Ardeshir R. Rastinehad
David N. Siegel
Editors

Peter A. Pinto
Bradford J. Wood
Associate Editors

Interventional Urology

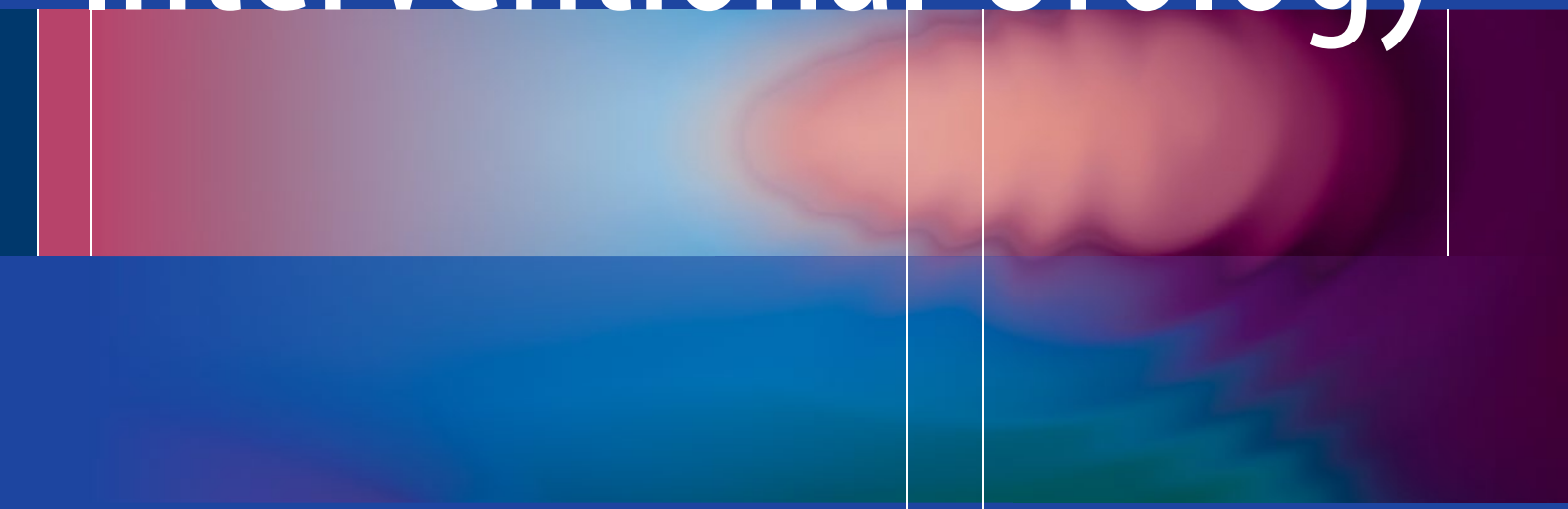

Springer

Ardeshir R. Rastinehad • David N. Siegel
Editors

Peter A. Pinto • Bradford J. Wood
Associate Editors

Interventional Urology

Springer

Editors
Ardeshir R. Rastinehad
Focal Therapy and Interventional
Urologic Oncology
Icahn School of Medicine at Mount Sinai
New York, NY
USA

David N. Siegel
Department of Radiology
Hofstra North Shore LIJ School of Medicine
New Hyde Park, NY
USA

Associate Editors
Peter A. Pinto
National Cancer Institute
National Institutes of Health
Bethesda, MD
USA

Bradford J. Wood
National Cancer Institute
National Institutes of Health
Bethesda, MD
USA

ISBN 978-3-319-23463-2 ISBN 978-3-319-23464-9 (eBook)
DOI 10.1007/978-3-319-23464-9

Library of Congress Control Number: 2015956038

Springer Cham Heidelberg New York Dordrecht London

Printed on acid-free paper

Springer International Publishing AG Switzerland is part of Springer Science+Business Media (www.springer.com)

Foreword

Major paradigm shifts in medicine are infrequent and germinal books that truly capture both context and content are rare. Simply stated, *Interventional Urology* is an outstanding work that presents the next era in the treatment of uropathology. The primary drivers of change in surgery are technical developments coupled with patient's desire for accurate treatment via least disruptive approaches. New imaging techniques not only provide accurate real-time non-invasive views inside of the human body but also provide associated physiologic data. Couple these advances with minimally invasive percutaneous techniques and we have arrived at the modern age of addressing urologic disease. The evolution of surgery from direct optically guided to image guided approaches is here to stay.

Drs. Siegel, Rastinehad, Pinto, and Wood have done a masterful job in assembling world-class experts to create a comprehensive opus reflecting contemporary approaches. Every present-day aspect of diagnostic and therapeutic urology is addressed. This textbook is both a state-of-the-art account of imaging in urology as well as linked achievable interventions. The chapters are well written, concise, and deliver practical applicable information for clinicians of various backgrounds.

The development of the field of interventional urology has required collaboration. Urologists, radiologists, interventionalists, and oncologists have to collaborate in non-traditional ways. The classic silo system will not permit optimal success in applying the lessons of this textbook. A breaking of barriers among specialties is required to facilitate the wisdom of these pages being applied to our patients. A quote by Henry Ford sums up the work that was needed to help advance both this text and what it represents: "Coming together is a beginning; keeping together is progress; working together is success." I laud the Editors for their successful work, both past and present, as well as anticipate their continued contributions to interventional sciences.

Hempstead, NY, USA — Louis R. Kavoussi, MD, MBA

Preface

The specialty of interventional urology is the manifestation of a true collaboration between disciplines. Given the pre-existing turf wars, cross-training a urology resident in all aspects of interventional radiology, not only those specific to urological diseases, was innovative as well as controversial. It was felt that this comprehensive and lengthy training was essential to the success of this program. Specifically, Dr. Rastinehad dedicated more than 6 months on the interventional radiology service during his residency, and following residency he spent 2 years training in both Urological Oncology and Interventional Radiology at the National Institute of Health in Bethesda, MD. We believe that what this has accomplished in terms of patient care and academics would not have been possible without this type of dedication. A debt of gratitude is owed to the others who, along with us, originally conceived of and facilitated the establishment of this program at the North Shore Long Island Jewish Health System; specifically, Dr. Louis Kavoussi, the Chairman of Urology, and the late Dr. Mitchell Goldman, who was the Chairman of Radiology at the time.

It is certainly not our expectation that any one individual can develop expertise in all the topics and techniques described in the following chapters, but rather this book should function as a road map and foundation for the development of this new area of medicine dedicated to the development of new minimally invasive methods for the management of urologic ailments. While it is unlikely that "Interventional Urology" will be formally established as a training platform for others in the near future, it is our hope that more people can receive similar collaborative training at institutions around the world and that this will serve as a model for other disciplines, where combining the traditional training in other specialties would be advantageous to patient care.

New York, NY, USA — Ardeshir R. Rastinehad, DO
New Hyde Park, NY, USA — David N. Siegel, MD

Contents

Contributors

Nnenaya Agochukwu, MD Department of Urology, Yale School of Medicine, New Haven, CT, USA

Noor Ahmad, MD Division of Interventional Radiology, Department of Radiology, New York Presbyterian Hospital/Weill Cornell Medical College, New York, NY, USA

Hashim Uddin Ahmed, PhD, FRCS(Urol), BM, BCh, BA Division of Surgery and Interventional Science, University College London, London, UK

Department of Urology, University College London Hospital NHS Foundation Trust, London, UK

Timothy Averch, MD Department of Urology, University of Pittsburgh School of Medicine, Pittsburgh, PA, USA

Gopal H. Badlani, MD Department of Urology, Wake Forest Baptist Medical Center, Winston-Salem, NC, USA

Ryan K. Berglund, MD Department of Urology, Cleveland Clinic Foundation, Cleveland, OH, USA

Shivank Bhatia, MD Department of Radiology, Jackson Memorial Hospital, University of Miami Hospital, Miami, FL, USA

Tiago Bilhim, MD, PhD Department of Radiology, Saint Louis Hospital and Nova Medical School, Faculdade de Ciências Médicas, Universidade Nova de Lisboa, Lisbon, Portugal

Vivian L. Bishay, MD Division of Interventional Radiology, Department of Radiology, Mount Sinai Hospital, New York, NY, USA

Jay T. Bishoff, MD, FACS Department of Urology, Intermountain Medical Center, Murray, UT, USA

Department of Surgery, University of Utah College of Medicine, Salt Lake City, UT, USA

Gennady Bratslavsky, MD Department of Urology, SUNY Upstate Medical University, Syracuse, NY, USA

Jeffrey A. Cadeddu, MD Department of Urology, University of Texas Southwestern Medical Center, Dallas, TX, USA

Drew M. Caplin, MD Department of Interventional and Diagnostic Radiology, Hofstra North Shore-LIJ School of Medicine, Hempstead, NY, USA

Mahmoud Chehab, MD Department of Urology, SUNY Upstate Medical University, Syracuse, NY, USA

Peter Choyke, MD Molecular Imaging Program, National Cancer Institute, National Institutes of Health, Bethesda, MD, USA

Brett Cox, MD Department of Radiation Medicine, North Shore LIJ Health System, Lake Success, NY, USA

John Michael DiBianco, MD Urologic Oncology Branch, National Cancer Institute, National Institutes of Health, Bethesda, MD, USA

Kefu Du, MD Division of Urology, University of Utah School of Medicine, Salt Lake City, UT, USA

Osama Elbuluk, BS Molecular Imaging Program, National Cancer Institute, National Institutes of Health, Bethesda, MD, USA

Ahmed El-Shater Bosaily, MSc, MBBCh Division of Surgery and Interventional science, University College London, London, UK

Division of Surgery and Interventional Science, Department of Urology, University College London Hospital NHS Foundation Trust, London, UK

Mark Emberton, MD, FRCS(Urol), FRCS, MBBS, BSc Division of Surgery and Interventional Sciences, University College London Hospital, London, UK

Aaron M. Fischman, MD Division of Interventional Radiology, Department of Radiology, Mount Sinai Hospital, New York, NY, USA

Barak Friedman, MD Department of Radiology, Hofstra North Shore LIJ School of Medicine, New Hyde Park, NY, USA

Pat F. Fulgham, MD Urology Clinics of North Texas, Dallas, TX, USA

Arvin K. George, MD Urologic Oncology Branch, National Cancer Institute, National Institutes of Health, Bethesda, MD, USA

Joseph D. Giardina, MD Vascular Interventional Radiology, Mallinckrodt Institute of Radiology, Washington University in St. Louis School of Medicine, St. Louis, Missouri, USA

Bruce R. Gilbert, MD, PhD Department of Urology, Hofstra North Shore LIJ School of Medicine, New Hyde Park, NY, USA

Stephanie Guillaumier, MD, MRCS, DipABRSM Division of Surgery and Interventional Science, University College London, London, UK

Marta E. Heilbrun, MD, MS Department of Radiology, University of Utah Health Sciences, Salt Lake City, UT, USA

John Hines, MD Department of Radiology, Hofstra North Shore LIJ School of Medicine, New Hyde Park, NY, USA

Jeremy Cash Horn, MD Division of Interventional Radiology, Department of Radiology, Mount Sinai Hospital, New York, NY, USA

Richard Ho Urologic Oncology Branch, The National Cancer Institute, National Institutes of Health, Bethesda, MD, USA

T. Idzenga, PhD, MSc Department of Urology, Amsterdam Medical Center, Amsterdam, The Netherlands

Liwei Jiang, MD Medical Research Scholars Program, National Institutes of Health, Bethesda, MD, USA

J. Stephen Jones, MD, MBA Department of Urology, Cleveland Clinic Foundation, Cleveland, OH, USA

Ilan Z. Kafka, MD Department of Urology, UPMC, Pittsburgh, PA, USA

Jay A. Karajgikar, MD Department of Radiology, Hofstra North Shore LIJ School of Medicine, New Hyde Park, NY, USA

Bruce R. Kava, MD Department of Urology, University of Miami Health System, Miami, FL, USA

No Kwak, MD Department of Radiology, North Shore LIJ Health System, New Hyde Park, NY, USA

Lucille Lee, MD Department of Radiation Medicine, North Shore LIJ Health System, Center for Advanced Medicine, Lake Success, NY, USA

Elliot Levy, MD Interventional Radiology Section, Radiology and Imaging Sciences Department, National Institutes of Health Clinical Center, Bethesda, MD, USA

Igor Lobko, MD Department of Radiology, North Shore LIJ Hofstra School of Medicine, New Hyde Park, NY, USA

Pamela Lombardi, MD Department of Radiology, Hofstra/North Shore LIJ School of Medicine, New Hyde Park, NY, USA

Robert A Lookstein, MD, FSIR Division of Interventional Radiology, Department of Radiology, Mount Sinai Hospital, New York, NY, USA

E. Justin Martinez, MD Department of Urology, University of Alabama at Birmingham, Birmingham, AL, USA

Jayadev R. Mettu, MBBS Department of Urology, Wake Forest School of Medicine, Winston-Salem, NC, USA

Adam R. Metwalli, MD Urologic Oncology Branch, National Cancer Institute, NIH, Bethesda, MD, USA

M. Mischi, PhD, MSc Department of Electrical Engineering, Eindhoven University of Technology, Eindhoven, The Netherlands

Anthony Mohabir, MD Department of Radiology, North Shore LIJ Hofstra School of Medicine, New Hyde Park, NY, USA

Prasoon P. Mohan, MD Department of Radiology, University of Miami Miller School of Medicine, Miami, FL, USA

Monica S.C. Morgan, MD Department of Urology, University of Texas Southwestern Medical Center, Dallas, TX, USA

Jeffrey W. Nix, MD Department of Urology, University of Alabama at Birmingham, Birmingham, AL, USA

Peter A. Pinto, MD Urologic Oncology Branch, The National Cancer Institute, National Institutes of Health, Bethesda, MD, USA

João Pisco, MD Interventional Radiology, Saint Louis Hospital and Faculdade Nova Medical School, de Ciências Médicas, Universidade Nova de Lisboa, Lisbon, Portugal

A.W. Postema, MD Department of Urology, Amsterdam Medical Center, Amsterdam, The Netherlands

Louis Potters, MD Department of Radiation Medicine, North Shore LIJ Health System, Center for Advanced Medicine, Lake Success, NY, USA

Soroush Rais-Bahrami, MD Departments of Urology and Radiology,
University of Alabama at Birmingham, Birmingham, AL, USA

Suraj Rambhia, MD Department of Radiology, North Shore-LIJ Medical Center,
New Hyde Park, NY, USA

Ardeshir R. Rastinehad, DO Departments of Urology and Radiology, Focal Therapy
and Interventional Urologic Oncology, Icahn School of Medicine at Mount Sinai,
New York, NY, USA

Gideon D. Richards, MD Arizona State Urological Institute, Gilbert, AZ, USA

Jean. J.M.C.H. De la Rosette, MD, PhD Department of Urology,
Amsterdam Medical Center, Amsterdam, The Netherlands

Marc H. Schiffman, MD Division of Interventional Radiology, Department of Radiology,
New York Presbyterian Hospital/Weill Cornell Medical College, New York, NY, USA

Brian Shuch, MD Department of Urology and Diagnostic Radiology,
Yale School of Medicine, New Haven, CT, USA

David N. Siegel, MD, FSIR Division of Vascular & Interventional Radiology,
Department of Radiology, Northshore-LIJ Health System, New Hyde Park, NY, USA

Thomas A. Sos, MD Division of Interventional Radiology, Department of Radiology,
New York Presbyterian Hospital/Weill Cornell Medical College, New York, NY, USA

Mario A. Taylor Howard University College of Medicine, Washington, DC, USA

E.J. Trabulsi, MD, FACS Department of Urology, Kimmel Cancer Center,
Thomas Jefferson University, Philadelphia, PA, USA

Hong Truong, MS, MD Department of Urology, Kimmel Cancer Center,
Thomas Jefferson University, Philadelphia, PA, USA

Baris Turkbey, MD Molecular Imaging Program, National Cancer Institute,
National Institutes of Health, Bethesda, MD, USA

Willemien van de Bos, PhD Department of Urology, Academic Medical Center,
Amsterdam, Netherlands

H. Wijkstra, PhD, MSc Department of Urology, Amsterdam Medical Center,
Amsterdam, The Netherlands

Department of Electrical Engineering, Eindhoven University of Technology,
Eindhoven, The Netherlands

Bradford J. Wood, MD NIH Center for Interventional Oncology,
National Institutes of Health, Bethesda, MD, USA

Interventional Radiology Section, National Institutes of Health, Bethesda, MD, USA

Vidhush K. Yarlagadda, MD Department of Urology,
University of Alabama at Birmingham, Birmingham, AL, USA

Part I

History

History of Interventional Urology

1

Ilan Z. Kafka and Timothy D. Averch

> Urology can be said to owe its existence as a specialty to the inventive genius of Thomas Edison and Wilhelm Conrad. Reed Nesbit, 1956 [1]

Interventional urology owes its roots to the breathtaking work of some of the greatest minds of the last two centuries. Physicist, chemist, engineers, and physicians, either alone or as part of a team, have come, sometimes by accident, to the discovery of technologies that have been responsible for shaping the world of medicine to the continuously evolving science that it is today.

X-Rays

X-rays have been used to noninvasively probe the human body since their discovery in Germany by physics professor Wilhelm Conrad Röntgen, on 8 November 1895 [2]. It took only 6 weeks for him to complete his first scientific research on this phenomenon, and on December 28, that same year, he submitted it to Würzburg's Physical-Medical Society journal with the title "*On a New Kind of Ray: A Preliminary Communication*" [3]. Within a few weeks of Röntgen's announcement, the use of X-rays spread fast and widely, and its first reported use under clinical conditions was by John Hall-Edwards in Birmingham, England, on 11 January 1896, when he used them to locate a needle stuck in the hand of an associate [4].

In 1896, a total of 49 books and brochures, and 1,044 scientific essays were written on the scientific aspects and possible applications of the newly discovered X-rays. A multitude of these publications dealt specifically with possible applications in medicine [5].

I.Z. Kafka, MD
Department of Urology, UPMC, Pittsburgh, PA, USA
e-mail: kafkaiz@upmc.edu

T.D. Averch, MD (✉)
Department of Urology, University of Pittsburgh
School of Medicine, Pittsburgh, PA, USA
e-mail: averchtd@upmc.edu

In the military, doctors started using X-rays to locate bullets in human flesh and photograph broken bones. X-rays were first used on casualties from the Abyssinian War of 1896, and the developing radiological technology rapidly progressed and was applied to military and general surgery [6] (Fig. 1.1).

X-Rays and Urology

Some of the earliest medical research involving X-rays involved the investigation and exposure of the biliary and renal tracts; John Macintyre, a Scottish doctor, imaged a kidney stone using X-rays. He was able to make a diagnosis of this stone only after five different patients suspected clinically of having renal calculus were photographed with negative results, but on the sixth attempt, in a patient previously known to have renal calculi, he was able to obtain a picture of an obliquely placed elongated deposit within the silhouette of the kidney. He confirmed the diagnosis in the subsequent operation and reported the case in the 11 July 1896 issue of *The Lancet* [8].

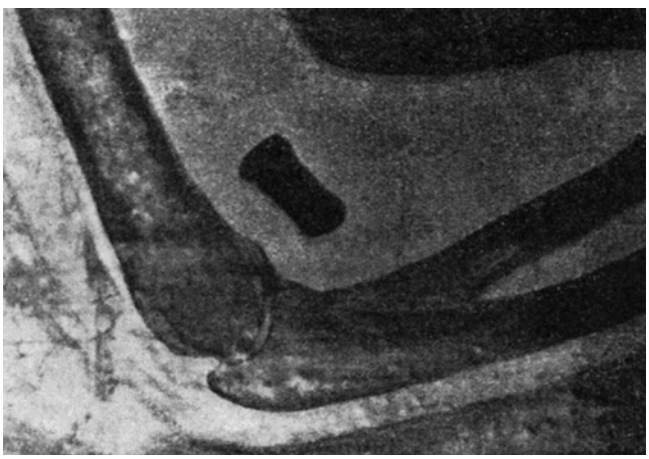

Fig. 1.1 A radiograph of a bullet in the elbow of a soldier 1897 (From Thomas [7] with permission)

A.R. Rastinehad, D.N. Siegel (eds.), *Interventional Urology*, DOI 10.1007/978-3-319-23464-9_1

Before 1895, the practice of urology was almost exclusively based on cystoscopy, itself a relatively new development, as well as on laboratory and physical examination. Röntgen's discovery changed the world of urology forever. Dr. Henry W. Cattell, Instructor of Anatomy at the University of Pennsylvania, in the United States, wrote, "… the manifold uses to which Roentgen's discovery may be applied in medicine are so obvious that it is even now questionable whether a surgeon would be morally justified in performing a certain type of operations without first having seen pictured by this rays the field of his work…" [9].

Adding Contrast

The first documented contrast study of the urinary tract was performed in 1897 by the French surgeon Théodore Tuffier. He passed a radiopaque catheter through the ureteral orifice in the bladder hereby outlining the course of the ureter [10].

The first ureteral catheters in use were radiolucent and mounted around a lead wire; this technique was subsequently replaced by making the ureteral catheters themselves radiopaque, by impregnating their walls with iron oxide. In 1914, the urologist Pasteau invented a catheter, which included a semiopaque centimeter scale, to localize stones precisely [11].

The search for better ways to visualize the urinary tract continued; next came the use of air as a contrast agent by Wittek, who succeeded in demonstrating cystolithiasis, thus giving birth to the air cystogram [12].

Replacing air as a contrast medium was the next step, and Wulff, in 1904, was the first to employ a radiopaque solution composed of 10 % bismuth subnitrate and starch, filling what was in all likelihood a huge diverticulum as well as the bladder itself [13].

This solution was soon replaced by a different liquid contrast agent containing a colloidal suspension of silver, giving better image quality, and, by injecting larger quantities of solution into the bladder, delineating the ureters and renal pelvises, giving birth to the first retrograde pyelograms [14]. The usefulness of this technique was quickly recognized but, unfortunately, so were the dangers associated with the silver-containing contrast agent. The search for safer materials began, and sodium iodide solutions, first described by Cameron in 1918, [15] became the contrast agents of choice for retrograde pyelography.

The next step in this evolutionary process was to eliminate the need to directly introduce the contrast agent into the urinary system. An indirect means might be faster and safer. The discovery of iodine as intravenous safe radio contrast agent was accidental. In the early 1920s, when iodine-containing compounds were used to treat syphilis, a team of workers at the Mayo Clinic, Earl Osborne (a syphilologist), Albert Scholl (a urologist), Charles Sutherland (a radiologist), and Leonard Rowntree (an internist), described the use of intravenous and oral sodium iodide to visualize the urinary tract. Osborne noticed that the urinary bladder was visible on radiographs of patients taking large doses of oral and intravenous sodium iodide for the treatment of syphilis. The visualization of the renal pelvis was poor, but the authors calibrated the dose of iodine against the urinary iodine concentration and the degree of bladder radioopacity, and thus they went on to perform the first successful clinical pyelogram. However, sodium iodine was far too toxic for clinical radiodiagnosis [16].

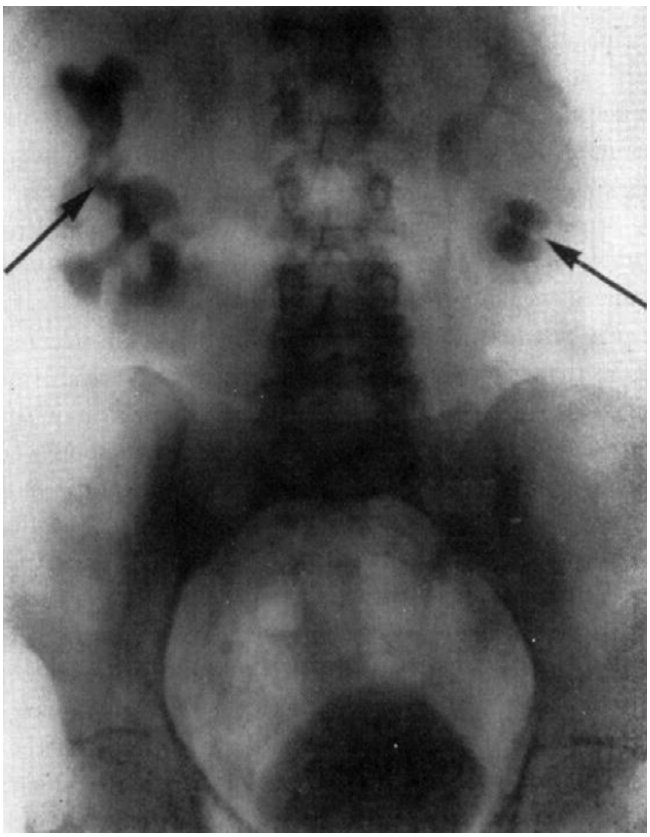

Fig. 1.2 Intravenous urography by Swick, (*arrows*) showing renal calyceal systems and bladder opacified (From Swick. [17] with permission)

A few years later, in 1928, Moses Swick, while an intern at Mount Sinai Hospital in the Department of Urology, traveled to Hamburg, Germany, on a research scholarship to work with Professor Leopold Lichtwitz in the treatment of human biliary infections with the use of iodinated drugs. It occurred to Swick that these drugs, containing iodine, might be of value in visualizing the renal tract by radiography [17]. He made several studies in laboratory animals. The initial studies were very encouraging, and, in order to gain access to the large number of patients, Swick transferred his work to Berlin to the urological department of Professor Alexander von Lichtenberg. Consequently, the first successful human intravenous urography (IVUs) was produced using a soluble iodinated pyridine compound solution (Uroselectan) [18–20] (Fig. 1.2).

In fact, iodinated pyridine compounds were routinely used to perform IV urography for the next 20 years.

Percutaneous Interventions

Percutaneous interventions on the urinary tract came much earlier than the discovery of X-rays. In 1686, Toler inserted cannulas through the perineum to relieve urinary retention from impassable urethral strictures.

Riolan used a suprapubic approach to the bladder, while Heisler, in 1770, left a suprapubic cannula in place permanently in men suffering from bladder outlet obstruction.

In the latter half of the tenth century, the Arab physician Serapion is said to have thrust a red-hot iron through the flank and extracted a renal calculus. A related story is the one of Hobson, British consul at Venice in the mid-seventeenth century, who, following surgery for renal colic, continued to pass urine through a fistula in his flank until one day his wife, using a small dagger for a probe, extracted a date-shaped calculus from the tract, after which the man had no more symptoms [21].

Thomas Hiller, a British pediatrician, in 1864, inserted a needle into the hydronephrotic kidney of a four-year-old boy and removed more than three liters of urine, repeating the procedure several times during the boy's life. [22] Several physicians took up this practice, but because of serious complications related to the procedure, especially peritonitis, caused it to be undertaken only under the most obliging circumstances, and it was eventually abandoned.

Interventional uroradiology as we know it today really began in 1939 when Archie Dean, an urologist at Memorial Hospital in New York, performed the first diagnostic percutaneous puncture of a renal mass. The return of clear fluid rather than blood made it possible to differentiate between cyst and neoplasms. However, in 1954, Wickbom, in Sweden [23], first utilized percutaneous puncture of the renal pelvis for antegrade pyelography and used this technique systematically in the diagnosis of outflow obstruction (Figs. 1.3 and 1.4).

A year later, Goodwin and Casey, from the University of California in Los Angeles, were the first to use percutaneous nephrostomy as a therapeutic approach for draining obstructed kidneys and gaining surgical access to the renal collecting system, leaving a length of polyethylene tubing for drainage [24].

Kurt Lindblom reported percutaneous puncture of both cystic and solid renal masses employing, for the first time, fluoroscopy for localization and contrast material instillation to outline the interior of the lesion [25].

The utility of upper urinary tract access was further expanded when Kapandji performed manometric studies of the renal pelvis following percutaneous puncture, serving as

Fig. 1.3 Antegrade pyelography (1954). After direct puncture of the left renal pelvis, contrast material demonstrates dilation of the pelvis and upper part of the ureter. There is complete obstruction of the ureter at the pelvic inlet (*arrow*) (From Wickbom. [23] with permission)

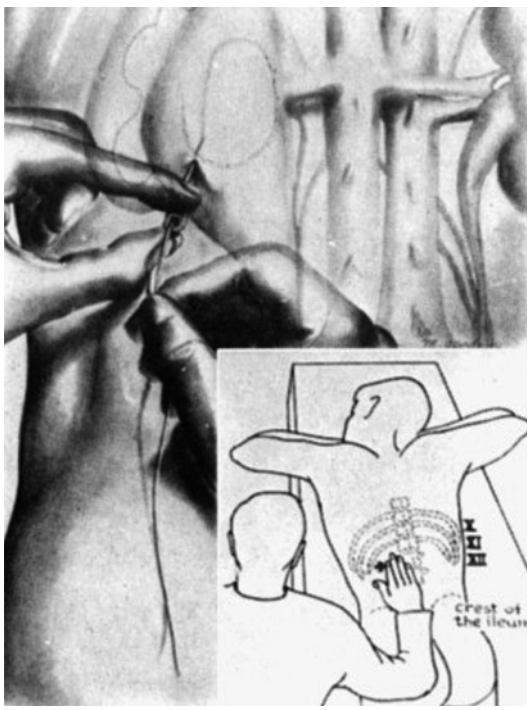

Fig. 1.4 Percutaneous trocar nephrostomy (1955): method and landmarks. Optimum puncture site is usually about five fingerbreadths lateral to midline and at a level where a 13th rib would be (From Wickbom. [23] with permission)

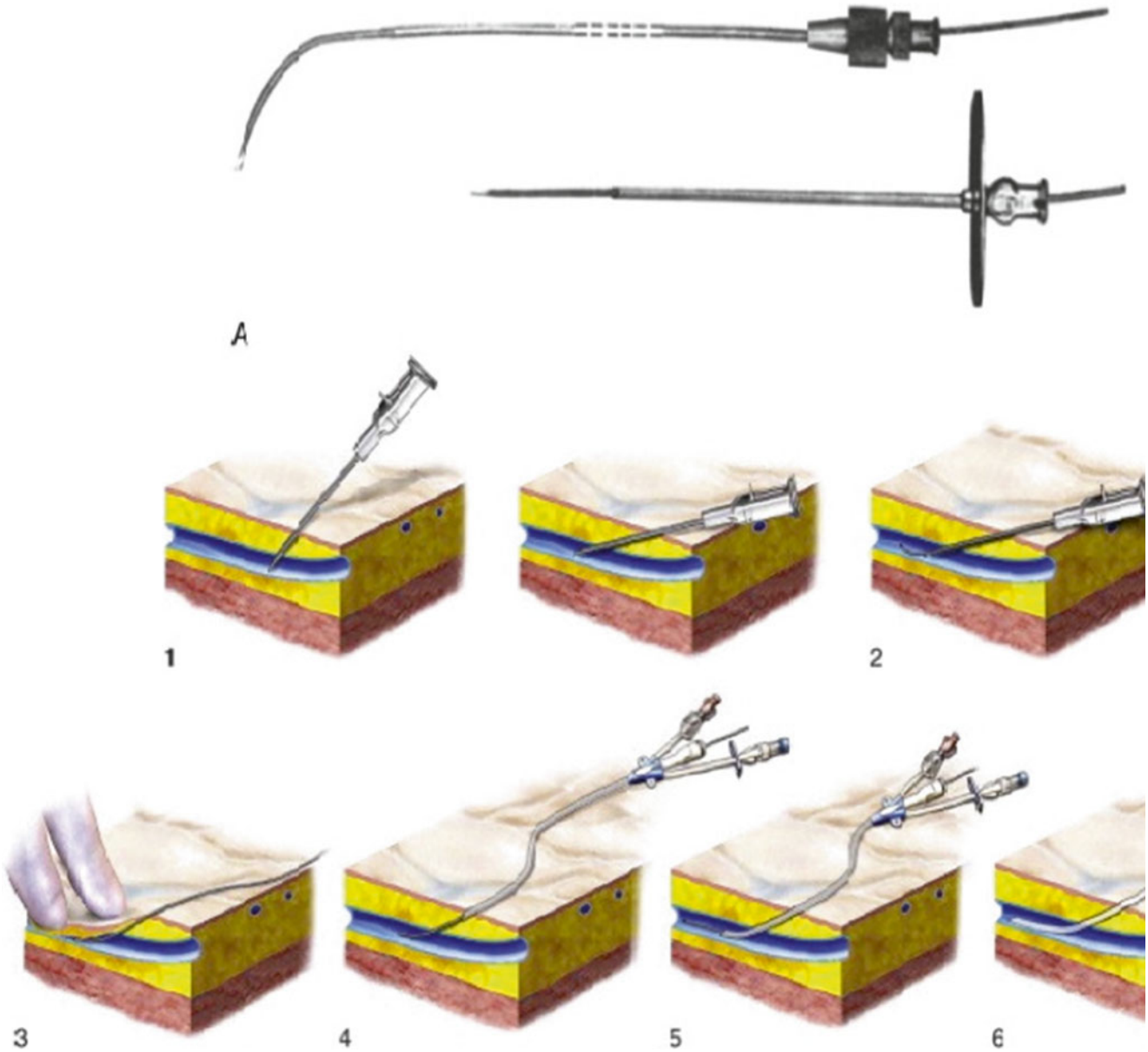

Fig. 1.5 Seldinger's technique (From Seldinger. [27] with permission). *1* Needle inserted into a vessel. *2* Wire guide inserted through the needle. 3. Needle comes out, leaving the wire guide in place 4–6 Catheter inserted over the wire and into the vessel

a base for the work of Robert Whitaker of Cambridge, England, who perfected the technique of pyeloureteral infusion with pressure-flow monitoring [26].

Goodwin and Casey's method was essentially blind, in order for them to insert a large trocar successfully, and it needed a markedly dilated renal collecting system. In 1965, Bartley and his associates in Göteborg in Sweden adapted Seldinger's method of vascular catheterization and implemented it in the placement of percutaneous nephrostomies (Fig. 1.5). They described the use of fluoroscopic localization, guide wires, and angiographic catheters, thereby giving rise to percutaneous nephrostomy (PCN) as it is similarly performed today [28].

In 1976, radiologist Ingmar Fernstrom and urologist Bengt Johansson published their benchmark work on removal of kidney and ureteral stones through a percutaneous approach and thus dramatically changed the practice of urology, giving birth to percutaneous nephrolithotomy (PCNL) [29].

Ultrasound

While at first renal biopsies were done "blindly," in 1956, Lusted and his associates introduced biopsy under fluoroscopic control. Subsequently, almost every imaging modality came to be utilized in localizing the kidney for biopsy [30].

Sonography-guided localization, which was first suggested by Berlyne in 1961, became the most popular method until this day [31].

The human application of ultrasound began in 1880 with the work of brothers Pierre and Jacques Curie, who discovered that when pressure is applied to certain crystals, they generate electric voltage [32].

In 1912, the sinking of the RMS Titanic sparked the public's desire for a device capable of echolocation. This was intensified 2 years later with the beginning of World War I, as submarine warfare became a vital part of war strategy. Canadian inventor Reginald Aubrey Fessenden—perhaps most famous for his work in pioneering radio broadcasting and developing the Niagara Falls power plant—volunteered during World War I to help create an acoustic-based system for echolocation. Within 3 months, he developed a high-power oscillator consisting of a 20 cm copper tube placed in a pattern of perpendicularly oriented magnetic fields that was capable of detecting an iceberg two miles away and being detected underwater by a receiver placed 50 miles away [33].

In 1936, German scientist Raimar Pohlman described an ultrasonic imaging method based on transmission via acoustic lenses, with conversion of the acoustic image into a visual entity. Two years later, Pohlman became the first to describe the use of ultrasound as a treatment modality when he observed its therapeutic effect when introduced into human tissues [34].

A few years later, in 1954, Dr. Joseph Holmes, a nephrologist, described the use of ultrasound to detect soft tissue structures with an ultrasonic "sonascope." This consisted of a large water bath in which the patient would sit, a sound generator mounted on the tub, and an oscilloscope which would display the images. The sonascope was capable of identifying a cirrhotic liver, renal cyst, and differentiating veins, arteries, and nerves in the neck [35] (Fig. 1.6).

In 1963, Japanese urologists Takahashi and Ouchi became the first to attempt ultrasonic examination of the prostate; however, the image quality that resulted was not interpretable and thus carried little medical utility. Progress was not made until in 1976 when Watanabe et al. demonstrated radial scanning that could adequately identify prostate and bladder pathology. Watanabe seated his patients on a chair with a hole cut in the center such that the transducer tube could be passed through the hole and into the rectum of the seated patient [36] (Fig. 1.7).

Astraldi, in 1925, was the first to carry out prostatic biopsies by the transrectal route. In 1930, Ferguson described a transperineal technique for aspirating prostatic tissue for cytological examination [37, 38]. Franzen first employed the currently used transrectal route for aspiration cytology in 1960.

The first to use real-time sonography for localizing the prostate for biopsy was done by Harada et al., while Ragde, Aldape, and Blasko adapted an automatic spring-loaded biopsy device (Biopty) for use in the prostate gland, making the procedure both more diagnostically accurate and less bothersome for patients [39–41].

Computed Tomography and Magnetic Resonance

Although the development of both CT and MRI technologies had almost a comparable timeline, each modality is based on a completely different principle. In 1917, Radon, a leading mathematician, found that formulas could be utilized to reconstruct a three-dimensional object from a very large number of two-dimensional projections of that object.

Based on Radon's principle and algorithms, in 1971, South African-born physicist Allan Cormack at Tufts University and English engineer Godfrey Hounsfield at EMI Laboratories in England, separately developed modern computer-based tomography scanning machines. In April 1972, at a seminar at the British Institute of Radiology, Hounsfield formally presented the results he had obtained using the EMI scanner, and descriptions of the device appeared in many publications, including The British Journal of Radiology.

Working independently, these two scientists later jointly received for their achievements the Nobel Prize for physiology or medicine in 1979.

In a very few months, by spring of 1974, computed tomography was recognized as a major improvement by radiologists throughout the world, and the name CT was soon known to politicians, government regulators, and the general public.

The first clinical CT scanners were installed between 1974 and 1976; they could only be used for the head and had a very slow scanning time of about 4.5 min for each image "slice." These were years of rapid growth in both use and media popularity of CT in neuroradiology practice. CT was not yet technically able to image other parts of the body with enough speed to be clinically useful [42–44].

Late in 1975, EMI, the original developer of the commercial CT scanner, announced a new CT unit, which successfully initiated a scanning technology with an eighteen-second scanning time that allowed practical imaging of the chest, abdomen, and pelvis. Body CT had arrived.

As advances in cross-sectional imaging allowed more expeditious acquisition of images, percutaneous biopsies started to be performed under CT guidance. The potent combination of accurate imaging with specific tissue diagnosis revolutionized the care of a wide range of patients and virtually ended the need for the exploratory laparotomy in specific cases [45, 46].

The drainage of intra-abdominal collections could be performed radiologically and percutaneously with

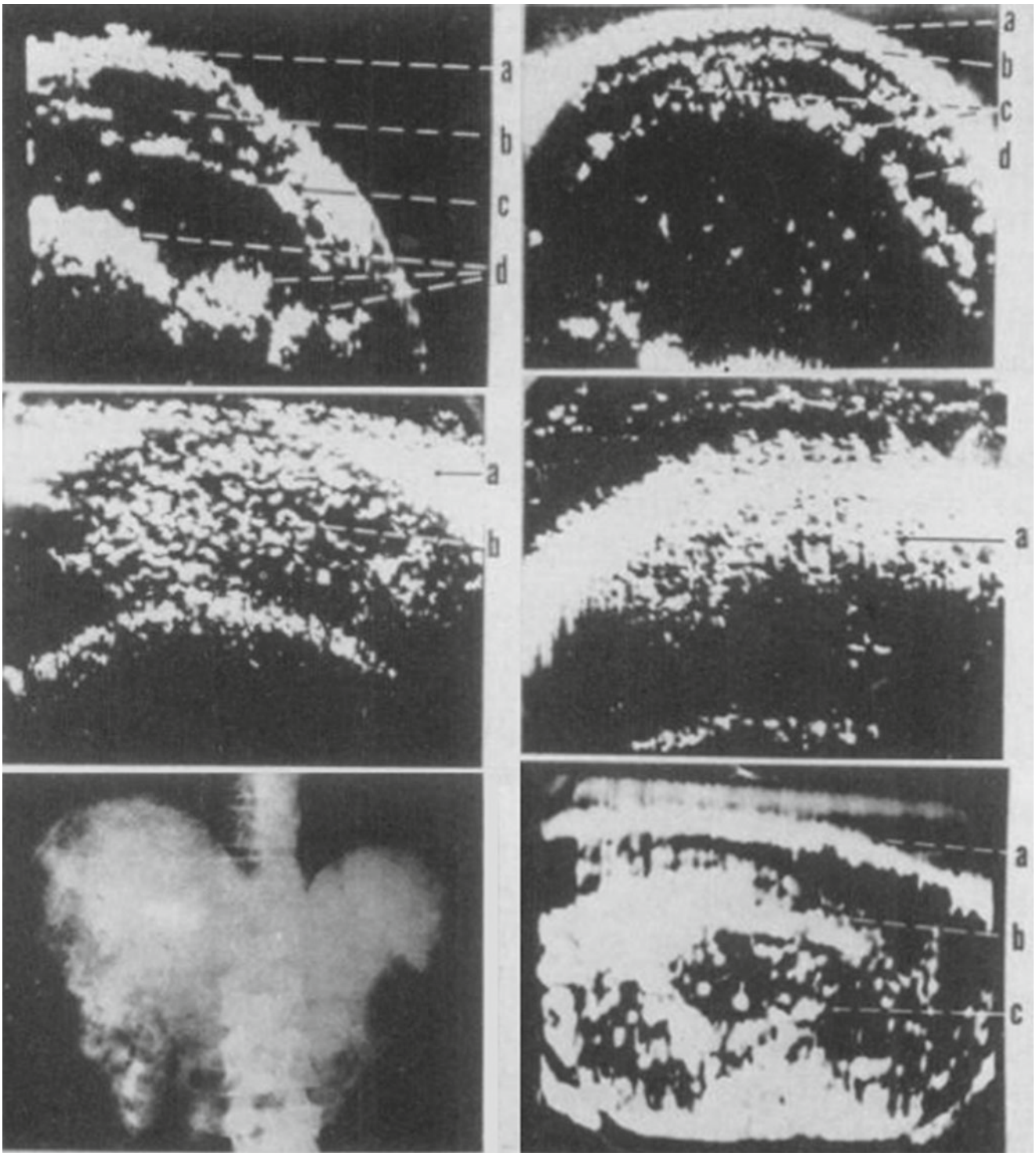

Fig. 1.6 Series of somagrams taken over the liver area of the abdomen. The first is of a normal individual as food is passing down the intestinal tract. (**a**) abdominal wall, (**b**, **c**) intestinal tract, (**d**) food. The second is of a patient with moderately advanced cirrhosis with hepatomegaly. (**a**, **b**) abdominal wall, **c** ascites, **d** enlarged liver (hepatomegaly). The third is of a patient with far-advanced cirrhosis where one can note the snowstorm-like appearance of the liver. (**a**) abdominal, (**b**) enlarged liver. The fourth is of a patient with diffuse miliary melanoma of the liver. (**a**) liver with diffuse melanoma. The fifth is a thorium dioxide radiograph of a patient with nodular metastases in the liver. The sixth picture is the corresponding somagram of the same patient. **a** abdominal wall, **b** liver, **c** liver metastasis. (From Holmes et al. [35] with permission)

small catheters instead of large surgical incisions. Percutaneous abscess drainage was soon to become a very popular standard of care with radiologists, surgeons, and patients [47].

The fast development of this imaging modality makes it an essential part of every medical discipline where the possibilities are endless: three-dimensional reconstruction, CT guided biopsies and tumor ablation, and presurgical planning.

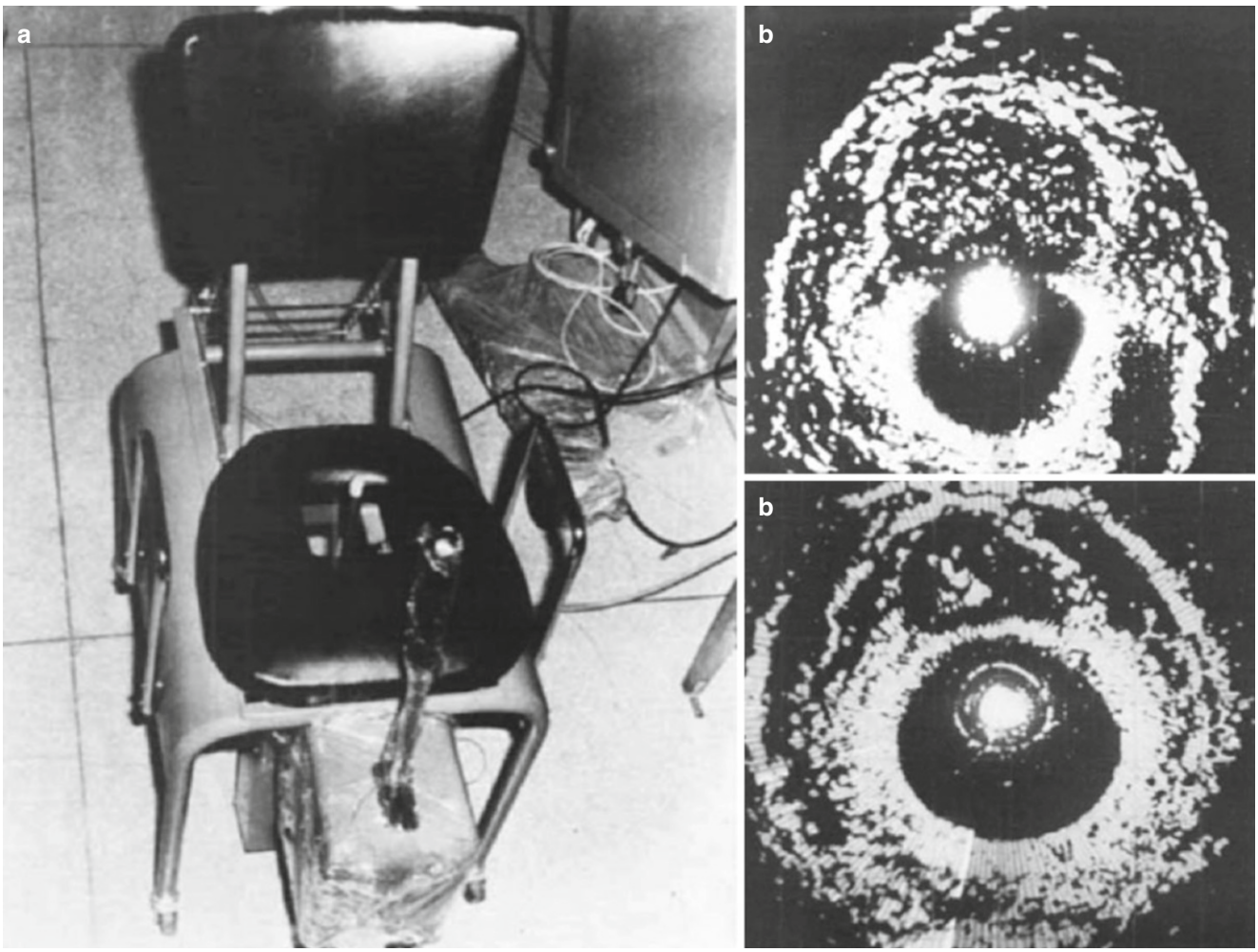

Fig. 1.7 (**a**) Watanabe's chair, (**b**) display of patient with BPH, (**c**) display of prostate with a nodule (From Watanabe et al. [36] Copyright 1957 John Wiley & Sons, Inc, with permission)

Magnetic resonance imaging (MRI) is one of the most important noninvasive imaging modalities in clinical diagnostics and research techniques that has evolved as a clinical modality over the past 30 years. The origins of MRI, or NMR (nuclear magnetic resonance), as it was termed in the past, however, can be traced back for over a century. Along the way, many scientists from diverse disciplines have made remarkable contributions that have brought the field to its present state. The success of MRI is in part brought about by the ability to image tissues with high resolutions in three dimensions, routinely down to 1 mm at clinical field strengths and smaller when necessary.

MRI was founded on the pioneering work of Felix Bloch and Edward Purcell in the field of NMR. These two independent groups discovered NMR almost simultaneously. Their investigations for which they received the Nobel Prize in 1952 focused on transition of magnetic nuclei and magnetic induction in bulk matter. In the same year, an American physicist by the name Herman Carr produced a one-dimensional MRI image [48].

In 1971, Raymond Damadian, a physician, at the Downstate Medical Center, State University of New York (SUNY), published a paper in *Science*, in which he reported that tumors and normal tissue can be distinguished in vivo by NMR [49].

In 1974, Paul C. Lauterbur, a chemist working in the United States, and Peter Mansfield, a physicist working in England, without knowledge of each other's work, described the use of magnetic field gradients for spatial localization of NMR signals. Their discoveries laid the foundation for Magnetic Resonance Imaging (MRI). For their contributions, Lauterbur and Mansfield were jointly awarded the 2003 Nobel Prize in Physiology or Medicine [50].

By 1975, Peter Mansfield and Andrew Maudsley proposed a line scan technique, which, in 1977, led to the first image of in vivo human anatomy of a cross section through a finger. In 1977, Hinshaw, Bottomley, and Holland succeeded with an image of the wrist [51] and Damadian et al. created a cross section of a human chest [52] More human thoracic and abdominal images followed, and, by 1978, Hugh Clow and Ian R. Young, working at the British company EMI,

reported the first transverse NMR image through a human head [53]. Two years later, William Moore and colleagues presented the first coronal and sagittal images through a human head.

The Fonar Corporation introduced the first commercial unit designed by Raymond Damadian, at the meeting of the American Roentgen Ray Society in June 1980.

In 1980, Edelstein et al. from Aberdeen University in Scotland demonstrated imaging of the body [54]. A single image could be acquired in approximately 5 min by this technique. By 1986, the imaging time was reduced to about 5 s without sacrificing significant image quality.

As larger-bore magnets were produced and surface coil technology was applied, MRI of the spine and larger body parts or regions became possible, and organs in the chest, abdomen, and pelvis became the subject of investigations. With the advent of surface coils, contrast agents, and faster pulse sequences, the scope of information that can be derived from MRI has greatly expanded.

Shortly after the introduction of clinical MRI, the first contrast-enhanced human MRI studies were reported in 1981 using ferric chloride as a contrast agent in the gastrointestinal tract. In 1984, Carr et al. first demonstrated the use of a gadolinium compound as a diagnostic intravascular MRI contrast agent [55] Currently, around one-quarter of all MRI examinations are performed with contrast agents.

The rapid and continuous development of imaging and interventional techniques is utterly important to urology and other surgical specialties as they try to focus on diagnosis and minimally invasive approaches to historically major surgical and diagnostic procedures.

The field of interventional urology owes its roots to these discoveries and their continuous technological evolution.

References

1. NESBIT RM. Radiology and its contribution to urology. Am J Roentgenol Radium Ther Nucl Med. 1956;75(5):995–6.
2. Alexi Assmus Beam line: the stanford linear accelerator center. Summer 1995;25(2):10–1.
3. Stanton A. Wilhelm Conrad röntgen on a New kind of rays: translation of a paper read before the würzburg physical and medical society, 1895. Nature. 1896;53(1369):274–6.
4. Meggitt G. Taming the rays: a history of radiation and protection. lulu.com; 2008. p. 3.
5. Glasser O. Wilhelm Conrad röntgen und die geschichte der röntgenstrahlen. Berlin: Springer; 1931.
6. Reynolds L. The history of the use of the roentgen ray in warfare. AJR. 1945;54:649–72.
7. Thomas AM. The first 50 years of military radiology 1895–1945. Eur J Radiol. 2007;63(2):214–9.
8. MacIntire J. Roentgen rays. Photography of the renal calculus; description of an adjustable modification in the focus tube. Lancet. 1896;148(3802):118.
9. Sherrow V. Medical imaging. New York: Benchmark Books; 2007. p. 25.
10. Tuffier T Sonde urétérale opaque. In: Duplay SE, Reclus P (1897–1899) Traité de chirurgie, Masson & Cie, Paris, 1897. p. 412–3.
11. Pasteau O. Les sondes urétérales opaques pour la radiographie. J Radiol Electrol. 1914;1:17–8.
12. Wittek A. Zur Technik der Röntgenphotographie (Lendenwirbel, Blasensteine). Förtsch Geb Rontgenstr. 1903–1904;7:26–7.
13. Wulff P. Verwendbarkeit der X•strahlen fur die diagnose der blasendifformitaten. Förtsch Rontgenstr. 1904;8:193–4.
14. Voelcker F, von Lichtenberg A. Pyelographie roentgenographie des nierenbeckens nach kollargolfulling. Munch Med Wschr. 1906;53:105–6.
15. Cameron DF. Aqueous solutions of potassium and sodium iodide as opaque mediums in roentgenography. JAMA. 1918;70:754–5.
16. Osborne ED, Sutherland CG, Scholl Jr AJ, et al. Roentgenography of urinary tract during the excretion of sodium iodide. JAMA. 1923;80:368–73.
17. Swick M. The discovery of intravenous urography: historical and development aspects of the urographic media and their role in other diagnostic and therapeutic areas. Bull NY Acad Med. 1966;42:128–51.
18. Swick M. Intravenous urography by means of the sodium salt of 5-iodo-2-pyridon-N-acetic acid. JAMA. 1930;95:1403–9.
19. Swick M. Intravenous urography by means of uroselectan. Am J Surg. 1930;8:405–11.
20. Von Lichtenberg A. Principles and new advances in excretory urography. Br J Urol. 1931;3:119–65.
21. Desnos EC. The history of urology up to the latter half of the nineteenth century. In: Murphy LJT, editor. The history of urology. Springfield: Charles, C. Thomas; 1972. p. 76.
22. Bloom DA, Morgan RJ, Scardino PL. Thomas hillier and percutaneous nephrostomy. Urology. 1989;33(4):346–50.
23. Wickbom I. Pyelography after direct puncture of the renal pelvis. Acta Radiolo. 1954;41(6):505–12. Ingmar Wickbom, Roentgen Department III, Sahlgrenska Sjukhuset, Gothenburg, Sweden.
24. Goodwin WE, Casey WC, Woolf W. Percutaneous trocar (needle) nephrostomy in hydronephrosis. J Am Med Assoc. 1955;157(11):891–4.
25. Lindblom K. Percutaneous puncture of renal cysts and tumors. Acta Radiol. 1946;27:66–72.
26. Whitaker RH. Diagnosis of obstruction in dilated ureters. Ann R Coll Surg Engl. 1973;53(3):153–66.
27. Seldinger SI. Catheter replacement of the needle in the percutaneous arteriography: a new technique. Acta Radiol. 1953;39:368–76.
28. Bertley O, Chidekel N, Radberg C. Percutaneous drainage of renal pelvis of uremia Due to obstructed urinary flow. Acta Chir Scand. 1965;129:443–6.
29. Fernstrom I, Johannsen B. Percutaneous pyelolithotomy: a New extraction technique. Scand J Urol Nephrol. 1988;10:257–9.
30. Lusted LB, Mortimer GE, Hoope J. Needle renal biopsy under image amplifier control. AJR. 1956;75:953–5.
31. Berlyne GM. UltraSonics in renal biopsy an Aid to determination of kidney position. Lancet. 1961;2:750–1.
32. Curie J, Curie P. Sur 'electricite polaire dans cristaux hemiedres a face inclinees. CR Acad Sci. 1880;91:383.
33. Seitz F. The cosmic inventor: Reginald Aubrey Fessenden (1866–1932). Am Philos Soc. 1999;89:41–6.
34. Jagannathan J, et al. High-intensity focused ultrasound surgery of the brain: part 1—a historical perspective with modern applications. Neurosurgery. 2009;64(2):201–10.
35. Holmes JH, et al. The ultrasonic visualization of soft tissue structures in the human body. Trans Am Clin Climatol Assoc. 1954;66:208–25.
36. Watanabe H, et al. Development and application of new equipment for transrectal ultrasonography. J Clin Ultrasound. 1974;2(2):91–8.

37. Astraltli A. Biopsie des tumeurs de la prostate. Arch Urol elin Necker. 1925;5:151.
38. Ferguson R. Cytology of prostatic specimens obtained by perineal aspiration biopsy. Am J Surg. 1925;9:507–11.
39. Franzen S, Giertz G, Zajicek J. Cytological diagnosis of prostatic tumors by transrectal aspiration biopsy. A preliminary report. Br J Urol. 1960;32:193.
40. Harada K, Igari D, Tanahashi Y. Gray scale transrectal ultransonography of the prostate. J Clin Ultrasound. 1979;7(1):45–9
41. Ragde H, Aldape HC, Blasko JC. Biopty: an automatic needle biopsy device—its use with an 18 gauge Tru-cut needle (bioptycut) in 174 consecutive prostate core biopsies. Endosonographique. 1987;3–5.
42. Ambrose J. Computerized transverse axial scanning (tomography)—part 2. Clinical applications. Br J Radiol. 1973;46: 1023–47.
43. Cormack AM. Reconstruction of densities from their projections, with applications in radiological physics. Phys Med Biol. 1973;18(2):195–207.
44. Hounsfield GN. Computerized transverse axial scanning (tomography)—part 1. Description of the system. Br J Radiol. 1973;46: 1016–22.
45. Isler RJ, Ferrucci Jr JT, Wittenberg J, et al. Tissue core biopsy of abdominal tumors with a 22 gauge cutting needle. AJR Am J Roentgenol. 1981;136:725–8.
46. Mueller PR, Wittenberg J, Ferrucci Jr JT. Fine needle aspiration biopsy of abdominal masses. Semin Roentgenol. 1981;16:52–61.
47. VanSonnenberg E, Ferrucci Jr JT, Mueller PR, Wittenberg J, Simone JF, Malt RA. Percutaneous radiographically guided catheter drainage of abdominal abscesses. JAMA. 1982;247:190–2.
48. Carr H, Free precession techniques in nuclear magnetic resonance, PhD thesis, Harvard University; 1952.
49. Damadian R. Tumor detection by nuclear magnetic resonance. Science. 1971;171(3976):1151–3.
50. Lautetbur PC. Image formation induced by local interactions: [examples employing nuclear magnetic resonance. Nature. 1973;242:190–1.
51. Hinshaw WS, Bottomley PA, Holland GN. Radiographic thinsection image of the human wrist by nuclear magnetic resonance. Nature. 1977;270:722–3.
52. Damadian R, Goldsmith M, Minkoff L. NMR in cancer: XVI. FONAR image of the live human body. Physiol Chem Phys. 1977;9:97–100.
53. Clow H, Young IR. Britain's brains produce first NMR scans. New Sci. 1978;80:588.
54. Edelstein WA, Hutchison JM, Johnson G, Redpath T. Spin warp NMR imaging and applications to human whole-body imaging. Phys Med Biol. 1980;25:751–6.
55. Carr DH, Brown J, Bydder GM, et al. Intravenous chelated gadolinium as a contrast agent in NMR imaging of cerebral tumours. Lancet. 1984;1(8375):484–6.

Imaging the Urinary Tract: Fundamentals of Ultrasound, Computed Tomography, and Magnetic Resonance Imaging

2

John Hines, Jay A. Karajgikar, Joseph D. Giardina, and Barak Friedman

Principles of Ultrasound

Ultrasound is a type of mechanical energy that produces vibrations as it traverses any given medium. These vibrations create varying areas of pressure. The alternations between areas of high and low pressure are measurable against time and termed the *wave frequency* with Hertz used as the unit of measurement. By convention, it is generally accepted that the speed of sound propagation is 1540 m/s, which represents the average speed at which sound travels in soft tissues. The unit of time of a cycle of the wave is called the *period*, and the distance between wave crests is termed *wavelength* [1–3].

Ultrasound in Tissue

In order to compose an ultrasound image, pulses of sound are sent into the target tissue. These pulses are very short, approximately 1 ms or less, and as they move through tissue, echo signals are produced and reflected back toward the source, termed a *transducer*. Different tissues interact differently with these sound waves. They are reflected, refracted, and/or absorbed by the tissue structures and then captured by the transducer, which then formulates an image. It is these differences in tissue interaction, the *echotexture*, that allow for anatomical imaging to be formulated. Structures that appear bright are termed *hyperechoic*, while structures that are dark are referred to as *hypoechoic* [1–3].

The amplitude of the echo signal of imaged tissues is dependent on the number of scatterers per unit volume, the acoustic impedance, the sizes of the scatterers, and the ultrasonic frequency. The term *hyperechoic* refers to tissue which yields higher scatter amplitude, and hypoechoic refers to tissue with lower scatter amplitude. Thus both are used to describe the scatter characteristics of tissue relative to the average background signal. Areas that appear hyperechoic are generally composed of greater numbers of scatterers and possess larger acoustic impedance differences as well as overall larger-sized scatterers. Acoustic scattering from nonspecular (diffuse) reflectors increases with frequency. Specular reflectors are largely independent of frequency. It is therefore usually possible to enhance the scattered echo signals by using higher ultrasound frequencies [1–3]:

Bright (hyperechoic): renal sinus fat and renal calculi
Dark (hypoechoic): renal pyramids
Uniform, midlevel echogenicity: renal cortex
Notable reflective surfaces: anterior surface of the kidney [3].

Smooth surfaces of tissue reflect sound waves in a rather predictable way, and when the angle of reflection is perpendicular to the tissue surface, a large proportion of the sound is reflected back to the transducer. This angle of reflection, termed the angle of incidence, is a key component of ultrasound imaging. When sound waves reflect off an irregular surface, a smaller proportion of the waves are reflected back to the transducer and often the strength of these waves is diminished. Thus these surfaces are termed diffuse (nonspecular) reflectors [1, 3, 4].

Impedance

Impedance is another factor in determining the strength of sound reflected by tissue surfaces or echoes. It describes differences in tissue density (denser and stiffer tissues having

J. Hines, MD (✉) • J.A. Karajgikar, MD • B. Friedman, MD
Department of Radiology, Hofstra North Shore LIJ School of Medicine, New Hyde Park, NY 11040, USA
e-mail: Jhines@nshs.edu; jaykarajgikar@nshs.edu; BFriedma@nshs.edu

J.D. Giardina, MD
Vascular Interventional Radiology, Mallinckrodt Institute of Radiology, Washington University in St. Louis School of Medicine, St. Louis, Missouri, USA
e-mail: giar55@gmail.com

A.R. Rastinehad, D.N. Siegel (eds.), *Interventional Urology*, DOI 10.1007/978-3-319-23464-9_2

greater impedance compared with those less dense tissues) and how sound is reflected differently at tissue interfaces. For example, the lung is much less dense than the liver, and thus, the liver has a higher impedance to sound waves than the lung. Sound is reflected differently at different tissue interfaces, and the sound that is not reflected is transmitted or absorbed. The echo strength is dependent on the amount of reflection and thus dependent on tissue interfaces with regard to their differences in impedance. Soft tissue adjacent to air-filled lungs provides a large difference in acoustic impedance. The sound waves incident on the soft tissue of the lungs are almost entirely reflected and appear very hyperechoic. In fact, so much of the beam is reflected that structures posterior to the air are not visualized. When adjacent tissues have similar acoustic impedances, only minor reflections of the incident energy will occur. Acoustic impedance gives rise to differences in transmission and reflection of ultrasound energy, which provides the foundation of pulse echo imaging [1, 3, 4].

Impedance values of biological tissue (unit = Z (rayl)):

Air-muscle—0.98
Fat-muscle—0.015
Liver-muscle—0.0003
Bone-muscle—0.41
Liver-kidney—0.00003 [3, 4]

Refraction

Similar to the behavior of waves of light energy, sound is refracted when it enters an interface at an angle which is non-perpendicular and when the densities of the mediums on both sides of the interface differ. The latter alters the speed at which the wave propagates and helps to create a change in the angle of propagation of the sound wave, termed the *refraction angle*. This angle increases with greater differences in tissue density and yields larger differences in the wave's speed as it travels through the two mediums. Refraction at interfaces between different tissues thus bends the sound wave beam and its reflected echoes. This is seen routinely at soft tissue-fluid as well as fat-muscle interfaces. A clinical example is demonstrated as *edge* (*refraction*) *artifact* encountered in the imaging of a simple cyst which demonstrates posterior acoustic enhancement with shadowing at the lateral edges (Fig. 2.1) [2–5].

Attenuation

Attenuation refers to decreases in sound beam strength as it travels through tissue. Frequency is a determining factor of attenuation, and the higher the frequency of the sound wave, the greater the attenuation. The penetrating power of sound is therefore limited at higher frequencies. Tissue density is another determining factor of attenuation. Reflections and refractions are some of the reasons for this phenomenon. Another is the conversion of the sound energy to heat.

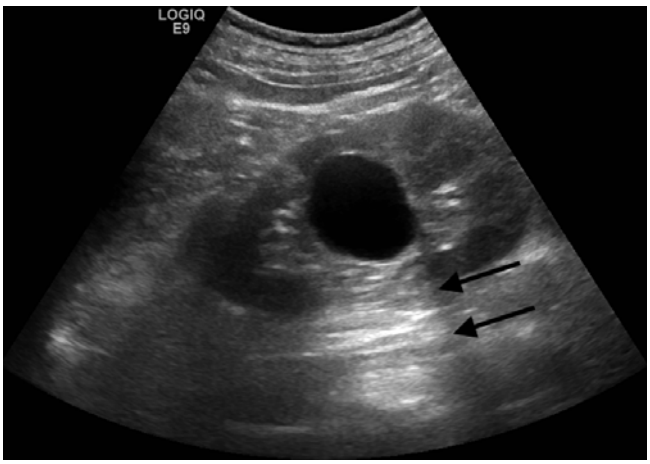

Fig. 2.1 Renal cyst. Sagittal sonographic image of the left kidney demonstrates a well-circumscribed, anechoic, thinly walled lesion with posterior acoustic enhancement (*black arrows*), a finding which is often used to definitively characterize a lesion as cystic. At the lateral edges of the enhanced echoes, there is a faint shadow representing *edge* (*refraction artifact*) which results from bending of the sound wave from its expected path

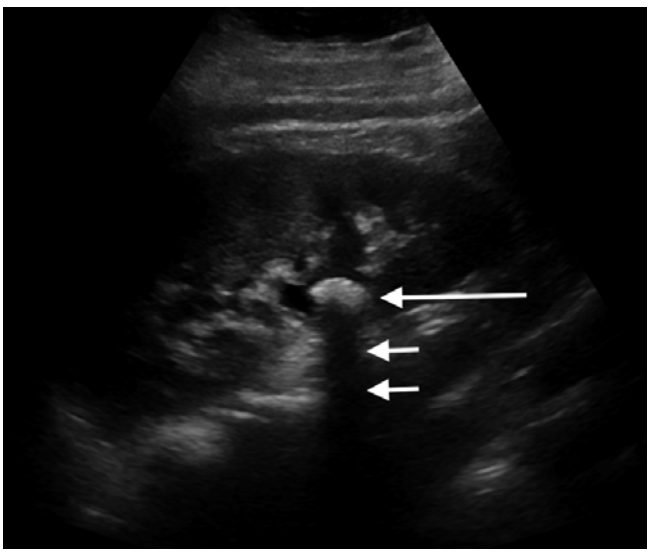

Fig. 2.2 Renal calculus. Sagittal sonographic image of the right kidney demonstrates a calcified renal stone (*large white arrow*) with the classic appearance of an echogenic lesion causing posterior acoustic shadowing (*small white arrows*)

Acoustic shadowing is an example of attenuation differences in action. The term refers to lost through transmission of the sound beam. An example is seen in renal calculi which both absorb and reflect the sound beam, resulting in acoustic shadows posterior to the calculus, due to marked attenuation of the sound beam (Fig. 2.2). In contrast, posterior acoustic enhancement is a phenomenon produced when attenuation of a structure is less than that of surrounding tissue, resulting in greater amplitude of the beam posterior to the structure.

This is falsely displayed as an increase in echogenicity of the tissue posterior to the weakly attenuating structure. In clinical practice, this is commonly seen in the setting of a simple renal cyst (Fig. 2.1) or any other fluid-containing structure, such as the urinary bladder [2–5]:

Attenuation coefficients for selected tissues at 1 MHz
Material attenuation coefficient (dB/cm)
Water 0.0002
Soft tissue 0.3–0.8
Fat 0.5–1.8
Bone 13–26
Air 40 [4]

Pulse-Echo Imaging Modes

Amplitude Mode (A-Mode)

A-mode is no longer utilized in the clinical setting. A short ultrasound pulse propagates into tissue and creates an echo, and this echo is received, amplified, and displayed as amplitude vs. distance [2, 3, 5].

Motion Mode (M-Mode)

Echo signal amplitudes are modulated according to levels of brightness and are displayed in a variety of shades of gray. The ultrasound beam is fixed at one position yet is observed in real time while scanning, allowing for the imaging of the motion of moving structures. A clinical example of M-mode use is in echocardiography, in which real-time evaluation of myocardial motion is performed [2, 3, 5].

Brightness Mode (B-Mode)

This mode produces a 2D image via modulating the echo signal amplitudes to various levels of brightness. This allows echoes to be displayed as lines with the imaged composed of "point-by-point variations in brightness level aka various shades of gray." In practice, structures that are more sound wave reflective appear more hyperechoic than those that are less reflective. Furthermore, the pulse line can be swept across tissue planes and produce cross-sectional imaging in the 2D plane [2, 3, 5].

Transducers

The sound beam is created by the transducer which makes use of a phenomenon called the piezoelectric effect to convert electrical energy into vibrational energy. This is accomplished by alternating electric current to the transducers crystal which causes expansion and contraction. Thus this produces vibrations and therefore sound waves. In addition to producing the sound beam, the transducer is also capable of receiving the reflected sound waves, referred to as echoes. Upon receipt, the crystal vibrates at the received echoes' frequency and converts that frequency into electrical current which is processed and converted into the ultrasound image [2, 3, 5].

Array technology allows for electronic focusing to a variety of depths with multiple focal zones from the same transducer. These capabilities yield better image quality/resolution/sharpness. Older transducers, in contrast, generated the sound beam with one element, causing the beam to converge at a focal zone, proximal to which was termed the *near field* and distal to which was termed the *far field*, where the sound waves diverged. The depth of the focal zone was determined by the characteristics of this single element [2, 3, 5].

Linear Array

Linear array transducers are composed of parallel scan lines which are perpendicular to the surface of the transducer. These utilize higher frequencies and provide high-resolution imaging of fascial planes that lay parallel to the skin surface. Linear arrays are most commonly used for imaging superficial and small parts and for musculoskeletal and vascular imaging where there is a need for highly detailed images [3, 5].

Curvilinear Array

These transducers are composed of crystals aligned in a convex arrangement, and thus, the scan lines diverge as the sound beam travels deeper into the scanned tissue. They typically utilize lower frequencies, allowing for deeper tissue penetration compared to linear high-frequency imaging. Interpolation is often required to fill in the gaps in the image produced by the diverging sound waves. The advantage of the curved array is that it produces a larger field of view for deeper tissue structures. It is often used for abdominal and obstetric imaging [3, 5].

Phased Array

These specialized transducers are composed of many more, often approximately 100, elements. They produce pulsed beams for each scan line, and thus, the beam can be steered in a different fashion than, for example, the linear array. The transducer also has a rather narrow face and the end result of

its image formation is one with a large lateral view of deeper tissue [3, 5].

A variety of modified transducer arrays are available for specialized imaging tasks by taking advantage of different focus strategies for specific anatomic regions. For example, endorectal probes are utilized for transrectal prostate biopsy, and endoesophageal probes are utilized for transesophageal echocardiography.

Types of Transducer Probes

Endorectal
Endoesophageal
Endovaginal
Endourethral
Endovascular [3, 5]

Image Resolution

Lateral Resolution

Lateral resolution refers to the minimum measurable separation of objects that lay parallel to the face of the transducer. Objects appear separated if their separation is in fact greater than the width of the sound beam. Higher-frequency transducers produce a longer near field, which is the narrowest portion of the beam. The near field is the region at which lateral resolution is the greatest. Higher-frequency transducers produce a narrow beam width, which decreases the amount of beam dispersion, which occurs in the far field. This thus allows for better lateral resolution [3, 5]. Focusing the beam further enhances lateral resolution by narrowing the beam width at a selected area of tissue.

Axial Resolution

Axial resolution refers to the minimum measurable separation of objects along the axis of the beam. The beam pulse length is the principal factor. A pulse length longer than twice the object separation will not generate resolvable echoes. Two basic techniques in which short pulses are generated are through broad bandwidth pulses and high-frequency beams. Therefore, broad bandwidth and high-frequency transducers are capable of producing short pulses and thus higher-resolution imaging [3, 5].

Elevational Resolution

Elevational resolution refers to slice thickness and is the same entity as lateral resolution but refers to the plane orthogonal to the image plane. The major contributing factor is beam width in this plane. Electronic control of transducers allows for other features that optimize image resolution. In modern ultrasound machines, the majority of these are automated upon selection of specific imaging protocols. These have the potential to improve image quality through the focus and filter of an echo upon its return to the transducer and help to enhance lateral resolution of the image by decreasing noise from the outer edges of the beam. Examples include:

Receive focus: received echoes from single pulse are electronically focused to account for location in the beam.
Dynamic aperture: aperture or sensitive area of the transducer is modified on reception to help eliminate side lobe or scattered signals from the edge of the beam.
Apodization: the sensitivity of individual transducer elements in an array is varied to help define the beam on transmit or reception [3, 5].

Transmit Power Control

The modulation of transmit power affects the pulse amplitude from the transducer. Stronger, greater amplitude pulses produce stronger returned echoes. This improves signal to noise ratio and increases the maximum depth of imaging. There is a potential risk of adverse bioeffects with prolonged exposure to high transmit power pulses in diagnostic ultrasonography; however, there are no reported confirmed cases. Nevertheless, "prudent and conservative" use of diagnostic sonography under the ALARA principle encourages the use of the lowest possible transmit power to produce diagnostic quality images [1, 5].

Frequency Selection

The ultrasound transducer has a broad frequency bandwidth which corresponds to the emitted pulse. The "nominal" frequency of a transducer is usually the center frequency of the bandwidth. As the frequency is increased, spatial resolution improves; however, the penetration of the beam decreases. Conversely, lower frequencies allow for greater penetration albeit with poorer spatial resolution. Thus the selection of transducer frequency is dependent on the clinical situation and requires a balance between the desired depth of penetration and spatial resolution [1, 5].

Doppler

Doppler ultrasound allows for clinical assessment of the presence or absence of flow within a vessel or tissue and can give information on blood flow direction, pulsatility,

and velocity. Doppler ultrasound processes frequencies of returning echoes from the imaged tissue to compose an image, as opposed to gray-scale sonography that utilizes the amplitude of the returning echoes. The foundation of Doppler ultrasound is the so-called Doppler effect. This refers to the change in frequency of a sound wave that occurs due to the relative motion of either the source, the observer (transducer), or the tissue medium. A commonly used example is the way in which the sound pitch of a moving train's whistle changes as it passes an observer. Clinically, blood cells act as moving reflectors of the ultrasound beam, and thus, blood flowing toward the transducer reflects the beam at a relatively higher frequency than blood flowing away [1, 6, 7]. The same transducers utilized for gray-scale imaging are capable of Doppler imaging. Three major Doppler imaging techniques are utilized clinically and discussed in the following sections.

Pulsed Wave (Spectral) Doppler

This is based on the velocity of a selected sample volume of blood flow and generates a waveform based upon directionality of flow: Flow toward the transducer is plotted above the baseline, and flow away from the transducer is plotted below. The velocity of the blood flow is demonstrated as the wave amplitude, and the characteristics of the waveform shape allow clinical inferences to be made about the type of flow. Spectral Doppler allows for the analysis of multiple different vessels at different depths and provides a high range of resolution and specificity due to the sampling component [1, 5, 7].

Color Doppler

This is a 2D depiction of blood flow which is superimposed on a gray-scale image of the tissue imaged. Relative direction of flow is depicted and based upon the average velocity of the blood. By convention, red typically is used for blood flowing toward the transducer and blue used for blood flowing away, although these settings can be easily switched. Color Doppler allows for the characterization of the quality of the blood flow, for example, turbulent vs. laminar flow. The intensity of the color display also varies as a depiction of the flow intensity (i.e., lighter shades depicting higher-frequency shifts). Objects that are stationary are depicted in gray scale only. Color Doppler therefore yields important clinical information about the overall flow to the imaged region and can help one choose where to place a spectral Doppler sampling window. The advantage of color Doppler is that it is a relatively easy technique for confirming the presence or absence of flow and visualizing small vessels, such as in the testes. Limitations include lower spatial resolution vs. gray-scale imaging as well as its relative insensitivity to slow flow or flow in small-caliber vessels for which spectral Doppler is superior [1, 5, 7].

Power Doppler

Power Doppler provides a display of the strength of the Doppler signal in contrast to the average shift of frequency. The color and shade displayed on the image are dependent upon the volume of the flowing blood. The primary advantage of power Doppler is a high sensitivity for detecting flowing blood. It is especially useful for the detection of slow flow or blood within very small vessels. Power Doppler is not susceptible to aliasing, in contrast to spectral and color Doppler. Unlike color and spectral Doppler, there is no reliance upon the Doppler angle, and thus, images of vessels in the perpendicular plane are possible to obtain. The disadvantages are that power Doppler does not provide any information about the directionality or velocity of blood flow. Power Doppler is vulnerable to motion, either of the transducer or of the tissue which manifests as an intense flash of color on the monitor, termed *flash artifact* [1, 5, 7].

Ultrasound Applications for the Genitourinary System

Normal Renal Anatomy

The normal ultrasound appearance of the kidneys is one of paired retroperitoneal structures. Each kidney is enclosed by a dense capsule, which itself is then surrounded by perinephric fat enclosed in Gerota's fascia. Sonographically, the kidney is conventionally imaged in the transverse and sagittal planes. Normal renal parenchyma in the longitudinal image is homogeneous with the normal cortex appearing more hyperechoic relative to the medulla. The medullary pyramids are thus hypoechoic in appearance relative to the cortex. They abut the renal sinus fat, which appears relatively hyperechoic. The center of the longitudinally displayed kidney is a complex of rather dense-appearing structures which include the peripelvic fat, renal vessels, lymphatic vessels, and normal collecting system. The normal vascular pedicle and the small intrarenal vasculature and renal perfusion are often well visualized and interrogated with the use of Doppler imaging to demonstrate the quality and quantity of flow [2, 8].

Renal Masses

Simple cysts (Fig. 2.1) are the most common benign adult renal mass, and ultrasound has proven an effective tool in evaluating renal cysts, allowing for differentiation from other cystic and solid renal masses. Simple cysts are commonly round, demonstrate a clearly defined thin wall, and lack internal echoes. The latter of these produce a characteristic feature known as *posterior acoustic enhancement*. The presence of internal septations, nodular components, internal echoes, and calcifications are more worrisome features.

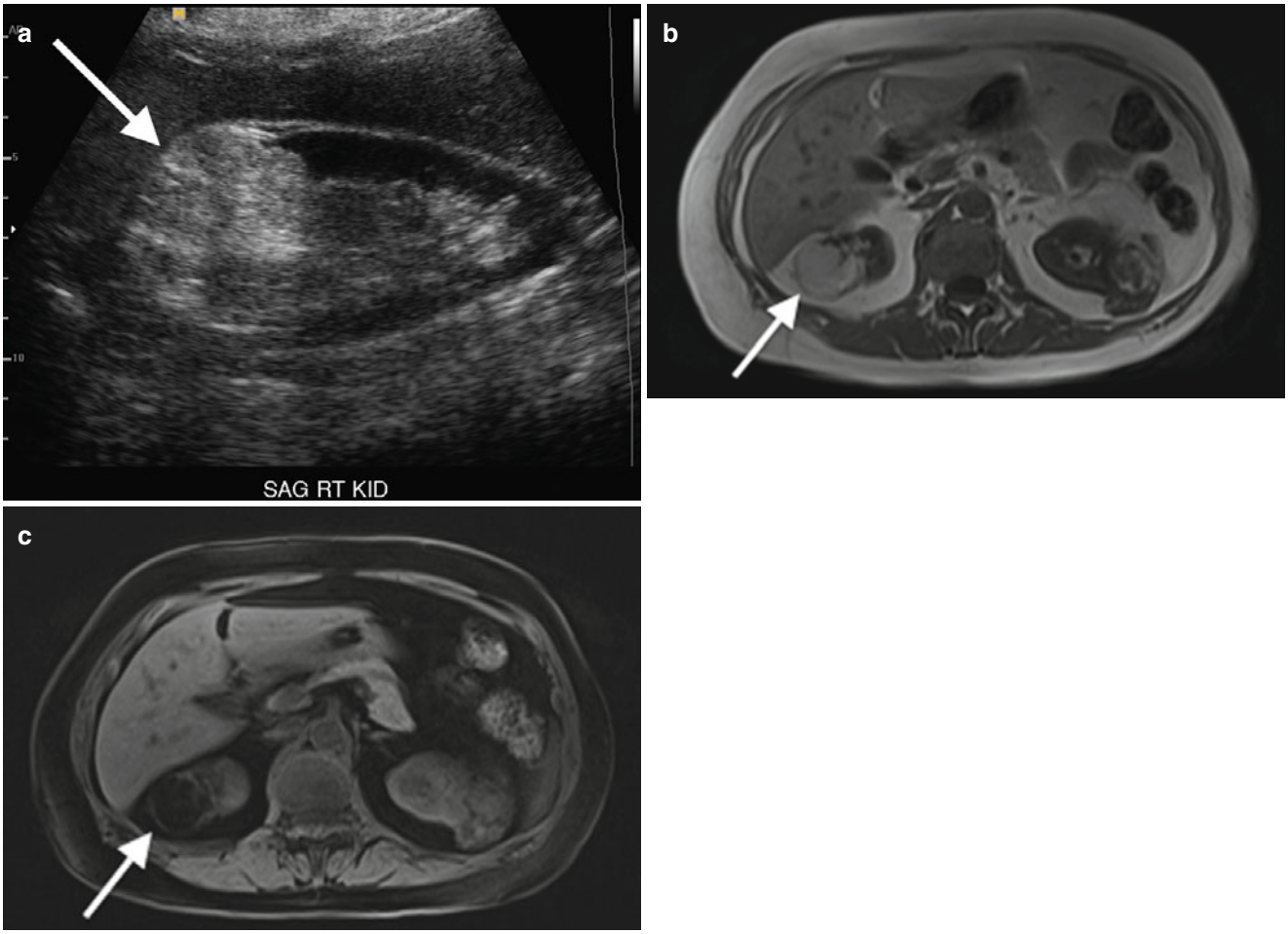

Fig. 2.3 Renal angiomyolipoma. Sagittal gray-scale sonographic image of the right kidney (**a**) demonstrates a rounded, hyperechoic, and nonshadowing solid mass at the upper pole of the kidney (*arrow*), consistent with angiomyolipoma. Accompanying non-contrast axial T1 in-phase (**b**) and T1 fat-saturated images (**c**) demonstrate the same mass to have high signal on the T1-weighted image (**b**) and diffuse signal loss (**c**) on the fat-suppressed image, confirming the diagnosis

Complex or septated cystic renal masses as well as solid masses raise suspicion of neoplasm (vs. abscess or hematoma) [2, 9, 10].

Sonographic characteristics of solid lesions include delineation of the posterior wall, lack of through transmission, and internal echoes. In the past, color flow and Doppler imaging were utilized to help differentiate different types of solid renal neoplasms. Ultrasound characterization of solid renal masses is more limited compared to cystic lesions, and more advanced imaging modalities such as CT and MR are indicated for further evaluation [2].

Angiomyolipoma (Fig. 2.3) is a benign, fat-containing renal mass that has a characteristic sonographic appearance. Lipid-rich lesions will demonstrate a characteristic homogeneous hyperechoic appearance and allow for a presumptive diagnosis, although infrequently this appearance can overlap with renal cell carcinoma. Therefore, additional imaging with CT is necessary to confirm the presence of macroscopic fat [9, 10].

Ultrasound can offer useful evaluation of mass lesions of the renal collecting system. Commonly, calcified calculi (Fig. 2.2) demonstrate the classic appearance of an echogenic focus with *posterior acoustic shadowing*. Even poorly or noncalcified calculi tend to demonstrate a hyperechoic echotexture and often shadow. Other lesions such as hematoma and neoplasm are often distinguishable from calculi, but their definitive diagnosis is better obtained via urologic procedures or additional imaging [2].

Overall, sonography is limited in its ability to stage the extent of malignant disease, which is better accomplished with CT and/or MRI.

Renal Failure

Ultrasound is commonly employed in the evaluation of renal failure as obstructive uropathy is an easily identifiable cause. Hydronephrosis (Fig. 2.4) is the hallmark of renal failure

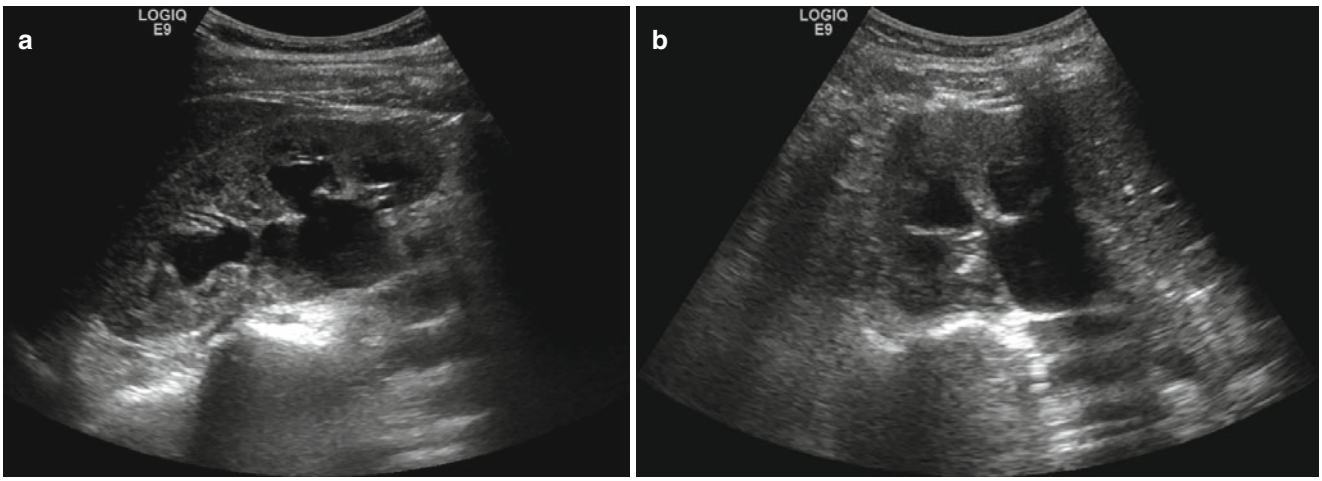

Fig. 2.4 Hydronephrosis. Sagittal (**a**) and transverse (**b**) sonographic images of the right kidney. The renal collecting system is symmetrically dilated, including dilatation of the renal calyces and central collecting system

due to obstruction and is characterized by the loss of the normally echogenic renal sinus which is replaced by a dilated hypoechoic collecting system. The level of dilatation of the calyces, infundibula, renal pelvis, and proximal ureter as well as the degree of parenchymal thinning can aid in inferring the degree and chronicity of the obstruction. Differential diagnostic considerations include parapelvic cysts, megacalyces, calyceal diverticula, and extrarenal pelvises. Post-intervention, ultrasound serves as an inexpensive and rapidly performed imaging study to assess for residual collecting system dilatation [2, 8].

Renal Transplant

The pelvic and superficial location of the transplanted kidney allows for it to be interrogated well by sonography. Postoperative perinephric collections, such as lymphoceles, urinomas, and hematomas, are usually identifiable. With decreased urine output, changes in renal volume and perfusion can be evaluated with sonography and allow for distinguishing obstruction from other transplant-related pathologies [2, 11].

Assessment of renal function is best accomplished with radionuclide imaging as the gray-scale ultrasound appearance in renal failure is rather nonspecific. Such findings include renal enlargement, increased cortical thickness, increased/decreased cortical echogenicity and loss of corticomedullary differentiation, prominent pyramids, thickness of the collecting system, and central sinus effacement. Ultrasound does however serve as an important tool in evaluating vascular complications of transplantation. Although conventional angiography remains the gold standard for the diagnosis of vascular complications, spectral and color Doppler ultrasound provide an excellent and noninvasive assessment of affected vessels. Pathologies typically encountered include renal arterial or venous occlusion or stenosis and pseudoaneurysms and arteriovenous fistulae [11].

Renal artery stenosis (Fig. 2.5) is the most common vascular complication of transplantation, reported in up to 10 % of patients. Color Doppler interrogation of a stenotic segment will demonstrate areas of focal aliasing. These regions can then be selected for spectral Doppler evaluation to quantify the degree of stenosis, which can then be evaluated with duplex Doppler techniques to characterize and grade the abnormality. Spectral Doppler criteria for significant stenoses include (a) velocities greater than 2 m/s or focal frequency shift greater than 7.5 kHz (when a 3-MHz transducer is used), (b) a velocity gradient between stenotic and prestenotic segments of more than 2:1, and (c) marked distal turbulence (*spectral broadening*). The presence of the classically described "*tardus parvus*" ("late, small" in Latin) waveforms may further support the diagnosis; however, they are not always present. If there is no significant flow abnormality demonstrated, renal arterial stenosis can be excluded [10–12].

Urinary Bladder

The normal sonographic appearance of the urinary bladder is a globular, hypoechoic structure whose shape is variable, depending on the level of distension and the patient's position at the time of examination. The wall appears hyperechoic, smooth, and diffusely symmetric in thickness. When the normal bladder is distended, the lumen should be anechoic [2].

Bladder tumors can sometimes be visualized sonographically. Polypoid lesions (Fig. 2.6) appear as intraluminal soft tissue projections which are fixed to the bladder wall and are

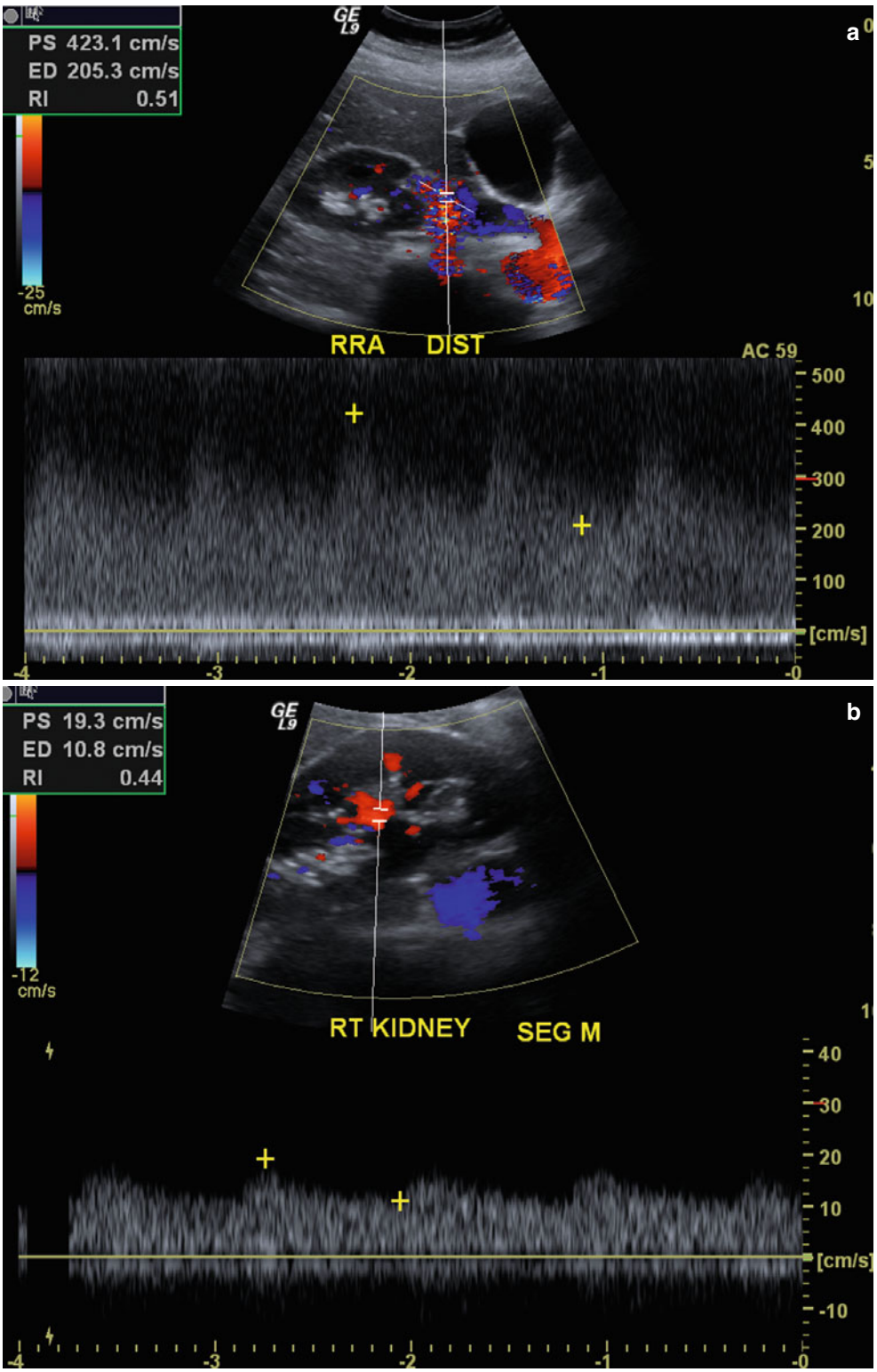

Fig. 2.5 Renal artery stenosis. Spectral Doppler sonographic images of the right renal artery, (**a**) at the level of a high-grade stenosis in the distal renal artery and (**b**) at the level of the segmental arteries, distal to the stenosis. (**a**, **b**) Abnormally high velocity is demonstrated at the level of the renal artery stenosis, while the arterial waveforms distal to the stenosis (**b**) show an abnormally delayed systolic upstroke with low amplitude ("tardus parvus") with corresponding low velocity. (**c**) Digitally subtracted image from renal arteriogram in the same patient shows a high grade mid-arterial stenosis (*arrow*). *Normal renal arterial waveform.* (**d**) A normal low-resistance waveform and velocity are demonstrated in the left renal artery in a different patient. Note the rapid systolic upstroke, with peak <150 cm/s and continuous low-resistance flow throughout diastole

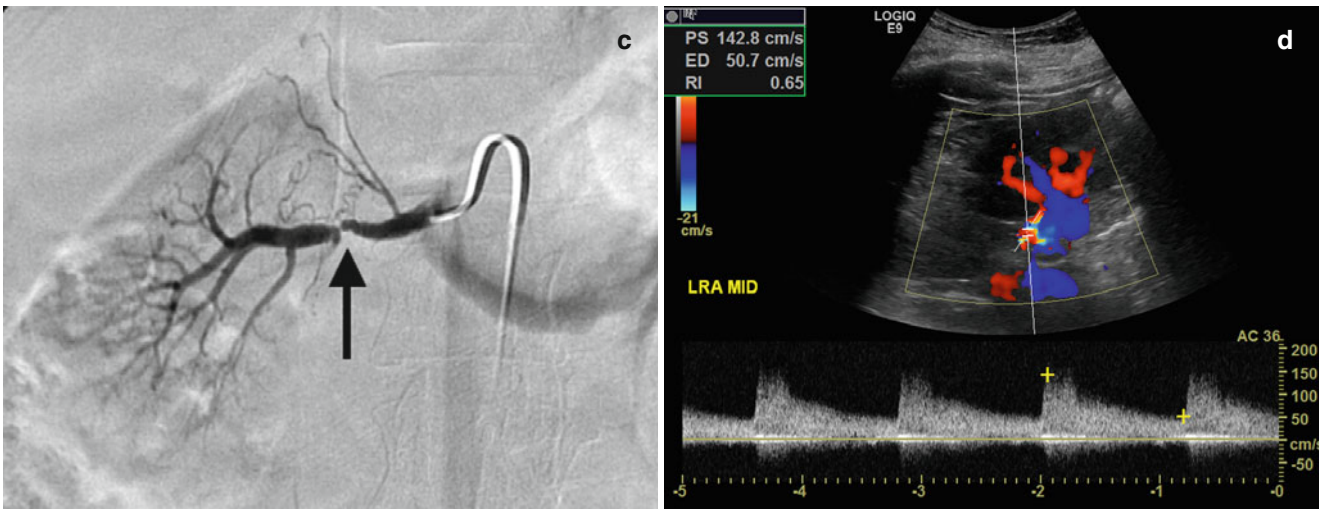

Fig. 2.5 (continued)

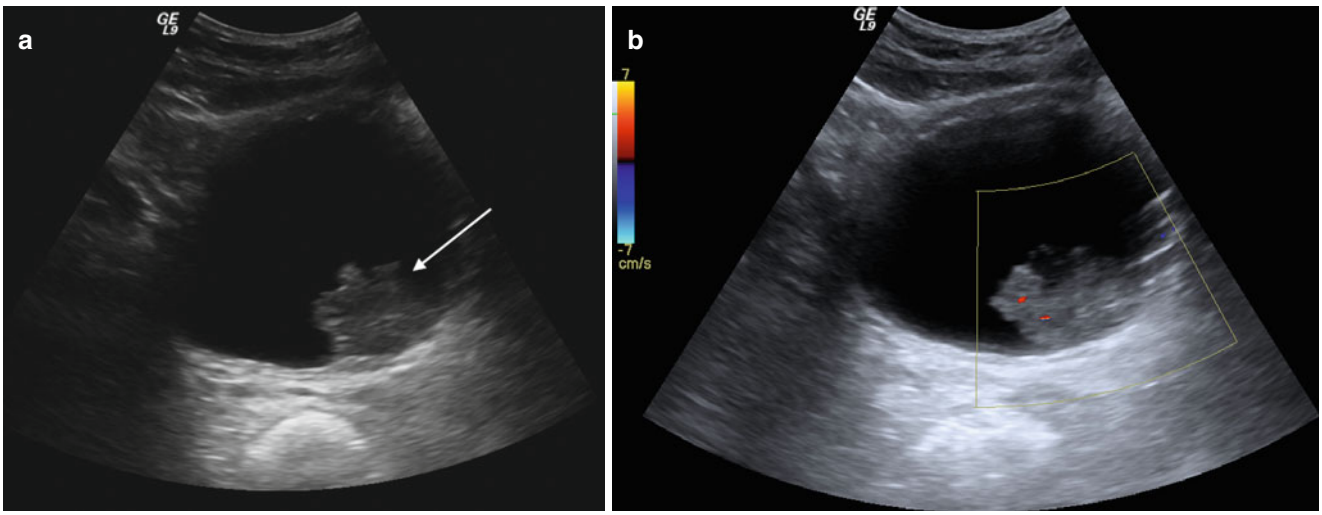

Fig. 2.6 Urinary bladder neoplasm. Transverse gray-scale (**a**) and color Doppler (**b**) sonographic images of the urinary bladder demonstrate a solid, exophytic mass within the urinary bladder lumen (*arrow* (**a**)) without any posterior acoustic shadowing and (**b**) with internal vascular color Doppler signal, indicative of a solid, vascularized lesion, rather than blood clot, adherent debris, or non-shadowing calculus

nonmobile with patient change in position, in contrast to mass-like lesions such as hematoma and calculi. Tumors are solid lesions in contrast to ureteroceles which, although they are also fixed to the bladder wall, have a distinct sonographic appearance with a thin echogenic wall and anechoic (cyst-like) center. Calculi within the bladder behave sonographically as in other areas of the GU tract with hyperechoic echotexture and posterior acoustic shadowing. Calculi will move as the patient changes position unless lodged at the ureterovesical junction [2].

Prostate

The normal sonographic appearance of the prostate is a symmetric triangular ellipsoid gland circumscribed by a fibrous capsule. The capsule itself appears as a continuous thin and hyperechoic layer of tissue. Internally the prostate demonstrates multiple fine diffuse homogeneous echoes which likely result from the interfaces of the myriad of small glands within. The posterior peripheral zone systolic velocity can typically be differentiated from the more anterior

peripheral zone, the central and transition zones, and the fibromuscular stroma [2].

Transrectal ultrasound has been shown to be useful in evaluating benign and malignant prostatic disease and plays a valuable role in biopsy and assessment of treatment of patients with prostate carcinoma (Fig. 2.7c). Note, however, that transrectal ultrasound is useful only to localize the prostate and not for the identification of lesions [2, 12–15].

Commonly used transrectal transducers used for prostate imaging range in frequency from 6.0 to 7.5 MHz. The higher frequency allows for detailed images; however, penetration of the beam is limited and thus the anterior prostate is often incompletely visualized. Most transducers are biplanar and provide images in the transverse and sagittal planes. The transverse plane allows for better visualization of the lateral margins, while the sagittal plane provides better images of the gland's apex and base [2, 12, 14, 15].

Currently, sonographic diagnostic evaluation of the prostate has a limited role in comparison with MRI (Fig. 2.7a, b). The anterior prostate is often insufficiently visualized, and

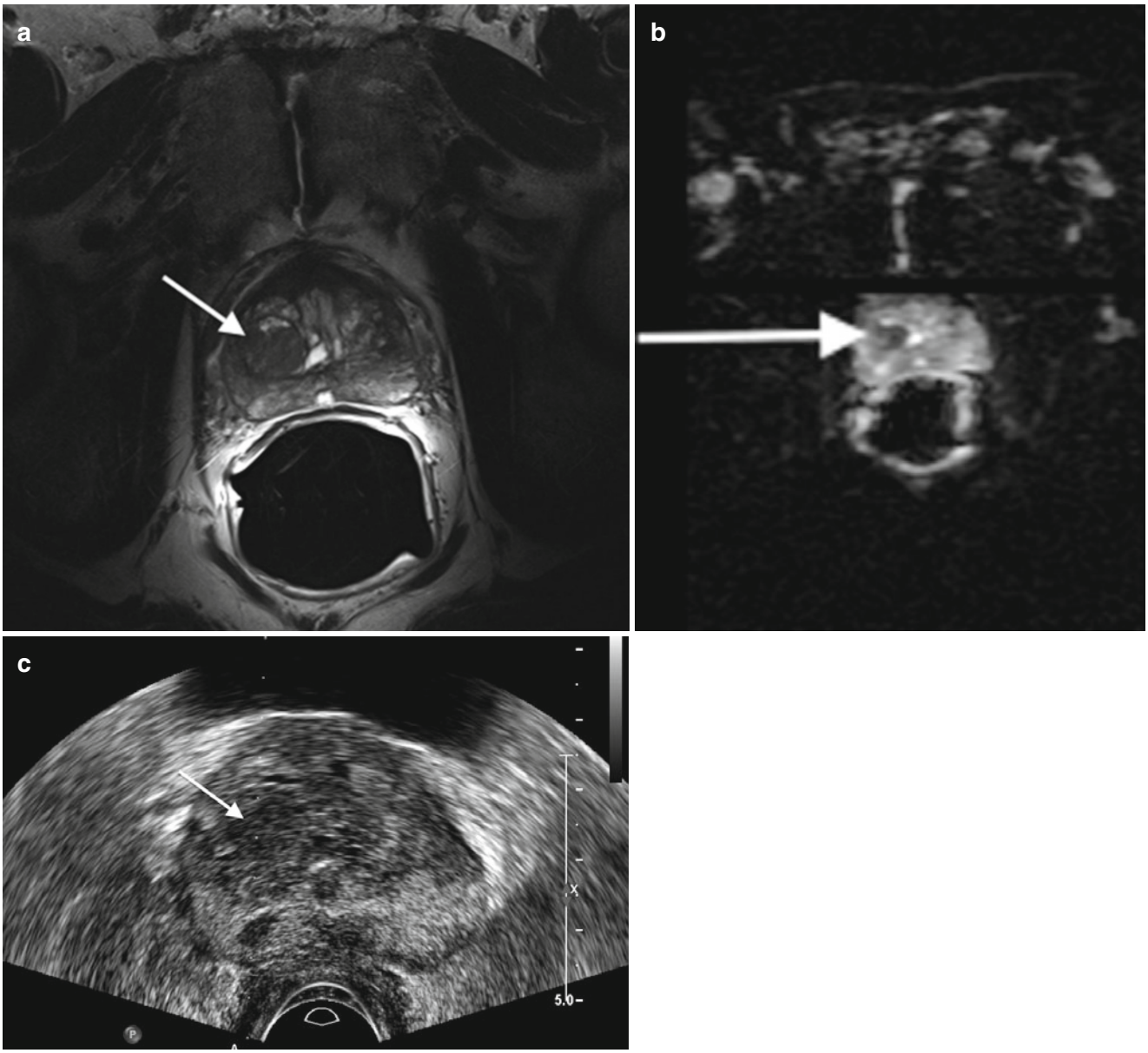

Fig. 2.7 Prostate carcinoma. (**a**) Axial T2- and (**b**) diffusion-weighted images of a right central prostate gland carcinoma (*arrows* (**a**, **b**)). (**c**) Transverse transrectal sonographic image of the prostate obtained during transrectal fusion biopsy demonstrates the lesion as a heterogeneous hypoechoic mass (*arrow*)

thus lesions in this region can go undetected. Additionally, many benign lesions as well as normal structures have similar sonographic appearances to small malignant lesions. Some carcinomas, in fact, are completely isoechoic and therefore the utility for diagnostic prostatic ultrasound is quite limited. It is becoming increasingly evident that supplementing the work-up of prostate cancer with prostate MRI when used in conjunction with transrectal ultrasound-guided biopsy will result in much higher yield for tissue diagnosis of malignancy [2, 12–15].

Penis

Sonographic evaluation of the penis is ideally conducted with a high-frequency linear transducer. This provides good visualization of the two corpora cavernosa, which are demonstrated as symmetric structures of homogenous mixed echogenicity which is due to the many interfaces of the vascular sinusoids. In contrast to the two corpus cavernosa, the corpus spongiosum normally appears mildly hypoechoic in comparison. The fibrous tunica albuginea appears as a hyperechoic line forming the intercavernous septum and provides a region of posterior acoustic shadowing between the corpora. Color and spectral Doppler sonography can evaluate penile vessel patency and characterize blood flow [2, 16].

Most applications of penile sonography occur in the acute setting. Acute conditions of the penis lend themselves to evaluation with ultrasound due to its wide availability and the real-time assessment it provides. Penile fracture results from tearing of the tunica albuginea leading to rupture of the corpora. Ultrasound is capable of demonstrating tears and the extent of the associated injury. The tear is visualized as a segmental discontinuity of the tunica albuginea, and associated hematoma may be visualized deep to the Buck fascia or subcutaneously. A secondary sign suggesting associated urethral injury is the presence of echogenic air in the cavernosa. The evaluation of the urethra with ultrasound is however limited, and when there is clinical concern of urethral injury, retrograde urethrography is indicated [2, 16].

Mondor disease of the penis, thrombophlebitis, or thrombosis occurs in the dorsal vein. Color Doppler evaluation serves in diagnosis and in monitoring patients. Sonographic findings include a lack of blood flow and noncompressibility of the dorsal vein, characteristic of thrombosis [2, 16].

Scrotal Ultrasound

The scrotum and its contents are superficial structures and thus well visualized with sonography. Scrotal pain and swelling prompt evaluation and sonography allows for differentiation between tumors, orchitis/epididymitis, torsion of the spermatic cord, and traumatic lesions such as fracture. Testicular and paratesticular malignant tumors are typically hypoechoic in appearance, and identification of such a mass demands surgical intervention in most scenarios. Nonseminomatous tumors can demonstrate increased vascular flow on Doppler imaging, while seminomas characteristically demonstrate homogeneous echotexture in contrast to embryonal tumors. Epididymitis is typically characterized by an enlarged and hypoechoic epididymis due to edema with hypervascularity on color Doppler imaging. Often, there is a reactive hydrocele accompanying the lesion. Epididymo-orchitis can have similar findings, as well as an enlarged and hypervascular testis [2, 17].

Clinically, distinguishing between testicular torsion (Fig. 2.8) and epididymo-orchitis can be difficult, and ultrasound has been found to be quite useful. In early torsion (approximately 1–3 h), echogenicity of the testes appears normal. As time goes on, there is enlargement of the torsed testis, and it will appear increasingly heterogeneous in echotexture. Evaluating the spermatic cord in suspected torsion is critical as a torsed cord can be visualized in the external inguinal orifice and aid in making the diagnosis. The intrascrotal portion of the torsed and edematous cord can appear as a rounded echogenic extratesticular mass. The orientation of the cord, testis, and epididymis can be inverted. The diagnosis is further strengthened with the evaluation of testicular blood flow, with the affected side demonstrating abnormal or absent flow compared to the normal testis. Comparative imaging with transverse views, including pulsed Doppler imaging can yield important information regarding decreased or reversed diastolic blood flow to the affected testis when compared to the normal side [17].

Traumatic injury to the scrotum lends itself to sonographic evaluation as the pain and swelling often limit physical examination. Findings include extratesticular hematoma and testicular rupture, the latter of which should be suspected in the case of poorly defined testicular margins and/or disruption of capsular blood flow. The echotexture of extratesticular/scrotal hematoma evolves over time with a more echogenic acute appearance transitioning to a more hypoechoic appearance in the subacute and later stages [17].

Varicocele

A varicocele (Fig. 2.9) will appear as a series of tortuous anechoic tubular structures either around, above, or below the testis. There is some variation in the caliber of the ves-

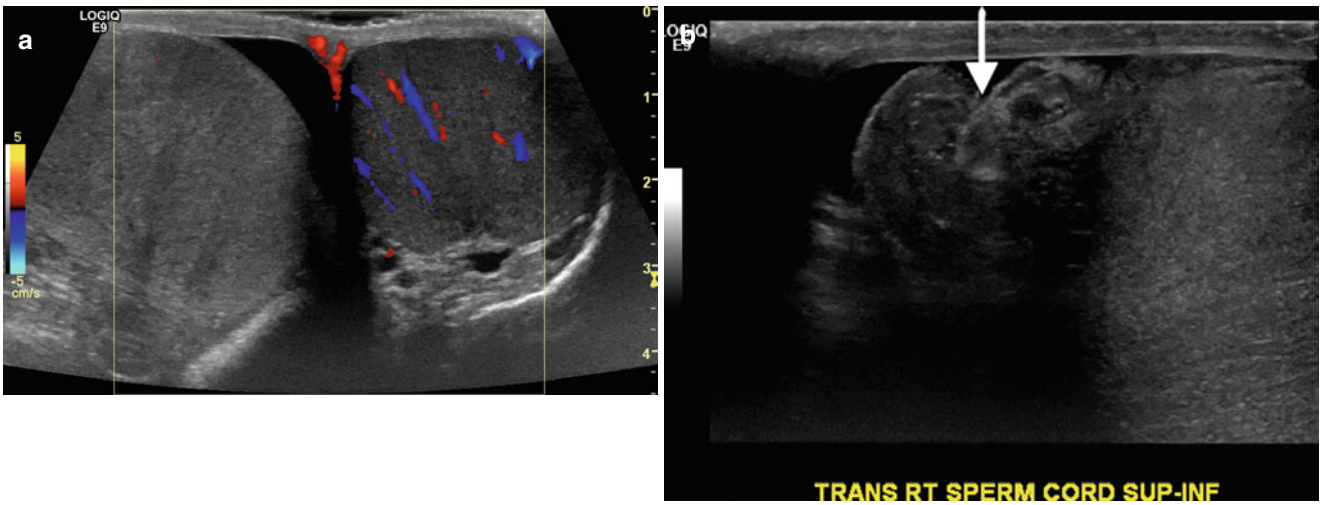

Fig. 2.8 Testicular torsion. Gray-scale and color Doppler images of the testes and gray-scale image of the spermatic cord in a young man presenting with acute right scrotal pain. (**a**) Color Doppler side-by-side transverse image demonstrates the absence of vascular flow to the right testicle compared the normal left testicle as manifested by the lack of color signal. (**b**) Transverse image demonstrating twisting of the spermatic cord (*arrow*)

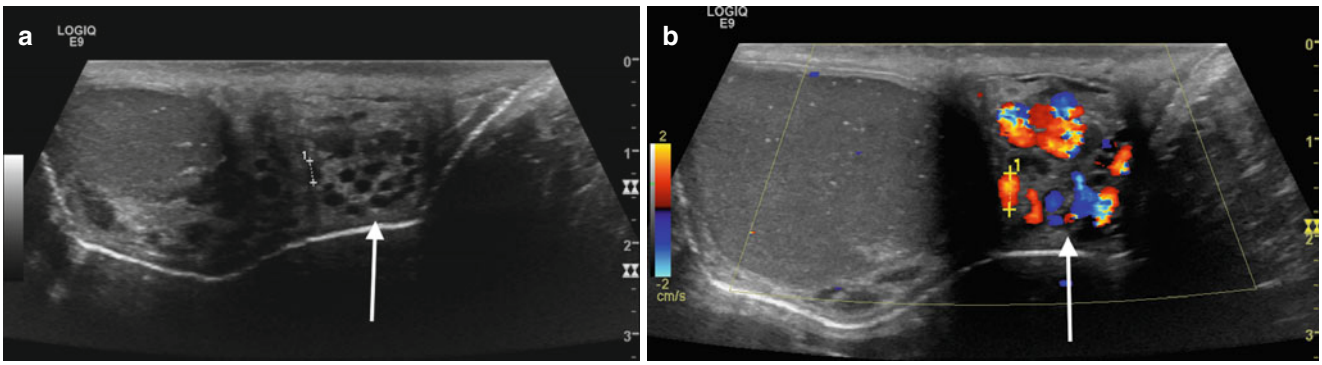

Fig. 2.9 Varicocele. Gray-scale (**a**) and color Doppler (**b**) sonographic images of the left testicle and an adjacent hydrocele. An extratesticular plexus of tortuous vessels (*arrows* (**a**, **b**)) is demonstrated with dilatation of the individual vessels upon Valsalva maneuver. Incidentally noted testicular microlithiasis can also be seen, manifested by scattered echogenic intratesticular foci

sels used by different authors, ranging typically from 2 to 3 mm. When utilizing color Doppler sonography at rest, blood flow within a suspected varicocele may be too slow for detection. With utilization of the Valsalva maneuver, the varicocele will enlarge and demonstrate reversal of flow. Color Doppler sonography is the accepted gold-standard technique for varicocele assessment as it provides accurate diagnosis and can also be used to stage lesions [18].

Computed Tomography (CT): Physical Principles and Genitourinary Applications

Physical Principles

The first CT scanner was developed by Sir Godfrey Hounsfield in Middlesex, Great Britain. In 1973, the first CT scanners were used clinically. Houndsfield and Allan Cormak were awarded the Nobel Prize in Medicine in 1979

for the development of CT technology [1, 19]. In the following decades, with constant advances in technology and computational power, cross-sectional imaging has revolutionized the practice of medicine, due to its capability to evaluate disease processes throughout the body in a noninvasive manner.

There are many urologic applications of CT, including, but not limited to, detection and characterization of renal stone disease; obstructive uropathy; benign and malignant tumors of the adrenals, kidneys, and upper and lower urinary tracts; traumatic injury; infection and its complications; and assessment of renal artery disease. Technologic advances over the years have greatly increased the capabilities of CT and have resulted in markedly greater speed of acquisition, anatomic coverage, and the ability to obtain dynamic contrast-enhanced images, all of which have worked to increase its diagnostic accuracy and image quality. This has also led to the development of newer applications, such as dual-energy CT, CT angiography, and CT urography. A drawback to the use of CT is its use of ionizing radiation, which results in a relatively large radiation dose. In recent years, however, dose reduction techniques have been implemented on a wide-scale basis, which have the potential to significantly reduce the dose from routine CT imaging.

A fundamental limiting factor of plain film radiography is that a three-dimensional object is reduced to a two-dimensional image, with the potential for multiple structures of varying radiodensity to be superimposed on one another, with the potential for the anatomy of interest to be obscured. Two distinct and extremely important advantages of CT over plain film radiography are (1) acquisition of a cross-sectional image with removal of any superimposed structures and (2) almost complete elimination of radiation scatter, which results in much greater sensitivity to differences in x-ray attenuation, thereby allowing excellent contrast between soft tissue structures. A CT examination is made up of multiple images, each one containing visual information from narrow anatomic sections through the imaged section of the body. The penetrating x-ray beam is collimated (shaped) into a very precise width [1, 19].

CT scanners are made up of two major components: the scanning component and computer components. The gantry consists of the scanning components, which surround the central aperture through which the patient is scanned. The computer components are located in the CT scanner control room. The scanning component includes the generator or power source, x-ray tube, collimators, detectors, data acquisition system computer components, image reconstruction, and scanner console.

Each detector, along with the focal spot of the x-ray tube, defines a ray. The detector measures the intensity of the x-rays within its ray. The intensity of the beam within each ray depends on the amount that x-rays are attenuated in the tissue through which it passes. Attenuation is a measurement of the fraction of radiation removed in passing through tissue. The attenuation of each boxlike element, or voxel, in the plane being scanned is measured by using many different rays acquired from many different angles over the course of the scan. The linear attenuation coefficient of a material indicates how strongly it absorbs or scatters (attenuates) x-ray photons. The linear attenuation coefficient depends on three properties: atomic number, physical density, and photon energy. The creation of a CT image is reliant upon the different attenuation characteristics of various tissues in the body [1, 19].

Once image detectors have assembled the data from each ray, images are reconstructed via analytical and iterative methods. The most commonly used reconstruction method is filtered backprojection, which has been used in the earliest CT scanners and is still used today. Filtered backprojection essentially determines the average density of each pixel by collecting sets of rays called projections, which are made across the patient in a particular direction in a section plane. Multiple projections are needed to determine average attenuation at each point, using rotational intervals of less than 1° [1, 19].

CT images are composed of gray-scale values, with each element of the image (pixel) assigned a gray-scale value dependent upon its average attenuation. Denser materials will cause greater attenuation of photons and will be brighter (whiter) on the CT image, while images that are less dense will be darker (blacker). Density measurements are standardized using the Hounsfield scale, in which water has a Hounsfield unit of zero, with other tissues ranging from −1000 (air) to +2000 (bone). Any voxel that has attenuation greater than water will have a positive HU value, and voxels which have attenuation less than water will have a negative HU. An attenuation value of specific tissue can be easily obtained by placing a cursor over the region of interest (ROI) at the workstation, for which the computer can average the attenuation of the voxels within the cursor. Attenuation values play great importance in tissue characterization and diagnosis and must be precisely calibrated on a regular basis [1, 19].

Detector arrays in multislice scanners are two dimensional. The number of detectors in the z-direction (in the head-to-toe direction of the patient) determines the maximum number of slices which can be simultaneously acquired. In a single-slice scanner, the slice width is determined by the width of the collimator. In multislice scanners, the slice width is determined by the width of the individual detectors. For instance, in a system with 64 detectors which are 0.625 mm in width, the slice thickness is 0.625 mm [19]. In actual practice, thicker slices are usually reconstructed for routine interpretation; however, thin sections are stored at the CT workstation and are available for review, if necessary.

Many imaging acquisition parameters determine image quality and patient dose. Two important acquisition parameters that affect radiation dose and image quality are peak tube voltage (kVp) and effective mAs. The effective mAs is the tube current (milliamperes) multiplied by the length of time that a given point in the patient is in the beam (seconds). The energy of the most energetic x-ray photon in the beam is always equal to the kVp. Pitch is another important acquisition parameter: this refers to the table movement per tube revolution divided by the beam width. Adjustments in pitch affect scan time, z-axis resolution, and radiation dose [1, 19].

Prior to the introduction of helical CT technology, scanners operated in axial or incremental mode. In axial CT scanners, the CT table is stationary during image acquisition, with the tube and detectors making one complete rotation. The x-ray beam is then turned off and the table repositioned [1, 19].

The design of modern CT scanner has been modified so that there are no hardwired connections between the generator and x-ray source and between the detector array and computer. This is achieved by slip-ring technology. Slip-ring technology, as well as advances in x-ray tube design and computer speed, made the development of helical scanning possible. Helical CT allows for uninterrupted motion of the x-ray source and the detector array, which rotate in a complete 360° arc around the patient. Simultaneously, the CT table (and patient) is moving in a continuous manner and at a predetermined speed [1, 19]. The result of these two different movements is that the beam takes a helical path through the patient. Helical scanners are capable of much faster scanning times and thinner slice acquisition than incremental CT scanners [19]. This improved temporal resolution has enabled dynamic studies after the administration of a bolus of intravenous iodinated contrast, whereby the entire abdomen and pelvis can be scanned on the order of seconds and images can be obtained in various phases of interest for a particular indication. For example, a typical examination for the evaluation of a renal mass would include arterial, nephrographic phases and sometimes excretory (pyelographic) phases as well as an unenhanced acquisition.

Dual-Energy CT

Dual-energy CT (DECT) scanners are built with two x-ray source/detector arrays. The tube voltage (kVp) settings for the two sources differ, resulting in two separate attenuation maps for the same object, one at a high energy level and one at a low energy level. As mentioned above, the linear attenuation coefficient of a specific material is dependent upon three properties: atomic number, density, and photon energy. DECT uses information obtained from both the high and low energy arrays to assess the rate of change in the linear attenuation coefficient of the structure being analyzed. As various elements and compounds commonly found in the human body have unique linear attenuation curves over a spectrum of energy, DECT is capable of providing information regarding specific chemical composition [20].

There are several ways in which the data obtained from DECT can be exploited to provide useful clinical and diagnostic information. Material-specific images can be formed by targeting a specific material's linear attenuation curves and removing it from the image. Common base materials targeted by DECT include water, iodine, and calcium. As enhancement on CT is produced from the effects of iodinated contrast medium, subtracting iodine results in a "virtual" non-contrast image, so that a single dual-energy scan could potentially replace two single-energy scans (pre- and post-contrast) [20]. This could have application in the evaluation of renal masses, calculous disease, adrenal nodules, and any other scenario where non-contrast images are necessary for lesion characterization or visualization. An additional benefit of virtual non-contrast images would be radiation dose reduction, due to elimination of a separate unenhanced acquisition.

Conversely, iodine-specific data sets (iodine maps) can be obtained. These are composed exclusively of the contribution of iodine to the image and may also be efficacious in renal mass characterization and other scenarios [21]. By enabling better visualization of iodine signal, enhancement within a mass may be more easily diagnosed on iodine-specific images. Studies have so far shown promising results for the use of virtual non-contrast and iodine-specific images in differentiating cystic from solid renal masses [21–23]; however, these techniques will require further study and validation. Future advances and refinements in dual-energy technology may even surpass the diagnostic capabilities of conventional, single-source CT.

Virtual non-contrast images have also shown promise in characterizing adrenal nodules [24, 25]. This is a promising development given the high frequency of adrenal nodules found on contrast-enhanced CT scans, which often need repeat CT examination with unenhanced images to better characterize.

Another active area of investigation of DECT is in renal stone characterization. DECT makes use of the distinctive absorption patterns of various stone components at both high and low energy levels to identify specific chemical composition [20]. This can expedite the work-up of renal stone disease, which can often involve lengthy laboratory and imaging investigation. Knowledge of stone composition can help improve treatment, as management of different stone types differs. DECT has shown to be reliable in differentiating uric acid stones from non-uric acid stones [20] and shows promise in the differentiation of other calculi (cystine, struvite, calcium oxalate monohydrate/calcium oxalate dihydrate/brushite, and hydroxyapatite/carbonate apatite calculi) [26, 27].

Applications of CT in the Urinary Tract

Kidneys

There are numerous indications for the use of CT in the evaluation of renal pathology. Some of the more common reasons include renal mass characterization, renal cancer staging, stone disease, trauma, inflammatory/infectious processes, obstructive uropathy, vascular disease, congenital urinary tract anomalies, and postoperative evaluation.

CT is a highly accurate modality for renal mass evaluation. Since the differential diagnosis often revolves around differentiating between a cystic and solid mass, the key element of such evaluation is the presence or absence of contrast enhancement [28]. Benign renal cysts are typically uniformly low in density (at or near the attenuation of water) on CT, with an imperceptible wall and no septations or mural nodules; however a significant minority will appear as high-attenuation lesions on CT due to the presence of hemorrhagic or proteinaceous debris. Because the density of these lesions (greater than 20 HU) overlaps with solid nodules, they cannot be differentiated by unenhanced or contrast-enhanced CT alone. Rather, both unenhanced and enhanced images must be acquired in the same sitting, with HU measurements obtained from both series. At this time, there is no true consensus on what constitutes significant enhancement; however, a threshold of >20 HU is used by some experts, with a 10–20 HU difference considered to be equivocal [28]. In the case of an enhancing soft tissue mass with no visible fat, there are no reliable CT findings to help differentiate a benign soft tissue mass, such as an oncocytoma or lipid-poor angiomyolipoma, from a renal cell carcinoma (RCC). Lymphoma and metastatic disease can also have a similar appearance to RCC, and attention to medical history and extrarenal findings must be made in order to make an accurate diagnosis. Nonneoplastic mimics of renal cell carcinoma include focal pyelonephritis, "pseudotumor" arising from congenital lobulation of the renal contour or from normal parenchyma adjacent to scarred cortex, and IgG-4 disease [29].

Artifacts, such as beam hardening from a patient who is unable to position his/her arms away from their sides or from pseudoenhancement, can give spurious results. Pseudoenhancement is a well-known artifact on CT, which causes increase in attenuation measurements in renal lesions on intravenous contrast-enhanced CT. This is due to an incorrect image reconstruction algorithm in areas adjacent to high-attenuation structures (in this case, the avidly enhancing renal parenchyma), with small, intraparenchymal lesions most likely to be affected [30, 31].

Cystic renal lesions are ubiquitous in the adult population, with simple cysts comprising the overwhelming majority of these masses. Cystic neoplasms do, however, arise in the kidney; therefore, the density (HU) measurement and internal composition of all cystic renal masses must be carefully assessed. The presence of enhancing septations and nodules increases the likelihood of a cystic neoplasm. The Bosniak classification of cystic renal masses categorizes lesions based on their morphology. Bosniak criteria include density, number, and thickness of septations; wall thickness; and soft tissue nodules (Fig. 2.10). The presence or absence of enhancement must be carefully assessed, as benign hemorrhagic cysts can have many of the features of a cystic neoplasm; however, any internal components should not enhance [28].

Angiomyolipomas are well assessed on CT and can be diagnosed when a renal mass contains macroscopic fat. This is a key element of renal mass characterization, as it is extremely rare for a renal cell carcinoma to contain fat. An unenhanced thin-section CT is the most sensitive test for fat detection and should be performed if fat is suspected in an enhancing renal mass. A small minority of angiomyolipomas will either contain no fat or an insufficient amount of fat to be detected at CT. Although these lesions often have features on CT that may suggest the diagnosis, they cannot be reliably distinguished from renal cell carcinoma without biopsy or surgery [28].

In cases of known renal malignancy, CT is an accurate modality for staging. The renal vein and IVC can be assessed for the presence and extent of tumor invasion. Tumor thrombus can often be distinguished from bland thrombus by enhancement in the former; however, there are limitations of both CT and MRI in assessing for invasion of the IVC wall, which can significantly impact prognosis [32]. Lymph node status is assessed based primarily on node size, with a cutoff of 1 cm in short axis diameter. This inevitably results in some false-positive (enlarged but benign nodes) and false-negative

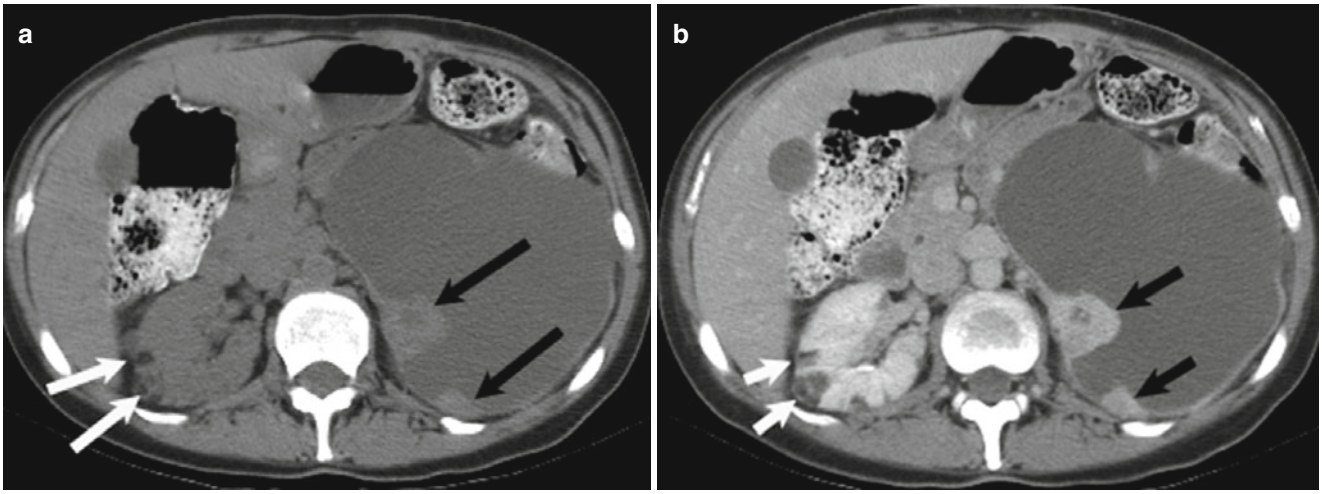

Fig. 2.10 Cystic renal cell carcinoma. Axial unenhanced (**a**, **b**) contrast-enhanced CT images demonstrates a large cystic left renal mass with nodular enhancing components (*black arrows*). Enhancement within a renal mass must be confirmed by comparison with unenhanced CT images. Also note two small fat density right renal lesions representing angiomyolipomas (*white arrows*)

(small but malignant nodes) cases. Johnson et al. reported a sensitivity of 83 % and specificity of 88 % for nodal assessment in the setting of renal cell carcinoma [33]. Distant metastases to the lung, liver, bone, and other sites are well depicted on CT.

In most cases of acute pyelonephritis, imaging is not necessary for diagnosis or management; however, CT does have a role in select subgroups of patients. These include those at high risk of complications, such as the immunocompromised, including diabetics, patients in whom there is poor response to standard treatment regimens, and in patients where there is clinical suspicion for complications, such as renal abscess, pyonephrosis, or emphysematous pyelonephritis (Fig. 2.11) [34, 35]. The typical finding on intravenous contrast-enhanced CT is one or multiple wedge-shaped areas of cortical hypoenhancement, reflecting involved areas of renal parenchyma (Fig. 2.12). Radiating linear bands of alternating decreased and normal enhancement, likely due to obstructed tubules with intervening normal tubules, can give rise to a "striated nephrogram." Secondary findings include global renal enlargement, thickening of Gerota's fascia, and urothelial thickening of the renal pelvis and ureter [34, 35]. CT can also demonstrate renal manifestations of less common infections, such as tuberculosis, fungal organisms, echinococcus, and xanthogranulomatous pyelonephritis (Fig. 2.13) [35].

Because of its availability, rapid patient throughput, and accuracy for diagnosing renal injury, CT is the first-line modality for the evaluation of blunt or penetrating renal trauma, including iatrogenic injury from surgical and percutaneous renal procedures. CT findings can be graded in conjunction with a renal trauma grading system, such as the American Association for the Surgery of Trauma (AAST) [36–38]. Intravenous contrast is essential when CT is used for renal trauma evaluation, in order to accurately demonstrate injuries to the kidney parenchyma and vasculature as well as perirenal and retroperitoneal hemorrhage (Fig. 2.14) and fluid collections. Excretory (delayed) phase images are necessary to evaluate for collecting system injury (AAST grade IV or V), which is diagnosed by extravasation of contrast-opacified urine from the damaged segment of the collecting system (Fig. 2.15) [38].

CT has become the gold standard for the evaluation of renal stone disease, replacing excretory urography and plain radiographs in most centers. CT has been shown to be highly sensitive (95–98 %) and specific (96–100 %) for diagnosing urolithiasis [39–41]. It is also readily available in most emergency departments, rapidly performed, does not require oral or intravenous contrast, and can detect stones of all sizes. CT can also help provide alternative diagnoses to stone disease either within (infection, neoplasm, congenital anomalies) or outside (e.g., pancreatitis, appendicitis, etc.) the urinary tract. The most direct sign of ureterolithiasis is the identification of a stone in the ureter. Secondary signs of an obstructing stone commonly seen on CT include hydroureteronephrosis and perinephric and periureteral fat stranding [42].

CT can provide essential information in patients undergoing stone removal procedures such as percutaneous nephrolithotomy (PCNL), ureteroscopy, or extracorporeal shock wave lithotripsy (ESWL). The preprocedure scan can help ascertain a safe route for needle access and the most appropriate calix to puncture in a patient undergoing PCNL and provide a stone to skin (SSD) distance prior to ESWL. Postintervention CT can be used to assess for any residual calculi or obstruction [43].

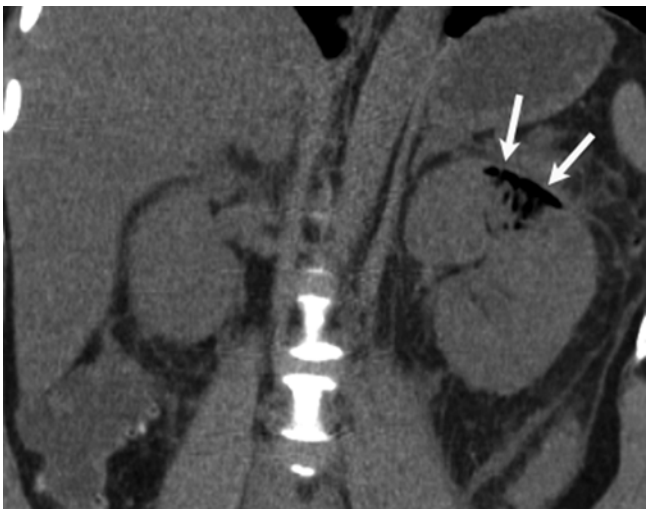

Fig. 2.11 Emphysematous pyelonephritis. Coronal unenhanced CT image demonstrates a wedge-shaped focus of gas (*arrows*) within the parenchyma of the left kidney

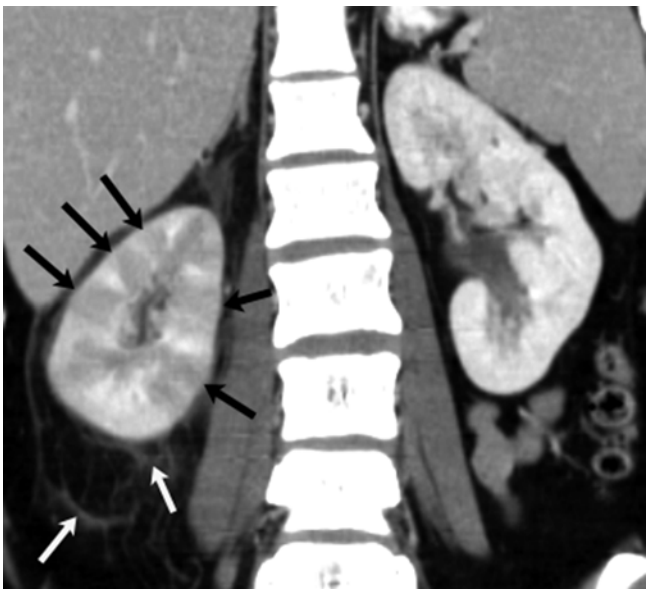

Fig. 2.12 Pyelonephritis. Coronal reformatted image from CT performed with intravenous contrast demonstrates multiple wedge-shaped areas (*black arrows*) of parenchymal hypoenhancement and perinephric stranding (*white arrows*)

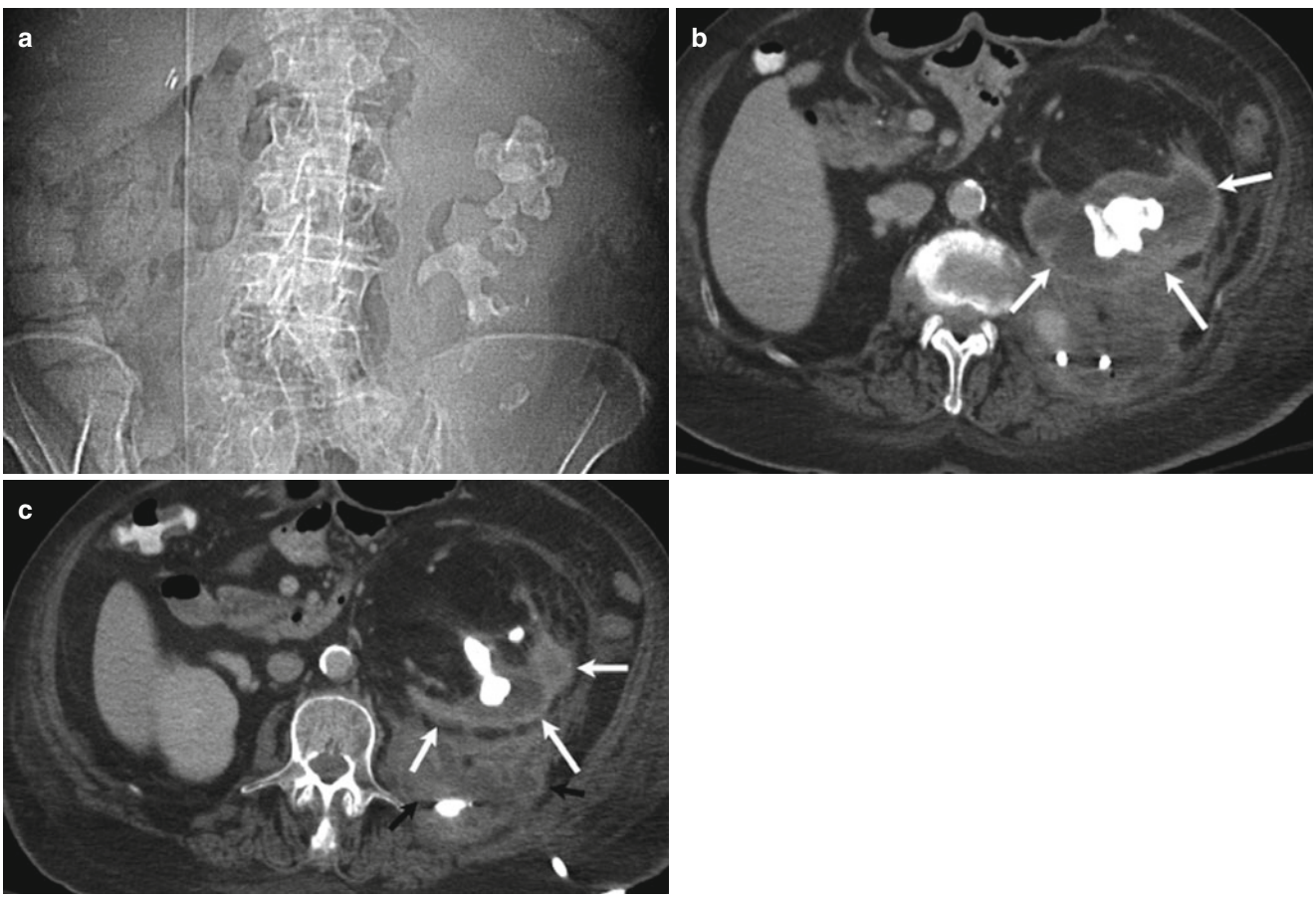

Fig. 2.13 Xanthogranulomatous pyelonephritis. Scout CT view (**a**) shows a large left staghorn calculus. Axial images from contrast-enhanced CT (**b**, **c**) demonstrate a nonfunctioning, hydronephrotic kidney (*white arrows*). Note abscess (*black arrows*) with drainage catheter in the posterior retroperitoneum

Congenital urinary tract anomalies are well evaluated with CT and often detected incidentally in the adult population; however, MRI is the preferred modality for the assessment of a known or suspected anomaly in a child due to the lack of ionizing radiation and the ability to perform a multiparametric examination.

Fig. 2.14 Renal injury with active bleeding. Contrast-enhanced coronal reformatted CT image demonstrates a full-thickness laceration of the left kidney. There is a large retroperitoneal hematoma (*arrows*) containing high-attenuation foci, representing vascular contrast extravasation (*arrowheads*)

Adrenal Glands

CT can be used to both characterize adrenal lesions and as a tool for surveillance of stability of an indeterminate nodule. The most common adrenal nodule is the adenoma. Due to their high frequency in the general population, these are often discovered as incidental findings on CT performed for other indications [44–46]. CT can be used to characterize a lesion as a benign adenoma in two manners. The first and simplest is by performing unenhanced CT. The majority of adenomas will contain intracellular lipid, which will reduce the attenuation of the nodule. Adrenal nodules measuring less than 10 HU on unenhanced CT can be diagnosed as adenomas with a 71 % sensitivity and 98 % specificity as reported in a meta-analysis by Boland et al. [47]. Unfortunately, about 30 % of adenomas will not meet this criterion. These so-called "lipid-poor" adenomas can be evaluated with a combined unenhanced and contrast-enhanced CT examination with washout analysis. Adenomas will usually have more rapid contrast washout than malignant nodules. The histopathologic basis for this is thought to be disorganized angiogenesis and vascular permeability in malignant nodules, leading to extravascular contrast leakage. Washout is calculated by comparing density measurements made on all three phases of the examination (unenhanced, dynamic contrast-enhanced, and delayed images obtained 15 min after contrast administration.) Established washout thresholds for the diagnosis of an adenoma are greater than 60 % absolute percentage washout (([HUcontrast - HUdelayed]/[HUcontrast-HUunenhanced]) × 100) or greater than 40 % relative percentage washout (([HUcontrast-HUdelayed]/[HUcontrast]) × 100). Using these

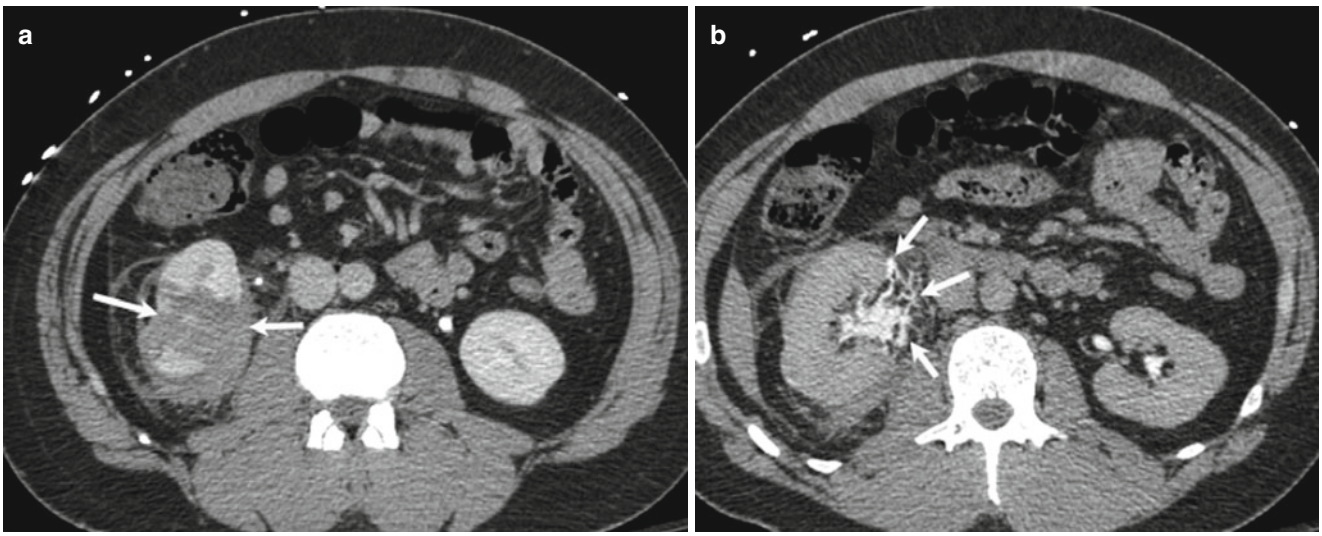

Fig. 2.15 Grade IV renal trauma. Axial contrast-enhanced images obtained in the nephrographic (**a**) and excretory (**b**) phases show a large parenchymal laceration (*arrows*, **a**) and extravasation of excreted contrast (*arrows*, **b**) diagnostic of collecting system injury

criteria, Caioli et al. successfully diagnosed 160/166 adenomas with 98 % sensitivity and 92 % specificity [48]. One important caveat to remember in adrenal washout imaging is that a pheochromocytoma can demonstrate washout levels similar to that of an adenoma. Such a lesion may be suspected if its absolute enhancement exceeds 110–120 HU after contrast administration [49].

Adrenal myelolipomas can be easily diagnosed in most cases due to the presence of macroscopic fat. Adrenal cysts are uncommon lesions, most often pseudocysts due to chronic hematoma. These lesions often demonstrate low attenuation and may contain wall calcification [44].

Other adrenal masses include hemorrhage, ganglioneuroma, metastatic disease, pheochromocytoma, adrenal cortical carcinoma, lymphoma, and collision tumor, as well as neuroblastoma in the pediatric population. Significant overlap exists in the CT features of these lesions, and further investigation with laboratory tests and possibly biopsy may be necessary to make an accurate diagnosis. Contrary to prior literature suggesting that ionic intravenous contrast administration may provoke a hypertensive crisis in patients with a pheochromocytoma [50], more recent studies have shown no adverse effects to nonionic intravenous contrast in patients with pheochromocytoma [51, 52].

Adrenal cortical carcinoma has a propensity for venous invasion, the extent of which can be characterized on contrast-enhanced CT scan. An adrenal mass with invasion of the inferior vena cava is highly suggestive of adrenal cortical carcinoma [53]. There are numerous causes of nontraumatic adrenal hemorrhage, which can mimic an adrenal tumor on imaging studies. Hemorrhage may be suspected in an adrenal mass with high attenuation on unenhanced imaging, with or without stranding of the periadrenal fat. The possibility of an underlying hemorrhagic neoplasm must also be entertained and can be further investigated using contrast-enhanced MRI with subtraction imaging [44].

Ureters and Bladder

With the exception of stone disease as discussed above, CT evaluation of the ureter usually necessitates IV contrast administration. Common indications for imaging of ureteral disease include hematuria, suspected tumor, known lower tract or previously treated upper or lower tract transitional cell carcinoma, investigation of ureteral obstruction, and after urinary diversion surgery. Comprehensive assessment of both the upper and lower tracts with CT is performed with CT urography. CT urography is usually performed as a triphasic study, with acquisition of unenhanced, nephrographic, and excretory phase series. Diuretic administration, typically low-dose intravenous furosemide, aids in the visualization of the upper and lower tracts by diluting the excreted contrast and increasing ureteral distention [54]. A biphasic study can be performed in younger patients to decrease radiation dose by using a "split bolus" technique, whereby a combined nephrographic and excretory series is obtained. This is accomplished by dividing the contrast volume into two doses: a smaller dose of 30 and 50 cc of contrast administered 8–10 min prior to scan initiation, with the remainder (approximately 100 cc) given 2 min prior to the scan (this technique allows time for the earlier dose to circulate and become excreted by the kidneys), while the second dose serves to provide a nephrographic phase [55]. Properly performed CT urography allows for detailed evaluation of the kidneys, collecting systems, ureters, and bladder and has been shown to be superior for the detection of transitional cell carcinoma as compared with excretory urography, with a meta-analysis finding a pooled sensitivity of 96 % and pooled specificity of 99 % [56]. Tumors will appear as a filling defect or wall thickening (either eccentric or circumferential) in the contrast-opacified collecting system (Fig. 2.16), with or without hydroureteronephrosis. In positive cases, CT allows for tumor staging to be performed simultaneously [54].

Other indications for CT urography of the ureters include trauma, including iatrogenic trauma from surgery or endoscopic urologic procedures, and infectious and inflammatory disorders (Fig. 2.17). CT urography can depict congenital anomalies, such as ureteropelvic junction obstruction, ureteric webs, duplicated collecting system, and megaureter, with excellent detail [54], although, as mentioned above, MRI, if available, is the preferred modality for such indications in the pediatric population.

Cystoscopy is typically the first-line method for the diagnosis of bladder tumor. When CT is performed for bladder tumor assessment, CT urography is indicated, in order to evaluate both the upper and lower urinary tracts, due to the tendency of urothelial neoplasms to be multicentric, with both synchronous and metachronous urinary tract involvements. There is the potential for some bladder tumors to be better visualized on the dynamic contrast-enhanced phase of the CT urogram rather than the excretory phase because (a) bladder cancers have been shown to have robust enhancement in the early phase of contrast administration [57] and (b) nonuniform opacification of the bladder due to mixing of contrast and urine can obscure or mimic a bladder nodule [58]. Sadow et al. reported a sensitivity of 79 % and specificity of 94 % for bladder cancer detection utilizing CT urography technique [59]. Limitations include underdistention of the bladder obscuring or potentially mimicking a tumor and flattening of the tumor from an overdistended bladder. CT

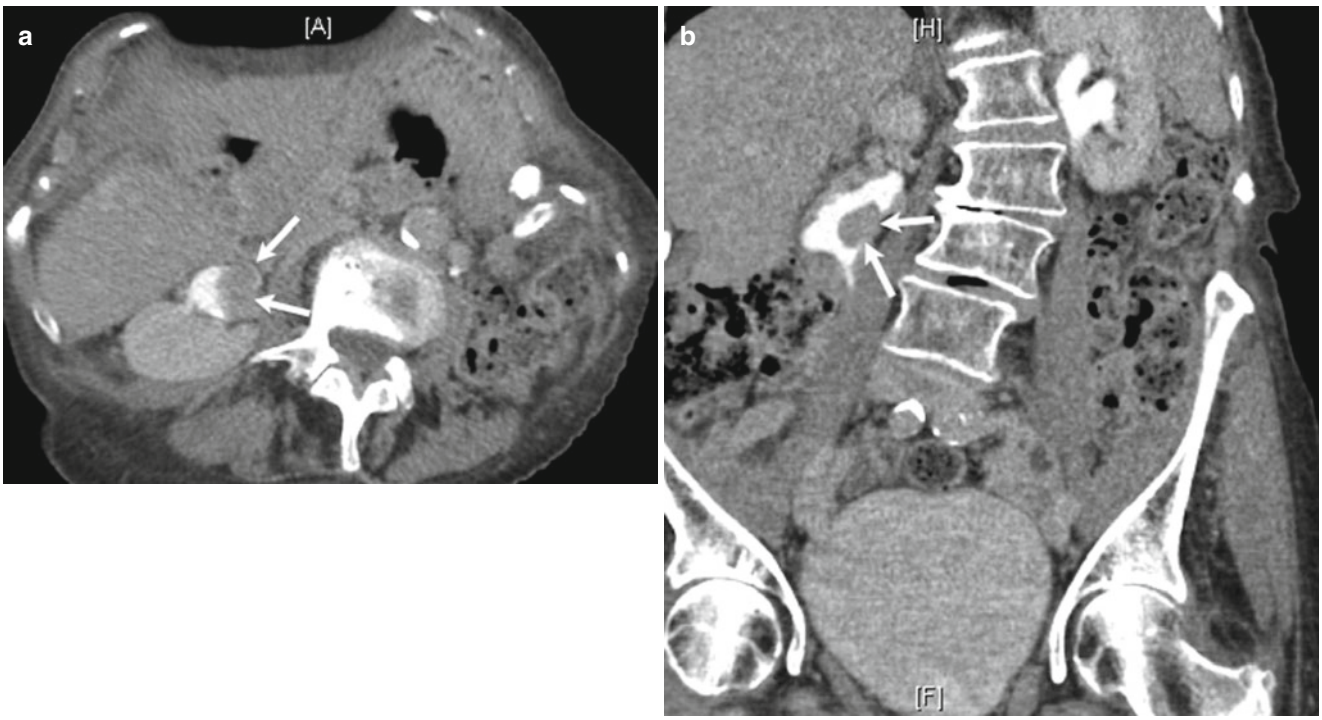

Fig. 2.16 Renal pelvis mass. Axial (**a**) and coronal (**b**) excretory phase images from CT urogram demonstrates a polypoid mass in the left renal pelvis (*arrows* (**a**, **b**)), outlined by opacified urine. This finding is suspicious for transitional cell carcinoma; however, tissue confirmation was not obtained due to the advanced age and comorbidities of the patient

may help visualize cancer within a bladder diverticulum, especially when the diverticulum is not accessible by cystoscopy (Fig. 2.18) [60].

CT is useful for detecting macroscopic extravesical tumor spread (T3b disease) from organ-confined tumor, although it will not detect microscopic perivesical fat invasion (T3a disease). CT can also be used to detect pelvic and retroperitoneal lymphadenopathy and distant metastatic deposits. Invasion of local organs, such as the prostate and rectum, can also be evaluated, although the lack of clear fat planes in the inferior pelvis can be a limiting factor in this regard. The inability of CT (and MRI) to resolve specific layers of the bladder wall significantly limits its overall accuracy in staging, especially between T1, T2, and T3 disease [29].

In addition to tumor detection and staging, other indications for CT of the bladder include trauma, fistulous disease, and assessment for rupture after biopsy, surgical procedure, or other instrumentation. Definitive evidence of bladder injury can be obtained with CT cystography which will show extravesical contrast extravasation in cases of bladder perforation and can also demonstrate whether the perforation is intra- or extraperitoneal, depending on the anatomic location of the extravasated contrast (Fig. 2.19). In the setting of blunt trauma, CT cystography has been shown to be accurate in demonstrating bladder rupture, with both sensitivity and specificity approaching 100 % [61, 62].

Magnetic Resonance Imaging: Basic Physics and Genitourinary Applications

Magnetism is an invisible force in nature, associated with the Earth, as well as many natural materials. Moving charges in an electric current flowing through a wire can produce a magnetic field. The unit of strength of a magnetic field is the tesla, with magnetic field strengths used in clinical MRI of approximately 0.5–3 T.

Protons also have a tiny associated magnetic field as a result of a spinning charge. This tiny magnetic field, called the magnetic dipole moment, can experience a force from an externally applied magnetic field. Biologic tissues are mostly composed of water molecules, which contain two hydrogen ions each consisting of a single proton. Clinical MRI applies to magnetism resulting from the proton, although electrons and neutrons have associated magnetism as well. In atomic nuclei with greater than one proton, protons will align with one another with opposite poles attracting. Pairs of protons with their unlike magnetic poles attracting lower the net magnetization of the pair. Thus, atoms with even atomic numbers will have no net magnetization.

Normally, the magnetic dipoles of hydrogen protons in tissue are randomly oriented. When exposed to an externally applied static magnetic field, such as in a clinical MRI magnet, the magnetic dipole will experience a force. The North pole of the hydrogen proton will be forced to align

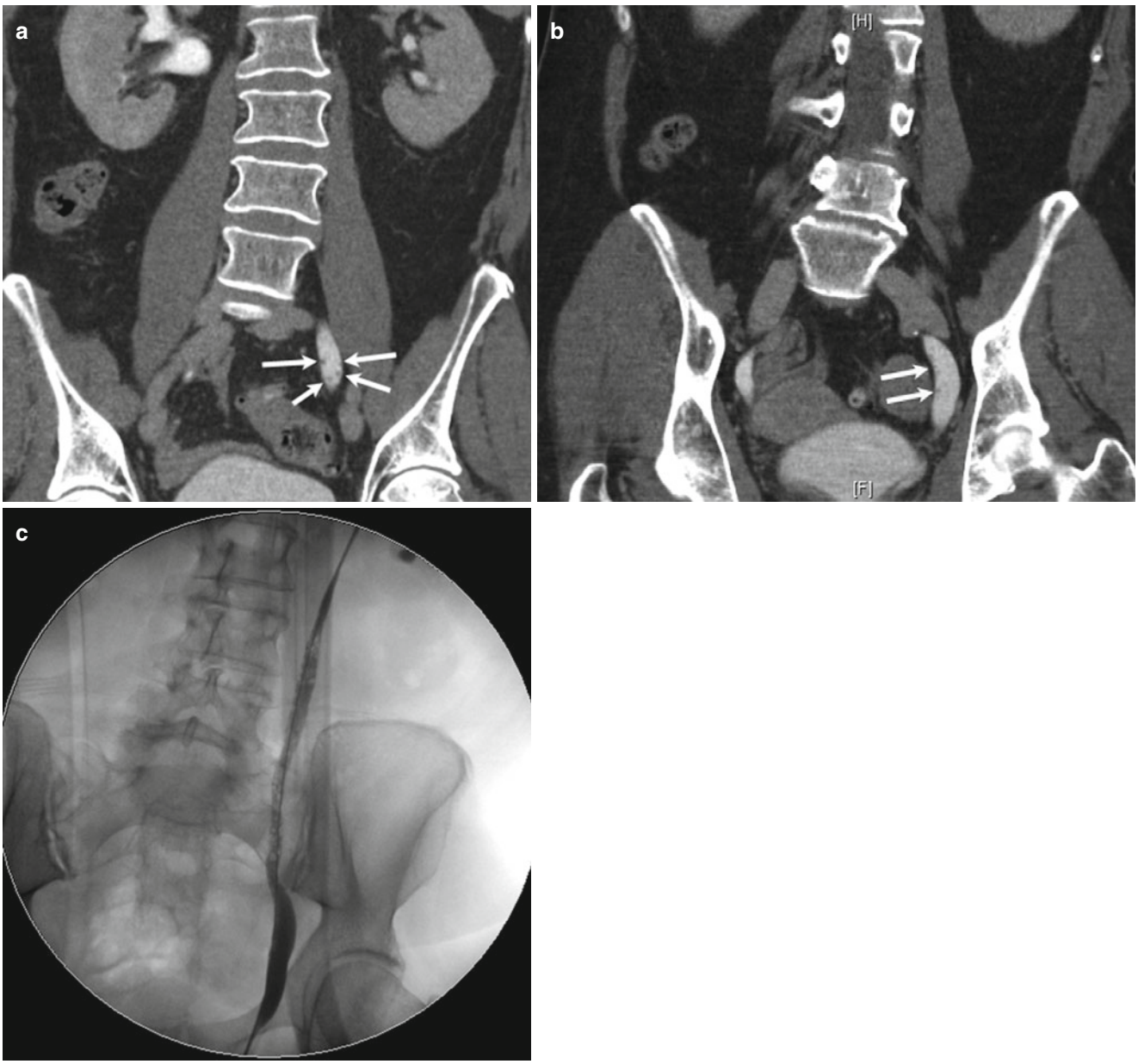

Fig. 2.17 Ureteritis cystica. Coronal images (**a**, **b**) from CT urogram demonstrate numerous tiny ureteral filling defects (*arrows*). Intraoperative fluoroscopic image obtained during retrograde pyelogram (**c**) better demonstrates the extent of ureteral involvement, with countless small intraluminal filling defects now visible

with the South pole of the external magnetic field. The proton is also forced into a spinning, precessional motion around the lines of the force of the external magnetic field, similar to that of a spinning top. The speed of proton precession, or precessional angular frequency (w), is influenced by the strength of the magnetic field and is known as the Larmor frequency. The relationship between proton precessional frequency and the external magnetic field is governed by the Larmor equation:

$$w=(y)\times(B0)$$

where (w) refers to the precessional angular frequency, (y) is the gyromagnetic ratio of the particular atom, and B0 is the strength of the external magnetic field.

When placed in a strong external magnetic field, protons are forced into parallel alignment, either with or against the direction of the magnetic field. A very slight majority of protons will align with the field, and it is this small excess which gives rise to MR signal, producing a vector (Mz) along the z-axis. This is known as the longitudinal vector.

In clinical MRI, a radiofrequency (RF) pulse in the same frequency range as the precessing protons is applied long

Fig. 2.18 Urinary bladder diverticulum with tumor. Axial contrast-enhanced CT image shows a left-sided urinary bladder diverticulum with nodular wall thickening suspicious for cancer (*arrows*)

Fig. 2.19 Urinary bladder perforation. Sagittal reformatted image from CT cystogram shows a defect in the wall of the bladder at the anterior dome and intraperitoneal contrast extravasation (*arrow*). The bladder was injured during cesarean section

enough to deviate the protons to a prescribed angle from the external magnetic field, which varies but is often 90 or 180°. This angle is known as the flip angle. Once the pulse is turned off, protons will return to their original state, a process known as relaxation, which has two components. The first is termed T1 relaxation and is defined as the time for the longitudinal magnetization to regain 63 % of its maximum value. Different tissues have different values of T1 and relax at different rates, with a short T1 relaxation time for adipose tissue and long T1 relaxation time for CSF.

The second effect of the applied RF pulse is that protons will synchronously precess, creating net transverse (Mxy) magnetization. Once net transverse magnetization is established and the RF pulse is turned off, protons will gradually precess in a more random fashion. Some protons will precess faster and others slower, a process called dephasing, resulting in decay of the Mxy vector, termed T2 relaxation. T2 relaxation time of tissue is the time it takes for the Mxy vector to decay to 37 % of its maximum value. Different tissues have different values of T2 and dephase at different rates, with short T2 relaxation time for the liver, muscle, and myocardium and long T2 relaxation time for CSF [63].

Image Formation

In addition to a static external magnetic field, the process of image formation requires the introduction of magnetic field gradients (slopes of magnetic strength), which are changes in the magnetic field strength as a function of location in the patient. Under the influence of a magnetic field gradient, resonant frequency of protons affected by the gradient varies according to location. Three different gradients are applied during image formation: slice-selection, phase-encoding, and frequency-encoding gradients, each of which is applied in one of the three spatial planes, with the information from each used to assign signal to a precise point on the image, or pixel, which is the term for the smallest resolvable unit of area on an image.

Assuming the patient is lying supine on the MRI table, gradient direction can be applied anterior to posterior, superior to inferior, or left to right to create sagittal, axial, and coronal spatial information. Initially, a slice-selection gradient is turned on, and an RF pulse with a specific bandwidth is administered to the patient, and tissue with a resonant frequency within this bandwidth is excited. The thickness of the section of tissue excited by the pulse determines the actual slice thickness and is inversely proportional to the strength of the gradient.

Subsequently, in the excited slice, a gradient is applied along the phase-encoding axis. Protons in the excited slice will be precessing at different speeds along the direction of the gradient. Protons precessing faster gain phase. After the phase-encoding gradient is turned off, the frequency-encoding gradient is applied along an axis perpendicular to the phase-encoding axis. The phase- and frequency-encoding gradients encode proton magnetic moments spatially, essentially labeling each pixel. During readout, the RF coil then detects the magnetization signal as a summation of all voxels which have each been uniquely labeled. Signal from each set of ensembles fills in one data point in k-space, which is then in turn processed into an image through Fourier transformation [63].

Pulse Sequences

An MRI pulse sequence diagram outlines the basic execution of an MRI scanner as follows: RF excitation, slice-selection

gradient, phase-encoding gradient, frequency-encoding gradient, data acquisition. These pulses are repeated many times during MRI imaging. The time between repetitions of pulse sequences is the repetition time (TR). The time between the RF pulse and the greatest MRI signal from transverse magnetization is the echo time or TE. The TR and TE are important tissue-related parameters having impact on image contrast. The TR is selected by the MRI operator and impacts the level of T1 contrast between tissues. If the TR is long, T1 relaxation differences between tissues are minimized. A short TR allows for greatest T1 contrast between tissues; therefore, T1-weighted images employ short TRs. T2-weighted sequences utilize a long TR in order to decrease T1 contrast and a long TE to optimize T2 contrast between tissues. Tissues with short T1 times will be brighter on T1-weighted images, while tissues with long T2 times will have higher signal on T2-weighted sequences [64–66].

Spin Echo

Spin-echo and fast spin-echo sequences are the mainstay of conventional MR imaging. This sequence begins with a 90° RF pulse followed by a 180° refocusing pulse at time TE/2. The signal produced at time TE fills one row of k-space. At time interval TR, the whole process is repeated to fill subsequent rows of k-space. TR and TE affect weighting as described above and can be tailored to provide either T1- or T2-weighted sequences. Spin-echo sequences have low sensitivity to magnetic field inhomogeneities and magnetic susceptibilities due to the application of the above-described 180° refocusing pulse [64–66].

Due to the very long imaging times of spin-echo sequences, they have largely been replaced by fast spin-echo (FSE). FSE is a variation on spin echo, whereby multiple rows of k-space are filled in a single TR interval. This results in much faster imaging times, with similar image quality, signal, and resolution to conventional spin-echo sequences [65, 66].

Gradient-Recalled Echo (GRE)

These sequences, of which there are numerous variations, begin with a small (<90° flip angle) which tips longitudinal magnetization and creates some transverse magnetization. Unlike spin-echo imaging, a 180° refocusing pulse is not applied in GRE. A negative frequency gradient pulse causes rapid dephasing of transverse magnetization followed by a positive frequency gradient pulse which rephases transverse magnetization and produces a gradient echo at TE.

Due to the use of small flip angles and the lack of a refocusing pulse, GRE images can be obtained with extremely short TR and TE values, allowing for rapid acquisition times. GRE sequence times are measured in seconds, as opposed to spin-echo sequences, which take minutes to complete, thus allowing breath-hold imaging to be performed. GRE sequences are vital for imaging the upper abdomen and to a lesser degree the pelvis, where fast sequences are necessary to minimize degradation from respiratory movements. GRE techniques also allow for volumetric imaging, including 3D magnetic resonance angiography and volumetric acquisitions [65, 67].

Inversion Recovery

This sequence begins with a 180° RF pulse causing inversion of the initial longitudinal tissue magnetization. A standard spin-echo sequence is then performed. During TI or inversion time, T1 relaxation causes different tissues to regain their longitudinal magnetization at different rates, which is the basis for T1 contrast. An inversion time (TI) can be chosen such that when a 90° spin-echo excitation occurs, a particular tissue magnetic moment will be at its "null point" and thus contribute very little to the overall signal. This property is utilized in short inversion time inversion-recovery (STIR) sequences for fat saturation and in fluid attenuated-inversion-recovery (FLAIR) sequences for saturation of water signal [64, 68, 69].

Diffusion-Weighted Imaging (DWI)

This is essentially a spin-echo T2-weighted sequence with a dephasing or diffusion-sensitizing gradient applied between the initial 90° RF pulse and the subsequent 180 pulse and a symmetric rephasing gradient applied after the 180° pulse. The basic idea behind DWI is to measure the degree of molecular motion during the time between these two gradients. DWI sequences can be performed with a range of B values. The B value refers to the strength of the diffusion-sensitizing gradient and is proportional to gradient amplitude, duration, and time interval between paired gradients.

The motion of water molecules in an environment of tightly packed cells or inflammatory debris will be restricted. Any change in phase acquired by the dephasing gradient is canceled by the rephasing gradient; thus signal from these tissues will be mostly preserved. Conversely, water molecules which are not restricted by their local environment can move relatively long distances after the initial gradient, and the effect of the first gradient will not be completely canceled out by the second gradient, resulting in net loss in signal intensity. In practice, this means that tissues with restricted diffusion will have higher signal than tissues with free diffusion. This difference in signal becomes more pronounced as the B value is increased. For instance, at a B value of 0, free water molecules have high signal intensity; signal and contrast from a B_0 image mirror that of a T2-weighted image. As the B value is increased, water molecules in a nonrestricted environment will lose their signal, while restricted tissues retain their signal.

Quantitative analysis of diffusion properties can be performed by the generation of apparent diffusion coefficient (ADC) maps, which are routinely obtained in clinical practice. Note that signal on the ADC maps is the opposite of

what is on the actual diffusion images described above: areas of restricted diffusion will be dark, while tissues with free diffusion will have bright signal [70, 71].

Fat Suppression

Due to differences in their local molecular environment, protons in fat have a slightly different resonant frequency than do protons in water. Fat suppression refers to the application of an RF pulse at the resonant frequency of fat protons, which selectively suppresses fat signal. Removal of high-signal fat has two important benefits in abdominal MR imaging. The first, more general benefit, is that fat suppression results in an image which is more sensitive to signal intensity differences, either from innate tissue properties or from contrast enhancement. This results in increased conspicuity of pathologic processes and enhancement. For these reasons, frequency-selective fat-suppressed imaging has become an essential element of the abdominal MRI exam.

A second and more specific benefit of fat suppression is the characterization of lesions containing macroscopic fat; such lesions will lose signal on fat-suppressed sequences as compared with the same sequence performed without fat suppression. Renal angiomyolipomas, adrenal myelolipomas, and retroperitoneal liposarcomas are examples of some of the more commonly encountered lesions in the urinary tract/retroperitoneum which contain macroscopic fat [67–69].

In- and Opposed-Phase (Chemical Shift) Imaging

This is a T1-weighted gradient echo sequence. Due to slight differences in their local chemical environment, water and fat protons will precess at slightly different frequencies. Over time, they will periodically resonate in phase and out of phase with each other at regular, predictable intervals, which is dependent on the magnetic field strength. This property is exploited with in- and opposed-phase imaging. Signal intensity on sequences obtained when water and fat protons are in phase with each other reflects the sum of the magnitude of water and fat signals. Conversely, opposed-phase imaging reflects the difference in magnitude of the opposed-phase water and fat vectors, as these vectors are opposed in direction and cancel each other out. Thus, tissues composed of 50 % fat and 50 % water will, in theory, have maximal signal loss (complete dropout) [67–69]. Conversely, tissues composed entirely or almost entirely of fat, such as some renal angiomyolipomas or adrenal myelolipomas, will have no change in signal as compared to the in-phase sequence (no dropout). Such lesions are best characterized on frequency-selective fat-suppressed sequences.

In- and opposed-phase imaging is routinely employed in urologic MR applications and plays a fundamental role in characterizing lesions containing microscopic fat. Examples of applications include fat detection in adrenal adenomas and clear-cell renal cell carcinoma. Opposed-phase images can be readily identified by a well-demarcated black line at any fat-water interface, the so-called India-ink artifact.

MR Urography

MR urography is an excellent method for noninvasive imaging of the urinary tract. Indications include evaluation of urinary tract obstruction, hematuria, congenital anomalies, and pre- and postsurgical anatomy. MR urography avoids the use of ionizing radiation and thus is of great benefit in evaluating pregnant patients and the pediatric population. MR urography is composed of two components: static-fluid MR urography and excretory MR urography.

In static-fluid MR urography, heavily T2-weighted sequences of the urinary tract are acquired, typically consisting of both high-resolution images and fast images acquired in rapid succession to create a cine series. Together, these can visualize the collecting systems, ureters, and bladder in their entirety. As visualization does not depend on excretion of contrast, static-fluid techniques are especially helpful in patients with dilated collecting systems and/or decreased renal function, in whom there may be poor contrast excretion and urinary tract opacification. Static-fluid techniques are also beneficial in subgroups of patients who are unable to receive intravenous contrast, including pregnancy, renal failure, and allergy.

Excretory MR urography, as its name implies, is performed in the excretory phase of contrast enhancement and can aid in the detection of mass lesions and assessment of renal function. Diuretic administration, usually low-dose furosemide, improves image quality in nondilated systems by enhancing urine flow, diluting the excreted contrast, and mildly distending the urinary tract.

Limitations of MR urography include long examination times, lower spatial resolution as compared with CT, and relative insensitivity to urinary tract calculi [72–74].

Basic Examination

The MRI exam begins with the patient being placed on a gantry which passes through the bore of the magnet. When exposed to a magnetic field, free water protons within atoms orient along the z-axis (head-to-toe axis) of the magnetic field. A radiofrequency coil is placed over the body part of interest. This typically consists of a coil which is placed outside the patient, positioned over the front and back of the patient; however, internal coils, such as endorectal coils, can be used for specific indications. The coil transmits the RF pulse through the patient. The effects of the RF pulse on the protons are expressed as a signal to obtain the magnetic

resonance image. Common generic sequences utilized in MR imaging of the GU tract include fast spin echo, single-shot fast spin echo with half-Fourier acquisition, 2D spoiled gradient echo, 3D spoiled gradient echo, and balanced steady-state gradient echo. Unfortunately, each MRI vendor has created unique trade names for these sequences, which often leads to undue confusion in trying to understand the properties, benefits, and limitations of each sequence [75].

Weighting of the image depends on TR and TE values as mentioned earlier in the general physics section. On T1-weighted images, fluid is low in signal, while on T2-weighted images, fluid is bright.

Relative and Absolute Contraindications

As there are many potential risks due to the strong magnetic field of MRI scanners, and previous adverse events and injuries have occurred involving patients, personnel, and equipment, the American College of Radiology recommends that all clinical and research MRI sites have a restricted zone, which includes the actual scanner room and an adjoining area, in which access is allowed only after careful MR safety screening. Any implantable device or potential foreign object must be carefully investigated for MR compatibility prior to the patient entering the restricted zone. These include, but are not limited to, vascular stents, stapes implant, implanted drug infusion device, neural growth stimulator, surgical clips, wire sutures, ocular prosthesis, joint replacement or prosthesis, bullets, and other foreign objects.

Contraindications to MRI include metal-containing implants which have the ability to heat or move when under the influence of a strong magnetic field or electronic implants which may be interrupted or permanently altered. These include pacemakers and defibrillators, metallic foreign body in the eye, deep brain stimulator, Swan-Ganz catheter, bullets or gunshot pellets, cerebral aneurysm clips, cochlear implants, magnetic dental implants, and drug infusion devices.

Other obstacles to MR examination include large patients that may be difficult to accommodate in the MRI bore, claustrophobic patients requiring sedation, significant pain limiting the patient's ability to lie still, and surgery in the previous 6 weeks [76].

Applications of MRI in the Urinary Tract

While CT is often the initial imaging modality for investigating genitourinary tract disease, advances in MRI, especially in terms of speed of image acquisition, have greatly improved the capabilities of MR imaging. MRI is superior to CT with regard to contrast resolution of soft tissue, often being able to further characterize equivocal CT or ultrasound findings. MRI can frequently provide substantial information when iodinated contrast for CT cannot be administered, even in situations where contrast cannot be administered for the MR examination. One important limitation of MRI with regard to CT is inferior spatial resolution. Below we will explore the specific applications of MR imaging of the genitourinary tract by organ.

Kidney

CT is usually the first-line modality for renal mass evaluation; however, contrast-enhanced MRI has been shown to be a highly accurate modality for both detection and characterization of renal lesions [77, 78]. MRI is often useful for more definitive characterization of indeterminate lesions seen on CT. Weakly enhancing neoplasms such as papillary renal cell carcinoma may demonstrate equivocal levels of enhancement on CT [79–81]. Detection of enhancement within small (<1.5 cm) lesions is frequently confounded on CT due to pseudoenhancement artifact [30, 31]. Intralesional high attenuation within hemorrhagic cysts or tumors can make detection of enhancement difficult on CT. In all of these scenarios, MRI can provide more definitive evidence of enhancement and thus guide management [28, 77, 78, 82]. When evaluating cystic renal lesions, MRI can readily detect a proteinaceous or hemorrhagic cyst as a nonenhancing lesion with high T1 signal and can accurately evaluate the presence or absence of septal enhancement (Fig. 2.20) [28]. Calcifications within a complex cyst may cause artifact on CT, however calcifications do not interfere with the detection of enhancement on MRI. Therefore, MRI can more accurately detect enhancement within the wall of a complex cyst than will CT. Subtraction images, obtained by electronically subtracting the pre-contrast sequence from the post-contrast sequence, generate images composed exclusively of contrast signal and are useful in assessing enhancement (Fig. 2.21) [78, 82].

MRI can be used for staging renal cell carcinoma, with several studies showing similar accuracies of CT and MRI in staging based on the TNM system, including detection of renal vein and inferior vena cava invasion (Fig. 2.22) [83].

MRI is also useful in detecting fat within angiomyolipomas (AMLs). T1 fat-suppressed images are virtually diagnostic for AML if there is signal loss in the lesion when compared with a similar sequence performed without fat suppression (Fig. 2.23). 4–5 % of AMLs are lipid poor and either contain no fat or insufficient fat to be detected on imaging; these lesions cannot be reliably differentiated from renal cell cancer with any imaging modality [84]. Some AMLs may also lose signal (dropout) on opposed-phase imaging due to the presence of microscopic amounts

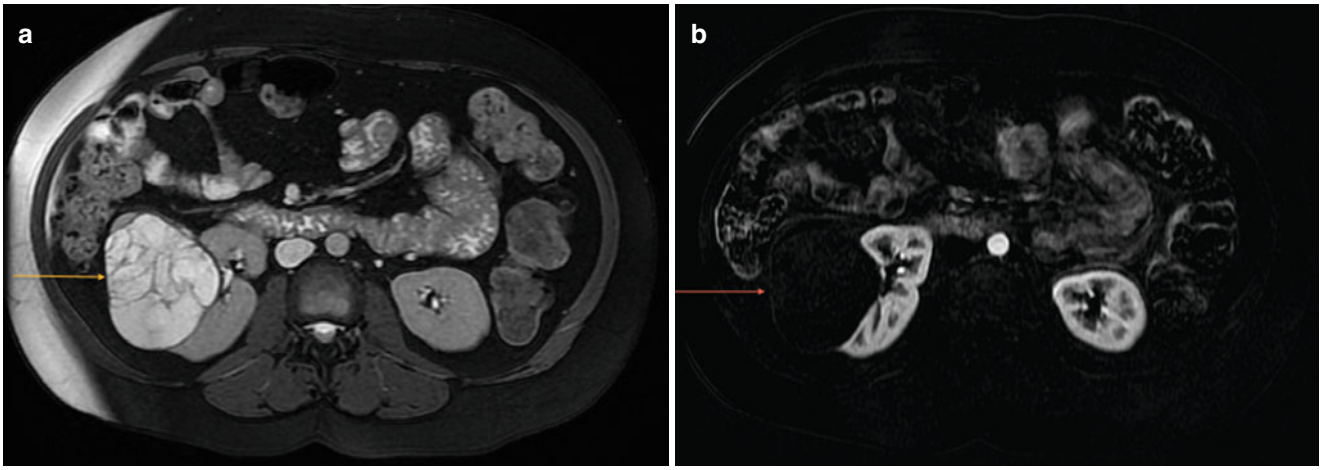

Fig. 2.20 Complex cystic renal mass. Axial T2-weighted (**a**) MRI image demonstrates a cystic right renal mass with numerous septations of varying thickness (*orange arrow* (**a**)). Contrast-enhanced subtraction image (**b**) shows the lack of enhancement within the wall of the mass or any of the septations (*arrow* (**b**)). The numerous septations in this mass raise suspicion for cystic renal cell carcinoma; however, the complete lack of enhancement suggests benignity: the septations may be sequelae of prior intracystic hemorrhage. This mass was stable for several years and thus likely benign

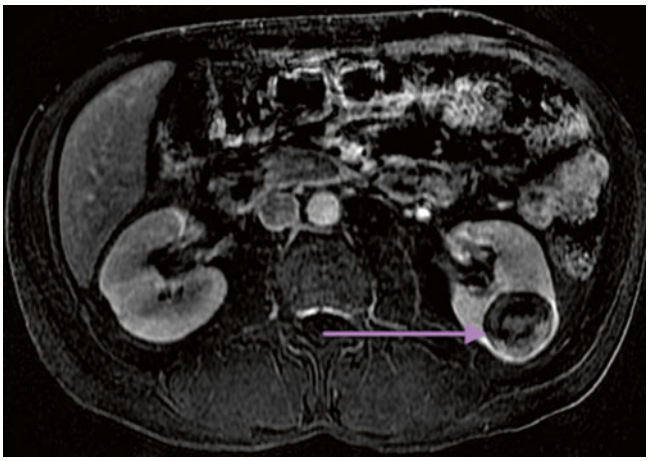

Fig. 2.21 Papillary renal cell carcinoma. Axial T1 post-contrast subtraction image at 100 s after contrast administration demonstrates mild heterogeneous enhancement of a left renal mass (*arrow*). Most papillary renal cell carcinomas demonstrate weak enhancement as compared with renal parenchyma. Subtraction images aid in evaluation of enhancement within a lesion. This finding was confirmed surgically

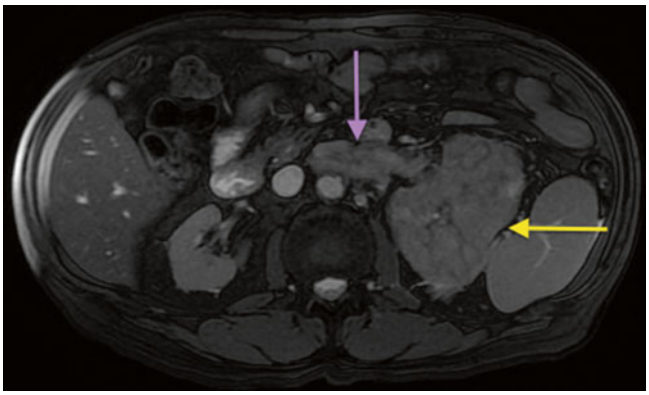

Fig. 2.22 Renal cell carcinoma with renal vein invasion. Axial "bright-blood" balanced gradient echo image demonstrates a large mass involving the left kidney (*yellow arrow*) with expansion of the left renal vein compatible with tumor thrombus (*purple arrow*). Note the difference in signal between the tumor-infiltrated left renal vein and the patent inferior vena cava. In patients who cannot receive intravenous contrast for MRI due to renal insufficiency, non-contrast imaging, including conventional, diffusion-weighted, gradient echo, and even MRA sequences, can often provide substantial information as compared to unenhanced CT scan

of fat within the tumor; however, caution should be exercised with this finding, as clear-cell renal cell carcinoma can also contain intracellular lipid and thus dropout on opposed-phase images (Fig. 2.24) [84, 85].

Adrenal

CT is the primary imaging modality for evaluating the adrenal glands; however, MRI plays a role in characterizing an adrenal mass in the setting of an equivocal CT and in patients who cannot receive iodinated contrast for CT. MRI is particularly useful in differentiating adrenal adenoma from metastasis.

Adrenal metastases and adenomas are differentiated on the basis of chemical shift imaging. Adrenal adenomas contain intracellular lipid, whereas metastases do not. If the lesion in question demonstrates signal dropout on opposed-phase imaging, then it likely represents an adenoma (Fig. 2.25), except in rare instances, such as metastatic disease from a clear-cell renal cell carcinoma. Lesions with no change in signal on out-of-phase imaging either do not contain lipid or contain insufficient quantities of lipid to be detected on MRI and are thus indeterminate. Such a lesion could represent a lipid-poor

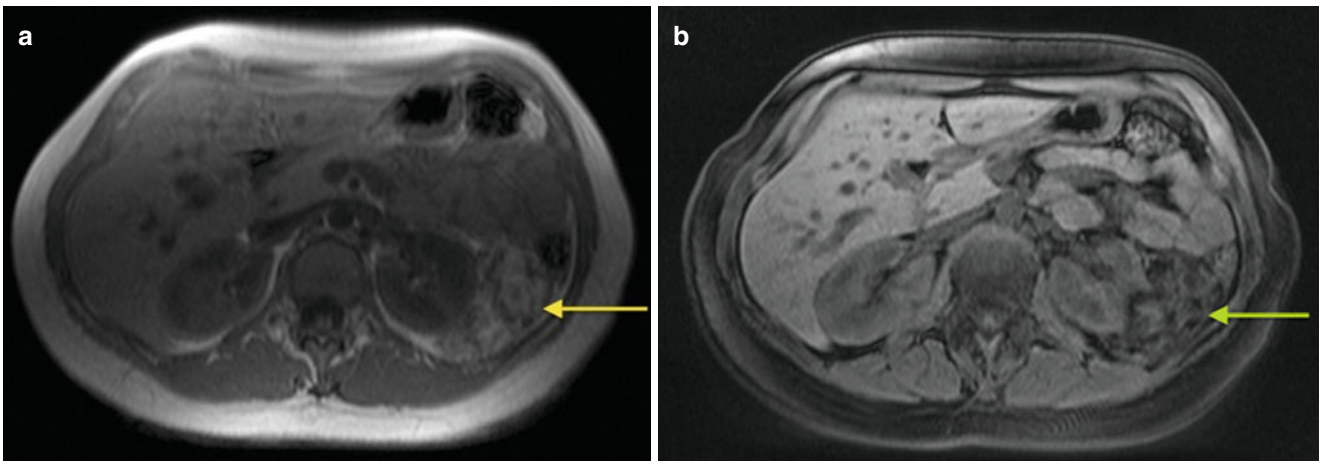

Fig. 2.23 Renal angiomyolipoma. Axial T1-weighted images obtained without (**a**) and with (**b**) fat suppression demonstrate a large, exophytic left renal mass (*arrows*) with areas of bulk fat which is bright on (**a**) and loses signal on the fat-suppressed image (**b**), compatible with an angiomyolipoma

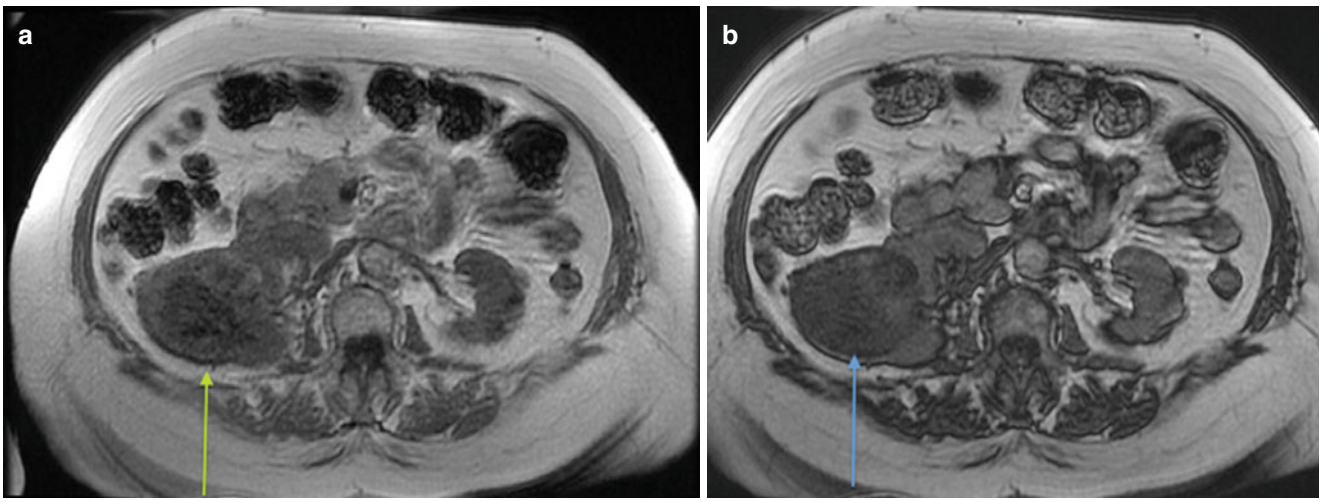

Fig. 2.24 Clear-cell renal cell carcinoma. Axial T1 in-phase (**a**) and opposed-phase (**b**) images demonstrate signal dropout within a large right renal mass (*arrows*) on opposed-phase imaging, confirming the presence of intracellular lipid. Dropout can also be seen in angiomyolipomas; however, in a lesion without macroscopic fat, this finding raises suspicion for clear-cell renal cell carcinoma, which was surgically confirmed

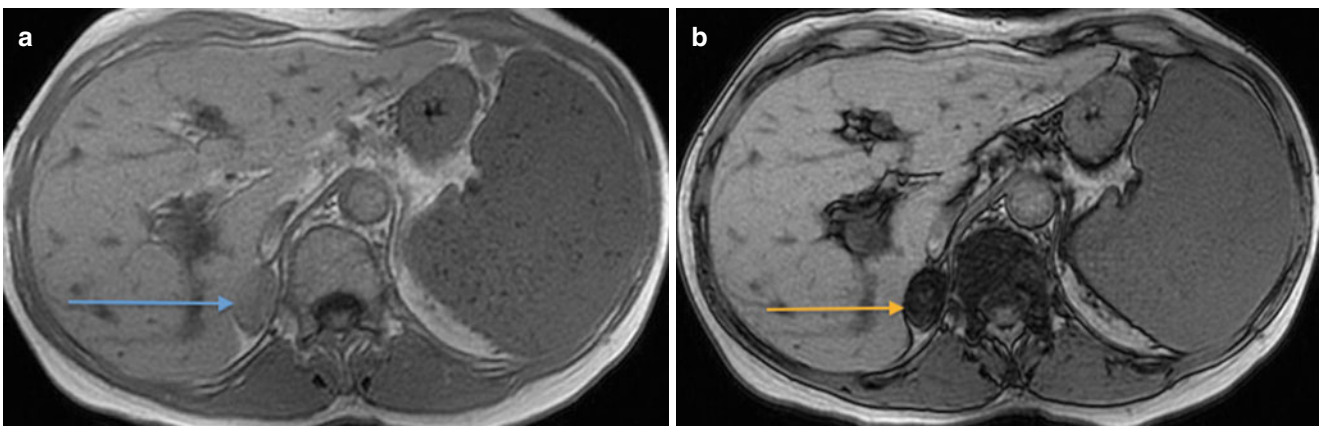

Fig. 2.25 Adrenal adenoma. Axial T1 in-phase (**a**) and opposed-phase (**b**) images demonstrate signal dropout of a right adrenal nodule (*arrows*) on opposed-phase imaging, confirming the presence of intracellular lipid and the diagnosis of an adrenal adenoma

adenoma or a non-adenomatous lesion. The sensitivity for adenoma detection with chemical shift imaging is approximately 80 % [86], which is similar to unenhanced CT.

Other adrenal lesions that can be specifically characterized by MRI include cyst and myelolipoma. However, the differential diagnosis of a non-cystic adrenal nodule devoid of fat is wide and must be correlated with a thorough biochemical and hormonal work-up for accurate diagnosis.

Approximately 65 % of pheochromocytomas are "light-bulb" bright on T2-weighted sequences; however, this is not a particularly sensitive or specific finding. A pheochromocytoma cannot be excluded on the basis of low T2 signal intensity, and other adrenal lesions, both benign and malignant, may have bright T2 signal [87, 88]. MRI, however, is an excellent modality for identifying extra-adrenal sites of pheochromocytoma, including the organ of Zuckerkandl, retroperitoneum, or carotid bulb.

Ureter and Bladder

MR urography is a useful method to evaluate the ureter and the bladder, especially in the pediatric age group and pregnant patients and in the setting of a contraindication to iodinated contrast. Congenital anomalies (Fig. 2.26), stenoses, obstruction, and filling defects due to stricture or neoplasm can be readily identified. MRI is significantly inferior to CT in the detection of ureteral calculi. The diagnosis of an obstructing ureteral stone on MRI is often made based on secondary findings, such as perirenal edema, ureteral dilatation, and perirenal fluid (Fig. 2.27) [72–74]. The role of MRI in bladder disease is not well established, although MRI has been used to detect tumors within diverticula, characterize intravesical pheochromocytoma, detect urachal tumors, and stage bladder cancer [89].

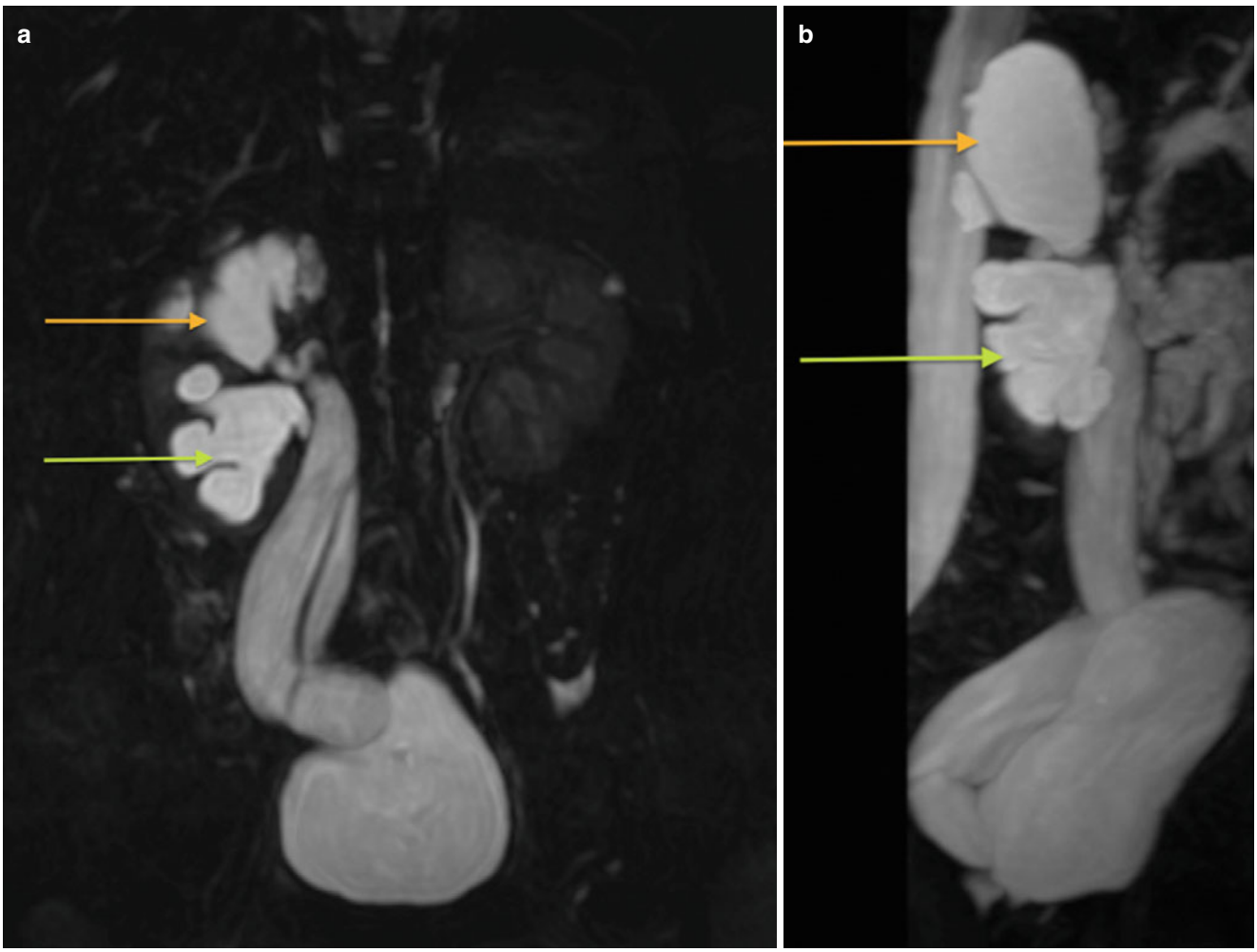

Fig. 2.26 Congenital duplicated renal collecting system with obstruction. Coronal (**a**) and sagittal (**b**) heavily T2-weighted images from an MR urogram demonstrate a right duplex collecting system with obstruction of the upper pole collecting moiety (*orange arrow*) and a low ectopic insertion of the ureter draining the upper pole (**b**). There is also dilatation of the lower pole collecting system (*green arrows*), possibly due to reflux

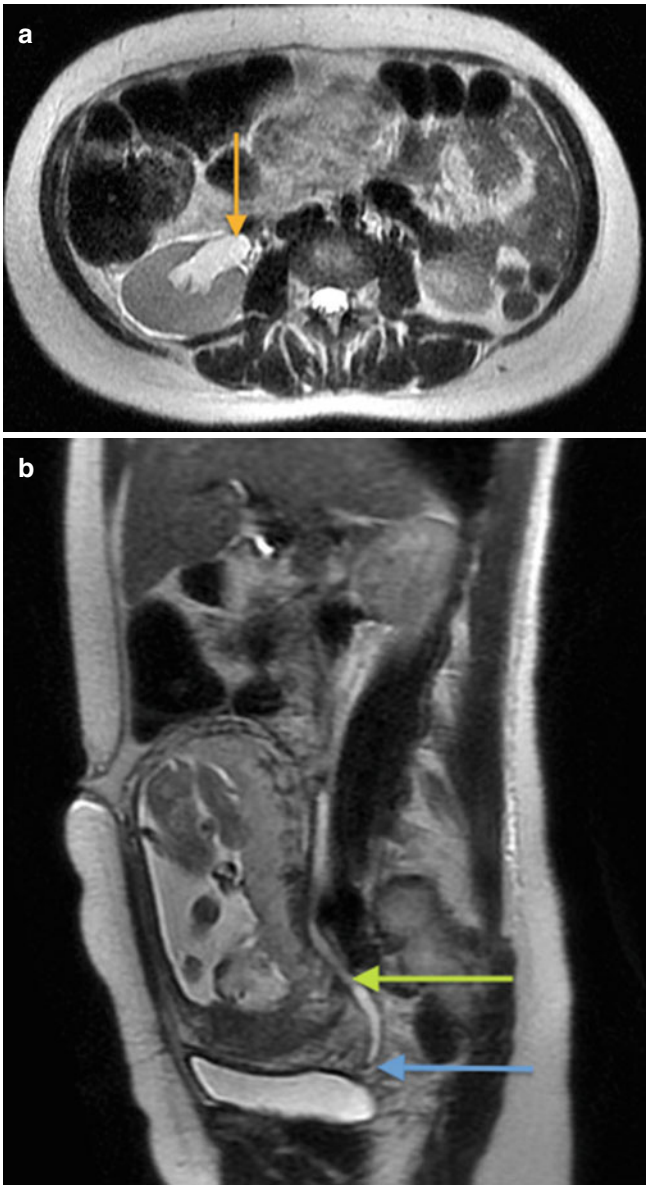

Fig. 2.27 Obstructing right ureteral calculus in a pregnant patient. Axial (**a**) and sagittal (**b**) T2-weighted images demonstrate mild right hydronephrosis (*orange arrow*) and hydroureter (*green arrow*) secondary to a low-signal distal right ureteral calculus (*blue arrow*). A gravid uterus is noted. In hydronephrosis of pregnancy, the ureter usually shows gradual tapering at the level of the pelvic brim, as opposed to this example, where the ureter remains dilated down to the ureterovesical junction

Prostate

MRI of the prostate offers accurate detection and local staging of prostate cancer. The advent of high-strength (3 T) magnetic fields and endorectal surface coils has led to signal to noise ratio increases, providing higher-resolution imaging of the prostatic surface and internal anatomy. A complete MRI exam of the prostate should include conventional T1- and T2-weighted spin-echo sequences, DWI with correlative ADC maps, and dynamic contrast-enhanced sequences. Prostate cancer typically appears as a region of hypointense T2 signal. The majority of cancers are located in the normally T2-hyperintense peripheral zone and often demonstrate diffusion restriction. Approximately 30 % of cancers occur in the central zone. Detection of these cancers may be more problematic due to the frequent presence of hyperplasia, resulting in a background of heterogeneous T2 signal and enhancement.

DWI now plays an important role in prostate cancer detection on MRI [90–92]. The use of high B values (1000 or greater) may increase sensitivity and specificity for lesion detection (Fig. 2.28) [93].

Contrast-enhanced imaging is typically performed with repeated ultrafast acquisitions after contrast injection, which provide high temporal resolution and the ability to assess contrast enhancement as a function of time. Prostate cancer generally demonstrates earlier and higher peak enhancement and early washout as compared with normal prostatic tissue [93].

MR spectroscopy is a technique which can separate out compounds in tissue based on their Larmor frequency (see discussion above). Citrate is found in relatively high concentrations in normal prostate and decreased amounts in prostate cancer (and other conditions such as prostatitis and hemorrhage). Choline can be detected on MRI spectroscopy as an aggregate peak of choline-containing cell membrane compounds. Choline is found in high amounts in prostate cancer due to rapid cell membrane turnover and relatively increased cell surface ratio. Increased choline concentration is the hallmark of prostate cancer, although it can be found in benign conditions such as prostatitis [93].

MRI is the most accurate imaging modality for differentiating between organ-confined (T1 or T2) and extracapsular (T3) diseases, although there are a wide range of sensitivities and specificities reported in the literature [93].

MRI is also playing a larger role in obtaining tissue diagnosis of prostate cancer. MR images can be coregistered with real-time ultrasound (US) imaging (MRI/US fusion biopsy), providing a target for US-guided biopsy. This has been shown to increase cancer detection rates compared with traditional transrectal US-guided biopsy, which is typically performed in blind fashion, by obtaining 12 core samples, without visualization of a target lesion. MRI/US fusion biopsy appears to be especially suited for patients with high suspicion for prostate cancer and negative US-guided biopsy [94].

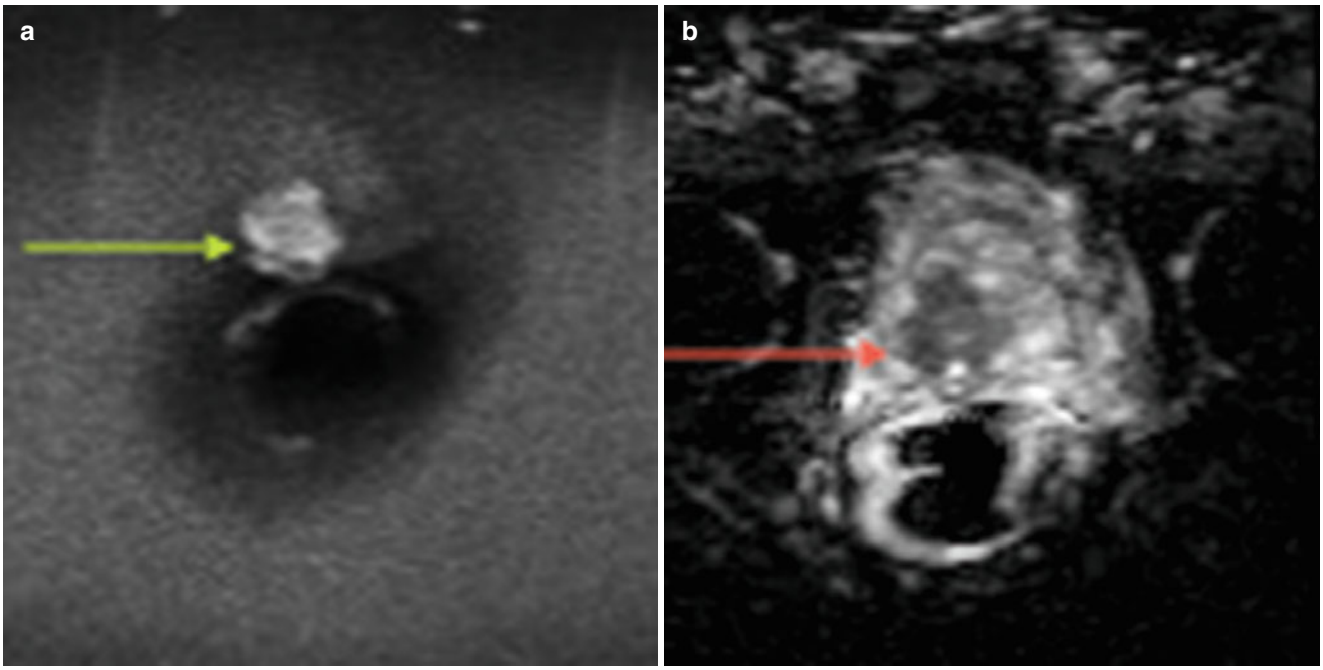

Fig. 2.28 Prostate cancer. b2000 diffusion-weighted image (**a**) and corresponding ADC map (**b**) demonstrate a large region of diffusion restriction within the peripheral zone of the prostate on the right, manifested by high signal on the diffusion image (*green arrow*, (**a**)) and low signal on the ADC map (*red arrow* (**b**)). Such markedly restricted diffusion is a highly suspicious finding for malignancy

Scrotum

Ultrasound is the primary imaging modality for the evaluation of the scrotum and testicles. MRI evaluation of the scrotum is limited by long examination times and lack of portability and availability, especially after hours. On MR, normal testes have homogeneous intermediate intensity on T1-weighted images and high signal on T2-weighted images. The testicles are surrounded by the fibrous tunica albuginea, which is low in signal intensity on T2-weighted images. The role of MRI in imaging the scrotum often revolves around adding additional information in cases where ultrasound findings are equivocal. For example, MRI can help define the pattern of injury in the setting of testicular trauma. An area of heterogeneous signal intensity on T2-weighted images should raise the possibility of testicular injury. Disruption in the normal low-signal tunica albuginea is diagnostic of testicular rupture; therefore, the tunica should be carefully assessed in all three planes [16, 95]. Another emerging application for scrotal MRI is in the differentiation of segmental testicular infarction versus small neoplasm. An avascular area on contrast-enhanced images with an enhancing rim is typically seen with infarction [16, 96]. Although not typically used in diagnosing and staging testicular cancer, MRI has been shown to be quite sensitive and specific in detecting testicular tumors, differentiating benign from malignant lesions (Fig. 2.29), and diagnosing local invasion [97].

Penis

Ultrasound is the primary modality in the evaluation of penile disease; however, MRI does have a role in the evaluation of blunt penile trauma. MR is able to depict the fascial layers of the penis in exquisite detail, demonstrating the presence and site of disruption of the normal low-signal tunica albuginea surrounding the corpus cavernosa (Fig. 2.30) and directing surgical repair [16, 98–100]. Other potential applications of MRI in evaluating penile disease include cancer staging, mass characterization, detection of plaques in Peyronie's disease, and localization of periurethral abscesses [16, 100].

Female Urethra

MRI plays a significant role in the diagnosis of urethral and periurethral disease in women, particularly in the evaluation of ureteral diverticula. The examination can be performed with a torso phased-array coil or an endoluminal coil

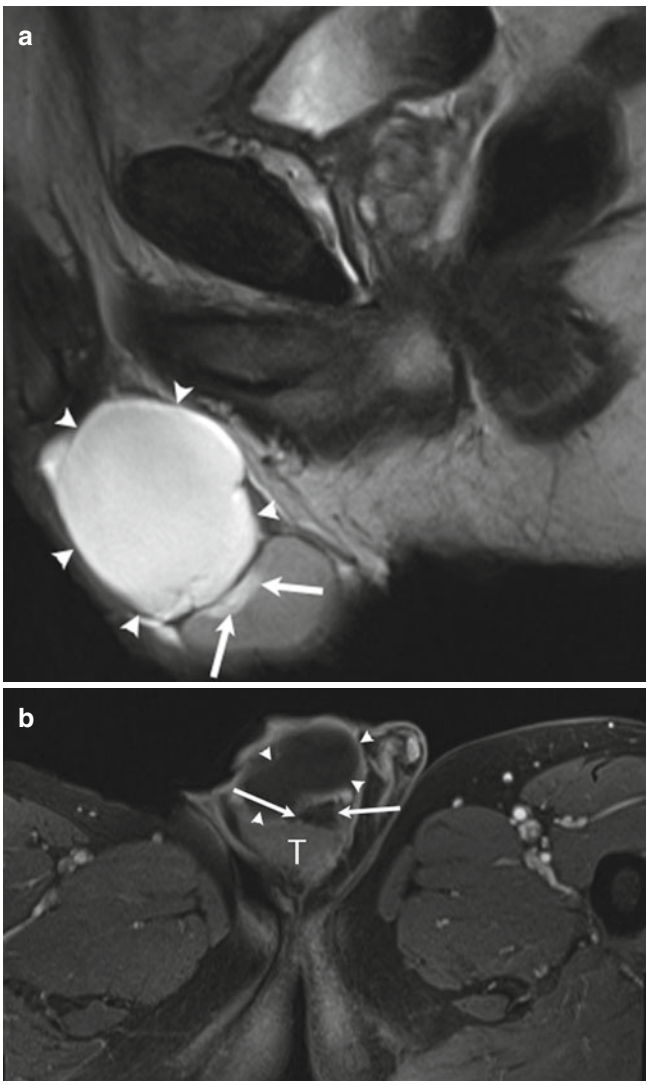

Fig. 2.29 Epididymal head cyst and dilatation of the rete testes. Sagittal T2-weighted (**a**) and axial T1-weighted gadolinium-enhanced images (**b**) demonstrate a large mass (*arrowheads*) above the right testicle ("T" in (**b**)). This is uniformly hyperintense on the T2-weighted and does not enhance, compatible with an epididymal head cyst. The patient had been referred to MRI for the evaluation of an indeterminate testicular lesion seen on ultrasound. The lesion (*arrows*) is bright on the T2-weighted sequence and does not enhance, compatible with a benign lesion, most likely dilatation of the rete testes

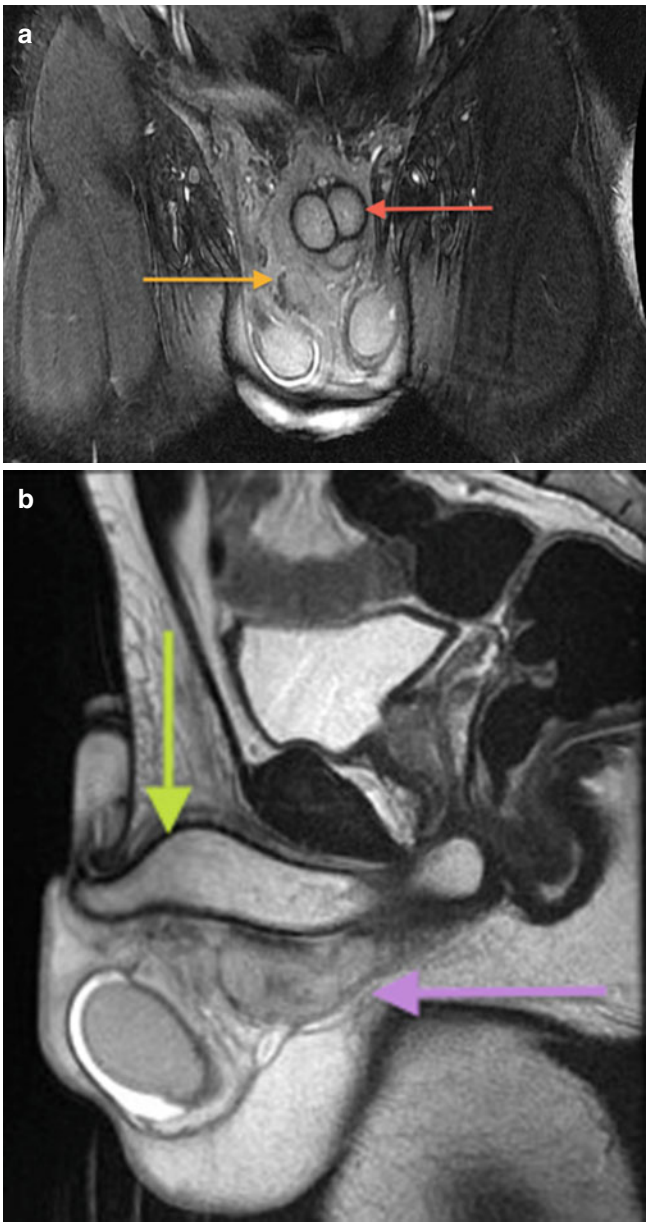

Fig. 2.30 Coronal (**a**) and sagittal (**b**) T2-weighted, fat-saturated MRI sequences demonstrate a mixed-signal collection inferior to the penile shaft (*orange arrow* in (**a**), *purple arrow* in (**b**)) compatible with a hematoma. The low-signal tunica albuginea is well visualized and is intact (*red arrow* in (**a**), *green arrow* in (**b**))

(endovaginal, endorectal, endourethral) to improve resolution and signal to noise ratio. Normally, on T2-weighted images, the urethral mucosa and muscle are hypointense, while the submucosa is hyperintense. A urethral diverticulum can be identified as single or multiple, unilocular, or multilocular on T2-weighted images. Circumferential involvement of the urethra, in a "saddle bag" configuration, is a common appearance of a urethral diverticulum. Post-contrast administration aids in the detection of diverticular inflammation or adenocarcinoma, depicted as a small enhancing soft tissue mass within the diverticulum. MRI is more sensitive than urethrography and urethroscopy for the diagnosis of urethral diverticulum and is indicated when clinical suspicion is strong and other modalities are inconclusive [101].

References

1. Bushberg JT, Boone JM. The essential physics of medical imaging. Philadelphia: Lippincott Williams & Wilkins; 2011.
2. Resnick MI, Spirnak JP. Basic principles of ultrasound. In: Gillenwater JY, editor. Adult and pediatric urology, vol. 1. Philadelphia: Lippincott Williams & Wilkins; 2002.
3. Scherzinger AL, Stamm E. Ultrasound-concepts and transducers. In: RSNA/AAPM Physics Modules members-only website. Retrieved from http://www.rsna.org/RSNA/AAPM_Online_Physics_Modules_.aspx.
4. Feldman MK, Katyal S, Blackwood MS. US artifacts 1. Radiographics. 2009;29(4):1179–89.
5. Badler R, Bordia R, Venkataramanan N. Interaction of ultrasound tissue and Doppler. In: RSNA/AAPM Physics Modules members-only website. Retrieved from http://www.rsna.org/RSNA/AAPM_Online_Physics_Modules_.aspx.
6. Evans KD, Layman R, Volz K. Image quality-artifacts-doppler-safety. In: RSNA/AAPM Physics Modules members-only website. Retrieved from http://www.rsna.org/RSNA/AAPM_Online_Physics_Modules_.aspx.
7. Merritt CR. Doppler US: the basics. Radiographics. 1991;11(1):109–19.
8. Daneman A, Navarro OM, Somers GR, Mohanta A, Jarrín JR, Traubici J. Renal pyramids: focused sonography of normal and pathologic processes 1. Radiographics. 2010;30(5):1287–307.
9. Hartman DS, Choyke PL, Hartman MS. From the RSNA refresher courses: a practical approach to the cystic renal mass 1. Radiographics. 2004;24 Suppl 1:S101–15.
10. Wagner BJ, Wong-You-Cheong JJ, Davis Jr CJ. Adult renal hamartomas. Radiographics. 1997;17(1):155–69.
11. Brown ED, Chen MY, Wolfman NT, Ott DJ, Watson Jr NE. Complications of renal transplantation: evaluation with US and radionuclide imaging 1. Radiographics. 2000;20(3):607–22.
12. Yacoub JH, Verma S, Moulton JS, Eggener S, Oto A. Imaging-guided prostate biopsy: conventional and emerging techniques. Radiographics. 2012;32(3):819–37.
13. Hernandez J, Thompson IM. Carcinoma core distribution in patients with palpable and nonpalpable prostate tumors. Cancer. 2005;103(9):1761–2.
14. Tamsel S, Killi R, Hekimgil M, Altay B, Soydan S, Demirpolat G. Transrectal ultrasound in detecting prostate cancer compared with serum total prostate-specific antigen levels. J Med Imaging Radiat Oncol. 2008;52(1):24–8.
15. Zisman A, Herbert M, Strauss S, Manor H, Liebovici D, Lindner A. Preoperative detection of locally advanced prostate cancer by using transrectal ultrasound-guided staging prostate biopsy. The Prostate J. 2000;2(3):130–6.
16. Avery LL, Scheinfeld MH. Imaging of penile and scrotal emergencies. Radiographics. 2013;33(3):721–40.
17. Aso C, Enríquez G, Fité M, Torán N, Piró C, Piqueras J, Lucaya J. Gray-scale and color Doppler sonography of scrotal disorders in children: an update 1. Radiographics. 2005;25(5):1197–214.
18. Pauroso S, Di Leo N, Fulle I, Di Segni M, Alessi S, Maggini E. Varicocele: ultrasonographic assessment in daily clinical practice. J Ultrasound. 2011;14(4):199–204.
19. Mahesh M. The AAPM/RSNA physics tutorial for residents: search for isotropic resolution in CT fr from conventional through multiple-Row detector. Radiographics. 2002;22(4):949–62.
20. Hartman R, Kawashima A, Takahashi N, Silva A, Vrtiska T, Leng S, Fletcher J, McCollough C. Applications of dual-energy CT in urologic imaging: an update. Radiol Clin North Am. 2012;50(2):191–205.
21. Song KD, Kim CK, Park BK, Kim B. Utility of iodine overlay technique and virtual unenhanced images for the characterization of renal masses by dual-energy CT. Am J Roentgenol. 2011;197(6):W1076–82.
22. Neville AM, Gupta RT, Miller CM, Merkle EM, Paulson EK, Boll DT. Detection of renal lesion enhancement with dual-energy multidetector CT. Radiology. 2011;259(1):173–83.
23. Graser A, Johnson TR, Hecht EM, Becker CR, Leidecker C, Staehler M, Stief CG, Hildebrandt H, Godoy MC, Finn ME, Stepansky F, Reiser MF, Macari M. Dual-energy CT in patients suspected of having renal masses: can virtual nonenhanced images replace true non-enhanced images? Radiology. 2009;252(2):433–40.
24. Gnannt R, Fischer M, Goetti R, Karlo C, Leschka S, Alkadhi H. Dual-energy CT for characterization of the incidental adrenal mass: preliminary observations. Am J Roentgenol. 2012;198(1):138–44.
25. Gupta RT, Ho LM, Marin D, Boll DT, Barnhart HX, Nelson RC. Dual-energy CT for characterization of adrenal nodules: initial experience. Am J Roentgenol. 2010;194(6):1479–83.
26. Boll DT, Patil NA, Paulson EK, Merkle EM, Simmons WN, Pierre SA, Preminger GM. Renal stone assessment with dual-energy multidetector CT and advanced postprocessing techniques: improved characterization of renal stone composition—pilot study 1. Radiology. 2009;250(3):813–20.
27. Zilberman DE, Ferrandino MN, Preminger GM, Paulson EK, Lipkin ME, Boll DT. In vivo determination of urinary stone composition using dual energy computerized tomography with advanced post-acquisition processing. J Urol. 2010;184(6):2354–9.
28. Israel GM, Bosniak MA. How i do it: evaluating renal masses. Radiology. 2005;236(2):441–50.
29. Taneja R, Bhargava P, Cuevas C, Dighe MK. Common and less-common renal masses and masslike conditions. Radiol Clin North Am. 2012;50(2):245–57.
30. Birnbaum BA, Maki DD, Chakraborty DP, Jacobs JE, Babb JS. Renal cyst pseudoenhancement: evaluation with an anthropomorphic body CT phantom. Radiology. 2002;225(1):83–90.
31. Wang ZJ, Coakley FV, Fu Y, Joe BN, Prevrhal S, Landeras LA, Webb EM, Yeh BM. Renal cyst pseudoenhancement at multidetector CT: what Are the effects of number of detectors and peak tube voltage? Radiology. 2008;248(3):910–6.
32. Ng CS, Wood CG, Silverman PM, Tannir NM, Tamboli P, Sandler CM. Renal cell carcinoma: diagnosis, staging, and surveillance. Am J Roentgenol. 2008;191(4):1220–32.
33. Johnson CD, Dunnick NR, Cohan RH, Illescas FF. Renal adenocarcinoma: CT staging of 100 tumors. Am J Roentgenol. 1987;148(1):59–63.
34. Hammond NA, Nikolaidis P, Miller FH. Infectious and inflammatory diseases of the kidney. Radiol Clin North Am. 2012;50(2):259–70.
35. Stunell H, Buckley O, Feeney J, Geoghegan T, Browne RFJ, Torreggiani WC. Imaging of acute pyelonephritis in the adult. Eur Radiol. 2007;17(7):1820–8.
36. Santucci RA, Wessells H, Bartsch G, Descotes J, Heyns CF, McAninch JW, Nash P, Schmidlin F. Evaluation and management of renal injuries: consensus statement of the renal trauma subcommittee. BJU Int. 2004;93(7):937–54.
37. Moore EE, Shackford SR, Pachter HL, McAninch JW, Browner BD, Champion HR, Flint LM, Gennarelli TA, Malangoni MA, Ramenofsky ML, Trafton PG. Organ injury scaling: spleen, liver, and kidney. J Trauma. 1989;29(12):1664–6.
38. Lee YJ, Oh SN, Rha SE, Byun JY. Renal trauma. Radiol Clin North Am. 2007;45(3):581–92.
39. Boulay I, Holtz P, Foley WD, White B, Begun FP. Ureteral calculi: diagnostic efficacy of helical CT and implications for treatment of patients. AJR Am J Roentgenol. 1999;172(6):1485–90.
40. Hamm M, Wawroschek F, Weckermann D, Knöpfle E, Häckel T, Häuser H, Krawczak G, Harzmann R. Unenhanced helical computed tomography in the evaluation of acute flank pain. Eur Urol. 2001;39(4):460–5.
41. Fielding JR, Fox LA, Heller H, Seltzer SE, Tempany CM, Silverman SG, Steele G. Spiral CT in the evaluation of flank pain: overall accuracy and feature analysis. J Comput Assist Tomogr. 1997;21(4):635–8.

42. Katz DS, Lane MJ, Sommer FG. Unenhanced helical CT of ureteral stones: incidence of associated urinary tract findings. AJR Am J Roentgenol. 1996;166(6):1319–22.
43. Kambadakone AR, Eisner BH, Catalano OA, Sahani DV. New and evolving concepts in the imaging and management of urolithiasis: urologists' perspective. Radiographics. 2010;30(3):603–23.
44. Berland LL, Silverman SG, Gore RM, Mayo-Smith WW, Megibow AJ, Yee J, Brink JA, Baker ME, Federle MP, Foley WD, Francis IR, Herts BR, Israel GM, Krinsky G, Platt JF, Shuman WP, Taylor AJ. Managing incidental findings on abdominal CT: white paper of the ACR incidental findings committee. J Am Coll Radiol. 2010;7(10):754–73.
45. Young Jr WF. The incidentally discovered adrenal mass. N Eng J Med. 2007;356(6):601–10.
46. Taffel M, Haji-Momenian S, Nikolaidis P, Miller FH. Adrenal imaging: a comprehensive review. Radiol Clin North Am. 2012; 50(2):219–43.
47. Boland GW, Lee M, Gazelle GS, Halpern EF, McNicholas MM, Mueller PR. Characterization of adrenal masses using unenhanced CT: an analysis of the CT literature. AJR Am J Roentgenol. 1998;171(1):201–4.
48. Caoili EM, Korobkin M, Francis IR, Cohan RH, Platt JF, Dunnick NR, Raghupathi KI. Adrenal masses: characterization with combined unenhanced and delayed enhanced CT. Radiology. 2002;222(3):629–33.
49. Johnson PT, Horton KM, Fishman EK. Adrenal imaging with multidetector CT: evidence-based protocol optimization and interpretative practice 1. Radiographics. 2009;29(5):1319–31.
50. Raisanen J, Shapiro B, Glazer GM, Desai S, Sisson JC. Plasma catecholamines in pheochromocytoma: effect of urographic contrast media. Am J Roentgenol. 1984;143(1):43–6.
51. Mukherjee JJ, Peppercorn PD, Reznek RH, Patel V, Kaltsas G, Besser M, Grossman AB. Pheochromocytoma: effect of nonionic contrast medium in CT on circulating catecholamine levels. Radiology. 1997;202(1):227–31.
52. Bessell-Browne R, O'Malley ME. CT of pheochromocytoma and paraganglioma: risk of adverse events with iv administration of nonionic contrast material. Am J Roentgenol. 2007;188(4):970–4.
53. Mezhir JJ, Song J, Piano G, Testa G, Raman J, Al-Ahmadie HA, Angelos P. Adrenocortical carcinoma invading the inferior vena cava: case report and literature review. Endocr Pract. 2008;14(6):721–5.
54. Bhargava P, Dighe MK, Lee JH, Wang C. Multimodality imaging of ureteric disease. Radiol Clin North Am. 2012;50(2):271–99.
55. Chow LC, Kwan SW, Olcott EW, Sommer G. Split-bolus MDCT urography with synchronous nephrographic and excretory phase enhancement. Am J Roentgenol. 2007;189(2):314–22.
56. Chlapoutakis K, Theocharopoulos N, Yarmenitis S, Damilakis J. Performance of computed tomographic urography in diagnosis of upper urinary tract urothelial carcinoma, in patients presenting with hematuria: systematic review and meta-analysis. Eur J Radiol. 2010;73(2):334–8.
57. Mouli S, Casalino DD, Nikolaidis P. Imaging features of common and uncommon bladder neoplasms. Radiol Clin North Am. 2012;50(2):301–16.
58. Knox MK, Cowan NC, Rivers-Bowerman MD, Turney BW. Evaluation of multidetector computed tomography urography and ultrasonography for diagnosing bladder cancer. Clin Radiol. 2008;63(12):1317–25.
59. Sadow CA, Silverman SG, O'Leary MP, Signorovitch JE. Bladder cancer detection with CT urography in an academic medical center. Radiology. 2008;249(1):195–202.
60. Vikram R, Sandler CM, Ng CS. Imaging and staging of transitional cell carcinoma: part 1, lower urinary tract. Am J Roentgenol. 2009;192(6):1481–7.
61. Chan DP, Abujudeh HH, Cushing Jr GL, Novelline RA. CT cystography with multiplanar reformation for suspected bladder rupture: experience in 234 cases. Am J Roentgenol. 2006;187(5):1296–302.
62. Quagliano PV, Delair SM, Malhotra AK. Diagnosis of blunt bladder injury: a prospective comparative study of computed tomography cystography and conventional retrograde cystography. J Trauma Acute Care Surg. 2006;61(2):410–22.
63. Balter S. An introduction to the physics of magnetic resonance imaging. Radiographics. 1987;7(2):371–83.
64. Pooley RA. Fundamental physics of MR imaging. Radiographics. 2005;25(4):1087–99.
65. Plewes DB. The AAPM/RSNA physics tutorial for residents. Contrast mechanisms in spin-echo MR imaging. Radiographics. 1994;14(6):1389–404.
66. Price RR. The AAPM/RSNA physics tutorial for residents. Contrast mechanisms in gradient-echo imaging and an introduction to fast imaging. Radiographics. 1995;15(1):165–78.
67. Bley TA, Wieben O, François CJ, Brittain JH, Reeder SB. Fat and water magnetic resonance imaging. J Magn Reson Imaging. 2010; 31(1):4–18.
68. Pokharel SS, Macura KJ, Kamel IR, Zaheer A. Current MR imaging lipid detection techniques for diagnosis of lesions in the abdomen and pelvis. Radiographics. 2013;33(3):681–702.
69. Delfaut EM, Beltran J, Johnson G, Rousseau J, Marchandise X, Cotten A. Fat suppression in MR imaging: techniques and pitfalls. Radiographics. 1999;19(2):373–82.
70. Qayyum A. Diffusion-weighted imaging in the abdomen and pelvis: concepts and applications. Radiographics. 2009;29(6): 1797–810.
71. Neil JJ. Measurement of water motion (apparent diffusion) in biological systems. Concepts Magn Reson. 1997;9(6):385–401.
72. Leyendecker JR, Barnes CE, Zagoria RJ. MR urography: techniques and clinical applications. Radiographics. 2008;28(1): 23–46.
73. Nolte-Ernsting CCA, Staatz G, Tacke J, Günther RW. MR urography today. Abdom Imaging. 2003;28(2):0191–209.
74. Leyendecker JR, Gianini JW. Magnetic resonance urography. Abdom Imaging. 2009;34(4):527–40.
75. Lin E. Body MRI sequences: a conceptual framework. Appl Radiol. 2012;41(1):16–23.
76. Kanal E, Barkovich AJ, Bell C, Borgstede JP, Bradley WG, Froelich JW, Gimbel JR, Gosbee JW, Kuhni-Kaminski E, Larson PA, Lester Jr JW, Nyenhuis J, Schaefer DJ, Sebek EA, Weinreb J, Wilkoff BL, Woods TO, Lucey L, Hernandez D. ACR guidance document on MR safe practices: 2013. J Magn Reson Imaging. 2013;37(3): 501–30.
77. Ho VB, Allen SF, Hood MN, Choyke PL. Renal masses: quantitative assessment of enhancement with dynamic MR imaging. Radiology. 2002;224(3):695–700.
78. Hecht EM, Israel GM, Krinsky GA, Hahn WY, Kim DC, Belitskaya-Levy I, Lee VS. Renal masses: quantitative analysis of enhancement with signal intensity measurements versus qualitative analysis of enhancement with image subtraction for diagnosing malignancy at MR imaging. Radiology. 2004;232(2):373–8.
79. Herts BR, Coll DM, Novick AC, Obuchowski N, Linnell G, Wirth SL, Baker ME. Enhancement characteristics of papillary renal neoplasms revealed on triphasic helical CT of the kidneys. Am J Roentgenol. 2002;178(2):367–72.
80. Roy C, Sauer B, Lindner V, Lang H, Saussine C, Jacqmin D. MR imaging of papillary renal neoplasms: potential application for characterization of small renal masses. Eur Radiol. 2007;17(1): 193–200.
81. Sun MR, Ngo L, Genega EM, Atkins MB, Finn ME, Rofsky NM, Pedrosa I. Renal cell carcinoma: dynamic contrast-enhanced MR imaging for differentiation of tumor subtypes—correlation with pathologic findings. Radiology. 2009;250(3):793–802.
82. Newatia A, Khatri G, Friedman B, Hines J. Subtraction imaging: applications for nonvascular abdominal MRI. Am J Roentgenol. 2007;188(4):1018–25.
83. Nikken JJ, Krestin GP. MRI of the kidney—state of the art. Eur Radiol. 2007;17(11):2780–93.

84. Silverman SG, Mortele KJ, Tuncali K, Jinzaki M, Cibas ES. Hyperattenuating renal masses: etiologies, pathogenesis, and imaging evaluation. Radiographics. 2007;27(4):1131–43.
85. Outwater EK, Bhatia M, Siegelman ES, Burke MA, Mitchell DG. Lipid in renal clear cell carcinoma: detection on opposed-phase gradient-echo MR images. Radiology. 1997;205(1): 103–7.
86. Outwater EK, Siegelman ES, Radecki PD, Piccoli CW, Mitchell DG. Distinction between benign and malignant adrenal masses: value of T1-weighted chemical-shift MR imaging. AJR Am J Roentgenol. 1995;165(3):579–83.
87. Varghese JC, Hahn PF, Papanicolaou N, Mayo-Smith WW, Gaa JA, Lee MJ. MR differentiation of phaeochromocytoma from other adrenal lesions based on qualitative analysis of T2 relaxation times. Clin Radiol. 1997;52(8):603–6.
88. Blake MA, Kalra MK, Maher MM, Sahani DV, Sweeney AT, Mueller PR, Hahn PF, Boland GW. Pheochromocytoma: an imaging chameleon. Radiographics. 2004;24 Suppl 1:S87–99.
89. Tekes A, Kamel I, Imam K, Szarf G, Schoenberg M, Nasir K, Thompson R, Bluemke D. Dynamic MRI of bladder cancer: evaluation of staging accuracy. Am J Roentgenol. 2005;184(1):121–7.
90. Haider MA, van der Kwast TH, Tanguay J, Evans AJ, Hashmi AT, Lockwood G, Trachtenberg J. Combined T2-weighted and diffusion-weighted MRI for localization of prostate cancer. Am J Roentgenol. 2007;189(2):323–8.
91. Tamada T, Sone T, Jo Y, Toshimitsu S, Yamashita T, Yamamoto A, Tanimoto D, Ito K. Apparent diffusion coefficient values in peripheral and transition zones of the prostate: comparison between normal and malignant prostatic tissues and correlation with histologic grade. J Magn Reson Imaging. 2008;28(3): 720–6.
92. Katahira K, Takahara T, Kwee TC, Oda S, Suzuki Y, Morishita S, Kitani K, Hamada Y, Kitaoka M, Yamashita Y. Ultra-high-b-value diffusion-weighted MR imaging for the detection of prostate cancer: evaluation in 201 cases with histopathological correlation. Eur Radiol. 2011;21(1):188–96.
93. Bonekamp D, Jacobs MA, El-Khouli R, Stoianovici D, Macura KJ. Advancements in MR imaging of the prostate: from diagnosis to interventions. Radiographics. 2011;31(3):677–703.
94. Vourganti S, Rastinehad A, Yerram NK, Nix J, Volkin D, Hoang A, Turkbey B, Gupta GN, Kruecker J, Linehan WM, Choyke PL, Wood BJ, Pinto PA. Multiparametric magnetic resonance imaging and ultrasound fusion biopsy detect prostate cancer in patients with prior negative transrectal ultrasound biopsies. J Urol. 2012;188(6):2152–7.
95. Kim SH, Park S, Choi SH, Jeong WK, Choi JH. The efficacy of magnetic resonance imaging for the diagnosis of testicular rupture: a prospective preliminary study. J Trauma Acute Care Surg. 2009;66(1):239–42.
96. Fernández-Pérez GC, Tardáguila FM, Velasco M, Rivas C, Dos Santos J, Cambronero J, Trinidad C, San Miguel P. Radiologic findings of segmental testicular infarction. Am J Roentgenol. 2005;184(5):1587–93.
97. Tsili AC, Argyropoulou MI, Giannakis D, Sofikitis N, Tsampoulas K. MRI in the characterization and local staging of testicular neoplasms. Am J Roentgenol. 2010;194(3):682–9.
98. Fedel M, Venz S, Andreessen R, Sudhoff F, Loening SA. The value of magnetic resonance imaging in the diagnosis of suspected penile fracture with atypical clinical findings. J Urol. 1996;155(6): 1924–7.
99. Choi MH, Kim B, Ryu JA, Lee SW, Lee KS. MR imaging of acute penile fracture 1. Radiographics. 2000;20(5):1397–405.
100. Pretorius ES, Siegelman ES, Ramchandani P, Banner MP. MR imaging of the penis 1. Radiographics. 2001;21 Suppl 1:S283–98.
101. Chou CP, Levenson RB, Elsayes KM, Lin YH, Fu TY, Chiu YS, Huang JS, Pan HB. Imaging of female urethral diverticulum: an update. Radiographics. 2008;28(7):1917–30.

Image Fusion Principles: Theory

3

Arvin K. George, John Michael DiBianco, and Ardeshir R. Rastinehad

Imaging has long played a vital role in the management of urologic diseases, providing information not available through physical examination. Initially being a purely diagnostic modality with individual interpretations obtained through separate and isolated modalities (X-ray, ultrasound, CT, MRI), it has grown to include investigations with computer-assisted detection and diagnosis applied to both isolated and combined imaging modalities [1–3]. Progress in technology and improvement in imaging techniques have evolved to encompass therapeutic roles.

History

In 1895, Wilhelm Roentgen demonstrated that X-ray images (radiographs) could portray the internal architecture of the human body [4]. The medical uses of radiography proceeded promptly, and within 2 weeks, a physician used imaging of a patient's hand and was able to remove an embedded needle thus performing the first image-guided procedure in history [4, 5]. Whether identifying a foreign body or a tumor, image-guided surgery (IGS) has the unique ability to guide the surgeon, to a specific location within the body, without direct visualization, using an approach through the least traumatic path [4]. In 1906, Horsley and Clarke developed the Cartesian coordinate system forming the basis for stereotaxic procedures, the next important advance in IGS [6, 7]. Utilized first in neurosurgery, each stereotactic procedure required a reference frame to be constructed. These various three-dimensional (3D) frames, affixed to the skull, acted as an external coordinate system allowing the surgeon to approach internal structures. Internal structures were mapped and their coordinates allocated by X-ray images of the skull with the spatial reference frame. The lack of a mechanism for real-time instrument tracking required fixation and precision of the reference frame during the operation [4]. A specific limitation of X-ray imaging was the lack of 3D information that resulted in the estimate of depth to be pure guesswork. The advent of tomographic studies, with their ability to provide 3D information, facilitated the use spatial information for cognitive guidance [8].

The development of real-time tracking capabilities using ultrasound, computed tomography (CT), or MR is able to visualize the location of an instrument or anatomical structure within the physical space [8]. This parallel registration of spaces (physical with image) is critical for the placement of an instrument for biopsy or treatment. Unlike the frame-based stereotaxic system, the location of an instrument or anatomical structure in the physical space could be located in real time in the image space [8]. The effectiveness of registration of the physical space with the image space has advanced rapidly, especially in fields with rigid landmarks, such as neurosurgery and orthopedics. The use of image guidance for abdominal and pelvic organs without rigid structures for orientation has taken longer to develop. Although various techniques for accessing the prostate have been developed, for instance, transperineal and transrectal approaches, the position of the prostate may be significantly altered by posture, respiration, and/or bladder fullness [8]. The necessity for real-time imaging is paramount. Transrectal ultrasound was introduced in the 1950s. In its infancy, it was used sparingly for the next three decades but eventually found to be of utility in the diagnosis of patients with prostate cancer with the introduction of the spring-loaded biopsy needle and needle guide. Transrectal ultrasound (TRUS)-guided prostate biopsy allowed an opportunity for urologists to incorporate TRUS into daily practice [9]. TRUS-guided prostate biopsies were a sign of significant improvement

A.K. George, MD (✉) • J.M. DiBianco, MD
Urologic Oncology Branch, National Cancer Institute, National Institutes of Health, Bethesda, MD, USA
e-mail: arvinkgeorge@gmail.com; john.dibianco@yahoo.com

A.R. Rastinehad, DO
Departments of Urology and Radiology, Associate Professor of Urology and Radiology and the Director of Focal Therapy and Interventional Urologic Oncology, Icahn School of Medicine at Mount Sinai, New York, NY, USA
e-mail: art.rastinehad@mountsinai.org

A.R. Rastinehad, D.N. Siegel (eds.), *Interventional Urology*, DOI 10.1007/978-3-319-23464-9_3

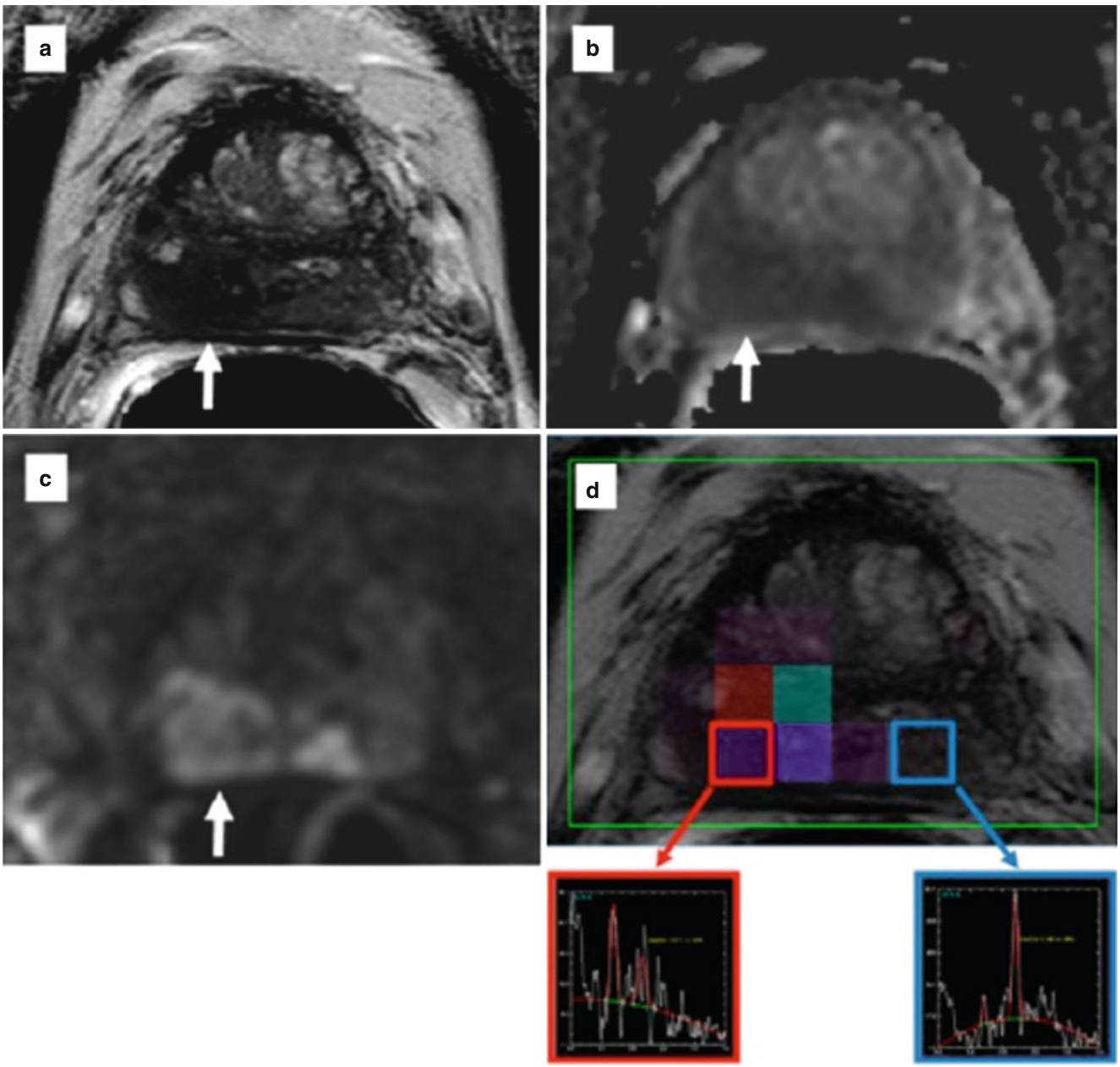

Fig. 3.1 (**a**) T2-weighted imaging, (**b**) ADC map from diffusion-weighted imaging, (**c**) dynamic contrast enhancement MRI demonstrating early and avid gadolinium enhancement, and (**d**) spectroscopic imaging depicting a right mid-base peripheral zone lesion (*arrow*) (Adapted from George et al. [13] with permission)

over the previously utilized digitally guided transrectal or transperineal biopsies [10–12].

An ultrasound-guided prostate biopsy is one of the earliest urologic image-guided procedures and remains in place today as one of the most commonly performed. By incorporating some of the newest imaging techniques, such as magnetic resonance and ultrasound (MR/US) fusion technology with tracking and 3D US mapping of the prostate, the process continues, as various investigators and academic centers study ways to improve sampling of the prostate (Fig. 3.1) [14, 15]. Throughout the modern era, the technological and procedural innovations in imaging have aided in the diagnosis and treatment of patients. Referring to image-guided procedures, Galloway has stated. The following is a discussion of the current state of the art, regarding the techniques in imaging and their applications in urologic interventions, with special attention to registration, image fusion, and tracking including diagnostic and therapeutic implementation.

Basics

Visualization and Application

Ultrasound (US) relies on the emission, reflection, and detection of high-frequency sound waves from organ boundaries and interface contingent on the change in density of the tissues contacted. This imaging technique is widely used in clinical practice, as a result of its many advantages including lack of patient exposure to toxic effects of radiation, real-time imaging capability, relatively low-cost, portability, and abbreviated learning curve for clinical use. Limitations of ultrasound imaging include its reliance on operator training and experience, reduced ability to access information about more distal structures or those hidden by variations of body habitus or those beyond low-density structures (lung, air-filled bowel loops, pneumoperitoneum), as resolution is distance and transmission dependent.

Developed in the 1970s, *computerized tomography* (CT) or X-ray computed tomography is a widely used imaging modality. It allows rapid high-resolution tissue imaging providing excellent delineation of anatomy. CT is a mainstay in the diagnosis and follow-up of clinical conditions in almost every medical and surgical specialty. CT has the capacity to guide the performance of percutaneous procedures, providing accurate location of instruments within three-dimensional regions of the body [16]. The main advantage of CT is its fast image acquisition and high resolution; significant disadvantages include exposure of the patient to ionizing radiation (especially cumulative exposure secondary to serial imaging) [17]. Ionizing radiation may expose patients to long-term cancer risk, particularly when exposed at early ages [18].

Positron emission tomography (PET) is a nuclear medicine technique which requires the administration of a radioisotope, a radioactively tagged chemical compound (radionuclide or tracer) to the patient. The subsequent gamma rays emitted from the patient as the radioisotope decays are captured, analyzed by computer, and portrayed as three-dimensional images locating the involvement of the functional processes of the administered chemical compound.

Fluoroscopy utilizes low-intensity X-rays to obtain "real-time" radiographic imaging. It is utilized as a diagnostic modality and during image-guided therapy [19]. The administration of intravascular contrast can allow for vessel mapping, facilitating therapeutic interventions such as drug delivery or angioembolization.

Magnetic resonance imaging (MRI) utilizes strong magnetic fields to polarize protons within the molecules of tissues via directed energy pulses. After magnetic alignment, protons move back to their aligned positions when the pulse is ended. The resulting waves are detected and captured so the computer may construct 3D images. By using both anatomical and functional MRI data, various tissue systems can be evaluated, based on the performance characteristics of each parameter, yielding high-quality diagnostic information.

Three-Dimensional Image Visualization

Typical radiographic imaging, X-ray, US, or fluoroscopy, is seen in the original plane as a two-dimensional (2D) image. More advanced imaging, CT, PET, and MRI, is computer processed allowing rendering in multiple planes. The multiplanar reconstruction (MPR) technique allows new images to be reformatted from their original plane (mostly axial) in coronal, sagittal, or oblique planes utilizing the pixel data acquired from the stack of planar images. MPR aids in visualization of anatomy by providing the perspective of structures within the entire volume that may not be readily apparent from base images. However, quality of MPR is dependent on base image acquisition and quality. The various approaches for 3D visualization and analysis of imaging datasets are subsequently described.

Surface rendering, or shaded surface display (SSD), operates on the assumption that a structure or organ can be displayed based on the surface estimated from an image (volume dataset) [20]. The surface is initially determined by segmentation which is accomplished by thresholding, or assigning each voxel intensity within the dataset to be within a predetermined attenuation range. Surface contours derived from the volume dataset are modeled as overlapping polygons, to represent the 3D object. SSD allows for swift image rendering; however, only a small portion of the dataset is employed, and it may be of limited utility where a discrete interface or boundary is not readily apparent [21].

Maximum intensity projection (MIP) rendering appraises each voxel along a continuous line throughout a dataset [22]. The maximum value voxel, or volumetric picture element, which essentially corresponds to a value on a grid in 3D space, is selected and used as the displayed value. Based on these displayed voxels, a 3D image is rendered. MIP is most commonly used in display and analysis of angiographic images and draws from only a small percentage of the entire volume dataset for rendering. Its shortcomings include lack of depth cues to assess spatial relationships and increased background "noise" due to display of only voxels with the highest intensity values.

Volume rendering is a technique that utilizes the entire volume dataset and assigns an opacity and color to each voxel which corresponds to tissue characteristics. It can display surfaces with shading and other parts of the volume simultaneously [23]. The highest image quality volume

rendering method from 3D scalar data is by volume ray casting. In volume ray casting, a "ray" is projected through the volume, and the amount of intersection between the ray and a voxel determines the contribution to the voxel value. Weighted measures of the voxel values are calculated for each pixel and scales to a range of gray-scale values from which an image is constructed. As volume rendering incorporates the whole dataset, it requires complex algorithms and powerful computer processing equipment but has the capacity to display multiple tissues in addition to giving information on spatial relationship within the volume.

Registration

The goal of medical image registration is to find the ideal transformation that optimally aligns the anatomic structures of interest from the acquired image datasets. Correspondence is established between features in image datasets using a transformational model such that mapping of coordinates between these images corresponds to the same anatomical point. Registration allows clinicians to integrate information from different imaging modalities or time points. The term "fusion" refers to the step subsequent to registration that creates an integrated display of the data involved. However, it is often used to refer to the entire process of co-registration and co-display of the registered datasets. Applications of image registration are diverse and include surgical guidance, radiation planning, computer-aided diagnosis, and fusion of anatomic and functional imaging [24–27].

Image registration was first accomplished by physicians using "cognitive registration," referring to the basic interpretations of imaging data and applying it to physical space based on cognitive estimations. Rapid technologic progress and research in the field has harnessed increased computational power to employ complex algorithms to deliver more accurate registration systems. Image registration is accomplished by incorporating information from one imaging modality and then applying it to a complementary modality and/or physical space to relate contrasting information from the different types of images. For example, when a suspicious lesion is only visualized on multiparametric MR imaging, MR/transrectal ultrasound fusion-guided biopsy can be performed whereby co-registration allows the real-time imaging advantage of US and resolution of MR to complement each other [13].

Current image registration techniques employ a combination of software-based algorithms and manual corrections to determine the spatial correspondence within 3D space. There are a number of algorithms that may be applied for registration, the common element being the ability to maximize a measure of similarity between a transformed "floating image" and a fixed "reference image" [28]. Intrinsic registration modalities rely solely on patient-derived imaging data and include intensity-based and geometric transformation-based models.

Geometric transformations require segmentation and include both landmark-based registration and surface-based registration techniques. Geometric transformation takes two forms, which are rigid and nonrigid or deformable algorithms. Rigid body registration is based on the notion that one image requires only translation and/or a rotation to achieve reasonable correspondence with a similar image, without change in the size or shape. Nonrigid or elastic registration is the more complex of the two types of transformations, where one image is elastically deformed to fit the second imaging and is used to describe changes in the shape, organ shift, or patient motion. Elastic registration employs a landmark-based approach in which corresponding landmarks (points, lines, surfaces, volumes) are forced (warped) to exactly match the other, potentially resulting in registration errors which may be compounded with each additional elastic transformation.

Landmark Based

Landmark-based registration identifies corresponding point landmarks as fiducial markers that appear in both images that are to be aligned [29]. These fiducial markers may be identifiable anatomical landmarks that remain unchanged such as bony points, cysts or calcifications, and the bifurcations of vessels. Alternatively, specific geometric features such as surface curvatures may be used. Point landmarks can be pins or markers attached to the patient's skin or screwed into the bone where anatomy is not well defined. There are advantages and disadvantages of each using each type. In such cases, it is important to ensure that the coordinate of each fiducial marker is calculated accurately and that the coordinate computed in each modality corresponds to the same point in physical space so as to minimize fiducial registration error (FRE) [30].

At a minimum, three non-collinear points in the 3D space are required to determine a transformation between two sets of images though intuitively, additional fiducials minimize registration error [31]. The "centroid" point between each corresponding set of coordinates is determined, followed by rotation to diminish the sum of the square displacements between them. In order to objectively measure the validity and accuracy of registration, both FRE and target registration error (TRE) are reported. An FRE is the distance between selected markers in the 3D datasets being registered. FRE does not necessarily represent or guarantee accuracy of the registration or the fusion, but a low FRE is required for an accurate registration (Fig. 3.2). Accuracy reflects the degree of coincidence of a point of interest within the registered

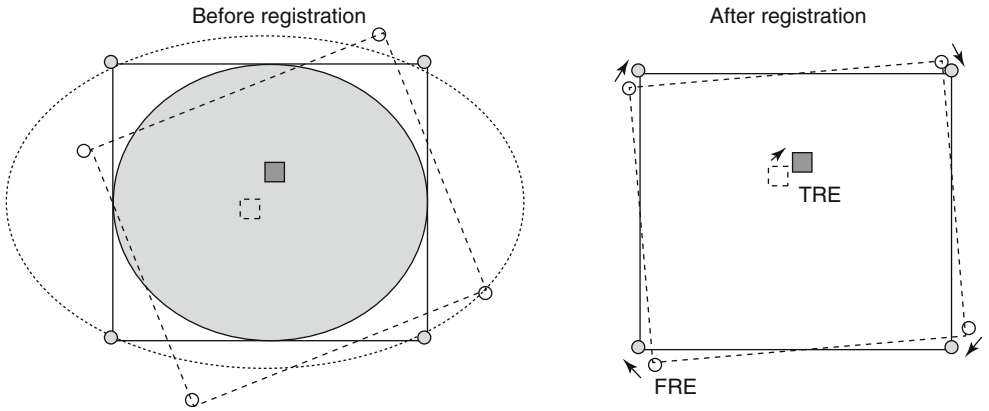

Fig. 3.2 Calculation of registration error. The fiducial registration error (*FRE*) is determined by the distance between corresponding fiducials in the reference dataset (*shaded circles*) and the floating dataset (*unshaded circles*) after registration is completed. The target registration error (*TRE*) is determined by the distance between the corresponding anatomical areas of interest in the two datasets (*squares*) after registration is completed (Adapted from Hutton and Braun [28] with permission)

images. The difference between the point of interest within the image and its actual locations is described as the TRE [23]. The reported accuracy of 3D inter-modality registration (CT/MRI, PET/MRI) is between 1 and 3 mm [32–35]. Landmark-based registration does often require the user to select the points in each image for matching, which can be time-consuming and require clinical expertise. However, the landmarks represent a small proportion of the original data, and thus, optimization can be performed quickly with the need for limited computational power.

Surface Based

Surface-based registration involves extraction of common features between sets of images, most often surfaces and curves. After surfaces are delineated, a transformation is computed that aims to minimize the distance between the two surfaces. The earliest algorithm, or "head and hat" algorithm, is a simplified manner in which performs the registration [36, 37]. The surfaces selected in the floating image set ("hat") are registered to the corresponding nearest edges in the reference image set ("head"), so as the "hat" is moved/manipulated in a manner that best fits the "head." Such methods are highly dependent on segmentation of surfaces that must correspond precisely and therefore necessitate high-resolution imaging to be most successful.

In an effort to overcome these limitations, the iterative closest point algorithm was proposed [38]. In the iterative closest point algorithm, the surface of one image is rendered using geometric primitives which may be facets or triangular sets, line segment sets, or parametric curves and surfaces. These primitives are then matched to the corresponding image, using a modeling equation by iteratively searching the closest points to minimize the disparity measure of this equation.

Voxel Intensity Based

Voxel intensity-based registration aligns images acquired from different imaging modalities based on imaging gray values, utilizing complementary information regarding similar structures without prior reduction as a result of segmentation [39]. As the full dataset is used, it requires high computational capacity. Paradigms for intensity-based registration include cross correlation (of extracted features), principal axes, and minimization of variance of intensity or histogram entropy. As intensity ratios between different modalities are often poorly correlated, increased interest has been given to the minimization of histogram entropy of different images. Entropy is essentially the probability of difference between the images being registered. The use of a 2D joint intensity histogram is correlated, point to point, between the images and their intensity. Each axis of the histogram represents possible gray-scale values in an imaging modality, and when images are perfectly aligned, the histogram is highly focused. The greater the error or difference in alignment, the greater the dispersion on the histogram is (Fig. 3.3) [40].

Tracking (Localizers)

Tracking refers to the transformation of image, patient, and instrument coordinates into a common reference system to identify its precise location within a 3D space. The clinical application of tracking or surgical navigation transcends medical specialties and has been exploited for percutaneous needle-based procedures (biopsy, catheter drainage, and ablation), endovascular interventions, minimally invasive surgical procedures, and even endoscopic procedures such as guidance for bronchoscopic biopsy of peripherally located lesions [41–43].

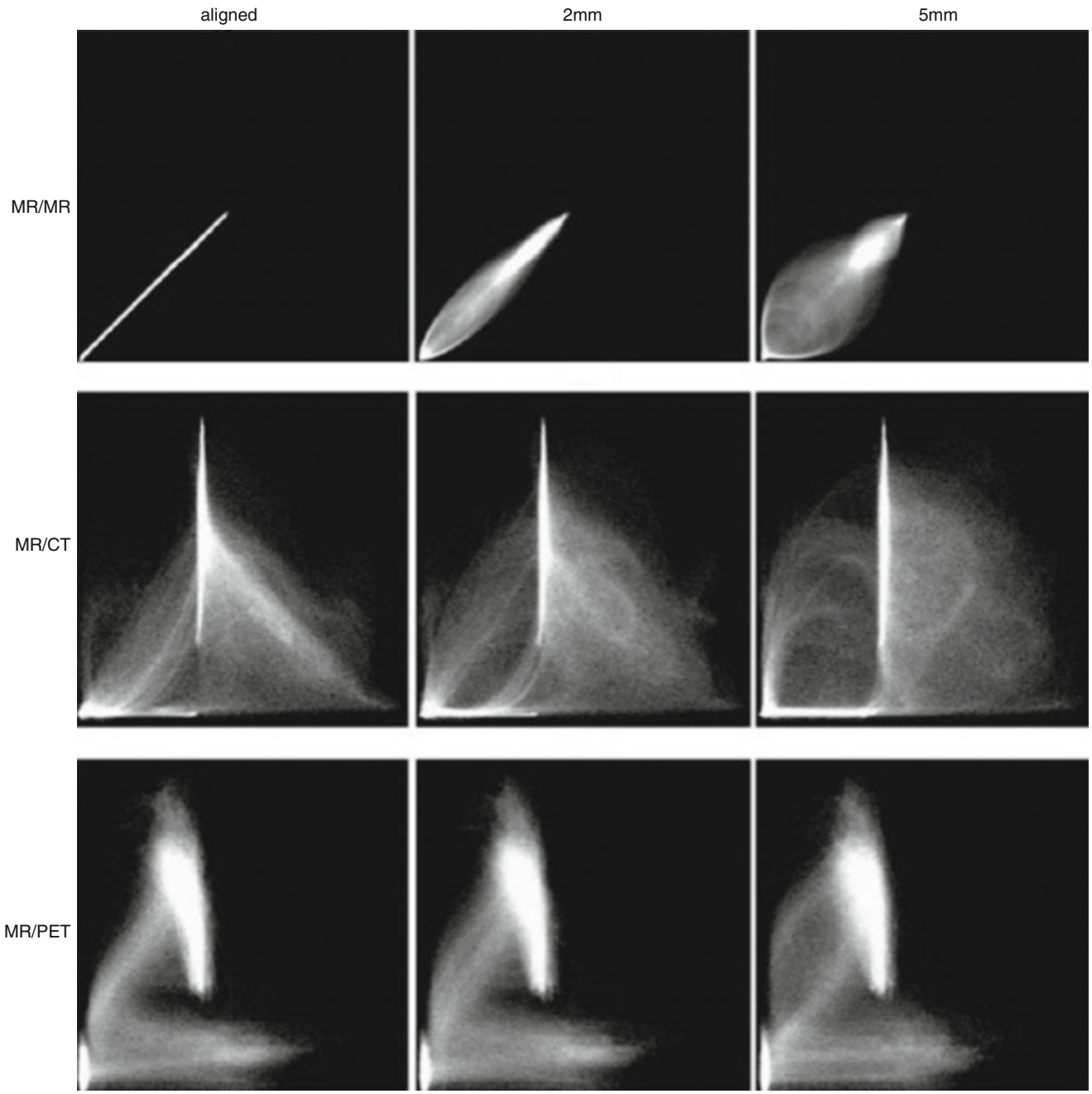

Fig. 3.3 Joint intensity histogram. Accuracy of voxel intensity-based registration can be visually represented by calculating joint entropy between the images being registered. When the modalities are similar and images are perfectly aligned, the histogram is highly focused. A greater degree of misregistration results in greater dispersion of "blur" within the histogram (Adapted from Hill et al. [29] with permission)

Optical tracking systems, the first to be widely adopted for clinical applications, operate via laser or infrared light emitting diodes and are tracked by reflection of light that is captured by an infrared camera. Alternatively, diodes placed on surgical instruments themselves may transmit signals back to a charge-coupled device camera. These systems represent the most accurate way of tracking instruments with spatial inaccuracy reported to be less than 1–3 mm [44, 45]. A major limiting factor in the use of optical tracking systems is the requirement of maintaining a "line of sight" (or unimpeded pathway) between the optical markers and the tracker camera [46]. As such, if an instrument tip is outside of the direct field, it is not visualized, but optically tracking the back of a rigid instrument allows for compensation by extrapolating the tips position. However, the line of sight requirement precludes the tracking of internal portions of an instrument, or if they are flexible or deformable [47].

Mechanical localizers are the earliest iterations that were employed for endonasal and neurosurgical therapies [48–51]. They consist of hardware with several degrees of freedom with encoders located at each joint, the entire device which is solely controlled by the operator. The exact location and orientation is calculated based on the feedback from geometric models derived from each encoder. These systems, though exhibiting a high degree of accuracy, can only track one object and may be large and cumbersome for use in a small operative field. A benefit of this system is that an instrument can be guided by the operator to a desired location within a physical space, fixed in a definite position and its location recorded [52].

The introduction of *electromagnetic (EM) tracking* systems was a proposed answer to the limitations of prior methods [53]. Electromagnetic tracking systems are based on the ability to localize a sensor which emits a weak electrical current in a weak pulsed electromagnetic field. An EM field generator is placed over the area of interest, creating a weak and differential electromagnetic field with a defined volume. The electric current emitted by sensor coils from skin fiducials, attached to or inside of instruments, is detected; and the strength of the signal based on its location within the EM field is triangulated to define its point in space [54]. Coils may be either 5 or 6 DOF (degrees of freedom). A single 5 DOF coil, though smaller, cannot determine the rotation component, which can be overcome by adding two or more 5 DOF coils, and most systems can track multiple coils within the geometry of the EM field. The reported accuracy is less than that of optical tracking systems (typically ~ 3 mm); however, "line of sight" tracking is not required allowing for tracking objects within the body within the EM field. Additionally, rapid technologic improvements now reportedly provide submillimeter tracking. A number of factors contribute to the utility of an individual EM tracking system. The refresh rate, working volume created by the field generator, and resilience must be considered [55]. A rapid refresh rate is needed when quantitative feedback is need such as during needle tracking, and images should be updated so as to not impede the physician performing the procedure. The size of the EM field created by the generator results in a fixed, arbitrary working volume in which the sensors must operate. As a result, it is imperative that the anatomy of interest and working area of a procedure be within the field. Signal intensity is dependent on proximity from the EM field generator; hence, the closer the coil is, the stronger the signal that is detected. Ferromagnetic materials from instruments and imaging equipment can cause interference resulting in distortions that may influence the accuracy of the system [56, 57]. A resilient system that employs direct current-driven tracking can minimize eddy currents created by metallic objects close to the operative field, and metal immune systems are now available.

Clinical Applications of Image Guidance

Augmented Reality

Augmented reality (AR) for surgical navigation uses a 3D image acquired preoperatively, rendering to a 2D live display captured intraoperatively. AR allows a surgeon to appreciate the objects and anatomical structures in the surgical field that are beyond the normal field of view. It can, for example, provide guidance for surgical resection of tumors deep to the visualized surface, or to appreciate vascular anatomy prior to being directly encountered [58].

In urologic surgery, it has successfully been used to assimilate information from imaging and visual information from the operative field during laparoscopic partial nephrectomy, adrenalectomy, and radical prostatectomy [59, 60]. Image overlay represents a significant advance over the status quo in which imaging data is usually only cognitively registered. AR models can be deployed in a variety of ways that not only require reliable registration but also tracking to ensure accuracy of the simulation. For robotic partial nephrectomy, an image-based surface tracking technique has been described that provides real-time stereoendoscopic visualization of preoperative imaging that obviates the need for markers or tracking devices yet accounts for both translational and rotational organ motion [61]. Additionally, the use of organ surface implantable navigation aids has been described to facilitate registration between intraoperative TRUS and the endoscopic image based on 2D and 3D point correspondences [62]. This system has been demonstrated in vivo successfully, with adequate surgical guidance and resection of the prostate and needle navigation markers [63].

The significant challenge for AR is to account for organ motion or deformation due to respiration or surgical manipulation [64]. Additional resources are being devoted to these questions, specifically how nonrigid registration algorithms may be optimized to compensate. Whether the cost and expertise translates into tangible benefits such as improved patient outcomes or safety is yet to be answered in a meaningful manner. This discipline is currently in its infancy, and AR techniques have not yet met with the initial enthusiasm of other fusion or tracking technologies.

Targeted Prostate Biopsy

Over the past 10 years, the design, development, and subsequent approval of fusion-guided prostate biopsy platforms have driven adoption and dissemination of this novel application of fusion/tracking technology. The use of fusion during prostate biopsy has allowed urologists to target MRI-identified areas suspicious for cancer rather than randomly

sampling the gland. Multiparametric MRI (MP-MRI)/US software-based registration platforms involve sending detailed information of preprogrammed target areas of interest along with the outlined/segmented images of the prostate to the fusion software platform. Once within the platform, real-time US images are taken and correlated with the previous imaging, such that the previous imaging and real-time imaging are "fused" and correlate correctly (Fig. 3.4).

The current role for imaging in the diagnosis, surveillance, and management of prostate cancer is not defined. MP-MRI TRUS fusion biopsies yield higher detection rates of clinically significant prostate cancer [65, 66] and allow for easier sampling of smaller prostatic lesions, identifying up to two-thirds more patients with clinically significant PCa [67]. In patients with an existing diagnosis of PCa who have decided to undergo definitive therapy, MP-MRI TRUS fusion biopsies have been shown to aid operative outcomes. Understanding the exact location and volume allows the surgeon to make appropriate decisions regarding nerve preservation techniques and possible margin approaches [68].

Focal Therapy

Due to the morbidity of systemic radical/whole gland treatment strategies, clinicians and patients are searching for feasible options to treat low-volume, low- and intermediate-risk PCa. Focal therapy, the selective targeting and treatment of specific areas of the prostate, has been utilized in carefully selected patients with amenable tumor size and topography. Treatment techniques include laser ablation, radiofrequency ablation, photodynamic therapy, high-intensity focused ultrasound (HIFU), irreversible electroporation (IRE), and cryotherapy [69]. Muller et al. reported the results from a consensus panel in 2014, in which they state that MP-MRI is the optimum imaging approach for focal therapy [69]. During treatment, real-time MRI and fusion platforms could also be used to aid tumor location, probe placement, and monitor treatment efficacy for focal therapy resulting in a truly "focal" treatment rather than regional therapies that have been employed to date [70, 71].

Computer-Aided Diagnosis

The use of computer assistance in the detection and diagnosis of urologic problems, for example, prostate cancer, is a maturing field of investigation with some exciting favorable, early findings [1, 72]. In one early report, computer assistance significantly improved the ability of less-experienced radiologists in classifying benign from malignant lesions, bringing their performance levels to that of those more experienced [73]. The work regarding computer assistance, to date, with multiparametric MRI has recently been comprehensively reviewed by Lemaitre et al. [1]

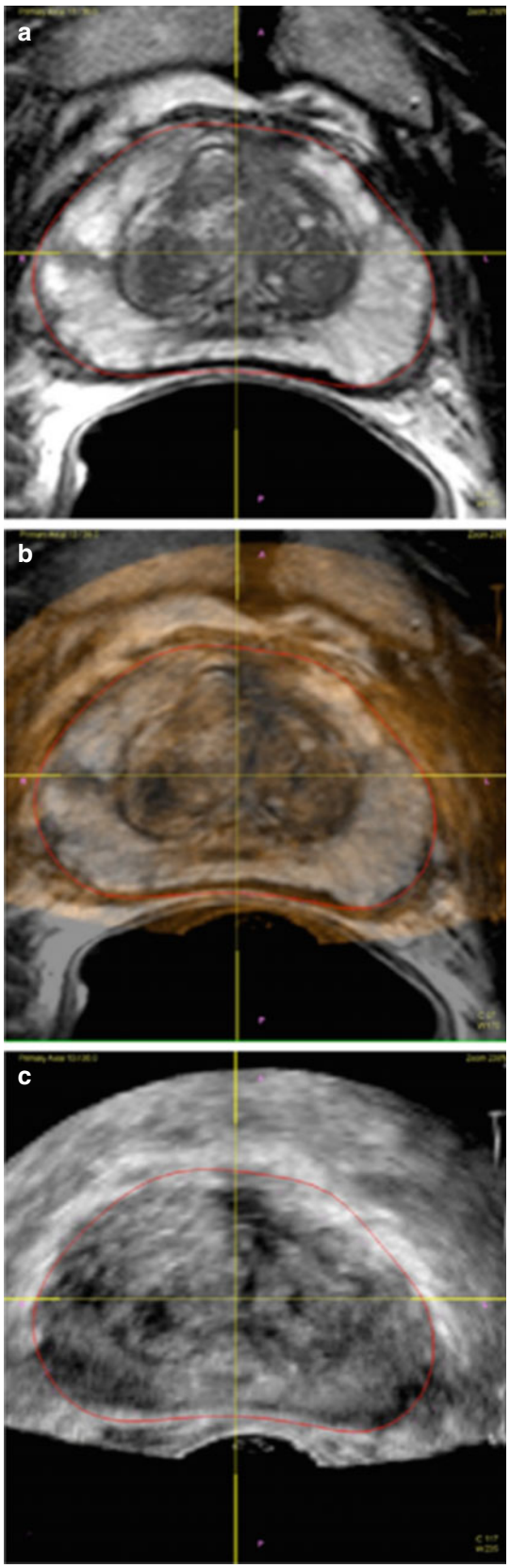

Fig. 3.4 MR/US fusion. (**a**) Axial T2-weighted MRI of the prostate, (**b**) MR/US overlay representing fusion of imaging modalities, and (**c**) US of the prostate in transverse view. When MRI and US are visualized on the same screen, presentation is termed image "co-display" (Adapted from Rothwax et al. [65] with permission)

Conclusion

The integration of imaging into the diagnosis, treatment, and surveillance of urologic disorders continues to evolve. A fundamental understanding of the principles upon which these new technologies are realized will undoubtedly provide an enhanced appreciation of its potential applications. Though urology by definition is an interventional surgical subspecialty, the exploration of more minimally invasive options by integration of imaging will enable the field to provide better outcomes to our patients.

References

1. Lemaitre G, Marti R, Freixenet J, et al. Computer-aided detection and diagnosis for prostate cancer based on mono and multiparametric MRI: a review. Comput Biol Med. 2015;60C:8–31.
2. Smeenge M, Mischi M, Laguna Pes MP, et al. Novel contrast-enhanced ultrasound imaging in prostate cancer. World J Urol. 2011;29:581–7.
3. Loch T, Carey B, Walz J, et al. EAU standardised medical terminology for urologic imaging: a taxonomic approach. Eur Urol. 2014;67(5):965–71.
4. Peters TM. Image-guidance for surgical procedures. Phys Med Biol. 2006;51:R505–40.
5. Webb S the physics of medical imaging institute of physics publishing 1988; 8.
6. Hayne R, Meyers JR. Characteristics of electrical activity of human corpus striatum and neighboring structures. J Neurophysiol. 1949;12:185–95.
7. al-Rodhan NR, Kelly PJ. Pioneers of stereotactic neurosurgery. Stereotact Funct Neurosurg. 1992;58:60–6.
8. Galloway RL. The process and development of image-guided procedures. Annu Rev Biomed Eng. 2001;3:83–108.
9. Lee F, Torp-Pedersen ST, Siders DB. The role of transrectal ultrasound in the early detection of prostate cancer. CA Cancer J Clin. 1989;39:337–60.
10. Pearlman CK. Transrectal biopsy of the prostate. J Urol. 1955;74:387–92.
11. Needell MH, Slotkin GE, Mitchell FD, et al. Prostatic needle biopsy. J Urol. 1955;74:138–41.
12. Onik G, Miessau M, Bostwick DG. Three-dimensional prostate mapping biopsy has a potentially significant impact on prostate cancer management. J Clini Oncol. 2009;27:4321–6.
13. George AK, Pinto PA, Rais-Bahrami S. Multiparametric MRI in the PSA screening era. Biomed Res Int. 2014;2014:465816.
14. Rastinehad AR, Baccala Jr AA, Chung PH, et al. D'Amico risk stratification correlates with degree of suspicion of prostate cancer on multiparametric magnetic resonance imaging. J Urol. 2011;185:815–20.
15. Xu S, Kruecker J, Turkbey B, et al. Real-time MRI-TRUS fusion for guidance of targeted prostate biopsies. Comput Aided Surg. 2008;13:255–64.
16. Neuzillet Y, Lechevallier E, Andre M, et al. Accuracy and clinical role of fine needle percutaneous biopsy with computerized tomography guidance of small (less than 4.0 cm) renal masses. J Urol. 2004;171:1802–5.
17. Hedlund E, Karlsson JE, Starck SA. Automatic and manual image fusion of in-pentetreotide SPECT and diagnostic CT in neuroendocrine tumor imaging - an evaluation. J Med Phy. 2010;35:223–8.
18. Smith-Bindman R, Aubin C, Bailitz J, et al. Ultrasonography versus computed tomography for suspected nephrolithiasis. N Engl J Med. 2014;371:1100–10.
19. Mahesh M. Fluoroscopy: patient radiation exposure issues. Radiographics. 2001;21:1033–45.
20. Gouraud H. Continuous shading of curved surfaces. IEEE Trans Comput. 1971;C-20:87–93.
21. Udupa JK, Hung HM, Chuang KS. Surface and volume rendering in three-dimensional imaging: a comparison. J Digit Imaging. 1991;1: 4:159–68.
22. Schreiner S, Galloway RL, Paschal CB. Comparison of projection algorithms used for the construction of maximum intensity projection images. J Comput Assist Tomogr. 1996;20:56–67.
23. Udupa JK. Three-dimensional visualization and analysis methodologies: a current perspective. Radiographics. 1999;19:783–806.
24. Miller K, Wittek A, Joldes G, et al. Modelling brain deformations for computer-integrated neurosurgery. Int J Numer Meth Biomed Eng. 2010;26:117–38.
25. Foskey M, Davis B, Goyal L, et al. Large deformation three-dimensional image registration in image-guided radiation therapy. Phys Med Biol. 2005;50:5869–92.
26. King AP, Rhode KS, Ma Y, et al. Registering preprocedure volumetric images with intraprocedure 3-D ultrasound using an ultrasound imaging model. IEEE Trans Med Imaging. 2010;29:924–37.
27. Sankineni S, George AK, Brown AM, et al. Posterior subcapsular prostate cancer: identification with mpMRI and MRI/TRUS fusion-guided biopsy. Abdom Imaging. 2015.
28. Hutton BF, Braun M. Software for image registration: algorithms, accuracy, efficacy. Semin Nucl Med. 2003;33:180–92.
29. Hill DL, Hawkes DJ, Crossman JE, et al. Registration of MR and CT images for skull base surgery using point-like anatomical features. Br J Radiol. 1991;64:1030–5.
30. Oliveira FP, Tavares JM. Medical image registration: a review. Comput Methods Biomech Biomed Engin. 2014;17:73–93.
31. Ukimura O, Hirahara N, Fujihara A, et al. Technique for a hybrid system of real-time transrectal ultrasound with preoperative magnetic resonance imaging in the guidance of targeted prostate biopsy. Int J Urol. 2010;17:890–3.
32. West J, Fitzpatrick JM, Wang MY, et al. Comparison and evaluation of retrospective intermodality brain image registration techniques. J Comput Assist Tomogr. 1997;21:554–66.
33. Barnden L, Kwiatek R, Lau Y, et al. Validation of fully automatic brain SPET to MR co-registration. Eur J Nucl Med. 2000;27:147–54.
34. Wong JC, Studholme C, Hawkes DJ, et al. Evaluation of the limits of visual detection of image misregistration in a brain fluorine-18 fluorodeoxyglucose PET-MRI study. Eur J Nucl Med. 1997;24: 642–50.
35. Fitzpatrick JM, Hill DL, Shyr Y, et al. Visual assessment of the accuracy of retrospective registration of MR and CT images of the brain. IEEE Trans Med Imaging. 1998;17:571–85.
36. Pelizzari CA, Chen GT, Spelbring DR, et al. Accurate three-dimensional registration of CT, PET, and/or MR images of the brain. J Comput Assist Tomogr. 1989;13:20–6.
37. Chen GTY, Pelizzari CA. Image correlation techniques in radiation therapy treatment planning. Comput Med Imaging Graph. 1988;13: 235–40.
38. Besl PJ, McKay NDA. Method for registration of 3-D shapes. IEEE Trans Pattern Anal Mach Intell. 1992;14:239–56.
39. Lee D, Nam WH, Lee JY, et al. Non-rigid registration between 3D ultrasound and CT images of the liver based on intensity and gradient information. Phys Med Biol. 2011;56:117–37.
40. Hill DL, Studholme C, Hawkes DJ. Voxel similarity measures for automated image registration. In: Roba RA, editor. Visualization in biomedical computing. 1994. p. 205–16.
41. Krucker J, Xu S, Glossop N, et al. Electromagnetic tracking for thermal ablation and biopsy guidance: clinical evaluation of spatial accuracy. J Vasc Interv Radiol. 2007;18:1141–50.
42. Giesel FL, Mehndiratta A, Locklin J, et al. Image fusion using CT, MRI and PET for treatment planning, navigation and follow up in percutaneous RFA. Exp Oncol. 2009;31:106–14.
43. Schwarz Y, Greif J, Becker HD, et al. Real-time electromagnetic navigation bronchoscopy to peripheral lung lesions using overlaid CT images: the first human study. Chest. 2006;129:988–94.

44. Peng JL, Kahler D, Li JG, et al. Characterization of a real-time surface image-guided stereotactic positioning system. Med Phys. 2010;37:5421–33.
45. Hassfeld S, Muhling J, Zoller J. Intraoperative navigation in oral and maxillofacial surgery. Int J Oral Maxillofac Surg. 1995;24: 111–9.
46. Phee SJ, Yang K. Interventional navigation systems for treatment of unresectable liver tumor. Med Biol Eng Comput. 2010;48:103–11.
47. Wood BJ, Kruecker J, Abi-Jaoudeh N, et al. Navigation systems for ablation. J Vasc Interv Radiol. 2010;21:S257–63.
48. Schlondorff G, Mosges R, Meyer-ebrecht D, et al. [CAS (computer assisted surgery). A new procedure in head and neck surgery]. HNO. 1989;37:187–90.
49. Adams L, Krybus W, Meyer-Ebrecht D, et al. Computer assisted surgery. IEEE Compu Graph. 1990;10:43–51.
50. Kosugi Y, Watanabe E, Goto J, et al. An articulated neurosurgical navigation system using MRI and CT images. IEEE Trans Biomed Eng. 1988;35:147–52.
51. Reinhardt HF In: Taylor R, Lavallee S, Burdea G, et al., editors. Neuronavigation: a ten year review. Cambridge: MIT Press; 1995.
52. Troccaz J, Peshkin M, Davies B, et al. The use of localizers, robots and synergistic devices in CAS. Lect Notes Comput Sc. 1997;1205:725–36.
53. Lugez E, Sadjadi H, Pichora DR, et al. Electromagnetic tracking in surgical and interventional environments: usability study. Int J Comput Assist Radiol Surg. 2015;10:253–62.
54. Wood BJ, Zhang H, Durrani A, et al. Navigation with electromagnetic tracking for interventional radiology procedures: a feasibility study. J Vasc Interv Radiol. 2005;16:493–505.
55. Yaniv Z, Wilson E, Lindisch D, et al. Electromagnetic tracking in the clinical environment. Med Phys. 2009;36:876–92.
56. Hastenteufel M, Vetter M, Meinzer HP, et al. Effect of 3D ultrasound probes on the accuracy of electromagnetic tracking systems. Ultrasound Med Biol. 2006;32:1359–68.
57. LaScalza S, Arico J, Hughes R. Effect of metal and sampling rate on accuracy of flock of birds electromagnetic tracking system. J Biomech. 2003;36:141–4.
58. Hughes-Hallett A, Mayer EK, Marcus HJ, et al. Augmented reality partial nephrectomy: examining the current status and future perspectives. Urology. 2014;83:266–73.
59. Greco F, Cadeddu JA, Gill IS, et al. Current perspectives in the use of molecular imaging to target surgical treatments for genitourinary cancers. Eur Urol. 2014;65:947–64.
60. Nicolau S, Soler L, Mutter D, et al. Augmented reality in laparoscopic surgical oncology. Surg Oncol. 2011;20:189–201.
61. Su LM, Vagvolgyi BP, Agarwal R, et al. Augmented reality during robot-assisted laparoscopic partial nephrectomy: toward real-time 3D-CT to stereoscopic video registration. Urology. 2009;73: 896–900.
62. Teber D, Simpfendorfer T, Guven S, et al. In-vitro evaluation of a soft-tissue navigation system for laparoscopic prostatectomy. J Endourol. 2010;24:1487–91.
63. Simpfendorfer T, Baumhauer M, Muller M, et al. Augmented reality visualization during laparoscopic radical prostatectomy. J Endourol. 2011;25:1841–5.
64. Nakamoto M, Ukimura O, Faber K, et al. Current progress on augmented reality visualization in endoscopic surgery. Curr Opin Urol. 2012;22:121–6.
65. Rothwax JT, George AK, Wood BJ, et al. Multiparametric MRI in biopsy guidance for prostate cancer: fusion-guided. Biomed Res Int. 2014;2014:439171.
66. Rastinehad AR, Turkbey B, Salami SS, et al. Improving detection of clinically significant prostate cancer: magnetic resonance imaging/transrectal ultrasound fusion guided prostate biopsy. J Urol. 2014;191:1749–54.
67. Wysock JS, Rosenkrantz AB, Huang WC, et al. A prospective, blinded comparison of magnetic resonance (MR) imaging-ultrasound fusion and visual estimation in the performance of MR-targeted prostate biopsy: the PROFUS trial. Eur Urol. 2014;66:343–51.
68. Park BH, Jeon HG, Jeong BC, et al. Influence of magnetic resonance imaging in the decision to preserve or resect neurovascular bundles at robotic assisted laparoscopic radical prostatectomy. J Urol. 2014;192:82–8.
69. Muller BG, van den Bos W, Brausi M, et al. Role of multiparametric magnetic resonance imaging (MRI) in focal therapy for prostate cancer: a Delphi consensus project. BJU Int. 2014;114: 698–707.
70. Partanen A, Yerram NK, Trivedi H, et al. Magnetic resonance imaging (MRI)-guided transurethral ultrasound therapy of the prostate: a preclinical study with radiological and pathological correlation using customised MRI-based moulds. BJU Int. 2013;112: 508–16.
71. Betrouni N, Colin P, Puech P, et al. An image guided treatment platform for prostate cancer photodynamic therapy. Conf Proc IEEE Eng Med Biol Soc. 2013;2013:370–3.
72. Hegde JV, Mulkern RV, Panych LP, et al. Multiparametric MRI of prostate cancer: an update on state-of-the-art techniques and their performance in detecting and localizing prostate cancer. J Magn Reson Imaging. 2013;37:1035–54.
73. Hambrock T, Vos PC, Hulsbergen-van de Kaa CA, et al. Prostate cancer: computer-aided diagnosis with multiparametric 3-T MR imaging--effect on observer performance. Radiology. 2013;266: 521–30.

Part II

Prostate

Prostate Imaging

4

Osama Elbuluk, Baris Turkbey, and Peter Choyke

In 2013, the American Cancer Society estimated that prostate cancer (PCa) would account for 28 % of all new cancers, more than twice that of any other malignancy [1]. It is the second leading cause of cancer-related mortality in Western men with approximately 30,000 deaths per year and is thus a major public health problem [1]. PCa, however, represents a broad spectrum of diseases ranging from indolent tumors with no risk of lethality to highly aggressive cancers that rapidly metastasize, leading to death. Similarly, treatment outcomes have been shown to vary greatly depending upon tumor staging. For example, treatment of cancer confined to the prostate is usually curative with a greater than 90 % 5-year survival, while treatment of advanced metastatic disease is far less effective with survival measured in months and accompanied by a poor quality of life. This has placed a significant emphasis on developing improved screening and staging methods.

Currently, the two major screening modalities are digital rectal examination (DRE) and serum prostate-specific antigen (PSA) measurement. Current clinical guidelines suggest that an abnormality found with either screening method prompts a transrectal ultrasound (TRUS)-guided systematic "random" biopsy. Unfortunately, this current algorithm often discloses low-grade cancers which are usually indolent and may not require treatment, while missing larger, high-grade tumors outside the typical biopsy template. DRE has a poor overall sensitivity (37 %) and positive predictive value (4–11 %) in patients with a PSA from 0 to 2.9 ng/mL [2]. PSA screening has a higher sensitivity, and, as a result, more cancers have been diagnosed earlier in their disease course. Currently, about 82 % of new cases are localized at the time of diagnosis [3]. However, PSA screening has a very low specificity (36 %) and has been found to be elevated in a variety of benign pathologies, such as prostatitis and benign prostatic hyperplasia (BPH) [4]. Also, the widely accepted PSA cutoff of 4.0 ng/mL sometimes fails to detect clinically significant cancer in patients with normal PSA values but leads to the overdiagnosis of nonclinically significant tumors [5]. Importantly, PSA screening has been associated with only modest survival benefits, which are counterbalanced by considerable degradation of quality of life in many men not benefiting from cancer detection. Consequently, the US Preventive Services Task Force has most recently given PSA testing a grade "D" recommendation, discouraging its use as a screening tool [6]. This is in part due to the limitations of PSA but also in part due to the limitations of TRUS biopsy both of which conspire to detect many low-grade, "insignificant" cancers that result in overtreatment. TRUS biopsy is performed blindly, without tumor visualization, and often fails to sample areas of the prostate which may harbor clinically significant disease, mainly the anterior gland, midline, and apex. This has resulted in an overdiagnosis of indolent disease (up to 50 %) in the posterior prostate as well as a high false-negative rate (up to 40 %) and the undesirable outcome of underdiagnosing lethal disease [7, 8]. Furthermore, TRUS biopsy results underestimate tumor Gleason grade in almost half of cases due to poor sampling [9]. This often leads to inappropriate assignment to active surveillance and delay in active treatment. The limitations of PSA and TRUS biopsy highlight the pressing need for better screening and imaging tools.

Advancements in magnetic resonance imaging (MRI) over the past 30 years have begun to address this need and are revolutionizing the way PCa is diagnosed and treated. When performed in a multiparametric fashion, combining anatomic and functional sequences, MRI provides valuable information for better detection, localization, and staging. Coupled with the developments of novel tracers for PET/CT, MR imaging may be the key to providing focal therapy in the near future. This chapter seeks to address current imaging techniques as they pertain to the management of PCa.

O. Elbuluk, BS • B. Turkbey, MD (✉) • P. Choyke, MD (✉)
Molecular Imaging Program, National Cancer Institute, National Institutes of Health, Bethesda, MD, USA
e-mail: oelbuluk@gmail.com; turkbeyi@mail.nih.gov; Pchoyke@mail.nih.gov

A.R. Rastinehad, D.N. Siegel (eds.), *Interventional Urology*, DOI 10.1007/978-3-319-23464-9_4

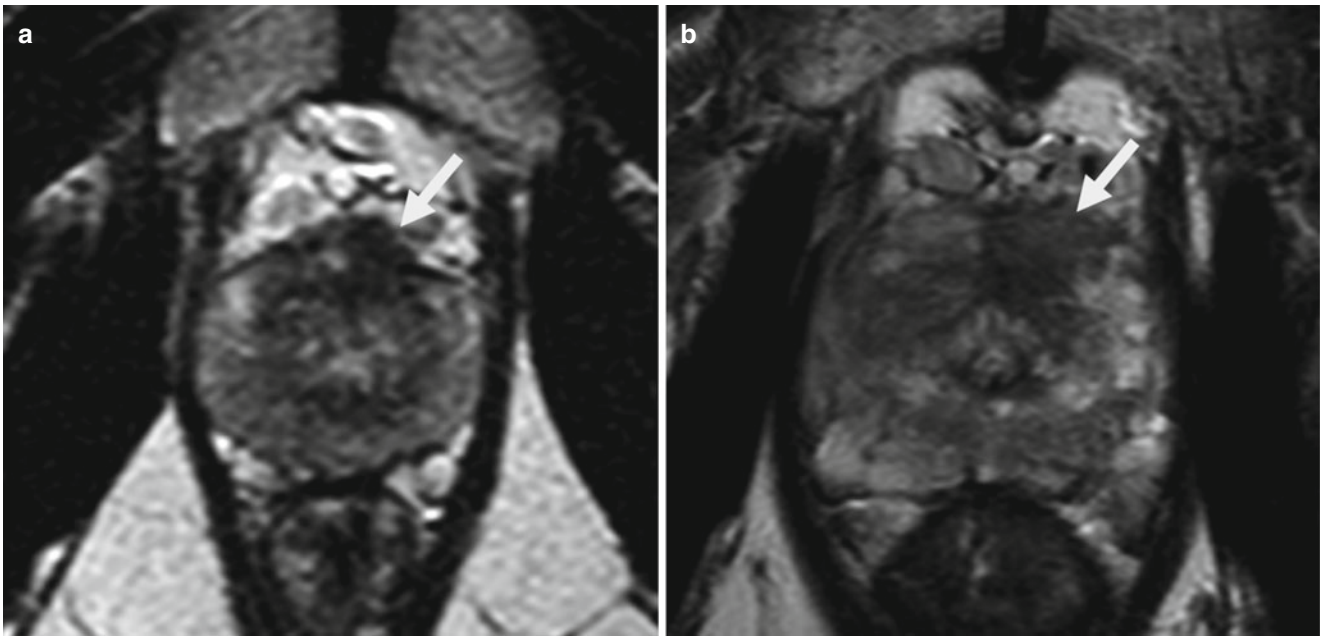

Fig. 4.1 Axial T2W MRI obtained at 1.5 T in a 59-year-old man (PSA = 7.12 ng/ml) showing a hypointense lesion in the left anterior transition zone (*arrow*). Targeted biopsy revealed Gleason 3 + 4 (40 %) prostate cancer within that lesion (**a**). Axial T2W MRI obtained at 3 T in a 65-year-old man (PSA = 7.94 ng/ml) shows a hypointense lesion in the left anterior transition zone (*arrow*), which revealed Gleason 3 + 3 (70 %) prostate cancer after a targeted biopsy (**b**). The image obtained at 3 T has a higher spatial resolution

MRI of the Prostate

MRI is the most promising imaging modality for the prostate as it has high spatial resolution and exceptional soft tissue contrast. The current practice is to perform a multiparametric MRI of the prostate, which consists of T2-weighted (T2W) imaging plus functional sequences such as diffusion-weighted imaging (DWI), dynamic contrast-enhanced (DCE) imaging, and magnetic resonance spectroscopy (MRS) imaging. However, many institutions have removed MRS imaging from their prostate MRI protocol because it is technically demanding and time consuming.

Prostate MRI can be performed using a 1.5 T or 3 T MRI scanner with or without the use of an endorectal coil (ERC). Quality is highly dependent on the scanner and the technique. Multiple studies have shown either no difference or better image quality at 1.5 T with endorectal coil versus 3 T with body phased-array coil [10–12]. However, since these studies change more than one variable at a time, it is difficult to isolate the importance of field strength and the endorectal coil. Certainly, there is agreement that 3 T imaging achieves equal or superior image quality to comparably performed 1.5 T imaging (Fig. 4.1). Generally, to optimize quality, 3 T is preferred as it has a higher signal-to-noise ratio (SNR) resulting in better image quality.

The use of endorectal coils is more controversial since they add time and cost to the study and are uncomfortable for patients. Much of the groundwork for prostate MRI was performed with 1.5 T scanners where the best results were obtained using both a phased-array body coil and an endorectal coil (ERC) [10, 13, 14]. However, the necessity of a coil at 3 T remains uncertain as some clinicians feel that the increased SNR may obviate the need for an ERC (Fig. 4.2). Turkbey et al. recently showed better sensitivity (76 % vs. 45 %) and positive predictive value (80 % vs. 64 %) for T2W plus DWI when performed with an endorectal dual coil than with a non-endorectal coil [15]; however, almost of the additional lesions detected with the coil were considered not clinically significant. Heijmink and colleagues also found endorectal coils to have better image quality and accuracy for tumor localization when compared to body array coils [13]. Given the lack of consensus, however, endorectal coils are usually omitted in the interest of the patient's comfort. When an endorectal coil is used, it should be properly distended and all air should be removed to eliminate artifacts due to gas [3]. If possible, the balloon surrounding the coil should be filled with fluorinert (PFC 770), which produces the least susceptibility artifact on DWI. However, this agent is not widely available and is sometimes replaced with barium. Confusion over how to fill the endorectal coil balloon has reduced interest in it further. Although there is no consensus, the general belief is that a non-endorectal coil MRI is sufficient for lesion detection and follow-up purposes, while the improved resolution with endorectal coil MRI is more necessary in tumor staging and before initiation of active surveillance or active treatment (surgery, radiotherapy, focal

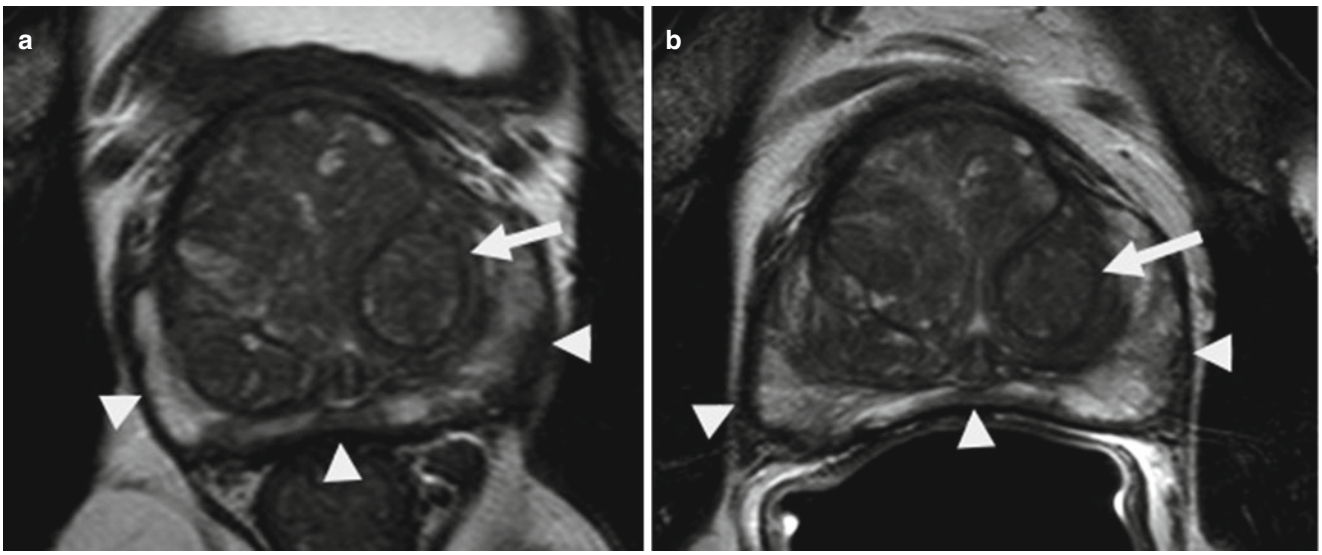

Fig. 4.2 Axial T2W MR images obtained without (**a**) and with (**b**) endorectal coil in a 53-year-old man (PSA = 8.82 ng/ml). Both axial T2W MR images show a well-defined BPH nodule in the left transition zone (*arrows in* **a**, **b**); additionally, the prostate capsule is accurately visualized in both images (*arrowheads in* **a**, **b**)

therapy). Realistically, however, it is difficult to justify two prostate MRIs in one workup of prostate cancer, so as a practical matter, prostate MRI is usually obtained without the endorectal coil.

Conventional (Anatomic) MRI: T1W MRI, T2W MRI

Conventional MR imaging is comprised of two sequences, T1-weighted (T1W) and T2-weighted spin echo imaging. T1W MR images have poor contrast in the prostate and fail to adequately differentiate the anatomic zones. They provide little utility for tumor detection and localization; however, they are of importance for identifying post-biopsy hemorrhage. Hemorrhage causes local magnetic field distortions and hinders the utility of T2W MRI by mimicking cancer in the peripheral zone (Fig. 4.3). On T1W MR images, biopsy hemorrhage appears as a hyperintense region. To preserve the value of T2W MRI, it is recommended that images be obtained at least 6–8 weeks after biopsy [16–19].

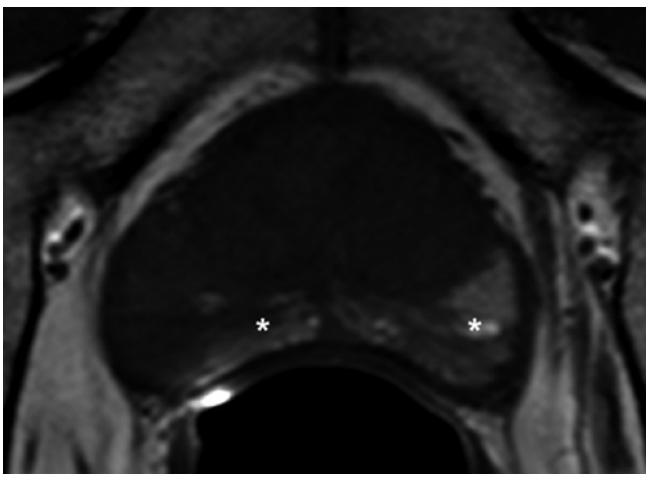

Fig. 4.3 A 61-year-old man (PSA = 15.26 ng/ml) who underwent a prostate biopsy 7 weeks before the MRI procedure. Axial T1W MR image shows biopsy-related residual hemorrhage within the entire left peripheral zone and in the medial half of the right peripheral zone (*asterisk*)

T2W is the mainstay of prostate MR imaging. It has high spatial resolution and allows for clear delineation of the intraprostatic zonal anatomy. Anatomically, the prostate gland is divided into a peripheral zone (PZ) and transitional zone (TZ) with a smaller central zone (CZ) collectively referred to as the central gland, the periurethral zone, and anterior fibromuscular stroma. The PZ is the site of about 65 % of prostate cancers and is normally high in signal intensity on T2W compared to the obturator muscle [20]. On the contrary, the central gland is of lesser intensity and far more heterogeneous due to BPH. The PZ and TZ are separated by a poorly defined "surgical pseudocapsule," while the true surgical capsule surrounds the prostate posteriorly and appears as a distinct hypointense rim [21]. The periurethral zone is a small ring of tissue that surrounds the urethra and has low signal intensity on T2W. The anterior fibromuscular stroma is an area of non-glandular tissue located anterior to the prostate and is also hypointense on T2W imaging. Other important surrounding structures include the neurovascular bundles and seminal vesicles. The neurovascular bundles are located on the posterolateral aspect of the true capsule and are seen as both hyper- and hypointense foci on T2W

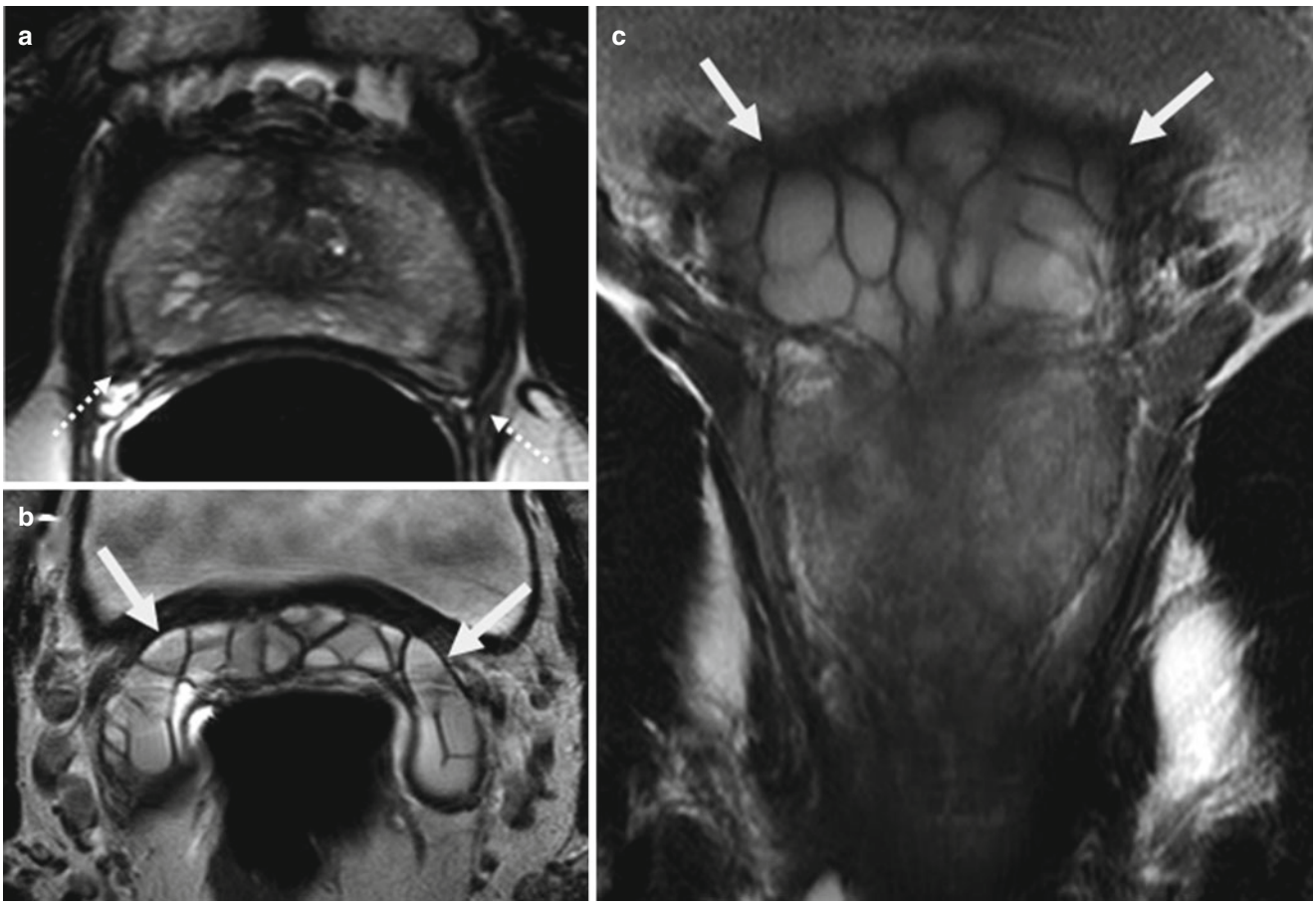

Fig. 4.4 A 44-year-old man (PSA = 1.7 ng/ml). Axial T2W MR images show the neurovascular bundles posterolateral to the prostate bilaterally (*dashed arrows*, **a**). Axial (**b**) and coronal (**c**) T2W MR images demonstrate the seminal vesicles (*arrows*) in the same patient

MRI. These bundles contain innervation essential for proper erectile function. The seminal vesicles are found superior to the prostate and posterior to the bladder base and appear as loculated, grape-like, hyperintense structures on T2W images (Fig. 4.4).

On T2W images, PCa in the PZ can appear as a poorly defined region of low signal intensity within the hyperintense PZ background (Fig. 4.5). Unfortunately, this pattern is nonspecific and can be seen in several benign conditions including atrophy, chronic prostatitis, hyperplasia, and post-treatment effects, caused by radiation, cryotherapy, or hormonal therapy [22]. Higher Gleason patterns of 4 or 5 have been shown to have lower T2 signal intensities than lower Gleason 3 patterns [23]. T2 signal intensity is also dependent upon tumor density and growth pattern. Langer and colleagues showed that PZ cancers mixed with normal tissue, which are often lower-grade tumors, can be isointense to background on T2 while dense, higher-grade tumors have lower intensities [24]. CG cancers account for approximately 30 % of prostate cancers and are much more difficult to diagnose on T2W MRI than are PZ cancers [20]. This is largely due to the expected heterogeneity of BPH and the ability of BPH nodules to mimic neoplastic lesions. BPH nodules can be classified as glandular or stromal (Fig. 4.6). In particular, stromal hyperplasia appears hypointense on T2W MRI and most closely mirrors cancer [25]. CG cancers are identified

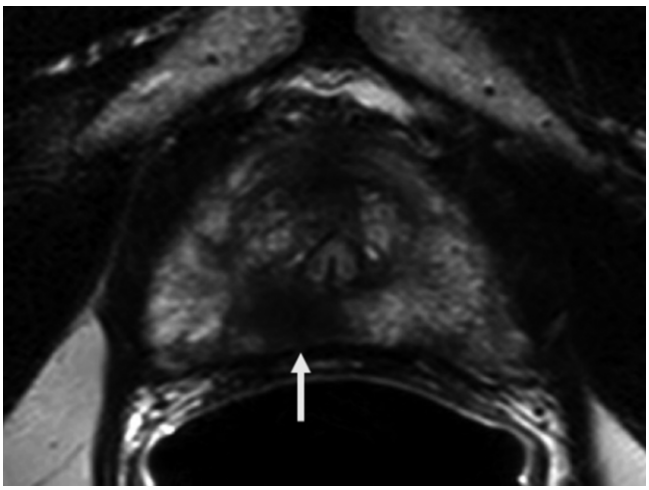

Fig. 4.5 Axial T2W MRI of a 64-year-old man (PSA = 2.65 ng/ml) with a hypointense lesion in the right apical peripheral zone (*arrow*), which is confirmed to include Gleason 4 + 4 prostate cancer

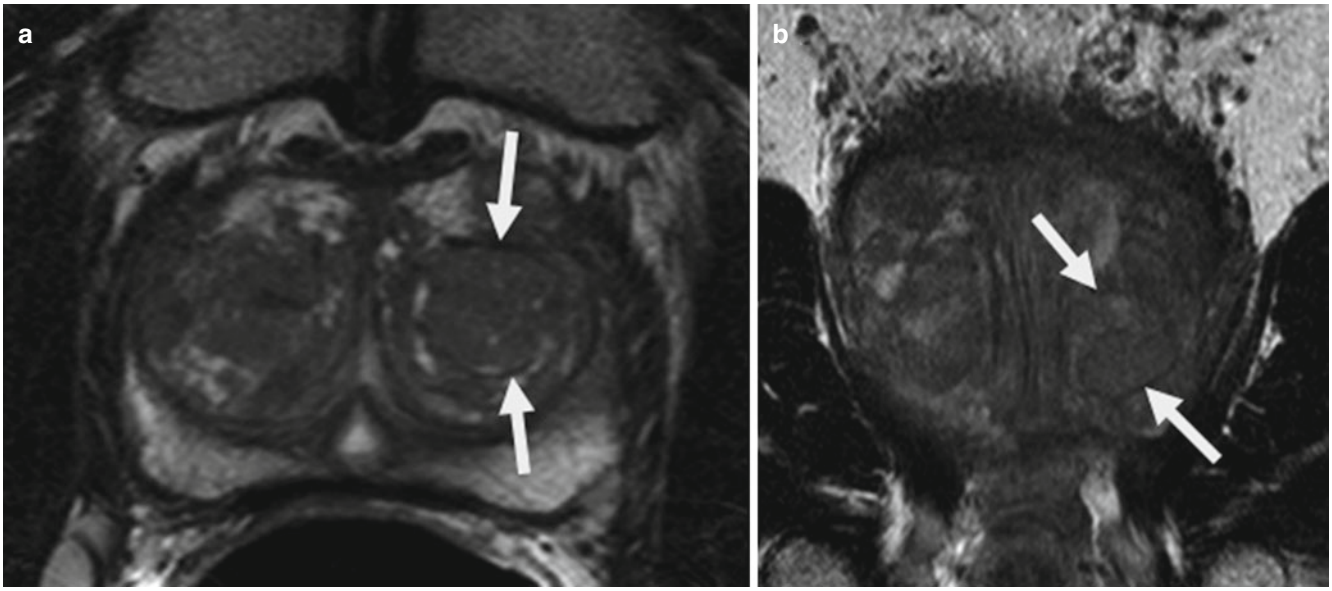

Fig. 4.6 Axial (**a**) and coronal (**b**) T2W MR images of a 67-year-old man (PSA = 6.49 ng/ml) show a hypointense lesion in the left apical mid-transition zone which mimics a prostate cancer lesion; however, the lesion has a well-demarcated capsule around it (*arrows in* **a**, **b**) which is consistent with a BPH nodule

based on their morphologic features such as homogenous hypointensity, ill-defined margins, absence of a capsule, and amorphous or lenticular shape [25–28]. T2W MR imaging has a wide range of sensitivities (27–100 %) and specificities (32–99 %) [29, 30]. This is largely attributed to differences in patient populations and MR methods across studies, as well as varying levels of experience of the MRI readers.

Nevertheless, T2W MRI does have some limitations. T2W MR imaging is highly susceptible to inter- and intraobserver variability. If findings cannot be reproduced, clinicians will continue to incorrectly stage cancers as seen with the current methods of PSA and TRUS biopsy. Efforts are currently underway to standardize the reporting of prostate MRI and improve reproducibility using the "PI-RADS" (Prostate Imaging – Reporting and Data System) scoring system [31].

Functional MRI: Diffusion-Weighted MR Imaging

Diffusion-weighted MRI is a functional MRI technique that is relatively quick, readily available, and does not require the use of intravenous contrast media. It evaluates the Brownian motion of free water within tissues. Typically, prostate cancers allow less diffusion of water relative to healthy tissue owing to their higher cellular density and loss of the normal tubular glandular structure of the prostate, which allows relatively high free water motion. DWI is quantified by calculating the apparent diffusion coefficient (ADC), which is related to the slope of change of the received signal as a function of magnetic gradient (b-value) strength, and is displayed as a parametric map reflecting the relative ADC [32]. Abnormal areas are represented on DW MRI as a bright signal associated with "restricted" diffusion which is dark on (ADC) maps (Fig. 4.7). ADC is a function of the freedom water molecules that has to travel within tissue [33]. The b-value is the measure of magnetic gradient strength and ranges from 0 to 2000 s/mm^2. The higher the b-value, the greater the loss of signal in unrestricted tissue and the more visible becomes pathologic tissue (Fig. 4.7). However, there is a loss of signal strength with increasing b-value placing practical constraints on its use. Recently, with improvements in technology, higher b-values, 1500–2000 s/mm^2, have been shown to both better depict cancers as well as minimize the effects of hemorrhage in the peripheral zone [34–38]. However, the higher the b-value, the worse the signal-to-noise ratio is, and it is imperative to find a balance between these two parameters.

DWI can be evaluated qualitatively and quantitatively. When evaluated qualitatively, the ADC map and the high b-value (b >1400 s/mm2) image should be evaluated together. Quantitatively, the ADC value is dependent upon many factors, including magnet strength, presence or absence of an endorectal coil, and the b-value, so that values cited in the literature vary greatly. Furthermore, it has been shown that ADC values in cancerous tissues can overlap significantly with healthy prostate and benign conditions, such as prostatitis [25, 39]. This has made it very challenging to establish a universal ADC cutoff value for PCa. ADCs have also been shown to have different accuracies for diagnosing cancer based on the anatomic location of the cancer within the prostate [40]. For instance, PZ cancers are easier to detect than

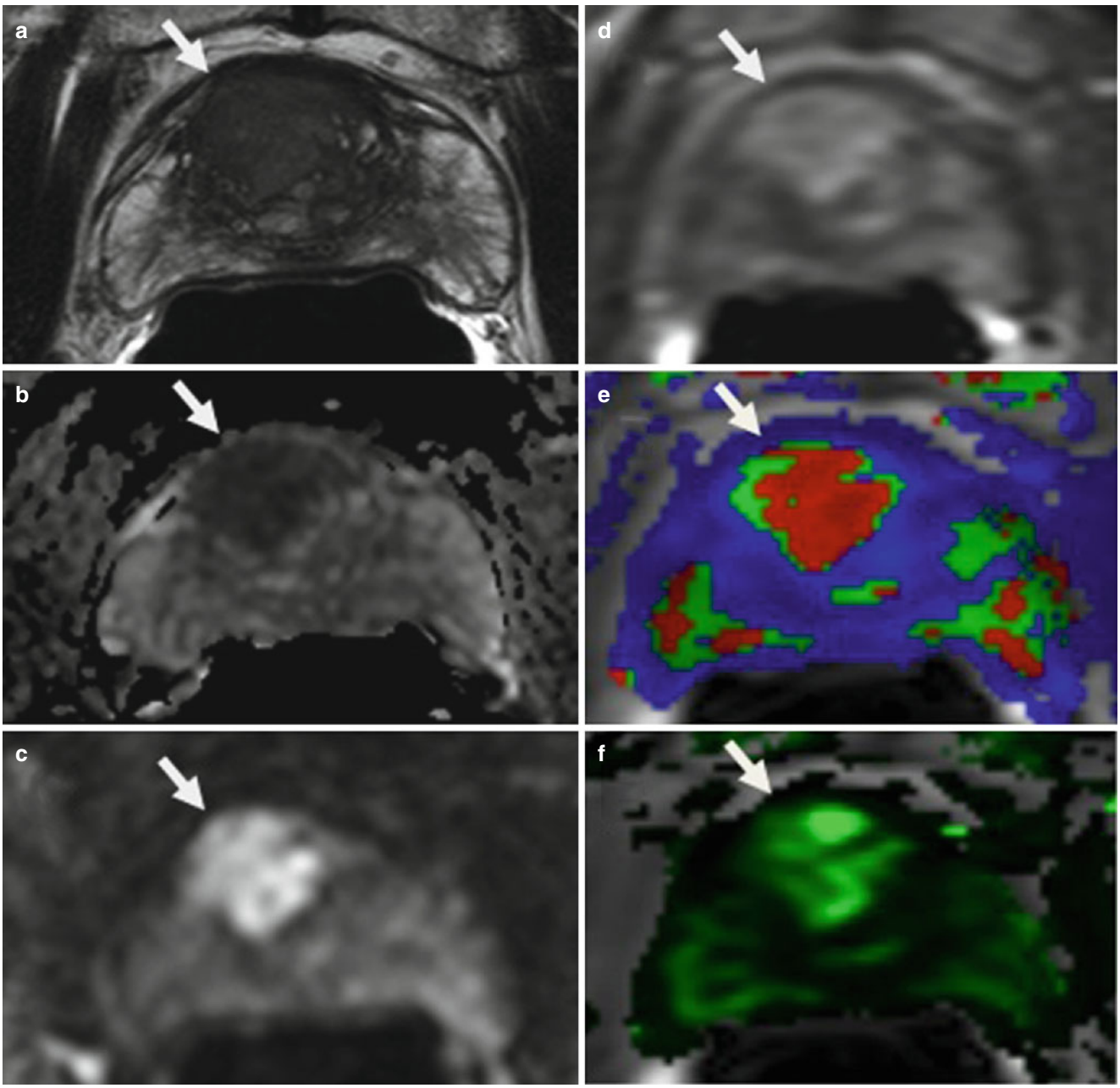

Fig. 4.7 A 65-year-old man with a PSA of 14.91 ng/ml. Axial T2W MRI shows a hypointense lesion in the right mid-anterior transition zone with capsular bulge (*arrow*) (**a**). ADC maps of DW MRI (**b**), b = 2000 DW MRI (**c**), raw DCE-MRI (**d**), K^{trans} (**e**), and k_{ep} (**f**) maps derived from DCE-MRI localize the right-sided lesion, which included Gleason 4 + 4 prostate cancer (*arrows*)

TZ cancers using ADC owing to the higher tubular composition of the normal PZ (causing background tissue to have high water diffusion) and more heterogeneous composition of the TZ (causing background tissue to have a mix of high and low water diffusion).

DWI is a practical and time-efficient MRI sequence and plays a leading role alongside T2W imaging. A meta-analysis of 5892 patients showed that DWI alone yielded higher sensitivity, specificity, and area under the ROC curve than T2W alone [41]. Similarly, DWI + T2W had a significantly better sensitivity and specificity than T2W alone. This is important because it is unlikely that DWI will ever be performed alone as this would eliminate the valuable, anatomic information obtained from T2W. Like most diagnostic tools, DWI has its shortcomings. It has a lower spatial resolution and is susceptible to bulk motion [42]. Moreover, air in the rectum can cause distortion of the prostate image due to susceptibility artifacts. With current efforts directed toward parallel

imaging and the implementation of higher field strength magnets, the shortcomings of DWI are being addressed. When used as part of multiparametric MRI protocols, it holds great utility for improving PCa detection and management.

Functional MRI: Dynamic Contrast-Enhanced (DCE) MRI

Angiogenesis is one of the hallmarks of cancer. During cancer growth, blood vessel proliferation is induced in response to oxygen and nutrient deprivation. In turn, these new vessels are more permeable and tortuous than the normal vasculature. This process can be monitored and imaged using a functional MRI technique known as DCE-MRI. DCE consists of consecutive T1W gradient echo images of the prostate before, during, and after an intravenous bolus of a low-molecular-weight gadolinium chelate. The entire prostate is rescanned continuously for several minutes, and the interval between consecutive scans is known as the temporal resolution. The temporal resolution can vary from 5 to 30 s with preference for the shorter times to catch the peak of enhancement after injection. DCE-MRI is carried on for approximately 5 min after contrast injection begins [19].

DCE-MRI can be evaluated qualitatively, quantitatively, or semiquantitatively (Fig. 4.7). Qualitatively, tumors exhibit early enhancement and early washout of the contrast relative to the surrounding prostate [43]. Quantitative analysis entails obtaining an enhancement curve from which a set of kinetic parameters which can be calculated by fitting the curves to a pharmacokinetic model such as the Tofts model. The Tofts model produces parameters, such as K^{trans} (transendothelial transport of contrast medium from vascular compartment to the tumor interstitium), k_{ep} (reverse transport parameter of contrast medium back to the vascular space), fpV (plasma volume fraction compared to whole tissue volume), and V_e (extravascular, extracellular volume fraction of the tumor) for describing tumor and tissue permeability [21]. K^{trans} and k_{ep} tend to differ in higher-grade tumors versus normal prostate tissue. However, these enhancement patterns can be nonspecific. For example, well-vascularized BPH nodules and cancers in the TZ enhance similarly [44]. Semiquantitative analysis entails analyzing the enhancement curve for a given region of interest in the prostate. For instance, pertinent parameters in this type of analysis are the slope of the washin and washout of the curve, time to peak, and peak enhancement. Semiquantitative analysis is fast and simple but is highly influenced by MRI hardware settings [45] and therefore may be less reproducible.

DCE-MRI holds significant value in improving tumor localization. It is limited by a low sensitivity as well as a lack of consensus guidelines over image acquisition parameters. Furthermore, quantitative parameters acquired using two-compartment models have a large standard deviation making it difficult to compare across studies and between different centers. Its greatest utility remains when it is used in a multiparametric manner with other MRI sequences.

Functional MRI: Magnetic Resonance Spectroscopy (MRS) Imaging

MRS is a functional MRI technique which displays the chemical concentrations of specific metabolites within the prostate, mainly citrate, choline, and creatine. Each metabolite has a resonance frequency reflective of the location of protons within the molecule, and this is displayed as a spectral profile which, in turn, can be converted into a metabolite map known as MRS imaging or MRSI. Choline, citrate, and creatine resonate at 3.2, 2.6, and 3.0 parts per million (ppm), respectively. Under normal physiologic conditions, the prostate has high levels of citrate and low levels of choline. Prostate epithelial cells are high in zinc content, which blocks the activity of aconitase in the Krebs cycle and this leads to a buildup of citrate. In cancer, zinc levels are diminished allowing aconitase to execute normal enzymatic activity and eliminate the buildup of citrate (Fig. 4.8). Additionally, choline compounds play a role in the synthesis and degradation of phospholipids used in maintaining the integrity of cell membranes. In cancer, the high choline concentration in the cytosol and interstitial tissue is simply reflective of increased cell turnover. It can be difficult to differentiate choline peaks from creatine peaks due to nonspecific peaks arising from other polyamines, so the choline-to-citrate ratio is often used as a more accurate marker of cancer.

MRS has a number of significant limitations. It is very technically demanding to perform relative to other MRI sequences and requires the presence of an onsite MRS physicist to achieve excellent results. This is due to the need to shim the magnet properly and eliminate signal from water and fat. Similarly, MRS is quite time consuming and this has caused many centers to omit it from their multiparametric protocols. The benefits of MRS in prostate cancer management are controversial. Casciani et al. evaluated the benefit of adding MRS to T2W for PCa diagnosis, and although there was an incremental benefit, it was not statistically significant [46]. Weinreb and colleagues investigated the same outcome in a large, multicenter trial of 134 patients and found that the accuracy of 1.5 T MRI + MRS was equivalent to that of MR imaging alone [30]. Others have shown some usefulness for MRS; for example, in a retrospective study of 67 patients, the volume of malignant metabolism on MRS was found to be an independent predictor of biochemical

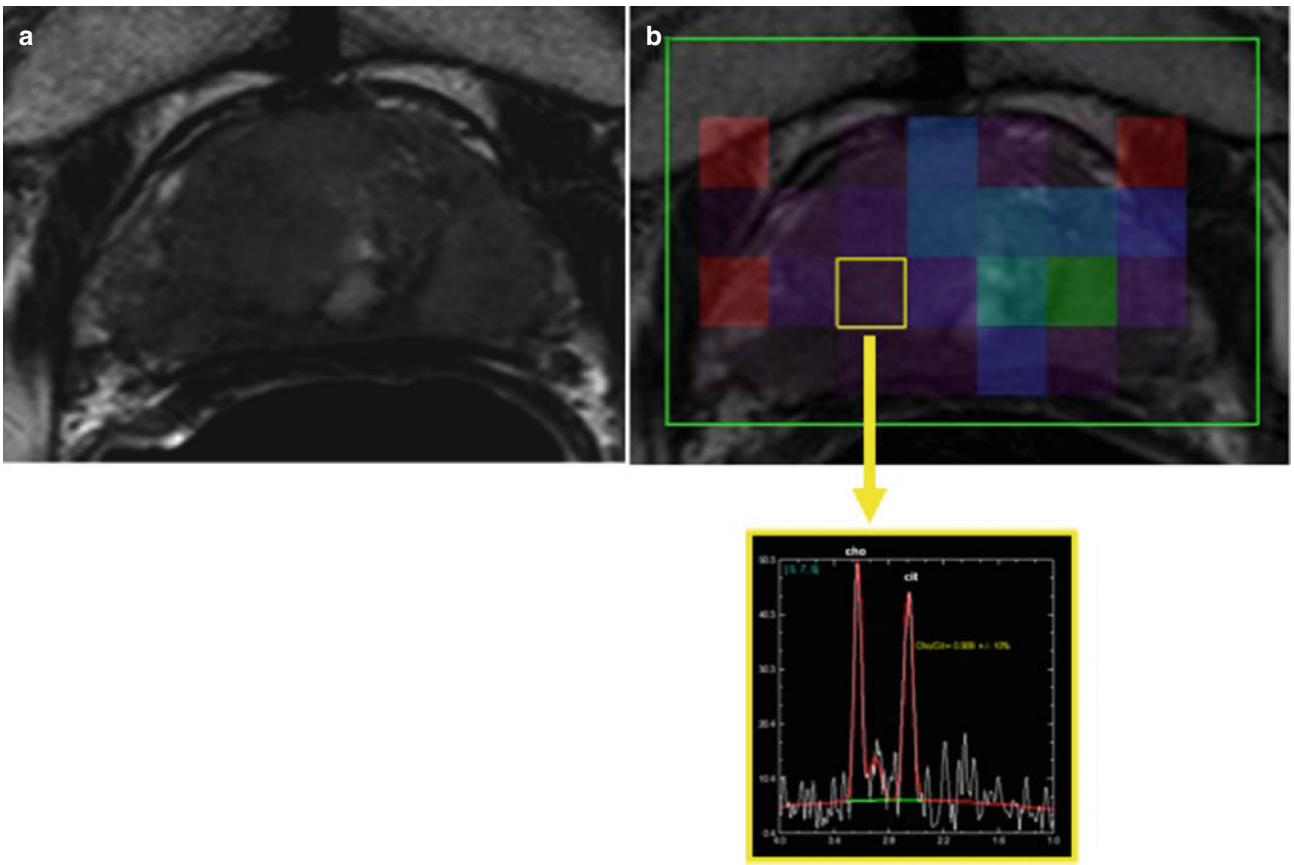

Fig. 4.8 Axial T2W MRI of a 67-year-old man (PSA = 8.321 ng/ml) shows a large lesion affecting almost the entire prostate gland (Gleason 4 + 4) (**a**). MR spectroscopy shows increased choline peak within the tumor lesion (**b**)

recurrence [47]. In summary, MRS has taken a backseat to both DWI and DCE in the realm of prostate cancer, but it remains to be seen if there is an appropriate niche for MRS implementation.

Clinical Applications of Multiparametric MRI

Each of the aforementioned MRI techniques has inherent strengths and weaknesses. To minimize shortcomings while optimizing utility, these techniques are often combined into a multiparametric MRI (mp-MRI) examination comprised of both conventional and functional sequences. The following section will address the use of mp-MRI for various aspects of PCa management.

Tumor Localization/Detection

As mentioned previously, TRUS biopsies often fail to detect cancer, which leads to repeat biopsies in order to establish a diagnosis even while PSA levels continue to rise. These repeat biopsies often have a lower yield than the initial biopsy [48]. It is thought that since MR imaging techniques are more specific than serum PSA measurement and TRUS biopsy; they could potentially improve tumor detection and decrease the number of biopsies. Furthermore, MR imaging could be particularly helpful in patients with an increasing PSA and negative biopsy [49, 50]. Unfortunately, it is difficult to compare findings across prospective studies due to differences in analysis, sample size, mean PSA of patient population, and criteria for cancer detection [42]. This is well evidenced in a recent meta-analysis by de Rooij and colleagues which only had seven studies which met inclusion criteria [51]. Pooled sensitivities and specificities were 74 % (0.66–0.81) and 88 % (0.82–0.92), respectively. Despite variability in technical parameters across studies, the high specificity suggests a likely role for performing mp-MRI prior to biopsies. Furthermore, MRI has proven to be most valuable in aiding tumor detection when it is used to guide biopsies. This has led to the advent of MRI fusion biopsy methods, which are covered at length in other areas of this book.

The diagnostic accuracy of multiparametric MRI has also been shown to be dependent upon the tumor location (TZ vs. PZ) and the underlying histology of the tumor. A prospective

study of 57 patients showed that sensitivity for mp-MRI drops from 80 to 53 % in the PZ versus the TZ, respectively [52]. The role of mp-MRI in diagnosing tumors in the TZ remains to be defined. Some studies have shown an added benefit with DWI, while others have shown no improvement with either DWI or DCE [52–54]. Recent work from Hoeks and colleagues found that at 3 T, localization accuracy did not differ between T2W and mp-MRI for all TZ cancers [55]. T2W imaging has proven vital for diagnosing TZ cancers, but the role of ADC maps and DCE parameters is still to be elucidated, and there may be great value to DWI obtained with high b-values (1400–2000 s/mm2) [37].

Lower-grade tumors, in general, are more difficult to detect [22, 56–58]. Pathologic features associated with an increased chance of detection include Gleason score (7 or greater), size (1 cm or greater), and solid growth [56]. A prospective study of 175 patients also found that detection rates were influenced by the following features: Gleason score, tumor volume, histological architecture, and location [59]. Multiparametric MRI is unique in that it is highly sensitive to histologic and morphologic changes in prostate cancer. This feature makes it useful in monitoring patients on active surveillance.

Tumor Staging

Local staging is an important application of MR imaging in prostate cancer. Current staging is performed using DRE, PSA, and TRUS-guided biopsy and such an approach understages disease in almost 60 % of cases [60]. Hence, many centers have evaluated the utility of MR imaging for PCa staging. Although numbers cited in the literature vary, the majority of the data supports the use of MRI as a staging tool. Most recently, Couñago et al. evaluated the accuracy of preoperative 3 T mp-MRI for local staging and found mp-MRI to correctly stage 79 % of cases while overstaging 6 % and understaging 15 % [61]. Furthermore, it was found that if mp-MRI was included in the decision-making process for radiation therapy, 34 % of cases would have been managed differently.

The presence of extraprostatic extension (EPE) upgrades tumor stage to T3a and is important to identify on imaging as it greatly influences the treatment approach. EPE usually presents as a disruption of the capsule with direct extension of the tumor into the periprostatic fat. Other signs of EPE include encasing of the neurovascular bundle, asymmetric neurovascular bundles, contour angulation, capsular irregularity or obscuration, tumor-capsule margin greater than 1.5 cm, and obliteration of the rectoprostatic angle [3]. In a retrospective study, assessing the value of ADC in predicting EPE, greatest % of cancer in all biopsy cores, biopsy-based Gleason score, and tumor ADC were all found to be independent predictors of EPE [62]. The AUC for ADC was 0.771 showing that ADC may be a potential marker for determining EPE preoperatively. In another retrospective study of 108 patients, DCE combined with T2W produced an overall sensitivity, specificity, positive predictive value, and negative predictive value of 75 %, 92 %, 79 %, and 91 %, respectively, for predicting EPE [63]. An equally important finding was that these percentages were achieved across all levels of reader experience. This data supports a role for 3 T MRI with endorectal coil as a tool for staging and detecting EPE.

Seminal vesicle invasion (SVI) is another important preoperative finding that upgrades tumor stage to T3b and is important for both management and prognosis. Patients with SVI often have higher grade, more aggressive tumors, and a higher risk for local recurrence [64, 65]. On T2W, SVI is identified by one of the following findings: extension of the tumor directly around or into the seminal vesicles, breakdown of normal seminal vesicle architecture, asymmetric wall thickening of the seminal vesicle, loss of the angle between the seminal vesicle and the prostate, or low signal intensity in the seminal vesicle [3]. For experienced readers, low signal intensity within the seminal vesicle and lack of preservation of seminal vesicle architecture have been found to be the most sensitive and specific [66]. A retrospective study of 131 patients found T2W alone to have high specificity and negative predictive value (>90 %) and moderate sensitivity and positive predictive value (50–60 %) [67]. DWI significantly improved specificity and positive predictive value but not AUC, while DCE did not provide any incremental value although focal enhancement of a low signal seminal vesicle is supportive of seminal vesicle invasion.

Assessment of Tumor Aggressiveness

Aggressiveness or severity in prostate cancer is defined by the Gleason score, the sum of the two most prevalent Gleason grades at histology [68, 69]. Unfortunately, TRUS random biopsies often incorrectly sample the tumor leading to upgrading and occasionally downgrading at surgery. This uncertainty leads to downstream errors in PCa treatment. Recent work has shown that mp-MRI holds potential for providing preoperative information on tumor aggressiveness. Many studies have shown a strong correlation between ADC value and Gleason grade [70–75]. In a retrospective study of 51 patients with a total of 62 PZ tumors, median ADC had a negative correlation with Gleason grade, and when stratified by high, intermediate, and low Gleason score, the ADC values were statistically significant between groups [74]. Verma and colleagues obtained a similar finding in the PZ but found no correlation with ADC values and Gleason grade in the TZ [73]. The D'Amico risk stratification system is another way to assess PCa aggressiveness and risk, and it incorporates

PSA, Gleason grade, and percent positive core biopsy [76]. Turkbey and colleagues showed a negative correlation with mean ADC of PZ tumors and both Gleason grade and D'Amico clinical risk scores [77]. ADC values were able to discern intermediate-to-high clinical risk scores from low clinical risk scores with a correct classification rate of 0.73. However, while encouraging, there is still much overlap among the categories so that in an individual patient, it is difficult to predict the Gleason score with great confidence.

A major way in which mp-MRI contributes to more accurate tumor characterization is in better localizing tumors for biopsy. By more accurately targeting lesions, larger samples of tumor are obtained, enabling the pathologist to have greater confidence regarding the ultimate Gleason score. This is reflected in reduced rates of upgrading at surgery when MRI is used preoperatively to biopsy the lesion.

Imaging of Nodal/Distant Involvement

The previous discussion of mp-MRI and PCa refers to scenarios where the cancer is localized to the prostate. However, in a select group of patients defined as high risk by the D'Amico stratification (PSA > 20 ng/dL, Gleason ≥8, clinical stage ≥ T2c), there is an increased risk of not only biochemical recurrence following primary treatment but metastatic spread and possibly death [78]. In these patients, there is an ever-growing need for methods to accurately detect nodal disease prior to surgery. Better imaging techniques may circumvent the need for patients to undergo unnecessary lymph node dissection and also improve outcomes by better staging disease preoperatively. A detailed review of imaging metastatic prostate cancer is beyond the scope of this chapter, but the following section aims to briefly address current and emerging imaging methods.

CT/MRI

CT and MRI are both readily available techniques for the evaluation of metastatic prostate cancer. Unfortunately, both techniques rely on morphologic criteria such as node size to discriminate between benign and malignant nodes and thus often fail to make an accurate diagnosis. Since prostate cancer is relatively slow growing, a cancer may spread to a lymph node without visibly changing the node's diameter over a long period. The Response Evaluation Criteria in Solid Tumors (RECIST) defines a lymph node as "metastatic" if the short-axis measures ≥1.5 cm [79]. Using these criteria, CT and MRI are very insensitive (<30 % in most studies) yet lead to false positives in the case of inflammation or nodal hyperplasia [80, 81]. Another common criterion is to define a metastatic pelvic lymph node as malignant if it is round and 8 mm or greater but less than 10 mm or if it is oval and 10 mm or greater [82]. In a retrospective study of 375 patients evaluated with CT, this criterion achieved a sensitivity of 34 % and a specificity of 97 % [83]. Furthermore, a meta-analysis of 24 studies assessing the diagnostic accuracy of CT and MRI in diagnosing lymph node metastases in PCa showed a pooled sensitivity of 42 % and 39 % for CT and MRI, respectively, and both had a specificity of 82 % [84]. Perhaps the shortcomings of CT and MRI have been best explained in a study by Heesakkers and colleagues in which they reported finding up to 80 % of lymph node metastases to be located in normal-sized lymph nodes of 8 mm or less [83]. Hence, a method that relies on node size can be predicted to fail. On the other hand, imaging that combines molecular and functional data with anatomic information may be more successful.

Of note, research studies with MRI suggest that nodal metastases can be detected with intravenous superparamagnetic contrast agents, which contain ultrasmall particles of iron oxide (USPIO). The general principle is that these particles are engulfed by macrophages in lymph nodes, causing reductions in signal within normal nodes on MRI, thus, allowing for visualization of millimeter-sized tumor involvement which does not lose signal [85]. The accumulation of the USPIO agent attenuates the signal of normal lymph node tissue on T2 and T2* images, but lymph nodes containing tumor still appear hyperintense [86, 87]. Multiple studies have shown utility of USPIO agents for improving detection of nodal disease [85, 88, 89]. The majority of experience with USPIO-enhanced MR lymphography is based on ferumoxtran-10, a dextran-coated USPIO, which is no longer available in the United States. Recently, a bolus injectable derivative of ferumoxtran-10, ferumoxytol, which is carbohydrate coated, is under investigation for its utility in lymph node staging of prostate cancer. Early studies suggest that ferumoxytol is less avidly taken up by macrophages than ferumoxtran-10, but it may still yield diagnostic studies.

Radionuclide Molecular Imaging

Conventional anatomic methods like CT and MRI do not have the sensitivity to detect molecular changes in tissue. Radionuclide molecular imaging, however, seeks to exploit these molecular changes and is a highly sensitive method for detecting both localized and distant cancer. One area in which radionuclide imaging has had a large impact is bony metastases. The current standard of care is to perform $^{99mTc\text{-}labeled}$ bone scintigraphy, which is taken up in osteoblastic lesions seen in metastatic PCa [90]. Unfortunately, bone scans lack sensitivity and specificity and similar lesions can be seen in other benign conditions such as benign neoplasms, trauma, and degenerative joint disease, all of which

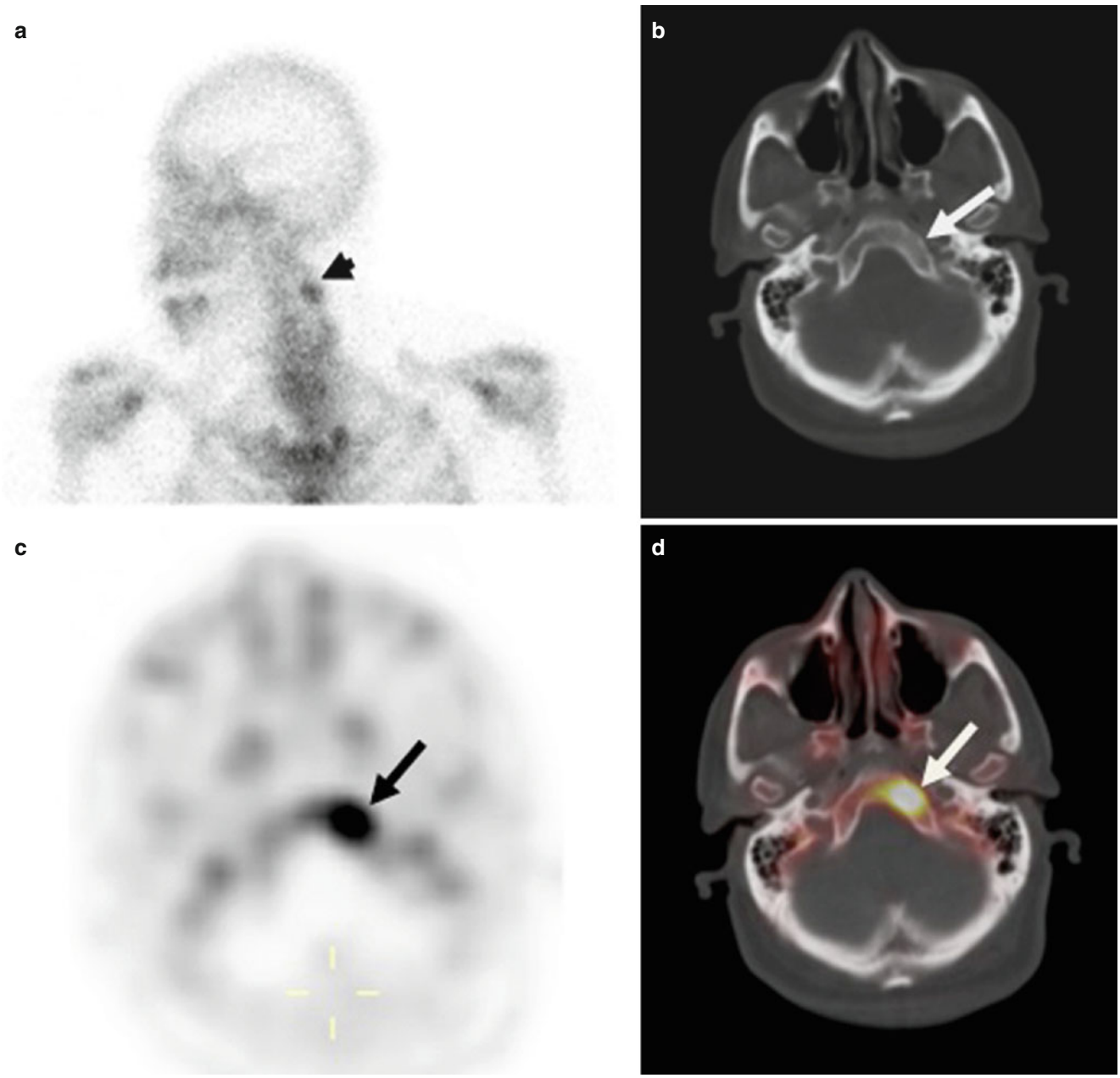

Fig. 4.9 A 55-year-old man (PSA = 41.44 ng/ml) with Gleason 5 + 5 prostate cancer. The Tc-99 m MDP bone scan reveals no pathologic uptake except for the uptake at the degeneration within the cervical vertebra (*arrowhead in* **a**). CT component of an ^{18F}NaF PET/CT shows a ground glass density within the left side of the clivus (*arrow in* **b**), which shows uptake on PET (**c**) and PET/CT (**d**) consistent with bony metastases

are commonly seen in PCa patients. These shortcomings have led to the development of ^{18}F – sodium fluoride (^{18}F-NaF) PET/CT as a potential alternative for detection of bony metastases (Fig. 4.9). In a prospective trial, Damle and colleagues evaluated the efficacy of ^{18}F-NaF versus that of ^{99m}Tc-bone scintigraphy in detecting bone metastases in patients with lung, breast, and prostate carcinoma [91]. ^{18}F-NaF outperformed the conventional bone scan in all test characteristics with respect to PCa and had a sensitivity and negative predictive value of 100 %. However, in practice, due to the high uptake of ^{18}F-NaF in normal bone and benign degenerative disease, these scans must be interpreted with great care and must be correlated with the co-registered CT.

Numerous other radiotracers are currently being researched for the advancement of PCa diagnostics. These include but are not limited to ^{18}F-choline and ^{11}C-choline, ^{11}C-acetate, ^{18}F-FACBC (radiolabeled leucine analog) ^{18}F-Dihydrotestosterone, and ^{18}F-DCFBC, which target prostate-specific membrane antigen (PSMA).

Conclusions

Traditionally, imaging has played a relatively minor role in the management of localized prostate cancer. However, the recent emergence of more powerful and accurate MRI techniques is changing the landscape of how we diagnose and treat localized and advanced disease.

MRI has emerged as the leading modality to assess localized disease. Multiparametric MRI employs a combination of T2W (+/− T1W, dependent upon time since biopsy) plus multiple functional sequences including DWI, DCE, and in some case MRSI. T2W provides the most detailed anatomic information, while DWI is the most practical functional technique and has already shown great promise in terms of improving MRI specificity. Dynamic contrast-enhanced MRI is sensitive for prostate cancer but mainly serves to increase the confidence of the reader. Using these sequences in combination may improve preoperative staging, localization, and biopsy techniques and will likely continue to have an impact on decisions regarding active surveillance and focal therapy. New methods such as iron oxide MR lymphography and PET/CT are emerging to improve the staging of prostate cancer.

References

1. Siegel R, Naishadham D, Jemal A. Cancer statistics, 2013. CA Cancer J Clin. 2013;63:11–30.
2. Schröder FH, et al. Evaluation of the digital rectal examination as a screening test for prostate cancer. Rotterdam section of the European randomized study of screening for prostate cancer. J Natl Cancer Inst. 1998;90:1817–23.
3. Yacoub JH, Oto A, Miller FH. MR imaging of the prostate. Radiol Clin North Am. 2014;52:811–37.
4. Schröder FH, et al. Early detection of prostate cancer in 2007. Part 1: PSA and PSA kinetics. Eur Urol. 2008;53:468–77.
5. Thompson IM, et al. Prevalence of prostate cancer among men with a prostate-specific antigen level < or =4.0 ng per milliliter. N Engl J Med. 2004;350:2239–46.
6. Moyer VA, Preventive Services US. Task force. Screening for prostate cancer: U.S. Preventive services task force recommendation statement. Ann Intern Med. 2012;157:120–34.
7. Miller AB. New data on prostate-cancer mortality after PSA screening. N Engl J Med. 2012;366:1047–8.
8. Levine MA, Ittman M, Melamed J, Lepor H. Two consecutive sets of transrectal ultrasound guided sextant biopsies of the prostate for the detection of prostate cancer. J Urol. 1998;159:471–5; discussion 475–476.
9. Noguchi M, Stamey TA, McNeal JE, Yemoto CM. Relationship between systematic biopsies and histological features of 222 radical prostatectomy specimens: lack of prediction of tumor significance for men with nonpalpable prostate cancer. J Urol. 2001;166:104–9; discussion 109–110.
10. Sosna J, et al. MR imaging of the prostate at 3 Tesla: comparison of an external phased-array coil to imaging with an endorectal coil at 1.5 Tesla. Acad Radiol. 2004;11:857–62.
11. Beyersdorff D, et al. MRI of prostate cancer at 1.5 and 3.0 T: comparison of image quality in tumor detection and staging. AJR Am J Roentgenol. 2005;185:1214–20.
12. Park BK, Kim B, Kim CK, Lee HM, Kwon GY. Comparison of phased-array 3.0-T and endorectal 1.5-T magnetic resonance imaging in the evaluation of local staging accuracy for prostate cancer. J Comput Assist Tomogr. 2007;31:534–8.
13. Heijmink SWTPJ, et al. Prostate cancer: body-array versus endorectal coil MR imaging at 3 T – comparison of image quality, localization, and staging performance. Radiology. 2007;244:184–95.
14. Engelbrecht MR, et al. Local staging of prostate cancer using magnetic resonance imaging: a meta-analysis. Eur Radiol. 2002;12:2294–302.
15. Turkbey B, et al. Comparison of endorectal coil and nonendorectal coil T2W and diffusion-weighted MRI at 3 tesla for localizing prostate cancer: correlation with whole-mount histopathology. J Magn Reson Imaging. 2014;39:1443–8.
16. White S, et al. Prostate cancer: effect of postbiopsy hemorrhage on interpretation of MR images. Radiology. 1995;195:385–90.
17. Barrett T, Vargas HA, Akin O, Goldman DA, Hricak H. Value of the hemorrhage exclusion sign on T1-weighted prostate MR images for the detection of prostate cancer. Radiology. 2012;263:751–7.
18. Qayyum A, et al. Organ-confined prostate cancer: effect of prior transrectal biopsy on endorectal MRI and MR spectroscopic imaging. AJR Am J Roentgenol. 2004;183:1079–83.
19. Barentsz JO, et al. ESUR prostate MR guidelines 2012. Eur Radiol. 2012;22:746–57.
20. McNeal JE, Redwine EA, Freiha FS, Stamey TA. Zonal distribution of prostatic adenocarcinoma. Correlation with histologic pattern and direction of spread. Am J Surg Pathol. 1988;12:897–906.
21. Tindall DJ. Recent advances in prostate cancer: basic science discoveries and clinical advances. Singapore: World Scientific; 2011.
22. Kirkham APS, Emberton M, Allen C. How good is MRI at detecting and characterising cancer within the prostate? Eur Urol. 2006;50:1163–74; discussion 1175.
23. Wang L, et al. Assessment of biologic aggressiveness of prostate cancer: correlation of MR signal intensity with Gleason grade after radical prostatectomy. Radiology. 2008;246:168–76.
24. Langer DL, et al. Intermixed normal tissue within prostate cancer: effect on MR imaging measurements of apparent diffusion coefficient and T2 – sparse versus dense cancers. Radiology. 2008;249:900–8.
25. Oto A, et al. Prostate cancer: differentiation of central gland cancer from benign prostatic hyperplasia by using diffusion-weighted and dynamic contrast-enhanced MR imaging. Radiology. 2010;257:715–23.
26. Akin O, et al. Transition zone prostate cancers: features, detection, localization, and staging at endorectal MR imaging. Radiology. 2006;239:784–92.
27. Li H, et al. Conventional MRI capabilities in the diagnosis of prostate cancer in the transition zone. AJR Am J Roentgenol. 2006;186:729–42.
28. Lemaitre L, et al. Dynamic contrast-enhanced MRI of anterior prostate cancer: morphometric assessment and correlation with radical prostatectomy findings. Eur Radiol. 2009;19:470–80.
29. Bloch BN, et al. Prostate cancer: accurate determination of extracapsular extension with high-spatial-resolution dynamic contrast-enhanced and T2-weighted MR imaging – initial results. Radiology. 2007;245:176–85.
30. Weinreb JC, et al. Prostate cancer: sextant localization at MR imaging and MR spectroscopic imaging before prostatectomy – results of ACRIN prospective multi-institutional clinicopathologic study. Radiology. 2009;251:122–33.
31. Turkbey B, et al. Prostate cancer: can multiparametric MR imaging help identify patients who are candidates for active surveillance? Radiology. 2013;268:144–52.
32. Stephenson SK, Chang EK, Marks LS. Screening and detection advances in magnetic resonance image-guided prostate biopsy. Urol Clin North Am. 2014;41:315–26.

33. Jacobs MA, Ouwerkerk R, Petrowski K, Macura KJ. Diffusion-weighted imaging with apparent diffusion coefficient mapping and spectroscopy in prostate cancer. Top Magn Reson Imaging. 2008;19:261–72.
34. Metens T, Miranda D, Absil J, Matos C. What is the optimal b value in diffusion-weighted MR imaging to depict prostate cancer at 3T? Eur Radiol. 2012;22:703–9.
35. Rosenkrantz AB, et al. T2-weighted prostate MRI at 7 tesla using a simplified external transmit-receive coil array: Correlation with radical prostatectomy findings in two prostate cancer patients. J Magn Reson Imaging. 2013. doi:10.1002/jmri.24511.
36. Kitajima K, et al. Clinical utility of apparent diffusion coefficient values obtained using high b-value when diagnosing prostate cancer using 3 tesla MRI: comparison between ultra-high b-value (2000 s/mm^2) and standard high b-value (1000 s/mm^2). J Magn Reson Imaging. 2012;36:198–205.
37. Katahira K, et al. Ultra-high-b-value diffusion-weighted MR imaging for the detection of prostate cancer: evaluation in 201 cases with histopathological correlation. Eur Radiol. 2011;21:188–96.
38. Ueno Y, et al. Ultra-high b-value diffusion-weighted MRI for the detection of prostate cancer with 3-T MRI. J Magn Reson Imaging. 2013;38:154–60.
39. Hosseinzadeh K, Schwarz SD. Endorectal diffusion-weighted imaging in prostate cancer to differentiate malignant and benign peripheral zone tissue. J Magn Reson Imaging. 2004;20:654–61.
40. Kim JH, Kim JK, Park B-W, Kim N, Cho K-S. Apparent diffusion coefficient: prostate cancer versus noncancerous tissue according to anatomical region. J Magn Reson Imaging. 2008;28:1173–9.
41. Tan CH, Wei W, Johnson V, Kundra V. Diffusion-weighted MRI in the detection of prostate cancer: meta-analysis. AJR Am J Roentgenol. 2012;199:822–9.
42. Hoeks CMA, et al. Prostate cancer: multiparametric MR imaging for detection, localization, and staging. Radiology. 2011;261:46–66.
43. Bonekamp D, Macura KJ. Dynamic contrast-enhanced magnetic resonance imaging in the evaluation of the prostate. Top Magn Reson Imaging. 2008;19:273–84.
44. Noworolski SM, Vigneron DB, Chen AP, Kurhanewicz J. Dynamic contrast-enhanced MRI and MR diffusion imaging to distinguish between glandular and stromal prostatic tissues. Magn Reson Imaging. 2008;26:1071–80.
45. Alonzi R, Padhani AR, Allen C. Dynamic contrast enhanced MRI in prostate cancer. Eur J Radiol. 2007;63:335–50.
46. Casciani E, et al. Contribution of the MR spectroscopic imaging in the diagnosis of prostate cancer in the peripheral zone. Abdom Imaging. 2007;32:796–802.
47. Joseph T, et al. Pretreatment endorectal magnetic resonance imaging and magnetic resonance spectroscopic imaging features of prostate cancer as predictors of response to external beam radiotherapy. Int J Radiat Oncol Biol Phys. 2009;73:665–71.
48. Djavan B, et al. Prospective evaluation of prostate cancer detected on biopsies 1, 2, 3 and 4: when should we stop? J Urol. 2001;166:1679–83.
49. Eberhardt SC, et al. ACR appropriateness criteria prostate cancer – pretreatment detection, staging, and surveillance. J Am Coll Radiol. 2013;10:83–92.
50. Heidenreich A, et al. EAU guidelines on prostate cancer. Part 1: screening, diagnosis, and treatment of clinically localised disease. Eur Urol. 2011;59:61–71.
51. De Rooij M, Hamoen EHJ, Fütterer JJ, Barentsz JO, Rovers MM. Accuracy of multiparametric MRI for prostate cancer detection: a meta-analysis. AJR Am J Roentgenol. 2014;202:343–51.
52. Delongchamps NB, et al. Multiparametric magnetic resonance imaging for the detection and localization of prostate cancer: combination of T2-weighted, dynamic contrast-enhanced and diffusion-weighted imaging. BJU Int. 2011;107:1411–8.
53. Jung SI, et al. Transition zone prostate cancer: incremental value of diffusion-weighted endorectal MR imaging in tumor detection and assessment of aggressiveness. Radiology. 2013;269:493–503.
54. Haider MA, et al. Combined T2-weighted and diffusion-weighted MRI for localization of prostate cancer. AJR Am J Roentgenol. 2007;189:323–8.
55. Hoeks CMA, et al. Transition zone prostate cancer: detection and localization with 3-T multiparametric MR imaging. Radiology. 2013;266:207–17.
56. Rosenkrantz AB, Mendrinos S, Babb JS, Taneja SS. Prostate cancer foci detected on multiparametric magnetic resonance imaging are histologically distinct from those not detected. J Urol. 2012;187:2032–8.
57. Vargas HA, Wassberg C, Akin O, Hricak H. MR imaging of treated prostate cancer. Radiology. 2012;262:26–42.
58. Doo KW, et al. Detectability of low and intermediate or high risk prostate cancer with combined T2-weighted and diffusion-weighted MRI. Eur Radiol. 2012;22:1812–9.
59. Bratan F, et al. Influence of imaging and histological factors on prostate cancer detection and localisation on multiparametric MRI: a prospective study. Eur Radiol. 2013;23:2019–29.
60. Bostwick DG. Staging prostate cancer – 1997: current methods and limitations. Eur Urol. 1997;32 Suppl 3:2–14.
61. Couñago F, et al. Role of 3.0 T multiparametric MRI in local staging in prostate cancer and clinical implications for radiation oncology. Clin Transl Oncol. 2014. doi:10.1007/s12094-014-1186-6.
62. Kim CK, Park SY, Park JJ, Park BK. Diffusion-weighted MRI as a predictor of extracapsular extension in prostate cancer. AJR Am J Roentgenol. 2014;202:W270–6.
63. Bloch BN, et al. Prediction of prostate cancer extracapsular extension with high spatial resolution dynamic contrast-enhanced 3-T MRI. Eur Radiol. 2012;22:2201–10.
64. Pierorazio PM, et al. A contemporary analysis of outcomes of adenocarcinoma of the prostate with seminal vesicle invasion (pT3b) after radical prostatectomy. J Urol. 2011;185:1691–7.
65. Sapre N, et al. Re-evaluating the biological significance of seminal vesicle invasion (SVI) in locally advanced prostate cancer. BJU Int. 2012;110 Suppl 4:58–63.
66. Sala E, et al. Endorectal MR imaging in the evaluation of seminal vesicle invasion: diagnostic accuracy and multivariate feature analysis. Radiology. 2006;238:929–37.
67. Soylu FN, et al. Seminal vesicle invasion in prostate cancer: evaluation by using multiparametric endorectal MR imaging. Radiology. 2013;267:797–806.
68. Gleason DF, Mellinger GT. Prediction of prognosis for prostatic adenocarcinoma by combined histological grading and clinical staging. J Urol. 1974;111:58–64.
69. Epstein JI, ISUP Grading Committee, Allsbrook Jr WC, Amin MB, Egevad LL. The 2005 International Society of Urological Pathology (ISUP) consensus conference on gleason grading of prostatic carcinoma. Am J Surg Pathol. 2005;29:1228–42.
70. Vargas HA, et al. Diffusion-weighted endorectal MR imaging at 3 T for prostate cancer: tumor detection and assessment of aggressiveness. Radiology. 2011;259:775–84.
71. Yoshimitsu K, et al. Usefulness of apparent diffusion coefficient map in diagnosing prostate carcinoma: correlation with stepwise histopathology. J Magn Reson Imaging. 2008;27:132–9.
72. Tamada T, et al. Apparent diffusion coefficient values in peripheral and transition zones of the prostate: comparison between normal and malignant prostatic tissues and correlation with histologic grade. J Magn Reson Imaging. 2008;28:720–6.
73. Verma S, et al. Assessment of aggressiveness of prostate cancer: correlation of apparent diffusion coefficient with histologic grade after radical prostatectomy. AJR Am J Roentgenol. 2011;196:374–81.

74. Hambrock T, et al. Relationship between apparent diffusion coefficients at 3.0-T MR imaging and Gleason grade in peripheral zone prostate cancer. Radiology. 2011;259:453–61.
75. Kobus T, et al. Prostate cancer aggressiveness: in vivo assessment of MR spectroscopy and diffusion-weighted imaging at 3 T. Radiology. 2012;265:457–67.
76. D'Amico A, et al. The use of clinical parameters in an interactive statistical package to predict pathological features associated with local failure after radical prostatectomy for prostate cancer. Clin Perform Qual Health Care. 1993;1:219–22.
77. Turkbey B, et al. Is apparent diffusion coefficient associated with clinical risk scores for prostate cancers that are visible on 3-T MR images? Radiology. 2011;258:488–95.
78. Bastian PJ, et al. High-risk prostate cancer: from definition to contemporary management. Eur Urol. 2012;61:1096–106.
79. Chalian H, et al. Radiologic assessment of response to therapy: comparison of RECIST versions 1.1 and 1.0. Radiographics. 2011;31:2093–105.
80. Campbell SC, Klein EA, Levin HS, Piedmonte MR. Open pelvic lymph node dissection for prostate cancer: a reassessment. Urology. 1995;46:352–5.
81. Tiguert R, et al. Lymph node size does not correlate with the presence of prostate cancer metastasis. Urology. 1999;53:367–71.
82. Outwater EK, Montilla-Soler JL. Imaging of prostate carcinoma. Cancer Control. 2013;20:161–76.
83. Heesakkers RAM, et al. MRI with a lymph-node-specific contrast agent as an alternative to CT scan and lymph-node dissection in patients with prostate cancer: a prospective multicohort study. Lancet Oncol. 2008;9:850–6.
84. Hövels AM, et al. The diagnostic accuracy of CT and MRI in the staging of pelvic lymph nodes in patients with prostate cancer: a meta-analysis. Clin Radiol. 2008;63:387–95.
85. Harisinghani MG, et al. Noninvasive detection of clinically occult lymph-node metastases in prostate cancer. N Engl J Med. 2003;348:2491–9.
86. Weissleder R, et al. Ultrasmall superparamagnetic iron oxide: an intravenous contrast agent for assessing lymph nodes with MR imaging. Radiology. 1990;175:494–8.
87. Wunderbaldinger P, Josephson L, Bremer C, Moore A, Weissleder R. Detection of lymph node metastases by contrast-enhanced MRI in an experimental model. Magn Reson Med. 2002;47:292–7.
88. Heesakkers RAM, et al. Prostate cancer evaluated with ferumoxtran-10–enhanced T2*-weighted MR imaging at 1.5 and 3.0 T: early experience. Radiology. 2006;239:481–7.
89. Heesakkers RAM, et al. Prostate cancer: detection of lymph node metastases outside the routine surgical area with ferumoxtran-10–enhanced MR imaging. Radiology. 2009;251:408–14.
90. Bouchelouche K, et al. PET/CT imaging and radioimmunotherapy of prostate cancer. Semin Nucl Med. 2011;41:29–44.
91. Damle NA, et al. The role of 18F-fluoride PET-CT in the detection of bone metastases in patients with breast, lung and prostate carcinoma: a comparison with FDG PET/CT and 99mTc-MDP bone scan. Jpn J Radiol. 2013;31:262–9.

Imaging of Benign Prostatic Conditions

5

E. Justin Martinez, Hong Truong,
and Soroush Rais-Bahrami

Benign Prostatic Hyperplasia

Benign prostatic hyperplasia (BPH) is a pathological process, characterized by the nonmalignant enlargement of the periurethral transition zone of the prostate. BPH involves a net increase in the number of stromal and epithelial cells in the prostate because of an imbalance between apoptosis and cell proliferation [1]. BPH can lead to constriction of the urethra and subsequent obstruction of urinary flow, inducing detrusor dysfunction. BPH is the most common cause of lower urinary tract symptoms (LUTS) in aging males, which include urinary frequency, urgency, nocturia, and dysuria. The prevalence of BPH increases with age. In the United States, BPH affects approximately 70 % of men 60–69 years old, 80 % of those 70 years and older and almost 90 % by age 90 [2, 3]. Although LUTS secondary to BPH are rarely life threatening, the effect of LUTS and BPH on older men's quality of life is significant and should not be underestimated. In men with prostates larger than 30 mL and severe LUTS, BPH can lead to serious complications including acute urinary retention, requiring catheterization, hydronephrosis, and acute renal injury [4].

In a number of population-based studies of the effect of BPH-associated LUTS on quality of life, the most important motivations for seeking treatment were severity of LUTS and the degree of bothersome impacts on quality of life. The American Urological Association (AUA) BPH guideline in 2010 recommends that the first step in evaluating patients presenting with LUTS is a medical history and focused physical examinations, including digital rectal and neurological examinations [5]. The goal is to establish that the symptoms are due to BPH and identify other causes of voiding dysfunction or comorbidities that may complicate treatment, such as diabetes, primary neurological disorder, urethral stricture, etc. Laboratory evaluations include urinalysis performed by dipstick testing and microscopic examination to screen for urinary tract infection, hematuria, and glucose. The seven symptom questions of the International Prostate Symptom Score, IPSS, are used to quantify symptom severity, monitor therapeutic response, and detect symptom progression.

Radiographic studies are not recommended in the initial evaluation of LUTS [5]. However, they are useful adjunctive tests in determining appropriate therapies for men with moderate to severe LUTS. Prostate size impacts the selection of appropriate medical therapy. BPH/LUTS are commonly treated with two classes of medication, alpha-adrenergic receptor blockers and 5-alpha reductase inhibitors (5-ARIs), or with surgical intervention. Alpha-adrenergic receptor blockers, such as doxazosin and tamsulosin, provide rapid symptom relief by reducing smooth muscle tension along the bladder neck, prostate, and urethra [6]. The 5-ARIs, which include finasteride and dutasteride, are antiandrogenic drugs that target the underlying disease process to reduce prostate size [6]. Patients with larger prostates may benefit more from 5-ARIs, whereas those with lower urinary tract symptoms and prostates less than 30 mL may benefit from alpha-adrenergic receptor blockers alone. When surgical options are considered, knowledge of prostate volume and configuration on imaging can assist clinicians in choosing minimally invasive surgery, transurethral prostate resection, or open prostatectomy. According to the European Association of Urology (EAU) guidelines, open surgery should be undertaken in patients with prostate volume greater than 80–100 mL, while transurethral incision of the prostate (TUIP) could also be used for prostate volumes less than 30 mL [7]. Transurethral resection of the prostate (TURP) would be the treatment of

E.J. Martinez, MD
Department of Urology, University of Alabama at Birmingham, Birmingham, AL, USA
e-mail: emartinez@uabmc.edu

H. Truong, MS, MD
Department of Urology, Kimmel Cancer Center, Thomas Jefferson University, Philadelphia, PA, USA
e-mail: hong.truong@jefferson.edu

S. Rais-Bahrami, MD (✉)
Departments of Urology and Radiology, University of Alabama at Birmingham, Birmingham, AL, USA
e-mail: soroushraisbahrami@gmail.com

A.R. Rastinehad, D.N. Siegel (eds.), *Interventional Urology*, DOI 10.1007/978-3-319-23464-9_5

choice for those with prostate volumes between 30 and 80 mL [7]. As a result, accurate estimation of gland volume constitutes an important guide in the management of men with BPH.

Ultrasound

Transabdominal Ultrasound

Historically, transabdominal prostatic US has been utilized to estimate the size and morphology of the prostate gland, such as the absence or presence of the middle lobe. Transabdominal ultrasound (TAUS) requires angling the probe beneath the pubic bone. The transverse plane is first evaluated to measure the height and width of the prostate gland. The transducer is then rotated to the sagittal plane to measure the length of the prostatic urethra, from the bladder neck to the apex of the prostate. The presence of the middle lobe and degree of intravesical prostatic protrusion (IPP) can also be assessed on the midsagittal plane. IPP severity is graded on a 3-point scale: grade 1, less than 5 mm; grade 2, 5–10 mm; and grade 3, more than 10 mm [8, 9]. It has been shown that IPP correlates well with urodynamic findings of bladder outlet obstruction (BOO) and detrusor dysfunction [8–10]. The positive predictive value (PPV) of grade 3 IPP for bladder outlet obstruction is found to be as high as 94 %, and the negative predictive value (NPV) is 79 % [8]. Other surrogate predictors of the severity of BPH and associated BOO such as post-void residual urine (PVR), bladder wall thickness, and bladder wall trabeculation can also be evaluated.

Due to its inherent limitations with respect to detailed imaging of the prostate and its surrounding tissues, TAUS has been shown to grossly overestimate prostate adenoma. Stravodimos and colleagues found that TAUS miscategorized 32.5 % of gland volumes as over 80 mL and led 25 patients to unnecessary open surgery [11]. Even though TAUS is a noninvasive and helpful imaging modality in assessing for IPP and BOO, it is not reliable in identifying patients for surgical interventions.

Transrectal Ultrasound (TRUS)

Since transrectal ultrasound (TRUS) of the prostate was first described in 1968 by Watanabe and colleagues [12], TRUS technology has become the standard first-line radiographic modality to evaluate appropriate patients for treatment of BPH. Handheld TRUS requires compression of the prostate to ensure adequate acoustic coupling between the probe and the prostate. To some extent this can be obviated with automated stepper devices that advance the probe in stepwise increments in the same plane. However, the degree of prostate distortion is highly operator-dependent. Indeed, a major problem with TRUS is its high intra-observer variability, estimated at −21 to +30 % of total prostate volume and −18 to +18 % of transition zone volume [13].

Another challenge in TRUS estimation of prostate volume is its assumption that the prostate has a regular ellipsoid shape. The ellipsoid model, which is the original and de facto standard method of calculating prostate volume, uses the formula length × width × height × π/6 [14]. However, the highly variable shape of the prostate, which is not typically a regular shape in most men, results in widely variable or outlier estimates of volume in individual cases that are not reflected in Pearson coefficient scores. Moreover, these eccentric volumes can be difficult to reproduce on serial imaging. As a result, TRUS has been shown to underestimate prostate volume for prostates larger than 50 mL and to overestimate prostate volume for glands smaller than 30 mL [15]. Despite its limitations, the TRUS method of prostate volume assessment is preferred in current clinical practice due to its availability, affordable cost, and time efficiency [16].

Magnetic Resonance Imaging (MRI)

MRI has been shown to be more reliable in prostate imaging, particularly in delineation of zonal anatomy, compared to TRUS. TRUS requires compression of the prostate to ensure adequate imaging which is highly operator-dependent. Furthermore, MRI allows for more accurate differentiation and segmentation of the transitional zone and peripheral zone [17, 18]. The axial T2W images are used for prostate volume measurements. The transitional zone of the prostate is characteristically recognizable by a thin band of fibromuscular tissue (pseudocapsule), which is low in signal intensity on T2-weighted MRI, and defines the border between the transitional zone and peripheral zone.

Turkbey and colleagues validated 3.0-Tesla MRI-derived total prostate volume with the weights of human radical prostatectomy specimens. The Pearson correlation coefficient revealed strong positive correlation between prostatectomy specimen volume and prostate volume estimates derived from manual segmentation ($R = 0.89$–0.91, $p < 0.0001$) and automated segmentation ($R = 0.88$–0.91, $p < 0.0001$) [19].

Computed Tomography (CT) Imaging

MRI and transrectal ultrasound are superior methods of imaging the prostate; however, given the frequency of CT scans (Fig. 5.1), it is important to have an understanding of pelvic anatomy including the prostate. Discrepancies exist between the imaging modalities. A study by Hoffelt et al. comparing the prostate volume between CT scan and TRUS found that the CT scan consistently overestimated the prostate volume by up to 50 % [20]. This tends to play a lesser role in BPH, but it is important in prostate cancer because an

Fig. 5.1 Non-contrast CT scan, axial cut demonstrating enlarged prostate

unnecessary larger dose of toxic radiation may be used. Conversely, another study comparing CT to TRUS prostate volume estimations found a close correlation between the two imaging studies. This particular study focused on brachytherapy implants, and they determined that if CT images were appropriately interpreted, CT is comparable to TRUS in measuring prostate volume [21]. Fiorino and colleagues showed that the same physician reviewing the same CT scan had greater than 1 mm differences in evaluating prostate contour [22].

Prostatitis

Prostatitis refers to inflammation of the prostate gland. Infection occurs when bacteria from the urethra or bladder enter the prostate. It has been reported that there are approximately 2 million outpatient visits yearly for prostatitis in the United States, accounting for 8 % of all urology office visits and 1 % of all primary care visits [23, 24].

The National Institutes of Health (NIH) established a classification of prostatitis into four categories: acute bacterial prostatitis, chronic bacterial prostatitis, chronic prostatitis/chronic pelvic pain syndrome (CP/CPPS), and asymptomatic inflammatory prostatitis. Acute bacterial prostatitis presents with dysuria, frequency, and other symptoms of a urinary tract infection. *E. coli* is the most common causative pathogen. Signs of systemic infection are related to infection of the prostate and include fever, malaise, and general aches. Treatment for acute bacterial prostatitis is directed at gram-negative enteric bacteria. Trimethoprim-sulfamethoxazole, fluoroquinolones, and ampicillin with gentamicin are all reasonable options while awaiting urine culture sensitivities and should continue for a total of 1 month duration. Additionally, alpha-adrenergic blockers can be used to help reduce obstruction and urinary reflux. Rarely, prostatitis requires surgery and this is generally seen in the setting of a prostatic abscess. Chronic bacterial prostatitis is seen in patients with repeated urinary tract infections, most commonly *E. coli*. Patients will present with dysuria and pelvic or low back pain. Positive urinary cultures can be seen in between periods of symptomatic bacteriuria. Chronic prostatitis/chronic pelvic pain syndrome (CP/CPPS) represents the most common type. Numerous medical therapies have been tried, but a definitive treatment still remains unknown. Patients in this subtype complain of LUTS and pelvic pain. Treatments to consider consist of anti-inflammatories, alpha-adrenergic blockers, and hormonal therapies. A recent study by Kong et al. evaluated the use of phosphodiesterase inhibitors, specifically mirodenafil, in combination with levofloxacin. The group receiving mirodenafil noted an improvement in LUTS; however, pain was unchanged [25]. CP/CPPS is further broken down into inflammatory and non-inflammatory. Noninflammatory chronic pelvic pain syndrome is characterized by the absence of WBCs in prostatic fluid and no prostatic bacterial infection. Inflammatory CP/CPPS also called nonbacterial prostatitis is defined as WBCs in prostatic fluid, but no active prostate infection. The etiology may be related to reflux of urine into the prostate causing an irritant prostatitis. Asymptomatic inflammatory prostatitis is seen during the workup for other genitourinary pathologies such as following a prostate biopsy. A common finding is a large concentration of leukocytes in semen [26]. Granulomatous prostatitis, which is not included in the NIH classification, is seen following bacillus Calmette-Guérin (BCG) intravesical therapy for bladder cancer and tuberculosis.

TRUS

Transrectal ultrasound to diagnose prostatitis is generally not used since the diagnosis is clinical; however, TRUS should be considered if there is clinical suspicion for a prostatic abscess. A study involving 45 men with a clinical diagnosis of acute bacterial prostatitis who underwent TRUS on admission and 1 month following antibiotic therapy demonstrated a mean reduction in prostate volume from 40.5 mL (sd: 17.9) to 24.3 mL (sd: 10.5) [27]. Several signs on TRUS were described in a 1989 article by Doble and Carter that have a high correlation with a prostatitis diagnosis. These included high-density and midrange echoes, echolucent zones, capsular irregularity and thickening, ejaculatory duct echoes, and periurethral zone irregularity. Their histopathological significance was also noted. Corpora amylacea were seen as the high-density echoes. Midrange echoes represented inflammation and/or fibrosis. The echolucent zones indicated inflammation. The specificity of midrange and high-density echoes was 51.9 % and 40.7 %, respectively. The sensitivity of the echolucent zones, capsular irregularity and thickening,

ejaculatory duct echoes, and periurethral zone irregularity ranged from 30.8 to 62.3 % [28].

A study comparing TRUS findings in the evaluation of men with chronic pelvic pain syndrome and chronic prostatitis revealed a statistically significant accumulation of prostatic calcifications and unilateral seminal vesicle gland alterations in men with chronic prostatitis. In patients with chronic pelvic pain syndrome, 22 % had prostatic calcifications and 11 % showed unilateral seminal vesicle gland alterations [29].

Color Doppler TRUS has been shown to be of value for monitoring acute bacterial prostatitis response to treatment. A study involving 25 patients treated for acute bacterial prostatitis had color Doppler and TRUS done at 1 week, 6 weeks, 3 months, and 6 months follow-up. The patients completed antibiotic therapy at 6-week follow-up ultrasound. 23 of the patients had blood flow to the entire prostate capsule at 1 week, and only two patients had blood flow to the entire capsule at 6 months. The patients in the same study were also noted to have an overall decrease in the amount and distribution of blood flow within the parenchyma based on a quantification system by the authors. They used the Doppler spot scale where they counted blood flow spots in the parenchyma and noted a decrease from mean 23.2 (sd: 11.1) spots at 1 week TRUS down to 7.9 (sd: 5.1) at 6 months [30].

MRI

The utilization of MRI in active surveillance for prostate cancer leads to more imaging of granulomatous prostatitis induced in patients previously treated with intravesical BCG for bladder cancer. Granulomatous prostatitis can mimic prostate cancer and may appear as a new hypointense lesion on T2W images with restricted diffusion. This was observed in a case report by Logan et al. about a patient undergoing multiparametric prostate MRI for active surveillance. These benign lesions may prompt earlier prostate biopsies [31]. Nagel and colleagues were able to show that diffusion-weighted MRI can show differences between prostatitis and prostate cancer in the peripheral zone and transition zone [32].

Prostatic Abscess

A prostatic abscess, though uncommon, should be suspected when a patient being treated for bacterial prostatitis fails to improve with antibiotic therapy. *E. coli* is the most common causative organism and is typically caused by the reflux of infected urine into the prostate gland. Additionally, hematogenous spread usually secondary to *Staphylococcus aureus* and direct inoculation following a prostatic procedure can lead to formation of a prostatic abscess. Patients may present with LUTS, perineal pain, fever, chills, low back pain, or even sepsis [33]. A fluctuation in areas of the prostate can be noted on digital rectal examination, but will not always be apparent. Immunosuppression and uncontrolled diabetes place a patient at an increased risk. Management is antibiotic therapy with abscess drainage. Surgical intervention includes transurethral unroofing and resection, perineal incision and drainage, and percutaneous drainage. Recurrence of a prostatic abscess can occur following initial treatment, so repeat imaging to confirm resolution of the abscess is recommended. This is commonly done with TRUS; however, CT and MRI are feasible options [33].

TRUS

Transrectal ultrasound is the diagnostic study of choice for a prostatic abscess. Hypoechogenic areas of varying sizes, which can be numerous, are a common finding. These areas are usually found in the transition zone and can distort the normal anatomy of the gland [33]. A small retrospective study involving nine patients by Oliveira et al. found all patients undergoing TRUS to have the above-described findings [34].

CT

CT scan is another useful method to diagnose and follow a prostatic abscess (Fig. 5.2a, b). A small prospective study followed seven patients with suspected prostatitis. Five of the patients had a CT scan alone and showed a homogenous area of low attenuation on CT after giving IV contrast. Two of the patients demonstrated enhancing rims around the abscess. CT scan has demonstrated to be useful in diagnosing and to follow resolution of the abscess. Both CT and TRUS can reveal septations; however, CT allows evaluation of adjacent tissue structures [35].

MRI

MRI will show a hypointense signal on T1 and hyperintense signal with peripheral enhancement on T2 [36] (Fig. 5.3a, b). Singh et al. evaluated the use of diffusion-weighted imaging (DWI) in two patients with a prostate abscess. DWI evaluates the diffusion of water molecules and calculates an apparent diffusion coefficient (ADC) between normal and pathological prostate. They demonstrated that the mean ADC levels in prostatic abscesses were low in comparison to normal peripheral zone prostate tissues and with malignant prostate tissue. The area of restricted diffusion represented an area of abnormality on T2 imaging [36].

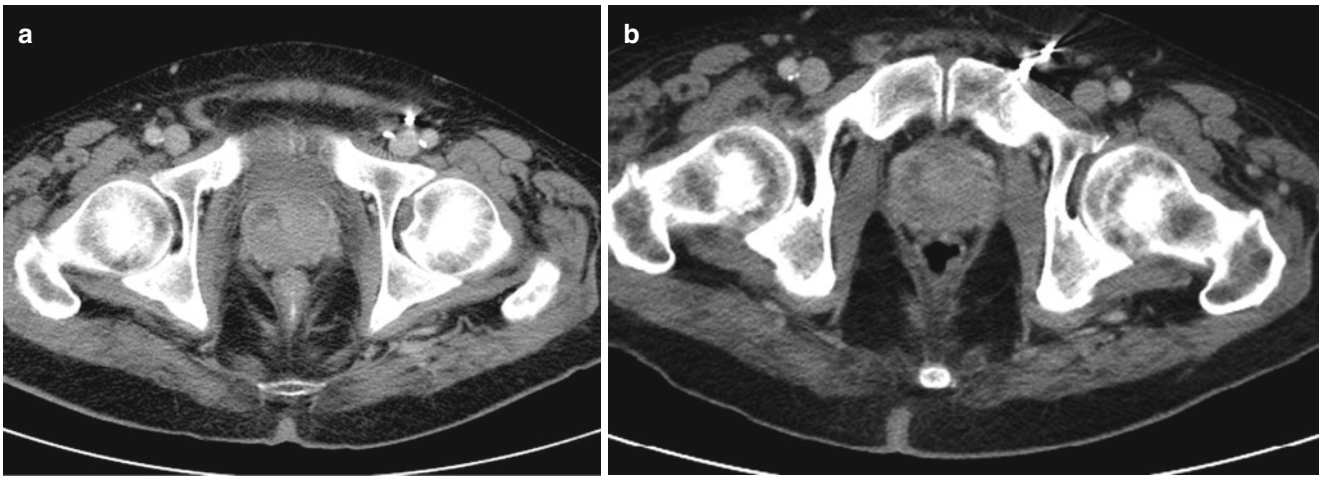

Fig. 5.2 (**a**) Contrast-enhanced CT scan, axial cut with a 1.3×1.2 cm hypoattenuating focus in the right anterior portion of the prostate with enhancement suggesting prostatic fluid collection concern for an abscess formation. (**b**) Contrast-enhanced CT scan, axial cut of the same patient several days later demonstrating a mild decrease in size of 0.7×0.5 cm

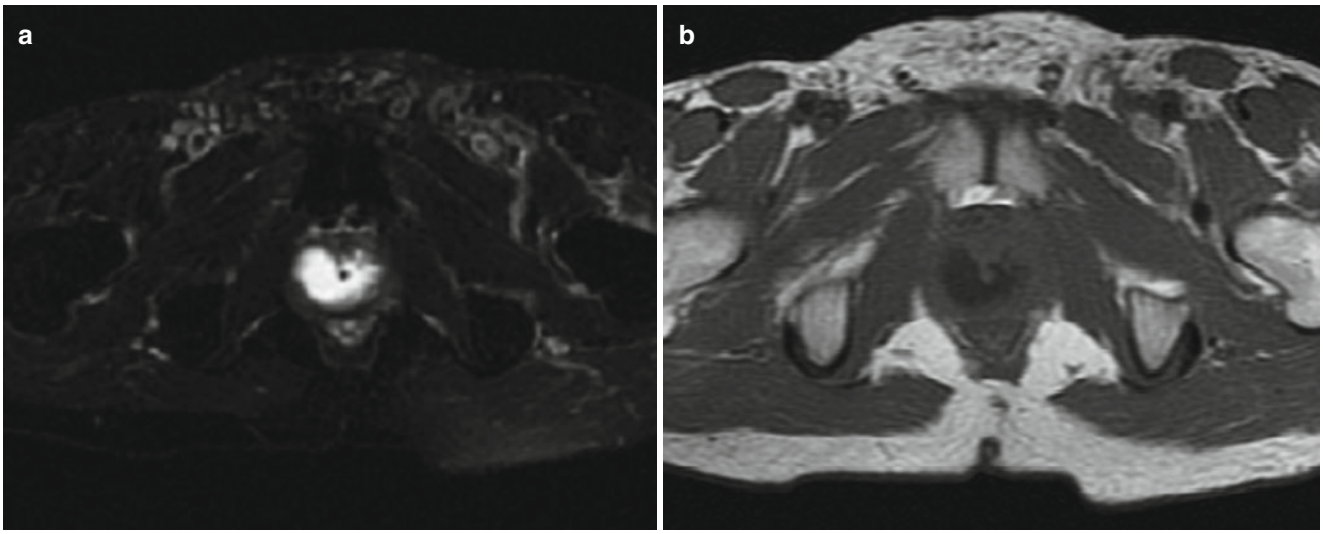

Fig. 5.3 (**a**) MR T2 axial cut of patient with suspected prostatic abscess and enlarged prostate. An intraprostatic periurethral high T2 signal suggesting fluid. (**b**) MR T1 axial cut of the same patient with suspected prostatic abscess and enlarged prostate. An intraprostatic periurethral abscess collection appearing as low signal on T1

Prostatic Cysts

A variety of cysts can exist in the prostate and can be asymptomatic or symptomatic depending on their origin and size. The overall prevalence of prostatic cysts is not known, but studies have shown medial cysts in up to 8 % of asymptomatic patients. Another small study found prostatic utricle (PU) cysts in 11 % of 150 infertile men, while no cysts were found in 30 fertile men. Prostatic cysts can be broken down into intraprostatic and periprostatic. Treatment is generally reserved for those cysts that may be associated with urinary obstruction, infertility, infection, or discomfort. The classification of prostatic cysts is based on their anatomic location which includes midline cysts, paramedian cysts, lateral cysts, and periprostatic cysts [37].

Galosi et al. proposed a new classification of prostatic cysts based on clinical and pathological features. They further described the appearance of the cystic lesions based upon imaging. Previous classifications have based cysts on clinical settings which included LUTS, oncology, infertility, and infectious disease [37]. They divided the cysts into six categories identified as type 1 through 6 in order: isolated medial cysts, ejaculatory duct cysts, parenchymal cysts, complicated cysts (hemorrhagic or infectious), cystic tumors, and parasitic cysts [37].

Midline cysts consist of PU cysts and Müllerian cysts. Müllerian cysts originate from remnants of the Müllerian duct, while PU cysts come from dilation of the prostatic utricle. These terms are sometimes used interchangeably; however, most literature classifies them as different entities. Midline cysts are located superior to the verumontanum in between the seminal vesicles. Müllerian cysts and PU cysts may be indistinguishable from one another on imaging, but there are differences on imaging to tell them apart. Müllerian duct cysts can originate lateral to midline given the anatomic location of the Müllerian ducts during embryology and anywhere along the Müllerian duct path. PU cysts should be precisely midline given the anatomic location the prostatic utricle. Aside from anatomic location, PU cysts communicate with the posterior urethra. This feature is not seen in Müllerian duct cysts. Müllerian duct cysts tend to be larger and occur later in life, while PU cysts occur in the first two decades of life. Lastly PU cysts have been associated with genitourinary abnormalities, while Müllerian duct cysts are isolated entities. Galosi also identified an enlarged PU in children, which is not a true cyst and is associated with an absent verumontanum and wide opening into the urethra. The enlarged PU is a tubular structure with squamous epithelium. A study involving 65 patients with Müllerian duct cysts evaluated the workup and management. Of the 65 patients, 27 underwent an invasive procedure which included transperineal or transrectal puncture in 9, endoscopic resection of the utricle meatus in 12, and large marsupialization in 6 patients. They noted improvement or cure in 82 % of the patients at roughly 4 years follow-up [38]. Halpern and Hirsch discuss a case report of a 35-year-old male with infertility found to have a Müllerian duct cyst. TRUS was used to guide transurethral laser incision of the cystic obstruction. Following incision, TRUS confirmed cystic decompression [39].

Ejaculatory duct cysts are paramedian cysts which can be congenital or acquired due to an ejaculatory duct obstruction. Evidence for an acquired ejaculatory duct cyst can be seen when there is a prostatic calculus or PU cysts. These cysts when aspirated contain spermatozoa or fructose [40].

Prostatic retention cysts are acquired and increase in frequency with advancing age in patients with BPH in the fifth and sixth decades of life. They result from the obstruction of prostate gland ductules resulting in upstream cystic dilation of the gland acini. On aspiration, spermatozoa are absent. BPH with cystic degeneration is the most common cystic lesion of the prostate and located in the transitional zone of the prostate gland [40]. They can be seen within the hyperplastic nodules and contain calculi and white or hemorrhagic fluid. The white fluid is corpora amylacea and hemorrhage is due to necrosis or infarction of prostatic nodules [40].

Other cystic lesions include cystadenoma which is a benign cystic tumor that may be associated with LUTS, pain, or urinary retention. They are noninvasive and appear on histology as a single layer of cuboidal cells with peribasal cells. Cavitary prostatitis is the result of static exudate occluding prostatic ducts and acini leading to weakened septa. The septa degenerate forming cavities in the prostate. Frequent genitourinary infections are commonly present in this population [40].

TRUS/CT

TRUS is the primary diagnostic imaging tool for prostatic and periprostatic cysts (Fig. 5.4). The majority of these lesions tend to be found incidentally during ultrasound for prostate biopsy. Cystic lesions may be simple or complex on imaging and appear hypoechoic on ultrasonography. Lesions may have septations, calcifications, or thickened walls. Müllerian duct cysts appear as midline or lateral to midline anechoic cystic lesions posterior to the urethra and can extend superior to the base of the prostate. Ejaculatory duct cysts are best seen in the sagittal plane and appear hypoechoic slightly lateral to midline [40].

On contrast enhanced CT scan, cysts will appear as non-enhancing hypodense structures within the prostate (Fig. 5.5a, b).

MRI

With the increase in use of MRI for targeted prostate biopsy during cancer workup, defining prostatic cysts become easier. On MR imaging, prostatic cysts are readily identified on T2-weighted imaging due to their high signal [41]. McDermott et al. describe the characteristic MR imaging features of prostatic cysts using a 1.5-T scanner with the patient in supine position as seen on axial, sagittal, and coronal T1/2-weighted images. They describe the characteristic pear-shaped PU cysts that give off high signal on T2-weighted imaging due to the straw-colored fluid which is devoid of sperm. Another defining feature is the PU cyst remains in the boundaries of the prostate, while Müllerian duct cysts when enlarged can extend above the prostate. Müllerian duct cysts are also of high signal on T2-weighted imaging due to a brown sperm-free fluid. On T1-weighted imaging Müllerian duct cysts that are hemorrhaging will appear hyperintense which is usually in association with a retrovesicular stone. Ejaculatory duct cysts appear as high signal on T2-weighted images and may be in association with a low-signal calculus. Prostatic retention cysts appear as round, smooth-walled unilocular cysts in any zone of the gland. Cystic BPH is located in the transitional zone of the prostate; however, they may appear in the peripheral

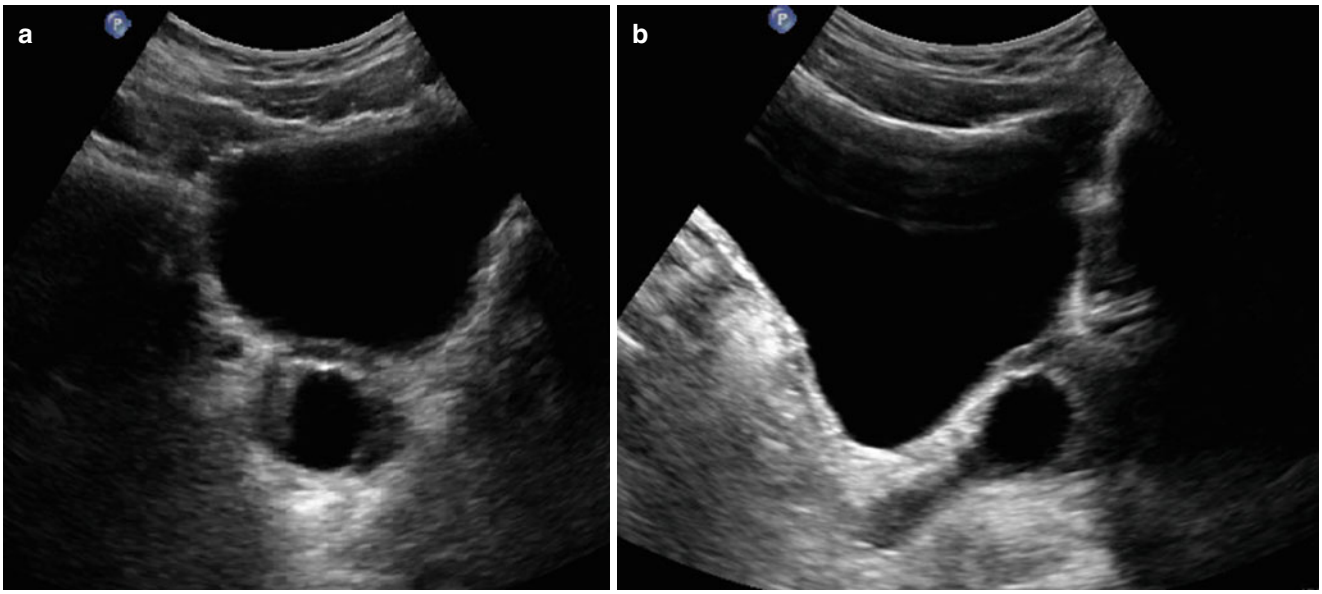

Fig. 5.4 (**a**) Transabdominal ultrasound in transverse plane of incidental finding of 1.9×1.7×2.1 cm anechoic cystic lesion associated with the prostate. (**b**) Same incidental prostatic cyst in longitudinal plane

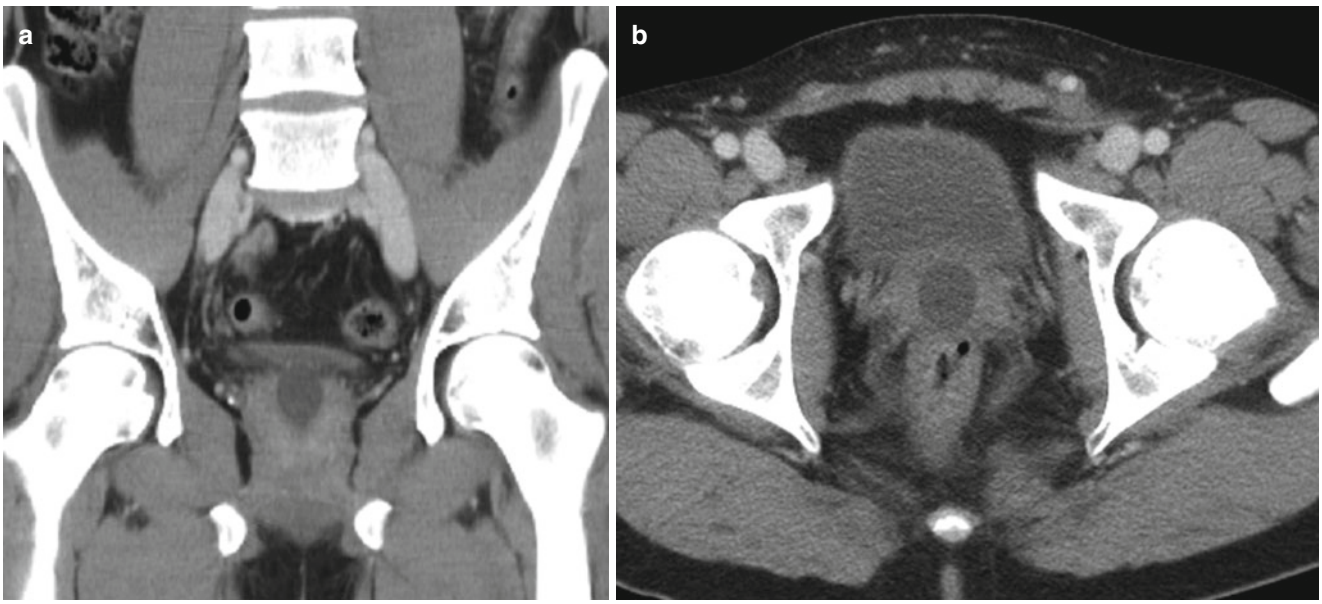

Fig. 5.5 (**a**) Contrast-enhanced CT scan, coronal section revealed incidental finding of round hypodense lesion within the central aspect of the prostate extending superior likely an utricle cyst. (**b**) Same utricle cyst in axial section

zone due to the enlarging transitional zone compressing the peripheral zone. On MR T2-weighted imaging, the lesion appears as high intensity.

Surgical management as previously discussed is reserved for patients with lower urinary tract symptoms and consists of aspiration and decompression to relieve obstruction or irritation. Different therapeutic treatments have been reported; however, therapy should be individualized for the patient.

Prostatic Calculi

Prostatic calculi are a common finding in men and may for the most part be completely asymptomatic and otherwise found during routine workup for other prostate-related diseases. The incidence is unknown but noted to be 7 % on pathological specimen, 20 % on autopsy, and 30 % on abdominal radiograph and thought to be higher on sonographic studies [42]. A study of 300 prostates from autopsies

from Søndergaard and colleagues found calculi in 99 % with a greater in number and size with age [43]. Prostatic calculi can be classified as true or false depending on their etiology. Calculi that form in the tissues or acini of the prostate glands are considered true prostatic calculi. Secondary or false prostatic calculi are those that may form in the kidneys, ureters, bladder, or diverticula of the urethra and migrate into the region of the prostatic urethra. Additionally, false calculi may develop after an abnormal connection between the prostate and urethra develops. It is believed they form after a calcareous substance deposits on corpora amylacea. The corpora amylacea convert calcium phosphate and calcium carbonate into calculi. Prostatic calculi tend to be less than 4 mm and multiple calculi are typically present. Patients usually have presenting symptoms associated with BPH or prostatitis. The calculi can act as a nidus for bacteria preventing resolution of prostatitis with antimicrobial therapy [44]. It has been shown that the larger the stone, the greater the severity of LUTS. The majority of prostatic stones are clinically silent and do not require intervention. When prostatic stones do produce severe obstruction by causing compression of the prostatic urethra, surgery may be required. Options include transurethral stone removal, open prostatolithotomy, and radical prostatectomy. A small study by Shoskes et al. of 16 men with CPPS refractory to multiple medical therapies were given a 3-month trial of daily suppository of 500 mg tetracycline, a vitamin, and ethylenediaminetetraacetic acid. 80 % of the patients experienced greater than 25 % improvement in symptoms. Ten patients underwent transrectal ultrasound following the 3-month treatment, and half of them showed a decrease in size or resolution of the prostatic calculi [45].

Imaging

Prostatic stones appear hyperechoic on transrectal or pelvic ultrasonography. On abdominal radiograph the stone will appear radiopaque above the pubic symphysis in patients with BPH. Prostatic calculi will appear radiopaque on CT scan. All three of these entities are generally ordered for the workup of another pathological process with prostatic calculi being an incidental finding. Rarely do prostatic calculi when diagnosed require intervention as a sole pathological finding not associated with other symptoms.

References

1. McNeal J. Pathology of benign prostatic hyperplasia. insight into etiology. Urol Clin North Am. 1990;17(3):477–86.
2. Berry SJ, Coffey DS, Walsh PC, Ewing LL. The development of human benign prostatic hyperplasia with age. J Urol. 1984;132(3):474–9.
3. Wei JT, Calhoun E, Jacobsen SJ. Urologic diseases in america project: benign prostatic hyperplasia. J Urol. 2005;173(4):1256–61. doi: S0022-5347(05)61064-6 [pii].
4. Kolman C, Girman CJ, Jacobsen SJ, Lieber MM. Distribution of post-void residual urine volume in randomly selected men. J Urol. 1999;161(1):122–7.
5. McVary KT, Roehrborn CG, Avins AL, et al. Update on AUA guideline on the management of benign prostatic hyperplasia. J Urol. 2011;185(5):1793–803.
6. Emberton M, Cornel EB, Bassi PF, Fourcade RO, Gomez JM, Castro R. Benign prostatic hyperplasia as a progressive disease: a guide to the risk factors and options for medical management. Int J Clin Pract. 2008;62(7):1076–86.
7. Madersbacher S, Alivizatos G, Nordling J, Sanz CR, Emberton M, de la Rosette JJ. EAU 2004 guidelines on assessment, therapy and follow-up of men with lower urinary tract symptoms suggestive of benign prostatic obstruction (BPH guidelines). Eur Urol. 2004;46(5):547–54.
8. Chia SJ, Heng CT, Chan SP, Foo KT. Correlation of intravesical prostatic protrusion with bladder outlet obstruction. BJU Int. 2003;91(4):371–4.
9. Nose H, Foo KT, Lim KB, Yokoyama T, Ozawa H, Kumon H. Accuracy of two noninvasive methods of diagnosing bladder outlet obstruction using ultrasonography: intravesical prostatic protrusion and velocity-flow video urodynamics. Urology. 2005;65(3):493–7. doi: S0090-4295(04)01211-7 [pii].
10. Keqin Z, Zhishun X, Jing Z, Haixin W, Dongqing Z, Benkang S. Clinical significance of intravesical prostatic protrusion in patients with benign prostatic enlargement. Urology. 2007;70(6):1096–9. doi: S0090-4295(07)01972-3 [pii].
11. Stravodimos KG, Petrolekas A, Kapetanakis T, et al. TRUS versus transabdominal ultrasound as a predictor of enucleated adenoma weight in patients with BPH: a tool for standard preoperative work-up? Int Urol Nephrol. 2009;41(4):767–71. doi:10.1007/s11255-009-9554-9.
12. Watanabe H, Kato H, Kato T, Morita M, Tanaka M. Diagnostic application of ultrasonotomography to the prostate. Nihon Hinyokika Gakkai Zasshi. 1968;59(4):273–9.
13. Zlotta AR, Djavan B, Damoun M, et al. The importance of measuring the prostatic transition zone: an anatomical and radiological study. BJU Int. 1999;84(6):661–6.
14. Tokgoz O, Tokgoz H, Unal I, et al. Diagnostic values of detrusor wall thickness, postvoid residual urine, and prostate volume to evaluate lower urinary tract symptoms in men. Diagn Interv Radiol. 2012;18(3):277–81.
15. Matthews GJ, Motta J, Fracchia J. The accuracy of transrectal ultrasound prostate volume estimation: clinical correlations. J Clin Ultrasound. 1996;24(9):501–5.
16. Tewari A, Indudhara R, Shinohara K, et al. Comparison of transrectal ultrasound prostatic volume estimation with magnetic resonance imaging volume estimation and surgical specimen weight in patients with benign prostatic hyperplasia. J Clin Ultrasound. 1996;24(4):169–74.
17. Hricak H, Dooms GC, McNeal JE, et al. MR imaging of the prostate gland: normal anatomy. AJR Am J Roentgenol. 1987;148(1):51–8.
18. Sommer FG, McNeal JE, Carrol CL. MR depiction of zonal anatomy of the prostate at 1.5 T. J Comput Assist Tomogr. 1986;10(6):983–9.
19. Turkbey B, Fotin SV, Huang RJ, et al. Fully automated prostate segmentation on MRI: comparison with manual segmentation methods and specimen volumes. AJR Am J Roentgenol. 2013;201(5):W720–9.
20. Hoffelt CS, Marshall LM, Garzotto M, et al. A comparison of CT scan to transrectal ultrasound-mesaured prostate volume in untreated prostate cancer. Int J Radiat Oncol Biol Phys. 2003;57:29–32.

21. Badiozamani KR, Wallner K, Cavanagh W, et al. Comparability of CT-based and TRUS-based prostate volumes. Int J Radiat Oncol Biol Phys. 1999;43:375–8.
22. Fiorino C, Reni M, Michalski J, et al. Intra- and inter-observer variability in contouring prostate and seminal vesicles: implications for conformal treatment planning. Radiother Oncol. 1998;47:285–92.
23. The national kidney and urologic diseases advisory board 1990 long-range plan: window on the 21st century. J Urol. 1991;145(3):568–93.
24. Collins MM, Stafford RS, O'Leary MP, Barry MJ. How common is prostatitis? A national survey of physician visits. J Urol. 1998;159(4):1224–8.
25. Kong do H, Yun CJ, Park HJ, Park NC. The efficacy of mirodenafil for chronic prostatitis/chronic pelvic pain syndrome in middle-aged males. Department of Urology, Pusan National University School of Medicine, Busan, Korea. pISSN: 2287–4208/eISSN: 2287–4690. World J Mens Health. 2014;32(3):145–50.
26. Krieger JN, Nyberg Jr L, Nickel JC. NIH consensus definition and classification of prostatitis. JAMA. 1999;282(3):236–7.
27. Horcajada JP, Vilana R, Moreno-Martínez A, Alvarez-Vijande R, Bru C, Bargalló X, Buñesch L, José Antonio M, Josep M. Transrectal prostatic ultrasonography in acute bacterial prostatitis: findings and clinical implications. Scand J Infect Dis. 2003;35(2):114–20.
28. Doble A, Carter SS. Ultrasonographic findings in prostatitis. St. Mary's hospital, London, England. Urol Clin North Am. 1989;16(4):763–72.
29. Ludwig M, Weidner W, Schroeder-Printzen I, Zimmermann O, Ringert RH. Transrectal prostatic sonography as a useful diagnostic means for patients with chronic prostatitis or prostatodynia. Br J Urol. 1994;73(6):664–8.
30. Palmas AS, Coelho MF, Fonseca JF. Color Doppler ultrasonographic scanning in acute bacterial prostatitis. Arch Ital Urol Androl. 2010;82(4):271–4.
31. Logan JK, Walton-Diaz A, Rais-Bahrami S, et al. Changes observed in multiparametric prostate magnetic resonance imaging characteristics correlate with histopathological development of chronic granulomatous prostatitis afer intravesicle bacillus Calmette-Guerin therapy. J Comput Assist Tomogr. 2014;38:274–6.
32. Nagel K, Schouten M, Hambrock T, Litjens G, Hoeks C, Haken B, Fütterer J. Differentiation of prostatitis and prostate cancer by using diffusion-weighted MR imaging and MR-guided biopsy at 3 T. Radiology. 2013;267:164–72.
33. Granados EA, Riley G, Salvados J, Vicente J. Prostatic abscess: diagnosis and treatment. J Urol. 1992;148:80–2.
34. Oliveira P, Andrade JA, Porto HC, Filho JE, Vinhes AF. Diagnosis and treatment of prostatic abscess. Int Braz J Urol. 2003;29(1):30–4.
35. Thornhill BA, Morehouse HT, Coleman P, Hoffman-Tretin JC. Prostatic abscess: CT and sonographic findings. AJR Am J Roentgenol. 1987;148:899–900.
36. Papanicolaou N, Pfister RC, Stafford SA, Parkhurst EC. Prostatic abscess: imaging with transrectalsonography and MR. AJR Am J Roentgenol. 1987;149:981–2.
37. Galosi AB, Montironi R, Fabiani A, Lacetera V, Galle G, Muzzonigro G. Cystic lesions of the prostate gland: an ultrasound classification with pathological correlation. J Urol. 2009;181:647–57.
38. Coppens L, Bonnet P, Andrianne R, de Leval J. Adult müllerian duct or utricle cyst: clinical significance and therapeutic management of 65 cases. J Urol. 2002;167(4):1740–4.
39. Halpern EJ, Hirsch IH. Sonographically guided transurethral laser incision of a müllerian duct cyst for treatment of ejaculatory duct obstruction. AJR Am J Roentgenol. 2000;175:777–8. 0361–803X/00/1753–777.
40. Nghiem HT, Kellman GM, Sandberg SA, Craig BM. Cystic lesions of the prostate. Radiographics. 1990;10:635–50.
41. McDermott VG, Meakem III TJ, Stolpen AH, Schnall MD. Prostatic and periprostatic cysts: findings on MR imaging. Am J Roentgenol. 1995;164:123–7.
42. Grayhack JT, McVary KT, Kozlowski JM. Benign prostatic hyperplasia. In: Gillenwater JY, Grayhack JT, Howards SS, Mitchell ME, editors. Adults and pediatrics urology, vol. 2. 4th ed. St. Louis: Mosby; 2002. p. 1401–70.
43. Søndergaard G, Vetner M, Christensen PO. Prostatic calculi. Acta Pathol Microbiol Immunol Scand A. 1987;95(3):141–5.
44. Venyo A. Prostatic calculi: a review of the literature. WebmedCentral Urol. 2012;3(6):WMC003463.
45. Shoskes DA, Thomas KD, Gomez E. Anti-nonbacterial therapy for men with chronic prostatitis/chronic pelvic pain syndrome and prostatic stones: preliminary experience. J Urol. 2005;173(2):474–7.

Transrectal Ultrasound of the Prostate

6

Gideon D. Richards, Pat F. Fulgham, and Bruce R. Gilbert

The urologist is uniquely qualified by training and experience to perform and interpret the transrectal ultrasound (TRUS) study of the prostate. TRUS enhances patient care by providing a minimally invasive procedure that gives real-time information for a rapid and accurate diagnosis. The goal of this chapter is to assist the physician in maintaining a high degree of proficiency in performing, interpreting, and documenting the transrectal ultrasound study and biopsy of the prostate.

Developmental Anatomy

Bladder and Urethra

The urogenital sinus is the embryonic structure that ultimately gives rise to the bladder, prostate, and majority of the urethra (Fig. 6.1). It is a structure that is of endodermal origin and develops from the cloaca as it is divided into anterior and posterior chambers by the ingrowth of the mesoderm. The anterior portion of the cloaca becomes the urogenital sinus and the posterior becomes the hindgut. The bladder forms from the superior portion of the urogenital sinus. The middle and lower parts of the urogenital sinus are also of endodermal origin and form the posterior (prostatic and membranous) urethra. The anterior portions of the urethra develop from both an endodermal (pendulous and bulbar urethra) and ectodermal (fossa navicularis and meatus) origin.

G.D. Richards, MD
Arizona State Urological Institute, Gilbert, AZ, USA
e-mail: gidrichards@gmail.com

P.F. Fulgham, MD
Urology Clinics of North Texas, Dallas, TX, USA

B.R. Gilbert, MD, PhD (✉)
Department of Urology, Hofstra North Shore LIJ School of Medicine, New Hyde Park, NY, USA
e-mail: bgilbert@gmail.com

The bladder is an *extraperitoneal* structure centrally positioned in the pelvis with three fixed landmarks important in bladder ultrasound:

1. The bladder base or trigone
2. The ureters, which enter the trigone approximately 2 cm lateral to the midline on each side
3. The bladder neck which is seen as a slightly open funnel at the base of the bladder

Identification of these landmarks allows for descriptive interpretation of prostate pathology as well as localization for TRUS biopsy.

Prostate and Accessory Glands

The seminal vesicles are of mesodermal origin. They differentiate during the 12th week of embryonic development from the mesonephric (Wolffian) duct near where they open into the urogenital sinus (Fig. 6.2). The prostate has both an endodermal and mesodermal origin. The glandular elements differentiate from the prostatic part of the urogenital sinus (endodermal) during the 12th week. The stroma and smooth muscle differentiate from mesodermal cells under the influence of dihydrotestosterone. The 12th week is also punctuated by the genesis of the bulbourethral (Cowper's) and urethral (Littré's) glands, which differentiate from protrusions along the urethra (endodermal).

The prostate is a *retroperitoneal* structure lying anterior to the rectum and inferior to the bladder, and it is separated from the rectum by an obliterated peritoneal plane (Denonvilliers' fascia). Lateral to the prostate are the levator ani and obturator internus muscles.

The "prostatic capsule" is not a true fibroelastic capsule, but rather periprostatic fat and stroma well visualized with ultrasound.

A.R. Rastinehad, D.N. Siegel (eds.), *Interventional Urology*, DOI 10.1007/978-3-319-23464-9_6

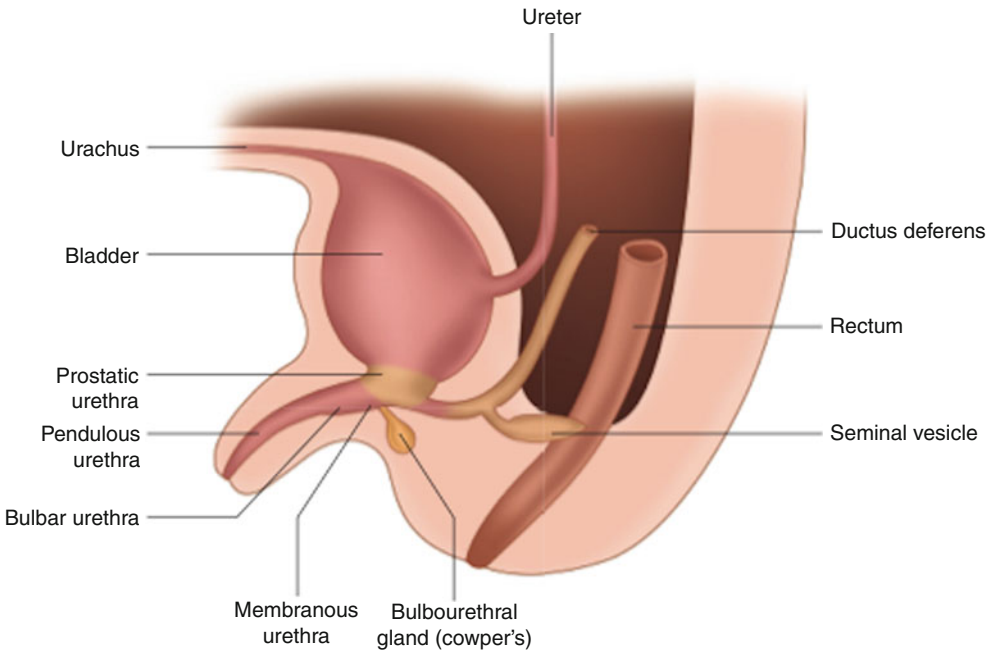

Fig. 6.1 Embryonic bladder and relationships with the ureters, male reproductive structures, and urethral components

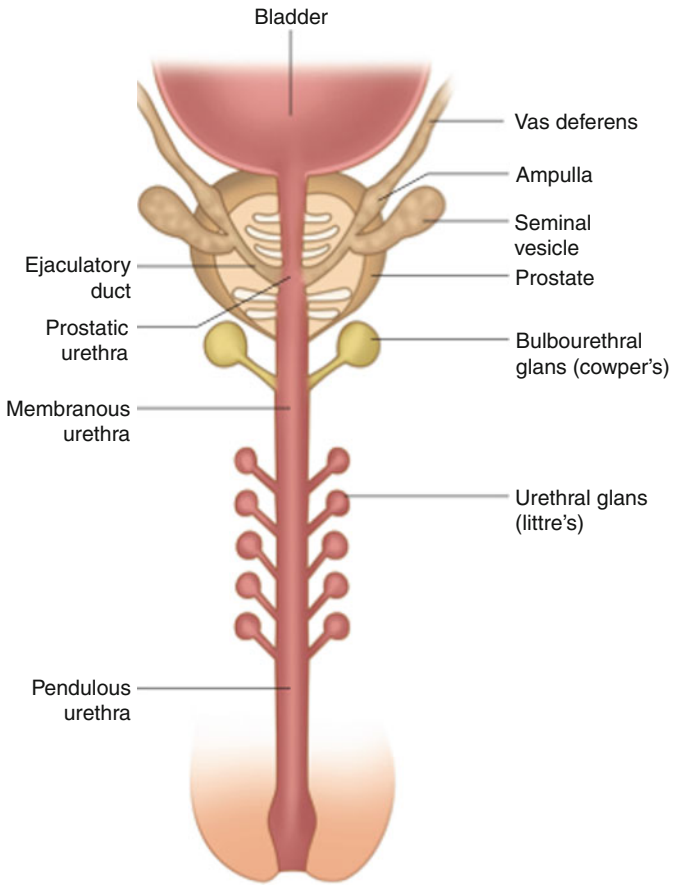

Fig. 6.2 The prostate and accessory glands of the urethra

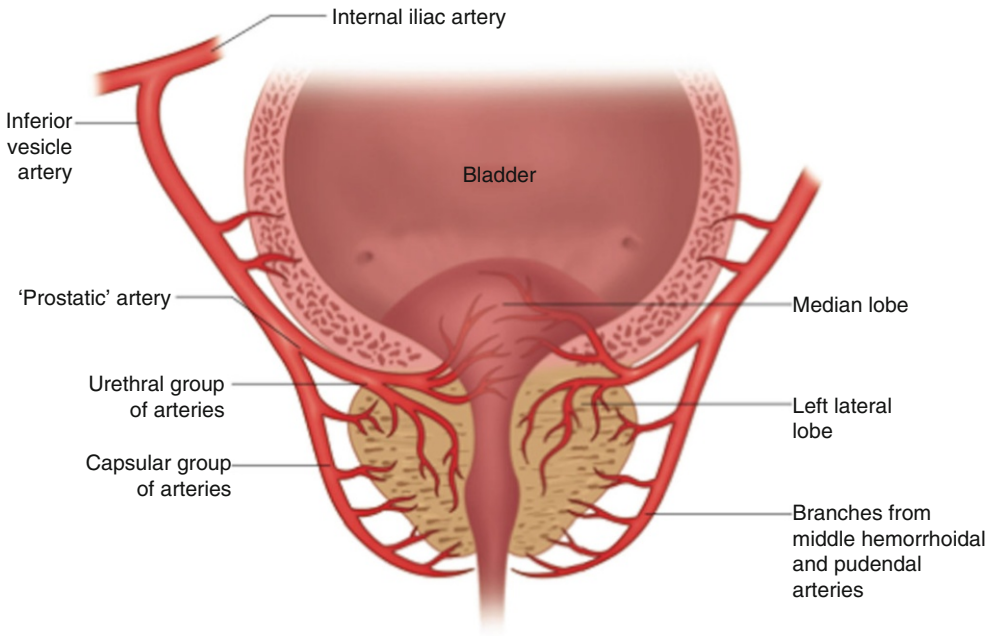

Fig. 6.3 Arterial supply to the prostate, bladder neck, and prostatic urethra

Vasculature

The prostate and seminal vesicles are supplied by the inferior vesical, internal pudendal, and middle rectal arteries (Fig. 6.3). The seminal vesicles are also supplied by a branch of the superior vesicle artery, the vesiculo-deferential artery.

Prostate Zonal Anatomy

Clinically, and from an ultrasound prospective, the prostate is best identified as being divided into four zones (Fig. 6.4). Three of which are glandular (central, transition, and peripheral zones) and one is nonglandular (anterior fibromuscular stroma).

The central zone regresses with age and is often difficult to identify on ultrasound. The periurethral transition zone increases in size with age and is a major contributor to benign prostatic hypertrophy. The surgical "capsule" is the line between the peripheral and central/transition zones. The nonglandular zone, the anterior fibromuscular stroma, is located entirely anterior to the urethra.

Understanding prostatic zonal anatomy is important for understanding disease distribution and biopsy considerations. Furthermore, it is invaluable for understanding the ultrasound appearance of the prostate.

Prostate Orientation

The standard orientation for transrectal ultrasound (TRUS) of the prostate in the sagittal longitudinal image places the anterior of the prostate at the top of the screen, posterior of the prostate at the bottom (Fig. 6.5). The base of the prostate is at the bladder neck (which lies to the left side of the screen), while the apex is where the prostatic urethra meets the bulbar urethra (falling more to the right side of the screen). It is oriented as if the observer were positioned to the right of the patient, looking through them sagittally, in cross section. The transverse ultrasound standard orientation is similar to the CT scan appearance with the anterior of the prostate at the top of the ultrasound display and the posterior at the bottom, while the right prostate is on the left side of the screen and left prostate on the right when looking at the ultrasound display. It is oriented as if the observer were positioned at the patient's feet looking up through them in cross section.

Clinical Interpretation

Patient Concerns

Our patients often present for ultrasound examinations, prostate ultrasound in particular, with much trepidation about the exam, especially when a biopsy is to be done, as well as a heightened anxiety regarding what our findings might be. It is essential that we understand our patients' concerns and make every effort to address them. Our patients appreciate the preprinted information about the ultrasound examination we provide. The brochure might include a discussion of the procedure, the preparation prior to the exam, what they might feel during the exam, as well as post-procedural instructions.

The examination is conducted in a warm room where the patient's privacy is maintained. Traffic in and out of the room is

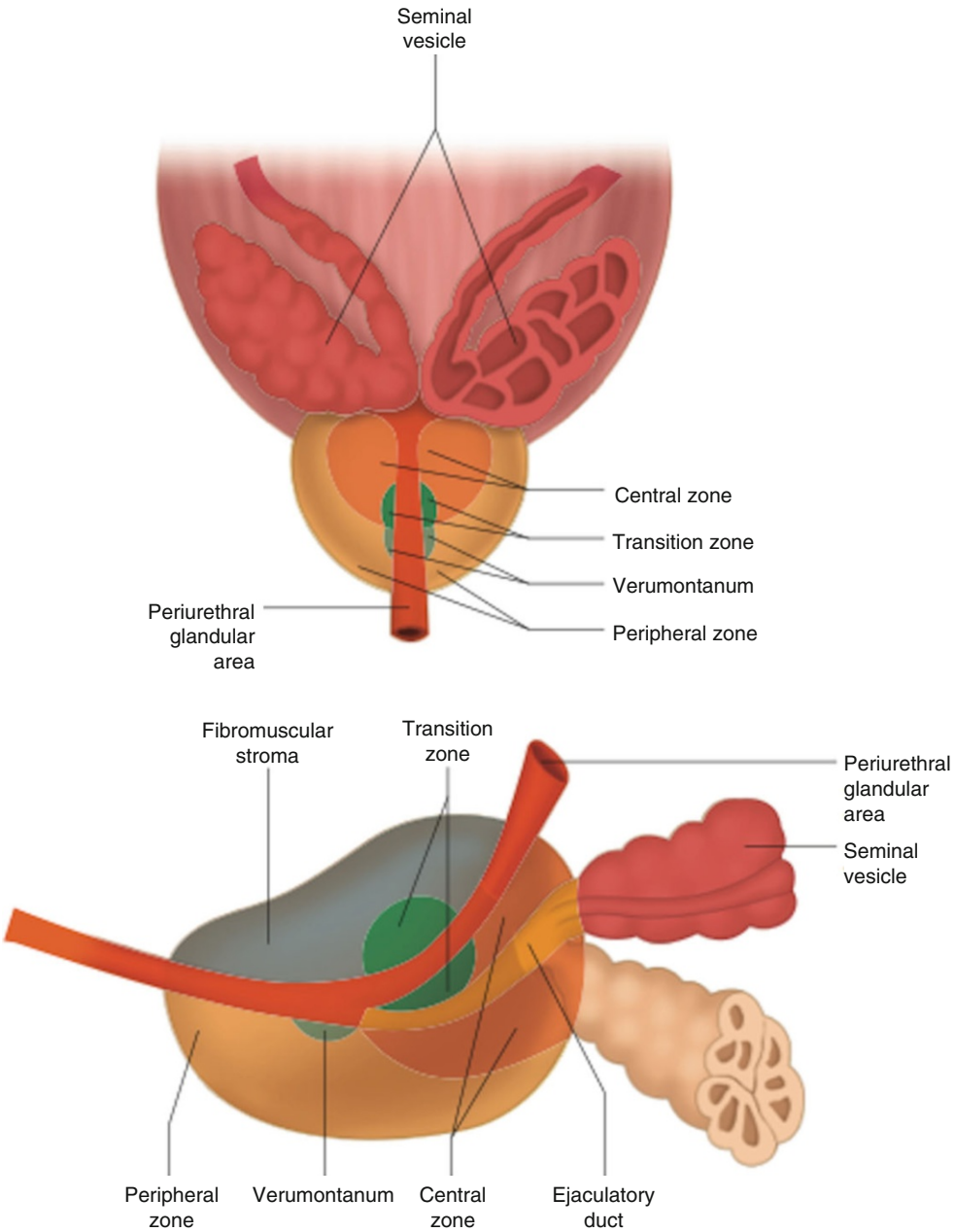

Fig. 6.4 Schematic of the prostate zonal anatomy

kept to a minimum during the procedure. All equipment is readied prior to the patient entering the room to ensure the procedure proceeds as rapidly as possible and to minimize patient anxiety.

Equipment Maintenance and Preparation

Transrectal ultrasound is a procedure that mandates disinfection of all equipment between patients. Biopsies should only be done with disposable single-use needles. The physician should document (in a procedure manual) policies for prevention of infectious disease, cleaning of ultrasound transducers, and a policy for equipment maintenance and calibration. Manufacturer guidelines should always be followed. Patient complications should be documented and logged.

Clusters of infectious complications or bleeding should be investigated for protocol violations or equipment failures.

Normal Imaging

The use of the standard terminology is important to describe ultrasound findings:

1. Hypoechoic is darker and more black.
2. Hyperechoic is brighter and more white.

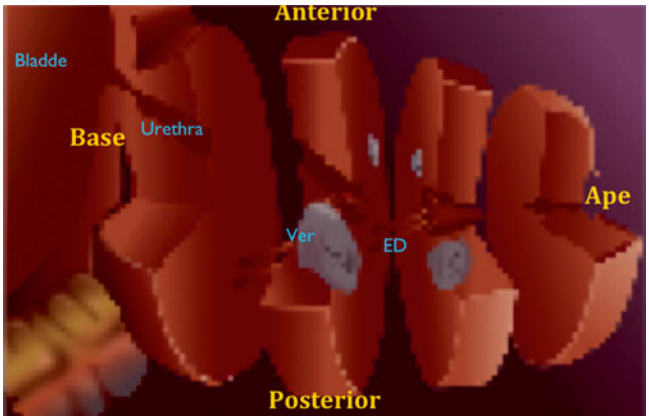

Fig. 6.5 Prostate orientation mimicking typical sagittal ultrasound view with the bladder to the left and the apex of the prostate to the right

3. Isoechoic is similar to the reference.
4. Anechoic is without echoes.
5. Homogeneous is of uniform echogenicity.
6. Heterogeneous is of mixed echogenicity.

High water content makes tissue appear hypoechoic, while high fat content makes tissue appear hyperechoic. Unlike renal and abdominal ultrasounds where the liver is usually used as the benchmark for comparisons of echogenicity, the prostatic ultrasound does not include the liver, and thus the left and right sides of the gland should always be compared to each other (Fig. 6.6).

The Adult Prostate

The young male prostate is homogenous with different zones often difficult to discern from each other. The "sonographic capsule" can be identified due to the impedance difference between the prostate and surrounding fat. The prominence of the urethra (u) is related to the surrounding low reflectivity of urethral muscles (Figs. 6.6 and 6.7).

In the young male, the peripheral zone (pz) is often hyperechoic compared to the central zone (cz) and transition zone (tz). The cz and tz are difficult to differentiate from each other, and the fibromuscular stroma (fs) is positioned anterior to the urethra.

In the older male the glandular and stromal elements enlarge, increasing the size of the tz and occasionally the pz. The tz is generally distinguishable from other zones. The cz is difficult to visualize (Fig. 6.7).

The base of the prostate is located at the superior aspect of the prostate contiguous with the bladder neck. The apex of the prostate is located at the inferior aspect of the prostate continuous with the striated muscles of the urethral sphincter (Fig. 6.5).

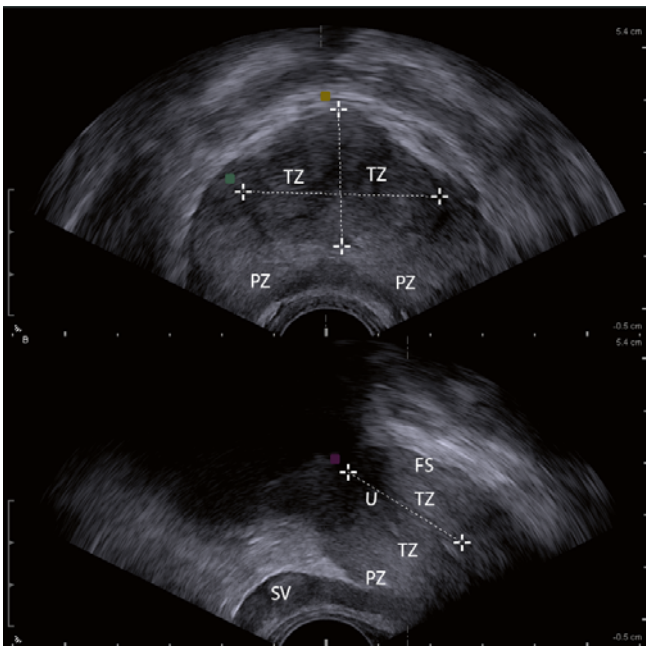

Fig. 6.6 The adult prostate. The top panel represents a transverse view and the bottom a longitudinal view. The transition zones (*TZ*), peripheral zones (*PZ*), anterior fibromuscular stroma (*FS*), seminal vesicle, and urethra (*U*) are indicated. The calipers are placed on the dimensions of the transition zone. Notice the symmetric echogenicity of the left and right sides in the top panel

Fig. 6.7 The prostate in a 35-year-old male (*top panel*) and 65-year-old male (*bottom panel*). Note the prominence of the transition zone in the older male

Scanning Protocol

A systematic scan will ensure that a comprehensive examination is performed and appropriately documented. A high-frequency (7.5–10 Mhz) transducer is usually used. This can be a biplanar or a single-plane transducer.

The patient is usually examined in the (left) lateral decubitus position with his legs flexed in the knee-to-chest position. It is essential to perform a digital rectal exam *prior* to inserting the ultrasound probe. *Any pain, tenderness, rectal stricture, mass, lesion, and/or bleeding that is encountered when performing the rectal exam or when inserting the probe might preclude the TRUS.*

The following represents one author's protocol for scanning the prostate. It should be viewed as a guide and modified as the physician deems appropriate.

Protocol

After probe insertion, perform a "survey" scan of the prostate from base to apex including the seminal vesicles and rectal wall. This provides the sonographer with an overview of the prostate and surrounding structures and allows for the development of a "road map" for more detailed evaluation.

The seminal vesicles are then examined in the transverse plane for comparative evaluation of echogenicity and measurements of seminal vesicle height and ampulla (vas deferens) diameter. Next the mid-prostate, transverse image of the prostate is examined and the AP and width measurements are taken. If using a biplane probe, the length measurement can also be obtained from the midsagittal longitudinal image. If not using a biplane probe, then obtain a *midsagittal longitudinal image* for the length measurement. Prostate volume, predicted prostate-specific antigen (PPSA), and prostate-specific antigen density (PSAD) can then be calculated usually by formulas already programmed in the ultrasound machine.

Continue the exam in the transverse plane, obtaining appropriate image documentation of both base and apex views. The sonographer should then rotate the probe (or switch views if using a biplane probe) into a longitudinal plane to slowly scan the prostate from the levator ani on the left to the levator ani on the right. Depending on the field of view, this may need to be done at several positions along the axial length of the prostate. Oftentimes there may be a need to angle the probe up to examine the right side of the gland and down to examine the left. Images of the right lateral longitudinal, left lateral longitudinal, and midsagittal planes should be captured for documentation.

As in many urologic applications of sonography, color Doppler can add valuable information. Inflammatory disease processes result in increased vascularity that is well demonstrated with transrectal ultrasound. In addition, the sensitivity for the detection of neoplastic processes can be increased with the use of color Doppler [1]. Therefore, the sonographer should document the vascularity of the gland and any abnormal vascular patterns. Make sure to label and document each view.

The bladder should also be evaluated with measurements of the wall thickness, size, and location of any diverticula, calculi, or other abnormalities. Again, color Doppler adds another dimension. Ureteral jets can be evaluated with color or power Doppler confirming patency of the ureteral orifices. Bladder volume and post-void residual (PVR), if appropriate, should also be measured and documented.

The rectal wall thickness must be evaluated and documented, as well as any other notable findings. The appearance of rectal abnormalities (Fig. 6.8) should be documented and should prompt referral to the appropriate medical specialist.

Fig. 6.8 A 62-year-old male with BPH found to have rectal mass. The mass is demonstrated as a thickening of the rectal wall on TRUS. The lower arrows on each panel point to the mass

The following are suggested images. They should be saved in a permanent medium, appropriately labeled, and attached to the written report:

1. Transverse view of the prostate at the base
2. Transverse view of the prostate at mid-gland with the mid-transverse anterior-posterior and width measurements indicated on the image
3. Transverse view of the prostate at the apex
4. Transverse view of the seminal vesicles
5. Transverse view of the bladder with the mid-transverse anterior-posterior and width measurements indicated on the image
6. Longitudinal (sagittal) view at midplane with the mid-sagittal longitudinal measurement indicated on the image
7. Longitudinal (sagittal) view of right side 30° to 45° from midline
8. Longitudinal (sagittal) view of left side 30° to 45° from midline
9. Longitudinal view of the seminal vesicles
10. Longitudinal view of the bladder with the midsagittal longitudinal measurement indicated on the image

Proper documentation of the ultrasound evaluation is an essential part of the examination. The goal is to provide a report that depicts what was observed and documents the features supporting the observations.

The report should include:

1. Patient identification.
2. Date of examination.
3. Measurement parameters and anatomical findings of the examination.
4. The indication for performing the examination is clear and provided on the report. The report is signed by the physician who performed the ultrasound examination.

Images should include the following:

1. Patient identification.
2. Date and time of each image.
3. Clear image with clearly labeled orientation and measurements.
4. Labeling of anatomy and any abnormalities.
5. Images should be attached to the report.

Disinfection of Probes

An important aspect of patient safety is the disinfection of the ultrasound probes. Low-level disinfection is for probes that come into contact with intact skin such as those used for renal and bladder ultrasound. Intermediate-level disinfection is used for some critical and some non-critical indications and includes transducers used for ultrasound of the scrotum. High-level disinfection is for semi-critical items that come in contact with mucous membrane or intact skin. This would include transvaginal and transrectal ultrasound when no biopsy is performed. *Critical-level disinfection* is used on materials that will enter tissues or when blood will flow through them. This would include intraoperative transducers as well as endorectal probes with biopsy guides and their attachments. Manufacturer's recommendations must be followed.

Indications for Prostate Ultrasound

Indications for prostate ultrasound are listed in Tables 6.1 and 6.2. It should be emphasized that these indications do not include routine screening.

Measurement of Prostate-Specific Antigen Density (PSAD)

Benign prostatic hypertrophy (BPH) occurs in most men and results in a rise in PSA not related to prostate cancer. PSAD is the blood PSA (ng/ml) level divided by the volume of the

Table 6.1 Indications for prostate ultrasound

1. Measurement of prostate volume for determination of PSA density
2. Abnormal digital rectal exam
3. Prostatic assessment with sonographic controlled biopsy
4. Cysts
5. Evaluation for and aspiration of prostate abscess
6. Assessment for suspected congenital abnormality
7. Lower urinary tract symptoms
8. Pelvic pain
9. Prostatitis/prostadynia
10. Hematospermia
11. Infertility
(a) Azoospermia
(b) Low-volume or poorly motile specimen
(c) Cysts
(d) Hypoplastic or dilated seminal vesicle
(e) Impaired motility
(f) Antisperm antibodies

Table 6.2 Indications for transrectal ultrasound-guided biopsy

To investigate an abnormal PSA or DRE
To follow up a biopsy with inconclusive or premalignant findings (e.g., ASAP, HGPIN)
To diagnose local recurrence after primary treatment for prostate cancer

prostate, as determined by TRUS. With most ultrasound software packages, the sonographer inputs the PSA and then measures the prostate with the mathematics performed electronically. With benign disease (BPH), the PSAD should not be more than 0.15 ng/ml/cm^3 of prostatic tissue. PSA levels exceeding 0.15 ng/ml/cc indicate the need for further evaluation.

Congenital Abnormality

Prostate Cysts

Most prostate cysts are benign. The location often defines the etiology (Fig. 6.9). Müllerian cysts do not communicate with the urethra, while utricle cysts are the fused caudal ends of the Müllerian ducts or urogenital sinus remnant and can communicate with the urethra. As with prostatic cysts, seminal vesicle cysts are suspected when ejaculate volume is low. They can also be seen with adult polycystic kidney disease.

Lower Urinary Tract Symptoms (LUTS)

TRUS is often used in the evaluation of lower urinary tract symptoms to evaluate prostate size, PVR, and evidence of lower urinary tract inflammation. However, controversy exists as to whether the measurements of the prostate and of the residual urine obtained through TRUS correlate with the patient symptoms [2]. Therefore, caution should be used in interpretation of the information obtained with TRUS in this scenario.

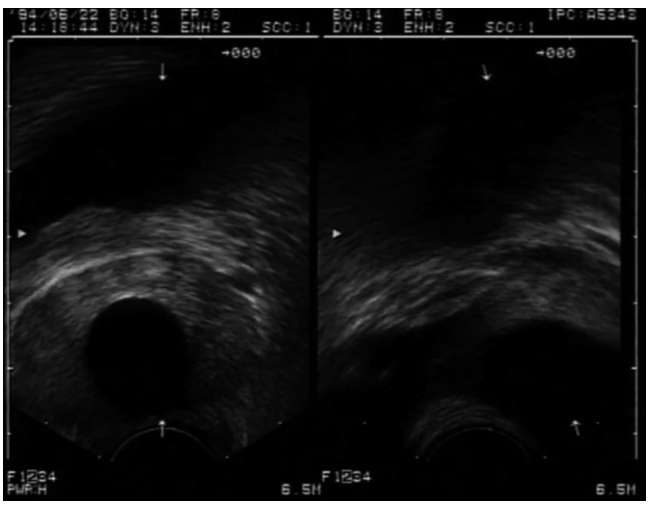

Fig. 6.9 Prostate cyst demonstrated in the midline prostate with transverse (*left panel*) and longitudinal (*right panel*) views. The cyst is anechoic and has well-demarcated walls, and the tissue on the opposite side of the cyst from the transducer has an increased echogenicity consistent with increased through-transmission

Chronic Prostate Inflammation/Abscess/ Prostate Pain Syndromes

Evaluation of chronic prostatitis or persistent pyuria can be assisted by TRUS. Granulomatous prostatitis has an appearance that generally includes multiple diffuse hypoechoic regions in multiple prostate zones; this appearance may also be seen in diffuse prostatic carcinoma. Occasionally, a focal hypoechoic area will be found to contain granulomatous prostatitis with TRUS biopsy (Fig. 6.10).

Prostatic abscesses have characteristic features that include a hypoechogenic appearance, increased peripheral vascularity with a loss of vascularity in the interior of the lesion, and a location usually within the central and transitional zones of the prostate. Inhomogeneous debris may be demonstrated within the hypoechoic abscess, and transrectal ultrasound-guided needle aspiration can be used to treat the condition [3].

Hematospermia

Transrectal ultrasonography has played an increasingly important role in the evaluation of men with hematospermia. Hematospermia is a common condition and causes great concern among men who experience it. Although often thought to be a common, benign condition, it can also be the sign of an underlying urologic disease.

Several studies have evaluated the utility of TRUS in the investigation of patients with chronic hematospermia. In a study of 52 patients, Etherington, Clements, Griffiths, and Peeling [4] found a significant number of patients with prostatic calculi and abnormalities of the seminal vesicles, including calculi, dilatation, and cysts.

Additionally, a paper by Worischeck and Parra [5] reported on the evaluation of 26 patients with hematospermia using TRUS. They found abnormalities in 92 % of patients, which included dilated seminal vesicles (30 %), ejaculatory duct cysts (15 %), ejaculatory duct calculi (15 %), seminal vesicle calculi (15 %), and Müllerian duct remnants (7 %).

Vascular anomalies including telangiectasia and varices have also been found on ultrasound in patients presenting with hematospermia.

Infertility: Azoospermia

There are specific indications for TRUS in the evaluation of the subfertile male. Suspicion is raised when men present with:

1. A low-volume ejaculate
2. A fructose-negative ejaculate

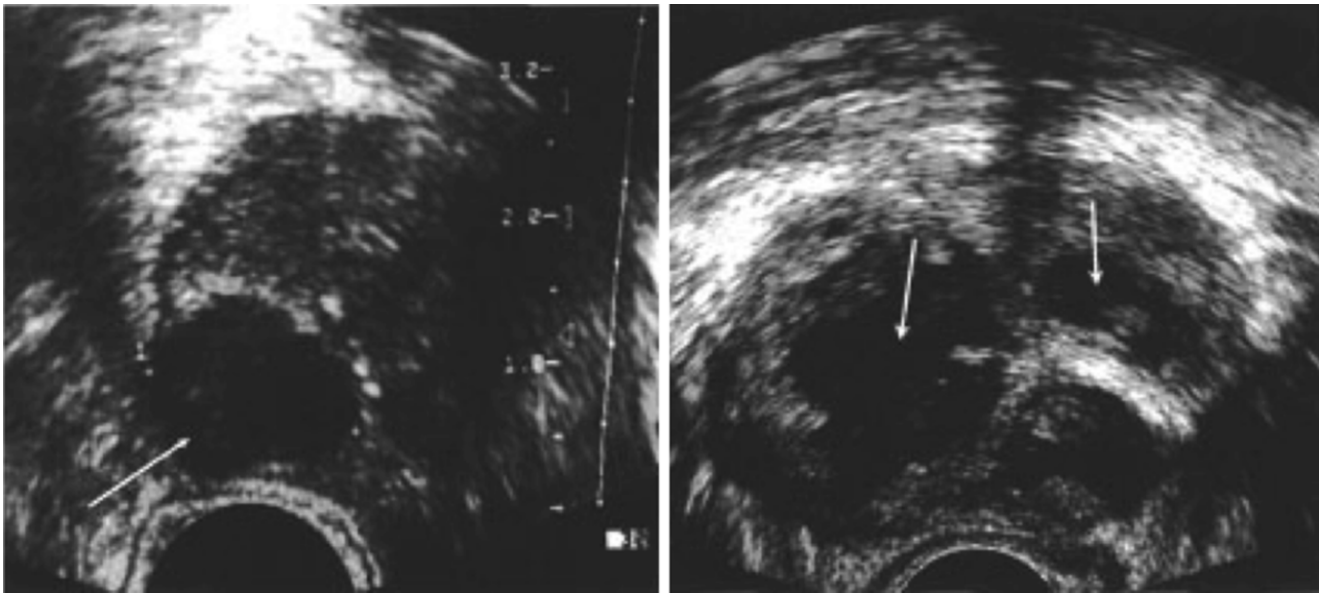

Fig. 6.10 Prostate inflammation and abscess, demonstrated as hypoechoic areas with regions of internal echoes

3. Pain on ejaculation
4. Urinary complaints of:
   (a) A decreased force of the urinary stream
   (b) Pain on urination
   (c) History of urinary tract infections

The presence of atrophic or dilated seminal vesicles, ejaculatory duct cysts, dilated seminal vesicles, and utricle or Müllerian cysts may be diagnostic and may be demonstrated by TRUS, and the presence or absence of these findings may direct therapy.

Prostate Biopsy for the Diagnosis of Prostate Cancer

Indications

Transrectal ultrasound-guided biopsy (TRUS-Bx) of the prostate is almost always initially performed for a specific clinical indication such as an elevation/change in the PSA or an abnormal digital rectal examination. High-grade prostatic intraepithelial neoplasia (HGPIN) and atypical small acinar proliferation (ASAP) on initial biopsy are considered by some to be indications for immediate or planned repeat biopsy [6, 7].

TRUS-Bx may be performed for a rising PSA after initial therapy. In the case of a patient with a rising PSA after radical retropubic prostatectomy ultrasound and biopsy of the prostatic fossa, any nodules encountered or the vesicourethral anastomosis may be used to diagnose local recurrence [8, 9]. After radiation therapy or cryotherapy, TRUS-Bx is employed to diagnose local treatment failure.

Ultrasound Findings

Regardless of the indication, ultrasound imaging plays a critical role in prostate biopsy. While needle guidance is a primary function of the ultrasound portion of the exam, any biopsy of the prostate should begin with a thorough diagnostic ultrasound. The sonographic characteristics of prostate cancer and the zonal distribution of cancer are well understood. It is clear that prostate cancers do not have a uniform pattern of echogenicity to allow accurate diagnosis on the basis of the imaging study alone. Approximately 70 % of prostate cancers will appear hypoechoic on ultrasound; however, microscopic cancers may be completely inapparent and indistinguishable from surrounding normal prostate tissue (Fig. 6.11). While 75 % of cancers are in the peripheral zone, at least 20 % may be in the transition zone and another 5 % in the central zone of the prostate (Fig. 6.12).

The increased microvasculature associated with some prostate cancers is too small to be seen by conventional scanning with a 7.5 mHz probe. However, increased regional blood flow associated with some prostate cancers is demonstrable with Doppler flow studies (intravascular ultrasound contrast agents may further facilitate identification of increased blood flow but are not currently FDA-approved for prostate ultrasound) [10].

While echogenicity provides clues to the location of prostate cancer, there are secondary findings which are valuable. For instance, deflection of the layer of corpora amylacea between the transition zone and peripheral zone (Fig. 6.13), asymmetry of the prostate, bulging of the prostatic capsule, and increased regional blood flow are sonographic signs that prostate cancer may be present (Fig. 6.14).

The appearance of prostate cancer is variable, but ultrasound should be used to take advantage of all available visual information (including blood flow, if Doppler capability is present) to maximize diagnostic yield from biopsy.

Patient Preparation

Informed Consent

The initial step in patient preparation should be to obtain informed consent. In addition to a discussion of potential adverse medical outcomes, the patient should be informed that there is a false-negative biopsy rate of 10–27 % [11, 12].

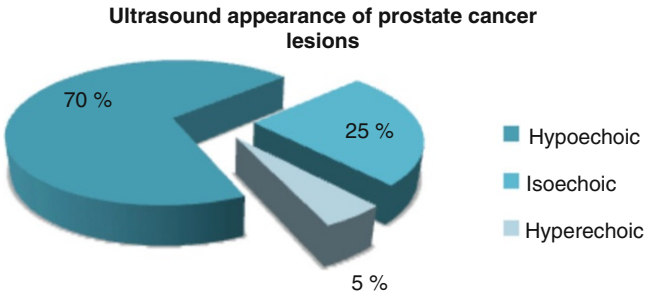

Fig. 6.11 Distribution of the various sonographic appearances of prostate cancer lesions

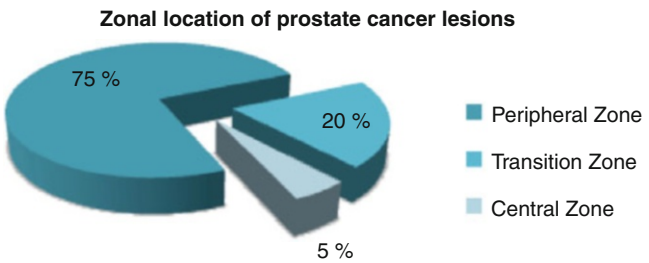

Fig. 6.12 Distribution of prostate cancer among the various zones of the prostate

Additionally, they should know that the diagnosis of small or clinically insignificant cancers may lead to treatments with significant morbidity.

Discontinue Anticoagulants

- Instruct patients to discontinue aspirin or aspirin-like products (NSAIDS), anticoagulants (vitamin E, Persantine, Coumadin, Plavix, etc.), and all herbal supplements (fish oil, chondroitin sulfate, etc.). These substances should not be restarted for 24 h after the procedure or until all bleeding has stopped. Some reports have suggested that low-dose aspirin (75–150 mg per day) may not increase bleeding risk [13–15]. The clinical risk associated with discontinuing anticoagulants will need to be weighed against the potential risk of bleeding after biopsy.

Preparation of Rectal Vault

- Instruct the patient to administer a Fleet enema 2–3 h prior to the biopsy. Although there is not universal agreement about the value of a cleansing enema with regard to

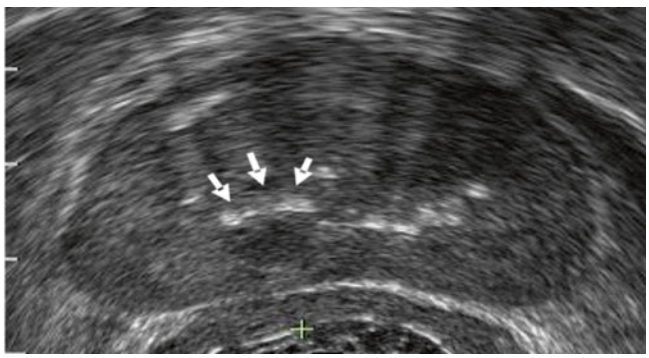

Fig. 6.13 Hypoechoicism with deflection of the junction between the transition zone and peripheral zone. The *arrows* demonstrate the upward deflection of the corpora amylacea

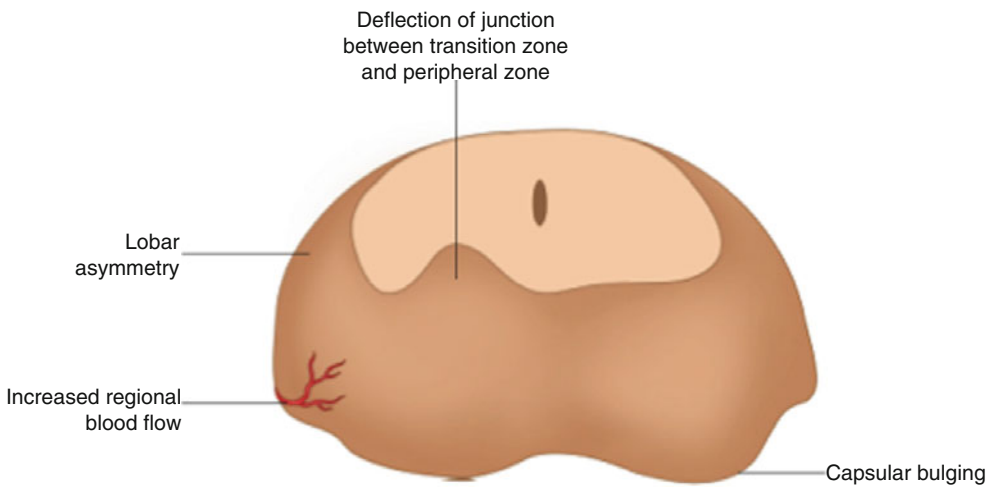

Fig. 6.14 Secondary sonographic findings suspicious for prostate cancer

subsequent infection, image quality is likely to be enhanced by removing stool and gas from the rectal vault. Jeon, Woo, Hyun, Choi, and Chai [16] demonstrated a decreased risk of infectious complications after TRUS-Bx for those patients who had rectal preparation via suppository (1.3 %) compared to those who did not have a preparation prior to biopsy (9.5 %). Lindert, Kabalin, and Terris [17] found that significantly more patients that developed bacteremia after TRUS-Bx had no rectal vault preparation in a group where patients were randomized to receive phosphate enemas or no vault preparation prior to biopsy.

Prophylactic Antibiotics

- Administer antibiotics prior to biopsy. Despite the risk of bacteriuria (44 %) and bacteremia (16 %) after biopsy demonstrated by Lindert et al. [17], the risk of an important clinical infection is low when antibiotic prophylaxis is used [18]. The best schedule for antibiotic prophylaxis is yet to be shown, but a single pre-biopsy dose and one post-biopsy dose seem justified. The evidence of multidrug-resistant *E. coli* secondary to the widespread use of broad-spectrum antibiotics suggests that the shortest course of appropriate antibiotic which protects the patient from serious clinical consequences would be desirable. We use one dose of a long-acting fluoroquinolone pre-biopsy and one dose 24 h after biopsy.
- The American Urological Association's best practice policy statement on urologic surgery recommends antimicrobial prophylaxis in *all* patients undergoing TRUS-Bx [19]. Fluoroquinolones, cephalosporins (first, second, and third generations), trimethoprim/sulfamethoxazole, gentamicin, and aztreonam are all identified as appropriate antibiotics for this purpose. Specific local antimicrobial resistance patterns should be considered in determining the regimen.
- Specific patient factors may also be used to direct antibacterial prophylaxis in the individual patient (e.g., a history of infections with fluoroquinolone-resistant organisms, adverse reactions with antibiotics or classes of antibiotics, comorbidities). Notably, many groups have reported a decrement in infection-related complications using rectal swab culture-directed antimicrobial prophylaxis [20, 21].

Urinalysis

- Though urinalysis is commonly performed prior to biopsy, there is no evidence that the risk of significant clinical infection is higher in the setting of an abnormal urinary sediment [22]. In patients with a history of bacteriuria especially those who may have hospital-acquired or multidrug-resistant organisms and in those where the consequences of bacteremia might be more profound (i.e., those who are immunosuppressed), evaluation of the urine sediment may assist the urologist in determining whether and when a biopsy should be performed.

Patient Position and Analgesia

Position

For office TRUS-Bx the patient may be placed in either the lateral decubitus position or lithotomy position. The lateral decubitus position allows the patient to assist with visualization of the prostate by varying the degree of hip flexion. Providing a monitor so the patient can watch the sonographic evaluation is often reassuring to the patient and helpful for explaining the findings.

Once the patient is in a satisfactory position, table height should be adjusted to provide maximal ergonomic advantage to the examiner. The ultrasound machine should be positioned so the urologist can make adjustments to maximize visualization of the image including adjusting the brightness and angle of the monitor (Fig. 6.15). Strategic placement of pads under the patient and on the floor to collect blood or body fluids associated with biopsy will facilitate cleanup between patients and minimize risk to those handling instruments and cleaning the room. A thorough digital rectal exam should be performed immediately prior to TRUS-Bx to dilate the rectal sphincter in anticipation of probe placement.

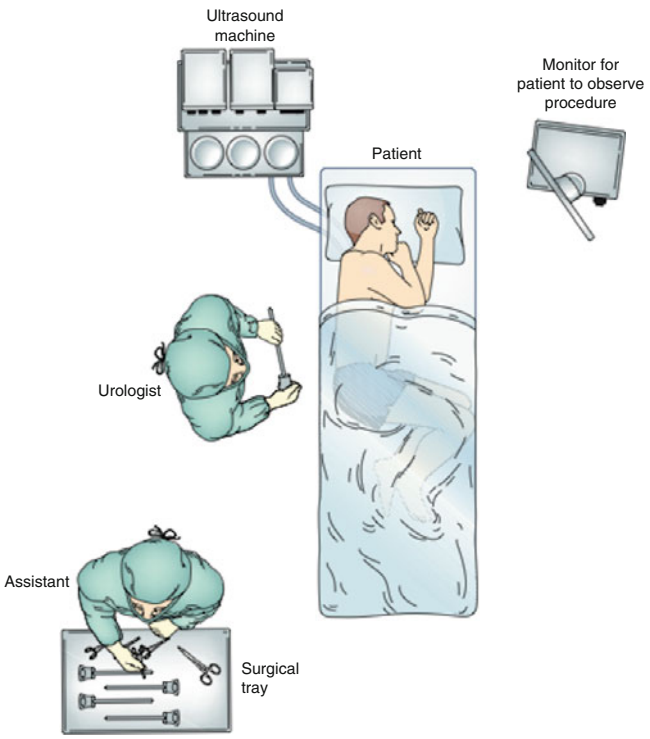

Fig. 6.15 Patient position and room setup for transrectal ultrasound-guided biopsy of the prostate

Additionally, the examiner will recall the position and size of palpable abnormalities. Attention should be given to extent of disease, prostatic symmetry, and involvement of the seminal vesicles or adjacent pelvic structures. The presence of internal or external hemorrhoids is noted. The evaluating finger should be directed posteriorly to assess for rectal lesions.

Analgesia

With smaller profile probes and the use of local anesthesia, it is possible to obtain a large number of biopsies with very little discomfort to the patient. The precise location and route by which the anesthetic agent should be given remains a point of some contention. The precise route by which the sensation of pain is transmitted during prostate biopsy is insufficiently understood. Pain may be induced by rectal distention during probe placement, pain fibers in the prostate capsule or prostatic parenchyma, and efferent pain fibers associated with the bladder neck or urethra. Satisfactory analgesia may be achieved with intrarectal lidocaine gel or a combination of lidocaine gel and DMSO as described by Kravchick et al. [23]. Periprostatic infiltration with lidocaine at the prostatoseminal vesicle junction is commonly employed to provide regional anesthesia during prostate biopsy (Fig. 6.16).

A long, 22-gauge needle may be used to infiltrate 15 cc of 1 % or 2 % Xylocaine into the vicinity of each of the two neurovascular bundles in this technique. A number of investigators have suggested modifications and alternatives including a single injection of 10 ml of 1 % lidocaine in the midline between Denonvilliers' fascia and the periprostatic fascia from base to apex [24], combined periprostatic and periapical infiltrations [25], and combined periprostatic and intraprostatic infiltrations [26]. Cevik, Dillioglugil, Zisman, and Akdas [25] found that the elapsed time from infiltration to biopsy strongly correlated with decreased pain sensation as reported by the patient and recommended 15 min between infiltration of analgesia and biopsy.

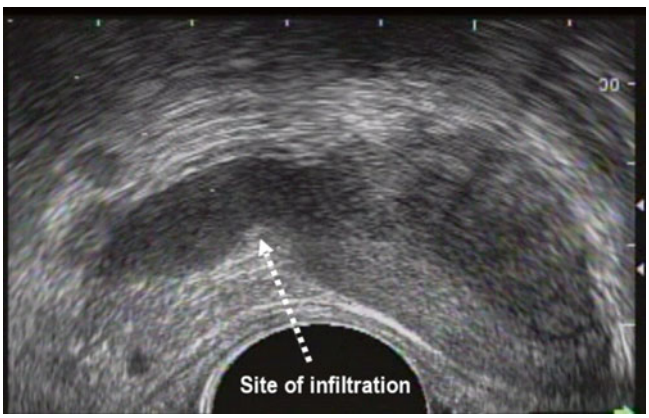

Fig. 6.16 Periprostatic infiltration with lidocaine at the junction of the seminal vesicle with the prostate in longitudinal view

Biopsy Technique

The goal of any biopsy should be to obtain adequate tissue from the locations of highest cancer probability while minimizing patient morbidity. The optimal technique for transrectal ultrasound and biopsy of the prostate remains controversial. For primary biopsy of the prostate, most clinicians would choose a transrectal route employing a template biopsy plus directed biopsies as indicated by findings from the ultrasound, magnetic resonance imaging (MRI), digital rectal exam, or prior biopsies. No one systematic template biopsy has proven substantially superior to the others. Cores taken from the lateral peripheral zones and apex have the highest statistical likelihood of containing cancer [27]. Therefore, biopsy strategies which maximize tissue taken from these areas are desirable. A typical biopsy scheme would be based on a sextant strategy with additional lateral cores (Fig. 6.17).

These cores are distributed to take maximum advantage of our understanding of the usual distribution of prostate cancer and its most common sonographic appearance. It has been shown convincingly that systematic biopsies will demonstrate cancers that are visually inapparent. It has also been shown that directing biopsies to hypoechoic or hypervascular areas of the prostate may yield a cancer diagnosis that would have been missed by systematic template biopsies alone [28] (Fig. 6.18).

Obtaining an increased number of cores based on prostate volume may improve the positive biopsy rate and decrease the rate of false-negative biopsies in large glands [29]. Occasionally there will be a palpable abnormality of the prostate that is not visible as an echogenic abnormality or as a disturbance in normal architecture. In an early study by Renfer, Schow, Thompson, and Optenberg [30] comparing sonographic to digitally directed biopsies, 12 % of cancers were detected only by digital guidance. In cases when a palpable abnormality is not demonstrable by ultrasound, it may be appropriate to perform digitally directed biopsy of the prostate, guiding the biopsy needle along the examiner's finger. A protective sheath or "trumpet" may be useful in performing such a digitally guided biopsy.

There does appear to be value in mapping the location of core biopsies in the sense that the extent and location of disease may influence treatment decisions, particularly when prostatic intraepithelial neoplasia or atypia is diagnosed on initial biopsy. Such mapping may provide information about the zones most likely to yield a positive biopsy on extended or repeat biopsy.

It is important when obtaining tissue from the prostate to use the automated biopsy needle to its best advantage. The tip of the needle should be advanced to the prostatic capsule. The distal excursion of the needle and the subsequent coverage of that needle by the hollow sheath will obtain a tissue

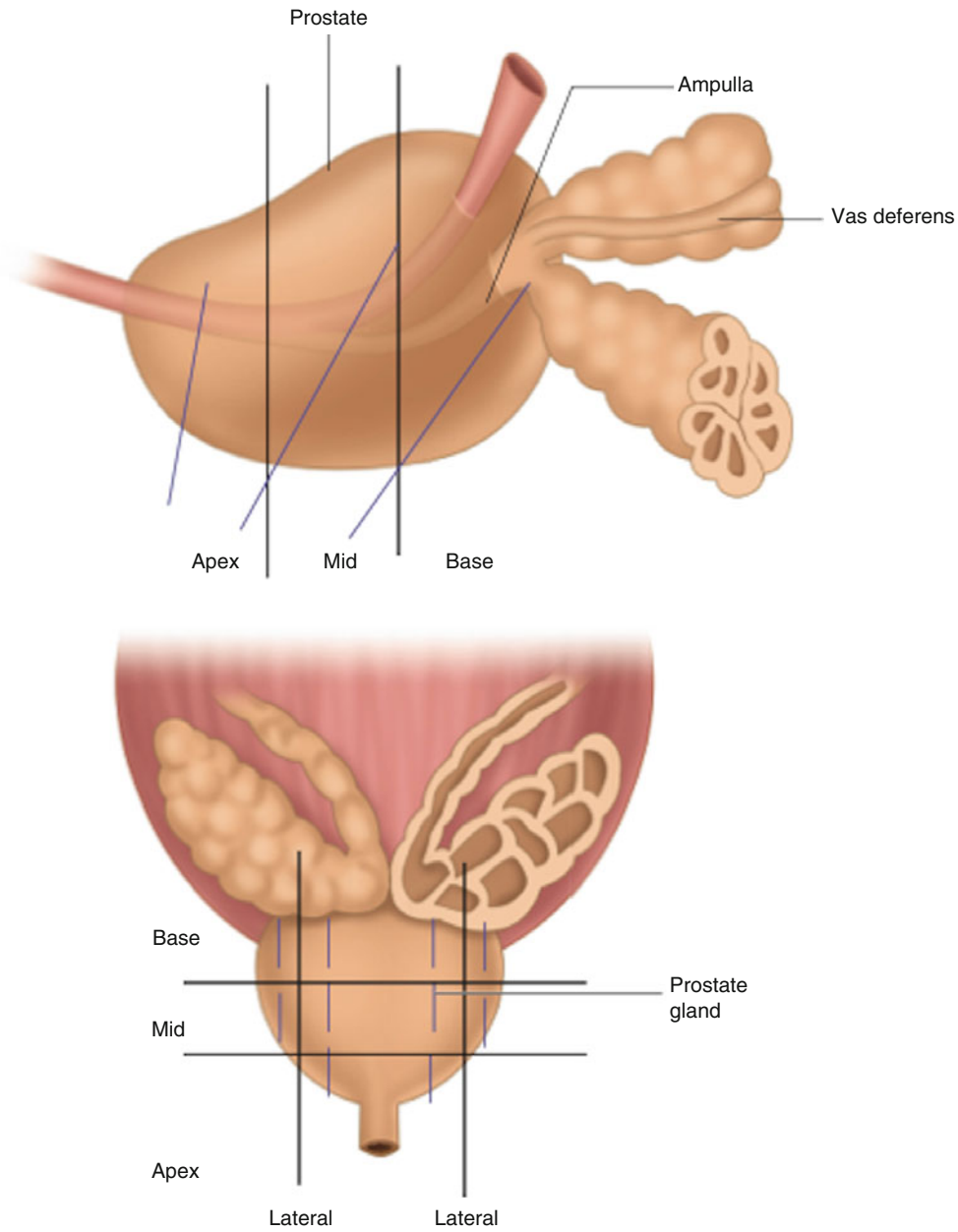

Fig. 6.17 Prostate template biopsy

specimen of approximately 17 mm. If the needle tip is corrected positioned at the beginning of the biopsy, the core will include the prostatic capsule (Figs. 6.19, 6.20, and 6.21).

Extended Biopsies

Extended biopsies are often performed when a patient has undergone one or more traditional template biopsies with negative results but with persistently worrisome clinical features such as a progressive increase in the PSA or a progressive abnormality on rectal exam. Extended biopsies are also considered when a patient has high-grade prostatic intraepithelial neoplasia or atypia.

The positive biopsy rate for patients who undergo immediate repeat biopsy for HGPIN is variously reported as 10–27 % [11, 12], suggesting that these patients are at no higher risk to harbor cancer than patients with accepted initial indications for biopsy. Nevertheless, it suggests false-negative biopsy results from most standard techniques may be as high as 30 %. This risk of a false-negative biopsy result should be discussed with the patient as part of the informed consent process. Extended biopsy strategies often employ 20–40 cores. Extended biopsies are typically done under sedation or general anesthesia. With the patient positioned in the left lateral decubitus position or lithotomy position, biopsies are performed in a systematic fashion, but additional cores from areas of previous abnormality are obtained. In

Fig. 6.18 Increased regional blood flow associated with prostate cancer. *Arrow* indicates region of increase blood flow on Doppler examination

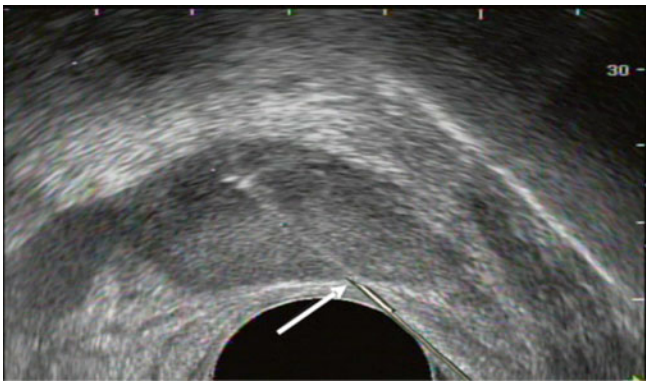

Fig. 6.19 Initial biopsy needle position with tip of the needle (*arrow*) at the capsule drawn superimposed over ultrasound image of the needle tract within the prostate during biopsy

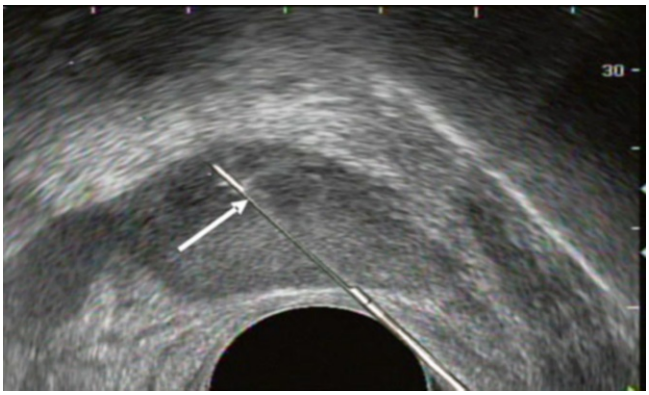

Fig. 6.20 Position of inner needle drawn superimposed over ultrasound image of the needle tract within the prostate during biopsy

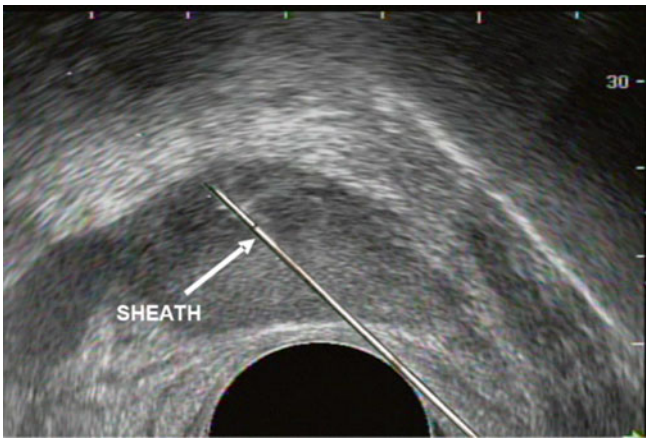

Fig. 6.21 Needle covered by sheath drawn superimposed over ultrasound image of the needle tract within the prostate during biopsy

addition, dedicated cores from each transition zone are usually obtained. Cores from anatomically different areas such as the anterior horns and apex are obtained.

Some investigators believe that the anterior lateral horns and the anterior prostate are less well sampled via the transrectal route than via a perineal approach. For a transperineal template approach, the patient is placed in the dorsal lithotomy position, and the transrectal ultrasound probe is arranged as it would be for brachytherapy. Using the template device as a guide, cores are taken from coronal sections of the prostate as described by Igel et al. [31].

Sonoelastography-Guided Biopsies

There are now commercially available ultrasound platforms that include the ability to perform real-time or shear wave elastography in addition to gray-scale imaging. Studies of the utility of sonoelastography-guided transrectal biopsy have shown that although the modality does not have sufficient sensitivity to supplant systematic template biopsies with biopsies targeted with sonoelastography [32], the addition of sonoelastographic guidance to a systematic template biopsy improves prostate cancer detection rates over gray-scale ultrasound [32–34].

Complications

Transrectal ultrasound-guided biopsy of the prostate is a generally safe and well-tolerated procedure. Despite the wide use of local anesthesia, a high percentage of men experience significant pain during the procedure [35]. Minor bleeding in the form of hematuria (39–58 %), hematospermia (28–45 %), and hematochezia (21–37 %) are so common they should be considered consequences of the procedure, rather than complications. Blood in the urine or stool typically occurs within 72 h, while blood in the ejaculate may persist for several weeks.

Serious complications after TRUS-Bx include febrile UTI/sepsis (<1 %) [19], rectal bleeding requiring transfusion or endoscopic procedure for control (0.7–4 %) [19, 36], vasovagal response, urinary retention, and epididymitis (<1 %) [37] (Table 6.3).

Patients are usually observed for a short period of time following biopsy to ensure there is no active rectal bleeding. Many patients experience transient nausea or rectal discomfort following biopsy without adverse sequelae, but nausea accompanied by tachycardia is often a sign of acute bleeding and rectal distention. In such cases it is helpful to have the patient visit the bathroom prior to leaving the office to be sure that they do not evacuate a large quantity of blood per rectum. When bleeding is suspected, compression of the rectal wall either by digital rectal examination or by reinsertion of the probe with direct application of pressure to the posterior aspect of the prostate may be tried. In more severe cases a large Foley catheter (24 F to 26 F) inserted into the rectum with the balloon inflated to 50 cc with sterile water will often provide enough compression to control local bleeding.

Infection, though often insidious, may pose a serious threat to the patient. Patients who experience infectious complications of TRUS-Bx will usually present within 24–48 h with chills and fever. These patients usually respond rapidly to oral antibiotic therapy. The emergence of quinolone-resistant bacterial species may require a change in antibiotic strategy. In some cases, microabscesses may form in the prostate, and the patient will experience a prolonged course of elevated temperature, difficulty voiding, and perineal pressure. In these cases it may be necessary to perform additional imaging studies and hospitalize the patient for IV antibiotics. Some patients may experience temporary difficulty voiding associated with irritation of the prostate or urethra or actual edema as a result of the biopsy. Up to 1 % of patients may develop acute urinary retention requiring temporary catheterization. Patients with marginal ability to void may be improved by the use of alpha-blockers. A vasovagal response occurs in 1–8 % of patients and is characterized by bradycardia and hypotension. These patients will often appear pale; yawning may be a premonitory sign of impending loss of consciousness. *Bradycardia is the most reliable differentiating sign between a vasovagal response and acute blood loss.* Most patients with a vasovagal response will recover within 15–20 min. Observation, serial vital signs, and fall precautions are appropriate. A brief period of observation with the patient sitting before he stands to dress may forestall some of the adverse sequelae of a vasovagal response and loss of consciousness.

Table 6.3 Complications of TRUS-Bx

Minor complications	*Incidence*
Hematuria	39–58 %
Hematospermia	28–45 %
Hematochezia	21–37 %
Major complications	
Febrile UTI/sepsis	0.3–1 %
Rectal bleeding requiring endoscopic procedure	0.7–4 %
Other: epididymitis, vasovagal response, acute urinary retention	<1 %

References

1. Kravchick S, Cytron S, Peled R, Altshuler A, Ben-Dor D. Using gray-scale and two different techniques of color Doppler sonography to detect prostate cancer. Urology. 2003;61(5):977–81.
2. Witjes WP, Aarinink RG, Ezz-el-Din K, et al. The correlation between prostate volume, transition zone volume, transition zone index and clinical and urodynamic investigations in patients with lower urinary tract symptoms. BJU Int. 1997;80(1):84.
3. Lim JW, Ko YT, Lee DH, et al. Treatment of prostatic abscess: value of transrectal ultrasonographically guided needle aspiration. J Ultrasound Med. 2000;19(9):609–17.
4. Etherington RJ, Clements R, Griffiths GJ, Peeling WB. Transrectal ultrasound in the investigation of haemospermia. Clin Radiol. 1990;41(3):175–7.
5. Worischeck JH, Parra RO. Chronic hematospermia: assessment by transrectal ultrasound. Urology. 1994;43(4):515–20.
6. Moore C, Karikehalli S, Nazeer T, et al. Prognosis of high grade prostatic intraepithelial neoplasia and atypical small acinar proliferation in the contemporary era. J Urol. 2005;173(1):70–2.
7. Borboroglu P, Sur R, Roberts J, Amling C. Repeat biopsy strategy with atypical small acinar proliferation or high grade prostatic intraepithelial neoplasia on initial prostate needle biopsy. J Urol. 2001;166(3):866–70.
8. Scattoni V, Roscigno M, Raber M, et al. Multiple vesico-urethral biopsies following radical prostatectomy: the predictive role of TRUS, DRE, PSA and the pathological stage. Eur Urol. 2003;44(4):407–14.
9. Deliveliotis C, Manousakas T, Chrisofos M, et al. Diagnostic efficacy of untrasound guided biopsy of the prostatic fossa in patients with rising PSA following radical prostatectomy. World J Urol. 2007;25(3):309–13.
10. Frauscher F, Klauser A, Volgger H, et al. Comparison of contrast enhanced color doppler targeted biopsy with conventional systematic biopsy: impact on prostate cancer detection. J Urol. 2002;167(4):1648–52.
11. Djavan B, Zlotta A, Remzi M, et al. Optimal predictors of prostate cancer on repeat prostate biopsy: a prospective study of 1,051 men. J Urol. 2000;163(4):1144–9.
12. Fowler J, Bigler S, Miles D, Yalkut D. Predictors of first repeat biopsy cancer detection with suspected local stage prostate cancer. J Urol. 2000;163(3):813–8.
13. Ghani K, Rockall A, Nargund V, Chinegwundoh F. Prostate biopsy: to stop anticoagulation or not? BJU Int. 2006;97(2):224–5.
14. Rodriguez LV, Terris MK. Risks and complications of transrectal ultrasound guided prostate needle biopsy: a prospective study and review of the literature. J Urol. 1998;160(6 pt 1):2115–20.
15. Maan Z, Cutting CW, Patel U, et al. Morbidity of transrectal ultrasonography-guided prostate biopsies in patients after the continued use of low-dose aspirin. BJU Int. 2003;91(9):798–800.
16. Jeon S, Woo S, Hyun J, Choi H, Chai S. Bisacodyl rectal preparation can decrease infectious complications of transrectal ultrasound-guided prostate biopsy. Urology. 2003;62(3):461–6.

17. Lindert K, Kabalin J, Terris M. Bacteremia and bacteriuria after transrectal ultrasound-guided prostate biopsy. J Urol. 2000;164(1):76–80.
18. Sieber P, Rommel F, Theodoran C, Hong R, Terzo M. Contemporary prostate biopsy complication rates in community-based urology practice. Urology. 2007;70(3):498–500.
19. AUA. Best practice policy statement on urologic surgery antimicrobial prophylaxis. 2008 updated 1 Jan 2014. http://www.auanet.org/education/guidelines/antimicrobial-prophylaxis.cfm.
20. Taylor AK, Zembower TR, Nadler RB, et al. Targeted antimicrobial prophylaxis using rectal swab cultures in men undergoing transrectal ultrasound guided prostate biopsy is associated with reduced incidence of postoperative infectious complications and cost of care. J Urol. 2012;187(4):1275–9.
21. Dupless CA, Bavaro M, Simons MP, et al. Rectal cultures before transrectal ultrasound-guided prostate biopsy reduce post-prostatic biopsy infection rates. Urology. 2012;79(3):556–61.
22. Gonzalez C, Averch T, Boyd L, et al. AUA/SUNA white paper on the incidence, prevention and treatment of complications related to prostate needle biopsy. 2012. http://www.auanet.org/education/other-aua-clinical-guidance-documents.cfm.
23. Kravchick S, Peled R, Ben-Dor D, et al. Comparison of different local anesthesia techniques during TRUS-guided biopsies: a prospective pilot study. Urology. 2005;65(1):109–13.
24. Taverna G, Maffezzini M, Benetti A, et al. A single injection of lidocaine as local anesthesia for ultrasound guided needle biopsy of the prostate. J Urol. 2002;167(1):222–3.
25. Cevik I, Dillioglugil O, Zisman A, Akdas A. Combined "periprostatic and periapical" local anesthesia is not superior to "periprostatic" anesthesia alone in reducing pain during tru-cut prostate biopsy. Urology. 2006;68(6):1215–9.
26. Lee H, Lee H, Byun S, et al. Effect of intraprostatic local anesthesia during transrectal ultrasound guided prostate biopsy: comparison of 3 methods in a randomized, double-blind, placebo controlled trial. J Urol. 2007;178(2):469–72.
27. Kravchick S, Cytron S, Peled R, et al. Optimal combinations for detection of prostate cancer: systematic sextant and laterally directed biopsies versus systematic sextant and color Doppler-targeted biopsies. Urology. 2004;63(2):301–5.
28. Hodge K, McNeal J, Terris M, Stamey T. Random systematic versus directed ultrasound guided transrectal core biopsies of the prostate. J Urol. 1989;142(1):71–5.
29. Remzi M, Fong Y, Dobrovits M, et al. The Vienna nomogram: validation of a novel biopsy strategy defining the optimal number of cores based on patient age and total prostate volume. J Urol. 2005;174(4):1256–61.
30. Renfer L, Schow D, Thompson I, Optenberg S. Is ultrasound guidance necessary for transrectal prostate biopsy? J Urol. 1995;154(4):1390–1.
31. Igel T, Knight M, Young P, et al. Systemic transperineal ultrasound guided template biopsy of the prostate in patients at high risk. J Urol. 2001;165(5):1575–9.
32. Nelson E, Slotoroff C, Gomeela L, Halpern E. Targeted biopsy of the prostate: the impact of color Doppler imaging and elastography on prostate cancer detection and Gleason score. Urology. 2007;70(6):1136–40.
33. Brock M, von Brodman C, Palisaar R, et al. The impact of real-time elastography guiding a systematic prostate biopsy to improve detection rate: a prospective study of 353 patients. J Urol. 2012;187(6):2039–43.
34. Aigner F, Pallwein L, Junker D, et al. Value of real-time elastography targeted biopsy for prostate cancer detection in men with prostate specific antigen 1.25 ng/ml or greater and 4.00 ng/ml or less. J Urol. 2010;184(3):913–7.
35. Altman A, Resnick M. Ultrasonographically guided biopsy of the prostate gland. J Ultrasound Med. 2001;20(2):159–67.
36. Ghani K, Dundas D, Patel U. Bleeding after transrectal ultrasonography-guided prostate biopsy: a study of 7-day morbidity after a six-, eight- and 12-core biopsy protocol. BJU Int. 2004;94(7):1014–20.
37. Donzella J, Merrick G, Lindert D, et al. Epididymitis after transrectal ultrasound-guided needle biopsy of prostate gland. Urology. 2004;63(2):306–8.

Fusion-Guided Prostate Biopsy

7

Liwei Jiang and Bradford J. Wood

The conventional method of prostate biopsy involves a systematic sampling of selected areas of the prostate in a regular but random sextant or extended fashion. This is somewhat blind and typically not directly navigated toward any specific target, but rather at a specific geographic region of the gland. Targeted prostate biopsy, on the other hand, directs sampling toward suspicious lesions found on a previous imaging study as magnetic resonance imaging (MRI). As such, targeted biopsy requires a combination of imaging modalities that pinpoint suspicious lesions (MRI) and that guide the biopsy needles (ultrasound).

No single imaging modality simultaneously offers precise lesion localization and quick office-based, cost-effective, real-time guidance [1]. Transrectal ultrasound (TRUS) possesses the ability to image in real time (high temporal resolution) but suffers from poor resolution (low spatial resolution) and low sensitivity to cancer. MRI, on the other hand, images prostate lesions in great detail (high spatial resolution), but typically not with real-time guidance (low temporal resolution).

In MRI-TRUS fusion, a multiparametric MRI study is performed before the biopsy procedure to localize suspicious targets. This generally consists of T2-weighted (T2W), diffusion-weighted imaging (DWI), and dynamic contrast-enhanced (DCE) sequences, with or without an endorectal coil. Such MRI is highly sensitive for the detection of aggressive, clinically significant prostate cancers, with a high positive predictive value. Histopathological correlation has demonstrated the positive predictive values of multiparametric MRI in detecting prostate cancer to be 98–100 % depending on the zone of the prostate [2]. In addition, multiparametric MRI is less sensitive in general for the detection of low-risk lesions [3]. This may have important implications for public health, given the debate about overdetection and overtreatment of low-grade prostate cancer in general. Although speculative, widespread reliance on MRI and fusion approaches in the future might theoretically result in less unnecessary treatment of low-grade cancers and more treatment of the cancers that carry more risk.

In gantry MRI-guided prostate biopsies are sometimes performed, but these procedures are often impractical because they require expensive MRI and personnel time as well as specialized MRI-compatible equipment. Techniques that fuse MRI and transrectal ultrasound (TRUS) allow the advantages of both the real-time imaging of TRUS and the high detection sensitivity of MRI while performing the procedure *outside* of the MRI in the office setting. This involves *bringing the MRI images to the patient, instead of the patient to the MRI imaging hardware*.

Ultrasound-MRI fusion may function for two parallel purposes: (1) guidance of needle to target defined by MRI and (2) to track, map, and record the locations of targeted and standard TRUS fusion biopsies for later referencing. This has special significance for patients with low Gleason scores who may elect active surveillance with or without focal therapies as treatment options.

With MRI data available to the operator during the biopsy, some operators perform the so-called "cognitive fusion" or visual registration, in which the location of lesions on TRUS is estimated mentally using the pre-procedural MRI as a reference. Although performing cognitive fusion represents a significant addition to the "blind" prostate systematic biopsy procedure that is traditionally guided with TRUS alone, the accuracy of cognitive fusion is highly operator-dependent and can be especially prone to error at the extreme apex and base, as well as anteriorly, which are defined differently on axial MRI (transverse to the anatomic pelvis) versus TRUS (2D imaging plane fans out)

L. Jiang, MD
Medical Research Scholars Program, National Institutes of Health, Bethesda, MD, USA

B.J. Wood, MD (✉)
NIH Center for Interventional Oncology, National Institutes of Health, Bethesda, MD, USA

Interventional Radiology Section, National Institutes of Health, Bethesda, MD, USA
e-mail: BWood@cc.nih.gov

A.R. Rastinehad, D.N. Siegel (eds.), *Interventional Urology*, DOI 10.1007/978-3-319-23464-9_7

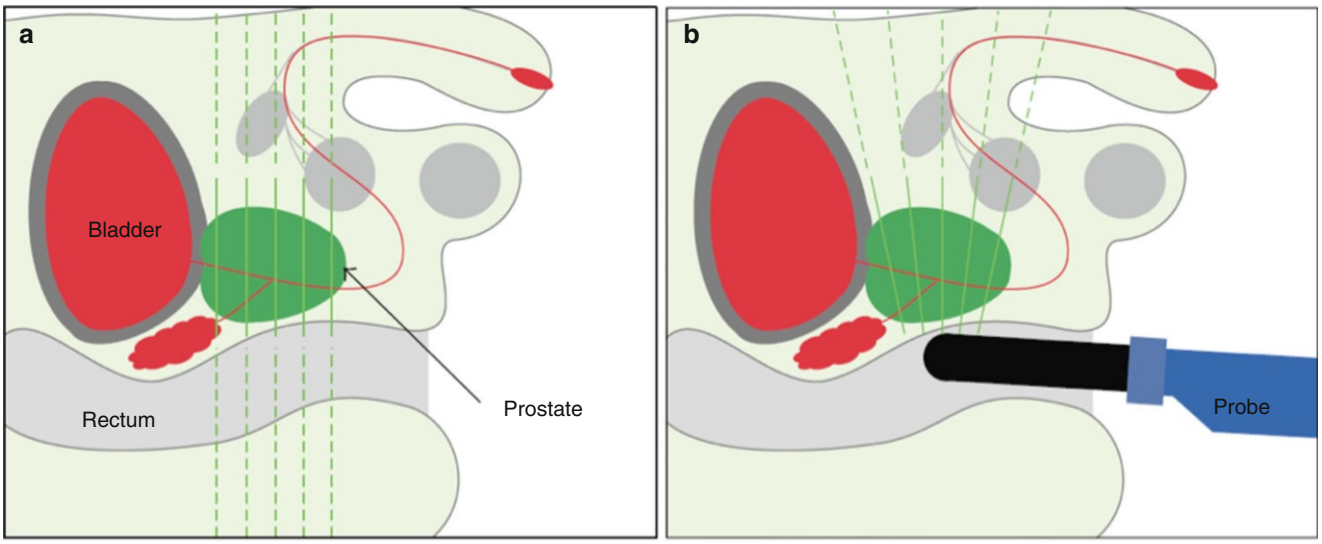

Fig. 7.1 MRI images (**a**) are often reported as axial to the anatomic pelvis, whereas TRUS images (**b**) are obtained with an end-fire or side-fire transducer, which are from very different planes, often fan shaped (From Kwak et al. [3], with permission)

(Fig. 7.1) which can make a TRUS-defined gland base very different from the perceived MRI-defined gland base [4]. To maximize the accuracy and consistency of the MRI-TRUS workflow, advanced MRI-TRUS fusion-guided prostate biopsy platforms (henceforth referred to as "fusion platforms") have been developed to semiautomatically align the real-time image obtained by TRUS to the pre-procedural MRI image. Using a combination of hardware and software approaches, these fusion platforms serve to guide the biopsy needle to the targets identified on MRI, as well as to track, map, and record the 3D locations of all biopsy samples taken for later referencing.

Multiple fusion platforms are now available commercially. To the authors' knowledge, no randomized clinical trials offering head-to-head comparisons across these platforms exist at the time of this writing. Further, MRI parameters and the definition of suspicious lesions vary by center, and patient selection biases preclude comparison of approaches across studies. While the workflow begins similarly with image analysis, prostate segmentation, and biopsy planning, the available platforms differ in (1) the image registration algorithm, (2) the method to track the biopsy needle position, (3) the interface to present the ultrasound and MRI images to the operator, (4) additional software capabilities such as mapping and navigation, and (5) the route of biopsy. In this chapter, these aspects are each discussed in general terms before specific fusion platforms are briefly reviewed. This discussion of such a dynamic arena is not intended to be comprehensive, but rather is an introduction to the technologies and techniques of fusion, to give the reader a general sense of the mechanisms and terminologies of the systems, processes, and workflows.

Image Analysis and Planning

After the patient undergoes a multiparametric MRI study, the images are analyzed for suspicious prostatic lesions. *Segmentation* of the prostate edge is performed, in which the margin of the prostate is defined semiautomatically and verified (and refined where necessary). Biopsy targets are defined as center points or volumes, and approach trajectories may be planned. After these steps, the prostate margin (segmentation volume) and target information are superimposed on anatomic T2W MRI images and transferred to the biopsy workstation for use during the procedure (Fig. 7.2). Although speculative, computer-aided detection platforms may facilitate the automation of this detection strategy, which may eventually prove a helpful assistance tool, given the expertise and subjective interpretation skill sets required for multiparametric image interpretation [5]. Workflow interfaces to PACS and the electronic health record may facilitate future data review in cases of active surveillance (Fig. 7.3).

Image Registration

In fusion biopsies, *registration* is the process of matching MRI to TRUS, thus aligning pre-procedural MRI images (along with segmentation and target information) to a TRUS 3D volume. TRUS volumes may be acquired in 3D or in 2D planes with the volume built by moving the TRUS probe across the prostate from base to apex (a "sweep"). Two software registration algorithms, rigid and elastic, differ in the degree of image distortion allowed for anatomic alignment (Fig. 7.4). *Rigid (non-deformable) registration* attempts to

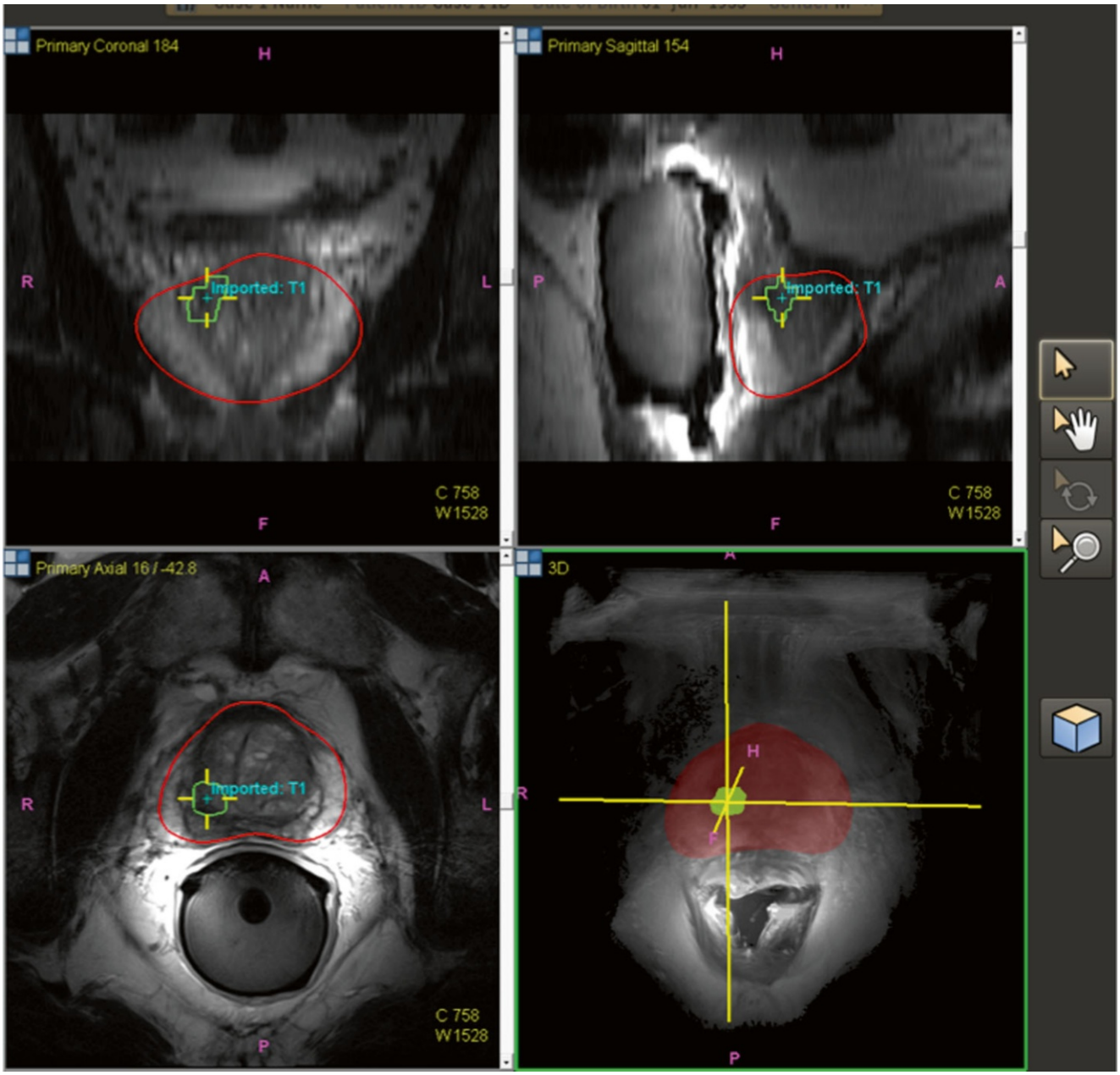

Fig. 7.2 Pre-procedural prostate segmentation on MRI (*red line*) and MRI target definition (*green line*) loaded into fusion workstation for registration to TRUS images

minimize image distortion by accommodating translation and rotation of images, but not local deformations (Fig. 7.5). While rigid registration maintains the true anatomic shapes and locations, the operator may need to manually adjust the alignment of TRUS and MRI images to account for local registration errors, which may occur from differences in prostate shape between TRUS and MRI images as well as prostate movements induced by pressure from the MRI endocoil or the TRUS probe during imaging [6]. *Elastic (deformable) registration*, on the other hand, attempts to maximize image alignment by accommodating local deformations in addition to translation and rotation. However, elastic registration may result in distortion of true anatomy to create a "good picture." On most systems, registration is performed semiautomatically, allowing the operator to fine-tune the alignment of edges and other important landmarks. Both rigid and elastic registration algorithms are available on most fusion systems, permitting the user to judge the most optimal alignment. The operator may toggle between rigid and elastic to determine the most optimal fit. The registration process is often repeated at several steps throughout a procedure, in order to maximize the matching or account for patient or

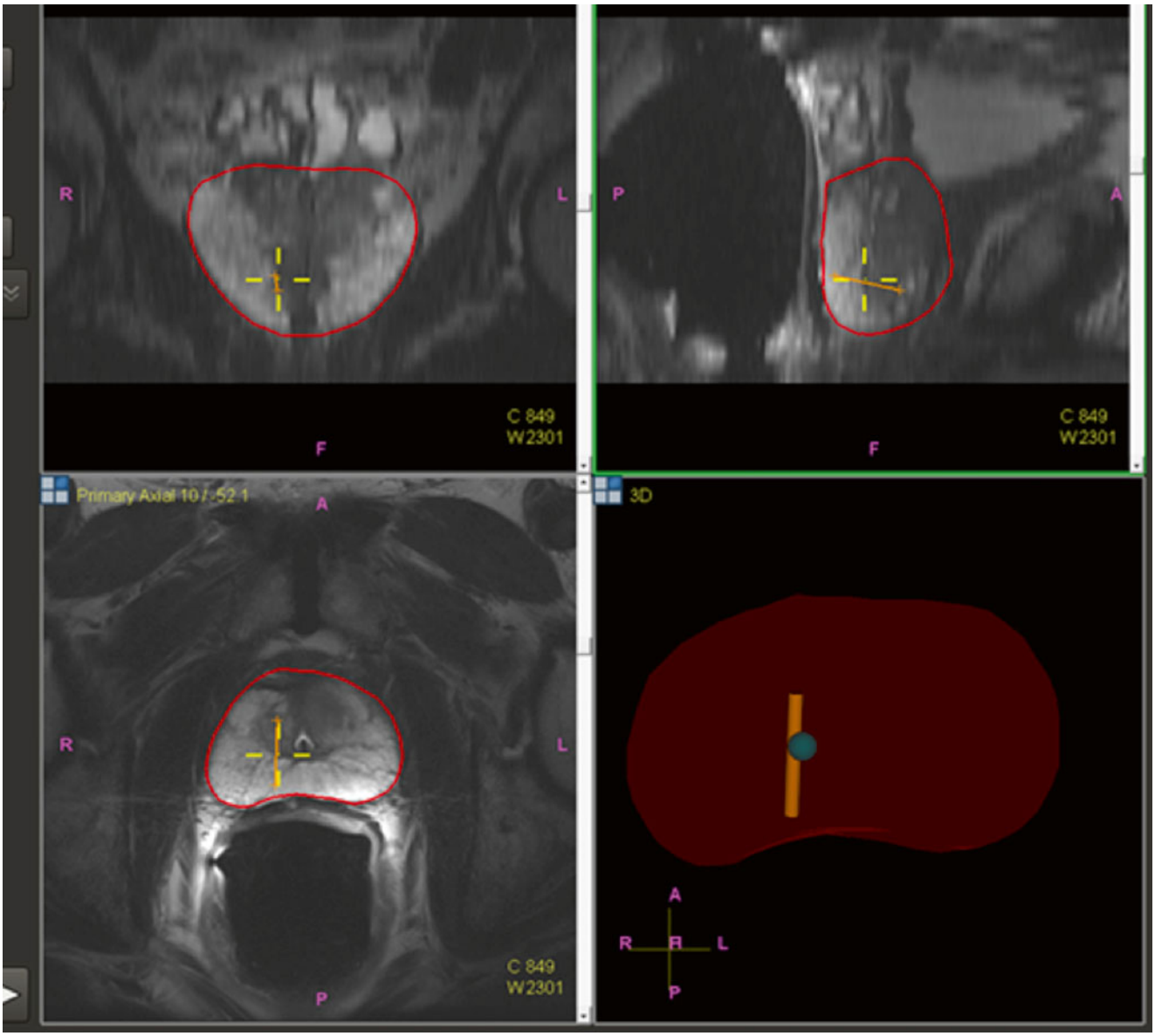

Fig. 7.3 Core biopsy location is tracked and mapped (*orange line*) for the medical record, for later focal ablation or brachytherapy, or for repeat biopsy at a later date as part of an active surveillance program

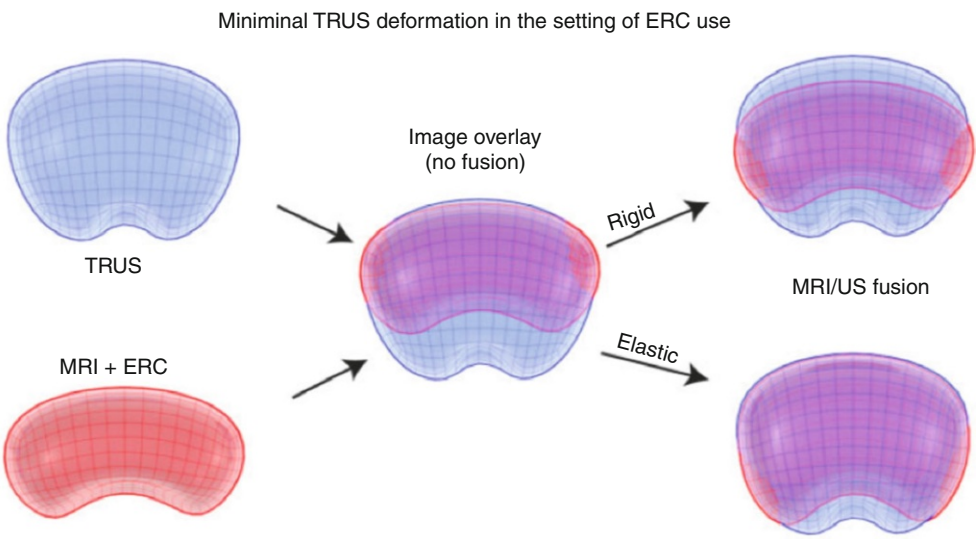

Fig. 7.4 Rigid and elastic registration. Although elastic registration matches the MRI and TRUS images, to make a better combined picture, the operator must be careful so as not to distort the true anatomy too much or move a target to an unrealistic location. Although not obvious, rigid registration with local matching of nearby anatomy and edges may be more accurate than elastic warping (From Logan et al. [6], with permission)

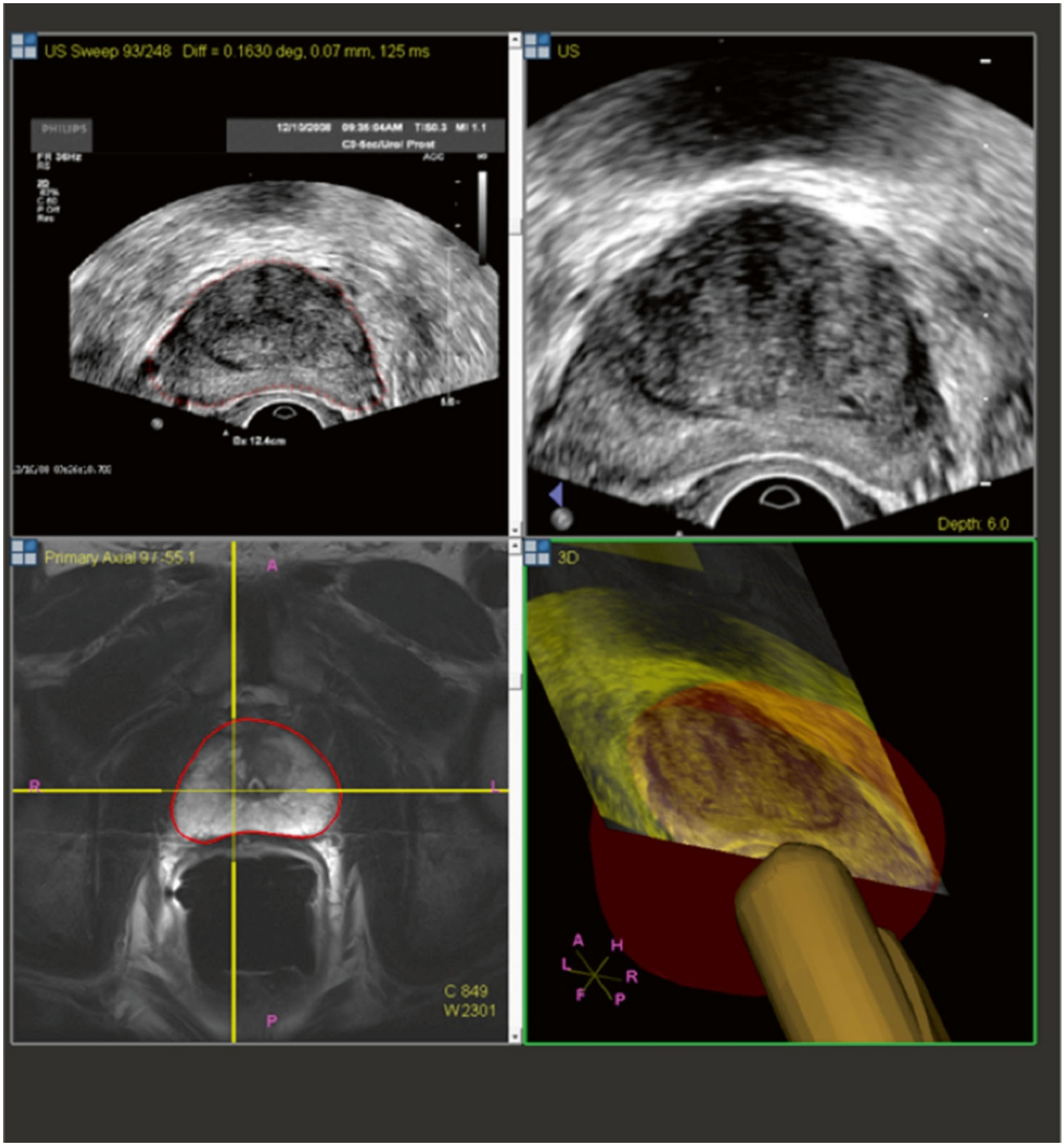

Fig. 7.5 In this case, rigid registration on TRUS and MRI involves similar shapes and may not require elastic registration

organ motion or deformation. It is important to ensure that high-quality matching remains valid throughout the navigation, as well as mapping biopsy processes.

Once MRI and TRUS data are fused, the way in which the resulting images are displayed to the user varies by fusion platform or operator preference. Some platforms overlay the MRI and TRUS images, reformatting the MRI volume to fit to the perspective of the TRUS probe. The standard axial, coronal, and sagittal planes may also be displayed. Other platforms display MRI and TRUS images side by side, either reformatted in the same orientation (Figs. 7.6 and 7.7) or using the tracking information supplied by the biopsy probe to select and display a single MRI slice in axial, coronal, and/or sagittal orientations. Both of these visualization options

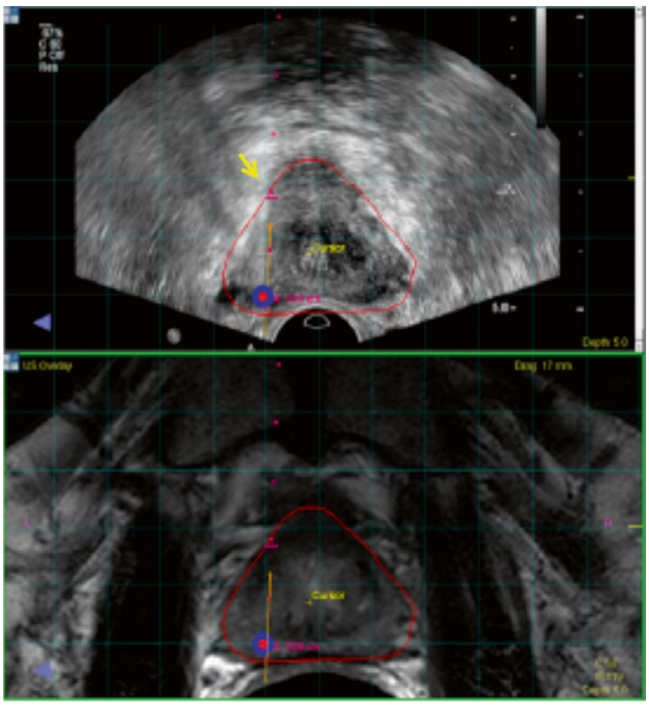

Fig. 7.6 Image co-display on the fusion workstation. *Top* ultrasound; *bottom* MRI. Target is displayed on each. *Small red dots* needle pathway. *Red and blue dots* target defined on MRI. Needle depth is determined visually by the echogenic white line (*arrow*) on real-time ultrasound

may be available on some fusion platforms. It is important to define an operator-specific workflow that is both workable and reproducible to maximize accuracy and standardization while maintaining the integrity of the fusion process. This may mean that much of the displayed information is excessive or extra and need not be reviewed from every possible viewpoint during the biopsy.

Tracking Approaches

In addition to the registration of MRI and TRUS images, fusion platforms may track and record the position of the biopsy probe in 3D space. This information may be used to present the relevant slices of the imaging data or be used for mapping and navigation (see below). There are three basic methods to attain MRI-TRUS fusion, which vary in their technologies, strengths, weaknesses, and initial intent of design. These are (1) electromagnetic tracking ("medical GPS"), (2) position-encoded joints in smart robotic arms, and (3) image-based tracking.

Some platforms (such as UroNav, Invivo; Virtual Navigator, Esaote; and Real-time Virtual Sonography, Hitachi) employ passive electromagnetic tracking, often dubbed "medical GPS," in which the position of a small sensor ("car") attached to the biopsy probe is detected by a magnetic field generator ("satellite") fixed to the operating table on an arm and external to the patient. Such tracking takes advantage of the Faraday principle or the fact that a coil (sensor) in the presence of different and changing magnetic fields (field generator) elicits an electrical current related to the different magnetic fields turned on sequentially by the field generator. The computer then converts this changing electrical current into a 3D position in space, in relation to the fused image which shares the X-Y-Z 3D Cartesian coordinates. Electromagnetic tracking preserves the conventional freehand biopsy approach, resulting in a relatively shallow learning curve [7, 8]. During the biopsy procedure, the operator typically performs an initial TRUS "sweep" of the prostate, after which the 3D ultrasound data are registered to the pre-procedural MRI data. Subsequently, the 3D position of the TRUS probe is used to guide the operator toward the planned approach trajectory (angle and position) for each suspicious lesion to be sampled (see "Mapping and Navigation" below) as well as to document the location of each biopsy core taken.

"Robotic" fusion platforms such as Artemis (Eigen), BiopSee (Pi Medical), and BioJet (BK Ultrasound) directly control the biopsy probe's angle and position. The biopsy probe is mounted on a mechanical stepper with position sensors or a more sophisticated articulating robotic arm that contains angle-sensing encoders. When the operator drives the robotic arm during the procedure, the angle and position are automatically calculated based upon the encoded joints. While the robotic aspect may add to the learning curve of this fusion platform, high accuracy in positional tracking may be achieved.

A third approach employs image-based software tracking methods, as exemplified by the Urostation (Koelis) platform that relies on retrospective TRUS-TRUS registration. Instead of utilizing real-time targeting, a 3D TRUS image acquired after each biopsy is registered with an initial 3D TRUS sweep to confirm the needle position [8]. In this manner, position tracking is achieved without the use of additional hardware such as electromagnetic generators or robotic arms. In addition, since the freehand biopsy approach is preserved, these image-based systems tend to most resemble the conventional TRUS technique, in terms of operator input. Initially designed for location mapping and recording, these systems may be modified and used for prospective navigation and guidance as well, with some potential limitations, such as performing a 3D TRUS volume after every needle, with the needle held in place during TRUS imaging.

Mapping and Navigation

To further help the biopsy operator, fusion systems offer varying degrees of mapping and navigation (or guidance) capabilities. *Mapping* refers to the process of tracking the imaging location

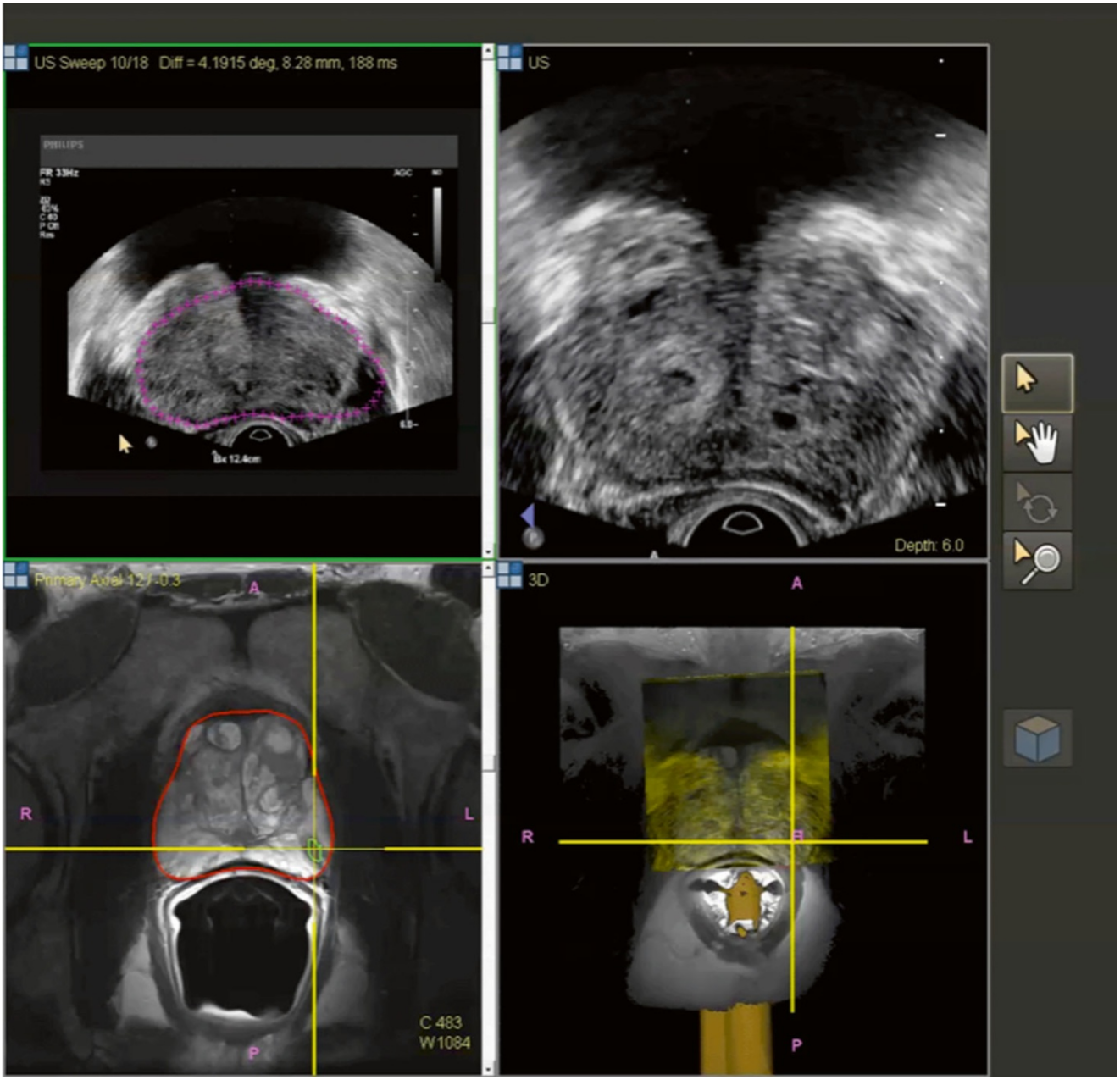

Fig. 7.7 Co-display of registered TRUS (*top*) and MRI (*bottom*) images after building a 3D volume on TRUS. Different shapes of prostate segmentation (*purple and red lines*) can be corrected by elastic registration and fusion

of a biopsy specimen and referencing it to pre-procedural MRI for later use. Mapping is done in order to better locate repeat biopsies in the setting of active surveillance of low-grade cancers (Fig. 7.3). *Navigation* (or *guidance*) refers to the platform's ability to aid prospective placement of a biopsy needle toward a target that was pre-identified on MRI but now targeted with TRUS, with the needle being directed transrectally and/or transperineally, depending on the platform. Mapping may be more important for blind or sextant biopsies that are positive, since the exact location may not otherwise be known or tracked, other than to say it was from the "left base," for example.

Route of Biopsy

Prostate biopsies can be performed transrectally or transperineally, with the former being the more commonly used technique. Given that the biopsy needle passes through the rectal mucosa in the transrectal approach, infection and sepsis following transrectal biopsy have been a concern. Recently, increasing rates of sepsis arising from transrectal biopsy have been reported, perhaps in part related to increasing prevalence of colonization with resistant organisms [9, 10]. A retrospective study of almost 5900 Japanese patients who

underwent transrectal and/or transperineal biopsies found no statistically significant difference in the overall rate of genitourinary tract infections between the transrectal (0.83 %) and the transperineal route (0.57 %), although the rate of febrile (≥38 °C) infections occurred more frequently after transrectal (0.71 %) than transperineal (0.16 %) biopsies ($P=0.04$) [11]. A prospective study of 245 transperineal biopsies performed at several centers in Melbourne, Australia, resulted in zero hospital readmissions for infection after transperineal biopsy [12]. These rates may be heavily impacted by local factors such as frequency of resistance to common prophylactic antibiotics. Consulting with a local infectious disease expert may be prudent to help develop local prophylactic standard procedures.

Major Platforms

Before exploring the technology, workflow, and strengths of each commercially available fusion platform, it is important to note that many platforms have evolved over time. Some were initially developed with one purpose (mapping *or* navigation) but have subsequently added the other capability. Likewise, some systems were initially developed with only rigid or elastic registration, or only the transrectal or transperineal approach, and have added the counterpart options more recently. Therefore, much of the data and characteristics of these systems in published literature likely represents one moment in time and may have evolved since publication. Further, the authors are most familiar with the UroNav system, having helped to develop that system over the past >12 years.

Electromagnetic Tracking

The *UroNav* platform (Invivo Corp., Gainesville, Florida, USA), developed at the National Institutes of Health in collaboration with Philips, began clinical trials in 2004 and was FDA 510(k)-cleared in 2006. The UroNav system and workstation are designed to be independent of TRUS vendor, functioning (initially) with Philips, General Electric, and BK Ultrasound systems. In addition, UroNav interfaces with the more general MRI image processing and segmentation software (DynaCAD, Invivo), for a unified MRI imaging and fusion platform. Pre-procedural MRI images are obtained (often from a 3 T scanner) with T2W, DCE, and DWI sequences (more recently without magnetic resonance spectroscopic imaging), to identify suspicious lesions. During the procedure, the patient is positioned decubitus per conventional TRUS biopsy, and an electromagnetic tracking "brick-like" generator is placed near the patient. Using a TRUS probe with an attached electromagnetic tracking sensor, the operator performs an initial ultrasound "sweep" of the prostate to obtain 3D TRUS data, which is then semiautomatically registered to the MRI data, with the option of either rigid or elastic registration. Manual adjustments are made to the image registration as necessary to improve alignment, which may be repeated throughout the case as needed. Once this initial phase is complete, the operator proceeds with the freehand TRUS approach. UroNav displays the fused TRUS and MRI images side by side (or as triplanar overlays) with a blending slider in the user interface to adjust relative transparencies. Navigation software guides the TRUS operator to the planned biopsy trajectory for each core, and mapping functionality documents the imaging location of each core taken. When using fusion to guide biopsy, the target is aligned with the TRUS needle guide by moving freehand the TRUS probe left/right, up/down, and in/out, one motion at a time, while watching the location of the target in relation to the needle guide pathway. Needle insertion depth is also monitored visually on the fused image, with the needle tip placed just short of the target prior to spring biopsy deployment across the target. Although automated, operator TRUS skill sets are helpful for optimal navigation. As described in the overview of electromagnetic tracking, because UroNav builds upon the conventional freehand transrectal biopsy approach, the learning curve is relatively low [7, 8]. In terms of the platform's accuracy, tracking error has been reported to be 5.8 ± 2.6 mm initially [13] and subsequently under 3 mm after technical improvements [14]. Initially developed for prospective navigation to MRI-defined targets, the mapping tool and elastic fusion were more recently added. The most recent version of the UroNav software permits the transperineal biopsy approach in addition to transrectal, demonstrating the evolution of fusion platforms over time. Fusion with UroNav both upgrades and detects higher Gleason score cancers than blind extended sextant biopsy [15], thus more appropriately triaging patients who need definitive treatment.

The *Virtual Navigator* (Esaote SpA, Genoa, Italy) and *Real-time Virtual Sonography* (Hitachi, Tokyo, Japan) platforms are both general-purpose fusion systems, initially designed to fuse real-time ultrasound to prior imaging studies such as CT, PET-CT, or MRI and subsequently adapted for prostate biopsy. Both platforms employ the freehand TRUS approach with electromagnetic tracking systems [7, 16]; as such, they inherit the characteristics of electromagnetic tracking-based systems as already described. Pre-procedural MRI is often obtained at 1.5 T using the T2W, DCE, and DWI sequences when using either platform. With Virtual Navigator, MRI data is registered to TRUS volume using only rigid registration, which has implications for local registration errors [6]. Real-time Virtual Sonography is able to biopsy both transrectally and transperineally; notably, during a prospective trial published in 2010, each patient

underwent transperineal targeted biopsy, transperineal systematic biopsy, and transrectal systematic biopsy, with a combined total of 12 cores taken per patient [17].

Mechanical Position Encoders

The *Artemis* platform (Eigen, Grass Valley, California, USA), US FDA 510(k)-cleared in 2007, has been used in clinical trials since 2009. The hardware cart features a standard, vendor-agnostic end-fire TRUS probe held by a robotic arm that contains angle-sensing encoders on its joints, which conveys spatial tracking information [18]. The hardware interfaces with an independent software workstation running the Eigen ProFuse software, which builds a 3D model of the prostate from pre-procedural MRI (often obtained at 3 T using the T2W, DCE, and DWI sequences) and allows delineation of suspicious lesions prior to biopsy. During the procedure, the patient is positioned at the edge of the bed in alignment with the robotic arm. By rotating the robotic arm, an initial ultrasound sweep is obtained, from which the software semiautomatically determines the boundaries of the prostate, with manual adjustments performed as necessary. Pre-procedural MRI annotated with the biopsy plan is loaded and fused with the TRUS image using rigid registration followed by elastic registration at the time of biopsy [7, 19]. Navigation software guides the operator to the planned targets. The system records the location of biopsy cores taken, and the operator can return to the site of a previous core with 2–3 mm accuracy [18]. Although the Artemis device is somewhat bulky and cumbersome [8], and requires user training [7], the use of the platform in the hands of an experienced operator has been reported to add only 5 min on average to the overall biopsy procedural time [16]. With high precision inherent in the direct, robotic tracking approach, this platform may yield highly accurate biopsies, assuming patient and prostate motion can be minimized.

The *BiopSee* platform (Pi Medical, Athens, Greece), with main clinical developments at the University Hospital Heidelberg, Heidelberg, Germany, is notable for eschewing the transrectal biopsy route altogether in favor of the transperineal route, although ultrasound imaging guidance is still done transrectally. The system consists of a TRUS probe attached to a mechanical stepper fixed to an operating table. The depth and rotation of the TRUS probe are tracked by embedded encoders. Pre-procedural multiparametric MRI is often performed at 3 T with T2W, DCE, and DWI sequences. During the biopsy, a 3D ultrasound volume is obtained by sweeping the TRUS probe from cranial to caudal, and MRI data is fused to the ultrasound volume via rigid registration or manually by simultaneously visualizing the axial, coronal, and sagittal planes [20, 21]. The limited range of motion of the TRUS probe may be a limitation of the system, increasing its learning curve [7]. The reported duration of the biopsy procedure was 60 min per patient for the first ten patients and 30 min per patient afterward [21].

Similar to Artemis, the *BioJet* platform (BK Ultrasound, Peabody, Massachusetts, USA; DK Technologies, Barum, Germany) employs a TRUS probe mounted on a mechanical arm with angle-sensing encoders. The system is capable of performing both transrectal and transperineal biopsies. Pre-procedural MRI is performed at 1.5 T [22] and later 3 T [23] with T2W, DCE, and DWI sequences. During the biopsy, MRI data is fused to the ultrasound volume via rigid registration. In the initial experience using the BioJet platform, patients were placed in the lithotomy position, and biopsy was carried out transperineally. The authors noted that the rigid registration algorithm required manual contour adjustments for proper fusion [22], implying the addition of elastic registration as a future direction.

Image-Based Tracking

The *Urostation* platform (Koelis, Grenoble, France) uses image-based registration to track needle position. It employs the freehand TRUS technique and relies on TRUS-TRUS image registration to retrospectively determine biopsy needle position. At the start of the biopsy procedure, a reference panorama 3D TRUS volume is obtained and registered to pre-procedural MRI data and target information. After each biopsy core is taken, a 3D TRUS image is acquired over 3 s with the needle in place, in order to image needle location. This is registered to the reference TRUS panorama to confirm needle location [24]. The operator is required to hold the probe in place during the 3 s TRUS acquisition; otherwise registration errors may occur. This is perhaps a limitation of the system [7, 8]. The Urostation system was designed to record the 3D location of biopsy samples for patients under active surveillance.

The *MIM Symphony* platform (MIM Software Inc., Cleveland, Ohio, USA) uses image-based registration and was originally designed for multimodality treatment planning for low-dose rate brachytherapy.

Discussion and Conclusions

Nowhere else in the human body are blind biopsies acceptable as a standard approach to diagnosing cancer. Standard blind TRUS prostate biopsies may be blind medicine for certain patients. Now, a number of fusion platforms exist, with differing strengths, weaknesses, workflows, and requirements for additional hardware or software. It remains difficult to compare across fusion platforms, since major published studies have been single-center trials that focused

on the platform in use at their respective institutions or addressed specific questions within prescreened and biased patient populations. Regardless, strong peer-reviewed evidence has demonstrated the promise of fusion-guided biopsies, irrespective of the fusion platform. It may not be speculative to say that the days of blind TRUS-guided prostate biopsies alone may equal suboptimal care for certain patients. Results from targeted biopsies suggest higher detection rates of clinically significant prostate cancer, lower detection rates of clinically insignificant lesions, and the ability to detect prostate cancer with fewer cores taken. However, it remains as work in progress how exactly to translate this information into standard clinical practice for specific patient populations.

In a prospective study involving more than 1000 men, compared to systematic biopsy, targeted biopsy using UroNav combined with systematic biopsy is associated with 30 % greater detection of high-risk cancer (Gleason 4+3 or greater) and 17 % fewer detection of low-risk cancer (Gleason 3+3 or low-volume Gleason 3+4) compared to systematic biopsy alone [3]. In addition, targeted biopsy using UroNav demonstrated a cancer detection rate of 37 % in 195 patients with prior negative biopsies; in the same study, systematic biopsies missed 12 of 21 (55 %) of high-grade cancers [25]. Using the Artemis platform, in 105 patients with prior negative biopsies, targeted biopsy improved the detection of clinically significant cancer (Gleason ≥3+4 or Gleason 6 with maximal core length ≥4 mm) (91 %) versus systematic biopsy (54 %) [26]. Furthermore, it was found that repeat biopsy of previously positive MRI targets demonstrated a higher detection rate (61 %) than repeat biopsy of previously positive systematic sites (29 %), with detection rate associated with core length [27]. With the Urostation platform, a higher detection rate of clinically significant prostate cancer (Gleason ≥3+4 or Gleason 6 with maximum cancer core length ≥4 mm) (43 %) compared to systematic biopsy (37 %) was reported in 152 patients undergoing first-round biopsies [28]. Similarly, targeted biopsies using the Virtual Navigator, Real-time Virtual Sonography, BiopSee, and BioJet platforms found higher cancer detection rates compared to systematic biopsies [6, 17, 21–23].

Thus far, most centers using fusion platforms have performed targeted biopsy in addition to systematic biopsy for each patient, an approach that increases sensitivity of detection while allowing direct comparison of the performance of targeted and systematic biopsies [29]. A 2014 meta-analysis of 14 qualifying papers reports that MRI-US fusion targeted biopsy detects more clinically significant cancers while sampling fewer cores than standard biopsy [30]. In patients with a previously negative 12-core standard biopsy and MRI suspicious targets, it may still be wise to obtain both targeted fusion and standard sextant biopsies in order to maximize detection rate.

The emergence of the MRI-TRUS fusion technique is likely increasing the number of patients who may benefit from prostate biopsy. Indications for fusion-guided biopsy are evolving, with no clear consensus at the time of this writing. Thus far the technology has commonly been used for patients with increased PSA level who previously had multiple rounds of negative systematic biopsies (Fig. 7.8), for targeted biopsies directed toward known suspicious MRI lesions, or for active surveillance of lower risk lesions. Exact consensus indications for fusion-guided prostate biopsy remain variable, and the additional value of standard sextant biopsy plus fusion versus fusion alone remains debatable at this time but should soon be better defined.

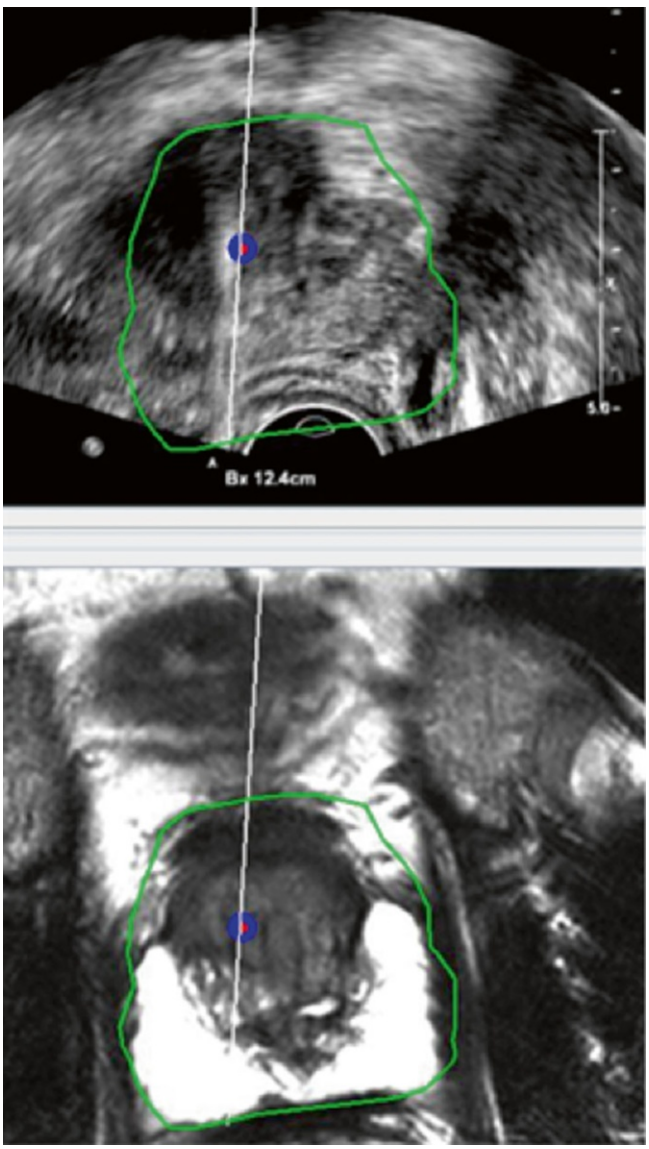

Fig. 7.8 Fusion biopsy of anterior target lesion with needle crossing target and Gleason 7 tumor that was negative on six prior random sextant biopsies over nearly a decade. This area is not well sampled, if at all, by conventional random blind sextant biopsy

Given the greater detection rate and efficiency of targeted biopsy, it is conceivable that the future of prostate biopsy may involve fewer blind cores, and fewer cores in general, and thus fewer biopsy-related complications, not to mention continued improvements in performance characteristics. Blind systematic biopsies may no longer be necessary when clinicians can both accurately localize suspicious lesions in preoperative imaging and accurately sample these lesions during the biopsy procedure itself. Given most platforms' ability to document the location of lesions biopsied, facilitating repeat sampling, active surveillance and focal therapy may play greater roles in management as alternatives to the more aggressive prostatectomy in appropriately screened patients with low-grade disease.

In sum, MRI-TRUS fusion-guided prostate biopsy is a novel, transformative, and potentially disruptive technique that unblinds the prostate biopsy, enabling targeted sampling that combines superior lesion detection of MRI with the real-time guidance of ultrasound. By bringing the imaging to the patient, fusion biopsy uses the imaging information when it is needed most, during the biopsy. Fusion systems provide accurate and efficient navigation and mapping that can be easily performed in the office outpatient setting with local nerve blocks alone. Better characterization and molecular profiling of prostate cancer are enabled by fusion platforms, which may advance the management of prostate cancer toward smarter, more personalized oncology and toward a world where needles are not driven into an organ blindly and randomly searching for disease when we know better. Information is power, and fusion applies that imaging information where and when it is needed. Welcome to the modern era of prostate cancer characterization.

Acknowledgments Dr. Liwei Jiang is part of the National Institutes of Health (NIH) Medical Research Scholars Program, a public-private partnership supported jointly by the NIH and generous contributions to the foundation for the NIH from Pfizer Inc., the Doris Duke Charitable Foundation, the Newport Foundation, the American Association for Dental Research, the Howard Hughes Medical Institute, and the Colgate-Palmolive Company, as well as other private donors.

For Dr. Wood, this research is supported in part by the Intramural Research Program of the NIH. The NIH (BW) holds intellectual property in this area. NIH and Philips (Invivo Corp.) have a cooperative research and development agreement.

References

1. Xu S, et al. Real-time MRI-TRUS fusion for guidance of targeted prostate biopsies. Comput Aided Surg Off J Int Soc Comput Aided Surg. 2008;13:255–64.
2. Turkbey B, et al. Multiparametric 3T prostate magnetic resonance imaging to detect cancer: histopathological correlation using prostatectomy specimens processed in customized magnetic resonance imaging based molds. J Urol. 2011;186:1818–24.
3. Kwak JT, et al. Is visual registration equivalent to semiautomated registration in prostate biopsy? BioMed Res Int. 2015;2015:394742.
4. Kwak JT, et al. Automated prostate cancer detection using T2-weighted and high-b-value diffusion-weighted magnetic resonance imaging. Med Phys. 2015;42:2368.
5. Delongchamps NB, et al. Prebiopsy magnetic resonance imaging and prostate cancer detection: comparison of random and targeted biopsies. J Urol. 2013;189:493–9.
6. Logan JK, et al. Current status of magnetic resonance imaging (MRI) and ultrasonography fusion software platforms for guidance of prostate biopsies: MRI/US fusion software for prostate biopsies. BJU Int. 2014;n/a–n/a. doi:10.1111/bju.12593
7. Sonn GA, Margolis DJ, Marks LS. Target detection: magnetic resonance imaging-ultrasound fusion-guided prostate biopsy. Urol Oncol. 2014;32:903–11.
8. Wagenlehner FME, et al. Infective complications after prostate biopsy: outcome of the Global Prevalence Study of Infections in Urology (GPIU) 2010 and 2011, a prospective multinational multicentre prostate biopsy study. Eur Urol. 2013;63:521–7.
9. Nam RK, et al. Increasing hospital admission rates for urological complications after transrectal ultrasound guided prostate biopsy. J Urol. 2013;189:S12–7; discussion S17–18.
10. Togo Y, et al. Occurrence of infection following prostate biopsy procedures in Japan: Japanese Research Group for Urinary Tract Infection (JRGU) – a multi-center retrospective study. J Infect Chemother. 2014;20:232–7.
11. Grummet JP, et al. Sepsis and 'superbugs': should we favour the transperineal over the transrectal approach for prostate biopsy? BJU Int. 2014;114:384–8.
12. Krücker J, et al. Electromagnetic tracking for thermal ablation and biopsy guidance: clinical evaluation of spatial accuracy. J Vasc Interv Radiol JVIR. 2007;18:1141–50.
13. Xu S, et al. Closed-loop control in fused MR-TRUS image-guided prostate biopsy. Med Image Comput Comput Assist Interv MICCAI Int Conf Med Image Comput Comput Assist Interv. 2007; 10:128–35.
14. Siddiqui MM, et al. Magnetic resonance imaging/ultrasound–fusion biopsy significantly upgrades prostate cancer versus systematic 12-core transrectal ultrasound biopsy. Eur Urol. 2013;64:713–9.
15. Brown AM, et al. Recent advances in image-guided targeted prostate biopsy. Abdom Imaging. 2015. doi:10.1007/s00261-015-0353-8.
16. Miyagawa T, et al. Real-time Virtual Sonography for navigation during targeted prostate biopsy using magnetic resonance imaging data. Int J Urol Off J Jpn Urol Assoc. 2010;17:855–60.
17. Natarajan S, et al. Clinical application of a 3D ultrasound-guided prostate biopsy system. Urol Oncol. 2011;29:334–42.
18. Sonn GA, et al. Targeted biopsy in the detection of prostate cancer using an office based magnetic resonance ultrasound fusion device. J Urol. 2013;189:86–91.
19. Hadaschik BA, et al. A novel stereotactic prostate biopsy system integrating pre-interventional magnetic resonance imaging and live ultrasound fusion. J Urol. 2011;186:2214–20.
20. Kuru TH, et al. Critical evaluation of magnetic resonance imaging targeted, transrectal ultrasound guided transperineal fusion biopsy for detection of prostate cancer. J Urol. 2013;190:1380–6.
21. Shoji S, et al. Manually controlled targeted prostate biopsy with real-time fusion imaging of multiparametric magnetic resonance imaging and transrectal ultrasound: an early experience. Int J Urol Off J Jpn Urol Assoc. 2014. doi:10.1111/iju.12643.
22. Tewes S, et al. Targeted MRI/TRUS fusion-guided biopsy in men with previous prostate biopsies using a novel registration software and multiparametric MRI PI-RADS scores: first results. World J Urol. 2015. doi:10.1007/s00345-015-1525-4.
23. Ukimura O, et al. 3-Dimensional elastic registration system of prostate biopsy location by real-time 3-dimensional transrectal ultrasound guidance with magnetic resonance/transrectal ultrasound image fusion. J Urol. 2012;187:1080–6.

24. Siddiqui MM, et al. Comparison of MR/ultrasound fusion-guided biopsy with ultrasound-guided biopsy for the diagnosis of prostate cancer. JAMA. 2015;313:390–7.
25. Vourganti S, et al. Multiparametric magnetic resonance imaging and ultrasound fusion biopsy detect prostate cancer in patients with prior negative transrectal ultrasound biopsies. J Urol. 2012;188:2152–7.
26. Sonn GA, et al. Value of targeted prostate biopsy using magnetic resonance-ultrasound fusion in men with prior negative biopsy and elevated prostate-specific antigen. Eur Urol. 2014;65:809–15.
27. Sonn GA, et al. Initial experience with electronic tracking of specific tumor sites in men undergoing active surveillance of prostate cancer. Urol Oncol. 2014;32:952–7.
28. Mozer P, et al. First round of targeted biopsies using magnetic resonance imaging/ultrasonography fusion compared with conventional transrectal ultrasonography-guided biopsies for the diagnosis of localised prostate cancer. BJU Int. 2015;115:50–7.
29. Salami SS, et al. In patients with a previous negative prostate biopsy and a suspicious lesion on magnetic resonance imaging, is a 12-core biopsy still necessary in addition to a targeted biopsy? BJU Int. 2015;115:562–70.
30. Valerio M, et al. Detection of clinically significant prostate cancer using magnetic resonance imaging-ultrasound fusion targeted biopsy: a systematic review. Eur Urol. 2014. doi:10.1016/j.eururo.2014.10.026.

Template Mapping Biopsies: An Overview of Technique and Results

8

Ahmed El-Shater Bosaily and Hashim U. Ahmed

Rationale and Background

Prostate cancer management is rapidly evolving. Currently, multiple options are available for men with localized prostate cancer ranging from active surveillance to whole-gland treatments. The results of several clinical trials have shown that accurate risk stratification is key to assigning the appropriate management option for men who would benefit most from it [1–9].

The current diagnostic pathway for patients with suspected prostate cancer remains reliant on transrectal ultrasound-guided biopsy (TRUS) with no utilization of pre-biopsy imaging. Annually, between 59,000 and 80,000 men have a TRUS biopsy in the UK and about one million in the USA [10]. TRUS-guided biopsy can be problematic. The random and systematic errors in diagnosis, which are inherent in TRUS-guided biopsies of the prostate, lead to a number of problems:

TRUS biopsies overdiagnose clinically insignificant prostate cancer. A man who undergoes TRUS biopsy has a 1 in 4 chance of being diagnosed with prostate cancer [11, 12]. This compares with a 6–8 % lifetime risk of having prostate cancer that would impact on his life expectancy. This overdetection of these small low-grade lesions is due in part to the random deployment of TRUS-guided biopsy needles [11–13] (Fig. 8.1).

TRUS-guided biopsies miss clinically significant cancers. They have an estimated false-negative rate of 30–45 % [13, 14]. TRUS biopsy's systematic error leads to significant cancer being missed as several parts of the prostate is systematically undersampled. First, the anterior part of the gland is missed as a result of its greater distance from the rectum (Fig. 8.2a). Second, areas in the midline are undersampled due to efforts to avoid the urethra. Third, the prostate apex is often inaccessible by the transrectal route [15–18].

TRUS-guided biopsies can be unrepresentative of the true burden of cancer. The random sampling error (Fig. 8.2 (b,c)) can mean that a biopsy does not hit the cancer lesion through its greatest diameter leading to either or both the size and the grade of cancer being underestimated [19] (Fig. 8.2c). Up to half of men deemed low risk on TRUS-guided biopsies can have higher burden or grade, or both, when a more accurate biopsy test is applied [16–18, 20–22]. As a result of the poor risk attribution, many men may not be able to receive the most suitable management in relation to their risk stratification.

TRUS-guided biopsy offers poor disease localization. As tissue preservative or focal therapy for prostate cancer depends on destroying the diseased tissue with minimal damage to healthy tissue, it is imperative to localize the diseased area in the prostate accurately to avoid undertreatment and recurrence on one hand and overtreatment and unnecessary increased morbidity on the other. TRUS biopsy is not able to provide such spatial information about the diseased area. And due to all above, the area diagnosed may not be the only area harboring clinically significant disease in the prostate.

Template transperineal prostate mapping (TPM) biopsies were conceived [23] to avoid the above issues and provide accurate risk assessment and location attribution of disease and have since gained increasing popularity and acceptance as a highly accurate diagnostic test [17, 18, 20, 21, 24].

Template Mapping Biopsies: Technique

Patient Preparation

In our routine practice at University College London, we do not prescribe preoperative preparation, although minimal

A. El-Shater Bosaily, MSc, MBBCh
H.U. Ahmed, PhD, FRCS(Urol), BM, BCh, BA (✉)
Division of Surgery and Interventional Science, University College London, London, UK

Department of Urology, University College London Hospital NHS Foundation Trust, London, UK
e-mail: a.shater@ucl.ac.uk, amshater@gmail.com; hashim.ahmed@ucl.ac.uk

A.R. Rastinehad, D.N. Siegel (eds.), *Interventional Urology*, DOI 10.1007/978-3-319-23464-9_8

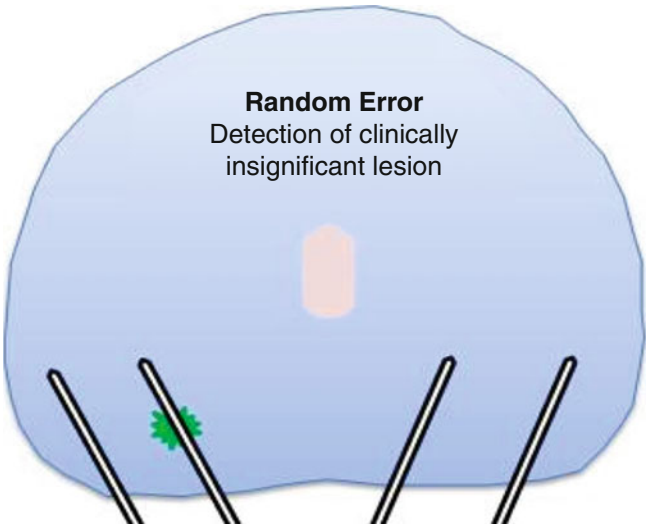

Fig. 8.1 Overdetection of insignificant prostate cancer

bowel preparation with a phosphate enema the night before or on the day of the procedure significantly improves ultrasound imaging of the prostate. An alpha-blocker such as tamsulosin or alfuzosin, although not essential, may be prescribed prior to the procedure (2–7 days). It is strongly recommended to prescribe a 2-week course of tamsulosin postoperatively in order to minimize the risk of acute urinary retention. Seven days prior to the procedure, antiplatelet agents should be stopped. Anticoagulants should be stopped after consultation with local guidelines.

Patient and Equipment Setup

The patient is positioned in the lithotomy position and a short-term urethral catheter is usually fitted. The catheter's main function is to delineate the urethra as a landmark to help align the prostate on ultrasound imaging and also to avoid injuring the urethra especially if it is deviated from the midline in nonsymmetrically enlarged glands usually due to benign prostatic hyperplasia. The catheter is spigotted, and the bladder should not be emptied to allow the bladder neck to be visualized on ultrasound. The scrotum and penis are taped to the abdomen. A biplanar ultrasound probe covered with an endocavity balloon mounted on a brachytherapy stepper is introduced into the rectum to visualize the prostate (Fig. 8.3). While inflating the balloon with water, it is essential to make sure most or all air bubbles are removed to avoid image artifacts (Fig. 8.4).

After the probe is introduced, the midline reference plane is established by visualizing the urethra and the catheter at the center of the sagittal plane or at the midline on the transverse plain on real-time ultrasound. This should be equivalent to the capital letter "D" on the 5 mm biopsy grid on transverse (axial) view (Figs. 8.5 and 8.6).

It is important to ascertain that the posterior aspect of the prostate is included within the biopsy grid by moving the probe and stepper anteriorly or posteriorly and inflating/deflating the balloon (Fig. 8.6) to ensure adequate sampling of the peripheral zone specially at the level of the prostate base.

It is important to establish the position of the anterior aspect of the prostate in relation to the bony pubic arch to ascertain needle access to the anterior aspect of the prostate. Avoiding the pubic arch obstructing the needle path can be established by a combination of further extended hip flexion, balloon deflation, and stepper repositioning (Fig. 8.5).

Once an acceptable setup is achieved, the perineum is cleaned and the patient is draped. Shaving the perineum is optional. A sterile plastic drape and a brachytherapy type 5 mm sterile disposable grid are attached (Fig. 8.7) to the stepper. It is important that the template grid is calibrated to match the 5 mm grid seen on the ultrasound screen.

Needle Deployment

On sagittal view, the prostate should be divided visually to cranial (basal) and caudal (apical) halves provided the prostate is large enough. The basal and the apical portions will be biopsied and potted separately. To perform a full template mapping biopsy, the biopsy needles are deployed through the template grid once apically and then basally before moving on to the next coordinate (hole) on the grid (Fig. 8.8) while avoiding injuring the urethra and the bladder. To avoid the urethra the midline plane anteriorly is always spared from biopsy (Fig. 8.5), which is usually the anterior coordinates along the D line in the grid. After obtaining a sample the needle should be rinsed in chlorhexidine and then in sterile water before it is reloaded and passed back to the operator. To save time two needles should be used in every procedure to allow the operator to biopsy while the sample is obtained from the other needle and allowing for it to be prepared, and reloaded for use. Figure 8.9 shows the scrub nurse's equipment setup. Once the whole gland is sampled, the catheter is removed and the patient can be discharged on the same day provided they are voiding urine well with no large residual volumes.

Assigning Zonal Anatomy to the Prostate

Biopsy cores can be labeled individually according to their *X*, *Y* coordinates on the grid and *Z* coordinates relating to whether it is basal or apical. The alternative is to divide the prostate into zones. There are also several ways to divide the

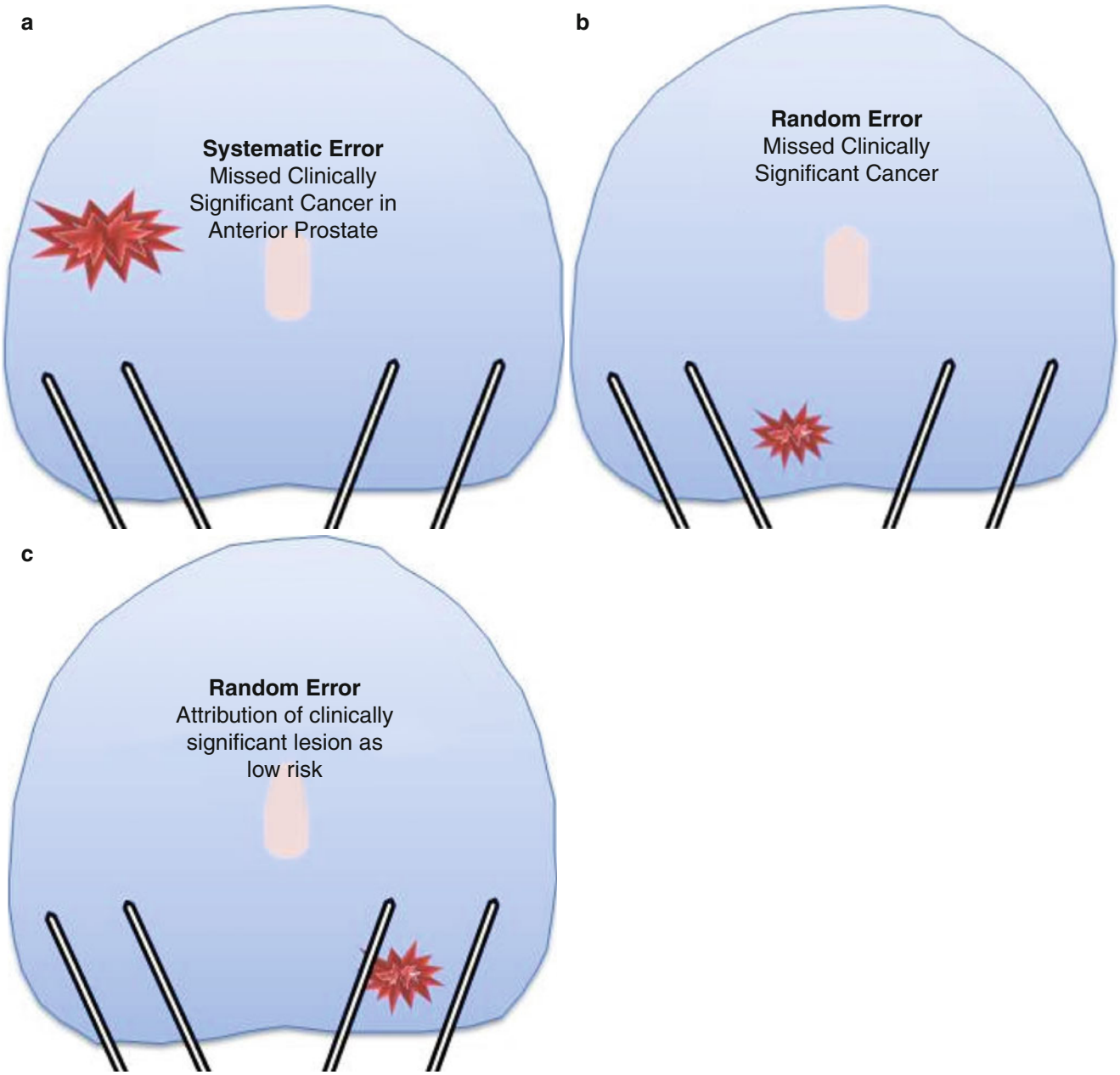

Fig. 8.2 TRUS biopsies underdiagnose clinically significant prostate cancer. (**a**) Random error. (**b**, **c**) Systematic error

prostate into anatomical zones. Barzell et al. initially divided the prostate into octants and then further divided them into three zones yielding 26 separate specimen pots [20]. Our group in University College London modified this further into the modified Barzell zones where the prostate is segmented into 20 zones (Fig. 8.10); then later reduced into 12 zones only to reduce the resource burden on pathology services (Fig. 8.11). The choice of approach should be driven first by the required accuracy of information and second by the amount of burden and logistics that can be tolerated. For example, if a TPM is used as a reference standard in a clinical trial validating a diagnostic modality like MRI as, for example, the PROMIS trial [25], a core-by-core coordinate record would yield the most accurate information at the expense of theater time, the need for logistical support, and histopathology processing cost. These issues can be mitigated using zonal sampling in which 5 mm sampling frequency is maintained but the cores geographically grouped and potted together. If the aim is for focal therapy, grouping the biopsies into zones should be sufficient to plan accurate treatment. In centers that only perform radical therapy, there is much less emphasis on the location of the disease and

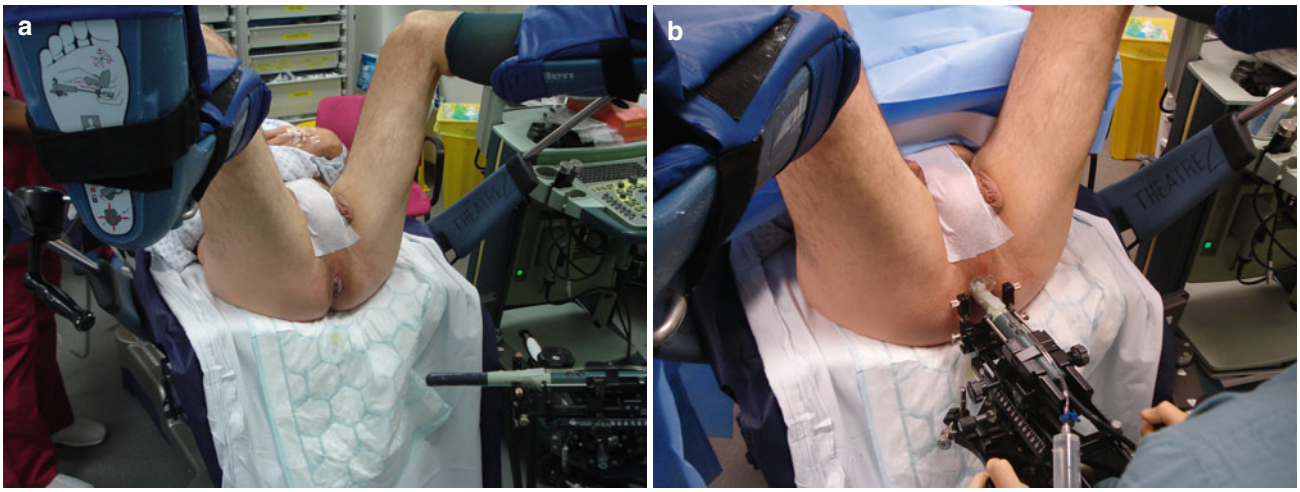

Fig. 8.3 Patient and probe setup. (**a**) Patient position. (**b**) Probe setup

Fig. 8.4 Probe in balloon cover with air bubbles emptied and sufficient gel coverage

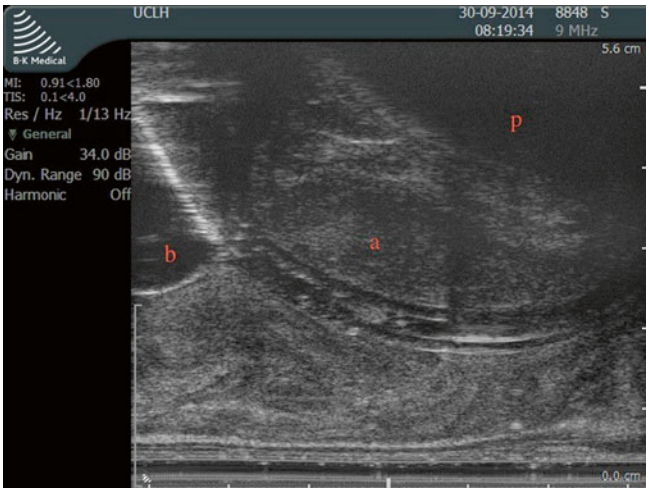

Fig. 8.5 Midline sagittal view of the prostate establishing the reference plain by visualizing the catheter in the urethra. Kindly note the catheter balloon and the bladder base (*b*). The bladder base and the symphysis pubis (*p*) position should be considered while planning the biopsy. (*a*) represents the anterior area of the transition zone spared from biopsy to avoid urethral injury

more on the risk stratification of the patient; hence, there will be no benefit in obtaining that level of detailed information.

Complications and Side Effects

With respect to morbidity and expected side effects, TPM biopsies have a similar side effect profile to that of TRUS-guided biopsy with three important differences. First, they carry a significantly lower risk of urosepsis (<0.5 %) – the most serious complication of TRUS-guided biopsy – as the needles do not traverse the rectal mucosa. Second, TPM biopsies confer a higher risk of self-limiting failure to void urine (5–10 %) as a result of greater gland swelling [26–28] compared to 1–2 % risk associated with TRUS-guided biopsy. Third, TPM biopsies require a general/spinal anesthetic, although in expert hands a limited mapping biopsy can be performed under sedation with local skin and periprostatic anesthesia [23]. On a more recent study by Losa et al. [29] comparing complication rates, according to the Clavien-Dindo classification, and changes in the quality of life, evaluated using the International Prostate Symptom Score, International Index of Erectile Function, and Functional Assessment of Cancer Therapy-Prostate questionnaires, before and 1 month after, template mapping biopsies did not appear to have a significant effect on the quality of life, and no life-threatening complications occurred, with negligible global Clavien-Dindo complication rates revealed.

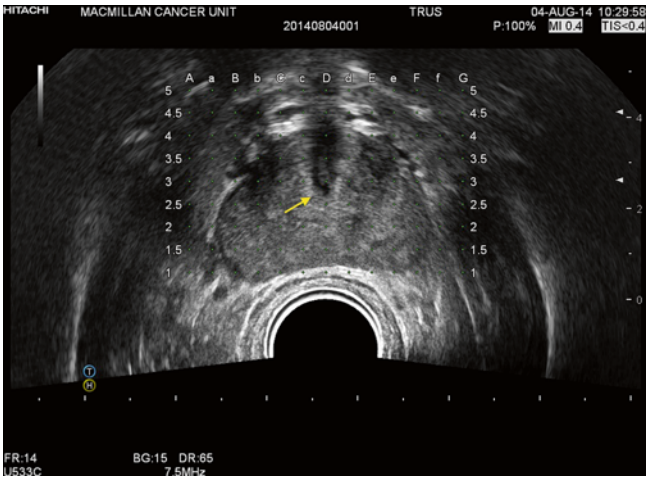

Fig. 8.6 Transverse (axial) view of the prostate showing the catheter and urethra (*arrow*) aligned at the coordinates D3 in the middle of the grid which confirms the midline alignment, divides the prostate into anterior and posterior aspects, and allows the operator to plan the biopsy zones. Please note that the peripheral zone is well covered by the biopsy grid

The Diagnostic Performance of Template Mapping Biopsies

Template mapping biopsies demonstrate a high diagnostic yield (Table 8.1). This has been demonstrated by several publications. In a case series of 191 consecutive biopsy naive patients, Bittner et al. documented 73.3 % positive diagnoses with 24.3 % of these cancers in areas not typically sampled in a TRUS biopsy [30]. Symons et al. reported a series of 409 patients and showed an overall detection rate of 56.7 %. When stratified between those having a primary TPM and those having a repeat biopsy (after a previous negative biopsy), the detection rates were 64.4 % and 35.6 %, respectively, with significantly higher detection rates in prostates <50 mL in volume compared to larger prostates (65.2 vs. 38.3 %) [31].

In series comparing findings on TPM and TRUS biopsy, TPM has been shown to have a significantly better performance than TRUS biopsy especially in the anterior aspect of the gland. This has been shown by Mabjeesh et al. on a 92-patient series who had at least 2 previous negative TRUS biopsies. Cancer was diagnosed in 26 % of the cohort with 83.3 % of these tumors located anteriorly in the prostate [32]. In terms of overall detection, [41] published a case series of 122 men who had 2 negative TRUS biopsies and showed a detection rate of 58 % [33]. Ekwueme et al. similarly showed 54.8 % detection rate in a cohort of 270 patients requiring repeat biopsy [34].

Also as discussed in the introduction of this chapter, TRUS biopsy may lead to misclassification of clinically significant disease as insignificant disease due to undersampling of the tumor; this may lead to inappropriate management. A cohort of 101 men with TRUS biopsy diagnosed with Gleason ≤3 + 3 who were on active surveillance underwent a restaging TPM that showed 34 % had more significant prostate cancer on restaging TPM compared with their TRUS biopsies. Of these men, 44 % had disease predominantly in the anterior part of the gland. In total, 33 % of these men were taken off active surveillance and had radical treatment [35].

In light of the high detection rates of cancer on TPM, tools such as the D'Amico risk stratification are not suitable, and a risk stratification strategy is needed to interpret the findings of TPM in terms of disease significance. In our center in UCL, Ahmed et al. [36] reconstructed 3D computer models of 107 whole-mount radical prostatectomies and performed 500 TPM simulations per case to assess the characteristics of clinically significant disease on TPM and assigned a more suitable risk stratification protocol. By combining the total cancer core length, the maximum cancer core length obtained, it was found that maximum cancer core length ≥6 mm found on a biopsy core represents a lesion with a volume of ≥0.5 ml. A cancer core length involvement ≥4 mm represents a cancer volume of ≥0.2 ml which was correlated to the Gleason score to produce the UCL (University College London) risk stratification system. Simulation studies have also been used to assess the diagnostic accuracy of template biopsy, which showed an overall accuracy (area under the receiver operating curve, AUC) of ≈0.90 compared with an AUC of 0.70–0.80 for TRUS biopsy [37]. TPM biopsies were able to rule out clinically significant disease with an AUC of 0.91 in Lecornet et al. work in comparison to an AUC of 0.75 on simulating TRUS biopsies [15].

Validation of Template Mapping Biopsies

Although methodologically challenging, TPM biopsies have been validated against whole-mount step-section radical prostatectomies. Crawford et al. validated TPM against 3D reconstructed radical prostatectomy specimens and showed that only one clinically significant lesion of 64 lesions was missed. When comparing the cumulative Gleason scores, 72 % had identical scores, 12 % were upgraded, and only 16 % were downgraded [24]. In Katz et al. work the sensitivity and specificity of TPM biopsies for prostate cancer detection was shown to be 86 % and 83 %, respectively [38]. On the other hand, Huo et al. [40] demonstrated much lower values in their earlier work on a series of 414 patients. The average sensitivity and specificity was 48 % and 84.1 %, respectively, with a statistically significant decrease in the sensitivity of larger prostates. Gleason grade concordance between biopsy and pathology specimens was achieved in 65.7 % of patients with upgrading of Gleason scores that occurred in 25.6 % of patients and downgrading in 8.8 %. In this particular paper this is likely due to the limited sampling protocol used in biopsies which yields much less information than a thorough radical prostatectomy protocol. The variation in the results between

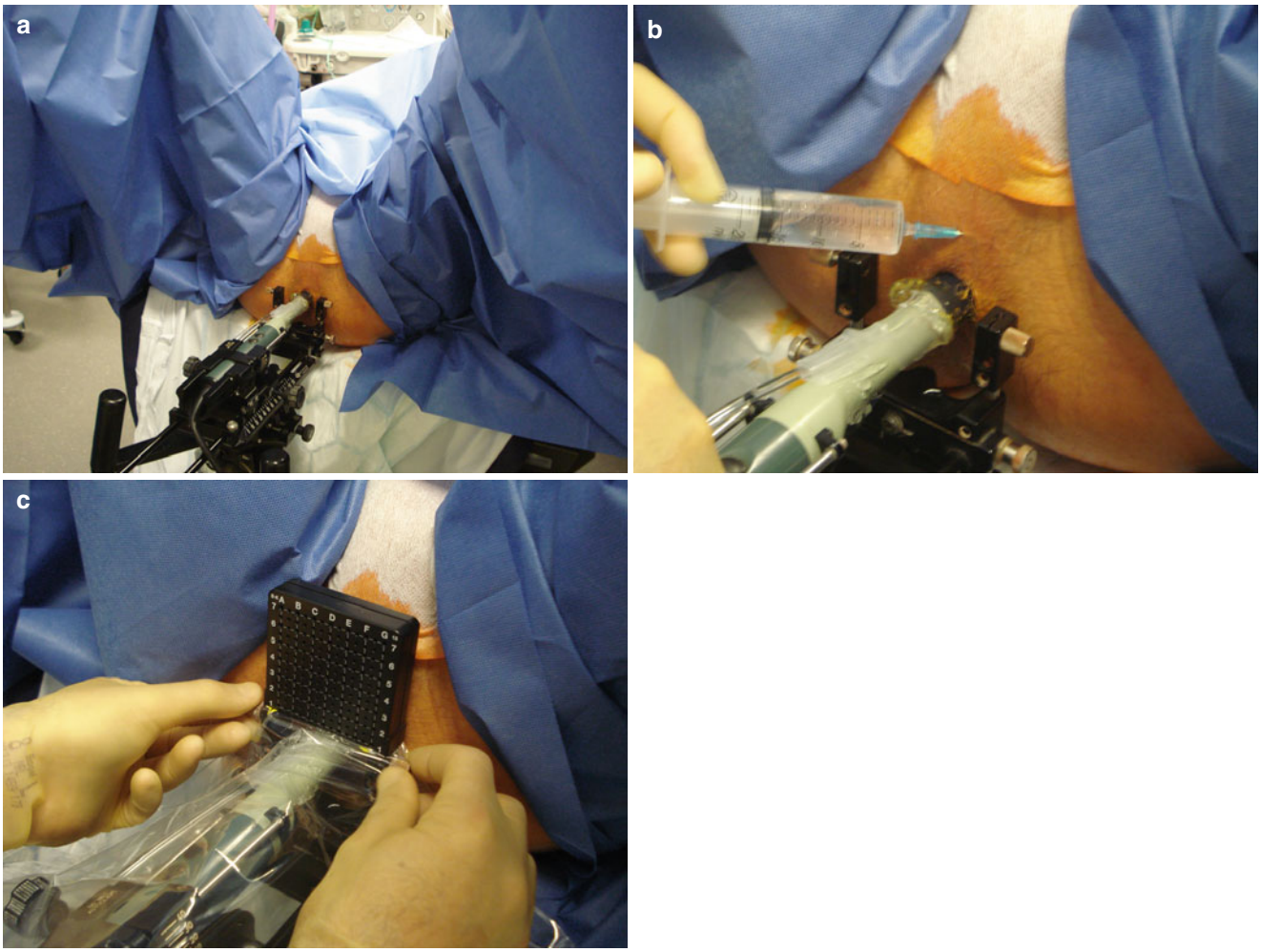

Fig. 8.7 Patient/probe preparation. (**a**) Patient draping and preparation. (**b**) Application of local anesthetic (bupivacaine with adrenaline 0.5 %). (**c**) Attachment of grid and plastic cover

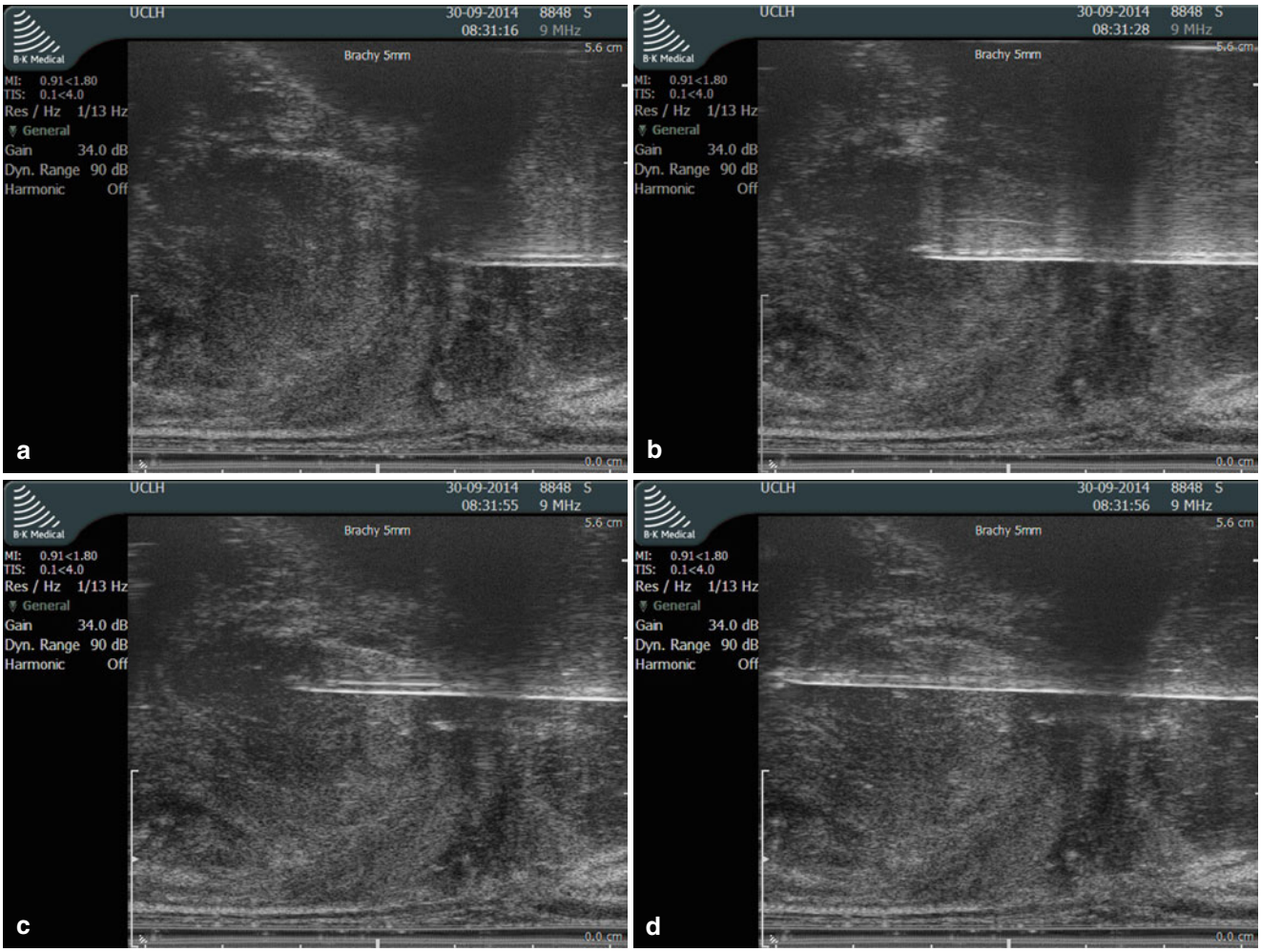

Fig. 8.8 Needle deployment. (**a**) Apical sampling: needle positioned against the apical capsule. (**b**) Apical sampling: needle deployed. (**c**) Basal sampling: needle positioned to sample the base where the previous biopsy tract ends, which can be tracked on the ultrasound screen and also felt as increased resistance once un-biopsied tissue is encountered. (**d**) Basal sampling: needle deployed stopping just short of the bladder base

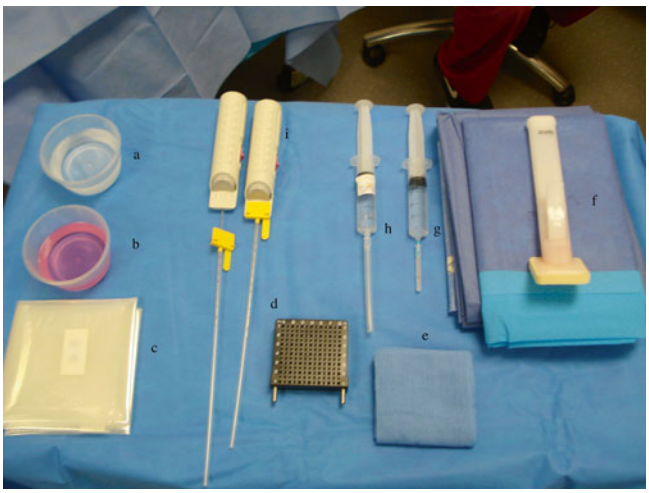

Fig. 8.9 (**a**) Sterile water. (**b**) Chlorhexidine. (**c**) Plastic probe cover. (**d**) 5 mm brachytherapy grid. (**e**) Sterile gauze. (**f**) Drapes. (**g**) Superficial local anesthesia (bupivacaine with adrenaline). (**h**) Deep local anesthesia: used only in templates under local anesthetic or sedation (without adrenaline). (**i**) Biopsy 18 g needles

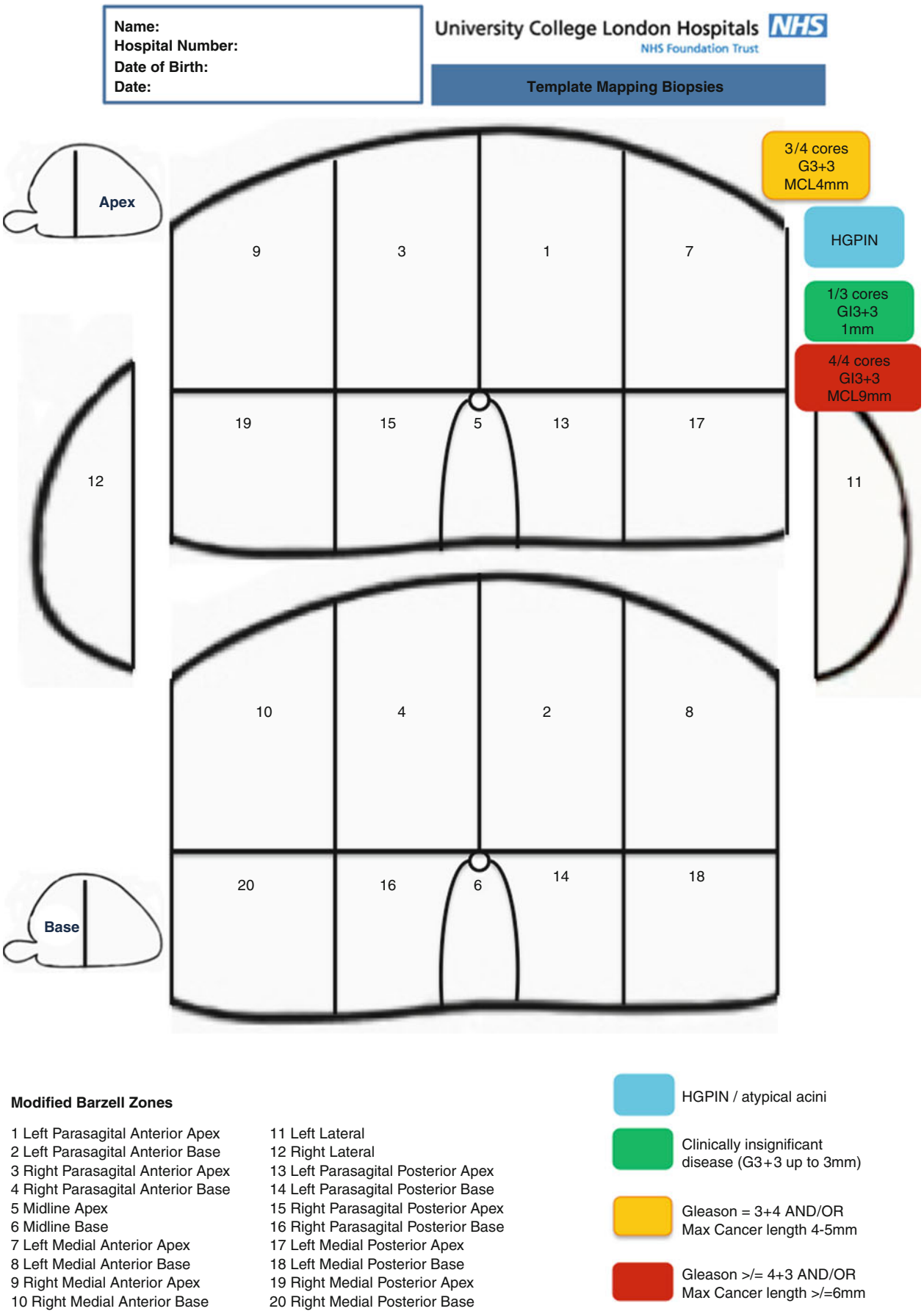

Fig. 8.10 Modified Barzell 20-zone approach similar to the approach used in PROMIS (Prostate MRI Imaging Study) and other diagnostic trials in UCL (Courtesy of University College London Hospitals, NHS Trust)

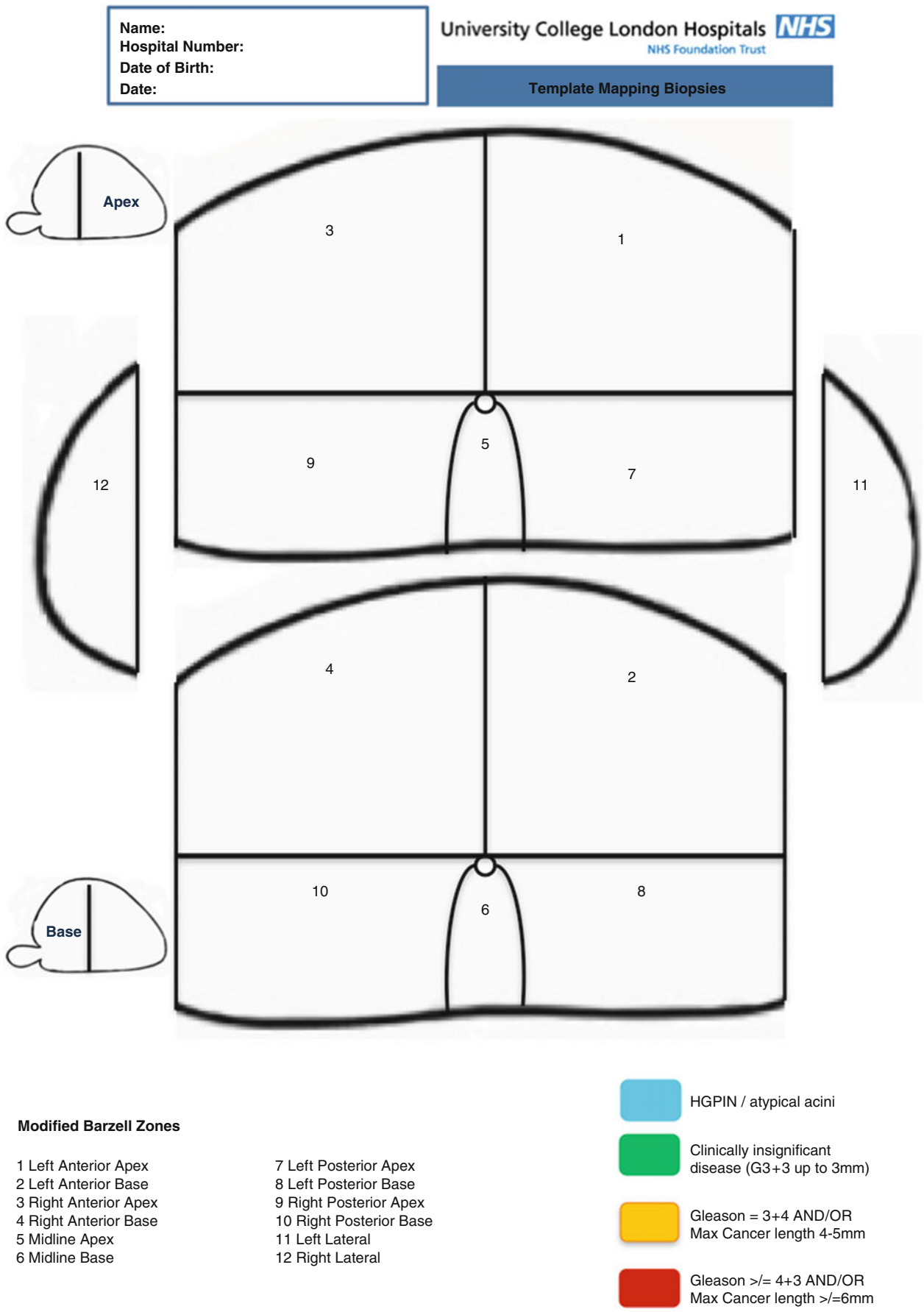

Fig. 8.11 Modified 12-zone approach applied in clinical practice in UCL (Courtesy of University College London Hospitals, NHS Trust)

Table 8.1 Variations in biopsy protocols and definitions of significance between publications

Study	Size	Age	PSA	Design	No. of cores	Technique	Definition	Measure	Results	Further info.
Ong et al. 2015 [39]	57	63[a]	5.8[a]	Bx naive	19[a]	*Variable*	GS≥7 or >3 cores positive	*CDR*	53 %	87 % of 53 % significant
	103		9.6[a]	negative TRUS	24[a]	*Variable*			36 %	81 % significant
Katz et al. [38]	17	–	5.6[a]	TPM/RP Validation	Density: no. of cores/volume [a]1.26	*Mapping*	GS ≥ 7 or >50 %/ core or >25 % Total/quadrant	Sensitivity and specificity	86 % and 83 %	
Nafie et al. 2014 [41]	50	67[b]	8[b]	Bx naive had TRUS then limited TPM	36 cores per patient	*Limited*	Any cancer	CDR	60 % positive, 32 % positive on both	No positive TRUS only. 28 % negative TRUS/+ve TPM
Pepe et al. [42]	226	64[a]	7.6[a]	Mixed cohort.	Bx naive: 22 cores[a] Repeat biopsy: 32 cores[a]	*Variable*	Any cancer	CDR anterior zone	11.8 % 8.8 %	
Klatte et al. (2013) [43]	50	57.5[b]	7.3[b]	Prior negative TRUS biopsy	24 cores per patient	*Variable*	Epstein criteria	CDR	48 %	25 % were insignificant
Vyas et al. (2013) [44]	634	63[a]	7.66[a]	Mixed cohort	Volume: <30 mL = 24 cores >50 mL = 38 cores	*Variable*	Any cancer	*CDR*	Bx naive: 54 % Prior TRUS: 36 %	29 % were upgraded from 3 + 3 disease
Symons et al. [31]	409	63[b]	9.7[b]	Mixed cohort	15[a]	*Limited*	Any cancer	*CDR*	56.7 %	Bx naive CDR64.4 % Prior Bx: 35.6 %
Gershman et al. (2013) [45]	34	66[b]	23[b]	Multiple negative Bx, rising PSA	24.8[b]	*Variable*	Any cancer	*CDR*	50 %	
Ekwueme et al. [34]	270	64[a]	10[a]	Previous –ve Bxs	7[a]	*Limited*	Any cancer	*CDR*	54.8 %	
Krughoff et al. 2013 [46]	161	61.6[b]	N/A	Low-volume disease on TRUS	61.4[b]	*Mapping*	Any cancer	Location of cancers missed on TRUS	Most were anterior	GS upgraded on TPM
Crawford et al. [24]	25	66[a]	5[a]	TPM followed by RP	49[a]	*Mapping*	Any cancer with further classification	Validation of GS and laterality	72 % similar GS 12 % upgraded on RP	80 % similar laterality
Takeshita et al. 2013 [47]	744	65[a]	6.1[a]	TRUS and TPBx	12 cores 14 cores	*Limited*	Any cancer	Cancers missed by TPBx	14 % missed	
Bittner et al. (2013) [48]	485	64.8[b]	8.7[b]	Prior –ve TRUS undergoing TPBx	55.6[b]	*Limited*	Any cancer with further classification of significance	*CDR*	46.6 %	
Losa et al. [29]	87	63.9[a]	6.9[a]	Low-risk cancer on TRUS	0.87 core/cm[a]	*Variable*	Any cancer	Complications	CDR 62.1 %	Complication profile favorable
Bittner et al. [30]	191	64.6[a]	5.2[a]	Biopsy naive	54[a]	*Limited*	Any cancer	CDR	73.3 %	
Huo et al. (2012) [40]	414	60.9[b]	7.7[b]	Bx naive TMP	23.5[b]	*Limited followed by RP*	Any cancer	Sensitivity and specificity	48 % and 84.1 %	25.60 % upgraded

Dimmen et al. (2012) [49]	69	64.5[a]	25.2[a]	negative TRUS	18.4[a]	*Limited followed by RP*	Any cancer	CDR	55 %	Assessed Gleason score only
Pal et al. (2012) [50]	40	63[b]	21.9[b]	2 negative TRUS	36[b]	*Limited*	Any cancer	CDR	68 %	
Ayres et al. (2012) [35]	101	68[a]	6.4[a]	Active surveillance patients	47[a]	*Limited*	N/A	Staging	34 % upstaged	
Lecornet al. (2012) [15]	96	N/A	2.1[a]	Computer simulation	N/A	*Mapping*	Any cancer	CDR	100 % (for lesions > 0.5 ml)	7 % of lesions 0.2–0.5 ml were missed by TTMB
Barqawi et al. (2011) [51]	215	60.5[a]	4.8[a]	negative TRUS	56[a]	*Mapping*	Any cancer	CDR	68.80 %	45.6 % upstaged
Abdollah et al. (2011) [52]	140	66.4[a]	10[a]	Mixed previous Bx cohort	24[a]	*Limited*	Any cancer	CDR	28.6 %	Methodological concerns
Taira et al. (2010) [22]	373	63.8[a]	8.3[a]	Mixed cohort	57[a]	*Limited*	>3+3 >50 %/core PSA density >0.15			
Onik et al. (2009) [17]	180	N/A	5.1[a]	Prior TRUS	50[a]	*Variable*	Any cancer	GS between TPM and TRUS	22.7 % GS upgraded	
Barzell et al. (2007)	80	69[a]	Density 0.14[a]	Prior TRUS	69[a]	*Mapping and repeat TRUS*	Any cancer	Benefit in treatment selection	N/A	
Onik et al. (2008)	110	N/A	7.4[b]	Unilateral cancer on TRUS	46[a]	*Mapping*	Any cancer	Laterality GS	55 % bilateral	23 % upstaged GS
Crawford et al. [18]	106	63.1[b]	N/A	Simulation study	N/A	*Mapping*	Any cancer	Comparison of 5 mm and 10 mm mapping	N/A	N/A

GS Gleason score, *Bx* biopsy, *TP* transperineal, *Limited* limited (non-5 mm) transperineal sampling, *Mapping* 5 mm mapping biopsy, *Variable* variable biopsy technique in the same study

[a]Median

[b]Mean

publications is mainly due to different definitions of clinically significant disease reported and the density of template mapping biopsies employed. It is also worth noting that the results improved with the increased cumulative experience in performing the procedure. Table 8.1 shows the variations in biopsy protocols and definitions of significance between publications.

Conclusion

To conclude, template prostate mapping biopsies are a highly accurate investigation of prostate cancer that can be applied to most men who are at risk of prostate cancer. They are characteristically better in detection of anteriorly located tumors and provide spatial information in the location and extent of diseased tissue which cannot be obtained via TRUS biopsy while confirming absence of the disease in the remaining prostate tissue. It is also an ideal procedure for validation of diagnostic biomarkers.

References

1. Djulbegovic M, Beyth RJ, Neuberger MM, et al. Screening for prostate cancer: systematic review and meta-analysis of randomised controlled trials. BMJ. 2010;341:c4543. Epub 2010/09/17.
2. Andriole GL, Crawford ED, Grubb 3rd RL, et al. Mortality results from a randomized prostate-cancer screening trial. N Engl J Med. 2009;360(13):1310–9. Epub 2009/03/20.
3. Hugosson J, Carlsson S, Aus G, et al. Mortality results from the Goteborg randomised population-based prostate-cancer screening trial. Lancet Oncol. 2010;11(8):725–32. Epub 2010/07/06.
4. Schroder FH, Hugosson J, Roobol MJ, et al. Prostate-cancer mortality at 11 years of follow-up. N Engl J Med. 2012;366(11):981–90. Epub 2012/03/16.
5. Schroder FH, Hugosson J, Roobol MJ, et al. Screening and prostate-cancer mortality in a randomized European study. N Engl J Med. 2009;360(13):1320–8. Epub 2009/03/20.
6. Holmberg L, Bill-Axelson A, Steineck G, et al. Results from the Scandinavian Prostate Cancer Group Trial Number 4: a randomized controlled trial of radical prostatectomy versus watchful waiting. J Natl Cancer Inst Monogr. 2012;2012(45):230–3. Epub 2012/12/29.
7. Wilt TJ. The Prostate Cancer Intervention Versus Observation Trial:VA/NCI/AHRQ Cooperative Studies Program #407 (PIVOT): Design and Baseline Results of a Randomized Controlled Trial Comparing Radical Prostatectomy With Watchful Waiting for Men With Clinically Localized Prostate Cancer. J Natl Cancer Inst Monogr. 2012;2012(45):184–90.
8. Barry MJ. Screening for prostate cancer — the controversy that refuses to die. N Engl J Med. 2009;360(13):1351–4.
9. Parker C, Emberton M. Screening for prostate cancer appears to work, but at what cost? BJU Int. 2009;104(3):290–2. Epub 2009/06/25.
10. Cross T, McPhail S. Clinical guideline prostate cancer: diagnosis and treatment. An assessment of need. A report to the National Collaborating Centre for Cancer. 2008.
11. Bangma CH, Roemeling S, Schroder FH. Overdiagnosis and overtreatment of early detected prostate cancer. World J Urol. 2007;25(1):3–9. Epub 2007/03/17.
12. Thompson IM, Goodman PJ, Tangen CM, et al. The influence of finasteride on the development of prostate cancer. N Engl J Med. 2003;349(3):215–24. Epub 2003/06/26.
13. Djavan B, Ravery V, Zlotta A, et al. Prospective evaluation of prostate cancer detected on biopsies 1, 2, 3 and 4: when should we stop? J Urol. 2001;166(5):1679–83. Epub 2001/10/05.
14. Scattoni V, Zlotta A, Montironi R, Schulman C, Rigatti P, Montorsi F. Extended and saturation prostatic biopsy in the diagnosis and characterisation of prostate cancer: a critical analysis of the literature. Eur Urol. 2007;52(5):1309–22. Epub 2007/08/28.
15. Lecornet E, Ahmed HU, Hu Y, et al. The accuracy of different biopsy strategies for the detection of clinically important prostate cancer: a computer simulation. J Urol. 2012;188(3):974–80.
16. Barzell WE, Melamed MR, Cathcart P, Moore CM, Ahmed HU, Emberton M. Identifying candidates for active surveillance: an evaluation of the repeat biopsy strategy for men with favorable risk prostate cancer. J Urol. 2012;188(3):762–8.
17. Onik G, Miessau M, Bostwick DG. Three-dimensional prostate mapping biopsy has a potentially significant impact on prostate cancer management. J Clin Oncol. United States 2009;27(26):4321–6. Epub 2009/08/05.
18. Crawford ED, Wilson SS, Torkko KC, et al. Clinical staging of prostate cancer: a computer-simulated study of transperineal prostate biopsy. BJU Int. 2005;96(7):999–1004.
19. Kulkarni GS, Al-Azab R, Lockwood G, et al. Evidence for a biopsy derived grade artifact among larger prostate glands. J Urol. 2006;175(2):505–9. Epub 2006/01/13.
20. Barzell WE, Melamed MR. Appropriate patient selection in the focal treatment of prostate cancer: the role of transperineal 3-dimensional pathologic mapping of the prostate—a 4-year experience. Urology. 2007;70(6):S27–35.
21. Onik G, Barzell W. Transperineal 3D mapping biopsy of the prostate: an essential tool in selecting patients for focal prostate cancer therapy. Urol Oncol. 2008;26(5):506–10. Epub 2008/09/09.
22. Taira AV, Merrick GS, Galbreath RW, et al. Performance of transperineal template-guided mapping biopsy in detecting prostate cancer in the initial and repeat biopsy setting. Prostate Cancer Prostatic Dis. 2010;13(1):71–7.
23. Barzell W, Whitmore W, Andriole G. How to perform transperineal saturation prostate biopsy: technique addresses diagnostic, therapeutic dilemmas that arise following TRUS biopsies. Urol Times. 2003;31:41.
24. Crawford ED, Rove KO, Barqawi AB, et al. Clinical-pathologic correlation between transperineal mapping biopsies of the prostate and three-dimensional reconstruction of prostatectomy specimens. Prostate. 2013;73(7):778–87. Epub 2012/11/22.
25. El-Shater Bosaily A, Parker C, Brown LC, et al. PROMIS - Prostate MR imaging study: A paired validating cohort study evaluating the role of multi-parametric MRI in men with clinical suspicion of prostate cancer. Contemp Clin Trials. 2015. Epub 2015/03/10.
26. Merrick GS, Taubenslag W, Andreini H, et al. The morbidity of transperineal template-guided prostate mapping biopsy. BJU Int. 2008;101(12):1524–9. Epub 2008/03/08.
27. Buskirk SJ, Pinkstaff DM, Petrou SP, et al. Acute urinary retention after transperineal template-guided prostate biopsy. Int J Radiat Oncol Biol Phys. 2004;59(5):1360–6. Epub 2004/07/28.
28. Miller J, Perumalla C, Heap G. Complications of transrectal versus transperineal prostate biopsy. ANZ J Surg. 2005;75(1–2):48–50. Epub 2005/03/03.
29. Andrea Losa GMG, Massimo Lazzeri, Giovanni Lughezzani, Giampiero Cardone, Massimo Freschi, Giuliana Lista, Alessandro Larcher, Luciano Dante Nava, Giorgio Guazzoni. Complications and Quality of Life After Template-assisted

Transperineal Prostate Biopsy in Patients Eligible for Focal Therapy. 2013;81(6):1291–6.
30. Bittner N, Merrick GS, Bennett A, et al. Diagnostic Performance of Initial Transperineal Template-guided Mapping Biopsy of the Prostate Gland. Am J Clin Oncol. 2013. Epub 2013/06/15.
31. Symons JL, Huo A, Yuen CL, et al. Outcomes of transperineal template-guided prostate biopsy in 409 patients. BJU Int. 2013;112(5):585–93. Epub 2013/04/05.
32. Mabjeesh NJ, Lidawi G, Chen J, German L, Matzkin H. High detection rate of significant prostate tumours in anterior zones using transperineal ultrasound-guided template saturation biopsy. BJU Int. 2012;110(7):993–7. Epub 2012/03/08.
33. Nafie S, Pal RP, Dormer JP, Khan MA. Transperineal template prostate biopsies in men with raised PSA despite two previous sets of negative TRUS-guided prostate biopsies. World J Urol. 2014;32(4):971–5. Epub 2013/12/18.
34. Ekwueme K, Simpson H, Zakhour H, Parr NJ. Transperineal template-guided saturation biopsy using a modified technique: outcome of 270 cases requiring repeat prostate biopsy. BJU Int. 2013;111(8):E365–73. Epub 2013/05/30.
35. Ayres BE, Montgomery BS, Barber NJ, et al. The role of transperineal template prostate biopsies in restaging men with prostate cancer managed by active surveillance. BJU Int. 2012;109(8):1170–6. Epub 2011/08/23.
36. Ahmed HU, Hu Y, Carter T, et al. Characterizing clinically significant prostate cancer using template prostate mapping biopsy. J Urol. 2011;186(2):458–64. Epub 2011/06/18.
37. Hu Y, Ahmed HU, Carter T, et al. A biopsy simulation study to assess the accuracy of several transrectal ultrasonography (TRUS)-biopsy strategies compared with template prostate mapping biopsies in patients who have undergone radical prostatectomy. BJU Int. 2012;110(6):812–20. Epub 2012/03/08.
38. Katz DJ, Pinochet R, Richards KA, et al. Comparison of transperineal mapping biopsy results with whole-mount radical prostatectomy pathology in patients with localized prostate cancer. Prostate Cancer. 2014;2014:781438. Epub 2014/06/06.
39. Ong WL, Weerakoon M, Huang S, et al. Transperineal biopsy prostate cancer detection in first biopsy and post-negative TRUS biopsy settings: The Victorian Transperineal Biopsy Collaboration experience. BJU Int. 2015. Epub 2015/01/07.
40. Huo AS, Hossack T, Symons JL, et al. Accuracy of primary systematic template guided transperineal biopsy of the prostate for locating prostate cancer: a comparison with radical prostatectomy specimens. J Urol. United States: Inc. Published by Elsevier Inc; 2012. p. 2044–9.
41. Nafie S, Mellon JK, Dormer JP, Khan MA. The role of transperineal template prostate biopsies in prostate cancer diagnosis in biopsy naive men with PSA less than 20 ng ml(-1.). Prostate Cancer Prostatic Dis. 2014;17(2):170–3. Epub 2014/03/05.
42. Pepe P, Dibenedetto G, Pennisi M, Fraggetta F, Colecchia M, Aragona F. Detection rate of anterior prostate cancer in 226 patients submitted to initial and repeat transperineal biopsy. Urol Int. 2014;93(2):189–92. Epub 2014/04/30.
43. Klatte T, Swietek N, Schatzl G, Waldert M. Transperineal template-guided biopsy for diagnosis of prostate cancer in patients with at least two prior negative biopsies. Wien Klin Wochenschr. 2013;125(21-22):669–73. Epub 2013/09/26.
44. Vyas L, Acher P, Kinsella J, et al. Indications, results and safety profile of transperineal sector biopsies (TPSB) of the prostate: a single centre experience of 634 cases. BJU Int. 2014;114(1):32–7. Epub 2013/09/24.
45. Gershman B, Zietman AL, Feldman AS, McDougal WS. Transperineal template-guided prostate biopsy for patients with persistently elevated PSA and multiple prior negative biopsies. Urol Oncol. 2013;31(7):1093–7. Epub 2012/02/07.
46. Krughoff K, Eid K, Phillips J, et al. The accuracy of prostate cancer localization diagnosed on transrectal ultrasound-guided biopsy compared to 3-dimensional transperineal approach. Adv Urol. 2013;2013:249080. Epub 2014/01/29.
47. Takeshita H, Numao N, Kijima T, et al. Diagnostic performance of initial transperineal 14-core prostate biopsy to detect significant cancer. Int Urol Nephrol. 2013;45(3):645–52. Epub 2013/03/27.
48. Bittner N, Merrick GS, Butler WM, Bennett A, Galbreath RW. Incidence and pathological features of prostate cancer detected on transperineal template guided mapping biopsy after negative transrectal ultrasound guided biopsy. J Urol. 2013;190(2):509–14. Epub 2013/02/19.
49. Dimmen M, Vlatkovic L, Hole K-H, Nesland JM, Brennhovd B, Axcrona K. Transperineal prostate biopsy detects significant cancer in patients with elevated prostate-specific antigen (PSA) levels and previous negative transrectal biopsies.
50. Pal RP, Elmussareh M, Chanawani M, Khan MA. The role of a standardized 36 core template-assisted transperineal prostate biopsy technique in patients with previously negative transrectal ultrasonography-guided prostate biopsies.
51. Barqawi AB, Rove KO, Gholizadeh S, O'Donnell CI, Koul H, Crawford ED. The role of 3-dimensional mapping biopsy in decision making for treatment of apparent early stage prostate cancer. J Urol. United States: Inc. Published by Elsevier Inc; 2011. p. 80–5.
52. Abdollah F, Novara G, Briganti A, et al. Trans-rectal versus transperineal saturation rebiopsy of the prostate: is there a difference in cancer detection rate? Urology. United States: 2011 Elsevier Inc; 2011. p. 921–5.

Contrast-Enhanced Ultrasound (CEUS) and Elastographic Imaging

9

T. Idzenga, Hong Truong, H. Wijkstra, A.W. Postema, M. Mischi, J.J.M.C.H. De la Rosette, and E.J. Trabulsi

Contrast-Enhanced Ultrasound (CEUS)

Ultrasound contrast agents (UCAs) are gas-filled microbubbles encapsulated in a biocompatible shell of protein, lipid, or polymer. UCAs were first introduced in 1968 by Gramiak and Shah [1]. They observed strong US echoes in blood as a result of air bubbles that were coadministered with the injection of a bolus of indocyanine green. This paragraph describes the development of UCAs, followed by various ultrasound imaging modalities that use UCAs and their application in interventional urology. Finally, we discuss the performance of these techniques in current urologic practice.

Ultrasound Contrast Agents

Ultrasound contrast agents are microbubbles in a saline solution to be administered intravenously either in the form of a bolus injection or a continuous catheter infusion into the bloodstream. UCAs pass through the smallest vessels and contribute to the detection of anatomic boundaries as well as microvasculature perfusion. Four generations of UCA have been developed. The classification of these generations is based on the ability of the UCA to pass the pulmonary capillaries and their half-life in the human body (Table 9.1). The first generation includes the early air microbubbles that were not stabilized by a shell, such as Echovist (Schering, Berlin, Germany), which was approved in Europe in the early 1990s. The second-generation agents were introduced in the mid 1990s and included the first encapsulated air bubbles, such as Albunex (Molecular Biosystems, San Diego, CA, USA) and Levovist (Schering, Berlin, Germany), whose shell was made of albumin and galactose respectively. The latest, third-generation microbubbles for ultrasound detection (including the commonly used SonoVue™, Definity™, and Sonazoid™) were composed of sulfur hexafluoride, octafluoropropane, or other perfluorocarbons encapsuled in a phospholipid, albumin, or polymer shell. The optimized use of a shell creates a strain that stabilizes bubbles against dissolution, which prolongs their half-life. These currently most frequently used UCAs have a mean diameter of 3–5 μm, approximately the size of a red blood cell. The fourth-generation UCAs are under development as a targeted contrast agent that could be used for molecular imaging and to carry genes and drugs to specific organ systems throughout the body (therapeutic UCAs).

Contrast agents are generally safe, and adverse reactions are very rarely observed [2, 3]. The main potential risks are US-induced cavitation or anaphylactic shock. The cavitation effect has been demonstrated in vitro with very high UCA concentration and acoustic power. With recommended clinical values, no significant biological effects have been observed. The components of the shell pose a risk of mostly mild allergic reactions.

CEUS Imaging Modalities

In conventional ultrasound (B-mode) imaging, UCAs produce an increase in gray-scale value, which makes blood

T. Idzenga, PhD, MSc • A.W. Postema, MD
J.J.M.C.H. De la Rosette, MD, PhD
Department of Urology, Amsterdam Medical Center, Amsterdam, The Netherlands
e-mail: t.idzenga@amc.uva.nl; a.w.postema@amc.nl; j.j.delarosette@amc.uva.nl

H. Truong, MS, MD • E.J. Trabulsi, MD
Department of Urology, Kimmel Cancer Center, Thomas Jefferson University, Philadelphia, PA, USA
e-mail: hong.truong@jefferson.edu; Edouard.Trabulsi@jefferson.edu

H. Wijkstra, PhD, MSc (✉)
Department of Urology, Amsterdam Medical Center, Amsterdam, The Netherlands

Department of Electrical Engineering, Eindhoven University of Technology, Eindhoven, The Netherlands
e-mail: h.wijkstra@amc.uva.nl

M. Mischi, PhD, MSc
Department of Electrical Engineering, Eindhoven University of Technology, Eindhoven, The Netherlands
e-mail: m.mischi@tue.nl

A.R. Rastinehad, D.N. Siegel (eds.), *Interventional Urology*, DOI 10.1007/978-3-319-23464-9_9

Table 9.1 Ultrasound contrast agents available for clinical or preclinical use

Agent	Manufacturer	Bubble size	Shell	Gas
First generation				
Echovist	Schering	8 μm	Galactose	Air
Second generation				
Albunex	Mallinckrodt	4.5 μm	Albumin	Air
Levovist	Schering	2–3 μm	Galactose	Air
Myomap	Quadrant		Albumin	Air
Quantison	Quadrant		Albumin	Air
Sonavist	Schering	2 μm	Cyanoacrylate	Air
Third generation				
Definity	Bristol-Myers Squibb	2.5 μm	Lipid	Octafluoropropane
Sonazoid	GE Healthcare	3 μm	Lipid	Perfluorocarbon
Imagent	Alliance	5 μm	Lipid	Perfluorohexane
Optison	GE Healthcare	2.25 μm	Albumin	Perfluorobutane
SonoVue	Bracco	2.5 μm	Lipid	Sulfurhexafluoride
PB 127	Point Biomedical	4.0 μm	Polymer	Nitrogen
Fourth generation				
Echogen	Sonus	2–5 μm	Colloid	Perfluoropentane
BR 55	Bracco	1.5 μm	Phospholipid	Perfluorobutane/Nitrogen

vessels appear hyperechoic. However, in small vessels the number of microbubbles is low and their signal is easily masked by that of the surrounding tissue.

Power/Color Doppler Imaging

Originally, the development of UCAs was intended to increase the amount of scatterers in the bloodstream to improve Doppler-based imaging of flow velocity in smaller vessels. With Doppler imaging, the echoes received from the moving scatterer (in this case red blood cells in the vessels) are slightly shifted in frequency with the transmitted ultrasound signal. This Doppler shift is related to the velocity of the scatterer. It is therefore possible to generate a map where the velocity and direction at each pixel is coded: color (directional) Doppler. Due to the sensitivity to motion artifacts, the Doppler signal of blood flow may be masked by that of tissue movements. Administering contrast agents to the blood flow increases the number of scatterers and, therefore, the Doppler signal. This is especially suitable for power (nondirectional) Doppler, which integrates the power from all moving scatterers.

Harmonic Imaging

Harmonic imaging exploits the nonlinear behavior of the microbubbles. When microbubbles are insonified with a certain frequency, they oscillate nonlinearly as a result of the shell structure (mechanical behavior) and the gas in the microbubble. The received signals contain multiples of the insonification frequency (so-called harmonics). Separating the harmonic part of the received ultrasound signal and processing this signal alone (either gray scale or Doppler) increases the so-called contrast-to-tissue ratio (CTR), i.e., it suppresses the tissue signal and enhances the UCA signal. Power Doppler in combination with harmonic imaging provides an effective tool for the detection of flow in the smaller vessels. For contrast-specific imaging, other frequency bands, such as subharmonics, ultraharmonics, and superharmonics, can also be used to increase the CTR [4].

Multi-pulse Imaging

The first multi-pulse imaging modality developed is the technique of pulse inversion imaging [5]. In this modality, a sequence of 2 US pulses is transmitted into the tissue. The second pulse is an inverted copy of the first. For a linear medium (e.g., biological tissue) the response to the second pulse is an inverted copy to that of the first pulse. The sum of the two responses is therefore equal to zero. For a nonlinear medium (e.g., microbubbles), the response will not be an exact inverted copy and the sum will therefore not be equal to zero. Different from harmonic imaging, which requires broadband transducers, pulse inversion can be implemented with a standard narrowband transducer. Pulse inversion is already effective at low insonating pressure (low mechanical index), which prolongs the half-life of the microbubbles and allows imaging with continuous transmission. Additional multi-pulse sequences for contrast-specific imaging are power modulation (PM) [6] and power-modulated pulse inversion (PMPI) [7], often referred to as contrast pulse sequencing (CPS). Similar to pulse inversion, CPS employs three low-power ultrasound pulses per image line with varied amplitudes and phases for transmission [7]. The received echoes from the contrast agent and the tissue are then separated using special processing algorithms. This sequence of pulses further suppresses the echoes from the tissue, thus allowing detection of small quantities of microbubbles.

Clinical Applications of CEUS in Interventional Urology

Contrast-enhanced ultrasound is a relatively new imaging technique that has found applications in several areas of interventional urology prior to treatment (diagnosis), after treatment (follow-up), and also during treatment (monitoring/guidance). The most frequent applications of CEUS are in the areas of prostate and renal disorders. Other, less frequent, applications are in the testis, the adrenal gland, and the bladder. Several procedures of utilizing the enhanced ultrasound signal from the contrast agents are in use. The first procedure is destruction-replenishment, a method during which all microbubbles within the ultrasound field are destroyed using acoustic pulses of high mechanical index. After destruction, the replenishment of the tissue with new microbubbles is monitored (Fig. 9.1a). This enables estimation of blood flow velocity and blood volume assuming a continuous infusion of microbubbles [8]. Another procedure is that of maximum intensity projection (MIP) imaging, a procedure in which the maximum intensity at each pixel is continuously mapped during perfusion of the tissue (see Fig. 9.1b). With this approach, each pixel value represents the maximum intensity at that pixel in the imaged area, which enables mapping the vessel trajectory. The third procedure consists of analyzing the intensity in a specific region of interest (ROI) as a function of time from the UCA wash in to the wash out; it is referred to as time intensity curve (TIC) analysis [9]. This technique enables assessment of blood volume and blood flow velocity in the investigated ROI [10]. A recently developed procedure uses these TICs to derive the dispersion of UCAs in the prostatic microvasculature [11], (Fig. 9.2). The dispersion kinetics is thought to reflect aspects of angiogenesis, such as microvessel density (MVD) and tortuosity of the microvessels. CEUS has shown to be a very attractive imaging technique and shows high potential in application prior to treatment, during treatment, and as follow-up after treatment in the field of interventional urology.

Prostate Diseases

Prostatitis, benign prostatic hyperplasia, and prostate cancer (PCa) are the three most common types of prostate diseases. In the area of prostate diseases, CEUS has been mainly applied in the diagnosis of PCa by transrectal ultrasound (TRUS). In 1997, Ragde et al. [12] proposed the combination of color Doppler sonography with the admission of a contrast agent (EchoGen™) for improved imaging of the prostate circulation. They found a clear enhancement of the blood vessels in the prostate and suggested that this might lead to more accurate identification of malignant lesions. This was the first technique used to study the microvasculature of the prostate for cancer detection, and the initial findings were confirmed in various studies [13–15]. The technique made it possible to image the neovasculature (angiogenesis) that supplies the (growing) tumor. It opened the door toward early detection of the aggressive prostate carcinoma. In 2005, Halpern et al. [16] introduced the technique of harmonic imaging for enhancement of the blood flow in the prostate. This technique already showed potential in assessing tumors/metastasis in the human liver [17] and perfusion of the myocardium [18]. In the following years, harmonic imaging has shown its value in various studies [19,

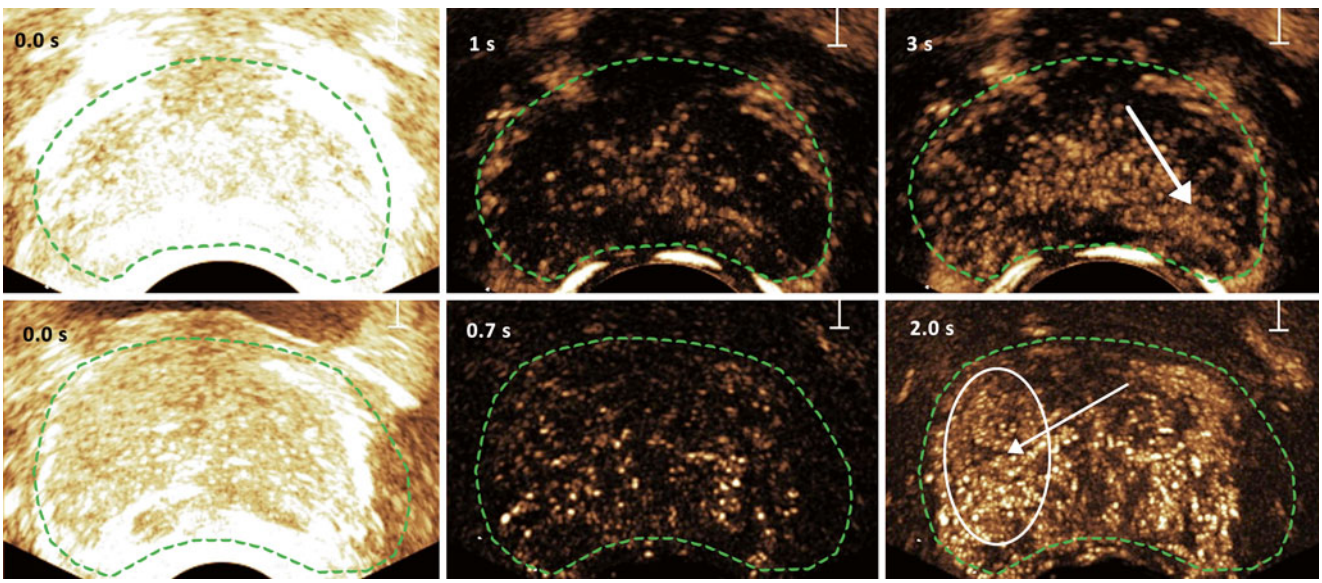

Fig. 9.1 Destruction and replenishment (*top*) and maximum intensity projection (*bottom*) imaging of microbubbles in the prostate. At 0 s all microbubbles present are destroyed by a strong acoustic pulse. The suspected areas (confirmed by histology) are indicated with an *arrow* in the right images

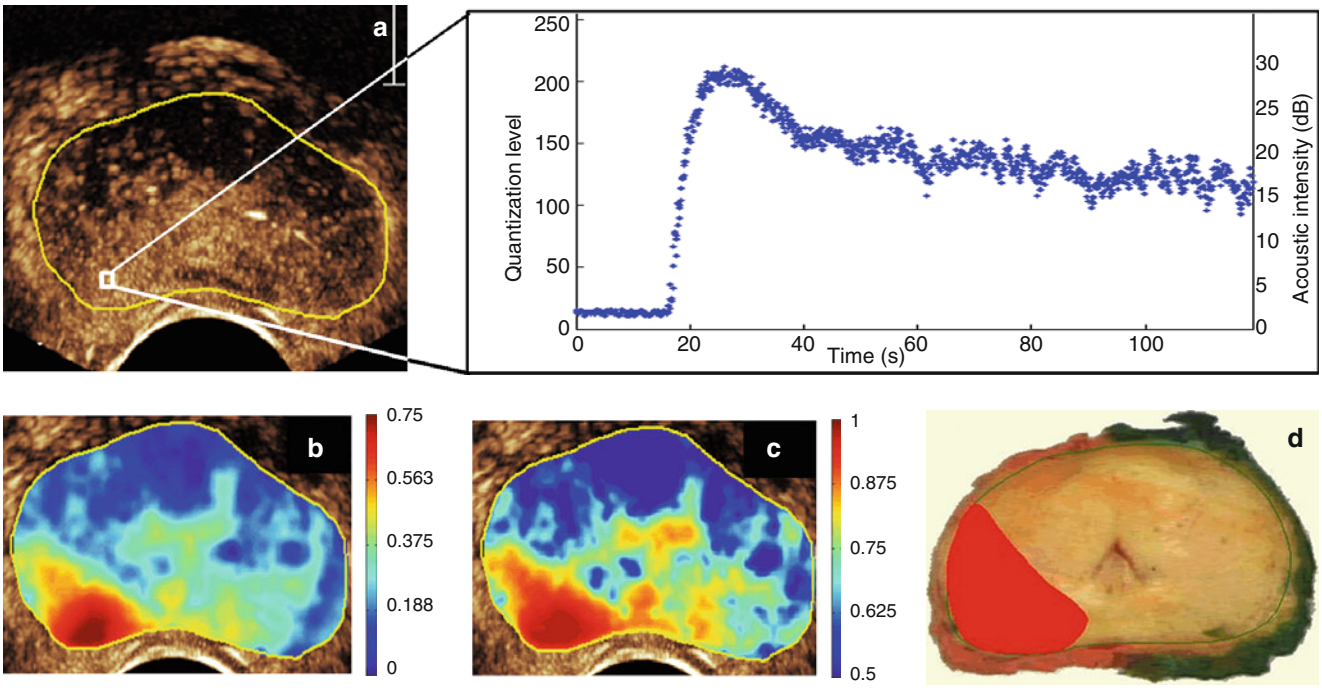

Fig. 9.2 Contrast-ultrasound dispersion imaging (CUDI) of the prostate based on coherence analysis of the TICs (**a**), dispersion-related time-intensity curve parameter κ (**b**), and coherence analysis (**c**). The corresponding histology slice of the excised prostate with carcinoma marked in *red* is shown in (**d**)

20]. The dispersion kinetics of UCAs in the microvasculature is hypothesized to reflect the underlying vessel architecture and therefore highlight the changes related to cancer angiogenesis [11, 21, 22].

Following the detection of PCa, treatments such as radical prostatectomy, HIFU, and cryotherapy can be used. In the follow-up on the treatments, CEUS is a potential candidate for assessing the treatment effect [23]. CEUS has been applied as a noninvasive method to assess the anastomotic leakage after radical prostatectomy [24, 25]. Sedelaar et al. used CEUS to measure the volume of the affected tissue after HIFU treatment [26]. The latter study was based on the lack of perfusion in the tissue affected by HIFU treatment.

Renal Disorders

One of the first publications on the application of CEUS in the kidney is by Brown et al. [27]. They assessed the utility of an intravenous contrast agent for visualization of visceral perfusion before and after segmental infarction in a canine model and found that the use of a contrast agent improved the evaluation of visceral ischemia. Following this publication, CEUS has been applied in diagnosing renal disorders, such as the detection and characterization of renal masses/cysts [28–31], renal artery stenosis [32, 33], and renal trauma [34] (Fig. 9.3). CEUS has been applied as a guidance/monitoring tool during radiofrequency ablation procedures [35] and the placement of renal allografts [36]. CEUS has also been used in the follow-up of treatments such as radiofrequency ablation [37] and cryoablation [38] and assessing the function of renal allografts [39, 40] after transplantation. In the follow-up after treatment of renal masses and the assessment of the renal allografts, the results were based on perfusion of the renal microvasculature. In the cases of ablation, non-perfusion of the ablated area indicated a successful treatment, whereas in the allografts a successful transplantation was indicated by perfusion of the renal tissue.

Other Disorders

Other areas of interventional urology where CEUS has been applied are noninvasive detection of bladder carcinoma [41] and differentiation between low- and high-grade bladder carcinoma [42], the assessment of testicular lesions [43], and assessment of female urethral vascularization [44] and diverticulum [45].

Performance of CEUS in Urologic Practice

The most common application of CEUS in urologic surgery is the detection of PCa. When the visualization of prostate adenocarcinoma improves, biopsy can be targeted more precisely with the goal of improving, if not replacing, random biopsy. The reported cancer detection rates of targeted CEUS biopsy ranged from 24.4 to 35 % [16, 46, 47]. Individual targeted CEUS cores were at least twice as likely cancer (OR = 2.0–3.1, $p < 0.001$) [16, 46, 47]. However, the cancer

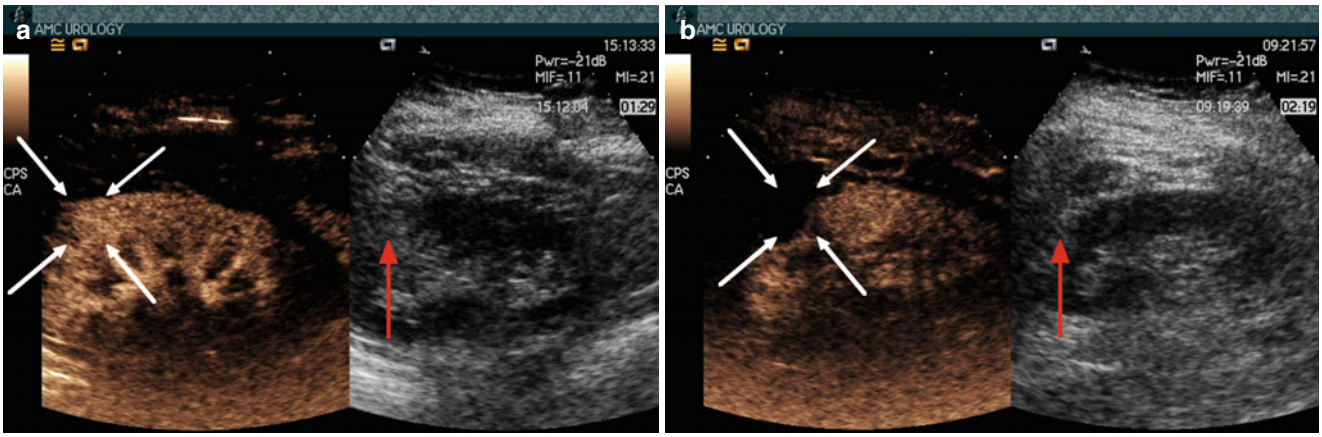

Fig. 9.3 (**a**) Contrast-enhanced US demonstrating hypervascularity of mass (*white arrows*) compared with normal renal cortex before cryotherapy. (**b**) Contrast-enhanced US at 2 weeks after cryoablation demonstrating lack of flow in the tumor (*white arrows*), consistent with successful cryoablation. The adjacent gray-scale images, however, are very similar (*red arrow*)

detection rates of targeted CEUS biopsy alone versus that of systematic sextant biopsy are not significantly different. CEUS alone missed 5–20 % of cancers that were diagnosed on standard sextant biopsy [16, 46, 47].

Several studies have shown that CEUS detects more and clinically significant cancers than standard biopsy. Mitterberger et al. evaluated systematic TRUS biopsy versus CEUS-targeted biopsy for the impact of Gleason grading [48]. They found that Gleason score detected by targeted CEUS cores was higher (mean Gleason score of 6.8) compared to those detected by standard biopsy (mean Gleason score of 5.4). Likewise, the targeted CEUS cores detected higher volume disease, involving ≥50 % core [15]. Roy et al. compared the diagnostic efficiency of CEUS for prostate cancer detection. They found that CEUS improves the sensitivity from 54 to 93 % without compromising the specificity of TRUS biopsy [15].

One significant drawback of CEUS is its poor discriminatory ability for PCa, ROC < 0.65, suggesting that CEUS imaging cannot adequately discriminate benign from malignant areas on prostate US [49]. Overall, even though targeted CEUS prostate biopsy improves the detection rate and diagnostic efficiency of PCa, it should only be used as an adjunct rather than replacement for standard systematic biopsy, even when abnormal vascularity targets are visualized in the prostate.

The renal application of CEUS in the differentiation of surgical versus nonsurgical cystic masses has also been investigated. Ascenti et al. compared the accuracy of CEUS with that of CT in the diagnosis of 31 patients with cystic renal masses. They found that CEUS and CT have similar accuracy (82 %) for diagnosis of malignant renal mass but CEUS is inferior to CT in the diagnosis of benign lesions, 75 % with CEUS and 100 % with CT [50]. Park et al. found CEUS upgraded the Bosniak classification in 26 % of cystic renal lesions [31]. CEUS was shown to be better in solid component in complex renal cysts than CT by providing better visualization of septa number and thickness.

Studies of CEUS in the diagnosis of cystic renal masses have revealed promising future possibilities for the technology. However, at this point, the accuracy of CT is still superior to that of CEUS because CEUS is operator dependent and influenced by lesion location. When there is a contraindication to iodinated contrast or gadolinium, due to renal insufficiency or allergy, CEUS of renal lesions can be helpful to better characterize complex renal masses on initial or follow-up sonographic evaluation.

Elastography

The term elastography has been coined by Ophir et al. in 1991 [51]. They described a new technique for quantitative imaging of stiffness in soft tissues. Elastography is based on the principle that soft tissue deforms more than hard tissue when a force is applied (stress). The change in size and shape (strain) of tissue as a result of the applied force yields an indication of the tissue elasticity. Elasticity of biological tissue is quantified in the Young's Modulus E (defined as stress/strain) in units of Pascal (Pa). To measure the strain in the tissue, a registration is made before and after the application of stress. From comparison of the pre- and post-deformation registration, local tissue displacements are estimated and strains are derived from these displacements resulting in strain images or elastograms. Lesions in biological tissue can then be identified from elastograms as regions with different strain or stiffness values [52]. This paragraph describes the various techniques of elastographic imaging and their application in interventional urology. Finally, we discuss the performance of these techniques in current urologic practice.

Techniques of Elastographic Imaging

The first step in elastographic imaging is deformation of the tissue by applying a stress to the tissue, either the result of a physiological force (e.g., the contraction of the cardiac muscle), an external applied force (e.g., the ultrasound probe pressing on the tissue), or an acoustic force (acoustic radiation force imaging: ARFI). The second step is estimating the tissue deformation resulting from the applied force. This can be done using ultrasound (US) or magnetic resonance imaging (MRI) and is generally referred to as deformation/strain imaging. When the applied stress is known and the resulting strain in the tissue is estimated, the Young's modulus of the tissue can be derived: elastographic imaging.

Physiological Deformation

One approach to deforming tissue is that of physiological processes that lead to deformation. An example is that of contraction of the cardiac muscle during the heart cycle. Using US imaging the resulting deformations and strain in the muscle can be estimated. Part of the cardiac muscle that is necrotic because they have been deprived from oxygen for a longer period of time (prolonged ischemia) will be hypokinetic (not contracting), showing poor or no strain. Since the stress applied by the physiological processes is generally not known, we need to rely on strain imaging to assess defects/dysfunction.

(Freehand) Quasi-Static Elastography

With the quasi-static displacement approach, an external force is applied to the tissue, e.g., by the transducer. This can be performed mechanically or manually (freehand). The force is applied for a certain amount of time to ensure that the tissue has reached a new quasi-static state. Displacements of the tissue between this new stabilized state and the previous (original) state are then estimated from the acquired ultrasound images (Fig. 9.4). In general, strain is estimated in the axial direction (along the ultrasound beam). In this direction, the strain estimation is more accurate and robust than in the lateral and elevational direction (both orthogonal to the ultrasound beam). Quasi-static elastography techniques have been implemented by a number of manufacturers such as General Electric (USA), Hitachi (Japan), Philips (The Netherlands), Siemens (Germany), and Toshiba (Japan) and have become commercially available on ultrasound systems in the clinical areas of breast, prostate, and thyroid imaging.

Acoustic Radiation Force Impulse (ARFI) Imaging

Acoustic radiation force impulse (ARFI) imaging is a third approach to elastographic imaging. With this technique, short-duration acoustic radiation forces (pushing pulses) are used to induce very local deformation of tissue and the recoil of the tissue is observed with ultrasound (tracking pulses) [53]. An ARFI imaging sequence usually consists of the transmission of one or more pushing pulses to deform the tissue, which is followed by a sequence of tracking pulses. Windowed cross-correlation of these tracking pulses is then used to estimate the displacements in the tissue. This process is repeated at different positions in the tissue to construct a spatial displacement map. This approach distinguishes itself by the highly localized forcing functions and

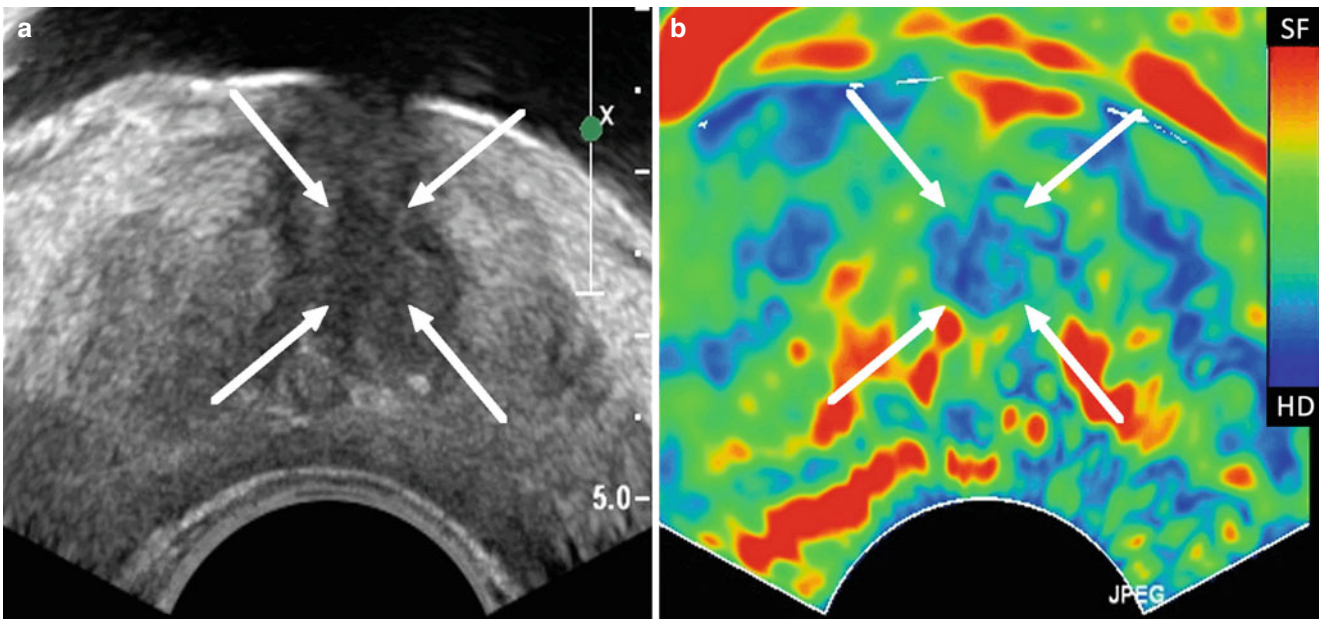

Fig. 9.4 Quasi-static transrectal ultrasound elastography of the prostate. The gray-scale TRUS image is shown in (**a**) and the corresponding elastogram in (**b**) with *blue* representing stiff tissue and *red* soft tissue. The suspected area is indicated on the gray-scale TRUS image and on the elastogram by *white arrows*. The suspected area was confirmed by biopsy as cancerous region (Gleason's score 3 + 4)

displacement profiles. A disadvantage of ARFI, however, is heating of the tissue as a consequence of the pushing pulses, which places a limit on the resulting displacements [54]. This technique has been implemented clinically by Siemens (Germany) in the form of "Virtual Touch® Tissue Imaging" and "Virtual Touch Tissue Quantification."

Vibro-Acoustography

Vibro-acoustography is a variant of acoustic radiation force imaging. The foci of two pushing pulses are placed in such a way that the ultrasound beams coincide at a crossover point within the tissue (Fig. 9.5). The two beams have slightly different frequencies (typically 25 kHz) to make the tissue in the focal region fluctuate at this beat frequency. The surrounding tissue in one beam or the other will however not fluctuate. The amplitude of the fluctuation depends on the local stiffness. With an external hydrophone, the acoustic emission at the beat frequency can be detected and used to create a spatial stiffness map when the focal point is moved in a two-dimensional plane. Vibro-acoustography is very sensitive and can measure displacements as small as a few nanometers, whereas other techniques require displacements in the order of micrometers. This technique is implemented on a GE Vivid 7 system [56].

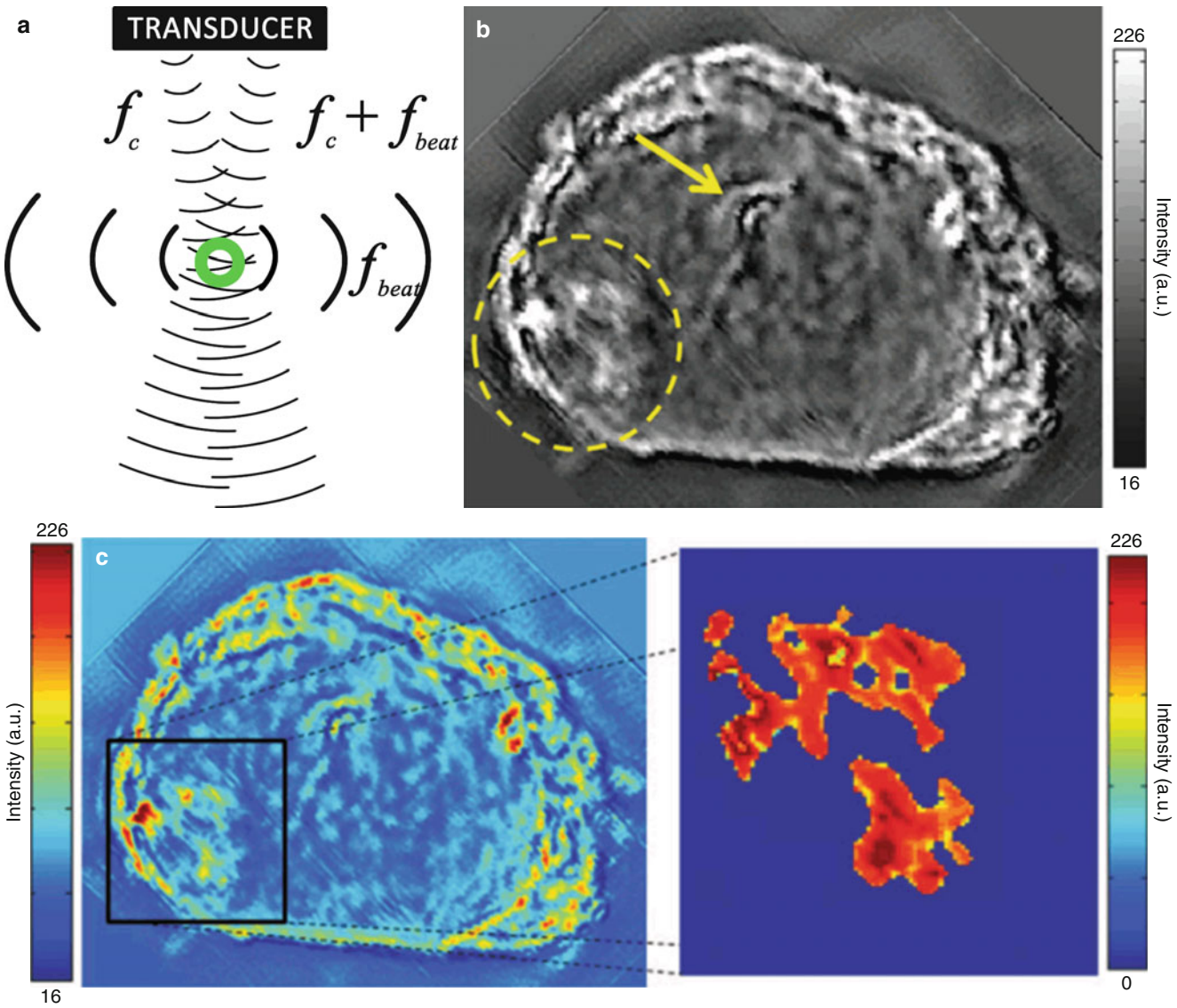

Fig. 9.5 Schematic illustration of the principle of vibro-acoustography (**a**) and a gray-scale vibro-acoustographic (VA) image of the axial section of an excised prostate (**b**). The VA image clearly shows the prostate anatomy, including the urethra (*arrow*) and a malignant lesion with bright and coarse texture in the peripheral zone (*dashed circle*). (**b**) The colored VA image and the selected ROI for classification process. (**c**) The selected ROI after threshold-based processing and boundary removal that identifies the lesion (From Alizad et al. [55], with permission)

Transient Elastography

Transient elastography utilizes a low-frequency short-pulsed excitation to excite the tissue of interest [57]. The mechanical stimulation causes the propagation of a low-frequency shear wave in the tissue with a velocity related to the tissue stiffness. The velocity at which the shear wave travels through tissue can be measured using an ultrasound pulse-echo mode. A spatial stiffness map can then be derived from the estimated propagation speed of the shear wave (Fig. 9.6). A current commercially available implementation of transient elastography is the Fibroscan® system produced by Echosens (France). The Fibroscan® is originally designed for use in the assessment of liver fibrosis by quantifying liver stiffness.

Shear Wave Elastography

Shear wave elastography (SWE) is a technique that does not require compression of the prostatic tissue as with quasi-static elastography. Quasi-plane shear waves are created by successfully focusing a pushing beam at different depths (Fig. 9.7). The resulting shear waves at each depth constructively create two quasi-planar shear waves that propagate in opposite directions. The propagation of these shear waves is then imaged at high frame rates in the order of kilohertz. The propagation speed of the shear waves are related to the local elastic properties. With shear wave elastography quantitative elasticity (expressed by the Young's modulus), maps of the tissue can be constructed in a few milliseconds. A major advantage of SWE is in that no pressure needs to be applied by the operator for inducing deformation of the tissue. This technique, however, requires an ultrasound scanner that can achieve high frame rates. This technique has been implemented by Supersonic Imagine (France) in their Aixplorer 3D UltraFast® ultrasound system.

Clinical Applications of Elastography in Interventional Urology

Ultrasound elastography is an imaging technique that has found applications in interventional urology prior to treatment (diagnosis), during treatment (monitoring), and after treatment (follow-up). The most frequent applications of elastography are in the areas of prostate and renal disorders.

Prostate Diseases

The first publications on elastic properties of the prostate for diagnosing PCa are from the University of Rochester [61, 62]. This is also the main application of elastography in prostate diseases. The techniques that are mainly used in the detection of PCa are quasi-static elastography prior to systematic biopsy [63], quasi-static elastography-targeted biopsies [64], and shear wave elastography prior to biopsy [65]. With quasi-static elastography, deformation of the prostate tissue is generally performed by a slight compression and decompression of the prostate. This is executed manually by

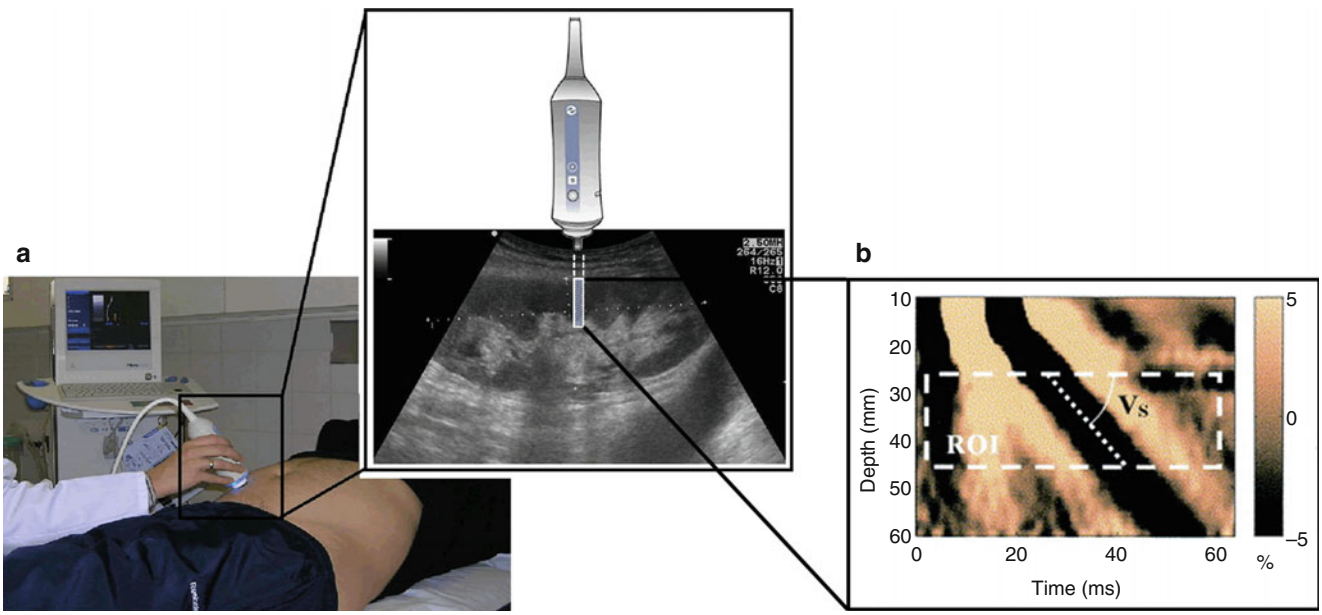

Fig. 9.6 Schematic illustration of applying transient elastography on assessment of lesions in the liver (**a**) and an example of a shear wave elastogram (**b**) (From Arndt et al. [58] and Sandrin et al. [59], with permission)

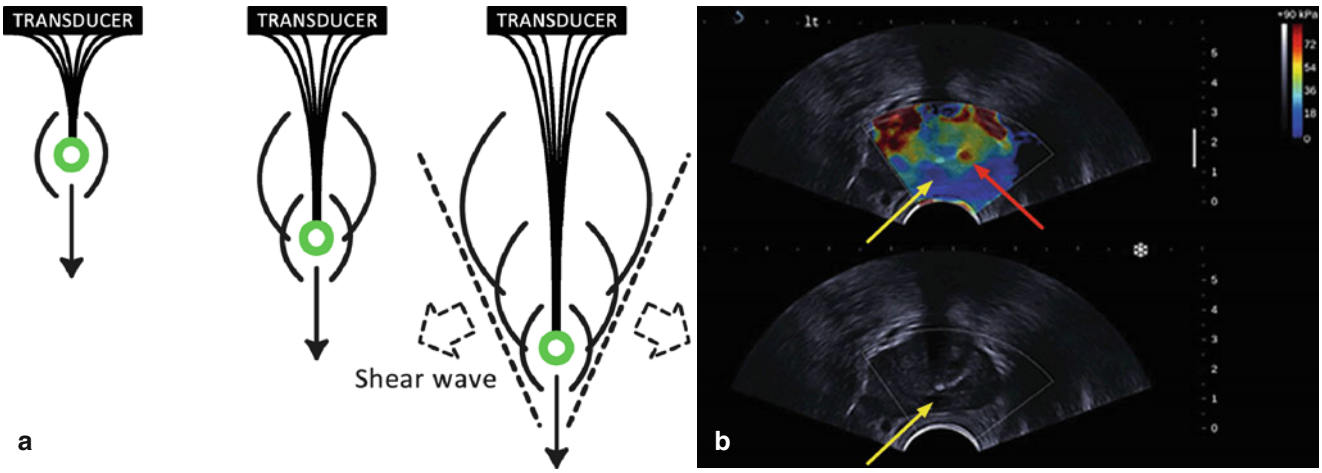

Fig. 9.7 (**a**) Schematic representation of the physical principles of shear wave generation in biological tissue. (**b**) Comparison of ultrasound and SWE. This patient presented with a hypoechoic nodule on ultrasound (black lesion with *arrow*). Shear wave elastography was preformed, and the nodule was found to be of low stiffness (G20 kPa). Note the *blue area* with a *yellow arrow*. However, another lesion was found with a high stiffness (75 kPa) and was found on biopsy to be PC with Gleason grade 7. Note the red lesion with a *red arrow* (From Barr et al. [60], with permission)

a physician using the tip of the transrectal ultrasound (TRUS) probe. The force that is applied to the prostate is then adjusted according to a visual indicator for compression on the ultrasound system. Another approach is the placement of a water-filled balloon between the probe and the rectal wall to improve the homogeneity of the deformation [66]. With shear wave elastography, no pressure needs to be applied to the prostate. For each acquisition plane, the transducer only needs to be maintained at a steady position for 2 to 4 s in order to stabilize the signals. The commercial ultrasound systems that are equipped with these techniques usually display the strain values (quasi-static elastography), the shear wave speed, or Young's modulus (both shear wave elastography) either in a color-coded overlay mode or a dual-view mode (Fig. 9.8). Another elastographic technique, vibro-acoustography, is applied to (3D) segmentation of the prostate, e.g., to aid intraoperatively in placement of the seeds for brachytherapy [68]. Another application of vibro-acoustography is the assessment of cryotherapy on the prostate [69].

Renal Disorders

In 1995, Emelianov et al. [70] published their hypothesis on elasticity imaging for early detection of renal pathology. In an in vitro animal model of nephritis, they have shown that the renal elastic properties change with renal damage. Since that publication, elastographic imaging has been applied to assess elastic properties of the kidney, degree of fibrosis in renal allografts, detection of renal carcinoma, and chronic kidney disease [71] (Fig. 9.9). In these studies, various elastographic imaging techniques have been used. In the first in vitro experiments, mainly quasi-static elastography was used [72]. Later on with in vivo experiments, acoustic radiation force impulse (ARFI) imaging [73], shear wave elastography [74], vibro-acoustography [75], and transient elastography [76] were used. The elastographic technique ARFI and shear wave elastography appear as the most appropriate techniques for assessment of the kidney elastic properties. Some caution with these techniques is however required. Syversveen et al. [77] showed that measurements of shear wave velocity using ARFI is depending on the pressure that is applied by the transducer. Furthermore, Gennisson et al. [78] showed that shear wave elastography is influenced by the blood perfusion and the urinary pressure in the kidney. Furthermore, shear wave velocity in the kidney showed an age dependency [79] and could possibly be used to identify chronic kidney disease [80]. Clevert et al. [81] actually used in their study on assessment of renal tumors of unknown etiology a combination of contrast-enhanced ultrasound and elastography. Their conclusion was that ARFI imaging improved the visualization of unclear renal masses as compared to B-mode ultrasound. Furthermore, contrast-enhanced ultrasound imaging allowed an early evaluation of renal masses.

Other Disorders

Other areas in interventional urology where elastography has been applied are, e.g., the assessment of testicular lesions [82] and bladder neck compliance [83]. In a pilot study Idzenga et al. monitored contractions of the detrusor muscle at the onset of voiding [84]. They estimated deformation of the detrusor, correlated these findings with the simultaneously recorded detrusor pressure, and found a significant correlation between deformation and pressure.

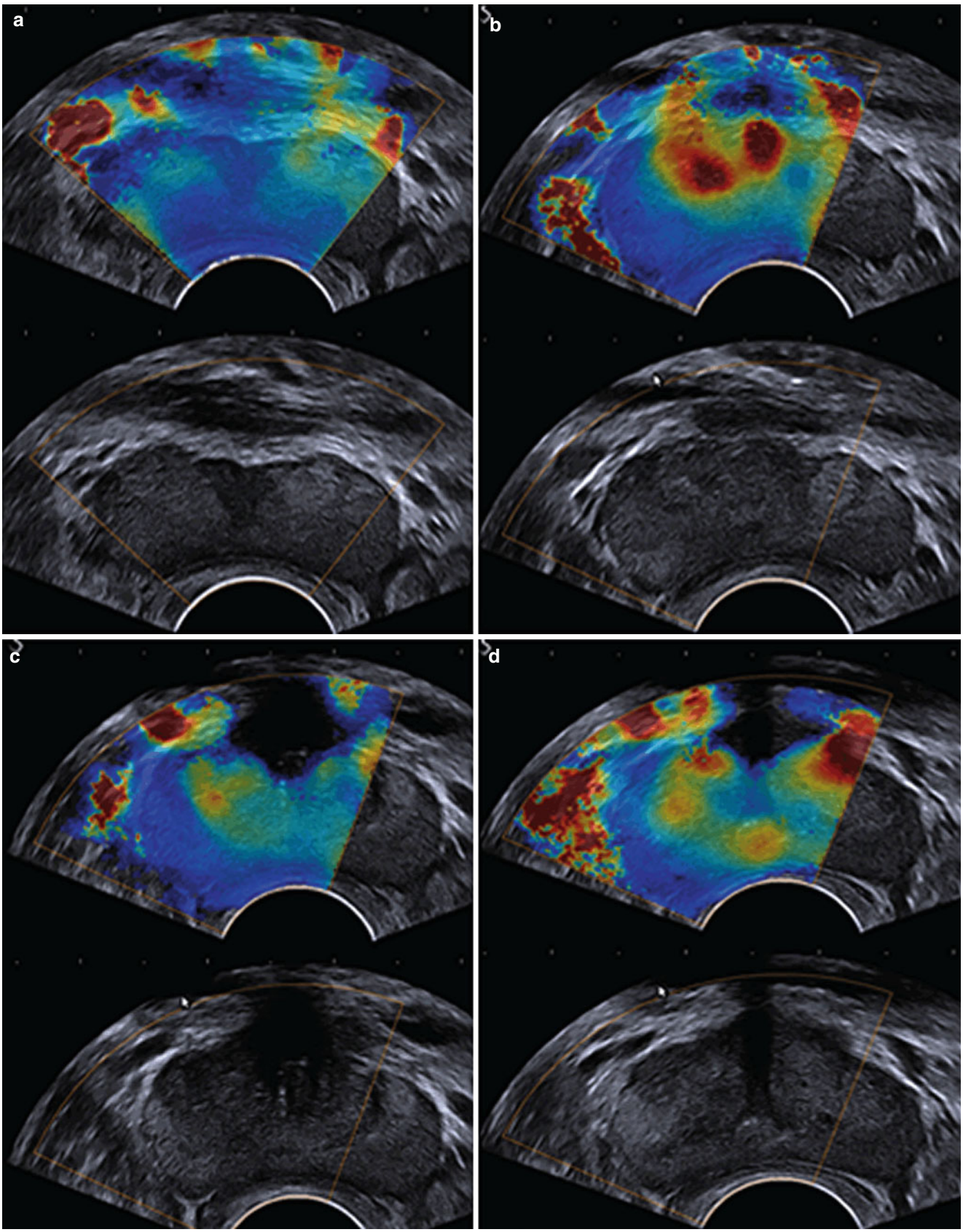

Fig. 9.8 A 32-year-old man, infertility, presenting with early benign prostate hypertrophy. Shear wave elastography with sections from the base to the apex (**a**–**d**) shows a very homogeneous and very soft peripheral zone, coded in blue, with mean elastography values below 10 kPa (the elasticity scale varies from 0 to 70 kPa). The central and transitional zones are already heterogeneous and contain nodules with increased hardness (From Correas et al. [67], with permission)

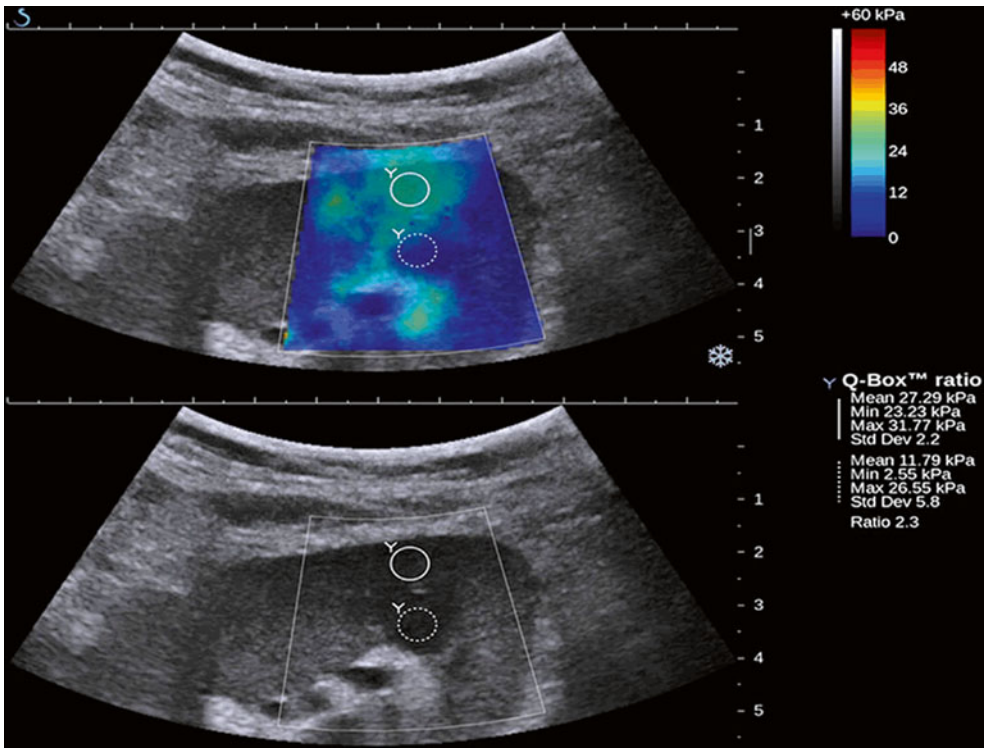

Fig. 9.9 Example of quantitative elasticity map of the lower pole of a kidney transplant. The regions of interest are positioned in the cortex (*open circle*) and the medulla (*dashed circle*) using the B-mode image. The color map is a distribution of elasticity values scaled from 0 to 60 kPa and calculated from shear wave velocity values using Young's modulus (From Grenier et al. [72], with permission)

Performance of Elastography in Urologic Practice

The main application of real-time sonoelastrography in urologic surgery is in the detection of PCa as an adjunct to TRUS prostate biopsy. Konig et al. reported that targeted sextant biopsies in 404 patients enhanced the PCa detection rate to 84.1 % from just 64.2 % in standard systematic biopsy [85]. Pallwein et al. conducted the largest prospective study in 2007 to determine whether a targeted elastography biopsy of the prostate would detect PCa as well as standard systematic TRUS biopsy. They found a combined cancer detection rate of 35 % in men undergoing both standard biopsy and targeted elastography biopsy, including 30 % by targeted elastography biopsy and 25 % by standard biopsy, though the difference is not statistically significant [63]. The contribution of elastography to PCa detection is in its enhanced diagnostic efficacy; elastography-targeted biopsy in a patient with PCa was 1.8- to 2.9-fold more likely to detect PCa than standard biopsy [63, 86].

In Pallwein and colleagues' studies comparing targeted elastography biopsy and standard TRUS biopsy, they found elastography has an overall sensitivity of 86 %, specificity of 72 %, and negative predictive value of 91.4 % [63, 87]. However, in a different study by Salomon et al. that investigated the performance of sonoelastography in a cohort of 109 patients undergoing radical prostatectomy, they reported 75 % sensitivity, 77 % specificity, 88 % positive predictive value, 59 % negative predictive value, and overall accuracy of 77 % [88]. The analysis by outer prostatic gland area revealed the best sensitivity for PCa detection at the apex (79–100 %) and mid-gland (94 %) [63]. Elastography yielded most false-negative biopsies of tumor located at the base of the prostate.

Junker et al. recently published a study that compared PCa detection rate of sonoelastography and multiparametric MRI in a cohort of 39 patients with biopsy-proven PCa who underwent radical prostatectomy. They found multiparametric MRI have better diagnostic performance compared to sonoelastography in both peripheral zone (90 % vs. 78 %, $p<0.05$) and more significantly transition zone (90 % vs. 18.2 %, $p<0.05$) [89]. In addition, volumetric measurements of PCa lesion were more reliable with T2-weighted MRI than with sonoelastography (Spearman rank correlation, 0.72 vs. 0.46) [89]. There were some preliminary studies, which compared the utility of elastography versus endorectal MRI in identifying extracapsular extension and seminal vesical invasion [90, 91]. Even though the initial data showed elastography may be comparable to endorectal MRI in predicting extracapsular extension of PCa, these results were not formally published. Endorectal MRI remains the image of choice for predicting extracapsular extension.

The main limitations of elastography are its user dependence and interobserver variability. In addition, elastography alone has been reported to miss a significant number of cancer foci. Elastography in conjunction with standard TRUS biopsy enhances the detection rate and diagnostic efficiency for PCa. More studies need to be done to determine the

adjunctive role of elastography to standard TRUS and whether elastography alone can add more useful preoperative risk stratification for men who need to undergo definitive treatment for PCa.

Conclusion

Enhanced ultrasound modalities utilizing contrast enhancement and sonoelastography represent novel techniques in the evaluation of the prostate and kidney in urology. For prostate evaluation, these techniques are a rational investigation of the well-demonstrated vascular alterations of prostate cancer foci with abnormal microvessel density and increased cellularity and tissue density, representing a clear mechanism for accurate targeting of these lesions. There are multiple putative benefits of enhanced ultrasound modalities, including improved targeting for prostate biopsy; improved characterization of suspicious renal masses, especially when contrast-enhanced axial imaging (CT or MRI) are contraindicated; and lower cost than CT or MRI. Further investigations and refinements are necessary to define the role of these techniques in current urologic practice.

References

1. Gramiak R, Shah PM. Echocardiography of the aortic root. Invest Radiol. 1968;3(5):356–66.
2. Main ML, Goldman JH, Grayburn PA. Ultrasound contrast agents: balancing safety versus efficacy. Expert Opin Drug Saf. 2009;8(1):49–56.
3. Piscaglia F, et al. Knowledge of the bio-effects of ultrasound among physicians performing clinical ultrasonography: Results of a survey conducted by the Italian Society for Ultrasound in Medicine and Biology (SIUMB). J Ultrasound. 2009;12(1):6–11.
4. Frinking PJ, et al. Ultrasound contrast imaging: current and new potential methods. Ultrasound Med Biol. 2000;26(6):965–75.
5. Simpson DH, Chin CT, Burns PN. Pulse inversion Doppler: a new method for detecting nonlinear echoes from microbubble contrast agents. IEEE Trans Ultrason Ferroelectr Freq Control. 1999;46(2):372–82.
6. Mor-Avi V, et al. Combined assessment of myocardial perfusion and regional left ventricular function by analysis of contrast-enhanced power modulation images. Circulation. 2001;104(3):352–7.
7. Phillips P, Gardner E. Contrast-agent detection and quantification. Eur Radiol. 2004;14 Suppl 8:P4–10.
8. Wei K, et al. Quantification of myocardial blood flow with ultrasound-induced destruction of microbubbles administered as a constant venous infusion. Circulation. 1998;97(5):473–83.
9. Eckersley RJ, et al. Quantitative microbubble enhanced transrectal ultrasound as a tool for monitoring hormonal treatment of prostate carcinoma. Prostate. 2002;51(4):256–67.
10. Greis C. Quantitative evaluation of microvascular blood flow by contrast-enhanced ultrasound (CEUS). Clin Hemorheol Microcirc. 2011;49(1–4):137–49.
11. Mischi M, Kuenen MP, Wijkstra H. Angiogenesis imaging by spatiotemporal analysis of ultrasound contrast agent dispersion kinetics. IEEE Trans Ultrason Ferroelectr Freq Control. 2012;59(4):621–9.
12. Ragde H, et al. Transrectal ultrasound microbubble contrast angiography of the prostate. Prostate. 1997;32(4):279–83.
13. Sedelaar JP, et al. Microvessel density: correlation between contrast ultrasonography and histology of prostate cancer. Eur Urol. 2001;40(3):285–93.
14. Bogers HA, et al. Contrast-enhanced three-dimensional power Doppler angiography of the human prostate: correlation with biopsy outcome. Urology. 1999;54(1):97–104.
15. Roy C, et al. Contrast enhanced color Doppler endorectal sonography of prostate: efficiency for detecting peripheral zone tumors and role for biopsy procedure. J Urol. 2003;170(1):69–72.
16. Halpern EJ, et al. Detection of prostate carcinoma with contrast-enhanced sonography using intermittent harmonic imaging. Cancer. 2005;104(11):2373–83.
17. Kono Y, et al. Gray scale second harmonic imaging of the liver: a preliminary animal study. Ultrasound Med Biol. 1997;23(5):719–26.
18. Becher H, et al. Harmonic power Doppler contrast echocardiography: preliminary clinical results. Echocardiography. 1997;14(6 Pt 1):637.
19. Halpern EJ. Contrast-enhanced ultrasound imaging of prostate cancer. Rev Urol. 2006;8 Suppl 1:S29–37.
20. Russo G, et al. Angiogenesis in prostate cancer: onset, progression and imaging. BJU Int. 2012;110(11 Pt C):E794–808.
21. Kuenen MP, et al. Spatiotemporal correlation of ultrasound contrast agent dilution curves for angiogenesis localization by dispersion imaging. IEEE Trans Ultrason Ferroelectr Freq Control. 2013;60(12):2665–9.
22. Kuenen MP, et al. Contrast-ultrasound dispersion imaging for prostate cancer localization by improved spatiotemporal similarity analysis. Ultrasound Med Biol. 2013;39(9):1631–41.
23. Wondergem N, De La Rosette JJ. HIFU and cryoablation – non or minimal touch techniques for the treatment of prostate cancer. Is there a role for contrast enhanced ultrasound? Minim Invasive Ther Allied Technol. 2007;16(1):22–30.
24. Schoeppler GM, et al. Detection of urinary leakage after radical retropubic prostatectomy by contrast enhanced ultrasound – do we still need conventional retrograde cystography? BJU Int. 2010;106(11):1632–7.
25. De Stefani S, et al. Transrectal contrast-enhanced (Levovist) ultrasonography in evaluation of urinary leakage after radical prostatectomy: a preliminary report. Urology. 2005;66(4):871–3.
26. Sedelaar JP, et al. The application of three-dimensional contrast-enhanced ultrasound to measure volume of affected tissue after HIFU treatment for localized prostate cancer. Eur Urol. 2000;37(5):559–68.
27. Brown JM, et al. Contrast enhanced sonography of visceral perfusion defects in dogs. J Ultrasound Med. 1997;16(7):493–9.
28. Houtzager S, et al. Evaluation of renal masses with contrast-enhanced ultrasound. Curr Urol Rep. 2013;14(2):116–23.
29. Xu ZF, et al. Renal cell carcinoma and renal angiomyolipoma: differential diagnosis with real-time contrast-enhanced ultrasonography. J Ultrasound Med. 2010;29(5):709–17.
30. Aoki S, et al. Contrast-enhanced ultrasound using a time-intensity curve for the diagnosis of renal cell carcinoma. BJU Int. 2011;108(3):349–54.
31. Park BK, et al. Assessment of cystic renal masses based on Bosniak classification: comparison of CT and contrast-enhanced US. Eur J Radiol. 2007;61(2):310–4.
32. Grzelak P, et al. Detection of transplant renal artery stenosis in the early postoperative period with analysis of parenchymal perfusion with ultrasound contrast agent. Ann Transplant. 2013;18:187–94.
33. Eriksson P, et al. Non-invasive investigations of potential renal artery stenosis in renal insufficiency. Nephrol Dial Transplant. 2010;25(11):3607–14.
34. Valentino M, et al. Contrast-enhanced ultrasonography in blunt abdominal trauma: considerations after 5 years of experience. Radiol Med. 2009;114(7):1080–93.

35. Zhao X, et al. Improved outcome of percutaneous radiofrequency ablation in renal cell carcinoma: a retrospective study of intraoperative contrast-enhanced ultrasonography in 73 patients. Abdom Imaging. 2012;37(5):885–91.
36. Ferramosca E, et al. Ultrasound-guided trans-hepatic embolization of a renal artery pseudoaneurysm in a patient with acquired solitary kidney and with chronic renal failure secondary to phenacetin abuse. J Ultrasound. 2014;17(1):65–9.
37. Meloni MF, et al. Follow-up after percutaneous radiofrequency ablation of renal cell carcinoma: contrast-enhanced sonography versus contrast-enhanced CT or MRI. AJR Am J Roentgenol. 2008;191(4):1233–8.
38. Barwari K, et al. Contrast-enhanced ultrasound for the evaluation of the cryolesion after laparoscopic renal cryoablation: an initial report. J Endourol. 2013;27(4):402–7.
39. Rennert J, et al. Identification of early complications following pancreas and renal transplantation using contrast enhanced ultrasound (CEUS) – first results. Clin Hemorheol Microcirc. 2014;58(2): 343–52.
40. Fernandez CP, et al. Diagnosis of acute cortical necrosis in renal transplantation by contrast-enhanced ultrasound: a preliminary experience. Ultraschall Med. 2013;34(4):340–4.
41. Nicolau C, et al. Accuracy of contrast-enhanced ultrasound in the detection of bladder cancer. Br J Radiol. 2011;84(1008):1091–9.
42. Drudi FM, et al. CEUS in the differentiation between low and high-grade bladder carcinoma. J Ultrasound. 2012;15(4):247–51.
43. Lock G, et al. Early experience with contrast-enhanced ultrasound in the diagnosis of testicular masses: a feasibility study. Urology. 2011;77(5):1049–53.
44. Siracusano S, et al. Application of ultrasound contrast agents for the characterization of female urethral vascularization in healthy pre- and postmenopausal volunteers: preliminary report. Eur Urol. 2006;50(6):1316–22.
45. Dai Y, et al. Diagnosis of female urethral diverticulum using transvaginal contrast-enhanced sonourethrography. Int Urogynecol J. 2013;24(9):1467–71.
46. Frauscher F, et al. Comparison of contrast enhanced color Doppler targeted biopsy with conventional systematic biopsy: impact on prostate cancer detection. J Urol. 2002;167(4):1648–52.
47. Pelzer A, et al. Prostate cancer detection in men with prostate specific antigen 4 to 10 ng/ml using a combined approach of contrast enhanced color Doppler targeted and systematic biopsy. J Urol. 2005;173(6):1926–9.
48. Mitterberger M, et al. Comparison of contrast enhanced color Doppler targeted biopsy to conventional systematic biopsy: impact on Gleason score. J Urol. 2007;178(2):464–8; discussion 468.
49. Halpern EJ, et al. Contrast enhanced transrectal ultrasound for the detection of prostate cancer: a randomized, double-blind trial of dutasteride pretreatment. J Urol. 2012;188(5):1739–45.
50. Ascenti G, et al. Complex cystic renal masses: characterization with contrast-enhanced US. Radiology. 2007;243(1):158–65.
51. Ophir J, et al. Elastography: a quantitative method for imaging the elasticity of biological tissues. Ultrason Imaging. 1991;13(2):111–34.
52. Krouskop TA, et al. Elastic moduli of breast and prostate tissues under compression. Ultrason Imaging. 1998;20(4):260–74.
53. Nightingale K, et al. Acoustic radiation force impulse imaging: in vivo demonstration of clinical feasibility. Ultrasound Med Biol. 2002;28(2):227–35.
54. Palmeri ML, Nightingale KR. On the thermal effects associated with radiation force imaging of soft tissue. IEEE Trans Ultrason Ferroelectr Freq Control. 2004;51(5):551–65.
55. Alizad A, Urban MW, Morris JC, et al. Application of vibro-acoustography in prostate tissue imaging. Med Phys. 2013;40(2):022902.
56. Urban MW, et al. Implementation of vibro-acoustography on a clinical ultrasound system. IEEE Trans Ultrason Ferroelectr Freq Control. 2011;58(6):1169–81.
57. Sandrin L, et al. Shear modulus imaging with 2-D transient elastography. IEEE Trans Ultrason Ferroelectr Freq Control. 2002;49(4):426–35.
58. Arndt R, Schmidt S, Loddenkemper C, Grünbaum M, Zidek W, van der Giet M, Westhoff TH. Noninvasive evaluation of renal allograft fibrosis by transient elastography – a pilot study. Transpl Int. 2010;23(9):871–7.
59. Sandrin L, Fourquet B, Hasquenoph JM, Yon S, Fournier C, Mal F, Christidis C, Ziol M, Poulet B, Kazemi F, Beaugrand M, Palau R. Transient elastography: a new noninvasive method for assessment of hepatic fibrosis. Ultrasound Med Biol. 2003;29(12):1705–13.
60. Barr RG, Memo R, Schaub CR. Shear wave ultrasound elastography of the prostate: initial results. Ultrasound Q. 2012;28(1):13–20.
61. Lerner RM, Huang SR, Parker KJ. "Sonoelasticity" images derived from ultrasound signals in mechanically vibrated tissues. Ultrasound Med Biol. 1990;16(3):231–9.
62. Parker KJ, et al. Tissue response to mechanical vibrations for "sonoelasticity imaging". Ultrasound Med Biol. 1990;16(3):241–6.
63. Pallwein L, et al. Sonoelastography of the prostate: comparison with systematic biopsy findings in 492 patients. Eur J Radiol. 2008;65(2):304–10.
64. Aigner F, et al. Value of real-time elastography targeted biopsy for prostate cancer detection in men with prostate specific antigen 1.25 ng/ml or greater and 4.00 ng/ml or less. J Urol. 2010;184(3):913–7.
65. Ahmad S, et al. Transrectal quantitative shear wave elastography in the detection and characterisation of prostate cancer. Surg Endosc. 2013;27(9):3280–7.
66. Tsutsumi M, et al. Real-time balloon inflation elastography for prostate cancer detection and initial evaluation of clinicopathologic analysis. AJR Am J Roentgenol. 2010;194(6):W471–6.
67. Correas JM, Tissier AM, Khairoune A, et al. Ultrasound elastography of the prostate: state of the art. Diagn Interv Imaging. 2013;94(5):551–60.
68. Mitri FG, et al. In vitro comparative study of vibro-acoustography versus pulse-echo ultrasound in imaging permanent prostate brachytherapy seeds. Ultrasonics. 2009;49(1):31–8.
69. Mitri FG, et al. Vibro-acoustography imaging of permanent prostate brachytherapy seeds in an excised human prostate – preliminary results and technical feasibility. Ultrasonics. 2009;49(3):389–94.
70. Emelianov SY, et al. Elasticity imaging for early detection of renal pathology. Ultrasound Med Biol. 1995;21(7):871–83.
71. Grenier N, et al. Renal ultrasound elastography. Diagn Interv Imaging. 2013;94(5):545–50.
72. Grenier N, et al. Quantitative elastography of renal transplants using supersonic shear imaging: a pilot study. Eur Radiol. 2012;22(10):2138–46.
73. Kallel F, et al. Elastographic imaging of low-contrast elastic modulus distributions in tissue. Ultrasound Med Biol. 1998;24(3):409–25.
74. Fahey BJ, et al. In vivo visualization of abdominal malignancies with acoustic radiation force elastography. Phys Med Biol. 2008;53(1):279–93.
75. Mitri FG, Kinnick RR. Vibroacoustography imaging of kidney stones in vitro. IEEE Trans Biomed Eng. 2012;59(1):248–54.
76. Sommerer C, et al. Assessment of renal allograft fibrosis by transient elastography. Transpl Int. 2013;26(5):545–51.
77. Syversveen T, et al. Assessment of renal allograft fibrosis by acoustic radiation force impulse quantification – a pilot study. Transpl Int. 2011;24(1):100–5.
78. Gennisson JL, et al. Supersonic shear wave elastography of in vivo pig kidney: influence of blood pressure, urinary pressure and tissue anisotropy. Ultrasound Med Biol. 2012;38(9):1559–67.

79. Lee MJ, et al. Age-related changes in liver, kidney, and spleen stiffness in healthy children measured with acoustic radiation force impulse imaging. Eur J Radiol. 2013;82(6):e290–4.
80. Guo LH, et al. Acoustic radiation force impulse imaging for noninvasive evaluation of renal parenchyma elasticity: preliminary findings. PLoS One. 2013;8(7), e68925.
81. Clevert DA, et al. Evaluation of Acoustic Radiation Force Impulse (ARFI) imaging and contrast-enhanced ultrasound in renal tumors of unknown etiology in comparison to histological findings. Clin Hemorheol Microcirc. 2009;43(1–2):95–107.
82. Jedrzejewski G, et al. Testicular adrenal rest tumors in boys with congenital adrenal hyperplasia: 3D US and elastography – do we get more information for diagnosis and monitoring? J Pediatr Urol. 2013;9(6 Pt B):p. 1032–7.
83. Ying H, et al. Quantitative assessment of bladder neck compliance by using transvaginal real-time elastography of women. Ultrasound Med Biol. 2013;39(10):1727–34.
84. Idzenga T, et al. Noninvasive 2-dimensional monitoring of strain in the detrusor muscle in patients with lower urinary tract symptoms using ultrasound strain imaging. J Urol. 2013;189(4):1402–8.
85. Konig K, et al. Initial experiences with real-time elastography guided biopsies of the prostate. J Urol. 2005;174(1):115–7.
86. Nelson ED, et al. Targeted biopsy of the prostate: the impact of color Doppler imaging and elastography on prostate cancer detection and Gleason score. Urology. 2007;70(6):1136–40.
87. Pallwein L, et al. Real-time elastography for detecting prostate cancer: preliminary experience. BJU Int. 2007;100(1):42–6.
88. Salomon G, et al. Evaluation of prostate cancer detection with ultrasound real-time elastography: a comparison with step section pathological analysis after radical prostatectomy. Eur Urol. 2008;54(6):1354–62.
89. Junker D, et al. Comparison of real-time elastography and multiparametric MRI for prostate cancer detection: a whole-mount step-section analysis. AJR Am J Roentgenol. 2014;202(3):W263–9.
90. Aigner F, et al. Prostate cancer and extracapsular extension (ECE): assessment by sonoelastography in comparison to MRI – a preliminary study. Eur Rad Suppl. 2007;17(1):294.
91. Pallwein L, et al. Early prostate cancer detection: sonoelastography and endorectal MRI-guided targeted biopsy. Radiology. 2006;(Abstract #1409 (SSJ05–05)).

High-Intensity Focused Ultrasound for Prostate Cancer

10

Stephanie Guillaumier, Mark Emberton, and Hashim Uddin Ahmed

Prostate cancer is the most common cancer in males and the second-leading cancer-related cause of death in the western world. Prostate-specific antigen (PSA) screening, and changes in the diagnostic pathway of prostate cancer, has resulted in proportionally more men being diagnosed with early stage prostate cancer still confined to the prostate. Patients are faced with an overwhelming choice of treatment options to treat their disease. Standard options include radical prostatectomy (RP) and external-beam radiotherapy (ERBT) which, although provide good long-term cancer control, are associated with significant side effects affecting the quality of life of these patients.

Various alternatives are now available. Tumour ablation in the prostate can be achieved through various energy modalities including the thermal effect of focalised ultrasound in HIFU. High-intensity focused ultrasound is a newly emerging technology for the treatment of localised prostate cancer. The body of evidence that has recently emerged in support of this technique suggests that achieving the trifecta of urinary continence, potency and oncological control is possible. Indeed, the oncological outcomes are comparable with other treatments. The advantages of HIFU are manifold: it is minimally invasive, can be performed in a single session, as a day-case procedure, can be repeated if necessary and patients can be offered other treatments in cases of residual or recurrent disease.

S. Guillaumier, MD, MRCS, DipABRSM
Division of Surgery and Interventional Science, University College London, London, UK

M. Emberton, MD, FRCS (Urol), FRCS, MBBS, BSc (✉)
Division of Surgery and Interventional Sciences, University College London Hospital, London, UK
e-mail: markemberton1@btinternet.com

H.U. Ahmed, PhD, FRCS(Urol), BM, BCh, BA
Division of Surgery and Interventional Science, University College London, London, UK

Department of Urology, University College London Hospital NHS Foundation Trust, London, UK
e-mail: Hashim.ahmed@ucl.ac.uk

There is a continuous search for new minimally invasive technologies and HIFU seems to have the potential to fill this void in prostate cancer. This technique has to date, mostly been assessed in cases of localised prostate cancer, whether primary (whole gland or focal) or as salvage therapy in cases of radiation failure. Therefore, HIFU has a role both as a primary and salvage treatment.

The Technology

Physical Principles

Ultrasound refers to mechanical vibrations produced by a crystal or transducer. These vibrations have a frequency above the threshold of human hearing (16 kHz) and are produced by applying an alternating voltage across a piezoelectric material, such as lead zirconate titanate. These materials oscillate at the same frequency as the alternating current. The ultrasound waves that are produced can travel through human tissue. This subsequently leads to alternating cycles of increased and reduced pressure, compression, and rarefaction, respectively.

Diagnostic ultrasound is of low frequencies (1–20 MHz) and results in insignificant energy deposit, which is therefore harmless. Therapeutic HIFU uses higher frequencies (0.8–4 MHz) and therefore deposits higher energy within the ultrasound beams. Therapeutic ultrasound can be divided into two groups: 'low' intensity (0.125–3 W/cm^2) or 'high' intensity (>5 W/cm^2). The former can stimulate normal physiological responses to injury. The latter can cause selective tissue destruction if delivered in a focused manner. The high-intensity ultrasound waves are converged by using an acoustic lens, bowl-shaped transducer or electronic phased array. Zones of high or low pressure are created as ultrasound waves travel through tissue. Tissue damage occurs when, during the high-pressure phase, the energy deposit at the focus is sufficiently high.

These pressure fluctuations result in shearing motions at a microscopic level. This in turn causes frictional energy.

A.R. Rastinehad, D.N. Siegel (eds.), *Interventional Urology*, DOI 10.1007/978-3-319-23464-9_10

Thus, mechanical energy is converted into heat energy. It is this heat energy that subsequently results in protein denaturation, disruption of the lipid cell membrane, coagulative necrosis and irreversible cell death. This is accompanied by an inflammatory response with formation of granulation tissue characterised by immature fibroblasts and new capillary formation at the periphery of the treated necrotic zone. Migration of polymorphonuclear leucocytes occurs 2 weeks after treatment and accompanied by fibrosis and scar tissue deposition as evidenced on multiparametric MRI of the prostate.

The volume of tissue ablation with each HIFU pulse is shaped like a grain of rice that is 1–3 mm transversely and 8–15 mm longitudinally (along beam axis). Each pulse is placed adjacent to each other to ablate larger volumes of tissue. Thermal toxicity is achieved at a temperature of 56 °C maintained for 1 s. The temperature achieved during HIFU is greater, up to 80 °C so even short pulses will achieve cell kill [1–3].

HIFU Devices

There are two main transrectal devices available for treatment of prostate cancer: Sonablate 500 (Focus Surgery, Indianapolis, IN) and Ablatherm Integrated Imaging (EDAP TMS SA, Vaulx en Velin, France). This chapter will primarily focus on these as the transurethral and MR-guided in-bore HIFU devices have little in the way of clinical data at the time of writing although we will summarise what data there is.

Sonablate 500

The Sonablate 500 device has two 4 MHz transducers operating at focal distances of 4.5, 4 or 3 cm. They are mounted back-to-back. Each transducer has a dual role. The centre is used as an imaging device and takes real-time ultrasound imaging; the periphery is used for treatment. The treatment head within the probe can be flipped according to the desired depth of penetration. The 4 cm transducer is routinely used for the anterior and the 3 cm one used for the posterior parts of the prostate glands. Pulse duration generally lasts for 3 s, followed by a 6 s gap to allow tissue cooling.

The combined imaging and therapeutic roles of the transducer allows for direct visualisation after each pulse of treatment cycle. The Sonablate device does not have a protocol-driven treatment. Rather, the power intensity of each pulse is guided by the grey-scale changes within the targeted area that represents steam. These grey-scale 'popcorning' changes have been termed 'Uchida' changes, named after the Japanese urologists who pioneered work with the Sonablate device.

The Sonablate machine allows for the treatment to be planned and executed in two or three separate blocks. The anterior part of the gland is treated first, followed by the mid-zone and posterior part. The transrectal probe will require adjustment between each block. The posterior block is always treated using the 3 cm focal length with lower energy levels to prevent rectal injury by heat build-up. Rectal cooling is achieved by pumping chilled degassed water at temperatures of 17–20 °C. Patients are placed in the dorsal lithotomy position for the Sonablate machine. The next generation now incorporates image fusion to deliver targeted therapy [4].

Ablatherm

The Ablatherm device uses two transducers: one for imaging (7.5 MHz) and one for treatment (3 MHz) and allows ablation within 25 mm of the prostate. Each pulse is of 4–5 s, followed by an interval of 4 7 s (Table 10.1).

This device uses predefined treatment algorithms with preset energy levels: as a primary procedure, as a re-treatment and for radiation failure. Therefore, the energy level, for each pulse, cannot be individually controlled by the operator. The treatment is planned slice by slice from the apex to bladder neck after the ultrasound scan of the prostate is obtained and reconstructed in 3D. Treatment is delivered to each lobe, anterior to posterior. The transrectal probe is incorporated into a table, which also holds the pump and cooling mechanism. The patient is placed on this table in the right lateral position. In addition, the Ablatherm device has a safety ring that stabilises the rectal wall intraoperatively as well as a patient motion detector [1, 3]. The new Focal One device, which incorporates image fusion, has very similar features to the previous Ablatherm generation and works very much in the same way to deliver the HIFU pulses although it is reported to be more precise.

Primary High-Intensity Focused Ultrasound: Outcomes

Whole-Gland HIFU

Treatment of localised prostate cancer with transrectal HIFU has initially been delivered as a minimally invasive therapy to the entire prostate gland. Historically, HIFU treatment was initially delivered in two sessions, one for each lobe. This was subsequently followed by a single session to treat the whole gland. Some centres combine TURP immediately before the HIFU treatment in a single session, to decrease the gland size, remove intra-prostatic calcification that could impede the ultrasound waves and reduce the risk of obstruction and urinary retention secondary to necrotic tissue (Fig. 10.1a, b).

Table 10.1 Comparison of Sonablate 500 and Ablatherm devices

	Ablatherm integrated imaging	Sonablate 500
Company	EDAP TMS SA, France	SonaCare Inc., USA
Since	2005	2001
Approval		
Table	Integrated	Standard
Patient position	Right lateral	Lithotomy or supine
Frequency	7.5 MHz for treatment planning; 3 MHz for treatment	4 MHz for treatment and planning
Focal point	4.5 cm	3–5 cm
Transducer	Single-treatment probe with two transducers	Single-treatment probe with two transducers of different focal lengths
Power	Predefined for each treatment	Manual adjustment by operator
Ablation temperature (°C)	>85	80–98
Imaging	Real time	Real time
Active cooling system	Yes	Yes
Rectal wall cooling	Yes	Yes

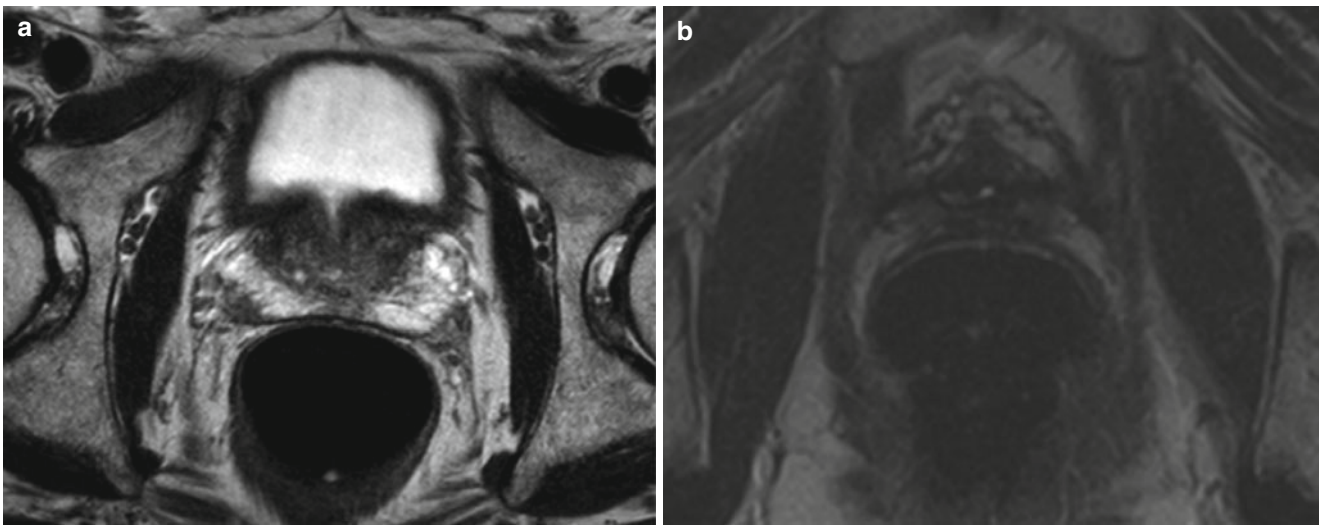

Fig. 10.1 (**a**) T2-weighted image on the left showing a left peripheral zone lesion. (**b**) T2-weighted image showing prostatic cavity with *whole-gland HIFU ablation*

Most HIFU studies have used PSA threshold values and biopsy results to assess failure. Many studies use the ASTRO or Phoenix definitions for biochemical failure. However, biochemical failure is difficult to define with HIFU, more so with focal HIFU.

Poissonnier et al. evaluated 227 patients with localised prostate cancer who were treated with whole-gland HIFU using the Ablatherm device. The HIFU session was combined with a TURP in 176 of these patients. With a follow-up of 27.5 + 20 months, the actuarial disease-free survival rate at 5 years was 66 %. The post-HIFU biopsies carried out after 3 months were negative in 86 % (196 patients). Using PSA nadir as a prognostic value, the patients were divided into three subgroups: nadir PSA <0.5 ng/ml, between 0.51 and 1 ng/ml and >1.1 ng/ml. The negative biopsy rates observed in each subgroup were 89 %, 76 % and 68 %, respectively [5].

The series presented by Blana et al. in 2008 analysed a total of 167 patients who underwent whole-gland HIFU, 116 of which underwent concomitant TURP. Of the 124 patients that had a follow-up biopsy, 115 patients (92.7 %) had no evidence of clinically significant cancer and 12.2 % transitioned into salvage treatment. Grade 1 urinary incontinence was found in ten (6.1 %) of patients, three (1.8 %) patients had grade 2 incontinence and none had grade 3 incontinence. Of 127 patients, 76 had no erectile dysfunction prior to the HIFU procedure. Of these, 42 (55.3 %) had full potency, and 34 (44.7 %) had erectile dysfunction [6].

The multicentre series described by Crouzet et al. followed up a total of 803 patients, of which only 589 patients

had biopsies post-HIFU. Of these, control biopsies were negative in 459 patients (77.9 %) and positive in 130 (22.1 %). 22.7 % (182) of patients subsequently had salvage treatment [7]. A further study from the same group followed a total of 1002 patients treated with HIFU to the whole gland with 63 % of patients achieving a PSA nadir of ≤0.3 ng/ml. A total of 37.1 % (371) patients exhibited a PSA rise and transitioned to salvage therapy [8].

Conversely, another French group, Ripert et al., reported on 53 patients with a mean follow-up or 45.4 months and adverse oncological outcomes, although not associated with any risk group. They found that overall, 36 (67.9 %) patients exhibited oncological failure [9].

Similarly, Pfeiffer et al. had a total of 191 consecutive patients and reported overall and cancer-specific survival rates of 86.3 % and 98.4 %, respectively. Metastases were detected in 7 (3.7 %) patients and oncological failure was experienced in 70 (36.6 %) [10].

Thuroff and Chaussy published the outcomes on their 15-year experience. With a total of 704 patients, the cancer-specific and metastases-specific survival rates were 99 % and 95 %, respectively. They report a re-treatment rate of 15 %, urinary incontinence in 4 %, infection in 2.1 % and obstruction in 4.6 % [11].

Similarly, Blana et al. published their long-term results in 2007. In a study incorporating 140 patients, they showed that good cancer control may be achieved with 114 of the 132 (86.4 %) patients who underwent post-HIFU biopsies being negative with no statistical differences between the low- and intermediate-risk groups. The overall survival rates at 5 and 8 years were 90 % and 83 % and only 15 % subsequently had salvage treatment [12]. Further results from the same group a year later with a study of 163 patients showing a disease-free survival rate of 66 % at 5 years with 16 % starting on salvage treatment [6].

These studies showed similar results to their registry analysis of 356 patients from nine centres over a period of 15 years. The rate of negative biopsies in the low-, intermediate- and high-risk groups were 86 %, 78.5 % and 74.2 %, respectively. The median PSA nadir achieved was 0.11 ng/ml at a mean of 14.4 weeks [13].

There are several series that have used the Sonablate device for whole-gland primary HIFU treatment.

Uchida et al. reported on their 5-year experience of whole-gland HIFU, a study incorporating a total of 517 men with T1c-T3N0M0 disease. The biochemical disease-free rate at 5 years was 72 %. Of the 483 who underwent post-HIFU biopsies, 401 (83 %) showed no evidence of clinically significant disease [14]. A further study from the same group focused on the quality of life parameters following HIFU treatment. Of 326 patients, 78 % of patients not receiving neoadjuvant hormonal therapy were potent 24 months after HIFU and the maximum flow rate and residual urine volume returned to baseline values at 12 or 24 months post-HIFU [15].

Another series from Japan looked at 137 patients, achieving a PSA nadir of <1.0 ng/ml was noted in 95 % of patients. Erectile dysfunction occurred in 37 % (22/59) who did not undergo hormonal therapy prior to HIFU. Of 137 patients, 133 underwent post-HIFU prostate biopsies. Of these, six were positive for malignancy [16].

Ahmed et al.'s group reported the first UK series of whole-gland HIFU in 2009. One hundred seventy-two men with a mean follow-up of 346 days showed that 70 % maintained potency by 12 months whilst only 7 % reported mild stress incontinence with no pad use, with a further 0.6 % of patients requiring pads. 92.4 % exhibited no evidence of disease showing that excellent cancer control can be achieved with HIFU [17] (Table 10.2).

Focal HIFU

Focal therapy has emerged as an alternative option to standard treatments. The main aim of focal therapy is tissue preservation with selective ablation, allowing preservation of existing functions and minimising the impact on the quality of life. There are a number of different ablative energies in existence, amongst which is HIFU.

HIFU was first established for use in benign prostatic hyperplasia (BPH). It was then translated for use in localised prostate cancer and one of the first focal HIFU series to be reported was Madersbacher et al.'s study on 29 patients who underwent focal HIFU prior to RP. These men were diagnosed with unilateral localised disease. They showed that focal HIFU was possible without compromising the integrity of intervening structures such as rectum and urethral sphincter [18]. The ability of HIFU to achieve well-defined areas of coagulative necrosis was later confirmed with another study demonstrating the potential for HIFU to treat localised prostate cancer in a focal manner [19] (Figs. 10.2a, b and 10.3a, b).

One of the next series to appear is by Muto et al. where whole-gland and focal HIFU were performed and compared. Indeed, no significant differences were noted in the 2-year biochemical DFS rates for the patients at low and intermediate risk between whole-gland and focal therapy. Interestingly to highlight, there were also no differences noted in the QOL parameters [20]. Indeed, Murat et al. looked at the outcome on erectile dysfunction after 56 patients underwent hemiablation HIFU. For the 52 patients with a pre-HIFU IIEF-5 of more than 17, 28 patients had a post-HIFU IIEF-5 score of more than 17. After the second HIFU session, 20 % of the 15 patients with an IIEF-5 of more than 17 remained with the same outcome [21].

Ahmed et al.'s group have published three series on focal HIFU for localised prostate cancer. The first comes from

Table 10.2 Primary whole-gland HIFU

Study	Device	D'Amico risk groups	Follow-up (months)	Post-HIFU histology	BFSR	Biochemical control	Metastasis-free survival (%)	Cancer-specific survival (%)
Posionner et al. (2006)	Ablatherm *N*=227	Not reported	27	86 % negative	66 %	84 % (PSA ≤ 0.5) 7 % (PSA 0.51–1) 8 % (PSA > 1.0)	Not reported	Not reported
Blana et al. (2007)	Ablatherm *N*=140	Low 51.4 %; inter 48.6 %	76.8	86.4 % negative	77 % at 5 years 69 % at 7 years	68.4 % (PSA ≤ 0.5) 31.6 % (PSA > 0.5)	Not reported	Not reported
Blana et al. (2008)	Ablatherm *N*=167	Low 51.5 %; inter 48.5 %	57.6	92.5 % negative	75 %	75 % (Phoenix) 86 % (PSA < 1.0) 64 % (PSA < 0.2)	Not reported	99.7 %
Blana et al. (2009)	Ablatherm *N*=285		56.4					
Crouzet et al. (2010)	Ablatherm *N*=803	Low 40.2 %; inter. 46.3 %; high 13.5 %	42	77.9 % negative		54.3 % (PSA ≤ 0.3) 21.4 % (PSA 0.3–1) 22.3 % (PSA > 1) 1.9 % (not determined)	97 %	99 %
Ripert et al. (2010)	Ablatherm *N*=53	Low 52.8 %; inter 47.2 %	45.4		21.7 %	20.8 % (PSA ≤ 0.2) 30.2 % (PSA0.21-1) 49 % (PSA > 1)	Not reported	100 %
Blana et al. (2012)	Ablatherm *N*=356	Low 44.9 %; inter 39.6 %; high 14.6 %	33.6	80.5 % (182/226) negative	85 % at 5 years 79 % at 7 years	PSA nadir 0.11 at	Not reported	Not reported
Uchida et al. (2009)	Sonablate *N*=517	Low 28 %; inter 38 %; high 34 %	24	83 % (401/483) negative	72 %	Not stated	Not reported	Not reported
Ahmed et al. (2009)	Sonablate *N*=172	Low 28 %; inter 38 %; high 34 %	12	92.4 % negative	Low 76 %; inter 63 %; high 57 %	61 % (PSA <0.2) 83 % (PSA <0.5)	Not reported	Not reported
Shoji et al. (2010)	Sonablate *N*=326				Low 84 %; inter 64 %; high 45 %		Not reported	Not reported
Inoue et al. (2011)	Sonablate *N*=137	Low 21 %; inter 50 %; high 29 %	36	95.5 % negative	Low 91 %; inter 81 %; low 62 %	95 % (PSA ≤ 1.0)	Not reported	Not reported
Pfeiffer et al. (2012)	Ablatherm *N*=191	Low 38 %; inter 63.6 %; high 28 %	52.8	Low 84.2 %; inter 63.6 %; high 67.5 % total 72.3 % (110/152) negative	Low 84.8 %, inter 64.9 %; low 54.9 %	74.1 % (PSA < 0.3)	Not reported	98.4 %
Thüroff and Chaussy (2013)	Ablatherm *N*=704	Low 21.6 %; inter 38.4 %; high 40 %	63.6				95 % (10 year)	99 % (10 year)
Crouzet et al. (2013)	Sonablate *N*=1002	Low 37 %; inter 45 %; high 17 %; undefined 1 %	76.8	63 % (485/774) negative	Low 86 %; inter 78 %; high 68 %	63 % (PSA ≤ 0.3) 56.6 % (PSA ≤ 0.2)	94 %	97 %

2011 as a phase I/II trial, where 20 men were treated with hemiablation HIFU. Ninety-five percent retained their potency whilst 95 % were pad-free. Eighty-nine percent of men achieved the trifecta status of cancer control, erections sufficient for intercourse and pad-free, leak-free continence at 12 months. These results demonstrate the feasibility of hemiablation as one form of focal therapy. However, with the increased precision in the diagnostic pathway of prostate

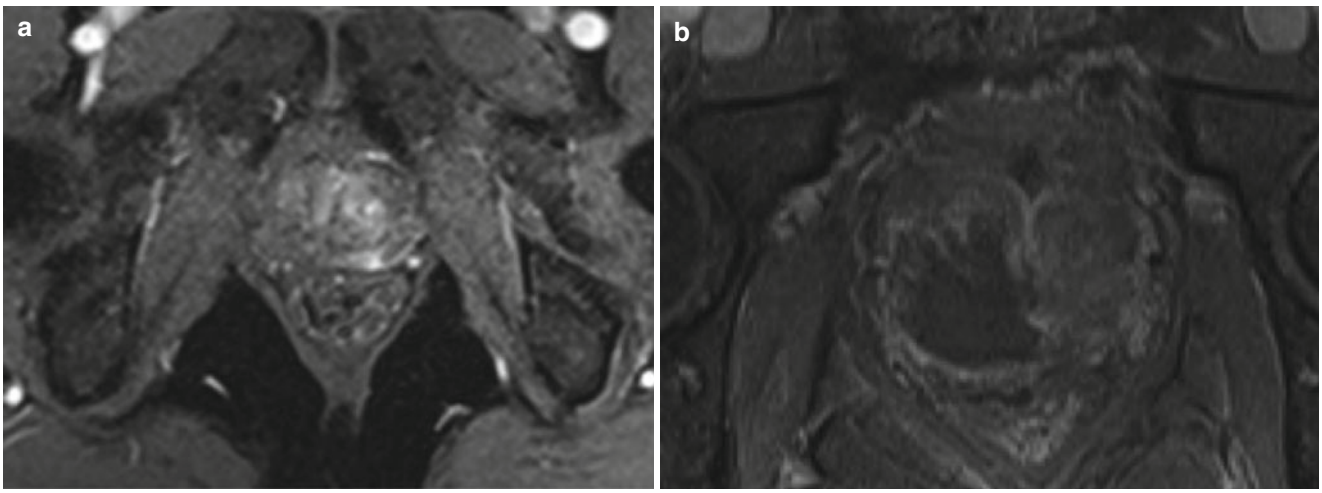

Fig. 10.2 (**a**) T2-weighted image showing a lesion in the right peripheral zone. (**b**) T2-weighted image showing treatment of the right peripheral zone lesion with *hemiablation HIFU*

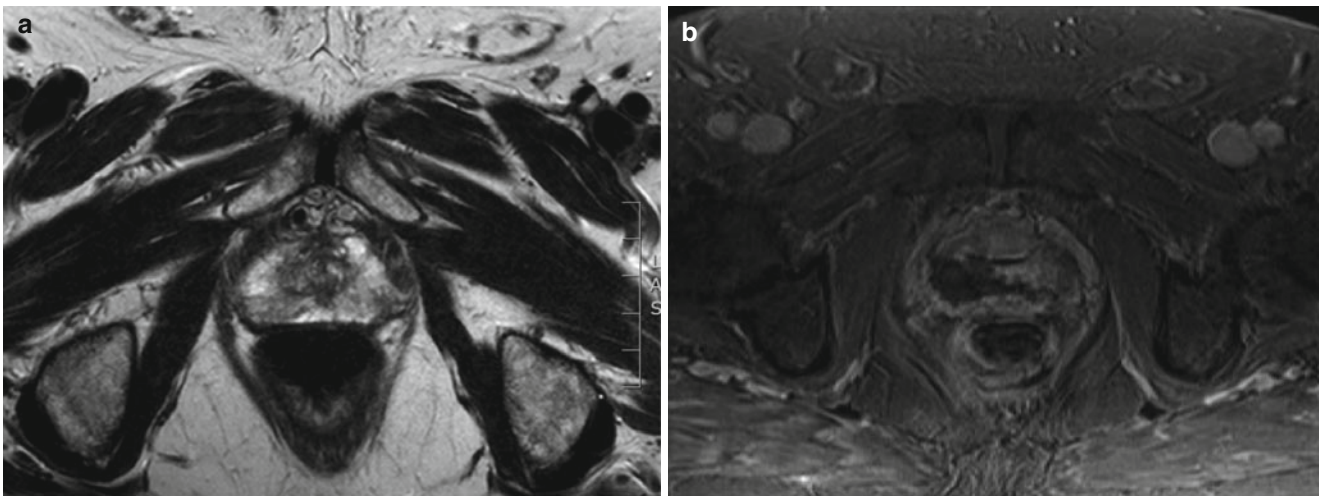

Fig. 10.3 (**a**) T2-weighted image showing right peripheral zone lesion. (**b**) T2-weighted image showing right *posterior quadrant ablation HIFU*

cancer, more precise characterisation has made treating the cancer more focally possible [22].

In fact, the same group published similar findings on 42 men who received focal HIFU with 92 % having no clinically significant cancer on follow-up biopsies in 30/39 men that were biopsied. Four men had re-treatment with no evidence of disease on MRI at 12 months. They report 89 % of men having sufficient erections for penetration, and all men with no baseline incontinence achieved pad-free continence at 12 months [23].

The third also reported similar findings. A total of 56 patients were treated with focal HIFU, of which 85.7 % had no measurable prostate cancer post-HIFU. Forty patients were leak-free, pad-free and had erections sufficient for penetration. Of 41 patients with good baseline function, 22 (53.7 %) achieved the trifecta status of pad-free, leak-free continence, good erectile function and absence of clinically significant disease [24].

El Fegoun et al. published the first series on focal HIFU in the elderly patient cohort. Hemiablation HIFU was performed in a total of 12 patients, 11 of whom had negative follow-up biopsies. One patient had re-treatment with HIFU and 4 were subsequently treated with androgen-deprivation therapy. The recurrence-free survival rate was 90 % at 5 years. Low morbidity rates are reported: none experience urinary incontinence, one patient suffered from an episode of acute urinary retention, and two had a urinary tract infection [25].

Targeting treatment to a discrete area of prostate tissue preserves surrounding structure and in doing so helps maintain patients' functions and quality of life. Focal HIFU has recently emerged as one of the minimally invasive techniques that provide acceptable morbidity rates whilst giving good oncological outcomes (Table 10.3).

Table 10.3 Primary focal HIFU

Study	Device	D'Amico risk groups	Mean follow-up	Post-HIFU histology (%)	BDFS	PSA kinetics	Secondary treatment actual (%)	Metastases-specific survival (%)	Cancer-specific survival (%)
Madersbacher et al. (1995)	Sonablate *N*=29	NR	NR	NR	NR	NR	NR	NR	NR
Beerlage et al. (1999)	Ablatherm *N*=14	NR	NR	28 % negative	NR	19 % (PSA<0.5) 50 % (PSA0.5-4.0) 30 % (PSA>4)	NR	NR	NR
Muto et al. (2008)	Sonablate *N*=29	Low 86.2 %; inter13.8 %	32 median	76.5 % negative	Low 83.3 % inter 53.6 %		NR	NR	NR
Murat et al. (2009)	NR *N*=56	NR	42 median	NR	76 % (3 years) 60 % (5 years)	PSA nadir 0.8 After 1st HIFU PSA nadir 0.47 After 2nd HIFU	NR	NR	NR
El Fougon et al. (2011)	Ablatherm *N*=12	NR	120 median	NR	NR	NR	NR	100 %	100 % (10 year)
Ahmed et al. (2011)	Sonablate *N*=20	Low 25 %; inter 75 %		89 % negative					
Ahmed et al. (2012)	Sonablate *N*=42	Low 27 %; inter 63 %; high 10 %							
Ahmed et al. (2015)	Sonablate *N*=56	Low 12.5 %; inter 83.9 %; high 3.6 %	NR	85.7 % negative	NR	NR	NR	NR	NR
Van Velthoven et al. (2014)	Ablatherm *N*=31	Low 54.8 %; inter 38.7 %; high 2 %	36.3	NR	66 % (5 years) 59 % (7 years)	68.4 % (PSA ≤ 0.5)	NR	NR	NR

Salvage High-Intensity Focused Ultrasound: Outcome Measures

After Radiation Failure

Up to 45 % of patients treated for localised prostate cancer with external-beam radiotherapy (EBRT) will experience biochemical relapse within 8 years [26–28]. Positive prostate biopsies after initial ERBT are associated with a higher risk of developing metastatic disease or death, with the median time for developing metastases after biochemical failure is approximately 3 years [29]. Most men receive androgen-deprivation therapy, which has a significant impact on the quality of life of patients as well as bone health and cardiac and metabolic implications. However, patients diagnosed with local recurrence after ERBT without any evidence of metastatic disease may be suitable for local salvage therapy and have four treatment options available: salvage radical prostatectomy, salvage brachytherapy, salvage cryotherapy and salvage high-intensity focused ultrasound [30]. There are several series that uses HIFU as a salvage therapy option in recurrent prostate cancer after ERBT failure (Fig. 10.4a, b).

Zacharakis et al. reviewed a series of 31 patients treated with salvage HIFU using the Sonablate 500 machine. They had previously received ERBT of 66–70 Gy and 18 out of 31 patients were on hormone therapy at the time of HIFU treatment. Three percent had recto-urethral fistula. Biopsies were carried out in 6 out of 1- patients that experienced PSA rise postoperatively. Seven percent of patients (2/31) were found to have local recurrence, 3 % of patients (1/31) revealed positive lymph nodes on MRI, with a further 10 % having confirmed metastatic disease. Overall, 71 % had no evidence of disease following salvage HIFU [31].

Another group, Gelet et al. included 71 patients in another similar series, with a follow-up of 14.8 months. Eighty percent (57/71) of patients had negative biopsies, and at the last follow-up, 44 % had no evidence of disease progression with 6 % developing rectal fistula, 7 % urinary incontinence and 17 % developing bladder neck stenosis [32].

From the same group, Murat et al. published their mid-term results, where 167 patients were included in the study

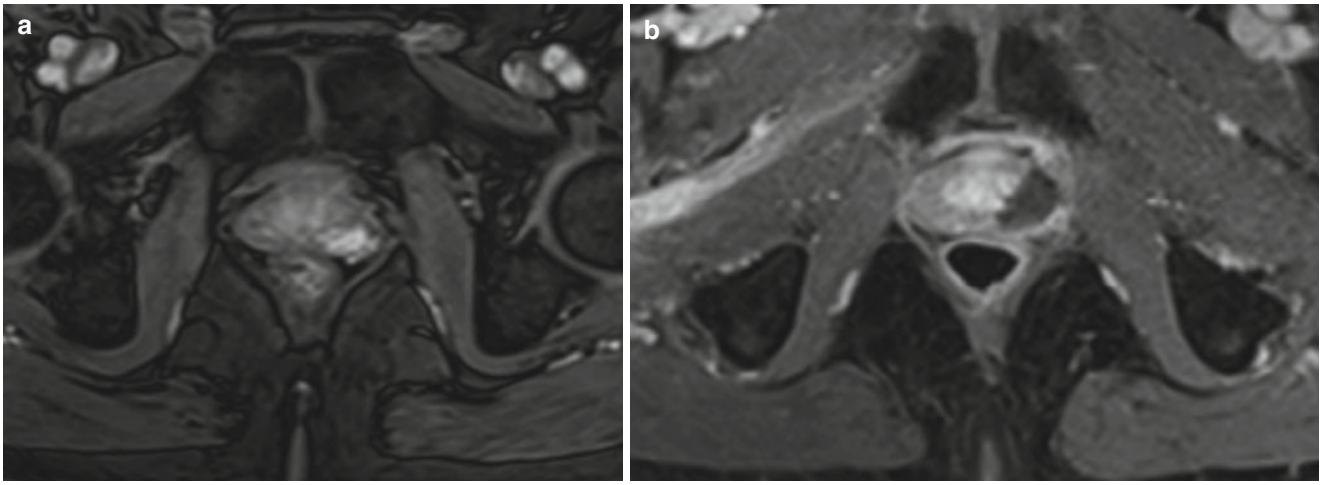

Fig. 10.4 (**a**) T2-weighted image showing left peripheral zone lesion. (**b**) T2-weighted image showing *salvage focal HIFU* treatment to the left posterior quadrant

with 194 HIFU sessions performed as 27 patients underwent two HIFU sessions. Ninety-five (56.8 %) patients had previously been treated with ADT, 81 of which had ADT as adjuvant therapy and 14 as cytoreduction treatment. Negative biopsy results were achieved in 122 (73 %) of patients with a median follow-up of 18.1 months. Overall survival was 84 % [30].

Early outcomes from salvage HIFU have been reported by Crouzet et al. on a cohort of 290 men with biopsy-confirmed radio-recurrent prostate cancer and a mean follow-up of 48 months. One hundred forty-five patients received androgen-deprivation therapy (ADT) prior to HIFU treatment. Sixty-five patients received this as combination therapy with ERBT, 66 as adjuvant therapy following ERBT and 14 patients as cytoreduction. All patients discontinued ADT prior to the salvage HIFU procedure. The side-effect profile included recto-urethral fistula (0.4 %) and urinary incontinence (19.9 %) [33].

Song et al. report on a small series that includes a total of 13 patients with a median follow-up of 44.5 months. The overall biochemical-free rate was 53.8 % with 38.5 % requiring interventions for complications [34].

Whole-gland salvage treatments such as salvage RP are associated with increased risk of bowel and genito-urinary complications. HIFU has a role as a focal salvage therapy for localised prostate cancer recurrence after EBRT, as described by Ahmed et al. in their pilot study where they treated 39 patients with focal HIFU. The median PSA nadir achieved was 0.57 ng/ml (0.1–2.3) and 44 % achieved a PSA nadir of <0.5 ng/ml. Of these, the 1-year, 2-year and 3-year biochemical-free survival rates were 86 %, 75 % and 63 %, respectively. For the group that did not achieve this PSA nadir, these rates decreased to 55 %, 24 % and 1 %, respectively. The pad-free rate was 87 % as measured at last follow-up [35].

This data is supported by a further study from Baco et al. who performed hemiablation HIFU in unilateral radio-recurrent disease in 48 patients. The mean PSA nadir achieved was 0.69 ng/ml at a median follow-up of 16.3 months. Disease progression occurred in 33 % (16/48) of which four had local recurrence in the untreated lobe and four, bilaterally. The progression-free survival rate at 12 and 24 months were 83 % and 52 %. Severe urinary incontinence only occurred in 8 % (4/48) of patients and 75 % (36/48) were pad-free [36].

HIFU as salvage therapy in patients with local recurrence after ERBT allows local control of the disease whilst preserving functional outcomes and quality of life. The morbidity associated with HIFU in salvage cases remains relatively low; however, longer-term follow-up is required (Table 10.4).

After Radical Prostatectomy

Radical prostatectomy (RP) is one of the standard primary curative treatment options for localised prostate cancer [37]. The recurrence rates of RP vary between 17–29 % [38].

An increase in the PSA level postoperatively is often a sign of local recurrence, in the absence of identifiable metastatic disease. This has traditionally been treated with salvage radiotherapy. HIFU is one of the minimally invasive therapies that can be used as a salvage option after prostatectomy failure.

Asimakopoulos et al. describe their findings on 19 patients with biopsy-proven locally recurrent prostate cancer after RP that were treated with a single session of salvage HIFU. 89.5 % (17/19) patients showed a PSA nadir of ≤0.1 ng/ml 3 months after HIFU. 8/17 patients were classified as failure during a median follow-up of 48 months and 9/17 (52.9 %)

Table 10.4 Salvage HIFU

Study	Device	D'Amico risk groups	Mean follow-up (months)	DFS	PSA kinetics	Cancer-specific survival (%)	Metastatic-specific survival (%)	Mortality (%)
Gelet et al. (2004)	Ablatherm	NR	NR	38 %	NR	NR	12.7 %	23.5 %
Zacharakis et al. (2008)	Sonablate 500	NR	7.4	NR	NR	NR	NR	NR
Murat et al. (2008)	Ablatherm	NR	18.1	Low 53 %; inter 42 %; low 25 %	NR	NR	NR	NR
Crouzet et al. (2012)	Ablatherm	Low 19 %; inter 31.4 %; high 43 %	48	Low 45 %; inter 31 %; high 21 %	60.7 % (PSA ≤ 0.3)	80 %	79.6 %	10 %
Song et al. (2014)	Ablatherm	Low-inter 54 %; high 46 %	44. 4	53.8 %	NR	NR	NR	NR
Baco et al. (2014)	Ablatherm	NR	16.3		NR	NR	NR	NR

patients continued to be a success. The overall 4-year biochemical disease-free rate was 47.4 % [39].

From Japan comes a case study by Hayashi et al. looking at biochemical recurrences after RP. It describes how four patients with local recurrence at the vesicourethral anastomotic site. Three patients were treated with ERBT and hormones as salvage therapy. They were then treated with HIFU using the Sonablate 500 device. Adenocarcinoma was confirmed by biopsy of lesion at the vesicourethral anastomotic lesion prior to HIFU treatment. Two of the patients were biochemically free of disease 24 months post-salvage HIFU, with PSA levels ≤0.02 ng/ml and three showed negative biopsies [40].

After Brachytherapy

Brachytherapy is well established as a primary treatment for localised prostate cancer. The biochemical recurrence-free survival rate has been reported to be 77 % at 12 years [41]. However, failure after brachytherapy poses a challenge in terms of further treatment options. Brachytherapy intra-prostatic seeds compromise and hamper the delivery of energy to the prostate tissue, impaired visualisation of the gland, as well as reflectivity towards the rectum [42].

Few studies have looked at salvage HIFU after brachytherapy failure. Yutkin et al. present their findings from 17 patients who underwent whole-gland salvage HIFU after biochemical failure following brachytherapy. A PSA response rate was achieved in 95 % of patients in 3 months and a biochemical recurrence-free survival rate of 73.6 % at a mean of 4.3 years.

MRI-Guided Transurethral Ultrasound Therapy

The implication of improved diagnostic methods for prostate cancer is an increase in the proportion of men diagnosed with low- or intermediate-risk disease who are still offered whole-gland radical therapies. This emphasises the need to detect clinically significant disease as well as treatments to improved morbidity.

Recent advances in imaging, notably the multiparametric MRI, have had a dramatic influence on the diagnostic pathway of prostate cancer. The exploration of MR within a therapeutic role follows on from this. Ultrasound has to date, dominated the treatment of prostate cancer with high-intensity focused ultrasound (HIFU). The limitation here is the inability to measure accurately the temperature distribution within the prostate gland intraoperatively, giving a more precise indication of cell kill. The temporal and spatial control of tissue temperature is vital during energy ablation therapy. There must be adequate destruction of the targeted tissue whilst preserving the surrounding tissues (neurovascular bundles, rectum, urethral sphincter and pubic bone) to prevent morbidity such as erectile dysfunction, fistulae and bone pain/necrosis. Control of heat energy deposition in MR thermometry offers a noninvasive measurement of tissue temperature, mainly by the proton resonant frequency shift method [43–45]. Combining HIFU with MR imaging for real-time temperature control could offer an increased accuracy of treatment.

There are currently two companies that have produced a device for the delivery of MR-guided transurethral ultrasound to the prostate. One is by Profound Medical Inc.; the other is the Sonalleve MR-HIFU by Philips Healthcare,

Vantaa, Finland. Ross et al. conducted a study on transurethral ultrasound applicators with highly directional energy deposition and rotational control. This study was carried out in canines and demonstrated that these techniques can result in selective coagulation of regions in the prostate with MRI monitoring and control of the treatment. Scanning using slow and discrete steps without allowing for cool down periods between rotations produced continuous sectored areas of coagulation extending to the prostatic capsule. They demonstrated that using a cooling balloon with the transurethral applicator and allowing water flow in the balloon kept the transducers from overheating, keeping the temperature around the urethra low. The study showed that 12 mm of tissue around the urethra remained viable after treatment. The MR used with an interventional open 0.5 Tesla magnet. Selective treatment using transurethral applicator is therefore feasible [46].

This study compliments Lafon et al.'s work published in the same year. Their work on a flat transducer applied to female rabbit livers demonstrated that it is capable of inducing coagulative necrosis and vessel haemostasis, with well-defined margins. They confirm that the heated zone remained confined to the dimensions of the transducer, making it possible to treat tissue in a targeted and well-controlled manner [47]. Further similar data from a preclinical study comes from Partanen et al.'s group on canine prostates [48].

The first phase 0 pilot study was performed in eight men diagnosed with localised prostate cancer immediately before radical prostatectomy. Transurethral ultrasound therapy was performed with the patient under spinal anaesthesia using a 1.5 T MRI.

The system used consists of a transurethral ultrasound heating applicator, a rotational positioning system, a flow circuit circulating degassed, deionised water through the transducer and a treatment delivery interface. All parts of the equipment are MRI compatible. The multielement transducer is inserted into the urethra and emits a high-intensity directional ultrasound beam, resulting in thermal delivery to tissues.

The rotational positioning system placed between the legs provides spatial control of the heat energy, which is achieved by performing the treatment within an MRI unit as this provides real-time temperature monitoring. A fibre-optic temperature sensor and an enema tip are inserted into the rectum to measure core temperature and evacuate any accumulated gas [49].

The resected gland was sliced in the plane of thermal damage for assessment. This demonstrated a spatial targeting accuracy of - 1.0 mm ± 2.6 and a continuous pattern of necrosis achieved, with a gradient of less than 4 mm between coagulated and normal tissue. The average procedure time was 3 h. This study shows that MRI imaging-controlled transurethral ultrasound therapy is feasible and well tolerated by patients [50].

Post-HIFU Follow-Up

PSA Surveillance and HIFU Failure

Biochemical failure is difficult to define after focal HIFU. To date, there is no consensus on the definition of biochemical failure in patients treated with HIFU. Many studies have applied either the ASTRO or Phoenix definitions. A study by Blana et al. addresses this issue. Their statistical model distinguishes between specificity and sensitivity, in that specificity prioritises local recurrences, regional or distant recurrences or death from prostate cancer whilst a high sensitivity prioritises cure. The study shows that a high PSA threshold value (2.0 mg/ml) is associated with an increase in specificity and low PSA threshold values are associated with high sensitivity. This study demonstrates that the biochemical events best predicting clinical failure were PSA threshold of 1.2–1.4 ng/ml: a PSA nadir plus 1.1–1.3 ng/ml, PSA doubling time of 1.25 and 1.75 years and PSA velocities of <0.3 ng/ml/year. The two definitions that best predicted clinical failure were 'nadir +1.2' and a 'PSA velocity of >0.2 ng/ml/year'. This study therefore suggests that the Stuttgart definition be added to the assessment of HIFU therapy. The Stuttgart definition in this study had a positive predictive value of 55 % suggesting that clinical judgement also needs to be applied.

Also important to note is the fact that PSA frequently rises to above nadir with therapies such as brachytherapy, ERBT and HIFU. The clinician must decide on how meaningful the PSA increase is. It is of concern if it rises to a level above nadir + 1.2, as demonstrated in the above-mentioned study [51].

HIFU may be repeated with little increase in morbidity. It may be necessary for repeated HIFU to return a patient to a disease-free state. Therefore, this should not be considered a biochemical failure unless their PSA fails to decrease below nadir + 1.2 or if their PSA increases above nadir + 1.2 [52]. It may be necessary in the future to further refine the definition of biochemical failure depending on the number of HIFU treatments per patient.

Post-HIFU Imaging

Advances in imaging, in particular the multiparametric MRI of the prostate, have allowed more accurate identification of individual lesions within the prostate. It has also developed as a tool for post-HIFU surveillance. The main aim is to detect residual or for residual or recurrent disease within the ablated tissue or in the untreated prostate gland.

MRI performed 1–2 weeks after HIFU therapy has been shown to exhibit enhancement at the periphery of the cavity due to the early inflammatory response to treatment. Further MRI of the prostate 12 months post-HIFU would allow

assessment of the treatment coverage as well as identifying viable malignant tissue. Since there is no consensus on biochemical failure after focal therapy, and due to residual secretion of PSA from benign tissue, PSA levels may not clearly indicate residual, recurrent or new tumour growth. Hence, mpMRI plays a vital role in detecting tumours and guide targeted post-HIFU prostate biopsies. Evaluating local recurrence after treatment with focal therapy is essential to planning second-line treatment.

Studies have shown that mpMRI is accurate in detecting local recurrences after whole-gland treatment with HIFU. MRI combining t2-weighted and DCE images is used to guide post-HIFU biopsies to areas containing recurrent tumour, increasing the probability of positive biopsies as compared to routine biopsies post-HIFU therapy [53, 54]. Little data is available on the appearances of the prostate after focal therapy, especially HIFU treatment. There is atrophy of the tissue in the ablated area, creating a cavity. Recurrences normally occur at the periphery of the treated zone. Pretreatment mpMRI is useful as a reference in these cases [55–57].

Tips And Tricks

Gland Size

The size and in particular the height of the prostate gland should be taken into account when planning treatment. It may be difficult for the ultrasound waves to reach part, or all, of the anterior gland. Previously, TURP was performed when planning whole-gland HIFU procedures, to debulk and obtain better access to the anterior gland, as well as reducing the risk of postoperative urinary retention. In cases of focal HIFU, preoperative treatment with 5-alpha reductase inhibitors may be used to reduce gland size.

Calcification

Calcification within the prostate leads to reverberation as well as shielding of the targeted prostate tissue from part of the ultrasound pulse, resulting in an inadequate heating of the tissue. Intra-prostatic calcification may be removed via TURP, but this would add significant length and morbidity to the procedure.

Patient Movement

Patient movement intraoperatively may lead areas of viable malignant tissue to remain after treatment. Precise planning and placement of the small HIFU pulses are necessary for the entire tumour to be successfully ablated. Hence, it is not advisable to perform this treatment under spinal/regional anaesthesia, and adequate muscle relaxation during general anaesthesia is essential.

Heat Sink Effect

The heat sink effect refers to an area of prostate tissue that overheats, preventing adequate transmission of ultrasound waves to the targeted area. This normally occurs if the time between the HIFU pulses is not adequate enough to allow tissue cooling. It may also occur if an area has high water content, such as a cyst. This effect can also occur in highly vascularised tissue, which is more resistant to thermal ablation due to the heat sink effect of the blood supply. Prostate tissue is as such. This cavitation phenomenon due to steam formation (gas micro-bubbles) and tissue disruption is difficult to control intraoperatively [3, 58].

Swelling of the Prostate

Swelling of the prostate occurs during the treatment requiring careful monitoring, and possible readjustment of treatment blocks may be necessary. Should the focal pulse points fall outside the contour of the prostate on the US images, treatment must be paused and treatment planning must be adjusted.

Complications

Rectal Wall Injury and Rectal Fistulae

Injury to the rectal wall during HIFU occurs due to overheating. This is prevented by rectal wall monitoring intraoperatively, by the device, as well as by circulating cool, degassed water around the transducer. Rectal fistulae rarely occur in the primary setting; however, HIFU in the salvage setting has been reported to result in 3–6 % recto-urethral fistulae (RUF) [31, 32]. The rate is even higher in those patients receiving salvage HIFU after a combination of ERBT and brachytherapy. Ahmed et al.'s group reported a rate of 3 out of 5 such patients developing a RUF, 5–8 months post-salvage HIFU [59] (Fig. 10.5).

Symptoms of RUF include pneumaturia, voiding of urine rectally, faeculant urine, recurrent UTI and suprapubic pain. RUF can be managed conservatively by insertion of suprapubic catheter and diverting the urine away from the fistula. Alternatively, if the RUF persists, a defunctioning colostomy and open surgical repair must be performed.

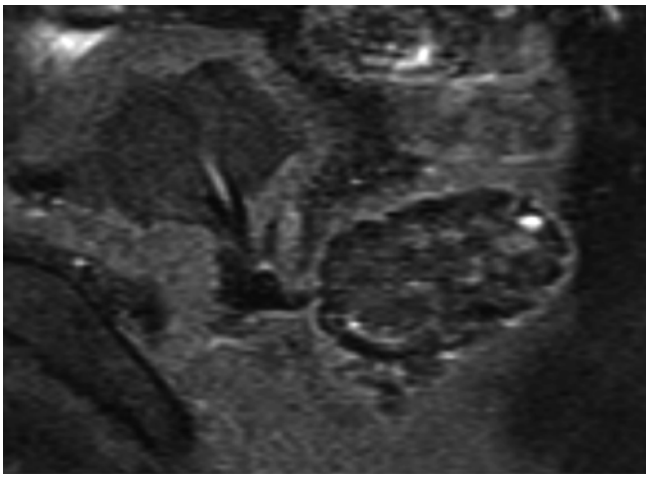

Fig. 10.5 T1-weighted images of recto-urethral fistula, catheter in situ

Future Perspectives

HIFU clearly has a significant role to play in the management of localised prostate cancer as well as a feasible option in cases of radiation failure. The future application of HIFU is focal therapy. Promising oncological and functional outcomes with focal HIFU have already been well published in several series.

Further advances in HIFU devices combined with refinement in imaging modalities will continue to propel this technology even further and may well place HIFU on the forefront of minimally invasive, image-guided options for the treatment of localised prostate cancer.

References

1. Murat F-JL, Gelet A. Current status of high-intensity focused ultrasound for prostate cancer: technology, clinical outcomes, and future. Curr Urol Rep. 2008;9:113–21.
2. Haar GT, Coussios C. High intensity focused ultrasound: physical principles and devices. Int J Hyperthermia. 2007;23:89–104.
3. Marberger M. Energy-based ablative therapy of prostate cancer: high-intensity focused ultrasound and cryoablation. Curr Opin Urol. 2007;17:194–9.
4. Dickinson L, et al. Image-directed, tissue-preserving focal therapy of prostate cancer: a feasibility study of a novel deformable magnetic resonance-ultrasound (MR-US) registration system. BJU Int. 2013;112:594–601.
5. Poissonnier L, et al. Control of prostate cancer by transrectal HIFU in 227 patients. Eur Urol. 2007;51:381–7.
6. Blana A, et al. Eight years' experience with high-intensity focused ultrasonography for treatment of localized prostate cancer. Urology. 2008;72:1329–33; discussion 1333–4.
7. Crouzet S, et al. Multicentric oncologic outcomes of high-intensity focused ultrasound for localized prostate cancer in 803 patients. Int Braz J Urol. 2011;37:128.
8. Crouzet S, et al. Whole-gland ablation of localized prostate cancer with high-intensity focused ultrasound: Oncologic outcomes and morbidity in 1002 patients. Eur Urol. 2014;65:907–14.
9. Ripert T, et al. Six years' experience with high-intensity focused ultrasonography for prostate cancer: Oncological outcomes using the new "Stuttgart" definition for biochemical failure. BJU Int. 2011;107:1899–905.
10. Pfeiffer D, Berger J, Gross AJ. Single application of high-intensity focused ultrasound as a first-line therapy for clinically localized prostate cancer: 5-year outcomes. BJU Int. 2012;110:1702–8.
11. Thüroff S, Chaussy C. Evolution and outcomes of 3 MHz high intensity focused ultrasound therapy for localized prostate cancer during 15 years. J Urol. 2013;190:702–10.
12. Blana A, et al. First analysis of the long-term results with transrectal HIFU in patients with localised prostate cancer. Eur Urol. 2008;53:1194–203.
13. Blana A, et al. Complete high-intensity focused ultrasound in prostate cancer: outcome from the @-Registry. Prostate Cancer Prostatic Dis. 2012;15:256–9.
14. Uchida T, et al. Transrectal high-intensity focused ultrasound for the treatment of localized prostate cancer: eight-year experience. Int J Urol. 2009;16:881–6.
15. Shoji S, et al. Quality of life following high-intensity focused ultrasound for the treatment of localized prostate cancer: a prospective study. Int J Urol. 2010;17:715–9.
16. Inoue Y, Goto K, Hayashi T, Hayashi M. Transrectal high-intensity focused ultrasound for treatment of localized prostate cancer. Int J Urol. 2011;18:358–62.
17. Ahmed HU, et al. High-intensity-focused ultrasound in the treatment of primary prostate cancer: the first UK series. Br J Cancer. 2009;101:19–26.
18. Madersbacher S, Pedevilla M, Vingers L, Susani M, Marberger M. Effect of high-intensity focused ultrasound on human prostate cancer in vivo. Cancer Res. 1995;55:3346–51.
19. Beerlage HP, Thüroff S, Debruyne FM, Chaussy C, de la Rosette JJ. Transrectal high-intensity focused ultrasound using the Ablatherm device in the treatment of localized prostate carcinoma. Urology. 1999;54:273–7.
20. Muto S, et al. Focal therapy with high-intensity-focused ultrasound in the treatment of localized prostate cancer. Jpn J Clin Oncol. 2008;38:192–9.
21. Murat FJ, et al. 854 Focal Therapy of Prostate Cancer (PCA) with HIFU: influence on erectile dysfunction (ED). Eur Urol Suppl. 2009;8:334.
22. Ahmed HU, et al. Focal therapy for localized prostate cancer: a phase I/II trial. J Urol. 2011;185:1246–54.
23. Ahmed HU, et al. Focal therapy for localised unifocal and multifocal prostate cancer: a prospective development study. Lancet Oncol. 2012;13:622–32.
24. Ahmed HU, et al. Focal ablation targeted to the index lesion in multifocal localised prostate cancer: a Prospective Development Study. Eur. Urol. 2015. doi:10.1016/j.eururo.2015.01.030.
25. El Fegoun AB, et al. Focal therapy with high-intensity focused ultrasound for prostate cancer in the elderly. A feasibility study with 10 years follow-up. Int Braz J Urol. 2011;37:212–3.
26. Zelefsky MJ, Reuter VE, Fuks Z, Scardino P, Shippy A. Influence of local tumor control on distant metastases and cancer related mortality after external beam radiotherapy for prostate cancer. J Urol. 2008;179:1368–73; discussion 1373.
27. Kuban DA, et al. Long-term multi-institutional analysis of stage T1-T2 prostate cancer treated with radiotherapy in the PSA era. Int J Radiat Oncol Biol Phys. 2003;57:915–28.
28. Agarwal PK, Sadetsky N, Konety BR, Resnick MI, Carroll PR. Treatment failure after primary and salvage therapy for prostate cancer: Likelihood, patterns of care, and outcomes. Cancer. 2008;112:307–14.

29. Lee WR, Hanks GE, Hanlon A. Increasing prostate-specific antigen profile following definitive radiation therapy for localized prostate cancer: clinical observations. J Clin Oncol. 1997;15:230–8.
30. Murat FJ, et al. Mid-term results demonstrate salvage high-intensity focused ultrasound (HIFU) as an effective and acceptably morbid salvage treatment option for locally radiorecurrent prostate cancer. Eur Urol. 2009;55:640–9.
31. Zacharakis E, et al. The feasibility and safety of high-intensity focused ultrasound as salvage therapy for recurrent prostate cancer following external beam radiotherapy. BJU Int. 2008; 102:786–92.
32. Gelet A, et al. Local recurrence of prostate cancer after external beam radiotherapy: early experience of salvage therapy using high-intensity focused ultrasonography. Urology. 2004;63:625–9.
33. Crouzet S, et al. Locally recurrent prostate cancer after initial radiation therapy: early salvage high-intensity focused ultrasound improves oncologic outcomes. Radiother Oncol. 2012;105: 198–202.
34. Song W, et al. High-intensity focused ultrasound as salvage therapy for patients with recurrent prostate cancer after radiotherapy. Korean J Urol. 2014;55:91–6.
35. Ahmed HU, et al. Focal salvage therapy for localized prostate cancer recurrence after external beam radiotherapy: a pilot study. Cancer. 2012;118:4148–55.
36. Baco E, et al. Hemi salvage high-intensity focused ultrasound (HIFU) in unilateral radiorecurrent prostate cancer: a prospective two-centre study. BJU Int. 2014. doi:10.1111/bju.12545.
37. Gerber GS, et al. Results of radical prostatectomy in men with clinically localized prostate cancer. JAMA. 1996;276:615–9.
38. Chun FK-H, et al. Anatomic radical retropubic prostatectomy-long-term recurrence-free survival rates for localized prostate cancer. World J Urol. 2006;24:273–80.
39. Asimakopoulos AD, Miano R, Virgili G, Vespasiani G, Finazzi Agrò E. HIFU as salvage first-line treatment for palpable, TRUS-evidenced, biopsy-proven locally recurrent prostate cancer after radical prostatectomy: a pilot study. Urol Oncol. 2012;30:577–83.
40. Hayashi M, Shinmei S, Asano K. Transrectal high-intensity focused ultrasound for treatment for patients with biochemical failure after radical prostatectomy. Int J Urol. 2007;14:1048–50.
41. Potters L, et al. 12-year outcomes following permanent prostate brachytherapy in patients with clinically localized prostate cancer. J Urol. 2005;173:1562–6.
42. Yutkin V, et al. Salvage high-intensity focused ultrasound for patients with recurrent prostate cancer after brachytherapy. Urology. 2014;84:1157–62.
43. Chen JC, et al. Prostate cancer: MR imaging and thermometry during microwave thermal ablation-initial experience. Radiology. 2000;214:290–7.
44. Hazle JD, et al. MRI-guided thermal therapy of transplanted tumors in the canine prostate using a directional transurethral ultrasound applicator. J Magn Reson Imaging. 2002;15:409–17.
45. Germain D, Chevallier P, Laurent A, Saint-Jalmes H. MR monitoring of tumour thermal therapy. MAGMA. 2001;13:47–59.
46. Ross AB, et al. Highly directional transurethral ultrasound applicators with rotational control for MRI-guided prostatic thermal therapy. Phys Med Biol. 2004;49:189–204.
47. Lafon C, Koszek L, Chesnais S, Theillère Y, Cathignol D. Feasibility of a transurethral ultrasound applicator for coagulation in prostate. Ultrasound Med Biol. 2004;30:113–22.
48. Partanen A, et al. Magnetic resonance imaging (MRI)-guided transurethral ultrasound therapy of the prostate: a preclinical study with radiological and pathological correlation using customised MRI-based moulds. BJU Int. 2013;112:508–16.
49. Chopra R, et al. MRI-compatible transurethral ultrasound system for the treatment of localized prostate cancer using rotational control. Med Phys. 2008;35:1346–57.
50. Chopra R, et al. MR imaging-controlled transurethral ultrasound therapy for conformal treatment of prostate tissue: initial feasibility in humans. Radiology. 2012;265:303–13.
51. Blana A, et al. High-intensity focused ultrasound for prostate cancer: comparative definitions of biochemical failure. BJU Int. 2009;104:1058–62.
52. Blana A, et al. Morbidity associated with repeated transrectal high-intensity focused ultrasound treatment of localized prostate cancer. World J Urol. 2006;24:585–90.
53. Ben Cheikh A, et al. MR detection of local prostate cancer recurrence after transrectal high-intensity focused US treatment: preliminary results. J Radiol. 2008;89:571–7.
54. Rouvière O, et al. Prostate cancer transrectal HIFU ablation: detection of local recurrences using T2-weighted and dynamic contrast-enhanced MRI. Eur Radiol. 2010;20:48–55.
55. Rouvière O, et al. MRI appearance of prostate following transrectal HIFU ablation of localized cancer. Eur Urol. 2001;40:265–74.
56. Susani M, Madersbacher S, Kratzik C, Vingers L, Marberger M. Morphology of tissue destruction induced by focused ultrasound. Eur Urol. 1993;23 Suppl 1:34–8.
57. Rouvière O, Gelet A, Crouzet S, Chapelon J-Y. Prostate focused ultrasound focal therapy—imaging for the future. Nat Rev Clin Oncol. 2012. doi:10.1038/nrclinonc.2012.136.
58. Tsakiris P, Thüroff S, de la Rosette J, Chaussy C. Transrectal high-intensity focused ultrasound devices: a critical appraisal of the available evidence. J Endourol. 2008;22:221–9.
59. Ahmed HU, et al. Rectal fistulae after salvage high-intensity focused ultrasound for recurrent prostate cancer after combined brachytherapy and external beam radiotherapy. BJU Int. 2009;103:321–3.

Laser Interstitial Thermal Therapy

11

Richard Ho, Arvin K. George, and Peter A. Pinto

Prostate cancer (PCa) continues to be the leading non-cutaneous cancer in men in the United States and responsible for nearly 30,000 deaths and 230,000 new cases per year [1]. The widespread use of prostate-specific antigen (PSA) testing has led to an overall increase in the proportion of men diagnosed with low-risk disease with concurrent decrease in disease-specific mortality [2]. According to the Surveillance, Epidemiology, and End Results (SEER) database, the advent of PSA screening in 1987 has since resulted in approximately a sevenfold increase in PCa incidence when compared to the pre-PSA era [3]. The increased detection of low-risk disease has also corresponded to a greater proportion of men diagnosed with PCa undergoing radical prostatectomy (RP) or radiation therapy (RT). The complications associated with these procedures such as urinary incontinence (20 % for RP and 5 % for RT) and erectile dysfunction (64 % for RP and 66 % for RT) in many cases outweigh the benefits [4]. The European Randomized Study of Screening for Prostate Cancer (ERSPC) trial also found that approximately half of those who underwent surgery were found to have cancers that were defined to be clinically indolent (<0.5 cm [3] tumor volume, organ-confined, Gleason score ≤6) [5]. Active surveillance (AS) has been an appealing alternative for managing low-risk disease, but concerns have been raised regarding potential decreases in long-term survival rates [6]. Studies with men offered with AS with selective delayed therapy have found a large number of patients who ultimately underwent RP to be harboring advanced disease [7]. The inaccuracy of disease risk stratification at the time of diagnosis has also led to 14–41 % of men assigned to AS converting to RP or RT due to upgrading or upstaging [8].

Focal therapy is gaining momentum as a viable therapeutic option due to advances in imaging modalities that can reliably characterize cancerous lesions as well as improvements in targeted biopsy techniques allowing for proper staging of suspicious lesions. Multiparametric magnetic resonance imaging (mpMRI) has been shown to be able to localize the site of clinically significant PCa prior to prostate biopsy [9]. Suspicious MRI focal abnormalities can be biopsied directly in the MRI unit or under transrectal ultrasound (TRUS) guidance using software that co-registers and fuses the MRI and ultrasound (US) images [10].

Prostate cancer is typically characterized as a multifocal disease with lesions often consisting of varying sizes and Gleason scores identified on MRI and biopsy. In the past, the multifocal nature of PCa has been a challenge for urologists to pursue minimally invasive focal therapy. Recent studies have supported the implication that the behavior of the index or dominant lesion may help predict disease progression [11]. Additionally, it has been shown that between 13 and 33 % of patients with PCa actually have a unifocal lesion and would be eligible for focal therapy [12]. The majority of secondary lesions are composed of Gleason 6 disease or lower, representing no immediate threat to the patient [13]. Though currently under investigation, the concept of focally ablating only the index lesion would theoretically be able to achieve oncologic control while minimizing the treatment-related morbidity associated with more invasive and extensive procedures [14].

Different energy sources have been investigated for focal therapy including cryotherapy [15], high-intensity focused ultrasound (HIFU) [16], photodynamic therapy [17], and laser ablation. Laser interstitial thermal therapy (LITT), also commonly referred to as focal laser ablation (FLA), is an evolving treatment paradigm that is able to destroy a predefined region of the prostate that harbors clinically significant disease. One of the main advantages associated with laser technology is that the fibers used avoid distortion of electromagnetic fields [18]. This allows for simultaneous real-time MRI imaging and magnetic resonance (MR) thermometry during treatment, providing accurate delivery of ablative energy to an intended focus with immediate visualization of the targeted treatment zone [19]. Laser ablation

R. Ho • A.K. George, MD • P.A. Pinto, MD (✉)
Urologic Oncology Branch, The National Cancer Institute, National Institutes of Health, Bethesda, MD, USA
e-mail: arvinkgeorge@gmail.com; pintop@mail.nih.gov

A.R. Rastinehad, D.N. Siegel (eds.), *Interventional Urology*, DOI 10.1007/978-3-319-23464-9_11

also results in more homogenous tissue necrosis, has a relatively lower cost, and is widely available [20].

Herein, we present the principles of LITT and the role of mpMRI for treatment monitoring and real-time visualization of targeted treatment zones and review the currently available literature.

Principles of Laser Ablation

LITT is used to destroy a tissue target by means of laser radiation energy. Rapid temperature elevation of targeted tissue causes protein denaturation resulting in in vivo tissue destruction generally when temperatures reach more than 60 °C [21]. Due to its optical absorption rate and relatively low vascularity, prostatic tissue is well suited for LITT [18]. When performed properly, LITT can accurately deliver laser energy to destroy the target tissue while sparing the surrounding tissues and neurovascular structures [22].

The introduction of the laser fiber can be performed either through a transperineal or transrectal procedure. In canine prostate models, Stafford et al. [19] used real-time three-dimensional (3D) MRI to accurately position and deliver laser energy within a mean (±SD) of 1.1 (±0.7) mm of a target site. They demonstrated that accurate laser fiber localization to soft tissue targets is a feasible task and that the use of real-time MRI can allow for precise estimates of the extent of tissue necrosis.

In LITT, focused electromagnetic energy is converted to thermal energy causing coagulative tissue necrosis. Different wavelengths and technologies of laser radiation have been used throughout the development of this technology. The first attempts of LITT of prostatic tissue used 1064 nm neodymium-doped yttrium aluminum garnet (Nd:YAG) lasers [23, 24], but 980 mm diode lasers are now being used for their portability, power, and cost-effectiveness [25]. Current diode lasers operate within the infrared spectrum with the use of a fiber-optic delivery accessory.

Role of MRI

Advances in MRI have helped to eliminate many hurdles in the adoption of focal therapy. MpMRI has been emerging as a useful modality to reliably detect and characterize clinically significant PCa due to its excellent ability to differentiate soft tissue. Although T2-weighted MRI alone demonstrates low sensitivity for tumor detection, the addition of parameters such as diffusion-weighted imaging (DWI), dynamic contrast-enhanced (DCE) sequences, and MR spectroscopy has significantly improved sensitivity and positive predictive value [26]. In addition, a negative mpMRI has a high negative predictive value for the lack of clinically significant PCa [27]. Bratan et al. [28] correlated preoperative mpMRI to postoperative surgical specimens in 175 men who underwent RP using a 27-grid diagram. They considered true positives as focal abnormalities on mpMRI whose diameters corresponded between 50 and 150 % to a region seen on histology. Using this method, they were able to achieve detection levels of 25, 48, and 71 % for Gleason 6 tumors; 63, 85, and 97 % for Gleason 7 tumors; and 80, 93, and 100 % of Gleason >7 tumors of <0.5, 0.5–2, and >2 cm diameter, respectively. Turkbey et al. [29] corrected for variations between histological lesion and MRI findings with a shrinkage factor and a co-registration method. Furthermore, custom 3D molds were made to accurately register specimen pathology to the mpMRI images. They found that mpMRI had a high sensitivity for lesions greater than 5 mm in diameter and Gleason scores greater than 7 (3+4), while low suspicious lesions reliably resulted in benign tissue or low-grade PCa on histopathology.

Focal therapy relies on the fact that a physician can identify the index lesion. A new biopsy method has emerged involving the co-registration of MRI with ultrasound images (MR/US) to detect PCa. This biopsy technique has demonstrated superior cancer detection rates of 54.4 % compared with 27–40.3 % for standard random biopsy [30]. Hadaschik et al. [31] reported a similar cancer detection rate of 59.4 % in a cohort of 106 patients undergoing perineal stereotactic prostate biopsy under MR/US fusion guidance. Siddiqui et al. [10] also found that in comparison to standard extended-sextant biopsy, MR/US-guided biopsies diagnosed 30 % more high-risk cancers and 17 % fewer low-risk cancers. MR/US-guided biopsy alone was able to differentiate low-risk from intermediate- and high-risk disease in 170 men with whole-gland pathology after prostatectomy better than standard biopsy or the 2 approaches combined (AUC 0.73, 0.59, and 0.67, respectively; p <0.05 for all comparisons).

Prior to using MRI for temperature monitoring, contrast-enhanced ultrasonography (CEUS) was used. Thermal effects created by the ablation process reduce blood perfusion significantly causing a decreased uptake of microbubbles in the ablated area. This leads to a loss in CEUS signal, producing clear delineation between viable and nonviable tissue [32]. Proton-resonance frequency (PRF) shift MR thermometry has now allowed real-time quantification of temperature using changes in the phase of gradient-recalled echo (GRE) images to estimate relative temperature changes [33]. This enhances the ability to minimize thermal destruction to surrounding tissues and neurovascular structures during the ablation process. Peters et al. [34] demonstrated on two in vivo canine prostate models that PRF shift MR thermometry correlated with temperature maps of histological sections and the thermal coagulation margins. The previously mentioned study by Stafford et al. [19] also showed that thermal damage predicted by an MRI and an Arrhenius

damage integral, a first-order thermochemical rate equation in which temperature history determines damage [35], correlated remarkably well with damage on 3D T1-weighted post-contrast images in the same plane (Pearson's $r^2=0.94$). Colin et al. [36] applied MRI-guided LITT to treat Dunning rat prostate tumors. Ellipsoid lesions visible on MRI correlated to coagulative necrosis within an ellipsoid-shaped lesion with volumes strongly correlating to histological analysis ($r=0.87$). Real-time MR thermometry has been shown to be an extremely useful tool in minimizing damage to surrounding organs and tissue during ablation of target lesions.

Current Status of LITT

A review of recent LITT studies is shown in Table 11.1. To date, almost all published studies involving LITT have been small non-randomized phase 1 studies with short-term follow-up.

In 2009, Atri et al. [32] introduced the application of CEUS-guided LITT. They treated a patient with biopsy-proven, solitary focus, low-risk PCa, visualized on mpMRI prior to the procedure. During and after photothermal therapy treatment, they observed large hypocontrast regions surrounding the treatment fibers, indicating the presence of an avascular lesion. The lesion they measured using CEUS also corresponded to tissue devascularization seen on a gadolinium (Gd)-enhanced MRI lesion 1 week after the procedure.

One of the first reported phase 1 studies assessing the feasibility of using a CEUS-guided focal laser with MRI was by Lindner et al. in 2009 [37]. They looked at 12 patients, including a patient from the 2009 Atri et al. study [32], with biopsy-proven low-risk PCa (T1c or T2a, PSA <10 ng/ml, Gleason score ≤6, only 1 of 12 cores <30 % cancer following transrectal ultrasound (TRUS)-guided biopsy) that underwent interstitial photothermal ablation. MRI was used to confirm and target the lesion, and a 3D ultrasound was fused to this to help guide the laser. Out of this cohort, 3 patients complained of perineal discomfort, 2 developed mild hematuria, 2 had hematospermia, and 1 complained of fatigue. There was no reported decrease in mean urinary or sexual function scores at 1, 3, and 6 months postoperatively. TRUS-guided 10-core systematic prostate biopsies performed 3–6 months after ablation showed 6 patients (50 %) had completely negative biopsies, 2 patients had a tumor found on the contralateral untreated side, and 4 patients had a residual tumor in previously treated areas. Of these 4 patients, 2 were found to have minimal disease on follow-up biopsy, and 2 were found to have cores greater than 50 % of Gleason 6 disease. This same group also performed a study of 4 patients who underwent LITT followed by RP in 2010 [38]. They correlated MRI-calculated ablated volume to the volume of homogenous necrosis seen on whole-mount histology. Their results showed there was a very good correlation ($r=0.89$) suggesting that post-ablation MRI could be a useful tool in determining the extent of actual tissue ablation.

One of the initial experiences in using real-time MRI guidance during LITT was performed by Raz et al. in 2010 [25]. MRI guidance allowed for improved visualization of the target, more accurate direction of the laser fiber, real-time monitoring of the ablation site and surrounding tissue, as well as immediate feedback on the extent of the treatment. The patients from this study were discharged without complications, and preservation of the neurovascular bundles was noted. There were also no adverse effects noted after 1 month of treatment.

Woodrum et al. in 2010 [39] also initially explored the feasibility of performing transperineal LITT for focal targets in the prostate using real-time MRI guidance. Previous studies had been focused on 1.5 T field strengths, but this study demonstrated the practicality of a 3.0 T MRI, which offered greater spatial and temporal resolution. They were able to verify that a perineal guidance grid allowed for accurate needle placement through a transperineal route at the appropriate depth in the prostate. Furthermore, they were able to correlate the gross appearance of the ablation zone to the temperature mapping estimates.

In 2011, Woodrum et al. [40] explored the use of 3.0 T MR focal laser thermal ablation therapy within the prostate

Table 11.1 Summary of clinical trials involving LITT of the prostate

Authors	Year	Study type	Patients (*n*)	MR field strength	Laser source	Treatment method	Real-time imaging
Atri et al.	2009	Patient	1	NA	830 nm (Indigo diode)	Transperineal	CEUS
Lindner et al.	2009	Patient	12[a]	NA	830 (Indigo diode)	Transperineal	CEUS
Lindner et al.	2010	Patient	4	NA	980 nm (Visualase diode)	Transperineal	CEUS
Raz et al.	2010	Patient	2	1.5 T	980 nm (Visualase diode)	Transperineal	MRI + CEUS
Woodrum et al.	2010	Human cadaver	5	3 T	980 nm (Visualase diode)	Transperineal	MRI
Woodrum et al.	2011	Patient	1	3 T	980 nm (Visualase diode)	Transperineal	MRI
Oto et al.	2013	Patient	9	1.5 T	980 nm (Visualase diode)	Transperineal	MRI

[a]The 12-patient cohort of Lindner et al. includes the 1-patient cohort of the Atri et al. study

bed in PCa recurrence. They reported a study in which they used LITT with real-time MR temperature mapping using the PRF shift to treat a patient with a documented recurrence after RP. The case was successful in treating the patient's recurrence with a decrease in PSA from 2.0 to 0.42 ng/ml at 2 months after therapy. Early follow-up showed no posttreatment incontinence, rectal wall injury, or other complications.

In 2013, Oto et al. [41] published the results of their phase 1 trial (federally registered NCT01192438) evaluating the safety and feasibility of MRI-guided focal laser therapy in men with clinically low-risk PCa (clinical stage T1c–T2a, PSA <10 ng/ml, Gleason ≤7, minimum of 12 biopsy cores with 3 or fewer containing cancer, no single biopsy with >50 % tumor involvement, and a suspicious lesion visible on MRI corresponding to the biopsy site). In total, 9 patients were treated with 8 having Gleason grade 6 cancer and 1 having grade 7 cancer. No major complications or serious adverse events after ablation occurred. MR imaging-guided biopsy of the ablation site was performed at 6 months follow-up. This revealed benign prostate in 7 patients and Gleason grade 6 cancer in 2. A retrospective review of the ablation images were performed showing that the lesion site was not completely covered by the ablation zone for the 2 patients with positive findings at follow-up biopsy. Quality-of-life (QOL) surveys were recorded at baseline and at 1, 3, and 6 months post-ablation. The study reported no statistically significant change from baseline in sexual function or urinary symptom assessments.

Lindner et al. also updated their phase 1 study to 38 men in 2013 continuing to show minimal complications after a year of posttreatment follow-up. A concerning outcome in this study was that 26 % of men treated showed a positive biopsy outside the ablated region at 4 months follow-up. This finding stresses the need for larger multi-institutional studies with longer follow-up to further elucidate the efficacy and side effect profile of focal therapies [42].

LITT Experience at the National Institutes of Health

The National Cancer Institute (NCI) at the National Institutes of Health (NIH) in Bethesda, Maryland, USA, is currently the site of an institutional review board-approved, phase 1 LITT trial [43]. The selection criteria include patients with organ-confined clinical T2a Gleason ≤7 (3+4) in 4 cores or less that also have been screened with mpMRI using a 3.0 T MRI scanner (Achieva, Philips Healthcare, Best, the Netherlands). Standardized MRI acquisition is composed of T2-weighted, axial DWI, 3D spectroscopy, and axial DCE sequences using a combination of a 16-channel cardiac surface coil (SENSE, Philips Healthcare) placed over the pelvis together with an endorectal coil (BPX-30, Medrad, Pittsburgh, Pennsylvania) filled with PFC-770. Suspicious lesions are independently evaluated and graded on a validated scoring system [27] incorporating the number of positive functional MRI modalities by two experienced genitourinary radiologists. Targeted biopsies are then performed using an MR/US fusion platform along with standard 12-core random TRUS biopsy. Within 6 months, biopsy-proven cancerous lesions are treated using the FDA-approved Visualase 980 nm diode laser system (Visualase Inc., Houston, Texas, USA).

The ablation procedure is performed in gantry, using a 3.0 T magnet to acquire an mpMRI image to help locate the desired tumor, guide laser fiber placement, and confirm optimal placement. A transperineal approach is utilized which reduces the risk of rectal wall damage with the advantage of improved access to the apical and anterior portions of the prostate. An MR-compatible transperineal template is fixed to an endorectal coil, and an MR image of the prostate is taken for grid registration and to ensure proper placement of the fiber before treatment. Titanium trocars and guide catheters are used to ensure proper depth of applicator placement confirmed by the planning software (Visualase Inc., Houston, Texas, USA). When the laser tip is confirmed to be in the desired location, the laser is activated at a power level insufficient to cause thermal injury so that appropriate placement of the applicator and proper operation of thermal imaging can be verified. A single ablation typically lasts 1–2 minutes with repeated imaging following cessation of laser activity to ensure cooling of the prostate. Real-time assessment of ablative zones is achieved using MR thermometry (Fig. 11.1).

Increasing laser power output, larger caliber fibers, and new lasers have allowed for larger ablation zones, which often help to achieve better tumor-free margins and decrease local tumor progression but risk unwanted collateral damage to nearby structures [18]. The use of hydrodissection has been incorporated in LITT at the NIH to facilitate tumors abutting the rectum, creating a buffer to protect vital structures. Although normal saline and 5 % dextrose are commonly used, migration of fluid is difficult to control and may require repeat instillation of fluid during the procedure. This had led to the design of a thermoreversible poloxamer solution that can be injected as a solution but forms a semisolid gel at room temperature [44]. Studies have shown favorable outcomes especially during percutaneous microwave ablation [45]. The NIH is currently working on using this versatile solution in hydrodissection during LITT.

Patients undergoing LITT at the NIH undergo scheduled mpMRI to monitor treatment outcomes (Fig. 11.2). Routine mpMRI is taken 1 day, 6 months, and 1 year after treatment with annual imaging taken subsequently. The accrual ceiling for the phase 1 study is now complete with a phase 2 study under way.

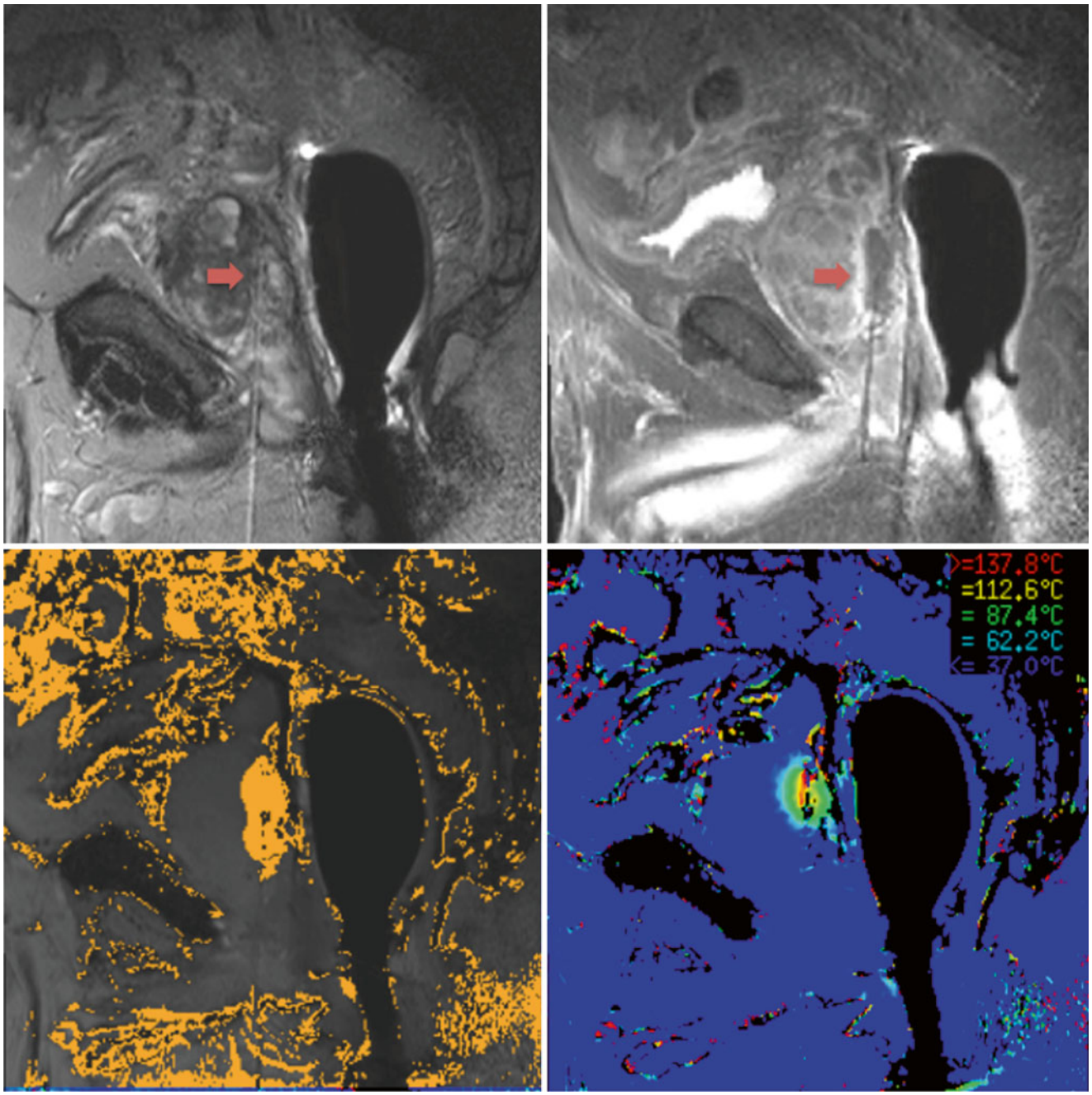

Fig. 11.1 MRI images obtained before (*top left*) and after (*top right*) LITT on a patient at the NIH. The tip of the needle can be visualized by the *red arrow*. Destruction mapping is seen on the *bottom left* and real-time thermometry is seen on the *bottom right*

Conclusion

Focal therapy is an evolving treatment paradigm that still requires further investigation. The application of focal treatment for PCa has been met with many difficulties: criteria for patient selection, precise localization, visualization and characterization of clinically significant cancer foci, accurate and precise guidance of ablative energy in the treatment zone, oncologic efficacy evaluation, and surveillance modalities [20]. Despite these challenges, preliminary phase 1 studies have shown that the LITT is feasible with good short-term efficacy and safety. Current uncertainties regarding long-term oncologic control will have to be answered as LITT moves out of its infancy and into larger clinical studies. The success of focal therapy revolves around the ability to accurately locate the tumor site as well as stage and risk-stratify patients, which has been progressing due to the recent advances in soft tissue imaging and mpMRI. Further advancements in using 3D

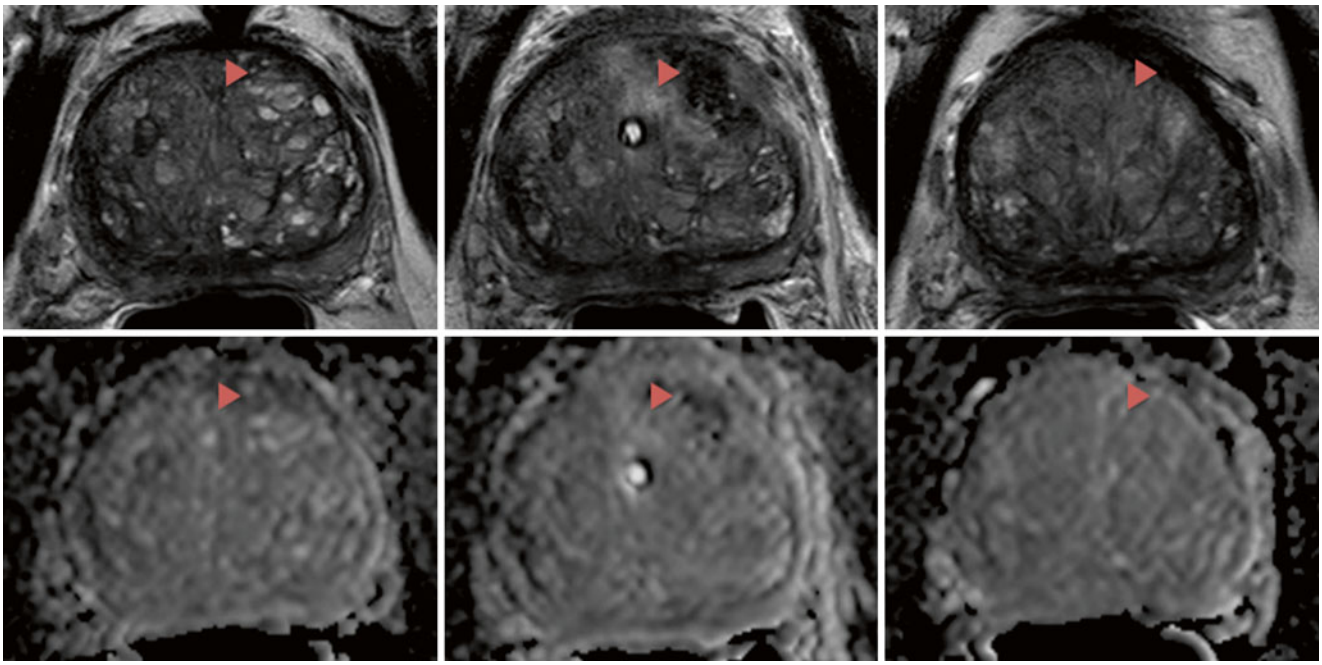

Fig. 11.2 T2 (*top row*) and DWI (*bottom row*) images of a patient who underwent LITT at the NIH. The patient had clinical T1 stage, Gleason 7 (3+4) disease involving the left mid-base anterior central gland with a pretreatment PSA of 6.5. The lesion, ablation zone, and scar tissue can be visualized by the red arrows before the ablative procedure (*left column*), 1 day after the ablation (*middle column*), and 1 year after the ablation (*right column*), respectively

MRI/US co-registration platforms will enable urologists to not only localize clinically significant disease more accurately but will serve as a tool to destroy MRI targets possibly under local anesthesia or in an office-based operating room [22]. It is likely that MRI-guided LITT will be adopted in the future as a powerful tool for urologists to treat prostate cancer.

References

1. Siegel RL, Miller KD, Jemal A. Cancer statistics, 2015. CA Cancer J Clin. 2015;65(1):5–29. doi:10.3322/caac.21254.
2. Loeb S, Bjurlin MA, Nicholson J, et al. Overdiagnosis and overtreatment of prostate cancer. Eur Urol. 2014;65(6):1046–55. doi:10.1016/j.eururo.2013.12.062.
3. Ries LAG, Melbert D, Krapcho M, et al. SEER cancer statistics review, 1975–2005. 2008. http://seer.cancer.gov/csr/1975_2005.
4. Sanda MG, Dunn RL, Michalski J, et al. Quality of life and satisfaction with outcome among prostate-cancer survivors. N Engl J Med. 2008;358(12):1250–61. doi:10.1056/NEJMoa074311.
5. Steyerberg EW, Roobol MJ, Kattan MW, van der Kwast TH, de Koning HJ, Schröder FH. Prediction of indolent prostate cancer: validation and updating of a prognostic nomogram. J Urol. 2007;177(1):107–12. doi:10.1016/j.juro.2006.08.068; discussion 112.
6. Bill-Axelson A, Holmberg L, Garmo H, et al. Radical prostatectomy or watchful waiting in early prostate cancer. N Engl J Med. 2014;370(10):932–42. doi:10.1056/NEJMoa1311593.
7. Klotz L. Active surveillance with selective delayed intervention for favorable risk prostate cancer. Urol Oncol. 2006;24(1):46–50. doi:10.1016/j.urolonc.2005.07.002.
8. Cooperberg MR, Carroll PR, Klotz L. Active surveillance for prostate cancer: progress and promise. J Clin Oncol. 2011;29(27):3669–76. doi:10.1200/JCO.2011.34.9738.
9. Turkbey B, Mani H, Aras O, et al. Prostate cancer: can multiparametric MR imaging help identify patients who are candidates for active surveillance? Radiology. 2013;268(1):144–52. doi:10.1148/radiol.13121325.
10. Siddiqui MM, Rais-Bahrami S, Turkbey B, et al. Comparison of MR/ultrasound fusion–guided biopsy with ultrasound-guided biopsy for the diagnosis of prostate cancer. JAMA. 2015;313(4):390. doi:10.1001/jama.2014.17942.
11. Stamey TA, McNeal JE, Yemoto CM, Sigal BM, Johnstone IM. Biological determinants of cancer progression in men with prostate cancer. JAMA. 1999;281(15):1395–400. http://www.ncbi.nlm.nih.gov/pubmed/10217055. Accessed March 17, 2015.
12. Meiers I, Waters DJ, Bostwick DG. Preoperative prediction of multifocal prostate cancer and application of focal therapy: review 2007. Urology. 2007;70(6 Suppl):3–8. doi:10.1016/j.urology.2007.06.1129.
13. Donin NM, Laze J, Zhou M, Ren Q, Lepor H. Gleason 6 prostate tumors diagnosed in the PSA era do not demonstrate the capacity for metastatic spread at the time of radical prostatectomy. Urology. 2013;82(1):148–52. doi:10.1016/j.urology.2013.03.054.
14. Bott SRJ, Ahmed HU, Hindley RG, Abdul-Rahman A, Freeman A, Emberton M. The index lesion and focal therapy: an analysis of the pathological characteristics of prostate cancer. BJU Int. 2010;106(11):1607–11. doi:10.1111/j.1464-410X.2010.09436.x.
15. Rees J, Patel B, MacDonagh R, Persad R. Cryosurgery for prostate cancer. BJU Int. 2004;93(6):710–4. doi:10.1111/j.1464-410X.2003.04746.x.
16. Uchida T, Shoji S, Nakano M, et al. Transrectal high-intensity focused ultrasound for the treatment of localized prostate cancer: eight-year experience. Int J Urol. 2009;16(11):881–6. doi:10.1111/j.1442-2042.2009.02389.x.
17. Arumainayagam N, Moore CM, Ahmed HU, Emberton M. Photodynamic therapy for focal ablation of the prostate. World J Urol. 2010;28(5):571–6. doi:10.1007/s00345-010-0554-2.

18. Lindner U, Lawrentschuk N, Trachtenberg J. Focal laser ablation for localized prostate cancer. J Endourol. 2010;24(5):791–7. doi:10.1089/end.2009.0440.
19. Stafford RJ, Shetty A, Elliott AM, et al. Magnetic resonance guided, focal laser induced interstitial thermal therapy in a canine prostate model. J Urol. 2010;184(4):1514–20. doi:10.1016/j.juro.2010.05.091.
20. Colin P, Mordon S, Nevoux P, et al. Focal laser ablation of prostate cancer: definition, needs, and future. Adv Urol. 2012;2012:589160. doi:10.1155/2012/589160.
21. Bomers JGR, Sedelaar JPM, Barentsz JO, Fütterer JJ. MRI-guided interventions for the treatment of prostate cancer. AJR Am J Roentgenol. 2012;199(4):714–20. doi:10.2214/AJR.12.8725.
22. Lee T, Mendhiratta N, Sperling D, Lepor H. Focal laser ablation for localized prostate cancer: principles, clinical trials, and our initial experience. Rev Urol. 2014;16(2):55–66. http://www.pubmedcentral.nih.gov/articlerender.fcgi?artid=4080850&tool=pmcentrez&rendertype=abstract. Accessed January 30, 2015.
23. Sander S, Beisland HO. Laser in the treatment of localized prostatic carcinoma. J Urol. 1984;132(2):280–1. http://www.ncbi.nlm.nih.gov/pubmed/6737577. Accessed January 27, 2015.
24. Sander S, Beisland HO, Fossberg E. Neodymion YAG laser in the treatment of prostatic cancer. Urol Res. 1982;10(2):85–6. http://www.ncbi.nlm.nih.gov/pubmed/7112783. Accessed January 27, 2015.
25. Raz O, Haider MA, Davidson SRH, et al. Real-time magnetic resonance imaging-guided focal laser therapy in patients with low-risk prostate cancer. Eur Urol. 2010;58(1):173–7. doi:10.1016/j.eururo.2010.03.006.
26. Turkbey B, Pinto PA, Mani H, et al. Prostate cancer: value of multiparametric MR imaging at 3 T for detection--histopathologic correlation. Radiology. 2010;255(1):89–99. doi:10.1148/radiol.09090475.
27. Rais-Bahrami S, Siddiqui MM, Turkbey B, et al. Utility of multiparametric magnetic resonance imaging suspicion levels for detecting prostate cancer. J Urol. 2013;190(5):1721–7. doi:10.1016/j.juro.2013.05.052.
28. Bratan F, Niaf E, Melodelima C, et al. Influence of imaging and histological factors on prostate cancer detection and localisation on multiparametric MRI: a prospective study. Eur Radiol. 2013;23(7):2019–29. doi:10.1007/s00330-013-2795-0.
29. Turkbey B, Mani H, Shah V, et al. Multiparametric 3T prostate magnetic resonance imaging to detect cancer: histopathological correlation using prostatectomy specimens processed in customized magnetic resonance imaging based molds. J Urol. 2011;186(5):1818–24. doi:10.1016/j.juro.2011.07.013.
30. Pinto PA, Chung PH, Rastinehad AR, et al. Magnetic resonance imaging/ultrasound fusion guided prostate biopsy improves cancer detection following transrectal ultrasound biopsy and correlates with multiparametric magnetic resonance imaging. J Urol. 2011;186(4):1281–5. doi:10.1016/j.juro.2011.05.078.
31. Hadaschik BA, Kuru TH, Tulea C, et al. A novel stereotactic prostate biopsy system integrating Pre-interventional magnetic resonance imaging and live ultrasound fusion. J Urol. 2011;186(6):2214–20. doi:10.1016/j.juro.2011.07.102.
32. Atri M, Gertner MR, Haider MA, Weersink RA, Trachtenberg J. Contrast-enhanced ultrasonography for real-time monitoring of interstitial laser thermal therapy in the focal treatment of prostate cancer. Can Urol Assoc J. 2009;3(2):125–130. http://www.pubmedcentral.nih.gov/articlerender.fcgi?artid=2666908&tool=pmcentrez&rendertype=abstract. Accessed March 19, 2015.
33. Rieke V, Kinsey AM, Ross AB, et al. Referenceless MR thermometry for monitoring thermal ablation in the prostate. IEEE Trans Med Imaging. 2007;26(6):813–21. doi:10.1109/TMI.2007.892647.
34. Peters RD, Chan E, Trachtenberg J, et al. Magnetic resonance thermometry for predicting thermal damage: an application of interstitial laser coagulation in an in vivo canine prostate model. Magn Reson Med. 2000;44(6):873–83. http://www.ncbi.nlm.nih.gov/pubmed/11108624. Accessed March 2, 2015.
35. Jankun J, Keck RW, Skrzypczak-Jankun E, Lilge L, Selman SH. Diverse optical characteristic of the prostate and light delivery system: implications for computer modelling of prostatic photodynamic therapy. BJU Int. 2005;95(9):1237–44. doi:10.1111/j.1464-410X.2005.05512.x.
36. Colin P, Nevoux P, Marqa M, et al. Focal laser interstitial thermotherapy (LITT) at 980 nm for prostate cancer: treatment feasibility in Dunning R3327-AT2 rat prostate tumour. BJU Int. 2012;109(3):452–8. doi:10.1111/j.1464-410X.2011.10406.x.
37. Lindner U, Weersink RA, Haider MA, et al. Image guided photothermal focal therapy for localized prostate cancer: phase I trial. J Urol. 2009;182(4):1371–7. doi:10.1016/j.juro.2009.06.035.
38. Lindner U, Lawrentschuk N, Weersink RA, et al. Focal laser ablation for prostate cancer followed by radical prostatectomy: validation of focal therapy and imaging accuracy. Eur Urol. 2010;57(6):1111–4. doi:10.1016/j.eururo.2010.03.008.
39. Woodrum DA, Gorny KR, Mynderse LA, et al. Feasibility of 3.0T magnetic resonance imaging-guided laser ablation of a cadaveric prostate. Urology. 2010;75(6):1514.e1–e6. doi:10.1016/j.urology.2010.01.059.
40. Woodrum DA, Mynderse LA, Gorny KR, Amrami KK, McNichols RJ, Callstrom MR. 3.0T MR-guided laser ablation of a prostate cancer recurrence in the postsurgical prostate bed. J Vasc Interv Radiol. 2011;22(7):929–34. doi:10.1016/j.jvir.2011.02.039.
41. Oto A, Sethi I, Karczmar G, et al. MR imaging-guided focal laser ablation for prostate cancer: phase I trial. Radiology. 2013;267(3):932–40. doi:10.1148/radiol.13121652.
42. Sankineni S, Wood BJ, Rais-Bahrami S, et al. Image-guided focal therapy for prostate cancer. Diagn Interv Radiol. 2014;20(6):492–7. doi:10.5152/dir.2014.14134.
43. Hoang AN, Volkin D, Yerram NK, et al. Image guidance in the focal treatment of prostate cancer. Curr Opin Urol. 2012;22(4):328–35. doi:10.1097/MOU.0b013e32835482cc.
44. Johnson A, Sprangers A, Cassidy P, et al. Design and validation of a thermoreversible material for percutaneous tissue hydrodissection. J Biomed Mater Res B Appl Biomater. 2013;101(8):1400–9. doi:10.1002/jbm.b.32959.
45. Moreland AJ, Lubner MG, Ziemlewicz TJ, et al. Evaluation of a thermoprotective Gel for hydrodissection during percutaneous microwave ablation: in vivo results. Cardiovasc Intervent Radiol. 2014. doi:10.1007/s00270-014-1008-9.

IRE for Prostate Cancer

12

Willemien van de Bos and Jean J.M.C.H. De la Rosette

Irreversible Electroporation (IRE)

Electroporation is a technique in which electric pulses, travelling between two or more electrodes, are used to create "nanopores" in the cell membrane. These pores allow for molecules to pass into the cell. The process can be temporary, reversible electroporation; however, above a certain threshold, the nanopores become permanent causing cell death due to the inability to maintain homeostasis, named irreversible electroporation (Fig. 12.1) [1, 2].

Among the uses for reversible electroporation is most importantly electrochemotherapy allowing for higher doses of chemotherapeutic agents to enter the cells. The occurrence of IRE during RE procedures was considered an unwanted treatment side effect. In recent years interest turned to IRE as a tumor ablation modality resulting in the development of commercially available medical equipment [3].

IRE has shown to effectively ablate tumor cells in vitro, in small and large animal experiments and in several safety and efficacy studies on the IRE of focal liver, pancreas, lesser pelvis, kidney, and lung tumors [4–6]. Tumor ablation experiments have shown that connective tissue structure could be preserved, and there is minor damage to associated blood vessels, neural tissue, or other vital structures [7–9].

The IRE lesions show a sharp demarcation between ablated and non-ablated tissue, whereas concurrent thermal ablation techniques often show a transitional zone of partially damaged tissue where insufficient temperatures were reached for definitive ablation [10].

W. van de Bos, PhD • Jean J.M.C.H. De la Rosette, MD, PhD (✉)
Department of Urology, Academic Medical Center,
Amsterdam, Netherlands
e-mail: j.j.delarosette@amc.uva.nl

Device

An IRE system consists of two major components, a low-energy direct current (LEDC) generator and the needle electrodes. The system is a commercially available technological platform based on the principles of irreversible electroporation (IRE) and is intended for applications that require the ablation of tissue that is primarily cellular. As a result, the potential applications are extremely broad [11].

The system is manufactured and distributed by AngioDynamics, Inc., under the trade name of NanoKnife™ and is approved by the regulatory authorities in Europe and meets several international recognized standards. The system and probes have been cleared for marketing by the US Food and Drug Administration and carry the CE mark for cell membrane electroporation in Europe. All cleared components are indicated for the surgical ablation of soft tissue.

IRE in Prostate Cancer

The major side effects of current prostate cancer treatments are incontinence, erectile dysfunction, bleeding, and bowel injury. The relatively high incidence (ranging 30–90 %) of erectile dysfunction is due to damage of the neurovascular nerve bundle and/or blood flow to the penis. The incidence of incontinence has been reported to be as high as 57 % and is due to damage of the distal urethral smooth muscle sphincter, the puboprostatic ligaments, and striated muscle along the length of the urethra. IRE has been shown to have an advantage over surgical and other ablation techniques of, the aforementioned, sparing surrounding tissue and vital structures such as blood vessels and nerve bundles (Table 12.1). It is therefore postulated that this advantage may help reduce or avoid these side effects [12].

A.R. Rastinehad, D.N. Siegel (eds.), *Interventional Urology*, DOI 10.1007/978-3-319-23464-9_12

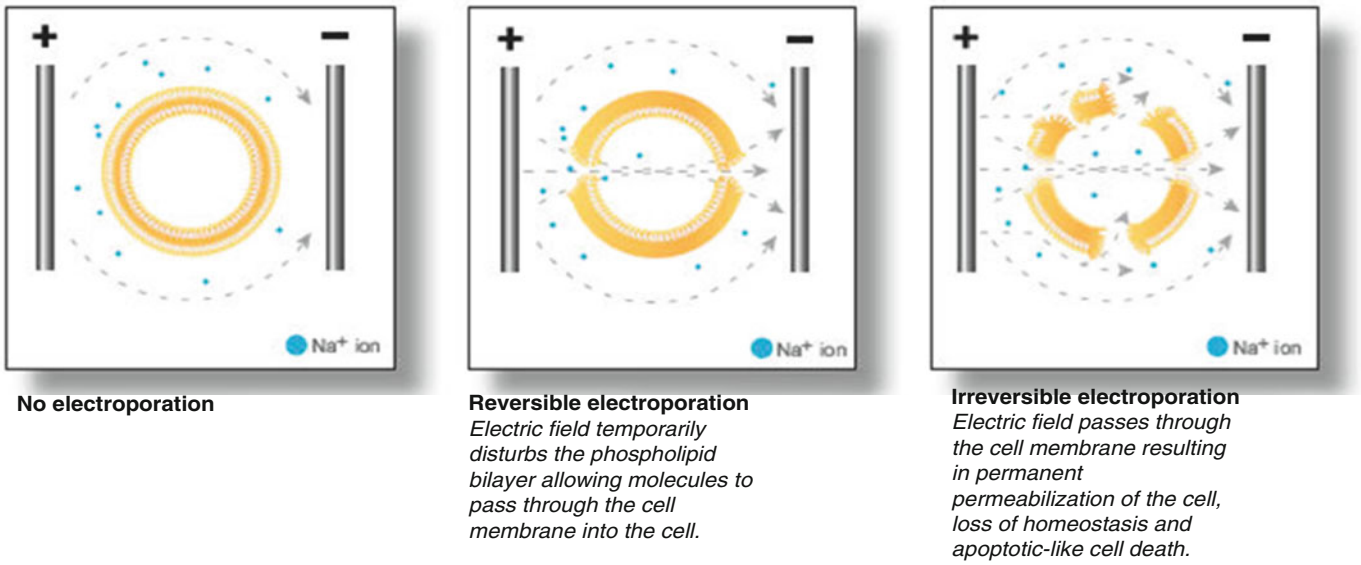

Fig. 12.1 Schematic illustration of the RE and IRE

Table 12.1 Advantages of IRE compared to current treatment options

Small needle electrodes with radiology guidance
Very short high-voltage pulses create permanent pores in cell membranes
Fast treatment
Rapid disappearance of targeted cells
No residual cavity or distortion
Almost no postoperative pain
Sparing of supporting and vital structures and consequently offers an alternative when thermal ablation and surgery are precluded

Procedure

The procedure will be performed under general anesthetic and full paralysis using rocuronium (dose 1 mg/kg). The procedure done under general anesthetic is a minimally invasive treatment [13].

A trigger can be used to supply the pulses at a cardiac autosynchronous rate to decrease the risk of cardiac arrhythmias. The patients are placed in the extended lithotomy position and sterile-draped, and a transurethral catheter is inserted (Fig. 12.2). The treated area will be destroyed under ultrasound (US) image guidance and the tumor cells by disrupting the cell membrane with short-duration, high-voltage direct current [14].

To define the treatment area, a biplane transrectal ultrasound system equipped with an endocavity probe will be used to visualize the prostate in both sagittal and axial directions. The volume and shape of the prostate have to be determined. This data will be entered into the planning software system. One specified treatment scenario will be chosen for ablation. The 19-gauge unipolar electrode needles will be inserted transperineally using a brachytherapy grid under continuous ultrasound guidance (Fig. 12.3).

Literature

Neal et al. published the results of two patients who underwent IRE procedure. The patients were aged 64 and 57 and had Gleason scores of 7 and 6 and PSA levels of 5.4 and 4.3 ng/ml, respectively [15]. Both patients received IRE electric pulse delivery and were discharged with a transurethral catheter that remained in situ for up to 10 days. Both patients experienced mild hematuria after the procedure and recovered in the post-IRE period without any other serious adverse event. Their prostatectomies were performed at 3 or 4 weeks post-IRE without complication. Histology showed regions of tissue necrosis surrounding the electrodes, all of which were contained within the healthy prostatic parenchyma. A variable extent of reactive stromal fibrosis and regenerative change in the epithelial lining of prostatic ducts were observed surrounding the necrotic focus. Inflammatory infiltrate was present, while squamous metaplasia and hemosiderin deposition were noted near the hemorrhagic margins. Reconstructing histologically determined IRE-altered prostate regions resulted in total volumes of 1.14 and 2.46 cm^3 for patient trials one and two, respectively.

Valerio et al. presented a study about the toxicity profile of irreversible electroporation in the focal treatment of prostate cancer [16].

Forty-five patients had grade 1–2 complications. Apart from two salvage patients treated for radiorecurrent disease

Fig. 12.2 Extended lithotomy position with ultrasound inserted

Fig. 12.3 The 19-gauge unipolar electrode needles inserted transperineally using a brachytherapy grid under continuous ultrasound guidance

who required necrotic tissue resection, no severe toxicity was recorded. The most frequent urinary complications were persistent dysuria and persistent debris hematuria. The PSA after 6 months was 3.2 ng/ml (0.04–26). Overall, secondary local treatment was needed in 8 of the 45 patients.

Conclusion

Irreversible electroporation is a promising focal therapy for the treatment of primary or recurrent prostate cancer. Focal Irreversibel electoporation remains investigational although appealing for the preservation of sexual function and avoiding of long-term urinary complaints.

References

1. Davalos RV, Mir LM, Rubinsky B. Tissue ablation with irreversible electroporation. Ann Biomed Eng. 2005;33:223–31.
2. Thomson KR, Cheung W, Ellis SJ, et al. Investigation of the safety of irreversible electroporation in humans. J Vasc Interv Radiol. 2011;22(5):611–21. doi:10.1016/j.jvir.2010.12.014.
3. Bertacchini C, Margotti PM, Bergamini E, Lodi A, Ronchetti M, Cadossi R. Design of an irreversible electroporation system for clinical use. Technol Cancer Res Treat. 2007;6(4):313–20.
4. Ball C, Thomson KR, Kavnoudias H. Irreversible electroporation: a new challenge in "out of operating theater" anesthesia. Anesth Analg. 2010;110(5):1305–9.
5. Garner AL, Cheng G, Cheng N, et al. Ultrashort electric pulse induced changes in cellular dielectric properties. Biochem Biophys Res Commun. 2007;362(1):139–44.
6. Scheffer HJ, Nielsen K, de Jong MC, et al. Irreversible electroporation for nonthermal tumor ablation in the clinical setting: a systematic review of safety and efficacy. J Vasc Interv Radiol. 2014;25(7):997–1011.
7. Onik G, Mikus P, Rubinsky B. Irreversible electroporation: implications for prostate ablation. Technol Cancer Res Treat. 2007;6:295–300.
8. Li W, Fan Q, Ji Z, et al. The effects of irreversible electroporation (IRE) on nerves. PLoS One. 2011;6(4):e18831.
9. Tsivian M, Polascik TJ. Bilateral focal ablation of prostate tissue using low-energy direct current (LEDC): a preclinical canine study. BJU Int. 2013;112:526–30.
10. Edd JF, Horowitz L, Davalos RV, Mir LM, Rubinsky B. In vivo results of a new focal tissue ablation technique: irreversible electroporation. IEEE Trans Biomed Eng. 2006;53(7):1409–15.
11. Lee EW, Loh CT, Kee ST. Imaging guided percutaneous irreversible electroporation: ultrasound and immunohistological correlation. Technol Cancer Res Treat. 2007;6:287–94.
12. Stock RG, Kao J, Stone NN. Penile erectile function after permanent radioactive seed implantation for treatment of prostate cancer. J Urol. 2001;165:436–9.
13. Miller L, Leor J, Rubinsky B. Cancer cells ablation with irreversible electroporation. Technol Cancer Res Treat. 2005;4:699–705.
14. Rubinsky B. Irreversible electroporation in medicine. Technol Cancer Res Treat. 2007;6(4):255–60.
15. Neal RE, Milar JL, Kavnoudias H, et al. In vivo characterization and numerical simulation of prostate properties for non-thermal irreversible electroporation ablation. Prostate. 2014;74(5):458–68.
16. Valerio M, Stricker PD, Ahmed HU et al. A pilot study assessing the toxicity profile of irreversible electroporation in the focal treatment of prostate cancer. Presented at 29th annual congress of the European Association of Urology, Stockholm. Session: Focal therapy for prostate cancer: New insights. Sunday, April 13, 2014.

Cryotherapy for Prostate Cancer

13

Ryan K. Berglund and J. Stephen Jones

Prostate cancer is the most common cause of cancer in men in the USA and the third leading cause of cancer death. The majority of men who develop prostate cancer will either have their cancer successfully treated or will die with and not of prostate cancer [1]. Since the introduction of PSA screening, the risk of an American man dying of prostate cancer has been reduced by over 40 %, but at a cost of treating many clinically insignificant cancers [2].

While a randomized trial has shown that radical surgery reduces the risk of mortality from prostate cancer as compared to nontreatment, the modest 5 % absolute reduction in mortality required 12 years to show a clinically significant difference, thus questioning radical treatment in the older and sicker patient population [3]. In fact, low-risk prostate cancers diagnosed in the PSA era have been subject to stage migration with very limited observed mortality after radical treatment up to 15 years postsurgery [4].

Radical treatments for prostate cancer, including surgery, brachytherapy, and external beam radiation therapy, are also associated with high rates of treatment-related morbidity. Treatment can affect urinary, sexual, and bowel functional domains and these complications are frequently permanent [5].

Cryotherapy, a method by which applying very low temperatures to induce apoptosis and necrosis in neighboring tissues, has been used as a method of ablating benign and malignant tissues since the 1960s. Initially, liquid nitrogen probes were placed under direct vision or via a perineal incision to ablate benign prostatic hyperplasia and prostate cancer. Outcomes from these treatments were unimpressive, and local complications, such as rectourethral fistula and urethral slough, were unacceptably high [6, 7].

Later, in the 1990s, the development of techniques for urethral warming and real-time monitoring of the cryotherapy iceball with transrectal ultrasound sparked new interest in treating prostate cancer with cryotherapy, but this was short lived. Although the iceball could be tracked and the urethra warmed, liquid nitrogen-cooled probes were difficult to rapidly regulate, and the urethral warmers were later withdrawn from the market. Impotence and urethral slough were commonplace, and there continued to be a high risk of rectourethral fistula, a dreaded complication from this procedure [8].

Since 2000, several technologies have allowed reintroduction of prostate cryotherapy into the market with FDA approval and an AUA consensus statement in 2008 [9]. First of all, ultrathin, 17-gauge cryoprobes that use argon gas to rapidly heat and cool tissues were produced. This allowed for close control of the freeze-thaw cycle with better control of the evolving iceball under improved real-time ultrasound guidance. The small size of the needles also allowed for placement of the probes via a brachytherapy-type perineal template yielding more precise iceball coverage. Second, effective urethral warmers have been introduced that substantially reduce the risk of urethral slough after the procedure. Lastly, ultrathin temperature probes are used which allow for real-time monitoring of the rectal and Denonvilliers fascia temperatures, therefore dramatically reducing the risk of rectourethral fistula [10, 11].

Adjustable cryoprobes have also recently been introduced, allowing for precise fine-tuning of the iceball. Figure 13.1a shows the Cryocare CS system, and Fig. 13.1b shows the newest adjustable Cryocare CryoProbe (Endocare, Irvine, CA).

Cancer cell death is achieved in cryotherapy via several pathways. In the coldest areas of the iceball, nearest the probe, ultralow temperatures create direct cell destruction via intra- and extracellular ice crystal formation which disrupts the cell membrane, dehydrates the cell, and leaves a hyperosmotic remnant. This results in tissue necrosis. Secondly, neighboring cells are exposed to thermal injury which induces inflammation and programmed cell death via apoptosis. Lastly, the cryotherapy effect also disrupts surrounding blood vessels, therefore restricting blood flow to

R.K. Berglund, MD (✉) • J.S. Jones, MD, MBA
Department of Urology, Cleveland Clinic Foundation, Cleveland, OH, USA
e-mail: BERGLUR@ccf.org; joness7@ccf.org

A.R. Rastinehad, D.N. Siegel (eds.), *Interventional Urology*, DOI 10.1007/978-3-319-23464-9_13

Fig. 13.1 (**a**) Cryocare CS system and (**b**) adjustable Cryocare cryoprobe (Used with permission of Endocare, Inc., a wholly owned subsidiary of HealthTronics, Inc. (c) 2015 HealthTronics, Inc. All rights reserved)

the treated tissues. To achieve cell death, a tissue temperature of −40 °C must be reached, although this is reduced to −20 °C if two freeze-thaw cycles are used. By rapidly cycling between freezing and thawing, which the newer argon probes allow, cells are unable to adapt, and this enhances the effect. It is generally regarded that two freeze-thaw cycles are necessary to achieve effective treatment [12].

Techniques

Patient preparation for cryotherapy includes preoperative evaluation of medical comorbidities with anesthesia clearance. Patient preparation includes nothing by mouth after midnight the night before surgery, with perioperative antibiotics given within 1 h prior to surgery with either a cephalosporin or quinolone.

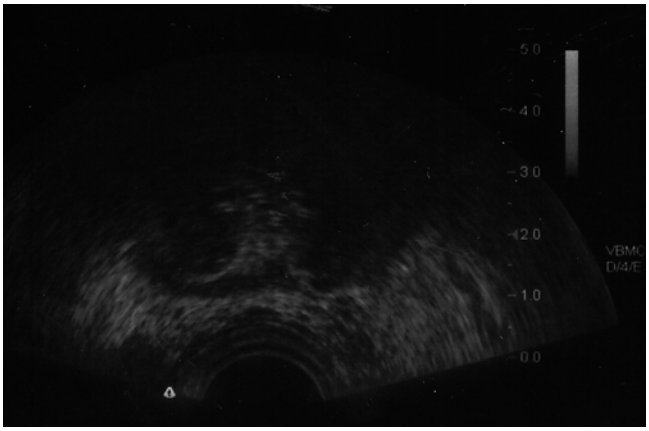

Fig. 13.2 Blacked-out area on ultrasound corresponds to location of the iceball

Surgery is performed under a general or spinal anesthetic in the exaggerated lithotomy position, with initial placement of a suprapubic tube for postoperative bladder decompression. A urethral catheter is then introduced via the urethra and into the bladder, and a brachytherapy template is attached to the table with a transrectal ultrasound allowing for real-time guidance and monitoring of the iceball during the procedure. A rectal and/or Denonvilliers fascia temperature probe is then deployed transperineally to allow real-time temperature monitoring during the procedure. At this point, prostate measurements are taken, and a treatment plan is devised. Cryoprobes are then deployed according to the plan with appropriate length settings. Care should be taken in keeping cryoprobes at least 8 mm from the urethra. Cryoprobe placement can be made for whole-gland treatment, hemiablation, and focal treatment. Cystoscopy to identify any misplaced probes is performed, and while the scope is in the bladder, a guidewire is placed. The scope is removed and a urethral warmer placed over the wire and secured in place to the drapes.

With the probes in place, rapid freezing is begun; with a target temperature of −40 °C. Rapid freezing increases the toxicity within the iceball while limiting the damage beyond it. Adjustments are made to the cooling of the probes to make a uniform iceball, and the blacked-out area on the transrectal ultrasound corresponds to its location (Fig. 13.2). On whole-gland treatment, a margin of 2–4 mm is obtained on the gland with the iceball abutting but not reaching the rectal wall with temperature measurements of the rectum confirming that it is not being frozen. Once the target temperature has been reached and a uniform iceball has reached beyond the margins, active thawing is started to stop the progression of the iceball. After an initial active thaw, passive thawing can be used with a goal of reaching >0 °C, at which time the prostate should become visible again on ultrasound, and a second freeze-thaw cycle is begun. With the completion of

the second thaw, the probes are then removed, the urethral warmer and temperature probe is removed, and the suprapubic tube or Foley catheter is placed to gravity drainage. The patient is then awaken from the procedure and taken to the postanesthesia recovery suite, with a discharge home in 1–2 h after the procedure.

Follow-up after the procedure includes suprapubic tube or Foley catheter removal at 1 week. Postoperative follow-up involves history and physical examination with PSA levels being drawn every 3 months for a year, every 6 months for the next 2 years, and annually thereafter. Some controversy exists as to how to monitor for prostate cancer recurrence after treatment. While some authors advocate for routine posttreatment biopsy at 12–18 months, many authors use the ASTRO 1997 criteria (three consecutive PSA rises) or the newer ASTRO Phoenix criteria (PSA nadir + 2 ng/ml) [13, 14].

Using this endpoint is somewhat controversial due to these criteria being validated only in patients treated with radiation and not cryotherapy. Levy and colleagues, using the Cryo On-Line Database (COLD) Registry, found that a nadir PSA was associated with recurrence outcomes. Eighty-five percent of patients achieved a nadir <0.6 ng/ml, 7 % had a nadir from 0.6 to 1.0 ng/ml, 6 % had a nadir of 1.1 to 2.5 ng/ml, and 2 % >2.5 ng/ml. The patients with a nadir <0.6 ng/ml had 5-year disease-free survival of 86, 67, and 51 % for low-, intermediate-, and high-risk disease, respectively. Patients with nadir of 0.6 ng/ml or higher had a 70 % disease-free rate at 2 years across risk groupings, leading the authors to conclude that patients with a nadir of 0.6 ng/ml or higher require closer follow-up and likely need repeat biopsy [15].

These authors subsequently showed that PSA <0.4 ng/ml was even more likely to assure 5-year biochemical disease-free survival so is the goal of contemporary whole-gland primary cryoablation [16].

Complications

As with any form of prostate cancer treatment, a number of complications can occur after prostate cryotherapy. The most common complication following prostate cryotherapy is erectile dysfunction. In whole-gland treatment, anywhere from 40 to 90 % of patients undergoing treatment report erectile dysfunction [14, 17, 18].

High rates of ED are anticipated with this approach given the proximity of the cavernous nerve to the prostate and the need to get a 2–4 mm iceball margin to achieve cancer control. Partial ablation techniques including subtotal ablation (where the contralateral nerve is spared), hemiablation, and focal ablation have much better potency rates of 71–85 %, but these are limited to low-risk patients with proven unilateral disease [19–23].

In general, whole-gland treatment should not be performed in men interested in preserving potency, and partial ablation should be limited to potent patients who meet stringent criteria for low-risk, unifocal disease. These cases should continue to be considered investigational [24].

Urinary complications are comparable to other radical treatment techniques such as surgery or radiotherapy. Urinary retention tends to be transient and associated with postoperative prostatic edema. Urinary incontinence is also comparable to other radical treatments with a less than 10 % incontinence rate observed. Data calculated from the COLD Registry shows a roughly 5 % pad use rate in whole-gland treatments [14], while partial ablation has even lower rates [23].

Urethral sloughing does occur in up to 15 % of patients with salvage treatment but is rare with primary treatment, but supportive therapy with brief urinary drainage with a suprapubic tube or Foley catheter is often sufficient to manage this complication. Rarely, a transurethral resection of the prostate is necessary, and subsequent urethral fistula is even more uncommon due to the effectiveness of current urethral warming devices [9, 14].

Pain occurs in upward of 50 % of treated patients, but this is usually transient [8, 9, 14, 25]. More severe pain syndromes include osteitis pubis, which occurs in about 3 % of patients, and penile pain in about 3 % of patients. These tend to be transient in nature and resolve with nonsteroidal anti-inflammatory medications [11, 26].

The most dreaded complication of prostate cryotherapy remains rectourethral fistula formation, and it is relatively uncommon with current cryotherapy devices. Jones and colleagues published the results of 1198 patients undergoing primary cryotherapy in the COLD Registry, and the rate of rectourethral fistula complication was 0.4 % [14].

Use of real-time temperature probes and real-time ultrasound monitoring has reduced this to a relatively rare phenomenon. This complication typically presents with watery diarrhea and fecaluria, and initial management is with Foley catheter drainage and a low-residue diet. In the rare cases that this fails to allow complete healing, definitive repair should be delayed for a minimum of 3–6 months allowing for healing from the initial procedure. In patients who have undergone prior radiation, repair is typically not possible, and permanent fecal and/or urinary diversion is usually necessary. Table 13.1 is a comparison of postprocedure continence, potency, and rectourethral fistula in an updated query of the COLD registry (Jones, unpublished data).

Robinson and colleagues published their quality-of-life results comparing patients randomized to treatment with prostate cryotherapy to another radical treatment, external beam radiation therapy. Two hundred and forty-four patients were randomized to one of those two treatments, with follow-up to 3 years posttreatment. Patients in both groups had

Table 13.1 Comparison of continence, potency, and rectourethral fistula from the COLD database (through 4099 cases)

Continence		
	Number of patients	Percent dry (no pads)
Full gland	2034	96.9
Partial gland	499	98.4
Salvage	236	87.7
Potency		
	Number of patients	Percent potent (intercourse)
Full gland	207	32.3
Partial gland	169	58.1
Salvage	24	40
Rectourethral fistula		
	Number of patients	Percent
Full gland	18	0.4
Partial gland	1	0.1
Salvage	9	1.5

Jones, unpublished data

overall high levels of quality of life, with cryotherapy patients having a slightly higher rate of acute urinary dysfunction, which resolved over time. At 3 months, both treatments had significantly reduced sexual quality of life, with the cryotherapy arm being statistically inferior in mean sexual function score at 3 years, with 13 % of cryotherapy patients reporting that sexual function was a moderate to severe problem [27].

Tips and Tricks

There are several tricks to making one's initial experience with prostate cryotherapy more straightforward. First of all, patient selection is important. Large glands (>60 g on transrectal ultrasound) should be avoided except in the most experienced hands. Larger glands require more cryoprobes to completely treat the gland and are harder to monitor on ultrasound. Areas that may harbor viable prostate cancer cells include the zones of tissue between probes and at the periphery of cryoprobe treatment zones, which are more likely to be found in larger glands [28].

Furthermore, reaching the anterior gland behind the pubis can be technically challenging. In select patients, pretreatment androgen deprivation therapy (ADT) with gonadotropin-releasing hormone analogs can be used to downsize the prostate, although ADT has a number of side effects that the patient needs to be made aware of. Furthermore, patients that have enlarged prostates that have been treated with prior transurethral resection or photovaporization for benign prostatic hyperplasia can be challenging to place probes in and monitor. In general, these patients are better served with other treatment modalities.

Patients with locally advanced disease also present challenges and, in general, should not be treated with primary cryotherapy. The AUA Best Practice Policy Statement on Cryosurgery for the Treatment of Localized Prostate Cancer advocates its use as a primary or salvage treatment for prostate cancer, but they caution against its use as a primary monotherapy in clinical stage T3 or greater disease. The presence of likely extraprostatic disease requires a greater treatment margin which endangers surrounding tissues. Also of concern is the margin of preserved tissue that surrounds the urethra with the urethral warmer. That tissue tends to be preserved during cryotherapy. Leibovich and colleagues found that up to 17 % of patients undergoing radical prostatectomy had disease touching the urethra, and those patients skewed heavily toward patients with locally advanced disease [28, 29].

Furthermore, cryotherapy does not allow for treatment of the regional lymph nodes as can be accomplished with surgery or external beam radiation therapy. Initial results with high-grade cancers (Gleason >7) in 77 patients from the COLD Registry showed that the actuarial 5-year biochemical disease-free survival using the ASTRO Phoenix criteria (nadir + 2 ng/ml) was only 45 %, although of those patients with biochemical recurrence, only 26 % had a posttreatment positive prostate biopsy [30].

During surgery, placement of a suprapubic tube may lessen the risks of acute urinary toxicities. Effective bladder drainage for 4 weeks reduces the risk of urinary retention and can allow management of an early urethral slough. This procedure has minimal morbidity and can be easily performed after the patient is put to sleep. During the case, the temperature and cryoprobes can be positioned as to tent the rectum away from the prostate to minimize the risk of rectal freezing and rectourethral fistula. Additionally, the presence of an experienced team and technician in the operating room can allow for effective communication and teamwork when performing the procedure.

Follow-up should be done every 3 months for the first year after treatment with a history and physical examination and PSA level, with the following 2 years being every 6 months, and then annually. Routine posttreatment prostate biopsy is likely unnecessary in patients with a PSA nadir below 0.6 ng/ml and without a PSA rise meeting the ASTRO Phoenix criteria of nadir + 2 ng/ml. Posttreatment prostate biopsy is advisable in patients with AUA high-risk disease, PSA nadir of 0.6 ng/ml or higher, or biochemical recurrence meeting the ASTRO Phoenix criteria. Furthermore, patients undergoing partial ablation of the prostate should undergo routine posttreatment biopsy as the biochemical endpoints routinely used (such as stable PSA values) are not validated in this setting.

Outcomes

Primary cryotherapy is an accepted, FDA-approved treatment for clinically localized prostate cancer, and the AUA has released a best practice guideline for its use. Cohen et al. presented retrospective 10-year data on prostate cryoablation as monotherapy for localized prostate cancer in 370 consecutive patients. AUA risk stratification for low-, intermediate-, and high-risk patients was 15 %, 38 %, and 47 %, respectively. Recurrence was determined using the ASTRO 1997 criteria (nadir PSA + three consecutive rises), ASTRO Phoenix (nadir PSA + 2 ng/ml), and posttreatment prostate biopsy. Using the ASTRO Phoenix definition, 10-year progression-free survival rates for low-, intermediate-, and high-risk patients were 81 %, 74 %, and 46 %, respectively. A prostate biopsy was recommended in all patients at 3–6 months postoperatively and at 2–5 years postoperatively, as well as in situations in which PSA increases were deemed clinically significant at the clinician's discretion. Patients underwent a total of two mean biopsies (range 0–6) per patient, with a 10-year negative biopsy rate of 77 % [13].

The Cryo On-Line Database (COLD) registry is a collaborative group consisting of 4 academic centers and 34 community urologists that prospectively collect cryotherapy data. Jones et al. published their data on 1198 patients undergoing primary cryoablation. With a mean follow-up of 24 months, patients were categorized according to AUA risk grouping, and both ASTRO 1997 and ASTRO Phoenix definitions were used to assess biochemical failure. Using the ASTRO 1997 criteria, 5-year biochemical progression-free survival was 85 %, 73 %, and 75 %, respectively, in the low-, intermediate-, and high-risk groups. Using the ASTRO 2005 Phoenix definition of nadir PSA plus 2 ng/ml, the 5-year biochemical progression-free survival rates were 91, 79, and 62 % in the low-, intermediate-, and high-risk groups. Figure 13.3a, b are Kaplan-Meier curves illustrating disease-free survival using both the old (a) and new (b) ASTRO definitions. Positive biopsy occurred in 38 % of patients with suspicion of recurrence and in 15 % of biopsies performed without cause [14].

Looking only at patients with high-grade cancer (Gleason 8–10), the COLD registry found that in 77 patients with a mean follow-up of 39 months, the 5-year biochemical progression-free survival rates were 64 and 45 % based on use of the ASTRO 1997 versus the ASTRO 2005 Phoenix criteria. When a posttreatment biopsy was performed in these patients, 26 % of patients had a positive biopsy [30].

The only randomized trial comparing cryotherapy to radical treatment was by Donnelly and colleagues. Two

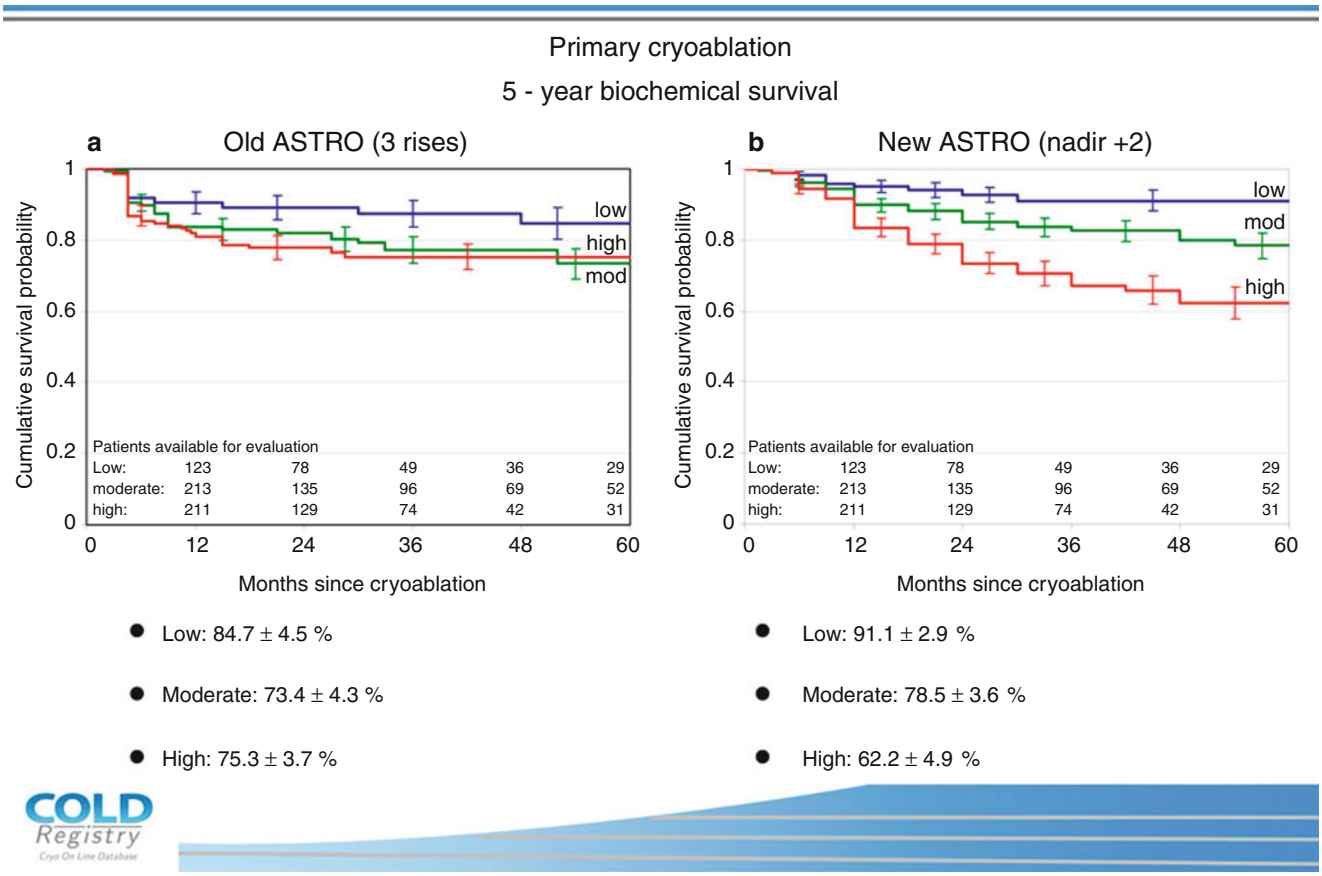

Fig. 13.3 Kaplan-Meier curves illustrating disease-free survival using both the old (**a**) and new (**b**) ASTRO definitions

hundred and forty-four men with clinically localized prostate cancer were randomized to either cryotherapy or external beam radiation therapy. The primary endpoint was disease progression measured by either radiologic progression, initiation of additional therapy, or biochemical failure (either ASTRO 1997 or ASTRO Phoenix). With a median follow-up of 100 months, disease progression was the same in both groups (24 % versus 24 %), with a higher positive posttreatment biopsy rate in the radiation arm of 29 % versus 8 % [31].

Another important use for prostate cryotherapy is in the salvage setting. Patients who have had a postradiation recurrence usually cannot receive additional radiation therapy, and salvage prostatectomy is associated with high urinary complication rates of up to 61 % [32].

Pisters and colleagues reported the COLD Registry experience with salvage cryotherapy. Two hundred and seventy-nine patients were followed for a median of 22 months, and the 5-year biochemical progression-free rate was 59 % (ASTRO 1997) and 55 % (ASTRO Phoenix), with a 33 % positive posttreatment biopsy rate. The complication rate was favorable by comparison to salvage prostatectomy, with a 4 % incontinence rate, 3 % urethral sloughing rate, and a 1 % rectourethral fistula rate [33].

Spiess and colleagues reported the results of therapeutic "bifecta" in salvage cryotherapy patients from the COLD Registry. They defined bifecta as a postcryotherapy nadir PSA level <0.6 ng/ml and no urinary incontinence. With 133 patients and a mean follow-up of 37 months, 73 % of patients had achieved bifecta [34].

Partial or focal cryoablation involves incomplete freezing of the prostate gland in order to reduce the risk of poor functional outcomes such as impotence and urinary incontinence. Given the incomplete treatment of the gland, care must be used in determining which patients qualify for this approach. These treatments should be limited to patients with a pretreatment evaluation consistent with unilateral, low-risk disease. And treatment can be limited to focal treatment of the lesion, gland hemiablation, or subtotal gland treatment with only sparing of the contralateral neurovascular bundle. Lambert and colleagues reported on their series of 25 patients treated with focal therapy. Through 28 months follow-up, only three patients had biochemical progression defined as PSA nadir <50 % pretreatment PSA and negative posttreatment biopsy. Interestingly, two out of three recurrences were on the contralateral side, and they were treated with additional cryotherapy. Seventy-one percent of the patients were potent defined as ability to achieve vaginal penetration sufficient for intercourse, with 41 % of the potent patients requiring oral agents. There were no cases of urinary incontinence, urethral slough, or fistula [20].

Ellis and colleagues published their series of 60 patients followed for a mean 15 months using the ASTRO 1997 criteria. All patients were treated with penile rehabilitation with a vacuum erection device, and 1/3 of their patients were intermediate or high risk. Eighty percent of patients were disease-free at last follow-up, and 20 % were undergoing retreatment. Seventy-one percent of patients were potent after treatment, and 4 % were incontinent (requiring pads). There were no cases of urethral slough or fistula [23].

This technique continues to be limited to investigational studies to assess safety and efficacy [9, 24].

Conclusions

Prostate cryotherapy for the treatment of primary or recurrent prostate cancer is efficacious and safe relative to the other radical treatments which are available. Focal cryotherapy remains investigational although appealing for the preservation of sexual function.

References

1. Jemal A, Siegel R, et al. Cancer statistics, 2009. CA: Cancer J Clin. 2009;59(4):225–49. Epub 2009 May 27.
2. Carroll PR. Early stage prostate cancer--do we have a problem with over-detection, overtreatment or both?-. J Urol. 2005;173(4): 1061–2.
3. Bill-Axelson A, Holmberg L, et al. Radical prostatectomy versus watchful waiting in localized prostate cancer: the Scandinavian prostate cancer group-4 randomized trial. J Natl Cancer Inst. 2008;100(16):1144–54. Epub 2008 Aug 11.
4. Stephenson AJ, Kattan MW, et al. Prostate cancer-specific mortality after radical prostatectomy for patients treated in the prostate-specific antigen era. J Clin Oncol. 2009;27(26):4300–5. Epub 2009 Jul 27.
5. Sanda MG, Dunn RL, Michalski J, et al. Quality of life and satisfaction with outcome among prostate-cancer survivors. N Engl J Med. 2008;358:1250.
6. Soanes WA, Gonder MJ, et al. Apparatus and technique for cryosurgery of the prostate. J Urol. 1966;96(4):508–11.
7. Flocks RH, Nelson CM, et al. Perineal cryosurgery for prostatic carcinoma. J Urol. 1972;108(6):933–5.
8. Cohen JK, Rooker GM, Miller Jr RJ, et al. Cryosurgical ablation of the prostate: treatment alternative for localized prostate cancer. Cancer Treat Res. 1996;88:167.
9. Babaian RJ, Donnelly B, et al. Best practice statement on cryosurgery for the treatment of localized prostate cancer. J Urol. 2008;180(5):1993–2004. Epub 2008 Sep 25.
10. Zisman A, Pantuck AJ, et al. Prostate cryoablation using direct transperineal placement of ultrathin probes through a 17-gauge brachytherapy template-technique and preliminary results. Urology. 2001;58(6):988–93.
11. Han KR, Cohen JK, et al. Treatment of organ confined prostate cancer with third generation cryosurgery: preliminary multicenter experience. J Urol. 2003;170(4 Pt 1):1126–30.
12. Baust JG, Gage AA, et al. The pathophysiology of thermoablation: optimizing cryoablation. Curr Opin Urol. 2009;19(2):127–32.
13. Cohen JK, Miller RJJ, Miller Jr RJ, et al. Ten-year biochemical disease control for patients with prostate cancer treated with cryosurgery as primary therapy. Urology. 2008;71(3):515–8.
14. Jones JS, Rewcastle JC, et al. Whole gland primary prostate cryoablation: initial results from the cryo on-line data registry. J Urol. 2008;180(2):554–8. Epub 2008 Jun 11.

15. Levy DA, Pisters LL, et al. Primary cryoablation nadir prostate specific antigen and biochemical failure. J Urol. 2009;182(3):931–7. Epub 2009 Jul 18.
16. Levy DA, Ross AE, Elshafei A, et al. Definition for biochemical success following primary whole gland prostate cryoablation. J Urol. 2014;192(5):1380–4.
17. Ellis DS. Cryosurgery as primary treatment for localized prostate cancer: a community hospital experience. Urology. 2002;60(2 Suppl 1):34–9.
18. Donnelly BJ, Saliken JC, Ernst DS, et al. Prospective trial of cryosurgical ablation of the prostate: five-year results. Urology. 2002;60:645.
19. Onik G, Narayan P, Vaughan D, et al. Focal "nerve-sparing" cryosurgery for treatment of primary prostate cancer: a new approach to preserving potency. Urology. 2002;60:109.
20. Lambert EH, Bolte K, et al. Focal cryosurgery: encouraging health outcomes for unifocal prostate cancer. Urology. 2007;69(6): 1117–20.
21. Onik G, Vaughan D, Lotenfoe R, et al. The "male lumpectomy": focal therapy for prostate cancer using cryoablation results in 48 patients with at least 2-year follow-up. Urol Oncol. 2008;26:500.
22. Nguyen CT, Jones JS. Focal therapy in the management of localized prostate cancer. BJU Int. 2011;107:1362.
23. Ellis DS, Manny Jr TB, et al. Focal cryosurgery followed by penile rehabilitation as primary treatment for localized prostate cancer: initial results. Urology. 2007;70(6 Suppl):9–15.
24. Eggener SE, Scardino PT, Carroll PR, et al. Focal therapy for localized prostate cancer: a critical appraisal of rationale and modalities. J Urol. 2007;178:2260.
25. Long JP, Fallick ML, LaRock DR, et al. Preliminary outcomes following cryosurgical ablation of the prostate in patients with clinically localized prostate carcinoma. J Urol. 1998;159:477.
26. Seigne JD, Pisters LL, von Eschenbach AC. Osteitis pubis as a complication of prostate cryotherapy. J Urol. 1996;156:182.
27. Robinson JW, Donnelly BJ, Siever JE, et al. A randomized trial of external beam radiotherapy versus cryoablation in patients with localized prostate cancer: quality of life outcomes. Cancer. 2009;115:4695.
28. Pisters LL. Cryotherapy for prostate cancer: ready for prime time? Curr Opin Urol. 2010;20:218.
29. Leibovich BC, Blute ML, Bostwick DG, et al. Proximity of prostate cancer to the urethra: implications for minimally invasive ablative therapies. Urology. 2000;56:726.
30. Jones JS, FAU-Rewcastle JC, Rewcastle JC. Primary cryoablation for Gleason 8, 9, or 10 localized prostate cancer: Biochemical and local control outcomes from the Cryo OnLine database registry. Indian J Urol. 2008;24(4):490–3.
31. Donnelly BJ, Saliken JC, Brasher PM, et al. A randomized trial of external beam radiotherapy versus cryoablation in patients with localized prostate cancer. Cancer. 2010;116:323.
32. Stephenson AJ, Scardino PT, et al. Morbidity and functional outcomes of salvage radical prostatectomy for locally recurrent prostate cancer after radiation therapy. J Urol. 2004;172(6 Pt 1):2239–43.
33. Pisters LL, Rewcastle JC, et al. Salvage prostate cryoablation: initial results from the cryo on-line data registry. J Urol. 2008;180(2):559–63; discussion 563–4. Epub 2008 Jun 12.
34. Spiess PE, Given RW, Jones JS. Achieving the 'bifecta' using salvage cryotherapy for locally recurrent prostate cancer: analysis of the Cryo On-Line Data (COLD) registry data. BJU Int. 2012;110:217.

Radiation Therapy: Brachytherapy

14

Brett Cox, Lucille Lee, and Louis Potters

Prostate brachytherapy is widely applied in the treatment of prostate cancer. Brachytherapy is a form of radiation therapy where a radiation source is placed inside or next to the area requiring treatment. A key feature of brachytherapy is that the radiation affects only a small area around the radiation sources with great intensity, with an exponential decline in dose intensity with greater distance from the source. Image guidance is an essential component of modern brachytherapy, as gains in the therapeutic ratio of prostate brachytherapy are achieved with meticulous spatial selection of target volumes. Modern image-guided technologies, especially high-clarity ultrasound, multiparametric magnetic resonance imaging (MRI), image fusion, and deformable registration, can help the radiation oncologist achieve high precision in the delivery of radiation sources to the target volume and permit avoidance of adjacent normal tissues.

Epidemiology

Prostate cancer has become the most common cancer in males based on Surveillance, Epidemiology, and End Results (SEER) data. In 2010, 217,730 cases were expected in the USA, and approximately 32,000 men died of prostate cancer [1]. Between 1999 and 2005, 92 % of cases were diagnosed in the locoregional stages, for which the 5-year relative survival approaches 100 %. Mortality has been declining since 1990, reflecting the use of screening prostatic serum antigen (PSA) and improvements in treatment [2].

B. Cox, MD
Department of Radiation Medicine, North Shore LIJ Health System, Lake Success, NY, USA

L. Lee, MD • L. Potters, MD (✉)
Department of Radiation Medicine, North Shore LIJ Health System, Center for Advanced Medicine, Lake Success, NY, USA
e-mail: lpotters@nshs.edu

Screening

The American Urological Association (AUA) recommends screening for prostate cancer in some men. Screening in men under 40 is not recommended, and screening for men 40–54 should not be generally performed, but can be considered for patients with risk factors such as positive family history or African-American race. For men aged 55–69 years old, PSA screening should be considered but done only after shared decision making between the physician and the patient. There is no role for PSA screening in men older than 70 years old with a life expectancy less than 10–15 years. PSA screening can be done once every 2 years to reduce overdiagnosis and false-positive findings. Recently, published randomized trials comparing the mortality outcomes of a screened group versus a non-screened group showed conflicting results, and controversy persists regarding screening [3, 4]. However, both studies suggested a high rate of overdetection and overtreatment. Therefore, specific patient recommendations emphasize an informed discussion of the risks and benefits of prostate cancer screening prior to biopsy and the option of active surveillance, instead of treatment for certain patients with prostate cancer.

Patient Evaluation

All potential candidates for brachytherapy should undergo a thorough history and physician examination. Any prior urologic surgery, including prior open or transurethral resection of the prostate, prostate needle ablation, or microwave therapy, should be noted. Any history of medicines for urinary obstructive symptoms should be considered. Sexual activity and potency should be thoroughly reviewed and considered in the context of management options. Prior oncologic history and treatments, especially for pelvic malignancies, should be considered, including prior history of chemotherapy or radiation therapy. Prior orthopedic surgeries or congenital misdevelopment of the pelvis and lower extremities

A.R. Rastinehad, D.N. Siegel (eds.), *Interventional Urology*, DOI 10.1007/978-3-319-23464-9_14

that can affect the ability to position the patient in a dorsal lithotomy position should be considered. Other relative contraindications to radiation therapy, especially inflammatory bowel disease and connective tissue disorders, should be carefully documented. When possible, using validated instruments such as the International Prostate Symptom Score (IPSS), International Index of Erectile Function (IIEF) score, and the Expanded Prostate Cancer Index Composite for Clinical Practice (EPIC-CP) to evaluate urinary function, erectile function, and gastrointestinal function should be utilized by the clinician. Finally the clinician must confirm that appropriate oncologic information has been obtained, including appropriately performed biopsy documenting adenocarcinoma within the past 12 months, full documentation of pathologic information including Gleason score, pretreatment PSA, and appropriate tests to complete clinical staging including digital rectal examination. All patients should be assigned an American Joint Committee on Cancer (AJCC) stage and National Comprehensive Cancer Network (NCCN) risk group classification.

Risk Stratification

Once the diagnosis of prostate cancer is made, a staging workup ensues in order to provide additional prognostic information for risk stratification, which may assist in management decisions. The NCCN Version 1.2015 provides recurrence risk stratification among patients with clinically localized disease based on PSA level, Gleason score, clinical stage, and biopsy specifics. The AJCC has incorporated PSA and Gleason score into a stage/prognostic group system (Table 14.1), while the tumor, node, and metastasis (TNM) system for clinical and pathologic staging remains the same. Imaging of the pelvis with computerized tomography (CT) or magnetic resonance imaging (MRI) is recommended for patients with T3/T4 disease or T1–T2 disease with a nomogram indicating probability of lymph node involvement >10 %. A bone scan is recommended for patients with any of the following: T1 disease and a PSA >20 ng/mL, T2 disease and a PSA >10 ng/mL, any T3/4 disease, or patients who report symptoms indicative of bony metastatic disease.

Table 14.1 Prostate cancer anatomic stage/prognostic group according to the American Joint Committee on Cancer

Group	T	N	M	PSA	Gleason
I	T1a–c	N0	M0	PSA <10	Gleason ≤6
	T2a	N0	M0	PSA < 0	Gleason ≤ 6
	T1–2a	N0	M0	PSA X	Gleason X
IIA	T1a–c	N0	M0	PSA <20	Gleason 7
	T1a–c	N0	M0	PSA ≥10–<20	Gleason ≤6
	T2a	N0	M0	PSA <20	Gleason ≤7
	T2b	N0	M0	PSA <20	Gleason ≤7
	T2b	N0	M0	PSA X	Gleason X
IIB	T2c	N0	M0	PSA any	Gleason any
	T1–2	N0	M0	PSA ≥20	Gleason any
	T1–2	N0	M0	PSA any	Gleason ≥8
III	T3a–b	N0	M0	PSA any	Gleason any
IV	T4	N0	M0	PSA any	Gleason any
	T any	N1	M0	PSA any	Gleason any
	T any	N any	M any	PSA any	Gleason any

Used with the permission of the American Joint Committee on Cancer (AJCC), Chicago, IL. The original source for this material is the *AJCC Cancer Staging Manual,* Seventh Edition (2010) published by Springer Science and Business Media LLC. www.springer.com

General Treatment Strategies

Common Treatment Strategies for Localized Prostate Cancer

General treatment strategies for early-stage prostate cancer include radical prostatectomy, external beam radiation therapy, brachytherapy, androgen deprivation therapy, and watchful waiting per NCCN Version 1.2015 guidelines for prostate cancer treatment. External beam radiation therapy, brachytherapy, and androgen deprivation therapy are often used as bi- or trimodality therapy combinations based on the aggressiveness of the disease in terms of probability of locoregional spread.

Role of Brachytherapy in Prostate Cancer Treatment

Prostate cancer patients with localized, organ-confined disease or limited extraprostatic extension are candidates for prostate brachytherapy. Table 14.2 summarizes general treatment guidelines for patients to be treated with brachytherapy. Patients with NCCN low-risk group disease are candidates for brachytherapy as monotherapy, patients with intermediate-risk group disease are candidates for brachytherapy with or without supplemental external beam radiotherapy, and patients with high-risk group disease should receive supplemental external beam radiotherapy and androgen deprivation therapy [5].

Selecting Patients for Brachytherapy

When deciding whether or not to use brachytherapy, either alone or in combination with EBRT, it is useful to consider pretreatment urologic symptoms and prostate size. Acute urologic symptoms may also be more severe with brachytherapy, which makes it less ideal for patients with

Table 14.2 Suggested treatment algorithm for low-, intermediate-, and high-risk prostate cancer to be treated with brachytherapy as recommended by the American Brachytherapy Society

	NCCN low-risk group	NCCN intermediate-risk group	NCCN high-risk group
Brachytherapy as monotherapy	Favored	Optional	Not recommended
Combination brachytherapy and external beam radiation	Not recommended	Optional	Optional
Inclusion of androgen deprivation	Not recommended[a]	Optional	Favored

Data from the American Brachytherapy Society
[a]Unless for short-term administration to achieve appropriate volume reduction to allow for implant

significant symptoms of benign prostatic hypertrophy (BPH) and those with large glands, the general cutoff being 50 cubic centimeters. Urinary symptoms are commonly rated using the AUA IPSS, which is the same as the BPH symptom score but with a quality-of-life (QOL) question added. In the phase III trial, RTOG 0815, patients with an AUA score of greater than 15 are not candidates for brachytherapy, and the size cutoff is less than 60 g. Also, a history of transurethral resection of the prostate (TURP) is considered a relative contraindication for brachytherapy because of the increased risk of urethral toxicity, including incontinence [6]. Other factors that may contribute to higher acute toxicity include a greater number of needles used to do the implant and the use of hormonal therapy [7].

The American Brachytherapy Society recommends the following absolute contraindications to TRUS-guided PPB: limited life expectancy, unacceptable operative risks including poor suitability for general or spinal anesthesia, presence of distant metastases, anatomic or surgical absence of the rectum such that TRUS guidance is not possible, large TURP defects which preclude seed placement and acceptable radiation dosimetry, and a history of ataxia-telangiectasia. Recommended relative contraindications include: IPSS >20, history of prior pelvis radiotherapy, prior TURP, prominent median lobe architecture, prostate volume >60 cubic centimeters, and history of inflammatory bowel disease [5]. It is emphasized that published reports demonstrate excellent clinical results in patients with relative contraindications if meticulous patient selection is used and treatment is performed by an experienced brachytherapy team in a multidisciplinary environment.

Combination External Beam Radiation Therapy and Brachytherapy

In theory, the higher incidence of extracapsular extension and seminal vesicle invasion in intermediate- to high-risk patients is more adequately covered by EBRT than brachytherapy, which is the rationale for combining EBRT and brachytherapy alone in these patients. On the other hand, certain intermediate-risk patients are likely to be candidates for brachytherapy alone. In a retrospective review of 668 brachytherapy patients, there was no statistically significant difference in the 8-year actuarial biochemical relapse-free survival (BRFS) between low- and intermediate-risk patients, 98.4 and 98.2 %, respectively [8]. These data suggest that most intermediate-risk patients have a low risk of micrometastatic disease in the pelvis. Even though the risk of extracapsular disease is higher in these patients, these areas may be adequately covered by an implant, since most extracapsular disease is located within 5 mm of the prostate capsule. In another series of combination therapy, where 63.4 % of the intermediate-risk patients had 50 % or more positive biopsy needle cores, there was an 80 % 15-year BRFS [8]. These data suggest excellent long-term control with the combined approach. However, despite high control rates, the additional use of EBRT may be detrimental in terms of higher rates of morbidity. Therefore, additional pathologic factors, such as number or percentage of positive cores, may be helpful to determine whether or not combination treatment should be used. There is a national trial RTOG 0232, which has accrued and closed at the time of publication, that randomized intermediate-risk group patients to brachytherapy alone versus combination therapy. The results of this trial will inform decision making regarding this patient group.

Imaging Correlations with Emphasis on Image Fusion Guidance

Only recently has imaging played a significant role in the diagnosis and staging of localized prostate cancer. Historically, bone scans and CT scans were used to assess for pelvic nodal metastases and distant metastatic disease, but there was little role for imaging to evaluate the primary tumor. However, with the influx of modern technologies, such as high-resolution ultrasound and multiparametric MRI, the primary tumor site can be anatomically and oncologically well characterized, leading to better staging and risk stratification of patients and refining the intraoperative interventional management of these patients. Accurate definition of the location of the tumor in the prostate gland improves the staging of prostate cancer and advises the patient's management team regarding decisions such as whether LDR or HDR brachytherapy may be a superior approach for a given patient or if supplemental treatments like external beam radiation therapy or androgen deprivation therapy should be recommended for a given patient.

Diagnosis

Transrectal ultrasound (TRUS) was the first modality widely to evaluate the local extent of prostate cancer and remains the most widely used imaging modality for biopsy guidance and image-guided treatments including brachytherapy source placement. However, even with improvements in ultrasound technology such as color Doppler, color power Doppler, microbubble contrast enhancement, and ultrasound elastography, TRUS is unable to reliably differentiate prostate cancer from normal prostate glandular tissue, and TRUS-guided biopsy can miss up to one-third of clinically significant prostate cancers [9, 10].

MRI of the prostate gland was first performed in the mid-1980s with excellent anatomic visualization [11]. The T2-weighted images provide excellent spatial resolution and can differentiate the more hyperintense peripheral from the lower signal intensity central and transition zones. In the T2 images, a focus of prostate cancer can appear with low signal intensity in the area of hyperintense parenchyma of the normal peripheral zone [12]. Hypointense lesions can also represent foci of benign hyperplasia, prostatitis, focal prostate atrophy, or post-biopsy hemorrhage or similar processes. The degree of signal reduction in a cancer lesion correlates, in some cases, with the grade and growth pattern of the tumor [13, 14]. T2-weighted MRI also offers the enormous benefit of assessing the extent of local disease. Extracapsular extension can be identified through asymmetry of the neurovascular bundles, obliteration of the rectoprostatic angle, irregular bulging of the prostatic margin, and low-signal tumor in the periprostatic fat. Seminal vesicle invasion can be similarly identified. Figure 14.1 demonstrates a T2 hypointense lesion with extracapsular extension.

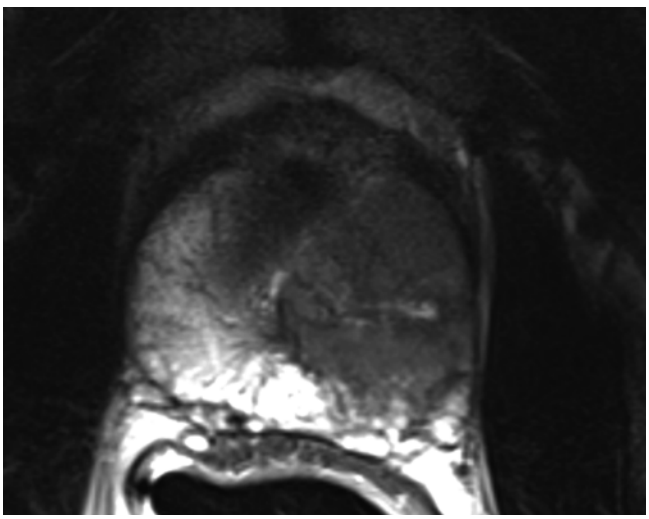

Fig. 14.1 MRI demonstrating a T2 hypointense lesion with extracapsular extension

More recently, the ability to obtain functional information from the MRI refined prostate cancer diagnosis and staging. Specifically, dynamic contrast-enhanced MRI (DCE-MRI), diffusion-weighted MRI (DW-MRI), and proton magnetic resonance spectroscopic imaging (MRSI) are all becoming more widely used in the evaluation of a potential prostate brachytherapy patient. DCE-MRI is able to detect changes in the local vasculature as prostate tumors secrete pro-angiogenic agents, such as vascular endothelial growth factor, leading to recruitment of neovasculature, increased vascular permeability, and increase in volume of the tumor interstitial space [15, 16]. With microcompartmental modeling, the time versus intensity curves of contrast enhancement can be plotted, and the parametric images can be fused with T2-weighed images. DWI-MRI is based on the thermally induced ransom molecular displacement (Brownian motion). An organ's diffusion properties are related to the amount of interstitial free water and tissue permeability. A prostatic neoplasm generally has more restricted diffusion due to higher cell densities and cancer cell membrane characteristics [17]. MRSI provides metabolic information by determining the chemical concentration of various compounds and metabolites in the prostate architecture. In prostate cancer, the choline-to-citrate ratio is generally used to identify lesions that are at high risk of representing prostate cancer [18].

Each of the MRI techniques offers distinct advantages and limitations, so the ideal use of MRI in prostate cancer is to use a combined multiparametric MRI (mpMRI) approach, where information from each technique is used to complement the information gained from the others. Modern software algorithms are able to register and fuse the information from different techniques to allow functional and anatomic colocalization. Typical mpMRI sequences include T1- and T2-weighted images combined with functional imaging techniques. There is increasing use of mpMRI in the diagnosis and staging of prostate cancer, but no formal recommendations of guidelines are available [19]. Efficient detection of prostate cancer is improved with performing targeted biopsies with MRI guidance, and sampling of the most abnormal area on a prostate MRI is likely to yield a positive diagnosis of prostate cancer [20, 21]. Accurate delineation of the prostate cancer lesions improves patient staging and also informs important brachytherapy treatment decisions regarding the need for supplemental external beam radiation therapy or androgen deprivation therapy.

Intraoperative Imaging

TRUS has been the mainstay imaging modality for intraoperative brachytherapy imaging and treatment planning due to its portability, ease of use, low cost, and safety. Suboptimal

source placement, in the past, was frequently a result of poor TRUS imaging during the procedure, a problem that is being mitigated with improvements in ultrasound technology and the ability to fuse ultrasound images with other modalities including CT and ultrasound.

Several institutions are exploring the concept of focal boost treatment strategies, where the whole prostate gland is treated but areas of dominant tumor are given a boost dose. In local failures after primary radiation therapy, there is a body of evidence that suggests the local recurrence happens at the dominant tumor locations [22, 23]. A focal brachytherapy boost could improve the therapeutic ratio of brachytherapy treatments by dose-escalating areas of bulky tumor while still allowing minimal increased dose to adjacent normal tissues.

Focal Brachytherapy

Due to the multifocal nature of prostate cancer, the use of any definitive radiotherapy has included the whole prostate gland as a target volume. With the advent of PSA screening and advanced imaging techniques, outlined above, that improve staging and finely hone risk group stratification, whole-gland treatment may represent overtreatment of low-grade, well-defined disease. Therefore, the concept of focal brachytherapy is being explored for patients with unifocal dominant lesions [24] with the assumption that the dominant lesion is responsible for total tumor volume, risk of recurrence, and Gleason score. In addition to brachytherapy, a variety of other focal ablative approaches are being explored, including photodynamic therapy, high-intensity ultrasound, cryotherapy, and thermal laser ablation.

Postoperative Dosimetry

A successful prostate implant demonstrates adequate coverage of the prostate gland and limitation of dose to adjacent normal tissues including the rectum, bladder, urethra, and neurovascular bundles. As detailed above, the ABS recommends post-implant dosimetry for all patients undergoing prostate brachytherapy. In this process, implanted sources are localized and correlated with prostatic anatomy to calculate the dosimetric parameters of interest. This process allows the radiation oncologist to correct systematic deficiencies in overall implant technique while identifying patients who are at risk for local failure or toxicity development. It is acknowledged that given the real-time nature of brachytherapy, there will be spatial variation in source placement from the intraoperative plan to the post-plan, and therefore a range of post-plan variabilities is to be anticipated.

The first published report of CT for post-implant dosimetry was in the 1990s, which allowed for the representation of organ and dose distribution together in spatial registration [25]. In contemporary practice, CT is recommended to evaluate post-implant dosimetry and is used in the vast majority of cases [26]. While CT is inexpensive and widely available and allows for easy identification for implant prostate seeds, it is not optimal for identification of the periphery of the prostate, particularly at the apex and base of the gland. Several authors have reported large uncertainties in prostate contours in post-implant CT scans [27, 28]. Additionally, the CT volume is generally different from the intraoperative volume and remains a confounding issue in the analysis and reporting of dosimetric outcomes [29].

Techniques

Brachytherapy of the prostate can be performed with a high-dose rate technique or a low-dose rate technique. LDR brachytherapy is an outpatient, minimally invasive, interventional procedure with a rapid recovery and ability to return to normal activities in a short period of time. In LDR prostate brachytherapy, permanent radioactive sources are placed in the prostate gland which deliver a certain amount of radiation before becoming nonradioactive. HDR brachytherapy is similar but may require a short inpatient stay and is performed with a temporary insertion of a high-dose radioactive source. Modern PPB techniques using ultrasound guidance and template-based placement of applicator needles were developed over 25 years ago and are widely still in use [30, 31].

Various interventional approaches regarding brachytherapy have been published with small differences in technique. There is not a uniformly accepted best defined approach nor a medicolegally defined standard for LDR or HDR brachytherapy. The standard approach for LDR seed implantation is to utilize a transperineal approach under TRUS guidance. Template guidance is used for needle placement. Figure 14.2 demonstrated the TRUS-guided transperineal approach with needle template in place. Some institutions use a preplanned approach, where a preoperative TRUS study is done to identify applicator needle and seed placement which is then later recreated in actual operative procedure. However, many centers are moving to an intraoperative approach, where needles are placed real time in the operative room with source placement finalized during the procedure after applicator needles have been placed. The intraoperative approach allows for a dynamic, real-time application of brachytherapy sources and obviates the challenging requirement to recreate the same patient and applicator anatomy used in the preplanning session.

The TRUS system used for implantation should be capable biplanar imaging and provide high-resolution ultrasonic frequencies between 5 and 12 MHz [5]. The system should

Fig. 14.2 Transrectal ultrasound-guided approach with needle delivery template used for prostate brachytherapy

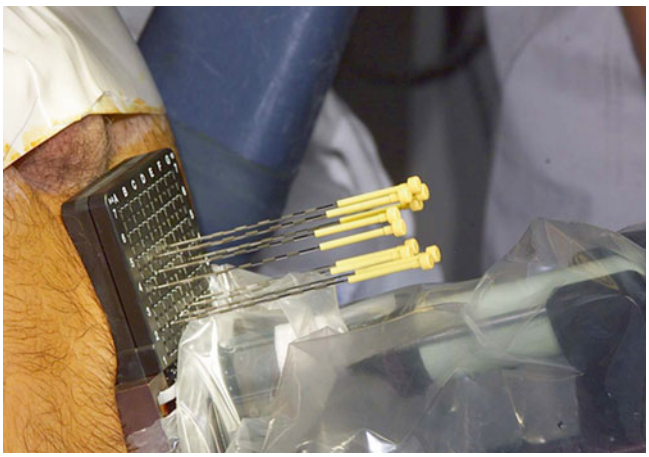

Fig. 14.3 Interstitial needles used for low-dose rate brachytherapy seed placement

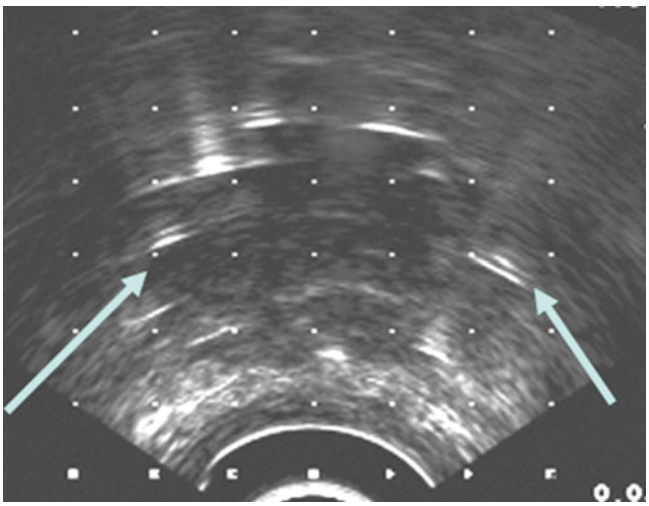

Fig. 14.4 Interstitial delivery needles on transrectal ultrasound-guided image

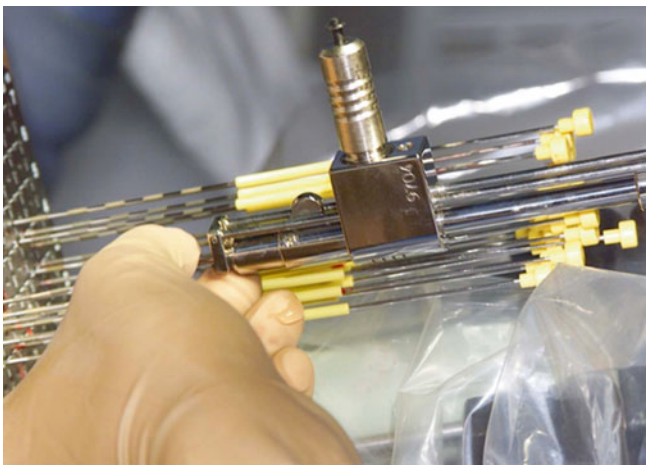

Fig. 14.5 Mick applicator with seed cartridge for delivery of loose, low-dose rate brachytherapy seeds

be capable of displaying an electronic grid that is calibrated and synchronized with the transperineal template docked to the ultrasound probe. Dedicated FDA-approved brachytherapy planning software should be used for the planning portion of the brachytherapy procedure. There have been multiple reports for the use of intraoperative fluoroscopy to complement ultrasound imaging [32] and for intraoperative dose computation [33], although this fluoroscopy is neither standard nor necessary for LDR interstitial brachytherapy. Similarly, there have been reports of intraoperative cone beam CT imaging (CBCT) for interventional guidance and for dose planning purposes.

During the procedure itself, the patient is anesthetized and placed in the dorsal lithotomy position. The perineum is sterilized and draped and the testicles are retracted away from the perineum. The ultrasound probe is placed into the rectum transanally, and adequate visualization of the prostate in the axial and longitudinal axes is confirmed. Applicator needles are placed into the prostate to facilitate delivery of the radioactive sources, as demonstrated in Fig. 14.3. Once applicator needles are placed, imaging is captured in the treatment planning system (Fig. 14.4), and a spatial reconstruction of the prostate, urethra, rectum, and other adjacent organs of risk is performed. A seed-loading pattern is either then generated with real-time planning or attempts are made to recreate the spatial arrangement of a preplan. Multiple effective strategies to source placement have been reported, including the use of a Mick applicator to place loose seeds individually [34] (Fig. 14.5), the use of preloaded needles where all the sources in a given needle are prearranged and deployed in a single motion [35], and the use of afterloading techniques [36]. During placement of sources, a "modified peripheral" loading pattern is generally recommended, in

which most seeds are placed at the periphery. The radioactive sources can be "loose" and placed one at a time or can be "stranded," where all the seeds in a given needle are linked via a bioresorbable polymer. The potential advantages and disadvantages of each approach have been reported, especially for loose seed migration with loose seed placement [37–46], but all approaches have been found to be safe and effective as long as appropriate dosimetric end points are ultimately met.

Generally recommended dose prescriptions for the planning target volume have been published by the ABS and are delineated in Table 14.3 [5]. Figure 14.6 demonstrates representative isodose lines from the intraoperative treatment planning system. In general, compliance with the American Association of Physics and Medicine Task Group's 43 and 137 reports is highly recommended, which give specific guidelines for treatment planning and dosimetric evaluation. There have been no prospective randomized trials to identify the optional dose and dosimetric evaluation of a prostate implant. Stock first reported the concept of D90 (the isodose encompassing 90% of the prostate) and its relationship to treatment outcome [47]. Numerous authors have also reported the predictive value of the V100, or the percentage volume of the prostate receiving 100 % of the prescribed dose [48]. To minimize the risk of urethral toxicity, it is recommended that significant portions of the urethra do not receive greater that 150 % of the prescribed dose [49]. The rectal volume receiving the prescription dose should be <1–2 cc [50]. At our institution, our primary intraoperative dosimetric goals used for our real-time, dynamic, and adaptive procedure are D90 >100 %, V100 >95 %, rectal max >2 cc, UD10 <150 %, and UD30 <130 %. CT-based postoperative dosimetry is recommended within the first 60 days after the implant (Figs. 14.7 and 14.8).

Table 14.3 Prescription doses as recommended by the American Association of Physics and Medicine and the American Brachytherapy Society

Isotope	Indication	Dose
Iodine-125	Monotherapy	140–160 Gy
	Combination therapy: EBRT dose	41.4–50.4 Gy (1.8–2.0 Gy/day)
	Combination therapy: brachytherapy dose	108–110 Gy
Pd-103	Monotherapy	110–125 Gy
	Combination therapy: EBRT dose	41.4–50.4 Gy (1.8–2.0 Gy/day)
	Combination therapy: brachytherapy dose	90–100 Gy

Data from the American Association of Physics and Medicine and the American Brachytherapy Society
EBRT external beam radiation therapy

Toxicity Profile

Anatomic Considerations

By virtue of its anatomic location, anterior to the rectum and posteroinferior to the bladder, treatment to the prostate results in mainly acute urinary and rectal side effects. The urethra, running right through the gland, can hardly be avoided. Neurovascular bundles responsible for erectile function run

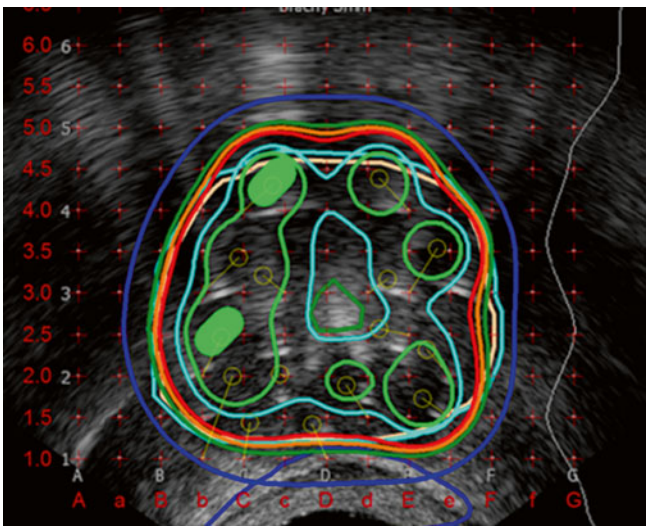

Fig. 14.6 Representative isodose lines from intraoperative planning for low-dose rate brachytherapy demonstrating excellent coverage while sparing the urethra

Fig. 14.7 Postoperative CT demonstrating excellent geometry and placement of low-dose rate brachytherapy seeds within the prostate gland

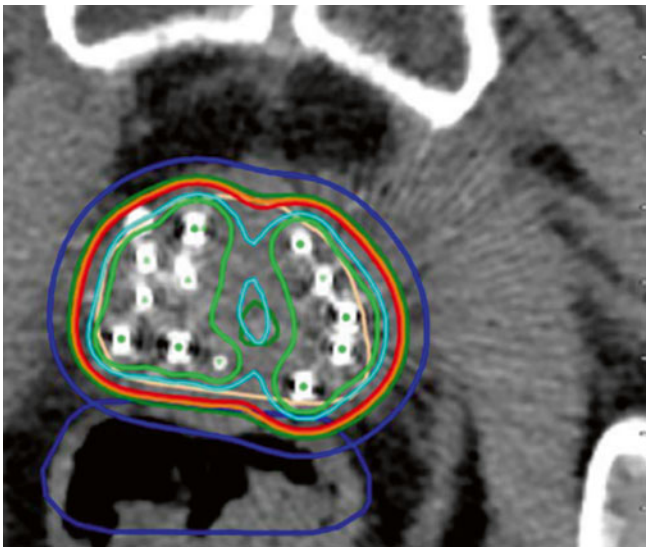

Fig. 14.8 Postoperative CT with isodose lines confirming excellent coverage while sparing the urethra

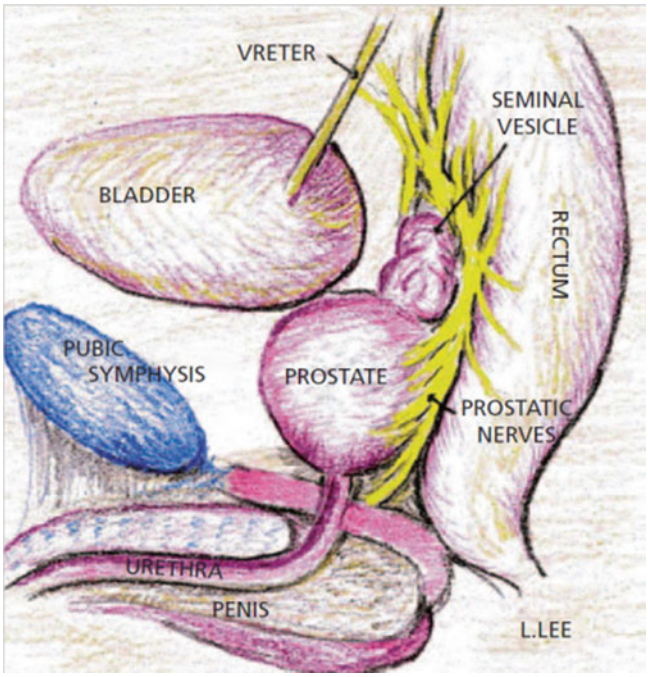

Fig. 14.9 Prostate in situ (Courtesy of L. Lee)

alongside the right and left posterolateral apical aspects of the gland (Fig. 14.9). As a result of their location, these structures receive a relatively high dose of radiation therapy and sustain most of the collateral damage from treatment. Imaging plays a primary role in locating these structures to assist in minimizing the planned dose and also maintaining precision of treatment delivery. The ultimate goal is to improve the therapeutic margin by increasing dose to the prostate while reducing dose particularly to the bladder and rectum.

Toxicity Grading

The EORTC/RTOG criteria of acute and chronic radiation morbidity are provided for all different clinical systems. Acute morbidities for lower gastrointestinal and genitourinary side effects, often cited for prostate cancer treatment, are listed in Table 14.4. The criteria for late effects are determined after the 90th day from the commencement of therapy and are listed in Table 14.5 [51]. Common Terminology Criteria for Adverse Events (CTCAE) provide similar information and are also frequently used. Version 4.0, released in May 2009 and updated in January 2015, includes a range of grades for various toxicities. The grading system ranges from 1 to 5: asymptomatic, symptomatic, severely altered function, life-threatening consequences, and death, respectively. Rectal toxicities include rectal fistula, hemorrhage, mucositis, necrosis, obstruction, pain, perforation, and ulcer. Urinary toxicities include urinary fistula, frequency, incontinence, retention, tract obstruction, tract pain, urgency, cystitis, and hematuria. Other adverse events that may apply to prostate cancer treatment include ejaculatory disorder and erectile dysfunction.

Outcomes

Low-Risk Group Patients

Five- and ten-year outcomes of brachytherapy monotherapy for patients with low-risk group disease range on the order of 90 % biochemical progression-free survival and 95 % disease-specific survival. Representative results are demonstrated in Table 14.6. Several authors have performed retrospective analyses comparing contemporary brachytherapy to external beam radiation therapy and/or radical prostatectomy, and similar results are noted regardless of modality [52–54].

Intermediate-Risk Group Patients

Intermediate-risk group patients represent a wide range of clinical situations, and therefore it is common to see heterogeneity in reported outcomes, especially because intermediate-risk group definition and patient selection criteria are different from series to series [55–62]. Also, the use of androgen deprivation with brachytherapy varies from center to center and affects the ability to report biochemical outcomes, and the ABS is unable to provide guidance regarding the use of androgen deprivation in combination with prostate brachytherapy [63]. Table 14.7 shows representative studies for patients with intermediate risk treated with brachytherapy as monotherapy.

Table 14.4 Radiation Therapy Oncology Group (RTOG) acute radiation morbidity scoring criteria

Score	0	1	2	3	4
Lower gastrointestinal	No change	Increased frequency or change in quality of bowel habits not requiring medication/ rectal discomfort not requiring analgesics	Diarrhea requiring parasympatholytic drugs/ mucus discharge not necessitating sanitary pads/ rectal or abdominal pain requiring analgesics	Diarrhea requiring parenteral support/severe mucus or blood discharge necessitating sanitary pads/abdominal distention (distended bowel loops on radiograph)	Acute or subacute obstruction, fistula, or perforation; GI bleeding requiring transfusion; abdominal pain or tenesmus requiring tube decompression or bowel diversion
Genitourinary	No change	Frequency of urination or nocturia twice pretreatment habit/ dysuria, urgency not requiring medication	Frequency of urination that is less frequent than every hour Dysuria, urgency, bladder spasm requiring local anesthetic (e.g., phenazopyridine)	Frequency with urgency and nocturia hourly or more frequently/dysuria, pelvic pain, or bladder spasm requiring regular frequent narcotic/gross hematuria with/ without clot passage	Hematuria requiring transfusion/acute bladder obstruction not secondary to clot passage, ulceration, or necrosis

From https://www.rtog.org/researchassociates/adverseeventreporting/acuteradiationmorbidityscoringcriteria.aspx, Radiation Therapy Oncology Group, with permission

Table 14.5 European Organisation for Research and Treatment of Cancer (EORTC)/Radiation Therapy Oncology Group (RTOG) criteria of late effects

Score	0	1	2	3	4
Small/large intestine	None	Mild diarrhea; mild cramping; bowel movements 5 times daily; slight rectal discharge or bleeding	Moderate diarrhea and colic; bowel movement >5 times daily; excessive rectal mucus or intermittent bleeding	Obstruction or bleeding requiring surgery	Necrosis/perforation, fistula
Bladder	None	Slight epithelial atrophy; minor telangiectasia (microscopic hematuria)	Moderate frequency; generalized telangiectasia; intermittent macroscopic hematuria	Severe frequency and dysuria; severe telangiectasia; frequent hematuria; reduction in bladder capacity (<150 mL)	Necrosis/contracted bladder capacity (<100 mL), severe hemorrhagic cystitis

From European Organisation for Research and Treatment of Cancer (EORTC)/Radiation Therapy Oncology Group (RTOG), with permission

Table 14.6 Results of brachytherapy monotherapy for low-risk group prostate patients

Author	Patients	Median follow-up	Percent bNED
Taira et al. [55]	575	148	98.6
Potters et al. [56]	481	82	89
Beyer et al. [57]	125	84	85
Grimm et al. [58]	125	81	87
Sharkey et al. [59]	528	72	87
Zelefsky et al. [60]	360	63	82
Hinnen et al. [61]	232	72	88
Henry et al. [62]	575	57	86

Table 14.7 Results of brachytherapy monotherapy for low-risk group prostate patients

Author	Patients	Median follow-up	Percent bNED	Percent use of ADT
Beyer et al. [57]	345	84	66	0
Cosset et al. [64]	276	43	94	68
Morris et al. [65]	419	54	96	100
Taira et al. [55]	144	74	96	0
Hinnen et al. [61]	369	69	61	18
Henry et al. [62]	430	57	86	N/R

Results of Combination Therapy with EBRT and Brachytherapy

The potential advantages of combination therapy are detailed above and have been well reviewed in the literature [35]. While some studies demonstrate a benefit to combination treatment, with bNED rates of 88, 80, and 53 % for low-, intermediate-, and high-risk group patients, respectively [8, 64–66], a number of studies have shown that there is not a difference in outcome between brachytherapy alone and combination therapy, especially for patients with intermediate-risk disease [52, 67]. The results of RTOG 0232 will further inform decision making in this patient category. It is widely accepted that for high-risk group patients, brachytherapy as monotherapy is generally not appropriate, and patients should receive supplemental external beam radiation and androgen deprivation therapy if at all feasible.

References

1. Jemal A, Siegel R, Xu J, Ward E. Cancer statistics, 2010. CA Cancer J Clin. 2010;60:277–300.
2. Greene KL, Albertsen PC, Babaian RJ, et al. Prostate specific antigen best practice statement: 2009 update. J Urol. 2013;189:S2–11.
3. Schroder FH, Hugosson J, Roobol MJ, et al. Screening and prostate-cancer mortality in a randomized European study. N Engl J Med. 2009;360:1320–8.
4. Andriole GL, Crawford ED, Grubb 3rd RL, et al. Mortality results from a randomized prostate-cancer screening trial. N Engl J Med. 2009;360:1310–9.
5. Davis BJ, Horwitz EM, Lee WR, et al. American Brachytherapy Society consensus guidelines for transrectal ultrasound-guided permanent prostate brachytherapy. Brachytherapy. 2012;11:6–19.
6. Chen AB, D'Amico AV, Neville BA, Earle CC. Patient and treatment factors associated with complications after prostate brachytherapy. J Clin Oncol. 2006;24:5298–304.
7. Keyes M, Miller S, Moravan V, et al. Predictive factors for acute and late urinary toxicity after permanent prostate brachytherapy: long-term outcome in 712 consecutive patients. Int J Radiat Oncol Biol Phys. 2009;73:1023–32.
8. Sylvester JE, Grimm PD, Blasko JC, et al. 15-Year biochemical relapse free survival in clinical Stage T1-T3 prostate cancer following combined external beam radiotherapy and brachytherapy; Seattle experience. Int J Radiat Oncol Biol Phys. 2007;67:57–64.
9. Rifkin MD, Zerhouni EA, Gatsonis CA, et al. Comparison of magnetic resonance imaging and ultrasonography in staging early prostate cancer. Results of a multi-institutional cooperative trial. N Engl J Med. 1990;323:621–6.
10. Beerlage HP, Aarnink RG, Ruijter ET, et al. Correlation of transrectal ultrasound, computer analysis of transrectal ultrasound and histopathology of radical prostatectomy specimen. Prostate Cancer Prostatic Dis. 2001;4:56–62.
11. Hricak H, Dooms GC, McNeal JE, et al. MR imaging of the prostate gland: normal anatomy. AJR Am J Roentgenol. 1987; 148:51–8.
12. Hricak H, White S, Vigneron D, et al. Carcinoma of the prostate gland: MR imaging with pelvic phased-array coils versus integrated endorectal – pelvic phased-array coils. Radiology. 1994;193: 703–9.
13. Wang L, Mazaheri Y, Zhang J, Ishill NM, Kuroiwa K, Hricak H. Assessment of biologic aggressiveness of prostate cancer: correlation of MR signal intensity with Gleason grade after radical prostatectomy. Radiology. 2008;246:168–76.
14. Langer DL, van der Kwast TH, Evans AJ, et al. Intermixed normal tissue within prostate cancer: effect on MR imaging measurements of apparent diffusion coefficient and T2 – sparse versus dense cancers. Radiology. 2008;249:900–8.
15. Bonekamp D, Macura KJ. Dynamic contrast-enhanced magnetic resonance imaging in the evaluation of the prostate. Top Magn Reson Imaging. 2008;19:273–84.
16. Alonzi R, Padhani AR, Allen C. Dynamic contrast enhanced MRI in prostate cancer. Eur J Radiol. 2007;63:335–50.
17. Jacobs MA, Ouwerkerk R, Petrowski K, Macura KJ. Diffusion-weighted imaging with apparent diffusion coefficient mapping and spectroscopy in prostate cancer. Top Magn Reson Imaging. 2008;19:261–72.
18. Mueller-Lisse UG, Scherr MK. Proton MR spectroscopy of the prostate. Eur J Radiol. 2007;63:351–60.
19. Sciarra A, Barentsz J, Bjartell A, et al. Advances in magnetic resonance imaging: how they are changing the management of prostate cancer. Eur Urol. 2011;59:962–77.
20. Futterer JJ, Heijmink SW, Scheenen TW, et al. Prostate cancer localization with dynamic contrast-enhanced MR imaging and proton MR spectroscopic imaging. Radiology. 2006;241:449–58.
21. Kim CK, Park BK, Lee HM, Kwon GY. Value of diffusion-weighted imaging for the prediction of prostate cancer location at 3T using a phased-array coil: preliminary results. Invest Radiol. 2007;42:842–7.
22. De Meerleer G, Villeirs G, Bral S, et al. The magnetic resonance detected intraprostatic lesion in prostate cancer: planning and delivery of intensity-modulated radiotherapy. Radiother Oncol. 2005;75:325–33.
23. Pucar D, Hricak H, Shukla-Dave A, et al. Clinically significant prostate cancer local recurrence after radiation therapy occurs at the site of primary tumor: magnetic resonance imaging and step-section pathology evidence. Int J Radiat Oncol Biol Phys. 2007;69:62–9.
24. Eggener S, Salomon G, Scardino PT, De la Rosette J, Polascik TJ, Brewster S. Focal therapy for prostate cancer: possibilities and limitations. Eur Urol. 2010;58:57–64.
25. Roy JN, Wallner KE, Harrington PJ, Ling CC, Anderson LL. A CT-based evaluation method for permanent implants: application to prostate. Int J Radiat Oncol Biol Phys. 1993;26:163–9.
26. Salembier C, Lavagnini P, Nickers P, et al. Tumour and target volumes in permanent prostate brachytherapy: a supplement to the ESTRO/EAU/EORTC recommendations on prostate brachytherapy. Radiother Oncol. 2007;83:3–10.
27. Dubois DF, Prestidge BR, Hotchkiss LA, Prete JJ, Bice Jr WS. Intraobserver and interobserver variability of MR imaging- and CT-derived prostate volumes after transperineal interstitial permanent prostate brachytherapy. Radiology. 1998;207:785–9.
28. Al-Qaisieh B. Pre- and post-implant dosimetry: an inter-comparison between UK prostate brachytherapy centres. Radiother Oncol. 2003;66:181–3.
29. Smith WL, Lewis C, Bauman G, et al. Prostate volume contouring: a 3D analysis of segmentation using 3DTRUS, CT, and MR. Int J Radiat Oncol Biol Phys. 2007;67:1238–47.
30. Charyulu KK. Transperineal interstitial implantation of prostate cancer: a new method. Int J Radiat Oncol Biol Phys. 1980;6:1261–6.
31. Holm HH. The history of interstitial brachytherapy of prostatic cancer. Semin Surg Oncol. 1997;13:431–7.
32. Buyyounouski MK, Davis BJ, Prestidge BR, et al. A survey of current clinical practice in permanent and temporary prostate brachytherapy: 2010 update. Brachytherapy. 2012;11:299–305.

33. Orio 3rd PF, Tutar IB, Narayanan S, et al. Intraoperative ultrasound-fluoroscopy fusion can enhance prostate brachytherapy quality. Int J Radiat Oncol Biol Phys. 2007;69:302–7.
34. Prestidge BR, Prete JJ, Buchholz TA, et al. A survey of current clinical practice of permanent prostate brachytherapy in the United States. Int J Radiat Oncol Biol Phys. 1998;40:461–5.
35. Blasko JC, Mate T, Sylvester JE, Grimm PD, Cavanagh W. Brachytherapy for carcinoma of the prostate: techniques, patient selection, and clinical outcomes. Semin Radiat Oncol. 2002;12:81–94.
36. Battermann JJ, van Es CA. The learning curve in prostate seed implantation. Cancer Radiother. 2000;4 Suppl 1:119s–22s.
37. Older RA, Synder B, Krupski TL, Glembocki DJ, Gillenwater JY. Radioactive implant migration in patients treated for localized prostate cancer with interstitial brachytherapy. J Urol. 2001;165:1590–2.
38. Tapen EM, Blasko JC, Grimm PD, et al. Reduction of radioactive seed embolization to the lung following prostate brachytherapy. Int J Radiat Oncol Biol Phys. 1998;42:1063–7.
39. Merrick GS, Butler WM, Dorsey AT, Lief JH, Benson ML. Seed fixity in the prostate/periprostatic region following brachytherapy. Int J Radiat Oncol Biol Phys. 2000;46:215–20.
40. Eshleman JS, Davis BJ, Pisansky TM, et al. Radioactive seed migration to the chest after transperineal interstitial prostate brachytherapy: extraprostatic seed placement correlates with migration. Int J Radiat Oncol Biol Phys. 2004;59:419–25.
41. Al-Qaisieh B, Carey B, Ash D, Bottomley D. The use of linked seeds eliminates lung embolization following permanent seed implantation for prostate cancer. Int J Radiat Oncol Biol Phys. 2004;59:397–9.
42. Fuller DB, Koziol JA, Feng AC. Prostate brachytherapy seed migration and dosimetry: analysis of stranded sources and other potential predictive factors. Brachytherapy. 2004;3:10–9.
43. Reed DR, Wallner KE, Merrick GS, et al. A prospective randomized comparison of stranded vs. loose ^{125}I seeds for prostate brachytherapy. Brachytherapy. 2007;6:129–34.
44. Heysek RV, Gwede CK, Torres-Roca J, et al. A dosimetric analysis of unstranded seeds versus customized stranded seeds in transperineal interstitial permanent prostate seed brachytherapy. Brachytherapy. 2006;5:244–50.
45. Lin K, Lee SP, Cho JS, Reiter RE, DeMarco JJ, Solberg TD. Improvements in prostate brachytherapy dosimetry due to seed stranding. Brachytherapy. 2007;6:44–8.
46. Fagundes HM, Keys RJ, Wojcik MF, Radden MA, Bertelsman CG, Cavanagh WA. Transperineal TRUS-guided prostate brachytherapy using loose seeds versus RAPIDStrand: a dosimetric analysis. Brachytherapy. 2004;3:136–40.
47. Stock RG, Stone NN, Tabert A, Iannuzzi C, DeWyngaert JK. A dose-response study for I-125 prostate implants. Int J Radiat Oncol Biol Phys. 1998;41:101–8.
48. Papagikos MA, Deguzman AF, Rossi PJ, McCullough DL, Clark PE, Lee WR. Dosimetric quantifiers for low-dose-rate prostate brachytherapy: is V(100) superior to D(90)? Brachytherapy. 2005;4:252–8.
49. Fogh S, Doyle L, Yu A, et al. A comparison of preplan transrectal ultrasound with preplan-CT in assessing volume and number of seeds needed for real-time ultrasound-based intra-operative planning in prostate (125)I seed implantation. Brachytherapy. 2010;9:335–40.
50. Crook JM, Potters L, Stock RG, Zelefsky MJ. Critical organ dosimetry in permanent seed prostate brachytherapy: defining the organs at risk. Brachytherapy. 2005;4:186–94.
51. Cox JD, Stetz J, Pajak TF. Toxicity criteria of the Radiation Therapy Oncology Group (RTOG) and the European Organization for Research and Treatment of Cancer (EORTC). Int J Radiat Oncol Biol Phys. 1995;31:1341–6.
52. Kupelian PA, Potters L, Khuntia D, et al. Radical prostatectomy, external beam radiotherapy <72 Gy, external beam radiotherapy > or =72 Gy, permanent seed implantation, or combined seeds/external beam radiotherapy for stage T1-T2 prostate cancer. Int J Radiat Oncol Biol Phys. 2004;58:25–33.
53. Colberg JW, Decker RH, Khan AM, McKeon A, Wilson LD, Peschel RE. Surgery versus implant for early prostate cancer: results from a single institution, 1992-2005. Cancer J. 2007;13:229–32.
54. D'Amico AV, Whittington R, Malkowicz SB, et al. Biochemical outcome after radical prostatectomy, external beam radiation therapy, or interstitial radiation therapy for clinically localized prostate cancer. JAMA. 1998;280:969–74.
55. Taira AV, Merrick GS, Butler WM, et al. Long-term outcome for clinically localized prostate cancer treated with permanent interstitial brachytherapy. Int J Radiat Oncol Biol Phys. 2011;79:1336–42.
56. Potters L, Morgenstern C, Calugaru E, et al. 12-year outcomes following permanent prostate brachytherapy in patients with clinically localized prostate cancer. J Urol. 2005;173:1562–6.
57. Beyer DC, Brachman DG. Failure free survival following brachytherapy alone for prostate cancer: comparison with external beam radiotherapy. Radiother Oncol. 2000;57:263–7.
58. Grimm PD, Blasko JC, Sylvester JE, Meier RM, Cavanagh W. 10-year biochemical (prostate-specific antigen) control of prostate cancer with (125)I brachytherapy. Int J Radiat Oncol Biol Phys. 2001;51:31–40.
59. Sharkey J, Cantor A, Solc Z, et al. 103Pd brachytherapy versus radical prostatectomy in patients with clinically localized prostate cancer: a 12-year experience from a single group practice. Brachytherapy. 2005;4:34–44.
60. Zelefsky MJ, Yamada Y, Cohen GN, et al. Intraoperative real-time planned conformal prostate brachytherapy: post-implantation dosimetric outcome and clinical implications. Radiother Oncol. 2007;84:185–9.
61. Hinnen KA, Battermann JJ, van Roermund JG, et al. Long-term biochemical and survival outcome of 921 patients treated with I-125 permanent prostate brachytherapy. Int J Radiat Oncol Biol Phys. 2010;76:1433–8.
62. Henry AM, Al-Qaisieh B, Gould K, et al. Outcomes following iodine-125 monotherapy for localized prostate cancer: the results of Leeds 10-year single-center brachytherapy experience. Int J Radiat Oncol Biol Phys. 2010;76:50–6.
63. Potters L, Torre T, Ashley R, Leibel S. Examining the role of neoadjuvant androgen deprivation in patients undergoing prostate brachytherapy. J Clin Oncol. 2000;18:1187–92.
64. Cosset JM, Flam T, Thiounn N, et al. Selecting patients for exclusive permanent implant prostate brachytherapy: the experience of the Paris Institut Curie/Cochin Hospital/Necker Hospital group on 809 patients. Int J Radiat Oncol Biol Phys. 2008;71:1042–8.
65. Morris WJ, Keyes M, Palma D, et al. Population-based study of biochemical and survival outcomes after permanent ^{125}I brachytherapy for low- and intermediate-risk prostate cancer. Urology. 2009;73:860–5. discussion 5-7.
66. Critz FA, Levinson K. 10-year disease-free survival rates after simultaneous irradiation for prostate cancer with a focus on calculation methodology. J Urol. 2004;172:2232–8.
67. Potters L, Freeman K. Prostatectomy, external beam radiation therapy, or brachytherapy for localized prostate cancer. JAMA. 1999;281:1584; author reply 5–6.

Selective Arterial Prostatic Embolization (SAPE): BPH Embolization

15

Tiago Bilhim and João Pisco

Different Treatment Options

Benign prostatic hyperplasia (BPH) consists of a proliferation of smooth muscle and epithelial cells within the transition zone of the prostate, leading to prostate enlargement (PE). BPH manifests clinically with lower urinary tract symptoms (LUTS) and bladder outlet obstruction (BOO) [1]. However, it can be difficult to make a direct link between BPH and LUTS. Many BPH patients don't have any clinically relevant symptoms, even though BOO may be present. On the other hand, many LUTS are not related to BPH but to the bladder (detrusor overactivity or underactivity), bladder neck, urethra, or kidney (nocturnal polyuria) or to neurological diseases [2].

Treatment strategies should be oriented to treat LUTS and not specific diseases or conditions. Many different treatment options exist and the patient should have a central role in decision making after being informed on the benefits and harms of treatment alternatives for LUTS secondary to BPH [1, 2]. Selective arterial prostatic embolization (SAPE) has been shown to be an effective treatment modality to control gross hematuria in patients with BPH and prostate cancer [3].

Watchful waiting (active surveillance) is accepted for patients with mild symptoms or moderate-to-severe symptoms who are not bothered by their LUTS and have no complications of LUTS and BOO (e.g., renal insufficiency, urinary retention, or recurrent infection). Medical therapy with alpha-blockers (alfuzosin, doxazosin, tamsulosin, and terazosin) is usually the first-line treatment option for men with bothersome, moderate-to-severe LUTS secondary to BPH. Alpha-blockers have a quick run-in period (up to a few weeks) and reduce the International Prostate Symptom Score (IPSS) by approximately 35–40 % and increase the maximum urinary flow rate (Qmax) by approximately 20–25 %, with long-lasting results (at least 4 years). 5-Alpha-reductase inhibitors (finasteride 5 mg or dutasteride 0.5 mg daily) may be used to prevent progression of LUTS secondary to BPH and to reduce the risk of urinary retention and future prostate-related surgery if the prostate volume is greater than 40 mL. The run-in period is approximately 3–6 months leading to a 15–30 % decrease in IPSS, an 18–28 % decrease in prostate volume, and a 1.5–2.0 mL/s increase in peak urinary flow rate (Qmax). Combination therapy (alpha-blockers + 5-alpha-reductase inhibitors) should be long-lasting (>1 year) in men with moderate-to-severe LUTS, enlarged prostates, and reduced Qmax (men likely to develop disease progression). Anticholinergic agents as monotherapy or in combination with an alpha-blocker are indicated for the management of predominantly irritative LUTS secondary to BPH in men without an elevated post-void residual (PVR) urine and without severe BOO. Phosphodiesterase 5 inhibitors (with or without alpha-blockers) significantly and consistently reduce IPSS by approximately 17–35 % and increase Qmax by 3.7–4.3 mL/s (24–38 %) and can be used for men with erectile dysfunction, failed alpha-blocker therapy, or pulmonary arterial hypertension or for those participating in LUTS clinical trials [1, 2].

Minimally invasive therapies (MISTs) include transurethral needle ablation (TUNA) of the prostate and transurethral microwave thermotherapy (TUMT). Both techniques are effective in partially relieving LUTS secondary to BPH and may be considered in men with moderate or severe symptoms refractory to or refusing medical therapy. TUNA induces an IPSS reduction from 40 to 70 % and Qmax increase from 26 to 121 %. However, 21.2 % of patients require additional treatment after 5 years. TUMT induces an IPSS reduction of 65 % and a Qmax improvement of 70 %; however a cumulative risk of treatment failure of 58.8 % at 5 years has been documented. Both MISTs are alternatives to

T. Bilhim, MD, PhD
Department of Radiology,
Saint Louis Hospital and Nova Medical School, Faculdade de Ciências Médicas, Universidade Nova de Lisboa,
Lisbon, Portugal

J. Pisco, MD (✉)
Interventional Radiology, Saint Louis Hospital and Nova Medical School, Faculdade de Ciências Médicas, Universidade Nova de Lisboa, Lisbon, Portugal
e-mail: martinspisco@hospitalsaintlouis.onmicrosoft.com

A.R. Rastinehad, D.N. Siegel (eds.), *Interventional Urology*, DOI 10.1007/978-3-319-23464-9_15

TURP for patients who wish to defer/avoid (complications of) TURP, but patients should be aware of significant re-treatment rates (low durability of results) and less improvement in symptoms and quality of life [1, 2]. Intraprostatic botulinum toxin or ethanol injections are considered experimental MIST and should be performed only in clinical trials. Transurethral incision of the prostate (TUIP) is another MIST limited to the treatment of smaller prostates (<30 mL), without significant median lobe.

Surgical interventions are appropriate for moderate-to-severe LUTS refractory to medical therapy or when patients refuse medical therapy, for men under acute urinary retention (AUR) or with other BPH-related complications (renal insufficiency secondary to BPH, recurrent urinary tract infections (UTI), gross hematuria due to BPH, bladder stones, and bladder diverticulum when associated with recurrent UTI or progressive bladder dysfunction). Open prostatectomies may be indicated for men with very enlarged prostates (>80–100 mL), bladder diverticula, or stones. Mono- or bipolar transurethral resection of the prostate (TURP) leads to an IPSS reduction of approximately 70 %, a mean Qmax increase of 125 % (9.7 mL/s), and re-treatment rates of 5.8, 12.3, and 14.7 % at 1, 5, and 8 years of follow-up, respectively. Most relevant complications of TURP include bleeding requiring blood transfusion (2.9 %), stress urinary incontinence (2.2 %), bladder neck stenosis and urethral stricture (up to 5 %), and retrograde ejaculation (65.4 %) [2]. TURP is the current standard procedure for men with indication to undergo surgery and prostate sizes of 30–80 mL. TURP provides subjective and objective improvement rates superior to medical or MIST therapies on the expense of higher morbidity. Transurethral laser surgery (holmium laser resection of the prostate, holmium laser enucleation of the prostate, transurethral side firing laser ablation, holmium laser ablation of the prostate, and photoselective vaporization) has similar clinical improvement and long-term complication rates to TURP but is able to treat patients with prostates larger than 80–100 mL. The shorter catheterization time and length of stay and decreased risk of perioperative complications (TUR syndrome, transfusions) must be weighted against the higher costs, long learning curve, and longer operative times [1, 2]. Retrograde ejaculation can occur in 75–80 % of patients after holmium laser enucleation (HoLEP) [2].

Imaging Evaluation

Clinical assessment (with IPSS measurement) with digital rectal examination and PSA measurements with or without uroflow studies are considered first-line approaches. No initial imaging is recommended in the standard patient [4]. Bladder ultrasound (US) may be useful to exclude bladder cancer, stone, or diverticulum and to evaluate the bladder wall thickness (that increases with long-standing BOO due to hypertrophy). Renal US may be useful to exclude renal cancer or obstruction due to BPH. Transrectal US (TRUS) of the prostate is the most reliable and less expensive technique to determine the prostate volume (transverse diameter × anteroposterior diameter × length × 0.52) and should be performed before surgery or MIST to help choose the best treatment option. The anteroposterior diameter (AP) is most accurately measured in the sagittal plane to avoid the "salami" distortion of measurements in the axial plane. TRUS also allows exploring the zonal anatomy and BPH patterns and identifying and measuring the protrusion index of the median lobe into the bladder base that may be associated with poorer outcomes after MIST procedures. Total prostate volume, proportion of central gland/total prostate volume, and lobar distributions have potential for the subtyping of BPH for effects on outcome [4].

Magnetic resonance imaging (MRI) in BPH patients is used to exclude cancer when high clinical suspicion and negative biopsy are present [5]. MRI also depicts the zonal anatomy and the protrusion index of the median lobe that may be predictors of treatment response. Multiparametric MRI with perfusion imaging is able to quantify the vascularity of the prostate and detect ischemia after embolization that may be important prognostic factors after prostate artery embolization (PAE). Diffusion imaging before and after PAE is another potential predictor of outcome after PAE.

Pre-procedural Patient Evaluation

The clinical severity of LUTS can be quantified using validated questionnaires as the IPSS that has seven questions (each scoring from 0 to 5 points, total score 35) that ask about storage-irritative symptoms (micturation frequency, urgency episodes, nocturia) and emptying symptoms (incomplete emptying, intermittence, weak urinary stream, straining at urination). Patients are classified as mildly symptomatic (0–7 points), moderately symptomatic (8–19 points), and severely symptomatic (20–35 points). The quality of life related to LUTS (QoL) or "bother score" is an eighth question that ranges from zero (delighted) to six (terrible) and is the strongest predictor for patient management as it directly reflects how the patient feels about his LUTS.

Erectile function should also be evaluated before and after because erectile dysfunction frequently coexists with BPH and/or can be a consequence of prostate medication or surgery. The use of validated questionnaires as the International Index of Erectile Function (IIEF) should be used routinely in BPH trials. In our practice we use the short (IIEF-5) version with five questions that can be easily and rapidly used.

Before PAE, patients undergo PSA measurement, prostate volume measurement with TRUS, and uroflow studies (to measure Qmax and PVR) [6]. Patients who have been counseled for prostate cancer screening in conjunction with an elevated PSA may undergo a workup to rule out prostate

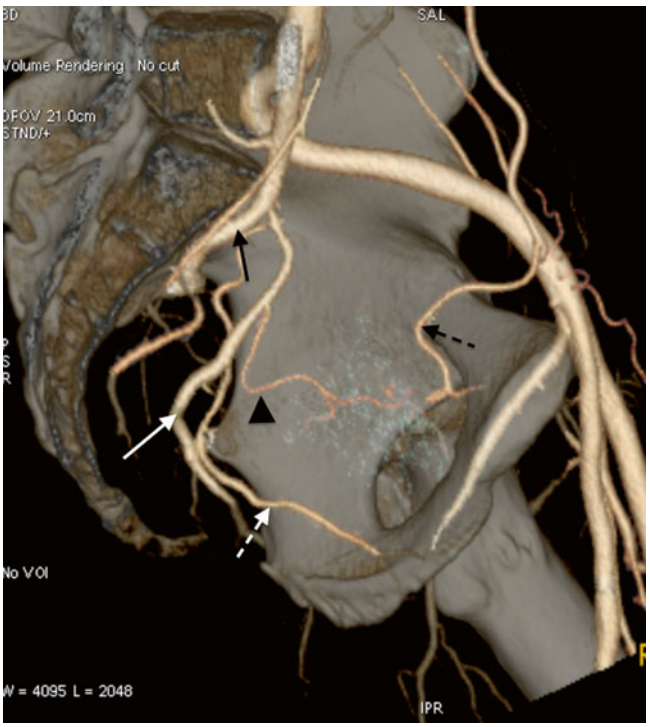

Fig. 15.1 CTA VR reformat of the left pelvic side. Type A bifurcation of the internal iliac artery (IIA). Posterior division with the superior gluteal artery (*black arrow*). Anterior division with the common gluteal-pudendal trunk bifurcating into inferior gluteal (*white arrow*) and internal pudendal (*white dashed arrow*) arteries. Only 1 prostate artery (PA) is seen (*black arrowhead*) arising from the common gluteal-pudendal trunk. The black dashed arrow marks an aberrant obturator artery arising from the inferior epigastric artery (external iliac artery)

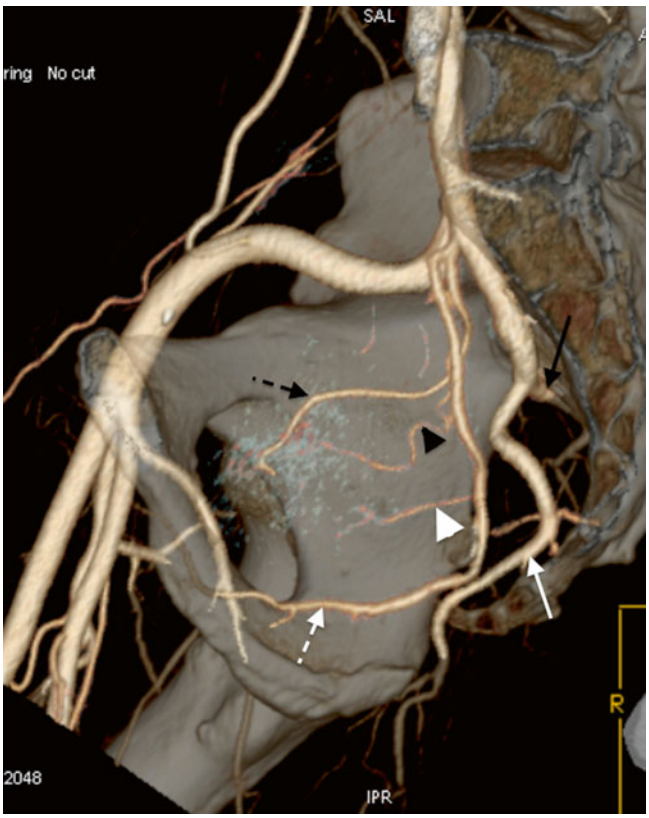

Fig. 15.2 CTA VR reformat of the right pelvic side. Type B bifurcation of the IIA. Posterior division with the superior gluteal (*black arrow*) and inferior gluteal (*white arrow*) arteries. Anterior division with the internal pudendal artery (*white dashed arrow*). Two PAs are seen arising from the internal pudendal artery. The *black arrowhead* marks the central gland PA, while the white arrowhead marks the peripheral gland PA. The *black dashed arrow* marks the obturator artery arising from the internal pudendal artery

cancer prior to treatment for their BPH. When the Qmax is very low (below 6 mL/s) and the flattened flow curve is suggestive of a urethral stricture, an urethrocystogram or urethrocystoscopy should be performed. When the Qmax is greater than 15 mL/s or when obstruction is doubtful, urodynamic pressure-flow studies should be performed to exclude bladder dysfunction (overactive or hypoactive bladder).

Technique

Vascular Anatomy Relevant for Embolization

One of the key aspects of PAE is finding the prostate arteries (PAs) that are usually 1–2 mm in diameter. Before finding these small arteries, it is important to identify all branches of the internal iliac artery (IIA) to facilitate navigation inside the male pelvis. We use the Yamaki classification [7–9] to help identify all major branches of the internal iliac artery. The most frequent branching pattern of the IIA is type A (60 %) where the anterior division gives off both internal pudendal and inferior gluteal arteries (common gluteal-pudendal trunk) (Fig. 15.1). The superior gluteal artery arises from the posterior division. In type B bifurcation (30 %), the posterior division seems larger because it gives rise to both superior and inferior gluteal arteries, while the anterior division only gives rise to the internal pudendal artery (Fig. 15.2). In type C (<10 %), all three major branches of the IIA (internal pudendal, superior, and inferior gluteal arteries) arise at the same time (Fig. 15.3). Group D is very rare (<0.5 %) and the posterior division gives rise to both superior gluteal and internal pudendal arteries, while the anterior division gives rise to the inferior gluteal artery. The obturator artery is another large branch that arises from the IIA in 70 % of the pelvis and from the inferior epigastric artery or external iliac artery in 30 % of the pelvis (thus called accessory or aberrant). The superior vesical artery is a smaller branch of the IIA, the main supplier to the bladder, and arises proximally from the anterior division of the IIA. PAs frequently arise from any of these arteries.

Knowledge of the radiological anatomy of all these major branches may help during PAE and facilitate the identification of the PAs [8, 9]. CTA is a valuable pre-procedural tool to help plan the procedure and study the vascular anatomy of the male pelvic arteries [10]. The prostate has a dual vascular

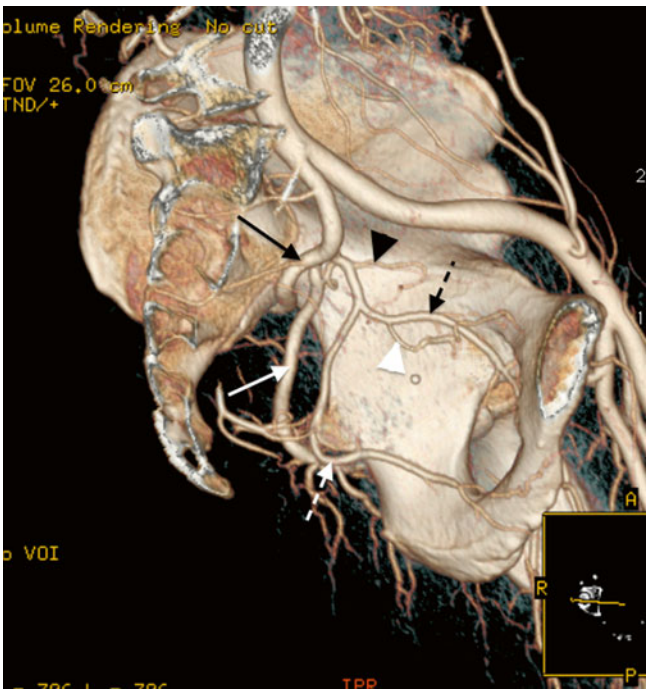

Fig. 15.3 CTA VR reformat of the left pelvic side. Type C bifurcation of the IIA. The superior gluteal artery (*black arrow*), the inferior gluteal artery (*white arrow*), and internal pudendal artery (*white dashed arrow*) arise simultaneously. Only 1 PA (*white arrowhead*) is seen arising from the obturator artery (*black dashed arrow*) that arises from the internal pudendal artery. The *black arrowhead* marks the superior vesical artery arising proximally from the anterior division of the IIA

Fig. 15.4 CTA sagittal-oblique MIP reformat of the left pelvic side (same patient from Fig. 15.1). Type A bifurcation of the IIA. Posterior division with the superior gluteal artery (*black arrow*). Anterior division with the common gluteal-pudendal trunk bifurcating into inferior gluteal (*white arrow*) and internal pudendal (*white dashed arrow*) arteries. Only 1 PA is seen (*black arrowhead*) arising from the common gluteal-pudendal trunk. The *black dashed arrows* mark the superior vesical artery branches feeding the bladder

supply with a central gland artery and a peripheral gland artery [11]. The central gland PA has a horizontal trajectory underneath the bladder neck (thus, also called vesicoprostatic artery) and penetrates the prostate capsule in the anterior-lateral quadrants (thus, also called anterior-lateral or medial PA). The peripheral gland PA has an oblique trajectory downward, forward, and inward and runs in the fat behind the prostate, in front of the rectum. The peripheral gland PA penetrates the prostate capsule in the posterior-lateral quadrants (thus, also called posterior-lateral or lateral PA) and frequently shares common origins or anastomoses with rectal branches. The central gland PA feeds most of the upper half and central gland of the prostate and may give rise to inferior vesical branches to the bladder neck or vesiculodeferential branches to the seminal glands along its trajectory. The peripheral gland PA feeds most of the lower half, apex, and peripheral prostate and frequently gives rise to rectal branches along its trajectory [11, 12].

The central gland and peripheral gland PAs may arise from one PA (Figs. 15.4, 15.5, 15.6, and 15.7) that bifurcates (60 % of pelvis) or from two independent PAs (40 % of pelvis) (Figs. 15.8, 15.9, 15.10, 15.11, 15.12, 15.13, 15.14, 15.15, 15.16, and 15.17). The PAs are larger when just 1 PA is present with approximately 2 mm in diameter, while PAs are smaller, approximately 1 mm in diameter, when two independent PAs are present. Prostate volume and PA diameter do not correlate,

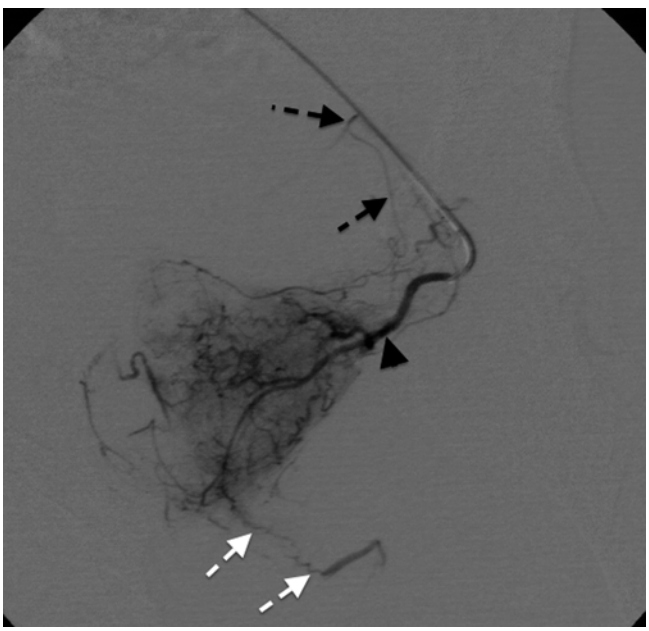

Fig. 15.5 Selective DSA of the left PA (*black arrowhead*) seen in Figs. 15.1 and 15.4. Anastomoses to the internal pudendal artery (*white dashed arrows*) and to the superior vesical artery (*black dashed arrows*) are seen

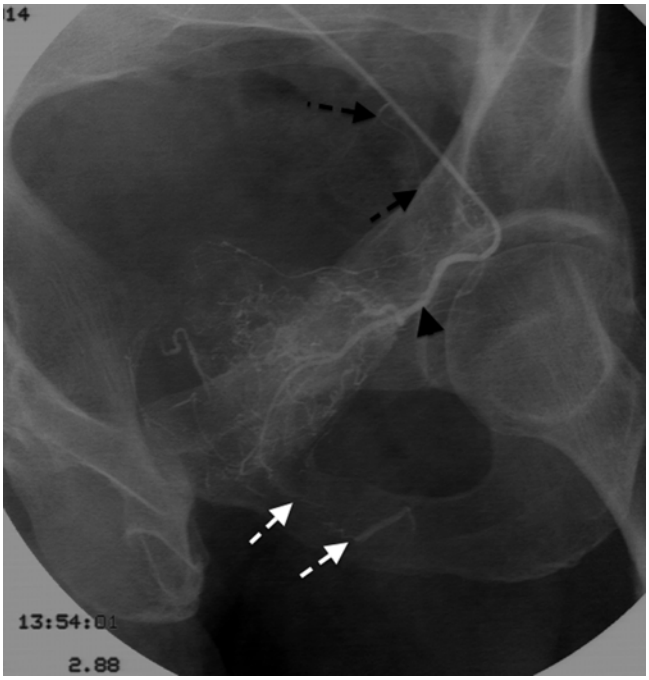

Fig. 15.6 Inverted image of Fig. 15.5 better depicting the vascularization of the central gland of the left hemiprostate. Anastomoses to the internal pudendal artery (*white dashed arrows*) and to the superior vesical artery (*black dashed arrows*) are seen

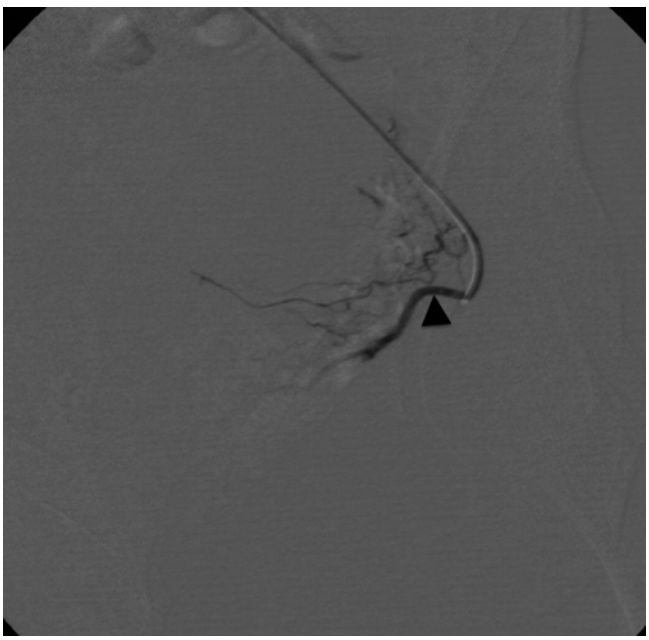

Fig. 15.7 Control angiogram after embolization of the left PA (*black arrowhead*) seen in Figs 15.5 and 15.6. Complete occlusion of the artery with no filling of the central gland of the prostate

Fig. 15.8 CTA sagittal-oblique MIP reformat of the right pelvic side (same patient from Fig. 15.2). Posterior division with the inferior gluteal artery (*white arrow*). Anterior division with the internal pudendal artery (*white dashed arrow*). Two PAs are seen arising from the internal pudendal artery. The *black arrowhead* marks the central gland PA, while the *white arrowhead* marks the peripheral gland PA

and patients with large prostates may have smaller PAs than patients with smaller prostates due to different number of PAs. PAs may arise from any of the IIA branches and even from outside the pelvic arteries [13]. The most frequent origins are the internal pudendal artery (30 %), superior vesical artery (20 %), and common gluteal-pudendal trunk (15 %). These origins are the "standard" anatomy representing up to 70 % of pelvis. The less frequent origins (20 %) are the obturator artery (12 %) and prostato-rectal trunks (8 %). Rare origins (<10 %) are the inferior (4 %) and superior (2 %) gluteal arteries, accessory pudendal arteries (2 %), and accessory obturator arteries (from the external iliac or inferior epigastric arteries, 2 %).

The PAs arising from prostato-rectal trunks are the peripheral gland PAs and usually there is a central gland PA arising proximally and independently from the IIA. Accessory pudendal arteries are the main blood supply to the corpora cavernosa in up to 4 % of pelvic sides or represent large anastomoses between the PAs and the penile arteries in up to 20 % of pelvis. Their identification is important to avoid untargeted ischemia to the penis or potential erectile dysfunction after PAE. PAs end at the prostate capsule, while accessory pudendal arteries run close to the prostate capsule but continue forward until they reach the pubic bone and anterior surface of the prostate. Then, instead of going into the prostate, they continue vertically downward behind the pubic bone and reach the penile hilum where they continue

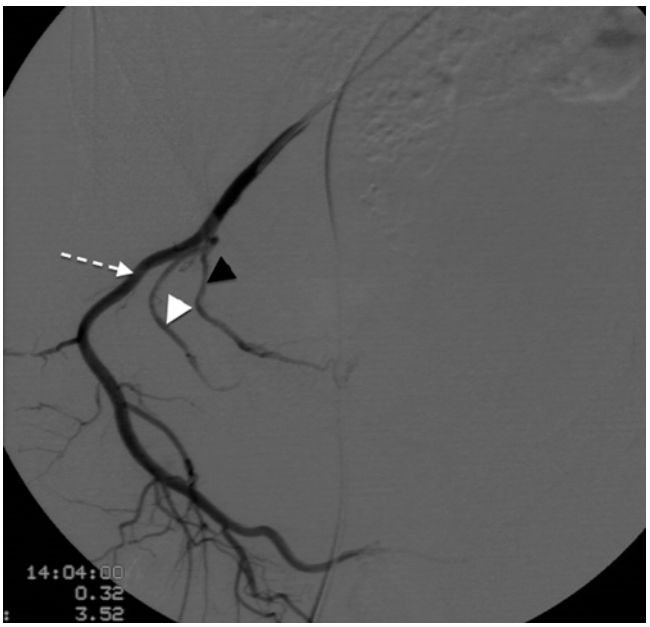

Fig. 15.9 DSA of the right internal pudendal artery (*white dashed arrow*) in ipsilateral anterior oblique projection (35°) and caudal-cranial angulation (−10°) of the same patient from Figs. 15.2 and 15.8. Two PAs are seen arising from the internal pudendal artery. The *black arrowhead* marks the central gland PA, while the *white arrowhead* marks the peripheral gland PA

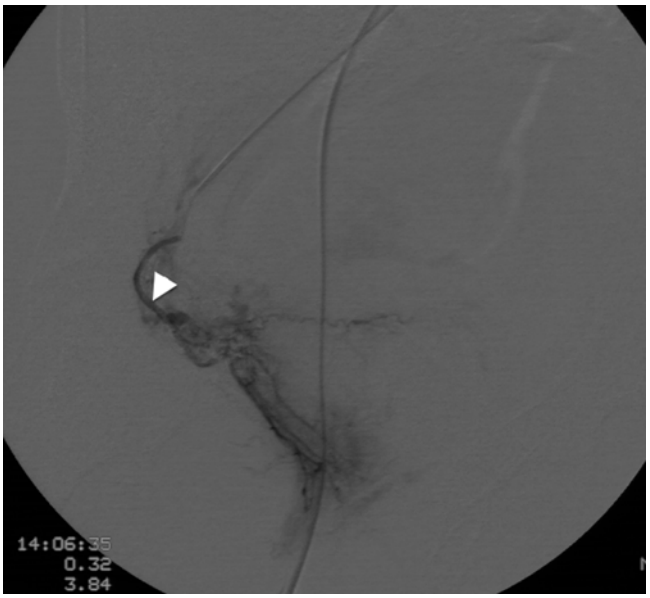

Fig. 15.10 Selective DSA of the right peripheral gland PA (*white arrowhead*) from the same patient in Figs. 15.2, 15.8, and 15.9. An oblique opacification of the peripheral gland and apex of the prostate is seen

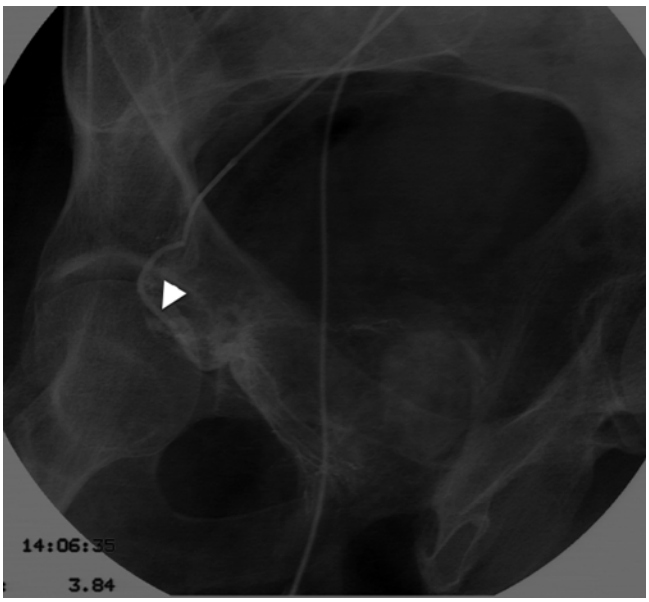

Fig. 15.11 Inverted image of Fig. 15.10 better depicting the vascularization of the peripheral gland of the right hemiprostate. Right peripheral gland PA (*white arrowhead*)

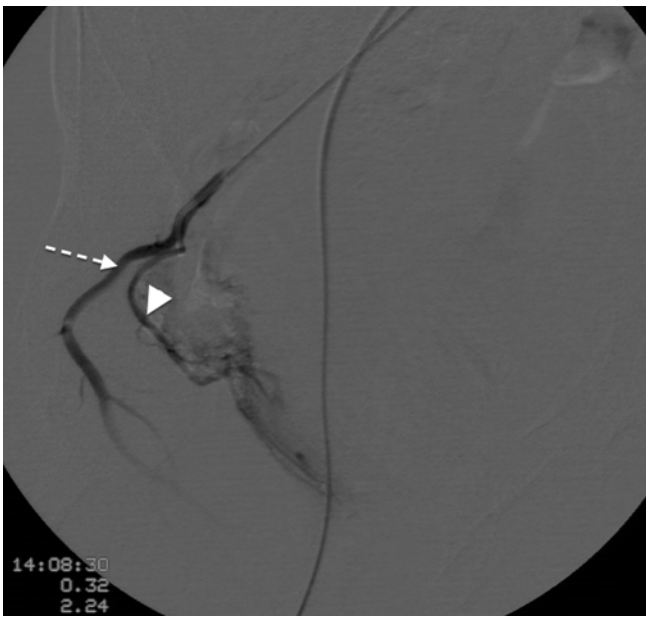

Fig. 15.12 Control angiogram after embolization of right peripheral gland PA (*white arrowhead*) seen in Fig. 15.10. Occlusion of the artery with no filling of the peripheral gland of the prostate and reflux into the internal pudendal artery (*white dashed arrow*)

forward with the dorsal artery of the penis or with the cavernosal artery, thus having an "S" trajectory that allows differentiation from the PAs (Figs. 15.18 and 15.19). In less than 2 % of pelvis, the PAs may arise from outside the IIA [13], from accessory obturator arteries (from the inferior epigastric or directly from the external iliac artery).

The DSA findings of the central and peripheral gland PAs are very different. The central gland PA has a globular and circumscribed appearance with parenchymal staining of the BPH adenomas. In up to 40 % of patients, the "corkscrew" pattern representing the typical tortuosity of the capsular branches may be detected. The central gland PA frequently

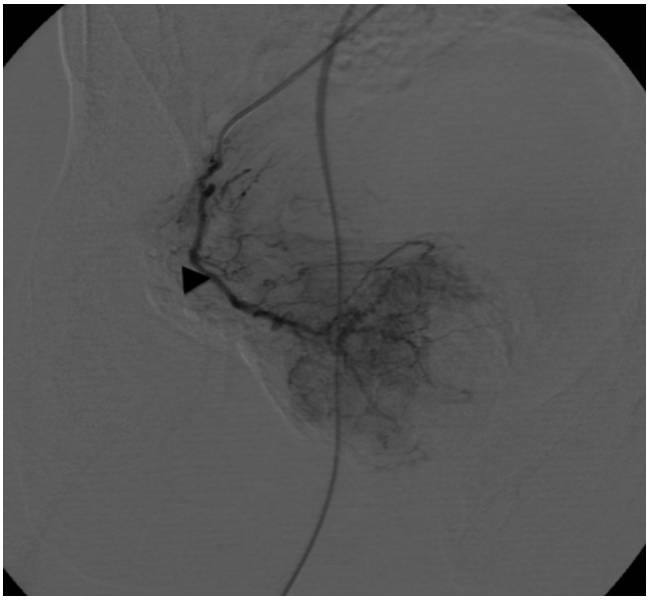

Fig. 15.13 Selective DSA of the right central gland PA (*black arrowhead*) from the same patient in Figs. 15.2, 15.8, and 15.9. A globular opacification of the central gland of the right hemiprostate with the corkscrew pattern of the capsular branches is seen

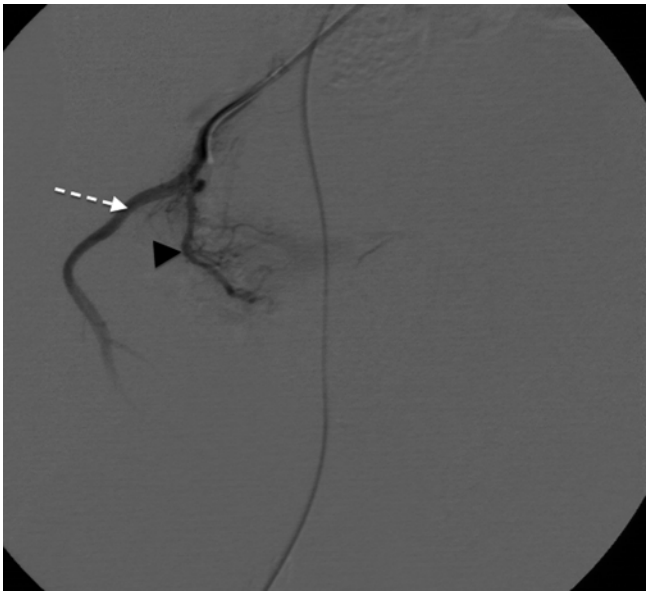

Fig. 15.15 Control angiogram after embolization of right central gland PA (*black arrowhead*) seen in Fig. 15.13. Occlusion of the artery with no filling of the central gland of the prostate and reflux into the internal pudendal artery (*white dashed arrow*)

Fig. 15.14 Inverted image of Fig. 15.13 better depicting the vascularization of the central gland of the right hemiprostate. Right central gland PA (*black arrowhead*)

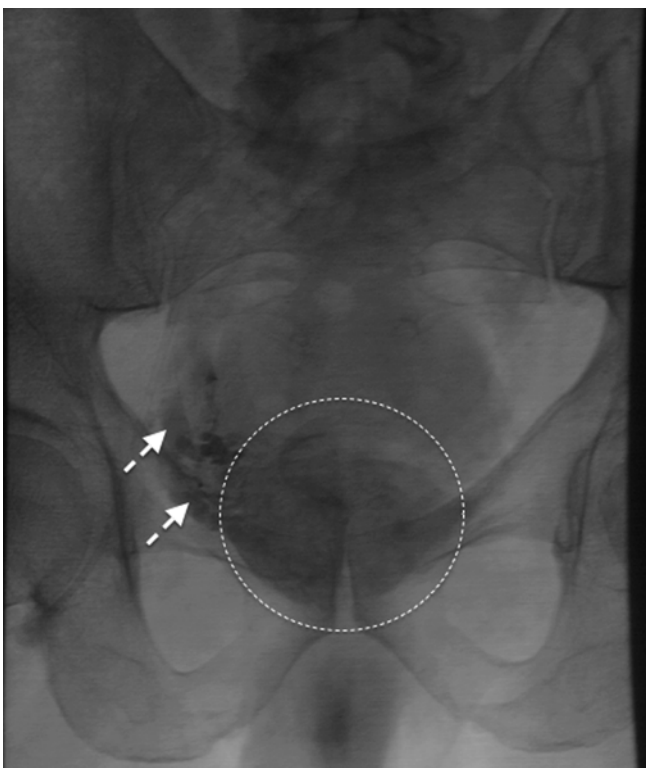

Fig. 15.16 Prostate staining with contrast after bilateral embolization (*inside circle*). Opacification of the right periprostatic venous plexus is depicted (*white dashed arrows*)

shares as common proximal origin with the superior vesical artery. It is important to differentiate the central gland PA from the superior vesical artery. The superior vesical artery has a straight trajectory forward into the bladder with a superior and more diffuse vascularization to the bladder wall, whereas the PAs first run downward frequently with an undulating trajectory until they reach the bladder base. Then, the PAs change trajectory forward into the central gland of the prostate running below the bladder base. The peripheral gland PAs have an oblique and diffuse vascularization without staining of the central gland BPH adenomas. There are frequent anastomoses or common origins with middle rectal

Fig. 15.17 CTA axial-oblique MIP reformat of the same patient from Figs. 15.1–15.16. Two independent PAs are seen on the right pelvic side, the central gland PA (*black dashed arrow*) and the peripheral gland PA (*black arrow*). On the left pelvic side, only one PA is seen bifurcating into central gland PA (*white dashed arrow*) and peripheral gland PA (*white arrow*)

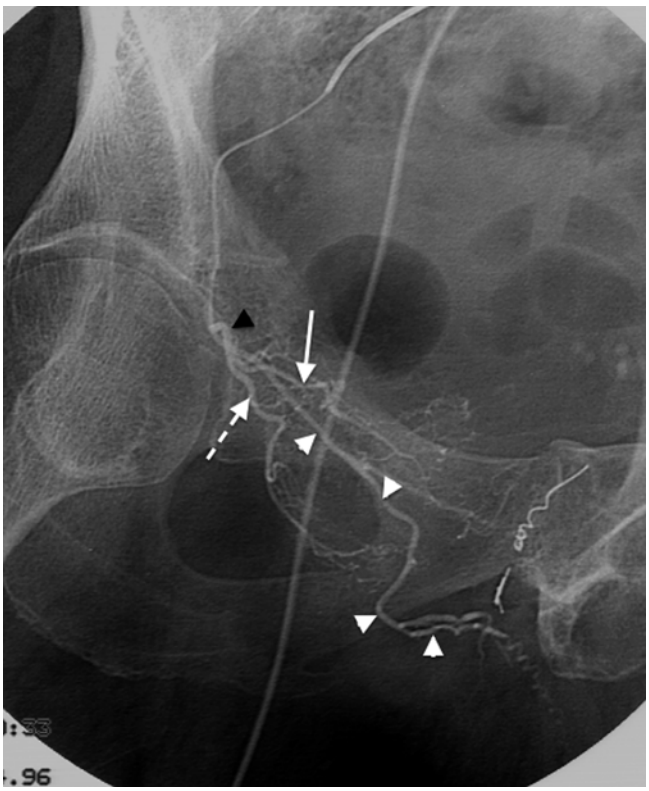

Fig. 15.18 DSA of a single right-sided PA (*black arrowhead*) in right anterior oblique projection (35°) and caudal-cranial (−10°) angulation. A large accessory pudendal artery (*white arrowheads*) is seen arising from the PA and finishing in the penile hilum (dorsal artery of the penis). The central gland PA (*white arrow*) and peripheral gland PA (*white dashed arrow*) arise from the PA. Coils on the opposite side from embolization of an accessory pudendal artery are seen

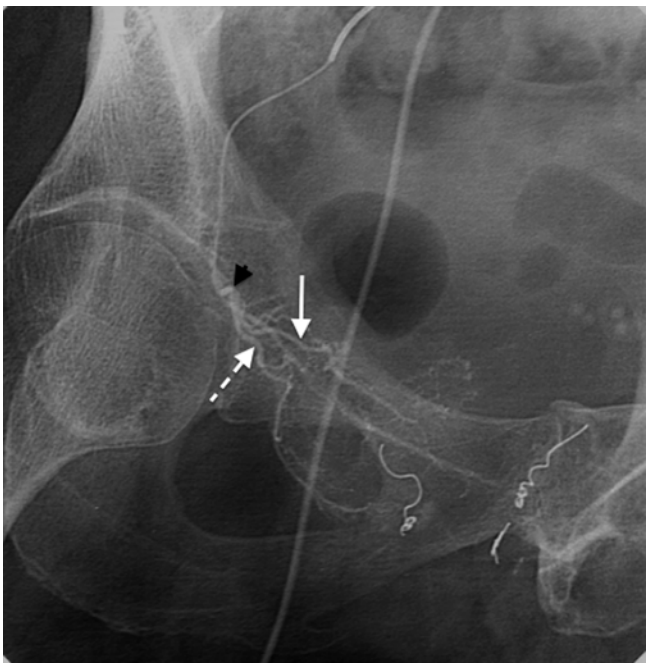

Fig. 15.19 DSA of a single right-sided PA (*black arrowhead*) in right anterior oblique projection (35°) and caudal-cranial (−10°) angulation from the same patient in Fig. 15.18 after coil embolization of the accessory pudendal artery. The central gland PA (*white arrow*) and peripheral gland PA (*white dashed arrow*) are seen but the penile artery is no longer opacified rendering embolization with particles safe

arteries; thus it is frequent to have retrograde filling of the inferior mesenteric artery. Differentiating the rectal arteries from the peripheral gland PA can be quite difficult and selective catheterization of the PAs challenging. The rectal arteries show an oblong and vertical opacification to the rectal wall with a prominent anal blush at the perineum and retrograde filling of the inferior mesenteric artery. When two independent PAs are present, it is frequent to have retrograde filling of one PA after selective catheterization and angiography of the other PA through intraprostatic anastomoses between central and peripheral gland PAs.

After selective catheterization of the PAs, it is very frequent to have anastomoses to adjacent organs (60 % of pelvis). With central gland PAs anastomoses to vesical (bladder), vesiculo-deferential (seminal glands) or internal pudendal and penile arteries may be present. Rectal anastomoses are more frequent with peripheral gland PAs. Anastomoses to contralateral PAs may be present in up to 20 % of patients.

Tips and Tricks

Our CTA protocol allows visualization and correct identification of the PAs in more than 95 % of patients [10, 11]. The use of high concentrations and volumes of iodine (100–120 mL at a concentration of 350–370 mg/mL iodine) is an important feature to obtain enough opacification of the PAs. We also give the patient a vasodilator before the acquisition

(Nitromint 0.5 mg, sublingual) to help identify the PAs. With this protocol the threshold for acquisition can be placed as high as 200 HU. With 16-row CT scanners, the acquisition time for the pelvis is approximately 13 s (scan range of around 30 cm). When using 64 or higher multirow detector CT scanners, it is important to adjust the pitch to have a scan time that is not too fast (below 10 seconds) because it may not give enough time to allow correct PA opacification. We always interpret the vascular anatomy of the male pelvic arteries reading the axial images (1.25 mm or less in thickness). Then, perform sagittal-oblique MIP reformats, coronal-oblique MIP reformats, axial-oblique MIP reformats, and VR reformats for each pelvic side. On the right pelvic side, the sagittal-oblique MIP reformat faces to the right and on the left to the left in order to correspond to the DSA runs of the IIA. We also perform a schematic drawing of the IIA on each side of the pelvis with the PA origin identified and have it available during PAE. The CTA VR reformats of the aorta and iliac arteries help plan PAE. We usually perform a unilateral femoral artery puncture and chose the side that has the least tortuous iliac arteries. When the iliac arteries are very tortuous on both pelvic sides, we perform a bilateral femoral puncture and access the internal iliac artery on each pelvic side with a RIM or Roche catheter.

With unilateral femoral punctures, we use the RUC catheter (Cook). It is possible to perform the crossover with a 0.035-inch shapable hydrophilic guidewire (Terumo) in most patients. When the aortic bifurcation is very acute angled, the crossover can be performed with a pigtail catheter and then change for the RUC catheter over the wire. After performing the crossover with the RUC catheter and removing the guidewire, we push and turn the catheter to reshape it into the secondary curve. The catheter has a radiopaque marker where it bends to reform with the secondary curve that has to be placed at the aortic bifurcation. With this configuration of the catheter, it is possible to navigate inside the IIA on both pelvic sides with only one-side femoral puncture. We usually go for the contralateral IIA first and then finish with the ipsilateral IIA. When removing the catheter, it is important to unbend and reform the catheter over the aortic bifurcation to avoid knots at the secondary curve.

When the catheter is inside the IIA, we place the tip at the proximal part of the anterior division and inject 6 mL at 3 mL/s with 350 mg/mL iodine. This allows correct opacification of all anterior division and posterior division (by reflux) branches of the IIA without reflux into the external iliac artery. If the catheter tip is placed too distally inside the anterior division of the IIA, proximal origins of the PA (from the superior vesical artery) may be missed. If the catheter is in the posterior division, the PA is frequently missed because it usually originates from branches of the anterior division. When placing the catheter tip very proximally in the IIA, reflux into the external iliac artery may become problematic. The DSA run of the IIA is performed in 35° ipsilateral anterior oblique projection and −10° caudal-cranial angulation. This projection allows easy recognition of all IIA branches and matches perfectly with the sagittal-oblique MIP reformat from CTA. The identification of the PAs is performed after looking at the schematic drawing and reformats of CTA and the DSA of the IIA on each pelvic side. After the identification of the PAs, we perform selective catheterization before embolization.

When just 1 PA is present, it frequently arises from the internal pudendal and common gluteal-pudendal trunk or obturator artery and 2.7 F microcatheter (Terumo) usually allows easy catheterization. We leave the catheter tip before the PA bifurcates and embolize both central and peripheral gland PAs. When 2 independent PAs are present, we try to catheterize the central gland PA and only embolize the peripheral gland PA if it provides significant supply to the prostate or when we can't enter the central gland PA. Entering central gland PAs arising from the superior vesical artery is frequently the most challenging technical aspect of PAE (Fig. 15.20). The superior vesical artery usually has an 90° angled origin and sometimes an atherosclerotic plaque may be present near the ostium. The PA also has another 90° angled origin from the superior vesical artery. This double 90° curve is usually very difficult to cross and forcing the microcatheter to go down into the PA distally to the superior vesical artery can sometimes be impossible. Frequently the RUC catheter tip can engage the ostium of the superior

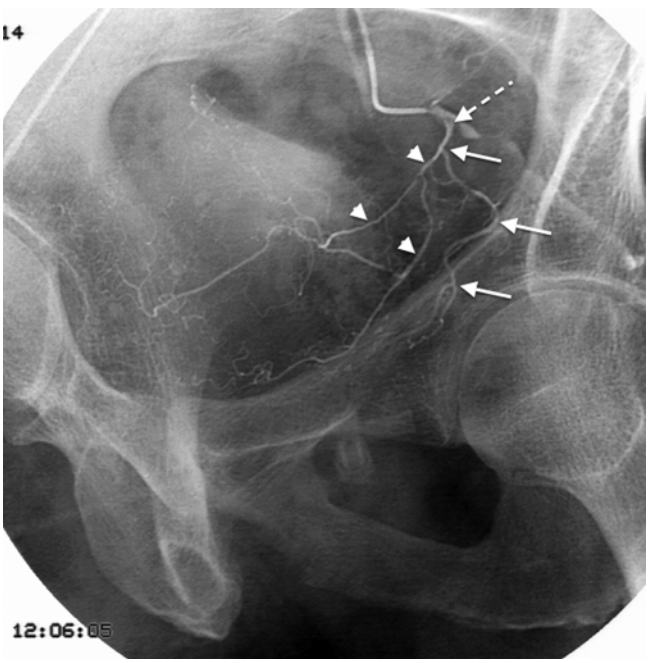

Fig. 15.20 DSA of a single left-sided PA (*white arrows*) in left anterior oblique projection (35°) and caudal-cranial (−10°) angulation. The PA arises at a 90° angle from the superior vesical artery. The superior vesical artery arises proximally from the anterior division of the IIA (*white dashed arrow*) at a 90° angle. The superior and inferior vesical arteries have a straight trajectory forward and vascularize the bladder (*white arrowheads*), while the PA first goes downward and then goes forward underneath the bladder into the prostate gland terminating into 2 branches (central and peripheral gland PAs). This double 90° angled origin is usually one of the greatest technical challenges for PAE

vesical artery and forcing the tip outward can help the microcatheter to go down into the PA instead of going forward into the superior vesical artery. With this type of anatomy, we use 0.016-inch hydrophilic guidewires (GT, Terumo) 90° angled or double angled. Nitinol, shapable 0.016-inch guidewires are another option and can be shaped to fit the PA origin angle. The microcatheters we use are 2.0-2.5 F (Cantata, Cook, or Progreat, Terumo). Angled-tip microcatheters may also be very useful. We frequently use a Swan-Ganz-tip-shaped microcatheter 2.4 F (Maestro, Merit) to facilitate catheterization of these arteries.

We advance the microcatheter into the PAs distally to vesical, rectal, or vesiculo-deferential branches. When large anastomoses between the PAs and penile arteries (accessory pudendal arteries) are present, we embolize them with microcoils, before embolizing the prostate (Figs. 15.18 and 15.19). If the accessory pudendal artery is the main supply to the penis, we try to advance the microcatheter distally into the PA and spare the accessory pudendal artery. We perform PAE with PVA particles (Cook or Boston Scientific), PVA microspheres (Bead Block, Biocompatibles), tris-acryl gelatin microspheres (Embospheres, Biosphere Medical), and polyzen-coated microspheres (Embozene, Celonova). With PVA particles we start embolization with 100 μm, continue with 200 μm, and finish with 300 μm. With Bead Block or Embospheres, we use 300–500 μm, and with Embozene we use 400 μm. We use smaller PVA particles than microspheres because they tend to clump and upsize, while microspheres are compressible and easily pass through smaller-sized arteries. Initially we would upsize particles if anastomoses were present between the PAs and surrounding organs, afraid of distal untargeted embolization. However, we have shown that with PVA particles, using smaller (100 μm) particles is as safe as using larger (200 μm) particles [14]. So, nowadays we do not upsize PVA particle size if we see anastomoses of the PAs. The end point for PAE should be as aggressive as possible with total occlusion of the PAs and concluded at the point reflux into the main artery is appreciated. This end point is easily achieved with microspheres (with only 3–5 mL for each PA), but may require larger volumes of PVA particles (10 mL for each PA). We prepare microspheres for embolization according to the manufacturer instructions (adding 4–6 mL of contrast to the vial) and use very diluted PVA particles (1 vial of PVA diluted into 80 mL of contrast/saline, 1/1 solution).

Cone-beam CT is a useful tool for PAE especially when no pre-procedural imaging with CTA has been performed or during the initial learning curve of the operators to certify correct catheter placement and avoid untargeted embolization to surrounding organs [15].

We plan PAE procedures with CTA and exclude patients with severe atherosclerosis of the iliac arteries and/or PAs (less than 5 %). Patients stop prostate medication if they are capable 2 weeks before embolization. After embolization they stop all prostate medication if they are clinically well. We advise patients that are dependent on alpha-blockers to maintain them 1 week after PAE and stop 2 weeks after embolization if they are feeling better. We give patients an acid-suppressing drug (omeprazole 20 mg, once daily) and an anti-inflammatory (naproxen 1000 mg, twice daily) for 2 days before the procedure and continue for 10 days following PAE. The anti-inflammatory drugs help to relieve symptoms from prostate inflammation after PAE. The use of prophylactic antibiotics can be performed during the procedure (cefazolin, 1 g i.v.). The use of antibiotics to treat urinary tract infections after PAE should be directed at specific agents. During embolization, analgesic and anti-inflammatory drugs are given intravenously (ketorolac tromethamine 30 mg i.v.; metamizol 2 g i.v.). We admit and discharge patients on the same day of the procedure and perform PAE on an outpatient basis in more than 90 % of patients. Most patients that stay in the hospital overnight are related to personal preferences.

Results

Technical failure (unable to embolize the PAs on both pelvic sides) may happen in up to 5 % of patients. Unilateral PAE may happen in up to 15 % of patients [16–19]. With pre-procedural CTA, the PAE procedure lasts around 90 min with mean fluoroscopy times of approximately 30 min [16, 17]. When no CTA is performed before PAE, the procedural times may go up to a mean of 200 min with mean fluoroscopy times of 90 min [19].

PAE is a painless procedure with most patients feeling no pain at all or only very light pain during or after embolization. No nausea or vomiting has been reported after PAE. Only one case has been reported of severe pain during and after PAE, and there was only major complication reported after PAE: bladder ischemia that had to be surgically repaired [16]. Minor adverse events after PAE include dysuria/urethral burning (20 %), irritative voiding (40 %), hematospermia (7 %), hematuria (5 %), rectal bleeding (2.5 %), urinary tract infection (2.5 %), balanoposthitis (1.6 %), temporary acute urinary retention lasting a couple of hours (2 %), perineal pain (8 %), and inguinal hematoma (5 %). These symptoms disappear spontaneously in the 1–2 weeks following PAE. From our experience persistent acute urinary retention after PAE occurs in less than 1 % of patients; we had two patients that had to undergo surgery due to acute urinary retention after embolization [16–19].

More than 90 % of patients under acute urinary retention are able to remove the bladder catheter and void spontaneously 7–28 days after PAE. In these patients it is important to maintain alpha-blockers until removal of the bladder catheter. When patients are unable to void spontaneously 2 months after PAE, we either repeat embolization or refer patients for

surgery. Clinical success at short-term (1–6 months) is approximately 80 % and at midterm (12–24 months) 75 %. After PAE there is a mean decrease of IPSS of 10–13 points (40–50 %) and of QoL of 1.5–2 points (40–50 %). There are a mean Qmax improvement of 3–6 mL/s (40–70 %) and a mean PVR reduction of 30 mL. The prostate volume reduces 20–30 % (18–30 mL) and the PSA 25–35 % (1.5–2 ng/mL). The mean IIEF improves 2–4 points (25–40 %) probably due to the discontinuation of prostatic medication [16–19].

Unilateral PAE is one of the reasons for clinical failure. Clinical failure rates after bilateral PAE are approximately 25 % and almost 50 % after unilateral PAE [17]. However, other factors are associated with poor outcome after PAE. Most patients with poor clinical outcome have bilateral and complete embolization of the PAs. Prostate volume does not reduce in up to 25 % of treated patients and no correlation was found between prostate volume reduction and clinical outcome, with some patients without prostate volume reduction improving significantly the LUTS severity, while others have impressive reductions in prostate volume but no improvement in LUTS severity. Patients medicated with 5-alpha-reductase inhibitors before PAE that stop the medication after embolization should be advised that prostate volume may go up 25 % and PSA up 50 % 3–6 months after PAE due to the washout effect of the medication. No correlation was found between urodynamic results and clinical outcome after PAE [16–19].

Posttreatment Follow-up (Imaging Applications)

We evaluate patients 1, 6, and 12 months and then yearly after PAE. At each time point, patients are clinically evaluated with the IPSS/QoL and IIEF scores. Objective measures are obtained with uroflowmetry (Qmax and PVR), TRUS (prostate volume), and PSA. Most clinical failures are nonresponders, patients that never improve after PAE. Up to 25 % of clinical failure patients are relapsers, patients that initially improved but had recurrent LUTS 6–12 months after PAE. We advise patients to wait at least 6 months before deciding on resuming prostate medication indefinitely, repeating PAE or undergoing surgery. Nowadays we repeat CTA before repeating PAE because many patients have occlusion of both PAs from the previous procedure and won't improve with the second embolization.

There are many potential predictors of clinical outcome. We believe that patients with high baseline PVR (>150 mL), large bladder diverticula, or stone have high likelihood of clinical failure because of bladder dysfunction. Also, patients severely obstructed (Qmax <6 mL/s) or with urethral strictures may respond poorly to PAE because the improvement in Qmax is very low and not enough to enable patients to void comfortably. We found no correlation between baseline prostate volume, LUTS severity, and clinical outcome. Other potential predictors of clinical outcome are bladder protrusion index of the median lobe and prostate vascularity (hyper- vs hypo-vascular prostates).

PSA in the first 24 h after PAE rises markedly, is a surrogate for prostate tissue destruction, and correlates with urodynamic and clinical outcomes [19]. MR-detected ischemia after PAE is another early potential predictor of clinical outcome.

The clinical improvement after PAE can be compared to other MISTs for BPH, with fewer side effects than TURP but lower clinical improvement rates and higher relapse rates. The results after PAE seem better than medication but do not have the immediate increase in flow rates associated with surgical therapies that remove obstructing tissue. The lack of long-term data, especially regarding the long-term improvement and relapse rates after PAE, is a key issue to assess the future role of the technique for BPH patients [20]. Many BPH patients on medication prefer to have minimally invasive procedures for LUTS relief and avoid surgery if possible and the associated complications; these are potential candidates for MIST and PAE. Multicenter, prospective trials comparing PAE with sham procedures and with TURP are important to assess the value of the technique.

References

1. McVary KT, Roehrborn CG, Avins AL, et al. Update on AUA guideline on the management of benign prostatic hyperplasia. J Urol. 2011;185:1793–803.
2. Oelke M, Bachmann A, Descazeaud A, et al. EAU guidelines on the treatment and follow-up of non-neurogenic male lower urinary tract symptoms including benign prostatic obstruction. Eur Urol. 2013;64:118–40.
3. Rastinehad AR, Caplin DM, Ost MC, et al. Selective arterial prostatic embolization (SAPE) for refractory hematuria of prostatic origin. Urology. 2008;71(2):181–4.
4. Wasserman NF. Benign prostatic hyperplasia: a review and ultrasound classification. Radiol Clin North Am. 2006;44:689–710.
5. Barentsz JO, Richenberg J, Clements R, et al. ESUR prostate MR guidelines 2012. Eur Radiol. 2012;22:746–57.
6. Pereira J A, Bilhim T, Duarte M, Rio Tinto H, Fernandes L, Martins Pisco J. Patient selection and counseling before prostatic arterial embolization. Tech Vasc Interv Radiol. 2012;15:270–5.
7. Yamaki K, Saga T, Doi Y, Aida K, Yoshizuka M. A statistical study of the branching of the human internal iliac artery. Kurume Med J. 1998;45:333–40.
8. Bilhim T, Casal D, Furtado A, Pais D, O'Neill JE, Pisco JM. Branching patterns of the male internal iliac artery: imaging findings. Surg Radiol Anat. 2011;33:151–9.
9. Bilhim T, Tinto HR, Fernandes L, Martins PJ. Radiological anatomy of prostatic arteries. Tech Vasc Interv Radiol. 2012;15:276–85.
10. Bilhim T, Pisco JM, Furtado A, et al. Prostatic arterial supply: demonstration by multirow detector angio CT and catheter angiography. Eur Radiol. 2011;21:1119–26.
11. Bilhim T, Pisco JM, Rio Tinto H, et al. Prostatic arterial supply: anatomic and imaging findings relevant for selective arterial embolization. J Vasc Interv Radiol. 2012;23:1403–15.

12. Bilhim T, Pereira JA, Tinto HR, et al. Middle rectal artery: myth or reality? Retrospective study with CT angiography and digital subtraction angiography. Surg Radiol Anat. 2013;35:517–22.
13. Bilhim T, Pisco JM, Campos Pinheiro L, Rio Tinto H, Fernandes L, Pereira JA. The role of accessory obturator arteries in prostatic arterial embolization. J Vasc Interv Radiol. 2014;25:875–9.
14. Bilhim T, Pisco J, Campos Pinheiro L, et al. Does polyvinyl alcohol particle size change the outcome of prostatic arterial embolization for benign prostatic hyperplasia? Results from a single-center randomized prospective study. J Vasc Interv Radiol. 2013;24:1595–602.e1.
15. Bagla S, Rholl KS, Sterling KM, et al. Utility of cone-beam CT imaging in prostatic artery embolization. J Vasc Interv Radiol. 2013;24:1603–7.
16. Pisco J, Campos Pinheiro L, Bilhim T, et al. Prostatic arterial embolization for benign prostatic hyperplasia: short- and intermediate-term results. Radiology. 2013;266:668–7.
17. Bilhim T, Pisco J, Rio Tinto H, et al. Unilateral versus bilateral prostatic arterial embolization for lower urinary tract symptoms in patients with prostate enlargement. Cardiovasc Intervent Radiol. 2013;36:403–11.
18. Bagla S, Martin CP, van Breda A, et al. Early results from a United States trial of prostatic artery embolization in the treatment of benign prostatic hyperplasia. J Vasc Interv Radiol. 2014;25:47–52.
19. Carnevale FC, da Motta-Leal-Filho JM, Antunes AA, et al. Quality of life and clinical symptom improvement support prostatic artery embolization for patients with acute urinary retention caused by benign prostatic hyperplasia. J Vasc Interv Radiol. 2013;24:535–42.
20. Golzarian J, Antunes AA, Bilhim T, et al. Prostatic artery embolization to treat lower urinary tract symptoms related to benign prostatic hyperplasia and bleeding in patients with prostate cancer: proceedings from a multidisciplinary research consensus panel. J Vasc Interv Radiol. 2014;25:665–74.

Treatments for Benign Conditions of the Prostate Gland

16

Bruce R. Kava, Jayadev R. Mettu, Shivank Bhatia, Prasoon P. Mohan, and Gopal H. Badlani

Benign Prostatic Hyperplasia

Histologically, the prostate is comprised of a network of branched tubuloalveolar glands that are surrounded by a richly innervated, well-vascularized fibromuscular stroma. Benign prostatic hyperplasia (BPH) is often referred to as the most common benign neoplasm in the aging male. It is a distinct histopathologic entity that is characterized by cellular proliferation of both components of the prostate: the glandular and stromal elements [1, 2]. From a clinical standpoint, this may be associated with age-dependent, bothersome, and progressive voiding symptoms.

The burden of BPH on society is enormous. It accounts for over 8 million outpatient physician visits annually in the United States, significantly impacts the quality of life of our aging population, and carries a price tag of more than 1.1 billion dollars in direct medical costs [3].

Definitions

The term *BPH* should be used exclusively to describe the specific histological findings of glandulo-stromal hyperplasia, seen within the transition zone (periurethral region) of the prostate (Fig. 16.1) [4]. While it is often used in the context of describing the constellation of voiding symptoms that occur in aging males, this should be discouraged. As we will see later, the very symptoms that are often attributable to BPH are not specific for BPH; they may occur even in its absence.

Lower urinary tract symptoms, or LUTS, is the accepted terminology used to describe the symptoms which are often associated with BPH and benign prostatic enlargement (BPE) [4, 5]. They reflect not only a direct (static) component of prostatic growth and obstruction but also a dynamic component of obstruction as well [6]. It is the static component of obstruction that results from an increase in number and volume of epithelial and smooth muscle cells, as well as connective tissue within the prostatic stroma. The dynamic component of obstruction results from an increase in the smooth muscle tone and resistance from the enlarging gland. Finally factoring into the LUTS perceived by the patient is the bladder response to obstruction, aging, and other less obvious influences [7]. This bladder component results in a spectrum of responses, varying from detrusor underactivity to detrusor overactivity.

LUTS can be broadly classified into one of three, often overlapping categories (Fig. 16.2) [8]. As mentioned above, none of the voiding symptoms under these categories are specific to BPH. In fact, cross-sectional studies performed in the United States and Europe have shown that the prevalence of LUTS in women is equivalent to that of men, suggesting that the pathophysiology of LUTS is much more complex than a simple obstructive process, as described above [9, 10]. However, under the right circumstances, in a male 45 years or older, in the absence of other potential non-BPH causes for LUTs, clinicians may safely attribute LUTs to BPH and BPE [6]. When confirmed by the presence of low flow and high voiding pressures on urodynamic studies, benign prostatic obstruction (BPO) is the most common diagnosis [4, 5, 8].

Measuring the Severity of BPH

The AUA Symptom Index (AUA-SI) and the International Prostate Symptom Score (IPSS) are identical, interchangeable,

B.R. Kava, MD
Department of Urology, University of Miami Health System, Miami, FL, USA

J.R. Mettu, MBBS
Department of Urology, Wake Forest School of Medicine, Winston-Salem, NC, USA

S. Bhatia, MD
Department of Radiology, Jackson Memorial Hospital, University of Miami Hospital, Miami, FL, USA

P.P. Mohan, MD
Department of Radiology, University of Miami Miller School of Medicine, Miami, FL, USA

G.H. Badlani, MD (✉)
Department of Urology, Wake Forest Baptist Medical Center, Winston-Salem, NC, USA
e-mail: gbadlani@wfubmc.edu

A.R. Rastinehad, D.N. Siegel (eds.), *Interventional Urology*, DOI 10.1007/978-3-319-23464-9_16

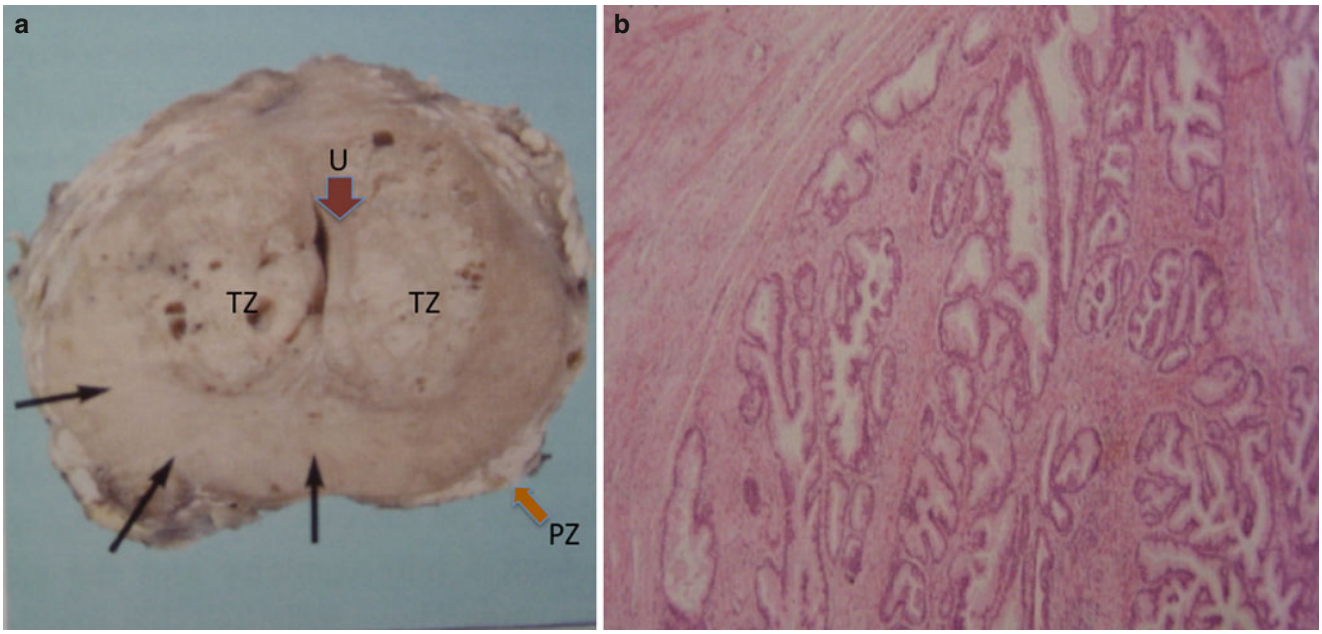

Fig. 16.1 (**a**) Surgical prostate specimen removed showing the characteristic gross features of BPH, including nodular growth within the transition zone (*TZ*) surrounding the urethra (*U*). The arrows point to additional areas within the transition zone which are enlarged and compress the peripheral zone (*PZ*) posteriorly against the prostatic capsule. (**b**) Histopathology of BPH showing glandulo-stromal hyperplasia

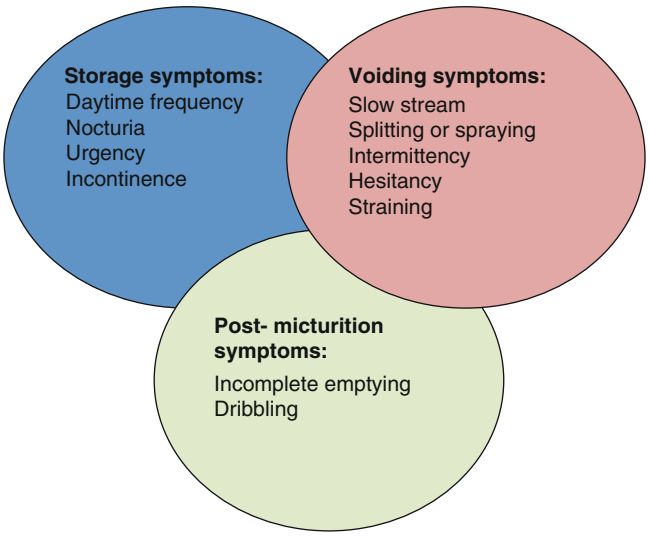

Fig. 16.2 Current classification system of lower urinary tract symptoms (LUTS) (From Abrams et al. [8], with permission)

validated instruments that have proven indispensable in grading both the severity of LUTS and their impact on an individual's quality of life [11, 12]. This seven-question, self-administered questionnaire elicits a 1-month account of the patient's symptoms that encompass storage (frequency, nocturia, urgency), voiding (force of stream, the need to strain to empty), and post-micturition (intermittency and sensation of incomplete voiding) symptoms. The overall score allows patients to be stratified into different categories of severity: mild (score 0–7), moderate (score 8–19), and severe (score 20–35). There is one additional quality of life (QoL) question that is designed to accompany the IPSS. It directly elicits the degree of bother associated with the severity symptom score.

Two additional objective parameters that are often used in the literature to describe the effects of a particular intervention are the maximal urinary flow rate (Qm) and the residual volume of urine detected in the urinary bladder after voiding (post-void residual, PVR). While urodynamics remains the standard for diagnosing BPO, these parameters are helpful in providing additional objective data about the voiding dysfunction. Of note, there is some temporal variation and lack of consistency on repeat testing in both of these parameters, which should never be used as the sole indicator of the value of an intervention.

The Burden of BPH and LUTS

Autopsy studies have demonstrated there is a gradual increase in the prevalence of BPH with each decade of life beyond age 30 years [13, 14]. This coincides with a generalized increase in the prevalence of BPE, based upon transrectal ultrasound [15] and MRI volumetric measurements [16]. Concomitant to these age-related increases in the prevalence of BPH and BPE, there is also a dramatic increase in the prevalence of LUTS [17, 18].

One of the most widely referenced observational studies is the Olmsted County Study, which demonstrated that

moderate LUTs (AUA symptom score 8 or higher) were present in 26 % of men in their 50s and in close to 50 % of men in their 80s. The problem transcends race, as 40 % of African-American males have moderate LUTS, and transcends global boundaries, as well [10].

Medical therapy has proven highly successful and is often the first line of therapy for bothersome LUTS that are associated with BPH [19]. Data suggest that up to 40 % of patients presenting for treatment of BPH are prescribed one or more pharmaceuticals, including alpha adrenoreceptor antagonists, 5-alpha reductase inhibitors, and anticholinergic agents [20]. Unfortunately, up to 30 % of men will ultimately discontinue therapy, because of bothersome adverse effects or lack of perceived benefit [21, 22].

While the utilization of medical therapy for BPH has increased over the last three decades, surgery continues to be used to treat symptoms resulting from this disorder. Data from the Medicare Carrier File [23] reveal that BPH procedures actually increased 44 % from 88,868 in 1999 to 127,786 in 2005, primarily due to an increase in the use of minimally invasive treatment options, such as lasers and thermotherapy (TUNA and microwave treatment). Interestingly, a recent update of this series showed that between 2005 and 2008, there was a slight decline in BPH surgery which is not easily explained and which affected almost all of the surgical modalities (Fig. 16.3). Nevertheless, the surgical treatment of BPH remains a very important part of the management of this disease.

Indications for Surgical Treatment of BPH

Surgical intervention is an appropriate treatment alternative for well-informed patients with moderate (IPSS score 9–19) or severe LUTs (IPSS score 20–35) and for patients who have developed acute urinary retention or other BPH-related complications [6, 24]. Many of these patients have symptoms that are unresponsive to medical therapy or are no longer desirous of long-term pharmacotherapy. BPH-related complications include chronic urinary retention, recurrent urinary infections resulting from BPO, recalcitrant hematuria, and renal impairment secondary to obstruction.

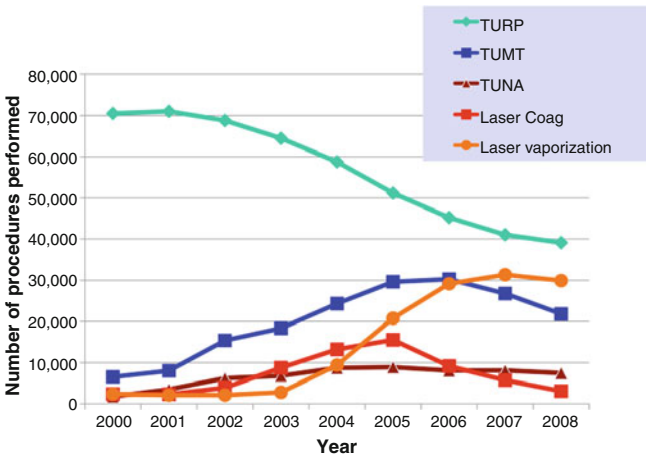

Fig. 16.3 Trends in the surgical treatment of BPH since the start of the millennium (From Malaeb et al. [23], with permission)

Surgical Options

Transurethral Resection of the Prostate (TURP)

Still recognized as the gold standard for surgical management of LUTS secondary to BPO in prostates < 80 ml, transurethral resection of the prostate (TURP) [6, 24] continues to evolve, despite almost 100 years in the urologic armamentarium. While a complete description of the technique is beyond the scope of this chapter, the basic premise of the TURP is to endoscopically resect all obstructing tissue within the transition zone, from the bladder neck to the verumontanum. This is a visible landmark on the floor of the prostate that demarcates the boundary of the striated sphincter and is where the ejaculatory ducts exit the gland.

While TURP represents a significant improvement over open prostatectomy in terms of recovery, it is far from perfect. In the perioperative period, adverse events associated with TURP (see Table 16.1) include a higher than acceptable risk of perioperative blood transfusions, TUR syndrome, perioperative urinary infections, delayed bleeding resulting in readmission, reoperation, and placement of a catheter [25–31]. Additional shortcomings of TURP are that the patient usually requires inpatient observation in the perioperative period, as well as requiring an indwelling catheter for a period of time following surgery. Between 6 and 15 % of patients undergoing TURP will require additional surgery for adenomatous regrowth, urethral strictures, or bladder neck contractures at 8–10 years [32, 33], and others will have permanent retrograde ejaculation or erectile dysfunction.

Over the last two decades, a number of improvements in instrumentation have resulted in a reduction of the perioperative morbidity associated with TURP, as can be seen in Table 16.1. These include dramatic improvements in fiberoptic technology and the utilization of increasingly high-definition camera units and monitors. By magnifying and enhancing the visibility of the operative field, these modifications have improved the precision of the surgical resection and have directly impacted the surgeon's ability to maintain adequate hemostasis. As a result, the transfusion risk associated with TURP has declined from nearly 20 % in the 1970s and 1980s to below 5 % in most contemporary series [28, 30–34].

The irrigant used for the standard TURP is usually glycine, which allows for a monopolar, high-frequency electro-

Table 16.1 Perioperative complications associated with TURP from select large series 1989–2011

Study	# pts.	Mortality (%)	Transfused (%)	TURP syndrome	Urinary infection (%)
Mebust et al. (1989) [25]	3885	0.23	6.4	2.0	2.3
Doll et al. (1992) [26]	388	2.8	22	NS	14
Horninger et al. (1996) [27]	1211	0	7.6	2.8	2.4
Uchida et al. [28]					
1971–1985	1930	0.2	20.2	0.5	2.5
1985–1996	1931	0.5	6.1	0.3	0.6
Berger et al. (2004) [29]	271	0	2.6	1.1	NS
Reich et al. (2008) [30]	9197	0.1	2.9	1.4	3.6
Mamoulakis et al. (2011) [31]	198	0.5	4	0.5	4.5

resection of prostatic tissue, with the ability to also use coagulation currents for hemostasis. Because glycine has an osmolarity of 200 mOsm/L, it does not cause hemolysis when it is systemically absorbed through the prostate during resections, as does sterile water. However, absorption of glycine may cause dilutional hyponatremia, particularly with prolonged resection times, during deep resections in which venous sinuses are exposed and when the height of the irrigant is more than 3 feet above the patient. This dilutional hyponatremia is the underlying mechanism for TUR syndrome, which may initially elicit visual changes, dizziness, headaches, nausea, and vomiting. As TUR syndrome progresses, it may precipitate apnea, seizures, and a variety of circulatory abnormalities (hypertension, hypotension, bradycardia, and arrhythmias). If left untreated, the patient may develop life-threatening pulmonary and cerebral edema, which must be addressed with diuresis. Clinical experience in treating this disorder is essential, as too rapid correction of the hyponatremia may elicit central pontine myelinolysis.

The incorporation of continuous flow irrigation systems in most contemporary resectoscope units is one measure that may or may not assist in prevention of TUR syndrome. The use of this system, which fosters continuous inflow and outflow of irrigant through separate channels within the resectoscope sheath, allows bladder pressures to remain relatively constant during the course of resection. By not having to disassemble the resectoscope numerous times during the procedure to empty the bladder of blood-tinged irrigation, it expedites the procedure, subsequently reducing the amount of blood loss and the amount of irrigation that the patient absorbs. There are no definitive studies that have proven that continuous flow resectoscopes are effective at preventing TUR syndrome, but most urologic surgeons prefer them in order to perform the resection in an uninterrupted fashion.

While contemporary instrumentation associated with monopolar TURP (M-TURP) has helped reduce the risk of perioperative complications, they have not entirely eradicated them. In fact, patients with larger prostates and those who present with preoperative indwelling catheters for urinary retention continue to pose special challenges for M-TURP. Generally, these situations require longer resection times and are associated with a higher risk of intraoperative blood loss [29, 30]. Other patients, such as those who have indwelling catheters, as well as those that need to continue anticoagulants in the perioperative period represent additional high-risk patients.

Bipolar-TURP and Bipolar Vaporization of the Prostate (BPVP)

The development of bipolar transurethral resection and vaporization procedures represents a very significant advance in the evolution of TURP. In traditional monopolar surgical units, electrical current travels through the patient's body to reach a grounding pad that is placed somewhere on the surface of the patient. Electrical current is readily diffused by ions within irrigation fluid. As a result, monopolar TURP (M-TURP) must be carried out in water, glycine, sorbitol, or mannitol. Bipolar circuitry is comprised of an active and a return pole attached to a single support on the resectoscope itself [34]. The electrical current that is generated with these units is not attenuated by ions within the irrigation solution. As a result, these units are quite functional in saline.

There are currently four bipolar resection devices that are available: the transurethral resection in saline (TURis) system (Olympus), the plasmakinetic system (Gyrus-PK), the Karl Storz bipolar device, and the Richard Wolf bipolar device. Each of these systems has the capability to resect or vaporize tissue, as well as perform coagulation functions.

Technique

Irrespective of whether the surgeon is using a bipolar loop electrode for a B-TURP or the button (Olympus) or half-moon (Karl Storz) electrodes for bipolar vaporization of the prostate (BPVP), the technical maneuvers, thought process, and overall strategic approach are very similar to the performance of an M-TURP (see Figs. 16.4, 16.5, and 16.6). This results in a relatively short learning curve for most urologic surgeons who are proficient in M-TURP.

Results

A recent meta-analysis identified 33 independent randomized clinical trials (RCTs) comparing B-TURP to M-TURP [36]. While RCTs suffer from relatively low patient numbers, are predominantly single-center series, provide poor long-term

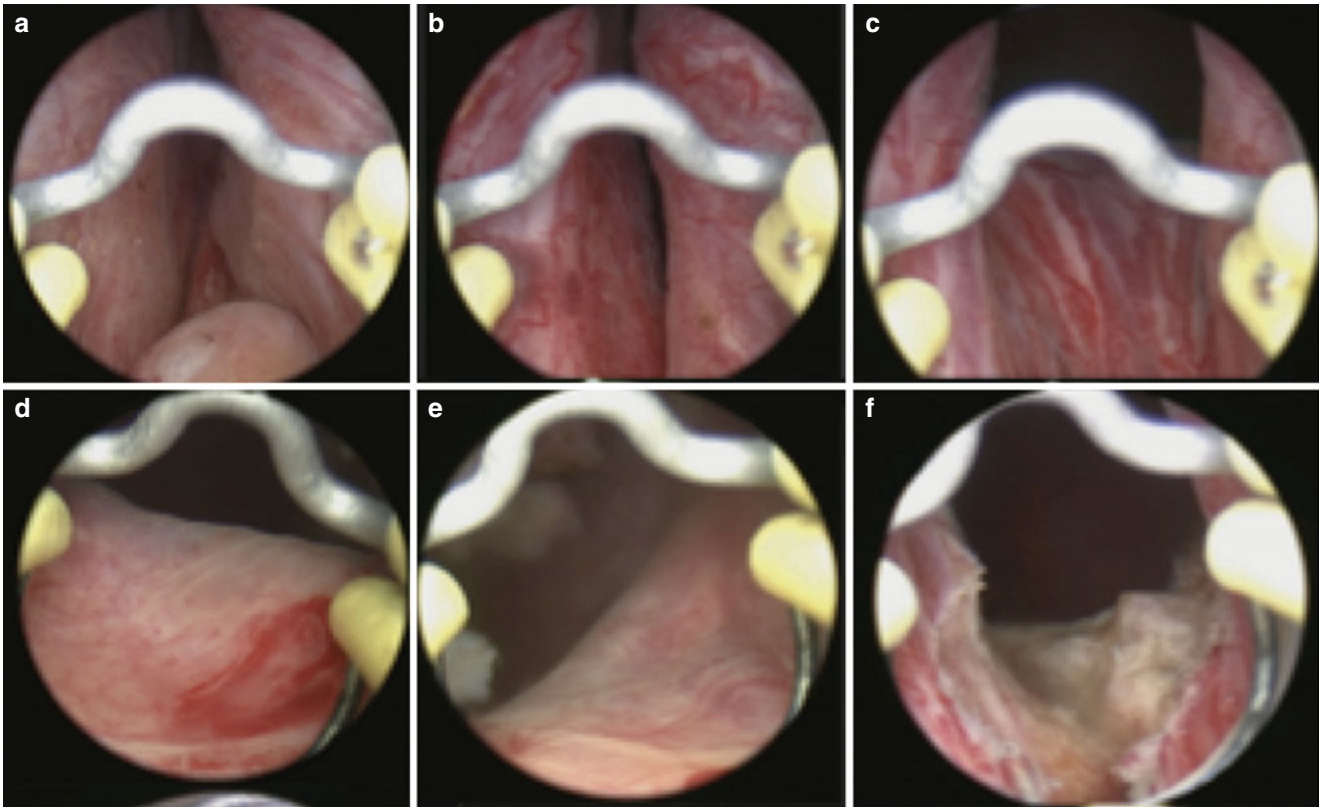

Fig. 16.4 Individual steps for B-TURP. In the upper panel, the prostate is visualized from the (**a**) verumontanum, (**b**) mid prostate, and (**c**) bladder neck. In the second row, the (**d**) right ureteral orifice and (**e**) left ureteral orifice are inspected prior to (**f**) resecting a portion of the floor to allow for chip mobilization and continuous fluid irrigation

follow-up, and lack patient and investigator blinding to the various procedures, B-TURP was found to have several advantages over M-TURP. First, B-TURP was associated with a significant reduction in the decline of perioperative serum Hb levels, which translated to a reduction in the need for blood transfusions. Of over 2800 evaluable patients from RCTs, the transfusion risk associated with B-TURP was half of that associated with M-TURP (2.2 % versus 4.4 %, $p=0.0009$). Additionally, the risk of TUR syndrome in 1339 patients undergoing M-TURP was 1.4 %, versus 0 of 1329 patients undergoing B-TURP, $p=0.002$. While the data supported a reduction in the length of stay and the duration of catheterization, these did not reach meaningful clinical relevance. The risk of clot retention and immediate return to the operating room was less following B-TURP, and with short-term follow up, there was no difference in the incidence of urethral strictures, bladder neck contractures, or urinary infections.

In terms of efficacy at 1 year, there was no difference between B-TURP and M-TURP in terms of IPSS, QoL score, PVR, or prostate volume. There was a slightly higher maximal flow rate (Qm) associated with B-TURP, but this was not clinically meaningful.

Tables 16.2 and 16.3 present complications and intermediate-level efficacy from five RCTs with follow-up between 18 and 48 months [35, 37–41]. This supports that B-TURP is comparable, in terms of efficacy as M-TURP. It also is associated with a lower risk of perioperative complications.

Laser Treatment of BPH

Lasers have increasingly been incorporated into the urological armamentarium for BPH surgery over the last 25 years. An array of laser systems have been developed, which by virtue of their intrinsic properties may produce a variety of effects on BPH tissue [42, 43]. These include desiccation, coagulation, and vaporization. Lasers may be used in a variety of capacities; they can be used for tissue ablation, incision, resection, and enucleation.

A fundamental working knowledge of laser physics is necessary in order to understand how and why particular lasers were chosen for management of BPH. As we will see, certain lasers are not well suited for treatment of BPH.

Basic Laser Physics

There are 92 different elements, each with a single nucleus and a variable number of electrons, which are constantly in motion. The addition of energy to a system of atoms causes excitation of the electrons, which absorb the energy and are

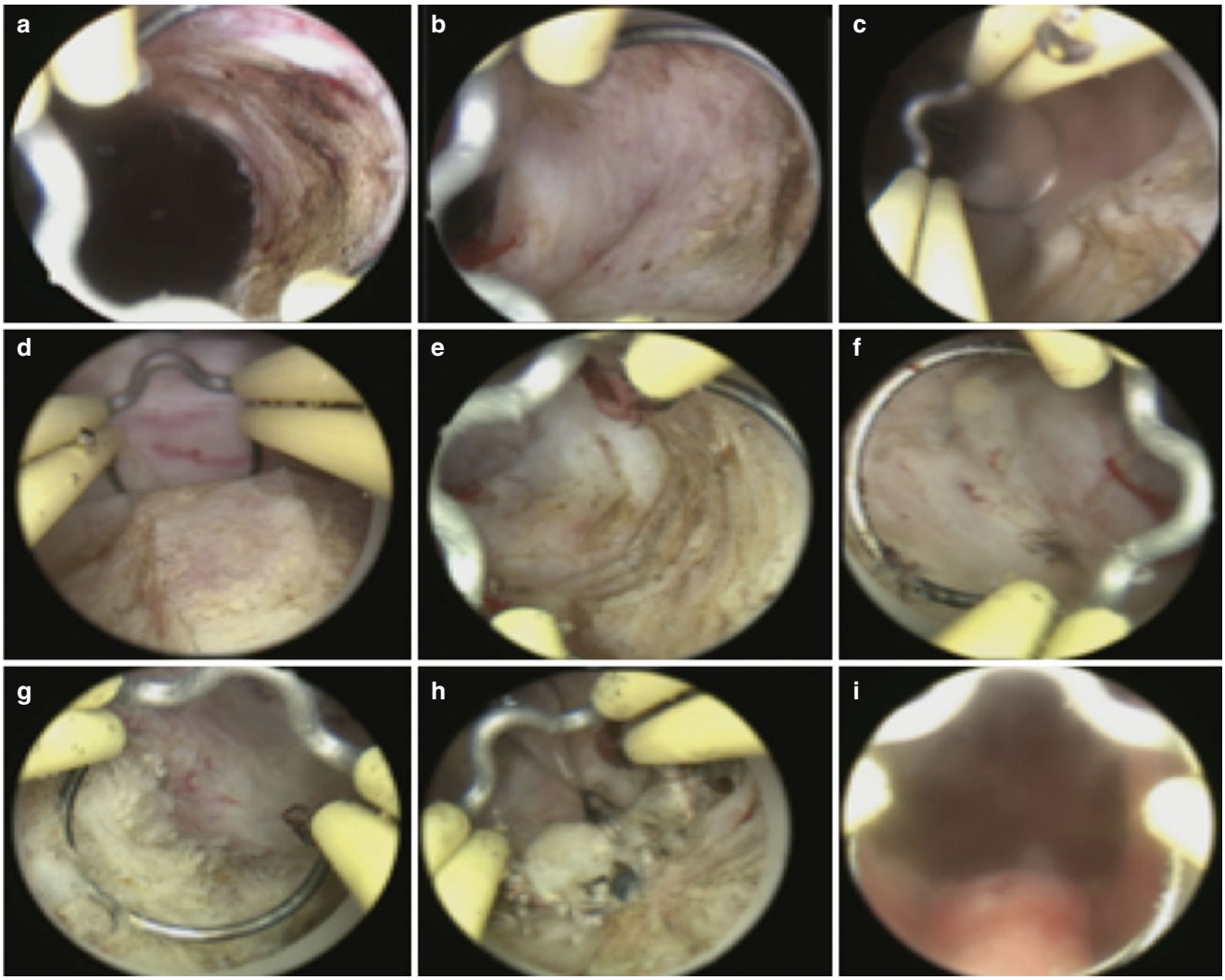

Fig. 16.5 B-TURP. The resection begins at the bladder neck at the 1 o'clock position (**a**). Adenoma is resected until the circular fibers of the surgical capsule can be seen (**b**). The resection then moves clockwise from 2 to 5 o'clock positions (**c**–**e**). The next step is to resect the right lateral lobe from the 11 o'clock position to the 7 o'clock position (**f**, **g**). The floor is then resected, and residual apical tissue is removed last (**h**). At the termination of the procedure, the prostatic capsule can be visualized from the verumontanum as completely devoid of residual adenoma (**i**)

raised into a higher state of energy. When the electron returns to its ground state, the energy emitted by the atom is released as a photon of light. The wavelength of the photon that is released is distinct and characteristic to the particular element.

Figure 16.7 demonstrates a very simple laser system. Energy is delivered to the atoms within the lasing medium by an external source. In this case it is the flash tube, which then excites the atoms. The excited atoms collide with other excited atoms, exponentially increasing the amount of energy within the laser chamber.

The photons of light released within the lasing medium are reflected in the laser chamber by a series of mirrors that are positioned at the ends of the laser chamber. One of these mirrors contains a small slit which allows some of the photons to escape. The escaping energy has all of the properties that are characteristics of light emitted by a laser: it is monochromatic, coherent, and unidirectional.

When a laser is directed into a medium, energy is absorbed and dissipated along the trajectory of entry. In the case of a well-vascularized, soft tissue medium such as the prostate, the absorbed laser energy is converted into heat, which may increase the temperature along the trajectory of the site of entry. The temperatures may reach 70–90 °C, at which time, desiccation and coagulation of the tissue occur. At higher temperatures, above 100 °C, tissue vaporization occurs.

Figure 16.8 indicates the specific wavelengths of a number of laser systems currently used to treat BPH. Superimposed on this graph are the absorption coefficients for hemoglobin water and melatonin, which ultimately dictate the effects of the particular laser on the tissue. This absorption coefficient indicates at what depth most of energy is absorbed by the tissue. Finally, the depth of penetration determines the linear depth that the laser into the tissue before it is completely absorbed.

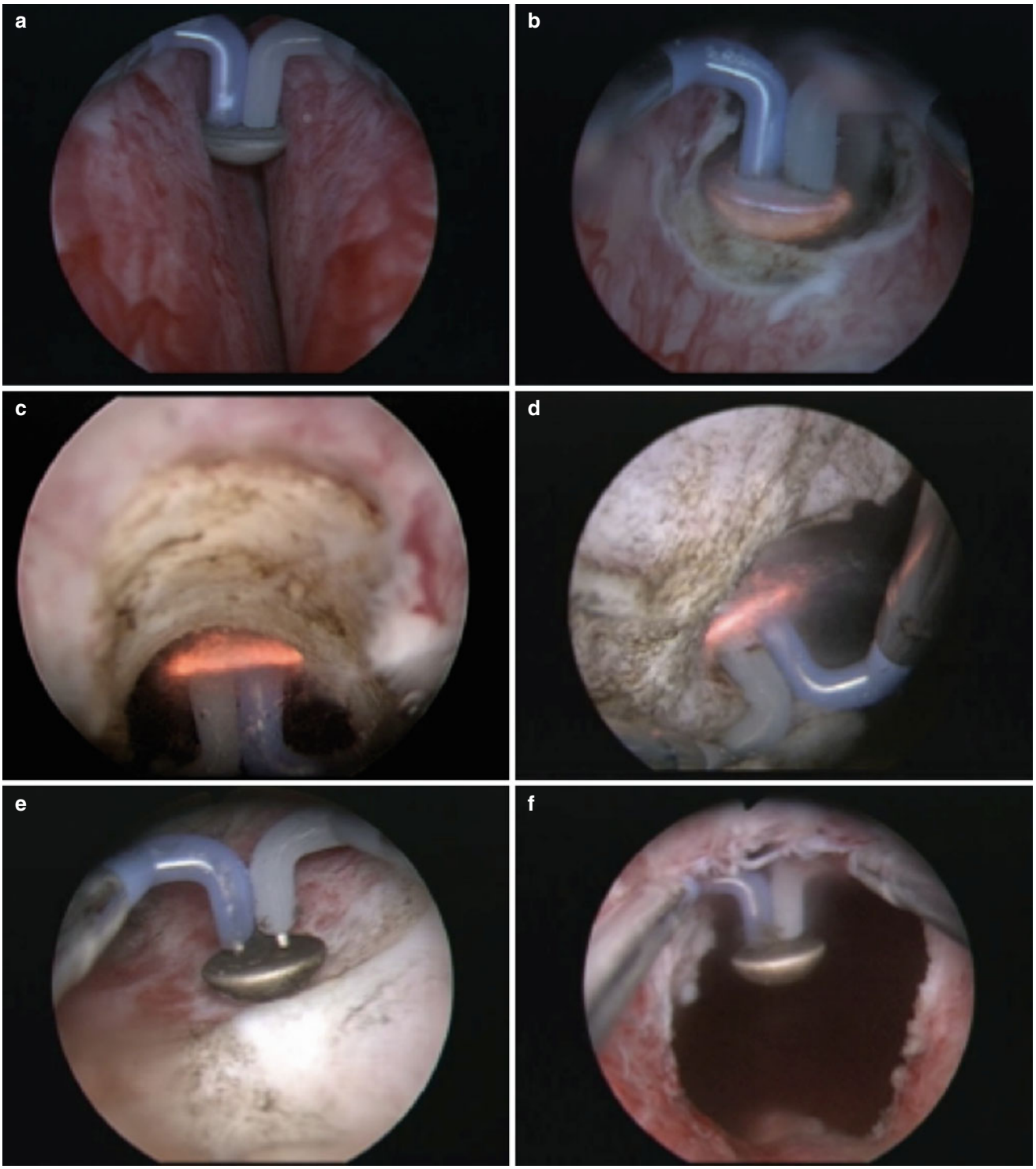

Fig. 16.6 Bipolar plasma vaporization (BPVP) of the prostate using the "button"-vapo-resection electrode (Olympus, Hamburg, Germany). During the procedure, the electrode is moved back and forth as it gently contacts the underlying prostatic tissue. As can be seen in panel **d**, a cloud of vaporization occurs as the tissue virtually disintegrates. The procedure offers excellent visualization, coagulation is used for addressing more prominent blood vessels, and the surgeon can readily identify the prostatic capsule (panel **e**) before moving on to another area (**a**) Bilateral prostate before initiating vaporization. (**b**) Vaporization at bladder neck. (**c**) Vaporization at 12 o'clock posterior anterior. (**e**) Vaporization of the floor of prostate with visible capsular fibers. (**f**) Bladder (black) visualized from the verumontanum at the completion of the procedure (From Geavlete et al. [35], with permission)

Table 16.2 RCTs with intermediate follow-up, comparing complications of bipolar TURP and monopolar TURP

Study	# pts.	F/U (Mos)	Volume (g)	Resection time (mins)	Transfused (%)	TUR syndrome (%)	Urethral strictures (%)	BN contracture (%)	Reoperation (%) for BPH
Autorino et al. (2009) [37]	32 B, PK-TURP	48	51.6	53	NS	NS	1.9	1.9	1.9
	31 M-TURP		47.5	49			4.0	2.0	2.0
Chen et al. (2010) [38]	50 B-TURP	24	60.2	59	2	0	4	2	NS
	50 M-TURP		59.1	60	6	0	6	4	NS
Geavlete et al. (2011) [39]	170 BPVP	18	54.1	39*	1.2	0	4.7	0.6	3.5
	170 B-TURP		53.7	52.1	1.8	0	6.5	3.5	9.4
	170 M-TURP		54.8	55.6	6.5*	1.8	5.3	4.1	8.8
Mamoudlakis et al. (2012, 2013) [31, 40]	141 B-TURP	36	63.8	39.5	6.4	0	8.2	6.6	18.9
	138 M-TURP		63.5	39.1	2.9	0.7	9.3	1.9	14.8
Komura et al. (2014) [41]	63 B-TURP	36	51	79.5*	1.6	0	NS	NS	0
	62 M-TURP		53	68.4	7	0	NS	NS	2

*Statistically significant ($p = 0.048$)

Table 16.3 Efficacy in RCTs with mid-level follow-up comparing monopolar TURP with bipolar procedures

Study	System (s)	# patients	Follow-up mos.)	Pre-/post-op IPSS (% change)	Pre-/post-op Qm (% change)	Pre-/post-op PVR (% change)
Autorino et al. (2008) [37]	PK-TURP	32 B, PK-TURP 31 M-TURP	48	24.2/6.4 (73) 24.3/6.9 (71)	7.1/19.8 (179) 6.2/21.2 (241)	80/42 (48) 75/45 (40)
Chen et al. (2010) [38]	TURis	50 B-TURP 50 M-TURP	24	22.8/3.7 (84) 21.8/3.8 (83)	7.1/25.5 (259) 7.9 /24.8 (214)	NS NS
Geavlete et al. (2011) [39]	Button-BPVP & TURis	170 BPVP 170 B-TURP 170 M-TURP	18	24.2/5.0 (79) 24/7.9 (67) 24.2/8.3 (66)	6.6/23.7 (259) 6.2/20.6 (232) 6.4/20.2 (215)	91/29 (68) 96/31 (67) 88/33 (63)
Mamoulakis et al. (2013) [31, 40]	AUTOCON II 400	122 B-TURP 107 M-TURP	24–36	23.4/8 (66) 23.1/7 (70)	8.8/19.5 (122) 8.8/19.4 (120)	91.8/27.8 (70) 100.5/20.2 (80)
Komura et al. (2014) [41]	TURis	63 B-TURP 62 M-TURP	36	23.7/5.2 (78) 22/4.2 (81)	6.4/16.8 (163) 7.1/18.6 (161)	43.7/10.3 (76) 47.4/6.6 (86)

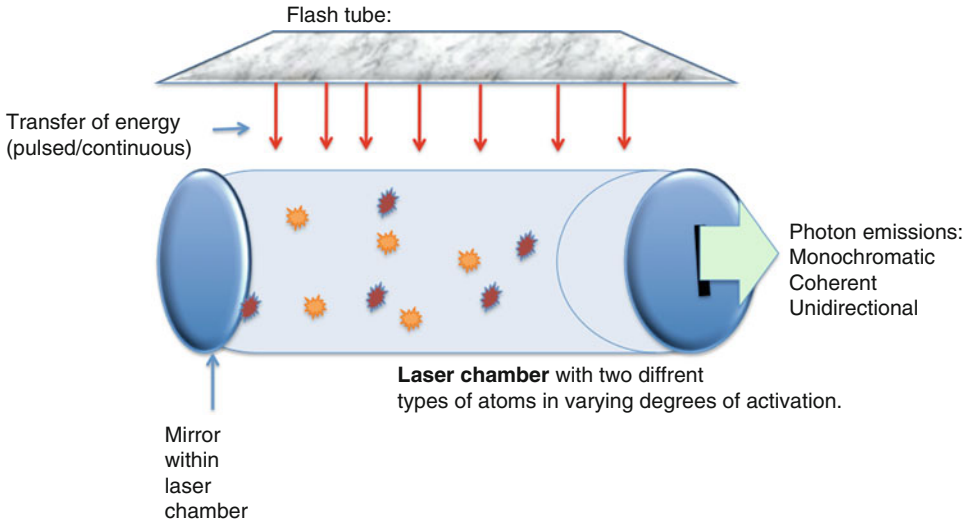

Fig. 16.7 Characteristics of a simple laser system. The flash tube delivers energy to the laser chamber either in a continuous or pulsatile fashion. This causes excitation of the atoms within the laser chamber which ricochet against each other and against the mirror at the end of the laser chamber. As energized atoms return to the ground state, the photons released are reflected within the chamber. Some will be released through the small slit-like opening in the right side of the chamber as laser light

Lasers Used for BPH

There are a number of different types of lasers that have been utilized in the management of BPH. It should be noted that this remains a work in progress. Improvements in the types of lasers, wavelength of energy used, optical delivery systems, precision of laser applications, and cost reduction continue to improve laser technology and extend its potential applications [44].

The Nd:YAG laser was one of the first laser systems used for treatment of BPH. From Fig. 16.8 one can see that this type of laser is well absorbed by hemoglobin, resulting in excellent hemostasis and coagulation. Because of the high

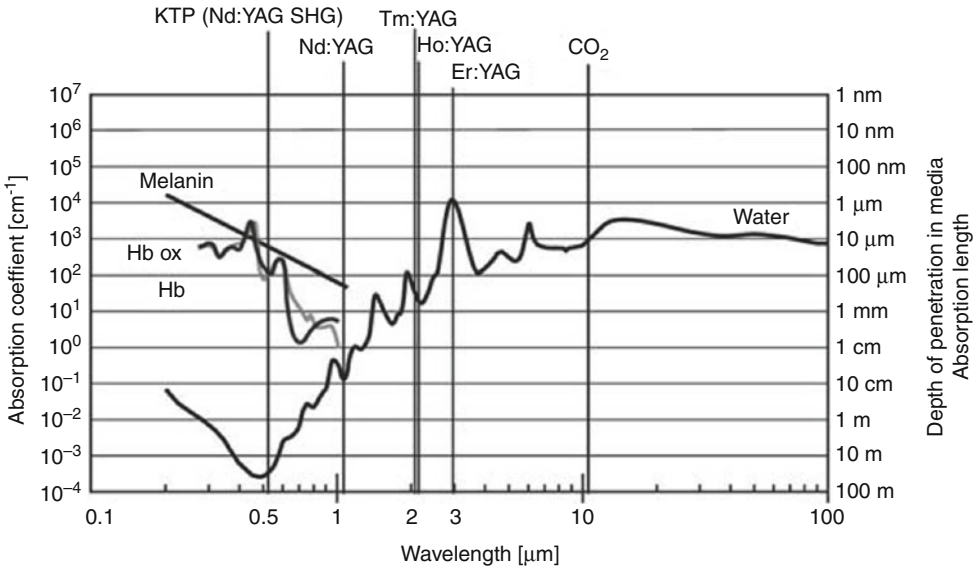

Fig. 16.8 Characteristics of various lasers used in the management of BPH (From Teichmann et al. [43], with permission)

penetration coefficient, however, most of the tissue effects resulting from treatment with the Nd:YAG laser occur deep within the prostate and not at the surface. As a result, patients who were subjected to BPH treatment with the Nd:YAG laser would often complain of pain, burning, and inflammatory symptoms for weeks, often requiring a catheter to be until the surface layers sloughed. As a result of these early experiences, the visual laser ablation of the prostate (VLAP) and transurethral ultrasound-guided laser-induced prostatectomy (TULIP), both using Nd:YAG laser technology, are no longer in use.

By adding a KTP crystal into the laser resonator, the KTP Nd:YAG laser emits energy with a wavelength of 532 nm, which is within the green spectrum of light. At this wavelength, the KTP Nd:YAG laser is strongly absorbed by hemoglobin, which is abundant in a well-vascularized tissue such as the prostate. With a short absorption length, there are rapid increases in tissue temperature at the point of entry into the tissue. This promotes surface vaporization with a seam of coagulation necrosis at the base [42].

Holmium (Ho):YAG lasers have also become very popular laser systems for treatment of BPH. Similar to the Nd:YAG, the crystalline matrix remains yttrium, aluminum, and garnet. Neodymium doping is replaced by a combination of chromium, thulium, and holmium. Chromium is excited easily by white light from a flash lamp. It then transfers energy to the thulium ions in the ground state, which doubles the number of excited ions with half the initial excitation energy. This facilitates energy transfer to the holmium ions, activating the laser, which then emits a wavelength of 2140 nm. The absorption length of the holmium laser is short due to strong absorption by water molecules, resulting in tissue effects that extend <0.5 mm into the tissue. This results in rapid onset of tissue vaporization with each laser pulse (Fig. 16.9).

From a practical standpoint, the holmium laser has been found to be extremely versatile. It is currently being used in both ablative and enucleation procedures. In the latter capacity, the holmium laser can create a pulsatile vaporization bubble, which separates the prostatic adenoma from the surgical capsule and creates a rim of coagulation necrosis underneath [45].

The Thulium:YAG laser (not shown in Fig. 16.9) emits at a wavelength of 2013 nm, which is very similar to the Ho:YAG. This accounts for its similar interactions within tissue. What makes the Thulium:YAG laser different is that the output is delivered as a continuous wave rather than in a pulsatile manner. This allows for faster and more efficient tissue vaporization [45].

Contemporary Laser Systems Used in the Treatment of BPH

KTP: Nd:YAG Lasers

By virtue of its selective absorption by hemoglobin, as well as its low penetration depth in tissue, the KTP laser vaporizes the surface layer of BPH tissue rapidly and hemostatically, with a 1–2 mm rim of coagulation [42]. As a result of these characteristics, the effect of the KTP laser is often referred to as photoselective vaporization of the prostate (PVP).

Technique

Photoselective vaporization of the prostate (PVP) became a viable option for treatment of BPH with the advent of a high-power, 80 W KTP laser. The system uses a side-firing glass fiber, which can be passed directly through either a 22.5 or 23 Fr continuous flow laser cystoscope or a standard 27 Fr continuous-flow resectoscope. Saline is the favored irrigant, which minimizes the risk of dilutional hyponatremia. The

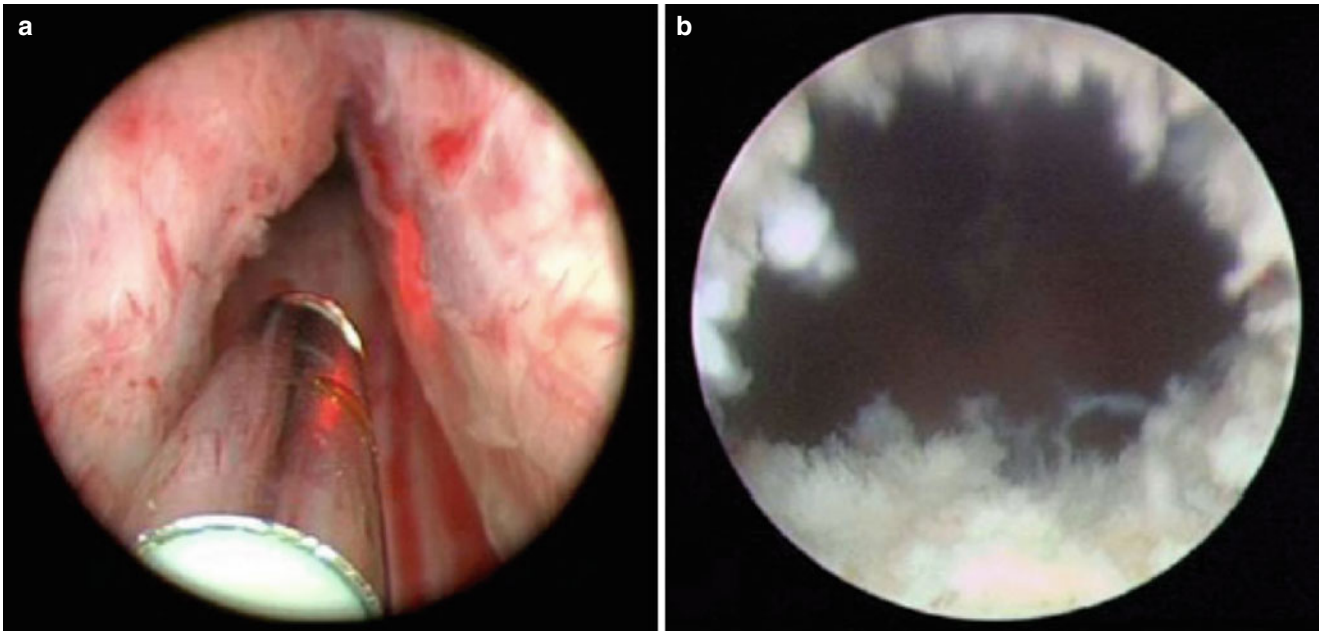

Fig. 16.9 Endoscopic view of holmium laser ablation of the prostate (HoLAP), demonstrating the post-treatment defect which appears blanched and irregular. (**a**) Endoscopic view of holmium laser of the prostate HoLAP, before initiating the procedure. (**b**) Demonstrating the post treatment defect which appears blanched and irregular

speed of tissue removal is a drawback with the PVP 80 W laser and is limited to 0.3–0.5 g/min [46]. This limits its use in larger prostates, which may take a considerable amount of time to complete the ablation.

The procedure is performed under general or spinal anesthesia, with the use of video endoscopy. Laser vaporization is accomplished by holding the laser fiber approximately 0.5–1 mm away from the tissue, while deploying a rotational motion over the adenoma. A 600 μm fiber with a 1.8 mm quartz capsule emits the beam at a 70° lateral deflecting angle [47].

The procedure usually begins at the bladder neck posteriorly. If there is a prominent median lobe, visual ablation of the obstructing adenomatous tissue can immediately be noted. By starting at this region, the operating surgeon allows for clearance of this tissue, which facilitates the passage of continuous-flow irrigant during the remainder of the procedure. The ureteral orifices should be noted at the outset, and great care should be exerted in avoiding injury to the bladder or either ureteral orifice.

Following ablation of the median lobe, similar to a TURP, the surgeon ablates the lateral lobes, the floor, and finally the apex. An attempt to vaporize tissue down to the level of the striated pseudocapsular fibers should be made. When arterial or venous bleeding is recognized, the laser can be moved away from the tissue, which defocuses the beam and allows for tissue coagulation. Alternatively a near contact technique can be used with lower power settings of 30–40 W [42].

Results

Following a series of single-center case reports [48, 49], Te et al. [50] reported on the results of the first multicenter prospective trial evaluating the 80 W KTP laser from the United States. With 139 men and 12-month follow-up, AUA-SI decreased from 23.9 to 4.3, QOL score decreased from 4.3 to 1.1, maximal urinary flow rate (Qm) increased from 7.8 to 22.6 ml/s, and the post-void residual urine volume (PVR) decreased from 114.3 to 24.8 ml. The transrectal ultrasound-estimated prostatic volume decreased from 54.6 to 34.4 ml, establishing this as a viable ablative option for select men with BPE. Approximately one third of patients did not require a catheter beyond the recovery room, and 86 % were hospitalized for less than 24 h. Complications occurred in 8.6 % of individuals and consisted of transient hematuria, dysuria, and urinary retention. At 1 year, two patients developed bladder neck contractures and one patient developed a soft urethral stricture.

Two randomized clinical trials (RCTs) comparing 80 W KTP with TURP have reported mixed results (Table 16.4). In the first, Bouchier-Hayes et al. [51] randomized 76 patients with medium-sized glands to KTP versus TURP. Overall KTP laser provided similar results to TURP, with respect to symptom score reduction, Qmax, and PVR. In the other RCT by Horasanli et al. [52], TURP significantly outperformed PVP in terms of all IPSS, Qm, and reduction of PVR.

As mentioned above, one of the limiting factors to the widespread adoption of the PVP initially was the slow rate of tissue vaporization. This caused problems, particularly when

Table 16.4 Efficacy of PVP with Greenlight 80 W, 120 W, and 180 W laser compared with traditional prostate surgery in several randomized clinical trials (RCTs)

Study	# patients	Follow-up (mos.)	Pre-/post-op IPSS (% change)	Pre-/post-op Qm (% change)	Pre-/post-op PVR (% change)
Bourchier-Hayes et al. (2010) [51]	46 PVP (80 W KTP) 39 TURP	12	25.3/8.9 (65) 25.4/10.9 (57)	8.8/18.6 (111) 8.9/19.4 (117)	129/ 22 (82) 111/17 (85)
Horasanli et al. (2008) [52]	39 PVP (80 W KTP) 37 TURP	6	18.9/13.1 (31)* 20.2/6.4 (68)	8.6/13.3 (55)* 9.2/20.7 (125)	183/78.9 (57)* 177/22.9 (87)
Skolarikos et al. (2008) [53]	65 PVP (80 W KTP) 60 OP	18	20/10 (50) 21/8.5 (60)	8.6/16 (86) 8.0/15 (87.5)	97/15 (85) 89/12 (87)
Lukacs et al. (2012) [54]	69 PVP (120 W KTP) 70 TURP	12	22/6 (77) 20/5 (70)	7.8/16.7 (115) 7.8 /16.8 (116)	89.5/0 (100) 79.5/7 (90)
Bachman et al. (2014) [55]	136 PVP (180 W KTP) 133 TURP	6	21.2/6.8 (68) 21.7/5.6 (74)	9.5/ 23.3 (145) 9.9/ 24.2 (144)	NS NS

*Statistically significant

treating larger prostates. Retreatment rates using the 80 W PVP, particularly for larger prostates, are higher than TURP or open prostatectomy [52, 53, 56].

Using laser diodes instead of an arc lamp to supply the energy to the Nd:YAG laser, the 120 W PVP laser was developed, which accelerated the speed of vaporization and significantly reduced the surgical time, even for prostates >80 ml [54, 57, 58]. A meta-analysis of the 9 randomized clinical trials evaluating 80 W and 120 W PVP and TURP found no differences in IPSS and Qm between PVP and TURP, but the data was limited to only 12-month follow-up [59].

Recently the 180 W XPS GreenLight laser system has been introduced, which utilizes a special MoXy fiber that expedites and improves the overall efficiency of prostatic vaporization. Preliminary results from a large, prospective multicenter RCT comparing XPS to TURP have been published [55]. The 269 patients randomized were balanced in terms of baseline IPSS scores, age, Qm, PVR, PSA, and TRUS volume, which was between 46 and 48 ml. At 6 months, patients undergoing TURP had a slightly better reduction of IPSS scores, which approached, but did not reach, statistical significance (post-treatment IPSS 6.8 ± 5.2 XPS versus 5.6 ± 4.9 TURP, $p = 0.056$). Qm, PVR, reduction in TRUS volume, and change in the serum PSA did not differ between the two arms. The perioperative safety of the two procedures was comparable. Only one patient undergoing a TURP required a blood transfusion. Interestingly, while the incidence of storage symptoms (frequency, urgency, urge incontinence) was comparable between the two modalities, urinary incontinence was seen in 11 % of XPS patients compared with 3 % of TURP patients ($p = 0.015$). Most of these cases were mild, but further evaluation of this treatment effect is certainly warranted.

With respect to safety, the literature has consistently reported that PVP is associated with reduced blood loss when compared to TURP [51–53, 57]. Few studies have evaluated long-term follow-up of patients undergoing PVP. Overall, there appears to be a relatively low risk of bladder neck contractures [53, 57], urinary incontinence, and erectile dysfunction [57]. Few studies have evaluated adverse sexual effects of PVP using standardized instruments. However there appears to be an equivalent incidence of retrograde ejaculation (approximately 50 %) when compared to TURP [52].

Holmium Lasers

The holmium laser is a pulsed, solid-state laser with a wavelength of 2140 nm. It is strongly absorbed by water and has a tissue penetration depth of only 0.2–0.4 mm. As a result, it rapidly vaporizes surface BPH tissue and simultaneously coagulates blood vessels at the depths of penetration. Due to these unique properties, the holmium laser is quite versatile and can be used for ablation, incision, resection, and enucleation of adenomatous prostatic tissue.

Holmium Laser Ablation of the Prostate (HoLAP)

Technique

Gilling and Fraundorfer [60] initially treated 79 patients with prostate volumes that varied from 45 to 133 cc. A 60 W laser was deployed, using a 70° side-fire fiber, through a 24 or 26 Fr cystoscope. Most of the reports indicate that the laser should used to ablate an area that appears to be sufficient for micturition, although based upon the overall principles of TURP, the surgical capsule should be exposed circumferentially within the prostatic fossa.

Results

There is only one randomized trial comparing 60 W and 80 W HoLAP to TURP [61]. With 36 patients randomized, the trial demonstrated that HoLAP was associated with less bleeding, shorter catheterization and hospital stay, and equivalent efficacy at 1 year, in terms of AUA-SI and Qm. Operative time was significantly longer in the HoLAP group. In response to this, higher-power 100 W holmium lasers, which allow for more rapid tissue vaporization, are now being utilized in most centers, although RCTs are not yet available.

Holmium Laser Enucleation of the Prostate (HoLEP)

Technique

With the development of a tissue morcellator [62], holmium laser enucleation of the prostate (HoLEP) is a technique that may be used for treatment of even extremely large prostate glands. While the technique described in the next few paragraphs seems relatively straightforward, there is a significant learning curve associated with HoLEP [63–67].

The holmium laser utilizes an end-firing bare contact fiber that is used to make two longitudinal incisions along the 5 and 7 o'clock positions, through the adenoma and directly onto the surgical capsule of the prostate. The incisions are carried out from the bladder neck toward the prostatic apex, where a third transverse incision is made, connecting the two longitudinal incisions. The beak of the cystoscope is then used to lift the apex of the prostate, on the bladder side of the verumontanum, similar to the manner in which a surgeon enucleates the prostate during open prostatectomy. The laser fiber is advanced and slowly develops an enucleation plane, ablating the adenoma that is visualized and leaving a rim of coagulated surgical capsule behind. At the bladder neck, the tissue is incised transversely by the laser, and pushed into the urinary bladder. By staying on the posterior portion of the surgical capsule, on occasion, the bladder neck can be undermined and the resection can inadvertently extend toward the ureteral orifices. The surgeon must keep this in mind, particularly as the bladder neck is approached. To avoid this, a transverse incision can often be made across the median lobe the surgeon approaches the bladder neck, allowing it to be sheared off. This avoids the problem of undermining the bladder neck.

Next, incisions are made at the 11 and 1 o'clock positions and the enucleation plane proceeds from 7 to 11 o'clock and 5 to 1 o'clock, starting at the apex and working toward the bladder neck. The lateral lobes are pushed into the urinary bladder.

The tissue morcellator is then deployed. The bladder is filled to capacity, in order to avoid the bladder wall from getting suctioned into the morcellator. Once all of the tissue has been morcellated and removed from the bladder, hemostasis is achieved by placing the laser fiber several millimeters from the tissue. By defocusing the beam at this distance, it can coagulate, rather than vaporize, the tissue.

Results

Table 16.5 outlines the results of several RCTs comparing HoLEP to TURP and open prostatectomy. In considering TURP versus HoLEP, length of stay, duration of catheterization, as well as the volume of tissue resected seem to favor HoLEP [66–76]. Mean operative time with HoLEP was consistently longer, however.

Once again data from HoLEP series suffers from relatively short-term follow-up. With 3-, 5-, and 6-year follow-up from several of series, HoLEP has proven to be durable and retains similar efficacy to TURP with respect to voiding parameters [71, 73, 76].

Two RCTs have compared open prostatectomy with HoLEP for those patients with larger prostates [74, 75]. As can be seen in the table, postoperative voiding parameters are generally comparable. While HoLEP is associated with a longer operative time (15–45 mins), there are significant benefits in terms of reduction in postoperative LOS, period of catheterization, and overall convalescence. Blood loss is

Table 16.5 Efficacy of HoLEP versus TURP and open prostatectomy

Study	# patients	Follow-up (months)	Pre-/postoperative IPSS (% change)	Pre-/postoperative Qm (% change)	Pre-/postoperative PVR (% change)
Tan et al. (2003) [66]	31 HoLEP 30 TURP	12	26.0/4.3 (83) 23.7/5.0 (79)	8.4/21.8 (159) 8.3/18.4 (122)	78/28 (64) 86/47 (45)
Kuntz et al. (2004) [68]	100 HoLEP 100 TURP	18	22.1/1.7(92)* 21.4/3.9(82)	4.9/27.9 (469) 5.9/27.7 (369)	237/5.3 (98) 216/ 26 (88)
Montorsi et al. (2004) [69]	52 HoLEP 48 TURP	12	21.6/ 4.1 (81) 21.9/ 3.9 (82)	4.3/15.5 (206) 4.3/ 12.1 (217)	NS NS
Gupta et al. (2006) [70]	50 HoLEP 50 TURP 50 TUVP	12	23.4/ 5.2 (78) 23.3/ 5.6 (76) 24.9/ 5.4 (78)	5.2/ 25.1 (387) 4.5/ 23.7 (427) 4.7/ 23.6 (407)	112/<20 (82) 84/ <20 (76) 103/ <20 (81)
Wilson et al. (2006) [71]	31 HoLEP 30 TURP	24	26/6.1 (77) 23.7/5.2 (78)	8.4/21.0 (150) 8.3/19.3 (133)	NS
Sun et al. (2014) [72]	82 HoLEP 82 TURP	12	24.4/4.9 (79) 24.5/7.5 (69)	5.3/19.8 (274) 5.7/18.2 (219)	116/12.7 (89) 108/23.2 (79)
Kuntz and Lerich (2002) [73]	60 HoLEP 60 OP	6	22.1/2.4 (89) 21.0/2.8 (87)	3.8/29.9 (686) 3.6/27.0 (650)	280/4.4 (99) 292/ 2.1 (99)
Naspro et al. (2010) [74]	41 HoLEP 39 OP	24	20.1/7.9 (61) 21.6/8.1 (63)	5.3/11.6 (146) 4.8/ 12.2 (142)	NS NS

*Statistically significant

reduced, which translates into a reduction in the need for homologous blood transfusions. Overall 8 of 60 (13 %) OP patients [75] and 2 of 39 (5.1 %) [74] OP patients from the two series required homologous transfusion versus none in the HoLEP groups. With 2- and 5-year follow-up [74, 77], HoLEP has proven to provide durable responses, which are similar to OP.

Thulium Lasers

Thulium lasers have absorption characteristics that are similar to that of holmium:YAG lasers, but due to the continuous-wave output accomplish more efficient tissue vaporization. Several techniques have been reported with the thulium:YAG laser for BPH. Unfortunately, there are few randomized clinical trials comparing these techniques with traditional treatments. Nevertheless, because of the similarity to holmium lasers, there will undoubtedly be more work in this area in the future.

Techniques

The basic skill sets required to utilize thulium lasers are similar to those of the holmium laser. Thulium vaporection (ThuVARP) is in many ways similar to TURP in that small tissue chips are resected from the gland. In one RCT [78] and one non-randomized clinical trial [79] comparing ThuVARP with M-TURP, thulium laser-treated patients showed a reduction in bleeding and transfusion rates, shorter hospitalization, and shorter catheterization time. Thulium vapoenucleation (ThuVEP) has been compared to HoLEP in a single randomized trial [80]. With short follow-up, voiding parameters were similar to TURP, with benefits in terms of reduced blood loss and perioperative morbidity.

Microwave Therapy of BPH

Under induction of a microwave field, water molecules, which have weak unequal dipoles, attempt to orient themselves within the field. The oscillation of the electromagnetic wave between negative and positive charges causes polar molecules to rotate, generating frictional heating and coagulation necrosis when temperatures reach above 60 °C. This is known as dielectric heating.

TUMT has undergone numerous modifications over the past 20 years. The route of administration has moved from a transrectal approach to a predominantly transurethral approach. The energy levels have also moved from low to higher energy as there has been the development of effective cooling systems to prevent damage to surrounding tissues. In particular, these cooling systems have enabled higher energy levels to be delivered the prostate for greater tissue effect and coagulation necrosis without causing urethral damage.

There are currently five FDA-approved systems in the United States. These include:

1. TherMatrx (American Medical Systems, Minnetonka, Minnesota, USA)
2. Prostatron (Urologix, Minneapolis, Minnesota, USA)
3. Targis (Urologix, Minneapolis, Minnesota, USA)
4. Prolieve (Boston Scientific Corporation, Natick, Massachusetts, USA)
5. CoreTherm (ProstaLund, Lund, Sweden)

All the available systems work in a similar fashion to deliver microwave energy to the prostatic tissue with a feedback system connected to a monitor displaying temperature levels and energy being delivered. The main difference between them is the design of the urethral catheter and microwave antenna. The antenna design has significant effect on the heating profile [81].

Technique

TUMT is a relatively simple, in-office procedure which can be performed under local anesthesia. The patient is positioned in the dorsal lithotomy position. The Microwave catheter is introduced in a similar fashion to that of a urethral catheter. The balloon is inflated within the urinary bladder, in order to insure that there is no movement of the catheter during treatment. Treatment is initiated and typically lasts from 30 to 60 min. A urethral catheter is left in place for a few days, at the discretion of the surgeon.

Results

In a pooled analysis of 540 patients across 6 trials [82], several conclusions regarding the use of microwave thermotherapy were reached:

1. The pooled mean symptom score for men undergoing TUMT decreased 65 % in 12 months (19.4–6.7) versus 77 % (19.6–4.5) in the men undergoing TURP.
2. TURP led to greater improvement in peak urinary flow than TUMT. The pooled mean peak urinary flow for men undergoing TUMT increased 70 % (from 7.9 to 13.5 mL/s) versus 119 % (from 8.6 to 18.7 mL/s) in men undergoing TURP.
3. TUMT participants (7.54/100 person-years) were more likely than TURP participants (1.05/100 person-years) to require retreatment for BPH symptoms ($P < 0.001$).

Overall, TUMT is a safe, in-office procedure which may be offered as an alternative treatment for BPH. Clearly, its overall efficacy is not as profound as TURP, and data regard-

ing durability and long-term complications are lacking as of this time.

Transurethral Needle Ablation of the Prostate (TUNA)

Transurethral needle ablation of the prostate (TUNA) uses low-level radiofrequency (RF) energy that is delivered by needles into the prostate [83]. Each of the needles is deployed under direct vision using a RFA-specific ablative catheter. The needles pierce the surface mucosa of the prostate and are positioned at fixed distances within the prostatic lobes. When the generator is started, this system increases the temperature within the prostate around the RFA needles and induces necrosis of prostatic tissue. There is cavitation caused by necrosis within the prostatic tissue, thereby reducing outflow resistance and the volume of the obstructing tissue. The advantage of TUNA is that it can be delivered under topical anesthesia to patients with symptomatic BPH, causing very precise and reproducible lesions within the prostate.

The Pro VU system from Medtronic or Prostiva System from Medtronic recently acquired by Urologix consists of a special catheter attached to a generator. The generator produces a monopolar RF signal between 460 and 490 kHz, which generates temperatures up to 100 °C. At the end of the catheter are two adjustable needles that are withdrawn into two adjustable shields made from Teflon. The needles are advanced into the prostatic tissue and can be placed accurately into the required position to produce desired coagulation necrosis.

The patient most likely to benefit from TUNA would be one who has predominantly lateral lobe enlargement and a prostate of 60 g or less [84]. Larger glands can be treated, but more time has to be spent treating each segment which can lead to delays in the office procedure and significant discomfort to the patient.

Technique

The patient is positioned in the dorsal lithotomy position. Topical anesthesia with 2 % intraurethral lidocaine (Xylocaine) may be used with low energy systems. Alternatively, spinal or general anesthesia may be used depending upon patient and physician preference. A local periprostatic nerve block may be used either transrectally or transperineally.

The RFA/TUNA catheter is advanced under direct vision using a 0° fiber-optic cystoscope, permitting direct visualization of the needles being introduced into the prostate. Preprocedural assessment of the size of the prostate allows calculation of the length of deployment of the needle within the prostate.

The thermal energy generated by the RFA/TUNA catheter may extend for up to 5–6 mm beyond the position of needle deployment with lesions measuring up to 20 × 10 mm; it is important to keep this in mind to avoid damage to surrounding tissue. When the position is deemed satisfactory, the Teflon shield on the proximal part of the needle is advanced to protect the urethral epithelium and the underlying tissue. Therefore the tip of the needle should not lie within 5–6 mm of the outer rim of the prostate. Additionally, the urethra is protected by the shields that extend from 5 to 6 mm from the TUNA catheter itself. The newer PROSTIVA systems come with a standard shield that does need have the need for an additional Teflon shield.

The number of cavitation lesions induced by the use of TUNA depends upon the size of the prostate, with the average being 12–16 lesions per session. There is some variability in the number of treatment lesions created, which varies by the size of the gland and the urologist's clinical judgment. Two treatment lesions are created by each TUNA cycle, as these needles are deployed at opposite sides of the prostate.

As a rule of thumb, it is generally recommended that one pair of lesions should be used to treat 20 g of prostate tissue; it can also be expressed in terms of length, with one pair of lesions, or treatment plane, being used for less than 3 cm of prostatic urethral length, two planes for 3–4 cm, and one extra plane of treatment cycle for every centimeter of additional urethral length. The procedure is then repeated on the opposite lobe.

The RF power that is delivered is 2–15 W for 5 min per lesion. In the newer PROSTIVA system, RF power is delivered for 2–2.5 min per lesion. In earlier models the treatment was begun at a low power, but now the whole thermal process is automated, with temperature levels at treatment areas preset. The temperature at the tip of the needle varies from 80 to 100 °C. The urethral temperature is kept below 46 ° C, and the temperature in the lesion is sustained for the treatment period.

At the end of the procedure, the decision to place a Foley catheter overnight is based upon the urologist's discretion. Many urologists do not place a catheter and allow the patients to go home after they have successfully voided.

Results

There have been several studies that have followed patients undergoing TUNA from 18 to 60 months. These are summarized in Table 16.6 [85–88].

Prostatic Urethral Lift (PUL)

The prostatic urethral lift (PUL) is a novel procedure that consists of the transurethral placement of suture-based implants, which hold the lateral prostatic lobes apart. The procedure differs from other ablative minimally invasive

Table 16.6 Efficacy of microwave treatment for BPH

Study	# patients	Follow-up (months)	IPSS pre-/post-treatment (% change)	Qm pre-/post-treatment (% change)	PVR pre-/post-treatment (% change)
Campo et al. (1997) [85]	120	18	20.8/6.7 (68)	8.2/14.1 (72)	NS
Steele and Sleep (1997) [86]	38	24	NS	6.6/11 (67)	76.1/36.9(52)
Murai et al. (2001) [87]	98	24	21.9/9.5(57)	7.6/11.5 (34)	21.9/9.5 (57)
Zlotta et al. (2003) [88]	188	60	20.9/8.7 (58)	8.6/12.1 (41)	20.9/8.7 (58)

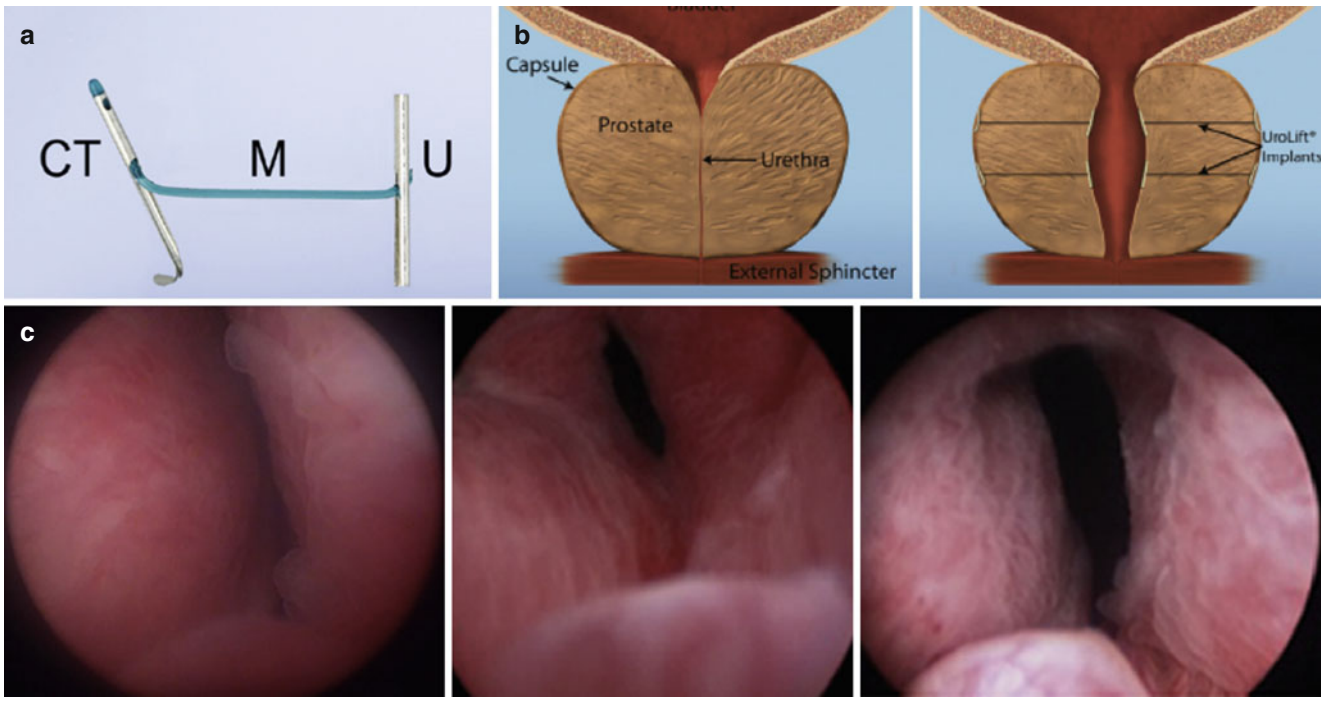

Fig. 16.10 (**a**) In the prostatic urethral lift, a novel monofilament (*M*) suture-based system is used to separate the lateral prostatic lobes between a stainless steel urethral (*U*) anchor and nitinol capsular tab (*CT*) [90]. (**b**) This figure conceptually demonstrates the rationale behind this approach [91]. (**c**) The endoscopic view of the prostate pre-operatively, immediately postoperatively, and at 6 months postoperatively is shown (**a** and **c** from McNicholas et al. [90]; **b** from Roerhborn et al. [91], with permission)

treatments for BPH in that it utilizes a mechanical means to address obstruction.

The prostatic urethral lift is well suited for those patients with predominantly lateral lobe enlargement. In fact, the presence of a large median lobe is a relative contraindication to the procedure. The size of the prostate does not seem to impact its success [89, 90], although smaller prostate size is preferred in the learning curve. Transrectal ultrasound determination of prostatic size, and a cystoscopic evaluation to exclude a predominant median lobe enlargement are mandatory prior to performing the procedure.

Technique

The patient is positioned in the dorsal lithotomy position. A periprostatic nerve block can be used, which makes it well suited as an office-based procedure. Alternatively 10 ml cold (4 °C) viscous lidocaine gel (2 %) can be inserted into the patient's bladder using a catheter, and a second 10 ml aliquot of viscous lidocaine gel (2) can be placed in the urethra. A clamp is applied to the penis for 20 min. General or regional anesthesia may alternatively be used.

Using a standard 20 Fr cystoscope and a 0° lens, the bladder and prostatic urethra are inspected. Once anatomical landmarks are identified, a custom implant delivery system that deploys suture-based anchors (The UroLift® System, NeoTract, Inc., Pleasanton, CA, USA) is placed into the cystoscopic sheath (Fig. 16.10). Targeted sites are defined, and a 19 G needle that houses a monofilament with metallic table is deployed into the prostatic urethra at the 10 o'clock and 2 o'clock positions. As the needle is retracted, the tab engages the prostatic capsule and there is tension applied to the anchoring suture. The intraurethral endpiece pulls the urethral lumen open, burying the endpiece into the tissue, where it eventually becomes buried under the mucosal layer, subsequently reducing the foreign body's contact with the urine.

Results

In a 2:1 randomized, multi-institutional study evaluating 206 patients who underwent PUL versus a sham procedure (cystoscopy and dilation) [91], patients undergoing PUL had significant reductions in AUA-SI (22.2 ± 5.5 baseline to 11.2 ± 7.7 post-procedure), increase in Qm (8.0 ± 2.4 baseline to 12.3 ± 5.4 post-procedure), and reduction in PVR (85.5 ± 69.2 baseline to 75.8 ± 83.9). This was significantly greater than the changes seen in the sham surgery group: AUA-SI (24.4 ± 5.8 baseline to 18.5 ± 8.6 post-procedure), Qm (7.9 ± 2.4 baseline to 9.9 ± 4.2 post-procedure), and PVR (85.6 ± 70.8 baseline to 63.4 ± 64). QOL improved significantly for the PUL (4.6–2.1) versus Sham (4.7–3.6), as well.

Long-term follow-up is lacking on PUL. The longest series reported to date is a multinational report evaluating 102 consecutive patients with symptomatic BPH, who were followed for 1 year following the procedure. Mean IPSS, QOL, and Qmax improved 36 %, 39 %, and 38 % by 2 weeks and 52 %, 53 %, and 51 % at 12 months, respectively.

Complications

Using several validated sexual function instruments in 40 patients undergoing PUL [92], there was minimal impact on erectile function and the majority of patients did not complain of retrograde ejaculation. Approximately 30–50 % of patients will require a postoperative catheter, hematuria and UTIs occur occasionally (<5 %), and fewer than 10 % of patients experience irritative symptoms. In general the procedure shows significant promise for select patients with primary lateral lobe hyperplasia, in terms of efficacy and safety.

Prostatic Abscess

Prostatic abscess is a relatively uncommon condition, with an incidence of 0.5 % among all prostatic diseases [93]. It may result from untreated or incompletely treated bacterial prostatitis [94]. Major causative pathogens are gram-negative bacilli, which are isolated in 65–85 % of cases [95, 96]. It is believed that the primary mechanism for the development of a prostatic abscess is via reflux of infected urine into the ejaculatory ducts in a patient with bladder outlet obstruction. The abscesses in such cases are more peripheral and the most frequent causative organism is *Escherichia coli* or other coliform bacteria [94]. The second mechanism is hematogenous spread from a distant source. Risk factors for prostatic abscess include bladder outlet obstruction, urethral manipulation, diabetes, liver disease, and immunocompromised state [97, 98]. Delay in treatment can result in complications such as rupture into the perineum, ischiorectal fossa, urethra, or rectum and subsequent septicemia [93].

The clinical diagnosis is often difficult, as the symptoms and signs are nonspecific and overlap with that of prostatitis. Symptoms include acute urinary retention, fever, dysuria, urinary frequency, perineal pain, hematuria, urethral discharge, and lower back pain. The finding of a tender, fluctuant mass on digital rectal examination is a specific but a non-consistent sign [93, 99]. It is important to distinguish between prostatitis and abscess as the management is different for both. In a patient who is being treated appropriately for a presumptive diagnosis of acute bacterial prostatitis does not improve, there should be a suspicion of a prostatic abscess.

Imaging modalities such as transrectal ultrasonography (TRUS), CT and MR imaging plays an important role in the diagnosis. TRUS is the most widely used technique as it is cheap and readily available and does not involve radiation [100]. One or more hypoechoic areas within the gland with thick walls are the most common appearance of abscess [101]. It is important to distinguish as abscess from prostate cancer which can be distinguished by blood flow on color and power Doppler examination.

Treatment

Patients should be started on broad-spectrum intravenous antibiotics with adequate gram-negative coverage. A Foley catheter may often be needed in patients developing acute urinary retention. Historically, primary treatment options included surgical interventions such as transurethral prostate incision, transurethral resection of the prostate (TURP), or transperineal drainage. Transurethral resection and incision are associated with several risks such as hemorrhage, retrograde ejaculation, and sepsis. Sepsis is particularly important due to the theoretical risk of irrigation fluid-induced bacteremia in the scenario of abscess.

Several studies have shown the safety and efficacy of TRUS-guided aspiration in treating prostatic abscess [94–96, 101, 102]. Advantages of TRUS-guided drainage include ease of performance, low morbidity rate, and potential of doing the procedure under local anesthesia/conscious sedation. TRUS enables precise puncture and drainage of even small abscesses, although repeat aspirations may be needed for complete treatment. The largest series was reported by Vyas et al., who successfully treated 48 patients with TRUS-guided aspiration. The authors proposed an algorithm which suggests that abscess greater than 2 cm be successfully treated with aspiration. For abscesses less than 2 cm, initial conservative treatment with intravenous antibiotics is suggested, failing which aspiration is recommended.

Transrectal drainage is preferred over transperineal drainage as is it is more comfortable for the patient and the needle

trajectory is shorter as the probe is in direct contact with prostate. Some authors have suggested placement of a drainage catheter (5); however this can be problematic as the catheter may be uncomfortable and it might be difficult to retain the catheter in place. There is also the theoretical risk of prostate-rectal fistula.

Prostatic Utricular Cyst and Mullerian Duct Cysts

A prostatic utricular cyst is an enlarged prostatic utricle that is most commonly associated with abnormal genitalia and is mostly diagnosed in pediatric population. The incidence is 11–14 % in association with hypospadias or intersex anomalies and it increases to more than 50 % in the presence of perineal hypospadias [103].

Prostatic utricular cysts (Fig. 16.11) are vesicular or tubular in shape and often communicate directly with the urethra. In contrast, Mullerian duct cysts (Fig. 16.12) are round, do not communicate with the prostatic urethra, and are discovered later in adults with normal genitalia. They result from the failure of involution of the Mullerian duct system in males [104]. Kim et al. found the incidence to be 5 % in general population and 17 % in men with infertility [105]. Both Mullerian duct cysts and utricular cyst appear as midline prostatic simple anechoic or complex echogenic cysts on TRUS and radiologic differentiation is not usually possible (see Fig. 16.9).

Although these cysts are most commonly asymptomatic, they can cause infertility by ejaculatory duct obstruction [106]. Symptoms include hematospermia, other ejaculatory disturbances, testicular or perineal pain, lower urinary tract irritative symptoms, lower urinary tract infection, and male infertility. Signs of duct obstruction include hypospermia (volume less than 2 cc), severe oligospermia or azoospermia, low fructose, and imaging findings of unilateral or bilateral dilatation of the seminal vesicle, ampulla, or vas deferens.

Diagnosis can be made by TRUS or MRI with endorectal coil; however, TRUS is preferred due to the availability and cost. Management options include TRUS-guided aspiration, endoscopic urethrotomy, and endoscopic marsupialization. In the largest series of 65 patients by Coppens et al., 9 were treated by TRUS-guided aspiration alone and symptom resolution was noted in 4 patients [103]. Because aspiration is safe and well tolerated, can be done on an outpatient basis, and does not compromise future treatment, it could be a good first step in management to relieve the irritative and obstructive symptoms. However, re-accumulation of the cyst fluid to some degree was seen in 7 patients. The authors suggest evaluation with TRUS in all patients presenting with abovementioned symptoms. They also emphasize the need to treat only symptomatic

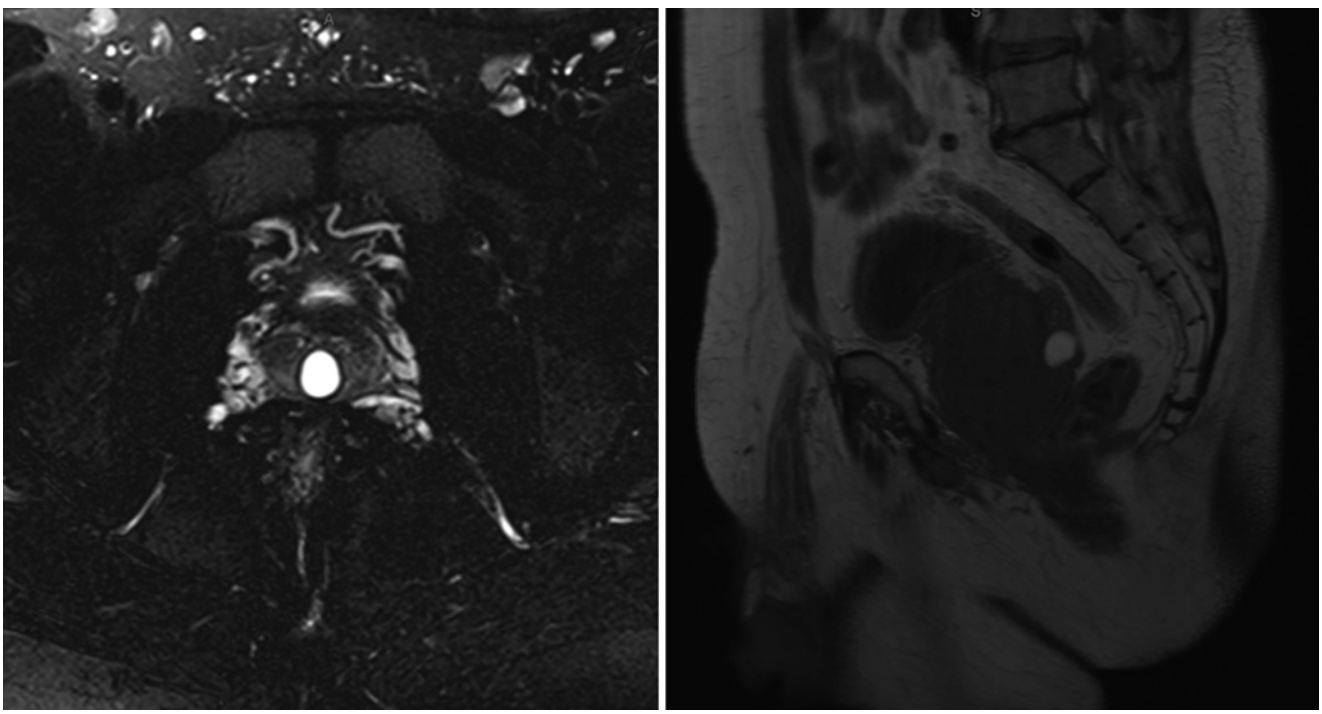

Fig. 16.11 Prostatic utricular cyst. As can be seen from the MRI T2-weighted images, the fluid-filled cyst is located very close to the midline, in close proximity to the prostatic urethra

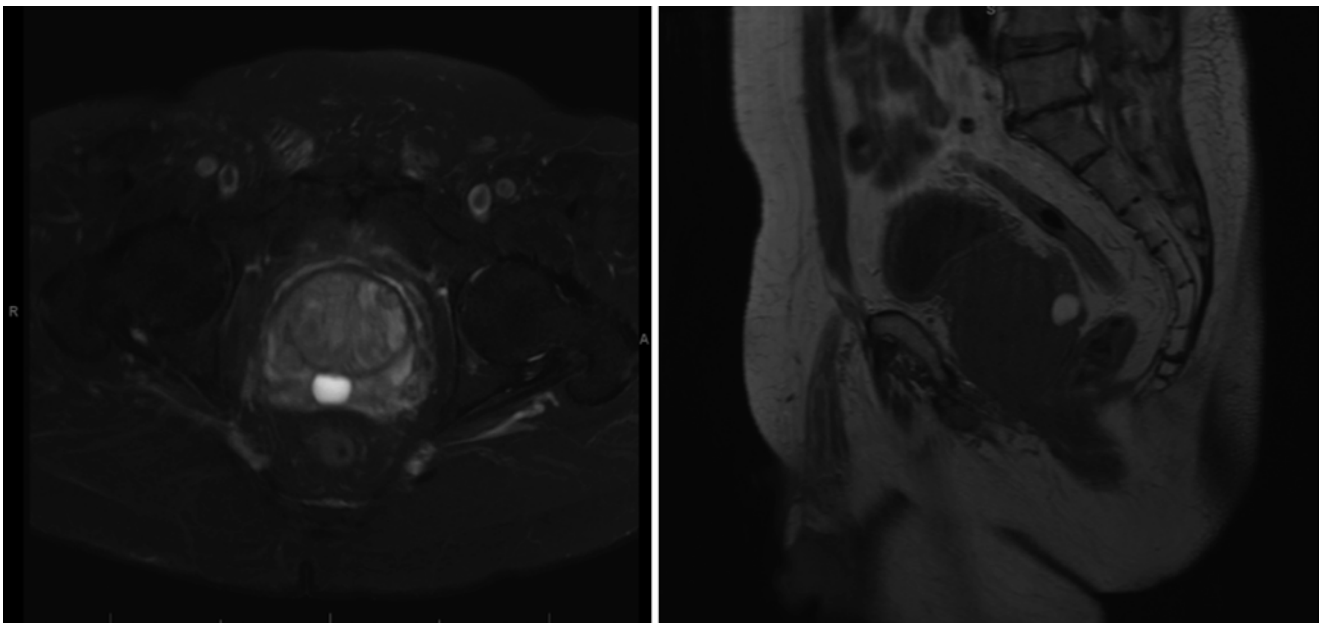

Fig. 16.12 Mullerian duct cyst: In these T2-weighted images of the prostate, the posterior fluid-filled cyst is noted in sagittal and coronal views. Because the cyst does not communicate directly with the prostatic urethra, it is not a utricular cyst

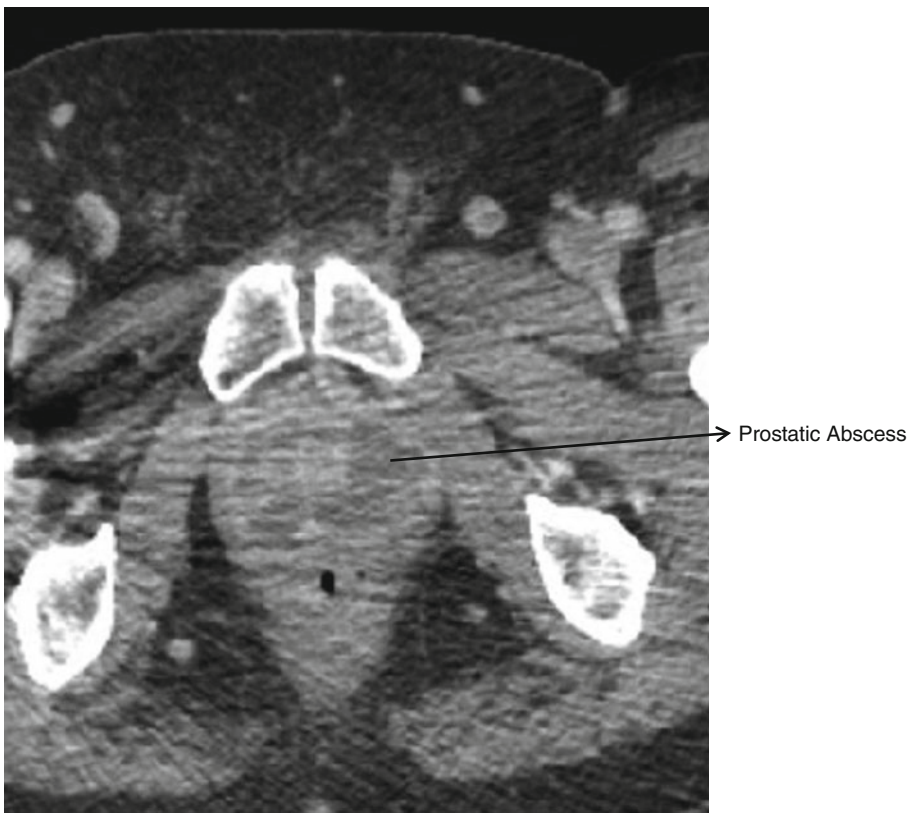

Fig. 16.13 Cross section view of a horse shoe abscess of the prostate

patients, regardless of the size of the cyst. Another study showed the usefulness of intraoperative TRUS during transurethral incision for precise targeting of the Mullerian duct cyst.

References

1. McNeal JE. Pathology of benign prostatic hyperplasia: insight into etiology. Urol Clin N Am. 1990;17:477–86.

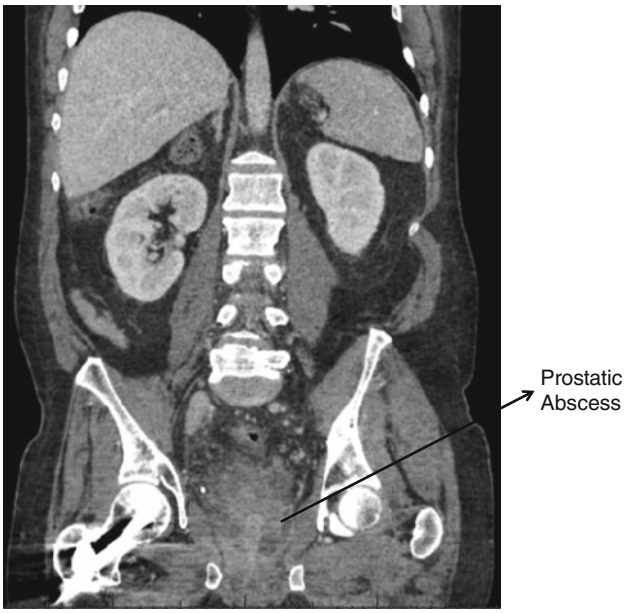

Fig. 16.14 CT scan demonstrating a hypoattenuated area in the proste representing an abscess

2. Lee C, Kozlowski J, Grayhack K. Intrinsic and extrinsic factors controlling benign prostatic growth. Prostate. 1997;31:131–8.
3. Wei JT, Calhoun E, Jacobsen SJ. Urologic diseases in America Project: benign prostatic hyperplasia. J Urol. 2005;173: 1256–61.
4. Abrams P. New words for old: lower urinary tract symptoms for "prostatism". BMJ. 1994;308(6934):929–30.
5. Abrams P. LUTS, BPH, BPE, BPO: a plea for the logical use of correct terms. Rev Urol. 1999;1:65.
6. McVary KT, Roehrborn CG, et al. American Urological Association Guideline: management of benign prostatic hyperplasia (BPH), revised 2010. J Urol. 2011;185(5):1793–803
7. Reynard J. Does anticholinergic medication have a role for men with lower urinary tract symptoms/benign prostatic hyperplasia either alone or in combination with other agents? Curr Opin Urol. 2004;14:13.
8. Abrams P, Cardozo L, et al. The standardization of terminology in lower urinary tract function: report from the standardization sub-committee of the International Continence Society. Urology. 2003;61:37–49.
9. Kupelian V, Wei JT, O'Leary MP, Kuseck JQ, Litman HJ, Link CL, McKinlay JB. Prevalence of lower urinary tract symptoms and effect on quality of life in a racially and ethnically diverse random sample. Arch Intern Med. 2006;166:2381–7.
10. Coyne KS, Sexton CC, Thompson CL, Milsom I, Irwin D, Kopp ZS, Chapple CR, Kaplan S, Tubaro A, Aiyer LP, Wein AJ. The prevalence of lower urinary tract symptoms (LUTS) in the USA, The UK and Sweden: results from the Epidemiology of LUTS (EpiLUTS) study. BJU Int. 2009;104:352–60.
11. Barry M, Fowler Jr F, O'Leary M, et al. The American Urological Association symptom index for benign prostatic hyperplasia. The Measurement Committee of the American Urological Association. J Urol. 1992;148:1549.
12. Barry M, Fowler Jr F, O'Leary M, et al. Measurement Committee of the American Urological Association. Med Care. 1995;22:AS145.
13. Franks LM. Benin nodular hyperplasia of the prostate: a review. Ann R Coll Surg Engl (Lond). 1954;14:92–106.
14. Berry SJ, Coffey DS, Walsh PC, Ewing LL. The development of human benign prostatic hyperplasia with age. J Urol. 1984;132:474–9.
15. Oesterling JE, Jacobsen SJ, et al. Serum prostate-specific antigen in a community-based population of healthy men: establishment of age-specific reference ranges. JAMA. 1993;270:860–4.
16. Roehrborn CG, Fuh V, et al. The relationship between total and free PSA, prostate volume and age in men age 40–60 with no clinical diagnosis of benign prostatic hyperplasia necessitating therapy. J Urol. 2000;163(Suppl):252.
17. Chute CG, Panser LA, Girman CJ, Oesterling JE, Gues HA, Jacobsen SJ, Lieber MM. The prevalence of prostatism: a population-based survey of urinary symptoms. J Urol. 1993;150:85–9.
18. Wei JT, Schottenfeld D, Cooper K, Taylor JM, Faerber GJ, Velarde MA, Bree R, Montie JE, Cooney KA. The natural history of lower urinary tract symptoms in black American men: relationships with aging, prostate size, flow rate, and bothersomeness. J Urol. 2001;165:1521–5.
19. McConnell JD, Roehrborn CG, Bautisa O, Andriole GL, Dixon CM, Kusek JW, et al. The long-term effect of doxazosin, finasteride, and combination therapy on the clinical progression of benign prostatic hyperplasia. N Engl J Med. 2003;349:2387–98.
20. Filson CP, Wei JT, Hollingsworth JM. Trends in medical management of men with lower urinary tract symptoms suggestive of benign prostatic hyperplasia. Urology. 2013;82:1386–93.
21. Roehrborn CG. Current medical therapies for men with lower urinary tract symptoms and benign prostatic hyperplasia: achievements and limitations. Rev Urol. 2008;10:14–25.
22. Verhamme KMC, Dielman JP, Bleumink GS, Bosch JLHR, Stricker BHC, Sturkenboom MCJM. Treatment strategies, patterns of drug use and treatment discontinuation in men with LUT suggestive of benign prostatic hyperplasia: the Triumph Project. Eur Urol. 2003;44:539–45.
23. Malaeb BS, Yu X, McBean AM, Elliot SP. National trends in surgical therapy for benign prostatic hyperplasia in the United States (2000–2008). Urology. 2012;79(5):1111–6.
24. Oelke M, Bachmann A, Descazeaud A, Emberton M, Gravas S, Michel MC, N'Dow J, Nordling J, de la Rosette JJ. EAU guidelines on the treatment and follow-up of non-neurogenic male lower urinary tract symptoms including benign prostatic obstruction. Eur Urol. 2013;64:118–40.
25. Mebust WK, Holtgrewe HL, Cockett ATK, Peters PC. Transurethral prostatectomy: immediate and postoperative complications, a cooperative study of 13 participating institutions evaluating 3,885 patients. J Urol. 1989;141:243–7.
26. Doll HA, Black NA, McPherson K, Flood AB, Williams GB, Smith JC. Mortality, morbidity and complications following transurethral resection of the prostate for benign prostatic hypertrophy. J Urol. 1992;147:1566–73.
27. Horninger W, Unterlechner H, Strasser H, Bartsch G. Transurethral prostatectomy: mortality and morbidity. Prostate. 1996;28:195–200.
28. Uchida T, Ohori M, Soh S, Sato T, Iwamura M, Ao T, Koshiba K. Factors influencing morbidity in patients undergoing transurethral resection of the prostate. Urology. 1999;53:98–104.
29. Berger AP, Wirtenberger W, Bektic J, Steiner H, Spranger R, Bartsch G. Safer transurethral resection of the prostate: coagulating intermittent cutting reduces hemostatic complications. J Urol. 2004;171:289–91.
30. Reich O, Gratzke C, Bachmann A, Seitz M, Schlenker B, Hermanek P, Lack N, Stief CG. Morbidity, mortality, and early outcome of transurethral resection of the prostate: a prospective multicenter evaluation of 10,654 patients. J Urol. 2008;180:246–9.
31. Mamoulakis C, Efthimlou I, Kazoulis S, Christoulakis I, Sofras F. The modified Clavien classification system: a standard platform for reporting complications in transurethral resection of the prostate. World J Urol. 2011;29:205–10.
32. Madersbacher S, Lackner J, Brossner C, Rohlich M, Stancik I, Willinger M, Schatzl G. Reoperation, myocardial infarction and

mortality after transurethral and open prostatectomy: a nationwide long-term analysis of 23,123 cases. Eur Urol. 2005;47: 499–504.
33. Varkarakis J, Bartsch G, Horninger W. Long-term morbidity and mortality of transurethral prostatectomy: a 10-year follow-up. Prostate. 2004;58:248–51.
34. Rassweiller J, Schulze M, Stock C, Teber D, de La Rosette J. Bipolar transurethral resection of the prostate- technical modifications and early clinical experience. Minim Invasive Ther Allied Technol. 2007;16:11–21.
35. Geavlete B, Stanescu F, Iacoboaie C, Geavlete P. Bipolar plasma enucleation of the prostate vs open prostatectomy in large benign prostatic hyperplasia cases- a medium term, prospective, randomized comparison. BJU Int. 2013;111:793–803.
36. Cornu J-N, Ahyai S, Bachmann A, de la Rosette J, Gilling P, Gratzke C, McVary K, Novara G, Woo H, Madersbacher S. A systematic review and meta-analysis of functional outcomes and complications following transurethral procedures for lower urinary tract symptoms resulting from benign prostatic obstruction: an update. Eur Urol. 2015;67(6):1066–96.
37. Autorino R, Damiano R, DiLorenzo G, Quarto G, Persona S, D'Armiento M, DeSio M. Four year outcome of a prospective randomized trial comparing bipolar plasmakinetic and monopolar transurethral resection of the prostate. Eur Urol. 2009;55: 922–31.
38. Chen Q, Zhang L, Fan QL, Zhou J, Peng YB, Wang Z. Bipolar transurethral resection in saline vs traditional monopolar resection of the prostate: results of a randomized trial with a 2-year follow-up. BJU Int. 2010;106:1339–43.
39. Geavelete B, Georgescu D, Multescu R, Stanescu F, Jecu M, Geavlete P. Bipolar plasma vaporization vs monopolar and bipolar TURP- a prospective, randomized, long-term comparison. Urology. 2011;78:930–6.
40. Mamoulakis C, Schulze M, Skolarikos A, Alivizatos G, Scarpa RM, Rassweiler JJ, de la Rosette JJMCH, Scaffone CM. Midterm results from an international multicentre randomized controlled trial comparing bipolar with monopolar transurethral resection of the prostate. Eur Urol. 2013;63:667–76.
41. Komura K, Inamoto T, Takai T, Uchimoto T, Saito K, Tanda N, Minami K, Uehara H, Takahara K, Hirano H, Nomi H, Kiyama S, Watsuji T, Azuma H. Could transurethral resection of the prostate using the TURis system take over conventional monopolar transurethral resection of the prostate? A randomized controlled trial and midterm results. Urology. 2014;84:405–11.
42. Te AE. The development of laser prostatectomy. BJU Int. 2004;93:262–5.
43. Teichmann H-O, Herrmann TR, Bach T. Technical aspects of lasers in urology. World J Urol. 2007;25:221–5.
44. Marks AJ, Teichman JMH. Lasers in clinical urology: state of the art and new horizons. World J Urol. 2007;25:227–33.
45. Hermann TRW, Liatsikos EN, Nagele U, Traxer O, Merseburger AS. EAU guidelines on laser technologies. Eur Urol. 2012;61:783–95.
46. Reich O, Bachmann A, Schneede P, Zaak D, Sulser T, Hofstetter A. Experimental comparison of high power (80W) potassium titanyl phosphate laser vaporization and transurethral resection of the prostate. J Urol. 2004;171:2502–4.
47. Bachmann A, Schurch L, Ruszat R, Wyler SF, Seifert H-H, Muller A, Lehmann K, Sulser T. Photoselective vaporization (PVP) versus transurethral resection of the prostate (TURP); a prospective bi-centre study of perioperative morbidity and early functional outcome. Eur Urol. 2005;48:965–72.
48. Sulser T, Reich O, Wyler S, Ruszat R, Casella R, Hofstetter A, Bachmann A. Photoselective KTP laser vaporization of the prostate: first experiences with 65 procedures. J Endourol. 2004;18:976–81.
49. Malek RS, Barrett DM, Kuntzman RS. High power potassium titanyl phosphate (KTP/532) laser vaporization prostatectomy: 24 hours later. Urology. 1998;51:254–6.
50. Te AE, Malloy TR, Stein BS, Ulchaker JC, Nseyo UO, Hai MA, Malek RS. Photoselective vaporization of the prostate for the treatment of benign prostatic hyperplasia: 12 month results from the first United States multicenter prospective trial. J Urol. 2004;172:1404–8.
51. Bouchier-Hayes DM, Van Appledorn S, Bugeja P, Crowe H, Challacombe B, Costello AJ. A randomized trial of photoselective vaporization of the prostate using the 80-W potassium-titanyl-phosphate laser vs transurethral prostatectomy, with a 1-year follow-up. BJU Int. 2010;105:964–9.
52. Horasanli K, Silay MS, Altay B, Tanriverdi O, Sarica K, Miroglu C. Photoselective potassium titanyl phosphate (KTP) laser vaporization versus transurethral resection of the prostate for prostates larger than 70ml: a short-term prospective randomized trial. Urology. 2008;71:247–51.
53. Skolarikos A, Papachristou C, Athanasiadis G, Chalikopoulos D, Deliveliotis C, Alivaizatos G. Eighteen-month results of a randomized prospective study comparing transurethral photoselective vaporization with transvesical open enucleation for prostatic adenomas greater than 80cc. J Endourol. 2008;22:2333–40.
54. Lukacs B, Loeffler J, Bruyere F, Blanchet P, Gelet A, Coloby P, De la Taille A, Lemaire P, Baron J-C, Cornu J-N, Aout M, Rousseau H, Vicaut E. Photoselective vaporization of the prostate with GreenLight 120-W laser compared with monopolar transurethral resection of the prostate: a multicenter randomized controlled trial. Eur Urol. 2012;61:1165–73.
55. Bachman A, Tubaro A, Barber N, d'Ancona F, Muir G, et al. 180-W XPS GreenLight laser vaporisation versus transurethral resection of the prostate for the treatment of benign prostatic obstruction: 6 month safety and efficacy results of a European multicentre randomized trail – the Goliath Study. Eur Urol. 2014;65:931–42.
56. Pfitzenmaier J, Gilfrich C, Pritsch M, et al. Vaporization of prostates of > or = 80ml using a potassium-titanyl-phosphate laser: mid-term results and comparison with prostates < 80ml. BJU Int. 2008;102:322–7.
57. Al-Ansari A, Younes N, Sampige VP, et al. Greenlight HPS 120-W laser vaporization versus transurethral resection of the prostate for treatment of benign prostatic hyperplasia: a randomized clinical trial with midterm follow –up. Eur Urol. 2010;58:349–55.
58. Tasci AI, Tugcu V, Sahin S, Zorluoglu F. Rapid communication photoselective vaporization of the prostate versus transurethral resection of the prostate for the large prostate: a prospective non-randomized bicenter trial with 2-year follow- up. J Endourol. 2008;22:347–53.
59. Thangasamy IA, Chalasani V, Bachmann A, Woo HH. Photoselective vaporisation of the prostate using 80W and 120W laser versus transurethral resection of the prostate for benign prostatic hyperplasia: a systematic review with meta-analysis from 2002 to 2012. Eur Urol. 2012;62:315–23.
60. Gilling PJ, Fraundorfer MR. Holmium laser prostatectomy: a technique in evolution. Curr Opin Urol. 1998;8:11–5.
61. Motet N, Anidjar M, Bourdon O, et al. Randomized comparison of transurethral electroresection and holmium:YAG laser vaporization for symptomatic benign prostatic hyperplasia. J Endourol. 1999;13:127–30.
62. Gilling PJ, Kennett KM, Das AK, Thomson D, Fraundorfer MR. Holmium laser enucleation of the prostate (HoLEP) combined with transurethral tissue morcellation: an update on the early clinical experience. J Endourol. 1998;12:457–9.
63. Tan AH, Gilling PJ. Holmium laser prostatectomy: current techniques. Urology. 2002;60:152–6.

64. Gilling P, Mackey M, Cresswell M, et al. Holmium laser versus transurethral resection of the prostate: a randomized prospective trial with 1-year follow up. J Urol. 1999;162:1640–4.
65. Kuntz RM. Laser treatment of benign prostatic hyperplasia. World J Urol. 2007;25:241–7.
66. Tan AHH, Gilling PJ, Kennett KM, Frampton C, Westenberg AM, Fraundorfer MR. A randomized trial comparing holmium laser enucleation of the prostate with transurethral resection of the prostate for the treatment of bladder outlet obstruction secondary to benign prostatic hyperplasia in large glands (40–200 grams). J Urol. 2003;170:1270–4.
67. Lerner LB, Tyson MD. Holmium laser applications of the prostate. Urol Clin North Am. 2009;36:485–95.
68. KuntzRM AS, Lehrich K, Fayad A. Transurethral holmium laser enucleation of the prostate versus transurethral electrocautery resection of the prostate: a randomized prospective trial in 200 patients. J Urol. 2004;172:1012–6.
69. Montorsi F, Naspro R, Salonia A, Suardi N, Briganti A, Zanoni M, Vanlenti S, Vavassori I, Rigatti P. Holmium laser enucleation versus transurethral resection of the prostate: results form a 2-center, prospective randomized trial in patients with obstructive benign prostatic hyperplasia. J Urol. 2004;172(5):1926–9.
70. Gupta N, Sivaramakrishna Kumar R, Dogra PN, Seth A. Comparison of standard transurethral resection, transurethral vapour resection and holmium laser enucleation of the prostate for managing benign prostatic hyperplasia of >40g. BJU Int. 2006;97:85–9.
71. Wilson LC, Gilling PJ, Williams A, Kennett KM, Frampton CM, Westenberg AM, Fraundorfer MR. A randomized trial comparing holmium laser enucleation versus transurethral resection in the treatment of prostates larger than 40 grams: results at 2 years. Eur Urol. 2006;50(3):569–73.
72. Sun N, Fu Y, Tian T, Gao J, Wang Y, et al. Holmium laser enucleation of the prostate versus transurethral resection of the prostate: a randomized clinical trial. Int Urol Nephrol. 2014;46:1277–82.
73. Ahyai SA, Lehrich K, Kuntz RM. Holmium laser enucleation versus transurethral resection of the prostate: 3 year follow up results of a randomized clinical trial. Eur Urol. 2007;52:1456–63.
74. Naspro R, Suardi N, Salonia A, et al. Holmium laser enucleation of the prostate versus open prostatectomy for prostates >70g: 24 month follow- up. Eur Urol. 2006;50:563–8.
75. Kuntz RM, Lehrich K. Transurethral holmium laser enucleation versus transvesical open enucleation for prostate adenoma greater than 100g: a randomized prospective trail of 120 patients. J Urol. 2002;168:1465–9.
76. Gilling PJ, Aho TF, Frampton CM, King CJ, Fraundorfer MR. Holmium laser enucleation of the prostate: results at 6 years. Eur Urol. 2008;53:744–9.
77. Kuntz RM, Lehrich K, Ahyai SA. Holmium laser enucleation of the prostate versus open prostatectomy for prostates greater than 100g: 5 year follow up results of a randomized clinical trial. Eur Urol. 2008;53:160–8.
78. Xia S-J, Zhuo J, Sun X-W, Han B-M, Shao Y, Zhang Y-N. Thulium laser versus standard transurethral resection of the prostate: a randomized prospective trial. Eur Urol. 2008;53:382–90.
79. Fu WJ, Zhang X, Yang Y, et al. Comparison of 2 micron continuous wave laser vaporesection of the prostate and transurethral resection of the prostate: a prospective, nonrandomized trial with 1-year follow up. Urology. 2010;75:194–9.
80. Shao Q, Zhang FB, Shang DH, Tian Y. Comparison of holmium and thulium laser in transurethral enucleation of the prostate. Zhonghua Nan Ke Xue. 2009;15:346–9 (in Chinese).
81. Bolmsjo M, Wagrell L, Hallin A, Eliasson T, Erlandsson BE, Mattiasson A. The heat is on–but how? A comparison of TUMT devices. Br J Urol. 1996;78(4):564–72.
82. Hoffman RM, Monga M, Elliott SP, Macdonald R, Langsjoen J, Tacklind J, Wilt TJ. Microwave thermotherapy for benign prostatic hyperplasia. Cochrane Database Syst Rev. 2012;(9):CD004135. doi:10.1002/14651858.CD004135.pub3.
83. Naslund MJ. Transurethral needle ablation of the prostate. Urology. 1997;50(2):167–72. doi:10.1016/S0090-4295(97)00277-X.
84. Bouza C, Lopez T, Magro A, Navalpotro L, Amate JM. Systematic review and meta-analysis of transurethral needle ablation in symptomatic benign prostatic hyperplasia. BMC Urol. 2006;6:14. doi:10.1186/1471-2490-6-14.
85. Campo B, Bergamaschi F, Corrada P, Ordesi G. Transurethral needle ablation (TUNA) of the prostate: a clinical and urodynamic evaluation. Urology. 1997;49(6):847–50.
86. Steele GS, Sleep DJ. Transurethral needle ablation of the prostate: a urodynamic based study with 2-year followup. J Urol. 1997;158(5):1834–8.
87. Murai M, Tachibana M, Miki M, Shiozawa H, Hirao Y, Okajima E. Transurethral needle ablation of the prostate: an initial Japanese clinical trial. Int J Urol. 2001;8(3):99–105.
88. Zlotta AR, Giannakopoulos X, Maehlum O, Ostrem T, Schulman CC. Long-term evaluation of transurethral needle ablation of the prostate (TUNA) for treatment of symptomatic benign prostatic hyperplasia: clinical outcome up to five years from three centers. Eur Urol. 2003;44(1):89–93.
89. Larcher A, Broglia L, Lughezzani G, Mistretta F, Abrate A, Lista G, Fossati N, et al. Urethral lift for benign prostatic hyperplasia: a comprehensive review of the literature. Curr Urol Rep. 2013;14:620–7.
90. McNicholas TA, Woo HH, Chin PT, Bolton D, Arjona MF, et al. Minimally invasive prostatic urethral lift: surgical technique and multinational experience. Eur Urol. 2013;64:292–9.
91. Roerhborn CG, Gange SN, Shore ND, Giddens JL, Bolton DM, Cowan BE, et al. The prostatic urethral lift for the treatment of lower urinary tract symptoms associated with prostate enlargement due to benign prostatic hyperplasia: The L.I.F.T. Study. J Urol. 2013;190:2161–7.
92. Woo HH, Bolton DM, Laborde E, Jack G, Chin PT, Rashid P, Thavaseelan J, McVary KT. Preservation of sexual function with the prostatic urethral lift; a novel treatment for lower urinary tract symptoms secondary to benign prostatic hyperplasia. J Sex Med. 2012;9:568–75.
93. Granados EA, Riley G, Salvador J, Vincente J. Prostatic abscess: diagnosis and treatment. J Urol. 1992;148(1):80–2.
94. Collado A, Palou J, Garcia-Penit J, Salvador J, de la Torre P, Vicente J. Ultrasound-guided needle aspiration in prostatic abscess. Urology. 1999;53(3):548–52.
95. Vyas JB, Ganpule SA, Ganpule AP, Sabnis RB, Desai MR. Transrectal ultrasound-guided aspiration in the management of prostatic abscess: a single-center experience. Indian J Radiol Imaging. 2013;23(3):253–7.
96. Jang K, Lee DH, Lee SH, Chung BH. Treatment of prostatic abscess: case collection and comparison of treatment methods. Korean J Urol. 2012;53(12):860–4.
97. Bachor R, Gottfried HW, Hautmann R. Minimal invasive therapy of prostatic abscess by transrectal ultrasound-guided perineal drainage. Eur Urol. 1995;28(4):320–4.
98. Trauzzi SJ, Kay CJ, Kaufman DG, Lowe FC. Management of prostatic abscess in patients with human immunodeficiency syndrome. Urology. 1994;43(5):629–33.
99. Jacobsen JD, Kvist E. Prostatic abscess. A review of literature and a presentation of 5 cases. Scand J Urol Nephrol. 1993;27(2):281–4.
100. Barozzi L, Pavlica P, Menchi I, De Matteis M, Canepari M. Prostatic abscess: diagnosis and treatment. AJR Am J Roentgenol. 1998;170(3):753–7.

101. Varkarakis J, Sebe P, Pinggera GM, Bartsch G, Strasser H. Three-dimensional ultrasound guidance for percutaneous drainage of prostatic abscesses. Urology. 2004;63(6):1017–20; discussion 20.
102. Lim JW, Ko YT, Lee DH, Park SJ, Oh JH, Yoon Y, et al. Treatment of prostatic abscess: value of transrectal ultrasonographically guided needle aspiration. J Ultrasound Med. 2000;19(9):609–17.
103. Coppens L, Bonnet P, Andrianne R, de Leval J. Adult mullerian duct or utricle cyst: clinical significance and therapeutic management of 65 cases. J Urol. 2002;167(4):1740–4.
104. Moukaddam HA, Haddad MC, El-Sayyed K, Wazzan W. Diagnosis and treatment of midline prostatic cysts. Clin Imaging. 2003;27(1):44–6.
105. Kim ED, Onel E, Honig SC, Lipschultz LI. The prevalence of cystic abnormalities of the prostate involving the ejaculatory ducts as detected by transrectal ultrasound. Int Urol Nephrol. 1997;29(6):647–52.
106. Halpern EJ, Hirsch IH. Sonographically guided transurethral laser incision of a Mullerian duct cyst for treatment of ejaculatory duct obstruction. AJR Am J Roentgenol. 2000;175(3):777.

Part III

Kidney

Kidney Imaging

17

Mahmoud Chehab and Gennady Bratslavsky

Renal imaging plays an essential role in the diagnosis and evaluation of renal pathology. In urology, it is most commonly used in the evaluation for hematuria, trauma, abdominal pain, and workup for genitourinary cancers. It is also utilized as a follow-up study for nephrolithiasis and surveillance of masses. Imaging modalities that play an important role in detecting disease regression, progression, recurrence, or metastasis include computerized tomography (CT) (Fig. 17.1), magnetic resonance imaging (MRI), diagnostic ultrasound (US), bone scan, and plain film x-ray. Positron emission tomography (PET) scanning with labeled antibody is under evaluation for imaging of renal cell carcinoma (RCC) and may play a role in the future, but it is currently not a standard or recommended diagnostic measure. Due to superior diagnostic accuracy, CT and MRI are both used for detection and characterization of neoplasms suspicious for RCC [1]. Kidney imaging has the ability to allow for a better surgical planning prior to either nephron-sparing surgery or radical nephrectomy for renal tumors. This chapter will focus on different modalities available to diagnose and differentiate renal pathology, such as renal mass, obstruction, calculi, and lymphoma. We will focus mostly on current and emerging techniques and modalities for the diagnosis of RCC and the role imaging plays as a biomarker of RCC subtypes.

Imaging for Kidney Pathology

The kidney plays an essential role in blood filtration and the maintenance of electrolyte levels. It is a well-vascularized organ receiving about 20 % of the cardiac output and plays an important role in the regulation of blood pressure. Several pathologies develop in the adult kidney and are not limited to renal masses, obstruction with and without hydronephrosis, nephrolithiasis, lymphoma, and urothelial carcinoma. Renal masses are found in the parenchyma or collecting system. Those are usually solid or cystic and are differentiated by imaging. Renal masses will be discussed in detail later in the chapter.

Collecting system or ureteral obstruction often leads to hydronephrosis and symptoms such as pain. Typically, patients with abdominal or flank/back pain are evaluated with US or CT. Both modalities are suitable to detect and grade hydronephrosis. Grading is done based on the Society for Fetal Urology (SFU) grading system established in 1993. Patients without calyx or pelvic dilation are classified as grade 0, pelvic dilation only as grade 1, mild calyx dilation as grade 2, severe calyx dilation as grade 3, and calyx dilation accompanied by renal parenchymal atrophy as grade 4 [2] (Tables 17.1 and Fig. 17.2).

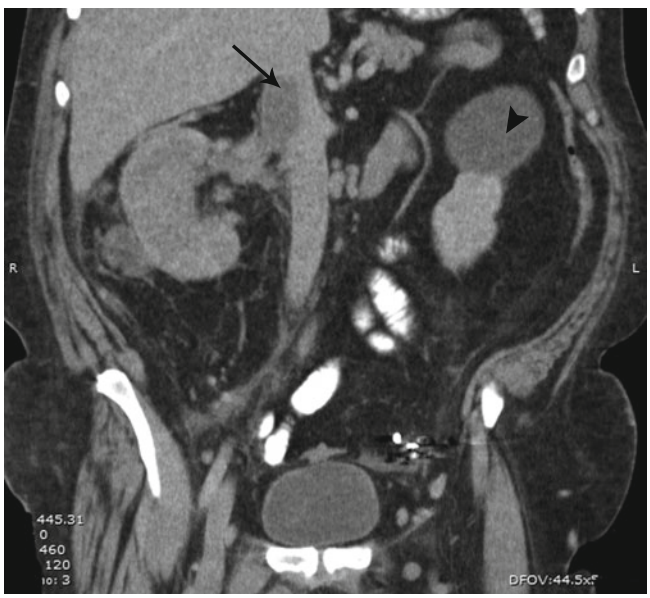

Fig. 17.1 CT scan with IV contrast showing a right renal mass with renal vein and IVC thrombus (*arrow*). The renal mass on the right is heterogeneous. The left kidney has an upper pole simple cyst that measures 9 HU (*arrowhead*)

M. Chehab, MD • G. Bratslavsky, MD (✉)
Department of Urology, SUNY Upstate Medical University, Syracuse, NY, USA
e-mail: bratslag@upstate.edu

A.R. Rastinehad, D.N. Siegel (eds.), *Interventional Urology*, DOI 10.1007/978-3-319-23464-9_17

Table 17.1 SFU grading of hydronephrosis

SFU grade	
0	No calyx or pelvic dilation
1	Pelvic dilation only
2	Mild calyx dilation
3	Severe calyx dilation
4	Calyx dilation accompanied by renal parenchymal atrophy

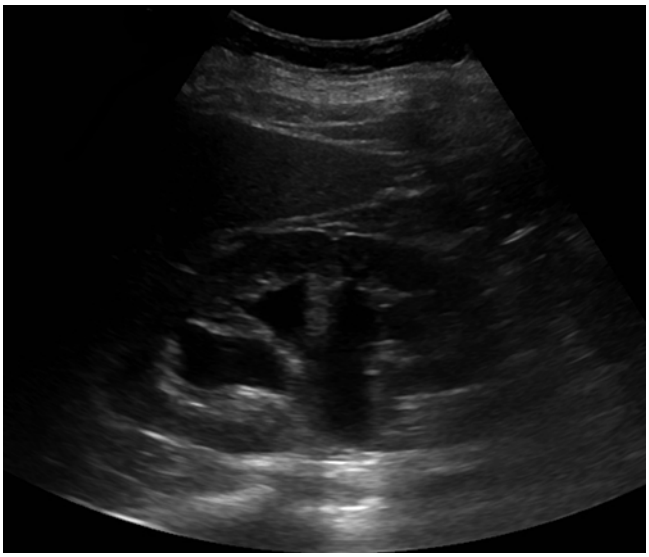

Fig. 17.2 Ultrasound image showing hydronephrosis with dilated pelvis and calyxes consistent with grade III SFU hydronephrosis

Nephrolithiasis is a major cause of obstruction and pathology of the kidney. While this topic is beyond the scope of this chapter, it will be discussed briefly. Imaging has an essential role in the diagnosis, management, and follow-up of patients with stone disease. A variety of imaging modalities are available for evaluation including conventional radiography such as x-ray of the kidney, ureters, and bladder (KUB), US, MR urography, and CT scans, each with its advantages and limitations. Intravenous urograms (IVU) were used in the past and this modality has declined in its utility with the increasing use of CT. In some scenarios, especially in patients with poor renal function, to better identify the exact stone location or collecting system anatomy, there may be a role for cystoscopy and a retrograde pyelogram.

There are several types of stones based on composition. The most common kidney stones in the United States are calcium based [3]. Other encountered stones include uric acid, magnesium ammonium phosphate, cystine, and indinavir stones. A KUB can be used to identify large calcium-based stones; however, uric acid stones are missed as the majority are radiolucent. Detection of stones by KUB may also be hindered by overlying bowel gas, patient body habitus, and extrarenal calcifications such as phleboliths. The advantages of a KUB include its wide availability, minimal radiation exposure, and low cost. US, the preferred imaging modality in pregnancy [4, 5], may be used in the evaluation of nephrolithiasis including uric acid stones. Advantages of US include its noninvasiveness, lack of radiation and intravenous contrast, and wide availability and relatively low cost. Limitations include poor sensitivity for ureteral stones and stones smaller than 3 mm [6]. In addition, US is highly nonspecific and may be unable to differentiate between ureteral obstruction secondary to calculi and physiologic hydronephrosis of pregnancy [5]. In these situations, further imaging with unenhanced CT, the gold standard for diagnosis of urinary calculi, may be required. Interestingly, the recent study published in the New England Journal of Medicine comparing US versus CT for nephrolithiasis showed that patients who were imaged with an US as the initial imaging modality were exposed to a lower total amount of radiation than were patients who received CT as the initial imaging modality, with no significant difference in high-risk diagnoses with complications, total serious adverse events, or related serious adverse events. The secondary outcomes of pain scores, hospital admissions, and emergency department readmissions during follow-up also did not differ significantly among the groups [7]. CT provides more information on the location of stones, nearby anatomy, and may aid in determining composition by measuring stone density using Hounsfield Unit (HU) measurements. Significant difference is seen in HU between pure uric acid stones and other stone types. Kuwahara et al. conclude that the determination of calculus composition by HU measurement is possible only for oxalate calculi of more than 1,600 HU and uric acid calculi of less than 500 HU [8]. CT is also useful in identifying other abdominal pathologies that may mimic symptoms of nephrolithiasis such as appendicitis, cholecystitis, and ovarian pathologies.

MRI is sometimes used in the evaluation of nephrolithiasis especially in pregnant women; however, it has a limited use in nephrolithiasis as it is expensive, time consuming, and not readily available. In addition, distinguishing stones from tumors or blood clot can be difficult because these entities all appear as a signal void [6]. While MRI is relatively insensitive for the direct detection of urinary calculi, it has the ability to detect the secondary effects of obstructive urolithiasis. Using rapid, single-shot abdominopelvic T2-weighted sequences with and without fat saturation provides an examination that can detect the sequelae of clinically active stone disease, in addition to alternate inflammatory processes that may mimic the symptoms of renal colic [9].

Other causes of obstruction include ureteropelvic junction (UPJ) obstruction congenital and acquired due to a crossing vessel (Fig. 17.3), stricture, trauma, etc. These conditions are commonly evaluated with CT and MRI. CT angiography may be used to evaluate UPJ obstruction due to a crossing vessel and can be used in surgical planning. Krepkin

Fig. 17.3 CT angiogram showing right hydronephrosis caused by a crossing vessel at the ureteropelvic junction. The artery can be seen branching off the aorta and supplying the lower pole of the right kidney (*arrow*)

et al. evaluated the use of MR renography (MRR) and concluded that in patients with UPJ obstruction MRR can measure split renal function, estimate the glomerular filtration rate with moderate correlation, and accurately discriminate mechanical from functional obstruction [10].

Urothelial Carcinoma

Solid masses can be present in the renal parenchyma or collecting system. When the collecting system is involved, urothelial carcinoma (UC) should be considered. Imaging with a delayed excretory phase is best for evaluation of the collecting system. Patients precluded from receiving intravenous contrast agents may particularly benefit from MR urography. UC occurs mainly in the bladder but could also develop in the upper urinary tract and account for 5–10 % of urothelial carcinomas. In the upper tract, it most frequently arises in the renal pelvis, followed by the infundibular and calyceal regions. Contrast-enhanced CT and MRI have become the most widely used imaging modalities for radiological evaluation of the upper urinary tract. On unenhanced studies, the intraluminal portion of a lesion often shows increased attenuation with respect to surrounding urine. UC does not typically deform the renal contour. In rare cases, invasion of sinus structures with infiltration of the sinus fat or collecting system elements may be subtle indicators of a UC presence on unenhanced images. After contrast administration, the mass typically enhances, although to a lesser degree than normal renal parenchyma and to a lesser degree than conventional RCC. CT urography which includes excretory-phase imaging improves visualization of collecting system abnormalities, and these lesions sometimes are seen as sessile filling defects. While CT urogram is the most common modality used for upper tract UC, diffusion-weighted MRI (DW-MRI) is gaining popularity. DW-MRI is a type of functional imaging, which is increasingly being utilized and provides helpful information for the diagnosis of UC in a noninvasive manner. The addition of DW-MRI to a routine MRI protocol requires only a few minutes, and it can be acquired using most current clinical MRI scanners. Growing evidence has emerged showing that DW-MRI can serve as an imaging biomarker for characterizing the pathophysiology of cancer. The imaging signal confers information about the biophysical properties of tissues, such as cell organization and density. The apparent diffusion coefficient (ADC) measures the magnitude of diffusion of water molecules within tissue using DW-MRI. Sasamori et al. found that the mean ADC of infiltrating UC was significantly lower than that of clear cell RCC, possibly reflecting the high cellularity of UC [11]. The potential of DW-MRI as an imaging biomarker is just emerging, and further studies are essential to validate and standardize this modality [12]. UC is typically isointense relative to the renal medulla on T1-weighted images, making the detection of small tumors in the collecting system virtually impossible. Larger infiltrative tumors may obliterate the fat in the renal sinus, which may be appreciated on T1-weighted images without the use of fat-saturation techniques. Enhancement of a focal filling defect in the collecting system is strongly suggestive of a UC. Differentiation between blood clots and enhancing filling defects is best accomplished by reviewing subtracted data sets.

Lymphoma

The kidney is one of the abdominal organs in which extranodal lymphoma can be found, and just like metastatic disease to the kidney, renal lymphoma is usually clinically silent. Lymphoma may involve the kidneys via hematogenous spread, in which a single mass or multiple bilateral masses are present, or by direct extension of retroperitoneal lymphoma. Lymphoma may mimic RCC and in some cases difficult to differentiate. Diffuse lymphomatous infiltration producing smooth generalized renal enlargement occurs in approximately 20 % of patients, and it is almost always bilateral. When lymphoma diffusely infiltrates a kidney, the kidney enlarges but maintains its reniform shape [13]. On CT imaging, renal lymphoma is seen as a soft tissue attenuation mass that enhances homogeneously but less intensely than normal renal parenchyma after contrast material administration. Nephrographic phase CT imaging is essential, since lymphomatous deposits in the kidney may be small and medullary in location, making them inconspicuous on corticomedullary phase images. On MRI, relative to the renal cortex,

lymphomatous masses are isointense or slightly hypointense on T1-weighted MRI and hypointense on T2-weighted images. Minimal heterogeneous enhancement is seen on early and delayed gadolinium-enhanced MRI in most patients. In addition, patients with renal lymphoma nearly always have evidence of disease elsewhere. If imaging findings are typical, then differentiation from RCC is usually not in question yet the biopsy is usually performed to confirm the diagnosis of lymphoma. In this situation, systemic therapy for lymphoma can be instituted, with the anticipation that the renal disease will respond in the same manner as the systemic disease. On rare occasions, renal lymphoma occurs as a solitary mass or exhibits unusual imaging characteristics, making differentiation from RCC difficult. In these circumstances, image-guided biopsy results are also diagnostic [14].

Renal Cysts and Masses

Renal masses are divided into cystic and solid. Renal cysts are among the most common renal lesions detected on cross-sectional imaging. While the majority are isodense to water with an attenuation values of <20 HU and easily diagnosed on CT, some renal cysts do not fulfill the established diagnostic criteria and can prove difficult to define. Simple cysts are best defined using sonographic criteria. These include (1) absence of internal echoes, (2) posterior enhancement, (3) round/oval shape, and (4) sharp, thin posterior walls. Since its publication in 1986, the Bosniak classification of renal cysts has been widely used to classify these lesions and to separate cystic lesions that can be safely followed from those requiring surgical resection (Table 17.2; Fig. 17.4) [15]. Because differentiating Bosniak II and III cysts was found to be particularly challenging, the original classification system was modified to a II F intermediate group [16]. Although other imaging modalities are frequently used in the evaluation of renal masses such as US and MRI, CT with and without contrast enhancement remains the primary diagnostic technique [17]. Currently, it is not recommended to use US for the initial evaluation of complex cystic renal masses largely because contrast enhancement, which is an important criterion for malignancy, cannot be assessed [18]. On the other hand, studies have shown that MRI features correlate well with histopathologic and CT findings and therefore MRI is an appropriate modality for cyst classification [18]. MRI may be used in equivocal cases to identify very thin septa or demonstrate enhancement not otherwise perceived on CT. The presence of enhancement within a renal lesion after the administration of gadolinium-based contrast material is the most reliable criterion for distinguishing solid masses from cysts. Comparison of pre- and postcontrast T1-weighted images is the key to the detection and characterization of renal lesions. Precontrast T1-weighted images are helpful in the characterization of certain aspects of cystic and solid lesions. Simple cysts are hypointense relative to the normal renal parenchyma on T1-weighted images due to their long relaxation time. Increased signal intensity within cysts may indicate the presence of hemorrhage or proteinaceous fluid. Similarly, hemorrhagic solid renal masses may display areas of increased signal intensity on T1-weighted images. Simple

Table 17.2 Bosniak classification of renal cysts

Category I: malignant risk less than 1 %; no follow-up required
Uncomplicated, simple benign cyst
Anechoic, posterior enhancement (through transmission), round or oval shape, thin, smooth wall
Homogeneous water content, sharp delineation with the renal parenchyma, no calcification, enhancement, or wall thickening
Category II: malignant risk less than 3 %; no follow-up required
<1 mm septations (hairline thin)
Fine calcifications within the septum or wall
<3 cm in diameter
Hyperdense cysts (>20 Hounsfield units)
Category IIF: malignant risk 5–10 %; follow-up recommended
Multiple thin septum
Septa thicker than hairline or slightly thick wall
Calcification, which may be thick
Intrarenal, >3 cm
No contrast enhancement
Category III: malignant risk 40–60 %; surgical excision recommended
Uniform wall thickening/nodularity
Thick/irregular calcification
Thick septa
Enhances with contrast
Category IV: malignant risk greater than 80 %; surgical excision recommended
Large cystic components
Irregular margins/prominent nodules
Solid-enhancing elements, independent of septa

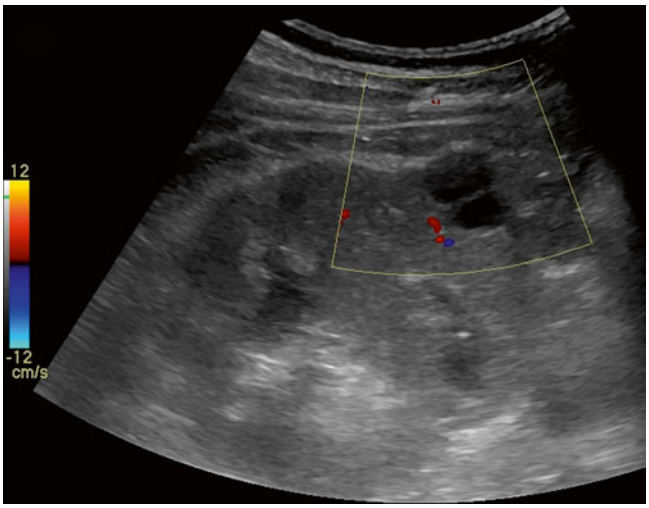

Fig. 17.4 Renal US of a patient showing a renal cyst with one septation

cysts are markedly T2 hyperintense, have a thin or imperceptible wall, display no internal architecture, and do not enhance. For cysts requiring follow-up, US and MRI are often used to minimize patient exposure to radiation.

Metastases to the Kidney

The most common tumor to metastasize to the kidney is carcinoma of the lung. Renal metastases may be multiple and bilateral and frequently are associated with metastases to other organs. Although they have nonspecific CT and MRI features, renal metastases commonly demonstrate infiltrative growth patterns. When the clinical history is available, the diagnosis may be obvious. In a patient with a history of malignancy without other metastases and a solitary renal mass, the renal mass is more likely to represent a renal cell carcinoma and not a metastasis. Nevertheless, it is possible that a single renal metastasis could occur, and differentiation from a renal cell carcinoma may not be obvious. In this situation, a renal biopsy may be diagnostic [13].

This chapter will now focus on imaging modalities to evaluate solid renal masses. As we have already discussed, different imaging modalities are available to the practicing urologist for the evaluation of a renal mass. The goal of renal lesion characterization by CT or MRI is to separate surgical lesions (RCC, cystic renal cell carcinoma, oncocytoma) from nonsurgical lesions (cyst, hemorrhagic cyst, angiomyolipoma (AML), pseudotumor). While US is a safe and readily available modality at a low cost, its use can be limited by body habitus as the sound waves are highly attenuated by the excess body tissue. 3–7 MHz transducers are used to evaluate the kidneys and surrounding structures such as the inferior vena cava (IVC) and renal veins. US can be helpful in assessing the IVC for tumor thrombus and evaluating the extent of the thrombus. However, CT and MRI have the advantage of identifying metastatic disease (Fig. 17.5) and to differentiate tumor thrombus from bland thrombus, because tumor thrombus is vascular unlike bland thrombus. US is also used intraoperatively to identify the extent of the thrombus as well as to locate multiple solid masses in multifocal RCC.

Contrast-Enhanced Ultrasound

Contrast-enhanced ultrasound (CEUS) is a modality developed over the last decade. It provides blood flow and tissue perfusion information based on a microbubble contrast agent and contrast-specific imaging software. Ultrasound contrast agents remain in the vascular system and are not excreted into the renal collecting system so these agents are not nephrotoxic and can be administered in patients with renal insufficiency. The microbubbles are removed from circulation by the lungs and liver. There is growing clinical evidence that CEUS is a reliable diagnostic tool in differentiating solid tumors and complicated cysts of the kidney and in the classification of cystic lesions as benign or malignant. Solid renal tumors generally show an early intense arterial enhancement equal or greater than that of the surrounding renal parenchyma. Intralesional areas without contrast enhancement suggest the presence of necrosis [19]. CEUS use has also been described to be as effective as CT and MRI for the follow-up of small renal masses after cryoablation [20]. While CEUS is being used in other countries for the evaluation of liver and kidney lesions, it is only approved in the United States by the FDA for use in cardiac imaging.

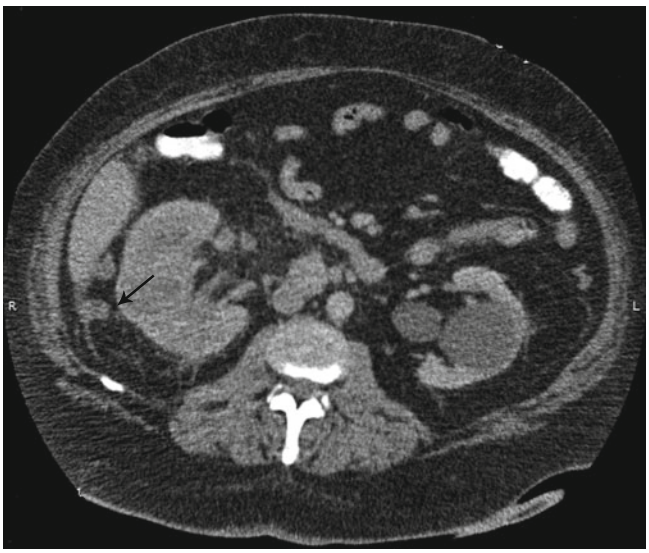

Fig. 17.5 CT scan with IV contrast showing a patient with right renal mass with retroperitoneal lymphadenopathy (*arrow*) and infiltration of Gerota's fascia (*arrow*)

Computed Tomography

Four distinct phases of renal enhancement can be imaged depending on acquisition time. The timing of these phases varies with the speed of intravenous contrast injection [21].

1. Arterial phase: This is a short phase, which occurs at about 15–25 seconds after the initiation of intravenous contrast injection; there is maximum opacification of the renal arteries during this phase. The renal veins also usually opacify in the late arterial phase.
2. Corticomedullary phase: This phase starts at about 25–70 seconds after the initiation of intravenous contrast injection. There is intense enhancement of the renal cortex due to preferential arterial flow to the cortex and glomerular filtration of the contrast material while the medulla remains relatively less enhanced. This phase

provides information about the vascularity of solid renal masses and is also the best phase for maximum opacification of the renal veins.
3. Nephrographic phase: This phase begins at 80–120 seconds and the contrast filters through the glomeruli into the collecting ducts and provides homogeneous enhancement of the normal renal parenchyma. This is the best phase for the detection of subtle parenchymal lesions.
4. Excretory phase: Starts at 180 seconds and at this point the contrast excretion allows opacification of the calyces, renal pelvis, and ureters, while the intensity of the nephrogram progressively declines. For a complete excretory phase, images at 240 seconds should be acquired to ensure opacification of the ureter.

For evaluation of renal masses, a minimum of two acquisition sequences are required for detection and characterization of renal lesions. An initial series of unenhanced scans provides a baseline to measure the enhancement within the lesion after the administration of intravenous contrast and a corticomedullary or nephrographic phase [22, 23]. Once a renal mass is identified, it is crucial to characterize it and differentiate clinically insignificant renal cysts from solid and potentially malignant renal tumors. Renal cysts are fluid filled and are avascular lesions lacking blood flow; they demonstrate no enhancement after intravenous contrast administration. In contrast, RCC has a rich vascular supply and enhances significantly after contrast; thus, accurate measurement of the degree of enhancement in renal masses is critical to distinguish complex cysts from solid and potentially malignant lesions. To determine lesion enhancement, attenuation values within the mass before and after intravenous contrast should be measured. This area is defined as the region of interest (ROI). The physician interpreting the study should attempt to measure the same ROI on two different phases. Enhancement values of more than 10–20 HU above precontrast measurements are considered significant as CT enhancement has been reported to correlate with microvessel density in RCC which is associated with hypervascularity of the tumor [24, 25]. Ye-Hua et al. also found that enhancement of clear cell RCC was negatively associated with Fuhrman grade and contributed this finding to the presence of histologic necrosis within the tumor. Areas of necrosis are usually hypovascular thus showing decreased contrast enhancement [23] (Fig. 17.6).

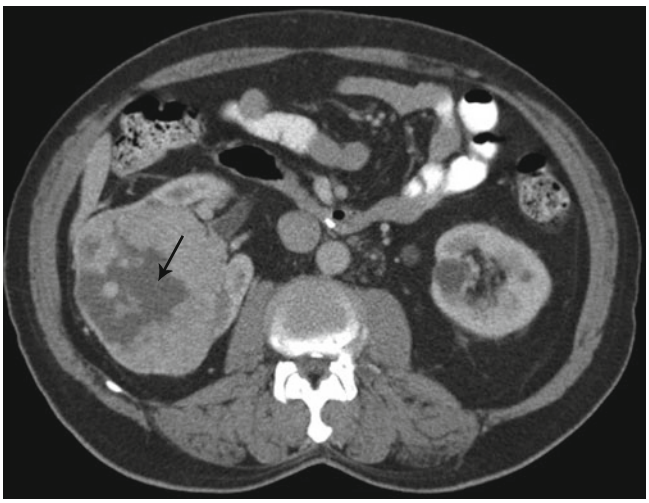

Fig. 17.6 CT scan with IV contrast showing a large right renal mass with central necrosis (*arrow*)

Magnetic Resonance Imaging

MRI is a useful tool for the characterization and presurgical staging of renal masses. MRI can be particularly helpful when renal lesions are detected but are not well characterized. The single greatest advantage of MRI imaging over US and CT is that MRI generates the highest intrinsic soft tissue contrast of any cross-sectional imaging modality (Fig. 17.7a, b). A protocol for effective MRI of the kidney should maximize soft tissue contrast, exploit the sensitivity of MRI to contrast material enhancement, and make full use of the multiplanar capability of this modality. The routine presurgical assessment of renal masses should include evaluation of the renal arterial supply and venous drainage. Correlating the anatomic findings and MRI signal intensity characteristics with the clinical features allows optimal diagnosis and staging. Diffusion-weighted imaging (DWI) is promising noninvasive imaging modalities that have been used in oncology. Recent advances in MRI technology enable DWI to show great potential in abdominal imaging and the ability to characterize renal lesions. DWI does not rely on intravenous contrast, so patients with renal failure who are at risk for nephrogenic systemic fibrosis or nephrotoxicity may particularly benefit from this technique in the evaluation for renal and upper urinary tract cancer. Several investigations have described the utility of DWI in normal kidneys, chronic renal disease, renal infection, and characterizing renal tumors. ADC value of the normal renal parenchyma is significantly higher compared to the tissues of kidney neoplasm. Mytsyk et al. showed that malignant renal tumors had significantly lower ADC values in contrast to benign tumors [26]. The ADC of a renal lesion can be potentially used as an additional parameter to help determine the appropriate clinical management.

Positron Emission Tomography

Fluorine-18-2-fluoro-2-deoxy-D-glucose (18 F-FDG) positron emission tomography (PET) is a molecular imaging modality that is the current mainstay for the management of

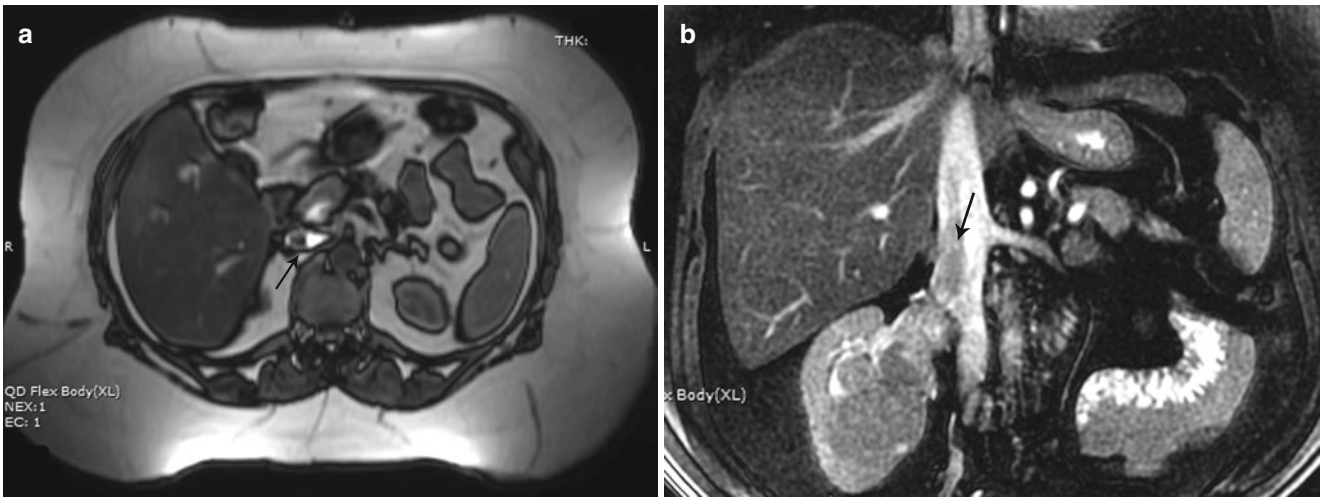

Fig. 17.7 (**a**) Axial MRI cuts showing a filling defect in the IVC from a tumor thrombus (*arrow*). (**b**) Coronal MRI cuts showing tumor thrombus extending from the right renal vein into the IVC (*arrow*)

patients with various types of cancer. This imaging technique depends on the fact that malignant tissues have a higher uptake of FDG than do the surrounding normal tissues. Increased glucose transfer across cancer cell membranes and/or increased glycolytic rates in cancer cells account for this increased uptake of FDG. Tumor cells exhibit high glucose transporter protein content and have higher levels of hexokinase and phosphofructokinase thus promoting glycolysis [27]. The clinical role of F-18 FDG PET in urologic oncology has yet to be determined, partly because of the physiological excretion of FDG through the kidneys, which makes it difficult to visualize the structures and tumors against the high background of FDG. Nakhoda et al. in a study to assess the diagnostic performance of 18 F-FDG PET/CT in 19 patients with 25 known solid malignant renal masses found an overall sensitivity of 88 % for detection of solid renal malignancies with sensitivities of 83 %, 100 %, and 100 % for RCC, secondary renal lymphomas, and renal metastases, respectively. 18 F-FDG PET/CT demonstrated some differences in metabolic activity based on renal tumor histopathological type and RCC subtype [28]. In a study by Özülker et al., a significant correlation was found between size and FDG uptakes of tumors. Fuhrman grades of tumors were also closely related with FDG avidity because the grades of FDG-positive tumors were significantly higher than the grades of FDG-negative tumors. In this study, overall sensitivity, specificity, and accuracy of F-18 FDG PET/CT for RCC were 46.6, 66.6, and 50 %, respectively [27]. F-18 FDG PET/CT imaging is highly sensitive in the detection of tumor thrombus from RCC, and it can also be used effectively for showing the malignant nature of the thrombus. Özülker et al. concluded that while PET may have limited role in the characterization of primary renal tumors, it is effective in the detection of distant metastases and can be used as a complementary tool in case the conventional imaging studies yield equivocal results [27].

A novel PET radiotracer, ^{124}I-cG250 a chimeric girentuximab labeled with 124I, is currently under clinical investigation to distinguish RCC from other benign and malignant renal masses. G250 is a monoclonal antibody that targets an epitope of carbonic anhydrase IX and has been shown in animal and human studies to bind to clear cell renal cell carcinoma. Carboxyl anhydrase IX (CAIX) protein is a transmembrane enzyme involved in cellular pH regulation, and it appears to play a role in the regulation of cell proliferation in response to hypoxic conditions in many tumors. In clear cell RCC, however, the underlying mechanism for expression of CAIX is different from that in other cancers. In clear cell RCC, hypoxia-inducible factor and CAIX are products of absence or nonfunctionality of the tumor-suppressor protein, von Hippel-Lindau, and resulting pseudohypoxia. Considering its high expression in clear cell RCC, CAIX has been investigated as an imaging target [29–31]. In a recent prospective PET-imaging trial with $^{124I\text{-}cG250}$, 94 % sensitivity and 100 % specificity support the potential clinical use of ^{124}I-cG250 antibody PET in renal masses as an alternative to biopsy for characterizing lesions. In the study, 26 patients were given a preparation of ^{124}I-cG250, all patients tolerated the ^{124}I-cG250 antibody infusion, there were no allergic or other adverse events related to the study agent or any agent-related toxic effects. The results of the study showed that of the 16 patients with a pathological diagnosis of clear cell RCC who received immunologically active antibody, 15 were identified correctly with PET, resulting in a sensitivity of 94 %. All nine patients who did not have clear cell RCC were identified correctly by PET, resulting in a specificity of 100 %. Positive predictive value for predicting clear cell RCC was 100 % and negative predictive for ruling out clear cell RCC was 90 % (55–100 %) [32].

Standardized Scoring Systems of Renal Masses

The centrality index (C-Index), preoperative aspects, and dimensions used for anatomic (PADUA) classification and the nephrometry score (RENAL) were developed as standardized scoring systems to quantify anatomic characteristics of kidney tumors. Okhunov et al. evaluated all three scoring systems and demonstrated reliability among observers [33]. Below, we will discuss the most commonly used scoring system.

The Nephrometry Score

The nephrometry score is the most widely used scoring system in the world and was developed by Drs. Kutikov and Uzzo as an imaging-based standardized reporting system of renal tumor size, location, and depth. CT or MRI imaging is used for the scoring. The RENAL Nephrometry Score consists of (R)adius (tumor size as maximal diameter), (E) xophytic/endophytic properties of the tumor, (N)earness of tumor deepest portion to the collecting system or sinus, (A) nterior (a)/posterior (p) descriptor, and the (L)ocation relative to the polar line. The suffix h (hilar) is assigned to tumors that abut the main renal artery or vein. In the initial study, the nephrometry scoring system was shown to accurately classify the complexity of 50 consecutive tumors [34]. The scoring system has also been shown in multiple studies to have good interobserver reliability [33, 35]. Currently, the nephrometry score is used to evaluate the complexity of a mass and helps in preoperative decision making. Reddy et al. evaluated the nephrometry scoring system as a predictor of complications after partial nephrectomy and found that an increase in the nephrometry score of one point resulted in greater odds of being in a higher Clavien-Dindo classification after controlling for RENAL suffix and type of surgical procedure. Furthermore, a patient with the RENAL suffix (p) had increased odds of developing more serious complications [31] (Fig. 17.8).

Radiographic Diagnosis of Histologic Subtypes

Bata et al. in a study to analyze the tumor attenuation characteristics in clear cell RCC and papillary RCC comparing the attenuation of the normal renal cortex in multiphase CT found significant differences in the attenuation ratios between clear cell and papillary RCC in the corticomedullary and nephrographic phases. Papillary RCC generally appeared as a less enhancing lesion compared with the normal renal cortex, and clear cell RCC appeared more hyperdense than papillary in these two phases [36].

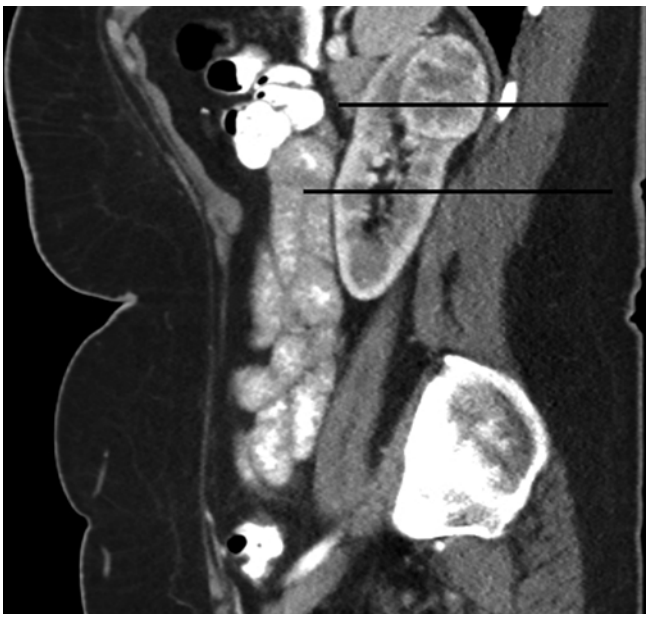

Fig. 17.8 CT scan shows a left heterogeneous renal mass in the upper pole that crosses the polar lines marked with *black lines*. Less than 50 % of the mass is exophytic and is within 2.3 mm from the collecting system. The diameter of the mass is 4.4 mm. The calculated RENAL nephrometry score was R.2 + E.2 + N.3 + A.P + L.2 = 9p

Pierorazio et al. did a study using multiphasic CT and evaluated the prediction of histologic diagnosis in small renal masses (SRMs) less than 4 cm. The group evaluated three distinct patterns of attenuation. They concluded that papillary RCC had the most distinct pattern, with relatively low levels of peak enhancement and relatively little fluctuation in attenuation from the corticomedullary through the delayed phase. Papillary RCC demonstrated low levels of absolute enhancement in the corticomedullary (≤30 HU) and nephrographic (≤40 HU) phases. This pattern does not exclude other tumor histology. However, tumors demonstrating a low, flat enhancement pattern have a >70 % likelihood of being papillary RCC [37]. The second pattern with rapid, high attenuation enhancement that quickly washes out in the delayed phase was indicative of clear cell RCC or oncocytoma. In a study of SRMs, Jinzaki et al. demonstrated that clear cell RCC and oncocytoma showed a peak enhancement >100 HU, whereas other tumors enhanced to <100 HU [24]. A small renal mass (SRM) that demonstrates a high, early enhancement pattern has a higher likelihood of being clear cell RCC than oncocytoma, chromophobe, AML, or papillary RCC. More than 70 % of tumors that retained actual enhancement of >80 HU were clear cell RCC [38]. Unfortunately, there was widespread crossover between benign and malignant histology within the third, intermediate pattern of enhancement. Most SRMs falling within the pattern of intermediate enhancement will be RCC, but this may not provide useful clinical data beyond what is known epidemiologically.

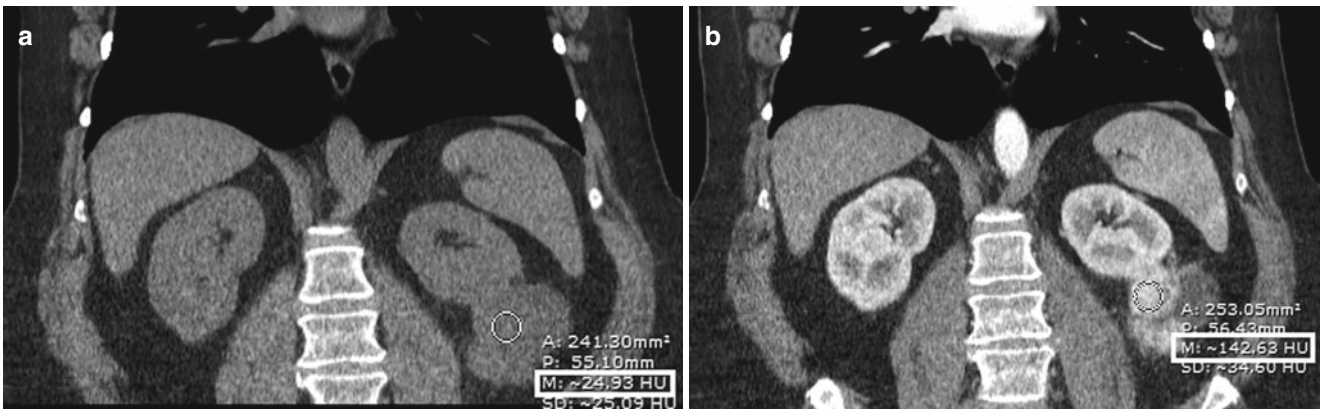

Fig. 17.9 CT scan with coronal cuts of a patient with pathologically proven clear cell RCC. (**a**) Noncontrast images, (**b**) nephrographic phase images. During the nephrographic phase, the left renal mass enhances up to 142 HU (by an additional 118 HU from noncontrast images) quite typical for clear cell RCC

In addition to a multiphasic CT, several other modalities continue to be evaluated as a predictor of malignancy or specific histology using MRI or PET CT (see MRI and PET sections above). Below are studies that specifically addressed the subtypes of RCC using any of the available modalities.

Clear Cell RCC

An additional tool to aid with diagnosis of renal mass histology is the washout formula introduced by Kopp et al. in 2013. An absolute enhancement washout value was calculated by the formula (mass nephrographic HU – mass delayed HU)/(mass nephrographic HU – mass noncontrast HU). Enhancement washout value <0 on CT imaging is highly specific for papillary RCC and non-clear cell RCC. Clear cell RCC is essentially excluded if the renal mass enhanced on all postcontrast phases. Washout value ≥0 is highly sensitive for clear cell RCC, oncocytoma, and AML [39].

In differentiating subtypes of RCC, the enhancement pattern is a useful parameter, particularly to differentiate clear cell from non-clear cell RCCs. Clear cell RCCs show stronger enhancement (Fig. 17.9) than do non-clear RCCs, which results from their rich vascular network and alveolar architecture at histological examination. Choi et al. in a recent study evaluated the three most common RCC subtypes; clear cell, chromophobe, and papillary using 3-T DWI MRI. This modality was found to be useful for differentiation of the three subtypes based on the apparent diffusion coefficient (ADC) maps [40]. The mean ADC values of all RCCs were statistically significantly lower than those of the normal renal parenchyma. Wang et al. also showed DWI at 3-T allows sensitive and specific differentiation of clear cell, papillary, and chromophobe RCCs. These findings suggest that DWI may be useful in the preoperative characterization of RCC [41]. The MRI appearance of clear cell RCC varies depending on the presence of hemorrhage and necrosis. Clear cell RCC most frequently demonstrates a signal intensity similar to that of the renal parenchyma on T1-weighted images and increased signal intensity on T2-weighted images. Central necrosis is common and is typically seen as a homogeneous hypointense area in the center of the mass on T1-weighted images and moderate to high signal intensity on T2-weighted images. In the presence of central necrosis, a solid rim of tumor is frequently seen at the periphery of the mass. Postcontrast images demonstrate lack of enhancement in areas of necrosis and marked enhancement in the viable components of the tumor. Hemorrhage into the tumor may occur and has a variable appearance depending on the stage of degradation of the component blood products. Subacute to chronic hemorrhage generally demonstrates high signal intensity on both T1- and T2-weighted images. Long-standing hemorrhage, which predominantly contains hemosiderin, is typically hypointense on both T1- and T2-weighted images. In addition, clear cell RCC tends to be hypervascular, with heterogeneous enhancement during the arterial phase. Renal vein tumor thrombus can be seen with aggressive higher-stage tumors. A tumor capsule of low signal intensity on T1- and T2-weighted images may be observed, and its interruption is associated with locally advanced disease and higher nuclear grade [42].

As discussed above in the PET section, novel imaging techniques are promising for detection of clear cell with excellent sensitivity and high specificity.

Papillary RCC

Papillary RCC demonstrates homogeneous low signal intensity on T2-weighted images and homogeneous low-level enhancement after intravenous contrast material administration (Fig. 17.10). Necrosis and hemorrhage may be present in low-grade type I tumors. Cytoplasmic or interstitial histiocytic hemosiderin deposition provides an accurate distinction from clear cell RCC, which typically exhibits heterogeneously increased signal intensity on T2-weighted images [42]. The overall sensitivity and specificity of MRI to predict the histologic subtype using a feature analysis are

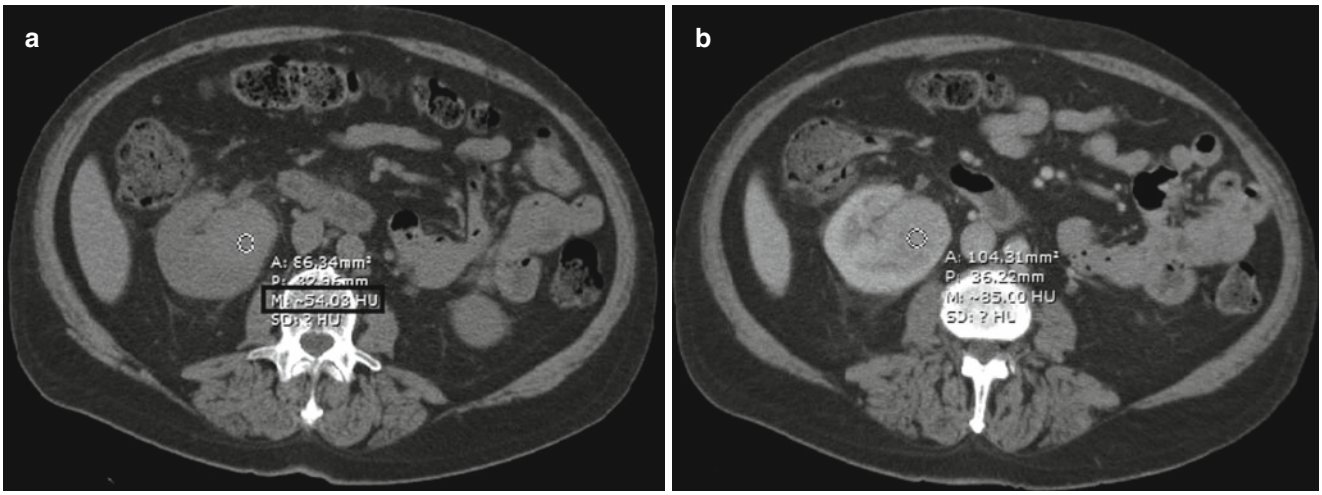

Fig. 17.10 Axial images of a patient with pathologically proven papillary RCC. (**a**) Noncontrasted image showing a mass in the right kidney measuring 54 HU. (**b**) Contrasted CT demonstrating enhancing renal mass 85 HU (by only additional 30 HU), quite typical for papillary RCC (see Fig. 17.8, demonstrating higher level of enhancement after IV contrast administration)

80 % and 94 %, respectively [43]. Enhancing papillary projections at the periphery of a cystic hemorrhagic mass are common and can be better depicted on subtraction images. Mileto et al. evaluated iodine quantification with a dual-energy multidetector CT to distinguish between clear cell and papillary RCC subtypes and found iodine quantification can be used to noninvasively discriminate between clear cell and papillary RCC subtypes at a single time point. Their data suggest that an iodine concentration threshold of 0.9 mg/mL optimizes the discrimination between clear cell and papillary RCC subtypes during the nephrographic phase of renal enhancement with an overall accuracy of 95.3 % [44].

Chromophobe RCC

Identifying chromophobe RCC is challenging. Chromophobe RCC tends to have a greater propensity for homogeneity and the presence of a central scar or necrosis [45]. Central necrosis may be absent even in very large chromophobe carcinomas. Their enhancement characteristics fall in between those of clear cell and papillary RCC, but there is considerable overlap. Although the imaging features of chromophobe RCC can be identical to those of clear cell RCC, the chromophobe subtype tends to have a better prognosis.

Angiomyolipoma

Angiomyolipomas (AMLs) are hamartomas containing varying proportions of fat, smooth muscle, and thick-walled blood vessels. AMLs can be symptomatic and patients may present with any of the following: pain, gross hematuria, anemia, and/or hypertension. Tumors greater than 4 cm carry an increased risk for potentially life-threatening hemorrhage, which has been reported in up to 10 % of these patients. A reliable diagnosis of AML can be made when fat is unequivocally demonstrated in a renal mass. AMLs with a predominant fatty component are isointense relative to fat with all MRI sequences, and they are hyperintense compared to renal parenchyma on T1-weighted images. In predominantly fatty AMLs, a characteristic India ink artifact is seen at the interface between the mass and the normal renal parenchyma on opposed-phase T1-weighted images, whereas the central portions of the lesion do not demonstrate changes in signal intensity compared with the in-phase images. The appearance of AML on T2-weighted images is variable and depends on the amount of bulk fat present in the lesion. Lipid-poor AMLs frequently demonstrate homogeneous low signal intensity relative to the renal parenchyma on T2-weighted images. Contrast-enhanced MRI does not help differentiate AML from other solid neoplasms as they can show different degrees of enhancement depending on the amount of vascularized tissue components they contain. On CT, the fatty portions of the lesion will measure −30 HU or less. If a very small amount of fat is suspected in a renal mass, it may be necessary to perform very thin sections without intravenous contrast to maximize the ability to depict fat within the lesion. In the extremely rare instance in which these lesions do not contain any fat (angiomyoma), the preoperative diagnosis of hamartoma cannot be made, and the lesion is indistinguishable from a renal cell carcinoma [13]. If a renal mass contains calcification in addition to fat, the possibility of renal cell carcinoma should not be ruled out. A clear diagnosis of AML cannot be made if calcium is present within a fat-containing lesion, and biopsy or surgery should be considered in these cases [13].

Oncocytoma

The MR imaging appearance of oncocytomas is variable and nonspecific. Oncocytomas are typically spheric and well-defined masses. Relative to the renal cortex, they have lower

signal intensity on T1-weighted images and higher signal intensity on T2-weighted images. The central scar if present can be seen as a stellate area of low signal intensity on T1-weighted MRI, high signal intensity on T2-weighted MRI, or on conventional CT. In a study attempting to distinguish oncocytoma from subtypes of RCC using CT, Bird et al. found a percentage enhancement of 500 % in the corticomedullary phase and a washout value of >50 % to be predictive of oncocytoma [38].

Imaging Guidelines for the Follow-Up of Clinically Localized Renal Neoplasms

The AUA has set forth guidelines including imaging for follow-up of renal neoplasms. Patients should undergo a baseline abdominal scan (CT or MRI) for nephron-sparing surgery and abdominal imaging (US, CT, or MRI) for radical nephrectomy within 3–12 months following renal surgery. In low-risk (pT1, N0, Nx) disease, following a radical nephrectomy imaging with US, CT, or MRI is optional if the initial postoperative baseline imaging is negative. Following a partial nephrectomy, US, CT, or MRI may be performed yearly for 3 years if the initial postoperative scan is negative. In moderate-to-high-risk patient (pT2-4 N0), a baseline chest and abdominal scan (CT or MRI) is recommended within 3–6 months following surgery with continued imaging (US, CXR, CT, or MRI) every 6 months for at least 3 years and annually thereafter to year five. Imaging beyond 5 years is left to the discretion of the clinician. Routine FDG PET scan is not indicated in the follow-up for renal cancer. In patients on active surveillance, a CT or MRI within 6 months of initiating active surveillance is recommended to establish a growth rate as well as an US, CT, or MRI obtained annually for continuous surveillance [1].

In conclusion, all imaging modalities have value. However, each modality has its own advantages and disadvantages and may be more or less appropriate in a given circumstance. It is important that physicians have the full array of imaging options available so that they can exercise their medical judgment to select the imaging modality that best meets the needs of any given patient.

References

1. Donat SM, et al. Follow-up for clinically localized renal neoplasms: AUA Guideline. J Urol. 2013;190(2):407–16.
2. Fernbach SK, Maizels M, Conway JJ. Ultrasound grading of hydronephrosis: introduction to the system used by the Society for Fetal Urology. Pediatr Radiol. 1993;23(6):478–80.
3. Arrabal-Polo MA, et al. Calcium nephrolithiasis and bone demineralization: pathophysiology, diagnosis, and medical management. Curr Opin Urol. 2014;24(6):633–88.
4. Semins MJ, Matlaga BR. Kidney stones during pregnancy. Nat Rev Urol. 2014;11(3):163–8.
5. Masselli G, et al. Imaging of stone disease in pregnancy. Abdom Imaging. 2013;38(6):1409–14.
6. Dhar M, Denstedt JD. Imaging in diagnosis, treatment, and follow-up of stone patients. Adv Chronic Kidney Dis. 2009;16(1):39–47.
7. Smith-Bindman R, et al. Ultrasonography versus computed tomography for suspected nephrolithiasis. N Engl J Med. 2014;371(12):1100–10.
8. Kuwahara M, et al. Computed tomography and composition of renal calculi. Urol Res. 1984;12(2):111–3.
9. Kalb B, et al. Acute abdominal pain: is there a potential role for MRI in the setting of the emergency department in a patient with renal calculi? J Magn Reson Imaging. 2010;32(5):1012–23.
10. Krepkin K, et al. Dynamic contrast-enhanced MR renography for renal function evaluation in ureteropelvic junction obstruction: feasibility study. AJR Am J Roentgenol. 2014;202(4):778–83.
11. Sasamori H, et al. Utility of apparent diffusion coefficients in the evaluation of solid renal tumors at 3T. Magn Reson Med Sci. 2014;13(2):89–95.
12. Yoshida S, et al. Role of diffusion-weighted magnetic resonance imaging in predicting sensitivity to chemoradiotherapy in muscle-invasive bladder cancer. Int J Radiat Oncol Biol Phys. 2012;83(1):e21–7.
13. Israel GM, Bosniak MA. Renal imaging for diagnosis and staging of renal cell carcinoma. Urol Clin North Am. 2003;30(3):499–514.
14. Dyer R, DiSantis DJ, McClennan BL. Simplified imaging approach for evaluation of the solid renal mass in adults. Radiology. 2008;247(2):331–43.
15. Whelan TF. Guidelines on the management of renal cyst disease. Can Urol Assoc J. 2010;4(2):98–9.
16. Bosniak MA. The use of the Bosniak classification system for renal cysts and cystic tumors. J Urol. 1997;157(5):1852–3.
17. Curry NS, Cochran ST, Bissada NK. Cystic renal masses: accurate Bosniak classification requires adequate renal CT. AJR Am J Roentgenol. 2000;175(2):339–42.
18. Ellimoottil C, et al. New modalities for the evaluation and surveillance of complex renal cysts. J Urol. 2014;192(6):1604–11.
19. Siracusano S, et al. The current role of contrast-enhanced ultrasound (CEUS) imaging in the evaluation of renal pathology. World J Urol. 2011;29(5):633–8.
20. Zeccolini G, et al. Comparison of Contrast-Enhanced Ultrasound Scan (CEUS) and MRI in the follow-up of cryoablation for small renal tumors. Experience on 25 cases. Urologia. 2014;81 Suppl 23:1–8.
21. Sheth S, Fishman EK. Multi-detector row CT of the kidneys and urinary tract: techniques and applications in the diagnosis of benign diseases. Radiographics. 2004;24(2):e20.
22. Yuh BI, et al. Comparison of nephrographic with excretory phase helical computed tomography for detecting and characterizing renal masses. Can Assoc Radiol J. 2000;51(3):170–6.
23. Zhu YH, et al. Low enhancement on multiphase contrast-enhanced CT images: an independent predictor of the presence of high tumor grade of clear cell renal cell carcinoma. AJR Am J Roentgenol. 2014;203(3):W295–300.
24. Jinzaki M, et al. Double-phase helical CT of small renal parenchymal neoplasms: correlation with pathologic findings and tumor angiogenesis. J Comput Assist Tomogr. 2000;24(6):835–42.
25. Wang JH, et al. Dynamic CT evaluation of tumor vascularity in renal cell carcinoma. AJR Am J Roentgenol. 2006;186(5):1423–30.
26. Mytsyk Y, et al. Value of the diffusion-weighted MRI in the differential diagnostics of malignant and benign kidney neoplasms – our clinical experience. Pol J Radiol. 2014;79:290–5.
27. Ozulker T, et al. A prospective diagnostic accuracy study of F-18 fluorodeoxyglucose-positron emission tomography/computed

tomography in the evaluation of indeterminate renal masses. Nucl Med Commun. 2011;32(4):265–72.
28. Nakhoda Z, et al. Assessment of the diagnostic performance of (18) F-FDG-PET/CT for detection and characterization of solid renal malignancies. Hell J Nucl Med. 2013;16(1):19–24.
29. Khandani AH, et al. PET/CT with (124)I-cG250: great potential and some open questions. AJR Am J Roentgenol. 2014;203(2):261–2.
30. Khandani AH, Rathmell WK. Positron emission tomography in renal cell carcinoma: an imaging biomarker in development. Semin Nucl Med. 2012;42(4):221–30.
31. Macis G, et al. Future perspectives for diagnostic imaging in urology: from anatomic and functional to molecular imaging. Urologia. 2013;80(1):29–41.
32. Divgi CR, et al. Preoperative characterisation of clear-cell renal carcinoma using iodine-124-labelled antibody chimeric G250 (124I-cG250) and PET in patients with renal masses: a phase I trial. Lancet Oncol. 2007;8(4):304–10.
33. Okhunov Z, et al. The comparison of three renal tumor scoring systems: C-Index, P.A.D.U.A., and R.E.N.A.L. nephrometry scores. J Endourol. 2011;25(12):1921–4.
34. Kutikov A, Uzzo RG. The R.E.N.A.L. nephrometry score: a comprehensive standardized system for quantitating renal tumor size, location and depth. J Urol. 2009;182(3):844–53.
35. Kolla SB, Spiess PE, Sexton WJ. Interobserver reliability of the RENAL nephrometry scoring system. Urology. 2011;78(3):592–4.
36. Bata P, et al. Clear cell renal cell carcinoma and papillary renal cell carcinoma: differentiation of distinct histological types with multiphase CT. Diagn Interv Radiol. 2013;19(5):387–92.
37. Pierorazio PM, et al. Multiphasic enhancement patterns of small renal masses (</=4 cm) on preoperative computed tomography: utility for distinguishing subtypes of renal cell carcinoma, angiomyolipoma, and oncocytoma. Urology. 2013;81(6):1265–71.
38. Bird VG, et al. Differentiation of oncocytoma and renal cell carcinoma in small renal masses (<4 cm): the role of 4-phase computerized tomography. World J Urol. 2011;29(6):787–92.
39. Kopp RP, et al. Differentiation of clear from non-clear cell renal cell carcinoma using CT washout formula. Can J Urol. 2013;20(3):6790–7.
40. Choi YA, et al. Subtype differentiation of renal cell carcinoma using diffusion-weighted and blood oxygenation level-dependent MRI. AJR Am J Roentgenol. 2014;203(1):W78–84.
41. Wang H, et al. Renal cell carcinoma: diffusion-weighted MR imaging for subtype differentiation at 3.0 T. Radiology. 2010;257(1):135–43.
42. Pedrosa I, Alsop DC, Rofsky NM. Magnetic resonance imaging as a biomarker in renal cell carcinoma. Cancer. 2009;115(10 Suppl):2334–45.
43. Pedrosa I, et al. MR classification of renal masses with pathologic correlation. Eur Radiol. 2008;18(2):365–75.
44. Mileto A, et al. Iodine quantification to distinguish clear cell from papillary renal cell carcinoma at dual-energy multidetector CT: a multireader diagnostic performance study. Radiology. 2014;273(3):813–20.
45. Raman SP, et al. Chromophobe renal cell carcinoma: multiphase MDCT enhancement patterns and morphologic features. AJR Am J Roentgenol. 2013;201(6):1268–76.

Renal Mass Biopsy

18

Nnenaya Agochukwu and Brian Shuch

Over the past few years, there has been an increase in the incidence of incidentally discovered small renal tumors, believed to be related to the widespread availability and utilization of cross-sectional imaging modalities [1, 2]. With early detection of incidental lesions, some centers have advocated a larger role of percutaneous renal mass biopsy for diagnostic purposes [3]. Traditionally, indications for renal mass biopsy were for diagnosis of suspected lymphoma or metastatic disease and had little role in management. Many centers now utilize renal mass biopsy for other indications such as obtaining a tissue diagnosis prior to ablative therapies, confirming histology prior to cytoreductive nephrectomy, and enrollment into active surveillance programs.

While interventional radiologists have traditionally performed the targeted renal mass biopsy, an increasing number of urologists with training in image-guided biopsies have began performing these procedures to aid their management. The goal of this chapter is to explore methods, safety, complications, and accuracy and to discuss current and expanding indications.

Accuracy of Renal Mass Biopsy

The diagnosis of renal cell carcinoma has differed from other solid malignancies in that a preoperative diagnosis has traditionally relied on imaging for suspicion of benign versus malignant disease. Most solid enhancing renal lesions are considered suspicious for renal cell carcinoma until proven otherwise and may be considered for surgical resection even in the absence of a tissue diagnosis [4]. Cystic renal lesions also have a distinct classification system based on cross-sectional imaging which is often used to guide management [5]. Despite improvements in imaging techniques, due to overlapping imaging characteristics of the various renal tumors, no imaging modality has sufficient sensitivity or specificity to predict benign disease [6]. The inability to predict benign disease with conventional modalities has led to a high rate of surgical removal of benign tumors. A study by Frank et al. found that 12.8 % of all masses removed at nephrectomy were actually benign with the incidence of benign pathology increasing with decreasing tumor size. For lesions ≤1 cm, 44 % were found to be benign after resection [7]. Loss of renal function after surgery has significant adverse health outcomes including renal and cardiac events [8]. Therefore, any reliable method to prevent unnecessary kidney loss would be an extremely useful clinical tool [8].

Renal Mass Biopsy Diagnosis of Malignancy

Image-guided biopsy of renal masses has proven to be safe and effective and have a high diagnostic yield. Overall, ≥80 % of renal mass biopsies contain enough material to make a pathologic diagnosis [9]. Depending on the series, the diagnostic sensitivity and specificity ranges from 80 % to 92 % and 83 % and 100 %, respectively [10]. A systematic literature review was performed by Lane and colleagues and evaluated the performance of nearly 2500 percutaneous renal biopsies. In this series, the positive and negative predictive value of a biopsy was 97.5 % and 82 %, respectively. Additionally, both the sensitivity and specificity were also nearly 92.1 % and 89.7 %, respectively.

Despite the accuracy of renal biopsy, there are times when there is insufficient material, and the biopsy is considered nondiagnostic. This may be avoided with an on-site cytopathology technologist reviewing the specimens prior to conclusion of the procedure. Success is greater for lesions that are larger and completely solid [11]. After a nondiagnostic biopsy, it's essential to look at the biopsy images to see if the trajectory of the needle went into the lesion in question. Occasionally, the prior biopsy may have clearly missed the

N. Agochukwu, MD
Department of Urology, Yale School of Medicine, New Haven, CT, USA

B. Shuch, MD (✉)
Department of Urology and Diagnostic Radiology, Yale School of Medicine, New Haven, CT, USA
e-mail: brian.shuch@yale.edu

A.R. Rastinehad, D.N. Siegel (eds.), *Interventional Urology*, DOI 10.1007/978-3-319-23464-9_18

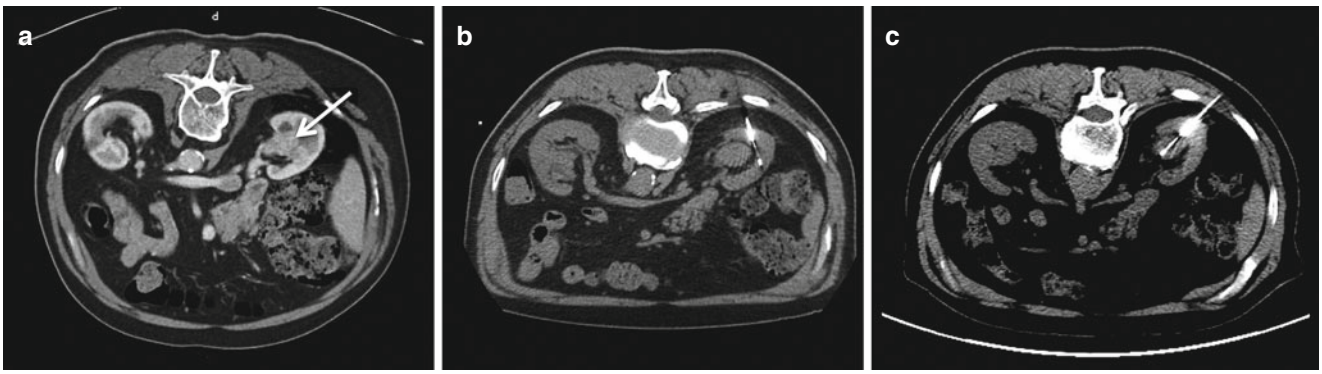

Fig. 18.1 An example of sampling error from a renal biopsy. (**a**) The tumor on contrast-enhanced imaging (*white arrow*). (**b**) The needle trajectory and biopsy performed from an outside hospital which showed normal parenchyma. (**c**) Repeat biopsy performed directly into the lesion between rib 11 and 12 which later demonstrated a Fuhrman grade III clear-cell kidney tumor

target lesion and caused a sampling error. In these cases, a repeat biopsy should be considered (Fig. 18.1a, b). Leveridge reported the outcome of 12 patients who underwent a repeat biopsy of a suspicious lesion and found that ten (83.3 %) had a successful tissue diagnosis.

Diagnosis of Histologic Subtype and Grade

Percutaneous renal biopsy may not only serve to diagnose renal cell carcinoma, but may provide further pathologic information including the identification of subtype and assessment of tumor grade. If a high-grade tumor or an aggressive subtype is found, a different management strategy may be worth considering. The diagnostic accuracy of distinguishing subtype of malignant tumors is approximately 80 % [12]. A study by Renshaw et al. assessed the accuracy of fine-needle aspiration (FNA) in identifying or distinguishing subtypes of renal cell carcinoma. There were 34 tumors studied, and of this, 74 % were correctly subtyped when compared to the nephrectomy specimen [13]. The accuracy of distinguishing grade and histology may be further improved with core needle biopsy. Neuzillet et al. assessed 88 patients who underwent a CT-guided core needle biopsy and found it accurate in identifying subtype and Fuhrman grade in 92 % and 69.8 %, respectively [14]. Incorporation of adjunct pathologic methods such as immunohistochemistry and assessment of cytogenetic changes may further improve the capability to characterize tumor subtype.

Biopsy Indications

Established Indications

There is no question that percutaneous renal biopsy will continue to expand and play a role in the diagnosis and management of renal masses. Currently, most experts recommend biopsy of renal masses when the diagnosis would change management, including the choice of surgery or systemic therapy. Established indications include patients with a renal mass who have an advanced, nonrenal malignancy such as melanoma, lung cancer, breast cancer, lymphoma, and colon cancer. Often, imaging may be suggestive of a metastasis when enhancement is less robust than for primary renal tumors; however, this characteristics is not definitive [15]. If the renal mass detected is a metastasis, the management is much different except in rare cases where there is a role for metastasectomy for an isolated lesion. In addition, patients with a renal mass that is deemed technically unresectable or who may not be a surgical candidate, a biopsy can help guide selection for systemic therapy. In patients who have a history of urinary tract infections such as pyelonephritis, a renal lesion may represent a focal abscess or carbuncle. In this setting, a percutaneous renal biopsy may avoid an unnecessary surgery. Finally, in patients with an atrophic kidney, it is not uncommon to have a spared region of parenchyma that may also resemble a tumor (a pseudotumor). It is often not possible to give patients intravenous contrast in this situation due to chronic kidney disease, and we prefer a confirmatory biopsy prior to offering management (Fig. 18.2a–c).

Emerging Indications

With improvements in detection of benign lesions and detection of subtype, there are emerging indications for biopsy. We consider a renal mass biopsy in elderly patients or those with small renal masses where identification of an oncocytoma or oncocytic tumor with a more indolent potential would lead to consideration of nonoperative management. Additionally, prior to enrollment in an active surveillance protocol, we believe identification of tumor characteristics provides insight into tumor biology. Occasionally, we identify an aggressive subtype or a high-grade lesion and consider treatment for these individuals. For patients who are considered for lapa-

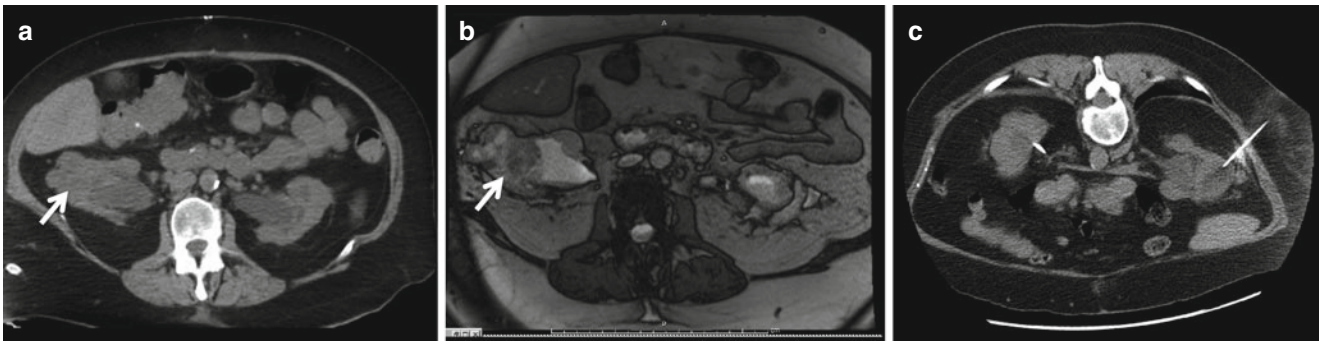

Fig. 18.2 Non-contrast (**a**) CT and (**b**) MRI in a 62-year-old female with CKD stage IV who had an irregular 4.5 cm right renal lesion (*white arrow*). (**c**) A percutaneous biopsy was performed for confirmation that this represented a mass versus asymmetric cortical hypertrophy. The biopsy confirmed the presence of a Fuhrman grade II clear-cell kidney tumor

roscopic or percutaneous ablation, many advocate for percutaneous biopsy before or at the time of treatment [4]. While both approaches are acceptable, we generally perform this in a separate setting prior to treatment and then proceed with ablation once a malignant histology is confirmed. We advocate combing procedures in certain circumstances such as when stopping anticoagulants is an issue. Finally, in cases of an extremely challenging partial nephrectomy where resection of the tumor will require collecting system entry and enucleation of the renal hilum, we occasionally utilize percutaneous biology to better characterize the lesion. In Fig. 18.3a–d, we demonstrate one such case in a lesion with a high nephrometry score (11) where three regions of the tumor were sampled and a Fuhrman grade II clear-cell RCC was identified. Due to the perceived lower grade and biologic potential, we did an open partial nephrectomy utilizing enucleative resection. Had this been a very high-grade lesion or an aggressive histologic type, we had discussed proceeding with a laparoscopic radical nephrectomy.

Complications of Renal Mass Biopsy

The initial experience with renal mass biopsy was associated with substantial morbidity. Recently, reviews have demonstrated that mortality is exceedingly rare and even minor complications are <2 % [9]. Complications of renal mass biopsy include tumor seeding, bleeding, infection, arteriovenous fistula, and pneumothorax. Each of these risks will be individually explored in the following sections. In light of the low rate of complications, the benefit of avoiding a morbid operation often outweighs the risk associated with renal mass biopsy.

Bleeding Risk

Hemorrhage is the most frequently encountered complication of renal biopsy. Modifiable factors such as coagulation parameters and hypertension should be optimized; however, even when these factors are controlled, there is still a high bleeding risk. It is recommended that patients on blood thinners be evaluated for cessation prior to biopsy, and those patients with history of bleeding diathesis be properly worked up. It has been widely believed that needle size plays a role in the risk of bleeding. For native kidneys, it has been demonstrated that the risk of bleeding can be fourfold greater if a 14 gauge needle is used versus smaller gauges [16]. However, in animal models, Gazelle and colleagues found no significant difference in bleeding risk between 18, 20, and 22 gauge needles [17]. We prefer to use a 17 gauge introducer with an 18 gauge needle to provide quality tissue cores with the theoretical benefit at limiting the risk of bleeding.

Identification of bleeding after biopsy is highly dependent on the use of post-procedural imaging. Ralls and colleagues investigated the incidence of bleeding by performing a CT scan and ultrasound 24–72 h after biopsy. CT scan was more sensitive and specific than US for detecting hemorrhage. A surprisingly high frequency of patients (90.8 %) were identified with a hemorrhage on CT scan. However, only two of these hematomas were clinically significant requiring treatment. While the risk of bleeding is high, generally, most patients will have a small hematoma that is not clinically significant.

Post-biopsy patients must be observed while lying supine to tamponade any bleeding. The optimal timing of observation after a renal mass biopsy has not been established. In the native renal biopsy literature, the timing of complications has been specifically addressed. Historically, patients were observed for 24 h for observation. Two large series assess the timing of major complications in patients who were kept for overnight observation. Several studies have suggested that 42–52 % and 85–95 % of complications are observed within 4 and 12 h, respectively [18, 19]. Most centers observe patients undergoing renal mass biopsies for approximately 4 h unless they are considered to have a significant risk of bleeding.

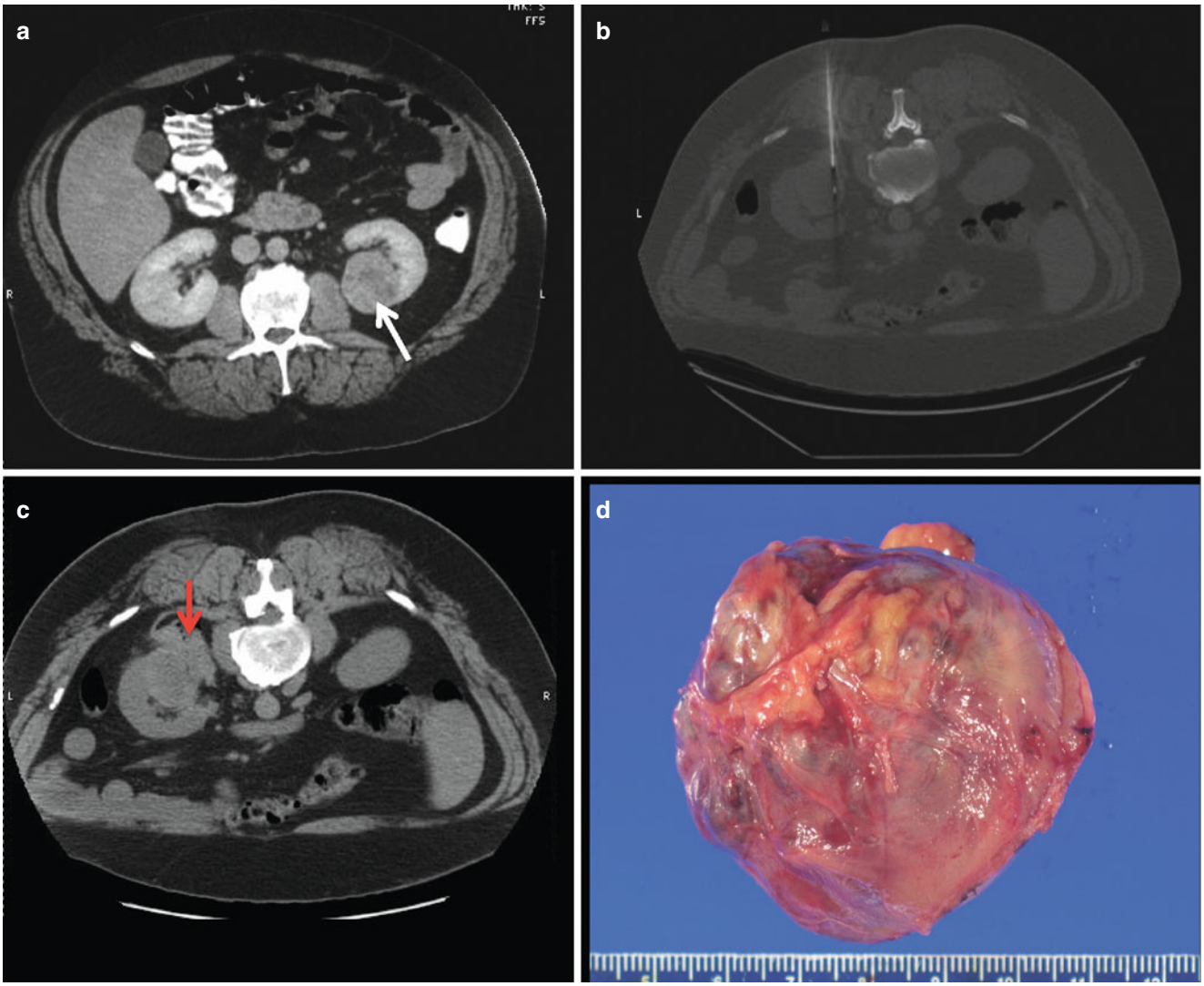

Fig. 18.3 (**a**) A 47-year-old man with an incidentally detected 5.5 cm left renal mass with a nephrometry score of 11 ph (*white arrow*). (**b**) A renal biopsy was performed to help guide the choice of therapy. (**c**) There was some mild asymptomatic hematoma (*red arrow*) after the procedure. (**d**) Once several cores demonstrated a Fuhrman grade 1–2 clear-cell renal mass, we proceeded with a complex partial nephrectomy confirming the presence of a low-grade T1b renal tumor

Significant bleeding complications appear to be higher in patients who need to undergo a random kidney biopsy for diagnosis of medical renal disease. Many of these patients may have platelet dysfunction from uremia or from aspirin or clopidogrel, thrombocytopenia, as well as having significant hypertension. A large meta-analysis was found; the overall rate of transfusion and gross hematuria is 1 % and 3.5 %, respectively, [16] much higher than what is observed in modern series of renal mass biopsies. Coprai and colleagues found that having elevated creatinine or being anemic are risk factors for post-biopsy hemorrhage with random kidney biopsies [16], which are obviously less frequent in patients who undergo a renal mass biopsy.

Occasionally, patients may develop hemodynamic instability for significant bleeding. In our experience, this is more common in frail patients or those on multiple hypertensive medications who have remained NPO for several hours before the procedure (Fig. 18.4a, b). Wood and colleagues examined clinically significant bleeding complications (requiring blood transfusion or embolization) after 79 renal mass biopsies. In this study, there were no major bleeding complications. In the case of a clinically significant bleed, rarely is surgery required. Conservative management with fluids and/or transfusion is generally all that is necessary. In the setting of a major post-biopsy hemorrhage, if angiography is available, we advocate for immediate selective embolization. While bleeding almost always stops with conservative management, embolization of active bleeding may prevent expansion into a large hematoma that could take months to reabsorb and cause a significant delay in surgical management.

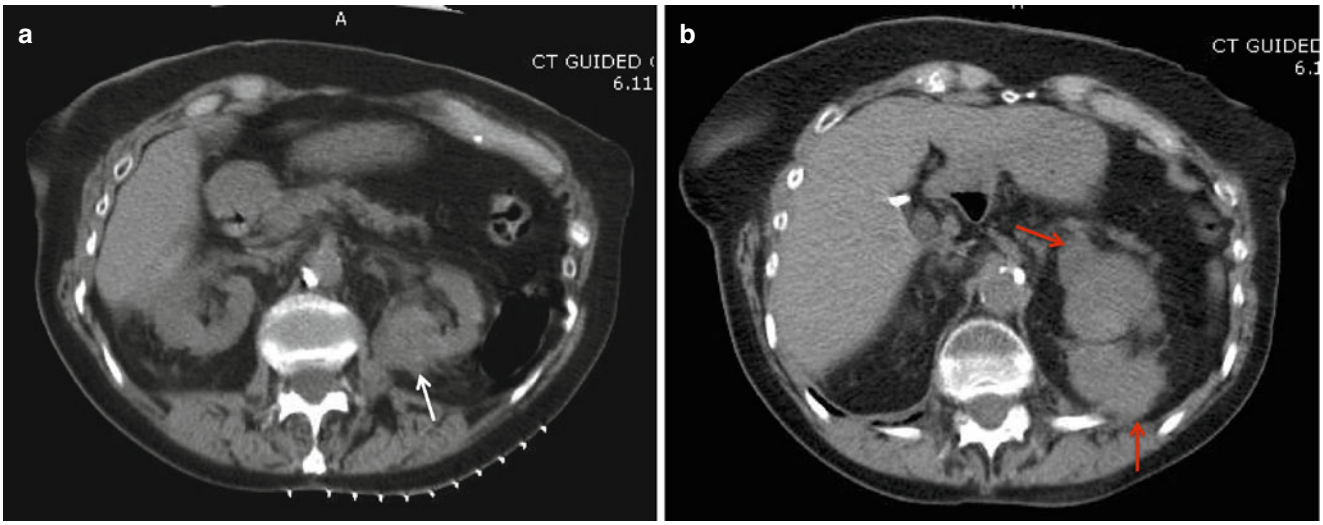

Fig. 18.4 (**a**) A posterior 3.8 cm renal lesion (*white arrow*) in an 86-year-old female. (**b**) After biopsy of the lesion, there was significant bleeding anterior and posterior to the lesion (*red arrows*). The patient was managed with admission and conservative measures

Risk of Seeding

The risk of needle track seeding of tumor cells is a concern in several solid nonrenal malignancies. In the kidney cancer literature, the risk is exceedingly low. Herts and colleagues estimate the risk of tumor seeding to be 0.01 % [20]. A study by Neuzillet et al. explored this risk in a series of 88 patients and found no reports of tumor seeding after biopsy [14]. Many believe the use of a coaxial sheath to pass the biopsy needle through for kidney biopsy could limit the risk of seeding. Additionally, there has been speculation that a large needle increases the risk of seeding [21]; however, no definitive evidence exists. This is the case for kidney tumors [22].

In the last 20 years, there is only one reported case of seeding in the literature. In this case, there was reported seeding of the biopsy tract after an ultrasound-guided biopsy of a Bosniak IIF renal cyst. In this report, there were four needle passes during FNA in addition to two core biopsies without the use of a coaxial sheath. On final pathology, the authors believed there was extrarenal extension of a 6.5 cm high-grade papillary tumor believed along one of the needle tracks [23]. This unique case occurred with a cystic lesion, that many centers would generally exclude from biopsy given the higher-risk cyst rupture and the potential for tumor spillage [24]. Additionally, while the authors believed the spread was along needle tracks, there is no definitive way to confirm the path of a biopsy needle ex vivo.

Due to the risk of seeding with upper tract urothelial cancers, some centers have avoided percutaneous biopsy for central lesions or those with collecting system involvement. However, since identification of tumor type has such an important implication on management, it sometimes is necessary prior to embarking on a treatment pathway. Ureteroscopic biopsies often provide limited tissue often with crush artifact. In the setting of suspected metastatic disease, we start with a percutaneous biopsy, as seeding may be irrelevant in this situation. For localized disease, if a ureteroscopic approach is attempted and is unsuccessful, since the risk of seeding is so exceedingly low, we proceed with a percutaneous biopsy [25].

Adjacent Organ Damage

The major organs at risk for damage from needle passage during percutaneous renal biopsy include the lung, pleura, liver, stomach, pancreas, colon, and spleen. An anterior approach with the patient in supine position is generally avoided due to the position of the bowels. However, for anterior tumors, we often position patients in a semi-flank position to shift the bowels inferiorly to provide a window to access the lesion (Fig. 18.5a–c). For upper pole lesions on the right side, if access to the lesion is difficult, a supine transhepatic approach can be performed (Fig. 18.6a, b). When necessary, we recommend use of a smaller gauge biopsy needle to limit bleeding complications.

When the biopsy is approached from a posterior intercostal approach, it is very important to keep breathing consistent. Patients should not be oversedated in order to cooperate with breathing instructions in order to minimize risk to adjacent organ injury. For patients with significant psychiatric illness or mental retardation, we have used general anesthesia for complete control of breathing. Adjacent organ injury is of particular concern for upper pole tumors due to the caudal extent of the pleural recess. A study by Hopper et al. examined the relationship of the surrounding organs to the upper pole of the kidney by evaluation of a prospective needle trajectory during inspiration and exhalation in both supine and prone positions [26]. In the prone position, there was more significant variation

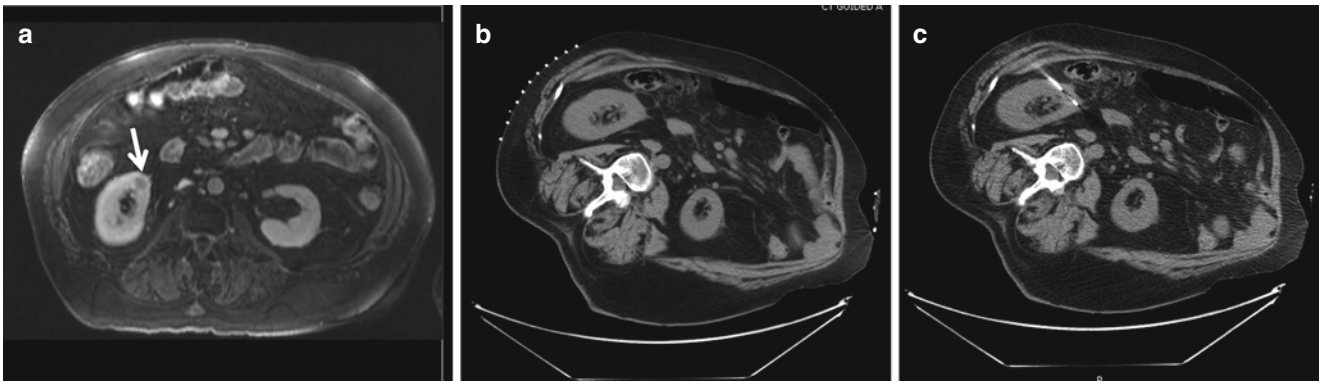

Fig. 18.5 (**a**) A 1 cm anteriomedial renal lesion (*white arrow*) that needed to be assessed prior to liver transplantation. (**b**) The patient was rolled into flank to shift the bowel and (**c**) facilitate ease of biopsy

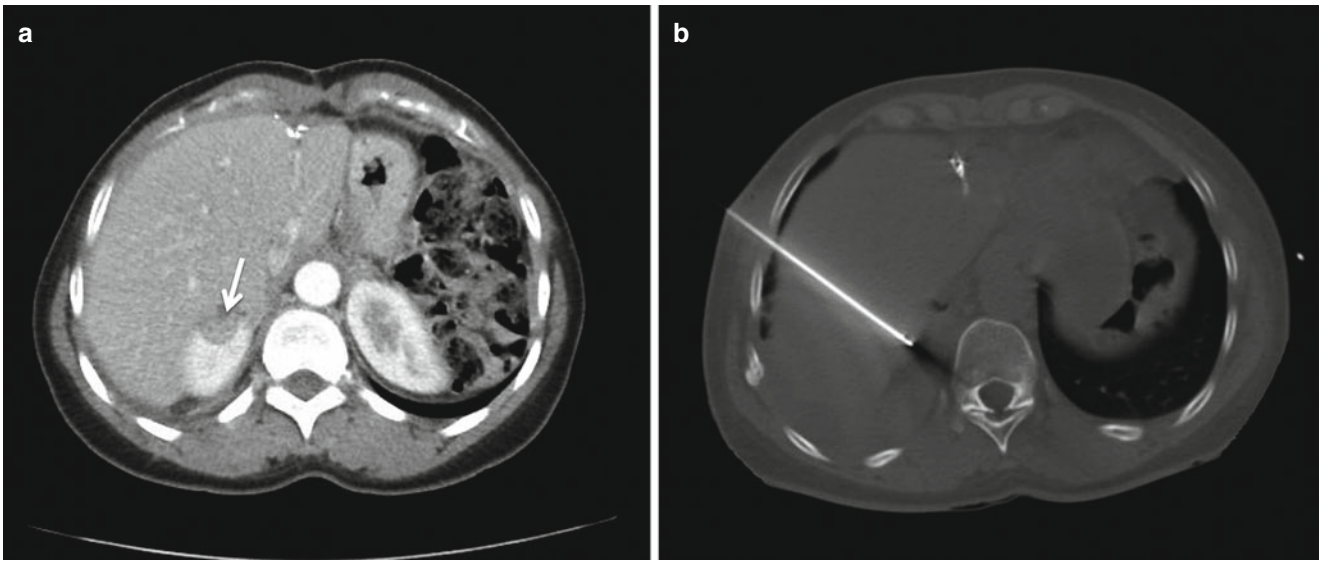

Fig. 18.6 (**a**) An upper pole, anterior renal mass (*white arrow*) in a patient with a prior history of metastatic cancer. (**b**) A transhepatic approach was used to access the lesion

between inspiration and expiration. If done after exhalation, the liver and spleen may be in the needle path in 14 % and 33 % of patients, respectively. These risks were minimized when performed during full inspiration. However, with this approach, there is a much higher rate of entry to the pleural, 14 % and 29 % on the left and right, respectively [26]. When attempting an intercostal approach above the 11th or 12th rib, despite a well-planned approach to the lesion, variations in breathing can still lead to pneumothorax (Fig. 18.7a–c). Picus et al. studied the risk of pleural injuries with a posterior intercostal approach and found 8 % of patients develop a pleural effusion and 4 % developed pneumothorax [27].

Biopsy Techniques

There are multiple methods of percutaneous renal mass biopsy that are both safe and effective. Each provider may have their own way of performing the procedure that works well in their hands. We will discuss several technical aspects of obtaining tissue, including using imaging modalities and guidance methods.

FNA Versus Core Biopsy

Fine-needle aspiration (FNA) and needle core biopsies are the two methods of obtaining renal tissue percutaneously. For FNA, a small sample of cells from the target area is aspirated through the needle into a syringe, and for the core biopsy, the needle is typically larger and a small cylinder of tissue is removed. A study by Scanga et al. assessed the utility of each method by assessing adequacy and diagnostic yield. When compared with FNA, core biopsies consistently had higher specimen adequacy, higher diagnostic accuracy, and higher reporting of RCC subtype and Fuhrman nuclear grade [28]. We generally perform core biopsies only, given the larger amount of tissue retrieved. For small lesions where

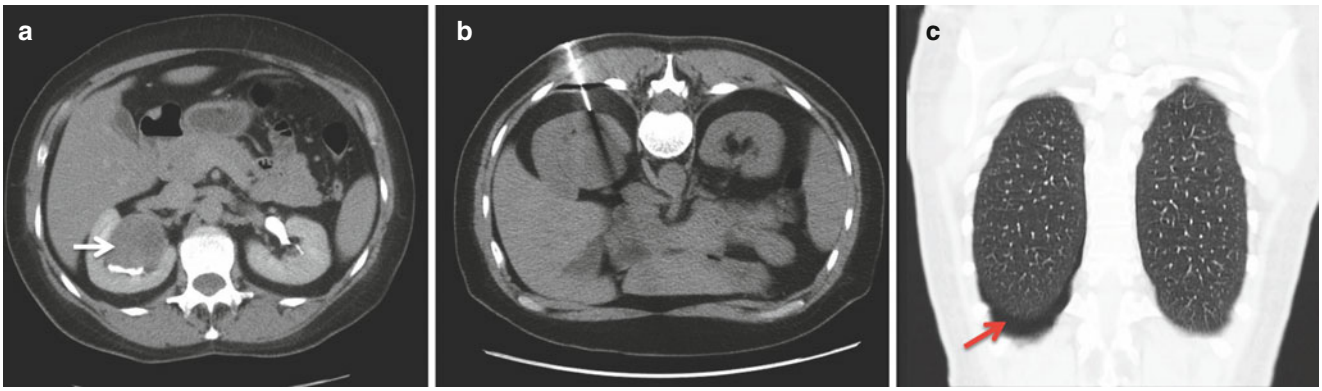

Fig. 18.7 (**a**) Upper pole, central right renal mass (*white arrow*) with borderline enhancement. (**b**) Despite targeting with the grid lines, the patient had erratic breathing leading to the needle transversing the lower pleural recess causing (**c**) A small pneumothorax seen on the coronal CT view

there is limited material to sample, we perform FNA in conjunction with the core biopsy to ensure one of the modalities obtains sufficient diagnostic material.

Imaging Modality

Multiple imaging modalities can be utilized for percutaneous renal mass biopsy. The most commonly used methods include ultrasound (US), computed tomography (CT), magnetic resonance imaging (MRI), and cone-beam CT-guided fluoroscopy. The most commonly used and best-studied modalities utilize CT and US. When deciding on the modality for renal mass biopsy, it is important to take several factors into consideration including the size and location of the renal mass, patient size, proximity to other vital organs, visibility, and the technical skill and comfort of the operator with each modality. In addition, other factors such as equipment availability, cost, and physician preference come into play.

US is commonly employed for normal kidney and renal mass biopsies. Use of US allows real-time multiplanar imaging, does not expose the patient to radiation, is low cost, is portable, and allows for accuracy of immediate post-biopsy hemorrhage. One major limitation of US-guided biopsy is there may be poor depth of tissue penetration and limited visualization in obese patients. If US is the modality used for renal mass biopsy, a detailed evaluation must be undertaken to optimize the image, identify the surrounding structures, select site of needle entry, and observe the needle passage directly into the lesion.

The benefits of CT include the ability to identify nearby structures thereby averting damage, better spatial resolution, and the option of using contrast to better delineate the lesion. For larger patients, a CT scan provides high-quality image guidance. Drawbacks of CT include radiation exposure, higher cost, and lack of real-time imaging. To minimize radiation, a lower radiation dose, a limited field, and larger slices (3.75–5 mm) can be utilized. Whenever we have concern of the potential for injury to adjacent structures or have an upper pole lesion, a CT approach may be beneficial in this scenario.

Other imaging modalities used in some centers include MRI and cone-beam CT-guided fluoroscopy. The availability and the expense of MRI make this imaging modality not feasible in many institutions. For most closed MRI units, the gantry is quite narrow, and placement and advancement of the biopsy needle can be challenging. Cone-beam CT-guided fluoroscopic platforms are emerging and represent an exciting technology for renal mass biopsy. Using fusion software, a prior scan can be overlaid with a low-dose cone-beam CT. Planning software can be used to design the trajectory of the needle. Fluoroscopic images can be used to denote the point of needle entry in the skin and advancement to the lesion. This technology is not available in all centers but serves as an attractive modality that provides quality-image guidance while limiting radiation exposure compared to conventional CT.

Localization Assistance

For ultrasound-guided renal mass biopsies, there are various brackets that can fasten to an ultrasound probe. Most ultrasound units have software available to demonstrate the path of a biopsy needle when placed directly into the needle guide. This is a very useful technique for beginners, as it will give a good idea of where the needle is heading. With the ultrasound probe demonstrating the renal mass in the longitudinal plane, the probe can be angled to direct the needle path into the tumor. Once the introducer is appropriately advanced, most needle brackets allow removal of the biopsy needle from the needle guide/ultrasound probe. This allows more freedom for the movement of the biopsy needle, additionally having control of the probe to optimize the angle of incidence for better visualization of the needle within the mass. With greater experience performing percutaneous ultrasound-guided biopsies,

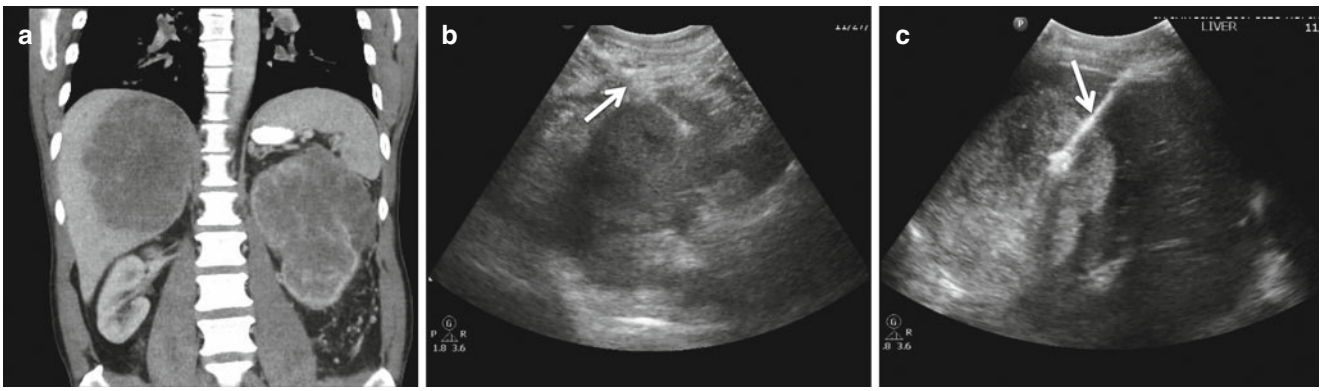

Fig. 18.8 (**a**) Patient with 15 cm kidney tumor and 12 cm liver metastasis. Use of an echogenic biopsy needle (*white arrows*) to guide localization into (**b**) renal mass and (**c**) liver lesion

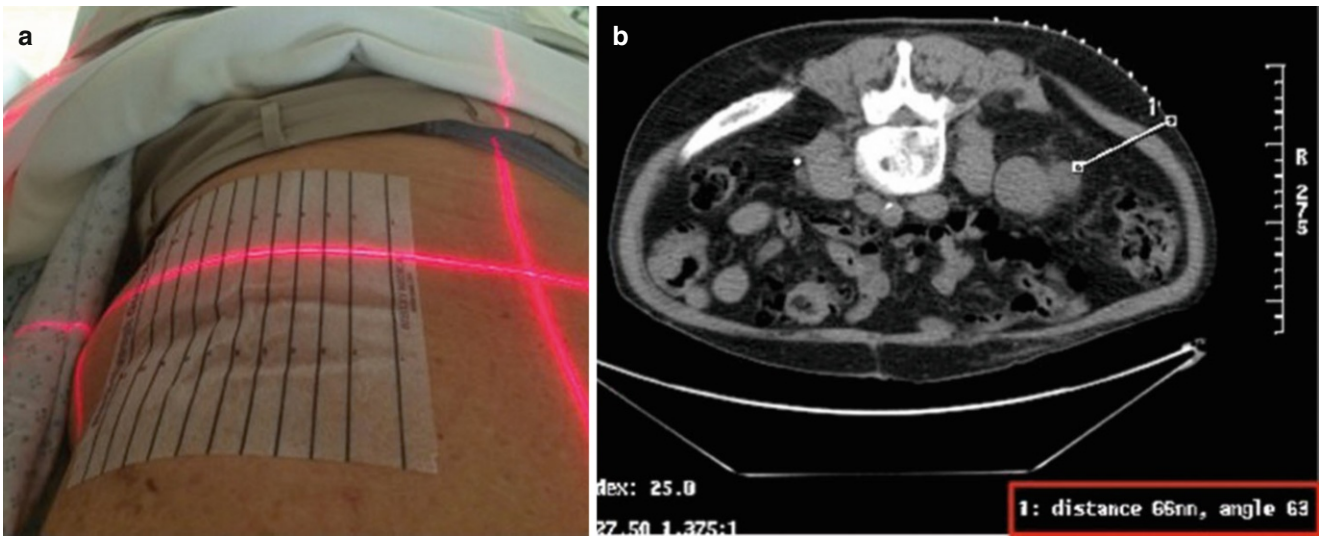

Fig. 18.9 (**a**) An example of a radiopaque localizing grid on a patient. The grid lines assist with sagittal localization, and the CT aiming beam shows the axial entry location. (**b**) The CT scan shows sagittal oriented grid lines and the distance/angle to the targeted lesion (*red box*)

most practitioners will prefer freehand placement of the introducer needle. One technique, which can improve the operator's ability to locate the needle, is using an echogenic needle with special etchings. This allows the needle to be hyperechoic on ultrasound to follow the path and the anticipated trajectory (Fig. 18.8a–c). If a echogenic needle is not available, scratches can be made on the outer surface of the introducer to make the needle more hyperechoic and visible during the biopsy.

For CT- and MRI-guided procedures, the use of a radiopaque localizing grid simplifies needle entry by allowing identification of the sagittal point of entry (Fig. 18.9a). Once the axial point of entry is determined, we note the angle and distance needed to get to the region of interest (Fig. 18.9b). Sometimes an isodense lesion does not alter the contour of the kidney and may be challenging to target. These lesions can easily be missed leading to a nondiagnostic biopsy. While anatomic landmarks are useful, often these may change when the patient is placed in prone or flank position as opposed to the supine position used to characterize the tumor. The use of IV contrast during cross-sectional imaging allows the technician to better visualize the location of the lesion (Fig. 18.10a–c). Once the lesion is localized, it facilitates targeting and improves the ability to obtain a diagnostic tissue sample.

Conclusions

Renal mass biopsy is an effective diagnostic procedure with an extremely low rate of major complications. Biopsy can be performed with a wide variety of imaging modalities, but most centers utilize either US or CT scans. Core needle biopsies yield a higher diagnostic accuracy than FNA with regard to identification of histologic subtype and grade. When done by an experienced practitioner, renal mass biopsy has proven to be very useful in guiding clinical management decisions.

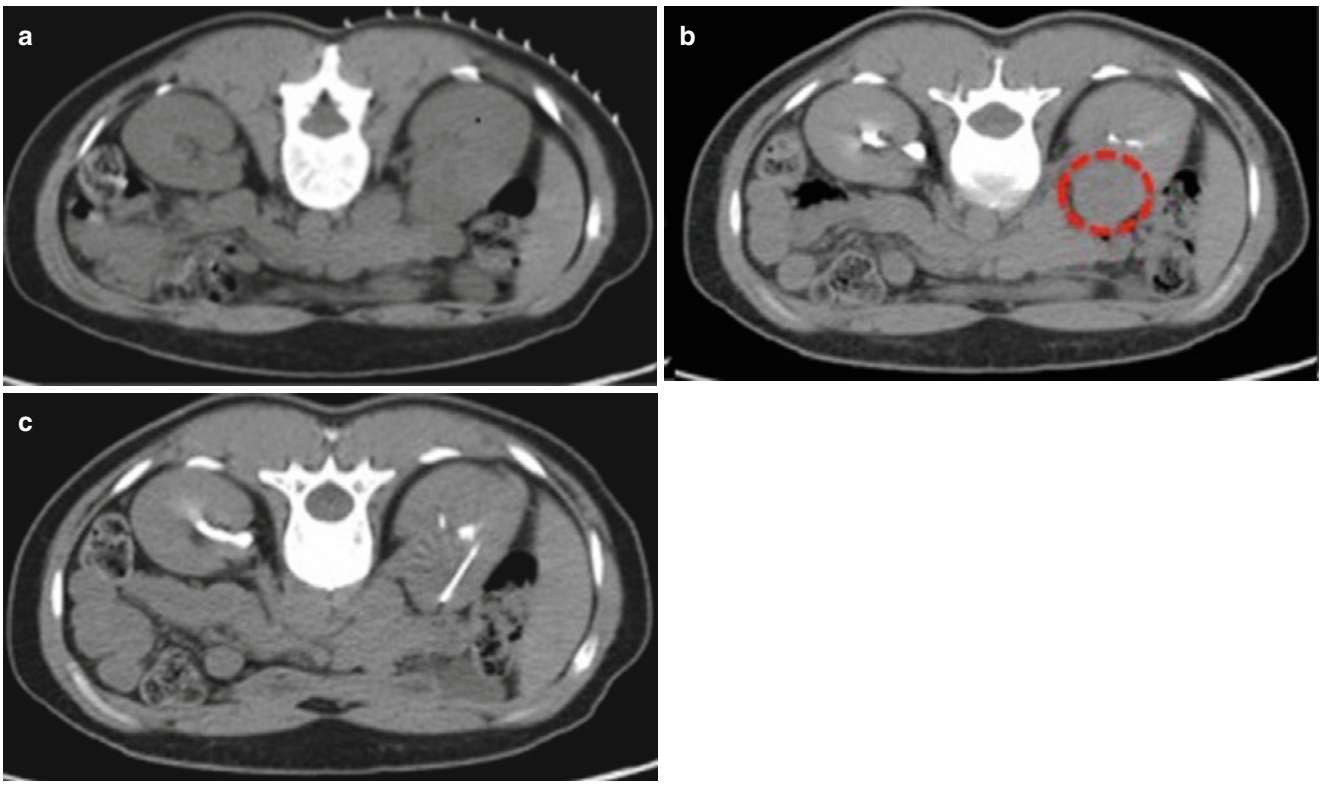

Fig. 18.10 (**a**) An endophytic 3 cm right renal mass that does not distort the contour of the kidney. (**b**) Use of IV contrast allows better delineation of the tumor location (*red arrows*) prior to placement of (**c**) percutaneous needle biopsy

References

1. Chow WH, Devesa SS, Warren JL, Fraumeni Jr JF. Rising incidence of renal cell cancer in the United States. JAMA. 1999;281:1628–31.
2. Hollingsworth JM, Miller DC, Daignault S, Hollenbeck BK. Rising incidence of small renal masses: a need to reassess treatment effect. J Natl Cancer Inst. 2006;98:1331–4.
3. Halverson SJ, Kunju LP, Bhalla R, et al. Accuracy of determining small renal mass management with risk stratified biopsies: confirmation by final pathology. J Urol. 2013;189:441–6.
4. Campbell SC, Novick AC, Belldegrun A, et al. Guideline for management of the clinical T1 renal mass. J Urol. 2009;182:1271–9.
5. Israel GM, Hindman N, Bosniak MA. Evaluation of cystic renal masses: comparison of CT and MR imaging by using the Bosniak classification system. Radiology. 2004;231:365–71.
6. Pedrosa I, Chou MT, Ngo L, et al. MR classification of renal masses with pathologic correlation. Eur Radiol. 2008;18:365–75.
7. Frank I, Blute ML, Cheville JC, Lohse CM, Weaver AL, Zincke H. Solid renal tumors: an analysis of pathological features related to tumor size. J Urol. 2003;170:2217–20.
8. Shuch B, Hanley JM, Lai JC, et al. Adverse health outcomes associated with surgical management of the small renal mass. J Urol. 2014;191:301–9.
9. Volpe A, Finelli A, Gill IS, et al. Rationale for percutaneous biopsy and histologic characterisation of renal tumours. Eur Urol. 2012;62:491–504.
10. Lane BR, Samplaski MK, Herts BR, Zhou M, Novick AC, Campbell SC. Renal mass biopsy--a renaissance? J Urol. 2008;179:20–7.
11. Leveridge MJ, Finelli A, Kachura JR, et al. Outcomes of small renal mass needle core biopsy, nondiagnostic percutaneous biopsy, and the role of repeat biopsy. Eur Urol. 2011;60:578–84.
12. Lechevallier E, Andre M, Barriol D, et al. Fine-needle percutaneous biopsy of renal masses with helical CT guidance. Radiology. 2000;216:506–10.
13. Renshaw AA, Granter SR. Metastatic, sarcomatoid, and PSA- and PAP-negative prostatic carcinoma: diagnosis by fine-needle aspiration. Diagn Cytopathol. 2000;23:199–201.
14. Neuzillet Y, Lechevallier E, Andre M, Daniel L, Coulange C. Accuracy and clinical role of fine needle percutaneous biopsy with computerized tomography guidance of small (less than 4.0 cm) renal masses. J Urol. 2004;171:1802–5.
15. Choyke PL, White EM, Zeman RK, Jaffe MH, Clark LR. Renal metastases: clinicopathologic and radiologic correlation. Radiology. 1987;162:359–63.
16. Corapi KM, Chen JL, Balk EM, Gordon CE. Bleeding complications of native kidney biopsy: a systematic review and meta-analysis. Am J Kidney Dis Off J Natl Kidney Found. 2012;60:62–73.
17. Gazelle GS, Haaga JR, Rowland DY. Effect of needle gauge, level of anticoagulation, and target organ on bleeding associated with aspiration biopsy. Work in progress. Radiology. 1992;183:509–13.
18. Whittier WL, Korbet SM. Timing of complications in percutaneous renal biopsy. J Am Soc Nephrol JASN. 2004;15:142–7.
19. Marwah DS, Korbet SM. Timing of complications in percutaneous renal biopsy: what is the optimal period of observation? Am J Kidney Dis Off J Natl Kidney Found. 1996;28:47–52.
20. Herts BR, Baker ME. The current role of percutaneous biopsy in the evaluation of renal masses. Semin Urol Oncol. 1995;13:254–61.
21. Huang GT, Sheu JC, Yang PM, Lee HS, Wang TH, Chen DS. Ultrasound-guided cutting biopsy for the diagnosis of hepatocellular carcinoma--a study based on 420 patients. J Hepatol. 1996;25:334–8.
22. Volpe A, Kachura JR, Geddie WR, et al. Techniques, safety and accuracy of sampling of renal tumors by fine needle aspiration and core biopsy. J Urol. 2007;178:379–86.

23. Mullins JK, Rodriguez R. Renal cell carcinoma seeding of a percutaneous biopsy tract. Can Urol Assoc J Journal de l'Association des urologues du Canada. 2013;7:E176–9.
24. Silverman SG, Gan YU, Mortele KJ, Tuncali K, Cibas ES. Renal masses in the adult patient: the role of percutaneous biopsy. Radiology. 2006;240:6–22.
25. Huang SY, Ahrar K, Gupta S, et al. Safety and diagnostic accuracy of percutaneous biopsy in upper tract urothelial carcinoma. BJU Int. 2015;115(4):625–32.
26. Hopper KD, Yakes WF. The posterior intercostal approach for percutaneous renal procedures: risk of puncturing the lung, spleen, and liver as determined by CT. AJR Am J Roentgenol. 1990;154:115–7.
27. Picus D, Weyman PJ, Clayman RV, McClennan BL. Intercostal-space nephrostomy for percutaneous stone removal. AJR Am J Roentgenol. 1986;147:393–7.
28. Scanga LR, Maygarden SJ. Utility of fine-needle aspiration and core biopsy with touch preparation in the diagnosis of renal lesions. Cancer Cytopathol. 2014;122:182–90.

Urinary Diversion and Drainage

19

Drew M. Caplin, Pamela Lombardi, and Suraj Rambhia

Urinary diversion and drainage procedures have been employed for over 100 years to minimally invasively treat disorders of the urinary tract. Percutaneous nephrostomy was first described in 1912 when Hugh Hampton Young passed a pediatric cystoscope percutaneously into a hydronephrotic kidney. In 1955, Willard Goodwin described percutaneous nephrostomy using a trocar technique similar to those used today [1]. Throughout the 1970s and 1980s, investigators in France, the United States, and Germany described percutaneous nephrostomy for the removal of renal calculi [2]. Over the last 25 years, the technical evolution of interventional radiologic and endourologic technique exploded in parallel with technological advances in imaging, catheters, and guidewires. Currently, percutaneous and endourologic techniques complement each other in the management of urinary tract pathology.

Percutaneous interventions are integral in the diagnosis and treatment of urinary tract disorders. A thorough knowledge of the anatomy, techniques, pearls, and pitfalls will equip the operator with the necessary armamentarium to treat a wide range of urinary tract pathologies.

Percutaneous Nephrostomy

Anatomy

An understanding of renal anatomy increases the safety and efficacy of percutaneous access and decreases the likelihood of complications. The kidneys are retroperitoneal organs, encased by perinephric fat and enclosed by the Gerota fascia. The kidney is obliquely situated, normally measuring approximately 10 cm on its axis, and parallels the psoas muscles with the upper pole oriented nearer the midline. The pleura extends posteriorly to the twelfth vertebral body, with about half of the right kidney and one third of the left kidney lying above this posterior pleural reflection [3].

The division of the renal artery into the major ventral and dorsal branches creates a relative avascular zone referred to as the *Brodel bloodless line of incision*. This zone is located posterior to the lateral convex border of the kidney and is the preferred route to traverse during percutaneous nephrostomy [4] (Fig. 19.1a, b). A posterolateral approach toward a posterior calyx minimizes bleeding risk and provides a straight vector for advancement of guidewires, dilators, and drainage catheters into the renal pelvis [3] (Fig. 19.1c).

Indications

The indications for PCN generally fall into one of four major categories: relief of urinary obstruction, urinary diversion, access for endourologic procedures, and diagnostic testing. The most common indication for percutaneous nephrostomy (PCN) is relief of urinary obstruction. Common causes of obstruction are calculi and malignancies of the renal collecting system and pelvis. Iatrogenic injuries and pelvic masses are less common causes of obstruction. Mass effect on the ureters from uterine fibroids or a gravid uterus can result in symptomatic obstruction. Pelvic malignancies include cervical and endometrial cancer, bladder cancer, and prostate cancer. Less common causes are congenital abnormalities, retroperitoneal fibrosis, and lymphoma. Emergent decompression is indicated in cases of obstruction coupled with urosepsis and/or acute renal failure. Other indications for decompression include obstruction with infection, declining renal function, or intractable pain, commonly when retrograde decompression has been attempted or is not indicated.

D.M. Caplin, MD (✉)
Department of Interventional and Diagnostic Radiology, Hofstra North Shore-LIJ School of Medicine, Hempstead, NY, USA
e-mail: dcaplin@nshs.edu

P. Lombardi, MD
Department of Radiology, Hofstra/North Shore-LIJ School of Medicine, New Hyde Park, NY, USA

S. Rambhia, MD
Department of Radiology, Hofstra/North Shore-LIJ School of Medicine, New Hyde Park, NY, USA

A.R. Rastinehad, D.N. Siegel (eds.), *Interventional Urology*, DOI 10.1007/978-3-319-23464-9_19

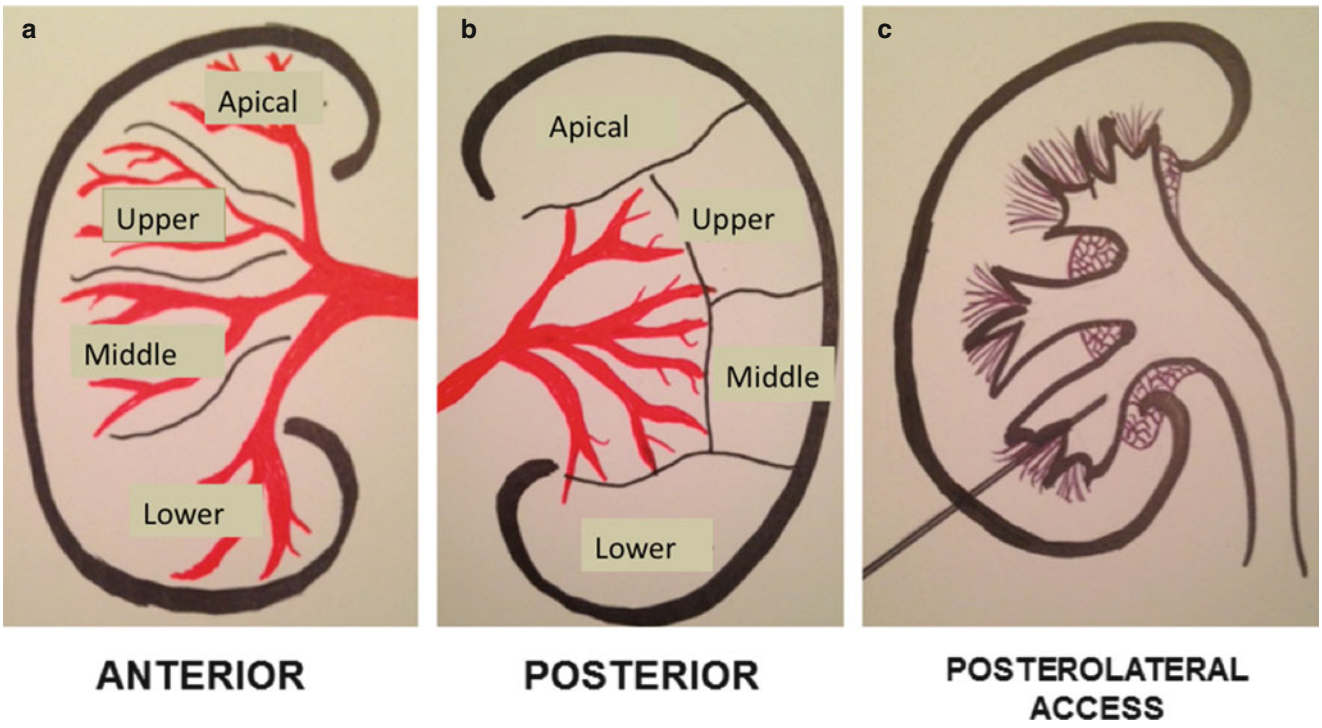

Fig. 19.1 Renal anatomy and vascular supply. Stylized images demonstrate the relative lack of blood flow of the posterolateral aspect of the kidney, known as Brodel bloodless line of incision (**a**, **b**). This is the rational for targeting a posterolateral calyx when obtaining percutaneous access to the renal collecting system (**c**)

In the setting of ureteral obstruction due to malignancy, a common approach in patients with bilateral obstruction due to pelvic malignancy is to initially drain the symptomatic or most hydronephrotic collecting system and only perform secondary PCN if renal function does not improve or in the presence of infection. This common practice is due to the high failure rate of stent placement in the setting of extrinsic compression due to pelvic malignancy [5].

Consultation for PCN is common in the setting of urinary leakage to divert downstream urine extravasation and to support healing and sealing of the ureteral injury. Urine leak, either traumatic or iatrogenic, can occur anywhere in the urinary tract or at the site of an anastomosis. In the setting of known malignancy, or inflammatory fistulas, PCN is indicated to divert urine in conjunction with stent placement [3]. Urgent urinary diversion is indicated in cases of hemorrhagic cystitis, which carries a mortality of 4 %.

Access for Interventions/Endourologic Procedures

PCN access is often the initial procedure prior to therapeutic interventions including lithotripsy, stone extraction, and treatment of ureteral strictures and possible direct infusion of antifungal agents. At times, the only indication for PCN access is when retrograde stent placement is not feasible or successful [5].

Nephroscopic-guided interventions and operations may be performed in conjunction with a Urologist, include but are not limited to resection of urothelial neoplasms, endopyelotomy, and intracavitary injection of chemotherapy for transitional cell carcinoma [3].

When the indication for PCN is nephrolithotomy and lithotripsy, the procedure is commonly performed in the operating room immediately prior to lithotomy or lithotripsy [5].

Diagnostic Testing

Nephrostomy access can provide urologists a conduit for biopsy of urothelial lesions with the aid of brushes and possibly forceps. In addition, although less common, PCN access allows for the performance of functional studies such as the Whitaker test. Rarely, access may be performed for foreign body retrieval in the setting of a fractured or migrated ureteral stent.

Contraindications

There are no absolute contraindications for percutaneous nephrostomy, so in the presence of a "relative contraindication," the risks must be carefully weighed in the setting of a critically ill patient requiring renal access or urinary diversion.

Relative Contraindications

Uncorrectable Coagulopathy

Nephrostomy catheter placement is considered a procedure with significant bleeding risk that may be difficult to detect or control. A relative contraindication is a severe coagulopathy that cannot be corrected or bleeding diathesis.

The consensus guidelines [5] for patients undergoing percutaneous nephrostomy tube placement include:

- INR: Correct above 1.5 (95 % consensus).
- Activated PTT: Stop or reverse heparin for values >1.5 times control.
- Platelets <50,000: Transfuse.

Severe Hyperkalemia (Potassium Level Greater Than 7 mEq/L)

Electrolyte abnormalities may result in arrhythmias and metabolic acidosis if uncorrected.

Terminally Ill Patients

In the setting of imminent death, nephrostomy placement may not improve quality of life to a significant degree.

Pregnancy

The use of fluoroscopy should be avoided in pregnancy, especially during the first trimester. While percutaneous nephrostomy insertion may be performed solely using ultrasound, limited fluoroscopy may be needed.

Preprocedural Evaluation

Imaging

Preprocedural imaging of any contributory modality should be reviewed to evaluate the location and anatomy of the target kidney, with attention to the expected needle trajectory to avoid transgressing the bowel, pleura, liver, or spleen. Ultrasonography is commonly the first-line imaging for obstructive disease as it can assess renal morphology and degree of hydronephrosis. The proximal ureter and bladder are also often evaluated. CT and MR have the advantage of the ability to evaluate the entire urinary tract and all surrounding abdominal and pelvic structures. The size, number, and configuration of calculi are readily seen on non-contrast CT.

Laboratory Analysis

It is good practice to review all available laboratory studies, not limited to platelets and the patient's coagulation profile. Abnormal coagulation and electrolyte results should be addressed and corrected, if the clinical scenario permits, prior to any intervention. A preprocedural documentation of the baseline serum creatinine can function as an indicator of improved renal function and postprocedural success.

Technical Aspects of Procedure

Anatomic Considerations/Patient Positioning

Standard positioning on the fluoroscopic table is prone or oblique prone, unless an anterior approach is indicated as often the case in transplant kidney interventions.

Prior to cleaning the skin, the targeted kidney may be imaged with ultrasound, CT, cone beam CT, or fluoroscopy to confirm prior imaging results, planned approach trajectory, and laterality.

Access through a specific calyx is occasionally required for stone extraction.

Antibiotics

The use of prophylactic antibiotics for PCN placement is directed toward preventing urosepsis from intravasation of organisms into the bloodstream during manipulation of the infected urinary system (Table 19.1) [6]. The need for such prevention may be stratified based on the at risk patient. Most authors recommend the use of prophylactic intravenous antibiotics for all obstructed patients; and all agree that high-risk patients with underlying comorbidities or immunosuppressed patients that are at high risk for infectious complications require prophylactic antibiotic coverage.

Sedation

Adequate sedation is a critical part of safe and effective nephrostomy placement. However, in situations when a patient cannot tolerate sedation and/or general anesthesia, a nephrostomy can be placed using only local anesthesia.

Prior to the procedure, the patient should refrain from oral intake for 8 h. Sedation should be performed in accordance with ASA guidelines, including maintained intravenous access and continuously monitored physiologic measurements throughout the procedure. Procedures in which the patient is in the prone position often facilitate airway management if the patient is breathing spontaneously with a supplemental oxygen mask or nasal cannula. Suction and supplemental oxygen must be immediately available and administered as needed. Securing the airway in the prone position with an endotracheal tube (ETT) is recommended for prolonged procedures, in patients with cardiopulmonary instability or when aspiration and loss of airway are likely [7].

According to ACR-SIR guidelines, intravenous sedative/analgesic drugs are given in incremental doses that

Table 19.1 Commonly used antibiotics for genitourinary procedures

Antibiotic	Dosage	Indication
Cefazolin IV	1 g	
Ceftriaxone IV	1 g	
Ampicillin and gentamicin IV	2 g and 1.5 mg	
Vancomycin or clindamycin +aminoglycoside		If penicillin allergic

are titrated to the desired endpoints of sedation and analgesia [8].

Access Approach

Methods

The practitioner performing the procedure should be aware that inspiratory effort is reduced with sedation; thus the kidney may be oriented cephalad compared to preprocedural imaging or access planning.

With the patient in the prone position, the laterality is confirmed and the overlying skin is prepared and draped. The skin and subcutaneous tissues overlying the intended entry site are infiltrated with local anesthetic and a small dermatotomy may be made with a scalpel. Needle access for PCN is usually obtained with sonographic guidance, fluoroscopic puncture, or varying levels of combining both methods. An 18 gauge trocar needle allows for less deflection and often has an echogenic diamond-shaped tip. The larger caliber 18 gauge needle has the ability to accept a 0.035 in. guidewire, thus minimizing the overall number of exchanges. If a 20–22 gauge trocar needle is used to access the renal pelvis, then a 0.018 in. wire and coaxial introducer catheter must be utilized prior to introducing a 0.035 in. stiff guidewire. The floppy tip of the wire reduces access trauma. Once there is enough purchase into the renal pelvis, the coaxial introducer is advanced over the guidewire and into position using the radio-opaque band to identify tip location of the sheath. Removal of the introducer and stiffening cannula permits advancement of a .038 in. diameter guidewire through the lumen of the sheath.

Usually, access to the collecting system is through a posterolateral approach with the needle directed toward a mid-to-lower pole calyx. Dryer [4] et al. describe the two tactile "pops" appreciated as the needle first traverses the renal capsule, followed by successful entry into the collecting system. Despite the access method, calyx entrance is confirmed by the chosen guidance modality and by aspirating urine. If the fluid is cloudy or there is a high clinical suspicion for infection, opacification of the collecting system may be avoided or performed with gentle caution.

Ultrasound

Under real-time sonographic guidance, an 18–22 gauge access needle is advanced directly into the target calyx using a "single-stick" technique. One should attempt to puncture a mid or lower pole calyx at an angle of 20–25° to the coronal plane (Fig. 19.2) [9].

Access is confirmed via sonography, the tactile "pop," and aspiration of urine. Contrast material may be injected under fluoroscopy for evaluation of calyceal location, morphology, and degree of hydronephrosis. Next, the access wire is advanced through the needle with an attempt to loop the wire within the renal pelvis which facilitates nephrostomy tube deployment. One must attempt to form the pigtail within the renal pelvis, as attempting to do so within the ureter or in a calyceal infundibulum may be difficult and traumatic.

Fluoroscopy

Fluoroscopy alone may be used to access the renal collecting system. If there is a radio-opaque calculus or indwelling ureteral stent or if the collecting system is opacified secondary to the administration of radio-opaque intravenous contrast or via retrograde injection through an existing ureteral catheter, these structures may be targeted in order to access the collecting system via a single or two-stick process. If no radio-opaque target is present, a 22 gauge needle may be advanced trans-retroperitoneal under fluoroscopy in a "blind" manner, guided by the renal outline or, if the outline cannot be seen, osseous landmarks and preoperative images [10]. Attempt to aspirate urine is performed by the operator as the needle is gently retracted. Upon aspiration of urine, the system may be opacified so the desired renal calyx may be defined and targeted with a second 18–22 gauge access needle.

Combination Method

Sonographic guidance of a 21–22 gauge needle into a renal calyx performed. Once in place, air can be injected to define the posterior calyx or the system can be opacified with contrast, in order to provide a radio-opaque target for larger needle access under fluoroscopy. There is a risk of causing an air embolus, if the needle is not within the collecting system.

CT

Although a less utilized form of guidance, a CT may be necessary in patients with variant renal anatomy, such as horseshoe or pelvic kidneys. Barbaric et al. [11] described a combine CT-fluoroscopy technique performed in a modified room where a C arm is fitted at the end of a CT table, allowing for fluoroscopy with the patient on the CT table. The CT-fluoroscopy technique was performed with the patient in the supine-oblique position, reporting no major complications and a 2 % minor complication rate.

Cone Beam/Fluoroscopic

Cone beam CT, especially with the use of needle guidance software, results in improved anatomic visualization compared to conventional CT and fluoroscopy. Newer hybrid systems can perform high-speed rotational scanning with or without simultaneous contrast injection and complete post processing within seconds. Siegel [12] describes the use of such software, allowing for the postprocessed dataset to be used to guide percutaneous interventions with the aid of interactive needle-path planning and guidance software.

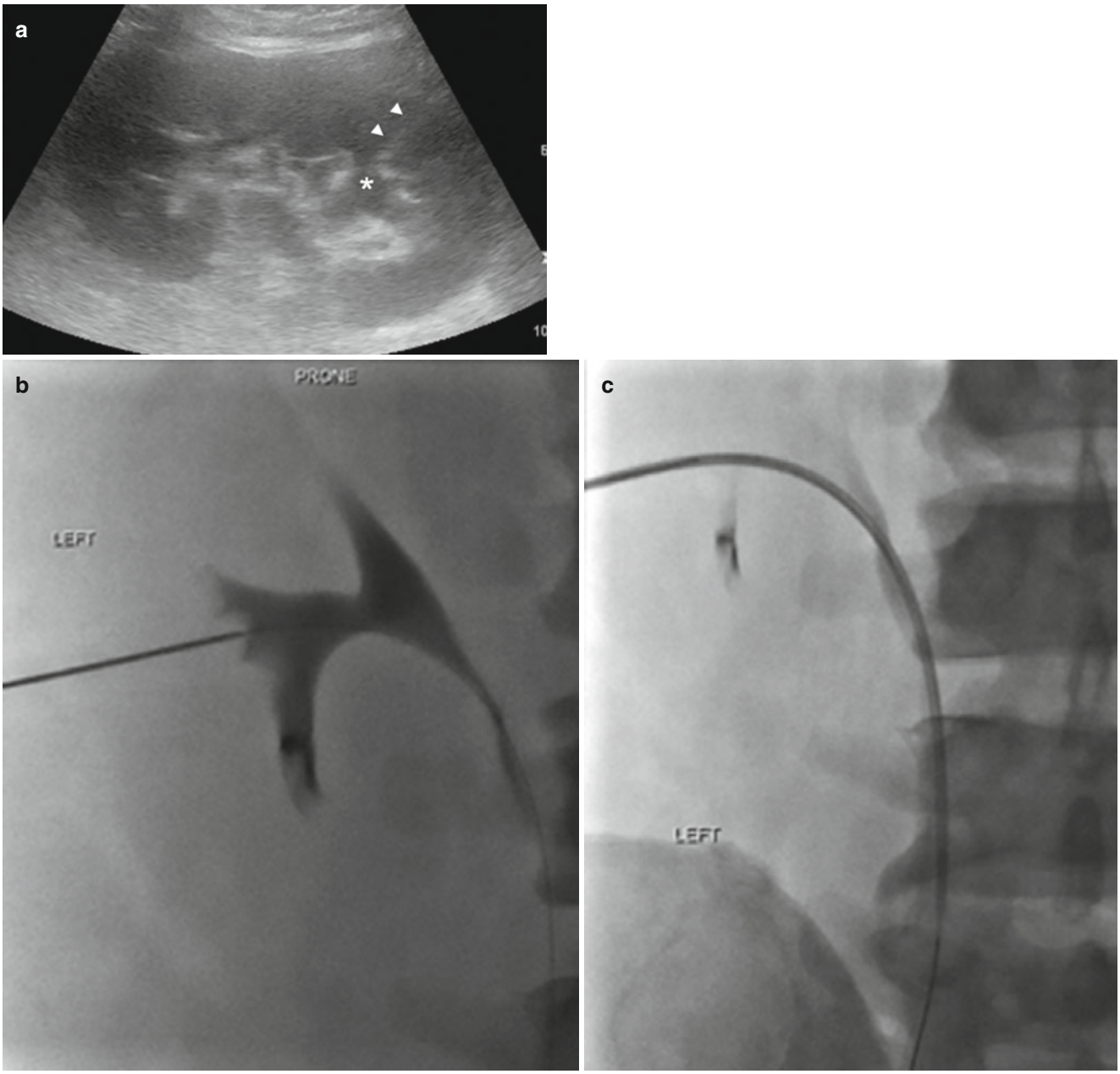

Fig. 19.2 Ultrasound-guided needle access for percutaneous nephrostomy. (**a**) Gray-scale ultrasound image of the left kidney. Lower pole calyx is denoted with an *asterisk*. Needle track is identified by the *arrowheads* with the intended target being a lower pole calyx. (**b**) Fluoroscopic images demonstrate contrast opacification of the renal collecting system. The operator proceeds with needle exchange over 0.018 in. wire for coaxial introducer sheath with contrast. (**c**) Subsequently, the operator passes a 0.035 in. guidewire through the coaxial introducer sheath and the lower pole calyx and down to the proximal ureter. (**d**) The introducer catheter is exchanged over 0.035 in. stiff wire for 8.5 French nephrostomy. Percutaneous nephrostomy drain is passed beyond the inner metal stiffener and into the ureter. The metal stiffener is stationed at the beginning of the curve of the wire and subsequently removed to allow for formation of pigtail end. The pigtail is positioned within the renal pelvis, and the pigtail loop is locked. (**e**) Injection of contrast confirms adequate placement of the pigtail catheter in a decompressed system, without filling defect

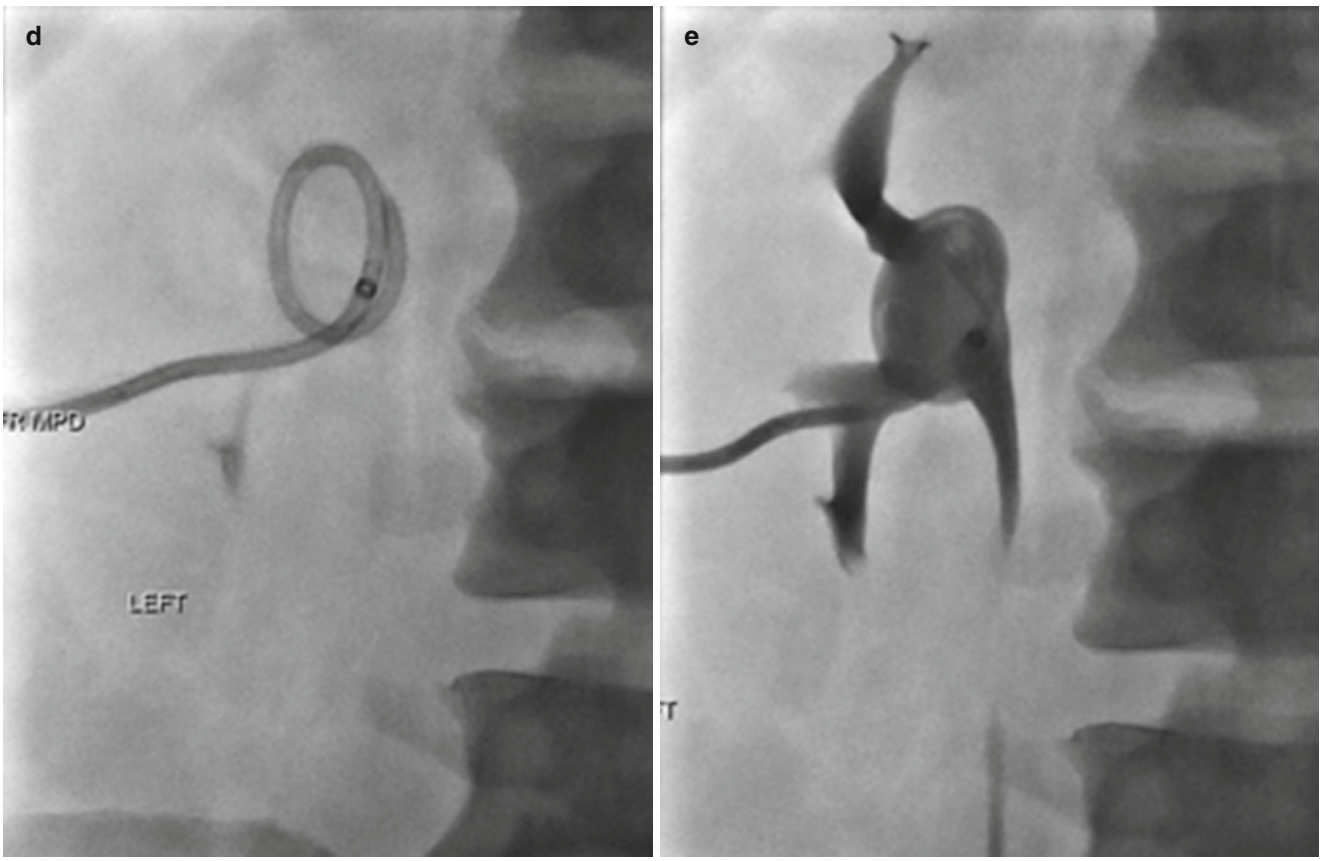

Fig. 19.2 (continued)

Outcomes

Success rates for PCN vary depending on the clinical scenario. The success rate in dilated systems approach is 99 % at most institutions, with lower rates reported in patients with non-dilated collecting systems, complex stone disease, and staghorn calculi. In complicated cases, reported success rates drop to 85 %.

Complications

The Society of Interventional Radiology stratifies the type of complication by outcome as listed below:

1. *Minor complications*:
   (a) No therapy, no consequence
   (b) Nominal therapy, no consequence; includes overnight admission for observation only
2. *Major complications*:
   (a) Require therapy, minor hospitalization (<48 h)
   (b) Require major therapy, unplanned increase in level of care, prolonged hospitalization (>48 h)
   (c) Permanent adverse sequelae
   (d) Death

Minor and major complications combined occur in approximately 10 % of patients [13] with sepsis and bleeding as the two major procedure-related complications.

Hemorrhage occurring after PCN is usually self-limited and resolves in a few days. If the urine remains bloody past 72 h with frank hemorrhage, upsizing of the nephrostomy tube may be considered. If bleeding persists and the urine remains grossly bloody after 3–5 days or when there is a drop in hematocrit, patients should undergo angiographic evaluation with embolization of injured vessels [3].

Other sources of a drop in hematocrit after PCN include retroperitoneal hemorrhage and should be considered in the appropriate clinical setting, especially if the urine is clear. Suspected retroperitoneal hemorrhage is best evaluated with CT.

The reported rate of sepsis is 1–3 %, with a higher incidence in patients undergoing PCN for suspected urosepsis or pyonephrosis.

Pleural complications rarely occur (approximately 0.2 % of decompressive nephrostomies) and include pneumothorax, empyema, hydrothorax, and hemothorax.

Nephroureteral Stents/Catheter/Tubes

A nephroureteral catheter is a unibody multiple side-hole internal/external drainage catheter. Typically the proximal locking loop, with drainage holes, is positioned in the renal pelvis, and the distal loop, also with drainage holes, is positioned in the bladder. This unibody catheter combines an external drainage tube and ureteral stent confers several advantages. The ability to drain patients both internally and externally provides maximal drainage. Simultaneous internal and external drainage maximally decompresses the patient ensuring that obstruction to urinary flow will be minimized. This may be desirable to facilitate healing of a urinary tract injury or to rapidly normalize renal function. Internal/external access may be desirable to facilitate stone extraction (Fig. 19.3). Finally, internal/external access may improve patient quality of life. In instances where ureteral stents are unable to be exchanged cystoscopically, nephroureteral tubes can remain capped and exchanged at regular intervals. This configuration provides emergency external drainage and facilitates catheter maintenance.

Nephroureteral catheters may be placed primarily or following a period of external drainage. Following access to the renal collecting system, an angled catheter is passed down the ureter to the level of concern. Prior to traversing the area of concern, a vascular sheath can be inserted into the collecting system or ureter over a stiff guidewire to protect access, to decrease trauma to renal parenchyma, and to increase support. The obstruction or injury is traversed using the catheter and a hydrophilic guidewire. Once entry into the bladder is confirmed, the approximate length of the ureter can be measured with a guidewire or catheter. The catheter and sheath are removed and exchanged for the nephroureteral catheter over a stiff wire. A long peel away sheath can be utilized, if necessary, to add support during catheter insertion through tortuous anatomy or severe stricture. The distal loop is positioned in the bladder and proximal loop is formed within the renal pelvis. Care should be taken to size the nephroureteral catheter appropriately as pressure on the trigone can decrease patient tolerance. Exchange is performed at regular intervals for long-term catheters and is usually over a guidewire and fairly straightforward.

Ureteral Stent Placement and Management

Generally, it is desirable to restore antegrade flow of urine without prolonged external drainage. It is inconvenient or uncomfortable for patients to have prolonged external drainage catheters whether they are capped or connected to drainage bags. The presence of an external drainage catheter exposes the patient to increased risk of dislodgement, leakage, access site irritation, or infection. To that end, internal drainage via double-J ureteral stents is better tolerated. Many times, they are placed as part of a staged procedure as issues such as urosepsis and uremia preclude extensive manipulation during primary drainage. Additionally, the presence of hydronephrosis and hydroureter can make it difficult to identify the point of obstruction. A staged procedure allows for accurate identification and possible treatment of a ureteral stricture or obstruction [14].

Double-J ureteral stents are catheters that have both proximal and distal loops, each with multiple drainage holes. Typically, one loop resides in the renal pelvis and one loop resides in the bladder. This configuration facilitates drainage and decreases the likelihood of dislodgement. Double-J ureteral stents are placed to restore continuity of antegrade flow through a ureteral blockage, stricture, or injury [15]. Typically, ureteral stents are placed by a urologist in a retrograde fashion. In instances when the urologist is unable to identify the ureteral orifice within the bladder or is unable to bypass a ureteral injury, obstruction, or stricture, they may be placed percutaneously in an antegrade fashion (Fig. 19.4).

Ureteral stents may be placed primarily, following a period of external drainage or in exchange for an indwelling percutaneous nephroureteral catheter. The procedure for antegrade ureteral stent placement is similar to PCNU placement (Fig. 19.3). Although placement of a covering nephrostomy tube is not mandatory following stent deployment, care should be taken not to lose access to the renal collecting system during deployment to facilitate covering nephrostomy tube placement. This tube may be left uncapped if there is significant hematuria to facilitate maximal drainage. A capping trial is performed to determine if the patient will tolerate internal drainage. Following a capping trial, the covering nephrostomy should be removed under fluoroscopy as it is possible that the locking loop of the nephrostomy catheter or its radiolucent retention string and proximal loop of the ureteral stent may be intertwined.

Antegrade Placement of Ureteral Stents via an Ileal Conduit

Following radical cystectomy for treatment of bladder carcinoma, an ileal conduit is often created. This is a loop of small bowel that is transposed, on its mesentery, to the abdominal wall. On one end, there is an incompetent ostomy, and the other end, a blind pouch. The ureters are anastomosed to this loop of bowel and urine drains to an ostomy bag. As the rate of anastomotic stricture is approximately 2–10 %, some surgeons elect to place ureteral stents at the time of surgery. However, most do not [16]. Patients with ureteral ileal anastomotic stricture present similarly to patients with chronic ureteral strictures from other causes and are managed similarly.

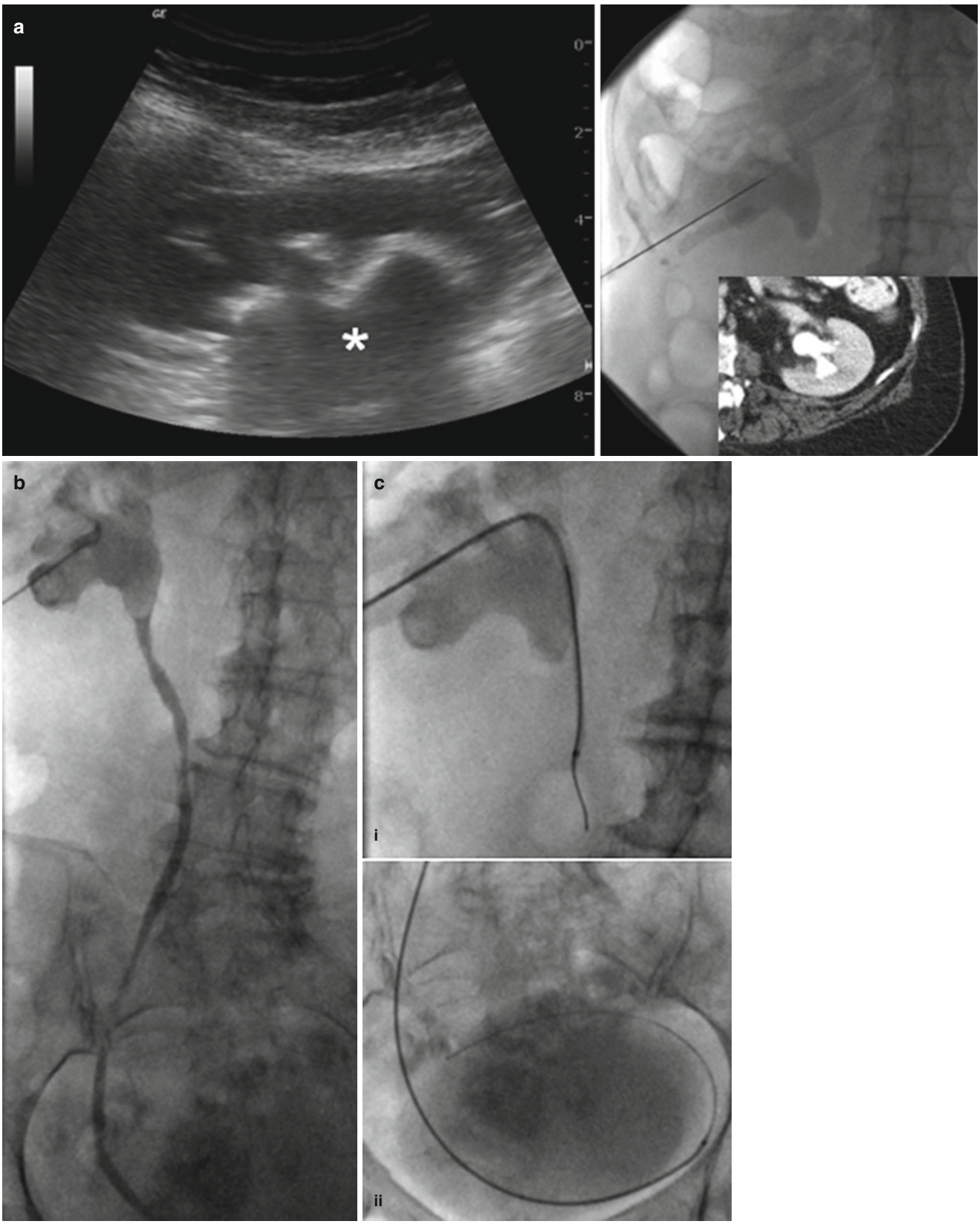

Fig. 19.3 Nephroureteral stent placement. Nephroureteral stent was placed in this patient with a staghorn calculus to provide access for percutaneous and endourologic stone extraction. (**a**) Gray-scale ultrasound, fluoroscopic, and CT images demonstrate needle puncture and access to kidney with large staghorn calculus (asterisk). (**b**) Contrast injection confirms access to the collecting system. (**c**) Catheter and wire are advanced to the proximal ureter (*i*) and subsequently the bladder (*ii*). (**d**) The nephroureteral stent is positioned appropriately. (**e**) Further contrast injection demonstrates patency and antegrade flow of contrast to the bladder

Fig. 19.3 (continued)

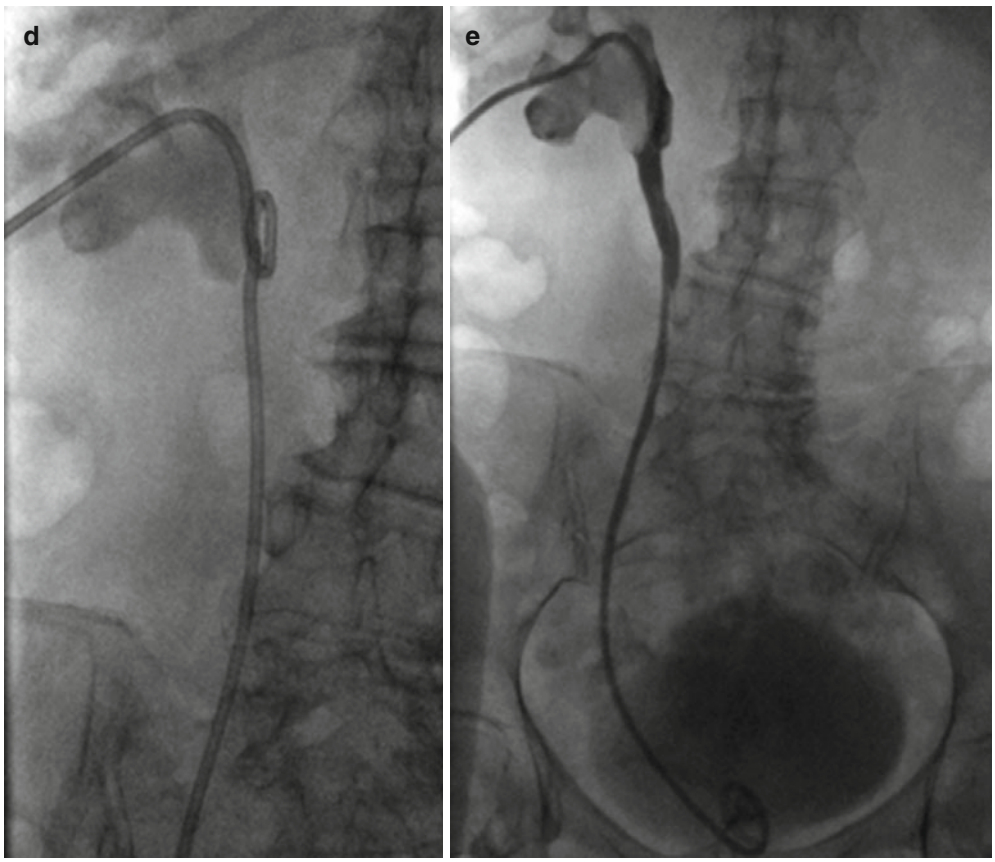

Initially, most patients are drained externally via a nephrostomy. However, like the majority of patients with nephrostomy tubes, the goal is internal drainage. Initially, the technique for stent placement is similar to antegrade double-J ureteral stent or nephroureteral tube placement. Once entry into the ileal conduit has been confirmed, a double-J ureteral stent may be placed with the distal loop within the conduit and proximal loop within the renal collecting system. This configuration is only used in the short term as the presence of mucous from the conduit usually causes stent obstruction within 2–3 months. Also, in this configuration, the distal stent is not within the ostomy bag, which decreases the likelihood of inadvertent dislodgment with ostomy bag manipulation. However, it increases the complexity of retrograde stent exchange as the distal end must be captured within the conduit. Often placing a finger into the ostomy is all that is needed to secure the distal loop. If this is not successful, the catheter may be captured using a vascular snare or via cystoscopy.

We prefer to place a locking loop catheter extending from the renal pelvis to the urostomy. As with other ureteral stent placements, catheter and wire are passed down the ureter and through the ureteral stricture. Once in the ileal conduit, the catheter and wire are advanced through the urostomy to the skin surface. At this time a second safety wire may be placed through the nephrostomy into the collecting system. A long stiff wire is placed through the catheter extending from the nephrostomy to the urostomy. A long locking pigtail catheter is placed retrograde, over the wire, extending from the urostomy to the renal pelvis. At the same time, a second locking pigtail catheter is placed over the same wire antegrade to the renal pelvis. Removal of the wire from the retrograde catheter facilitates formation of both locking loops within the renal pelvis. The nephrostomy tube is left to external drainage with the hub of the ureteral catheter left to drain within the urostomy bag (Fig. 19.5). In this way, the stent lumen is not exposed to the mucous produced within the conduit.

Catheter Exchange

Routine maintenance is important for all chronically indwelling catheters. Over time, urinary tract catheters fail due to wear and tear, become encrusted with mineral deposits or clog with mucous or proteinaceous material. It is good practice to periodically exchange all indwelling urinary tract catheters. We routinely exchange catheters every 3–6 months depending on each patient's clinical situation.

Nephrostomy tube exchange can easily be performed under fluoroscopy in the prone position using local anesthetic only. Injection of contrast material confirms placement with in the renal pelvis. The catheter is exchanged over a stiff

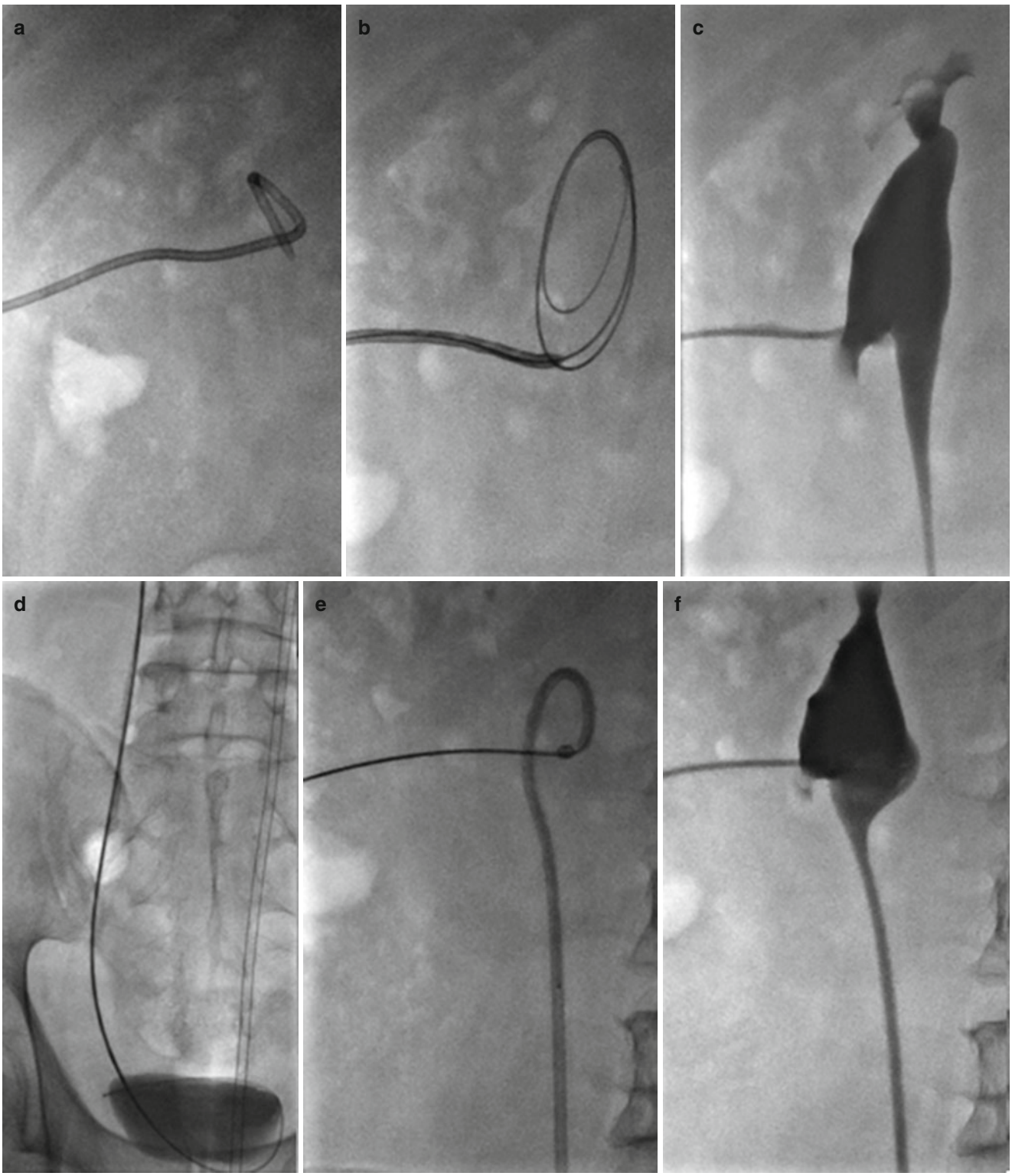

Fig. 19.4 Antegrade double-J ureteral stent placement. (**a**) Scout fluoroscopic image demonstrates nephrostomy tube access on the left. (**b**) The nephrostomy tube is uncoiled and removed over a wire. (**c**) A 5 French angled catheter and a hydrophilic wire are advanced to the bladder with contrast opacification. (**d**) Catheter is exchanged over a stiff 0.035 guidewire for 8 French stent. The distal part of the stent is advanced to the bladder. (**e**) Proximal part of the stent is advanced with "pusher" and deployed. (**f**) Confirmation of stent patency with appropriate placement in the renal pelvis and (**g**) bladder. (**h**) Proximal part of stent visualized after contrast has passed in antegrade fashion. Chronic double-J ureteral stents are generally exchanged at regular intervals over a guidewire

Fig. 19.4 (continued)

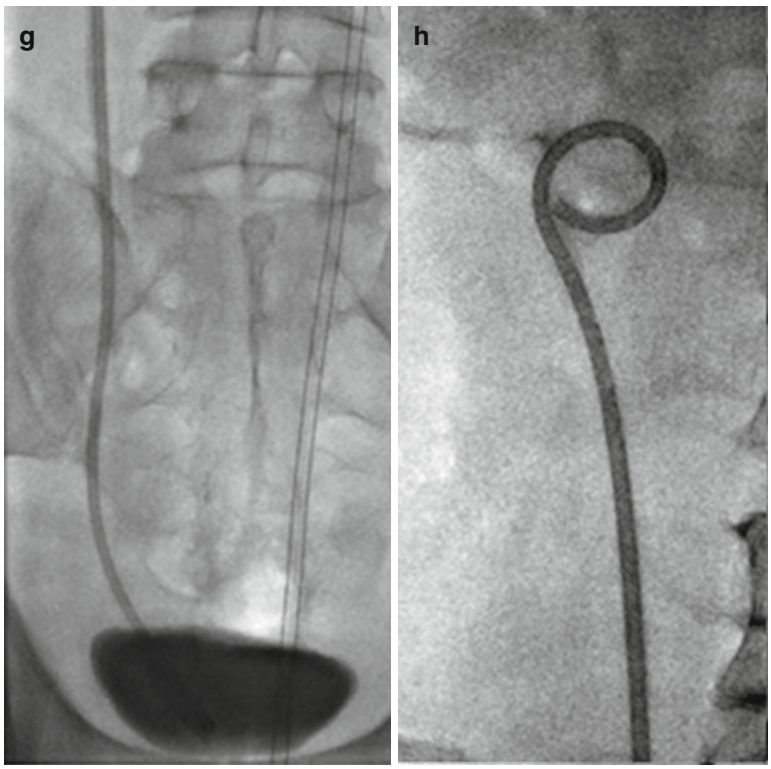

0.035 in. guidewire for a new nephrostomy tube which is formed within the renal pelvis.

Nephroureteral catheters are exchanged in a similar fashion as nephrostomy tubes but may be considerably more uncomfortable for the patient. Exchange often requires more manipulation to reduce the proximal loop and often results in catheter and wire pressure upon the bladder trigone. Furthermore, difficulty may be encountered during replacement through chronic strictures or tortuous ureters. To that end, we usually provide sedation for some of our patients.

Double-J ureteral stent exchange is typically performed by a urologist in a retrograde fashion. Usually exchange is via cystoscopic and possibly fluoroscopic guidance. In cases where this is not possible, stents may either be exchanged in an antegrade or retrograde fashion. Patients are usually given conscious or deep sedation. If there is a nephrostomy tube in place, the nephrostomy tube is exchanged for a vascular sheath. A snare is introduced through the sheath into the renal pelvis and is used to capture the proximal loop. The loop is brought out through the nephrostomy to the skin surface and the ureteral stent is exchanged over a long stiff guidewire. Following exchange, the nephrostomy tube may be replaced depending on the needs of the patient (Figs. 19.6 and 19.7). If there is no nephrostomy tube present and the urethra is unable to be catheterized, a stent may be retrieved via a new percutaneous nephrostomy. Ureteral stent exchange via an ileal conduit is usually performed in a supine, awake patient. In cases where a double-J ureteral stent has been placed, the distal loop is secured as described above and the stent is exchanged over a stiff guidewire (Fig. 19.8). In cases where a locking loop catheter is present, exchange is analogous to nephrostomy tube exchange (Fig. 19.9). Care should be taken to prevent prolapse of the catheter and wire through the ileal ureteral anastomosis into the conduit. If access to the ureter is lost, catheterization of the anastomosis is extremely difficult. The ureteral anastomosis may be identified upon contrast opacification of the ileal conduit or via cystoscopy [17]. Most times, loss of access requires percutaneous nephrostomy.

Unfortunately, there are instances where catheters become encrusted with mineral deposits or clogged. Catheter exchange can become challenging and frustrating for both the patient and operator. In instances where a catheter or stent is clogged with blood or proteinaceous material, clearance can often be achieved by flushing the catheter with normal saline within a small volume syringe. Alternatively, catheters are often cleared by probing with a stiff hydrophilic guidewire. If the lumen is unable to be cleared, a sheath can often be placed over the catheter into the urinary tract facilitating removal while preserving access [18]. On rare occasions where a tube is casted both inside and out with mineral deposits and unable to be exchanged, lithotripsy can be performed to free the catheter for exchange [19].

Catheters can become dislodged requiring emergent replacement. In instances where a chronic nephrostomy tube has become dislodged, replacement is through the established

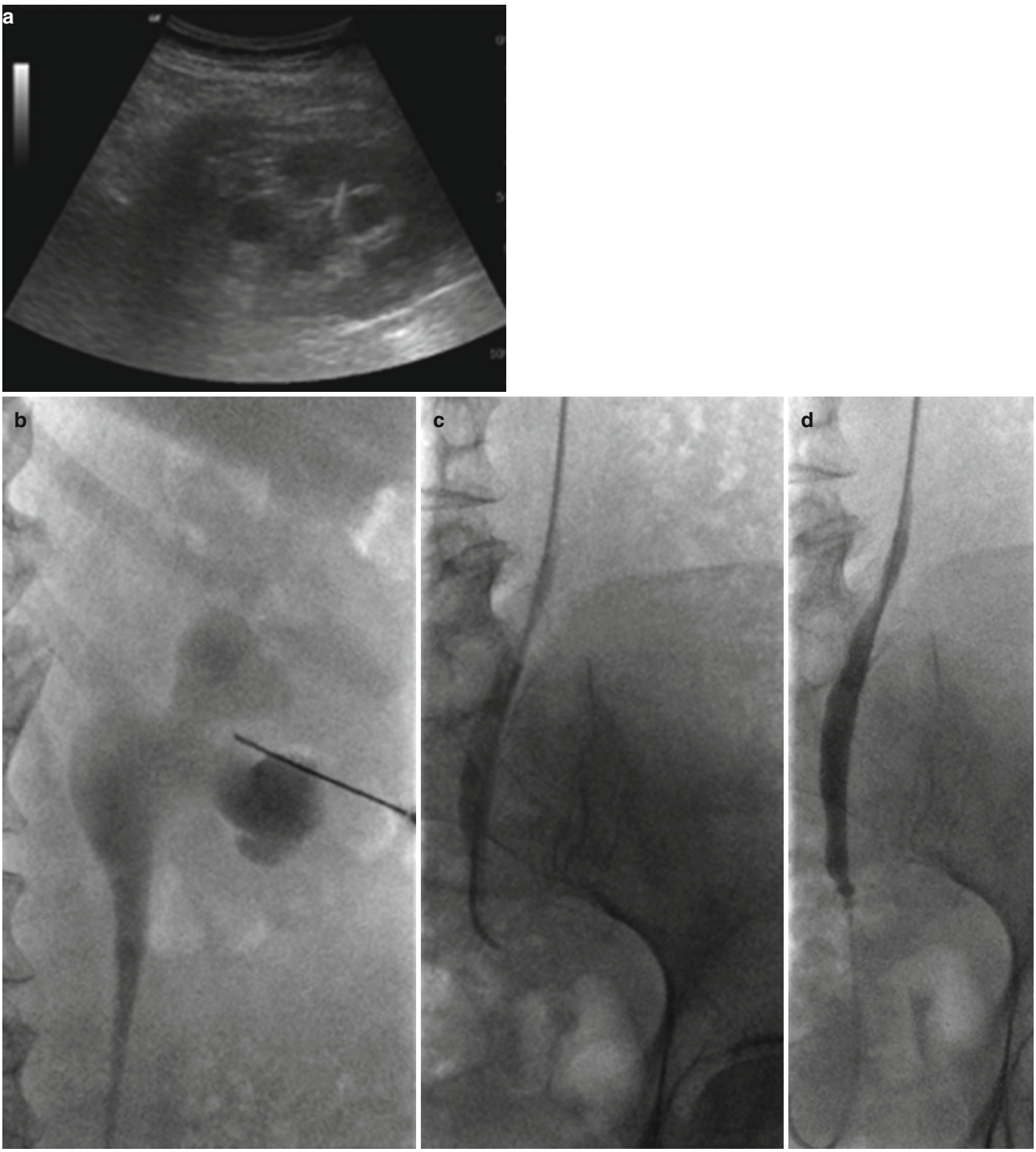

Fig. 19.5 Percutaneous access and ureteral stent placement via ileal conduit for treatment of ureteroileal sticture. (**a**) Ultrasound-guided access is confirmed with fluoroscopy. (**b**) Contrast opacification is noted to the distal ureter. (**c**) Angled catheter and guidewire are advanced to ureteroileal stricture. (**d**) Catheter and wire are passed through stricture into ileal conduit. (**e**) Contrast opacification of the ileal conduit. (**f**) A stiff 0.035 in. wire is advanced through the catheter via "flossing" maneuver. The wire extends from nephrostomy to the urostomy. (**g**) Retrograde passage of 8.5 French × 45 cm drainage catheter from the urostomy to the renal pelvis is demonstrated. (**h**) Retrograde injection of contrast confirms placement. (**i**) Final position of "upside-down" ureteral stent

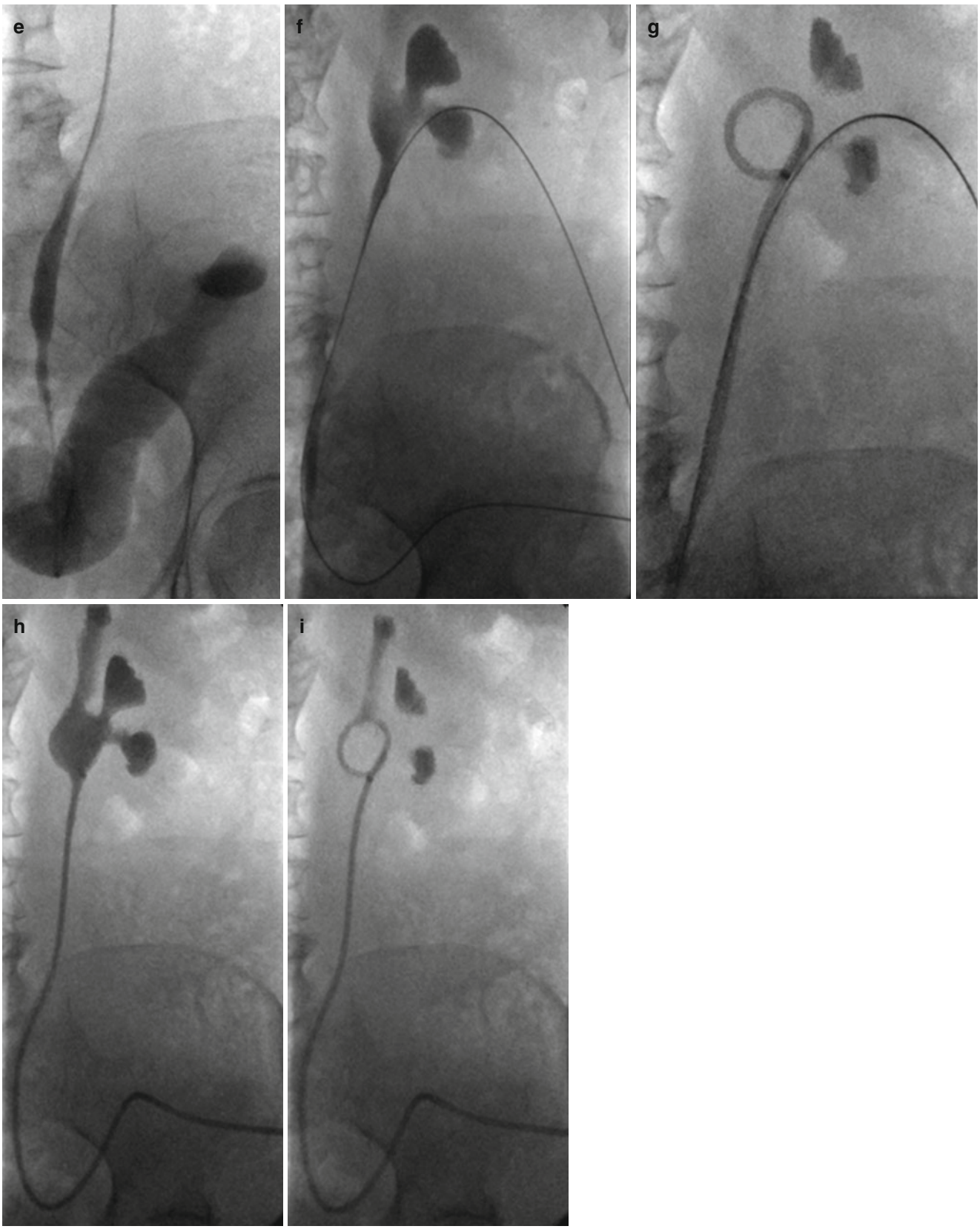

Fig. 19.5 (continued)

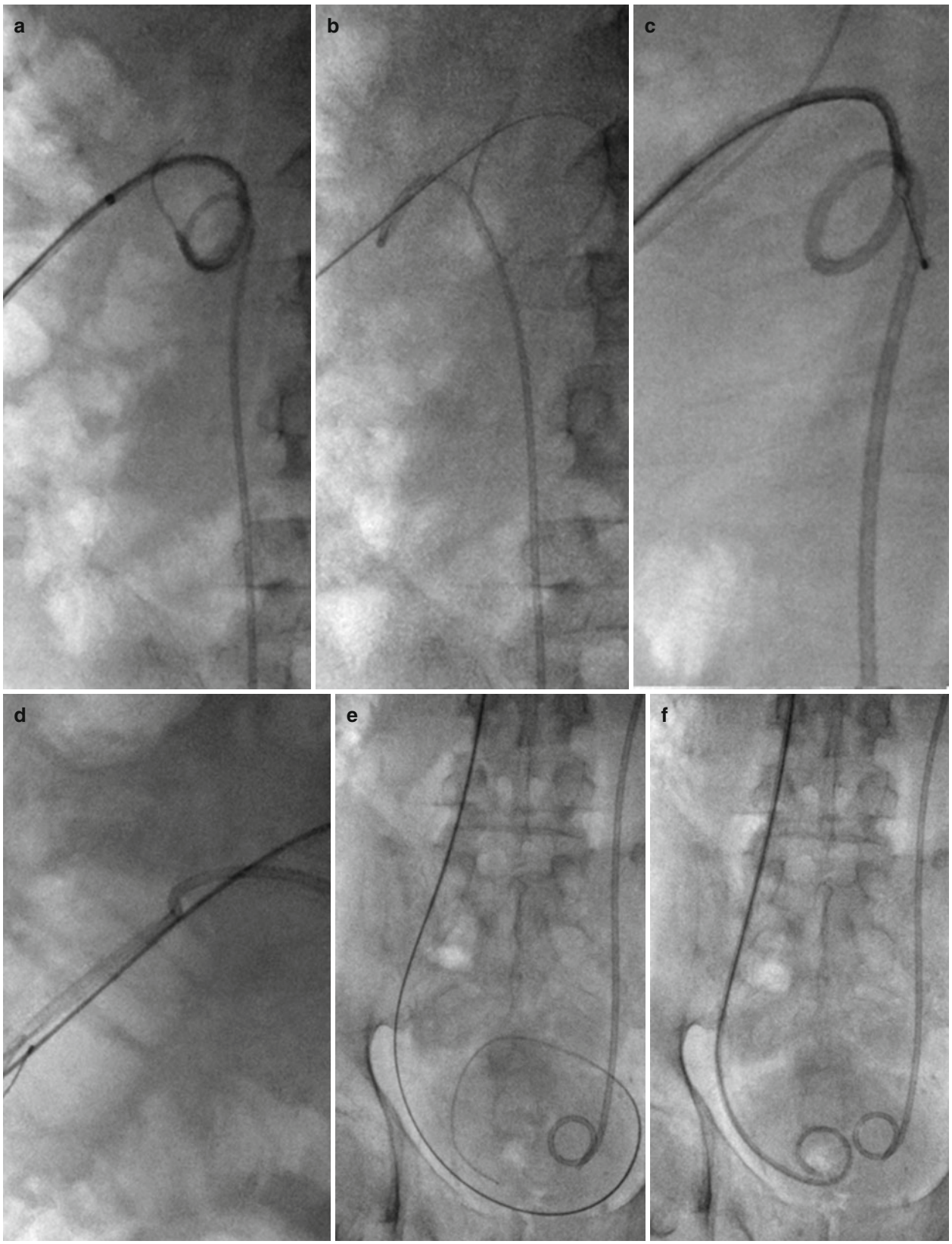

Fig. 19.6 Antegrade ureteral stent retrieval and exchange to nephroureteral stent. (**a**) Indwelling nephrostomy tube was removed over 0.035 in. stiff wire. (**b**) Wire is advanced so that it is well within the renal collecting system. (**c**) A vascular sheath, snare catheter, and "safety wire" are placed in an effort to capture the stent while maintaining percutaneous access. (**d**) The stent is captured and removed to the skin surface. (**e**) Wire is placed through the captured stent and advanced to the bladder. (**f**) The stent is replaced with nephroureteral tube. The same procedure was performed on the opposite side. (**g**, **h**) Demonstration of configuration of bilateral tubes (**g**) before and (**h**) after exchange

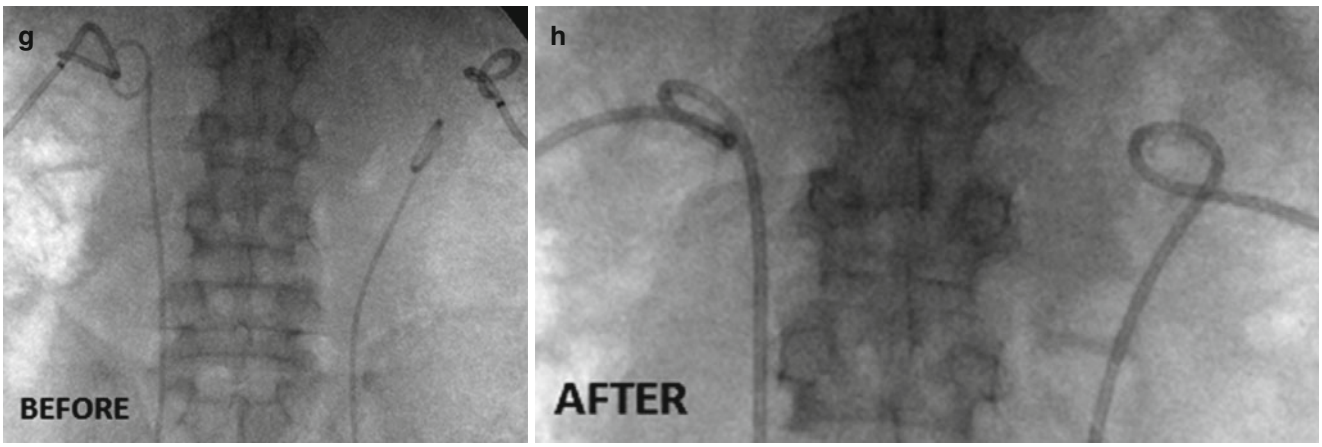

Fig. 19.6 (continued)

tract (Fig. 19.10). The tract is opacified confirming communication with the renal collecting system and is then traversed with a catheter and a guidewire. If the tract is not established, replacement is more urgent as the tissue layers may fall out of alignment or the nephrostomy may close entirely. Often, through contrast opacification and probing with a catheter and hydrophilic guidewire, the tract can be recannulated resulting in successful nephrostomy reinsertion. In instances where the tract is unable to be recannulated, a fresh nephrostomy may be indicated.

If a covering nephrostomy is dislodged, it may dislodge the indwelling ureteral stent as well if the two loops are intertwined. Similar to exchange, replacement of the double-J ureteral stent and covering nephrostomy or dislodged percutaneous nephroureteral catheter may require sedation. The ability to replace a dislodged ileal conduit ureteral stent depends on its relationship to the ureteral ileal anastomosis. If access to the ureter is preserved, most are routine guidewire exchanges. However, if access to the ureter is lost, the patient may require percutaneous nephrostomy.

Ureteral Stricture Treatment

A ureteral stricture is a narrowing of the ureteral lumen causing a functional obstruction. Strictures may be classified by benign or malignant, extrinsic or intrinsic. Extrinsic malignant compression of the distal ureter is usually secondary to pelvic malignancies arising from the prostate, colon, cervix, uterus, and bladder. Extrinsic malignant compression of the proximal to mid ureter is usually secondary to retroperitoneal lymphadenopathy. Extrinsic benign compression can be secondary to idiopathic retroperitoneal fibrosis, fibroid uterus, or gravid uterus [20]. Malignant intrinsic ureteral obstructions are most commonly caused by transitional cell carcinoma. Benign intrinsic ureteral strictures are either congenital or acquired. The most common site of benign intrinsic ureteral obstruction is the UPJ. Most commonly, strictures result from stone impaction and the techniques used for their removal. However, benign strictures can also result from injuries sustained during surgery or radiation therapy or at an anastomosis [21].

Traditionally, ureteral strictures have been treated with open surgery. However, the morbidity and difficulty of such procedures drove the need for minimally invasive therapies. Endourologic therapies were developed using catheter and wire techniques borrowed largely from endovascular techniques. Currently, ureteral strictures are usually initially treated endourologically. Often, placement of a chronic large diameter (eight French or greater) ureteral stent is all that is necessary to remodel a ureteral stricture. However, in cases where the stricture is high grade and resistant, balloon dilatation may be utilized [21]. High-pressure balloons frequently used in dialysis access can be utilized with success to dilate ureteral strictures. Dilation of short-segment, acute, benign strictures have the highest likelihood of success. After a stricture is crossed, a high-pressure balloon is centered upon the stricture over a stiff guidewire. Successive or prolonged dilations can be performed followed by the placement of a ureteral stent [22].

Ureteral Embolization

Ureteral embolization is a minimally invasive technique to achieve permanent urinary diversion. The most common indication is for treatment of lower urinary tract fistulae. Although infrequent, the most common cause is post hysterectomy. However, they may result from trauma, malignancy, radiation, inflammation, or infection. Surgical repair is often difficult and most resolve following urinary diversion with bilateral nephrostomy tubes and placement of a foley catheter. On rare occasions, when diversion does not allow the fistula to dry and heal,

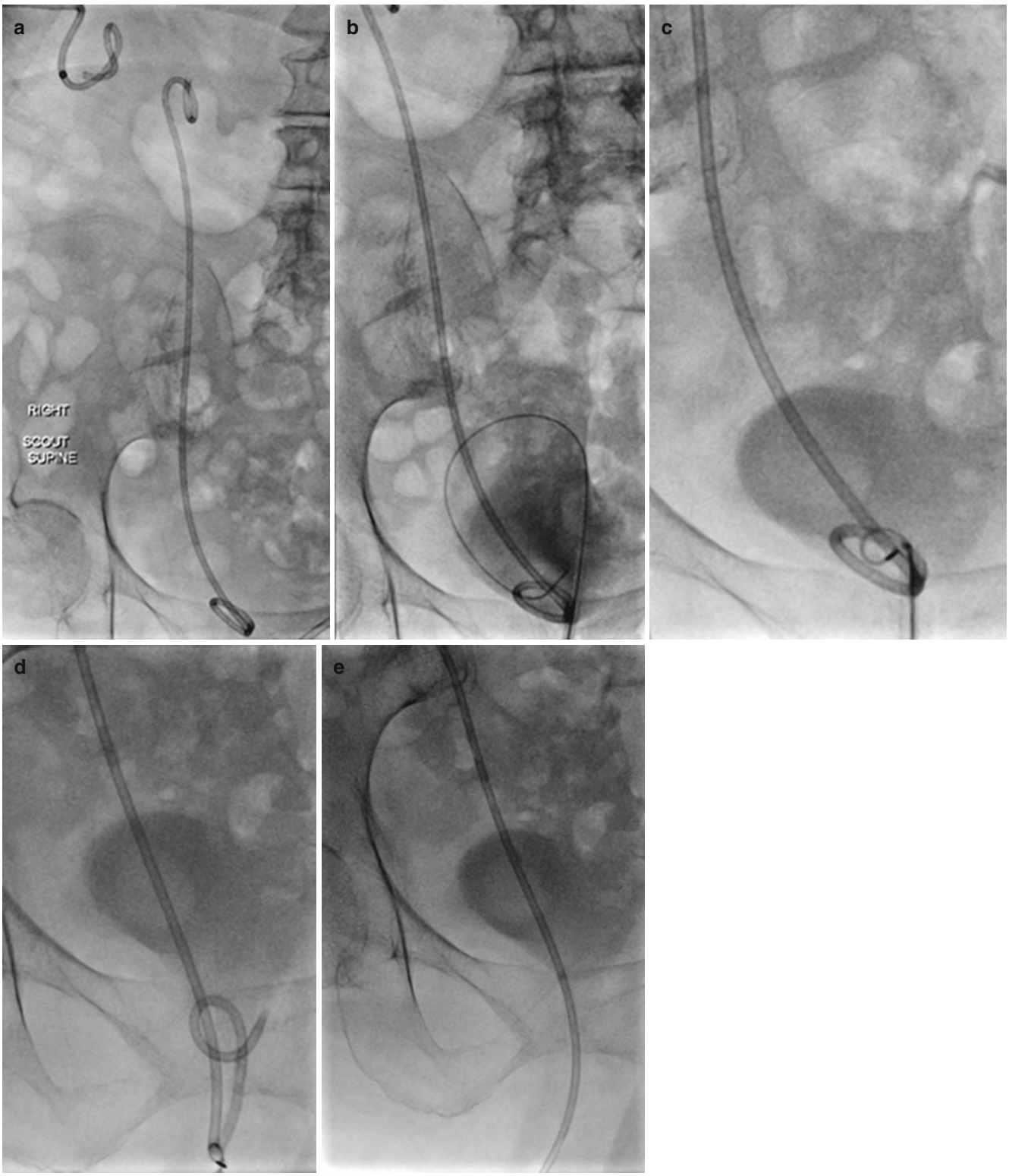

Fig. 19.7 Retrograde capture of indwelling ureteral stent. (**a**) Double-J ureteral stent and dislodged nephrostomy tube. (**b**) Angled catheter and glidewire are used to traverse urethra into the bladder. The catheter is exchanged over a stiff wire for a vascular sheath and tip-deflecting wire. (**c**) Tip-deflecting wire is used to capture distal urethral stent. (**d**) The stent in the process of being withdrawn. (**e**) The stent is withdrawn through the urethra, where it can be exchanged or fully removed

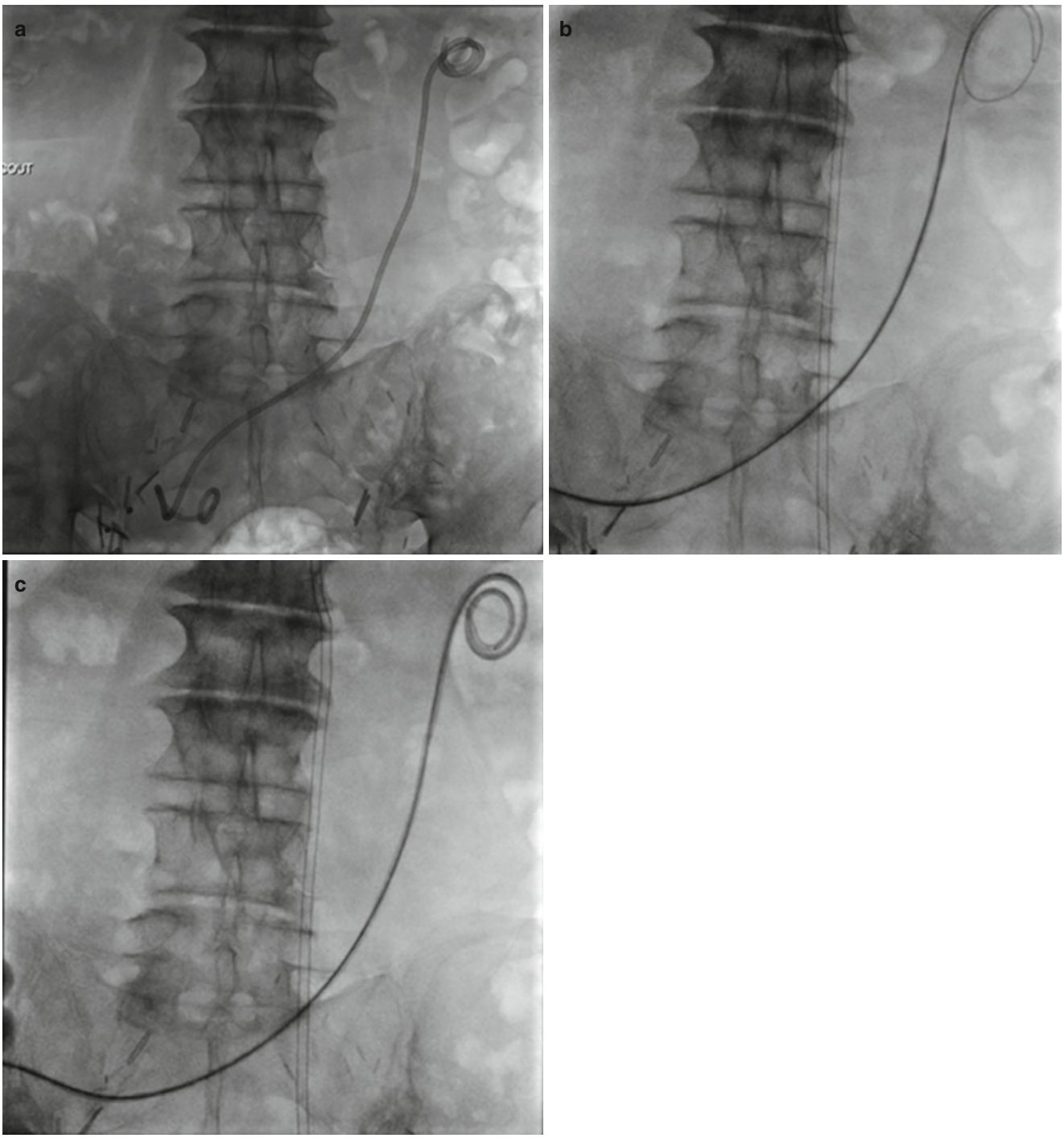

Fig. 19.8 Exchange of double-J stent via ileal conduit. (**a**) Indwelling double-J ureteral stent extends from the renal pelvis to the proximal ileal conduit. (**b**) Manual capture of distal loop by digital manipulation of the urostomy. (**c**) Exchange over a guidewire for 7 French × 30 cm variable length stent

embolization may be considered. As in the treatment of urinary strictures, endovascular techniques are utilized. Various agents such as coils, gelfoam, vascular plugs, and n-butyl cyanoacrylate glue can be used singularly or in combination to occlude the ureter with success rates approaching 100 % [4].

Transplant Kidney Interventions

The indications for transplant nephrostomy tube and/or ureteral stent placement are largely similar to those for native kidneys [23]. Additionally, a percutaneous nephrostomy may be placed in order to determine if renal

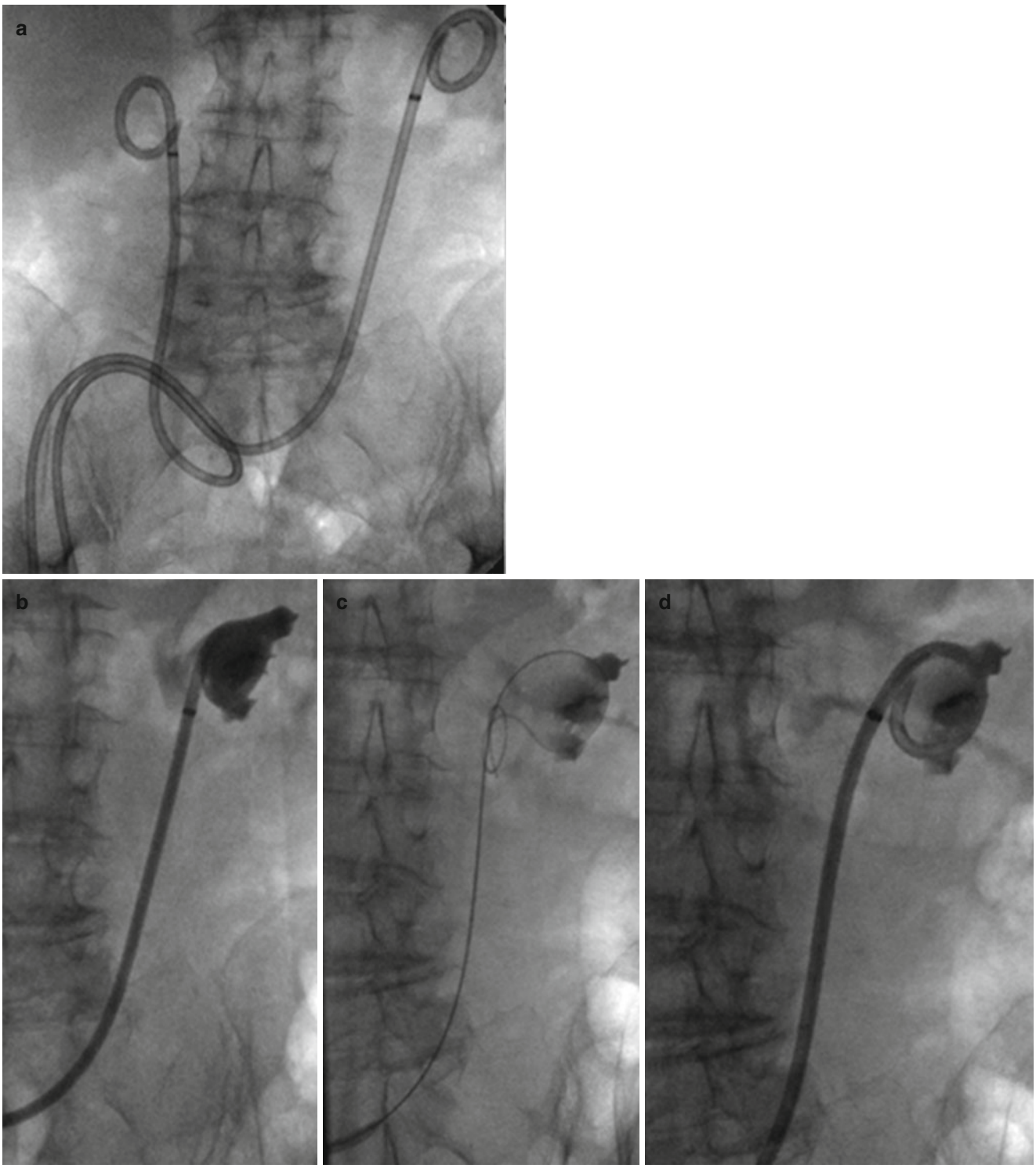

Fig. 19.9 Exchange of "upside-down" pigtail ureteral stents via the ileal conduit. (**a**) Bilateral ureteral stents are in place. Distal pigtails are within renal pelvis and catheter hubs are within the urostomy bag. (**b**) Retrograde contrast opacification confirms placement within renal pelvis. (**c**) Exchange of catheter is performed over 0.035 in. guidewire. (**d**) Fresh catheter end is formed after retrograde exchange of ureteral stent via ileal conduit

failure is secondary to obstruction or rejection [24]. Ischemia during harvest and transplant predisposes patients to ureteral anastomotic strictures and leaks [25]. These cases may necessitate placement of a nephrostomy tube and/or ureteral stent. It is important to know the location of the transplant kidney prior to attempting access.

Although placement is primarily within the pelvis, the laterality and configuration of the transplant are variable. Preliminary sonography, CT, or MRI is valuable to locate the transplant kidney, to assess its configuration, to assess the degree of hydronephrosis, and to identify any interposed structures [26].

Access to the transplant kidney, placement of nephroureteral tubes and antegrade double-J ureteral stents is performed using techniques previously described. However, due to the length of the ureter, pediatric nephroureteral tubes (Fig. 19.11) and double-J ureteral stents are usually preferable (Fig. 19.12).

Suprapubic Catheterization

Suprapubic catheterization is performed to relieve urinary retention when transurethral catheterization is contraindicated or unsuccessful. Urethral injury, urethral transection, urethral obstruction, bladder neck masses, prostate cancer, and benign prostatic hypertrophy are all conditions which may preclude or prevent urethral catheterization [27].

The procedure may be performed under sonographic, fluoroscopic, or CT guidance or a combination of modalities. The operator should not rely on anatomic landmarks alone, but should visualize the distended bladder prior to proceeding.

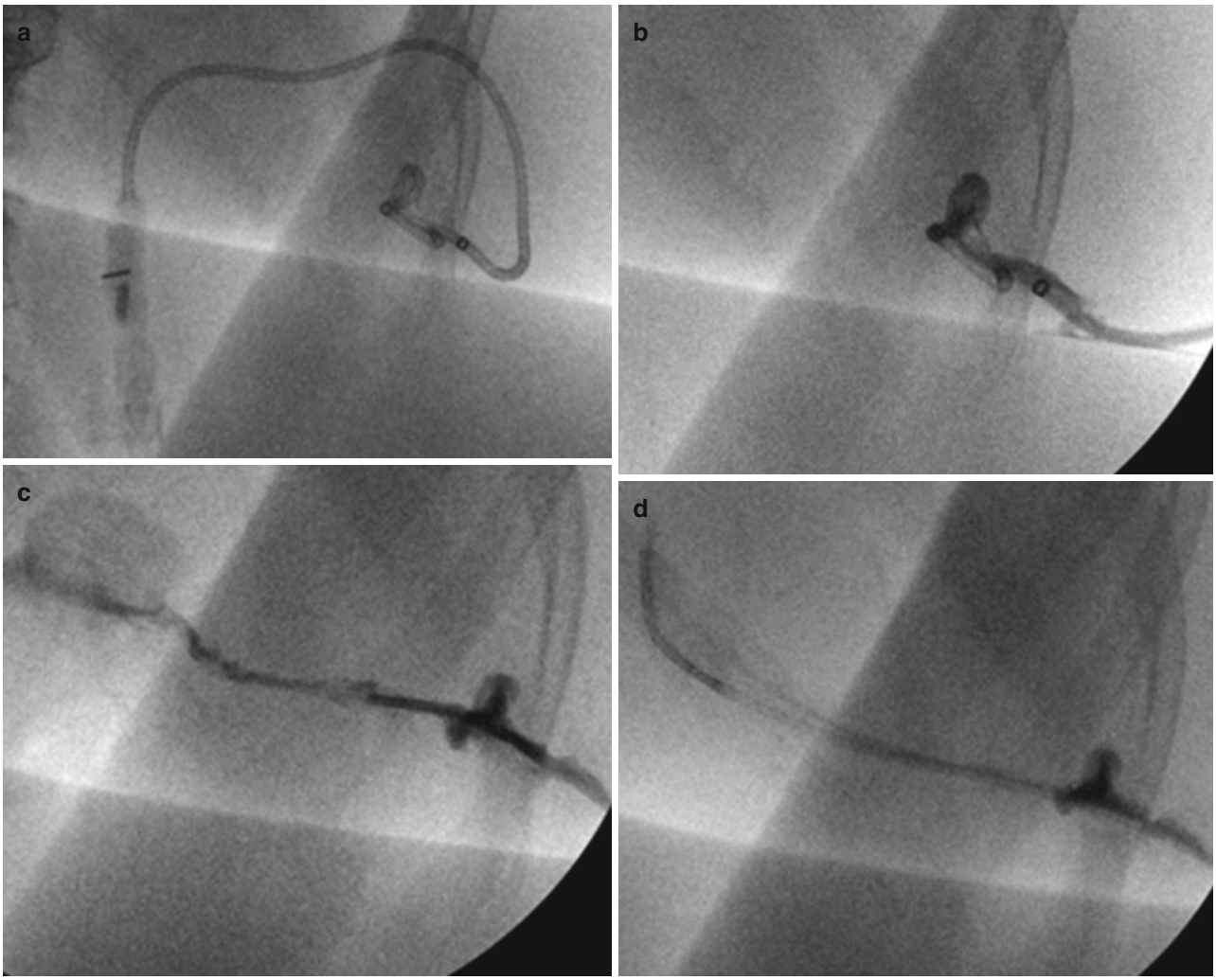

Fig. 19.10 Dislodged nephrostomy tube replacement with recanalization of nephrostomy tube tract. (**a**) Scout image demonstrates deformed catheter locking loop. (**b**) Zoomed view of catheter morphology and location. (**c**) After catheter removal, a 5 French angled catheter was placed into the nephrostomy. Opacification of the tract demonstrates communication with the renal collecting system. (**d**) Catheter is advanced, along with a 0.035 in. glidewire, into the renal pelvis. (**e**) Contrast opacification confirms hydronephrosis of the kidney and placement of the catheter in the renal collecting system. (**f**) Angled catheter is then exchanged over 0.035 in. guidewire. (**g**) Pigtail nephrostomy catheter is replaced and positioned in the renal pelvis

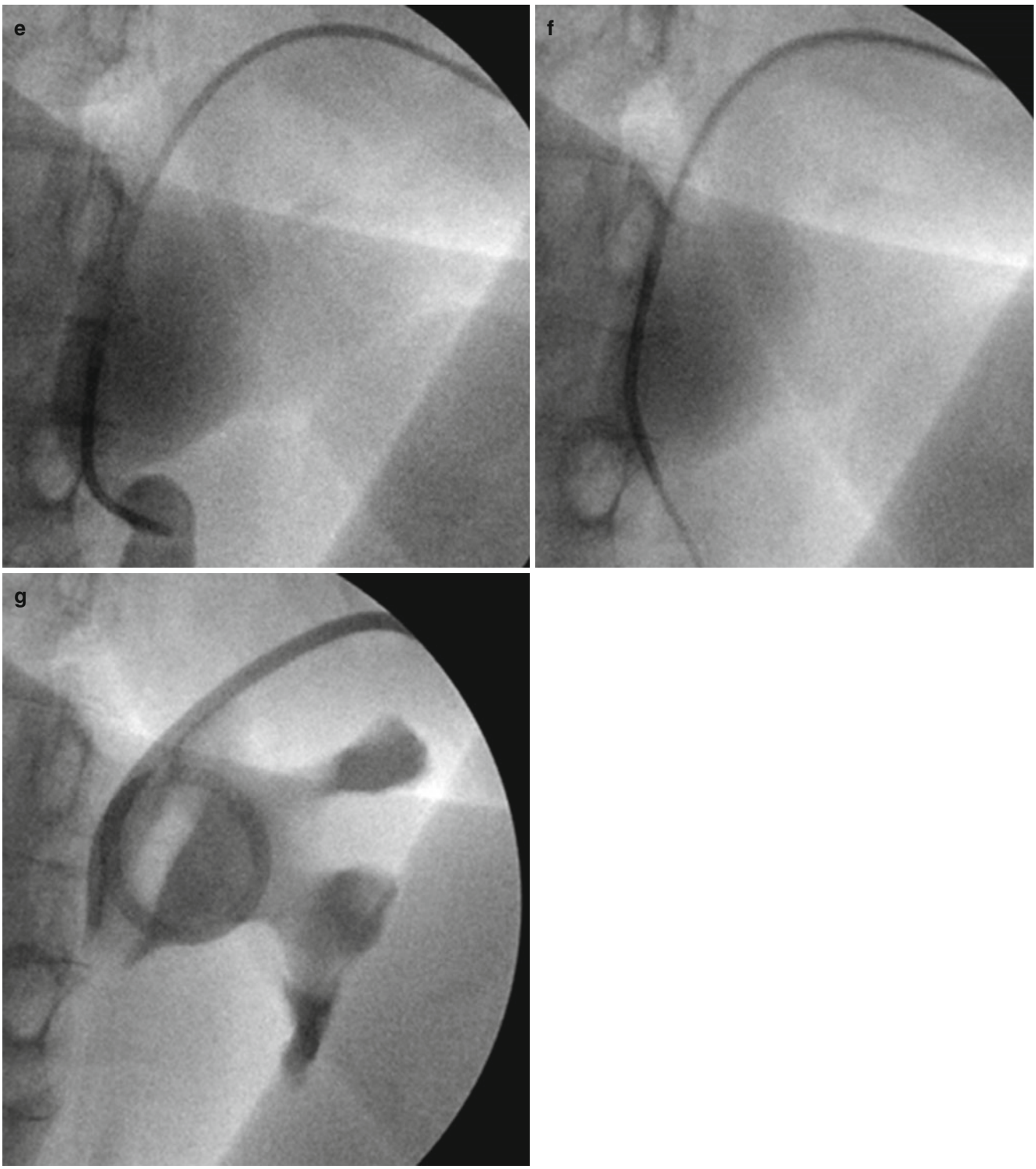

Fig. 19.10 (continued)

For most patients, ultrasound is sufficient to safely guide the procedure. However, in patients who have had multiple abdominal surgeries or pelvic masses or are morbidly obese, CT may be preferred. The patient is placed in the supine position. The pubic area is shaved, if necessary, and prepared and draped in a sterile fashion. Ideally, the bladder is entered on the midline, approximately 4–5 cm above the pubic bone. However, preprocedural imaging may dictate an alternate approach. We favor an ultrasound and fluoroscopic-guided approach. Using this approach, there is real-time visualization

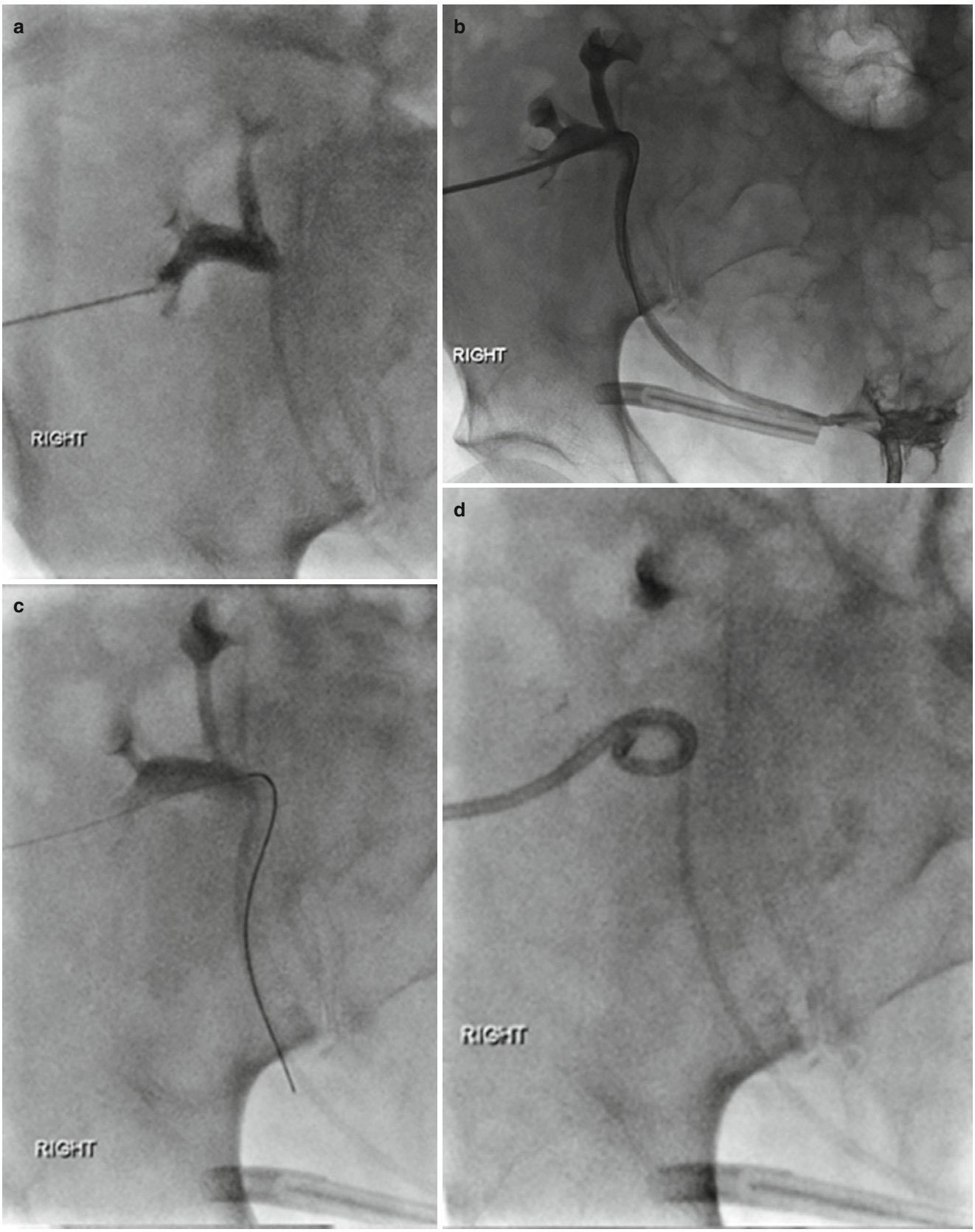

Fig. 19.11 Primary percutaneous nephrostomy placement in a patient with known polycystic kidney disease and a right lower quadrant renal transplant. (**a**) Needle access of the transplant collecting system is demonstrated in a lateral calyx. (**b**) Placement of guidewire into the proximal right transplant collecting system/ureter. (**c**) Patency of the transplant collecting system is demonstrated to the bladder. (**d**) Formation of distal end of 8.5 French nephrostomy catheter in right lower quadrant transplant renal collecting system

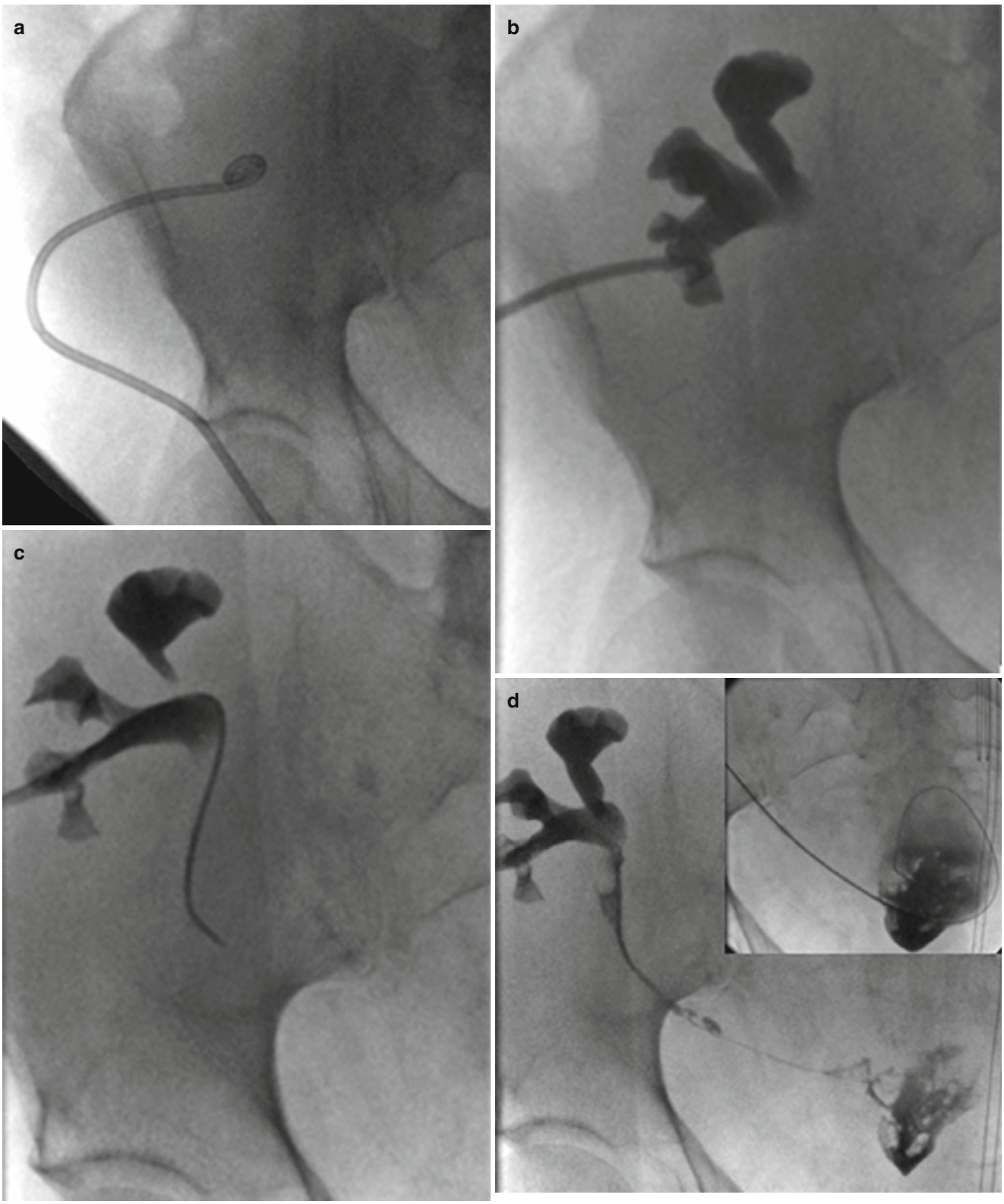

Fig. 19.12 Double-J stent placement in a transplant kidney via nephrostomy tube. (**a**) Nephrostomy tube is noted of right lower quadrant transplant kidney in the same patient as Fig. 19.11. (**b**) Contrast opacification of the transplant renal collecting system is demonstrated. (**c**) Nephrostomy tube is removed over the wire. The wire and an angled catheter are advanced into the proximal ureter. (**d**) Contrast opacification through the catheter demonstrates patency of the collecting system to the urinary bladder. Inset demonstrates advancement of stent catheter and wire into the urinary bladder. (**e**) Stent catheter is pushed until the proximal and distal ends are located in the renal collecting system and bladder, respectively. (**f**) Deployment of the proximal end of the double-J ureteral stent is demonstrated along with replacement of nephrostomy catheter

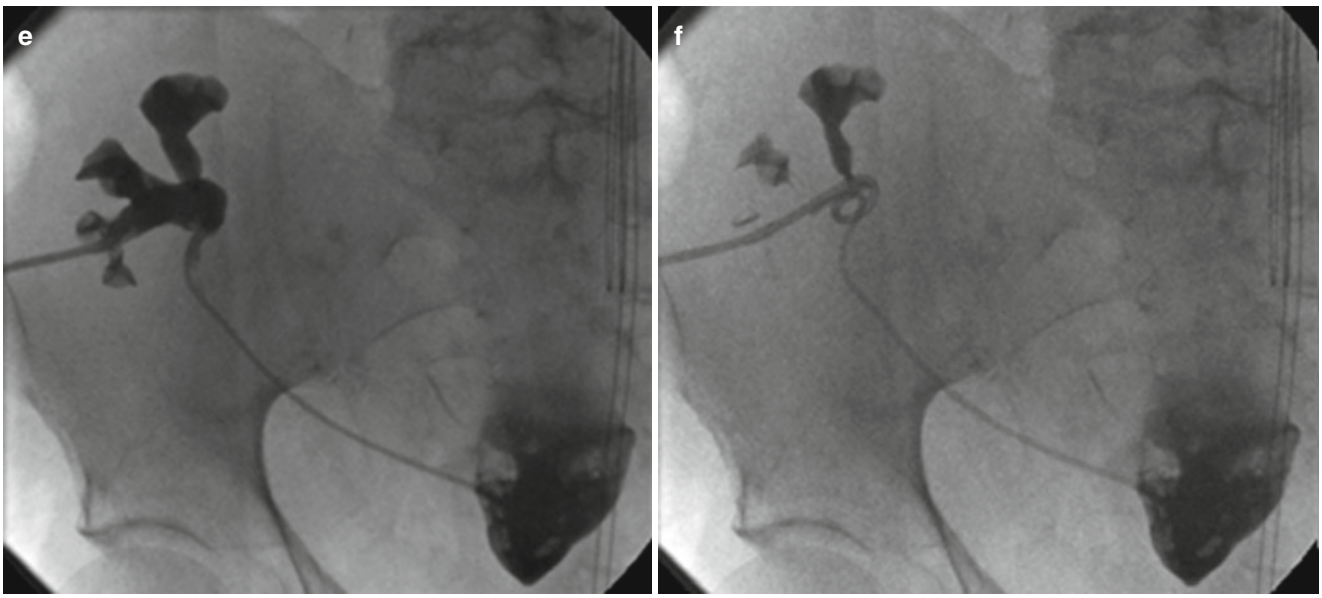

Fig. 19.12 (continued)

of needle and catheter approach. Placement is via Seldinger technique, typically utilizing 8–10 French drainage catheters. However, operator preference and the clinical circumstances may dictate placement of alternate catheter types and diameters (Fig. 19.13). A urine sample is typically submitted for culture and drainage is to gravity. Postprocedural care and maintenance of suprapubic drainage catheters are similar to nephrostomy catheters.

Urinoma Drainage

Urinomas are urine-filled fluid collections. They are most commonly found in the retroperitoneum in the perinephric space. However, the location may be variable in the postoperative and renal transplant patient (Fig. 19.14). Common causes are primarily due to obstruction but also include trauma, surgery, or urinary tract instrumentation. Urinomas appear as simple or complex cystic masses on ultrasound. On cross-sectional imaging, the fluid appears simple and low density, similar to the urine within the bladder. Differential diagnosis includes abscess, seroma, lymphocele, or liquefied hematoma. Occasionally, there is contrast extravasation into the urinoma during intravenous urogram. Small urinomas typically resolve over time. However, if the urinoma is large, persistent, or symptomatic, drainage should be considered.

Urinoma drainage is approached in a similar fashion to drainage of any symptomatic abdominal or pelvic fluid collection (Fig. 19.14). Patient positioning is dependent on accessibility. Imaging guidance modalities include CT, coned beam CT, fluoroscopy, transcutaneous ultrasound, endorectal ultrasound, and endovaginal ultrasound as acceptable options. The chosen modality depends on the location of the fluid collection, local resources, and practices. Following access to the fluid collection, a fluid sample is submitted for culture and creatinine, triglycerides, and possibly cell count. Although the appearance of the fluid is usually an indicator of its origin, the results obtained can help to narrow down its origin and to guide treatment. Following drainage catheter placement and evacuation of the cavity contents, injection of contrast material may be performed to evaluate the morphology of the fluid cavity, to confirm optimal drainage catheter placement, to demonstrate loculations or daughter collections, and to identify communication to the urinary tract. Due to the patulous nature of most urinoma cavities at initial drainage, demonstrating fistulas to the urinary tract at initial presentation is infrequent. Furthermore, if there is suspicion for infection or the patient is symptomatic, injection is not performed as pressurization of the cavity may result in bacteremia or sepsis.

Urinoma drainage may be combined with nephrostomy and bladder drainage to divert the urine stream to promote healing (Fig. 19.15). Follow-up evaluation is based on clinical status and may include CT scans and drainage catheter evaluation under fluoroscopy. If there is adequate drainage, the urinoma cavity will shrink over time. Contrast injection of the drainage catheter under fluoroscopy will usually demonstrate the urinary tract fistula after the urinoma cavity has contracted. The clinical endpoint is complete collapse and contraction of the urinoma cavity and closure of the fistula to the urinary tract. With continued diversion of the urine stream, the fistula tract will usually eventually heal.

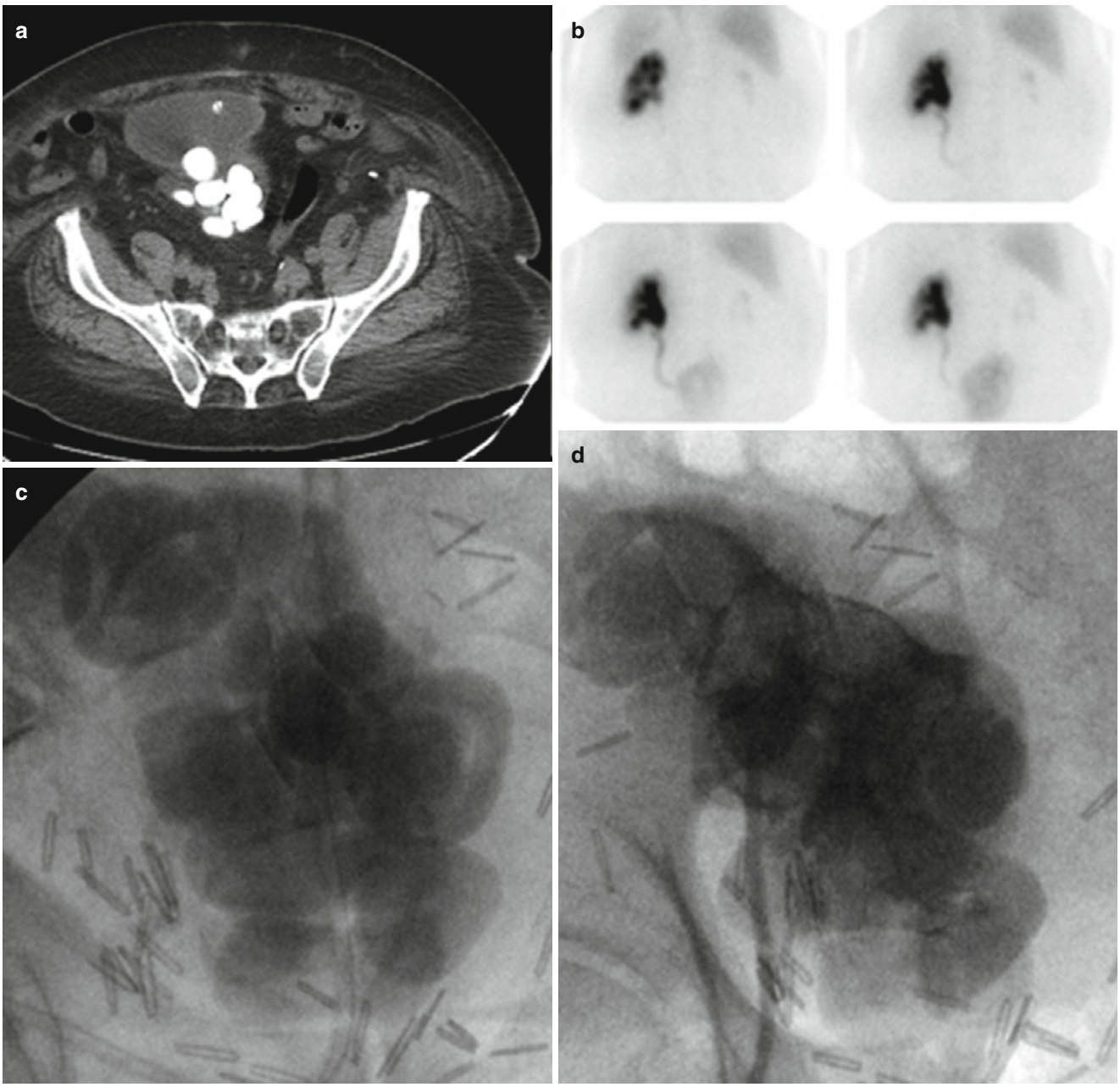

Fig. 19.13 Suprapubic catheter exchange. (**a**) Axial CT image demonstrates bladder with multiple large rounded calculi which prevented foley catheter placement. Suprapubic catheter is also present. (**b**) Renal Lasix scan demonstrates presence of one functional kidney. (**c**) Fluoroscopic image demonstrates bladder filled with stones and presence of suprapubic catheter. (**d**) Contrast opacification of the bladder demonstrates patency of the catheter, which is subsequently exchanged over a guidewire (**e**)

Fig. 19.13 (continued)

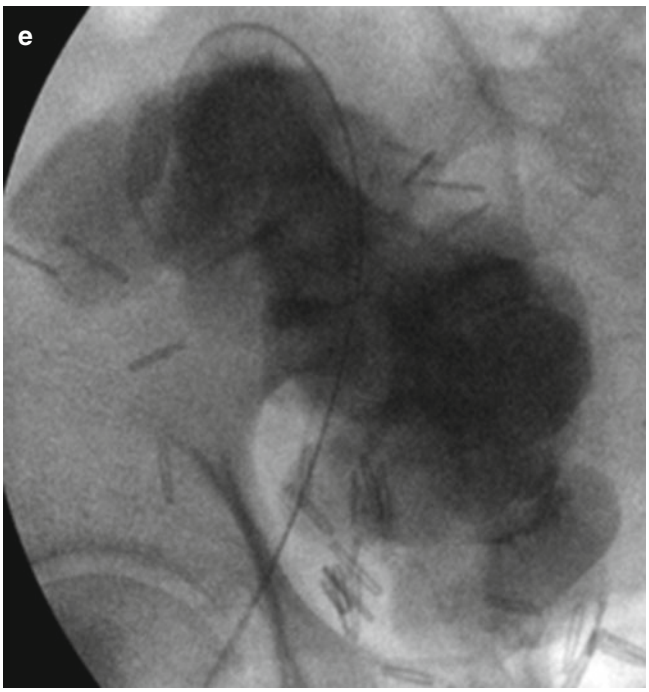

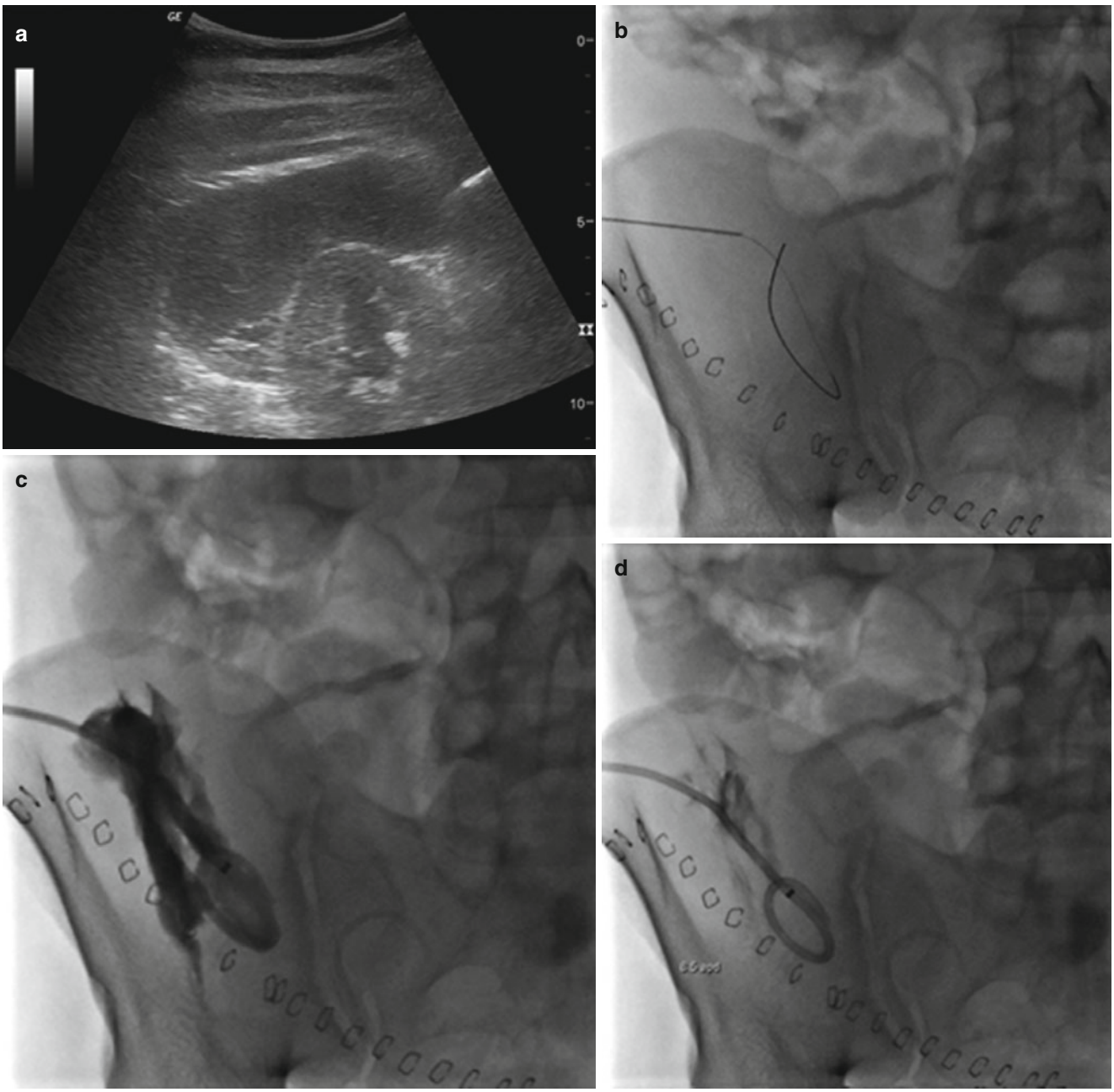

Fig. 19.14 Urinoma drainage in patient with right lower quadrant transplant. (**a**) Gray-scale ultrasound image demonstrates needle access in perinephric collection. Needle is demarcated with arrowhead. (**b**) Fluoroscopy shows wire access into the collection. (**c**) Drainage catheter is advanced over the wire, and placement is confirmed with contrast injection. (**d**) Contrast and fluid in the collection are removed and the formed catheter is left to drain any re-accumulating fluid

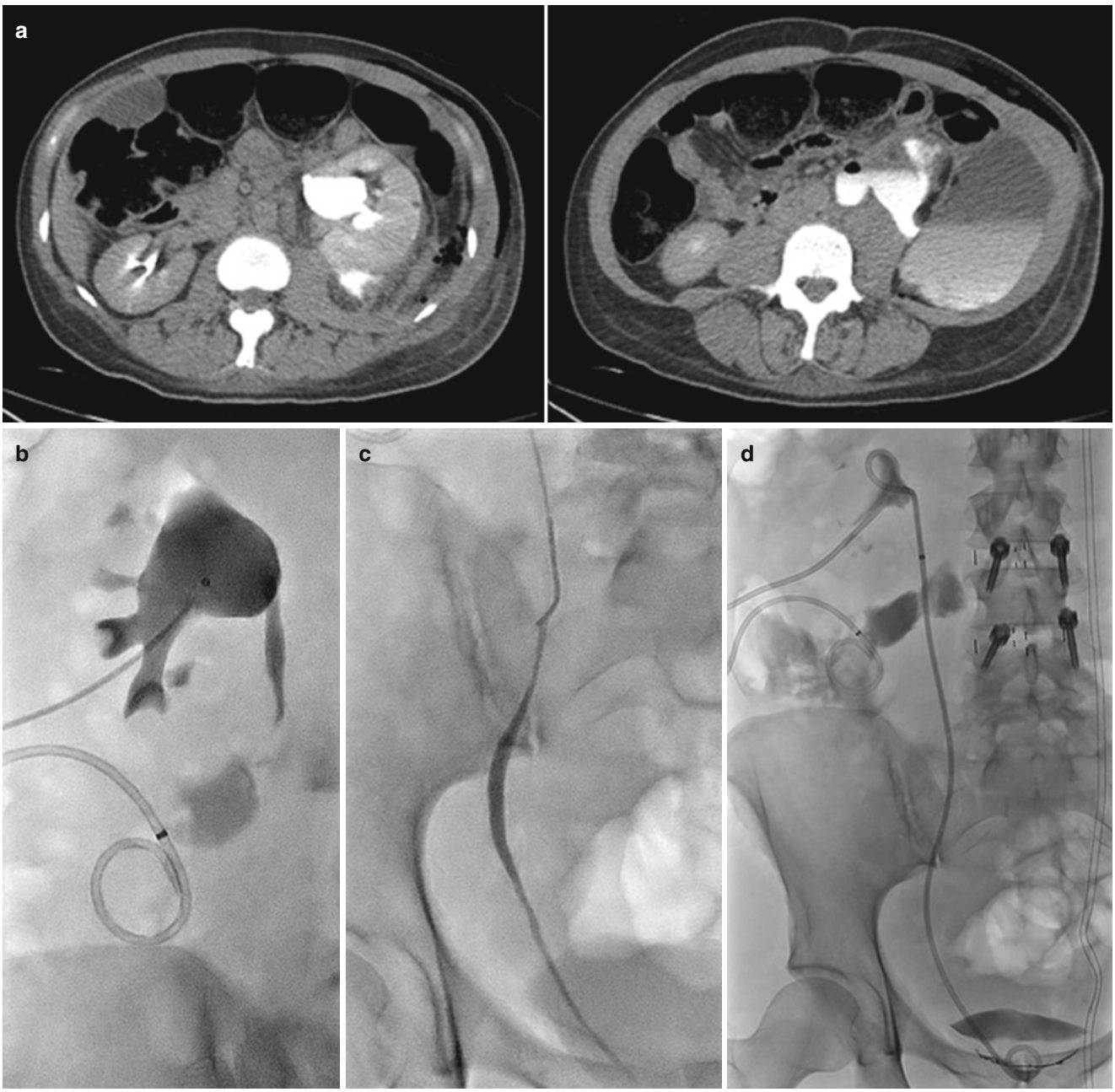

Fig. 19.15 Concomitant use of drainage and diversion in a patient who had ureteral injury in the process of anterior approach lumbar spinal surgery. (**a**) Two axial slices from CT urogram protocol demonstrate hydronephrotic left kidney with large left perinephric collection consistent with ureteral injury and obstruction of the left collecting system. (**b**) Fluoroscopic image demonstrates percutaneous access to hydronephrotic left kidney after patient already had percutaneous drainage of left perinephric collection. Contrast injection shows persistent left mid-ureteral leak. (**c**) Passage of contrast to the distal left ureter is demonstrated. (**d**) Left-sided nephroureteral stent bypasses the site of ureteral injury and allows for ureteral healing. Percutaneous drain for urinoma remains in place

Conclusion

Urinary drainage and diversion encompass some of the more traditional procedures in interventional radiology. A broad spectrum of techniques is employed to gain access to the kidney, ureter, and bladder to achieve diagnostic and therapeutic goals. The planning, approach, and execution overlap with those of other interventional radiologic disciplines. Traditionally, procedures were performed under fluoroscopy, using landmarks for guidance. As technology has evolved, the technique has been refined. Today, operators may use ultrasound, fluoroscopy, CT, or cone beam CT alone or in combination to confidently access and treat the urinary tract, even in non-distended systems. Advances in other areas of interventional radiology continue to have application to urinary drainage and diversion, expanding diagnostic and therapeutic options.

References

1. Goodwin WE, Casey WC, Woolf W. Percutaneous trocar (needle) nephrostomy in hydronephrosis. J Am Med Assoc. 1955;157(11): 891–4.
2. Alken P, Hutschenreiter G, Gunther R, et al. Percutaneous stone manipulation. J Urol. 1981;125(4):463–6.
3. Valji K. Practice of interventional radiology. In: Urologic and genital systems. p. 684–71.
4. Dyer R, et al. Percutaneous nephrostomy with extensions of the technique: step by step. Radiographic. 2002;22:503–25.
5. Malloy PC. Consensus guidelines for periprocedural management of coagulation status and hemostasis risk in percutaneous image-guided interventions. J Vasc Interv Radiol. 2009;20(7 Suppl):S240–9.
6. Beddy P, Ryan JM. Antibiotic prophylaxis in interventional radiology—anything new? Tech Vasc Interv Radiol. 2006;9(2):69–76.
7. Bui T. Airway management of patients undergoing non-OR procedures. Anesthesiology News. 2008.
8. Caplin D. ACR-SIR practice guideline for sedation/analgesia. Reston: American College of Radiology (ACR); 2010.
9. Millward S. Percutaneous nephrostomy: a practical approach. JVIR. 2000;11:955–64.
10. Saad W. Percutaneous nephrostomy: native and transplanted kidneys. Tech Vasc Interv Radiol. 2009;12(3):172–92.
11. Barbaric Z, et al. Percutaneous nephrostomy: placement under CT and fluoroscopy guidance. AJR. 1997;169:151–5.
12. Sigel D. 3D imaging in the angiography suite advances interventional patient care. Appl Radiol. 2012.
13. Cardella J. Society of interventional radiology. Standards of Practice Committee. Percutaneous Nephrostomy. 2014.
14. Makramalla A, Zuckerman DA. "Nephroureteral stents: principles and techniques.". Semin Intervent Radiol. 2011;28(4). Thieme Medical Publishers.
15. Hausegger KA, Portugaller HR. Percutaneous nephrostomy and antegrade ureteral stenting: technique—indications—complications. Eur Radiol. 2006;16(9):2016–30.
16. Tal R, et al. "Management of benign ureteral strictures following radical cystectomy and urinary diversion for bladder cancer.". J Urol. 2007;178(2):538–42.
17. Drake MJ, Cowan NC. Fluoroscopy guided retrograde ureteral stent insertion in patients with a ureteroileal urinary conduit: method and results. J Urol. 2002;167(5):2049–51.
18. Farooq A, Agarwal S, Jones V. Safe removal of an encrusted nephrostomy tube using a vascular sheath: a technique revisited. Cardiovasc Intervent Radiol. 2013;36(3):820–3.
19. Weedin JW, Coburn M, Link RE. The impact of proximal stone burden on the management of encrusted and retained ureteral stents. J Urol. 2011;185(2):542–7.
20. Chung SY, Stein RJ, Landsittel D, Davies BJ, Cuellar DC, Hrebinko RL, et al. 15-year experience with the management of extrinsic ureteral obstruction with indwelling ureteral stents. J Urol. 2004;172(2):592–5.
21. Hafez KS, Wolf Jr JS. Update on minimally invasive management of ureteral strictures. J Endourol. 2003;17(7):453–64.
22. Kwak S, Leef JA, Rosenblum JD. Percutaneous balloon catheter dilatation of benign ureteral strictures: effect of multiple dilatation procedures on long-term patency. AJR Am J Roentgenol. 1995;165(1):97–100.
23. Mostafa SA, et al. Percutaneous nephrostomy for treatment of post-transplant ureteral obstructions. Urol J. 2008;5(2):79–83.
24. Peregrin JH, et al. "Nephrostomy in early posttransplantation period in patients with nonfunctional graft and nondilated collecting system.". Cardiovasc Intervent Radiol. 2014;37(2):458–62.
25. Fayek SA, et al. Ureteral stents are associated with reduced risk of ureteral complications after kidney transplantation: a large single center experience. Transplantation. 2012;93(3):304–8.
26. Kobayashi K, et al. Interventional radiologic management of renal transplant dysfunction: indications, limitations, and technical considerations 1. Radiographics. 2007;27(4):1109–30.
27. Harrison SC, et al. British Association of Urological Surgeons' suprapubic catheter practice guidelines. BJU Int. 2011;107(1):77–85.

Renal Ablations

20

Monica S.C. Morgan and Jeffrey A. Cadeddu

Management of renal cell carcinoma has undergone a paradigm shift over the last two decades. The incidence of localized renal cell carcinoma (RCC) has dramatically increased due to the greater use and refinement of modern cross-sectional imaging [1–3]. In addition to cancer-specific survival, this trend has allowed urologists to increase the focus on preservation of renal function, avoidance of treatment-related morbidity, and quality-of-life outcomes.

Renal tumor ablative therapies offer a myriad of advantages compared to extirpative surgery. Particularly, they are less technically demanding than partial nephrectomy (open, laparoscopic, or robotic), not requiring hilar dissection or renorrhaphy. Moreover, they are associated with fewer complications and shorter convalescence [4].

Cryoablation

Cryoablation (CA) refers to the concept of the application of extreme cold temperatures to destroy tissue. Dr. James Arnott, an English physician, first described this using a combination of ice and salt to topically palliate breast and cervical cancers with variable success [5]. The first modern-day probe using pressurized liquid nitrogen was developed by Dr. Irving S. Cooper, a neurosurgeon from New York. This revolutionary self-contained probe controlled temperatures of −196 °C and allowed for intra-abdominal treatment of large volumes; however, its application was limited due to the lack of availability of intraoperative imaging to monitor the expanding frozen tissue. In the mid-1980s, Onik and colleagues discovered the application of intraoperative ultrasonography during cryosurgery which addressed many of its aforementioned shortcomings [6, 7]. Newer argon gas-based systems were developed in the late 1990s due to the inefficiency of the liquid nitrogen system. These probe systems rely on the Joule-Thomson principle (low temperatures are achieved by rapid expansion of high-pressure, inert gas) to generate temperatures of −185.7 °C within treatment tissues. In addition to being more efficient, these systems provide a more reliable target temperature [8]. Now the majority of commercially available CA units employ argon gas-based systems (Visual-ICE®, Galil Medical, Arden Hills, MN; CryoCare, CryoCare CS, Endocare, Irvine, CA; SeedNet, Oncura, Philadelphia, PA) (Fig. 20.1).

M.S.C. Morgan, MD • J.A. Cadeddu, MD (✉)
Department of Urology, University of Texas Southwestern Medical Center, Dallas, TX, USA
e-mail: Jeffrey.Cadeddu@UTSouthwestern.edu

Mechanism

Tissue injury during CA is multifaceted and occurs during both the freezing and thawing cycle [9–11]. During rapid freezing in the field closest to the cryoprobe, ice crystals form within the intracellular space causing mechanical trauma to plasma membranes and organelles leading to ischemia and apoptosis. With gradual freezing spreading further from the probe, the cooling process is slower, therefore promoting extracellular ice crystal formation, thus creating an osmotic gradient resulting in intracellular fluid depletion which leads to dehydration and membrane rupture. During the thawing phase, ice crystals melt causing a decrease in extracellular osmolarity, resulting in an influx of water back into the cells, cellular edema, and further cell membrane disruption [12]. During the freezing process, injury to blood vessel endothelium results in platelet activation; vascular thrombosis and tissue ischemia also occur.

Principles of Treatment

Treatment Temperature and Adequate Ablation Zone

Cell damage depends on the number of freeze-thaw cycles [13], the cooling rate, the lowest temperature achieved, and the hold time at subzero temperatures [14, 15]. For normal renal parenchyma, destruction is possible at −19.4 °C;

A.R. Rastinehad, D.N. Siegel (eds.), *Interventional Urology*, DOI 10.1007/978-3-319-23464-9_20

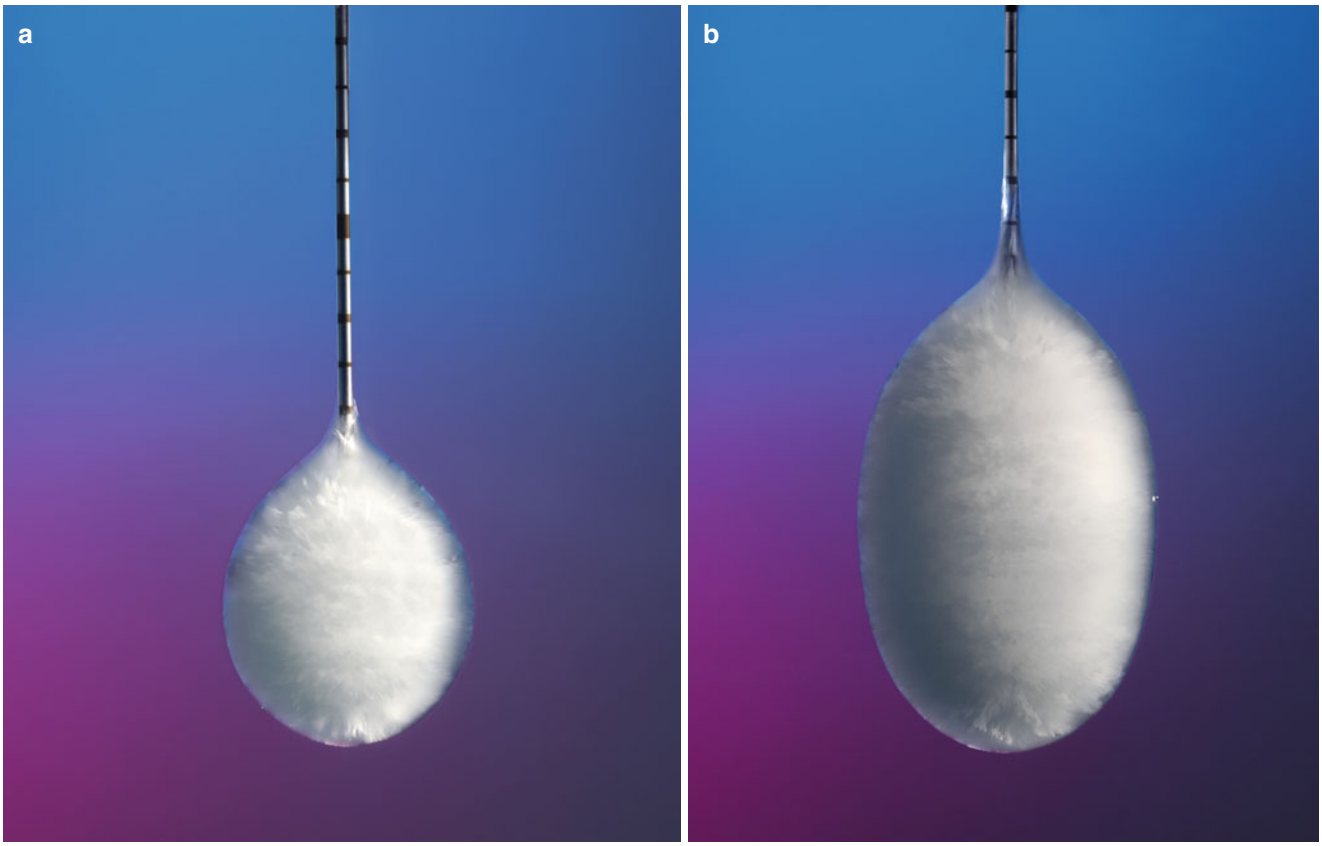

Fig. 20.1 Two types of cryoablation needles used with the Visual-ICE® Cryoablation System. (**a**) IceSeed®, (**b**) IceRod® (Used with permission. © Galil Medical)

however, CA of small animal models indicates that temperatures as low as −50 °C may be necessary to assure complete cellular death of malignant tissue owing to its more fibrous nature [14, 16, 17]. Currently, the preferred target tissue temperature during CA is −40 °C or below. Moreover, preclinical models have demonstrated that the aforementioned threshold temperature of −20 °C was obtained 3.1 mm inside the edge of the evolving ice ball [16, 18]. Thus, to achieve an adequate ablation zone, most authors advocate that CA should be performed at least 5–10 mm beyond the edge of the target lesion. The ablation zone is dependent on the number and type of CA needles placed, tissue and tumor characteristics, thermal heat sink from surrounding vasculature, and treatment duration (Fig. 20.2).

Freeze-Thaw Cycles

The optimal number of cycles is still controversial; early in vivo studies have demonstrated that multiple cycles promoted a larger, more adequate area of liquefactive necrosis consequently improving cure rates [13, 19]. Thus, to ensure complete cellular death, the current recommendation is to perform a double freeze-thaw cycle. Apart from the number of cycles, experimental data suggests that active thawing, with helium gas at 15–20 °C/min, does not differ in the degree or reproducibility of tissue destruction compared to passive thawing [13]. Moreover, active thawing is clearly more efficient therefore reducing procedural time as well as allowing the surgeon to more rapidly address posttreatment bleeding [4].

Duration of Treatment

Little data exists regarding the optimal duration of the freeze cycle. Preclinical studies have demonstrated complete cellular necrosis extending 10 mm or more beyond the probes with a treatment time of 10–15 min. Furthermore, tissue treated for 5 min or less have excessive bleeding and greater than 15 min may fracture and have subsequent hemorrhage [20]. Therefore, most contemporary series utilize a freeze cycle of 8–10 min, while the second cycle is generally shorter (6–8 min) [21, 22].

Radiofrequency Ablation

Mechanism

Radiofrequency energy was first described in 1891 by d'Arsonval but was not implemented in surgery until 1928

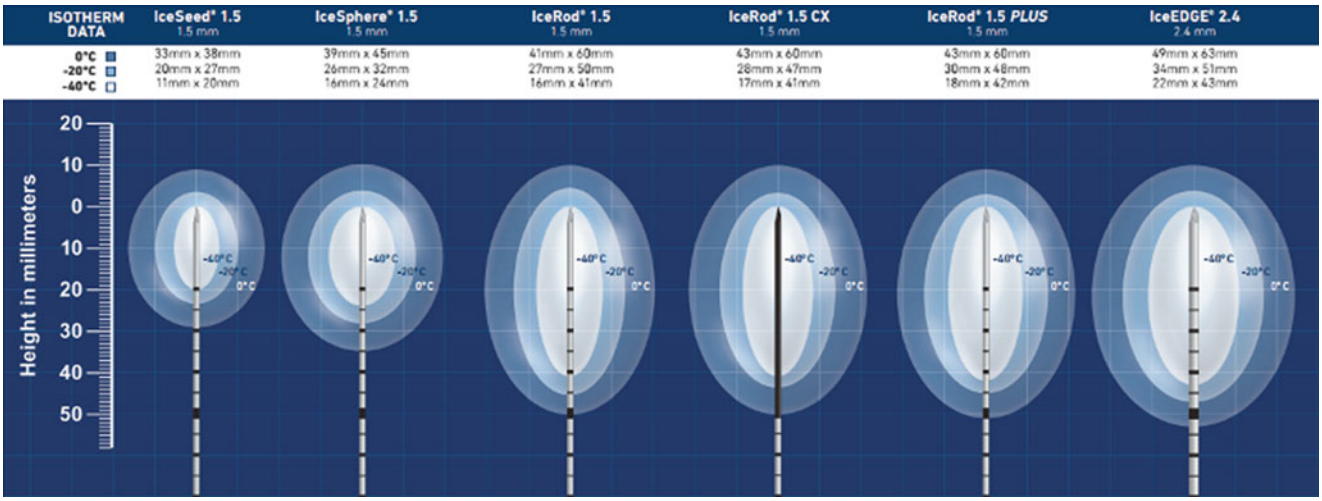

Fig. 20.2 Guide for cryoablation needle(s) use demonstrating in vitro ice ball dimensions for each needle. In vitro studies were performed in room temperature gel that underwent two 10-min freeze cycles separated by a 5-min passive thaw cycle. Accuracy is ±3 mm width and ±4 mm length (Used with permission. © Galil Medical)

when Cushing and Bovie developed the electrocautery knife. Radiofrequency ablation (RFA) uses radiofrequency energy to heat tissue causing subsequent cellular death. High-frequency, monopolar alternating current produced by the RF generator is delivered directly to target tissue at a frequency of 450–1200 kHz resulting in molecular friction and heat production. Increasing temperature within target tissue leads to membrane disruption, protein denaturation, vascular thrombosis, and ultimately, coagulation necrosis [23, 24].

Principles of Treatment

RF Electrodes and Systems

In 1990, probes that could be used for percutaneous RFA were developed by two individual groups simultaneously, consisting of a layer of insulation down to an exposed metal tip, allowing for percutaneous passage of the needle to deeper target tissues [25, 26]. With the use of these probes, the volume of tissue destruction can be controlled by adjusting the length of exposure of the uninsulated portion of the needle. While utilizing the initial design of these probes, development of modern-day RFA probes and generators has led to the capability of treating larger, more complex lesions.

RF generators are either temperature or impedance based. Temperature-based systems monitor tissue temperatures at the tip of the electrode by using thermocouples and determine treatment completion when tissue adjacent to the probe has reached target temperature for a predetermined period of time. Impedance-based systems monitor the level of impedance at the electrode tip, and RF energy is delivered until it achieves a predetermined impedance level indicating complete tissue ablation. Dedicated animal models have demonstrated similar efficacy with these two systems [27]. Clinical data does not explicitly support superiority of either system.

The initial single-electrode monopolar probes were designed and controlled by varying the exposed uninsulated tip, but were only capable of treating tumors no larger than 2 cm [28]. A variety of systems have been developed in pursuit of larger treatment volume. LeVeen introduced an insulated monopolar probe with twelve tines that deploy into an umbrella shape in order to create a spherical treatment zone (Boston Scientific, Natick, MA, USA) (Fig. 20.3) [29]. These tines function as RF antennae for wider distribution of current and monitor impedance, redirecting current to lower impedance if high impedance is encountered. The Valleylab system (Mansfield, MA, USA) is another impedance-based system consisting of a single 17-gauge "cool tip" electrode, cooled with chilled normal saline to prevent charring of adjacent tissue. The RITA probe (AngioDynamics, Queensbury, NY, USA), which is Christmas tree-shaped, uses thermistors embedded in five of the nine electrical tines to modulate average temperature of all the electrodes as well as the temperature of each electrode (Fig. 20.4). In clinical studies, multi-tine electrodes have shown more complete necrosis and superior treatment outcomes [30–32]. RF energy can also be delivered via either bipolar or monopolar electrodes. Traditional monopolar devices work based on electrical transmission through the exposed probe tip dissipating through a grounding pad on the skin of the patient. Bipolar devices generate current between two electrodes (one active and one negative). The theoretical advantages of bipolar devices are induction of higher temperatures and a larger focus of coagulation necrosis [33]. However, rather than a spherical treatment zone, an elliptical area is produced. Considering most renal tumors are spherical, bipolar devices have not been widely adapted.

Fig. 20.3 RFA LeVeen needle electrode with deployed multi-tine array (Courtesy of Boston Scientific, Natick, MA, USA)

Fig. 20.4 14-gauge Starburst XL RFA probe (Courtesy of AngioDynamics, Queensbury, NY, USA)

Wet Versus Dry RFA

RF energy can be applied using needles positioned directly into the lesion (dry RFA) or with perfusion of ionic solutions to decrease the charring effect (carbonization) and act as an energy conductor (wet RFA). Early dry RFA systems, although highly successful in treating small lesions, encountered tissue impedance and therefore lacked efficacy in treating lesions larger than 4 cm. Wet RFA probes deliver a constant saline infusion into the tissue adjacent to the probe, lowering the probe tip temperature, therefore mitigating the charring effect and corresponding premature rise in impedance, allowing for a larger ablation zone [34–37]. Although wet RFA allows a larger treatment zone, it may lead to overtreatment of the target zone and disruption of normal parenchyma as there is less control over the exact size of ablation [38].

Treatment Measure/Temperature

The volume of ablated tissue directly correlates with the amount of RF energy applied to the tissue. Electrical impedance must remain low in order to create an expanding sphere of tissue damage emanating outward from the probe. If the amount of RF energy is applied too high or current is administered too rapidly, charring occurs, thus dehydrating the tissue, abruptly increasing impedance. Energy transfer is then blocked arresting the heating process [15, 39]. Therefore, impedance-based systems generally start at 40–80 W and increased at 10 W/min to a maximum of 130–200 W until they reach an impedance of 200–500 Ω. With the temperature-based system, this phenomenon is prevented by keeping target temperatures at or below 105 °C. Walsh and colleagues demonstrated that the minimum target temperature that is lethal to human RCC in vitro is 70 °C [40].

Techniques and Approaches

Percutaneous Approach

Percutaneous tumor ablation may be performed under conscious sedation with local anesthesia or under general endotracheal anesthesia. Currently, the majority of percutaneous ablations are performed with sedation by anesthesia. General endotracheal anesthesia is generally reserved for patients that cannot tolerate the positioning. Regardless, it is usually performed on an outpatient basis or 24-h observation. Depending on physicians' preference, ablation is performed under ultrasound, CT, or MR guidance [41, 42]. Most investigators prefer CT guidance, which allows precise electrode placement. Following intravenous administration of prophylactic antibiotics, the patient is positioned in either a modified flank, supine, or prone position depending on the tumor location.

First, a non-contrast CT is obtained to confirm tumor size and position. An optional contrast-enhanced CT may be obtained to delineate the tumor and assist with guidance in

cases where no other landmarks are available. With the help of a grid that is placed on the patient's skin, a 20-gauge "finder needle" is often inserted under CT guidance near the location of the tumor. Position is confirmed with repeated imaging. Using the finder needle as a guide, the ablation probe(s) is then positioned for treatment. The treatment duration and number of probes are determined based on size of the lesion and manufacturer's recommendations. Placement of the probes/tines is confirmed by serial imaging. A histologic diagnosis is key in providing uniformity of treatment and improving outcome-based data. The American Urological Association Guidelines Panels concerning small renal mass and follow-up for clinically localized renal neoplasms recommends that biopsy be performed at or prior to time of ablation [43, 44]. If tumor biopsy has not been performed, an 18-gauge core biopsy needle is used. Specimens are obtained and sent for permanent section prior to ablation. It is important for treatment probes to be placed prior to the biopsy as a possible perirenal hematoma after biopsy may interfere with proper visualization of the lesion. In the case were the patient is under general endotracheal anesthesia, adjustments of probe and biopsy needle may be performed with breath holding in order to standardize the position of the mobile kidney. For CA, probes should be positioned to ensure cryolesion overlap. This is accomplished by placing them in parallel to one another in a triangular or quadratic configuration. The probe tips should be advanced just beyond the tip of the deepest tumor margin.

Cryoablation allows for imaging during treatment to monitor efficacy. Although low temperatures of −140 to −190 °C are reached at the cryoprobe tips, there exists a steep temperature gradient which falls to 0 °C at the ice ball edge. This ice edge-normal tissue interface can be identified with CT or US. As previously stated, the ice ball should evolve 5–10 mm beyond the tumor margin to ensure complete treatment (Fig. 20.5). After the second thaw cycle is completed, the probe is gently twisted, and if no resistance exists, it is gently removed.

As previously mentioned, to monitor treatment efficacy during RFA, tissue temperature or impedance is measured

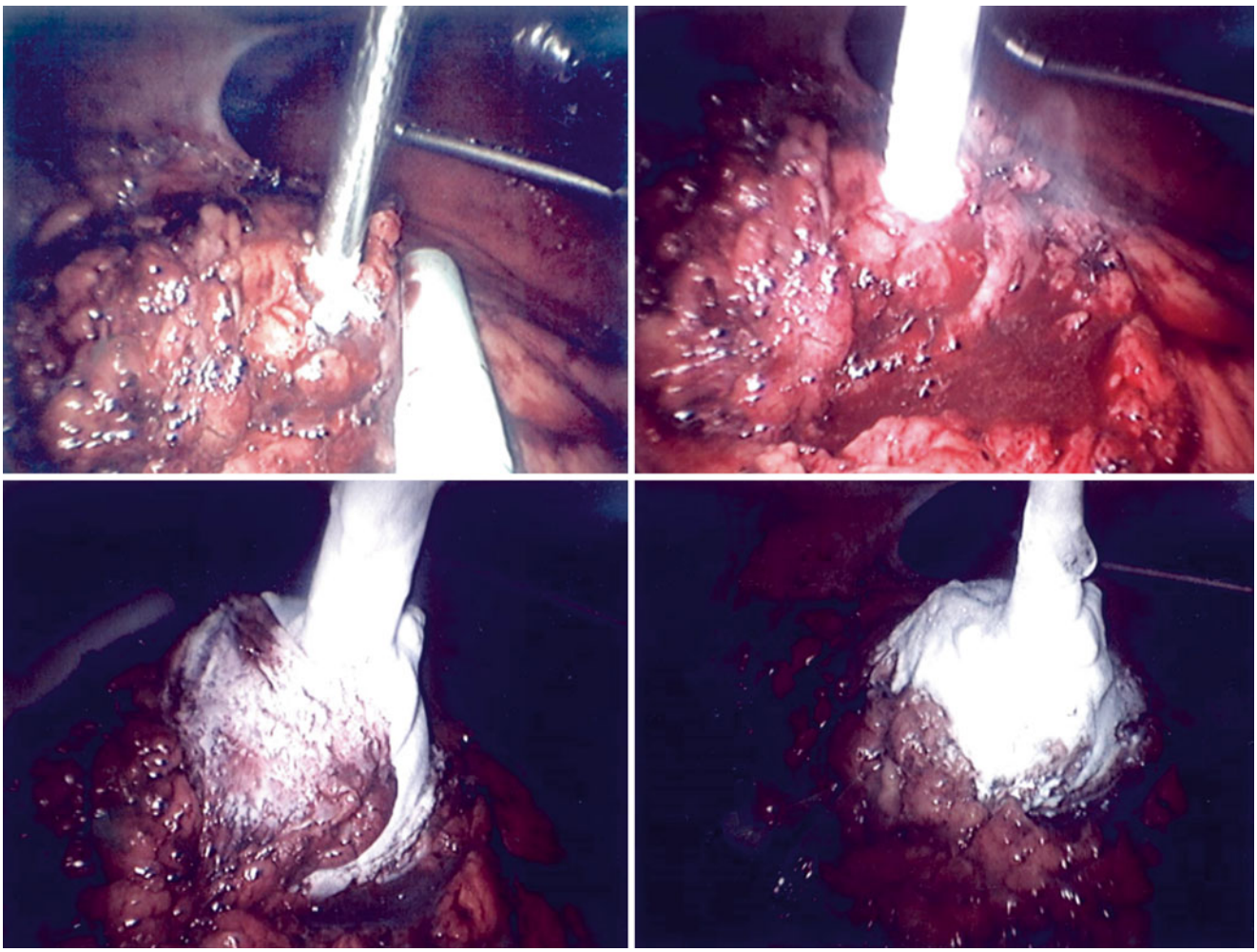

Fig. 20.5 Laparoscopic cryoablation of right renal mass demonstrating progressive ice ball formation

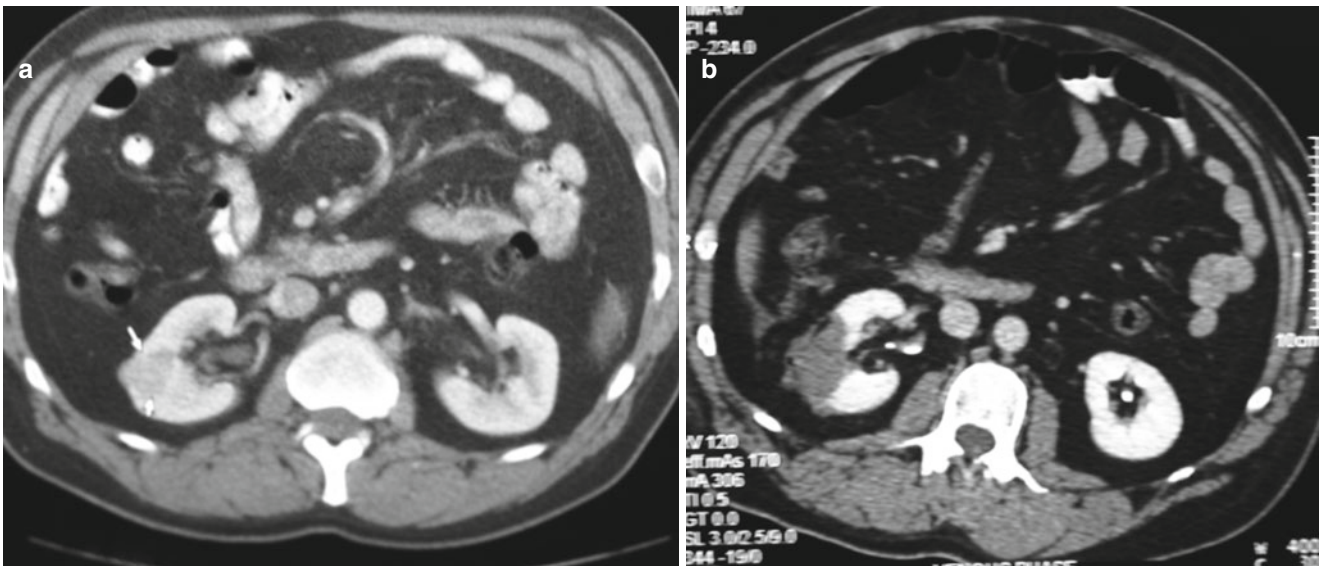

Fig. 20.6 Right midpole posterolateral renal mass (**a**) prior to and (**b**) immediately post cryoablation

using either single multi-tined probes (with incorporated thermistors) or multiple single-shaft probes that measure tissue impedance. The authors use a 14-gauge Starburst XL (Angiodynamics, Queensbury, NY, USA) RFA probe that is deployed and adjusted to ensure complete coverage of the lesion with at least 5 mm margin. This is achieved with the use of serial non-contrast CT scans with 3-mm cuts. For tine deployments of <2, 2–3, and 3–4 cm, the ablation cycles are timed at 5, 7, and 8 min at a target temperature of 105 °C, respectively. After a 30-s cooldown, a second cycle of similar duration is performed. During both cooldown cycles, the passive tissue temperature in each quadrant must be greater than 70 °C, confirming absence of a large heat sink.

Posttreatment, a contrast-enhanced CT, is repeated to evaluate completeness of ablation and to assess for complications (Fig. 20.6). However, post CA, the ice ball will obscure the zone of true ablation and therefore will overestimate the area being treated. As per AUA guidelines, the follow-up of renal mass ablation includes a contrast-enhanced CT or MRI at 3 and 6 months following ablation, then annually for 5 years [44]. Therefore, treatment success is truly evaluated during follow-up. Following treatment, patients are discharged in a same-day fashion. Those with comorbidities or complications are typically admitted overnight.

Laparoscopic Approach

Laparoscopic ablation may be delivered using either a retroperitoneal or transperitoneal approach, depending on tumor location. Mobilization of the kidney is performed using a three-port technique. Gerota's fascia is opened in a fashion similar to that employed for a laparoscopic partial nephrectomy. The fat overlying the lesion is excised and may be placed in a specimen bag and sent for pathologic analysis. Placement of the CA or RFA probes can be performed percutaneously, leaving the ports free for instrumentation (Fig. 20.7). Probe placement and probe depth are confirmed by direct visualization and intraoperative ultrasonography, respectively.

Tips and Tricks

Appropriate patient selection, preoperative planning, and good surgical technique are keys to a successful ablation. In order to determine whether a tumor should be managed laparoscopically or percutaneously, cross-sectional imaging is imperative. When there is concern regarding adjacent organs, further imaging may be obtained in different positions in order to plan the most appropriate probe placement. Laparoscopic ablation should be considered in patients with anterior tumors, tumors near the collecting system, or when a suitable access tract on imaging is not possible. Other options include intra-procedural hydrodissection, pneumo-dissection, or balloon dissection to displace adjacent organs. The ideal renal masses for percutaneous ablation are posterior tumors, those located >0.5 cm from the ureteropelvic junction or collecting system, and those >1 cm from surrounding bowel.

Oncologic Outcomes

As renal ablation is relatively new compared to extirpative surgery, long-term data is just now being reported. The American Urological Association recently recognized ablation as an alternative treatment to small renal masses in patients with primarily T1a (<4 cm) tumors with risk factors that may increase surgical morbidity [43]. Furthermore,

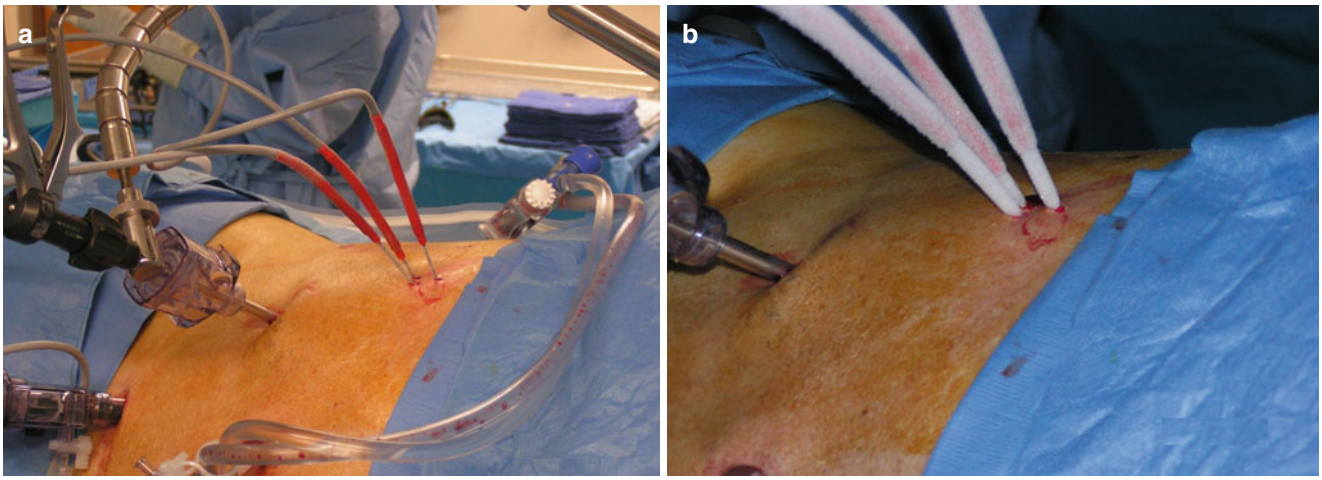

Fig. 20.7 (**a**) Laparoscopic cryoablation setup with a camera port, two working ports, and percutaneous probe insertion; (**b**) percutaneous deployment of the probes in a triangular configuration

Table 20.1 Cryoablation for biopsy-proven RCC: intermediate and long-term outcomes

Author, year	No. patients (no. of tumors)	Technique	Tumor size, cm (range)	Follow-up (years) (range)	5-year LRFS (%)	5-year CSS (%)	5-year OS (%)
Aron et al., 2010 [51]	55 (55)	Laparoscopic	Mean 2.3 (0.9–5.0)	Median 7.8 (5–11)	87.3	92	84
Guazzoni et al., 2010 [68]	44	Laparoscopic	Median 2.14 (0.5–4)	Mean 5.1	93.2[a]	100	93.2
Tanagho et al., 2012 [49]	35	Laparoscopic	Mean 2.5 (SD 0.98)	Mean 6.3 (SD 3.3)	80[b]	100[b]	76.2[b]

LRFS local recurrence-free survival, *CSS* cancer-specific survival, *OS* overall survival
[a]These patients underwent salvage RFA or radical nephrectomy, but were not included in the recurrence analysis
[b]6-year LRFS, CSS, OS

based on its success, the AUA guidelines now recommend that CA and RFA be discussed with healthy patients as an alternative to surgical treatment, keeping in mind the slight increased risk of tumor recurrence and possible difficulty of surgical salvage.

Due to the heterogeneity of the literature, interpretation of oncologic success may be more of a challenge. Quality of evidence is improving as renal ablative literature continues to mature. Regarding CA, local recurrence-free survival ranges between 80 and 86 % while RFA ranges between 88 and 92 %. Metastasis-free survival and cancer-specific survival exceed 90 % in practically all reported series. Data suggests progression-free survival and disease-specific survival exceed 90 % as well and are similar for ablative therapy and extirpative procedures. RCC-specific outcomes are for CA, and RFA in select series with intermediate and long-term follow-up is summarized in Tables 20.1 and 20.2, respectively.

Local Recurrence-Free Survival (LRFS)

The risk of local tumor recurrence following CA and RFA has been evaluated in several meta-analyses [43, 45, 46]. In these studies, local recurrence was generally defined ablation. The AUA SRM Guidelines Panel examined the literature concerning CA and RFA and determined LRFS of 90.6 % (83.8–94.7 %) for cryoablation and 87.0 % (83.2–90 %) for RFA [43]. When compared to surgical treatment, both ablative therapies demonstrated significantly higher local recurrence rates in spite of shorter follow-up. There was no significant difference in LRFS between CA and RFA and no difference in metastasis-free survival or cancer-specific survival between ablation and extirpative therapy.

El Dib et al. performed a more recent meta-analysis, reviewing 31 case series (20 CA, 11 RFA) and found no difference between the two treatments in terms of efficacy (CA 89 %, RFA 90 %) [46]. Of note, a recent cohort study, using the Surveillance, Epidemiology and End Results (SEER) database reported that patients who underwent nephron-sparing surgery had an improvement of 1.7 % in 5-year disease-specific survival (DSS) compared to ablation [47]. The difference in DSS decreased over time, perhaps due to improved patient selection, increased experience, and modifications in technique. As well, long-term follow-up data suggests that tumor size is a significant indicator of success [48–50].

Table 20.2 Radiofrequency ablation of biopsy-proven RCC: intermediate and long-term outcomes

Author, year	No. of patients (no. of tumors)	Technique	Tumor size, cm (range)	Follow-up (years) (range)	5-year LRFS (%)	5-year CSS (%)	5-year OS (%)
McDougal et al., 2005	16 (20)	Percutaneous	Mean 3.2 (1.1–7.1)	Mean 4.6 (4–6)	91[a]	100[a]	68.7[a]
Levinson et al., 2008	18 (18)	Percutaneous	Mean 2.1 (1–4)	Mean 4.8 (3.4–6.7)	79.9	100	58.3
Tracy et al., 2010	160 (179)	Percutaneous and laparoscopic	Mean 2.4 (1.0–5.4)	Mean 2.25 (0.13–7.5)	90	99	85[b]
Zagoria et al., 2011	41 (48)	Percutaneous	Median 2.6 (0.7–8.2)	Median 4.67 (IQR 3–5.3)	88	1/41 (2.4 %) died of RCC	66
Olweny et al., 2012	37 (37)	Percutaneous and laparoscopic	Median 2.1 (IQR 1.8–2.8)	Median 6.5 (IQR 5.8–7.1)	91.7	97.2	97.2
Psutka et al., 2013	185 (185)	Percutaneous	Median 3 (1–6.5)	Median 6.43 (0.5–13.4)	95.2	99.4	73.3
Atwell et al., 2013	222 (256)	Percutaneous	Mean 1.9 (0.6–3)	Mean 2.8 (1.2–4.1)	98.1	98.7[c]	–

LRFS local recurrence-free survival, *CSS* cancer-specific survival, *OS* overall survival
[a]4-year LRFS, CSS, OS
[b]OS for entire cohort, including 22 % with benign or non-diagnostic histology
[c]No prior history of RCC

Metastatic Recurrence-Free Survival (MRFS)

The AUA guidelines evaluated MRSF, which was defined as "any disease present in the body other than in the treated kidney or associated renal fossa following primary treatment." Mean MRFS was 95.3 % (91.1–97.5 %) for CA and 97.5 % (94.8–98.8 %) for RFA [43]. No significant difference was found in MRFS between ablative therapy and extirpative procedures. However, ablative therapy had shorter follow-up, highlighting the need for long-term data.

Over the last several years, authors have reported intermediate and long-term outcomes, including greater than 5-year follow-up data for CA [49, 51] and RFA [23, 48, 50, 52, 53]. This data supports the fact that outcomes for ablative therapy are durable greater than 5 years and up to 10 years.

Cancer-Specific Survival (CSS) and Overall Survival (OS)

The AUA meta-analysis additionally evaluated the risk of mortality from RCC following CA or RFA. CSS was 95.2 % (89.2–97.9 %) and 98.1 % (95.2–99.2 %) with CA and RFA, respectively. Laparoscopic partial nephrectomy had a significantly higher CSS compared to CA, but not for RFA. However, no significant difference was found between the two ablative therapies. Recent publications have reported CSS ranging from 78 to 100 % for CA [49, 51] and approximately 98 % for RFA [50, 52, 53].

Overall survival rates published by the AUA Guidelines Panel were 95.8 % (87.2–98.7 %) for CA and 93.7 % (85.4–97.4 %) for RFA. However, the reports included in this analysis reflect shorter follow-up. Recently reported 5-year OS rates following ablative procedures range from 75 to 85 %, which is consistent with an older patient population with more comorbidities than those who undergo extirpative procedures [23, 50, 52].

Complications

The AUA Guidelines Panel published a meta-analysis comparing urologic and non-urologic complications following CA, RFA, and extirpative therapy [43]. Major complications included hemorrhage requiring transfusion or intervention, urine leakage, abscess, and unforeseen loss of renal function. Major urologic complications post CA and RFA were 4.9 % (3.3–7.4 %) and 6.0 % (4.3–8.2 %), respectively. There was no significant difference in urologic complications between CA and RFA. The risk of major urologic complications was lower with ablation than with open or laparoscopic partial nephrectomy. Major non-urologic issues occurred in 5 % (3.5–7.2 %) of patients who underwent CA and 4.5 % (3.2 %–6.2 %) of those who underwent RFA.

Pain or paresthesia at the probe insertion site is the most common minor complication following renal tumor ablation, occurring in up to 8 % of patients [54]. The most recent generation of cryoprobes are designed with thermal insulation along the shaft, which has led to a decline in freezer burns observed with older generations. RFA probes are equipped with the active portion along the most distal aspect. During RFA, when performing tract ablation, the active portion should not surpass Gerota's fascia, therefore avoiding nerve injury. Prior to RFA, grounding pads should be placed at the exact same level on the posterior aspect of the patient's thigh, perpendicular to its long axis, in order to avoid electrical skin burns, which are possible, but extremely rare [55].

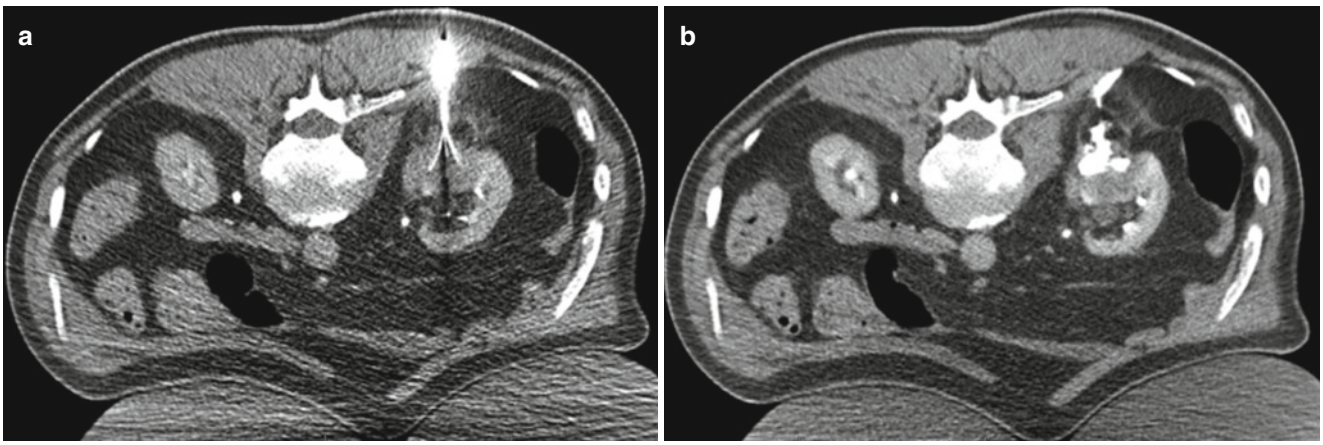

Fig. 20.8 Radiofrequency ablation of left midpole posterior renal mass. (**a**) Deployed RF probe tines, (**b**) extravasation of contrast from the collecting system demonstrating a urine leak

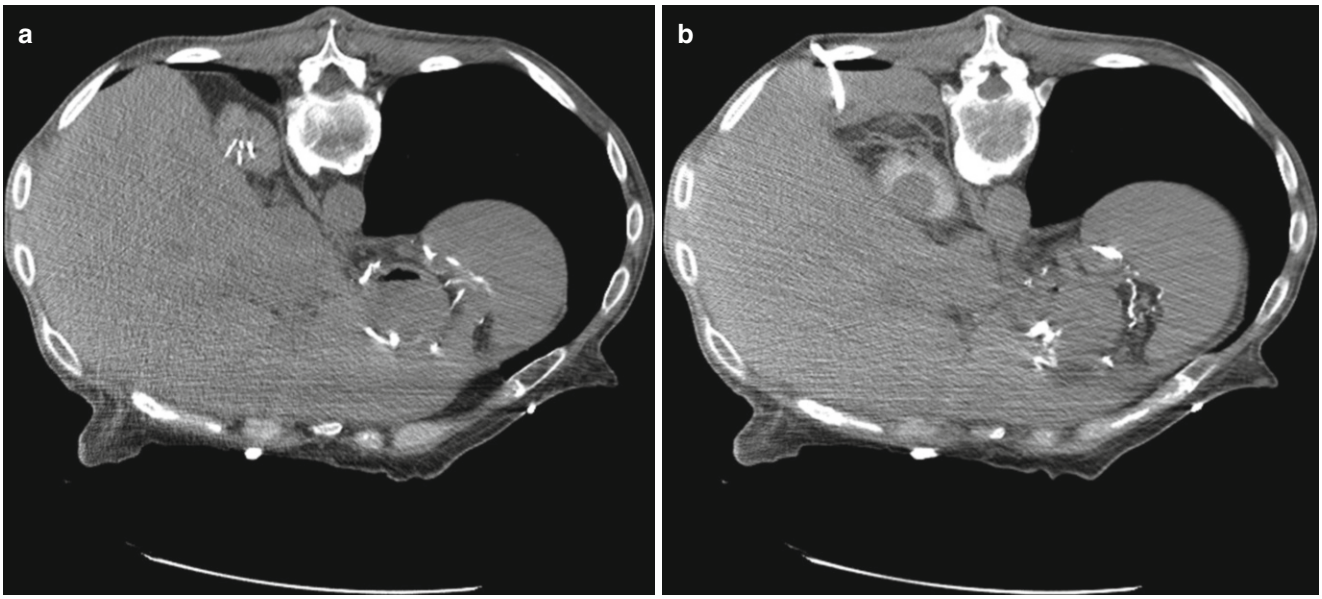

Fig. 20.9 Radiofrequency ablation of 2.1 cm right upper pole renal tumor. (**a**) Deployed RF probe tines, (**b**) complicated by hemothorax and loculated pneumothorax which warranted right chest tube placement

Injury to the urothelium may range from minor to major hematuria with clots or may present as obstruction. Patients with hematuria should undergo conservative management; however, angioembolization should be considered in the presence of significant hemorrhage. In severe cases, damage to the collecting system may result in perirenal urinoma formation or cutaneous urinary fistula. Urinary obstruction or leakage may either be managed conservatively or with placement of an indwelling stent (Fig. 20.8).

Injury to adjacent organs can occur. If probes are placed above the twelfth rib in order to treat an upper pole lesion, this can result in injury to the pleural cavity causing a pneumothorax or hemothorax (Fig. 20.9). This is usually recognized during the procedure. A simple pneumothorax may be treated by aspiration using a small needle inserted into the pleural space at the end of the case. A large or persistent pneumothorax may require chest tube placement. Post-procedure, shortness of breath, or chest pain should elicit suspicion of a pneumothorax, and an upright chest radiograph should be performed promptly.

Colon injury may also occur, but is exceedingly rare and is largely preventable with appropriate surgical technique. During percutaneous ablation, saline may be injected in order to hydro-dissect tissues in the setting where the tumor is in close proximity to bowel. However, these lesions may be more suitable for the laparoscopic approach where bowel can be safely dissected away from the surgical field. A colon injury should be managed with general surgery. Frank perforation should be managed with prompt surgical exploration. Initial management of a controlled colo-renal fistula should

include placement of a ureteral stent, while a persistent or colo-cutaneous fistula may require surgical diversion [56].

Intra- or postoperative hemorrhage has been cited in up to 11–27 % of patients treated with ablative renal procedures [57]. Transfusion rate is 3.2 % (2–4.9 %) with CA and 2.4 % (1.4–4 %) with RFA [43]. The use of multiple probes for larger renal masses is the primary risk factor for hemorrhage [58]. During CA, adequate thaw time decreases the risk of tumor "fracture," while premature probe removal increases risk of "fracture" and hemorrhage. Needle placement may cause bleeding, which may be controlled by just proceeding with ablation, specifically with the coagulative capabilities of RFA. During laparoscopic ablation, bleeding may be managed using hemostatic agents in combination with direct pressure. Consideration should be given for selective angioembolization if bleeding continues post-ablation.

Postoperative infection may occur in the absence of large hematoma or urinoma; however, they are extremely rare, yet may be lethal [59]. Patients with increased risk for infection are those with active infection at time of ablation or those with chronic colonization of the urinary tract [60, 61]. Patients at risk should undergo screening by urine culture and be treated appropriately preceding ablation. Administration of perioperative antibiotic prophylaxis at the time of the procedure should be considered.

New Ablative Approaches

There exist a number of promising ablation modalities in prospect; however, most should be considered investigational in the present time. These modalities include high-intensity focal ultrasonography (HIFU), radiation therapy, stereotactic ablative body radiation (SABR), laser interstitial thermal therapy (LITT), irreversible electroporation (IRE), microwave ablation (MWA), and target embolization prior to ablation. The most promising of these appear to be IRE, MWA, and SABR. IRE is a nonthermal process where nanoscale pores are irreversibly generated across cellular membranes by the application of an electrical field. This increases cell membrane permeability ultimately leading to cell death. Potential benefits are avoiding heat sink, preservation of tissue scaffolding, extracellular matrix, ductal structures, and blood vessels [62, 63]. MWA functions in a similar manner to RFA. It conveys energy through semiflexible probes directly inserted into the target lesion. Microwave energy creates rapid water ion oscillation and frictional heat in the tissue. Unlike RFA, it is not limited by charring and desiccation, and it has capabilities of achieving treatment temperatures higher than 60 °C more rapidly. This may potentially increase efficiency and decrease susceptibility to heat sink [64]. However, the degree of heat production and penetration relies on tissue water content, therefore making it more challenging to predict in a heterogeneous environment such a renal parenchyma [32, 65]. Finally, SABR is a "treatment method to deliver a high dose of radiation to the target, utilizing either single dose or a small number of fractions with a high degree of precision within the body" as defined by the American Society of Therapeutic Radiology and Oncology [66]. It uses an image-guided three-dimensional coordinate tracking system that is dependent on a constant reference point, the fiducial marker, which is continually identified by the linear accelerator. As opposed to conventional radiation therapy techniques, SABR compensates for movement secondary to respiration and radiation scatter by tracking, identification, and correction of target lesion movement, omitting patient repositioning or treatment interruption. Potential benefits include accuracy and precision of treating target tissue and also the ability to use high doses of radiation to a focal zone without scatter therefore not compromising adjacent parenchyma [67]. Further investigation of the modalities is necessary to determine their potential in comparison to long-established methods of CA and RFA.

Conclusions

CA and RFA have grown from being considered experimental to a viable treatment option for patients with comorbidities. Now they are currently considered as viable alternatives to extirpative surgery. These two renal ablative therapies offer many advantages. They are less technically challenging than nephron-sparing surgery, have less treatment-related morbidity, and offer comparable renal function preservation. Ultimately, the use of ablative technology to treat a small renal mass should consider patient demographics and comorbidities, tumor-related characteristics, and the patient's desires.

References

1. Sun M, Thuret R, Abdollah F, et al. Age-adjusted incidence, mortality, and survival rates of stage-specific renal cell carcinoma in North America: a trend analysis. Eur Urol. 2011;59:135–41.
2. Smaldone MC, Kutikov A, Egleston B, et al. Assessing performance trends in laparoscopic nephrectomy and nephron-sparing surgery for localized renal tumors. Urology. 2012;80:286–91.
3. Volpe A, Panzarella T, Rendon RA, Haider MA, Kondylis FI, Jewett MA. The natural history of incidentally detected small renal masses. Cancer. 2004;100:738–45.
4. Desai MM, Aron M, Gill IS. Laparoscopic partial nephrectomy versus laparoscopic cryoablation for the small renal tumor. Urology. 2005;66:23–8.
5. Arnott J. Practical illustrations of the remedial efficacy of a very low or anaesthetic temperature in cancer. Lancet. 1850;2:257–9.
6. Onik G, Cooper C, Goldberg HI, Moss AA, Rubinsky B, Christianson M. Ultrasonic characteristics of frozen liver. Cryobiology. 1984;21:321–8.
7. Onik G, Gilbert J, Hoddick W, et al. Sonographic monitoring of hepatic cryosurgery in an experimental animal model. AJR Am J Roentgenol. 1985;144:1043–7.

8. Rewcastle JC, Sandison GA, Saliken JC, Donnelly BJ, McKinnon JG. Considerations during clinical operation of two commercially available cryomachines. J Surg Oncol. 1999;71:106–11.
9. Mazur P. The role of intracellular freezing in the death of cells cooled at supraoptimal rates. Cryobiology. 1977;14:251–72.
10. Ishiguro H, Rubinsky B. Mechanical interactions between ice crystals and red-blood cells during directional solidification. Cryobiology. 1994;31:483–500.
11. Hoffmann NE, Bischof JC. The cryobiology of cryosurgical injury. Urology. 2002;60:40–9.
12. Erinjeri JP, Clark TW. Cryoablation: mechanism of action and devices. J Vascu Intervent Radiol JVIR. 2010;21:S187–91.
13. Woolley ML, Schulsinger DA, Durand DB, Zeltser IS, Waltzer WC. Effect of freezing parameters (freeze cycle and thaw process) on tissue destruction following renal cryoablation. J Endourol/Endourol Soc. 2002;16:519–22.
14. Gage AA, Baust J. Mechanisms of tissue injury in cryosurgery. Cryobiology. 1998;37:171–86.
15. Finelli A, Rewcastle JC, Jewett MA. Cryotherapy and radiofrequency ablation: pathophysiologic basis and laboratory studies. Curr Opin Urol. 2003;13:187–91.
16. Chosy SG, Nakada SY, Lee Jr FT, Warner TF. Monitoring renal cryosurgery: predictors of tissue necrosis in swine. J Urol. 1998;159:1370–4.
17. Larson TR, Rrobertson DW, Corica A, Bostwick DG. In vivo interstitial temperature mapping of the human prostate during cryosurgery with correlation to histopathologic outcomes. Urology. 2000;55:547–52.
18. Campbell SC, Krishnamurthi V, Chow G, Hale J, Myles J, Novick AC. Renal cryosurgery: experimental evaluation of treatment parameters. Urology. 1998;52:29–33; discussion –4.
19. Neel 3rd HB, Ketcham AS, Hammond WG. Requisites for successful cryogenic surgery of cancer. Arch Surg. 1971;102:45–8.
20. Auge BK, Santa-Cruz RW, Polascik TJ. Effect of freeze time during renal cryoablation: a swine model. J Endourol/Endourol Soc. 2006;20:1101–5.
21. Breen DJ, Bryant TJ, Abbas A, et al. Percutaneous cryoablation of renal tumours: outcomes from 171 tumours in 147 patients. BJU Int. 2013;112:758–65.
22. Kim EH, Tanagho YS, Bhayani SB, Saad NE, Benway BM, Figenshau RS. Percutaneous cryoablation of renal masses: Washington University experience of treating 129 tumours. BJU Int. 2013;111:872–9.
23. Tracy CR, Raman JD, Donnally C, Trimmer CK, Cadeddu JA. Durable oncologic outcomes after radiofrequency ablation: experience from treating 243 small renal masses over 7.5 years. Cancer. 2010;116:3135–42.
24. Hsu TH, Fidler ME, Gill IS. Radiofrequency ablation of the kidney: acute and chronic histology in porcine model. Urology. 2000;56:872–5.
25. Mcgahan JP, Browning PD, Brock JM, Tesluk H. Hepatic ablation using radiofrequency electrocautery. Invest Radiol. 1990;25:267–70.
26. Rossi S, Fornari F, Pathies C, Buscarini L. Thermal lesions induced by 480 Khz localized current field in guinea pig and pig liver. Tumori. 1990;76:54–7.
27. Gettman MT, Lotan Y, Corwin TS, et al. Radiofrequency coagulation of renal parenchyma: comparison of effects of energy generators on treatment efficacy. J Endourol/Endourol Soc. 2002;16:83–8.
28. Mcgahan JP, Schneider P, Brock JM, Tesluk H. Treatment of liver tumors by percutaneous radiofrequency electrocautery. Semin Intervent Rad. 1993;10:143–9.
29. LeVeen RF. Laser hyperthermia and radiofrequency ablation of hepatic lesions. Semin Intervent Rad. 1997;14:313–24.
30. Rossi S, Buscarini E, Garbagnati F, et al. Percutaneous treatment of small hepatic tumors by an expandable RF needle electrode. Am J Roentgenol. 1998;170:1015–22.
31. Curley SA, Izzo F, Ellis LM, Vauthey JN, Vallone P. Radiofrequency ablation of hepatocellular cancer in 110 patients with cirrhosis. Ann Surg. 2000;232:381–9.
32. Rehman J, Landman J, Lee D, et al. Needle-based ablation of renal parenchyma using microwave, cryoablation, impedance- and temperature-based monopolar and bipolar radiofrequency, and liquid and gel chemoablation: Laboratory studies and review of the literature. J Endourol/Endourol Soc. 2004;18:83–104.
33. Nakada SY, Jerde TJ, Warner TF, et al. Bipolar radiofrequency ablation of the kidney: comparison with monopolar radiofrequency ablation. J Endourol. 2003;17:927–33.
34. Goldberg SN, Gazelle GS, Halpern EF, Rittman WJ, Mueller PR, Rosenthal DI. Radiofrequency tissue ablation: importance of local temperature along the electrode tip exposure in determining lesion shape and size. Acad Radiol. 1996;3:212–8.
35. Lorentzen T, Christensen NEH, Nolsoe CP, TorpPedersen ST. Radiofrequency tissue ablation with a cooled needle in vitro: ultrasonography, dose response, and lesion temperature. Acad Radiol. 1997;4:292–7.
36. Collyer WC, Landman J, Olweny EO, et al. Comparison of renal ablation with cryotherapy, dry radiofrequency, and saline augmented radiofrequency in a porcine model. J Am Coll Surg. 2001;193:505–13.
37. Pereira PL, Trubenbach J, Schenk M, et al. Radiofrequency ablation: In vivo comparison of four commercially available devices in pig livers. Radiology. 2004;232:482–90.
38. Frich L, Edwin B, Brabrand K, et al. Gastric perforation after percutaneous radiofrequency ablation of a colorectal liver metastasis in a patient with adhesions in the peritoneal cavity. AJR Am J Roentgenol. 2005;184:S120–2.
39. Djavan B, Partin AW, Hoey MF, Roehrborn CG, Dixon CM, Marberger M. Transurethral radiofrequency therapy for benign prostatic hyperplasia using a novel saline-liquid conductor: the virtual electrode. Urology. 2000;55:13–6.
40. Walsh LP, Anderson JK, Baker MR, et al. In vitro assessment of the efficacy of thermal therapy in human renal cell carcinoma. Urology. 2007;70:380–4.
41. Shingleton WB, Sewell Jr PE. Cryoablation of renal tumours in patients with solitary kidneys. BJU Int. 2003;92:237–9.
42. Davis K, Kielar A, Jafari K. Effectiveness of ultrasound-guided radiofrequency ablation in the treatment of 36 renal cell carcinoma tumours compared with published results of using computed tomography guidance. Can Assoc Radiol J. 2012;63:S23–32.
43. Novick AC, Belldegrun A, Campbell SC, et al. Guideline for management of the clinical T1 renal mass. J Urol. 2009;182:1271–9.
44. Donat SM, Diaz M, Bishoff JT, et al. Follow-up for clinically localized renal neoplasms: AUA guideline. J Urol. 2013;190:407–16.
45. Kunkle DA, Egleston BL, Uzzo RG. Excise, ablate or observe: the small renal mass dilemma--a meta-analysis and review. J Urol. 2008;179:1227–33; discussion 33–4.
46. El Dib R, Touma NJ, Kapoor A. Cryoablation vs radiofrequency ablation for the treatment of renal cell carcinoma: a meta-analysis of case series studies. BJU Int. 2012;110:510–6.
47. Whitson JM, Harris CR, Meng MV. Population-based comparative effectiveness of nephron-sparing surgery vs ablation for small renal masses. BJU Int. 2012;110:1438–43; discussion 43.
48. Best SL, Park SK, Youssef RF, et al. Long-term outcomes of renal tumor radio frequency ablation stratified by tumor diameter: size matters. J Urol. 2012;187:1183–9.
49. Tanagho YS, Roytman TM, Bhayani SB, et al. Laparoscopic cryoablation of renal masses: single-center long-term experience. Urology. 2012;80:307–14.
50. Psutka SP, Feldman AS, McDougal WS, McGovern FJ, Mueller P, Gervais DA. Long-term oncologic outcomes after radiofrequency ablation for T1 renal cell carcinoma. Eur Urol. 2013;63:486–92.

51. Aron M, Kamoi K, Remer E, Berger A, Desai M, Gill I. Laparoscopic renal cryoablation: 8-year, single surgeon outcomes. J Urol. 2010;183:889–95.
52. Zagoria RJ, Pettus JA, Rogers M, Werle DM, Childs D, Leyendecker JR. Long-term outcomes after percutaneous radiofrequency ablation for renal cell carcinoma. Urology. 2011;77:1393–7.
53. Olweny EO, Park SK, Tan YK, Best SL, Trimmer C, Cadeddu JA. Radiofrequency ablation versus partial nephrectomy in patients with solitary clinical T1a renal cell carcinoma: comparable oncologic outcomes at a minimum of 5 years of follow-up. Eur Urol. 2012;61:1156–61.
54. Farrell MA, Charboneau WJ, DiMarco DS, et al. Imaging-guided radiofrequency ablation of solid renal tumors. AJR Am J Roentgenol. 2003;180:1509–13.
55. McDougal WS, Gervais DA, McGovern FJ, Mueller PR. Long-term followup of patients with renal cell carcinoma treated with radio frequency ablation with curative intent. J Urol. 2005;174:61–3.
56. Vanderbrink BA, Rastinehad A, Caplin D, Ost MC, Lobko I, Lee BR. Successful conservative management of colorenal fistula after percutaneous cryoablation of renal-cell carcinoma. J Endourol/Endourol Soc. 2007;21:726–9.
57. Finley DS, Beck S, Box G, et al. Percutaneous and laparoscopic cryoablation of small renal masses. J Urol. 2008;180:492–8.
58. Lehman DS, Hruby GW, Phillips CK, McKiernan JM, Benson MC, Landman J. First prize (tie): laparoscopic renal cryoablation: efficacy and complications for larger renal masses. J Endourol/Endourol Soc. 2008;22:1123–7.
59. Schmit GD, Thompson RH, Kurup AN, et al. Usefulness of R.E.N.A.L. nephrometry scoring system for predicting outcomes and complications of percutaneous ablation of 751 renal tumors. J Urol. 2013;189:30–5.
60. Brown DB, Bhayani SB. Persistent urine leak after cryoablation of a renal tumor in a patient with an ileal conduit. J Vasc Interv Radiol. 2007;18:1324–7.
61. Bandi G, Wen CC, Hedican SP, Moon TD, Lee FT, Nakada SY. Cryoablation of small renal masses: assessment of the outcome at one institution. BJU Int. 2007;100:798–801.
62. Edd JF, Horowitz L, Davalos RV, Mir LM, Rubinsky B. In vivo results of a new focal tissue ablation technique: irreversible electroporation. IEEE Trans Biomed Eng. 2006;53:1409–15.
63. Deodhar A, Monette S, Single Jr GW, et al. Renal tissue ablation with irreversible electroporation: preliminary results in a porcine model. Urology. 2011;77:754–60.
64. Liang P, Wang Y. Microwave ablation of hepatocellular carcinoma. Oncology. 2007;72 Suppl 1:124–31.
65. Moore C, Salas N, Zaias J, Shields J, Bird V, Leveillee R. Effects of microwave ablation of the kidney. J Endourol/Endourol Soc. 2010;24:439–44.
66. Potters L, Kavanagh B, Galvin JM, et al. American Society for Therapeutic Radiology and Oncology (ASTRO) and American College of Radiology (ACR) practice guideline for the performance of stereotactic body radiation therapy. Int J Radiat Oncol Biol Phys. 2010;76:326–32.
67. Vricella GJ, Ponsky LE, Cadeddu JA. Ablative technologies for urologic cancers. Urol Clin North Am. 2009;36:163–78. viii.
68. Guazzoni G, Cestari A, Buffi N, et al. Oncologic results of laparoscopic renal cryoablation for clinical T1a tumors: 8 years of experience in a single institution. Urology. 2010;76:624–9.

Renal Angiography and Embolization

21

Igor Lobko and Anthony Mohabir

Renal embolization can be lifesaving, be used to facilitate perioperative hemostasis, and often eliminate the need for a surgical intervention in patients with life-threatening renal hemorrhage. Renal angioembolization is also used to electively treat benign renal masses and has been used in the preoperative setting for large renal masses with/without renal vein thrombosis. At times, this technique can be surprisingly simple or quite difficult and, in the majority of cases, extremely clinically satisfying. A high level of expertise and preparedness is sometimes required to deal with an unexpected course.

Renal Arterial Anatomy

In order to safely and effectively perform renal arterial interventions, a fundamental understanding of the normal and variant renal vascular anatomy is essential. The renal arteries most commonly originate from the aorta approximately 1 cm distal to the origin of the superior mesenteric artery, at the level of the lower 1st and upper 2nd lumbar vertebrae (Fig. 21.1). In a majority of patients (approximately 70 %), there is a single renal artery to each kidney. The left renal artery is shorter than the right, given its proximity to the aorta. The kidney is composed of five segments: apical, upper, middle, lower, and posterior. The posterior division artery is usually the first branch of the main renal artery and supplies the posterior segment of the kidney. The anterior division splits into three terminal segmental arteries: superior to the upper segment, middle or medial to the middle segment, and inferior to the lower segment. The vascular supply to the apical segment is usually provided by the anterior division artery but in approximately 10 % of cases may have supply from the posterior division. There are also smaller branches supplying the renal pelvis and proximal ureter, which can originate from the main renal artery and its branches [1, 2].

Variant anatomy of the renal arteries is found in approximately 35 % of cases. The most common variation is the presence of so-called "accessory," "aberrant," or "supernumerary" renal arteries which present in about 30 % of these patients (Fig. 21.2). They commonly originate directly from the aorta but can be seen coming off of almost any artery between the diaphragm and pelvis. Usually, the superior accessory artery supplies the apical segment, and the inferior branch supplies the lower segment. Accessory renal arteries arising above the main trunk are more common than the ones originating below it, and they are also more common on the left than the right. Very often a right-sided accessory renal artery may be found in front of the inferior vena cava. Doubled renal arteries present in about 10 % of all cases. Accessory renal arteries more commonly supply blood to the inferior segment than to the superior one.

It is important to remember that as the renal arteries can originate from almost any artery in the abdomen and pelvis, they can also give off branches to the surrounding organs. The commonly seen extrarenal arteries originating from the renal vasculature are inferior phrenic, adrenal, hepatic, gonadal, pancreatic, colonic, and lumbar arteries.

Adrenal Vasculature

The adrenal glands may be supplied by up to 3 arteries (Fig. 21.3). They usually originate from the inferior phrenic arteries, the renal arteries, or the aorta. Adrenal blood flow is supplied in approximately 34 % by all three arteries, 61 % by any of the two arteries, and 6 % by a single vessel.

Horseshoe Kidney

In utero during the 4th–9th weeks of gestation, the closely situated metanephric buds of the lower abdomen/pelvis are developing into the bilateral kidneys. During this process

I. Lobko, MD (✉) • A. Mohabir, MD
Department of Radiology, North Shore LIJ Hofstra School of Medicine, New Hyde Park, NY, USA
e-mail: ilobko@lij.edu

A.R. Rastinehad, D.N. Siegel (eds.), *Interventional Urology*, DOI 10.1007/978-3-319-23464-9_21

Fig. 21.1 Renal arterial anatomy. (**a**) Digital subtracted angiography (DSA) of the right kidney demonstrates common right renal arterial anatomy. The first branch descends posteriorly and supplies the posterior segment (*arrowheads*). (**b**) Un-subtracted angiography image of the right kidney demonstrates common right renal arterial anatomy. The anterior branch is seen supplying the apical (*white arrow*), middle (*black open arrow*), and lower renal segments (*black arrow*)

Fig. 21.2 Aortogram and variant renal artery anatomy. Right kidney upper pole accessory renal artery (*arrow*). Duplicated left renal arteries (*arrowheads*)

they externally rotate bilaterally and ascend to the retroperitoneum. As the metanephros ascend, their vascular supply stems from sequentially higher levels of aortic arteries. The most common anomaly of renal ascent is a solitary malrotated kidney in the retroperitoneum. However, if there is disturbance in the separation and ascent of the metanephic buds, a fusion anomaly may occur, most commonly in a form of the horseshoe kidney.

Horseshoe kidneys are typically formed by fusion of the lower poles of the metanephros (Fig. 21.4) [3]. The kidney may ascend until the upper border of the isthmus reaches the inferior mesenteric artery. Vascular supply to the horseshoe kidney varies; there may be single bilateral, duplicate bilateral, or multiple aortic and iliac arteries.

When renal arterial interventions are performed, it is important to evaluate for normal branching patterns as well as variants, as these findings may greatly change the outcome of the intervention.

Technical Issues

Vascular Access

Vascular access is the start of any angiographic procedure. The well-executed arterial access is the first step to a successful outcome. The common femoral artery access, utilizing modified Seldinger technique, is the most traditional and still most commonly used approach. Axillary, brachial, or

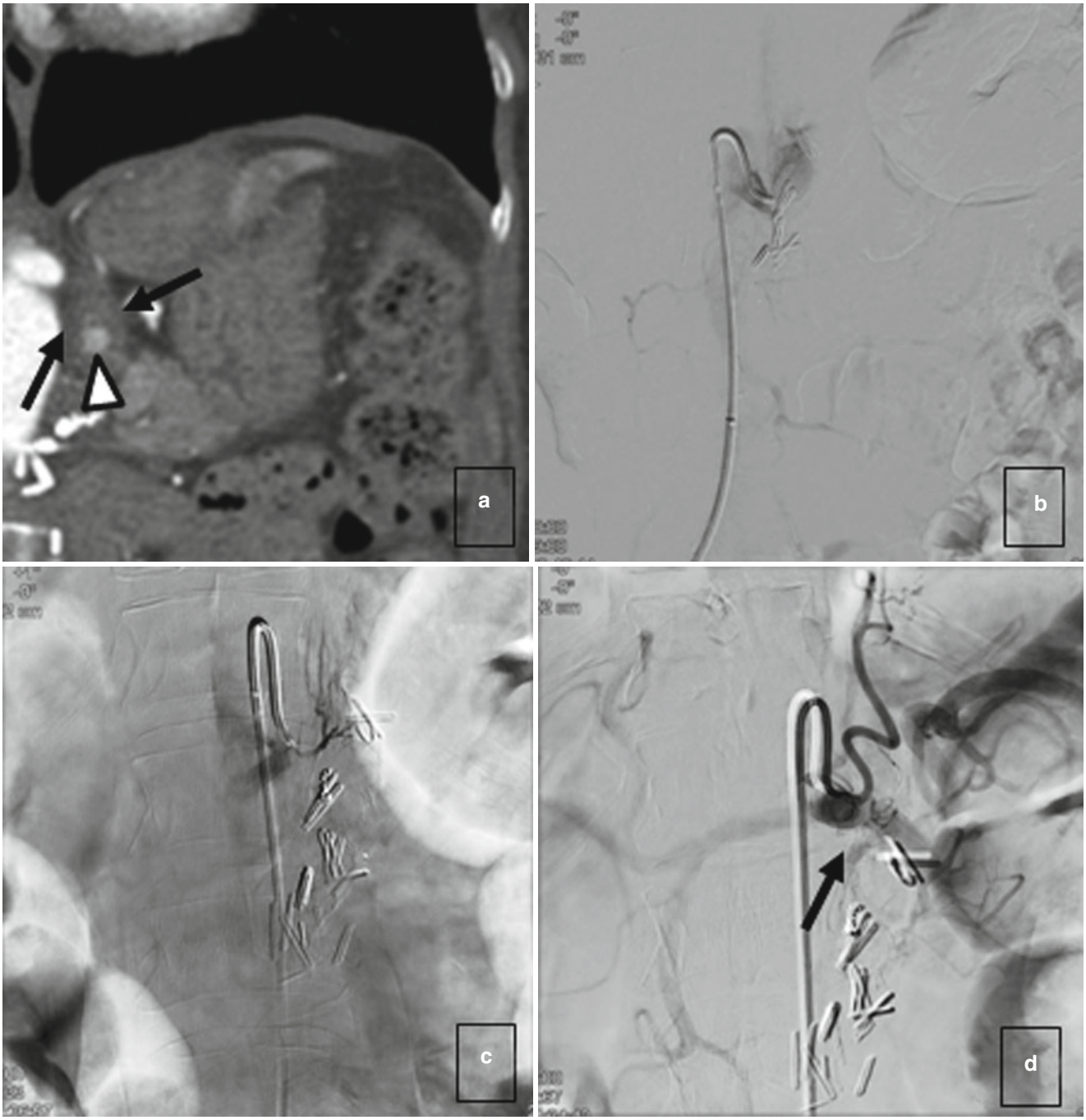

Fig. 21.3 Adrenal artery. (**a**) Coronal CTA image of the abdomen demonstrates status post adrenal-sparing left nephrectomy with contrast blush (*arrowhead*) noted between the limbs of the adrenal gland (*black arrows*), compatible with pseudoaneurysm. (**b**) The inferior adrenal artery arises from the left renal artery stump. (**c**) Middle adrenal artery is a branch off of the aorta. (**d**) Celiac trunk injection shows left inferior phrenic artery which gives rise to superior adrenal artery (*black arrow*)

radial arterial access may be used in patients where the femoral artery access is not feasible [4, 5].

Most commonly, arterial puncture is performed utilizing real-time ultrasound guidance with a 21 gauge micropuncture needle. A vascular sheath is placed into the common femoral artery following initial access. The size of the sheath may vary, in accordance with the type of devices planned to be used, but commonly ranges between 4 and 6 French. When performing vascular interventions on a neonate or small child, the procedure could be performed with a 4 French system without a vascular sheath in order to decrease the size of the arteriotomy. In rare cases, when the intervention has to be done within the first few days of life, the angiogram can be attempted via the umbilical artery.

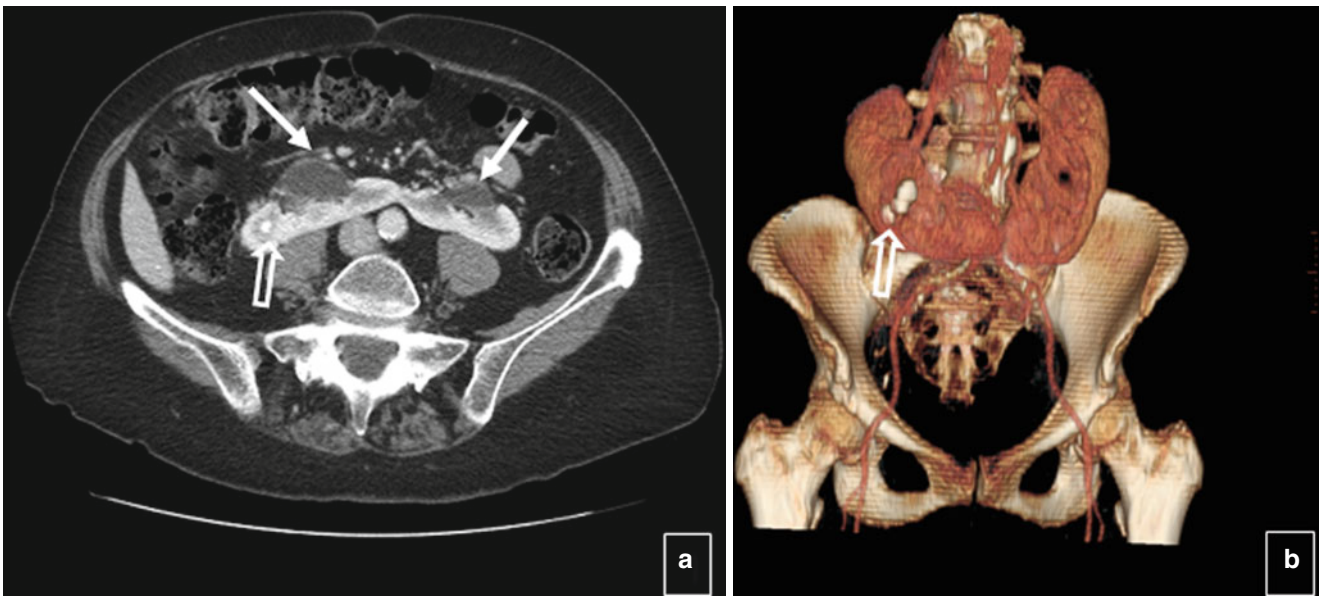

Fig. 21.4 Horseshoe kidney. (**a**) Axial CT image demonstrates renal fusion at the lower poles, diagnostic for a horseshoe kidney. Additional note is made of prominent collecting systems bilaterally (*white arrows*) and a nonobstructing stone on the right (*open white arrows*). (**b**) 3D reformat image clearly depicts right renal stone and identifies several feeding vessels from the anterior aspect of the aorta

Renal Artery Catheterization

Although an abdominal aortogram in most cases is not needed before the selective renal arterial catheterization, it could be an important asset if aberrant arteries can't be readily localized. Selective renal artery catheterization can be performed with different catheters. The catheter choice in most cases is based on operator preference. In some situations, such as the left renal artery catheterization or when dealing with a stenotic origin, a reverse curve catheter may provide more stable access. Selective catheterization of distal renal artery branches is obtained with microcatheters using coaxial technique. Microcatheters allow for an embolization of distal renal artery branches providing an opportunity to preserve as much renal parenchyma as possible.

Embolization Materials

Embolization materials can be classified in several different ways. They can be temporary, dissolving over time which allows for vascular recanalization, or permanent, staying within the vessel for the rest of the patient's life following the embolization. Temporary arterial embolization agents, such as gelatin foam, microfibrillar collagen, or biodegradable particles, may be used to devascularize specific arterial segments or an entire kidney. An occlusive effect, depending on material, may last approximately 3–90 days.

Permanent embolization may be achieved with a variety of agents or devices including coils, vascular plugs, particles, and liquid embolic materials.

Coils can be nondetachable or detachable. Detachable coils provide the possibility of removing the coil before detachment if it is not appropriately positioned within the vessel. This additional control significantly decreases the chance of nontarget embolization.

Embolization particles are made from a variety of different materials and supplied in sizes ranging from 40 to 2000 μm. Small particles, 40–300 μm, are traditionally used for a distal tumor embolization in order to achieve tumor necrosis and minimize neovascularization. For some tumors like angiomyolipomas, somewhat larger particles can achieve an effective tumor necrosis too. In general, the larger particles are used to obtain rapid vascular occlusion where tissue necrosis is not the goal, such as for preoperative devascularization. In addition, the larger particles can be used to minimize possible arteriovenous shunting often seen during tumor embolization. Particles are considered a permanent embolic agent although the above-described temporary agents also belong to this category. Recently a new calibrated biodegradable particle has been introduced and likely will be widely available in the near future.

Liquid embolic agents include ethanol, glue, or acrylic and newer nonadhesive agents. Concentrated ethanol (94–99 %) induces instantaneous endothelial damage resulting in rapid vessel occlusion. Ethanol may be diluted with radiopaque iodized oil. The iodized oil makes injection of the ethanol visible. Additionally, the radiopaque iodized oil increases the

duration that the ethanol is in contact with the vascular endothelium, potentially producing a greater effect for a given volume of ethanol. Of note, ethanol injection can be painful, and the patients require adequate intra-procedural pain management.

N-butyl-2-cyanoacrylate glue is a liquid embolic agent which polymerizes upon contact with blood or any ionic substance. The glue is diluted with a radiopaque iodized oil. Depending on the blood flow characteristics, the glue dilution is adjusted to optimize the vascular occlusion and to prevent nontarget delivery. The use of glue therefore requires significant expertise and experience. A nonadhesive liquid agent composed of ethylene vinyl alcohol copolymer dissolved in radiopaque tantalum powder is also available. This forms a dense cast which is malleable for several minutes which allows for slow arterial injection within a selected vessel potentially providing additional control during delivery.

Following renal embolization, a post-embolization arteriogram should be performed. Usually the embolized vessel or the closest proximal artery is injected initially followed by a main renal arteriogram. The main renal arteriogram is performed to evaluate the effect of the vascular occlusion and to assess for the presence of additional arteries which could supply the targeted area. In cases of postoperative bleeding, the main renal arteriogram can also reveal additional areas of bleeding not seen on the initial arteriogram.

The angiographic procedure is completed with the removal of the access sheath or the catheter. Hemostatic control of the vascular access can be accomplished with manual compression of the puncture site with or without hemostatic patches or use of the compression-assisted devices especially common with the radial artery approach. Utilization of the different available vascular closure devices generally makes vascular access site management more secure and comfortable for patients and operating physicians.

Post-embolization Management

Post-embolization course includes protection of the arterial access site from bleeding, such as strict bed rest with extension of the punctured extremity and management of the post-embolization symptoms. Common post-embolization symptoms include flank, back and/or abdominal pain, as well as nausea, vomiting, low-grade fever, or leukocytosis. Pain, fever, nausea/vomiting, and leukocytosis following embolization define the post-embolization syndrome which usually develops within first 72 h following the procedure. Adequate pain management, antiemetic medications, anti-inflammatory medications, and intravenous fluids that are required until the patient is able to tolerate PO diet and medications are the key parts of post-embolization management. It is important to remember that post-embolization fever and leukocytosis do not usually require a septic workup.

Angiography and Embolization for Treatment of the Traumatic and Iatrogenic Hemorrhage

Renal trauma may be due to blunt force or penetrating injury [6, 7]. During peace times, blunt trauma is much more common, and penetrating renal injuries usually occur following medical interventions—such as surgery, biopsies, or percutaneous urological procedures (Fig. 21.5).

Blunt renal trauma is typically graded with CT scanning and, according to the American Association for the Surgery of Trauma, can directly need surgical intervention. Grade I–II renal injuries are treated conservatively with inpatient observation and blood transfusions as needed. Grade III–V injuries typically require intervention with either surgical exploration or therapeutic angiography and embolization (Table 21.1). Embolization of large renal lacerations that are actively bleeding can be done prior to nephrectomy or may be performed alone as a nonsurgical kidney-sparing procedure [8].

In order to successfully identify a hemorrhagic source, knowledge of the angiographic signs of bleeding is crucial. These are divided in two groups: direct and indirect. Most common indirect signs of bleeding are hematoma, vascular spasm, and deviation of the arteries from their expected course, commonly due to underlying hematoma. The common direct signs of bleeding are contrast extravasation, abrupt termination of the artery the so-called vessel cutoff sign, formation of a pseudoaneurysm and/or development of an arteriovenous fistula. Contrast extravasation corresponds to a site of active bleeding (Figs. 21.6 and 21.7). The abrupt vessel termination is usually secondary to an arterial thrombosis either due to complete or partial transection. Pseudoaneurysm is an area of lobular contrast accumulation outside of the ruptured vessel surrounded by the adjacent tissue providing temporary hemostasis. These pseudoaneurysms present with intermittent bleeding which happens when the surrounding tissues burst due to continuously increasing pressure. The arteriovenous fistula represents an abnormal communication between the artery and vein. This abnormality is represented by early filling of a draining vein (Fig. 21.8).

In postoperative patients with renal hemorrhage, renal angiography reveals a demonstrable and treatable etiology with a high rate of efficacy. Angiography should be considered first line for intractable and delayed bleeding in these settings.

Angiography and Embolization of Renal Tumors

Before discussing the specific tumors, it is necessary to be aware of angiographic futures of the so-called "tumor

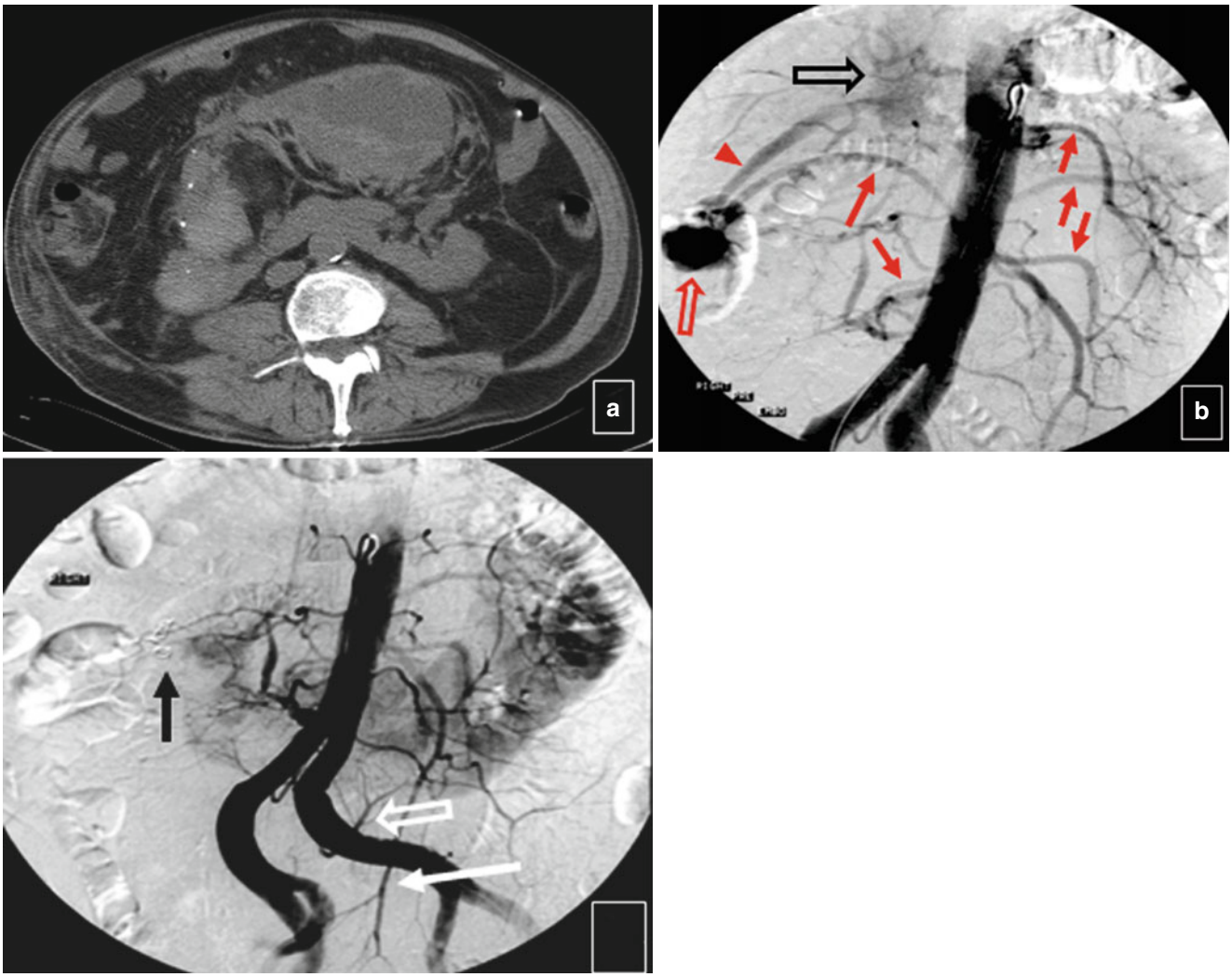

Fig. 21.5 Horseshoe kidney with hematoma, pseudoaneurysm, and arteriovenous fistula. (**a**) Axial CT images of a horseshoe kidney status post percutaneous stone extraction demonstrates a large adjacent mixed density collection; the dense components of the collection are compatible with hematoma. (**b**) Hematuria status post percutaneous stone extraction from the right collecting system of a horseshoe kidney. Multiple renal arteries are identified (*red arrows*). Additionally, lobulated contrast accumulation is noted, reflective of a *pseudoaneurysm* (*open red arrow*). Simultaneous filling of a right-sided renal vein (*arrowhead*) and IVC (*open black arrow*) is identified, compatible with an *arteriovenous fistula* (AVF). (**c**) Post-coil embolization aortogram—resolution of the pseudoaneurysm and AVF. Coil (*black arrow*), the iliac branch renal artery feeding the renal isthmus (*open white arrow*), and the inferior mesenteric artery (*white arrow*)

Table 21.1 CT grading of the renal trauma

Category	Description	Management
1	Minor contusion with microscopic or gross hematuria; urological studies should be otherwise normal. Alternatively, a subcapsular nonexpanding hematoma without an associated parenchymal laceration	Conservative
2	Nonexpanding perirenal hematoma confines to the retroperitoneum. Or laceration less than 1 cm of the parenchymal depth of the renal cortex without urinary extravasation	Conservative
3	Laceration of the greater than 1 cm depth of the renal cortex without collecting system rupture or urinary extravasation	Embolization and/or surgical exploration
4	Parenchymal laceration through the renal cortex, medulla, and collecting system. Or main renal artery or vein injury with contained hemorrhage	Embolization and/or surgical exploration
5	Completely shattered kidney or avulsion of the renal hilum which devascularized the kidney	Embolization and/or surgical exploration

From Federle et al. [6], with permission

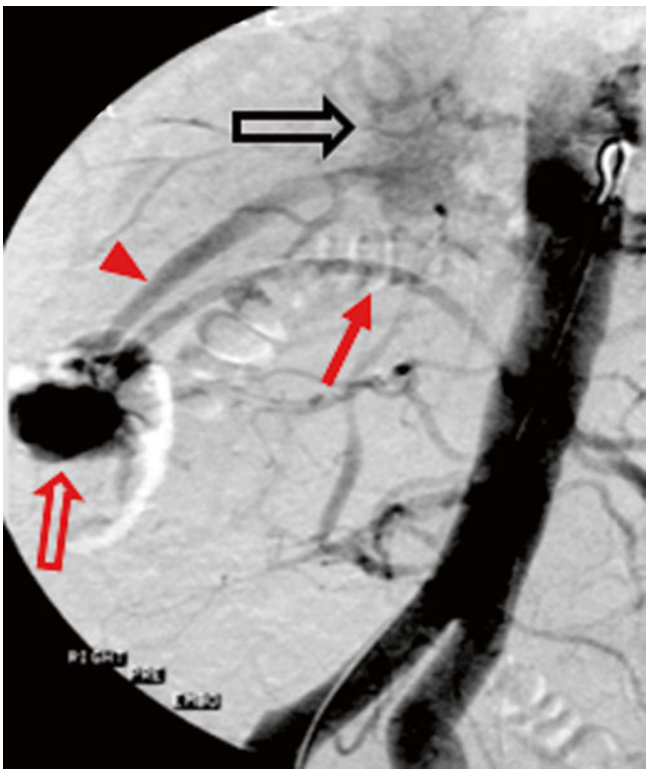

Fig. 21.6 Direct signs of vessel injury. Pseudoaneurysm and arteriovenous fistula. Aortogram demonstrates filling of a right renal artery (*red arrow*) with lobulated contrast, reflective of a *pseudoaneurysm* (*open red arrow*). Simultaneous filling of a right-sided renal vein (*arrowhead*) and IVC (*open black arrow*) is identified, compatible with an *arteriovenous fistula* (AVF)

vascularity" (Fig. 21.9). Neoplastic processes anywhere in the body have similar vascular changes. They include abnormal vascular tortuosity, vascular lumen irregularity, formation of a true and pseudoaneurysms, hypervascularity, early contrast opacification, and delayed washout—also called "mother-in-law sign," arteriovenous shunting, and parasitic vascularization with vessels recruited from the adjacent structures and organs. Tumor vessels are more porous and do not have the same ability to contract and control bleeding as normal arteries and for that reason are prone to bleed especially when masses increase in size. When some tumors become large, they can become a source of vascular sequestration. In many situations it is impossible to determine the nature of the tumor based on angiographic appearance, and correlation with the cross-sectional imaging is extremely important.

Renal Angiomyolipomas

Renal angiomyolipomas (AML) are nonmalignant neoplasms which contain fat, vascular, and smooth muscle components. AMLs are sporadic in 80 % of cases (Figs. 21.10 and 21.11) [9]. Sporadic tumors are more common in women and are asymptomatic in approximately 75 % of cases at presentation. About 15 % of patients present with bleeding and in 15 % they are multiple. 20 % of AMLs are associated with phakomatoses, primarily tuberous sclerosis, von Hippel-Lindau syndrome, and neurofibromatosis type 1. AMLs are often noted incidentally; however, some patients may present with a palpable mass, flank pain, urinary tract infection, hematuria, renal failure, or hypertension. Renal angiomyolipomas pose a significant hemorrhagic risk. The risk of bleeding is proportional to a lesion size and the general consensus is that when they reach 4 cm, preemptive embolization should be performed. Surgery is another option but, in the current era, is generally reserved for the minority of cases, where embolization cannot be performed.

Angiographically AMLs are hypervascular tumors with sharp borders, irregularly dilated vessels, early arterial filling, micro- or macro-aneurysms, and absence of arteriovenous shunting. The sporadic AMLs, more often than the tumors associated with the other conditions, have a single feeding artery. Particle embolization results in decreased vascularity, tumor size, and likelihood of hemorrhage (Figs. 21.12 and 21.13). Renal AMLs treated with embolization undergo continued follow-up and may require re-embolization in approximately 1/3rd of the cases. Additionally, AMLs that demonstrate acute hemorrhage can be successfully treated with emergent embolization. Selective arterial embolization of AMLs is a standard, safe, and durable and an effective nephron-sparing therapy [10].

Preop Embolization for Large Tumors

Large renal tumors, particularly renal cell carcinomas (RCC), should undergo radical surgery in patients where there is a curative intent. Highly vascular RCC is associated with significant intraoperative hemorrhage [8]. Preoperative renal arterial embolization has been a long-standing method to decrease perioperative morbidity and mortality. Arterial embolization is performed typically within 24 h of the intended radical nephrectomy (Fig. 21.14). Devascularization of large renal tumors yields decreased intravascular tumor extension which leads to easier surgical dissection planes. This in turn can result in shorter operative times and decreased intraoperative hemorrhage.

Pediatric Renal Tumors

Pediatric renal tumors typically consist of Wilms' tumors, AMLs, and more rare etiologies (malignant rhabdoid tumors, metanephric adenomas, etc.) [11–13]. Selective renal arterial embolization serves as a means to prevent or treat hemorrhage, as in the case of AMLs. In rare cases of advanced

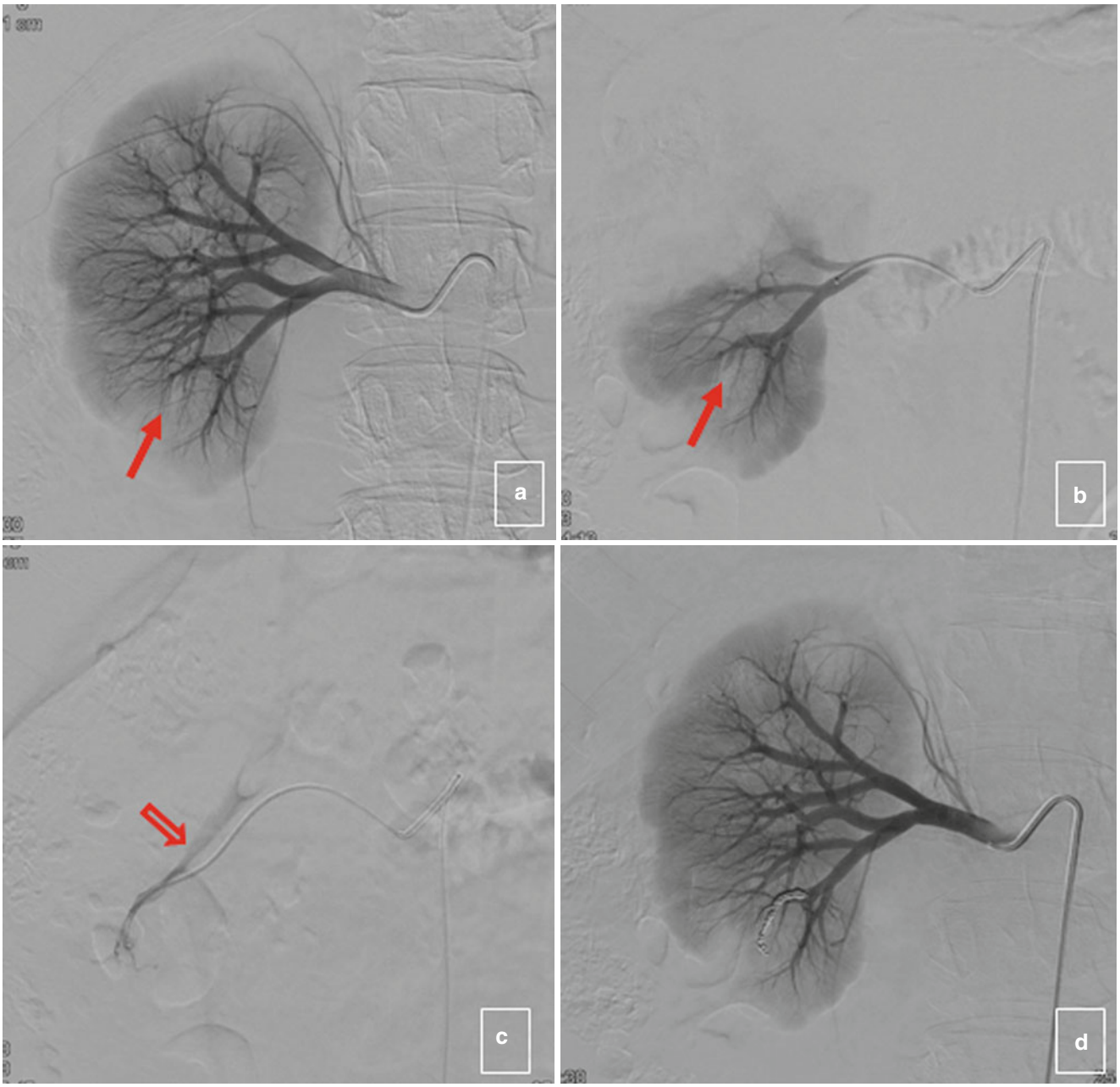

Fig. 21.7 Direct signs of vessel injury. Arterial cutoff sign in a patient status post laparoscopic partial nephrectomy. (**a**) Arterial angiography of the right kidney demonstrates an abrupt end to a lower segment renal artery branch (*red arrow*). (**b**) Lower segment renal arteriography confirms the finding, commonly known as the *arterial cutoff sign* (*red arrow*). (**c**) Microcatheter placed through the level of the occlusion demonstrates immediate venous filling, consistent with arteriovenous fistula (*open arrow*). (**d**) Post-embolization arteriogram demonstrates successful occlusion of the vessel

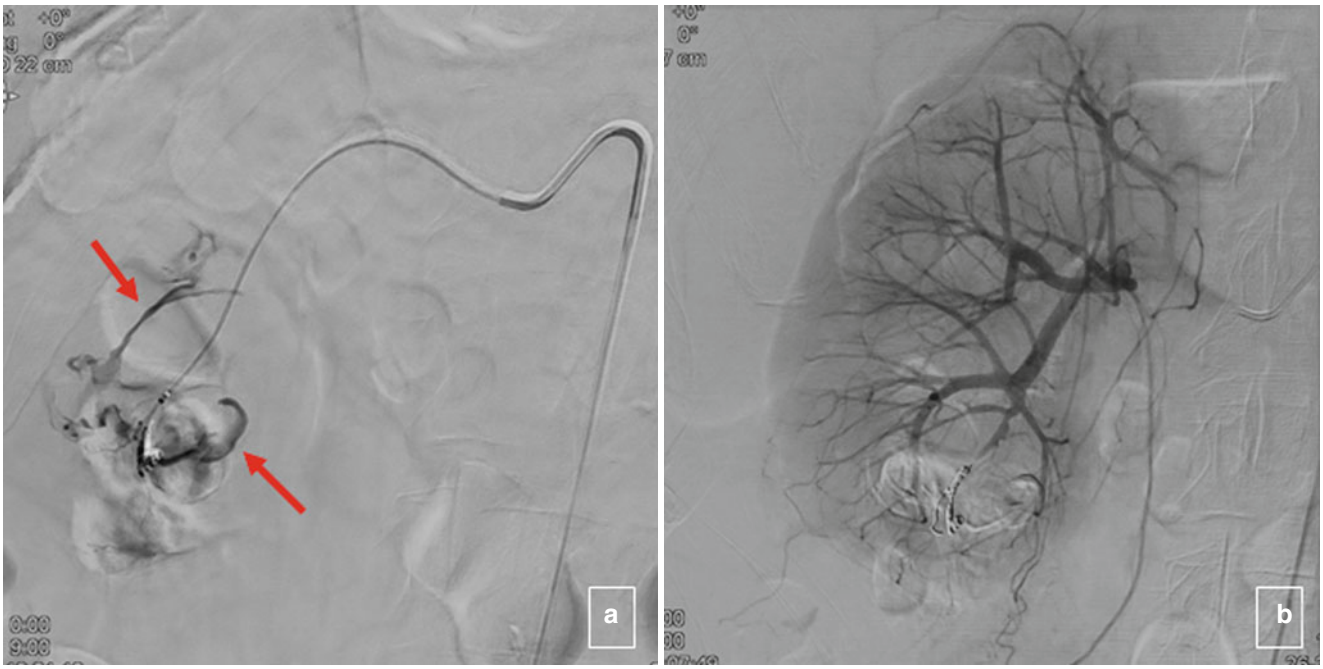

Fig. 21.8 Direct signs of vessel injury. Active contrast extravasation/active bleeding. Right renal hemorrhage status post laparoscopic resection of a right lower pole mass. (**a**) Arterial angiography of the right kidney demonstrates contrast extravasation superiorly and medially (*red arrows*) to the microcatheter. (**b**) Post-coil embolization arteriogram—occlusion of the bleeding artery

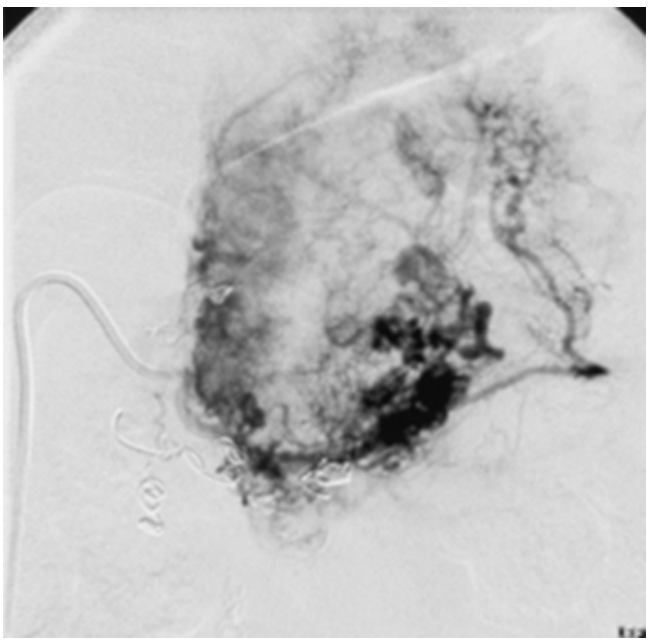

Fig. 21.9 Tumor vascularity. Selective angiogram of the left kidney demonstrates tumor neovascularity which consists of tortuous irregular vessels with multiple small aneurysms, pseudoaneurysms, and contrast blush. Note: multiple embolic coils from prior embolizations of several hemorrhagic AMLs

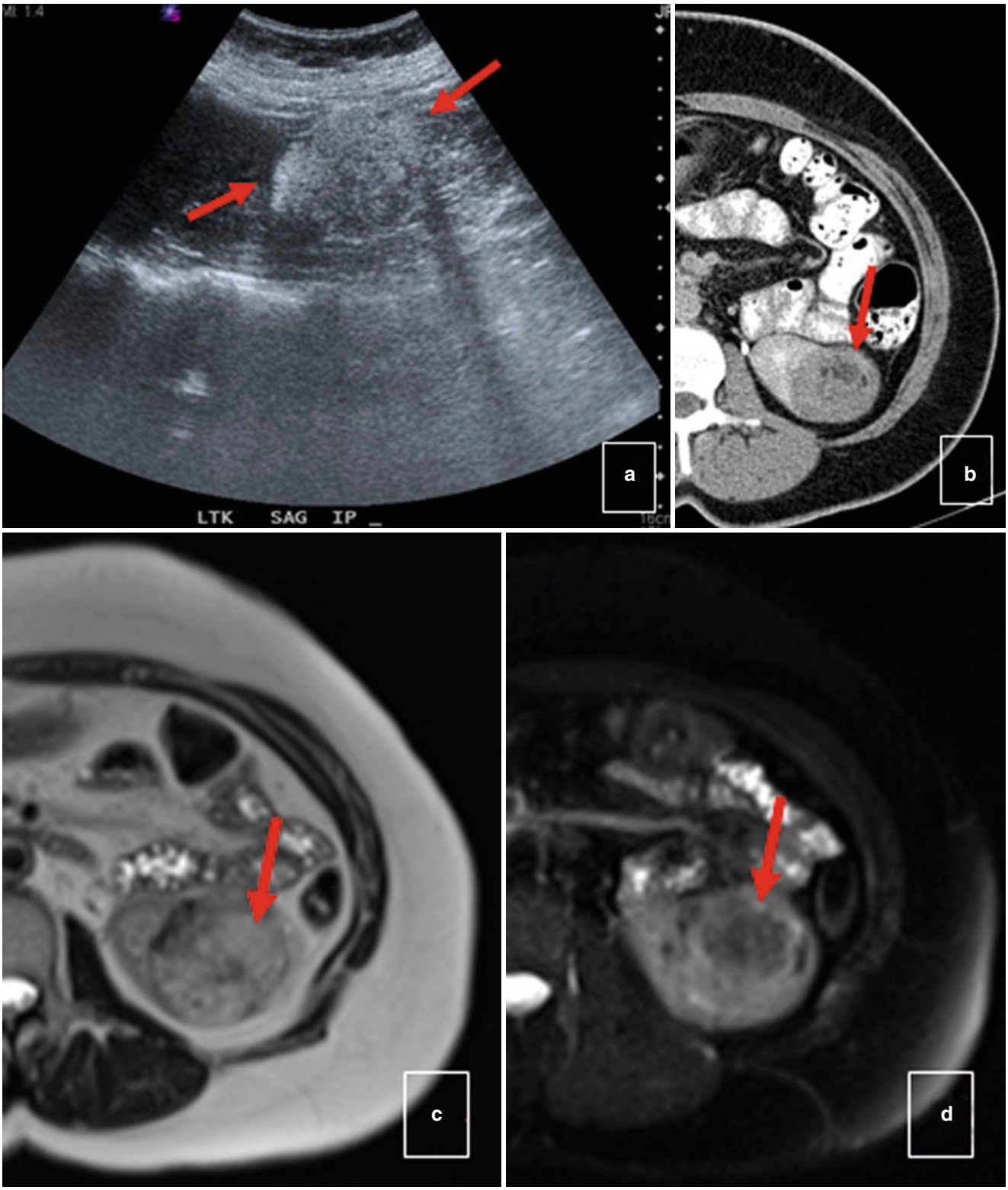

Fig. 21.10 Sporadic angiomyolipoma. (**a**) Ultrasound image of the left kidney demonstrates a hyperechoic left lower pole renal lesion with shadowing (*red arrows*). (**b**) Contrast-enhanced CT of the same patient demonstrates a fat/low attenuation (−37 Hounsfield units) containing mass (*arrows*) in left upper renal pole. (**c**) MRI T2 confirms a fat containing left upper pole renal lesion. (**d**) Note the fat suppression within the tumor on the T2 fat-saturated image. All modalities are diagnostic of an angiomyolipoma

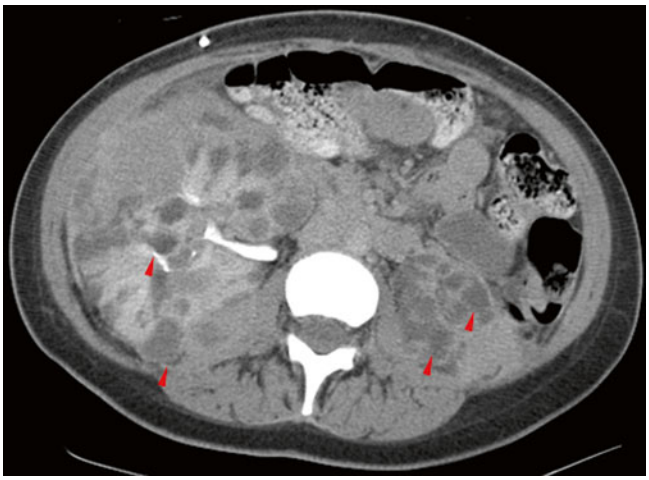

Fig. 21.11 Bilateral angiomyolipomas. Axial contrast-enhanced images of the abdomen demonstrate bilateral lipid-rich lesions (*arrowheads*), compatible with renal angiomyolipomas in a patient with tuberous sclerosis

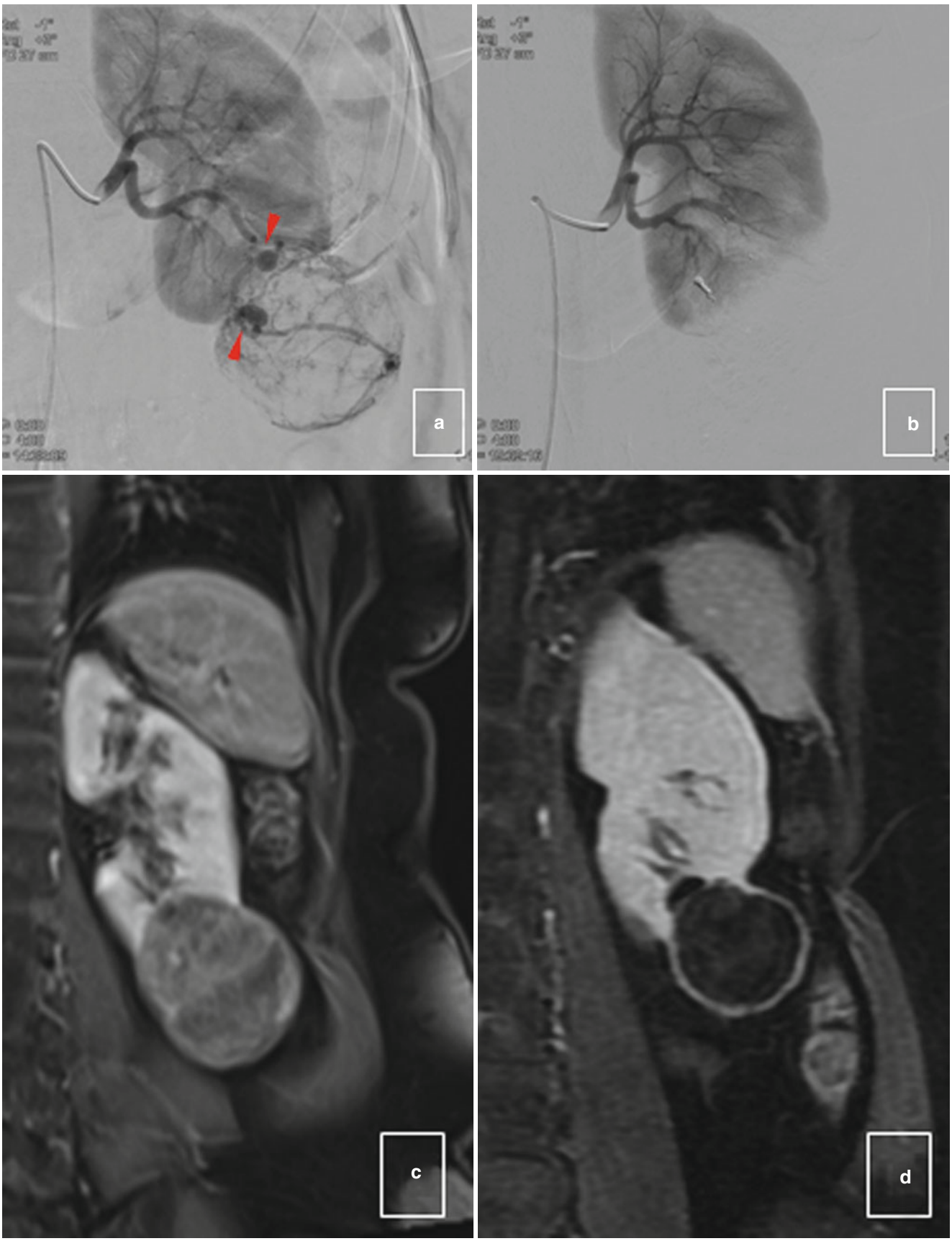

Fig. 21.12 Sporadic angiomyolipoma with interval treatment. (**a**) Angiographic images of the left kidney demonstrate a left lower renal pole exophytic mass with dilated irregularly shaped vessels. Note the presence of the saccular aneurysms along the vessels (*arrowheads*). (**b**) Post-embolization angiogram—absence of previously identified tumor vascularity. (**c**) Pre-procedural Post-contrast coronal T1 MRI images of the left kidney demonstrate an enhancing left lower renal pole angiomyolipoma. (**d**) 6-month follow-up repeat MRI demonstrates decreased tumor size with only minimal peripheral enhancement

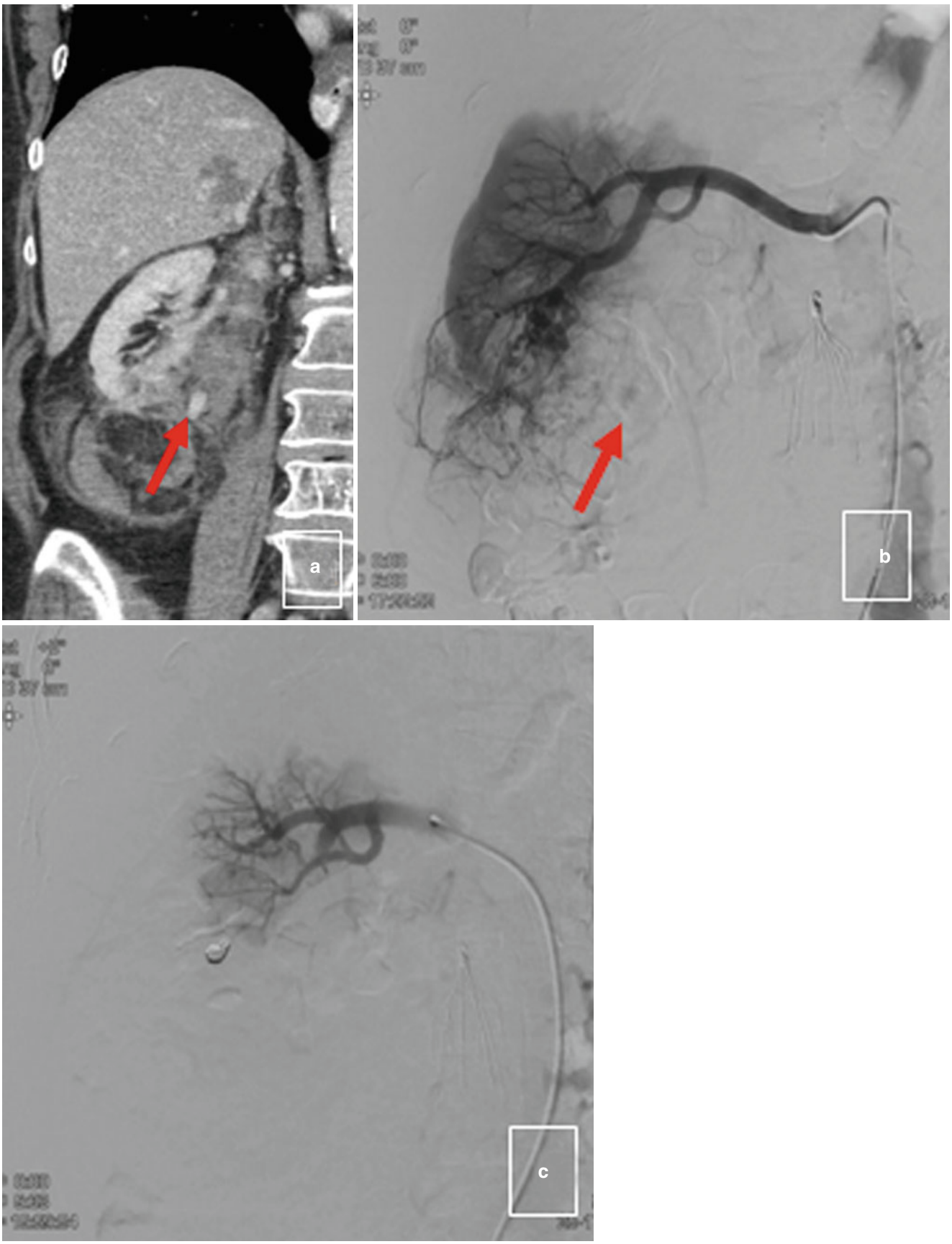

Fig. 21.13 Hemorrhagic angiomyolipoma. (**a**) Coronal reformatted contrast-enhanced arterial phase CT image demonstrates a large right renal angiomyolipoma with contrast accumulation medially (*arrow*), compatible with pseudoaneurysm. (**b**) Renal angiography demonstrated irregularly dilated and tortuous tumor arteries with the presence of a pseudoaneurysm (*arrow*). (**c**) Post-coil embolization angiogram demonstrates successful arterial occlusion with preservation of the middle, upper, and posterior segments

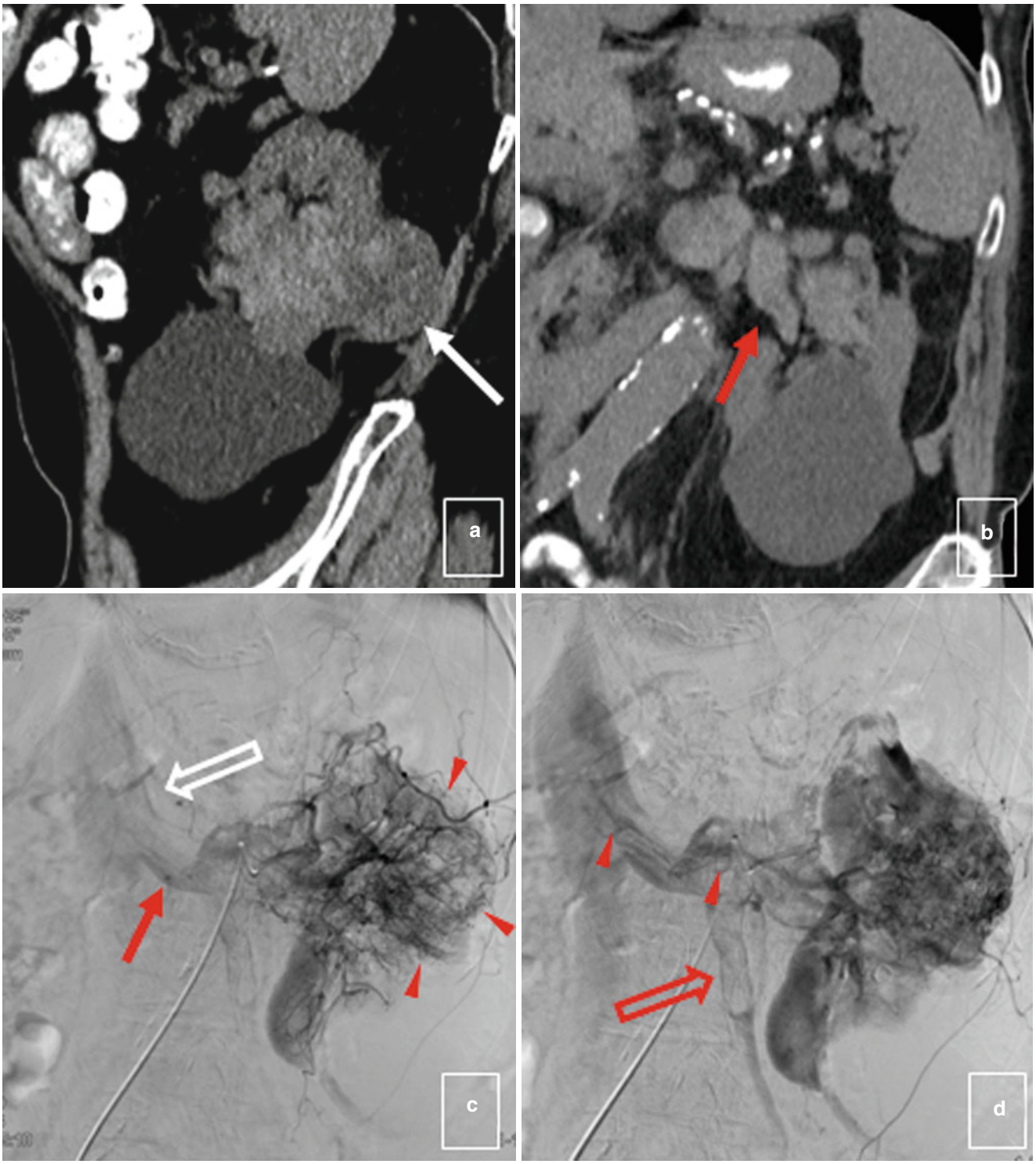

Fig. 21.14 Renal cell carcinoma. (**a**) Contrast-enhanced sagittal and coronal reformatted CT images of the abdomen demonstrate an exophytic posterior left renal mass (*white arrow*). (**b**) Tumor thrombus is seen extending to the left renal vein (*arrow*). (**c**) Angiography confirms a hypervascular renal tumor (*arrowheads*) with tumor extension into the left renal vein (*arrow*) and the IVC (*open white arrow*). (**d**) Slightly delayed imaging demonstrates prominent tumor vascularity in the left renal vein (*arrowheads*) and tumor extension into the left gonadal vein (*open arrow*)

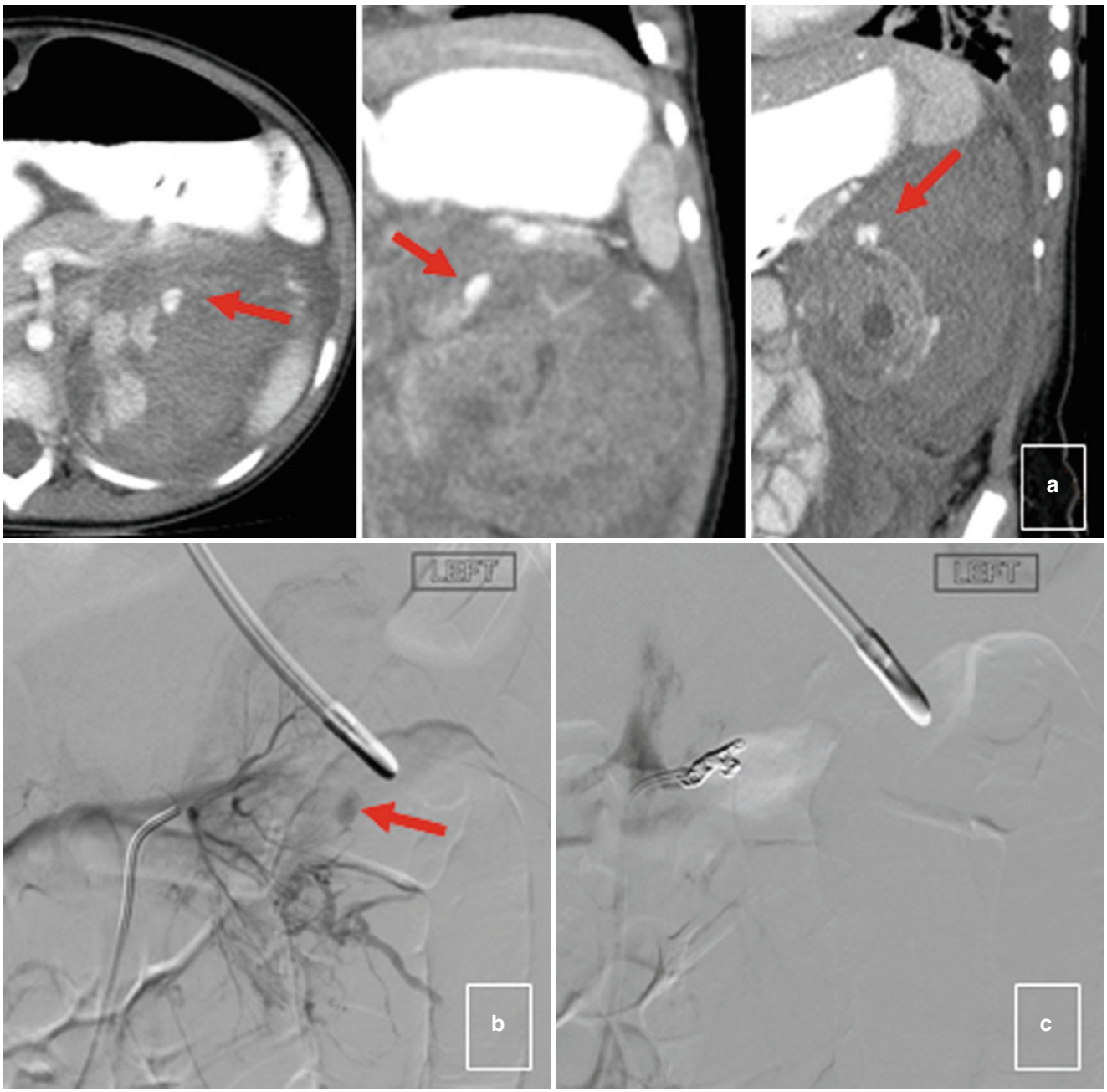

Fig. 21.15 Hemorrhagic Wilms' tumor. (**a** composite): Axial, coronal, and sagittal images of a contrast-enhanced CT of the abdomen demonstrate an enlarged hemorrhagic left renal mass in a 2-year-old male, compatible with a hemorrhagic Wilms' tumor. Note the pseudoaneurysm seen on multiple projections (*arrows*). (**b**) Left renal angiography depicts prominent tumor vascularity, increased density corresponding to the adjacent hematoma, medial displacement of the kidney, and the pseudoaneurysm (*arrow*). (**c**) Post-embolization angiogram—successful emergent devascularization of the left kidney. The embolization coils spare the proximal renal artery to facilitate uncomplicated intraoperative renal artery ligation

ruptured Wilms' tumors, embolization may temporize bleeding in order to prepare patients for surgery (Fig. 21.15).

Conclusion

Renal angiography and embolization is a significant asset to any urological practice. The ability to perform these minimally invasive procedures to prevent or control renal hemorrhage greatly improves morbidity and mortality within this patient population. There are ongoing technological advancements—with the generation of new catheters, embolic agents, and imaging techniques to say the least; this provides almost unimaginable diagnostic and therapeutic capabilities for continuous improvement in treatment outcomes.

References

1. Rocco F, Cozzi LA, Cozzi G. Study of the renal segmental arterial anatomy with contrast-enhanced multi-detector computed tomography. Surg Radiol Anat. 2014;37:517–26.
2. Kumar S, Neyaz Z, Gupta A. The utility of 64 channel multidetector CT angiography for evaluating the renal vascular anatomy and possible variations: a pictorial essay. Korean J Radiol. 2010;11(3):346–54.
3. Decter RM. Chapter 92. Renal fusion and ectopia. In: Glenn's urologic surgery. 7th ed. Philadelphia, PA: Lippincott, Williams and Wilkins; 2010:487–92.
4. Muller A, Rouvière O. Renal artery embolization – indications, technical approaches and outcomes. Nat Rev Nephrol. 2014;11:288–301.
5. Sauk S, Zuckerman DA. Renal artery embolization. Semin Intervent Radiol. 2011;28(4):396–406. Thieme Medical Publishers.
6. Federle M, Pollack HM, et al. Chapter 51. Evaluation of renal trauma. In: Clinical urography. 1st ed. Saunders; 1990:1472–94.
7. Lee R, et al. Hemorrhage following percutaneous renal surgery: characterization of angiographic findings. J Endourol. 2008;22(6):1129–35.
8. Zargar H, et al. Renal artery embolization prior to nephrectomy for locally advanced renal cell carcinoma. ANZ J Surg. 2014;84(7–8):564–7.
9. Umeoka S, et al. Pictorial review of tuberous sclerosis in various organs. Radiographics. 2008;28(7):e32.
10. Chan CK, et al. The efficacy, safety and durability of selective renal arterial embolization in treating symptomatic and asymptomatic renal angiomyolipoma. Urology. 2011;77(3):642–8.
11. Lowe LH, et al. Pediatric renal masses: Wilms tumor and beyond. Radiographics. 2000;20(6):1585–603.
12. Li M-J, et al. A retrospective study of the preoperative treatment of advanced Wilms tumor in children with chemotherapy versus transcatheter arterial chemoembolization alone or combined with short-term systemic chemotherapy. J Vasc Interv Radiol. 2011;22(3):279–86.
13. Ruff S, et al. Emergency embolization of a Wilms' tumor for life-threatening hemorrhage prior to nephrectomy. J Pediatr Surg Case Rep. 2014;2(6):280–3.

Nutcracker Syndrome

22

Suraj Rambhia and David N. Siegel

Nutcracker syndrome (NCS), also known as left renal vein entrapment syndrome, is a rare clinical entity caused by compression of the left renal vein between the superior mesenteric artery and abdominal aorta. This anatomic configuration was first described as analogous to a "nutcracker" in 1937 by Grant [1] (Fig. 22.1). The first venographic study of a patient with this clinical syndrome was reported by Schepper [2] in 1972. When symptomatic, NCS can present as persistent hematuria accompanied by flank pain and/or pelvic pain, with or without the formation of lower extremity and pelvic varices in female or varicocele in male patients [3]. In females, severe cases can lead to abdominopelvic pain as well as other symptoms of pelvic congestion, including dysmenorrhea, dyspareunia, and dysuria [4]. The standard workup for hematuria to evaluate for infectious, inflammatory, or neoplastic causes of persistent hematuria is usually negative leading to the sometimes used nomenclature of "essential hematuria," suggesting the rarer clinical entity of NCS [5, 6]. The following chapter discusses the diagnosis and current surgical and minimally invasive treatment options for this disorder.

Imaging Diagnosis

In a patient with an unremarkable workup for the common causes of hematuria and/or flank pain, a multimodality approach of Doppler US followed by either CT or MR venography will often suggest a diagnosis of NCS. Direct transcatheter venous pressure measurement demonstrating a gradient between the renal vein and IVC is the gold standard in establishing the diagnosis [7].

Ultrasound imaging can often demonstrate the compressed renal vein and allow for measurement of the vein diameter and stenosis secondary to the compression (Fig. 22.2). Examination in long axis using color Doppler will reveal the presence of a velocity gradient from the perihilar to mesoaortic region [8–10]. The presence of increased flow within collateral vessels is further evidence of renal venous hypertension. Although ultrasound can elegantly display the stenosis and collaterals, studies have shown poor correlation between Doppler and the gold standard renocaval pullback pressure measurements [11, 12], which we believe is on the basis of variation in collateral decompression of the renal vein. For this reason, direct measurement of the pressure between the left renal vein and IVC remains important for establishing a diagnosis of NCS, with a pressure differential greater than 5 mmHg considered significant [3].

As CT and MR allow the evaluation of anatomical details in multiple planes, the extrinsic compression of the left renal vein as well as presence of collateral vessels [13–15] can be demonstrated (Fig. 22.3). Extrinsic compression of the left renal vein can result from abnormal origin of the SMA [16, 17] or anomalous anatomy of the left renal vein itself [7, 18] (Fig. 22.4).

The veins normally draining into the left renal vein include the left gonadal vein, left ureteral vein, left inferior phrenic vein, and left adrenal veins [19]. In NCS, these vessels are often engorged due to the decreased outflow of the left renal vein. These collaterals lead to elevated pressures in the gonadal vein and in turn, elevated pressures in the smaller and more delicate vesicular veins and pampniform plexus, resulting in varicocele formation. Finally, as collaterals often inadequately decompress the obstructed renal vein, hematuria occurs, from transposition of blood across delicate renal sinusoids into to the collection system. In the author's experience, hematuria, while often microscopically present, is rarely gross and/or clinically problematic in NCS patients

S. Rambhia, MD
Department of Radiology, North Shore LIJ Medical Center, New Hyde Park, NY, USA
e-mail: SRambhia13@nshs.edu

D.N. Siegel, MD, FSIR (✉)
Division of Vascular and Interventional Radiology, Department of Radiology, Northshore-LIJ Health System, New Hyde Park, NY, USA
e-mail: dsiegel@nshs.edu

A.R. Rastinehad, D.N. Siegel (eds.), *Interventional Urology*, DOI 10.1007/978-3-319-23464-9_22

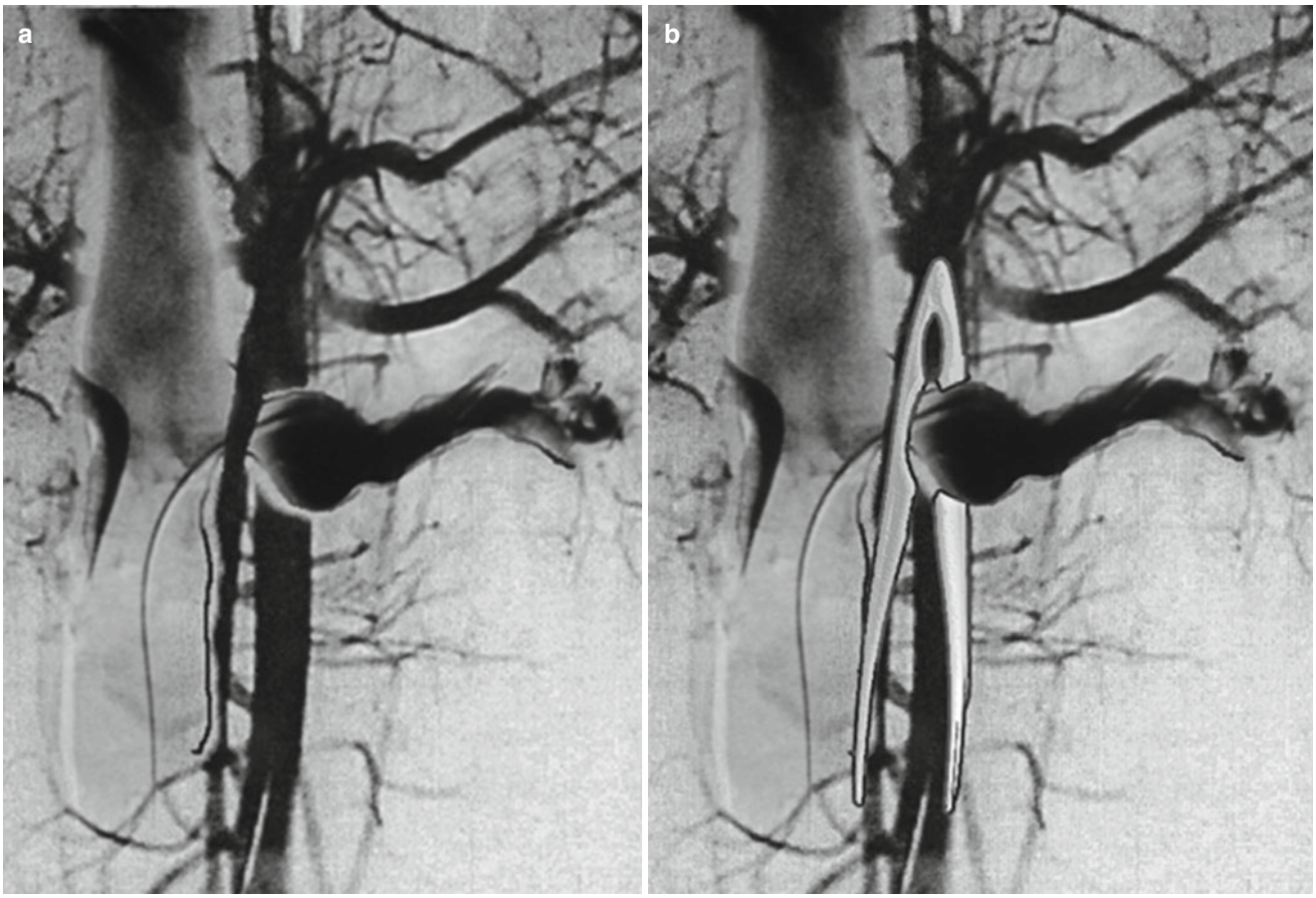

Fig. 22.1 Anatomy of nutcracker syndrome. (**a**) Combined venogram and arteriogram demonstrates compression of the left renal vein between the superior mesenteric artery and aorta. (**b**) Anatomical configuration of left renal vein entrapment syndrome conforms to the shape of a nutcracker (overlaid)

Fig. 22.2 Ultrasound depiction of nutcracker syndrome. Transverse ultrasound image demonstrates compression of the left renal vein (*LRV*) between the superior mesenteric artery (*SMA*) and aorta (*AO*) (Courtesy of Ahmad Alomari, MD)

with symptoms of pelvic congestion or varicocele, and NCS patients with persistent gross hematuria rarely have symptoms of varicocele or pelvic congestion. We believe that this is on the basis of renal vein pressures, and those with robust collaterals are likely decompressed well enough to avoid hematuria and vice versa.

Clinical Management and Treatment Options

A wide array of treatment approaches have been employed in an attempt to either decrease venous hypertension or alleviate the predominating symptoms of hematuria or pelvic congestion. Severity of symptoms, patient demographic, and understanding of available minimally invasive techniques can guide the clinician as to when and how to intervene.

The first reported case of treated NCS was in 1974 [20]. Since then, a number of surgical approaches have been described. These include direct reimplantation of the left renal vein [21, 22], SMA transposition [23, 24], nephropexy

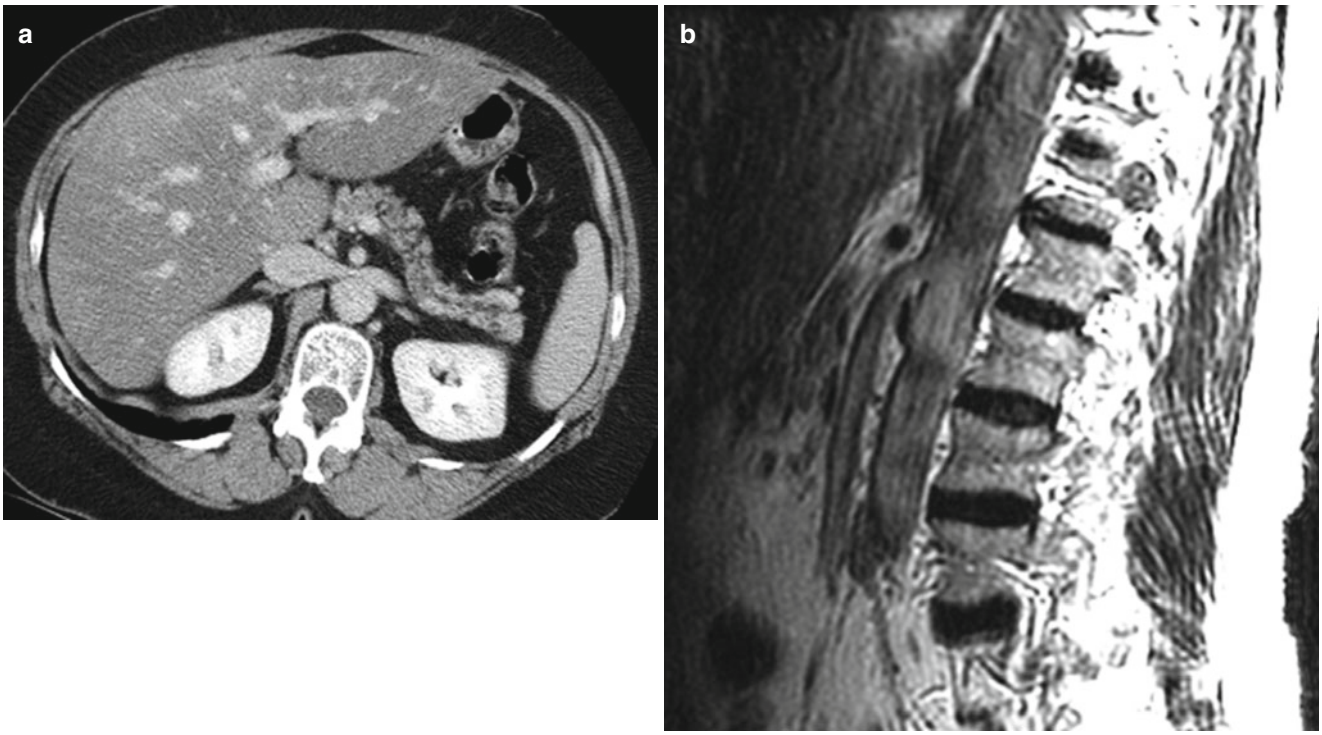

Fig. 22.3 Cross-sectional imaging of nutcracker syndrome. (**a**) Axial CT demonstrates compression of the left renal vein between the superior mesenteric artery and aorta. (**b**) Sagittal T1 MR also demonstrates the most commonly recognized anatomic configuration of nutcracker syndrome

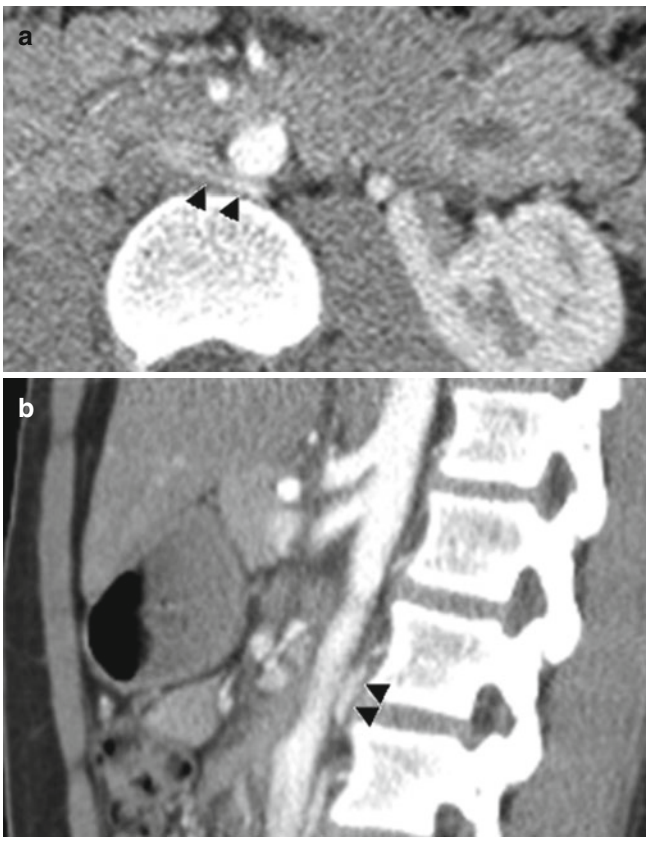

Fig. 22.4 Retro-aortic left renal vein. Axial (**a**) and sagittal (**b**) CT images showing retro-aortic course of the left renal vein (*arrowheads*). The left renal vein is compressed between the aorta and spine

[25], autotransplantation of left kidney [26, 27], nephrectomy alone [28], and external stenting or bracing of the LRV [4, 29–31]. Most of these approaches were developed to decrease underlying venous hypertension. LRV transposition is the most commonly described surgical approach successfully utilized to alleviate pelvic congestion symptoms and hematuria [23, 32–36]. Some approaches, such as left gonadal vein ligation [30], gonadocaval bypass [4], splenorenal venous bypass [29], and/or embolization and sclerosis of pelvic varices are more directed to treat pelvic congestion symptoms. Ligation of collateral vessels, coil embolization of gonadal veins, and ablation of varices have been employed in conjunction with renocaval pressure gradient relieving procedures in cases where pelvic congestion resulted from NCS [3, 37].

For pediatric patients, some authors have described intermittent hematuria and proteinuria as a byproduct of anatomical changes of normal growth [12], providing support for a conservative approach, where patients are monitored up to 24 months to evaluate for resolution of symptoms [3, 21]. Severe pain and hematuria requiring transfusion are among the gamut of symptoms that would require more urgent intervention [3, 12].

More recently, endovascular stenting of the left renal vein has been reported. The WALLSTENT, first used in 1996 [37], continues to be the most commonly utilized stent in the United States because of its availability in large calibers and lengths that best correspond to LRV dimensions. Since that

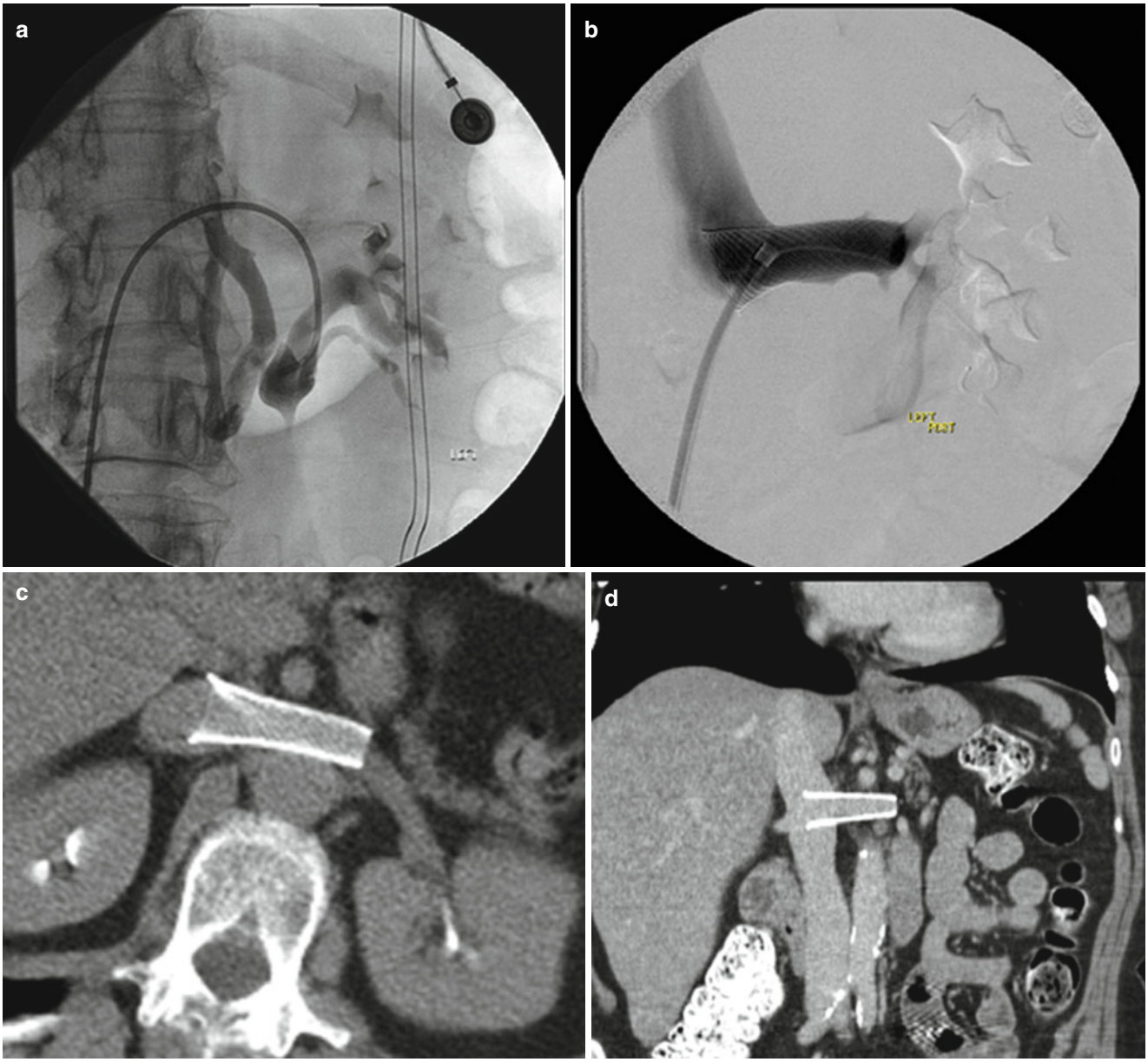

Fig. 22.5 Pre- and posttreatment images. (**a**) Venogram prior to stenting in a patient with nutcracker syndrome demonstrates drainage through numerous collateral vessels. (**b**) Post stent placement in the left renal vein; there is return of drainage into the IVC. Images **c** and **d** show stent placement CT images in the axial and coronal plane, respectively

report, several studies have described LRV stenting with alleviation of symptoms of NCS [23, 38–45] (Fig. 22.5).

Several complications of LRV stenting including stent migration, thrombosis, and restenosis have been reported [40, 42, 45], and the theoretical long-term risk of stent erosion has also been discussed in the literature [12], which is especially relevant as these patients are generally younger. Given the paucity of cases in the literature and lack of data regarding long-term consequences of endovascular stenting, these authors feel the decision to pursue any intervention should be guided by clinical and radiological findings on a case-by-case basis.

Conclusion

Left renal vein entrapment syndrome, also known as nutcracker syndrome, involves compression of the left renal vein and can present with abdominopelvic pain, hematuria, and symptoms of pelvic congestion syndrome. Noninvasive ultrasound and cross-sectional imaging can show the anatomic abnormality; however, the diagnosis is only suggested if anatomic findings correlate with the clinical picture and is confirmed by direct renocaval pressure gradient measurement. Though LRV transposition and now LRV stenting are commonly employed methods for treatment of nutcracker syndrome, judicious

management of NCS should take into consideration patient's age, severity, and chronicity of symptoms along with current lack of data regarding long-term outcomes of stent placement.

References

1. Grant JCB. Method of anatomy. Baltimore: Williams & Wilkins; 1937. p. 158.
2. de Schepper A. "Nutcracker" phenomenon of the renal vein and venous pathology of the left kidney [in Dutch]. J Belge Radiol. 1972;55(5):507–11.
3. Rudloff U, et al. Mesoaortic compression of the left renal vein (nutcracker syndrome): case reports and review of the literature. Ann Vasc Surg. 2006;20:120–9.
4. Scultetus AH, et al. The nutcracker syndrome: its role in the pelvic venous disorders. J Vasc Surg. 2001;34:812–9.
5. Russo D, et al. Gross hematuria of uncommon origin: the nutcracker syndrome. Am J Kidney Dis. 1998;32:E3.
6. MacMahon HE, Latorraca R. Essential renal hematuria. J Urol. 1954;71:667–76.
7. Venkatachalam S, et al. Basic data underlying clinical decision-making in endovascular therapy: the nutcracker syndrome. Ann Vasc Surg. 2011;25(8):1154–64.
8. Kim WS, et al. Hemodynamic investigation of the left renal vein in pediatric varicocele: Doppler US, venography, and pressure measurements. Radiology. 2006;241(1):228–34.
9. Shin JI, et al. Doppler ultrasonographic indices in diagnosing nutcracker syndrome in children. Pediatr Nephrol. 2007;22(3):409–13.
10. Cheon JE, et al. Nutcracker syndrome in children with gross haematuria: Doppler sonographic evaluation of the left renal vein. Pediatr Radiol. 2006;36(7):686–6.
11. Takebayashi S, et al. Diagnosis of the nutcracker syndrome with color Doppler sonography: correlation with flow patterns on retrograde left renal venography. Am J Roentgenol. 1999;172(1):39–43.
12. Kurklinsky AK, Rooke TW. Nutcracker phenomenon and nutcracker syndrome. Mayo Clin Proc. 2010;85(6):552–9.
13. Lamba R, et al. Multidetector CT of vascular compression syndromes in the abdomen and pelvis. Radiographics. 2014;34(1):93–115.
14. Butros SR, et al. Venous compression syndromes: clinical features, imaging findings and management. Br J Radiol. 2013;86:20130284.
15. Kim KW, et al. Diagnostic value of computed tomographic findings of nutcracker syndrome: correlation with renal venography and renocaval pressure gradients. Eur J Radiol. 2011;80(3):648–54.
16. Fitoz S, et al. Nutcracker syndrome in children: the role of upright position examination and superior mesenteric artery angle measurement in the diagnosis. J Ultrasound Med. 2007;26:573–80.
17. Basroum MK, et al. Patient with both Wilkie syndrome and nutcracker syndrome. Vasc Med. 2008;13(3):247–50.
18. Urban BA, et al. Three-dimensional volume-rendered CT angiography of the renal arteries and veins: normal anatomy, variants, and clinical applications. Radiographics. 2001;21(2):373–86.
19. Federle M, et al. Diagnostic and surgical imaging anatomy: chest, abdomen. Pelvis Clinical Anatomy. 2007;21:463.
20. Pastershank SP. Left renal vein obstruction by a superior mesenteric artery. J Can Assoc Radiol. 1974;25(1):52–4.
21. Shin JI, et al. Factors affecting spontaneous resolution of hematuria in childhood nutcracker syndrome. Pediatr Nephrol. 2005;20(5):609–13.
22. Stewart BH. Left renal venous hypertension "nutcracker" syndrome. Managed by direct renocaval reimplantation. Urology. 1982;20:365–9.
23. Zhang H, et al. The left renal entrapment syndrome: diagnosis and treatment. Ann Vasc Surg. 2007;21(2):198–203.
24. Thompson PN, et al. A case of nutcracker syndrome: treatment by mesoaortic transposition. J Vasc Surg. 1992;16(4):663–5.
25. Shaper KR, et al. The nutcracker syndrome: an uncommon cause of haematuria. Br J Urol. 1994;74:144–6.
26. Xu D, et al. Management of renal nutcracker syndrome by retroperitoneal laparoscopic nephrectomy with ex vivo autograft repair and autotransplantation: a case report and review of the literature. J Med Case Reports. 2009;3:82.
27. Chuang CK, et al. The nutcracker syndrome managed by autotransplantation. J Urol. 1997;157(5):1833–4.
28. Hohenfellner M, et al. The nutcracker syndrome: new aspects of pathophysiology, diagnosis and treatment. J Urol. 1991;146(3):685–8.
29. Chung BI, et al. Laparoscopic splenorenal venous bypass for nutcracker syndrome. J Vasc Surg. 2009;49:1319–23.
30. Rogers A, et al. Transperitoneal laparoscopic left gonadal vein ligation can be the right treatment option for pelvic congestion symptoms secondary to nutcracker syndrome. Vascular. 2007;15:238–40.
31. Barnes RW, et al. Mesoaortic compression of the left renal vein (the so-called nutcracker syndrome): repair by a new stenting procedure. J Vasc Surg. 1988;8(4):415–21.
32. Reed NR, et al. Left renal vein transposition for nutcracker syndrome. J Vasc Surg. 2009;49(2):386–613.
33. Hohenfellner M, et al. Transposition of the left renal vein for treatment of nutcracker phenomenon: long term follow up. Urology. 2002;59(3):354–7.
34. Salehipour M, et al. Left renal vein transposition for treatment of the Nutcracker syndrome. Arch Iran Med. 2006;9:161–2.
35. Kim JY, et al. Transposition of the left renal vein in nutcracker syndrome. Eur J Vasc Endovasc Surgery. 2006;31(1):80–2.
36. Wang L, et al. Diagnosis and surgical treatment of nutcracker syndrome: a single-center experience. Urology. 2009;73:871–6.
37. Neste MG, et al. Endovascular stent placement as a treatment for renal venous hypertension. J Vasc Interv Radiol. 1996;7(6):859–61.
38. Chen W, et al. Endovascular stent placement for the treatment of nutcracker phenomenon in three pediatric patients. J Vasc Interv Radiol. 2005;16(11):1529–33.
39. Basile A, et al. Percutaneous nitinol stent implantation in the treatment of nutcracker syndrome in young adults. J Vasc Interv Radiol. 2007;18(8):1042–6.
40. Kim SJ, et al. Long-term follow-up after endovascular stent placement for treatment of nutcracker syndrome. J Vasc Interv Radiol. 2005;16(3):428–31.
41. Wei SM, et al. Intravenous stent placement for treatment of the nutcracker syndrome. J Urol. 2003;170(5):1934–5.
42. Hartung O, et al. Endovascular stenting in the treatment of pelvic vein congestion caused by nutcracker syndrome: lessons learned from the first five cases. J Vasc Surg. 2005;42:275–80.
43. Park YB, et al. Nutcracker syndrome: intravascular stenting approach. Nephrol Dial Transplant. 2000;15:99–101.
44. Cohen F, et al. Endovascular treatment of circumaortic nutcracker syndrome. J Vasc Interv Radiol. 2009;20:1255–7.
45. Gagnon LO, et al. Nutcracker syndrome in a 20-year-old patient treated with intravascular stent placement: a case report. Can J Urol. 2009;16:4765–9.

Renal Artery Stenosis

23

Noor Ahmad, Marc H. Schiffman, and Thomas A. Sos

Renal artery stenosis, resulting in renovascular hypertension, is a major cause of secondary hypertension [1]. When both kidneys are affected, ischemic nephropathy with diminished renal function also results. The most common cause of renal artery stenosis is atherosclerotic, usually ostial, narrowing of the renal artery. The second most common cause of renal artery stenosis is fibromuscular dysplasia. In most cases, aRAS is treated with stent placement and FMD with angioplasty alone. Nonrandomized single-center series for revascularization for both atherosclerotic Renal Artery Stenosis (aRAS) and fibromuscular dysplasia (FMD) have reported excellent outcomes [2, 3]. In recent years, however, large prospective randomized trials have disputed these previously reported outcomes in the management of aRAS [4, 5]. Despite many flaws in these trials, the importance of proper patient selection and performance of appropriate endovascular technique by skilled operators has been emphasized. In this chapter, the authors review patient selection factors, describe standard techniques for renal revascularization, and provide technical "tips" that can be utilized during intervention. In addition, the authors will review reported outcomes, in particular, from several large retrospective studies including the primarily US-based "Cardiovascular Outcomes in Renal Atherosclerotic Lesions" (CORAL) trial.

Renal artery stenosis (RAS) refers to a fixed narrowing of the renal artery which can lead to renin-mediated renovascular hypertension (RVH) and ischemic nephropathy (IN). It is the most common cause of secondary hypertension and accounts for 1–4 % of all patients with hypertension [6].

Renal artery stenosis secondary to atherosclerosis (aRAS) accounts for 90 % of patients with RVH, with fibromuscular dysplasia (FMD) accounting for the second most common cause [6]. Angiographically, most aRAS lesions occur within the ostium or the first centimeter of the renal artery and are due to plaque within the aorta engulfing the ostium of the renal artery resulting in the stenosis [3]. The narrowing within FMD usually occurs in the mid to distal third of the renal artery and medial fibroplasia, with a "string of beads" appearance, which accounts for most cases [4].

Indications for treatment with renal artery catheter-based interventions must include renal artery stenosis documented to be *hemodynamically significant*, particularly when associated with renal dysfunction, poorly controlled hypertension, or recurrent pulmonary edema [7]. Renal revascularization certainly has a significant role in the management of aRAS patients; however, careful selection is necessary to identify patients who will benefit the most from intervention. Treatment for aRAS has been renal revascularization with renal artery angioplasty and stenting; however, this has been controversial secondary to several large-scale retrospective studies in recent years [4, 5]. Treatment for FMD with renal angioplasty has been shown to be widely accepted and efficacious.

Techniques

Patient Selection

Appropriate patient selection for intervention in patients with significant renal artery stenosis is based on clinical, anatomic, and physiologic (hemodynamic) criteria. Renal artery stenosis can be an independent clinically asymptomatic condition, or it can overlap with multiple clinical syndromes including hypertension or renal insufficiency [8]. All three clinical conditions can occur independently or may be causally linked to each other (Fig. 23.1). For example, patients with essential hypertension may have renal artery stenosis, which does not result in renovascular hypertension. It is important to stratify these separate clinical conditions in order to guide safe, effective, and appropriate treatment.

N. Ahmad, MD (✉) • M.H. Schiffman, MD • T.A. Sos, MD
Division of Interventional Radiology, Department of Radiology, New York Presbyterian Hospital/Weill Cornell Medical College, New York, NY, USA
e-mail: TAS2003@med.cornell.edu

A.R. Rastinehad, D.N. Siegel (eds.), *Interventional Urology*, DOI 10.1007/978-3-319-23464-9_23

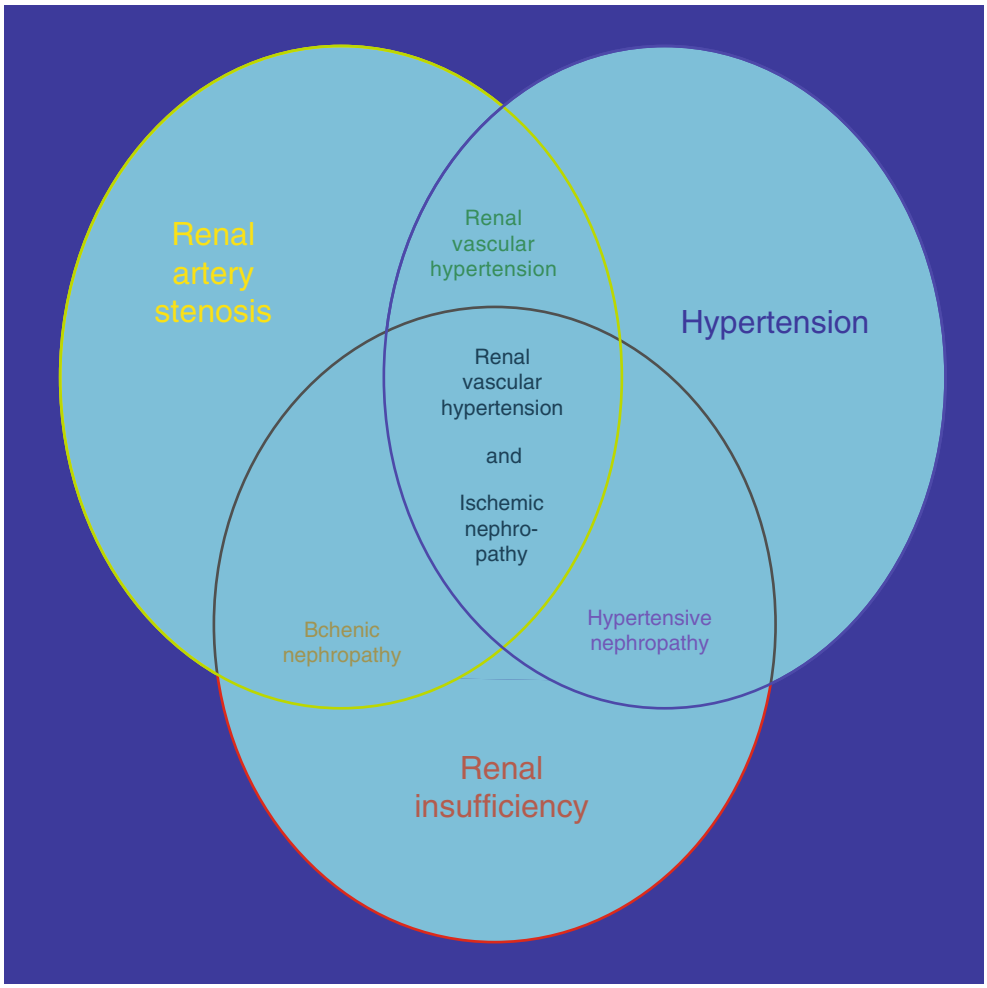

Fig. 23.1 Complex overlapping relationship between renal artery stenosis, hypertension, and renal insufficiency

Clinical Criteria

According to the Seventh Report of the Joint National Committee on Prevention, Detection, Evaluation, and Treatment for High Blood Pressure, testing for identifiable causes of nonessential hypertension is not indicated unless blood pressure control is not achieved despite attempt with optimal doses of three drugs of different classes [9]. The Society of Interventional Radiology and American Heart Association states that patients should undergo further testing with imaging in the following group of patients: patients with onset of hypertension before 30 years of age; patients with severe hypertension after the age of 55; accelerated, resistant, or malignant hypertension; new azotemia; worsening renal function after administration of angiotensin converting enzyme inhibiting agents or angiotensin receptor blocking agents; size discrepancy between kidneys greater than 1.5 cm or sudden; and unexplained pulmonary edema [10, 11]. Physical exam and imaging findings in patients with suspected RAS may include continuous epigastric bruit, retinopathy, and asymmetric renal atrophy. Laboratory results, which should prompt further investigation with diagnostic imaging or angiography, include elevated plasma renin activity, hypokalemia, and/or proteinuria [11].

Anatomic Criteria/Screening Diagnostic Exams

In patients with suspected renovascular hypertension, imaging technique selection for diagnostic screening should be guided and based on the American College of Radiology Appropriateness Selection Criteria [12]. These include ultrasound, nuclear medicine exam, computed tomography (CT), and magnetic resonance angiography (MRA). CT and MRA have the added benefit of not just being screening exams but can be vital in the pre-procedural planning prior to angiography.

Duplex Doppler ultrasound (US) has the highest rating in appropriateness criteria for the evaluation of patients with high index of suspicion of renovascular hypertension and diminished renal function and second highest in patients with normal renal function [12]. US provides real-time anatomic and hemodynamic information by utilizing gray scale,

color flow Doppler, and Doppler spectral analysis to evaluate the renal arteries. A diagnosis of RAS on ultrasound requires a peak systolic velocity in the renal artery exceeding 180 or 200 cm/s and a renal artery/aortic velocity ratio exceeding 3.5. Doppler US can also be helpful in predicting outcomes for renal artery interventions. Resistive indices of greater than 0.8 have been shown to predict poor outcome after attempts at reducing hypertension and improving renal function [13], but others dispute its predictive value. Unfortunately, US is operator dependent and also may be compromised by the patient's body habitus. These limitations may become significant when patients are serially followed and the exam is performed by different operators.

Nuclear medicine screening exams offer the added advantage of providing functional renal assessment along with limited anatomic information. Renal perfusion, renal function, and renal excretion can be qualitatively and quantitatively assessed. For the diagnosis of renal artery stenosis, the study of choice is angiotensin converting enzyme inhibitor scintigraphy. Kidneys affected by renovascular hypertension demonstrate impaired function due to angiotensin converter enzyme inhibition. The reported sensitivity of ACE-inhibitor renal scintigraphy for renovascular hypertension ranges from 34 to 93 % and with specificity of 100 % [14].

Computed tomography angiography (CTA) uses multidetector row helical scanners to generate high-resolution two-dimensional images and volume or surface renderings in three dimensions to provide detailed anatomic information [15]. According to the ACR Appropriateness Criteria, CTA is rated the highest in patients with high index of suspicion of renovascular hypertension and normal renal function [12]. Along with detailed anatomic information, additional information about the renal arteries that CTA can provide includes the extent and distribution of atherosclerotic plaque as well as secondary signs of RAS including post-stenotic dilatation, changes in renal size and volume, and cortical changes [16]. Although CTA can be useful in evaluating renal artery stents and in stent stenosis, imaging artifact from high-density materials including calcified arterial plaques can cause beam hardening and limit evaluation of surrounding structures. A major limitation of CTA besides the use of significant doses of ionizing radiation is the use of nephrotoxic iodinated contrast – alas in patients who need it most, those with IN, it often cannot be used.

Along with CTA, magnetic resonance angiography (MRA) is a highest rated exam of choice according to the ACR Appropriateness Criteria in patients with a high index of renovascular hypertension and normal renal function (Fig. 23.2). MRA is also the highest rated exam of choice in patients with diminished renal function given the ability to obtain information without the use of an iodine-based contrast agent [12]. Gadolinium-based MRA contrast unfortunately has been associated with nephrogenic systemic fibrosis (NSF) in patients with IN. Newer noncontrast MRA sequences with steady-state free precession (SSFP) and arterial spin labeling techniques and safer Gad-based contrast can overcome these problems. MRA uses magnetic fields and radiofrequency energy to produce high detailed images, which provide information in identifying RAS, vascular anatomy, renal anatomy, and technique planning. The negative predictive value of unenhanced MRA compared to CTA and DSA is 96 % suggesting negative MRAs essentially nearly rule out renal artery stenosis [17, 18]. Newer techniques, such as blood oxygen level-dependent (BOLD) MRI, are being developed to provide physiologic information that may help identify patients who will benefit from the intervention [19–22].

Physiologic Criteria: Catheter-Based Angiography with Pressure Measurements

Catheter-based angiography is the gold standard for diagnosing significant renal artery stenosis [23]. Catheter arteriography has high spatial resolution for evaluating the main renal arteries as well as branch renal arteries. The anatomic minimum threshold of hemodynamically significant renal artery stenosis is greater than 70–80 % diameter [24, 25]. Visual estimation of a stenosis based on angiography is notoriously inaccurate and must be confirmed by physiological/hemodynamic objective assessment with pressure gradients across a stenosis. Hemodynamically significant stenoses include lesions with a peak systolic gradient of greater than 10–20 mmHg or 10 % of the peak systolic pressure [26–28].

Multiple studies have proven that pressure gradients are the most effective and reliable indicator for how well a patient will respond to angioplasty and stenting. Leesar et al. in 2009 and Mangiacapra et al. in 2010 compared systolic pressure gradients, renal fractional flow reserve, quantitative angiography, and intravascular ultrasound and found that systolic pressure gradients had the best receiver operator characteristic curve for predicting blood pressure response post renal artery stenting [26, 28].

Renal Vein Renin Sampling

Although the usefulness has been controversial, renal vein renin (RVR) sampling can be an additional physiological indicator of how much a renal artery stenosis is contributing to a patient's hypertension. In addition, it can be a useful predictor in determining which patients will benefit the most after revascularization for renovascular hypertension [7]. Studies have shown, though, that RVR is neither sensitive nor specific enough to exclude patients who do not have RVH [29–32]. RVR secretion that lateralizes to the affected side, however, has as strong positive predictive value [33].

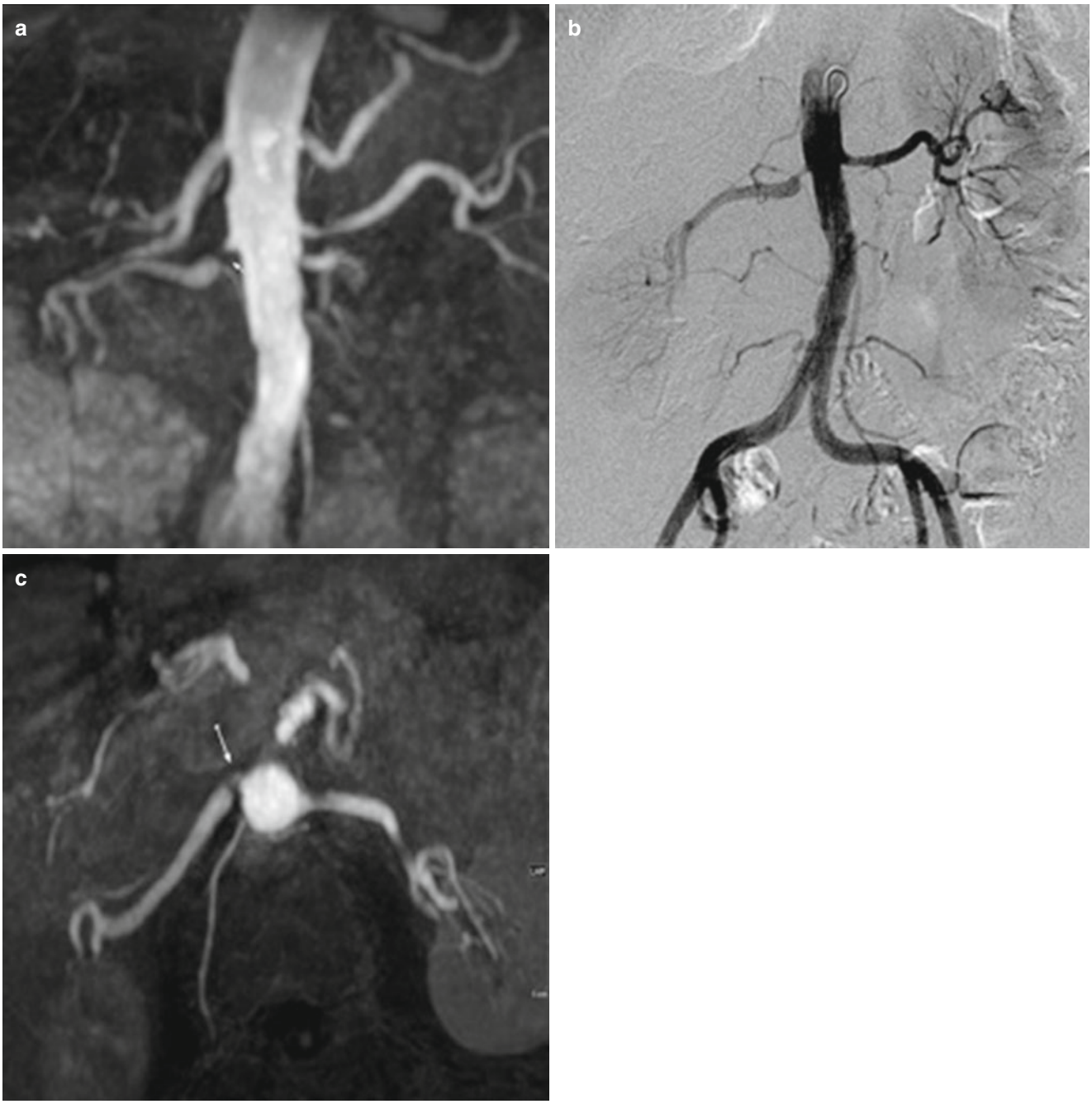

Fig. 23.2 Patient presenting with symptoms of renovascular hypertension with suspected right-sided renal artery stenosis on pre-procedural MRA (**a**) and confirmed on angiography (**b**) after pressure measurements obtained. Axial slice from MRA (**c**) demonstrates ostial stenosis of the right renal artery, which arises approximately 30° ventrally along the right anterolateral aspect

Venous samples should be taken from the right main renal vein, from the left renal vein, and from the infrarenal IVC. The renin levels can be analyzed by the simple ratio method or the incremental ratio method. The simple ratio method takes the ratio of the RVR activity in the involved size divided by the activity in the non-involved side with a positive ratio being 1.5:1.0 (sensitivity 62 % and specificity 60 %) [7]. The incremental ratio method calculates the net secretion of the renin from each kidney. Hypersecretion of renin from the stenotic kidney ($[V-A]/A>50$ %) and contralateral suppression release from the normal kidney are strong predictors of curability of hypertension with therapeutic revascularization for the affected kidney [30].

Potential pitfalls in RVR sampling, which can result in poor predictive values, include sampling renal veins in patients who are chronically blocked with ACE inhibitors or

beta-blockers. In addition, failure to identify normal anatomic variants or accessory renal veins and not sampling distal to the gonadal vein in the left renal vein can both lead to suboptimal studies [7].

Summary: Algorithms for Treatment

After clinical suspicion of renovascular hypertension or renal insufficiency is raised and a screening diagnostic exam is positive for renal artery stenosis, the anatomic and hemodynamic significance of stenosis must be confirmed by pressure gradient, and the patients should be treated. Finally, safe and reasonable anatomic and medical conditions for access and therapy should be present. A summary of the algorithm for workup and management in patients with suspected renovascular hypertension and renal insufficiency is shown in Fig. 23.3.

Absolute contraindications to treatment include a hemodynamically insignificant stenosis and a medically severely unstable patient. Relative contraindications include a long-segment occlusion, an atrophic kidney, and a severely diseased aorta predisposing to increased risk of embolization of atheroma. Newer catheters and techniques performed by skilled operators, however, allow interventionalists to proceed despite these relative contraindications [7] (Fig. 23.4).

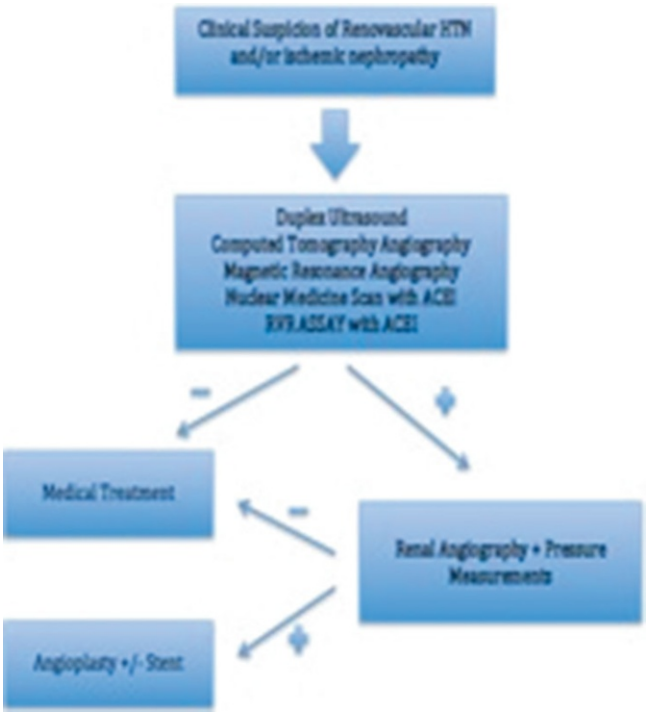

Fig. 23.3 Algorithm for the management of patients with renovascular hypertension secondary to suspected renal artery stenosis

Diagnostic Catheter-Based Aortography

Initial puncture is usually made through the common femoral artery. Interventional cardiologists are increasingly using the radial artery, and vascular surgeons are increasingly using the brachial artery [34]. Specific anatomic considerations, which may affect the puncture selection, have to be taken into account during pre-procedure planning and include the obliquity of the renal arteries at their origin from the aorta (see section "Tips").

After puncture, a standard 10 cm 5 Fr vascular sheath is placed, and a flush catheter, such as a 4 Fr Omniflush™ (Angiodynamics, Queensbury, NY) catheter, is used for standard aortography. The advantage of using the OmniFlush™ catheter is its ability to deliver a more concentrated bolus to the area of interest because its side holes and end hole are directed laterally and caudally [7]. The catheter is positioned at the T12–L1 interspace since the renal arteries usually originate at the upper endplate of the L1 vertebral body. After aortography, the renal artery should be selected with a soft atraumatic wire, such as a Bentson wire, and a recurved catheter such as the Sos Omni™ selective (Angiodynamics, Queensbury, NY). Hydrophilic guidewires should be avoided as much as possible given their propensity to result in vascular perforation; however, if they are used to cross difficult stenosis, whenever possible, they should be exchanged for a non-hydrophilic wire. Multiple visceral recurved diagnostic catheters can be used for selecting the renal arteries including a Simmons, Sidewinder, Shepherd's crook, and Sos Omni Selective™ or the nonrecurve Cobra Tips for selecting the renal artery is discussed in greater detail below within the section "Tips."

Pressure Gradient Measurements

After successfully crossing a lesion with a soft atraumatic wire and a recurved catheter, the transtenotic pressure gradient should be measured, ideally with a 0.014″ pressure-sensing wire [35]. This translesional gradient should then be compared to a simultaneous aortic pressure measured, ideally, with a multichannel monitor. Serial alternating pressures can be compared if a multichannel monitor is not available. If a pressure-sensing wire is not available, pressure measurements can be obtained through a 4 Fr catheter; however, it should be noted, and this catheter contributes to the existing stenosis [7]. Since visual assessment of anatomic stenosis is very unreliable, even in seemingly very severe stenosis, pressure gradients must always be measured.

Angioplasty

Percutaneous transluminal renal angioplasty (PRTA) is a nonsurgical method of restoring blood flow within RAS. Balloons

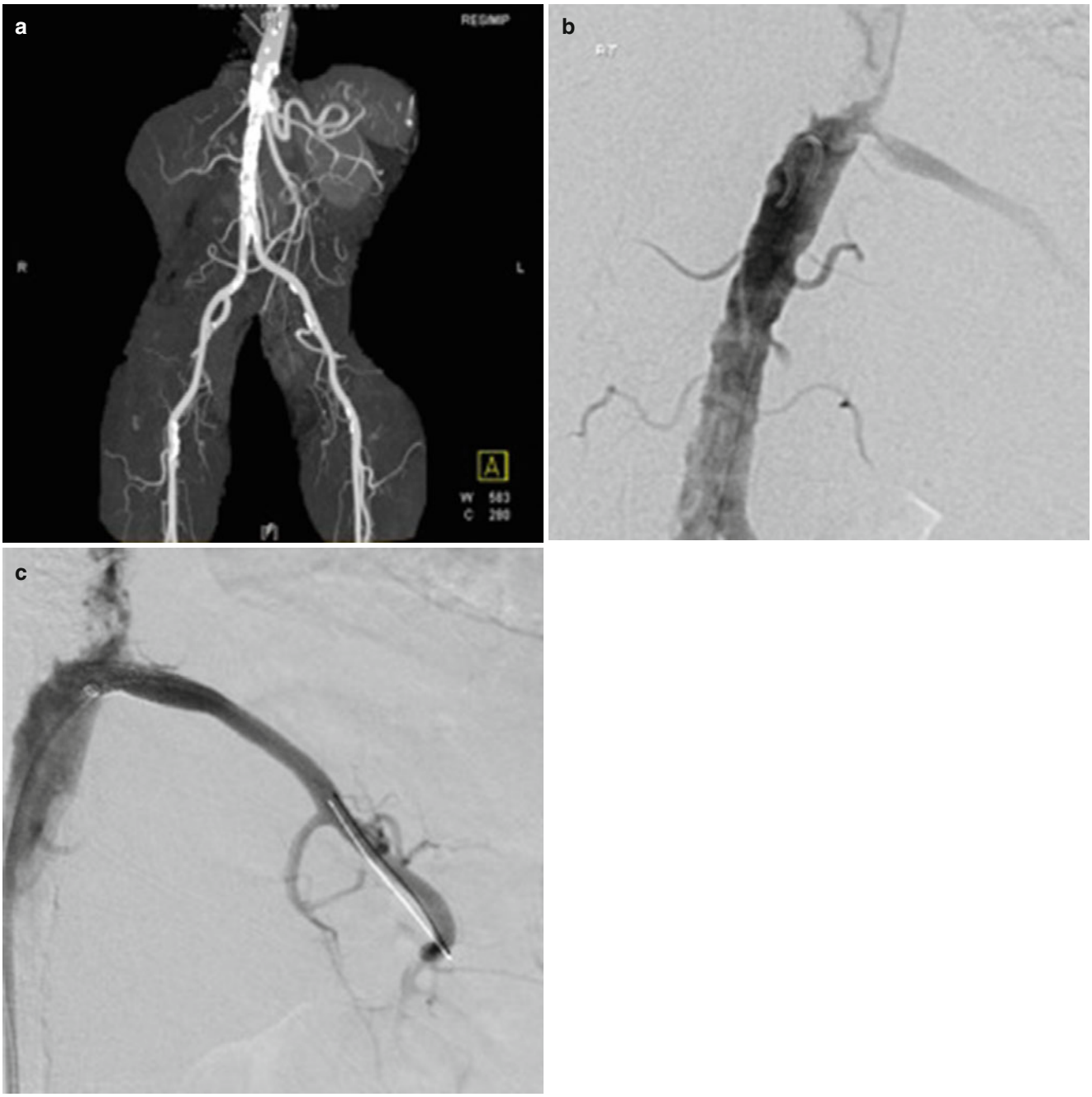

Fig. 23.4 An 82-year-old female with refractory hypertension and imaging findings of left renal artery stenosis, right renal artery occlusion, and severe atheromatous aorta (**a**). Angiography and pressure measurements confirmed left renal artery stenosis with a trans-stenotic mean arterial pressure gradient of 22 mmHg and severe suprarenal aortic plaque (**b**). Successful stent placement across left renal artery stenosis (**c**)

vary tremendously in length, diameter, shape, compliance, and material. Choosing a balloon depends on several factors, which include the length and severity of stenosis, diameter of the non-stenotic portion of the renal artery, tortuosity, and branching pattern. PTRA alone has been found to be more successful in non-ostial (1 cm from the origin) lesions and is indicated in stenosis due to either atherosclerosis or fibromuscular dysplasia. In aRAS ostial lesions, PTRA alone fails in up 75 % of cases [36]; primary stenting is the preferred treatment. Complications from PTRA and stenting include distal embolization, cholesterol embolization, renal artery injury, and access site hematoma [7].

Initially diagnostic aortography and selective renal artery catheterization with trans-stenotic pressure measurements are performed, as previously described. When PTRA is planned, careful selection of the size of the balloon diameter should be

made. Generally, a balloon diameter that is 10 % larger than the estimated "normal" diameter of the vessel based on the arteriogram is recommended. Sub 4 Fr balloon systems are used with 0.014″–0.018″ guidewires or a 5 Fr balloon system over a 0.035″ guidewire if necessary [7]. A soft-tipped but relatively stiff shaft wire is used to select and cross the stenosis, and patients are systemically heparinized once the lesions are crossed. The diagnostic catheter used to cross the stenosis is then exchanged for a longer sheath/guide system or directly for the balloon catheter; alternatively, the sheath can be introduced initially and all maneuvers performed through it. After placing the balloon markers across the lesion, the balloon is slowly inflated until the balloon is fully inflated or has reached its rated maximum pressure. In long-segment FMD, overlapping inflations may be necessary, starting distally and proceed centrally. After removing the balloon catheter, a "post-" PTRA angiogram is performed, ideally utilizing a technique that preserves wire position across the lesion. In addition a post-PTRA pressure gradient is performed to ensure that the gradient has been resolved. This is the strongest indicator for posttreatment success rates [28].

Stenting

Renal artery stenting improves the efficacy of PTRA by offsetting the recoil force of arteries and atherosclerotic plaque, especially at the ostium [7]. Almost all aRAS stenoses at the ostium require a stent. After diagnostic angiography, the renal artery and stenosis are crossed, as described previously in the renal angioplasty section (Fig. 23.5). Multiple techniques exist for proper stent deployment, in particular for renal ostial lesions. With renal artery stenting, a guiding catheter/sheath system is almost always used for stent deployment. The sheath or guiding catheter typically acts as support or "backbone" to help with crossing tight renal artery stenosis. In addition, it allows for contrast injections, while equipment including balloons, wires, and stents are in place [37]. A stent and dilating balloon, which will adequately cover the lesion, extend a few millimeters into the aorta and match the normal vessel diameter that is used.

A 0.018 or 0.014 in. atraumatic wire and a diagnostic catheter are utilized to cross the lesion, and the wire tip is positioned in the distal main renal artery or a proximal first or second order branch. The stent is pre-mounted on a balloon catheter and is delivered through a 5 Fr or 6 Fr guide sheath or catheter. In cases of severe stenosis, the 5 Fr sheath may be advanced through the stenosis to ascertain stent passage and then slowly withdrawn leaving the balloon/stent combination over the guidewire in the stenosis [38]. For low-profile pre-mounted Monorail balloon-expandable stents, after a stiff guidewire is placed across a lesion, the stent is positioned across the lesion with about 2 mm extending into the aorta. Accurate positioning is confirmed by injecting contrast through the sidearm of the sheath, the balloon is then inflated, and the stent is deployed. To achieve long-term patency, it is mandatory for the stent to cover the stenosis extending from the ostium into the aorta and a few mm distal to the stenosis. Completion arteriography is performed through injection of the sidearm of the sheath after it is withdrawn into the proximal stent or aorta. Overlapping stents reduce patency; if they are necessary, approximately 2 mm of stent overlap is recommended. Gaps within a series of stents may promote intimal hyperplasia. Once completed, repeated angiograms through the sheath and pressure measurements should be taken to evaluate positioning, residual stenosis, or residual abnormal pressure gradients.

Specific Situations

Bilateral Renal Artery Stenosis and/or Occluded Renal Artery

Treatment of bilateral renal artery stenosis should be performed during the same session, if possible. If both sides have lesions thought to be hemodynamically significant, the technically easier side, which is often that with the larger kidney, should be attempted first; if the first procedure is successful and both the operator and patient are still fresh, the second more difficult side can be attempted but rescheduled or postponed if significant difficulties are encountered.

If the technically more difficult and functionally less important side were attempted first and resulted in a complication or were unsuccessful, a tired operator and patient may have to perform/undergo the second "rescue" procedure which probably would have been successful if it had been performed initially, but now under adverse conditions, it is less likely to succeed. If for any reason, the technically more challenging cannot be treated, the patient has the benefit of at least one side being treated.

In cases of renal artery occlusion, recanalization should only be attempted if the patient is anatomically or physiologically uninephric or after the contralateral kidney is successfully treated. Criteria for intervention of a completely occluded renal artery include clinical significance and adequate kidney size, if a clear stump is seen on angiography and if there is increased renin production [39]. Pre-procedure planning with CTA or MRA will assist in determining the anatomy of the occlusion. A straight hydrophilic guidewire can be used to cross the occluded segment through a catheter which can pull/push the wire and catheter through the occlusion. Typically a stiff one piece 5 F AngiOptic Sos Omni™ or similar recurve selective catheter is used; however, great care should be taken given the significant risk of vessel or collecting system perforation with the stiffer hydrophilic guidewire [40]. As soon as the occlusion is crossed, a control

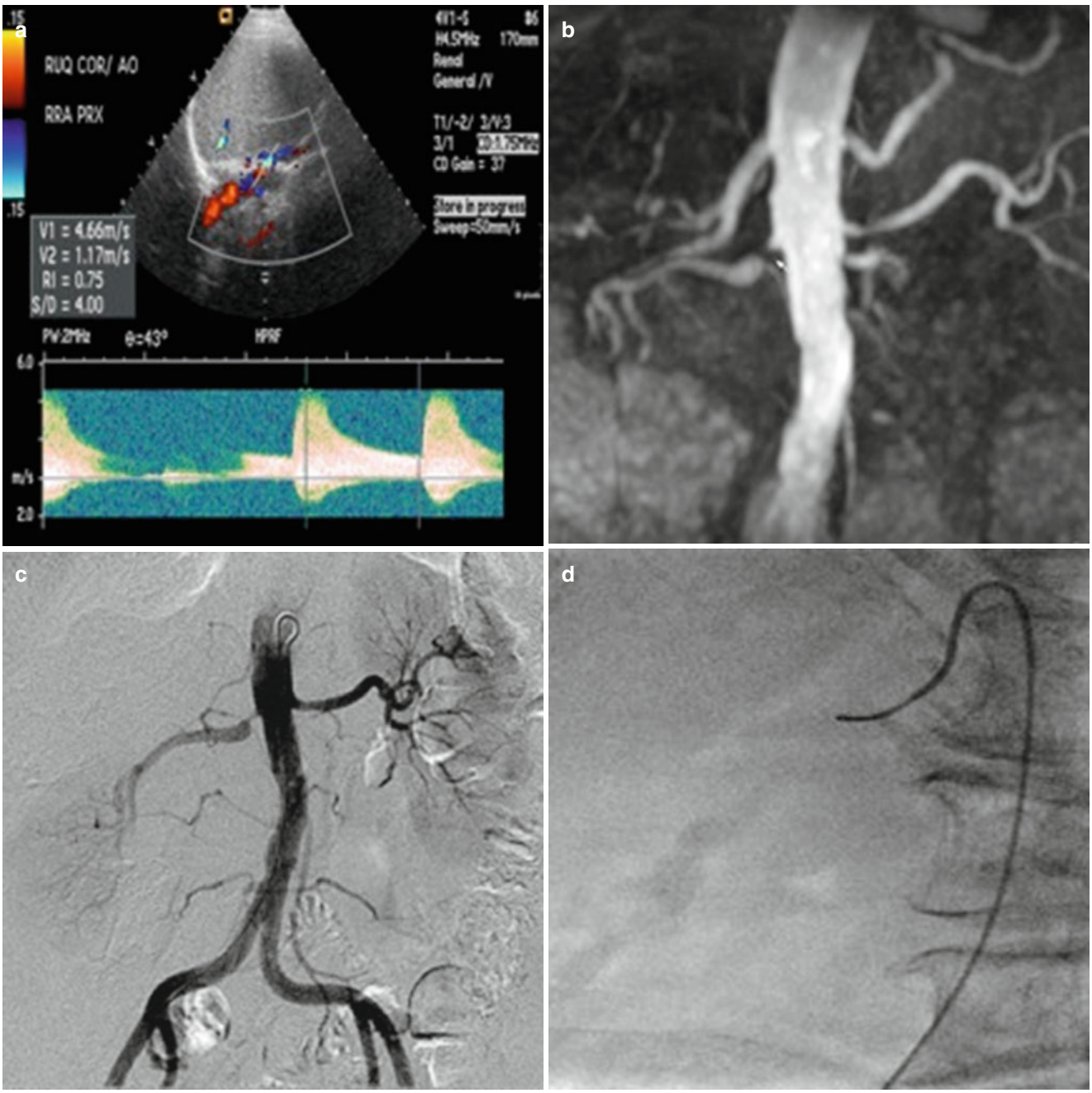

Fig. 23.5 A 77-year-old female with refractory hypertension on ACEI and two additional antihypertensives with elevated plasma renin activity. (**a**) Ultrasound demonstrates elevated peak systolic velocity and elevated arterial resistive indices suggestive of renal artery stenosis. (**b**) MRA demonstrates severe stenosis at origin of right renal artery with post-stenotic dilatation. (**c**-**j**) A 4 French Sos Omni 2 catheter and a Bentson wire were used to select the right renal artery. Pressure measurements demonstrated a 49 mmHg mean arterial trans-stenotic pressure gradient. The Bentson was exchanged for a 0.018″ Ironman, and the Sos Omni 2 Catheter and sheath were exchanged for a long 5 French Ansel Sheath. A 5 mm × 15 mm Express Tm SD Renal and Biliary Pre-mounted (Monorail) Stent System (Boston Scientific, Marlborough, MA) was successfully placed in the proximal right renal artery

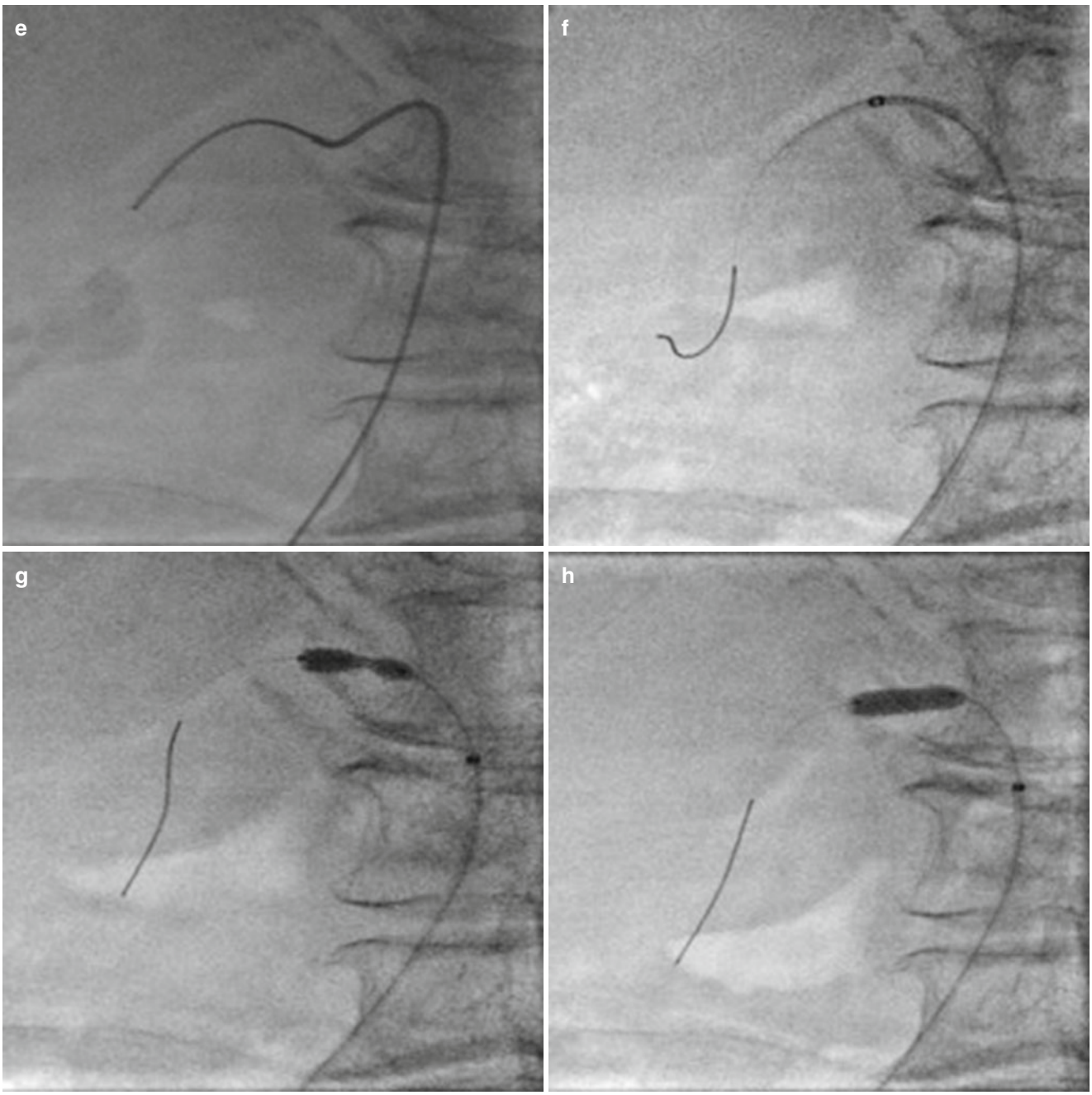

Fig. 23.5 (continued)

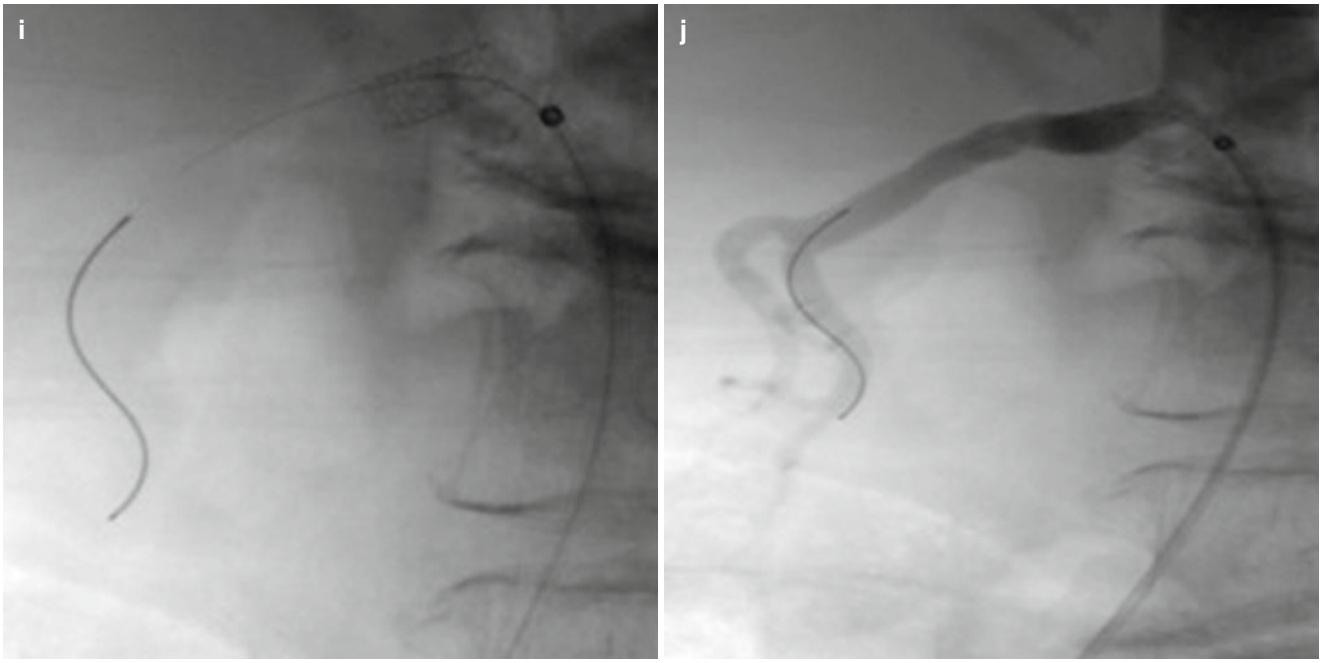

Fig. 23.5 (continued)

arteriogram through the sheath must be performed to ascertain that the wire tip is in the distal lumen. If the recanalization resulted in extravascular passage, the procedure should be stopped and the vessel observed for bleeding for at least an hour and even embolized if necessary. If the recanalization was successful, the hydrophilic guidewire should be immediately exchanged with a non-hydrophilic soft platinum-tipped stiffer shaft wire and stenting continued.

Transplant Renal Artery Stenosis

Transplant renal artery stenosis is the most frequent vascular complication in patients with post renal transplantation. The most common time period in which transplant renal artery stenosis presents is at between 3 months and 2 years [41]. Renal revascularization is the treatment after medication regimen has failed and there is suspicion of renal artery stenosis based on a screening exam such as duplex ultrasound and/or magnetic resonance angiogram (Fig. 23.6). In cases with recurrent stenoses or an ostial stenosis, such as at an end-to-side renal to iliac artery anastomosis, stenting is recommended. Angioplasty, alone, usually in an end-to-end renal to hypogastric artery anastomosis – a procedure now rarely performed – has a reported success rate of greater than 80 % [42]. Stent placement has also been reported to have high clinical success, including significant early improvement of hypertension and creatinine, with minimal complications [43]. Eighty-eight to one hundred percent clinical success rates have been reported based on clinical outcome such as hypertension control, reduction in antihypertensive drugs, and graft function and preservation [44, 45].

Diagnostic transplant renal arteriography is usually performed via a femoral artery approach. A contralateral approach is recommended in patients with an end-to-end anastomosis to the internal iliac artery and ipsilateral in patient with end-to-side anastomosis to the external iliac artery [46]. The angle of anastomosis is also important to assess in the pre-procedural phase. A nonselective ipsilateral iliac angiogram is performed to exclude an inflow/pre-anastomotic problem. The transplant renal artery is then selected and the stenosis crossed using a recurved catheter and a soft-tipped atraumatic wire. Pressure measurements should be obtained prior to treatment. If an arterial mean gradient greater than 10 % is present, renal endovascular revascularization is recommended [45].

Pediatric Patients

Secondary hypertension due to renovascular hypertension is the cause of about 3.0–8.5 % of patients with pediatric hypertension. The most common cause of renovascular hypertension in the pediatric population is fibromuscular dysplasia; however, other causes include Takayasu's arteritis and neurofibromatosis I; rarer causes include William's syndrome, Marfan's syndrome, congenital rubella syndrome, and Kawasaki's and Crohn's disease [47].

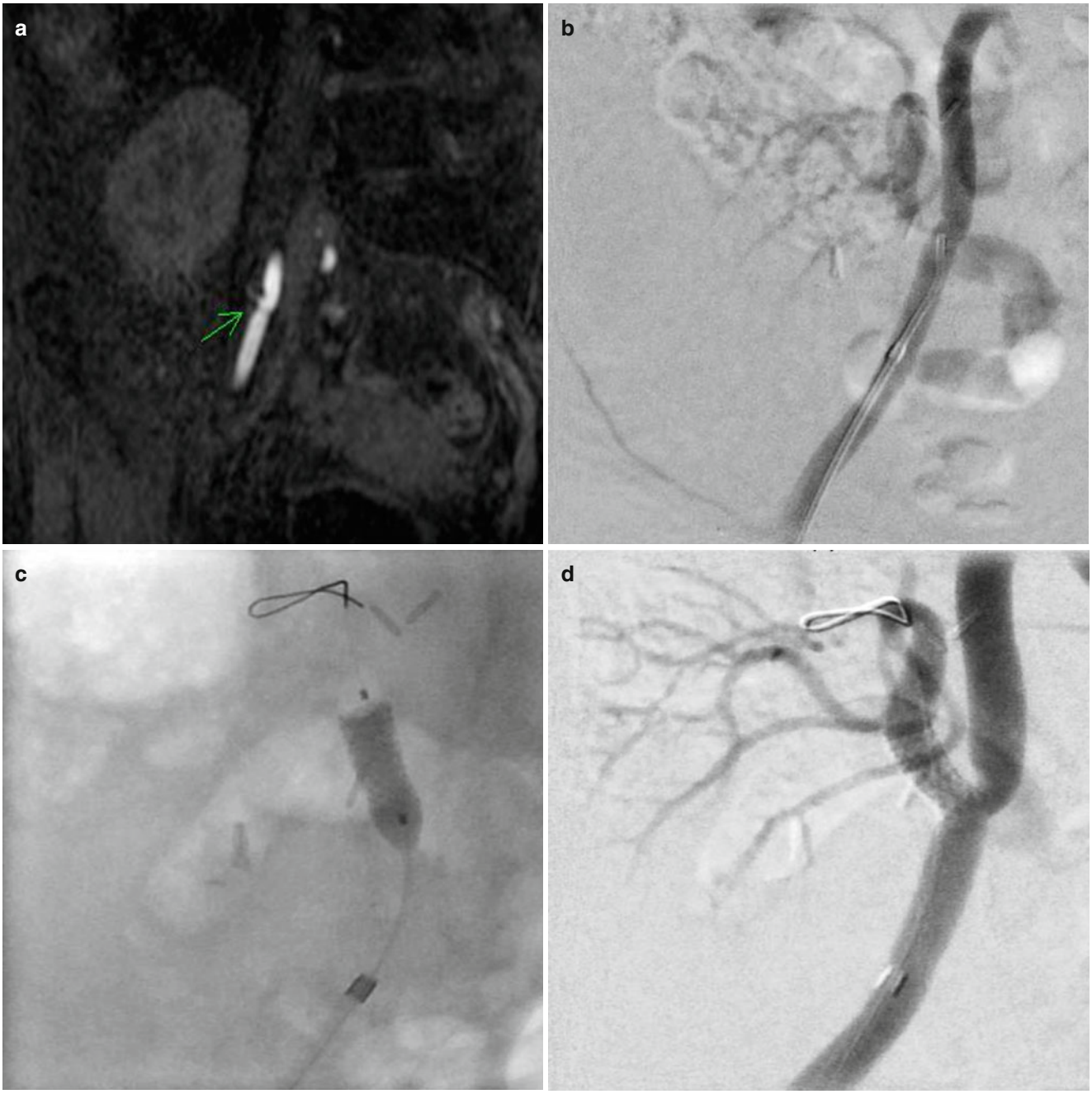

Fig. 23.6 A 43-year-old female status post kidney transplant with elevated creatinine and worsening hypertension 4 months post-transplant. Ultrasound and MR angiography findings were suggestive of stenosis of the transplant renal artery. The transplanted kidney renal artery anastomosis is to the right external iliac artery. Severe stenosis of the transplant artery at the anastomosis with post-stenotic dilatation (**a**) with successful placement of a 6 mm × 14 mm Express SD balloon-expandable stent (**b**, **c**). Post angiography shows no residual transplant renal artery stenosis (**d**) (Courtesy of Dr. Darren Schneider, Weill Cornell Medical College)

Medical therapy should be the first line in management for pediatric patients with RAS to allow for maximal body growth before any endovascular or surgical intervention. If medical therapy fails and signs of end organ damage are present, renal revascularization, specifically angioplasty, should be considered [48]. Renal artery stent placement should only be used in pediatric patients who develop flow-limiting dissection after angioplasty, or focal arterial rupture [49]. Children with mid-aortic syndrome with hypoplastic proximal renal arteries do not respond to angioplasty! Vigorous attempts at angioplasty should not be made since rupture may result.

Tips

Fluoroscopy Views

Appropriate views should be obtained to best visualize the renal arteries, including their origin. The right renal usually artery arises approximately 30° ventral, and the left renal artery arises slightly dorsal to the "equator" of the aorta. Given these anatomic considerations, optimal obliquities should be obtained (Fig. 23.7). For example, a 30° left anterior oblique for the right renal artery should be obtained to optimize a profile view of the right renal artery ostium. If there is clinical suspicion for fibromuscular dysplasia, at least two oblique views of the bilateral renal arteries should be obtained [7]. Rarely, additional caudo-cranial and cranio-caudal angulations may need to clarify the anatomy.

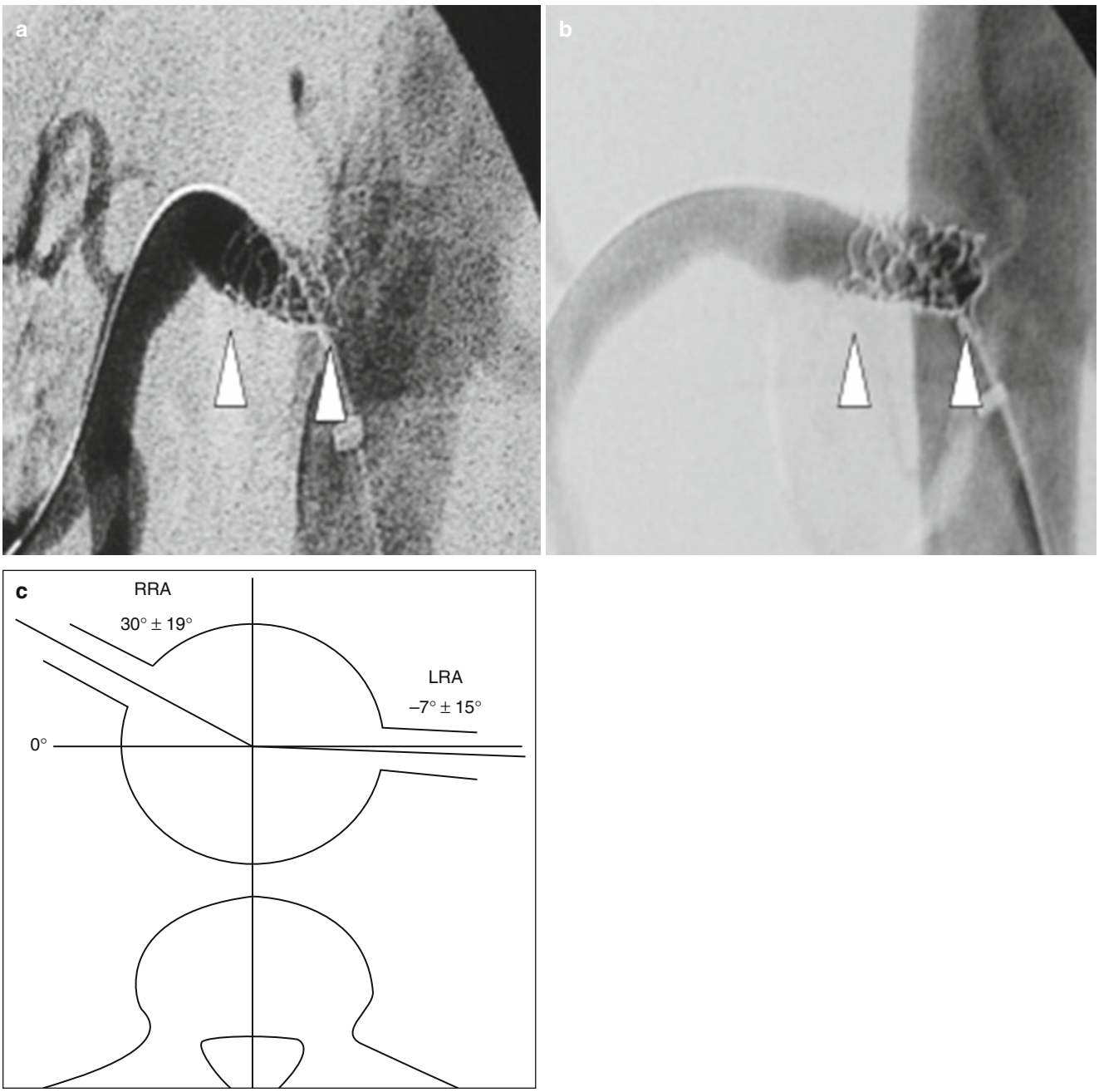

Fig. 23.7 Importance of the correct obliquity during stent placement. (**a**) 30° left anterior oblique projection demonstrates an appropriately placed right renal artery stent with a few millimeters projecting into the aorta. (**b**) 40° left anterior oblique projection demonstrates more than half the stent extending into the aorta. If the stent was placed in this projection, the stent would have been malpositioned, and the ostium would not have been covered. (**c**) Orientation of the right and left renal arteries along an axial plane. The right renal artery origin is 30° ventral, and the left renal artery is 7° dorsal to the mid-coronal plain of the aorta

Avoidance of Contrast-Induced Nephropathy

Iodinated contrast-induced nephropathy or acute renal failure is reported to occur in 1–6 % of cases and in up to 40–50 % of diabetics with already compromised renal function [50–52]. While iodinated contrast is required for at least some portions of the exam, carbon dioxide, or gadolinium can be used as a non- or less nephrotoxic contrast agent. In addition, N-acetylcysteine can be used as a nephroprotective agent in preventing contrast-induced nephropathy in high-risk individuals. Although its efficacy has been questioned, given the potential benefit, low likelihood of adverse effects, and low cost, its use is recommended in these cases [50–52]. Pretreatment hydration with saline and bicarb is the most well documented and useful to prevent or minimize nephrotoxicity [50, 53]. The use of iodinated contrast material is a limitation in patients with renal failure and in patients with a contrast allergy.

The practice of iodinated contrast-sparing techniques during procedures is the most effective way to reduce the risk of contrast-induced nephropathy. The total amount of iodinated contrast medium should be limited. The nephrotoxicity of all iodinated contrast media, including low-osmolar ones, is related to the total volume and concentration of iodinated particle. Renal revascularization procedures can be performed with the use of 30–50 % (or half strength) contrast medium (150 mg I/mL). In addition, catheter techniques during certain parts of the procedure, such as the "Sos Flick" (described below) technique during selection of the renal arteries, can result in significant reduction of contrast volume for the entire procedure.

Patients with Atherosclerotic Renal Artery Stenosis (aRAS)

A significant concern, when working within a diseased aorta in patients with aRAS, is the risk of micro-cholesterol embolization and shifting of plaque during catheter manipulation [54]. Multiple techniques exist which can potentially reduce the risk of cholesterol embolization, including the growing use of embolization protection devices (EPD).

"No Touch" Technique

A variation of the standard technique is the "no touch" technique. This technique is used in patients with extensive atherosclerotic plaque within the aorta or patients with an ectatic aorta. The goal of the "no touch" technique is to prevent dislodgement of macroscopic or microscopic plaque which can then result in embolization (Fig. 23.8). The guiding catheter is positioned just below the renal artery orifice. Two wires are advanced through the sheath. The first wire is a 0.035 in. wire which is advanced into the suprarenal aorta and

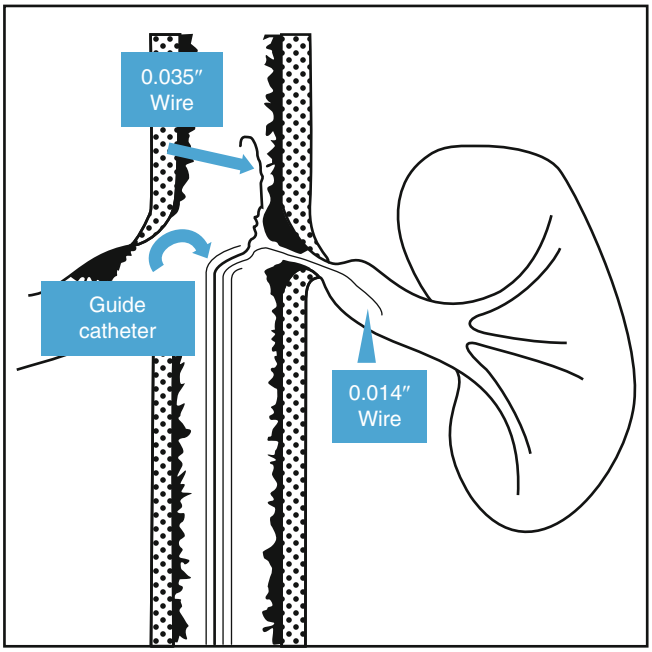

Fig. 23.8 "No touch" technique. A 0.035″ guidewire is used to deflect the guide catheter away from the aortic wall while a 0.014 guidewire is advanced through the aRAS

"deflects" the catheter away from the aortic wall preventing dislodgement of atherosclerotic plaque from the wall. A second 0.018 or 0.014 in. wire is advanced through the sheath and used to select the renal artery [37].

The "Sos Flick" Technique

The "Sos Flick" technique minimizes the extent of catheter manipulations and minimizes contact of the diagnostic catheter with the diseased aortic wall [7]. An additional and important advantage is that this technique significantly reduces the amount of contrast used during test "puff" injections when attempting to engage the renal artery origin with a catheter or wire (Fig. 23.9). The "Sos Flick" technique uses a Sos Omni Selective™ (Angiodynamics, Queensbury, NY). After the Sos Omni Selective catheter tip is reformed, a soft atraumatic guidewire is withdrawn until approximately 1–2 cm of the wire extends from the catheter tip. The catheter, with the wire tip out, is slowly advanced cranially with the catheter tip pointing laterally in the plane of the origin of the renal artery. Once the wire engages into the stenotic origin of the renal artery, a characteristic lateral "flick" is noted. The wire and the catheter can then gently be advanced across the stenosis.

Use of Embolic Protection Devices and Platelet Inhibitors

Micro-cholesterol embolization is a serious and potentially irreversible risk of all renal artery interventions. The risk of atheroembolism during a procedure is often underestimated

and has been thought to be a significant contributor to renal failure after renal artery stenting [55]. The risk for embolization is present during all portions of renal artery revascularization including prior to selection of the renal artery within the aorta, as well as during catheter manipulations within the renal artery. Embolic protection devices (EPD) have gained popularity over the last couple of years, for the theoretical advantage of preventing showering emboli from lodging distally and occluding branches [56].

None of the currently available EPDs has been specifically designed for the renal artery. In most cases, EPDs have been approved for carotid artery stenting. Nevertheless, the popularity of EPDs in renal arteries has increased, although no level 1 evidence currently exists to support its use in this specific setting.

A major limitation of current EPDs is the pore size of 100 μm of typical filter designs. During typical catheter manipulations in aRAS, millions of emboli smaller than 10 μm were

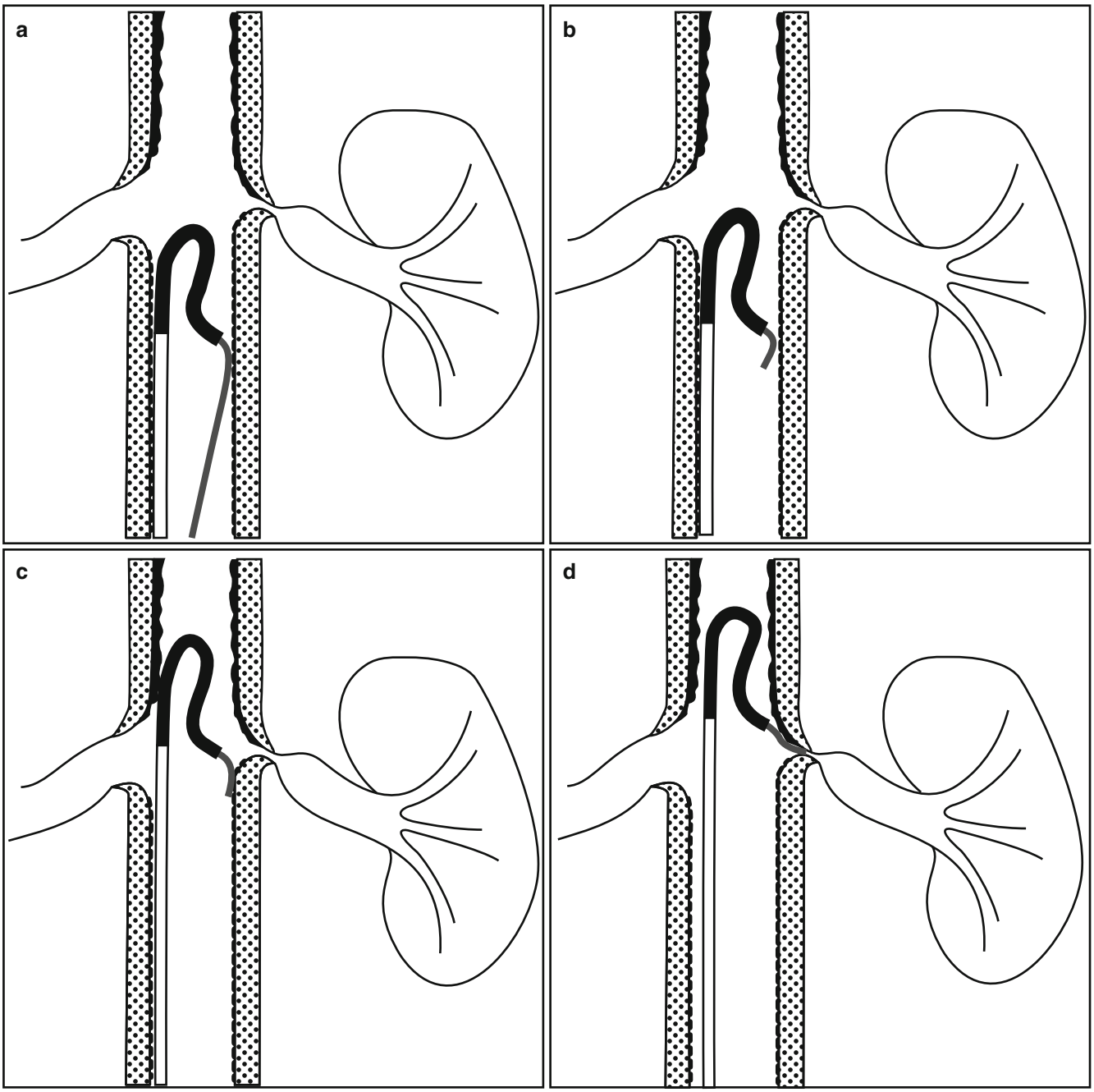

Fig. 23.9 (**a**–**e**) "Sos Flick" technique. As a Sos Omni Selective^{Tm} recurve-type catheter and small amount of wire are advanced cranially, the wire "flicks" laterally into the stenotic renal artery

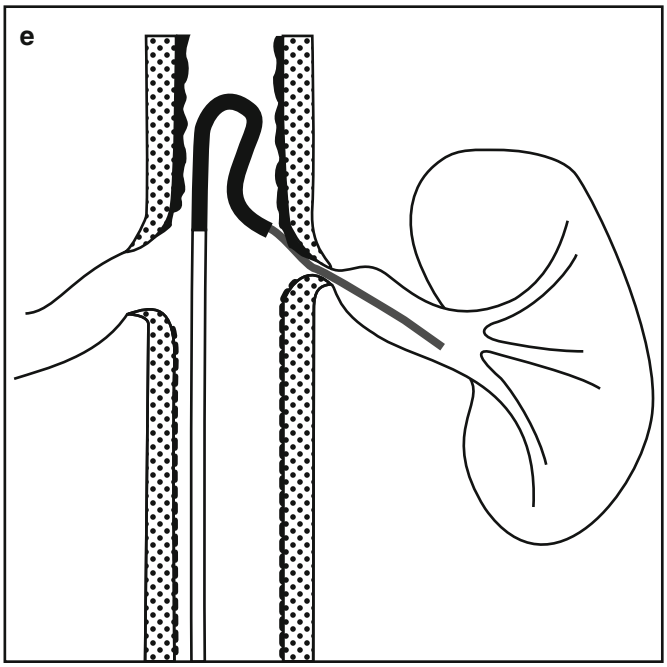

Fig. 23.9 (continued)

produced; however, only a few particles 1 mm or larger were produced. Additional limitations include a guiding catheter or sheath which must be advanced across the renal lesion and limits the possibility to deploy stents using the "bareback" technique. The bulkiness of the EPD may also add to potential micro-cholesterol embolization distal to a stenosis while crossing a lesion [57]. Along with embolization, the technique also poses a risk for dissection and/or renal artery spasm. Finally, actually deploying a filter generally requires a relatively long "landing zone" distal to the stenosis within the renal artery [58]. The main renal artery is approximately 40 mm long in adults, but early branching occurs in 20–30 % of cases with the current combined length between filter and balloon stent systems being between 30 and 35 mm.

Holden et al. in 2003 and 2006 demonstrated the potential benefits of EPDs including the most significant benefit of preserving function and preventing deterioration post endovascular revascularization for aRAS [59]. The study evaluated 63 patients, and at 6 months follow-up, the renal function either improved or stabilized in 97 % of patients. Another report described captured debris within 80 % of procedures with filter-type embolic protection device with 99 % stabilization or improvement of renal function noted 2 years after stenting [55, 56]. The role of glycoprotein IIB/IIIa inhibitors/antiplatelet therapy such as abciximab has also been used extensively with EPDs. The Prospective Randomized Study Comparing Renal Artery Stenting (RESIST) with or Without Distal Protection trial evaluated the role of an EPD and abciximab. Interestingly, the RESIST compared four groups including patients who had renal artery stenting alone, stenting with an EPD only, stenting with abciximab only, and stenting with the combination of the EPD and abciximab. The only groups shown to have a decrease in the decline of renal function/glomerular filtration rates were the patients with the combination of EPD and abciximab suggesting a synergistic effect between the two [55, 56]. The potential advantages of EPDs for renal artery revascularization may become routine, if they can show level 1 scientific evidence.

Patients with Fibromuscular Dysplasia (FMD)

Multiple selective oblique views of the renal artery may be necessary to fully characterize the extent of renal artery stenosis in FMD patients. Patients with the medial form of FMD generally respond very well to low-pressure angioplasty alone [60]. Patients with intimal fibroplasia are usually resistant to angioplasty; however, in many cases over the course of several weeks to months, blood pressure improves, and the arteriographic appearance of the lesion becomes normal. After a guidewire is passed across the stenosis, pressure measurements through a microcatheter or a 0.014 pressure-sensing wire is suggested (Fig. 23.10). Pressure measurements may be inaccurate because the passage of a catheter may open the offending flap-like membranes of the beaded stenosis thereby providing a perceived reduction in pressure. Intra-procedural Doppler can also be used to confirm the location and presence of the renal artery stenosis.

After selecting the renal artery, a floppy tipped but stiff shaft guidewire should be used to cross the stenosis. A hydrophilic guidewire is not recommended because they are prone to cause dissection within the beaded stenoses of FMD. The risk of dissection is elevated in these cases, and great care should be taken when attempting to cross a stenosis with any wire. Maneuvers such as having the patient cough or take a deep breath and exhale to change the orientation of the wire tip to the stenosis may be beneficial. Once the stenosis is crossed, a selective arteriogram over the guidewire is recommended, given that the initial location and length of the stenosis may have been changed by the presence of the guidewire. Angioplasty, mostly with low-pressure inflations, should effectively eliminate the beaded stenosis completely. If a stenosis persists, re-dilating with a 1 mm greater balloon diameter can be considered. A completion renal arteriogram is necessary post-angioplasty to ensure complete resolution of the stenosis and to evaluate for any complications.

Treatment of fibromuscular dysplasia can be more challenging than treatment of atherosclerotic renal disease. FMD lesions are not uncommonly located within the distal main renal artery, branch points, and intrarenal branches, and treatment of these areas can be difficult. Percutaneous transluminal renal angioplasty (PTRA) is still the first line of treatment for these locations. In fact, technical outcome has

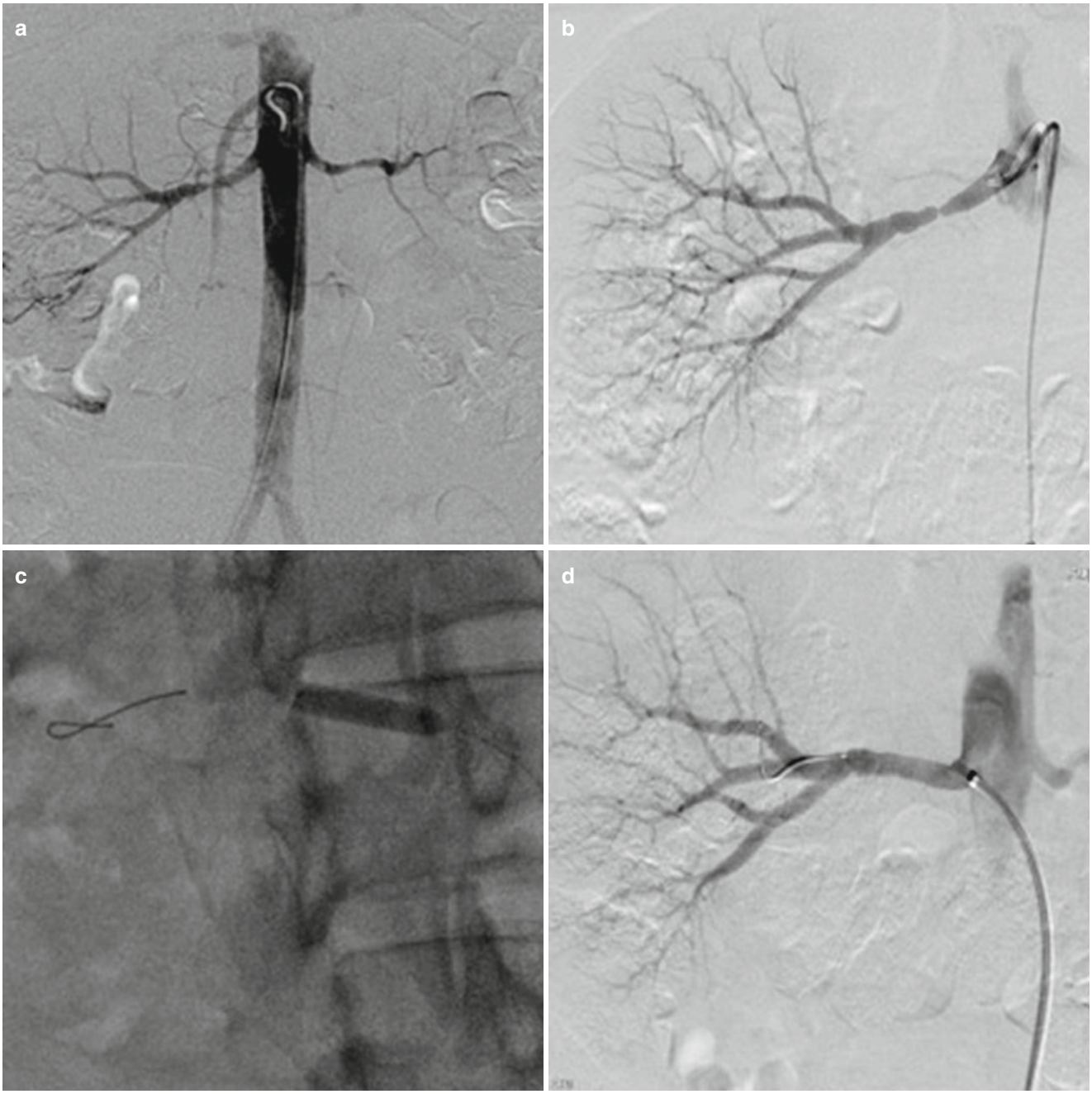

Fig. 23.10 A 34-year-old female patient with refractory hypertension secondary to bilateral fibromuscular dysplasia (**a**) on three antihypertensives prior to treatment. Pressure gradient across stenosis prior to angioplasty measured approximately 100 mmHg for each renal artery. Successful angioplasty performed for both renal arteries with the right shown above (**b**–**d**). Patient was subsequently weaned off of all three antihypertensives

been shown to be successful with PTRA alone with results shown to be similar to those reported for the main renal artery [61]. Smaller balloon systems (0.014–0.018 in. balloon catheter systems) are low in profile, flexible, and tracked better than the larger systems allowing for use in these intrarenal locations [62].

Rupture of the renal artery during treatment is uncommon and occurs in approximately 2–6 % of cases. Rupture occurs most often in association with complex fibromuscular dysplasia lesions. Initial treatment to stop the leaking is with prolonged balloon treatment. Depending on the size and severity of the rupture, other options for treatment may be required. In some cases, covered stents can be used to exclude the area of rupture. In more severe situations, open surgery may be necessary after initial hemostasis is achieved with a balloon [63, 64].

Outcomes

Percutaneous renal revascularization, compared to surgical techniques, is safe, fast, and better tolerated and has long-term patency rates comparable to open bypass [65]. With proper patient selection, revascularization with angioplasty and stenting produces excellent results that have been shown to both reduce systemic blood pressure and preserve or even improve renal function [66–68].

Recently, however, there has been great controversy regarding the benefits of renal artery stenting versus treatment with medical therapy alone. In 2009, the Stent Placement in Patients with Atherosclerotic Renal Artery Stenosis and Impaired Renal Function (STAR) trial compared medical treatment of renal artery stenosis with medical treatment and stent placement in 150 patients across ten European centers. The study concluded that intervention had minimal or no benefit but with high a complication rate. The validity of the conclusions was questionable, however, because the study was underpowered and included many patients with less than 50 % stenosis. In addition, pressure gradients were not used to evaluate the stenoses. Given the poor patient selection, these results should have been expected [69, 70].

The Angioplasty and Stenting for Renal Artery Lesions (ASTRAL) trial in 2010 was a large randomized study to evaluate the effectiveness of catheter-based interventions in patients with "substantial" renal artery stenosis whose physicians were not certain whether the patients should have stenting or medical therapy. ASTRAL randomized 806 patients to renal artery stenting with medical therapy or medical therapy alone. Again, the authors of this study concluded that there was no additional clinical benefit from renal artery stenting over and above medical treatment given the risks for intra-procedural complications. Patient selection, however, was a major flaw. Many patients with less than 70 % stenosis were included in the study, and some with greater than 70 % of stenosis (patients who would have been expected to benefit) were excluded. In addition, visual estimates of stenosis are notoriously unreliable and pressure gradients were not obtained [71]. Finally, there was significant variability of operator experience given that there were 56 participating centers, with only 5 centers enrolling more than 30 patients and 45 centers enrolling 10 or fewer patients [71, 72].

The Cardiovascular Outcomes in Renal Atherosclerotic Lesions (CORAL) trial published in January of 2014 was the largest trial to evaluate catheter-based intervention compared to medical therapy [4]. The trial included 947 patients who were randomized at more than 100 sites, which compared patients who had renal artery stent placement and medical therapy compared to patients with medical therapy alone. The study evaluated clinical events such as mortality, stroke, heart attacks, and progressive kidney disease. CORAL concluded that renal artery stenting, when added to comprehensive, multifactorial medical therapy in patients with renal artery stenosis and hypertension or chronic kidney disease, did not have significant benefit in preventing clinical events.

Again, patient selection was a major flaw. Along with the STAR and ASTRAL studies, the CORAL study did not routinely measure pressure gradients, and thus, the number of patients with a hemodynamically significant aRAS with clearly defined indication for renal artery stenting is not known. Additionally, some patients were not included in the randomized study because they or their physicians thought that they would benefit from stenting.

Early in the study, CORAL authors attempted to correct inadequate criteria for patient selection in the ASTRAL and STAR trials. They proposed to identify patients with clinically and hemodynamically significant renal artery stenosis by the following inclusion characteristics: systolic blood pressure greater than 155 mmHg on at least two antihypertensive medications, stenosis of at least 60 %, and renal artery systolic pressure gradient of greater than 20 mmHg in patients with 60–79 % stenosis. These criteria were dropped or eased early on in the study to increase patient and study site recruitment. Patients with RAS detected by duplex ultrasound, MRA, and CTA were included.

CORAL attempted to address a limitation in previous studies of the great inter-observer and intra-observer variation in interpreting the severity of stenosis of angiographic images by including computerized measurement in the core laboratory. However, because most lesions are ostial, the measurement of pre-stenotic segment is limited or impossible. Comparison is also made to the post-stenotic segment; however, this measurement is also limited because the post-stenotic segment can undergo dilatation or collapse in more severe cases.

The patients included in the CORAL trial had an average stenosis of only 67 % by core lab. In dog studies, hemodynamically significant stenosis was not seen until renal artery constriction by US was greater than 75 %, and in humans, renin secretion was only observed in patients with greater than 80 % stenosis; thus, it is likely that in the CORAL patients with less than 70 % stenosis, stenosis may not have been hemodynamically significant.

Conclusion

Endovascular catheter-based renal revascularization is safe and effective in carefully selected patients who have clinically and hemodynamically significant renal artery disease. Experienced operators should perform renal artery angioplasty and/or stenting using the best available techniques. Clinical signs and symptoms combined with a choice from a plethora of appropriate laboratory tests and noninvasive diagnostic imaging assist in identifying patients who could benefit from the intervention.

Ultimately, confirmation with an elevated trans-stenotic arterial pressure gradient should direct whether or not to proceed with endovascular treatment. Despite the recent large negative retrospective trials discouraging the use of endovascular revascularization, appropriately selected patient's endovascular revascularization can prevent progression of renal failure and control secondary hypertension and ultimately preserve kidneys.

References

1. Fatica RA, Port FK, Young EW. Incidence trends and mortality in end-stage renal disease attributed to renovascular disease in the United States. Am J Kidney Dis. 2001;37(6):1184.
2. Takumi T, Mathew V, Barsness GW, et al. The association between renal atherosclerotic plaque characteristics and renal function before and after renal artery intervention. Mayo Clin Proc. 2011;86:1165–72.
3. White CJ. Catheter based therapy for atherosclerotic renal artery stenosis. Circulation. 2006;113:1464–73.
4. Cooper CJ, Murphy TP, Cutlip DE, et al. Stenting and Medical therapy for atherosclerotic renal artery stenosis. N Engl J Med. 2014;370:13–22.
5. ASTRAL Investigators, Wheatley K, Ives N, Gray R, et al. Revascularization versus medical therapy for renal-artery stenosis. N Engl J Med. 2009;361:1953–62.
6. Cherry DK, Hing E, Woodwell DA, et al. National ambulatory medical care survey: 2006 summary. Hyatts- ville, MD: National Health Statistics; 2006.
7. Trost D, Sos T. Renal artery angioplasty and stents. Handbook of interventional radiologic procedures. 2010;20:205–18.
8. Fields LE, Burt VL, Cutler JA, Hughes J, Roccella EJ, Sorlie P. The burden of adult hypertension in the United States 1999 to 2000: a rising tide. Hypertension. 2004;44:398–404.
9. Hirsch AT, et al. ACC/AHA guidelines for the management of patients with peripheral arterial disease (lower extremity, renal, mesenteric, and abdominal aortic): a collaborative report from the American Associations for Vascular Surgery/Society for Vascular Surgery, Society for Cardiovascular Angiography and Interventions, Society for Vascular Medicine and Biology, Society of Interventional Radiology, and the ACC/AHA Task Force on Practice Guidelines (writing committee to develop guidelines for the management of patients with peripheral arterial disease) – summary of recommendations. J Vasc Intervent Radiol. 2006;17(9):1383–97.
10. Martin LG, et al. Quality improvement guidelines for angiography, angioplasty, and stent placement for the diagnosis and treatment of renal artery stenosis in adults. J Vasc Intervent Radiol. 2010;21(4):421–30.
11. Anderson JL, et al. Management of patients with peripheral artery disease (compilation of 2005 and 2011 ACCF/AHA guideline recommendations)a report of the American College of Cardiology Foundation/American Heart Association Task Force on practice guidelines. J Am Coll Cardiol. 2013;61(14):1555–70.
12. Amis Jr ES, et al. Radiologic investigation of patients with renovascular hypertension. American College of Radiology. ACR appropriateness criteria. Radiology. 2000;215(Suppl):63–70.
13. Zierler RE. Is duplex scanning the best screening test for renal artery stenosis? Semin Vasc Surg. 2001;14(3):177–85.
14. Sfakianakis GN, et al. Single-dose captopril scintigraphy in the diagnosis of renovascular hypertension. J Nucl Med. 1987;28(9):1383–92.
15. Urban BA, et al. Three dimensional volume rendered CT angiography of the renal arteries and veins: normal anatomy, variants, and clinical applications. Radiographics. 2001;21(2):373–86.
16. Rountas C, et al. Imaging modalities for renal artery stenosis in suspected renovascular hypertension: prospective intraindividual comparison of color Doppler US, CT angiography, GD-enhanced MR angiography, and digital substraction angiography. Ren Fail. 2007;29(3):295–302.
17. Vasbinder GB, et al. Diagnostic tests for renal artery stenosis in patients suspected of having renovascular hypertension: a meta-analysis. Ann Intern Med. 2001;135(6):401–11.
18. Vasbinder GB, et al. Accuracy of computed tomographic angiography and magnetic resonance angiography for diagnosing renal artery stenosis. Ann Intern Med. 2004;141(9):674–82.
19. Schoenberg SO, et al. Diagnosis of renal artery stenosis with magnetic resonance angiography: update 2003. Nephrol Dial Transplant. 2003;18(7):1252–6.
20. Fain SB, et al. High-spatial-resolution contrast-enhanced MR angiography of the renal arteries: a prospective comparison with digital subtraction angiography. Radiology. 2001;218(2):481–90.
21. Tan KT, et al. Magnetic resonance angiography for the diagnosis of renal artery stenosis: a meta-analysis. Clin Radiol. 2002;57(7):617–24.
22. Notohamiprodjo M, Reiser MF, Sourbron SP. Diffusion and perfusion of the kidney. Eur J Radiol. 2010;76(3):337–47.
23. Kim D, et al. Renal artery imaging: a prospective comparison of intra-arterial digital subtraction angiography with conventional angiography. Angiology. 1991;42(5):345–57.
24. Imanishi M, Akabane S, Takamiya M, et al. Critical degree of renal arterial stenosis that causes hypertension in dogs. Angiology. 1992;43:833–42.
25. Simon G. What is critical renal artery stenosis? Am J Hypertens. 2000;13:1189–93.
26. Leesar MA, Varma J, Shapira A, et al. Prediction of hypertension improvement after stenting of renal artery stenosis: comparative accuracy of translesional pressure gradients, intravascular ultrasound, and angiography. J Am Coll Cardiol. 2009;53:2363–71.
27. De Bruyne B, Manoharan G, Pijls NH, et al. Assessment of renal artery stenosis severity by pressure gradient measurements. J Am Coll Cardiol. 2006;48:1851–5.
28. Mangiacapra F, Trana C, Sarno G, et al. Translesional pressure gradients to predict blood pressure response after renal artery stenting in patients with renovascular hypertension. Circ Cardiovasc Interv. 2010;3:537–42.
29. Strong CG, Hunt JC, Sheps SG, et al. Renal venous renin activity: enhancement of sensitivity of lateralization by sodium depletion. Am J Cardiol. 1971;27:602–11.
30. Vaughan ED, Buhler FR, Laragh JH, et al. Renovascular hypertension: renin measurements to indicate hypersecretion and contralateral suppression, estimate renal plasma flow, and score for surgical curability. Am J Med. 1973;55:402–14.
31. Foster JH, Maxwell MH, Franklin SS, et al. Renovascular occlusive disease: results of operative treatment. JAMA. 1975;231:1043–8.
32. Canzanello VJ, Millan VG, Spiegel JE, et al. Percutaneous transluminal renal angioplasty in management of atherosclerotic renovascular hypertension: results in 100 patients. Hypertension. 1989;13(2):163–72.
33. Burket MW, Cooper CJ, Kennedy DJ, et al. Renal artery angioplasty and stent placement: predictors of a favorable outcome. Am Heart J. 2000;139(1 Pt 1):64–71.
34. Sos TA. Upper extremity access for renal artery stenting: radial, brachial and axillary access: how to do them safely and pitfalls to avoid. J Cardiovasc Surg. 2010;51:741–6.
35. Colyer Jr WR, et al. Utility of a 0.014" pressure-sensing guidewire to assess renal artery translesional systolic pressure gradients. Catheter Cardiovasc Interv. 2003;59(3):372–7.
36. Eldrup-Jorgensen J, Harvey HR, Sampson LN, Amberson SM, Bredenberg CE. Should percutaneous transluminal renal artery angioplasty be applied to ostial renal artery atherosclerosis? J Vasc Surg. 1995;21:909–14, 914–5.

37. Funaki B. Renal ostial angioplasty and stenting. The routine procedure. Semin Intervent Radiol. 2009;26:74–81.
38. Lederman RJ, Mendelsohn FO, Santos R, Phillips HR, Stack RS, Crowley JJ. Primary renal artery stenting: characteristics and outcomes after 363 procedures. Am Heart J. 2001;142:314–23.
39. Rehan A, Almanaseer Y, Desai DM, Ali A, et al. Complete resolution of acute renal failure after left renal artery angioplasty and stent placement for total renal artery occlusion. Cardiology. 2007; 108:51–4.
40. Laird JR, Rundback J, Zierler RE, et al. Safety and efficacy of renal artery stenting following suboptimal renal angioplasty for de novo and restenotic ostial lesions: results from a nonrandomized, prospective multicenter registry. J Vasc Interv Radiol. 2010;21(5): 627–37.
41. Bruno S, Remuzzi G, Ruggenenti P. Transplant renal stenosis. J Am Soc Nephrol. 2004;15:134.
42. Fervenza RF, Lafayette RA, Alfrey EJ, Peterson J. Renal artery stenosis in kidney transplantation. Am J Kidney Dis. 1998;31:142–8.
43. Beecroft JR, Rajan DK, Clark T, Robinette M, Stavropoulos SW. Transplant renal artery stenosis: outcome after percutaneous intervention. J Vasc Interv Radiol. 2004;15:1407–13.
44. Chow K, Szeto CC, Lee PSF, et al. Revascularization for post transplant renal artery stenosis. Nephrology. 2007;12:406–12.
45. Seratnahaei A, Shah A, Bodiwala K, Mukherjee D. Management of transplant renal artery stenosis. Angiology. 2010;62:219–24.
46. Rundback JH, Weintraub JL. Renovascular interventions. Image guided interventions. 2014;58:404–10.
47. Daniels SR, Loggie JM, McEnery PT, Towbin RB. Clinical spectrum of intrinsic renovascular hypertension in children. Pediatrics. 1987;19:698–704.
48. Tullus K, Brennan E, Hamilton G, Lord R, McLaren CA, Marks SD, Roebuck DJ. Renovascular hypertension in children. Lancet. 2008;19:1453–63.
49. Radanovic B, Cacic Z, Perkov D, Smiljanic R, Coric SR, Ilakovac K. Endovascular therapy of renovascular hypertension in children: single center analysis. Pediatr Surg. 2009;19(3):135–40.
50. Waybill MM, Waybill PN. Contrast media-induced nephrotoxicity: identification of patients at risk and algorithms for prevention. J Vasc Interv Radiol. 2001;12(1):3–9.
51. Kerns SR, Hawkins IF. Carbon dioxide administration angiography: expanding applications and technical evolution. AJR. 1995;164:735–41.
52. Lautin EM, Freeman NJ, Schoenfeld AH, et al. Radiocontrast-associated renal dysfunction: incidence and risk factors. AJR Am J Roentgenol. 1991;157(1):49–58.
53. Merten GJ, Burgess WP, Gray LV, et al. Prevention of contrast-induced nephropathy with sodium bicarbonate: a randomized controlled trial. JAMA. 2004;291(19):2328–34.
54. Zeller T, Frank U, Müller C, et al. Predictors of improved renal function after percutaneous stent-supported angioplasty of severe atherosclerotic ostial renal artery stenosis. Circulation. 2003;108: 2244–9.
55. Edwards MS, Corriere MA, Craven TE, et al. Atheroembolism during percutaneous renal revascularization. J Vasc Surg. 2007;46: 55–61.
56. Edwards MS, Craven BL, Stafford J, et al. Distal embolic protection during renal artery angioplasty and stenting. J Vasc Surg. 2006;44:128–35.
57. Kawarda O, Yokoi Y, Takemoto K. The characteristics of dissemination of embolic materials during renal artery stenting. Catheter Cardiovasc Interv. 2007;70:784–8.
58. Talenfeld AD, Schope RB, Alper HJ, Cohen E. MDCT angiography of the renal arteries in patients with atherosclerotic renal artery stenosis: implications for renal artery stenting with distal protection. Am J Roentgenol. 2007;188(6):1652–8.
59. Arthurs Z, Starnes B, Cuadrado D, et al. Renal artery stenting slows the rate of renal function decline. J Vasc Surg. 2007;45:726–31.
60. Chryssant SS, et al. Treatment of hypertension in patients with renal artery stenosis due to fibromuscular dysplasia of the renal arteries. Diagn Ther. 2014;4(1):36–43.
61. Cluzel P, Raynaud A, Beyssen B, Pagny JY, Gaux JC. Stenoses of renal branch arteries in fibromuscular dysplasia: results of percutaneous transluminal angioplasty. Radiology. 1994;193(1):227–32.
62. Meuse MA, Turba UC, Sabri SS, Park AW, Saad WEA, Angle JF, Matsumoto AH. Treatment of renal artery fibromuscular dysplasia. Tech Vasc Interv Radiol. 2010;13(2):126–33.
63. Bonelli FS, McKusick MA, Textor SC, et al. Renal artery angioplasty: technical results and clinical outcome in 320 patients. Mayo Clin Proc. 1995;70(11):1041–52.
64. Gottsater A, Lindblad B. Optimal management of renal artery fibromuscular dysplasia. Ther Clin Risk Manag. 2014;10:583–95.
65. Tegtmeyer CJ, Kellum CD, Ayers C. Percutaneous transluminal angioplasty of the renal artery. Results and long-term follow-up. Radiology. 1984;153(1):77–84.
66. Sos TA, et al. Percutaneous transluminal renal angioplasty in renovascular hypertension due to atheroma or fibromuscular dysplasia. N Engl J Med. 1983;309(5):274–9.
67. Miller GA, et al. Percutaneous transluminal angioplasty vs. surgery for renovascular hypertension. AJR Am J Roentgenol. 1985; 144(3):447–50.
68. Sos TA. Angioplasty for the treatment of azotemia and renovascular hypertension in atherosclerotic renal artery disease. Circulation. 1991;83(2 Suppl):I162–6.
69. White CJ. The need for randomized trials to prove the safety and efficacy of parachutes, bulletproof vests, and percutaneous renal intervention. Mayo Clin Proc. 2011;86(7):603–5.
70. White CJ, Olin JW. Diagnosis and management of atherosclerotic renal artery stenosis: improving patient selection and outcomes. Nat Clin Pract Cardiovasc Med. 2009;6(3):176–90.
71. Mann SJ, Sos TA. Misleading results of randomized trials: the example of renal artery stenting. J Clin Hypertens (Greenwich). 2010;12(1):1–2.
72. White CJ. Kiss my astral: one seriously flawed study of renal stenting after another. Catheter Cardiovasc Interv. 2010;75(2):305–7.

Part IV

Bladder/Ureter

Hemorrhagic Cystitis

24

Vidhush K. Yarlagadda, Jeremy Cash Horn,
Aaron M. Fischman, and Jeffrey W. Nix

Hemorrhagic cystitis (HC) is a symptom complex that refers to bleeding caused by an irritation of the bladder mucosa that can be of insidious or rapid onset. Patients present with some degree of gross hematuria as well as lower urinary tract symptoms (LUTS); however, the range to which these symptoms manifest is wide with varying degrees of resistance to treatment depending on the underlying etiology. A proposed underlying mechanism is urothelial cell irritation with subsequent mucosal edema followed by cell death. The bladder muscle and vasculature are exposed to urine, which contains urokinase, a serine protease with fibrinolytic activity [1]. The resultant bleeding can be difficult to control and begins to explain why this condition can be so difficult to treat.

Categorizing and Grading HC

HC can be categorized into two broad groups: infectious and noninfectious. Infectious HC is uncommon; however, when present, it is typically viral in nature and is often seen in immunocompromised patients. Bacterial, fungal, and parasitic infections are also known to cause HC, though the incidence is significantly less. Noninfectious HC can be further divided into chemical, radiation, and interstitial cystitis (IC). It is the severe manifestations of all of the above etiologies for cystitis that can lead to HC. HC is commonly stratified based on severity of symptoms [2] (Table 24.1). Grade I and II HC can be managed conservatively with hydration, whereas grades III and IV require urologic intervention. Hemorrhagic cystitis is also characterized into acute and chronic phases, though there can be significant overlap with recurrent acute flare-ups superimposed on a bladder with chronic changes. In some cases, cessation of the offending agent leads to resolution of symptoms with little or no residual effect.

Infectious Etiology

Infectious HC is most commonly seen in immunocompromised patients, especially those that are undergoing bone marrow or hematopoietic stem cell transplant. In fact, between 10 and 25 % of bone marrow transplant (BMT) patients suffer from HC [3]. The majority is seen with viral-mediated HC; however, one can see other forms of infectious HC as discussed below.

Viral-Mediated HC

The immunosuppression in transplant patients increases the risk of opportunistic infection, and polyoma viruses (BK and JC virus) along with adenoviruses are the most common causative agent of HC in this population. Infection with polyoma virus is opportunistic, as up to 80 % of all adults are colonized. The virus infects many different cell types including urothelial cells of the renal pelvis, ureters, and bladder [4–6]. In immunocompetent hosts, they lie dormant following infection – viral reactivation requires a combination of predisposition to reactivation, target organ damage, and host immune dysfunction.

Table 24.1 Hemorrhagic cystitis grade by symptoms

Grade	Symptoms
I	LUTS without gross hematuria
II	LUTS + gross hematuria
III	LUTS + gross hematuria + clots
IV	LUTS + gross hematuria + clots causing urinary retention

V.K. Yarlagadda, MD • A.M. Fischman, MD • J.W. Nix, MD (✉)
Department of Urology, University of Alabama at Birmingham, Birmingham, AL, USA
e-mail: jnix@uabmc.edu

J.C. Horn, MD
Division of Interventional Radiology, Department of Radiology, Mount Sinai Hospital, New York, NY, USA

A.R. Rastinehad, D.N. Siegel (eds.), *Interventional Urology*, DOI 10.1007/978-3-319-23464-9_24

Adenovirus represents another common infectious agent associated with HC in immunocompromised patients. The incidence of adenovirus infection ranges from 10 to 20 %, with renal transplant patients being at increased risk of HC associated with infection [7, 8]. Children have been shown to have onset of symptoms sooner than adults (30 vs. 90 days) [9].

While polyoma virus and adenovirus infection cause HC in immunocompromised hosts, infection with cytomegalovirus (CMV) has recently been shown to cause HC despite seemingly normal immune function. In one report, an otherwise healthy 3-year-old boy with gross hematuria had cystoscopic evidence of HC – bladder biopsy was consistent with CMV infection and viral DNA was present in both serum and urine samples. In this patient, symptoms resolved spontaneously with conservative management 1 month after onset [10].

Diagnosis

Onset is usually within the first 30–90 days following initiation of immunosuppression, though symptoms can arise as far as 1 year later. Symptom severity correlates with increased rates of complication including bladder perforation, hydronephrosis, and kidney injury [11]. Viral shedding in the urine is seen both in active and dormant infection, though studies have shown that patients with viruria prior to immunosuppression are at almost twice the risk of developing HC (9 % vs. 16 %) [12]. Diagnosis can be made with urine cytology or PCR testing for viral DNA. These patients should be monitored closely so that intervention can be timely. Adenovirus viruria is present during active disease and can be detected with PCR testing of the urine [13].

Infectious causes of HC share similar imaging findings. Bladder ultrasound as well as computed tomography (CT) can show a thickened bladder wall along with increased attenuation of urine and intraluminal clots. Magnetic resonance imaging will show inflammation and edema within the bladder wall [14, 15].

Management

Management of HC caused by polyoma virus includes reduction of immunosuppression, treatment with antibiotic and/or antiviral agents along with supportive treatment targeted at preventing urinary clot retention and hemorrhagic anemia, as well as symptom control (discussed below). In patients with additional risk factors for renal failure or concern for renal transplant graft dysfunction, reduction of immunosuppression alone can be quite effective and avoids the use of nephrotoxic agents. One study demonstrated that a 50 % reduction in immunosuppressive agents resulted in clearance of BK viremia in 58 % of patients [16]. Cidofovir is viral DNA synthesis inhibitor and has demonstrated utility in treating patients with polyoma virus-associated HC, with the limiting factor of nephrotoxicity [17–19]. Most studies have investigated intravenous cidofovir, though there are also reports of effectiveness in intravesical instillation. This is useful in patients where the nephrotoxicity of intravenous cidofovir is prohibitive. In a retrospective study, treatment with IV cidofovir resulted in 67 % of patients with complete resolution of HC and another 12 % with partial resolution [20]. In the same study, 60 % treated with intravesical cidofovir had complete resolution of symptoms and another 20 % had partial resolution. Another agent shown to be effective in polyoma virus infection is leflunomide, a pyrimidine synthesis inhibitor with both immunosuppressive and antiviral properties. One study demonstrated an 88 % reduction in viremia following treatment with leflunomide combined with reduction in immunosuppression [21]. Finally, fluoroquinolones are effective both in prophylaxis and treatment of polyoma virus-associated HC [22, 23]. A retrospective study of 92 consecutive patients demonstrated that prophylaxis with ciprofloxacin prior to and during immunosuppression led to a significant reduction in the incidence of BK virus-associated HC (2.6 % vs. 20.9 %) [24].

The principles of therapy are similar to that for polyoma virus such as reduction of immunosuppression, the use of antivirals, and symptomatic control are the same as that for adenovirus in general. There are no specific antiviral treatments for adenovirus, though agents such as ganciclovir, vidarabine, ribavirin, and cidofovir have all been used with some success [25–28]. The best studied of these agents include ribavirin and cidofovir, though to date, there are no randomized controlled trials (RCT) investigating their effect.

Nonviral Infectious HC

While viral HC is most common, bacterial, fungal, and parasitic infection can also cause HC. Bacterial cystitis, though usually a benign disease, has been reported in rare but severe cases to progress to HC with potentially fatal outcomes including spontaneous bladder perforation [29]. The most common bacterial causes are *E. coli*, *Proteus spp.*, *Klebsiella spp.*, *and S. saprophyticus* [30]. There is a recent report of a patient with acalculous cholecystitis and acute HC caused by *S. typhi* [31]. Regardless of the causative agent, management of bacterial HC relies on culture-driven antimicrobial therapy along with symptom control.

HC is also a known sequelae of tuberculosis of the bladder. This is seen in the immigrant population and affected individuals usually have concurrent renal tuberculosis [32].

Fungal causes of HC are rare and usually associated with treatment of bacterial cystitis [33]. Organisms reported to cause hemorrhagic complications include *Candida albicans*, *Cryptococcus neoformans*, *Aspergillus fumigatus*, and *Torulopsis glabrata*. Characteristic findings include white plaques overlying the urothelium. As with bacterial cystitis, symptoms resolve following treatment of the underlying

infection [34]. In the United States, parasitic HC is rare. However, bladder schistosomiasis is a serious health concern in developing nations, primarily in Africa [35]. Infection starts with exposure to contaminated water, where larvae penetrate the skin. Following maturation in the lungs and liver, adult worms travel to the pelvic veins and deposit eggs in the bladder wall. The eggs incite an inflammatory reaction with subsequent fibrosis. During the inflammatory phase, nodular bladder wall thickening is seen on CT urography. In the chronic fibrotic phase, bladder volume is decreased and imaging shows a thickened calcified bladder [36].

Treatment with praziquantel will treat the infection but the chronic fibrotic changes cannot be reversed [37]. In rare cases, hemorrhagic cystitis has been noted in association with hydatid cyst disease caused by *Echinococcus granulosus* [38]. Treatment with albendazole leads to resolution of symptom.

Noninfectious Etiology

Radiation-Induced HC

Radiation-induced cystitis is seen in adult patients with pelvic malignancy and pediatric patients following whole-body radiation in preparation for bone marrow transplantation. Its presentation can be divided into acute and late radiation cystitis.

The overall incidence of radiation cystitis ranges from 5 to 10 %. This number varies greatly depending on the series and the patient population studied. Patients receiving larger doses of radiation or radiation directed at the bladder have an increased risk of developing radiation cystitis of worsening severity [39]. It is therefore not surprising that patients who have undergone radiation treatment for bladder cancer have the highest rates of radiation cystitis, with almost 10 % of patients having small shrunken bladders [40]. Patients treated with radiation for either prostate or cervical cancer have a 6–8 % risk of grade III/IV HC [41, 42]. Acute radiation cystitis occurs either during or shortly after radiation therapy (usually within 3 months) and is caused by injury to the fast dividing cells of the bladder mucosa. The symptoms are typically self-limiting and include dysuria, urgency, and frequency. These can usually be managed conservatively. In the acute phase, imaging findings are similar to those seen in infectious HC. Late radiation cystitis develops anywhere between 6 months and 20 years after therapy. It is caused by damage to vascular and connective tissues, which have a much slower cell turnover rate than the bladder mucosa. Endothelial cell damage and perivascular fibrosis are seen months to years after radiation and can result in vascular occlusion/bladder ischemia [43]. The vascular ischemia causes late bladder fibrosis and contraction which can be seen on CT imaging. Radiation also damages smooth muscle cells, causing them to be replaced by fibroblasts, which will lead to decreased bladder compliance. Histologically, these late changes present as a progressive obliterative endarteritis that leads to mucosal ischemia, cellular depletion, and fibrosis. The hypoxia results in tissue breakdown and sloughing of the necrotic bladder mucosa, which leads to hematuria. Telangiectasia also develops which can further contribute to the hematuria. The impaired tissue healing and fibrosis lead to a reduction in bladder capacity and can cause LUTS [44].

Chemically Induced HC

Oxazophorine-Induced HC

There are a wide variety of drugs that have been implicated in the development of hemorrhagic cystitis. The best studied of these agents include the oxazophorine compounds such as cyclophosphamide and ifosfamide. These are alkylating agents that are used in the treatment regimens of several cancers including Hodgkin's disease, small cell lung carcinoma, and breast cancer. Cyclophosphamide is also used in nonneoplastic disorders such as Wegener's granulomatosis, systemic lupus erythematosus, and rheumatoid arthritis [45]. The dose-limiting step of the oxazophorine compounds is typically urotoxicity. Hemorrhagic cystitis can develop in up to 40 % of patients after treatment with cyclophosphamide or ifosfamide with the toxicity typically being dose related and occurring within 48 h [46, 47]. In around 4 % of patients, the bleeding can become uncontrollable and even life threatening [48].

The pathophysiological mechanism of oxazophorine urotoxicity involves the breakdown of the drugs into acrolein. Cyclophosphamide and ifosfamide are both metabolized by hepatic microsomal enzymes into a mustard derivative (the antineoplastic metabolite) and acrolein. Acrolein is an unsaturated aldehyde with no significant antitumor activity that is excreted through the urine and can interact with the urothelium to produce toxic effects [49]. Acrolein enters the cells both directly and indirectly (through nuclear factor kappa B and activator protein-1) and causes an increase in reactive oxygen species and nitric oxide, which leads to peroxynitrite production. The increase in peroxynitrite levels causes lipid peroxidation, protein oxidation, DNA strand breaks, and eventual necrotic cell death [50]. Clinically, this causes bladder mucosal edema, vascular dilation, increased capillary fragility, and hemorrhage. This can result in chronic fibrosis of the bladder wall, which may lead to a small, fibrotic, noncompliant bladder [51].

The three main approaches for prophylaxis of oxazophorine-induced hemorrhagic cystitis are sodium 2mercaptoethane sulfonate (mesna), hyperhydration with forced diuresis, and continuous bladder irrigation (CBI). The common mechanism of these 3 methods is to reduce the

contact of acrolein with the bladder epithelium. CBI and forced diuresis accomplish this through dilution and forced excretion of the toxic compound. Mesna is a thiol-containing compound that can be coadminstered with cyclophosphamide and ifosfamide. It is excreted into the urinary tract where the sulfhydryl group of mesna can combine with the terminal methyl group of acrolein to form a nontoxic thioether [52]. Mesna works only as a prophylactic method and has no role in treating HC after it has developed. The results of prophylaxis with mesna versus CBI have been examined in a prospective randomized controlled trial. A study of 200 patients receiving either mesna or CBI found that the incidence of hematuria was diminished in the group receiving mesna (76 % vs. 53 %; $p=0.007$); however, the incidences of grade 3 and 4 hematuria were the same in each group (18 %). The group receiving CBI also had significantly increased incidence of moderate to severe bladder discomfort/spasms and UTIs compared to group receiving mesna [53]. More recently, a nonrandomized clinical study showed hemorrhagic cystitis occurred in 50 % of patients after prophylaxis with mesna, hydration, and an alkalizing regimen versus 32 % of patients when CBI was added to the prophylaxis regimen ($p=0.11$). Moreover, they found that in the CBI group, there was a significant reduction in the mean duration of hemorrhagic cystitis (10 vs. 18 days; $p=0.02$), in duration of hospitalization (30.2 vs. 39.6; $p<0.001$), and in lateonset hemorrhagic cystitis ($p=0.001$) [54]. Future prospects for prophylactic agents include compounds such as amifostine and glutathione as well as a wide variety of plant derivatives such as flavonoids and polyphenols [55].

Other Chemotherapeutics

There are several other chemotherapeutic drugs that are less commonly associated with hemorrhagic cystitis. In all cases, management includes stopping the offending agent and supportive management. Busulfan is an alkylating agent that is used in the treatment of CML and in conjunction with cyclophosphamide as a conditioning agent prior to bone marrow transplantation. It has been reported to cause hemorrhagic cystitis in up to 16 % of patients [56, 57]. Bleomycin, a glycopeptide antibiotic used in the treatment of Hodgkin's lymphoma, squamous cell carcinoma, and testicular cancer, has been shown to cause HC as well [58, 59]. Temozolomide is an alkylating agent used in the treatment of brain masses and was first reported to be associated with HC in 2002 in a patient being treated for breast cancer with brain metastasis [60]. Docetaxel is a microtubule inhibitor used in treating hormone-independent prostate cancer and, in rare cases, has been shown to cause HC [61]. Cabazitaxel is a microtubule inhibitor used in prostate cancer patients who have developed resistance to docetaxel. There are reports of patients starting this drug and developing HC soon after. Of note, all patients who developed HC after starting cabazitaxel had previously undergone radiation therapy for prostate cancer and cystoscopic findings were very similar to that seen in radiation-induced HC. In all patients, however, symptoms resolved after cabazitaxel was discontinued [62]. Given the timeline of development and resolution of symptoms, it seems that cabazitaxel precipitated radiation HC. Gefitinib, an EGFR inhibitor used in treating non-small cell lung cancer, has been shown to precipitate HC – discontinuation of the agent led to resolution of symptoms [63].

Miscellaneous Drug Agents

Along with chemotherapeutic agents, other medications have been shown to cause HC. In rare cases, penicillins have precipitated hemorrhagic cystitis, though this has only been reported in severely ill patients. This reaction is thought to be caused by an immune-mediated process – all patients were reported to have eosinophilic infiltration on the bladder wall along with peripheral eosinophilia. Immunofluorescent staining of the submucosal tissue shows the presence of immunoglobulin G and M along with C3 [46]. Piperacillin, methicillin, carbenicillin, ticarcillin, and penicillin G have all been associated with HC [64, 65]. Symptoms typically begin 2–4 weeks of starting the antibiotic and resolution of symptoms occurring with discontinuation of the drug [66–69]. Of note, all patients reported to have penicillin-associated HC were being treated for severe systemic infection, suggesting that the systemic inflammatory response played some role in precipitating the hemorrhagic event. However, with the limited amount of data on the topic, further research is needed to determine the exact mechanism involved. Danazol, a synthetic steroid, was shown to cause hemorrhagic cystitis in 19 % of a series of patients with hereditary angioedema. Neither the dose nor the duration of danazol treatment affected the severity, and in all the patients but one, the symptoms resolved after discontinuation of the drug [70]. Tiaprofenic acid is a nonsteroidal anti-inflammatory drug used in the treatment of osteoarthritis and rheumatoid arthritis. It can cause hemorrhagic cystitis with reports of onset ranging from 2 days to 3 years after starting the drug. As with most medications, stopping the drug will most often reverse the symptoms [71]. Cystoscopic and biopsy findings are similar to interstitial cystitis.

Topical agents that are introduced into the bladder can also cause hemorrhagic cystitis through direct irritation of the bladder mucosa. Nonoxynol-9 is a spermicide used as a vaginal contraceptive suppository. Accidental insertion into the bladder causes hemorrhagic cystitis due to the acidic nature of the suppository [72, 73]. All patients presented with acute onset of LUTS and gross hematuria. Cystoscopic findings reveal diffuse inflammation of the bladder mucosa with decreased bladder volumes and associated ulceration and hemorrhage. Ether has been used to declog Foley balloon

ports. Rupture of the balloon can result in an ether cystitis that can be resistant to treatment [74, 75]. The effects on bladder function can be so severe that bladder augmentation can be needed to restore normal micturition.

Occupational Agents

Occupational exposure to toxic compounds is known to cause HC. o- and p-toluidine, organic compounds used in the synthesis of chemical dyes, have a well-known association with hemorrhagic exposure. As the geopolitical industrial climate has shifted and manufacturing is moved overseas, the incidence of HC is becoming rarer and rarer in the United States while there are increasing reports coming from nations with large manufacturing industries [76, 77]. Chlordimeform, a pesticide used against ticks and moths, has also been reported to cause HC after occupational exposure. Cystoscopic findings are consistent with acute inflammatory changes and hemorrhage, and symptoms usually resolve with conservative management [78]. Organophosphate toxicity, which is well known for its anticholinergic symptoms, has recently been shown to cause grade IV HC. CT imaging reveals inflammatory changes of the bladder and ureters. Given the acute nature of the insult, symptoms resolve with conservative management [79].

Abuse of the anesthetic agent ketamine, an NMDA receptor antagonist that has become increasingly popular in the past decade, is showing a growing association with HC. Multiple case series describe patients who were daily ketamine users presenting with grade III and IV HC. CT imaging revealed classic inflammatory changes including diffuse bladder wall thickening and perivesicular stranding. Cystoscopic examination revealed bladder ulceration, diffuse hemorrhage, and reduced bladder capacities. Biopsy showed acute and chronic inflammation with an eosinophilic infiltrate suggesting a possible allergic mechanism. Cessation of use along with oral hyaluronic acid led to improvement of symptoms [80].

Management

Overall Management

The initial management of HC begins with careful history, physical examination, and labs as needed to determine not only the underlying etiology but also the degree of the blood loss, as patients should be resuscitated appropriately with fluids and/or blood product based on standard critical care guidelines. Urinalysis and urine culture should be performed, and all patients should be presumed to have urinary tract infection until culture data shows otherwise. Diagnosis should rule out other conditions including medical renal disease, UTI, urolithiasis, coagulopathy, and neoplasm of the bladder or upper urinary tract. In cases of bleeding caused by these mechanisms, treatment of the underlying disorder leads to resolution of symptoms. Even in such cases, hemorrhage itself must be managed and can be done so using the same algorithm used in all other forms of HC.

In determining appropriate management strategies, it is important to understand the severity as well as chronicity of the symptoms. In grade I and II hematuria, management involves treating the underlying cause combined with increased fluid intake. Increased fluids dilute the urokinase found in urine allowing bleeding to resolve with normal coagulation. In patients with grade III and IV HC (Table 24.1), treatment by a urologist is often necessary. These patients are characterized by hemorrhage severe enough to cause urinary retention secondary to clot obstruction of the bladder neck and urethra.

Prevention

Of course, the ideal strategy would be that of prevention. For patients undergoing radiation treatment, this involves tailoring the treatment as much as possible to the region of interest and limiting the dose delivered to the bladder. For chemical-induced cystitis, such as that caused by acrolein, minimizing exposure through treatments that are very effective (i.e., mesna) is the best treatment as it prevents HC. In many patients, once chronic changes are present, they are irreversible and the effect of urokinase in the urine on the underlying bladder muscle and vasculature propagates a cycle of irritation, causing hemorrhage that is very difficult to control.

Initial Bedside Management

Irrigation and Clot Evacuation

When bleeding is severe enough to warrant urologic consultation, care should follow as such. Residual hematoma and urinary stasis provide an excellent culture medium for bacteria to grow, and patients can quickly progress to urosepsis, and again, the treatment of any possible infection is of utmost importance. In the setting of ongoing hemorrhage or urinary clot obstruction, bladder irrigation at the bedside is warranted using a large, stiff-walled catheter as one must evacuate and remove all clots from the bladder [54]. Given that the bladder wall is friable and delicate in HC, the urologist should always be weary of bladder perforation, especially in the case of a chronically fibrotic, shrunken bladder that may be seen in late-stage radiation cystitis. Irrigation is usually performed with a large, catheter-tipped syringe and should continue until there is no clot remaining, and this can often require multiple liters of irrigation.

Continuous Bladder Irrigation

Once all clots have been removed, patients who continue to have low-volume bleeding should be placed on continuous bladder irrigation. It is often the practice of these authors to place patients on continuous bladder irrigation (CBI) for at least several hours if we are consulted for severe HC that requires catheter placement and irrigation. The rate of irrigation can be titrated by nursing staff as long as the urine remains free of clot. Once bleeding has resolved and the urine has remained free of blood for 24 h, the catheter can be removed. If bleeding is persistent for greater than 24 h and requires multiple hand irrigations, then cystoscopy and fulguration under anesthesia or intravesical installation should be considered. If the clinician is concerned that all of the clot is not able to be removed, then cystoscopy under anesthesia with clot evacuation and fulguration is most likely the best next step. This is because intravesical treatments are not likely to work with residual clot in the bladder. However, if the clinician feels that the clot is removed but it is continuously bleeding that is necessitating the CBI, then intravesical therapies may be a good next option as there are some that do not require anesthesia. It is most likely that a patient with grade IV HC will need cystoscopic clot evacuation before proceeding to possible bedside intravesical instillations to ensure clots are removed.

Bedside Intravesical Instillations

Aluminum (Alum)

Aluminum salts can control bladder hemorrhage by causing protein precipitation at the cell surface and within the interstitial space. The resulting vascular protection reduces edema, inflammation, and exudate, all of which contribute to the promotion of further bleeding. As opposed to HA or chondroitin sulfate, alum instillation can be used for severe HC. The first use of intravesical aluminum salt (alum) irrigation is described in a 1982 report of six patients with severe HC following radiation for bladder cancer [81]. Patients were irrigated with a 1 % alum solution in sterile water via a large rigid three-way catheter at the bedside. Subsequent reports have confirmed the utility of intravesical alum irrigation with minimal adverse events [82]. The precipitates formed after alum instillation can cause catheter obstruction, and in rare cases, alum irrigation has been reported to cause systemic side effects including anemia, osteomalacia, and renal failure with associated encephalopathy [83, 84]. Alum should be instilled utilizing a 1 % solution intravesically with a rate of 250–300 ml/h to prevent clotting of the tubing. Clinicians should be checking serum alum levels as well as neuro checks for signs of aluminum toxicity. These signs include lethargy, confusion, seizures, and metabolic acidosis. Clinicians should be cautious of using alum in patients with renal failure as well as patients with significant allergic history.

Amicar

Another agent that can be used at the bedside for intravesical irrigation is ε-aminocaproic acid (Amicar), which is a lysine derivative that acts as an inhibitor of tissue plasminogen and related enzymes. Amicar is particularly useful in HC as it also inhibits urokinase, which, as discussed above, is an integral component of propagating bladder hemorrhage. A study of 37 patients with refractory HC treated with intravesical Amicar showed resolution of bleeding in 89 % of subjects. Patients were treated with 200 mg/L solution of Amicar in normal saline irrigated continuously until 24 h after bleeding resolved [85]. An important consideration in planning treatment with Amicar is ensuring that the bladder is clot-free prior to therapy, as Amicar causes hardening of clots making them difficult to remove. Thus, patients being considered for Amicar should undergo clot evacuation either by hand irrigation or cystoscopically and then be placed on CBI in preparation for treatment.

Procedural Interventions

Cystoscopy and Fulguration

Electrocautery

In those patients whose bleeding does not resolve, or clot removal is not possible with hand irrigation, cystoscopic intervention with electrocautery fulguration of bleeding sites and clot evacuation is indicated [86, 87]. Care should be taken as the underlying tissue can be very friable and bladder perforation can occur. Though the data is sparse, approximately 60 % of patients will see resolution of bleeding after a single treatment with cystoscopic clot evacuation. However, patients requiring further clot evacuations have a significantly reduced chance of responding and often require more aggressive means of treatment [88].

Nd:YAG

Nd:YAG is utilized and has been reported as effective option. However, the mechanism for its effect is thermal coagulation and thus, the tissue will eventually slough just as it will with electrocautery and then must heal. This is a concern in patients with radiation-induced cystitis where healing may be affected [89].

Argon Beam

Other options for cystoscopy management of ongoing hemorrhage include the use of argon plasma, which can be useful in cases with more diffuse bleeding that cannot be controlled with traditional electrocautery [87, 90, 91].

Greenlight KTP Laser

A recent report has described 10 patients with refractory radiation-induced HC treated with Greenlight KTP laser coagulation, which is traditionally used in transurethral resection of the prostate for benign prostatic hyperplasia. In this series, 9 out of 10 patients had no recurrence of bleeding at 6-month follow-up [92]. Another retrospective review of 20 patients showed that the KTP laser was able to selectively ablate the vasculature while persevering the overlying mucosa. Ninety-two percent of the patients had successful treatment with average hematuria-free periods of 11.8 months [89].

Intravesical Therapy Refractory

Intravesical formalin has been extensively studied and has demonstrated excellent results in treating HC that is refractory to conservative measures [93]. Formalin is an aqueous solution of formaldehyde and acts similarly to alum when instilled in the bladder. It causes precipitation of cellular proteins [94] and its fixative properties stabilize the telangiectatic changes seen in HC. Its use was first described in 1969 [95] – a 10 % formalin solution was used in patients with severe HC and improvement in symptoms was seen in 90 % of those treated. Since the initial study, variations to treatment protocols, including formalin concentration as well as contact time and subsequent irrigation, have been studied. It has been shown in these studies that intravesical formalin is highly effective in controlling severe HC with success rates of 80–93 % [96]. Of note, formalin instillation is extremely painful, and either general or spinal anesthesia is required during instillation. General principles of formalin instillation include the following:

- Make sure all clots removed from the bladder and fulgurate any obvious bleeding vessels.
- Protect external skin areas such as vaginal packing to prevent leakage around catheter and Vaseline to skin around penis.
- Perform cystography to make sure vesicoureteral reflux (VUR) is not present.
- Start with a low concentration (1–2 %) and repeat with incrementally increased concentrations as necessary.
- Minimize the volume of formalin used.
- Minimize formalin dwell time in the bladder (15 min).
- In our experience, obstruction of the ureters with ureteral dilators prior to instillation is another effective approach to minimizing VUJ/ureteric complications.

The major limiting factors to the use of formalin include local and systemic complications, which include a small and contracted bladder, incontinence, vesicoureteral reflux (VUR), ureteral strictures, acute tubular necrosis, urinary fistulas, bladder perforation, and toxic effects on the myocardium [97–104]. Using a lower concentration of formalin and minimizing exposure to the ureters and vesicoureteral junction can minimize many of these side effects [105]. Patients with radiation-induced HC have been shown to require higher concentrations of formalin and/or repeat instillations compared with bleeding secondary to cyclophosphamide or bladder cancer.

In patients with focal areas of bleeding, formalin-soaked pledgets were applied cystoscopically. Similar to instillation, lower concentrations appear to be equally effective – use of 4 % formalin was equally effective as 10 % [105].

Other Intravesical Options

Silver nitrate, which is commonly used to treat bleeding wounds at the bedside, can also be used intravesically. The data is sparse, but one study showed improvement in eight out of nine subjects [106]. There are reports of patients suffering subsequent renal failure secondary to precipitation of silver salts in the ureters [107]. Renal function improved after ureteroscopic removal of precipitates, but this complication emphasizes the importance of ruling out VUR prior to intravesical therapy. Irrigation with phenol has also been described in a case report [108], though the deleterious effects of phenol persisting in the bladder require neutralization and large-volume irrigation following instillation [109]. Given the paucity of data and significant risks, this is not a recommended treatment modality.

Intravesical prostaglandin has been described both in the United States and abroad to be effective in treating refractory HC. Though the exact mechanism is not known, it is thought that prostaglandins cause vasoconstriction and promote platelet aggregation. These agents are especially useful as they can be administered at the bedside, have very few associated adverse effects, and are generally well tolerated by patients [110]. A 1984 report describes a BMT patient with refractory HC who had previously required multiple transfusions and failed conservative management. The patient's bladder was filled with a 3.75 mg/L solution of PGE2 in normal saline, which remained in place for 4 h before being drained. This was repeated for 5 days, at the end of which hematuria resolved [111]. PGE1 and PGF2-alpha have also been reported to be effective [110, 112, 113], and often, the choice between which prostaglandin to use is decided based on availability. Finally, carboprost, a synthetic PGF2-alpha analogue that is commonly used in severe postpartum hemorrhage, can be used as well [114, 115]. In one study, 24 patients with severe HC underwent hourly bedside intravesical carboprost instillation every 6 h with doses being titrated daily until bleeding resolved. Responses were seen within 7 days in most patients, though half of those who saw initial improvement in symptoms ultimately had recurrence of bleeding requiring more aggressive treatment modalities [116]. The most common side effect of intravesical

prostaglandin is bladder spasm, which can be effectively controlled with anticholinergics and rarely is severe enough to warrant discontinuation of therapy. Taken together, intravesical prostaglandin is a well-tolerated effective treatment for moderate HC and can be used as a temporizing measure in more severe cases until definitive therapy is provided.

Systemic Therapies

Hyperbaric Oxygen Therapy

Another useful treatment modality in refractory HC is hyperbaric oxygen therapy (HBOT). Patients sit in an enclosed pressurized space for a set amount of time every day and breath 100 % O_2 leading to saturation of hemoglobin and an elevated PaO_2. The increased oxygen tissue promotes angiogenesis and wound healing making it especially useful in ischemic tissue. To date, there are many studies, including small prospective series, highlighting the effectiveness of HBOT. Most studies have found that around 80 % of patients with severe grade III/IV HC have a durable response to treatment after an average of around 30 treatments [117, 118]. While HBOT has traditionally been reserved for persistent refractory HC, there is a new shift toward earlier use. Recent data has shown improved efficacy and a reduced number of treatments if patients are started on HBOT soon after HC is detected [119]. The major benefit of HBOT is a lack of adverse effects. There is an ongoing randomized controlled trial to determine the long-term effects on the bladder mucosa after HBOT to treat refractory HC. However, its use is limited by a couple of different factors. HBOT requires twenty sessions with daily session 5–6 times a week that usually require weeks before a therapeutic effect is seen. Therefore, ongoing hemorrhage must be stopped or at least be slowed while the patient is undergoing therapy. Hyperbaric chambers tend to be very small and claustrophobia is a significant concern in many patients that preclude its use. However, in those that can tolerate it, HBOT is an excellent treatment modality that will likely see increasing use in HC in the coming years.

Other Systemic Therapies

In addition to intravesical therapy, there are some agents that can be administered orally or intravenously to treat HC. The use of both factors VI and XIII have been previously reported to effectively stop hemorrhage in refractory HC, and one study even reports control of hemorrhage with Factor VII after failure of 4 % intravesical formalin [120–122]. However, a trial in 2003 that attempted to control refractory HC with human factor VII showed no benefit. These agents can be especially useful in patients with severe hemorrhage leading to coagulopathy. Amicar, which was discussed above as an intravesical agent, can also be administered intravenously either alone or in combination with intravesical administration and has been reported to effectively control bleeding as soon as 24 h after starting treatment [123].

Surgical and Interventional Procedures

Urinary Diversion

Urinary diversion can range from percutaneous nephrostomy tubes to more definitive procedures such as cystectomy with an ileal conduit.

Nephrostomy Tubes

Nephrostomy tubes are the simplest way to divert urine flow from the bladder without requiring extirpative surgery; however, its ability to control significant bleeding is questionable. Patients where the bladder has been left in situ, such as in the above scenario, have reported complications up to 80 % with high readmission rates and 25 % requiring eventual cystectomy [124, 125]. However, as is most of the literature in HC, this is based on single institutional retrospective reviews in small cohorts.

Cystectomy

Most urologists attempt to avoid primary cystectomy for patients with severe HC secondary to patient and disease-related complexities. The largest series to date looking at cystectomy for refractory HC identified patients commonly had low preoperative hemoglobin, high ASA score, and advanced age. Patients had a high rate of severe perioperative complications (Clavien III–IV) of 42 % with a 90-day mortality rate of 16 %. Since the majority of these cases were secondary to radiation (95 %), there were 4 patients that had to undergo supratrigonal cystectomy secondary to severe fibrosis and 2 patients where the procedure was aborted with only ureteral ligation [126]. In the same study, 1- and 3-year overall survival rates were 84 % and 52 %, respectively. This treatment may have to be considered for patients; however, it should be utilized only if other conservative therapies fail.

Embolization

Finally, in the case of acute life-threatening hemorrhage that requires immediate control, embolization can achieve this. Blood supply to the urinary bladder is predominately derived from branches of the internal iliac artery. Specifically, both the superior and inferior vesical arteries usually arise from the anterior division of the internal iliac artery. In men, prostatic arteries may also supply portions of the urinary bladder and arise from the internal pudendal artery. Endovascular embolization of the arteries supplying the urinary bladder can be performed to control bleeding in cases of hemorrhagic

cystitis that have failed more conservative treatments. First described in 1976 [127], transcatheter embolization performed to control intractable bladder hemorrhage is infrequently reported but has been shown to have good clinical success rates (control of bleeding) ranging from 70 to 100 % [128–133].

Vascular access is most commonly obtained via retrograde percutaneous catheterization of the femoral artery on one or both sides. A distal aortogram can first be performed with a high-flow pigtail or straight catheter to better delineate the iliac anatomy. Selective angiography is subsequently performed of the internal iliac arteries, most commonly using pre-curved Cobra or Simmons type 2 catheters. The catheter tip is then placed as subselectively as possible into the anterior division of the internal iliac artery; a coaxial microcatheter can subsequently be used to catheterize vesicular branches based on angiographic findings. More recent studies have demonstrated good success with more superselective embolizations, which allow for better target embolization and less complications from nontarget embolization [130].

Embolization is most frequently performed with polyvinyl alcohol (PVA) particles or trisacryl gelatin microspheres mixed with contrast to monitor particle infusion and potential reflux. Initially, smaller 100–300 μm particles are used; as the distal branches fill, larger particles are used, usually 300–500 μm.

If there is difficulty subselecting the vesical or prostatic arteries, coil blockade is performed. A coil is placed in the ostium of nontarget arteries, often the superior gluteal artery, and the catheter tip is then retracted. Embolization is then performed with the catheter tip in the proximal internal iliac artery. The theory is that flow will be steered into the vesical or prostatic branches while protecting the coiled vessel. Perfusion will be maintained in the vascular bed of the coiled vessel due to collaterals and retrograde filling [130]. DSA is then performed of the internal iliac artery following embolization to evaluate efficacy and technical success. The same procedure is usually then repeated on the contralateral side, as unilateral embolization has a higher risk of rebleeding [133, 134].

Radiation- or chemotherapy-induced hemorrhagic cystitis is a morbid and therapeutically challenging disease. Patient's often require multiple blood transfusions as well as prolonged or repeat hospital admissions requiring repeat bladder irrigations. As these patients are often older and with multiple comorbidities, a surgical approach is frequently not an option if conservative options have failed. Endovascular embolization allows for control of bleeding in a minimally invasive manner. Although there have only been small case series investigating this technique, a literature review demonstrated high technical success rates ranging from 92.6 to 100 % [135]. In these studies, the initial clinical success was very high, with repeat bleeding seen more frequently in cases of radiation cystitis compared to other causes of intractable hematuria [131]. These cases may require repeat embolizations for control of hemorrhage.

Although infrequently reported following vesicular embolization, potential complications include gluteal ischemia (paresis, pain, or skin necrosis), Brown-Sequard syndrome, or bladder necrosis. Occasionally, patients report experiencing post-embolic syndrome, which can manifest with nonspecific symptoms including fever, nausea, and vomiting.

In conclusion, endovascular catheter-directed embolization of the arteries supplying the urinary bladder is a safe option to control the bleeding in cases of hemorrhagic cystitis if conservative methods fail. Most frequently, embolization is performed with PVA particles or trisacryl gelatin microspheres. Efforts should be made to perform bilateral embolizations as subselectively as possible to decrease the rate of complications from nontarget embolization. It is important to note that in cases of radiation cystitis or hemorrhagic cystitis caused by chemotherapeutic agents, embolization should be viewed as a palliative measure aimed at bleeding control and improving patient comfort by decreasing the need for blood transfusions.

Experimental Therapies

GAG Layer Replenishment

As discussed earlier, the epithelium of the bladder is coated by a thick layer of glycosaminoglycans (i.e., the GAG layer). This is a nonspecific defense against bacterial adherence as well as protection against irritants. The components of the GAG layer include hyaluronic acid as well as chondroitin sulfate [135, 136]. Therefore, many have theorized that the repair and rebuilding of the GAG layer can function to treat HC. A small randomized prospective trial compared hyaluronic acid (HA) to hyperbaric oxygen therapy (HBOT) and showed HA to be as effective as the HBOT therapy in patients with HC. It was also very well tolerated; however, there were no patients in this group with grade IV HC and it should be reserved as experimental and for patients with mild grade III or lower symptoms [137]. Sodium hyaluronate is given weekly via intravesical installation of 40 mg/50 ml for a duration of up to 6 weeks [138]. There is little evidence in regard to chondroitin sulfate for the indication of HC. However, a large observational study of 266 patients with severe forms of chronic cystitis showed it to be effective and well tolerated; however, the results need to be confirmed in a controlled trial [139].

Stem Cell Therapy

NCT02174536 is an ongoing randomized controlled trial to evaluate efficacy of using placenta-derived decidual stromal cells.

Orgotein

The use of 5-azaDC, nicotinamide, or Anakinra also was possibly studied. Another trial NCT01295645 trial to test efficacy of cidofovir for BK virus induced HC.

Fibrin Glue

Cystoscopic application of fibrin glue to bleeding sites has shown effectiveness in treating ongoing hemorrhage [140], and a recent case series of 35 patients treated with fibrin glue showed resolution of hemorrhage in 83 % of patients at 50-day follow-up [141].

Conclusion

Though there are many different etiologies and management options for HC, the overall paradigm is quite straightforward. HC is ultimately secondary to a denuded bladder mucosa with irritation of the underlying bladder musculature and vasculature. The compounding effect of ongoing irritation combined with the presence of urokinase leads to hemorrhage that is difficult to control. Management should start with resuscitation as needed, and any offending agents should be immediately discontinued. Traditionally, treatment follows a stepwise fashion progressing from less invasive bedside procedures to more invasive intravesical therapies and diversion – the particular progression often depends on patient-specific characteristics and institutional practices.

Given the rare incidence of HC, there remains a paucity of data on the topic. The literature is primarily comprised of retrospective reviews with only a few prospective trials. Further research is needed to better predict which patients are at increased risk of developing HC and which therapy is most likely to stop hemorrhage and restore urinary function, all while minimizing adverse effects associated with many of the established treatments.

References

1. Hong SY, Pyo SJ, Lee HB. Effect of serum urokinase on urine fibrinolytic activity. Nephron. 1990;55:287–91.
2. Droller MJ, Saral R, Santos G. Prevention of cyclophosphamide-induced hemorrhagic cystitis. Urology. 1982;20:256–8.
3. J. MA, G. D, J. B. et al. Transplantation. 8:704–10.
4. Boldorini R, Veggiani C, Barco D, Monga G. Kidney and urinary tract polyomavirus infection and distribution: molecular biology investigation of 10 consecutive autopsies. Arch Pathol Lab Med. 2005;129:69–73.
5. Boldorini R, et al. Periodic assessment of urine and serum by cytology and molecular biology as a diagnostic tool for BK virus nephropathy in renal transplant patients. Acta Cytol. 2005;49:235–43.
6. Das D, Shah RB, Imperiale MJ. Detection and expression of human BK virus sequences in neoplastic prostate tissues. Oncogene. 2004;23:7031–46.
7. Flomenberg P, et al. Increasing incidence of adenovirus disease in bone marrow transplant recipients. J Infect Dis. 1994;169:775–81.
8. Hierholzer JC. Adenoviruses in the immunocompromised host. Clin Microbiol Rev. 1992;5:262–74.
9. Carrigan DR. Adenovirus infections in immunocompromised patients. Am J Med. 1997;102:71–4.
10. Taktak A, Acar B, Gür G, et al. Cytomegalovirus-related hemorrhagic cystitis in an immunocompetent child. Ren Fail. 2014;36:1148–50.
11. Riachy E, et al. Risk factors and predictors of severity score and complications of pediatric hemorrhagic cystitis. J Urol. 2014;191:186–92.
12. Silva Lde P, et al. Hemorrhagic cystitis after allogeneic hematopoietic stem cell transplants is the complex result of BK virus infection, preparative regimen intensity and donor type. Haematologica. 2010;95:1183–90.
13. Mufson MA, Belshe RB. A review of adenoviruses in the etiology of acute hemorrhagic cystitis. J Urol. 1976;115:191–4.
14. McCarville MB, Hoffer FA, Gingrich JR, Jenkins JJ. Imaging findings of hemorrhagic cystitis in pediatric oncology patients. Pediatr Radiol. 2000;30:131–8.
15. Schulze M, et al. Computed tomography findings of human polyomavirus BK (BKV)-associated cystitis in allogeneic hematopoietic stem cell transplant recipients. Acta Radiol. 2008;49:1187–94.
16. Hymes LC, Warshaw BL. Polyomavirus (BK) in pediatric renal transplants: evaluation of viremic patients with and without BK associated nephritis. Pediatr Transplant. 2006;10:920–2.
17. Mackey MC. Intravesicular cidofovir for the treatment of polyomavirus-associated hemorrhagic cystitis. Ann Pharmacother. 2012;46:442–6.
18. Ortiz A, et al. Tubular cell apoptosis and cidofovir-induced acute renal failure. Antivir Ther. 2005;10:185–90.
19. Meier P, Dautheville-Guibal S, Ronco PM, Rossert J. Cidofovir-induced end-stage renal failure. Nephrol Dial Transplant. 2002;17:148–9.
20. Cesaro S, et al. Cidofovir for BK virus-associated hemorrhagic cystitis: a retrospective study. Clin Infect Dis. 2009;49:233–40.
21. Williams JW, et al. Leflunomide for polyomavirus type BK nephropathy. N Engl J Med. 2005;352:1157–8.
22. Randhawa PS. Anti-BK virus activity of ciprofloxacin and related antibiotics. Clin Infect Dis. 2005;41:1366–7; author reply 1367.
23. Portolani M, et al. Suppression of BK virus replication and cytopathic effect by inhibitors of prokaryotic DNA gyrase. Antiviral Res. 1988;9:205–18.
24. Miller AN, Glode A, Hogan KR, et al. Efficacy and safety of ciprofloxacin for prophylaxis of polyomavirus BK virus-associated hemorrhagic cystitis in allogeneic hematopoietic stem cell transplantation recipients. Biol Blood Marrow Transplant. 2011;17:1176–81.
25. Arav-Boger R, Echavarria M, Forman M, et al. Clearance of adenoviral hepatitis with ribavirin therapy in a pediatric liver transplant recipient. Pediatr Infect Dis J. 2000;19:1097–100.
26. Bordigoni P, Carret AS, Venard V, Witz F, Le Faou A. Treatment of adenovirus infections in patients undergoing allogeneic hematopoietic stem cell transplantation. Clin Infect Dis. 2001;32:1290–7.
27. Hoffman JA, Shah AJ, Ross LA, Kapoor N. Adenoviral infections and a prospective trial of cidofovir in pediatric hematopoietic stem cell transplantation. Biol Blood Marrow Transplant. 2001;7:388–94.
28. Nakazawa Y, et al. Urinary excretion of ganciclovir contributes to improvement of adenovirus-associated hemorrhagic cystitis after allogeneic bone marrow transplantation. Pediatr Transplant. 2009;13:632–5.
29. Rodríguez Rodríguez A, et al. Spontaneous bladder perforation secondary to bacterial cystitis. Cause of acute abdomen in diabetic elderly. Actas Urol Esp. 1995;19:393–7.

30. Ronald AR. Current concepts in the management of urinary tract infections in adults. Med Clin North Am. 1984;68:335–49.
31. Beyazal Polat H, Beyazal M, Beyazal Çeliker F. A case report of acute acalculous cholecystitis and acute hemorrhagic cystitis due to salmonella typhi. Case Rep Med. 2014;2014:758583.
32. Stoller JK. Late recurrence of mycobacterium bovis genitourinary tuberculosis: case report and review of literature. J Urol. 1985;134: 565–6.
33. Haldar S, Dru C, Bhowmick NA. Mechanisms of hemorrhagic cystitis. Am J Clin Exp Urol. 2014;2:199–208.
34. Fisher JF, et al. Urinary tract infections due to Candida albicans. Rev Infect Dis. 1982;4:1107–18.
35. Neal PM. Schistosomiasis--an unusual cause of ureteral obstruction: a case history and perspective. Clin Med Res. 2004;2: 216–27.
36. Wong-You-Cheong JJ, Woodward PJ, Manning MA, Davis CJ. From the archives of the AFIP: inflammatory and nonneoplastic bladder masses: radiologic-pathologic correlation. Radiographics. 2006;26:1847–68.
37. Kramer CV, Zhang F, Sinclair D, Olliaro PL. Drugs for treating urinary schistosomiasis. Cochrane Database Syst Rev. 2014;(8): CD000053.
38. Hansman DJ, Brown JM. Eosinophilic cystitis: a case associated with possible hydatid infection. Med J Aust. 1974;2:563–5.
39. Denton AS, Clarke NW, Maher EJ. Non-surgical interventions for late radiation cystitis in patients who have received radical radiotherapy to the pelvis. Cochrane Database Syst Rev. 2002;(3): CD001773.
40. Goodman GB, Hislop TG, Elwood JM, Balfour J. Conservation of bladder function in patients with invasive bladder cancer treated by definitive irradiation and selective cystectomy. Int J Radiat Oncol Biol Phys. 1981;7:569–73.
41. Fuentes-Raspall R, et al. Late rectal and bladder toxicity following radiation therapy for prostate cancer: predictive factors and treatment results. Rep Pract Oncol Radiother. 2013;18:298–303.
42. Levenback C, Eifel PJ, Burke TW, Morris M, Gershenson DM. Hemorrhagic cystitis following radiotherapy for stage Ib cancer of the cervix. Gynecol Oncol. 1994;55:206–10.
43. Russell NS, Bartelink H. Radiotherapy: the last 25 years. Cancer Treat Rev. 1999;25:365–76.
44. Marks LB, Carroll PR, Dugan TC, Anscher MS. The response of the urinary bladder, urethra, and ureter to radiation and chemotherapy. Int J Radiat Oncol Biol Phys. 1995;31:1257–80.
45. Brock N. Oxazaphosphorine cytostatics: past-present-future. Seventh Cain Memorial Award lecture. Cancer Res. 1989;49:1–7.
46. Cox PJ. Cyclophosphamide cystitis – identification of acrolein as the causative agent. Biochem Pharmacol. 1979;28:2045–9.
47. Stillwell TJ, Benson RC. Cyclophosphamide-induced hemorrhagic cystitis. A review of 100 patients. Cancer. 1988;61:451–7.
48. Gray KJ, Engelmann UH, Johnson EH, Fishman IJ. Evaluation of misoprostol cytoprotection of the bladder with cyclophosphamide (Cytoxan) therapy. J Urol. 1986;136:497–500.
49. Schoenike SE, Dana WJ. Ifosfamide and mesna. Clin Pharm. 1990;9:179–91.
50. Korkmaz A, Topal T, Oter S. Pathophysiological aspects of cyclophosphamide and ifosfamide induced hemorrhagic cystitis; implication of reactive oxygen and nitrogen species as well as PARP activation. Cell Biol Toxicol. 2007;23:303–12.
51. Kimura M, Tomita Y, Morishita H, Takahashi K. Presence of mucosal change in the urinary bladder in nonhematuric patients with long-term exposure and/or accumulating high-dose cyclophosphamide. Possible significance of follow-up cystoscopy on preventing development of cyclophosphamide-induced hemorrhagic cystitis. Urol Int. 1998;61:8–11.
52. Dorr RT. Chemoprotectants for cancer chemotherapy. Semin Oncol. 1991;18:48–58.
53. Vose JM, et al. Mesna compared with continuous bladder irrigation as uroprotection during high-dose chemotherapy and transplantation: a randomized trial. J Clin Oncol. 1993;11:1306–10.
54. Hadjibabaie M, et al. Continuous bladder irrigation prevents hemorrhagic cystitis after allogeneic hematopoietic cell transplantation. Urol Oncol. 2008;26:43–6.
55. Batista CK, et al. Amifostine and glutathione prevent ifosfamide- and acrolein-induced hemorrhagic cystitis. Cancer Chemother Pharmacol. 2007;59:71–7.
56. Tsuboi K, et al. Multivariate analysis of risk factors for hemorrhagic cystitis after hematopoietic stem cell transplantation. Bone Marrow Transplant. 2003;32:903–7.
57. Ansari M, et al. Association between busulfan exposure and outcome in children receiving intravenous busulfan before hematopoietic stem cell transplantation. Ther Drug Monit. 2014;36: 93–9.
58. Komiya I, Nojiri M, Kuriya S, Saito Y. Hemorrhagic cystitis caused by bleomycin treatment. Jpn J Med. 1991;30:392.
59. Cantwell BM, Harris AL, Patrick D, Hall RR. Hemorrhagic cystitis after i.v. bleomycin, vinblastine, cisplatin, and etoposide for testicular cancer. Cancer Treat Rep. 1986;70:548–9.
60. Islam R, Isaacson BJ, Zickerman PM, Ratanawong C, Tipping SJ. Hemorrhagic cystitis as an unexpected adverse reaction to temozolomide: case report. Am J Clin Oncol. 2002;25:513–4.
61. Ntekim AI, Ajekigbe A. Hemorrhagic cystitis in a patient receiving docetaxel for prostate cancer. Clin Med Insights Oncol. 2010;4:11–3.
62. Grellety T, et al. Hemorrhagic cystitis in patients treated with cabazitaxel: a radiation recall syndrome? Ann Oncol. 2014;25:1248–9.
63. Laterza MM, Chiurazzi B, Brangi M, Riccardi F, Cartenì G. Gefitinib in non-small cell lung carcinoma: a case report of an unusual side effect and complete response in advanced disease. Tumori. 2013;99:3e–5.
64. Marx CM, Alpert SE. Ticarcillin-induced cystitis. Cross-reactivity with related penicillins. Am J Dis Child. 1984;138:670–2.
65. Bracis R, Sanders CV, Gilbert DN. Methicillin hemorrhagic cystitis. Antimicrob Agents Chemother. 1977;12:438–9.
66. Cook FV, Farrar WE, Kreutner A. Hemorrhagic cystitis and ureteritis, and interstitial nephritis associated with administration of penicillin G. J Urol. 1979;122:110–1.
67. Adlam D, Firoozan S, Gribbin B, Banning AP. Haemorrhagic cystitis and renal dysfunction associated with high dose benzylpenicillin. J Infect. 2000;40:102–3.
68. Toma Y, et al. Penicillin G-induced hemorrhagic cystitis with hydronephrosis. Intern Med. 2009;48:1667–9.
69. Kim MK, et al. Penicillin G-induced hemorrhagic cystitis: a case and review of the literature. Korean J Intern Med. 2013;28:743–5.
70. Andriole GL, et al. Danazol-induced cystitis: an undescribed source of hematuria in patients with hereditary angioneurotic edema. J Urol. 1986;135:44–6.
71. Crawford ML, Waller PC, Wood SM. Severe cystitis associated with tiaprofenic acid. Br J Urol. 1997;79:578–84.
72. Mayersak JS, Viviano CJ. Severe chemical cystitis from the transurethral intravesical insertion of a vaginal contraceptive suppository: a report of 3 cases and proposed method of management. J Urol. 1993;149:835–7.
73. Pliskin MJ, Dresner ML. Inadvertent urethral insertion of a contraceptive suppository. J Urol. 1988;139:1049–50.
74. Nellans RE, Ellis LR, Kenny GM. Ether cystitis. JAMA. 1985;254:530.
75. Lebowitz RL, Effmann EL. Ether cystitis. Urology. 1978;12:427–8.
76. LYONS JS. Hematuria in workmen in aniline dye industry due to 5-chloro-ortho-toluidine; six case reports. J Urol. 1947;58:277–81.
77. Song P, Li X, Yan Y. Analysis of the literature on acute aromatic amino or nitro-compounds poisoning. Zhonghua Lao Dong Wei Shei Zhi Ye Bing Za Zhi. 2014;32:366–9.

78. Jurincic C, Horlbeck R, Metz K, Klippel KF. Acute hemorrhagic cystitis following chlordimeform poisoning. Dtsch Med Wochenschr. 1991;116:816–8.
79. Jain M, Palmo D, Agrawal V, Garg PK. Hemorrhagic cystitis: a rare manifestation of organophosphate poisoning. Urol Ann. 2014;6:271–2.
80. Chen CH, Lee MH, Chen YC, Lin MF. Ketamine-snorting associated cystitis. J Formos Med Assoc. 2011;110:787–91.
81. Ostroff EB, Chenault OW. Alum irrigation for the control of massive bladder hemorrhage. J Urol. 1982;128:929–30.
82. Goel AK, et al. Intravesical irrigation with alum for the control of massive bladder hemorrhage. J Urol. 1985;133:956–7.
83. Perazella M, Brown E. Acute aluminum toxicity and alum bladder irrigation in patients with renal failure. Am J Kidney Dis. 1993;21:44–6.
84. Phelps KR, Naylor K, Brien TP, Wilbur H, Haqqie SS. Encephalopathy after bladder irrigation with alum: case report and literature review. Am J Med Sci. 1999;318:181–5.
85. Singh I, Laungani GB. Intravesical epsilon aminocaproic acid in management of intractable bladder hemorrhage. Urology. 1992;40:227–9.
86. Rabinovitch HH. Simple innocuous treatment of massive cyclophosphamide hemorrhagic cystitis. Urology. 1979;13:610–2.
87. Ohhara M, et al. Severe cyclophosphamide hemorrhagic cystitis controlled with transurethral electrocoagulation: a case report. Hinyokika Kiyo. 1985;31:1045–8.
88. Kaplan JR, Wolf Jr JS. Efficacy and survival associated with cystoscopy and clot evacuation for radiation or cyclophosphamide induced hemorrhagic cystitis. J Urol. 2009;181:641–6.
89. Talab SS, McDougal WS, Wu C-L, Tabatabaei S. Mucosa-sparing. KTP laser coagulation of submucosal telangiectatic vessels in patients with radiation-induced cystitis: a novel approach. Urology. 2014;84:478–83.
90. Quinlan DM, Naslund MJ, Brendler CB. Application of argon beam coagulation in urological surgery. J Urol. 1992;147(2):410–2.
91. Suzuki S, et al. Successful use of endoscopic argon plasma coagulation for hemorrhagic radiation cystitis: a case report. Jpn J Clin Oncol. 2014;44:692–5.
92. Zhu J, Xue B, Shan Y, Yang D, Zang Y. Transurethral coagulation for radiation-induced hemorrhagic cystitis using Greenlight™ potassium-titanyl-phosphate laser. Photomed Laser Surg. 2013; 31:78–81.
93. Kumar S, Rosen P, Grabstald H. Intravesical formalin for the control of intractable bladder hemorrhage secondary to cystitis or cancer. J Urol. 1975;114:540.
94. Shah BC, Albert DJ. Intravesical instillation of formalin for the management of intractable hematuria. J Urol. 1973;110:519–20.
95. Brown RB. A method of management of inoperable carcinoma of the bladder. Med J Aust. 1969;1(1):23–4.
96. Choong S, Walkden M, Kirby R. The management of intractable haematuria. BJU Int. 2000;86:951–9.
97. Spiro LH, Hecht H, Horowitz A, Orkin L. Formalin treatment for massive bladder hemorrhage. Complications. Urology. 1973;2:669–71.
98. Godec CJ, Gleich P. Intractable hematuria and formalin. J Urol. 1983;130:688–91.
99. Rao MS, et al. Fatal complication of intravesical formalin during control of intractable hemorrhage from radiation cystitis. Urology. 1978;11:588–90.
100. Chugh KS, Singhal PC, Banerjee SS. Acute tubular necrosis following intravesical instillation of formalin. Urol Int. 1977;32: 454–9.
101. Kalish M, Silber SJ, Herwig KR. Papillary necrosis. Result of intravesical instillation of formalin. Urology. 1973;2(3):315–7.
102. Scott MP, Marshall S, Lyon RP. Bladder rupture following formalin therapy for hemorrhage secondary to cyclophosphamide therapy. Urology. 1974;3:364–5.
103. Finkelstein LH, Arsht DB, Trenkle D. Vesicoileal fistula: an unusual complication following the use of formalin for control of refractory post-irradiation bladder hemorrhage. J Urol. 1977;117: 168–70.
104. Lourie JA, Drysdale HC, Wynne EJ. Death following intravesical formalin instillation. Br J Urol. 1977;49:476.
105. Lojanapiwat B, Sripralakrit S, Soonthornphan S, Wudhikarn S. Intravesicle formalin instillation with a modified technique for controlling haemorrhage secondary to radiation cystitis. Asian J Surg. 2002;25:232–5.
106. Kumar AP, et al. Silver nitrate irrigation to control bladder hemorrhage in children receiving cancer therapy. J Urol. 1976;116:85–6.
107. Raghavaiah NV, Soloway MS. Anuria following silver nitrate irrigation for intractable bladder hemorrhage. J Urol. 1977;118: 681–2.
108. Susan LP, Marsh RJ. Phenolization of bladder in treatment of massive intractable hematuria. Urology. 1975;5:119–21.
109. Lebowitz RL. Intravesical chemical cauterization and methemoglobinemia. Pediatrics. 1980;65:630.
110. Levine LA, Jarrard DF. Treatment of cyclophosphamide-induced hemorrhagic cystitis with intravesical carboprost tromethamine. J Urol. 1993;149:719–23.
111. Mohiuddin J, Prentice HG, Schey S, Blacklock H, Dandona P. Treatment of cyclophosphamide-induced cystitis with prostaglandin E2. Ann Intern Med. 1984;101:142.
112. Trigg ME, et al. Prostaglandin E1 bladder instillations to control severe hemorrhagic cystitis. J Urol. 1990;143:92–4.
113. Shurafa M, Shumaker E, Cronin S. Prostaglandin F2-alpha bladder irrigation for control of intractable cyclophosphamide-induced hemorrhagic cystitis. J Urol. 1987;137:1230–1.
114. Miller LJ, Chandler SW, Ippoliti CM. Treatment of cyclophosphamide-induced hemorrhagic cystitis with prostaglandins. Ann Pharmacother. 1994;28:590–4.
115. Levine LA, Kranc DM. Evaluation of carboprost tromethamine in the treatment of cyclophosphamide-induced hemorrhagic cystitis. Cancer. 1990;66:242–5.
116. Ippoliti C, et al. Intravesicular carboprost for the treatment of hemorrhagic cystitis after marrow transplantation. Urology. 1995;46:811–5.
117. Corman JM, McClure D, Pritchett R, Kozlowski P, Hampson NB. Treatment of radiation induced hemorrhagic cystitis with hyperbaric oxygen. J Urol. 2003;169:2200–2.
118. Dellis A, Deliveliotis C, Kalentzos V, et al. Is there a role for hyberbaric oxygen as primary treatment for grade IV radiation-induced haemorrhagic cystitis? A prospective pilot-feasibility study and review of literature. Int Braz J Urol. 2014;40(3):296–305.
119. Oscarsson N, Arnell P, Lodding P, Ricksten SE, Seeman-Lodding H. Hyperbaric oxygen treatment in radiation-induced cystitis and proctitis: a prospective cohort study on patient-perceived quality of recovery. Int J Radiat Oncol Biol Phys. 2013;87:670–5.
120. Connolly SS, D'Arcy FT, Corcoran MO. Recombinant activated factor VII to control life-threatening haemorrhagic radiation cystitis. Ir J Med Sci. 2010;179:431–3.
121. Geisler JP, Linnemeier GC, Manahan KJ. Recombinant factor VIIa to treat late radiation-induced hemorrhagic cystitis: a case report. J Reprod Med. 2008;53:360–2.
122. Demesmay K, Tissot E, Bulabois CE, et al. Factor XIII replacement in stem-cell transplant recipients with severe hemorrhagic cystitis: a report of four cases. Transplantation. 2002;74:1190–2.
123. Aroney RS, Dalley DN, Levi JA. Haemorrhagic cystitis treated with epsilon-aminocaproic acid. Med J Aust. 1980;2:92.
124. Eigner EB, Freiha FS. The fate of the remaining bladder following supravesical diversion. J Urol. 1990;144:31–3.
125. Fazili T, Bhat TR, Masood S, Palmer JH, Mufti GR. Fate of the leftover bladder after supravesical urinary diversion for benign disease. J Urol. 2006;176:620–1.

126. Linder BJ, Tarrell RF, Boorjian SA. Cystectomy for refractory hemorrhagic cystitis: contemporary etiology, presentation and outcomes. J Urol. 2014;192:1687–92.
127. Schuhrke TD, Barr JW. Intractable bladder hemorrhage: therapeutic angiographic embolization of the hypogastric arteries. J Urol. 1976;116:523–5.
128. Appleton DS, Sibley GN, Doyle PT. Internal iliac artery embolisation for the control of severe bladder and prostate haemorrhage. Br J Urol. 1988;61:45–7.
129. Nabi G. Therapeutic transcatheter arterial embolization in the management of intractable haemorrhage from pelvic urological malignancies: preliminary experience and long-term follow-up. BJU Int. 2003;92:245–7.
130. Rastinehad AR. Selective arterial prostatic embolization (SAPE) for refractory hematuria of prostatic origin. Urology. 2008;71: 181–4.
131. Delgal A, et al. Outcome of transcatheter arterial embolization for bladder and prostate hemorrhage. J Urol. 2010;183: 1947–53.
132. Lang EK. Transcatheter embolization of hypogastric branch arteries in the management of intractable bladder hemorrhage. J Urol. 1979;121:30–6.
133. Loffroy R, et al. Current role of transcatheter arterial embolization for bladder and prostate hemorrhage. Diagn Interv Imaging. 2014;95:1027–34.
134. Hald T, Mygind T. Control of life threatening vesical hemorrhage by unilateral hypogastric artery muscle embolization. J Urol. 1974;112:60–3.
135. Berradinis D. Superselective embolization of bladder arteries in the treatment of intractable bladder hemorrhage. Int J Urol. 2005;12:503–5.
136. Lilly JD, Parsons CL. Bladder surface glycosaminoglycans is a human epithelial permeability barrier. Surg Gynecol Obstet. 1990;171(6):493–6.
137. Shao Y, Lu G-l, Shen Z-j. Comparison of intravesical hyaluronic acid instillation and hyperbaric oxygen in the treatment of radiation-induced hemorrhagic cystitis. BJU Int. 2012;109:691–4.
138. Thompson A, et al. Guidelines for the diagnosis, prevention and management of chemical-and radiation-induced cystitis. J Clin Urol. 2014;7:25–35.
139. Nordling J, van Ophoven A. Intravesical glycosaminoglycan replenishment with chondroitin sulphate in chronic forms of cystitis. A multi-national, multi-centre, prospective observational clinical trial. Arzneimittelforschung. 2007;58:328–35.
140. Purves JT, Graham ML, Ramakumar S. Application of fibrin glue to damaged bladder mucosa in a case of BK viral hemorrhagic cystitis. Urology. 2005;66(3):641–3.
141. Tirindelli MC, et al. Fibrin glue therapy for severe hemorrhagic cystitis after allogeneic hematopoietic stem cell transplantation. Biol Blood Marrow Transplant. 2014;20:1612–7.

Endovascular Management of Priapism and Erectile Dysfunction

25

Jeremy Cash Horn, Vivian L. Bishay, Aaron M. Fischman, and Robert A. Lookstein

Relevant Anatomy and Physiology

The penis is composed of three cylindrical cavernous bodies of erectile tissue: the paired corpora cavernosa dorsally and the single corpus spongiosum ventrally, which contains the urethra. Each cylinder has an outer fibrous capsule called tunica albuginea. The three bodies are composed of erectile tissue—an anastomosing network of cavernous vascular spaces lined with endothelia within a loose connective tissue support.

Although there is frequent anatomic variation, the arterial supply to the penis is supplied mainly by branches of the internal pudendal arteries, which usually arise from the anterior division of the internal iliac artery (Fig. 25.1). After giving off the inferior rectal arteries and the perineal-scrotal artery (as well as smaller branches including the bulbar artery and urethral artery), the internal pudendal artery becomes the penile artery. There are two terminal branches of the penile artery: the dorsal artery of the penis and the deep artery of the penis (cavernosal artery). The dorsal arteries of the penis are paired arteries that run on each side of the single deep dorsal vein in the dorsal groove between the corpora cavernosa. Deep arteries of the penis run near the center of each corpora cavernosa, supplying the erectile tissue after dividing into helicine arteries, which enter the lacunar spaces of the corpora. Additionally, superficial and deep branches of the external pudendal arteries supply the penis and anastomose with the branches of the internal pudendal arteries.

Venous drainage of the cavernous spaces is via three sets of veins (Fig. 25.2). The superficial dorsal vein drains the skin and subcutaneous tissues of the penis, ultimately draining into the superficial external pudendal vein. The deep dorsal vein drains the glans penis, the corpus spongiosum, and part of the corpora cavernosa. The cavernous veins are a venous plexus that drain the corpora and join the deep dorsal vein of the penis, which drains into the prostatic venous plexus.

Erection is a neurovascular event. During the flaccid state, blood flow to the cavernous spaces is minimal due to vasoconstriction of the vasculature and shunting of blood flow away from the cavernous spaces. In response to sexual arousal, the parasympathetic nerves innervating the vascular smooth muscle of the deep arteries release nitric oxide, initiating a cascade that results in muscular relaxation. The vasodilation allows blood to flow into the cavernous spaces to induce engorgement and erection. This also has the effect of increasing pressure on the veins in the penis, reducing venous drainage.

Priapism

Priapism is a persistent erection of the penis that occurs hours beyond or in the absence of sexual stimulation [1]. Typically, priapism only affects the corpora cavernosa and is related to differences in the arterial inflow and venous outflow. Classically, two forms of priapism have been described—low flow (veno-occlusive, ischemic) and high flow (arterial, non-ischemic)—both of which differ in the etiologic pathophysiology and the available treatment options.

Low-Flow Priapism

Low-flow (veno-occlusive, ischemic) priapism is the most common type and is caused by impaired outflow from the corpora cavernosa. This leads to painful engorgement of the corpora cavernosa and subsequent ischemia of a cavernous tissue. This form of priapism is considered a form of compartment syndrome and therefore a urological emergency due to the potential for permanent damage to penile tissue and high frequency of erectile dysfunction if left untreated.

J.C. Horn, MD • V.L. Bishay, MD • A.M. Fischman, MD
R.A. Lookstein, MD, FSIR (✉)
Division of Interventional Radiology, Department of Radiology, Mount Sinai Hospital, New York, NY, USA
e-mail: robert.lookstein@mssm.edu

A.R. Rastinehad, D.N. Siegel (eds.), *Interventional Urology*, DOI 10.1007/978-3-319-23464-9_25

The duration of priapism is the most important predictor of the development of subsequent erectile function in the setting of low-flow priapism [2]. Low-flow priapism can be associated with sickle cell disease, hematological malignancies, or medications; however, it most commonly is idiopathic in etiology [3]. Treatment of this form of priapism involves decompression of the corpora cavernosa via needle aspiration, which allows recovery of intracorporeal blood circulation. If this fails, direct injection of sympathomimetic agents is recommended prior to initiating surgical intervention [1]. There is little or no role of endovascular therapy in the management of low-flow priapism.

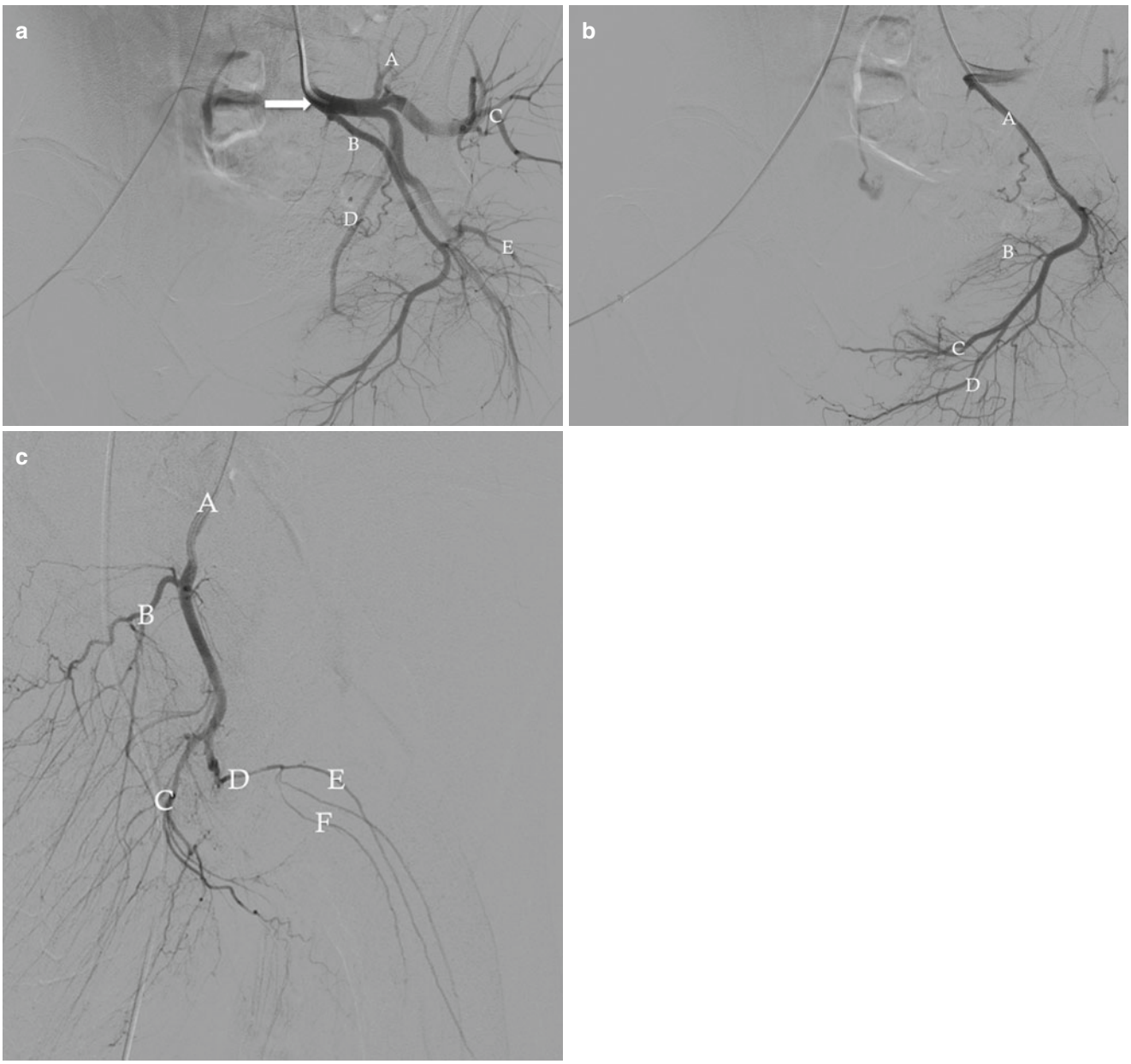

Fig. 25.1 (**a**): *Arrow*: Catheter tip in the left internal iliac artery demonstrating a selective digital subtraction angiography (DSA) of left internal iliac artery anatomy. *A*: Lateral sacral artery. *B*: Internal pudendal artery. *C*: Superior gluteal artery. *D*: Obturator artery. *E*: Inferior gluteal artery. (**b**) Selective DSA of normal internal pudendal artery anatomy. *A*: Internal pudendal artery. *B*: Inferior rectal branches. *C*: Penile artery. *D*: Perineal-scrotal artery. (**c**) Selective DSA of the internal pudendal artery demonstrating more distal branches. *A*: Internal pudendal artery. *B*: Inferior rectal arteries. *C*: Perineal-scrotal artery. *D*: Penile artery. *E*: Dorsal artery of the penis. *F*: Cavernosal artery. (**d**) Schematic drawing of the arterial anatomy supplying the penis. (**e**) Schematic drawing of the cross-sectional vascular anatomy of the penis

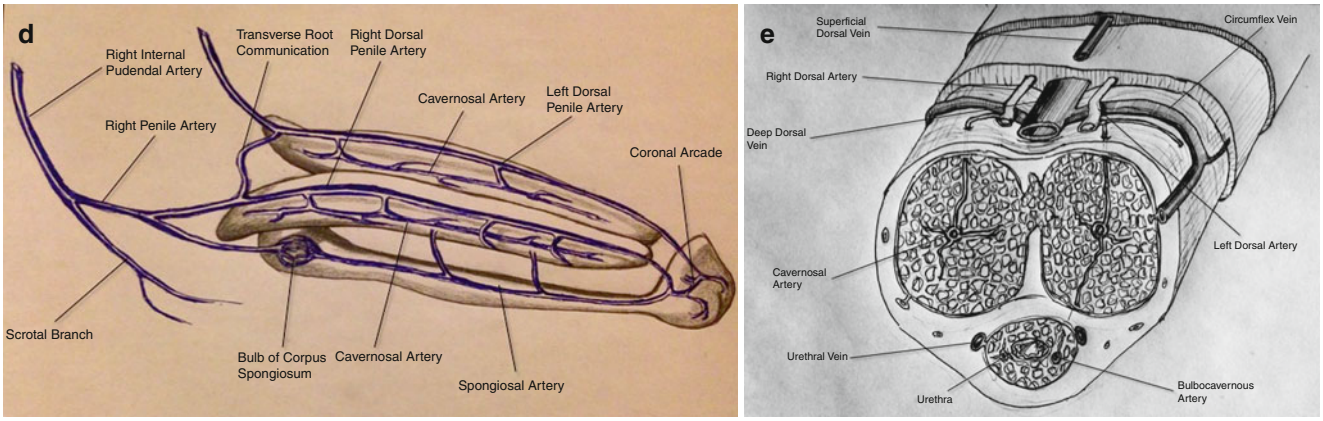

Fig. 25.1 (continued)

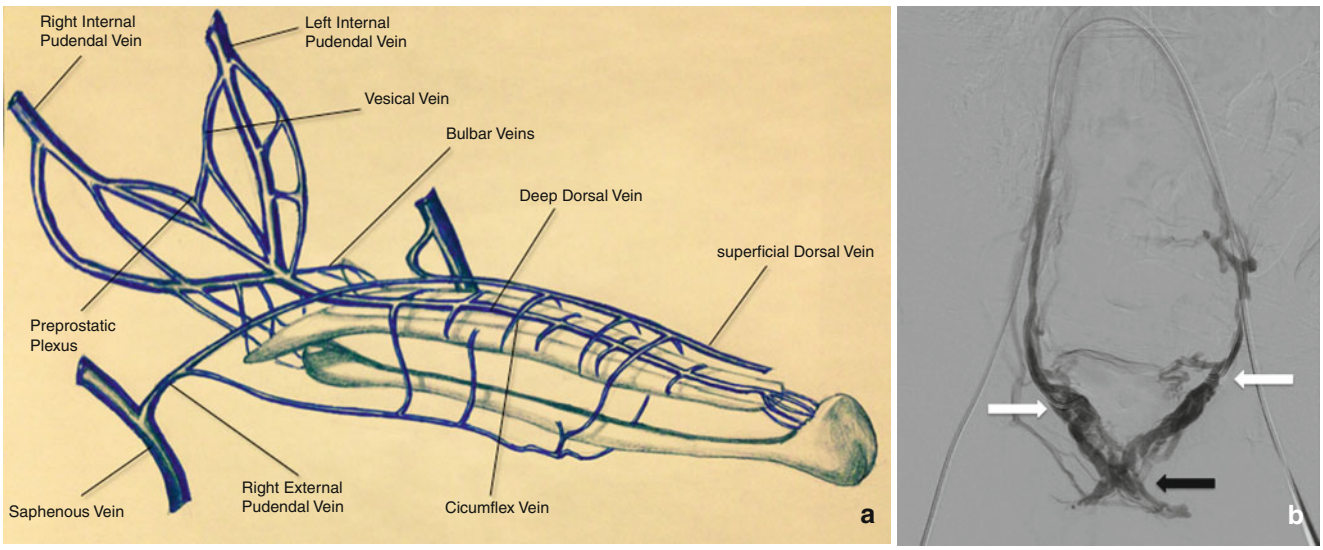

Fig. 25.2 (**a**) Schematic drawing of the venous drainage of the penis. (**b**) Venogram depicting the prostatic venous plexus. Access was obtained through the bilateral femoral veins. The catheters are seen extending through the contralateral internal iliac veins, with bilateral catheter tips at the junction of the internal pudendal veins/prostatic plexus (*white arrows*). Contrast is seen refluxing into the prostatic plexus (*black arrow*)

High-Flow Priapism

Classification and Pathophysiology

High-flow priapism, also called nonischemic or arterial priapism, is a rare condition that usually results from perineal or penile trauma, which leads to arteriocavernous fistula formation. Blood flows from one of the terminal branches of the internal pudendal artery—usually the cavernosal artery—into the lacunar spaces of the corpora cavernosa. The lacunar endothelium is then exposed to oxygenated blood with high velocity and turbulent flow causing shearing forces, which stimulate the release of nitric oxide. This results in arterial and trabecular dilatation throughout the corpora cavernosa [4, 5].

High-flow priapism can develop immediately following trauma or may not develop for a number of days following the inciting event. Arterial priapism is not a medical emergency because venous outflow remains intact and therefore the penis is not ischemic. The priapism can therefore persist for long periods of time without permanent damage of penile tissues [6].

Presentation

Clinically, a patient with high-flow priapism typically reports an erection that is not associated with pain and is frequently intermittent or not fully rigid. Typically there is a delay between the injury and the development of the priapism that may be up to a few days or longer. On physical examination, the corpora

are tumescent but not fully rigid (in contrast to low-flow priapism), and there may be signs of perineal or penile trauma.

Diagnostic Evaluation

Needle aspiration, while not utilized in the treatment of high-flow priapism, can have a diagnostic role as one of the initial steps in determining if the priapism can be characterized as high or low flow. Diagnostic evaluation can also utilize ultrasound, which will show hypoechoic regions in the region of the arterial-sinusoidal fistula as well as direct visualization of the fistula on color Doppler imaging [4, 7]. Both computed tomography angiography (CTA) and magnetic resonance angiography (MRA) have also been demonstrated as an effective tool for displaying penile arterial and venous anatomy and localizing the site of the fistula [8, 9].

Management

The American Urological Association states that the majority of arterial priapism cases resolve spontaneously and recommend conservative management as the first-line treatment for this form of priapism [1]. However, some studies suggest a low rate of resolution with conservative management [10] or only temporary resolution with conservative options, including ultrasonographic compression or intracavernous injection of alpha-adrenergic agents [11]. Many centers now manage this form of priapism by performing radiologic embolization of the feeding artery (Fig. 25.3). This technique was first described in 1977 utilizing autologous clot [12]. Since that time a number of studies have been published describing the technique with a variety of embolic agents, including Gelfoam, PVA, microcoils, and NBCA [10, 13, 14]. Although rare cases of bilateral fistulas have been described, unilateral embolization is recommended to avoid the risk of gangrene and erectile dysfunction. If bilateral embolization is necessary, absorbable embolic materials are preferred.

Overall clinical success rates with embolization are high, with resolution of the priapism seen within 24 h following the procedure. Recurrence rates ranging from 7 to 27 % have been reported after a single embolization treatment [15], also usually seen within the first 24 h following the procedure.

Erectile Dysfunction

Erectile dysfunction is the inability to achieve an erection or maintain an erection sufficient for satisfactory sexual performance [16]. The overall prevalence in the US male population over the age of 20 is approximately 18 %. The incidence increases with age, with approximately 70.25 % of men aged 70 years or older affected [17]. It is particularly associated with cardiovascular risk factors, including diabetes mellitus, hypertension, vascular disease, and dyslipidemia.

The AUA recommends that the initial evaluation of ED includes a complete medical, sexual, and psychosocial history [16]. The international index of erectile function (IIEF) is a questionnaire that has been developed to objectively assess erectile function [18]. The first-line therapy includes lifestyle and pharmacotherapy modification, as well as oral therapy with phosphodiesterase-5 inhibitors [19].

Further diagnostic testing is performed in a case-by-case manner and is based on the findings found during routine diagnostic workup. Because normal sexual function requires interactions among vascular, neurogenic, hormonal, and psychological systems, ED can result from the dysfunction of any one of these systems. Once psychogenic, neurogenic, and hormonal factors have been eliminated as possible causes, the focus shifts to an investigation of possible vasculogenic factors. Specific vascular causes of ED may be related to veno-occlusive dysfunction (VOD) or arterial insufficiency, both of which may be amenable to endovascular therapy.

Veno-Occlusive Dysfunction

With veno-occlusive dysfunction, incomplete relaxation of the corporeal smooth muscles causes incomplete resistance to outflow of blood from the corpora (previously termed "venous leakage") and thus incomplete erection [20]. Patients with VOD often fare poorly with oral pharmacotherapy and frequently require long-term intracavernosal injection therapy [21]. Abnormalities of the venous system in erection can be diagnosed by cavernosometry, and the site of the venous "leakage" can be assessed with cavernosography. Both techniques are generally employed in young men who are already diagnosed with ED to evaluate for VOD.

In traditional cavernosography, two intracavernosal 19- to 21-gauge butterfly needles are placed dorsolaterally in each corpus cavernosum, approximately halfway down the shaft. Contrast medium diluted at approximately 1:4 with heparinized saline is slowly infused through one of the needles at a rate starting at 40 ml/min, with the rate slowly increased over time. Only one side needs to be injected because the septum between the corpora cavernosa is fenestrated. The contrast medium will be seen filling both corpora and the superficial and deep veins draining the pelvis. The second catheter is attached to a pressure transducer to record intracavernous pressure change. The flow rates needed to induce and maintain an erection are recorded [22].

In normal patients, infusion of approximately 80–120 mL of fluid will produce tumescence and finally an erection, with erection maintained at flow rates between 15 and 50 mL/min. Intracavernous pressure will rise to at least 80 mmHg for the duration of the erection. Veno-occlusive dysfunction is characterized by the absence of erection without significant

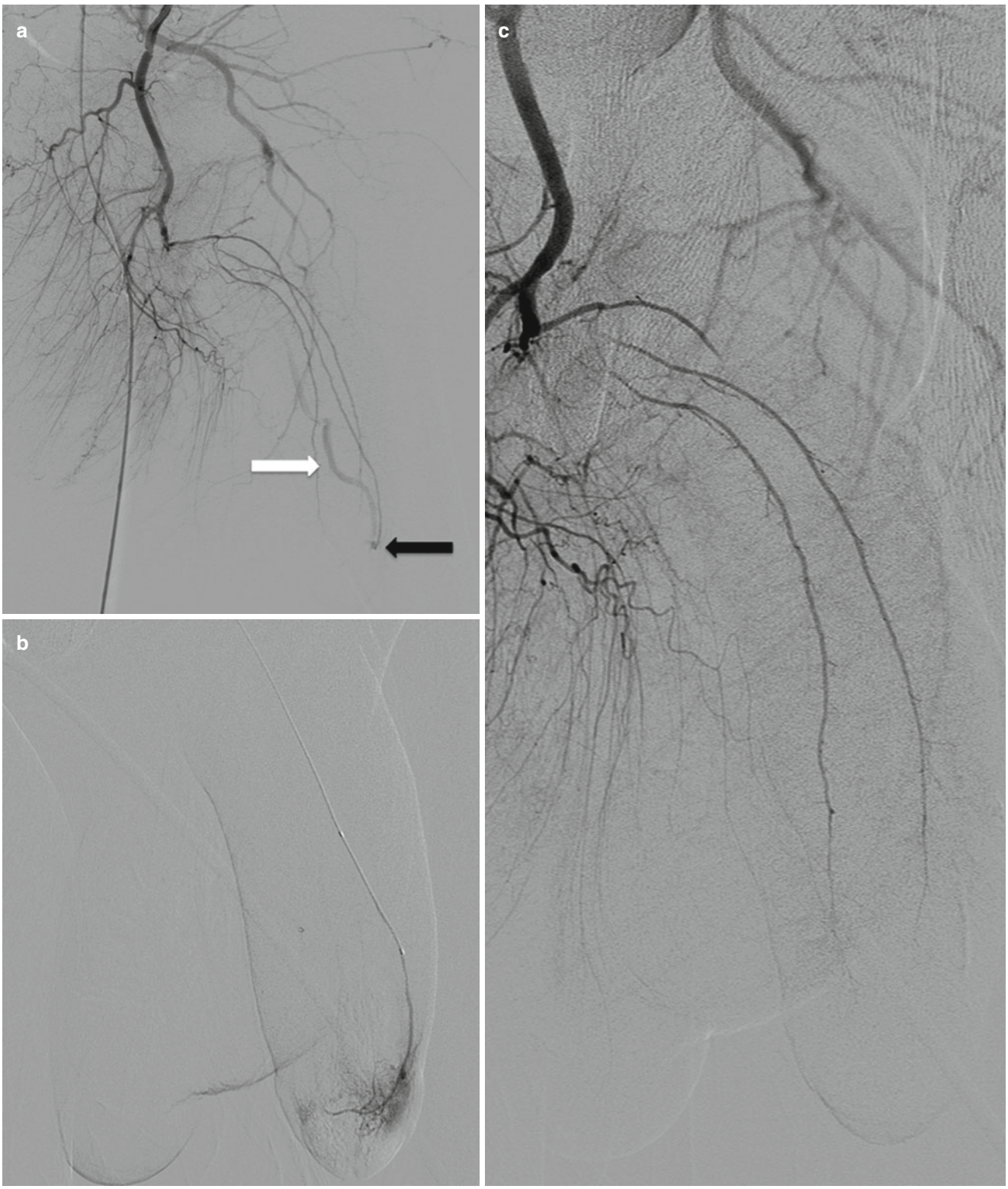

Fig. 25.3 (**a**) Selective catheterization of the left internal pudendal artery demonstrates early filling of the deep dorsal vein of the penis (*white arrow*) via an AV fistula in the distal aspect of the penis (*black arrow*). (**b**) More distal catheterization demonstrates the AV fistula with contrast filling the lacunar spaces of the distal corpora. (**c**) Control angiogram after embolization with Gelfoam demonstrates no visualization of the AV fistula. Patient's intermittent priapism resolved within 2 weeks following the procedure

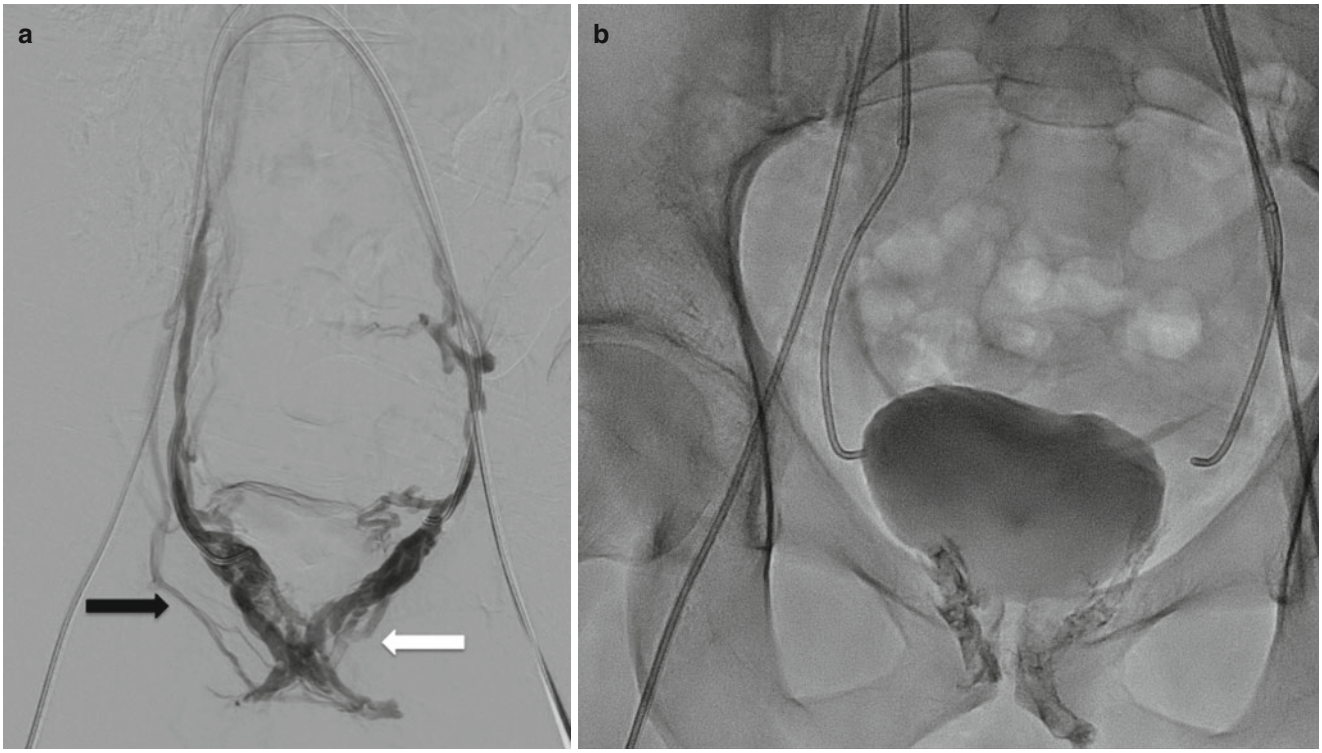

Fig. 25.4 (**a**) Selective venography of the bilateral internal pudendal veins demonstrates reflux of contrast into the periprostatic venous plexus (*white arrow*) and right external pudendal vein (*black arrow*). (**b**) Following injection of NBCA mixed with contrast, there is occlusion of flow within the periprostatic plexus. The patient reported an improvement in his erectile dysfunction in the month following the procedure

increase of the intracavernous pressure. In many patients with VOD, much higher flow rates are needed to induce and subsequently maintain an erection [23].

Dynamic infusion cavernosometry and cavernosography (DICC) is a more comprehensive technique to evaluate the hemodynamic function of the penis. Unlike conventional cavernosography, DICC is performed after the intracavernosal injection of vasoactive agents, which lead to a pharmacologically induced erection, with subsequent provocative tests to determine the ability of the corpora cavernosa to optimally increase their venous outflow resistance. Systolic occlusion pressures in the left and right cavernosal arteries are also measured, which can help identify arterial occlusion or stenosis in the cavernous arterial bed [24].

Historically, erectile dysfunction caused by veno-occlusive dysfunction was treated by surgical ligation of the deep dorsal vein. Since that time, other surgical approaches have been described that include venous stripping or penile vascularization [25]. Subsequent research has investigated the role of interventional embolization of the deep dorsal vein of the penis in the treatment of erectile dysfunction caused by veno-occlusive dysfunction [20, 21, 26–30].

Ultrasound-guided catheterization of the deep dorsal vein of the penis is the most commonly described method for embolization. After gaining access, venography can be performed to allow visualization of the periprostatic venous plexus as well as the internal and external pudendal veins. The endpoint of the embolization procedure is complete occlusion of the periprostatic venous plexus and related efferents. The most common embolic material that has been described has been NBCA [20, 21, 30] mixed with a contrast agent. It is recommended that application of the embolic material is performed during Valsalva maneuver to reduce the incidence of distal progression of the glue.

An alternative technique that has been described is retrograde access to the periprostatic venous plexus via a femoral vein approach (Fig. 25.4) [29–31]. Using this technique, the venous anatomy can be evaluated first by selective venography of the internal pudendal vein, followed by subsequent selective catheterizations leading up to the confluence of the dorsal penile vein into the venous prostatic plexus. Attempt should be made to reach the most distal venous point when using this approach.

Follow-up should involve the use of the IIEF-6, a questionnaire that quantifies erectile function. Repeat cavernosometry and cavernosography should also be performed. Studies have described varying success following DDV embolization, with reported clinical success (the ability to reach and maintain an erection) ranging from 68 to 89 %.

Arterial Insufficiency

Arterial insufficiency of the penis may result from atherosclerotic arterial lesions of the internal pudendal arteries or their terminal branches to the penis or from microangiopathy of the deep arteries (helicine arteries) of the corpora cavernosa. Decreased arterial inflow due to aortoiliac occlusions, as in Leriche syndrome, has also been associated with erectile dysfunction [32]. It has been well documented that erectile dysfunction shares common risk factors and often coexists with cardiovascular disease, as well as acting as an independent risk factor for future cardiovascular events [33, 34]. Thus, it is unsurprising that arterial disease can play a significant role in the pathogenesis of erectile dysfunction. Importantly, arteriogenic erectile dysfunction is associated with decreased rates of response to PDE5 inhibitors, suggesting the need for alternative therapy in this patient population [35].

In patients that are candidates for penile arterial angioplasty on the basis of DICC evaluation, conventional angiography or computed tomographic angiography (CTA) studies can be performed to demonstrate the anatomy and distribution of arterial lesions [36]. In order to achieve excellent visualization of the small arteries that constitute the penile blood supply, it is beneficial to maximize penile arterial inflow via pharmacologic induction of an erection [24].

Although arterial stenoses could theoretically be present anywhere in the ilio-pudendal-penile arterial system in patients with arteriogenic erectile dysfunction, studies have shown that the majority of lesions (up to 90 %) are located in the common penile and internal pudendal arteries [37]. Lesions are most frequently multifocal, and isolated internal pudendal artery intervention will therefore be unsuccessful without simultaneous intervention of the more distal penile artery. The average diameters of the penile and internal pudendal arteries are 1–2 and 2–3 mm, respectively [37]. Early interventional treatment of arteriogenic erectile dysfunction was directed toward the larger arteries, including the common iliac and internal iliac arteries [38, 39]. However, with advancement in interventional techniques, more recent research has been directed toward treatment of these smaller caliber arteries—including both the internal pudendal and penile arteries [37, 40, 41].

For transluminal angioplasty of the distal internal pudendal or penile arteries, either an ipsilateral or contralateral femoral approach can be used. Arterial flow should be augmented with intracavernosal injection of papaverine (30–60 mg) [42]. An alternative option is the injection of intra-arterial nitroglycerin (150–200 ug) [37, 43]. Unilateral dilatation is usually sufficient to provide clinical success, as the patency of a single cavernosal artery can provide adequate blood flow and pressure for erection [41].

Although there is limited research investigating the role of angioplasty in the treatment of ED, recent research has demonstrated improvement in erectile function in up to 60 % of patients with erectile dysfunction not initially responsive to PDE5 inhibitors with penile artery stenoses [37]. Newer studies are investigating the role of drug-eluting stents for focal atherosclerotic lesions of the internal pudendal arteries in patients with erectile dysfunction, with reported clinical success of 68 % [44].

References

1. Montague DK, Jarow J, Broderick GA, Dmochowski RR, Heaton JP, Lue TF, et al. American Urological Association guideline on the management of priapism. J Urol. 2003;170(4 Pt 1):1318–24. PubMed.
2. Salonia A, Eardley I, Giuliano F, Hatzichristou D, Moncada I, Vardi Y, et al. European Association of Urology guidelines on priapism. Eur Urol. 2014;65(2):480–9. PubMed.
3. Broderick GA, Kadioglu A, Bivalacqua TJ, Ghanem H, Nehra A, Shamloul R. Priapism: pathogenesis, epidemiology, and management. J Sex Med. 2010;7(1 Pt 2):476–500. PubMed.
4. Bertolotto M, Quaia E, Mucelli FP, Ciampalini S, Forgacs B, Gattuccio I. Color Doppler imaging of posttraumatic priapism before and after selective embolization. Radiographics. 2003;23(2):495–503. PubMed.
5. Kim N, Vardi Y, Padma-Nathan H, Daley J, Goldstein I, Saenzde Tejada I. Oxygen tension regulates the nitric oxide pathway. Physiological role in penile erection. J Clin Invest. 1993;91(2):437–42. PubMed Pubmed Central PMCID: 287949.
6. Bastuba MD, Saenz de Tejada I, Dinlenc CZ, Sarazen A, Krane RJ, Goldstein I. Arterial priapism: diagnosis, treatment and long-term followup. J Urol. 1994;151(5):1231–7. PubMed.
7. Feldstein VA. Posttraumatic "high-flow" priapism evaluation with color flow Doppler sonography. J ultrasound Med. 1993;12(10):589–93. PubMed.
8. White C, Gulati M, Gomes A, Rajfer J, Raman S. Pre-embolization evaluation of high-flow priapism: magnetic resonance angiography of the penis. Abdom Imaging. 2013;38(3):588–97. PubMed.
9. Suzuki K, Nishizawa S, Muraishi O, Fujita A, Hyodoh H, Tokue A. Post-traumatic high flow priapism: demonstrable findings of penile enhanced computed tomography. Int J Urol. 2001;8(11):648–51. PubMed.
10. Zhao S, Zhou J, Zhang YF, Zhang XL, Long QY. Therapeutic embolization of high-flow priapism 1 year follow up with color Doppler sonography. Eur J Radiol. 2013;82(12):e769–74. PubMed.
11. Mizutani M, Nakano H, Sagami K, Nihira H. Treatment of post-traumatic priapism by intracavernous injection of alpha-stimulant. Urol Int. 1986;41(4):312–4. PubMed.
12. Wear Jr JB, Crummy AB, Munson BO. A new approach to the treatment of priapism. J Urol. 1977;117(2):252–4. PubMed.
13. Towbin R, Hurh P, Baskin K, Cahill AM, Carr M, Canning D, et al. Priapism in children: treatment with embolotherapy. Pediatr Radiol. 2007;37(5):483–7. PubMed.
14. Ozturk MH, Gumus M, Donmez H, Peynircioglu B, Onal B, Dinc H. Materials in embolotherapy of high-flow priapism: results and long-term follow-up. Diagn Interv Radiol. 2009;15(3):215–20. PubMed.
15. Bertolotto M, Zappetti R, Pizzolato R, Liguori G. Color Doppler appearance of penile cavernosal-spongiosal communications in patients with high-flow priapism. Acta Radiol. 2008;49(6):710–4. PubMed.
16. Montague DK, Jarow JP, Broderick GA, Dmochowski RR, Heaton JP, Lue TF, et al. Chapter 1: the management of erectile dysfunction: an AUA update. J Urol. 2005;174(1):230–9. PubMed.

17. Selvin E, Burnett AL, Platz EA. Prevalence and risk factors for erectile dysfunction in the US. Am J Med. 2007;120(2):151–7. PubMed.
18. Rosen RC, Cappelleri JC, Gendrano 3rd N. The International Index of Erectile Function (IIEF): a state-of-the-science review. Int J Impot Res. 2002;14(4):226–44. PubMed.
19. Heidelbaugh JJ. Management of erectile dysfunction. Am Fam Physician. 2010;81(3):305–12. PubMed.
20. Peskircioglu L, Tekin I, Boyvat F, Karabulut A, Ozkardes H. Embolization of the deep dorsal vein for the treatment of erectile impotence due to veno-occlusive dysfunction. J Urol. 2000;163(2): 472–5. PubMed.
21. Rebonato A, Auci A, Sanguinetti F, Maiettini D, Rossi M, Brunese L, et al. Embolization of the periprostatic venous plexus for erectile dysfunction resulting from venous leakage. J Vasc Interv Radiol. 2014;25(6):866–72. PubMed.
22. Delcour C, Wespes E, Vandenbosch G, Schulman CC, Struyven J. Impotence: evaluation with cavernosography. Radiology. 1986;161(3):803–6. PubMed.
23. Delcour CP, Vandenbosch GA, Struyven JL. Cavernosography and cavernosometry in the evaluation of impotence. Urol Radiol. 1988;10(3):144–50. PubMed.
24. Rosen MP, Schwartz AN, Levine FJ, Greenfield AJ. Radiologic assessment of impotence: angiography, sonography, cavernosography, and scintigraphy. AJR Am J Roentgenol. 1991;157(5):923–31; discussion 32–4. PubMed.
25. Lewis RW. Venous surgery for impotence. Urol Clin North Am. 1988;15(1):115–21. PubMed.
26. Courtheoux P, Maiza D, Henriet JP, Vaislic CD, Evrard C, Theron J. Erectile dysfunction caused by venous leakage: treatment with detachable balloons and coils. Radiology. 1986;161(3):807–9. PubMed.
27. Schwartz AN, Lowe M, Harley JD, Berger RE. Preliminary report: penile vein occlusion therapy: selection criteria and methods used for the transcatheter treatment of impotence caused by venous-sinusoidal incompetence. J Urol. 1992;148(3):815–20. PubMed.
28. Schild HH, Mildenberger P, Kersjes W. Effectiveness of platinum wire microcoils for venous occlusion: a study on patients treated for venogenic impotence. Cardiovasc Intervent Radiol. 1994;17(3):170–2. PubMed.
29. Basche S, Eger C, Elsebach K, Ulshofer B. [Veno-occlusive dysfunction as a cause of erectile impotence: therapy of venous leak with retrograde embolization of the internal pudendal vein]. VASA Zeitschrift fur Gefasskrankheiten. 2003;32(1):47–50. PubMed Venookklusive Dysfunktion als Ursache der erektilen Impotenz: Therapie des venosen Lecks durch retrograde Embolisation der V. pudenda interna.
30. Aschenbach R, Steiner T, Kerl MJ, Zangos S, Basche S, Vogl TJ. Endovascular embolisation therapy in men with erectile impotence due to veno-occlusive dysfunction. Eur J Radiol. 2013;82(3):504–7. PubMed.
31. Schild HH, Muller SC. Retrograde penile venoablation. Ann Acad Med Singapore. 1993;22(5):675–8. PubMed.
32. Spiliopoulos S, Shaida N, Katsanos K, Krokidis M. The role of interventional radiology in the diagnosis and management of male impotence. Cardiovasc Intervent Radiol. 2013;36(5):1204–12. PubMed.
33. Gandaglia G, Briganti A, Jackson G, Kloner RA, Montorsi F, Montorsi P, et al. A systematic review of the association between erectile dysfunction and cardiovascular disease. Eur Urol. 2014;65(5):968–78. PubMed.
34. Thompson IM, Tangen CM, Goodman PJ, Probstfield JL, Moinpour CM, Coltman CA. Erectile dysfunction and subsequent cardiovascular disease. JAMA. 2005;294(23):2996–3002. PubMed.
35. Gamidov SI, Mazo EB, Ovchinnikov RI, Andranovich SV, Iremashvili VV. [Prediction of clinical efficacy of levitra (vardenafil) in patients with arteriogenic erectile dysfunction]. Urologiia. 2006;(4):44–9. PubMed.
36. Kawanishi Y, Lee KS, Kimura K, Kojima K, Yamamoto A, Numata A. Feasibility of multi-slice computed tomography in the diagnosis of arteriogenic erectile dysfunction. BJU Int. 2001;88(4):390–5. PubMed.
37. Wang TD, Lee WJ, Yang SC, Lin PC, Tai HC, Hsieh JT, et al. Safety and six-month durability of angioplasty for isolated penile artery stenoses in patients with erectile dysfunction: a first-in-man study. EuroIntervention. 2014;10(1):147–56. PubMed.
38. Castaneda-Zuniga WR, Smith A, Kaye K, Rusnak B, Herrerra M, Miller R, et al. Transluminal angioplasty for treatment of vasculogenic impotence. AJR Am J Roentgenol. 1982;139(2):371–3. PubMed.
39. Goldwasser B, Carson 3rd CC, Braun SD, McCann RL. Impotence due to the pelvic steal syndrome: treatment by iliac transluminal angioplasty. J Urol. 1985;133(5):860–1. PubMed.
40. Zumbe J, Drawz G, Wiedemann A, Grozinger K, Engelmann U. Indications for penile revascularization and long-term results. Andrologia. 1999;31 Suppl 1:83–7. PubMed.
41. Valji K, Bookstein JJ. Transluminal angioplasty in the treatment of arteriogenic impotence. Cardiovasc Intervent Radiol. 1988;11(4): 245–52. PubMed.
42. Bookstein JJ, Valji K, Parsons L, Kessler W. Pharmacoarteriography in the evaluation of impotence. J Urol. 1987;137(2):333–7. PubMed.
43. Bookstein JJ, Lang EV. Penile magnification pharmacoarteriography: details of intrapenile arterial anatomy. AJR Am J Roentgenol. 1987;148(5):883–8. PubMed.
44. Rogers JH, Goldstein I, Kandzari DE, Kohler TS, Stinis CT, Wagner PJ, et al. Zotarolimus-eluting peripheral stents for the treatment of erectile dysfunction in subjects with suboptimal response t o phosphodiesterase-5 inhibitors. J Am Coll Cardiol. 2012;60(25): 2618–27. PubMed.

Part V

Adrenal

Adrenal Imaging

26

Kefu Du, Marta E. Heilbrun, and Jay T. Bishoff

Anatomy

The adrenal glands are retroperitoneal organs located on the lateral edges of the vertebral column in front of the 12th rib on the right and the 11th and 12th ribs on the left [1]. They lie superior or superomedial to the upper pole of the kidneys and anterior to the crus of the diaphragm. The left gland is bound medially by the aorta and covered anteriorly by the stomach, pancreas, and splenic vessels. The right adrenal gland lies lateral to the inferior vena cava and posterior to the liver [2]. Both are embedded in the perirenal fat and enclosed by the Gerota's fascia [1, 2]. The left adrenal is crescent-shaped, and the right adrenal is triangular in shape [1, 3]. Each adrenal gland is approximately 5 × 3 × 1 cm in size and weighs between 4 and 6 g [1, 3]. The superior adrenal arteries arise from the inferior phrenic arteries and provide the main blood supply; the middle adrenal arteries branch from the aorta; and the inferior adrenal arteries branch from the renal arteries [2, 4]. The left adrenal vein joins the inferior phrenic vein and drains into the left renal vein, while the short right adrenal vein drains directly into the posterior surface of the inferior vena cava. [1, 2, 4]. The main lymphatic drainage of the adrenal glands is through the para-aortic lymph nodes on the left and the paracaval lymph nodes on the right [2].

K. Du, MD
Division of Urology, University of Utah School of Medicine, Salt Lake City, UT, USA

J.T. Bishoff, MD, FACS (✉)
Department of Urology, Intermountain Medical Center, Murray, UT, USA

Division of Urology, University of Utah School of Medicine, Salt Lake City, UT, USA
e-mail: Jay.Bishoff@imail.org

M.E. Heilbrun, MD, MS
Department of Radiology, University of Utah School of Medicine, Salt Lake City, UT, USA

Embryology

The adrenal cortex is derived from the intermediate mesoderm of the urogenital ridge, and the adrenal medulla arises from the neural crest cells in the adjacent neuroectoderm sympathetic ganglia at the level of the celiac plexus [5]. Since the adrenals and kidneys have separate embryologic origins, the ipsilateral adrenal is usually present and normally located in cases of renal agenesis, malrotation, or malposition, but they assume a discoid shape [5]. At birth, the adrenal gland is twice the weight of an adult gland and is roughly one third the size of the neonatal kidney, whereas the size of the adult gland is about 8 % of that of the kidney [5, 6]. The fetal cortex rapidly regresses and disappears by 6 months of age, while the adult zona glomerulosa and fasciculata fully differentiate by age three. Zona reticularis develops after 4 years of age and may take up to 15 years of age to fully differentiate [6].

Physiology

The adrenal gland consists of the cortex and medulla. The cortex contains three zones, each with specific steroid hormone production from cholesterol as the common precursor [7]. The zona glomerulosa produces the mineralocorticoid aldosterone (100–150 μg/day) [7]. It is chiefly activated by angiotensin II through the renin-angiotensin-aldosterone pathway and directly by serum potassium [7]. Aldosterone regulates electrolyte metabolism by stimulating the distal renal tubules and cortical collecting ducts to reabsorb Na^+ and Cl^- while secreting H^+ and K^+. The sodium reabsorption is accompanied by reuptake of free water, thus affecting total body fluid volume [7, 8]. The zona fasciculata produces the glucocorticoid cortisol (10–20 mg/day), is primarily influenced by adrenocorticotropic hormone (ACTH), and follows a strict circadian schedule with peak cortisol production occurring in the early morning [9]. The zona reticularis produces adrenal androgens

A.R. Rastinehad, D.N. Siegel (eds.), *Interventional Urology*, DOI 10.1007/978-3-319-23464-9_26

dehydroepiandrosterone (DHEA), dehydroepiandrosterone sulfate (DHEAS), and androstenedione (>20 mg/day), and it also appears to be under control of ACTH and exhibits circadian patterns [7]. These adrenal androgens represent an important component of circulating androgens in premenopausal women but a much smaller contribution in men. However, adrenal androgen excess may be of clinical significance even in men [10]. The adrenal medulla is responsible for the production of epinephrine (80 %), norepinephrine (19 %), and dopamine (1 %), and it is innervated by preganglionic sympathetic fibers from T11 to L2 [11]. The conversion of norepinephrine to epinephrine is catalyzed by the enzyme phenylethanolamine-N-methyltransferase, which is relatively unique to the adrenal medulla (other than the brain and the organ of Zuckerkandl) [2, 12]. Epinephrine and norepinephrine are metabolized to metanephrine and normetanephrine, respectively, by catechol-O-methyltransferase (COMT). In the liver, monoamine oxidase, COMT, and other enzymes subsequently convert the catecholamine metabolites to the primary metabolic end product, vanillylmandelic acid (VMA) [12].

Adrenal Incidentaloma

Adrenal incidentaloma is defined as an unsuspected adrenal mass greater than 1 cm in diameter identified on examination for non-adrenal purposes, with no presenting signs or symptoms of adrenal disorder [13]. It has an incidence of approximately 5 % and is found at autopsy in 1–8.7 % [14, 15]. More women have incidental adrenal masses, but this likely reflects the sex distribution of the population undergoing imaging procedures [15, 16]. The incidence increases with age, with risk of less than 0.2 % in patients younger than 30 years old and 6.9 % in those over 70 years of age [17]. In patients with known extra-adrenal malignancy, approximately 50 % of adrenal incidentalomas represent metastases [18]. Nearly 20 % of incidental adrenal masses potentially require surgical treatment (Table 26.1) [19].

Table 26.1 Characteristics of adrenal incidentalomas

Adrenal lesions	Percent of total ($n=2005$)
Functioning adenoma	11.4
Subclinical Cushing's syndrome	5.3
Aldosterone-producing adenoma	1.0
Pheochromocytoma	5.1
Malignant	7.2
Adrenal cancer	4.7
Metastasis	2.5
Total potentially surgical lesions	18.6
Apparent nonfunctioning adenoma	82.4

From Young [19], with permission

Size and Growth

Median size of an adrenal incidentaloma at presentation is approximately 3 cm [15, 20]. Malignant potential increases with size [4, 15, 21], and adrenocortical carcinoma (ACC) accounts for 2 % of tumors up to 4 cm in size, 6 % of tumors that are 4.1–6 cm, and 25 % of tumors that are greater than 6 cm [16, 22]. In contrast, benign adrenal adenomas account for less than 15 % of masses greater than 6 cm [16]. Benign to malignant ratio has been estimated to be 5–1 5:1 at a cutoff of greater than 3 cm in diameter and 3–1 3:1 at a cutoff of greater than 4 cm [15]. While masses greater than 6 cm should be considered malignant until proven benign and generally require surgical excision [2, 16], many experts recommend 4 cm as the cutoff diameter for surgical resection in otherwise healthy patients [2, 13, 20, 23]. The 4 cm criterion has a 93 % sensitivity and 42 % specificity for detecting malignancy and is felt to minimize number of unnecessary operations while avoid missing virtually all ACC [20, 23]. However, ACC is more commonly found in younger patients and the incidence of benign adrenal adenomas increases with age [13, 20]. Therefore, the decision regarding adrenalectomy for an incidentaloma should integrate the assessment of metabolic activity, tumor size, imaging characteristics, patient age, comorbidity status, surgical risk, presence of other malignancies, and tumor growth kinetics [2, 4, 13].

A minority of adrenal masses grow over time, with approximately 9 % growing more than 1 cm in a mean period of 3 years [15]. Even in the group of growing masses, the rate of malignant transformation is exceedingly low at around 1 in 1000, with rapid growth as a worrisome sign [13, 15, 24]. Growth by 1 cm or more during the period of observation has been recommended as a criterion to consider surgical removal [4, 13, 15]. The current recommendations for for repeat imaging are at 6, 12, and 24 months [2, 4, 13, 16, 25]. Suspicious and unusual masses may require more frequent imaging protocol, while small (<2 cm), uniform, hypodense nodules in patients with no history of malignant disease may be monitored less frequently [13].

Biopsy of Adrenal Masses

Adrenal biopsy has limited role in the workup of adrenal masses. While biopsies have high positive and negative predictive values in patients with a known non-adrenal malignancy [26, 27], they cannot reliably differentiate benign from malignant adrenocortical tumors [2, 4, 13, 16, 23]. Although complication rate for adrenal biopsies is low, some complications, such as needle track seeding, hemorrhage, pneumothorax, and hemothorax, can seriously affect patient well-being and limit surgical options [2, 4, 13, 23]. Therefore, adrenal

biopsy should be pursued only when its result is certain to influence management and radiologic and metabolic diagnostic limitations have been reached [2, 4, 13]. Prior to performing an adrenal biopsy, the possibility of pheochromocytoma must be evaluated with metabolic testing in order to prevent life-threatening hypertensive crises [16, 25].

Adrenal Mass Imaging

Computed tomography (CT) and magnetic resonance imaging (MRI) are able to discriminate with high degree of accuracy among the various types of incidentally detected adrenal lesions [3], but ultrasonography is suboptimal for detection and characterization of adrenal tumors [28, 29]. Important attributes, such as size, laterality, homogeneity, density, and anatomic relationships, are also accurately assessed by MRI and CT [2]. Large size, irregular shape, vague contour, and invasion into surrounding structures generally indicate malignancy [29]. However, metastatic lesions can be homogeneous and similar in appearance to adenomas [30]. Characterization of adrenal lesions relies on the identification of intracellular lipid, perfusion differences, and metabolic activity that differentiate a benign adenoma from nonadenomas [30, 31]. Since most (>70 %) adrenal adenomas contain much higher intracellular lipid content than other adrenal lesions, lipid sensitive imaging is highly effective in their identification [30, 32]. Nevertheless, CT or MRI characteristics do not eliminate the need for a complete metabolic workup of all adrenal tumors [2, 16].

Computed Tomography

The ideal adrenal CT should include unenhanced, 60 s postcontrast, and 15 min postcontrast images [2, 3], but an unenhanced CT is perhaps the single best and most easily interpretable test to diagnose an adrenal adenoma [2]. Adrenal adenomas demonstrate a low attenuation value on unenhanced CT due to their high lipid content. The measurement of attenuation value should involve a region of interest (ROI) that is one-half to two-thirds of the lesion's surface area through the center of the lesion and avoid areas of necrosis [3, 30]. A Hounsfield unit (HU) of 0 or less is 100 % specific but only 47 % sensitive for a benign adenoma [33]; an attenuation value of 10 HU or less, which is currently the most widely adopted threshold, improves the sensitivity to a clinically acceptable 71 % while maintaining specificity of 98 % [30, 34]. In order to improve the sensitivity for detection of adenomas on unenhanced CT, some have advocated use of histogram analysis, where individual attenuation values of all pixels in the ROI are plotted against their frequency, and the amount of lipid in the mass is proportional to the number of negative pixels (less than 0 HU) [3, 30]. Up to 91 % sensitivity with threshold of >10 % negative pixel has been demonstrated [35, 36], but its utility in clinical practice remains unproven [30]. Unlike an unenhanced CT, the utility of a single contrast-enhanced (CE) CT is limited as tremendous overlap in postcontrast attenuation values exists between adenomas and nonadenomas [37].

Up to 30 % of adrenal adenomas are lipid-poor and have an attenuation of greater than 10 HU on unenhanced CT, making them indistinguishable from other lesions [34]. They demonstrate rapid washout of contrast, a property that is unique to adenomas [3, 29, 30]. While the absolute attenuation measurement on a delayed CT is not useful, the ratio of adrenal attenuation comparing washout-delayed scan to the initial dynamic enhanced scan is able to characterize adrenal lesions with great precision [30]. If an unenhanced CT has been obtained, the percentage of absolute contrast enhancement washout (ACEW) can be calculated by [3, 30]:

$$\text{ACEW} = \frac{\text{CE CT attenuation at 60 s} - \text{CE CT attenuation at 15 min}}{\text{CE CT attenuation at 60 s} - \text{unenhanced CT attenuation}} \times 100$$

Frequently in clinical practice, the unenhanced CT is unavailable. The relative contrast enhancement washout (RCEW) is calculated in these scenarios [3, 30]:

$$\text{RCEW} = \frac{\text{CE CT attenuation at 60 s} - \text{CE CT attenuation at 15 min}}{\text{CE CT attenuation at 60 s}} \times 100$$

An ACEW of >60 % and a RCEW of >40 % after 15 min delay are both highly sensitive and specific for an adenoma (sensitivity 88 and 96 %, specificity 96 and 100 %, respectively), and these thresholds are adopted most commonly [3, 30, 38] (Fig. 26.1). Although a >50 % RCEW after 10 min has been reported to have a high sensitivity and specificity [30, 39], the 10 min protocol was later found to lack sufficient accuracy for routine clinical practice [40].

Magnetic Resonance Imaging

Standard adrenal MRI should include T1, T2, chemical shift imaging (CSI) in- and opposed-phase, and T1 fat-saturated sequences [3]. The normal adrenal has a uniform intermediate T1 and a low-to-intermediate T2 signal intensity, and it is better demonstrated on T1 fat-saturated images due to the

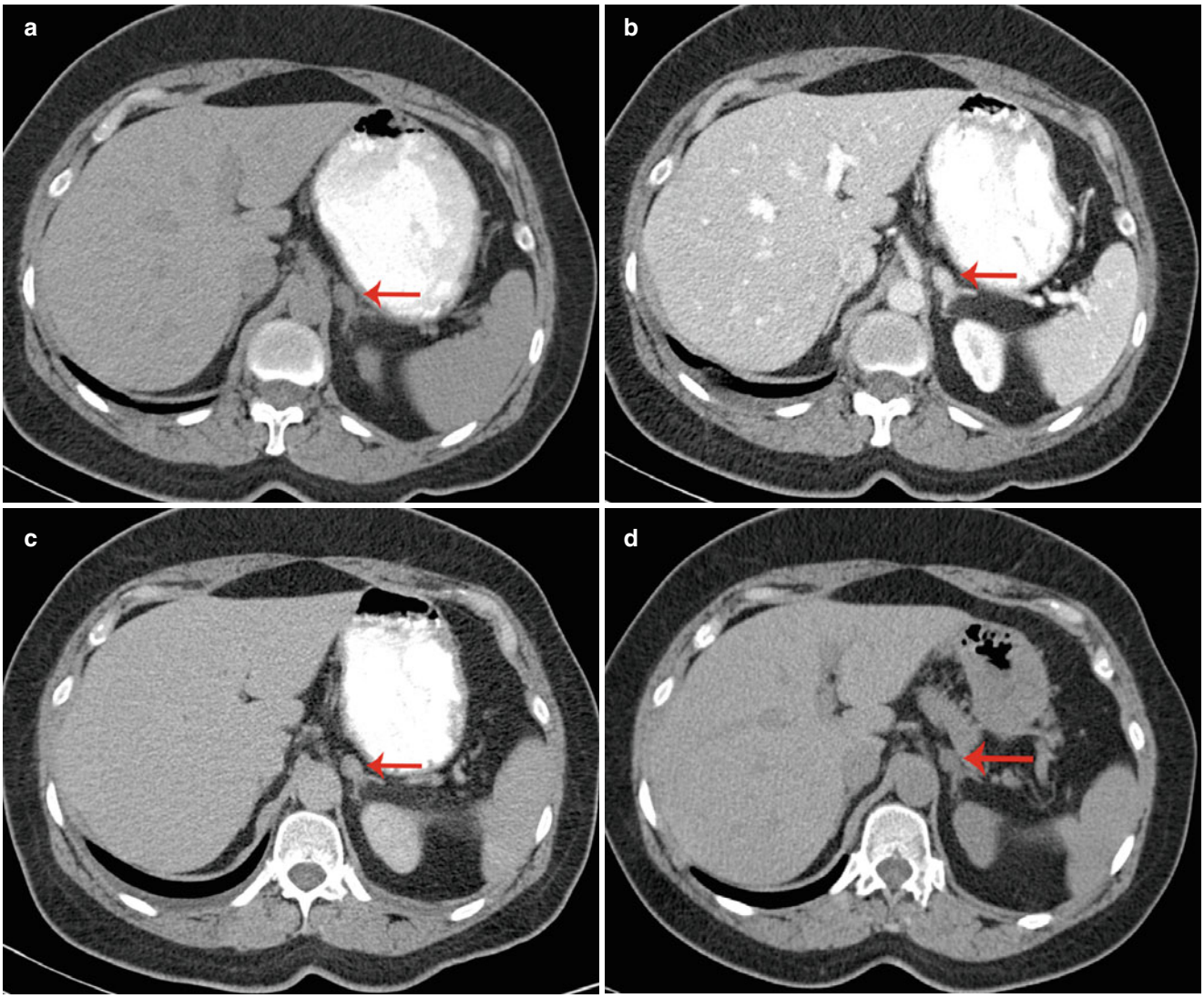

Fig. 26.1 A 53-year-old woman underwent an adrenal protocol CT for evaluation of a left adrenal nodule found during workup of hyperaldosteronism. (**a**) Unenhanced CT shows a left adrenal nodule (*arrow*) with an attenuation value of 14 HU, indicating an indeterminate mass. (**b**) Delayed images 60 s after contrast injection show that the mass has an attenuation value of 142 HU (*arrow*). (**c**) Delayed images 15 min after contrast injection show that the mass has an attenuation value of 60 HU (*arrow*). The mass is consistent with an adenoma with an absolute contrast enhancement washout of 64 % and relative contrast enhancement washout of 58 %. (**d**) Unenhanced CT 6 months later shows unchanged mass size (*arrow*)

suppression of signal from surrounding retroperitoneal fat [3]. CSI detects intracellular lipid in adenomas by exploiting the different frequency of proton oscillation in water and lipid molecules [3, 30, 41]. In adenomas that contain intracellular lipid, the signal intensity on opposed-phase sequences drops out compared to in-phase images, whereas it remains unchanged in malignant lesions and pheochromocytomas, which lack intracellular lipid [3, 30, 32, 41] (Fig. 26.2). In general, simple visual assessment of relative signal intensity loss is sufficient, but equivocal cases may need quantitative evaluation [3, 41, 42]. The adrenal-to-spleen chemical shift ratio of <70 or signal intensity index of >16.5 % may be used to identify lipid-rich adenoma [3, 30, 42, 43]. In lipid-rich adenoma, CSI is similar to unenhanced CT in accuracy and avoids ionizing radiation, although at significantly higher cost [30]. However, in lipid-poor adenomas, particularly those with unenhanced CT attenuation values between 10 and 30 HU, CSI appears to be superior [44, 45]. Further modification of CSI to subtraction CSI, where the opposed-phase images are subtracted from the in-phase images, can be helpful in equivocal cases to further improve diagnostic accuracy [46]. Unlike contrast-enhanced CT washout studies, gadolinium-enhanced MR washout studies do not exhibit sufficient diagnostic strength [2–4]. Nevertheless, adenomas demonstrate certain enhancement patterns that may aid in discriminating them from malignant lesions, such as homogeneous enhancement, ring enhancement, and early peak enhancement [47].

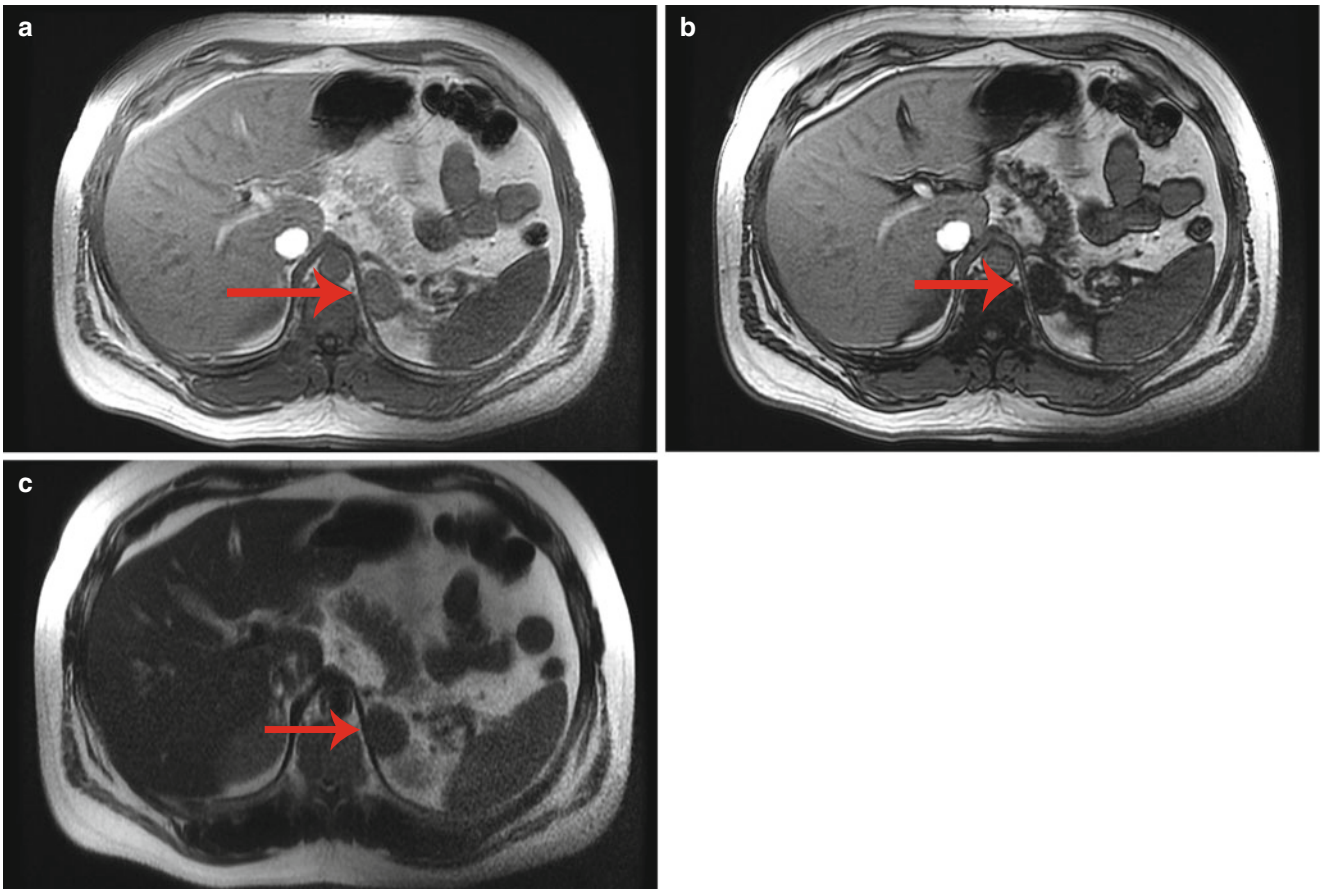

Fig. 26.2 A 45-year-old man underwent a 1.5 T MRI with CSI that was consistent with left adrenal adenoma. (**a**) In-phase T1-weighted imaging demonstrates a left adrenal mass (*arrow*) with signal isointense to muscle. (**b**) Opposed-phase T1-weighted imaging shows dropout of signal in the left adrenal lesion (*arrow*) relative to the in-phase imaging. (**c**) Single-shot T2 weighted spin echo imaging reveals the left adrenal nodule (*arrow*) with low signal intensity

Functional Imaging

^{18}F-fluorodeoxyglucose positron emission tomography (^{18}F-FDG-PET) has demonstrated high sensitivity and specificity in identification of malignant adrenal tumors, including adrenocortical carcinomas, metastatic pheochromocytomas, and metastatic lesions to the adrenal gland [48–50]. ^{11}C-metomidate, a radiotracer that is preferentially taken up by adrenocortical cells, is used to distinguish adrenocortical and non-cortical lesions, but its use is significantly limited by its inability to differentiate benign adenomas from adrenocortical carcinomas [51–53].

Radionuclide scintigraphy with ^{131}I-6β-iodomethyl-norcholesterol (NP-59), another marker of adrenocortical tissue, can distinguish lesions of adrenocortical origin from other space-occupying lesions [17]. However, NP-59 is also unable to identify adrenal adenomas from adrenocortical carcinomas, and it is currently not approved by the US Food and Drug Administration [2, 3, 30]. ^{131}I or ^{123}I metaiodobenzylguanidine (MIBG) is an analogue of norepinephrine that is incorporated into catecholamine storage vesicles and is used to identify pheochromocytomas [29, 54]. However, MIBG scintigraphy has suboptimal sensitivity and specificity, particularly in extra-adrenal, malignant, and certain familial diseases, limiting its utility [2, 50]. Overall, the indication for functional imaging in the workup of adrenal incidentalomas is restricted due to the high diagnostic accuracy of biochemical evaluation and cross-sectional imaging [2, 4, 25, 30].

Biochemical Evaluation

More than 10 % of adrenal incidentalomas are metabolically functional [19]. Metabolic testing for cortisol and catecholamine is recommended for all adrenal incidentalomas [16]. Aldosterone hypersecretion should also be assessed in patients with a history of hypertension [13, 16, 55]. Since sex steroid hypersecretion is exceedingly rare, routine testing for sex hormones is not recommended [13, 16].

Testing for Cortisol Hypersecretion

The three initial tests for Cushing's syndrome in patients with adrenal incidentalomas are overnight low-dose (1 mg)

dexamethasone suppression test (1-mg DST), late-night salivary cortisol test, and 24-h urinary free cortisol test (UFC). Practice guidelines from the Endocrine Society recommend the 1-mg DST or late-night salivary cortisol test over UFC due to their superior sensitivity in this population [56].

For the 1-mg DST, 1 mg dexamethasone is given between 2300 and 2400 h on the night before, and serum cortisol is obtained between 0800 and 0900 h. Alternatively, some endocrinologists prefer a 48 h, 2-mg/day DST for potential improved sensitivity. Patient's failure to suppress cortisol level is indicative of Cushing's syndrome [56]. A cutoff value of >1.8 μg/dL, with a sensitivity of >95 % and specificity of 70–80 %, is recommended for this screening test [56]. Various pharmaceuticals may affect DST via their effect on CYP 3A4, such as phenytoin, phenobarbital, carbamazepine, rifampin, and alcohol. Therefore, patients receiving antiepileptic medications known to affect dexamethasone metabolism should not undergo DST [56]. Oral contraceptives should be avoided since its estrogen component causes high false-positive rates by increasing cortisol-binding globulin concentration and thus total (but not bioavailable) cortisol levels [56].

Late-night salivary cortisol examines the loss of circadian rhythm in Cushing's syndrome [56]. Measurements collected between 2300 and 2400 h with normal cutoff of <145 ng/dL have sensitivity and specificity of >90 % [56]. This test may be influenced by patient factors including depression, altered sleep patterns, chronic illness, and tobacco use [56].

Twenty-four-hour urinary free cortisol evaluation directly measures free bioavailable cortisol. This test is most accurate in patients with a glomerular filtration rate >60 mL/min. It is the recommended test in pregnant patients, although cutoff values two to three times the normal threshold must be used to account for the physiologic hormonal changes [56].

Testing for Aldosterone Hypersecretion

Although hypersecretion of aldosterone by adrenal masses is rare, with only 1 % adrenal incidentalomas causing Conn syndrome [19], nearly 5 % newly hypertensive patients referred to hypertension centers have been found with aldosterone-producing adenoma [57]. The screening test of choice for aldosterone hypersecretion is a morning plasma aldosterone (ng/dL) to renin (ng/mL/h) ratio, where a ratio >20 or 30 and simultaneous aldosterone concentration >15 ng/dL are indicative of Conn syndrome [13, 16, 58, 59]. Patients with hypokalemia should normalize their potassium levels [13]; patients on beta blockers, potassium-sparing diuretics such as amiloride, and mineralocorticoid receptor blockers such as spironolactone should stop those medications to prevent false results [13, 59]. Confirmatory testing is necessary for patients with positive screening test, usually with a 3-day oral sodium challenge followed by 24-h urinary aldosterone measurement, and endocrinology referral should be considered [2, 13, 59, 60].

Testing for Catecholamine Hypersecretion

Approximately 5 % of adrenal incidentalomas are pheochromocytoma [19]. Biochemical testing to rule out this disease should be performed in normotensive as well as hypertensive patients, as about half of patients with pheochromocytoma are not hypertensive [20, 61]. Either plasma-free metanephrine or 24-h urinary-fractionated metanephrine tests should be the initial biochemical testing for pheochromocytoma [50, 62, 63]. The superiority of the two tests has not been established [50], and both provide sensitivity of 97 % and specificity around 90 % [64, 65]. Inherent characteristics of each test should be considered when choosing between the two. For example, plasma-free metanephrine is applicable in patients with renal failure, where urine collection may be inappropriate [50, 62, 63]. Conversely, it is recommended that blood be sampled after patient has been supine for 30 min, thus requiring more time and effort from the medical staff [50, 62, 63]. A number of medications, including acetaminophen, tricyclic antidepressants, phenoxybenzamine, monoamine oxidase inhibitors, and α-methyldopa, cause false-positives and should be avoided [50]. Physiologic stress associated with extreme illness can also elevate plasma or urine metanephrines [50]. If results are equivocal, repeat testing after elimination of confounding medications, sampling errors, and physiologic stress should be performed. If abnormal results continue, referral to an endocrinologist is recommended [2, 50], and additional investigation, such as clonidine suppression test and chromogranin measurements, may be performed [50].

Adrenal Diseases

Cushing's Syndrome

Cushing's syndrome is defined as inappropriately high exposure of tissue to glucocorticoids [56]. Hypercortisolism can cause diverse effects on different organ systems (Table 26.2), and some physical features include reddish purple striae, plethora, proximal muscle weakness, and easy bruising [56]. Causes of Cushing's syndrome can be divided into exogenous, due to iatrogenic glucocorticoid administration, and endogenous, which is further separated into ACTH-dependent and ACTH-independent [2, 56]. The most common cause of Cushing's syndrome is use of supraphysiologic amounts of exogenous glucocorticoids [66]. Of the endogenous Cushing's syndrome, ACTH-dependent hypercortisolism accounts for 80–85 %, with Cushing's disease, or primary pituitary hypersecretion of ACTH, being the most common cause [66]. Ectopic ACTH production nearly

Table 26.2 Effects of glucocorticoids

System	Effect
Central nervous system	Depression Psychosis
Endocrine system	Decreased LH, FSH release Decreased TSH release Decreased GH secretion Menstrual irregularity
Eyes	Glaucoma
Cardiovascular/renal systems	Salt and water retention Hypertension
Gastrointestinal tract	Peptic ulcerations
Carbohydrate/lipid metabolism	Increased hepatic glycogen deposition Increased peripheral insulin resistance Increased gluconeogenesis Increased free fatty acid production Type 2 diabetes
Adipose tissue distribution	Visceral obesity
Genitourinary system	Urolithiasis Erectile dysfunction Decreased libido
Bone and calcium metabolism	Vertebral osteoporosis
Skin/muscle/connective tissue	Protein catabolism/collagen breakdown Skin thinning Muscular atrophy Buffalo hump Hirsutism or female balding Acne
Immune system	Anti-inflammatory actions Immunosuppression
Growth and development	Decreased linear growth

Data from Refs. [10, 56, 66]
FSH follicle-stimulating hormone, *GH* growth hormone, *LH* luteinizing hormone, *TSH* thyroid-stimulating hormone

always arise from malignant processes, most commonly from small-cell carcinoma of the lung and bronchial carcinoid tumors [10, 66, 67]. An extremely rare cause is production of corticotrophin-releasing hormone (CRH) by malignancies, most commonly bronchial carcinomas [67]. ACTH-independent Cushing's syndrome is most often caused by unilateral adrenal tumors, including benign adenomas and adrenocortical carcinomas, in approximately 60 and 40 % of cases, respectively [66]. Other rare causes of Cushing's syndrome include ACTH-independent bilateral macronodular adrenal hyperplasia, as seen in McCune-Albright syndrome, and primary pigmented nodular adrenocortical disease, as seen in Carney complex [66–68].

After diagnosing Cushing's syndrome (see section "Testing for Cortisol Hypersecretion"), the cause of hypercortisolism should be determined with endocrinologic referral [56, 66]. ACTH-independent causes are distinguished from ACTH-dependent ones by a low serum ACTH, and abdominal imaging is employed to identify the adrenal source [66]. For ACTH-dependent Cushing's syndrome, direct downstream measurement of ACTH in the inferior petrosal sinus following CRH stimulation is the gold standard for separating ectopic ACTH production from Cushing's disease [66, 67].

The main treatment option for Cushing's disease is transsphenoidal surgical resection, and salvage radiation therapy is reserved for persistent or recurrent cases [66, 67]. For unilateral cortisol-producing adrenal masses, laparoscopic resection is preferred [66, 67]. Bilateral adrenalectomy with lifelong replacement therapy may be pursued for bilateral hyperplasia or ACTH-dependent causes that are not amenable to surgical resection of the source of ACTH [66]. For patients who are not candidates for surgical intervention, medical blockade with metyrapone, ketoconazole, mitotane, or etomidate may be attempted, although it is associated with significant toxicity [10, 66, 69, 70].

Primary Hyperaldosteronism

Primary hyperaldosteronism, or Conn syndrome, occurs in 5–13 % of hypertensive patients [22, 60]. In this disease, aldosterone secretion is independent of the renin-angiotensin-aldosterone system and suppresses plasma renin levels [2, 71]. Patients are usually diagnosed in the third to sixth decades of life [2, 71]. Signs and symptoms include refractory hypertension, hypokalemia, periodic paralysis, muscle weakness and cramping, polydipsia, and polyuria [60, 71]. However, no characteristic is specific to this syndrome, and hypokalemia is frequently absent [60, 71]. The vast majority of primary hyperaldosteronism is caused by bilateral adrenal hyperplasia (60 %) and adrenal adenoma (35 %) [60]. Comparatively, aldosterone-producing adenomas are associated with more profound hypertension and hypokalemia [57]. Less common causes of primary hyperaldosteronism include unilateral adrenal hyperplasia (2 %), adrenocortical carcinoma (<1 %), familial hyperaldosteronism (<1 %), and ectopic aldosterone-producing adenoma or carcinoma (<1 %) [60]. Conn syndrome is associated with earlier and worse cardiac and renal damage, underlying the need for treatment [72, 73].

Indications for primary hyperaldosteronism screening are listed in Table 26.3. Once screening and confirmatory testing achieve the diagnosis of the disease (see section "Testing for Aldosterone Hypersecretion"), subtype differentiation is essential to determine surgically correctable disease, including aldosterone-producing adenoma or carcinoma, primary unilateral adrenal hyperplasia, or ectopic aldosterone-producing tumors [2, 55]. An adrenal CT scan is indicated to evaluate for presence of adrenal nodules in potential surgical candidates [2]. Correct lateralization is more important with advancing age as the incidence of adrenal incidentalomas increases [55]. A young patient (<40 years old) with primary

Table 26.3 Indications for primary hyperaldosteronism screening

Hypertension with hypokalemia
Resistant hypertension
Adrenal incidentaloma with hypertension
Early onset hypertension (<20 years) or stroke (<50 years)
Severe hypertension (≥160 mmHg systolic or ≥110 mmHg diastolic)
Whenever considering secondary causes of hypertension
Unexplained hypokalemia (spontaneous or diuretic induced)
Evidence of target organ damage disproportionate to degree of hypertension

Data from Refs. [2, 60]

hyperaldosteronism who has an adrenal adenoma >1 cm and a morphologically normal contralateral adrenal gland may proceed with surgical resection of the adenoma without need for further imaging given the rarity of incidental adenomas in this population [2, 55, 60, 74, 75]. Patients considering surgery who are older, with bilateral abnormal glands or with unilateral microadenoma(s), should undergo bilateral adrenal vein sampling for lateralization of aldosterone secretion [2, 55, 74, 76]. The details of adrenal vein sampling will be discussed in the next chapter.

Treatment for primary hyperaldosteronism aims to remove the source of excess aldosterone or to block its effect on target organs [60]. Laparoscopic unilateral adrenalectomy is preferred for aldosterone-producing adenomas or unilateral adrenal hyperplasia [60, 74]. Although blood pressure control improves in 100 % of patients postoperatively, long-term cure rate of hypertension ranges from 30 to 72 %, most likely due to concurrent primary hypertension [60, 77, 78]. Medical therapy with aldosterone antagonists spironolactone or eplerenone is indicated for patients who have surgically uncorrectable subtypes and those who are not surgical candidates [60, 74].

Pheochromocytoma

Pheochromocytoma is a tumor arising from catecholamine producing adrenomedullary chromaffin cells [50]. Its prevalence in hypertensive patients in general outpatient clinics varies between 0.2 and 0.6 % [50]. Approximately 3–5 % of adrenal incidentalomas are pheochromocytomas [19, 20, 79]. About 10 % of pheochromocytomas are located bilaterally [59]. Up to a quarter of pheochromocytomas are extra-adrenal and are known as paragangliomas, as they arise from paraganglia that anatomically parallel the sympathetic and parasympathetic ganglia of the head, neck, thorax, abdomen, and pelvis [2, 50, 80]. Pheochromocytoma may be malignant, which can only be defined by the presence of clinical metastasis [2]. While less than 5 % of adrenal pheochromocytomas are malignant, metastases accompany a third of extra-adrenal diseases [81]. The 5-year survival rate of malignant pheochromocytoma is less than 50 % without treatment [82]. More than a third of patients have been found to harbor germline mutations [50]. The most common genes involved in germline mutations are mitochondrial succinate dehydrogenase subunit B and D (SDHB, SDHD), von Hippel-Lindau (VHL), rearranged transfection protooncogene (RET), and neurofibromatosis type 1 (NF1) [50] (Table 26.4). Of the familial forms of pheochromocytoma, mutations of SDHB lead to metastatic disease in more than 40 % of patients [50, 83–85].

The main clinical feature of pheochromocytoma is paroxysmal hypertension, but nearly 50 % of patients with incidentally discovered pheochromocytoma may be normotensive [86]. Classic triad hallmark of the disease includes sudden headache, palpitations, and sweating [59]. Sporadic forms of pheochromocytoma are most often diagnosed in patients aged 40–50 years, while hereditary forms are more commonly diagnosed before age 40 [81]. Malignant lesions tend to be larger (>5 cm) and exhibit elevated dopamine levels, and the most common metastatic sites are bone, lungs, liver, and lymph nodes [81].

Biochemical testing is the first step in evaluation of a patient suspected of having pheochromocytoma [2] (see section "Testing for Catecholamine Hypersecretion"). Once there is clear biochemical evidence of pheochromocytoma, imaging studies are needed for localization of the lesion [50]. On imaging, pheochromocytomas usually appear as smooth, round, well-circumscribed lesions [2, 13, 30]. Their internal architecture varies depending on the degree of central necrosis and may be homogeneous, heterogeneous, solid, cystic, or calcified [3, 50]. Due to its rich vascularity and low lipid content, pheochromocytomas typically have an attenuation of >10 HU on unenhanced CT [13, 86]. On enhanced CT, pheochromocytomas characteristically demonstrate intense contrast enhancement and slow washout on delayed images [3, 4, 13, 17, 30, 87]. The use of nonionic contrast dye is safe without the need for adrenergic receptor blockade [50]. While CT with contrast provides excellent spatial resolution and is recommended as the initial imaging modality [50], MRI is useful in children, pregnant women, and patients who have allergy to CT contrast [50, 81]. Pheochromocytomas are typically isointense to the liver on T1-weighted images and do not exhibit signal dropout on opposed-phase sequences of CSI [3, 4, 22]. Classically, bright signal intensity on T2-weighted imaging, known as the "light bulb" sign, is associated with pheochromocytomas, but this imaging characteristic is neither specific nor sensitive enough for diagnosis [2, 50, 86] (Fig. 26.3). In metastatic disease, ^{18}F-FDG-PET/CT is the preferred imaging modality [50]. Use of ^{123}I-MIBG scintigraphy is suggested when radiotherapy using ^{131}I-MIBG is planned and occasionally in patients who have an increased risk of metastasis, such as those with a large primary tumor (>5 cm), extra-adrenal, multifocal, or recurrent disease [50, 81].

Table 26.4 Hereditary forms of pheochromocytoma

Syndrome	Clinical characteristics	Gene	% of all PHEO patients	Risk of PHEO (%)	Rate of malignant disease (%)
Familial paraganglioma syndrome type 4	Carotid body tumors Vagal, jugular, tympanic, thoracic, or abdominal paragangliomas	SDHB	10.3	20	>40
Familial paraganglioma syndrome type 1	Carotid body tumors Vagal, jugular, tympanic, thoracic, or abdominal paragangliomas	SDHD	8.9	20	<3
Von Hippel-Lindau syndrome	Renal cell carcinomas and cysts Brain and retinal hemangioblastoma Pancreatic neoplasms and cysts Epididymal cystadenomas Endolymphatic sac tumors	VHL	7.3	10–20	5
Multiple endocrine neoplasia type 2A	Medullary thyroid cancer Primary hyperparathyroidism Cutaneous lichen amyloidosis	RET	<5	50	3
Multiple endocrine neoplasia type 2B	Medullary thyroid cancer Mucocutaneous neuromas Skeletal deformities (Marfanoid body habitus) Joint laxity Myelinated corneal nerves Intestinal ganglioneuromas (Hirschsprung disease)	RET	<5	50	3
Neurofibromatosis type 1	Neurofibromas Café au lait skin spots Malignant peripheral nerve sheath tumor Optic glioma Lisch nodule Skeletal abnormalities	NF1	3.3	1	11

Data from Refs. [50, 81, 84, 85]
PHEO pheochromocytoma

Surgical resection is the mainstay of treatment, where minimally invasive adrenalectomy is preferred for small tumors, while open resection should be performed for large (>6 cm) or invasive pheochromocytomas to ensure complete resection, prevent tumor rupture, and avoid local recurrence [2, 50, 62]. Preoperative catecholamine blockade should be performed in all patients with a hormonally functional pheochromocytoma in order to prevent intraoperative hypertensive crises and cardiac arrhythmias [50, 62]. Phenoxybenzamine irreversibly blocks the α-receptor and is the most commonly used preoperative catecholamine blockade [88]. Beta blockade is used when necessary to treat reflex tachycardia and arrhythmia that may result with α-blockade initiation, and it must never be started prior to appropriate α-blockade to avoid exacerbation of hypertensive crisis due to unopposed stimulation of the α-adrenergic receptors [50, 62]. Calcium channel blockers and metyrosine may be used in combination with α-blockers when the hypertension is resistant to α-blockade alone [50, 88]. Restoration of intravascular volume with liberal salt and fluid intake is necessary to prevent severe hypotension after tumor removal [50, 88]. After surgery, lifelong biochemical screening is recommended due to high rate of recurrence [50]. Finally, treatment of metastatic pheochromocytoma incorporates surgical metastatectomy, radioactive ^{131}I-MIBG therapy, and chemotherapy [62].

Adrenocortical Carcinoma

Adrenocortical carcinoma (ACC) is a rare malignancy with an incidence of 0.7–2 per million [89]. Median age of diagnosis is between fourth and fifth decades of life, with a second peak of increased incidence during childhood less than 5 years of age [90]. Although the majority of ACCs are sporadic, certain syndromes are associated with the disease (Table 26.5). Common mutations found in sporadic cases include loss of tumor protein p53 (TP53) function, increased insulin-like growth factor (IGF) expression, and constitutive activation of the Wnt/β-catenin pathway [89]. The most common metastatic sites are lungs, liver, and bone [91]. Approximately 60 % of patients with ACC present with functional tumors,

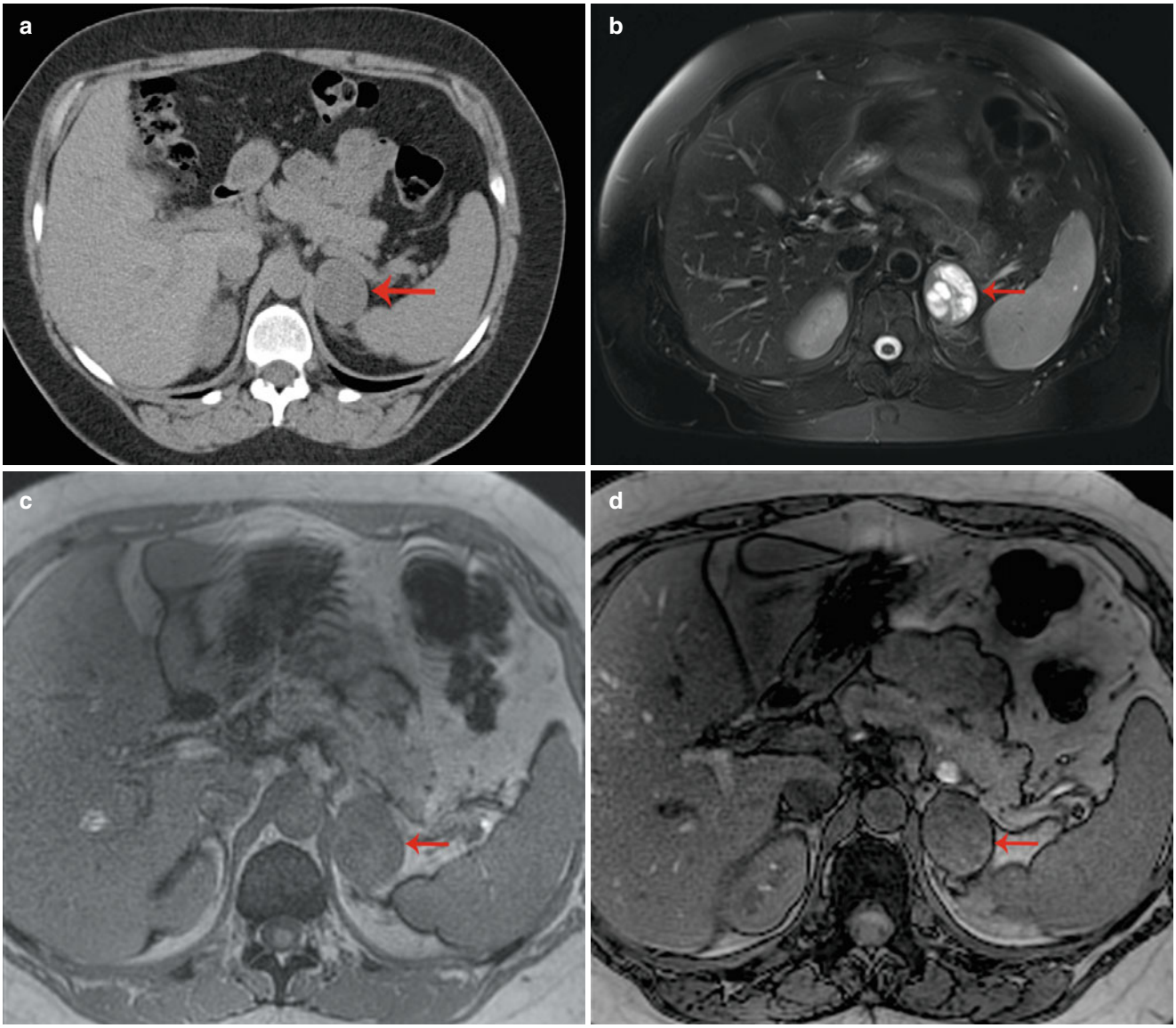

Fig. 26.3 A 44-year-old woman had a 3.8 cm left adrenal mass with classic appearance of pheochromocytoma. (**a**) Unenhanced CT shows a left heterogeneous adrenal mass (*arrow*) with attenuation value of 15 HU. (**b**) The mass is heterogeneously hyperintense on T2-weighted MRI, showing the "light bulb" sign (*arrow*). (**c**) In-phase T1-weighted MRI shows that the left adrenal mass (*arrow*) is isointense to the liver. (**d**) The mass shows no significant signal dropout on opposed-phase T1-weighted MRI (*arrow*)

and 50 % of them exhibit signs and symptoms of Cushing's syndrome [90] (see Table 26.2) but with more marked virilization due to higher rate of 17-ketosteroid and DHEA secretion [92]. Feminization may occur in men due to peripheral conversion of androgens to estrogens, causing gynecomastia and testicular atrophy [91]. Aldosterone hypersecretion is a rare presentation, and mineralocorticoid effect is more commonly mediated by high cortisol levels [91]. A third of patients with ACC present with nonspecific symptoms related to mass effect associated with local tumor growth, such as abdominal or flank pain, abdominal fullness, or early satiety [90, 91]. On the contrary, 90 % of pediatric patients present with evidence of hormonal hyperfunction, where virilizing signs and symptoms are seen in 55 % of children [92].

Initial evaluation after a thorough history and physical examination should include basic metabolic assessment with creatinine, liver enzymes, and a complete blood count. Evaluation of functional status of adrenal tumors is essential. Initial imaging studies should include CT or MRI of abdomen and pelvis and CT of the chest [91]. Excess secretion of glucocorticoids, mineralocorticoids, sex steroids including DHEAS and testosterone, and steroid precursors should be evaluated, and these hormones can serve as surveillance tumor markers if elevated [89–91]. Biochemical exclusion of pheochromocytoma is warranted [91] (see section "Biochemical Evaluation"). On cross-sectional imaging, common characteristics of ACC include large size (often >6 cm), heterogeneous enhancement, central necrosis,

Table 26.5 Hereditary syndromes associated with adrenocortical carcinoma

Syndrome	Clinical characteristics	Gene	Prevalence in general population	Prevalence in ACC patients
Li-Fraumeni syndrome	Sarcoma Choroid plexus tumor Brain cancer Early breast cancer Leukemia Lymphoma	TP53	1:20,000 to 1:1 million	3–7 % adults, 50–80 % children
Multiple endocrine neoplasia type 1	Foregut neuroendocrine tumors Pituitary tumors Parathyroid hyperplasia Collagenoma Angiofibroma Adrenal adenoma or hyperplasia	MENIN	1:30,000	1–2 % adults
Lynch syndrome	Colorectal cancer Endometrial cancer Sebaceous neoplasms Ovarian cancer Pancreatic cancer Brain cancer Upper tract urothelial carcinoma [93]	Mismatch repair gene mutations	1:440	3 % adults
Beckwith-Wiedemann syndrome	Wilms' tumor Hepatoblastoma Macrosomia Adrenocortical cytomegaly, adenoma, or cyst Hemihypertrophy Macroglossia Omphalocele Ear pits	IGF2, CDKN1C, H19	1:13,000	Very rare, only in children
Familial adenomatous polyposis	Intestinal polyps Colon cancer Duodenal carcinoma Thyroid cancer Desmoid tumor Adrenal adenoma Supernumerary teeth Congenital hypertrophy of the retina Osteoma Epidermoid cysts	APC	1:30,000	<1 %
Neurofibromatosis type 1	Neurofibromas Café au lait skin spots Malignant peripheral nerve sheath tumor Optic glioma Lisch nodule Skeletal abnormalities	NF1	1:3000	<1 %
Carney complex	Primary pigmented nodular adrenal disease Large-cell calcifying Sertoli cell tumors Thyroid adenoma Myxoma Somatotroph pituitary adenoma Lentigines	PRKAR1A	~700 patients worldwide	Very rare (case reports only)

From Else et al. [91], with permission

hemorrhage, irregular borders, calcifications, and invasion of surrounding structures [30, 90, 91] (Fig. 26.4). ACC has significantly higher attenuation on unenhanced CT imaging (39 HU vs <10 HU) compared to adrenal adenomas and lack of contrast washout on delayed contrast CT imaging [4, 30, 87, 91]. It also typically does not show homogeneous signal

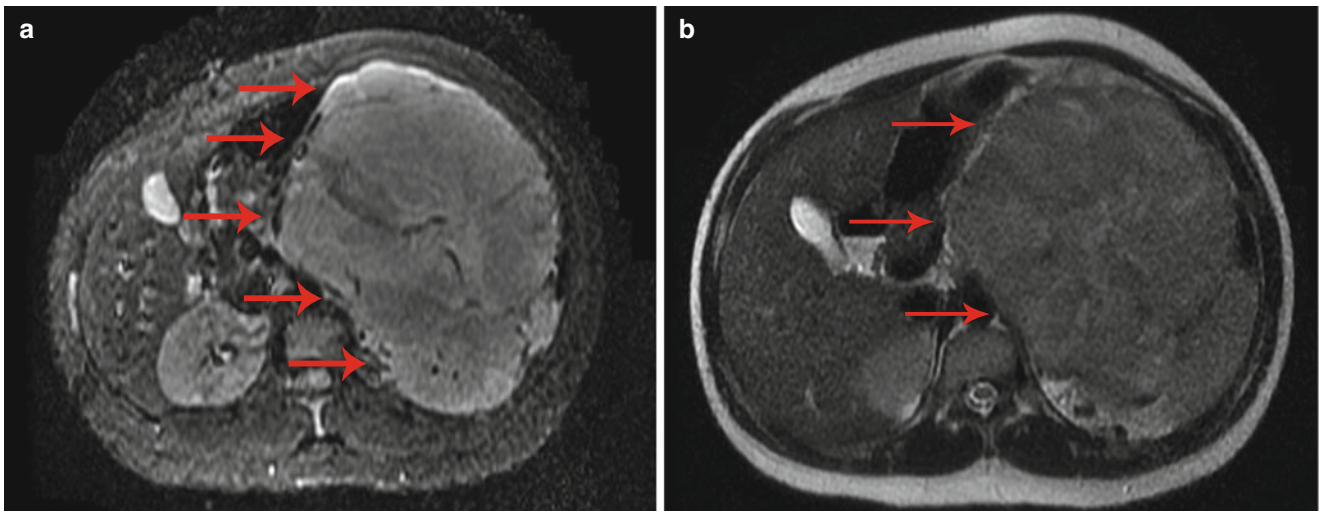

Fig. 26.4 A 65-year-old woman with a large left heterogeneously enhancing adrenocortical carcinoma on a 1.5 T abdominal MRI. (**a**) Moderately weighted T2 STIR images show a hyperintense signal (*arrows*). (**b**) Heavily weighted T2 single-shot fast spin echo shows an isointense signal (*arrows*). These findings are all dependent on the degree of T2 weighting

dropout on chemical shift MRI [30, 41, 91]. ^{18}F-FDG-PET/CT is useful for staging ACC and evaluating local recurrence, but it has limited ability to characterize lesions <10 mm in size and cannot distinguish ACC from other malignant lesions [91] (see section "Adrenal Mass Imaging"). Pathologic evaluation most commonly uses the Weiss criteria, incorporating nine histologic features to help distinguish benign from malignant tumors, including high mitotic rate, atypical mitoses, high nuclear grade, low percentage of clear cells, necrosis, diffuse architecture of tumor, and invasion of venous, sinusoidal, and capsular structures [90, 93, 94].

Complete surgical excision offers the best chance for cure, prolonging median survival to 74 months compared to 12 months for those who undergo incomplete resection [95]. However, cure rate is low, as up to 80 % of patients who undergo curative resection may develop local or distant recurrences [92]. Due to the tumor's often large size and invasion of local structures, an open surgical approach is standard in order to maximize the chance for complete excision [89–91]. Tumor debulking for unresectable disease is palliative and may alleviate tumor-related symptoms [89–91], and an operation should be considered if more than 90 % of disease burden can be removed [96]. Resection of recurrent ACC has been shown to be helpful in long-term disease control [89, 90]. Mitotane is currently the only approved medical therapy for advanced ACC [89, 91]. Recently, combination chemotherapy of etoposide, doxorubicin, cisplatin, and mitotane has been validated for treatment of locally advanced and metastatic ACC [89, 91]. Radiotherapy has limited role as primary treatment of ACC, but it may offer significant improvement in disease control in both the adjuvant and palliative settings [91]. Follow-up after initial treatment should continue for many years given the possibility for late recurrences as long as 10–12 years after resection [90]. Recommendations for surveillance indicate evaluation of hormone markers that were elevated before treatment, as well as cross-sectional imaging of the chest, abdomen, and pelvis [91]. Initial 3-month interval surveillance may be increased to 6-month intervals after a recurrence-free time of 2–3 years [91].

Metastases

The adrenal glands are common sites for metastases. The most common primary sites include the kidney, melanoma, thyroid, colon, lung, and breast [18, 97]. Radiographically, metastatic lesions appear well circumscribed and homogeneous and do not usually demonstrate specific morphologic imaging features [30] (Fig. 26.5). They generally exhibit attenuation >10 HU on unenhanced CT and lack significant contrast loss on washout studies, and they are not infrequently bilateral [4, 30]. Biopsy of the adrenal lesion in the setting of known non-adrenal malignancy can be helpful when imaging is equivocal [13]. Treatment of metastatic tumors of the adrenal glands requires a multidisciplinary approach, and resection of metastatic adrenal lesions has been associated with long-term survival for certain malignancies, such as non-small-cell lung cancer, melanoma, and renal cell carcinoma [2, 4, 18, 98].

Myelolipoma

Adrenal myelolipomas are rare benign tumors that are composed of mature adipose and hematopoietic tissue [99]. Although usually asymptomatic, they can present with flank pain, palpable mass, or hematuria resulting from tumor growth and compression, necrosis, or hemorrhage [100].

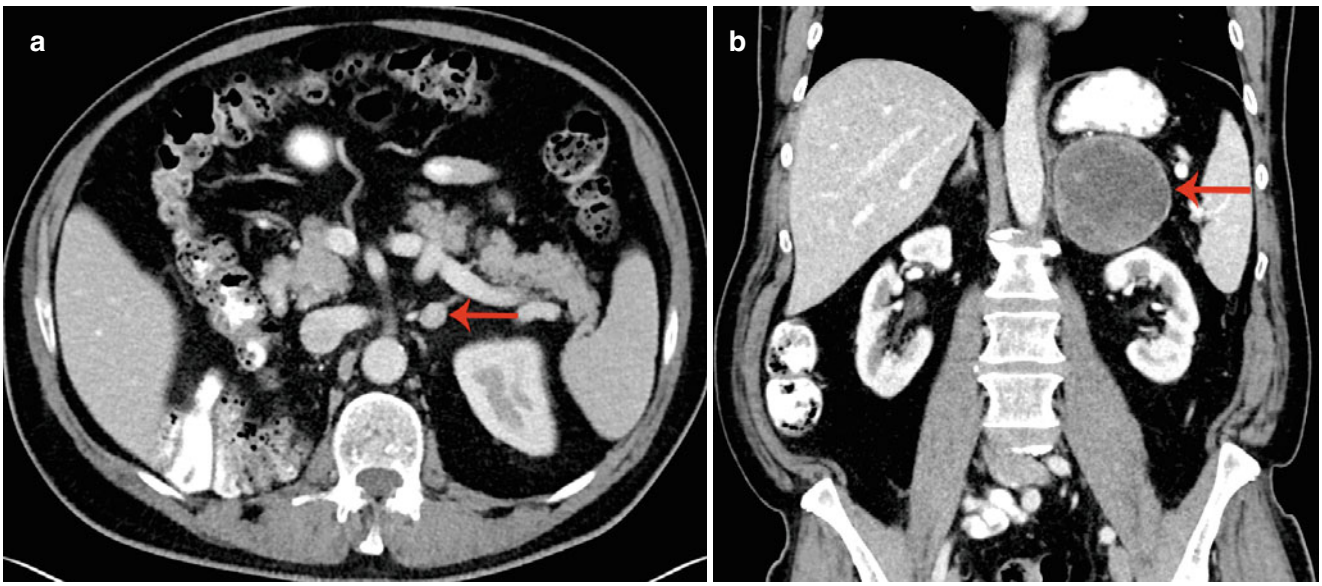

Fig. 26.5 Metastases to adrenal glands. (**a**) A 61-year-old male with history of right radical nephrectomy for clear cell renal cell carcinoma presents with enlarging left adrenal lesion (*arrow*) on enhanced CT, measuring 1.6 cm compared to 0.9 cm 6 months prior. (**b**) A 62 year-old male with history of metastatic melanoma was found to have increasing size of heterogeneous left adrenal mass (*arrow*) on enhanced CT, from 2.1 to 10.2 cm in 6 months

While myelolipomas are classically metabolically inactive, they can coexist with hyperfunctional adrenal diseases, such as Cushing's syndrome, pheochromocytomas, and congenital adrenal hyperplasia [99]. Although they are usually unilateral, bilateral myelolipomas have been reported [101]. Diagnosis is often based on cross-sectional imaging. The lesion is typically well encapsulated, heterogeneous with low density of mature fat (< −30 HU) interspersed with more dense myeloid tissue that enhances with contrast administration on CT imaging [99, 100], and about a quarter of the lesions exhibit calcifications [102]. Myelolipomas have a signal intensity equal to subcutaneous and retroperitoneal fat on MRI, typically showing high signal intensity on T1- and T2-weighted images and loss of signal intensity with fat suppression [3, 99, 100] (Fig. 26.6). In general, asymptomatic adrenal myelolipomas are treated conservatively with observation as they follow a benign clinical course [99]. However, some have advocated excision of tumors larger than 10 cm because of a small but distinct risk of developing abdominal pain or life-threatening shock from spontaneous hemorrhage [103].

Adrenal Hemorrhage and Hematoma

Due to its rich blood supply, adrenal glands are predisposed to hemorrhage [41]. Causes include coagulopathy, antiphospholipid antibody syndrome, trauma, biopsy, tumor, and severe physiologic stress such as meningococcal septicemia in Waterhouse-Friderichsen syndrome [3, 104]. Traumatic adrenal hemorrhage is usually associated with injuries of higher severity and accompanying injuries to surrounding structures [104]. Adrenal hematomas characteristically appear as well-defined round or oval [3, 104]. On unenhanced CT imaging, acute to subacute hematomas contain areas of high attenuation that usually range from 50 to 90 HU [105] (Fig. 26.7). On MRI, hematomas in acute stage (less than 7 days) typically appear isointense or slightly hypointense on T1-weighted images and markedly hypointense on T2-weighted images [105]. Subacute hematomas (7 days to 7 weeks) appear hyperintense on T1- and T2-weighted images [105]. Chronic hematomas (>7 weeks) present with a hypointense rim on T1- and T2-weighted images [105]. Over time, an adrenal hematoma decreases in size and may calcify or organize [105].

Adrenal Oncocytoma

Adrenal oncocytomas are extremely rare tumors, with less than 150 cases reported in the literature [106]. They are most often detected incidentally, since only 17 % are functional [106]. Although they are mostly benign lesions, about 20 % demonstrate some elements of malignancy [106]. CT and MRI cannot reliably identify or differentiate benign and malignant oncocytic tumors, and diagnosis is made upon surgical pathology [106, 107]. While prognosis is good for benign oncocytomas, adrenocortical oncocytic carcinoma has a poor survival rate of only 5 years [106].

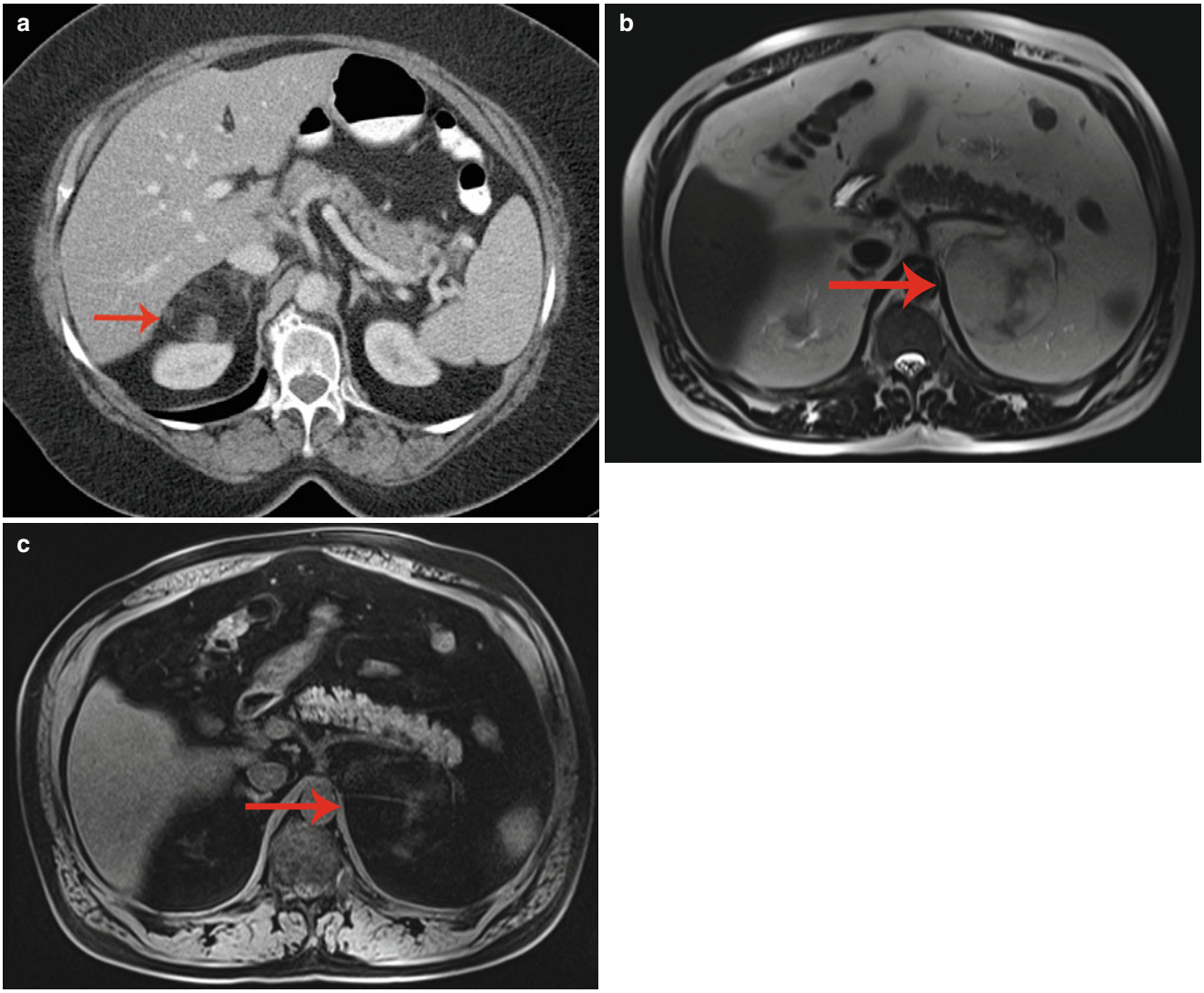

Fig. 26.6 Adrenal myelolipomas. (**a**) A 79-year-old woman with a 5.5 cm right adrenal mass on contrast-enhanced CT with mostly fat density and more nodular solid components in the periphery, consistent with adrenal myelolipoma (*arrow*). (**b**) A 44-year-old male underwent a 1.5 T MRI showing a left adrenal lesion consistent with myelolipoma. T2 single-shot spin echo demonstrates the adrenal mass (*arrow*) with signal isointense to abdominal fat. (**c**) T1 fat-suppressed unenhanced imaging shows loss of signal within the mass (*arrow*) consistent with gross fat

Adrenal Cysts

Adrenal cysts are uncommon lesions that are usually discovered incidentally on imaging examinations [108]. The peak incidence is between third and sixth decades, and a definite female predilection exists [108]. Patients are usually asymptomatic but can present with abdominal or flank pain, abdominal mass, spontaneous intracystic hemorrhage, or cyst rupture [108, 109]. Adrenal cysts are classified into four major histopathologic categories: endothelial (45 %), pseudocysts (39 %), epithelial (9 %), and parasitic (7 %) [108, 109]. Interval enlargement of adrenal cysts is frequent and may not indicate malignancy [108], but up to 7 % of adrenal cysts may be associated with malignancy such as adrenocortical carcinoma [110, 111]. Routine metabolic workup is recommended to exclude active lesions [2, 108]. On imaging, the lesions demonstrate expected imaging characteristics of cysts, including fluid attenuation on CT, lack of enhancement following contrast administration, anechoic appearance on ultrasound, and homogeneous low T1 and high T2 signal characteristics on MRI [3, 30, 41, 112]. They usually have thin walls and may contain internal septations. Higher attenuation values (>30 HU) can be seen due to hemorrhage, intracystic debris, and calcification [113] (Fig. 26.8). Conservative management with serial imaging has been proposed for asymptomatic, small, thin-walled (≤3 mm) nonfunctioning lesions [108, 114, 115]. Surgical excision, preferably with laparoscopic approach, is indicated for adrenal cysts that are large (>6 cm), heterogeneous, thick-walled, symptomatic, or parasitic [114].

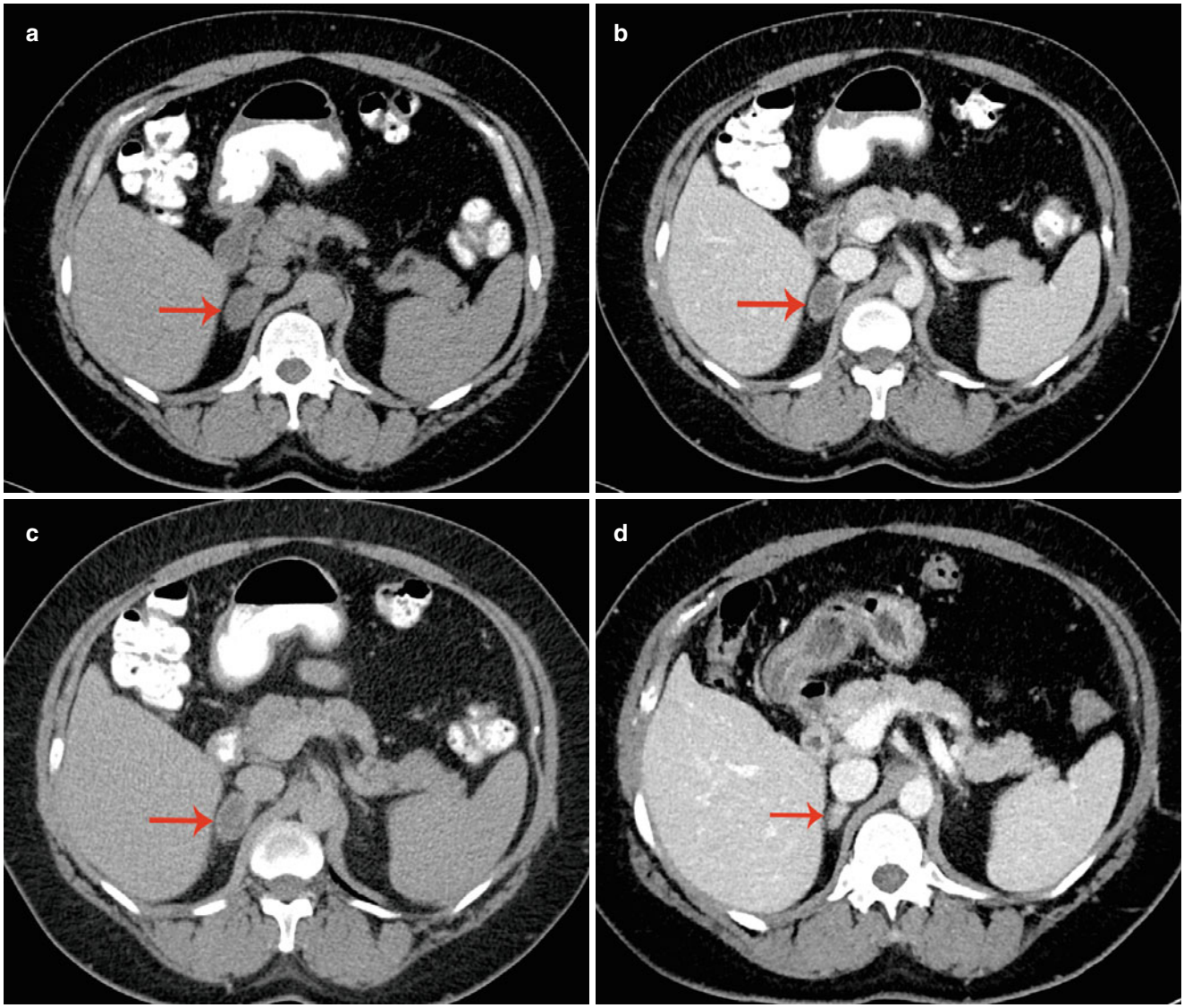

Fig. 26.7 A 52-year-old woman who sustained a motor vehicle collision was found with a 2.9 cm right adrenal mass (*arrows*). CT images (**a**) prior to, (**b**) 60 s after, and (**c**) 15 min after contrast injection show attenuation values of 16 HU, 24 HU, and 20 HU, respectively. This derives an absolute contrast enhancement washout of 50 % and relative contrast enhancement washout of 17 %, consistent for a nonadenoma. (**d**) However, follow-up imaging at 6 months shows interval decrease in size to 1.6 cm, indicating that the mass is most consistent with a resolving adrenal hematoma

Congenital Adrenal Hyperplasia

Congenital adrenal hyperplasia (CAH) is a group of autosomal recessive disorders of cortisol biosynthesis, where 95 % of the cases involve deficiency of the enzyme 21-hydroxylase [116]. It is characterized by cortisol deficiency and androgen excess, and patients may present as salt-wasting or non-salt-wasting, depending on presence or absence of mineralocorticoid deficiency [116]. Due to lack of negative feedback on corticotrophin-releasing hormone and ACTH, chronic enlargement of adrenal glands and increased prevalence of benign adrenal tumors are associated with CAH [116–118] (Fig. 26.9). About 30–50 % of men with CAH develop testicular adrenal rest tumors, especially those with poor medical management or severe deficiency [117]. Patients are treated with sufficient glucocorticoids to suppress adrenal androgen secretion, and mineralocorticoids are given to normalize electrolyte and plasma renin activity [116]. Bilateral adrenalectomy has been tried to remove adrenocortical stimulation and improve medical management, but it remains controversial due to high dose of glucocorticoids required to prevent hyperpigmentation, activation of adrenal rest tissues, and a possible increase in susceptibility to adrenal crisis and sudden death [116].

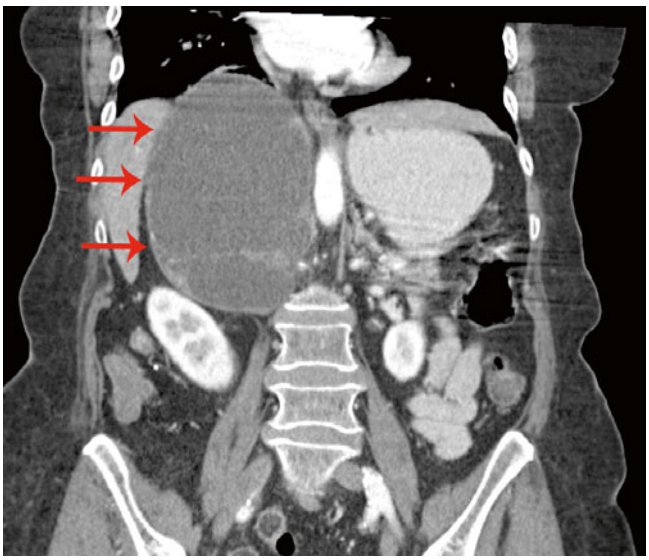

Fig. 26.8 An 84-year-old woman presented with shortness of breath and was found with a 15.7 cm right cystic adrenal mass (*arrows*) on contrast-enhanced CT, showing enhancing septations and displacement of the right kidney, liver, inferior vena cava, and diaphragm. The contour of the mass was seen on chest X-ray 2 years prior to presentation, indicating size stability

Fig. 26.9 A 26-year-old man with history of congenital adrenal hyperplasia due to 21-hydroxylase deficiency. CT images show diffuse nodular enlargement of bilateral adrenal glands (*arrows*) with preservation of normal adreniform configuration

Neuroblastoma

Neuroblastoma is derived from the cells of the neural crest that develop into the adrenal medulla and sympathetic ganglia [119]. It is the most common malignancy in the first month of life and most common adrenal mass in a young child, usually presenting with a palpable abdominal mass [112, 119]. Neuroblastomas are aggressive tumors that invade adjacent organs or displace or encase adjacent vessels [119, 120], and over 50 % of patients present with metastatic disease [85]. They produce high levels of catecholamines that are detected by urinary vanillylmandelic acid, homovanillic acid, or dopamine in 90 % of cases [3, 85, 120]. On imaging, these tumors are heterogeneous, irregularly shaped, lobulated, and unencapsulated and contain coarse, amorphous, or mottled peripheral calcifications [3]. Treatment involves surgical excision for localized disease, while chemotherapy is indicated in intermediate- and high-risk diseases [119, 120].

Conclusion

The adrenal glands serve vital functions in homeostatic regulations and are integrally involved in physiologic functions of the entire body. Adrenal masses are commonly seen on imaging, and careful evaluation is key for appropriate diagnosis and treatment. Knowledge of adrenal physiology and pathophysiology is important in proper management of patients presenting for treatment of adrenal diseases.

References

1. Avisse C, Marcus C, Patey M, Ladam-Marcus V, Delattre JF, Flament JB. Surgical anatomy and embryology of the adrenal glands. Surg Clin North Am. 2000;80(1):403–15.
2. Kutikov A, Crispen PL, Uzzo RG. Pathophysiology, evaluation, and medical management of adrenal disorders. In: Wein AJ, Kavoussi LR, Novick AC, Partin AW, Peters CA, editors. Campbell-Walsh urology. 10th ed. Philadelphia: Elsevier Saunders; 2011. p. 1685–736.
3. Sahdev A, Reznek RH. Adrenal imaging. In: Grainger & Allison's diagnostic radiology. Edinburgh: Churchill Livingstone Elsevier; 2014;(44).
4. Kutikov A, Mehrazin R, Uzzo RG. Assessment and management of an adrenal mass in urological practice. Linthicum: American Urological Association; 2014. p. 194–9.
5. Barwick TD, Malhotra A, Webb JA, Savage MO, Reznek RH. Embryology of the adrenal glands and its relevance to diagnostic imaging. Clin Radiol. 2005;60(9):953–9.
6. Kempná P, Flück CE. Adrenal gland development and defects. Best Pract Res Clin Endocrinol Metab. 2008;22(1):77–93.
7. Arlt W, Stewart PM. Adrenal corticosteroid biosynthesis, metabolism, and action. Endocrinol Metab Clin North Am. 2005;34(2):293–313, viii.
8. White PC. Disorders of aldosterone biosynthesis and action. N Engl J Med. 1994;331(4):250–8.
9. Jacobson L. Hypothalamic-pituitary-adrenocortical axis regulation. Endocrinol Metab Clin North Am. 2005;34(2):271–92, vii.
10. Stewart PM, Krone NP. The adrenal cortex. In: Melmed S, Polonsky KS, Larsen PR, Kronenberg HM, editors. Williams textbook of endocrinology. 12th ed. Philadelphia: Saunders Elsevier; 2011.
11. de Diego AM, Gandía L, García AG. A physiological view of the central and peripheral mechanisms that regulate the release of catecholamines at the adrenal medulla. Acta Physiol (Oxf). 2008;192(2):287–301.
12. Eisenhofer G, Kopin IJ, Goldstein DS. Catecholamine metabolism: a contemporary view with implications for physiology and medicine. Pharmacol Rev. 2004;56(3):331–49.

13. Young WF. Clinical practice. The incidentally discovered adrenal mass. N Engl J Med. 2007;356(6):601–10.
14. Song JH, Chaudhry FS, Mayo-Smith WW. The incidental adrenal mass on CT: prevalence of adrenal disease in 1,049 consecutive adrenal masses in patients with no known malignancy. AJR Am J Roentgenol. 2008;190(5):1163–8.
15. Barzon L, Sonino N, Fallo F, Palu G, Boscaro M. Prevalence and natural history of adrenal incidentalomas. Eur J Endocrinol. 2003;149(4):273–85.
16. Grumbach MM, Biller BM, Braunstein GD, Campbell KK, Carney JA, Godley PA, et al. Management of the clinically inapparent adrenal mass ("incidentaloma"). Ann Intern Med. 2003; 138(5):424–9.
17. Kloos RT, Gross MD, Francis IR, Korobkin M, Shapiro B. Incidentally discovered adrenal masses. Endocr Rev. 1995; 16(4):460–84.
18. Lenert JT, Barnett CC, Kudelka AP, Sellin RV, Gagel RF, Prieto VG, et al. Evaluation and surgical resection of adrenal masses in patients with a history of extra-adrenal malignancy. Surgery. 2001;130(6):1060–7.
19. Young WF. Management approaches to adrenal incidentalomas. A view from Rochester, Minnesota. Endocrinol Metab Clin North Am. 2000;29(1):159–85.
20. Mantero F, Terzolo M, Arnaldi G, Osella G, Masini AM, Alì A, et al. A survey on adrenal incidentaloma in Italy. Study Group on Adrenal Tumors of the Italian Society of Endocrinology. J Clin Endocrinol Metab. 2000;85(2):637–44.
21. Angeli A, Osella G, Alì A, Terzolo M. Adrenal incidentaloma: an overview of clinical and epidemiological data from the National Italian Study Group. Horm Res. 1997;47(4–6):279–83.
22. Cicala MV, Sartorato P, Mantero F. Incidentally discovered masses in hypertensive patients. Best Pract Res Clin Endocrinol Metab. 2006;20(3):451–66.
23. Thompson GB, Young WF. Adrenal incidentaloma. Curr Opin Oncol. 2003;15(1):84–90.
24. Libè R, Dall'Asta C, Barbetta L, Baccarelli A, Beck-Peccoz P, Ambrosi B. Long-term follow-up study of patients with adrenal incidentalomas. Eur J Endocrinol. 2002;147(4):489–94.
25. Singh PK, Buch HN. Adrenal incidentaloma: evaluation and management. J Clin Pathol. 2008;61(11):1168–73.
26. Welch TJ, Sheedy PF, Stephens DH, Johnson CM, Swensen SJ. Percutaneous adrenal biopsy: review of a 10-year experience. Radiology. 1994;193(2):341–4.
27. Harisinghani MG, Maher MM, Hahn PF, Gervais DA, Jhaveri K, Varghese J, et al. Predictive value of benign percutaneous adrenal biopsies in oncology patients. Clin Radiol. 2002;57(10):898–901.
28. Suzuki Y, Sasagawa, Suzuki H, Izumi T, Kaneko H, Nakada T. The role of ultrasonography in the detection of adrenal masses: comparison with computed tomography and magnetic resonance imaging. Int Urol Nephrol. 2001;32(3):303–6.
29. Heinz-Peer G, Memarsadeghi M, Niederle B. Imaging of adrenal masses. Curr Opin Urol. 2007;17(1):32–8.
30. Boland GW, Blake MA, Hahn PF, Mayo-Smith WW. Incidental adrenal lesions: principles, techniques, and algorithms for imaging characterization. Radiology. 2008;249(3):756–75.
31. Boland GW. Adrenal imaging: why, when, what, and how? Part 2. What technique? AJR Am J Roentgenol. 2011;196(1):W1–5.
32. Korobkin M, Giordano TJ, Brodeur FJ, Francis IR, Siegelman ES, Quint LE, et al. Adrenal adenomas: relationship between histologic lipid and CT and MR findings. Radiology. 1996;200(3):743–7.
33. Lee MJ, Hahn PF, Papanicolaou N, Egglin TK, Saini S, Mueller PR, et al. Benign and malignant adrenal masses: CT distinction with attenuation coefficients, size, and observer analysis. Radiology. 1991;179(2):415–8.
34. Boland GW, Lee MJ, Gazelle GS, Halpern EF, McNicholas MM, Mueller PR. Characterization of adrenal masses using unenhanced CT: an analysis of the CT literature. AJR Am J Roentgenol. 1998;171(1):201–4.
35. Halefoglu AM, Bas N, Yasar A, Basak M. Differentiation of adrenal adenomas from nonadenomas using CT histogram analysis method: a prospective study. Eur J Radiol. 2010;73(3):643–51.
36. Ho LM, Paulson EK, Brady MJ, Wong TZ, Schindera ST. Lipid-poor adenomas on unenhanced CT: does histogram analysis increase sensitivity compared with a mean attenuation threshold? AJR Am J Roentgenol. 2008;191(1):234–8.
37. Korobkin M, Brodeur FJ, Yutzy GG, Francis IR, Quint LE, Dunnick NR, et al. Differentiation of adrenal adenomas from nonadenomas using CT attenuation values. AJR Am J Roentgenol. 1996;166(3):531–6.
38. Korobkin M, Brodeur FJ, Francis IR, Quint LE, Dunnick NR, Londy F. CT time-attenuation washout curves of adrenal adenomas and nonadenomas. AJR Am J Roentgenol. 1998;170(3):747–52.
39. Peña CS, Boland GW, Hahn PF, Lee MJ, Mueller PR. Characterization of indeterminate (lipid-poor) adrenal masses: use of washout characteristics at contrast-enhanced CT. Radiology. 2000;217(3):798–802.
40. Sangwaiya MJ, Boland GW, Cronin CG, Blake MA, Halpern EF, Hahn PF. Incidental adrenal lesions: accuracy of characterization with contrast-enhanced washout multidetector CT – 10-minute delayed imaging protocol revisited in a large patient cohort. Radiology. 2010;256(2):504–10.
41. Davarpanah AH, Israel GM. MR imaging of the kidneys and adrenal glands. Radiol Clin North Am. 2014;52(4):779–98.
42. Mayo-Smith WW, Lee MJ, McNicholas MM, Hahn PF, Boland GW, Saini S. Characterization of adrenal masses (<5 cm) by use of chemical shift MR imaging: observer performance versus quantitative measures. AJR Am J Roentgenol. 1995;165(1):91–5.
43. Fujiyoshi F, Nakajo M, Fukukura Y, Tsuchimochi S. Characterization of adrenal tumors by chemical shift fast low-angle shot MR imaging: comparison of four methods of quantitative evaluation. AJR Am J Roentgenol. 2003;180(6):1649–57.
44. Israel GM, Korobkin M, Wang C, Hecht EN, Krinsky GA. Comparison of unenhanced CT and chemical shift MRI in evaluating lipid-rich adrenal adenomas. AJR Am J Roentgenol. 2004; 183(1):215–9.
45. Haider MA, Ghai S, Jhaveri K, Lockwood G. Chemical shift MR imaging of hyperattenuating (>10 HU) adrenal masses: does it still have a role? Radiology. 2004;231(3):711–6.
46. Savci G, Yazici Z, Sahin N, Akgöz S, Tuncel E. Value of chemical shift subtraction MRI in characterization of adrenal masses. AJR Am J Roentgenol. 2006;186(1):130–5.
47. Inan N, Arslan A, Akansel G, Anik Y, Balci NC, Demirci A. Dynamic contrast enhanced MRI in the differential diagnosis of adrenal adenomas and malignant adrenal masses. Eur J Radiol. 2008;65(1):154–62.
48. Blake MA, Slattery JM, Kalra MK, Halpern EF, Fischman AJ, Mueller PR, et al. Adrenal lesions: characterization with fused PET/CT image in patients with proved or suspected malignancy – initial experience. Radiology. 2006;238(3):970–7.
49. Chong S, Lee KS, Kim HY, Kim YK, Kim BT, Chung MJ, et al. Integrated PET-CT for the characterization of adrenal gland lesions in cancer patients: diagnostic efficacy and interpretation pitfalls. Radiographics. 2006;26(6):1811–24; discussion 24–6.
50. Lenders JW, Duh QY, Eisenhofer G, Gimenez-Roqueplo AP, Grebe SK, Murad MH, et al. Pheochromocytoma and paraganglioma: an endocrine society clinical practice guideline. J Clin Endocrinol Metab. 2014;99(6):1915–42.
51. Zettinig G, Mitterhauser M, Wadsak W, Becherer A, Pirich C, Vierhapper H, et al. Positron emission tomography imaging of adrenal masses: (18)F-fluorodeoxyglucose and the 11beta-hydroxylase tracer (11)C-metomidate. Eur J Nucl Med Mol Imaging. 2004;31(9):1224–30.

52. Blake MA, Prakash P, Cronin CG. PET/CT for adrenal assessment. AJR Am J Roentgenol. 2010;195(2):W91–5.
53. Minn H, Salonen A, Friberg J, Roivainen A, Viljanen T, Långsjö J, et al. Imaging of adrenal incidentalomas with PET using (11) C-metomidate and (18)F-FDG. J Nucl Med. 2004;45(6):972–9.
54. Kaltsas G, Korbonits M, Heintz E, Mukherjee JJ, Jenkins PJ, Chew SL, et al. Comparison of somatostatin analog and meta-iodobenzylguanidine radionuclides in the diagnosis and localization of advanced neuroendocrine tumors. J Clin Endocrinol Metab. 2001;86(2):895–902.
55. Zeiger MA, Thompson GB, Duh QY, Hamrahian AH, Angelos P, Elaraj D, et al. The American Association of Clinical Endocrinologists and American Association of Endocrine Surgeons medical guidelines for the management of adrenal incidentalomas. Endocr Pract. 2009;15 Suppl 1:1–20.
56. Nieman LK, Biller BM, Findling JW, Newell-Price J, Savage MO, Stewart PM, et al. The diagnosis of Cushing's syndrome: an endocrine society clinical practice guideline. J Clin Endocrinol Metab. 2008;93(5):1526–40.
57. Rossi GP, Bernini G, Caliumi C, Desideri G, Fabris B, Ferri C, et al. A prospective study of the prevalence of primary aldosteronism in 1,125 hypertensive patients. J Am Coll Cardiol. 2006; 48(11):2293–300.
58. Mulatero P, Stowasser M, Loh KC, Fardella CE, Gordon RD, Mosso L, et al. Increased diagnosis of primary aldosteronism, including surgically correctable forms, in centers from five continents. J Clin Endocrinol Metab. 2004;89(3):1045–50.
59. Anagnostis P, Karagiannis A, Tziomalos K, Kakafika AI, Athyros VG, Mikhailidis DP. Adrenal incidentaloma: a diagnostic challenge. Hormones (Athens). 2009;8(3):163–84.
60. Young WF. Primary aldosteronism: renaissance of a syndrome. Clin Endocrinol (Oxf). 2007;66(5):607–18.
61. Sutton MG, Sheps SG, Lie JT. Prevalence of clinically unsuspected pheochromocytoma. Review of a 50-year autopsy series. Mayo Clin Proc. 1981;56(6):354–60.
62. Pacak K, Eisenhofer G, Ahlman H, Bornstein SR, Gimenez-Roqueplo AP, Grossman AB, et al. Pheochromocytoma: recommendations for clinical practice from the First International Symposium. October 2005. Nat Clin Pract Endocrinol Metab. 2007;3(2):92–102.
63. Grossman A, Pacak K, Sawka A, Lenders JW, Harlander D, Peaston RT, et al. Biochemical diagnosis and localization of pheochromocytoma: can we reach a consensus? Ann N Y Acad Sci. 2006;1073:332–47.
64. Perry CG, Sawka AM, Singh R, Thabane L, Bajnarek J, Young WF. The diagnostic efficacy of urinary fractionated metanephrines measured by tandem mass spectrometry in detection of pheochromocytoma. Clin Endocrinol (Oxf). 2007;66(5):703–8.
65. Lenders JW, Pacak K, Walther MM, Linehan WM, Mannelli M, Friberg P, et al. Biochemical diagnosis of pheochromocytoma: which test is best? JAMA. 2002;287(11):1427–34.
66. Newell-Price J, Bertagna X, Grossman AB, Nieman LK. Cushing's syndrome. Lancet. 2006;367(9522):1605–17.
67. Porterfield JR, Thompson GB, Young WF, Chow JT, Fryrear RS, van Heerden JA, et al. Surgery for Cushing's syndrome: an historical review and recent ten-year experience. World J Surg. 2008;32(5):659–77.
68. Lacroix A, Bourdeau I. Bilateral adrenal Cushing's syndrome: macronodular adrenal hyperplasia and primary pigmented nodular adrenocortical disease. Endocrinol Metab Clin North Am. 2005;34(2):441–58, x.
69. Feelders RA, Hofland LJ, de Herder WW. Medical treatment of Cushing's syndrome: adrenal-blocking drugs and ketoconazole. Neuroendocrinology. 2010;92 Suppl 1:111–5.
70. Kamenický P, Droumaguet C, Salenave S, Blanchard A, Jublanc C, Gautier JF, et al. Mitotane, metyrapone, and ketoconazole combination therapy as an alternative to rescue adrenalectomy for severe ACTH-dependent Cushing's syndrome. J Clin Endocrinol Metab. 2011;96(9):2796–804.
71. Young WF. Endocrine hypertension. In: Melmed S, Polonsky KS, Larsen PR, Kronenberg HM, editors. Williams textbook of endocrinology. 12th ed. Philadelphia: Saunders Elsevier; 2011.
72. Rossi GP, Bernini G, Desideri G, Fabris B, Ferri C, Giacchetti G, et al. Renal damage in primary aldosteronism: results of the PAPY Study. Hypertension. 2006;48(2):232–8.
73. Tanabe A, Naruse M, Naruse K, Hase M, Yoshimoto T, Tanaka M, et al. Left ventricular hypertrophy is more prominent in patients with primary aldosteronism than in patients with other types of secondary hypertension. Hypertens Res. 1997;20(2):85–90.
74. Young WF. Primary aldosteronism: management issues. Ann N Y Acad Sci. 2002;970:61–76.
75. Mulatero P, Bertello C, Rossato D, Mengozzi G, Milan A, Garrone C, et al. Roles of clinical criteria, computed tomography scan, and adrenal vein sampling in differential diagnosis of primary aldosteronism subtypes. J Clin Endocrinol Metab. 2008;93(4):1366–71.
76. Toniato A, Bernante P, Rossi GP, Pelizzo MR. The role of adrenal venous sampling in the surgical management of primary aldosteronism. World J Surg. 2006;30(4):624–7.
77. Meyer A, Brabant G, Behrend M. Long-term follow-up after adrenalectomy for primary aldosteronism. World J Surg. 2005;29(2):155–9.
78. Lumachi F, Ermani M, Basso SM, Armanini D, Iacobone M, Favia G. Long-term results of adrenalectomy in patients with aldosterone-producing adenomas: multivariate analysis of factors affecting unresolved hypertension and review of the literature. Am Surg. 2005;71(10):864–9.
79. Kasperlik-Zaluska AA, Roslonowska E, Slowinska-Srzednicka J, Otto M, Cichocki A, Cwikla J, et al. 1,111 patients with adrenal incidentalomas observed at a single endocrinological center: incidence of chromaffin tumors. Ann N Y Acad Sci. 2006;1073:38–46.
80. Ilias I, Pacak K. Current approaches and recommended algorithm for the diagnostic localization of pheochromocytoma. J Clin Endocrinol Metab. 2004;89(2):479–91.
81. Lenders JW, Eisenhofer G, Mannelli M, Pacak K. Phaeochromocytoma. Lancet. 2005;366(9486):665–75.
82. Eisenhofer G, Bornstein SR, Brouwers FM, Cheung NK, Dahia PL, de Krijger RR, et al. Malignant pheochromocytoma: current status and initiatives for future progress. Endocr Relat Cancer. 2004;11(3):423–36.
83. Amar L, Baudin E, Burnichon N, Peyrard S, Silvera S, Bertherat J, et al. Succinate dehydrogenase B gene mutations predict survival in patients with malignant pheochromocytomas or paragangliomas. J Clin Endocrinol Metab. 2007;92(10):3822–8.
84. Dluhy RG. Pheochromocytoma – death of an axiom. N Engl J Med. 2002;346(19):1486–8.
85. Fung MM, Viveros OH, O'Connor DT. Diseases of the adrenal medulla. Acta Physiol (Oxf). 2008;192(2):325–35.
86. Kannan S, Remer EM, Hamrahian AH. Evaluation of patients with adrenal incidentalomas. Curr Opin Endocrinol Diabetes Obes. 2013;20(3):161–9.
87. Szolar DH, Korobkin M, Reittner P, Berghold A, Bauernhofer T, Trummer H, et al. Adrenocortical carcinomas and adrenal pheochromocytomas: mass and enhancement loss evaluation at delayed contrast-enhanced CT. Radiology. 2005;234(2):479–85.
88. Pacak K. Preoperative management of the pheochromocytoma patient. J Clin Endocrinol Metab. 2007;92(11):4069–79.
89. Fassnacht M, Kroiss M, Allolio B. Update in adrenocortical carcinoma. J Clin Endocrinol Metab. 2013;98(12):4551–64.
90. Lafemina J, Brennan MF. Adrenocortical carcinoma: past, present, and future. J Surg Oncol. 2012;106(5):586–94.
91. Else T, Kim AC, Sabolch A, Raymond VM, Kandathil A, Caoili EM, et al. Adrenocortical carcinoma. Endocr Rev. 2014;35(2): 282–326.

92. Roman S. Adrenocortical carcinoma. Curr Opin Oncol. 2006; 18(1):36–42.
93. Mork M, Hubosky SG, Roupret M, Margulis V, Raman J, Lotan Y, et al. Lynch Syndrome: A Primer for Urologists and Panel Recommendations. J Urol. 2015;194(1):21–9.
94. Weiss LM. Comparative histologic study of 43 metastasizing and nonmetastasizing adrenocortical tumors. Am J Surg Pathol. 1984;8(3):163–9.
95. Schulick RD, Brennan MF. Long-term survival after complete resection and repeat resection in patients with adrenocortical carcinoma. Ann Surg Oncol. 1999;6(8):719–26.
96. Schteingart DE, Doherty GM, Gauger PG, Giordano TJ, Hammer GD, Korobkin M, et al. Management of patients with adrenal cancer: recommendations of an international consensus conference. Endocr Relat Cancer. 2005;12(3):667–80.
97. Hess KR, Varadhachary GR, Taylor SH, Wei W, Raber MN, Lenzi R, et al. Metastatic patterns in adenocarcinoma. Cancer. 2006; 106(7):1624–33.
98. Branum GD, Epstein RE, Leight GS, Seigler HF. The role of resection in the management of melanoma metastatic to the adrenal gland. Surgery. 1991;109(2):127–31.
99. Daneshmand S, Quek ML. Adrenal myelolipoma: diagnosis and management. Urol J. 2006;3(2):71–4.
100. Patel VG, Babalola OA, Fortson JK, Weaver WL. Adrenal myelolipoma: report of a case and review of the literature. Am Surg. 2006;72(7):649–54.
101. Bishoff JT, Waguespack RL, Lynch SC, May DA, Poremba JA, Hall CR. Bilateral symptomatic adrenal myelolipoma. J Urol. 1997;158(4):1517–8.
102. Lam KY, Lo CY. Adrenal lipomatous tumours: a 30 year clinicopathological experience at a single institution. J Clin Pathol. 2001;54(9):707–12.
103. Meyer A, Behrend M. Presentation and therapy of myelolipoma. Int J Urol. 2005;12(3):239–43.
104. Johnson PT, Horton KM, Fishman EK. Adrenal imaging with MDCT: nonneoplastic disease. AJR Am J Roentgenol. 2009; 193(4):1128–35.
105. Kawashima A, Sandler CM, Ernst RD, Takahashi N, Roubidoux MA, Goldman SM, et al. Imaging of nontraumatic hemorrhage of the adrenal gland. Radiographics. 1999;19(4): 949–63.
106. Mearini L, Del Sordo R, Costantini E, Nunzi E, Porena M. Adrenal oncocytic neoplasm: a systematic review. Urol Int. 2013;91(2): 125–33.
107. Tirkes T, Gokaslan T, McCrea J, Sandrasegaran K, Hollar MA, Akisik F, et al. Oncocytic neoplasms of the adrenal gland. AJR Am J Roentgenol. 2011;196(3):592–6.
108. Ricci Z, Chernyak V, Hsu K, Mazzariol FS, Flusberg M, Oh S, et al. Adrenal cysts: natural history by long-term imaging follow-up. AJR Am J Roentgenol. 2013;201(5):1009–16.
109. Guo YK, Yang ZG, Li Y, Deng YP, Ma ES, Min PQ, et al. Uncommon adrenal masses: CT and MRI features with histopathologic correlation. Eur J Radiol. 2007;62(3):359–70.
110. Neri LM, Nance FC. Management of adrenal cysts. Am Surg. 1999;65(2):151–63.
111. Erickson LA, Lloyd RV, Hartman R, Thompson G. Cystic adrenal neoplasms. Cancer. 2004;101(7):1537–44.
112. Lockhart ME, Smith JK, Kenney PJ. Imaging of adrenal masses. Eur J Radiol. 2002;41(2):95–112.
113. Sanal HT, Kocaoglu M, Yildirim D, Bulakbasi N, Guvenc I, Tayfun C, et al. Imaging features of benign adrenal cysts. Eur J Radiol. 2006;60(3):465–9.
114. Castillo OA, Litvak JP, Kerkebe M, Urena RD. Laparoscopic management of symptomatic and large adrenal cysts. J Urol. 2005;173(3):915–7.
115. Rozenblit A, Morehouse HT, Amis ES. Cystic adrenal lesions: CT features. Radiology. 1996;201(2):541–8.
116. Merke DP, Bornstein SR. Congenital adrenal hyperplasia. Lancet. 2005;365(9477):2125–36.
117. Auchus RJ, Arlt W. Approach to the patient: the adult with congenital adrenal hyperplasia. J Clin Endocrinol Metab. 2013;98(7): 2645–55.
118. Gupta P, Bhalla A, Sharma R. Bilateral adrenal lesions. J Med Imaging Radiat Oncol. 2012;56(6):636–45.
119. McHugh K. Renal and adrenal tumours in children. Cancer Imaging. 2007;7:41–51.
120. Kushner BH. Neuroblastoma: a disease requiring a multitude of imaging studies. J Nucl Med. 2004;45(7):1172–88.

Adrenal Interventions

27

Mario A. Taylor and Adam R. Metwalli

Percutaneous Adrenal Biopsy

Incidence

Adrenal incidentaloma (AI) is the term used to describe lesions of the adrenal gland discovered as a secondary finding in radiologic imaging ordered for a medically unrelated reason. Adrenal masses classified as AI are found in as many as 4 % of the imaged patient population whereas autopsy studies have found adrenal masses in 9 % of patients and in a quarter of cancer patients [1–3]. Although nonfunctioning adenomas represent the vast majority of AIs, reported at up to 82 %, other common pathologies include cortisol-secreting adenomas, pheochromocytomas, adrenocortical carcinomas, metastatic lesions, and aldosteronomas [2]. Nonfunctioning benign lesions include nonfunctioning adenomas, myelolipomas, adrenal cysts, and ganglioneuromas. The adrenal gland is also a common site of metastasis in lung, beast, and prostate cancer [4]. Once discovered, incidentalomas should be assessed for functionality and malignancy risk. It is generally accepted that all functioning and malignant lesions should be surgical removed. The role of the consulting surgeon is to determine the functionality and malignancy risk of AIs. Surgeons should collaborate with radiologists and endocrinologists to help interpret radiologic studies and biochemical panels.

Differential Diagnosis

Initial evaluation of an AI is to determine whether it is a functioning, hormone-secreting tumor. Despite the fact that the vast majority of AIs are nonfunctional, all lesions require biochemical evaluation to rule out cortisol-secreting adenoma and pheochromocytoma as these must be managed markedly differently. Careful physical examination is critical as this may inform the hormonal evaluation most appropriate. For example, if physical examination reveals evidence of excessive androgen production such as hirsutism or gynecomastia, then androgenic steroid hormones should also be included in addition to the standard catecholamines and mineralocorticoids.

Laboratory Evaluations

Cortisol-Producing Adenoma

Cushing's syndrome is diagnosed following an elevated 24-h urine free cortisol level or by failure to suppress cortisol production after overnight low-dose dexamethasone. Patients with primary-cortisol producing adenomas will present with elevated cortisol, low ACTH, and an adrenal mass on CT or other radiographic imaging. Some patients will also present with subclinical Cushing's syndrome which does not lead to the full expression of all Cushing syndrome symptoms. This subset of patients with subclinical Cushing's syndrome may also experience obesity, hypertension, diabetes, and osteoporosis.

Aldosteronoma

Primary hyperaldosteronism is the leading cause of secondary hypertension in all hypertensive patients [2, 5, 6]. Only patients who present with hypertension and/or hypokalemia with AI should receive biochemical screening for hyperaldosteronism. Screening consists of calculating the patient's plasma aldosterone concentration (PAC) to plasma renin activity (PRA) ratio, which is referred to as APR. An APR of >30 is indicative of hyperaldosteronism and should be followed by further assessment to demonstrate the subtype of primary hyperaldosteronism and the location of the hyper secretion. Adrenal venous sampling (AVS), which will be discussed in detail later in this chapter, can differentiate between lateralized aldosteronoma and bilateral adrenal nodular hyperplasia. This differentiation

M.A. Taylor
Howard University College of Medicine,
Washington, DC, USA

A.R. Metwalli, MD (✉)
Urologic Oncology Branch, National Cancer Institute,
NIH, Bethesda, MD, USA
e-mail: adam.metwalli@nih.gov

A.R. Rastinehad, D.N. Siegel (eds.), *Interventional Urology*, DOI 10.1007/978-3-319-23464-9_27

Table 27.1 Medications that affect the plasma-free metanephrine levels

Class of drug	Effect on urine/plasma normetanephrine and metanephrine
Tricyclic antidepressants	Increase
Tricyclic antidepressants (acute administration)	Decrease
Selective serotonin reuptake inhibitors	Increase
a-Adrenergic receptor blockers (selective)	No effect
a-Adrenergic receptor blockers (nonspecific)	Increase
β-Adrenergic receptor blockers	Increase
Monoamine oxidase inhibitors (MAOI)	Large increase

is crucial because management strategies differ dramatically depending on diagnosis.

Metastases

The adrenal gland is a common site of metastatic spread for malignant tumors. Lung, breast, prostate, and malignant melanoma represent some of the most common types of malignant carcinomas that spread to the adrenal gland [4]. In patients with a history of a previous malignancy, particularly those listed, adrenal biopsy should be considered to confirm the diagnosis. In general, patients with a single metastatic lesion should undergo surgical resection. If multiple tumors are discovered, the patient should be referred to an oncologist for further treatment.

Myelolipomas

Myelolipomas represent another type of benign nonfunctioning adrenal mass. These lesions are easily identified on computed tomography imaging due to the pathognomonic macroscopic fat and bone marrow contents.

Pheochromocytoma

Patients symptomatic with pheochromocytoma typically present with tachycardia, hypertension, cardiac palpitation, anxiety, and/or sweating. All patients with discovered AI should be screened for pheochromocytoma even if they present with no symptoms. Plasma-free metanephrine and normetanephrine levels are easily obtained via blood draw and are reliable markers for pheochromocytoma. Plasma-free metanephrine levels of three to four times the normal range are indicative of pheochromocytoma. The sensitivity of this assessment ranges from 77 to 97 % while the specificity ranges from 69 to 98 %. When used along with plasma-free normetanephrine levels, the sensitivity and specificity of the assessments increase to 97–100 and 85–89 %, respectively [7]. Some medications may falsely increase the plasma-free metanephrine levels and therefore should be discontinued prior to testing (Table 27.1).

Adrenocortical Carcinoma

Adrenocortical carcinoma is a rare type of tumor that should be suspected when lesions are >6 cm in size and/or if the patient presents with virilizing symptoms. Patients with AI and possible ACC should be biochemically screened for hypersecretion. One study determined 66 % of ACC were hormone-secreting tumors [7, 8].

Diagnostic Evaluation

Imaging (CT, PET/CT, MRI)

It is important to choose the appropriately indicated study type to most accurately determine pathology. While the majority of AIs are benign, there are certain radiologic characteristics that are pathognomonic for specific lesions. Some AI can be immediately characterized with CT if certain features are clearly present. Cortical adenomas are homogenous and have low attenuation; myelolipomas usually display macroscopic fat; ACCs are usually large (>6 cm) and heterogeneous; and cysts show fluid density. There are also characteristics that may indicate malignancy such as local invasion of surrounding tissue, tumor necrosis, heterogeneity of mass, irregular borders, and regional lymphadenopathy. Any relevant prior imaging studies performed should be evaluated. If a lesion is stable for at least 6 months, the likelihood that the lesion is malignant is remote.

Most patients with AI will have undergone contrast-enhanced CT as the initial study but contrast-enhanced CT singularly has little use in characterizing adrenal lesion by densitometry. AI lesions can be characterized by an adrenal CT protocol including unenhanced CT followed by contrast washout measurements. On unenhanced CT, adrenal cortical adenomas normally have low attenuation (<10 HU), indicating a lipid-rich lesion, while ACCs more commonly have higher attenuation (≥10 HU), indicating a lipid-poor lesion. An increased probability of malignancy can be determined when contrast washout levels are evaluated. Most malignant lesions have an absolute washout of <60 % and a relative percentage washout of <40 %, while benign lesions show an absolute washout of >60 % and a relative washout >40 % [7, 9]. Absolute and relative washout are related to the characteristics of the lesion, with benign adenomas displaying a more rapid washout of contrast, while the opposite is true for malignant lesions. Each can be calculated as follows:

$$\text{Absolute washout} = \text{Enhanced CT(HU)} - \text{Delayed CT(HU)} \Big/ \text{Enhanced CT(HU)} - \text{Unenhanced CT(HU)} \times 100\%$$

$$\text{Relative washout} = \text{Enhanced CT(HU)} - \text{Delayed CT(HU)} \Big/ \text{Enhanced CT(HU)} \times 100\%$$

The accuracy of MRI in distinguishing benign and malignant adrenal masses is similar to that of CT imaging.

On MRI, normal adrenal gland tissue and adenoma demonstrate a low to intermediate signal on T1- and T2-weighted imaging, while malignant lesions are usually hypointense on T1 and hyperintense on T2 imaging. Adrenocortical carcinoma appears heterogeneous such as in CT imaging but may have a loss of signal intensity on out of phase MRI images leading to a mistaken diagnosis of benign lesion. The typical teaching that pheochromocytomas are usually hyperintense on T2-weighted images but may also exhibit low SI on T2-weighted images.

Another useful tool for distinguishing benign from malignant lesions is 18-fluoro-2-deoxy-D-glucose position emission tomography, ^{18}F-FDG-PET. Patients with a persistently indeterminate adrenal mass even following an appropriately performed CT should undergo an FDG-PET. Adrenal FDG uptake is considered malignant when intensity is higher than hepatic uptake [10]. Malignant tumors also have demonstrated larger max uptake of FDG when compared to benign lesions [11]. A large multicenter prospective study including 77 patients demonstrated that FDG-PET successfully distinguished ACC from adenoma with a sensitivity of 100 % and a specificity of 88 % [11]. However FDG-PET is primarily useful when attempting to diagnose the highly malignant ACC from an indeterminate nonfunction adenoma because FDG-PET may result in a false positive when imaging functional adenomas and pheochromocytomas since these lesions exhibit uptake similar to that of malignant lesions.

Adrenal Vein Sampling (AVS)

If a preliminary diagnosis of primary hyperaldosteronism is made, further biochemical testing in the form of adrenal venous sampling should be performed to confirm diagnosis. Adrenal venous sampling involves sampling blood from the adrenal veins and comparing the aldosterone concentration to the contralateral side and that found in the periphery. This technique will be discussed in-depth later in this chapter.

Indications and Contradictions for Adrenal Biopsy

Lesions definitively characterized as adenomas by imaging do not require biopsy. Functioning adenomas should be surgically excised while nonfunctioning adenomas should be followed up with interval imaging. Other benign nonfunctioning adrenal lesions include myelolipomas and adrenal cysts which also do not require biopsy. Suspected pheochromocytomas should not be biopsied; a thorough and properly performed biochemical assessment of plasma metanephrines can confirm this diagnosis. An unnecessary biopsy of a pheochromocytoma may cause a sudden hypertensive crisis due to the release of excessive catecholamines into circulation. These lesions should be treated with surgical resection. Lesions that cannot be confidently characterized by standard radiologic or laboratory criteria and lesions that are larger than 4 cm and lesions with markedly heterogeneous appearance on imaging should be referred for adrenal biopsy [12]. However, masses which are highly suspicious for adrenocortical carcinoma such as those isolated adrenal mass >4 cm with irregular margins/central necrosis and no known primary malignancy should be considered for wide surgical excision rather than biopsy. AIs found in patients with a medical history of extra-adrenal malignancy may be considered for adrenal biopsy. Mazziglia et al. showed that 40–75 % of AIs in this population indicate metastatic disease [13]. By comparison other studies have demonstrated a 0 % rate of malignancy in 973 patients with no history of cancer who presented with adrenal incidentaloma [14, 15]. Historically, percutaneous adrenal biopsy has had relatively limited indications due to high non-diagnostic rate, risk of tumor seeding, and possible catecholamine surge if the lesion may be a pheochromocytoma. A retrospective study performed by Mazzaglia et al. determined that needle biopsy of AI is often inadequate for distinguishing benign lesions from malignant lesions due to histologic similarity and recommend that biopsy only be considered for making diagnosis of metastatic disease in patients with known or suspected extra-adrenal malignancy [13]. As such, these lesions usually present as large (>4 cm), heterogeneous lesions.

Pre-procedure

Routine coagulation parameters such as INR and platelet count must be checked before biopsy to mitigate risk of hemorrhage. Anticoagulants should be discontinued at least 2–5 days prior to the procedure depending on the specific medication used (Table 27.1). In patients at high risk for deep vein thrombosis, a bridging technique can be utilized before and after biopsy using low-molecular-weight heparin [16]. Some radiologists will forego these recommendations with patients who are healthy and have no history of abnormal bleeding or use of anticoagulants. Adrenal biopsy is usually well tolerated and can be administered under local anesthesia or with conscious sedation. Prophylactic antibiotics are normally not recommended.

Relevant Anatomy and Procedure Technique

The adrenal glands are located in the retroperitoneum directly superior to the kidneys and encased in Gerota's fascia (Fig. 27.1). There are rare anatomic variations in adrenal gland location. In the cases of solitary kidney or pelvic kidney, adrenal glands will be found in the same location but appear differently on imaging.

Fig. 27.1 Anatomical considerations for adrenal biopsy. Left-sided 4.3 cm adrenal mass (*red asterisk*). Paraspinous needle placement (*black arrow*) is often the safest approach given the close proximity of the spleen (*red arrow*), stomach (*green arrow*), kidney (*blue arrow*), and pleura (*yellow arrow*). Representative images of contrast-enhanced CT abdomen (**a**) axial view, (**b**) coronal view, and (**c**) sagittal view

In cases in which fine-needle aspirate is necessary, small-caliber needles (20–22 gauge) should be used. For histologic analysis, cutting needles are to be used to provide core biopsy samples. During adrenal biopsies, coaxial technique using 16–19 gauge guide needles is used to allow for the retrieval of fine-needle aspirates and core biopsies. Chiba needles with slightly curved tips are commonly used to enhance redirecting, while Hawkins needles with interchangeable tips can be utilized if saline injection is anticipated for paravertebral widening [17].

Patients are oriented in the decubitus position which decreases diaphragmatic movements, lessening the risk of lung transgression. Patients can also be placed prone in order to attempt a posterior approach to the adrenal glands. If neither approach works, an anterior approach can be used, though it is associated with higher rates of complications [18]. A caudal-to-cephalic approach may be utilized to minimize risk of pleural transgression in both the prone and decubitus positions. In cases where the paravertebral space is minimal, injection of saline can be administered to widen the space. The saline will displace the parietal pleura laterally, decreasing the risk of pleural transgression. Ultrasound guidance can be used for large adrenal masses and gives the advantage of real-time observation. Otherwise, CT guidance is the standard imaging modality used for adrenal biopsy.

Results and Complications

Complication rates for adrenal biopsy range from 0 to 12 % [19–22]. The most common complications associated with adrenal gland biopsy are pneumothorax and hemorrhage. Needle track seeding, hypertensive crisis, and adrenal abscesses are other less common complications that have be noted in literature. Following biopsy, patients usually remain under care for another 3 h to monitor hemostasis [17]. When post-biopsy hemorrhage does occur, it usually occurs in the abdomen or thorax and normally resolves without intervention [17]. Literature has demonstrated an increase in morbidity and mortality when the transhepatic approach and the anterior approach to the left adrenal gland which traverses the pancreas have been utilized [18]. In cases in which the pleural space was transgressed, a chest x-ray (CXR) must be ordered as well as 3 h follow-up CXR after the procedure to evaluate for a progressive pneumothorax. Patients found to have pneumothorax should be treated with a small-bore chest tube. Another serious complication of adrenal gland biopsy that may occur during the procedure is hypertensive crisis propagated by the release of catecholamines from the gland. Approximately 2.4 % of pheochromocytomas present atypically on imaging and thus can lead to unsuspecting biopsy of a catecholamine-secreting tumor [23]. If an acute hypertensive crisis does occur during biopsy, it can be treated with 1 mg of phentolamine via IV followed by an IV phentolamine drip. Intravenous nitroprusside can also be utilized to control hypertension as well as beta-adrenergic blockers to treat cardiac arrhythmias or hypotension. For lesions in which pheochromocytoma has not been conclusively ruled out, administration of alpha-blockers prior to the procedure should be considered.

The sensitivity of adrenal biopsy for detecting malignancy ranges from 81 to 100 % [24–26]. Several studies have reported that adrenal biopsy in this setting is unreliable and variable [13, 27, 28]. However, one prospective study of 220 adrenal biopsy demonstrated a correct diagnosis 76.8 % of biopsies. The study included 39 malignant tumors and showed a sensitivity of 94.6 % and a specificity of 95.3 % when determining malignancy [29]. While these results are exceptional, they may not be reflective of common adrenal biopsy practice since the radiologic selection criteria were very strict enriching the study cohort for malignant lesions; in addition, ACC-specific immunohistochemistry stains were used on core samples improving the diagnostic results as well. As it stands though, adrenal biopsy should be indicated for AI lesions that remain indeterminate after appropriately performed imaging (CT/PET and/or MRI) and biochemical assays which both may discourage adrenal biopsy.

Discussion

Adrenal gland lesions are extremely common and are often found incidentally on radiographic imaging studies performed for other reasons. The vast majority of lesions can be diagnosed accurately with radiographic criteria alone. Furthermore, the overwhelming prevalence of benign adenomas even in patients with a history of malignancy results in a limited role for adrenal biopsy. Most published data indicate that adrenal biopsies have an unacceptably high non-diagnostic rate and do not reliably differentiate between benign and malignant primary adrenal tumors. Additionally, a small but significant risk of a hypertensive crisis due to an unrecognized or atypical pheochromocytoma also limits the application of adrenal biopsy. Finally, the theoretical risk of tumor seeding and increasing complexity of subsequent surgery are additional concerns that limit widespread application of adrenal biopsy. Currently, the usage of core biopsy for the differentiation of benign tumors from malignant tumors in the adrenal gland is not part of standard diagnostic algorithms for adrenal masses.

Adrenal gland lesions are indicated for biopsy if the mass is indeterminate after imaging and the patient has a history of malignancy or if the mass is indeterminate and larger than 4 cm. All patients should undergo plasma screening for catecholamines prior to the biopsy to rule out pheochromocytoma. Adrenal biopsy is a generally well-tolerated procedure, and in experienced hands complication risks are low. In specific and well-characterized patient populations, biopsy can be useful for the diagnosis of adrenal incidentalomas.

Common Tips for Success

- Target-side down decubitus positioning often is the safest paraspinal access.
- To visualize a clear path for the biopsy needle, gantry angulation may be needed. Many CT scanners allow up to 30° of gantry tilt which is usually enough to visualize a clear access route.
- Smaller Chiba and spinal FNA needles (21–23 ga) may be preferable if lesion appears hypervascular on pre-biopsy imaging.
- Core biopsy specimens are preferred for diagnosis of lymphoma.
- Etched needles may enhance visualization under ultrasound guidance, and manual scratching of needle with metal clamp will achieve effect with no added cost.

Adrenal Venous Sampling

Adrenal venous sampling is the current standard of care for identifying and lateralizing surgically curable cases of hyperaldosteronism caused by aldosterone-secreting adrenal tumors. Studies have reported sensitivity of 95 % and specificity of 100 % for adrenal venous sampling for lateralizing aldosterone hypersecretion [30–36]. This technique, though, remains underutilized. It is often described as a technically challenging procedure with problematical complications such as adrenal vein rupture and embolism [35, 37]. Adrenal venous sampling also lacks a universally accepted set of standards for performance and interpretation of results. The classic presentation of primary aldosteronism (PA) is hypertension with hypokalemia and metabolic alkalosis. Most times, though, patients do not present with all three symptoms. The Endocrine Society has established guidelines to screen select patient populations. Patients with hypertension and hypokalemia, refractory hypertension, hypertension with an adrenal incidentaloma, or hypertension with history of familial/early onset hypertension should be screened for primary aldosteronism [38]. Diagnostic workup for primary aldosteronism includes plasma renin assay (PRA) and plasma aldosterone concentration (PAC), both retrieved peripherally. Decreased plasma renin with an increased PAC/PRA ratio is indicative of primary aldosteronism. Normal PAC/PRA ratio is usually in the range of 4–10 while patients with PA will have a ratio of 30–50 [39, 40]. Recent studies have suggested that primary aldosteronism accounts for 5–13 % of all hypertensive patients and that up to 62.3 % of patients with primary hyperaldosteronism may be curable with surgical resection [40–42]. It is important to note that the two most common causes of primary hyperaldosteronism are bilateral idiopathic hyperplasia and unilateral aldosterone-producing adenoma (as well as a chance of bilateral functioning adenomas) [38, 43]. This distinction is critical because clinical management of patients depends on accurate diagnoses. Patients with bilateral hyperplasia must be managed medically due to the inability to treat surgically. These patients are best treated with long-term usage of spironolactone or other aldosterone antagonist [38]. Adrenal venous sampling can be used to accurately lateralize functioning adenomas for surgical resection. Recent studies have shown that localizing the source of aldosterone-producing adenomas and bilateral lesions using MRI and CT is difficult and often leads to equivocal findings [44]. One prospective study of 203 patients noted that up to 46.4 % of patients may have been incorrectly treated based on CT-imaging alone [36]. This includes patients that may have had an inappropriate adrenalectomy and patients that would have been excluded for adrenalectomy. Another large study showed 37.8 % of the 950 patient population had CT/MRI results in disagreement with adrenal venous sampling outcome [44]. Mounting evidence continues to demonstrate the need for AVS usage when CT imaging is equivocal and/or when lateralization of lesion(s) is required.

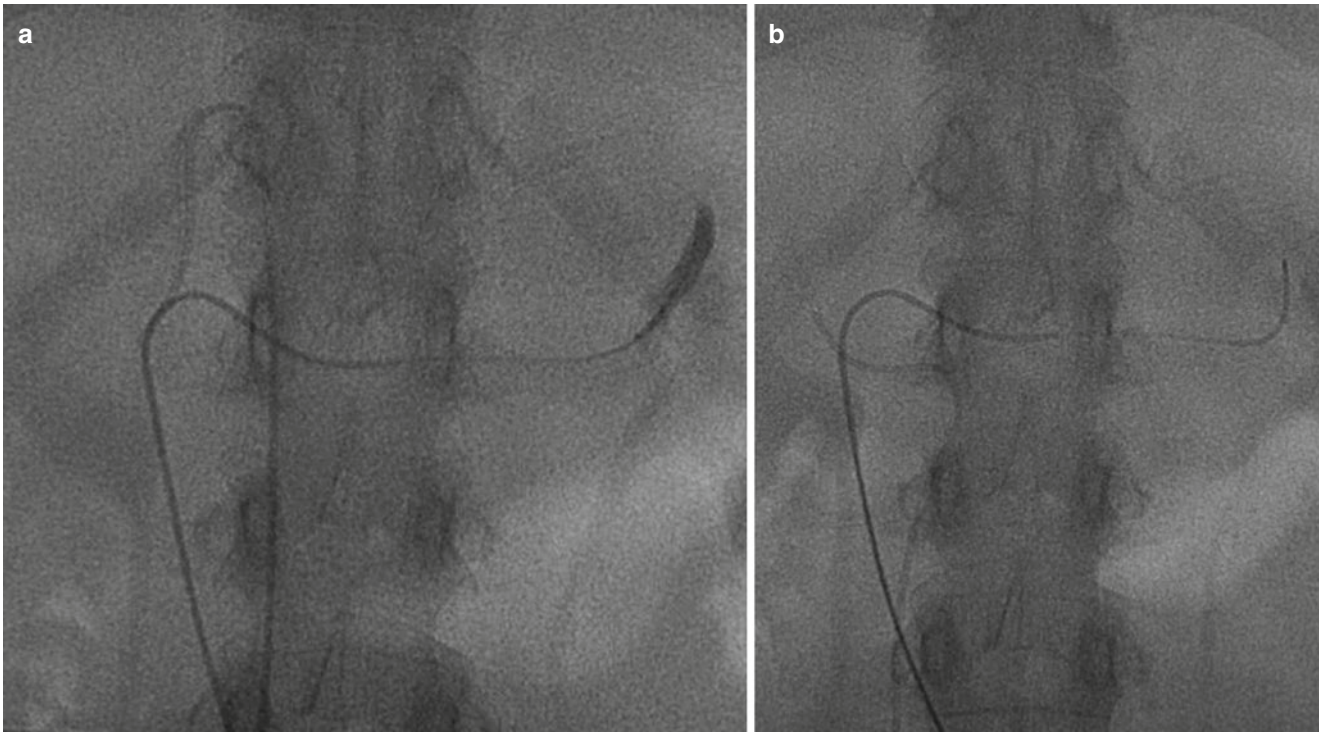

Fig. 27.2 Adrenal vein sampling. Two-catheter technique for AVS. Note the left catheter traversing the length of the left renal vein with cephalad deflection into the left adrenal vein. The right catheter is in the right adrenal vein and shorter as would be expected anatomically

AVS Technique

Currently, there is no universally standard protocol for performing adrenal venous sampling. Adrenal venous sampling involves the catheterization of the left and right adrenal, sampling the venous drainage. There are several major variations in technique that can be employed when performing this procedure. Both adrenal veins can be sampled simultaneously using two catheters (Fig. 27.2) or sequentially using only one catheter at a time for each of the veins. Furthermore, the use of intraprocedural ACTH stimulation is another technical option dependent on practitioner preference. If ACTH stimulation is desired, cosyntropin, synthetic ATCH, can be administered as a bolus or as a continuous intravenous infusion. Sacks et al. suggest utilizing three initial sets of simultaneously obtained samples. This set is followed by administration of a 0.25 mg bolus of cosyntropin and removing samples at 5, 10, and 15 min intervals after bolus administration [45]. Mathur et al. utilized a different technique that included two baseline samples taken 5 min apart from both adrenal veins and the iliac vein [46]. After the initial samples, an intravenous bolus of 0.25 mg of ACTH followed by an infusion of ACTH of 0.25 mg in 250 mL of normal saline was given at a rate of 150 cc/h. Venous samples were collected at 5, 10, and 15 min intervals after ACTH infusion.

The role of synthetic ACTH in AVS is to induce ACTH-sensitive adenomas to produce aldosterone and/or cortisol in excess of normal physiological levels. This process is the main mechanism behind AVS and allows clinicians to lateralize lesions to either or both adrenal glands. As stated before, there is no standard for whether a bolus, infusion, or both should be used during this procedure, though generally most centers use a combination of both techniques. There has been data published demonstrating the possibility that the administration of ACTH is unwarranted and may confound the results of the procedure [47]. One study investigating the usage of three different amounts of ACTH dosage (high, intermediate, and low) found that the high and intermediate dosage groups led to an incorrect lateralization in 3 and 12.5 % of cases, respectively [47]. The authors have suggested that this may be due to the tendency for the ACTH to stimulate the normal adrenal glandular tissue instead of the adenoma. As of now, more data is needed to determine the optimal protocol for administration of ACTH stimulation.

The *Adrenal Venous Sampling International Study* showed that about 66 % of centers used sequential sampling technique with cosyntropin stimulation [48]. The remaining centers used simultaneous sampling with no cosyntropin stimulation. Although there is the possibility of creating an artificial gradient when sampling sequentially, when cortisol secretion is maximally stimulated using cosyntropin, the

time difference between sampling is irrelevant when assessing selectivity. The pulsatile nature of aldosterone secretion, though, makes measurements susceptible to temporal variability in aldosterone concentration in each adrenal vein. This fact is important to consider for determining the *lateralization index (LI).*

Once the catheter has been placed, samples are removed and assayed to determine what is referred to as the *selectivity index (SI).* This index is used to confirm the placement of the catheter by comparing the concentrations of cortisol from the adrenal vein samples to samples taken from the inferior vena cava. A selectivity index, defined as plasma cortisol concentration$_{\text{adrenal vein}}$/plasma cortisol concentration$_{\text{IVC}}$, ≥2–5 indicates cortisol levels are more concentrated in the adrenal veins and confirms selectivity [46, 48–50]. Another way to confirm placement of the catheter is using gentle retrograde venography. Contrast filling the right and left adrenal veins confirms placement. The simultaneous and sequential techniques are described below.

The simultaneous technique is started when catheters with side holes located toward the distal end (generally 4-F Simmons 1 and 4-F Simmons 2 catheters; Cook, Bloomington, IN) are directed through the right common femoral vein and placed in the right and left adrenal veins [51]. Small amounts of nonionic contrast are injected to verify the locations of the catheters. During this time, a 3000 unit bolus of intravenous heparin should be administered. The baseline samples are removed simultaneously from the right and left adrenal veins to be tested for aldosterone and cortisol concentrations. Cosyntropin is administered as a 0.25 mg bolus followed by 0.25 mg in 5 mL of normal saline infused over 10–15 min. After ACTH stimulation via cosyntropin, blood is removed simultaneously from the right and left adrenal veins. Following the completion of the infusion, blood is drawn from the IVC.

In the sequential technique, a single set of post-infusion samples are obtained following bilateral catheterization. Patients receive a continuous intravenous infusion of 0.25 mg per 500 mL of normal saline of cosyntropin at a rate of 100 mL/h. Infusion is initiated 1 h before sampling as well as throughout the procedure. Access to the right adrenal vein is gained through the right common femoral vein with a 5-F HS2 catheter (Cook) with a side hole located near the distal end [51]. A sample is drawn to determine aldosterone and cortisol concentrations. As stated above, retrograde injection is used to verify catheter location. Directly following this, the catheter is switched for a 5-F Simmons 2 catheter and catheterization and sampling of the left adrenal vein is performed. Once again, retrograde injection is performed to verify catheter location. Drawn blood samples are measured for aldosterone and cortisol concentrations. The catheter is then retracted into the IVC where another set of samples are drawn for aldosterone and cortisol measurement [51].

Diagnostic Evaluation

Once the PAC/PRA ratio is used to confirm a diagnosis of primary aldosteronism, PRA, PAC, and a basic metabolic panel may indicate the etiology of the PA. Unilateral aldosteronomas are responsible for 30–60 % of cases and usually cause greater hypertension, greater hypokalemia, and higher concentrations of aldosterone when compared to bilateral adrenal hyperplasia [46]. Literature has reported a sensitivity of 100 % and specificity of 61 % in diagnosing aldosteronomas using a PAC/PRA ratio >32 [37]. If findings remain equivocal, the lateralization index can be used to assess the location of aldosterone hypersecretion. The LI is defined as PAC/PCC$_{\text{dom}}$: PAC/PCC$_{\text{nondom}}$: PAC and PCC from both adrenal veins with the higher PAC/PCC ratio divided by the lower [50]. This value is then compared to a cutoff value which differs between studies. The AVIS study showed centers using LI cutoffs ranging from 2.0 to 4.0, depending on whether or not cosyntropin stimulation was used and was sufficient [48]. Mathur et al. have demonstrated lateralization to be most accurate using cosyntropin stimulation with simultaneous catheterization and a cutoff value >4.0. These authors report a success rate of 98 % with cosyntropin as well as a 95 % success rate pre-ACTH stimulation [46]. There is still significant debate over the LI cutoff to achieve successful lateralization. The choice of a higher/stricter cutoff, with and without stimulation, leads to selection of patients with a higher probability of being successfully treated with unilateral adrenalectomy. Although useful, this selection may exclude a few patients with aldosteronomas that produce low or varying amounts of aldosterone. It should be noted that because the majority of aldosterone-producing adenomas are benign, a false negative, due to a stricter LI cutoff, will result in a patient being managed medically. On the contrary, a false positive results in a patient undergoing an unnecessary surgery, exposing them to all associated risks. As such, it would be prudent to use a stricter cutoff for LI index.

Another important consideration is that large aldosterone-producing adenomas >3 cm sometimes co-secrete cortisol which leads to suppression of cortisol production in the contralateral adrenal gland. This phenomenon lowers the SI on the contralateral side and increases the PAC/PCC ratio and thus changing the LI [33, 50]. In these cases with lesions >3 cm, biochemical assessments should be used to rule out hypercortisolism. If hypercortisolism is confirmed, the lesion should be resected without prior AVS being performed.

Some authors have suggested the usage of secondary characteristics such as absolute value of the PAC/PRA ratio and measurement of other steroid levels when AVS results in equivocal findings. Some aldosteronomas have been found to secrete 18-hydroxycortisol and 18-oxocortisol [52].

A ratio of 18-hydroxtcortisone (precursor) to aldosterone seems to be around 1.5–3 on the ipsilateral side of the lesion and >5 on the contralateral side. These criteria though have only been used in small studies and although promising lack sufficient formal evidence. Auchus et al. have suggested that in cases where LI is 2–4, if the IVC aldosterone/cortisol ratio is significantly higher (>1.5×) than the nondominant adrenal vein, then the case can be considered lateralized to the dominant side. These authors report accurately identifying several patients with this approach [49]. More comprehensive evidence is needed before these can be incorporated into standard of care algorithms.

Complications

Early studies have reported adrenal vein sampling complication rates ranging from 0.2 to 13 % [50]. The AVIS study has noted that most sites with large volume of AVS report a complication rate of <1 % [48]. The most common complication has consistently been reported as adrenal vein rupture, while other complications include vascular dissection, thrombosis, and intraglandular and periadrenal hematoma [50]. Not surprisingly, the AVIS study concluded that the number of adrenal vein ruptures was inversely proportional to the number of AVS performed per radiologist and per medical center [48]. Adrenal vein rupture is defined by constant pain following AVS and should be confirmed with imaging studies. It can usually be treated conservatively with no major clinical sequelae. The other less common complications may cause permanent adrenal insufficiency which can, oddly, be curative if occurring ipsilateral to the aldosterone-producing adenoma. In general, AVS is a safe and diagnostically accurate procedure with an extremely low complication rate in experienced hands.

Results and Conclusion

Although adrenal venous sampling is a technically challenging procedure, it is a proven diagnostic tool for subtyping primary aldosteronism. Its high diagnostic accuracy and low complication rate support its usage as the gold standard for diagnosing PA. The limitations of CT/MR imaging and basic biochemical laboratory results alone make it an important tool for clinicians. High-resolution CT/MR imaging, as used to distinguish between unilateral and bilateral lesions, may still miss small lesions or detect clinically irrelevant nonfunctional adrenal incidentalomas. Going forward, additional studies are needed to optimize the use of ACTH stimulation in conjunction with AVS as well as establish standards for SI and LI values.

Percutaneous Image-Guided Adrenal Ablation

Adrenal tumors represent a large heterogeneous group of neoplasms. Primary adrenal tumors include nonfunctioning adenomas, cortisol-secreting adenomas, aldosterone-secreting adenomas, pheochromocytomas, and adrenocortical carcinomas [53]. The adrenal gland is also a common site of metastatic disease from the lungs, kidneys, prostate, and/or melanoma [4]. Surgical resection has been the standard practice for the treatment of malignant and/or functioning tumors. Recently though, there has been increased investigation into minimally invasive procedures that aim to minimize the morbidity of adrenal interventions. These procedures have been useful for patients with metastatic/multifocal diseases and patients with multiple comorbidities. The most commonly used ablation techniques for adrenal lesions are radiofrequency ablation (RFA), cryoablation (CA), microwave ablation (MWA), and chemical ablation (ChA) with RFA being by far the most utilized.

Patient Evaluation

Pre-intervention assessment of a patient an adrenal tumor should include a multispecialty consultation with surgical, endocrine and/or urologic oncologists, interventional radiologists, radiation oncologists, and endocrinologists. This approach is required to manage the many intricacies of adrenal neoplasms. Clinicians should weigh the risks, benefits, and suitability of ablative interventions for the particular patients. Patients for whom ablative therapy is indicated must undergo pre-procedural imaging studies in the form of multiphase CT or MRI with gadolinium for tumor staging and grading. Ablation is indicated when isolated adrenal metastases are found on imaging but is contraindicated if extensive systemic metastases are discovered [54]. Other routine laboratory measurements should also be made. If a functioning tumor is suspected, patients should have appropriate biochemical assessments to rule out hypersecretion. Currently, ablative techniques for adrenal tumors are indicated for patients that are poor surgical candidates, patients that have unresectable lesions, patients with a past surgical history of attempted removal, and/or patients who refuse surgery. Ablative therapies may offer a minimally invasive technique to effectively treat patients in this cohort.

Although ablative techniques appear promising, standardization of care is ongoing. For example, pre-ablation biopsy is recommended in most cases but may be avoided if a definitive diagnosis can be made from the patient's medical history and noninvasive imaging [55]. One author suggests that, when referring to renal tumors, pre-ablation biopsy makes

for a more definitive diagnosis, avoiding possibly unnecessary treatment and allowing for correct interpretation of ablation effectiveness and efficacy [56]. However, pre-ablation biopsy is not performed in all cases at this time.

Another major consideration when performing adrenal ablations is the need for pre-, intra-, and post-procedural therapy. The adrenal glands are complex, highly active organs that synthesize and release potent hormones, such as catecholamines and corticosteroids, directly into the blood circulation. As such, pre- and intraprocedural adrenergic blockage may be necessary. Ablation of the adrenal gland, without or with pheochromocytoma, may result in a surge of catecholamines into the bloodstream and may lead to an acute hypertensive crisis or cardiac and/cerebral ischemia/infarction. Some authors suggest alpha- and beta-adrenergic blockade for a number of weeks before and during any adrenal ablation as well as careful monitoring of hemodynamics intraprocedurally [57]. These medications are normally prophylactically used for cases in which pheochromocytoma is suspected or confirmed. Yet, no formal recommendations exist to date, so while it is now strongly suggested to initiate adrenergic blockade prior to any adrenal ablation, variations in practice persist [58]. Venkatesan et al. investigated the effectiveness of RFA for seven pheochromocytoma lesions in six patients [57]. Five of six patients were premedicated for 7–21 days prior to intervention using phenoxybenzamine, atenolol, and alpha-methyl-paratyrosine and for alpha-blockage, beta-blockage, and catecholamine synthesis inhibition, respectively. Six of the seven lesions were successfully treated, defined as lack of enhancement on CT at follow-up. The authors also report a single complication, a pneumothorax that was treated intraprocedurally and resulted in no further difficulties.

Patients with cortisol-secreting tumors should be medicated with peri-procedural hydrocortisone. Adrenal insufficiency is of special note when treating these patients. In keeping with widespread lack of standardization, post-ablation hydrocortisone replacement has been reported as long as 1–3 years following RFA of cortisol-secreting tumors [59].

Radiofrequency Ablation

Radiofrequency ablation is the most common technique used for ablation of adrenal lesions [53]. RFA employs an alternating electric current in the radiofrequency range to generate heat. The patient, grounding pads, a needle electrode, and a radiofrequency generator are all placed in series to create a closed circuit. When the alternating currents are applied, the heat generated causes thermal damage and tissue necrosis of the tumor. The amount and extent of tissue damage will depend on the temperature and duration of the ablation. The temperature necessary for effective tumor necrosis is 50–60 °C [60]. Most authors have found a treatment time of 8–10 min sufficient to reach the appropriate temperature and achieve complete tumor destruction [53]. Intratumoral temperature should be monitored during and after the ablation to ensure the adequate lethal temperature has been achieved.

The efficacy of RFA treating malignant and functioning adrenal tumors has been well documented in the literature. In addition to the previously cited small series by Venkatesan et al., Wolf et al. reported the efficacy of RFA and MWA in treating 23 metastatic lesions in 22 patients [57, 61]. Of the 16 tumors treated with RFA, 13 were successfully ablated while 3 were confirmed incomplete ablations. Two of the three tumors were successfully retreated at a later date. The authors reported two complications, retroperitoneal hematoma and intraprocedural hypertensive crisis and MI, in the RFA-treated patient cohort. Another study reports on the treatment of 15 primary adrenocortical carcinomas or metastatic disease in 8 patients [62, 63]. The authors state a technical success rate of 53 % with a higher success rate of 67 % when considering lesions ≤5 cm while incurring no major complications. All patients in this study were poor surgical candidates or had unresectable tumors necessitating a minimally invasive alternative. Lala et al. reported a 100 % clinical success rate in a retrospective study of 13 patients with functioning adrenal tumors. Clinical success was defined by the resolution of clinical symptoms and the normalization of biochemical imbalances [63].

It is important to note that communication between the interventional radiologist and anesthesiologist should be prioritized and maintained throughout the procedure. The interventional urologist/radiologist should communicate with the anesthesiologist whenever the adrenal gland is going to be manipulated, such as insertion or readjustment of the RFA probe. This allows the anesthesiologist to prepare for any possible consequences that may occur such as hypertensive crisis.

Radiofrequency ablation technical success is widely accepted as the lack of enhancement on CT imaging of the ablation zone immediately following the procedure and at 1–3 months of follow-up [53]. While RFA is the most commonly used modality for adrenal ablation, most published series are quite small so larger series and longer term efficacy data are necessary.

Cryoablation

Cryoablation involves the application of subfreezing temperatures to tumors to initiate tissue destruction. Currently, most cryoablation devices use argon gas through an internal aperture to cool the cryoablation probe and create the ice ball. Expansion of the gas causes rapid cooling that

allows the probe to reach temperatures ranging from –80 °C to −150 °C [53]. A range of 1–8 applicators can be used, with more applicators used to reach lower temperatures. A cryoablation treatment session involves two 10 min freezing sections with each followed by an 8 min thaw cycle. The main causes of cell death include the formation and melting of intracellular ice crystals, cell rupture, protein denaturation, and ischemia secondary to hypoxia [64]. Cryoablation also causes microvascular thrombosis that decreases bleeding, a resultant that occurs with RFA and MWA via cauterization. One advantage that cryoablation has over RFA or MWA is the capability of the interventional radiologist to visualize the expansion of the ice crystal using CT imaging or US. This difference decreases the risk of damaging adjacent structures.

Currently there is limited data examining the efficacy and effectiveness of cryoablation in adrenal tumors. Welch et al. reported success in obtained local control in 11 of 12 adrenal metastases in a cryoablation model [65]. As with all minimally invasive thermal ablation techniques, more data is needed not only to determine efficacy vis-à-vis the gold standard of surgical extirpation but also to distinguish if any particular method of thermal ablation is advantageous.

Microwave Ablation

Microwave ablation involves the usage of electromagnetic energy in the microwave range to induce cell death. This necrosis is achieved when the electromagnetic energy agitates water molecules, creating frictional heat. Microwave ablation is similar to RFA in that both procedures damage tissue via coagulation necrosis. Potential advantages of MWA over other types of ablation are higher peak tissue temperatures, capability to treat larger tumor volumes, faster ablation times, and the ability to successfully ablate cystic tumors. However, the rapid temperature elevation in MWA makes incrementally increases in tissue temperature difficult to achieve and thus this approach is considered somewhat more technically challenging. The MWA procedure involves placing a microwave probe directly into the tumor followed by the generation of electromagnetic microwaves. In one series, researchers successfully used MWA to successfully treat four out of four metastatic tumors with one complication, a case of intraprocedural hypertension [61]. In the only other series, Li et al. successfully obtained 100 % local control of 10 adrenal malignancies with a mean follow-up of 11.3 months [66]. As with cryoablation, limited evidence for the usage of MWA in adrenal ablation is available in the literature and further investigation is needed to characterize the use of MWA for adrenal lesions.

Chemical Ablation

Chemical ablation of the adrenal gland can be performed either by direct percutaneous injection of ethanol or acetic acid into the tumor or by embolization through the ipsilateral adrenal artery. Ethanol induces coagulative necrosis and microvascular thrombosis via protein denaturation. Although chemical ablation is not utilized widespread in the USA, the largest study to date examined chemical ablation of 46 primary and metastatic tumors. The authors report a success rate of 92.6 % when treating primary tumors and a lower 30 % success rate when treating metastatic tumors [67].

Technical Considerations

Adrenal gland tumors are most accessible posteriorly with the patient in an ipsilateral decubitus position. The position decreases the movement of the diaphragm and the ability of the ipsilateral lung to expand, which leads to hypoinflation. This minimizes the risk of lung transgression and pneumothorax. Supine transhepatic and paraspinal are two other possible approaches for adrenal ablation. One important consideration to consider when performing ablations is protecting surrounding structures from damage. This can be accomplished using hydrodissection to create a spatial border between structures and the target area. Under the guidance of ultrasound and/or CT imaging, a catheter with distal side holes is placed in the area in between the adrenal gland and the protected structure. The addition of 10 mL of iodinated contrast to a 500 mL bag of fluid assists in visualizing the solution on CT imaging [53]. The amount of 5 % dextrose in water injected is dependent upon the desired displacement to avoid damage to the nontarget structure. Saline solution and other ionic solutions conduct electricity and thus are not good choices for RFA, though they are not contraindicated for microwave and cryoablation.

As stated earlier, communication between the interventional radiologist and the anesthesiologist is critical during all adrenal gland ablations but is especially important in cases of pheochromocytoma. All technical manipulations (insertion/adjustment/removal of the ablation probe/initiation of current) of the adrenal gland or tumor should be announced to the anesthesiologist in preparation for possible hemodynamic consequences. In cases of confirmed or suspected pheochromocytoma, patients should be prophylactically medicated with alpha-adrenergic and beta-adrenergic blockers to prevent hypertensive crises.

Complications

The most common complications of adrenal gland ablation are bleeding, infection, hypertensive crisis, and thermal damage to adjacent organs [53]. Adrenal insufficiency is another possible complication that may lead to long-term medical management with appropriate hormones [59]. Needle seeding of tumor cells is a theoretical possibility but has not been reported following percutaneous adrenal ablation. The risk of seeding may possibly be minimized by ablating the probe track during removal through there is no evidence to support this technique.

Follow-up

Following ablation, patients should have a short-term follow-up that includes imaging and clinical evaluation. Regular interval imaging with contrast-enhanced modalities is useful for detecting the technical success of ablation and also to detect incomplete ablation or recurrent tumors. Currently there are no established guidelines for the length and intervals of follow-up after ablation. Wolf et al. reported follow-up within 30 days after ablation, 3 months after ablation, and 6 months after ablation [61]. Other authors suggest follow-up 1–3 months after ablation then again at 6–12 month intervals [55]. This latter scheduled is probably more commonly adopted and results in adequate follow-up without unnecessary clinic visits or imaging. A successful ablation is defined as a lack of enhancement within the ablation area and a gradual decrease in size of the ablation zone. Enhancement and/or enlargement of the ablation zone may be indicative of a recurrent tumor or failed ablation. Patients who were treated for functioning tumors should also have full biochemical evaluation. Clinically successful treatments should return patients to their normalized blood levels.

Conclusion

Percutaneous ablative therapies appear to be effective approach to manage patients who are poor surgical candidates, due to either multiple comorbidities or metastatic disease. All modalities have scant but promising data for ablation of adrenal tumors and all need to be investigated more fully to determine their true safety and usefulness in the adrenal gland. While these techniques may be well established in other organs, the intricacies of the adrenal gland make it a challenging treatment location. As more data becomes available, the role of minimally invasive ablative techniques for adrenal tumors will be better characterized and treatment algorithms standardized.

References

1. Young Jr WF. Clinical practice. The incidentally discovered adrenal mass. N Engl J Med. 2007;356(6):601–10.
2. Barzon L, et al. Prevalence and natural history of adrenal incidentalomas. Eur J Endocrinol. 2003;149(4):273–85.
3. Tsitouridis I, et al. CT guided percutaneous adrenal biopsy for lesions with equivocal findings in chemical shift MR imaging. Hippokratia. 2008;12(1):37–42.
4. Wagnerova H, Lazurova I, Felsoci M. Adrenal metastases. Bratisl Lek Listy. 2013;114(4):237–40.
5. Young WF. Primary aldosteronism: renaissance of a syndrome. Clin Endocrinol (Oxf). 2007;66(5):607–18.
6. Aronova A, Iii TJ, Zarnegar R. Management of hypertension in primary aldosteronism. World J Cardiol. 2014;6(5):227–33.
7. Bittner JGT, Brunt LM. Evaluation and management of adrenal incidentaloma. J Surg Oncol. 2012;106(5):557–64.
8. Icard P, et al. Adrenocortical carcinomas: surgical trends and results of a 253-patient series from the French Association of Endocrine Surgeons study group. World J Surg. 2001;25(7):891–7.
9. Sharma KV, et al. Image-guided adrenal and renal biopsy. Tech Vasc Interv Radiol. 2010;13(2):100–9.
10. Arnaldi G, Boscaro M. Adrenal incidentaloma. Best Pract Res Clin Endocrinol Metab. 2012;26(4):405–19.
11. Groussin L, et al. ^{18}F-Fluorodeoxyglucose positron emission tomography for the diagnosis of adrenocortical tumors: a prospective study in 77 operated patients. J Clin Endocrinol Metab. 2009;94(5):1713–22.
12. Arellano RS, et al. Image-guided percutaneous biopsy of the adrenal gland: review of indications, technique, and complications. Curr Probl Diagn Radiol. 2003;32(1):3–10.
13. Mazzaglia PJ, Monchik JM. Limited value of adrenal biopsy in the evaluation of adrenal neoplasm: a decade of experience. Arch Surg. 2009;144(5):465–70.
14. Song JH, Chaudhry FS, Mayo-Smith WW. The incidental adrenal mass on CT: prevalence of adrenal disease in 1,049 consecutive adrenal masses in patients with no known malignancy. AJR Am J Roentgenol. 2008;190(5):1163–8.
15. Song JH, Chaudhry FS, Mayo-Smith WW. The incidental indeterminate adrenal mass on CT (>10 H) in patients without cancer: is further imaging necessary? Follow-up of 321 consecutive indeterminate adrenal masses. AJR Am J Roentgenol. 2007;189(5):1119–23.
16. BRIDGE Study Investigators. Bridging anticoagulation: is it needed when warfarin is interrupted around the time of a surgery or procedure? Circulation. 2012;125(12):e496–8.
17. Ahrar K, Gupta S. Percutaneous image-guided biopsy. New York: Springer; 2014. x, 375 pages.
18. Kane NM, et al. Percutaneous biopsy of left adrenal masses: prevalence of pancreatitis after anterior approach. AJR Am J Roentgenol. 1991;157(4):777–80.
19. Bernardino ME, et al. CT-guided adrenal biopsy: accuracy, safety, and indications. AJR Am J Roentgenol. 1985;144(1):67–9.
20. Heaston DK, et al. Narrow gauge needle aspiration of solid adrenal masses. AJR Am J Roentgenol. 1982;138(6):1143–8.
21. Mody MK, Kazerooni EA, Korobkin M. Percutaneous CT-guided biopsy of adrenal masses: immediate and delayed complications. J Comput Assist Tomogr. 1995;19(3):434–9.
22. Gervais D, Sabharwal T. Interventional radiology procedures in biopsy and drainage, Techniques in interventional radiology. London/New York: Springer; 2011. xiv, 199 p.
23. Sharma P, et al. Can hybrid SPECT-CT overcome the limitations associated with poor imaging properties of ^{131}I-MIBG?: comparison

with planar scintigraphy and SPECT in pheochromocytoma. Clin Nucl Med. 2013;38(9):e346–53.
24. de Agustin P, et al. Fine-needle aspiration biopsy of the adrenal glands: a ten-year experience. Diagn Cytopathol. 1999;21(2):92–7.
25. Saboorian MH, Katz RL, Charnsangavej C. Fine needle aspiration cytology of primary and metastatic lesions of the adrenal gland. A series of 188 biopsies with radiologic correlation. Acta Cytol. 1995;39(5):843–51.
26. Welch TJ, et al. Percutaneous adrenal biopsy: review of a 10-year experience. Radiology. 1994;193(2):341–4.
27. Grumbach MM, et al. Management of the clinically inapparent adrenal mass ("incidentaloma"). Ann Intern Med. 2003;138(5):424–9.
28. Quayle FJ, et al. Needle biopsy of incidentally discovered adrenal masses is rarely informative and potentially hazardous. Surgery. 2007;142(4):497–502; discussion 502–4.
29. Saeger W, et al. High diagnostic accuracy of adrenal core biopsy: results of the German and Austrian adrenal network multicenter trial in 220 consecutive patients. Hum Pathol. 2003;34(2):180–6.
30. Fauci AS. Harrison's principles of internal medicine. 17th ed. New York: McGraw-Hill; 2008.
31. Magill SB, et al. Comparison of adrenal vein sampling and computed tomography in the differentiation of primary aldosteronism. J Clin Endocrinol Metab. 2001;86(3):1066–71.
32. McKenzie TJ, et al. Aldosteronomas – state of the art. Surg Clin North Am. 2009;89(5):1241–53.
33. Mulatero P, et al. Impact of different diagnostic criteria during adrenal vein sampling on reproducibility of subtype diagnosis in patients with primary aldosteronism. Hypertension. 2010;55(3):667–73.
34. Phillips JL, et al. Predictive value of preoperative tests in discriminating bilateral adrenal hyperplasia from an aldosterone-producing adrenal adenoma. J Clin Endocrinol Metab. 2000;85(12):4526–33.
35. Stewart PM, Allolio B. Adrenal vein sampling for Primary Aldosteronism: time for a reality check. Clin Endocrinol (Oxf). 2010;72(2):146–8.
36. Young WF, et al. Role for adrenal venous sampling in primary aldosteronism. Surgery. 2004;136(6):1227–35.
37. Khan SL, Angle JF. Adrenal vein sampling. Tech Vasc Interv Radiol. 2010;13(2):110–25.
38. Funder JW, Carey RM, Fardella C, et al. Case detection, diagnosis, and treatment of patients with primary aldosteronism: an endocrine society clinical practice guideline. J Clin Endocrinol Metab. 2008;93(9):3266–81.
39. Weinberger MH, Fineberg NS. The diagnosis of primary aldosteronism and separation of two major subtypes. Arch Intern Med. 1993;153(18):2125–9.
40. Young Jr WF, Hogan MJ. Renin-independent hypermineralocorticoidism. Trends Endocrinol Metab. 1994;5(3):97–106.
41. Rossi GP, Seccia TM, Pessina AC. Primary aldosteronism – part I: prevalence, screening, and selection of cases for adrenal vein sampling. J Nephrol. 2008;21(4):447–54.
42. Lim PO, et al. Potentially high prevalence of primary aldosteronism in a primary-care population. Lancet. 1999;353(9146):40.
43. Vongpatasin W. Resistant hypertension: a review of diagnosis and management. JAMA. 2014;311(31):2216–24.
44. Kempers MJ, et al. Systematic review: diagnostic procedures to differentiate unilateral from bilateral adrenal abnormality in primary aldosteronism. Ann Intern Med. 2009;151(5):329–37.
45. Sacks BA, Brook OR, Brennan IM. Adrenal venous sampling: promises and pitfalls. Curr Opin Endocrinol Diabetes Obes. 2013;20(3):180–5.
46. Mathur A, et al. Consequences of adrenal venous sampling in primary hyperaldosteronism and predictors of unilateral adrenal disease. J Am Coll Surg. 2010;211(3):384–90.
47. Seccia TM, et al. Adrenocorticotropic hormone stimulation during adrenal vein sampling for identifying surgically curable subtypes of primary aldosteronism: comparison of 3 different protocols. Hypertension. 2009;53(5):761–6.
48. Rossi GP, et al. The Adrenal Vein Sampling International Study (AVIS) for identifying the major subtypes of primary aldosteronism. J Clin Endocrinol Metab. 2012;97(5):1606–14.
49. Auchus RJ, et al. What we still do not know about adrenal vein sampling for primary aldosteronism. Horm Metab Res. 2010;42(6):411–5.
50. Rossi GP, et al. An expert consensus statement on use of adrenal vein sampling for the subtyping of primary aldosteronism. Hypertension. 2014;63(1):151–60.
51. Carr CE, et al. Comparison of sequential versus simultaneous methods of adrenal venous sampling. J Vasc Interv Radiol. 2004;15(11):1245–50.
52. Nakamura Y, et al. 18-oxocortisol measurement in adrenal vein sampling as a biomarker for subclassifying primary aldosteronism. J Clin Endocrinol Metab. 2011;96(8):E1272–8.
53. Ethier MD, Beland MD, Mayo-Smith W. Image-guided ablation of adrenal tumors. Tech Vasc Interv Radiol. 2013;16(4):262–8.
54. Gunjur A, et al. Surgical and ablative therapies for the management of adrenal 'oligometastases' – a systematic review. Cancer Treat Rev. 2014;40(7):838–46.
55. Venkatesan AM, et al. Percutaneous ablation of adrenal tumors. Tech Vasc Interv Radiol. 2010;13(2):89–99.
56. Tuncali K, et al. Evaluation of patients referred for percutaneous ablation of renal tumors: importance of a preprocedural diagnosis. AJR Am J Roentgenol. 2004;183(3):575–82.
57. Venkatesan AM, et al. Radiofrequency ablation of metastatic pheochromocytoma. J Vasc Interv Radiol. 2009;20(11):1483–90.
58. Atwell TD, et al. Malignant hypertension during cryoablation of an adrenal gland tumor. J Vasc Interv Radiol. 2006;17(3):573–5.
59. Arima K, et al. Image-guided radiofrequency ablation for adrenocortical adenoma with Cushing syndrome: outcomes after mean follow-up of 33 months. Urology. 2007;70(3):407–11.
60. Rhim H, et al. Essential techniques for successful radio-frequency thermal ablation of malignant hepatic tumors. Radiographics. 2001;21(Spec No):S17–35; discussion S36–9.
61. Wolf FJ, et al. Adrenal neoplasms: effectiveness and safety of CT-guided ablation of 23 tumors in 22 patients. Eur J Radiol. 2012;81(8):1717–23.
62. Wood BJ, et al. Radiofrequency ablation of adrenal tumors and adrenocortical carcinoma metastases. Cancer. 2003;97(3):554–60.
63. Mendiratta-Lala M, et al. Efficacy of radiofrequency ablation in the treatment of small functional adrenal neoplasms. Radiology. 2011;258(1):308–16.
64. Beland MD, Mayo-Smith WW. Ablation of adrenal neoplasms. Abdom Imaging. 2009;34(5):588–92.
65. Tsoumakidou G, et al. Life-threatening complication during percutaneous ablation of adrenal gland metastasis: Takotsubo syndrome. Cardiovasc Intervent Radiol. 2010;33(3):646–9.
66. Li X, et al. CT-guided percutaneous microwave ablation of adrenal malignant carcinoma: preliminary results. Cancer. 2011;117(22):5182–8.
67. Xiao YY, et al. CT-guided percutaneous chemical ablation of adrenal neoplasms. AJR Am J Roentgenol. 2008;190(1):105–10.

Part VI

Retroperitoneum

Varicocele and Pelvic Congestion Syndrome

28

No Kwak

Varicocele

Varicocele is a commonly encountered venous disease characterized by varicosities of the pampiniform plexus secondary to gonadal vein reflux. Often found in adolescence, the incidence of varicocele is approximately 16 %, and its prevalence increases with each decade reaching 42 % in the elderly population [1, 2]. While most men with varicocele are asymptomatic, clinical presentations include male infertility, scrotal pain, and/or low serum testosterone level [3]. It is estimated that 19–41 % of the infertile men present with varicocele as the only identifiable cause of infertility, and these individuals frequently manifest with testicular hypotrophy and abnormal semen parameters [4–8].

The etiology of varicocele is believed to be multifactorial and includes anatomical difference in the venous drainages of the left and right gonadal veins, valvular absence or dysfunction, and venous obstruction from external compression. Varicocele generally occurs on the left side accounting for approximately 80–90 % of the cases although some authors have argued for the bilateral phenomenon of varicocele [9]. The venous drainage of the left gonadal vein into the "high-pressure" left renal vein as well as the longer course and perpendicular insertion of the left gonadal vein may explain the predominance of the left-sided varicocele. It is estimated that up to 40 % of the population presents with congenital valvular absence. Valvular absence or dysfunction is believed to facilitate the venous reflux in the pampiniform plexus leading to the development of varicocele. However, some authors dispute this notion, based on the cadaver data showing the absence of the valves in the spermatic vein in men with and without varicocele [10]. Although rare, compression of the left renal vein by the superior mesenteric artery as in the nutcracker syndrome can cause secondary varicocele. Isolated right varicocele is rare and necessitates further workup for retroperitoneal lymphadenopathy or renal tumors responsible for the venous obstruction [11–14].

The pathophysiology of varicocele leading to male infertility remains elusive despite the extensive investigation in the past decades. Alteration in the hypothalamic-pituitary-gonadal axis, testicular hyperthermia, hypoxia, and reflux of the renal and adrenal metabolites are among the proposed mechanisms of varicocele-mediated male infertility. Stagnation of blood in the microcirculatory vessels and ischemic degenerative changes of the seminiferous tubules have been reported in the testicular biopsies of men with varicocele [9, 15]. Recently, a large body of evidence has suggested the role of reactive oxygen species on sperm DNA damage detected as DNA fragmentation and 8-OHdG although the exact mechanism is yet unclear [16, 17].

Diagnosis and Imaging

Varicocele manifests as a "bag of worms" on scrotal examination. It is classified as grade 0 (no palpable varicocele during Valsalva maneuver), grade 1 (palpable only during Valsalva maneuver), grade 2 (palpable at rest), and grade 3 (visible and palpable at rest) [18].

Venography is the most definitive diagnostic study and is commonly used as the reference value for many investigators comparing the efficacy of different diagnostic modalities including contact thermography and ultrasonography. However, it is an invasive procedure and is typically reserved until the time of interventional treatment. Ultrasonography is the imaging modality of choice as it enables the real-time visualization of venous dilatation and reflux in the pampiniform plexus and allows the assessment of the other intra- and extratesticular pathology.

Sonographic examination is generally performed using a high-frequency transducer (7–10 MHz) while the patient stands upright performing the Valsalva maneuver. On ultrasonography, varicocele is best visualized superior or lateral to the testis

N. Kwak, MD
Department of Radiology, North Shore LIJ Health System, New Hyde Park, NY, USA
e-mail: NKwak@NSHS.edu

A.R. Rastinehad, D.N. Siegel (eds.), *Interventional Urology*, DOI 10.1007/978-3-319-23464-9_28

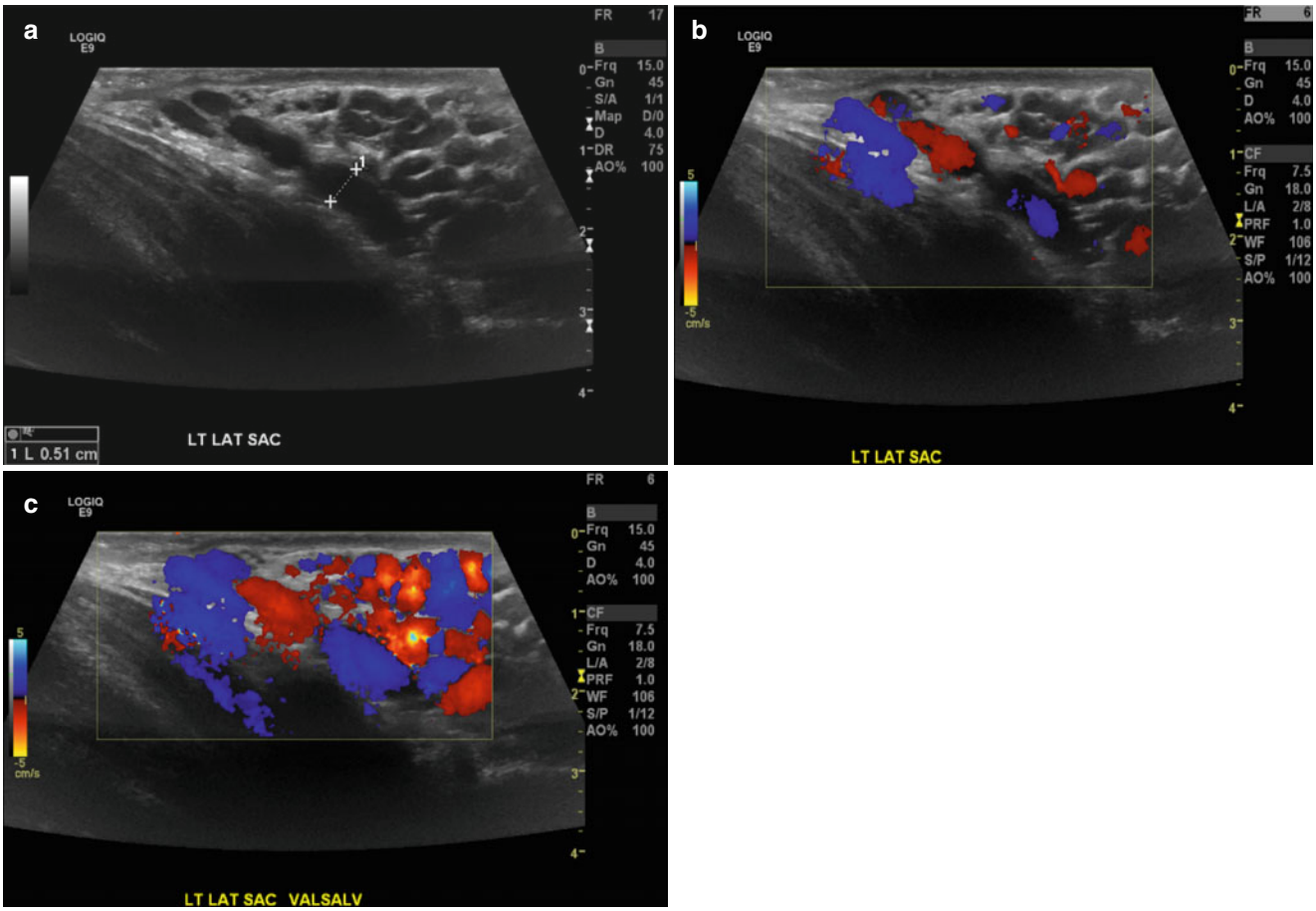

Fig. 28.1 A 19-year-old male with left-sided varicocele. (**a**) The gray-scale sonography shows dilated veins in the pampiniform plexus measuring 5 mm. (**b**, **c**) The color Doppler sonography demonstrates reflux during the Valsalva maneuver indicated by the increase in color flow

and is characterized by multiple, serpiginous, and tubular structures (Fig. 28.1). The veins of the pampiniform plexus normally range from 0.5 to 1.5 mm in diameter. The diagnosis of varicocele is made when the veins in the pampiniform plexus measure greater than 3 mm and demonstrate reflux during the Valsalva maneuver [19, 20]. In the report by Pilatz et al., clinically significant varicoceles (grade I–III) were reliably diagnosed with sensitivity and specificity of greater than 80 % using the diameter values of 2.45 mm at rest and 2.95 mm during the Valsalva maneuver [21]. When the presence of reflux in the veins of the pampiniform plexus was used as criteria, Petros et al. reported a high sensitivity of 93 % but a specificity of only 33 % [22]. When the reflux criterion was further refined as greater than 1 s, Trum et al. reported high sensitivity and specificity of 97 and 94 %, respectively [23].

Treatment

Varicocele treatment is indicated in patients with clinical varicocele with (1) male infertility and with abnormal semen parameters or function test, (2) greater than 20 % testicular volume differential that persists for more than a year in the pediatric population, (3) scrotal discomfort or pain, or (4) hypogonadism [3, 24–27].

Varicocelectomy

Basic surgical approaches in ligating the internal spermatic vein include retroperitoneal, inguinal, and subinguinal. Various varicocele ligation techniques have been developed over the past decades. Open (Palomo) or laparoscopic retroperitoneal, macroscopic inguinal (Ivanissevich), and microscopic subinguinal techniques are among the many available options [4, 28, 29]. For the high retroperitoneal approach, a transverse incision is made medial and inferior to the anterior superior iliac spine at the level of the inguinal ring. By incising the external oblique fascia and retracting the internal oblique muscle, the internal spermatic veins are exposed, dissected, and ligated. Doppler probe is typically used to facilitate the identification of the testicular artery. Laparoscopic varicocelectomy is generally performed transperitoneally, while retroperitoneal and extraperitoneal approaches have been described. Laparoscopic technique provides higher magnification and is performed nearer the

left renal vein where there are fewer large draining gonadal veins, far from the takeoff of the testicular artery.

For the inguinal approach, the incision is made just above the pubic symphysis. Incision of the external oblique fascia allows mobilization of the spermatic cord, and the internal spermatic veins are exposed and ligated after the spermatic fascia is incised.

Microsurgical subinguinal varicocelectomy is the newest technique that has gained popularity among the male infertility specialists because of its favorable outcomes. For the subinguinal approach, an incision is made at the external inguinal ring avoiding division of the abdominal fascia and muscle. Use of 8–15 power optical magnification and microvascular Doppler allows clear identification of vessels and lymphatics minimizing the risk of accidental ligation.

Recent meta-analysis by Cayan et al. has reported overall spontaneous pregnancy in 39 % of 4473 subfertile or infertile men undergoing varicocele treatment with various techniques. The highest spontaneous pregnancy rate of 39 % was achieved after varicocele repair [30]. The highest spontaneous pregnancy rate of 42 % was achieved in the microscopic subinguinal technique, compared to 38 % in the Palomo, 30 % in the laparoscopic, and 36 % in the macroscopic inguinal techniques. The lowest recurrence rate of 1 % was seen in the microscopic subinguinal technique while 15, 4.3, and 2.6 % recurrence rates were seen in the Palomo, laparoscopic, and Ivanissevich techniques, respectively. The lowest hydrocele formation rate of 0.4 % was reported in the microscopic subinguinal technique, compared to 8, 2.8, and 7 % in the Palomo, laparoscopic, and macroscopic inguinal techniques. Rare complications included testicular atrophy after incidental artery ligation and intraperitoneal injury to bowel, bladder, or neurovascular bundles.

Percutaneous Embolization

Retrograde gonadal vein embolization is the standard procedure for primary varicocele treatment or salvage therapy for recurrent varicocele. Retrospective study of varicocele treatment with surgical ligation and percutaneous embolization by Shlansky-Goldberg et al. has reported comparable improvement in seminal parameters and pregnancy rates of 39 and 34 % after embolization and surgery, respectively [31]. Advantages of percutaneous varicocele embolization include anatomic delineation of the venous collaterals and sparing of injury to the lymphatic drainage and testicular artery. While hydrocele formation is a major postoperative complication after surgical ligation, it has never been reported after embolization.

Embolization is generally performed via a right femoral vein approach. A 5–6 French Cobra catheter is typically used to catheterize the left renal vein then the orifice of the left gonadal vein. Use of a coaxial system with a 6–7 French preformed long sheath or guiding catheter provides additional stability. Use of a microcatheter facilitates the catheterization of the small caliber veins with less risk of vasospasm or perforation. The origin of the right gonadal vein typically drains into the right anterolateral aspect of the IVC inferior to the right renal vein. A sidewinder-type catheter like a Mickelson, Sos Omni, or Simmons catheter is usually used on the right. Given the size of most IVCs, a catheter with larger secondary curve may aid in access due to its reverse curvature and larger secondary curve which can brace itself against the IVC wall. Internal jugular or basilic vein approach can be used in the setting of unsuccessful catheterization of the right gonadal vein via the femoral approach.

After catheterizing the gonadal vein, venography is performed with the patient placed in the reverse Trendelenburg position. Venograms are obtained at various levels while advancing the catheter from the orifice of the gonadal vein to the level of the pubic symphysis for mapping of the highly variable venous collateral pathways. In general, the gonadal vein branches into the medial and lateral divisions at the level of L4. While the medial division drains are joined by the periureteral veins to form a venous plexus along the ureter draining into the left renal vein or IVC, the lateral division joins the renal capsular and colonic veins. Cross communication between the left and right spermatic veins has been reported in 55 % of the human cadavers [10]. Duplication of the gonadal vein in the inguinal region and communication with the retroperitoneal veins such as the lumbar, renal capsular, iliac, and rarely circumaortic renal veins are among the common collateral pathways (Fig. 28.2). Incomplete interruption of these collateral pathways contributes to the persistence or recurrence of varicocele after surgical or interventional treatment [32–34].

Various embolic agents are used in embolization including coils, vascular plugs, and sclerosants. Coils are the most commonly used embolic agents and can be classified based on the mechanisms of deployment and occlusion. A detachable coil has many advantages as its release mechanism allows precise positioning of the coil mass and safe withdrawal prior to deployment, in cases of inappropriate sizing relative to the vein diameter or inaccurate positioning. However, a detachable coil tends to be more costly. While a fibered coil induces thrombosis around the coil mass, a hydrogel-coated coil can expand up to nine times its original volume leading to vessel occlusion [35]. Coil embolization of the gonadal vein is performed by placing a nest of coils at the lowest collateral branch, usually at the level of the inguinal ligament. Microcoils are available if a microcatheter is utilized for catheterization at this level. During the retraction of the catheter toward the renal vein, coils are deployed at multiple levels. Generally, coils are placed at four levels: (1) the inguinal ligament, (2) lower sacroiliac joint, (3) upper sacroiliac joint, and (4) several centimeters below the renal vein insertion. Branching points are embolized in an effort to achieve interruption of the collateral pathways (Fig. 28.3).

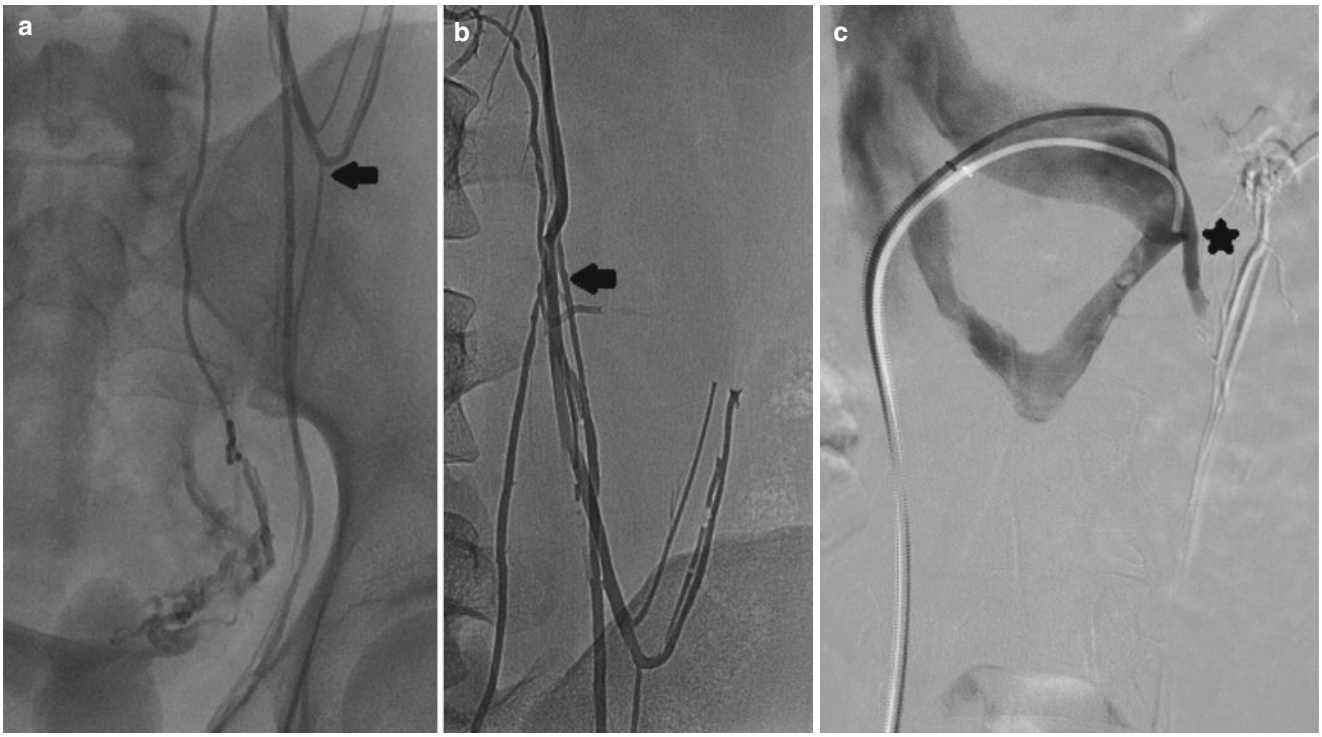

Fig. 28.2 A 24-year-old male with bilateral scrotal pain elicited when lifting weights. (**a**, **b**) Duplicated gonadal veins join retroperitoneal veins (*arrows*) at the level of the upper sacroiliac joint. (**c**) The left gonadal vein drains into the circumaortic renal vein (*asterisk*)

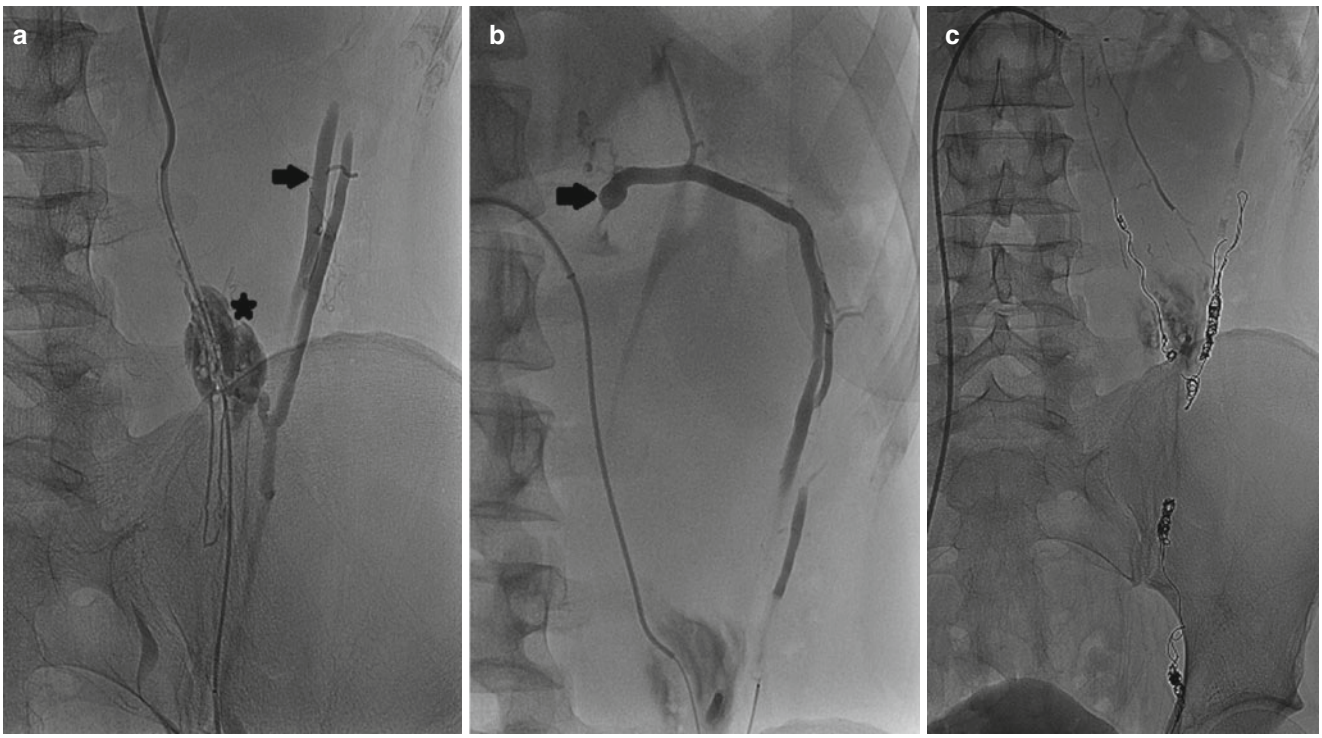

Fig. 28.3 A 25-year-old male with left-sided varicocele and scrotal pain. (**a**, **b**) The left gonadal and accessory gonadal veins join the renal capsular veins draining into the left renal vein (*arrows*). Contrast extravasation is seen at the confluence (*asterisk*) indicating small perforation. A microcatheter is used to traverse the short segment of venous perforation. (**c**) Multiple coils are deployed in the gonadal and renal capsular veins

Amplatzer vascular plugs offer a simple, efficient way to occlude large caliber veins. Technical success rate of 96 % has been reported with spontaneous pregnancy rate of 40 % and statistically significant improvement in the semen parameters [36, 37]. Overall complication rate is 11 % including minor complications, contrast extravasation from vascular perforation, coil migration, allergy to contrast agent, and thrombophlebitis of the pampiniform plexus. Major complication rates are about 1 %.

Various sclerosing agents have been used including boiling contrast material, ethanol, sodium tetradecyl sulfate, and sodium morrhuate. Currently, sodium tetradecyl sulfate is the only FDA-approved sclerosant in the United States. Sodium tetradecyl sulfate is typically mixed with air and vigorously agitated between two syringes through a three-way stopcock (Tessari technique) in order to create foam consistency. Upon injection, chemical injury is believed to produce inflammatory reaction leading to endothelial necrosis. A retrospective study by Gandini et al. has reported spontaneous pregnancy rate of 39 % and resolution of testicular pain in 96.5 % of the patients [38]. Similarly, Li et al. have reported technical success rate of 91.4 % with no subsequent recurrence. However, sclerotherapy is often associated with significant inflammatory pain during injection, and reflux of the sclerosant into the undesired venous beds can result in rare complications such as pampiniform thrombophlebitis or renal vein thrombosis.

Coils and sclerosants are often used together in the sandwich technique. After the first nest of coils is deployed at the level of the internal inguinal ring, a sclerosant can be injected on top of the coils. Advantage of this technique is the occlusion of the numerous small collateral channels. In the pediatric population, pain relief and catch-up testicular growth have been reported in 91–94 % of the patients [39, 40].

Pelvic Congestion Syndrome

Chronic pelvic pain is defined as noncyclical pain of at least 6 months duration. Pelvic pain affects approximately one third of all women accounting for 20 % of outpatient gynecologic appointments and numerous diagnostic tests including laparoscopy [41]. The etiology of chronic pelvic pain is varied including gynecologic, urologic, gastrointestinal, neurological, and psychosocial disorders. Pelvic congestion syndrome is characterized by the presence of ovarian and pelvic varicosities in the setting of chronic pelvic pain. Clinical manifestations of pelvic congestion syndrome include pelvic pain exacerbated by prolonged standing, dysmenorrhea, dyspareunia, postcoital ache, and hip pain [42, 43]. Pelvic venous congestion is typically seen in the multiparous women with its prevalence in the general population reaching approximately 10% as reported in the study of healthy female kidney donors undergoing screening renal angiography [44]. However, up to 40 % of asymptomatic women have incidental findings of pelvic varicosities [45, 46]. Hence, pelvic congestion syndrome remains as a diagnosis of exclusion requiring a multidisciplinary evaluation and discussion.

Pelvic congestion is characterized by ovarian venous reflux and dilatation associated with varicosities in the ovarian, uterine, rectal, vesical, vulvar, and/or upper thigh venous systems. The etiology of pelvic congestion is believed to be multifactorial involving mechanical and hormonal factors [47]. Anatomic differences in the left and right ovarian venous drainages, absence of valves in ovarian veins, and markedly increased pelvic venous capacity during late pregnancy are among the proposed mechanical factors leading to venous incompetence and development of pelvic varices. Venous compressions from nutcracker and May-Thurner syndromes are secondary causes of venous engorgement [10–12, 48]. Increased prevalence in multiparous and premenopausal women, presence of polycystic ovaries, and pain relief after administration of progestins or GnRH agonists have been reported, implicating the role of a hyperestrogenic state in pelvic congestion [45, 49, 50]. The cause of pain in pelvic congestion syndrome remains unclear, but pain receptor activation is felt to be the most likely possibility [47, 49].

Diagnosis and Imaging

Pelvic congestion syndrome remains a diagnosis of exclusion after thorough history and physical examination in a multidisciplinary framework. Venography is the "gold standard" because it allows evaluation of the venous reflux and extent of varices in the ovarian, uterine, rectal, vesical, vulvar, and even lower extremity venous systems. Pelvic supply to the varicose veins of the lower extremity has been reported in up to 25 % of women treated for varicose veins [50]. However, venography is not a practical approach due to its invasiveness. Ultrasonography and MRI have gained increasing popularity as initial diagnostic tools because they allow direct visualization of pelvic varices and, more importantly, assess for other pelvic disorders such as endometriosis, uterine myoma, and uterine adenomyosis.

Transabdominal and transvaginal sonographic examination is performed using 2–4 MHz convex and 5–9 MHz intracavitary transducers, respectively, with the patient in the supine position performing the Valsalva maneuver. Dilated ovarian vein with reflux, presence of pelvic varices with dilated cross-uterine arcuate veins, and polycystic changes of the ovary have been reported in pelvic congestion syndrome [51]. Park et al. reported the ovarian vein diameter of 7.9 mm in patients with pelvic congestion syndrome compared to 4.2 mm in the control group. The positive predictive value was 83 % when a cutoff value of the left ovarian diameter was set at 6 mm [52]. However, there is still no uniform

criterion on the size of the ovarian vein, and furthermore, some authors have argued that the ovarian diameter alone is not a reliable criterion in the absence of venous reflux [53].

MRI/MRV is the most preferred imaging modality of choice because it allows the anatomic assessment of the abdominopelvic structures without the radiation exposure of CT scan as well as the functional evaluation of the ovarian veins and pelvic varicosities [54]. Varicose veins appear as tortuous, dilated tubular structures around the ovaries and uterus on T1- and T2-weighted images. On dynamic imaging after intravenous administration of the contrast, reflux in the left ovarian vein can be sequentially imaged showing contrast passing through the parametrial and uterine venous plexus to the contralateral side (Fig. 28.4). Using dynamic imaging, diagnosis of nutcracker or May-Thurner syndrome can be reliably made as well.

Treatment

Hormonal Therapy

Daily oral administration of medroxyprogesterone has been shown to reduce pelvic pain when co-administered with psychotherapy. In a double-blinded RCT comparing GnRH agonists and medroxyprogesterone, Soyal et al. have reported efficacy of both hormonal therapies with GnRH leading to improvements in pain, depression, and sexual function. MPA is given orally 30 mg/day for 6 months, while goserelin is administered as an injection of 3.6 mg monthly for 6 month. Side effects of progestins include bloating and weight gain, while those of GnRH agonists are hot flashes, vaginal dryness, and mood changes [49, 55].

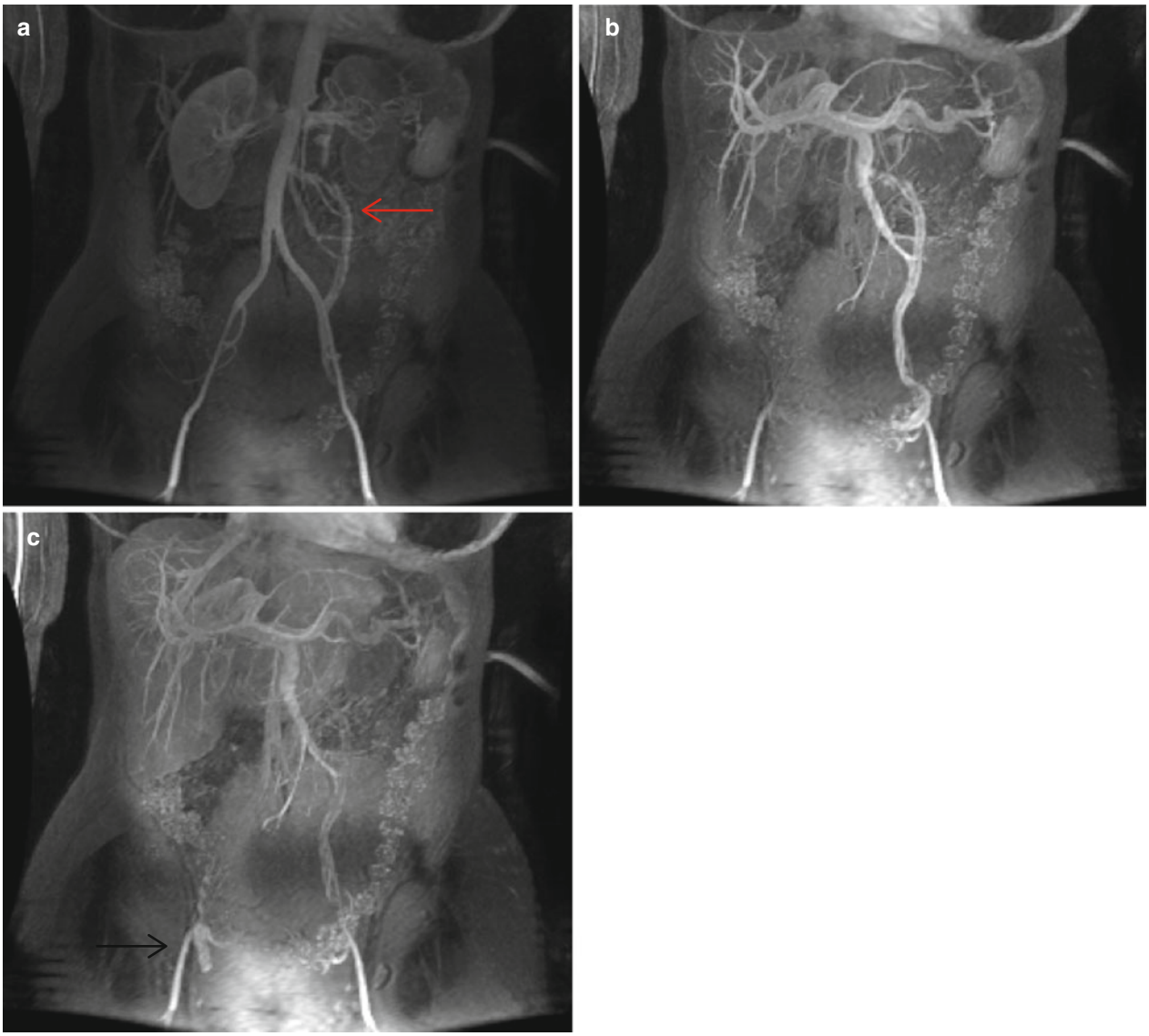

Fig. 28.4 Time-resolved imaging of contrast kinetics. (**a**) During the arterial phase there is enhancement of the left renal vein with reflux in the left ovarian vein (*red arrow*). (**b**, **c**) During the portal venous and delayed phases, there is enhancement of the parametrial varices and contralateral ovarian and internal iliac veins (*black arrow*)

Percutaneous Embolization

The fundamental techniques of percutaneous embolization of ovarian veins are similar to that of varicocele as described previously. Key differences in techniques include venography of the internal iliac veins after catheterization using a 5 F Cobra catheter in order to delineate the communication between the ovarian and internal iliac veins. Adequate delineation of these bridging veins is imperative prior to sclerosing the ovarian, parametrial, and uterine varices in order to avoid accidental reflux of sclerosant, typically sodium tetradecyl sulfate, into the common femoral veins. When necessary, embolization of the bridging vein between the ovarian and internal iliac veins is achieved using detachable coils or a vascular plug if a 5 F or larger catheter can be positioned in the communicating vein (Fig. 28.5). In a series of 56 patients undergoing percutaneous embolization of ovarian

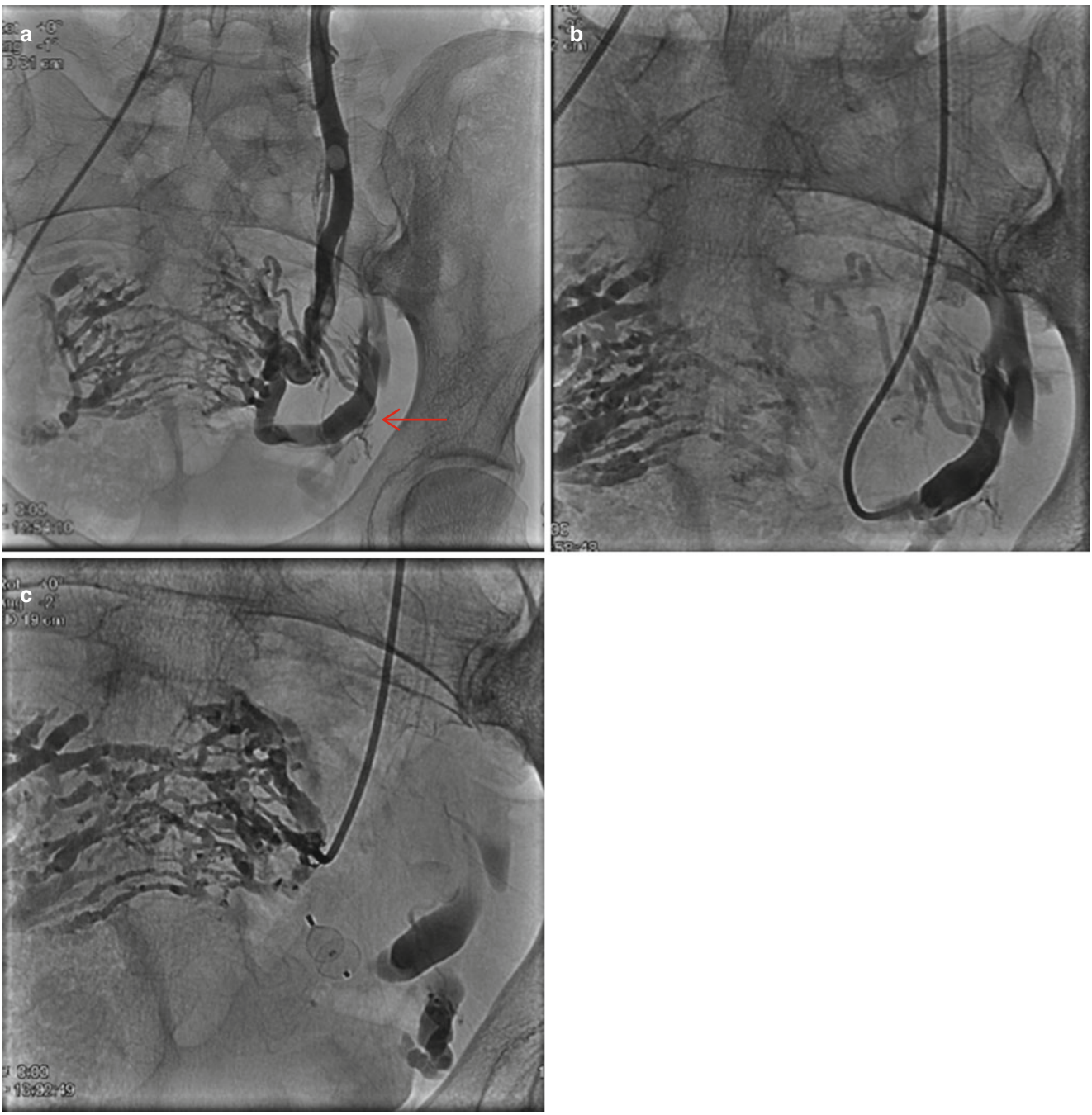

Fig. 28.5 A 34-year-old female with chronic pelvic pain. (**a**) The left ovarian venogram demonstrates dilated parametrial veins. Contrast crosses the midline and opacifies numerous dilated arcuate veins and contralateral parametrial varices. A large bridging vein is identified between the left ovarian and internal iliac veins (*arrow*). (**b**, **c**) The bridging vein is catheterized with a 5 French Cobra catheter, and an Amplatzer vascular plug is deployed, followed by sclerosis of the parametrial and arcuate veins

and internal iliac veins, Venbrux et al. reported a technical success rate of 100 % with 96 % of the patients experiencing significant improvement in pain. Similar results have been reported by Kwon et al. with technical success rate of 100 % with complete pain resolution in 8 % and significant pain relief in 75 % of the patients. In a series of 202 patients undergoing percutaneous embolization for pelvic congestion, 94 % of the patients experienced significant pain relief with 33.5 % reporting complete pain resolution. Overall complication rate was 3 % including coil migration to the pulmonary circulation and left renal vein [56–58].

References

1. Belloli G, D'Agostino S, Pesce C, Fantuz E. Varicocele in childhood and adolescence and other testicular anomalies: an epidemiological study. Pediatr Med Chir. 1993;15:159–62.
2. Levinger U, Gornish M, Gat Y, Bachar G. Is varicocele prevalence increasing with age? Andrologia. 2007;39:77–80.
3. Schlegel P, Goldstein M. Alternate indications for varicocele repair: non-obstructive azoospermia, pain, androgen deficiency and progressive testicular dysfunction. Fertil Steril. 2011;96:1288–93.
4. Pryor J, Howards S. Varicocele. Urol Clin North Am. 1987;14: 499–513.
5. Diamond D, et al. Relationship of varicocele grade and testicular hypotrophy to semen parameters in adolescents. J Urol. 2007;178:1584–8.
6. Gorelick J, Goldstein M. Loss of fertility in men with varicocele. Fertil Steril. 1993;59:613–6.
7. Sakamoto H, Ogawa Y, Yoshida H. Relationship between testicular volume and varicocele in patients with infertility. Urology. 2008;71:104–9.
8. Sigman M, Jarow J. Ipsilateral testicular hypotrophy is associated with decreased sperm counts in infertile men with varicoceles. J Urol. 1997;158:605–7.
9. Gat Y, Zukerman Z, Chakraborty J, Gornish M. Varicocele, hypoxia and male infertility. Fluid mechanics analysis of the impaired testicular venous drainage system. Hum Reprod. 2005;20:2614–9.
10. Wishahi M. Detailed anatomy of the internal spermatic vein and the ovarian vein. Human cadaver study and operative spermatic venography: clinical aspects. J Urol. 1991;145:780–4.
11. Reed N, et al. Left renal vein transposition for nutcracker syndrome. J Vasc Surg. 2009;49:386–94.
12. Wang X, et al. Results of endovascular treatment for patients with nutcracker syndrome. J Vasc Surg. 2012;56:142–8.
13. Auldist A. Wilm's tumor presenting as a varicocele. J Pediatr Surg. 1976;11:471–2.
14. Roy C, et al. Varicocele as the presenting sign of an abdominal mass. J Urol. 1989;141:597–9.
15. Agarwal A, et al. Role of oxidative stress in pathogenesis of varicocele and infertility. Urology. 2009;73:461–9.
16. Smit M, et al. Decreased sperm DNA fragmentation after surgical varicocelectomy is associated with increased pregnancy rate. J Urol. 2013;189:S146–50.
17. Thomson L, Zieschang J, Clark A. Oxidative deoxyribonucleic acid damage in sperm has a negative impact on clinical pregnancy rate in intrauterine insemination but not intracytoplasmic sperm injection cycles. Fertil Steril. 2011;96:843–7.
18. WHO. Manual for the standardized investigation, diagnosis and management of the infertile male. Cambridge: Cambridge University Press; 2000.
19. Dogra V, Gottlieb R, Oka M, Rubens D. Sonography of the scrotum. Radiology. 2003;227:18–36.
20. Woodward P, et al. Extratesticular scrotal masses: radiologic-pathologic correlation. Radiographics. 2003;23:215–40.
21. Pilatz A, et al. Color Doppler ultrasound imaging in varicoceles: is the venous diameter sufficient for predicting clinical and subclinical varicocele? World J Urol. 2011;29:645–50.
22. Petros J, Andriole G, Middleton W, Picus D. Correlation of testicular color Doppler ultrasonography, physical examination and venography in the detection of left varicoceles in men with infertility. J Urol. 1991;145:785–8.
23. Trum J, Gubler F, Laan R, van der Veen F. The value of palpation, varicoscreen contact thermography and color Doppler ultrasound in the diagnosis of varicocele. Hum Reprod. 1996;11:1232–5.
24. Diamond D, Gargollo P, Caldamone A. Current management principles for adolescent varicocele. Fertil Steril. 2011;96:1293–8.
25. Jarow J, et al. Best practice policies for male infertility. J Urol. 2002;167:2138–44.
26. The American Society of Reproductive Medicine. Report on varicocele and infertility. Fertil Steril. 2008;90:S247–9.
27. Jungwirth A, et al. European association of urology guidelines on male infertility: the 2012 update. Eur Urol. 2012;62:324–32.
28. Iacarino V, Venetucci P. Interventional radiology of male varicocele: current status. Cardiovasc Intervent Radiol. 2012;35:1263–80.
29. Chan P. Management options of varicoceles. Indian J Urol. 2011;27(1):65–73.
30. Cayan S, Shavakhabov S, Kadioglu A. Treatment of palpable varicocele in infertile men: a meta-analysis to define the best technique. J Androl. 2009;30:33–40.
31. Shlansky-Goldberg R, et al. Percutaneous varicocele embolization versus surgical ligation for the treatment of infertility: changes in seminal parameters and pregnancy outcomes. J Vasc Interv Radiol. 1997;8:759–67.
32. Sze D, et al. Persistent and recurrent postsurgical varicoceles: venographic anatomy and treatment with N-butyl cyanoacrylate embolization. J Vasc Interv Radiol. 2008;19:539–45.
33. Kim J, et al. Persistent or recurrent varicocele after failed varicocelectomy: Outcome in patients treated using percutaneous transcatheter embolization. Clin Radiol. 2012;67:359–65.
34. Rais-Bahrami S, et al. Angiographic of primary versus salvage varicoceles treated with selective gonadal vein embolization: an explanation for surgical treatment failure. J Endourol. 2012;26:556–60.
35. Maleux, et al. Prospective comparison of hydrogel-coated microcoils versus fibered platinum microcoils in the prophylactic embolization of the gastroduodenal artery before Yttrium-90 radioembolization. J Vasc Interv Radiol. 2013;24:797–803.
36. Nabi G, Asterlings S, Greene D, Marsh R. Percutaneous embolization of varicoceles: outcomes and correlation of semen improvement with pregnancy. Urology. 2004;63:359–63.
37. Bechara C, et al. Percutaneous treatment of varicocele with microcoil embolization: comparison of treatment outcome with laparoscopic varicocelectomy. Vascular. 2009;17 Suppl 3:S129–36.
38. Gandini R, et al. Male varicocele: transcatheter foam sclerotherapy with sodium tetradecyl sulfate – outcome in 244 patients. Radiology. 2008;246:612–8.
39. Reiner E, et al. Initial experience with 3% sodium tetradecyl sulfate foam and fibered coils for management of adolescent varicocele. J Vasc Interv Radiol. 2008;19:207–10.
40. Storm D, Hogan M, Jayanthi V. Initial experience with percutaneous selective embolization: a truly minimally invasive treatment of the adolescent varicocele with no risk of hydrocele development. J Pediatr Urol. 2010;6:567–71.
41. Reiter RC. Chronic pelvic pain. Clin Obstet Gynecol. 1990;33:117–8.
42. Beard RW, Geginald PW, Wardworth J. Clinical features of women with chronic lower abdominal pain and pelvic congestion. Br J Obstet Gynaecol. 1988;95:153–61.

43. Huang C, Shelkey J. Chronic hip pain as a presenting symptom in pelvic congestion syndrome. J Vasc Interv Radiol. 2013;24: 753–5.
44. Belenky A, Bartal G, Atar E, et al. Ovarian varices in healthy female kidney donors: incidence, morbidity, and clinical outcome. AJR Am J Roentgenol. 2002;179:625–7.
45. Rozenblit AM, Ricci ZJ, Tuvia J, Amis ES. Incompetent and dilated ovarian veins: a common CT finding in asymptomatic parous women. AJR Am J Roentgenol. 2001;176:119–22.
46. Hiromura T, Nishioka T, Nishioka S, et al. Reflux in the left ovarian vein: analysis of MDCT findings in asymptomatic women. AJR Am J Roentgenol. 2004;183:1411–5.
47. Phillips D, Deipolyi AR, Hesketh RL, et al. Pelvic congestion syndrome: etiology of pain, diagnosis, and clinical management. J Vasc Interv Radiol. 2014;25:725–33.
48. Reginald P, Beard R, Kooner J. Intravenous dihydroergotamine to relieve pelvic congestion with pain in young women. Lancet. 1987;2:351–3.
49. Soysal ME, et al. A randomized controlled trial of goserelin and medroxyprogesterone acetate in the treatment of pelvic congestion. Hum Reprod. 2001;16:931–9.
50. Whiteley A, et al. Pelvic venous reflux is a major contributory cause of recurrent varicose veins in more than a quarter of women. J Vasc Surg: Venous and Lym Dis. 2014;2:411–5.
51. Ignacio E, et al. Pelvic congestion syndrome: diagnosis and treatment. Semin Intervent Radiol. 2008;25(4):361–8.
52. Park SJ, Lim JW, Ko YT, et al. Diagnosis of pelvic congestion syndrome using transabdominal and transvaginal sonography. AJR Am J Roentgenol. 2004;182:683–8.
53. Dos Santos SJ, Holdstock JM, Harrison CC, et al. Ovarian vein diameter cannot be used as an indicator of ovarian venous reflux. Eur J Vasc Endovasc Surg. 2014;49:1–5.
54. Leiber L, et al. MRI and venographic aspects of pelvic venous insufficiency. Diagn Interv Imaging. 2014;95:1091–102.
55. Tu F, Hahn D, Steege J. Pelvic congestion syndrome-associated pelvic pain: a systematic review of diagnosis and management. Obstet Gynecol Surv. 2010;65:332–40.
56. Venbrux A, et al. Pelvic congestion syndrome (pelvic venous incompetence): impact of ovarian and internal iliac vein embolotherapy on menstrual cycle and chronic pelvic pain. J Vasc Interv Radiol. 2002;13:171–8.
57. Kwon S, et al. Transcatheter ovarian vein embolization using coils for the treatment of pelvic congestion syndrome. Cardiovasc Intervent Radiol. 2007;30:655–61.
58. Laborda A, et al. Endovascular treatment of pelvic congestion syndrome: visual analog scale (VAS) long-term follow-up clinical evaluation in 202 patients. Cardiovasc Intervent Radiol. 2013;36:1006–14.

Retroperitoneal Biopsy: Indications and Imaging Approach

29

Elliot Levy

The contents of the retroperitoneum are defined by the boundaries of the potential space behind the posterior abdominal parietal peritoneum and the fascia investing the lumbar musculature. Primary retroperitoneal neoplasms are a rare group of tumors which do not arise from a specific organ but rather originate from tissues or rests of embryonic cells which exist in the retroperitoneum [1]. The most common variety is sarcoma, which accounts for up to 90 % of lesions after lymphoma is excluded. Liposarcomas and leiomyosarcomas are the next most common types, accounting for up to 15 % of tumors. The average age of presentation is during the fifth to seventh decades, and the tumors are often large in size at diagnosis due to the paucity of symptoms associated with growth of retroperitoneal tumors in general. Excluding lymphomas, the most frequent primary retroperitoneal malignancies in decreasing order include liposarcoma, MFH, leiomyosarcoma, rhabdomyosarcoma, and malignant nerve sheath tumors [2]. Both Hodgkin's and non-Hodgkin's lymphoma may also occur in the retroperitoneum. Epithelial tumors may rise from the kidney, adrenal gland, and pancreas, and metastatic disease from germ cell tumors, primary carcinomas, or melanomas can also occur. Benign tumors may have neurogenic origins as well (schwannomas, neurofibroma, paraganglioma) [3].

Retroperitoneal tumors are diagnosed at physical examination if they are particularly large, or commonly by imaging when the patient presents with insidious onset of non-localizing symptoms such as lower extremity or genital edema, weight loss, anorexia, urological symptoms, or back pain.

E. Levy, MD
Interventional Radiology Section, Radiology and Imaging Sciences Department, National Institutes of Health Clinical Center, Bethesda, MD, USA
e-mail: levyeb@cc.nih.gov

Imaging of Retroperitoneal Tumors

Precise localization and compartmentalization of large masses can be difficult as the size the mass obscures its focus of origin. Displacement of anatomic structures may help to localize the origin. Cross-sectional imaging including MRI and CT provides a complete overview of the peritoneal cavity and retroperitoneal spaces. MRI imaging can exquisitely "characterize" retroperitoneal masses [4], although no specific tumor histology features unique or diagnostic imaging characteristics by virtue of shared tissue components. At the same time, these common tumor tissue components may provide important clues to the origin of large retroperitoneal tumors, including fat signal associated with lipoma, liposarcoma, and teratoma, and myxoid stromal seeding in neurogenic tumors as well as myxoid liposarcomas and malignant fibrous histiocytoma.

A concise review of the imaging of retroperitoneal masses is provided by Rajiah et al. [5]. Additional radiographic signs which may aid in the identification of mass origin include beak sign, embedded organ sign, and embedded organ sign [2]. Nishino et al. [2] also summarize patterns of tumor spread around and between normal structures which may provide clues to retroperitoneal tumor origins, e.g., tumor extension along and around normal structures as a characteristic of tumors of sympathetic ganglia origin [6]. Viable tumor often shows some degree of enhancement after the administration of intravenous contrast material, while necrotic material shows reduced density, hyperintensity on T2W imaging, and absence of contrast enhancement. Fat-containing tumors show high signal intensity on T1-weighted MR imaging, as well as corresponding loss of signal on fat-suppressed image sequences. Myxoid stroma characteristically appears hyperintense on T2W MR imaging and may show delayed enhancement after gadolinium injection [6]. Teratomas may feature fluid attenuation, fat-fluid levels, and calcifications [7]. Neurogenic lesions such as schwannomas typically appear hypointense on T1W and T2W noncontrast imaging and exhibit heterogeneous patterns of contrast

A.R. Rastinehad, D.N. Siegel (eds.), *Interventional Urology*, DOI 10.1007/978-3-319-23464-9_29

enhancement [5]. Malignant fibrous histiocytoma displays heterogeneous signal characteristics on all MR pulse sequences [4].

Benign retroperitoneal masses include lymphangioma, lipoma, myelolipoma, angiomyolipoma, lipoblastoma, hibernoma, nerve sheath tumors, and paraganglioma. Lymphangiomas have a unilocular or multilocular cystic appearance and are diagnosed in infancy, while lipoblastomas typically present in childhood or teenage years. Hibernoma is a rare tumor composed of fetal or brown fat which is most frequently diagnosed in the fourth decade of life. Lipomas rarely occur in the retroperitoneum. These tumors typically grow rather slowly and present as large retroperitoneal masses whose radiographic appearance is characterized by their fat content. These tumors must be distinguished from pelvic lipomatosis as well as liposarcoma; even pathological diagnosis of lipoma should be suspected as under sampled liposarcoma [8].

Myelolipoma is also characterized by an abundance of adipocytes but more commonly arises from the adrenal glands. Extra-adrenal examples are exceedingly uncommon and may be misinterpreted at biopsy [9]. Extrarenal angiomyolipoma is an extremely rare tumor which typically presents as incidental findings during investigations for other purposes, or with abdominal pain and hemorrhagic shock [10].

Paragangliomas, the extra-adrenal equivalent of pheochromocytomas which arise from residual adrenal medullary chromaffin cells, are most commonly found in proximity to the aorta and sympathetic ganglia. Malignant paragangliomas may be difficult to distinguish from benign lesions, with malignancy established by the recognition of local invasion or metastases.

Peripheral nerve sheath tumors comprise another group of benign retroperitoneal neoplasms. The most common peripheral nerve tumor is the schwannoma, which is typically discovered as a large, well-circumscribed mass featuring cystic degeneration.

Lymphoma is the most common form of retroperitoneal malignancy. Non-Hodgkin's lymphoma tends to involve a larger variety of lymph node groups than Hodgkin's lymphoma. Malignant lymph nodes may show moderate homogeneous to patchy inhomogeneous enhancement postgadolinium administration. In contrast to metastatic lymphadenopathy, primary lymphoma usually does not demonstrate nodal necrosis. [Retroperitoneal fibrosis after lymphoma therapy may be difficult to distinguish from but fibrosis most likely has low T2W signal]. Retroperitoneal lymphadenopathy is typically seen in other nonneoplastic conditions such as mycobacterium avium-intracellulare infection (MAI) or Castleman's disease (giant lymph node hyperplasia).

Liposarcoma is the most common malignant primary retroperitoneal neoplasm. Although difficult to distinguish from benign lipoma, the presence of proportionally larger nonadipose components and greater enhancement of septations may be more suggestive of malignancy.

The retroperitoneum is the second most common site for malignant fibrous histiocytoma, the most common type of adult soft tissue sarcoma [11]. This tumor is frequently associated with invasion of adjacent organs, together which large size conveys a poorer prognosis. Calcification has been identified in 7–20 % of lesions [5]. Solid lesions often demonstrate a peripheral nodular enhancement pattern or "pseudocapsule" on precontrast MRI imaging [4].

Germ cell tumors uncommonly originate in the retroperitoneum and are more commonly observed in men [5]. Rajiah et al. [5] further observe that extragonadal germ cell tumors are often observed in the midline between the T6 and S2 vertebrae and that a mass in this location is more suggestive of a primary extragonadal germ cell tumor than metastasis.

Biopsy Indications and Image-Guided Approach

Diagnosis of retroperitoneal tumors often requires tissue sampling; Strauss et al. [3] propose that for patients with (1) retroperitoneal tumors for which diagnosis is uncertain from the radiological appearance, (2) histologies for which neoadjuvant therapy may be appropriate as induction therapy, and preoperative biopsy is "mandatory." Surgical tissue sampling is invasive and associated with fixed morbidity [12]. In the past, fine needle aspirations were recommended primarily to reduce the risk of hemorrhage or injury to adjacent organs, but the safety and efficacy of cutting needles has been firmly established [13]. Image-guided percutaneous biopsy has been shown to provide satisfactory yield with reduced morbidity and mortality [14]. Tissue sampling is also important to characterize retroperitoneal lesions for therapy planning.

Biopsy needle selection has been based primarily upon efficacy of tissue sampling for lymphoma. Knelson et al. [15] reviewed CT-guided needle biopsy for retroperitoneal lesions, and both the diagnosis and the histological subtyping of lymphoma could be determined in 10 of 11 cases using the 14-gauge Tru-Cut needle, but it was not possible to make the specific diagnosis in any of the lymphoma patients using the 20-gauge Chiba needle. Agid et al. [16] reported that CT-guided core needle biopsies were sufficient to establish a diagnosis in 83 % of the patients with lymphoproliferative disorders and they suggested that it should be used as the first step in the diagnosis of lymphomas. Stattaus et al. [17] reported that the correct lymphoma subtype could be revealed for retroperitoneal masses in 87 % of the patients by using a 16- or 18-gauge core biopsy system with the coaxial technique under CT guidance. In the study of Tomozawa et al. [18], 43 (96 %) of 45 patients

had a defined diagnosis with the correct histological subtype determined with an 18-gauge core needle, and subsequent treatment was performed on the basis of the biopsy results. Although needle size will be best determined by suspected histology as well as local expertise, most core needle biopsies performed with 18-guage needles will provide diagnostic material.

Imaging guidance is often provided by static CT imaging, CT fluoroscopy, cone beam CT, or ultrasound, although the specific guidance modality is often dictated by operator preference. The simplest and preferred biopsy path trajectory is often a straight line to the tumor target from the skin entry site in a single axial plane. Off-plane approaches are possible and often aided by combinations of imaging systems and biopsy planning software packages. UItrasound, CT fluoroscopy, and cone beam CT packages which link CT coordinates to the active fluoroscopic image can provide real-time visualization of the biopsy needle in the trajectory to the target lesion. These advantages may shorten procedure time, reduce nontarget punctures, and reduce radiation exposure [19].

Ultrasound guidance enjoys the advantage of avoiding patient exposure to ionizing radiation. Ultrasound images of the retroperitoneum are generated based upon the differential ability of tissue to reflect or transmit sound of frequency between 3.5 and 7 MHz in the clinical realm. Ultrasound permits the operator to monitor needle placement in real-time fashion without ionizing radiation as metallic needles are sonoreflective. In addition, sonography with color Doppler technology can identify significant intra-tumoral vascularity to be avoided by needle puncture. Deep abdominal and pelvic targets are best imaged with a curved array 3.5–5 MHz probe, while more superficial targets can be imaged with improved resolution with 5 MHz and greater linear array probes. Needle guidance can be accomplished "freehand" or with the use of specifically designed needle guides which attach to the transducer. Ultrasound delineation of retroperitoneal masses may be obscured by overlying bowel gas, necessitating placing the patient in a lateral decubitus or prone position for visualization. Yarram et al. observed an ultrasound-guided pelvic mass biopsy success rate of 95.4 % compared with 84.6 % for CT guidance [20].

A pre-procedure CT or MRI scan can provide a basis for biopsy path and target planning. In general, the planned needle biopsy path should exclude the viscera, the pleura, and the visible blood vessels. Other structures to be avoided which are inconstantly imaged or not visualized include the ureters and sciatic and genitofemoral nerves. In some instances, target selection must be refined toward viable regions of tumors as opposed to more necrotic regions. Tumor viability is indirectly evidenced by increased soft tissue density comparable to the muscle as well as observed enhancement following the administration of vascular contrast material (CT or MRI). CT showing low-density tissue in the central portion of the tumor may be related to liquifactive or hemorrhagic necrosis and should be avoided during tissue sampling. Leiomyosarcomas in particular may demonstrate significant zones of necrosis [21]. Hypervascularity may be recognized according to the presence of adjacent discrete blood vessels, increased density following vascular contrast administration (CT), or by noting increased blood flow within portions of the lesion according to color Doppler sonography. Characteristic tissue components not only aid in radiographic diagnosis but also may inform biopsy planning; liposarcomas will have varying amounts of fat, with high-grade liposarcomas having the least amount. Tissue sampling of suspected liposarcoma from areas of increased tissue density may increase diagnostic yield. Myxoid tissue has well-recognized specific MR imaging characteristics [6]. Neurogenic tumors more typically contain myxoid tissue, although liposarcomas and myxoid malignant fibrous histiocytoma may also exhibit myxoid tissue [5].

MRI has been employed both as a diagnostic imaging and an imaging guidance modality. Previous reports have predominantly documented the value of MRI guidance with biopsies of hepatic dome masses, masses visible only at MRI, or in instances where ultrasound is not feasible [22]. Kariniemi et al. (2005) [23] demonstrated high sensitivity and specificity ranging from 71 to 100 % of both aspiration and core biopsies guided by low-field MRI in 31 consecutive patients with liver, lymph node, retroperitoneal, adrenal, and splenic masses for whom ultrasound-guided procedures were not feasible. However, optical tracking was used in this study to determine the skin entrance site as well as the puncture route. MRI-guided procedures require the use of MRI-compatible (nonferromagnetic) needles in order to avoid magnetic susceptibility artifacts.

Percutaneous image-guided biopsy for diagnosis and subtyping may be occasionally be limited by the presence of fibrosis, necrosis, and limited ability to specifically target viable tumor cells, but PET imaging have the capability to further refine biopsy target selection based upon tissue viability and exclusion of necrotic tumor. Kitajima et al. (2013) [24] summarize the ^{18}F-FDG-PET/CT findings of patients with retroperitoneal tumors. Absence of FDG uptake may be seen with necrosis, and corresponding areas should be avoided for tissue sampling. With large and/or previously treated lesions, PET scans can identify portions of tumor which are viable and suitable for sampling. Specifically registered PET images can be used to target lesions inconspicuous at nonenhanced CT or malignant portions of lesions which also contain benign tissue such as fat [25]. Care must be exercised, as activity in a suspected lesion shows SUV close to the cutoff value, or alternatively when a lesion shows FDG uptake due to posttreatment inflammation [26].

Additional Imaging Considerations

Image Registration for Biopsy Guidance

When conventional CT is used for biopsy guidance, images are most frequently obtained without administration of intravenous contrast. In some instances, viable or otherwise suitable tumor tissue for biopsy may not be apparent on the nonenhanced CT images. In these instances, nonenhanced images can be manually or automatically registered with imaging obtained with an alternative modality, permitting image-guided biopsy based upon the intra-procedural nonenhanced CT images. Contrast-enhanced CT, MRI, as well as PET-CT can be registered in this fashion and the combined images displayed in such a manner which guides biopsy needle placement.

Lesions which are out of the convenient transaxial plane with reference to the skin entrance site may also be approached for biopsy using image registration with magnetically tracked instruments [27]. This approach relies on the successful and accurate registration of the imaging (often CT) Cartesian coordinate system with a simultaneous magnetic reference field. With this approach, the magnetically tracked biopsy needle position can be displayed using the registered CT dataset. Real-time needle position information is available to the operator without CT or fluoroscopic imaging until final needle position is verified.

Alternatively, an ultrasound probe can be electromagnetically tracked after registration of the magnetic field positional coordinates with a coincidentally or previously obtained CT dataset. In this fashion, although the needle may be visualized with ultrasound, the needle position can be displayed in multiplanar format determined by the tracked ultrasound probe. Under optimal conditions, the severity of the registration error between imaging and magnetic coordinates should be less than 3 mm.

Developments in flat panel detector technology have permitted implementation of cone beam CT mounted on imaging suite fluoroscopic C-arm to deliver first computed rotational 3D digital subtraction angiography and subsequently cone beam computed tomographic imaging (CBCT). Orth et al. (2008) [28] review the technical innovations featured in current clinical CBCT systems. CBCT systems allow automatic registration of three-dimensional CT data with live fluoroscopic imaging, while a software package displays a biopsy trajectory planned with the 3D dataset to be superimposed upon the live fluoroscopic images. Furthermore, pre-procedure contrast-enhanced conventional CT or MRI as well as PET-CT images can be registered with intra-procedural cone beam CT to further refine a biopsy target according to enhancement pattern, FDG-PET avidity, or MRI appearance observed prior to the planned procedure. Cone beam CT systems potentially reduce the amount of contrast material as well as radiation required to complete image-guided biopsies.

Cytogenetics

Molecular and genetic profiling of tumors is likely to play a significantly increased role in the optimization of treatment of tumors in individual patients. Identification of specific mutations and improvements in tissue arrays will contribute to improve more specific diagnoses as well as development of specifically targeted therapeutic agents. Conyers et al. summarized the cytogenetics of liposarcomas [29]. In the past, the pathological differentiation of a benign lipoma from a well-differentiated liposarcoma has been difficult. The oncogene MDM2 is seen in 100 % of well-differentiated and dedifferentiated liposarcomas, for example, and amplification of CDK4 has been described in 90 % of liposarcomas as well. In addition to differentiating lesions based upon biopsy histopathology, these markers may have prognostic value and may predict the risk of transformation.

The role of percutaneous biopsy for the procurement of samples for molecular or genetic profiling in addition to diagnostic histopathology has not been defined. The ability to perform molecular or genetic profiling on small caliber biopsy samples is evolving as advances in tissue array technology and next-generation sequencing are introduced into clinical practice. The efficacy of percutaneous needle biopsy for the molecular profiling of non-small cell lung cancer, for example, has been demonstrated [30]. It seems likely that specimens adequate for molecular profiling could be efficiently and safely obtained percutaneously from retroperitoneal tumors with imaging guidance.

Tips and Tricks

Patient Preparation Normal status of the retroperitoneal biopsy patient candidate's coagulation parameters should be confirmed prior to biopsy attempt. The Society of Vascular and Interventional Radiology Standards of Practice Committee has designated retroperitoneal biopsies (excluding renal biopsies) as Category 2 procedures with moderate risk of bleeding [31]. Correction of INR to <1.5 and platelet count >50,000/μL is recommended according to these practice standards.

Although percutaneous core needle biopsy of the retroperitoneum is not often associated with significant pain, individual patients may require conscious sedation for relief of anxiety related to anticipation of pain. Patients receiving

conscious sedation should observe an overnight fast prior the procedure. Coagulopathy and severe thrombocytopenia are relative contraindications for percutaneous biopsy, and coagulation parameters should be confirmed and corrected prior to planned biopsy.

Coaxial approach: Use of a coaxial technique allows for diagnostic aspirations to confirm cellularity and cell viability prior to obtaining core biopsies. A coaxial approach for suspected lymphoma also facilitates sampling for flow cytometry studies and core specimens using a single puncture. De Bazelaire et al. [32] described that a coaxial introducer provided with an additional blunt tip stylet allows safe access to difficult-to-reach lymph nodes in the chest, abdomen, and pelvis under CT control.

Biopsy path planning: Biopsies of lesions adjacent to the aorta and vena cava are most often approached posteriorly with the patient prone or in lateral decubitus position in order to avoid bowel loops, large vessels, and viscera such as the pancreas. Large masses can often be approached using an anterolateral trajectory in the supine position. A safe trajectory can often be facilitated by a change in the patient's position; a bowel loop can be displaced medially or laterally out of a planned needle trajectory by rotating the patient into a lateral decubitus position, for example.

Additional measures to successfully biopsy lesions with limited access include hydrodissection, blunt needle technique, and alternative transgluteal and transosseous approaches in addition to the anterior extraperitoneal approach through the iliopsoas muscle. These approaches are systematically reviewed by Gupta et al. [33]. Hydrodissection with sterile physiological saline may displace an interposed bowel loop, where displacement is by as little as 1 cm which might otherwise facilitate a planned approach. Alternatively, small mesenteric blood vessels can be displaced and biopsy accomplished using a coaxial approach with a blunt tip needle such as the Hawkins ™ blunt needle access system. Alternatively, infrarenal or perivascular lesions which may appear obscured for biopsy purposes in some instances can be accessed using a transvenous approach as described by Maleux et al. [34].

Lesions or lymph nodes in the internal or external iliac chain may be obscured by overlying bowel loops and adjacent vessels. In these cases, a transmuscular biopsy trajectory through the iliopsoas muscle may avoid bowel injury or injury to the external iliac vessels. The transgluteal approach is particularly advantageous for presacral or pararectal masses, although care must be taken to avoid injury to the sciatic nerve by planning the needle trajectory adjacent to the sacrum rather than the posteromedial margin of the iliac bone. In rare instances, access to a biopsy target lesion can be obtained using a transosseous approach through the iliac bone [33].

References

1. Rodríguez JAV, José M, Moreno D, Navarro HP, Carrión P. Primary retroperitoneal tumors: review of our 10-year case series. Arch Esp Urol. 2010;63(1):13–22.
2. Nishino M, Hayakawa K, Minami M, Yamamoto A, Ueda H, Takasu K. Primary retroperitoneal neoplasms: CT and MR imaging findings with anatomic and pathologic diagnostic clues. Radiographics. 2003;23(1):45–57. doi:10.1148/rg.231025037.
3. Strauss DC, Hayes AJ, Thomas JM. Retroperitoneal tumours: review of management. Ann R Coll Surg Engl. 2011;93:275–80. doi:10.1308/003588411X571944.
4. Elsayes KM, Staveteig PT, Narra VR, Chen Z-M, Moustafa YL, Brown J. Retroperitoneal masses: magnetic resonance imaging findings with pathologic correlation. Curr Probl Diagn Radiol. 2007;36(June):97–106. doi:10.1067/j.cpradiol.2006.12.003.
5. Rajiah P, Sinha R, Cuevas C, Dubinsky TJ, Bush WH, Kolokythas O. Imaging of uncommon retroperitoneal masses. Radiographics. 2011;31:949–76. doi:10.1148/rg.314095132.
6. Nishimura H, Zhang Y, Ohkuma K, Uchida M, Hayabuchi N, Sun S. MR imaging of soft-tissue masses of the extraperitoneal spaces. Radiographics. 2001;21:1141–54. doi:10.1148/radiographics.21.5.g01se141141.
7. Lee J, Hiken J, Semelka S. Retroperitoneum. In Lee J, Sagel S, Stanley R, Heiken J editors, Computed tomography with MRI correlation. 3rd ed. 1996. p. 1023–1086.
8. Craig WD, Fanburg-Smith JC, Henry LR, Guerrero R, Barton JH. Fat-containing lesions of the retroperitoneum: radiologic-pathologic correlation. Radiographics. 2009;29(1):261–90. doi:10.1148/rg.291085203.
9. Butori N, Guy F, Collin F, Benet C, Causeret S, Isambert N. Retroperitoneal extra-adrenal myelolipoma: appearance in CT and MRI. Diagn Interv Imaging. 2012;93(3):204–7. doi:10.1016/j.diii.2011.12.010.
10. Tsutsumi M, Yamauchi A, Tsukamoto S, Ishikawa S. A case of angiomyolipoma presenting as a huge retroperitoneal mass. Int J Urol : Off J Jpn Urol Assoc. 2001;8(8): 470–1. Retrieved from http://www.ncbi.nlm.nih.gov/pubmed/11555018.
11. Ahlén J, Enberg U, Larsson C, Larsson O, Frisk T, Brosjö O, Rosen A, Bäckdahl M. Malignant fibrous histiocytoma, aggressive fibromatosis and benign fibrous tumors express mRNA for the metalloproteinase inducer EMMPRIN and the metalloproteinases MMP-2 and MT1-MMP. Sarcoma. 2001;5(3):143–9. doi:10.1080/13577140120048601.
12. Hopper KD. Percutaneous, radiographically guided biopsy: a history. Radiology. 1995;196(2):329–33. doi:10.1148/radiology.196.2.7617841.
13. Nolsøe C, Nielsen L, Torp-Pedersen S, Holm HH. Major complications and deaths due to interventional ultrasonography: a review of 8000 cases. J Clin Ultrasound : JCU; 1990;18(3):179–84. Retrieved from http://www.ncbi.nlm.nih.gov/pubmed/2155937.
14. Moulton JS, Moore PT. Coaxial percutaneous biopsy technique with automated biopsy devices: value in improving accuracy and negative predictive value. Radiology. 1993;186(2):515–22. doi:10.1148/radiology.186.2.8421758.
15. Knelson M, Haaga J, Lazarus H, Ghosh C, Abdul-Karim F, Sorenson K. (1989). Computed tomography-guided retroperitoneal biopsies. J Clin Oncol : Off J Am Soc Clin Oncol. 7(8):1169–73. Retrieved from http://www.ncbi.nlm.nih.gov/pubmed/2754451.
16. Agid R, Sklair-Levy M, Bloom AI, Lieberman S, Polliack A, Ben-Yehuda D, Sherman Y, Libson E (2003). CT-guided biopsy with cutting-edge needle for the diagnosis of malignant lymphoma: experience of 267 biopsies. Clin Radiol. 58(2):143–7. Retrieved from http://www.ncbi.nlm.nih.gov/pubmed/12623044.

17. Stattaus J, Kalkmann J, Kuehl H, Metz K, Metz KA, Nowrousian MR, Forsting M, Ladd SC. Diagnostic yield of computed tomography-guided coaxial core biopsy of undetermined masses in the free retroperitoneal space: single-center experience. Cardiovasc Interv Radiol. 2008;31:919–25. doi:10.1007/s00270-008-9317-5.
18. Tomozawa Y, Inaba Y, Yamaura H, Sato Y, Kato M, Kanamoto T, Sakane M. Clinical value of CT-guided needle biopsy for retroperitoneal lesions. Korean J Radiol. 2011;12(3):351–7. doi:10.3348/kjr.2011.12.3.351.
19. Braak SJ, van Strijen MJL, van Es HW, Nievelstein RAJ, van Heesewijk JPM. Effective dose during needle interventions: cone-beam CT guidance compared with conventional CT guidance. J Vasc Interv Radiol: JVIR. 2011;22(4):455–61. doi:10.1016/j.jvir.2011.02.011.
20. Yarram SG, Nghiem HV, Higgins E, Fox G, Nan B, Francis IR. Evaluation of imaging-guided core biopsy of pelvic masses. AJR Am J Roentgenol. 2007;188(5):1208–11. doi:10.2214/AJR.05.1393.
21. Shah J, Kirshenbaum M, Shah K. CT characteristics of primary retroperitoneal tumors and the importance of differentiation from secondary retroperitoneal tumors. Curr Probl Diagn Radiol. 2008;31(17):1–5.
22. Lu DS, Silverman SG, Raman SS. MR-guided therapy. Applications in the abdomen. Magn Reson Imaging Clin North Am. 1999;7(2):337–48. Retrieved from http://www.ncbi.nlm.nih.gov/pubmed/10382165.
23. Kariniemi J, Blanco Sequeiros R, Ojala R, Tervonen O. MRI-guided abdominal biopsy in a 0.23-T open-configuration MRI system. Eur Radiol. 2005;15:1256–62. doi:10.1007/s00330-004-2566-z.
24. Kitajima K, Kono A, Konishi J, Suenaga Y, Takahashi S, Sugimura K. ^{18}F-FDG-PET/CT findings of retroperitoneal tumors: a pictorial essay. Jpn J Radiol. 2013;31:301–9. doi:10.1007/s11604-013-0192-x.
25. Tatli S, Gerbaudo VH, Mamede M, Tuncali K, Shyn PB, Silverman SG. Abdominal masses sampled at PET/CT-guided percutaneous biopsy: initial experience with registration of prior PET/CT images. Radiology. 2010;256(1):305–11. doi:10.1148/radiol.10090931.
26. Kobayashi K, Bhargava P, Raja S, Nasseri F, Al-Balas HA, Smith DD, George SP, Vij MS. Image-guided biopsy: what the interventional radiologist needs to know about PET/CT. Radiographics. 2012;32:1483–501. doi:10.1148/rg.325115159.
27. Wallace MJ, Gupta S, Hicks ME. Out-of-plane computed-tomography-guided biopsy using a magnetic-field-based navigation system. Cardiovasc interv Radiol. 2006;29(November 2005):108–13. doi:10.1007/s00270-005-0041-0.
28. Orth RC, Wallace MJ, Kuo MD. C-arm cone-beam CT: general principles and technical considerations for use in interventional radiology. J Vasc Interv Radiol: JVIR. 2008;19(4):814–20. doi:10.1016/j.jvir.2008.02.002.
29. Conyers R, Young S, Thomas DM. Liposarcoma: molecular genetics and therapeutics. Sarcoma. 2011;2011:483154. doi:10.1155/2011/483154.
30. Albanna AS, Kasymjanova G, Robitaille C, Cohen V, Brandao G, Pepe C, Small D, Agulnik J. Comparison of the yield of different diagnostic procedures for cellular differentiation and genetic profiling of non-small-cell lung cancer. J Thorac Oncol: Off Publ Int Assoc Study of Lung Cancer. 2014;9(8):1120–5. doi:10.1097/JTO.0000000000000230.
31. Patel IJ, Davidson JC, Nikolic B, Salazar GM, Schwartzberg MS, Walker TG, Saad WA. Consensus guidelines for periprocedural management of coagulation status and hemostasis risk in percutaneous image-guided interventions. J Vasc Interv Radiol. 2012;23(6):727–36. doi:10.1016/j.jvir.2012.02.012.
32. De Bazelaire C, Farges C, Mathieu O, Zagdanski AM, Bourrier P, Frija J, De Kerviler E. Blunt-tip coaxial introducer: a revisited tool for difficult CT-guided biopsy in the chest and abdomen. Am J Roentgenol. 2009;193(August):144–8. doi:10.2214/AJR.08.2125.
33. Gupta S, Nguyen HL, Morello Jr FA, Ahrar K, Wallace MJ, Madoff DC, Murthy R, Hicks ME. Various approaches for CT-guided percutaneous biopsy of deep pelvic lesions: anatomic and technical considerations. Radiographics. 2004;24:175–89. doi:10.1148/rg.241035063.
34. Maleux G, Hertogh GD, Lavens M, Oyen R. Transvenous biopsy of retroperitoneal tumoral masses : value of cone-beam CT guidance. J Vasc Interv Radiol. 1830;25(11):1830–2. doi:10.1016/j.jvir.2014.07.006.

Index

A.R. Rastinehad, D.N. Siegel (eds.), *Interventional Urology*, DOI 10.1007/978-3-319-23464-9